GEORISK 2011

Geotechnical Risk Assessment & Management

Geotechnical Special Publication No. 224

ASCE

Edited by
C. Hsein Juang, Kok Kwang Phoon,
Anand J. Puppala, Russell A. Green,
and Gordon A. Fenton

G-I GEO-INSTITUTE ASCE

GEOTECHNICAL SPECIAL PUBLICATION NO. 224

GEORISK 2011

GEOTECHNICAL RISK ASSESSMENT AND MANAGEMENT

PROCEEDINGS OF GEORISK 2011

June 26–28, 2011
Atlanta, Georgia

SPONSORED BY
Geo-Institute of the American Society of Civil Engineers

EDITED BY
C. Hsein Juang
Kok Kwang Phoon
Anand J. Puppala
Russell A. Green
Gordon A. Fenton

Published by the American Society of Civil Engineers

Copyright and Disclaimer

ISBN: 978-0-7844-1183-4

Any statements expressed in these materials are those of the individual authors and do not necessarily represent the views of ASCE, which takes no responsibility for any statement made herein. No reference made in this publication to any specific method, product, process or service constitutes or implies an endorsement, recommendation, or warranty thereof by ASCE. The materials are for general information only and do not represent a standard of ASCE, nor are they intended as a reference in purchase specifications, contracts, regulations, statutes, or any other legal document.

ASCE makes no representation or warranty of any kind, whether express or implied, concerning the accuracy, completeness, suitability, or utility of any information, apparatus, product, or process discussed in this publication, and assumes no liability therefore. This information should not be used without first securing competent advice with respect to its suitability for any general or specific application. Anyone utilizing this information assumes all liability arising from such use, including but not limited to infringement of any patent or patents.

Copyright © 2011 by the American Society of Civil Engineers.
All Rights Reserved.

ASCE and American Society of Civil Engineers—Registered in U.S. Patent and Trademark Office.

American Society of Civil Engineers
ASCE International Headquarters
1801 Alexander Bell Drive
Reston, VA 20191-4400 USA

Call Toll-Free in the U.S.: 1-800-548-2723 (ASCE)
Call from anywhere in the world: 1-703-295-6300
Internet: http://www.pubs.asce.org

Preface

This Geotechnical Special Publication is the official proceedings of GeoRisk 2011, the Geo-Institute (G-I) conference on Geotechnical Risk Assessment and Management. GeoRisk 2011 is the first G-I specialty conference held in this field since the 1996 "Uncertainty in the Geologic Environment: from Theory to Practice" conference presented in Madison, Wisconsin.

Uncertainties in the geologic environment, and their effects, are well recognized by geotechnical engineers. Use of higher factors of safety in geotechnical practice than in other disciplines is a reflection of the greater uncertainties the geotechnical engineers face. In his 1965 Terzaghi Lecture, Arthur Casagrande introduced the concept of "calculated risk" as a means for accounting for these uncertainties in design. This concept was further elaborated by Robert V. Whitman in his 1981 Terzaghi Lecture on "evaluating calculated risk" and by Norbert R. Morgenstern in his Casagrande Lecture in 1995 on "managing risk." Over the past few decades, geotechnical engineers have become increasingly aware of the need and benefits of risk assessment and management in geotechnical engineering, as well as of the need to effectively communicate risk among and between engineers, clients, regulatory agencies, and the public. Risk assessment and management is also a critical aspect of geotechnical practice from perspective of private industry. This Geotechnical Special Publication contains peer-reviewed technical papers that address such issues, covering new and continuing work on geohazard mitigation, uncertainty modeling, and risk assessment and management in all fields of geotechnical engineering from theory to practice.

Held in Atlanta, Georgia, on June 26-28, 2011, this GeoRisk 2011 conference was initially proposed by C. Hsein Juang of the G-I Technical Committee on Risk Assessment and Management and approved by the G-I Conference Coordination Committee (CCC) in April 2008. Steve Kramer was appointed as the CCC liaison to the Organizing Committee of the Conference, which included C. Hsein Juang (Chair), Kok-Kwang Phoon and Glenn Rix (Co-Chairs), Gordon A. Fenton, Edward Glynn, Russell A. Green, D.V. Griffiths, Anand Puppala, and Xiong "Bill" Yu. In addition to papers submitted in response to the Call for Papers, the conference proceedings also includes the keynote lectures delivered by the following world renowned experts:

"Risk of Limit-Equilibrium Failure of Long Earth Slopes: How it Depends on Length" by Erik Vanmarcke
"Development of a Risk-based Landslide Warning System" by Wilson Tang
"Unresolved Problems in Geotechnical Risk and Reliability" by John Christian and Gregory Baecher
"Learning to Live with Geohazards: From Research to Practice" by Suzanne Lacasse and Farrokh Nadim
"Geo-Risks in the Business Environment" by William Brumund
"The Practical Application of Risk Assessment to Dam Safety" by Gregg Scott

All papers, both "submitted" and "keynote" papers, were reviewed following the same procedures and using the same technical standards of practice of the Geo-Institute of the American Society of Civil Engineers. More than 260 abstracts and 155 papers were received in response to the Call for Papers. All papers were subject to a peer review process coordinated by the various session organizers and supervised by the conference editors. Two positive reviews

were required for acceptance and two negative reviews were required for exclusion. Standard editorial review forms (online version) were applied to maintain uniform technical standards of the papers. As a result, 127 papers were accepted for presentations at the conference and published in this Geotechnical Special Publication. The editors expect that diverse assortment of papers written by a distinguished group of national and international authors will be both stimulating and inspiring to their readers. The papers are eligible for discussion in the *Journal of Geotechnical and Geo-environmental Engineering* and for ASCE award nominations.

A publication of this quality would not have been possible without the dedication and professionalism of the session organizers and paper reviewers, the names of which appear in our subsequent acknowledgment. For those additional reviewers who were inadvertently omitted, we offer our sincere apologies.

We wish to acknowledge the marvelous efforts of the invited keynote speakers, authors, reviewers, and session organizers for their significant contributions. We also wish to extend our special thanks to the organizers and panelists of the three important discussion panels,

"Impact of Public Policy on Risk"
"The Future of Risk, Reliability, and Probabilistic Methods in Geotechnical Engineering"
"Geotechnical Business Risk"

The first panel on "Impact of Public Policy on Risk" was organized by Robert B. Gilbert and its panelists included Joe D. Manous, Marty McCann, Jr., and Brian Pallasch. The second panel on "The Future of Risk, Reliability, and Probabilistic Methods in Geotechnical Engineering" was organized by John T. Christian and Gregory B. Baecher and its panelists included Gregory B. Baecher, William Roberds, and Robert C. Patev. The third panel on "Geotechnical Business Risk" was organized by Todd H. Rees and its panelists included Michael Davis, Roger Jinks, Alan J. Krause, W. Allen Marr, and William F. Brumund.

We also wish to convey our sincere gratitude to Steve Kramer, the CCC liaison to the Organizing Committee of the GeoRisk 2011 Conference, and the ASCE/G-I staff especially Elaine Watson, Robert Schweinfurth, Sean Scully, Lauren Tighe and Helen Cook for their coordination and enthusiastic support to this conference. All of the submission activities of the papers for this conference were managed online by MIRA SMART and we wish to express our thanks to Patrick Driscoll for his unceasing effort. The editors also wish to acknowledge the assistance of Ms. Kate Gunberg of Virginia Tech and Ms. Donna Dickert at ASCE Geo-Institute in the final production of this Geotechnical Special Publication.

Editors

C. Hsein Juang (Clemson University)
Kok Kwang Phoon (National University of Singapore)
Anand J. Puppala (University of Texas at Arlington)
Russell A. Green (Virginia Tech)
Gordon A. Fenton (Dalhousie University)

Acknowledgments

List of Technical Session Organizers:

Jose Andrade
Ronald Andrus
Laurie Baise
Omer Bilgin
Mohammed Gabr
Edward Glynn
Russell Green
Hongwei Huang
Nick Hudyma
Jeff Keaton
Dianqing Li
Zenon Medina-Cetina
Shadi Najjar
Anand Puppala
Nadarajah Ravichandran
Krishna R. Reddy
Lance Roberts
Adrian Rodriguez-Marek
Marika Santagata
Kallol Sett
Mingjiang Tao
Wang Yu
Xiong Yu
Lianyang Zhang
Limin Zhang

List of Paper Reviewers:

Murad Abu-Farsakh
Sami Akbas
Linda Al Atik
Tamara Al Bittar
Jose Andrade
Ron Andrus
Marwan Aouad
Chloe Arson
Adda Athanasopoulos
Muhunthan Balasingam
Laurie Baise
Paola Bandini
Munwar Basha
Dipanjan Basu
Reza Behrou
Michelle Bernhardt
Ömer Bilgin
Ross Boulanger
Aaron Bradshaw
Scott Brandenberg
Ashly Cabas
Michele Calvello
Zijun Cao
Jose Cepeda
Ronald A. Chadderton
Debanik Chaudhuri
Jie-Ru Chen
John Chen
Qun Chen
Yonggang Cheng
Jianye Ching
Bhaskar Chittoori
Deepankar Choudhury
Richard Coffman
Brady Cox
Don De Groot
Juan Du
Saba Esmailzadeh
Luis Fargier-Gabaldon
Du Feng
Gordon A. Fenton
Damon Fick

Kevin Foster
Kevin Foye
Mo Gabr
Sivapalan Gajan
Patricia Gallagher
Louis Ge
Anthony Goh
Russell A. Green
Kathryn A. Gunberg
Seungwoon Han
Kianoosh Hatami
Ahmed Hedayat
Francisco Hernandez
Dennis Hiltunen
Roman Hryciw
Austin Huang
Fu-Kuo Huang
Hongwei Huang
Wen Chao Huang
Nick Hudyma
Magued Iskander
Mark Jaksa
Allen Jones
C. Hsein Juang
Ronnie Kamai
Siddharth Khandelwal
Yazen Khasawneh
Arash Khosravifar
William Kitch
Harald Klammler
Murali Krishna
Kiseok Kwak
Sam Lasley
Christian Ledezma
Jongwon (John) Lee
Junhwan Lee
Kyu Lee
Steve Levorson
Dianqing Li
Jinhui Li
Xu Li
Nina Liu
Yan Liu
Zhen Liu
Barbara Luke
Ronaldo Luna
Antony Martin
Zenon Medina-Cetina
Paul Michaels
Stanley Miller
Anil Misra
Nisha Mohanan
Mohammad Mohseninfar
Gonzalo Montalva
Eugene Morgan
Robb Moss
Farrokh Nadim
Shadi Najjar
Arpita Nandi
Soheil Nazarian
Guney Olgun
Thomas Oommen
Jun Kyung Park
Ming Peng
Thomas Pennington
Marry Perlea
Vlad Perlea
Michael Perlow Jr
Kok-Kwang Phoon
Pouya Pishgah Gilani
Widjojo Prakoso
Monica Prezzi
Anand Puppala
Byron Quan Luna
Marco Rannalli
Nadarajah Ravichandran
Lance Roberts
Adrian Rodriguez-Marek
J. David Rogers
Michel Saad
David Saftner
Anastasia Santoso
Jessee Scarborough
Brian Schleppi
Bernd Schuppener
Aniruddha Sengupta
Kallol Sett
Ajay Shara

N. Shariatmadari
Amit Shrivastava
Raj Siddharthan
Brian Simpson
Ida Solhell
Abdul-Hamid Soubra
Dan Spikula
Victor Taboada
Nima Tafazzoli
Junliang Tao
Mingjiang Tao
Eric Thompson
Laura Tonni
Fulvio Tonon
Thalia Travassarou
John Tripp
Mesut Turel
Thomas Tye
Marco Uzielli
Miranda Vanderpool
Giovanna Vessia
Jui-Pin Wang
Yu Wang
Joseph Wartman
Lei Wei
Andrea L. Welker
Haijia Wen
Yiping Wu
Ryan Yan
Shaoli Yang
John Yao
Negin Yousefpour
Dalia Youssef Abdel Massih
Xinbao Yu
Xiong Yu
Dimitrios Zekkos
Ioannis E. Zevgolis
Bin Zhang
Gregg Zhang
Jie Zhang
Lianyang Zhang
Limin Zhang
Lulu Zhang
Don Zhao
Gongdan Zhou

Table of Contents

Keynote Lectures

Risk of Limit-Equilibrium Failure of Long Earth Slopes: How It Depends on Length 1
Erik Vanmarcke

Development of a Risk-Based Landslide Warning System 25
Wilson H. Tang and L. M. Zhang

Unresolved Problems in Geotechnical Risk and Reliability 50
John T. Christian and Gregory B. Baecher

Learning to Live with Geohazards: From Research to Practice 64
Suzanne Lacasse and Farrokh Nadim

Geo-Risks in the Business Environment 117
William F. Brumund

The Practical Application of Risk Assessment to Dam Safety 129
Gregg A. Scott

Characterization and Modeling of Variability of Soils across Scales

Random Field Model Parameters for Columbia River Silt 169
Armin W. Stuedlein

Reliability-Based Design for Allowable Bearing Capacity by Considering Differential Settlement on Highly Fractured Rock Masses 178
Jianye Ching, Yu-Gang Hu, Zon-Yee Yang, and Jang-Quang Shiau

Assessment of Levee Site Variability As a Function of the Number of Explorations 186
Christopher B. Groves, Hollie L. Ellis, and N. Kyle Tabor

Influence of Geotechnical Dataset on the Range of Influence of Undrained Shear Strength 193
Site Onyejekwe and Louis Ge

Reliability Based Approach to Quantify Montmorillonite Mineral in Expansive Clays 201
Bhaskar Chittoori and Anand J. Puppala

Probabilistic/Simulation Methods

Subset Simulation and Its Application to a Spatially Random Soil 209
Ashraf Ahmed and Abdul-Hamid Soubra

Probabilistic Analysis of Basal Heave in Deep Excavation 217

Y. G. Tang and Gordon T. C. Kung

Influence of the Scale of Fluctuation of the Friction Angle on the Face Stability of a Pressurized Tunnel in Sands 225

M. Guilhem Mollon, Kok-Kwang Phoon, Daniel Dias, and Abdul-Hamid Soubra

Probabilistic Finite Element Analysis of a Raft Foundation Supported by Drilled Shafts in Karst 233

D. V. Griffiths, D. Dotson, and J. Huang

Probabilistic Slope Stability Analysis As a Supplement to a Deterministic Study 240

Nishant Dayal, A. Rafael Prieto, J. Paul Lewis, and R. David Scherer

Liquefaction Probability by Probabilistic Version of Robertson and Wride Model 247

Chih-Sheng Ku, C. Hsein Juang, Jianye Ching, and Der-Her Lee

Uncertainty Modeling

Design Criteria for the Differential Settlement of Landfill Foundations Modeled Using Random Fields 255

K. C. Foye and X. Zhao

Bayesian Updating of Load Settlement Curves for Footings on Cohesionless Soil 263

Shadi S. Najjar and Michel Saad

Stochastic vs. Deterministic Analysis of Consolidation Problem in Natural Alluvial Deposits 271

Pouya Pishgah Gilani and Reza Jamshidi Chenari

Bearing Capacity of Strip Footings on Spatially Random Soils Using Sparse Polynomial Chaos Expansion 279

Tamara Al-Bittar and Abdul-Hamid Soubra

Spatial Variability of Aperture in a Rough-Walled Crack in Surface Soil 287

J. H. Li, Z. F. Wang, and L. M. Zhang

Parameter Estimation and Uncertainty Analysis Incorporating Engineering Judgement by Bayesian Inversion 295

C. P. Lin and Y. C. Hung

Earthquake Engineering and Soil Dynamics I

Site Response Effects on Partially Ergodic PSHA 303

G. A. Montalva and A. Rodriguez-Marek

A Case Study of Alternative Site Response Explanatory Variables in Parkfield, California 310

E. M. Thompson, L. G. Baise, Robert E. Kayen, Eugene C. Morgan, and James Kaklamanos

Estimating Repair Cost and Downtime Due to Earthquake-Induced Damage at Container Ports 318
L. M. Ivey, G. J. Rix, S. D. Werner, and A. L. Erera

Effect of Fabric Anisotropy on Seismic Response of Strip Foundations 326
Bo Li, Xiangwu Zeng, and Hao Yu

Seismic Response of Reinforced Soil Retaining Walls: Is PGA-Based Design Adequate? 336
J. B. Varnier and K. Hatami

Performance Based Assessment of Dynamic Soil-Structure Interaction Effects on Seismic Response of Building Frames 344
Behzad Fatahi, Hamid Reza Tabatabaiefar, and Bijan Samali

Geotechnical Assessment, Characterization, and Design for Risk Management I

Effects of Slenderness Ratio on Seismic Behavior of Vertical Micropiles 352
Gholamreza Saghaee and Reza Noorzad

Multichannel Analysis of Surface Waves (MASW) at the National Geotechnical Engineering Site at Texas A&M University (NGES/TAMU) 361
R. T. Williams and D. Penumadu

Probabilistic Compressible Soil Thickness from Field Settlement Data 371
Sangho Lee and Masud Alam

A Novel Application of Risk Analysis Methods to Evaluate the Future Viability of Two Large Concrete Stormwater Detention Tanks 379
M. Eddleston and P. J. Mason

Risk Management for Large-Scale Foundation Design and Construction in Challenging Karst Geology 387
John I. Yao and Emad Farouz

Effect of Spatial Variability and Model Uncertainty on the Design of Sockets in Weak Carbonate Rocks 395
Khaled H. Charif and Shadi Najjar

Engineering Geology and Site Characterization

CPT-Based Probabilistic Characterization of Effective Friction Angle of Sand 403
Zijun Cao, Yu Wang, and Siu-Kui Au

Prediction of Embankment Settlement from PCPT Measurements: A Case Study at Courtableau Bridge 411
Xinbao Yu and Murad Abu-Farsakh

Geochemical and Geotechnical Features of Terra Rossa in Karst Areas of Southern Appalachians 420

A. Nandi and J. Moore

Characterizing Spatial Variability of Cone Penetration Testing through Geostatistical Evaluation **428**
D. A. Saftner, R. A. Green, R. D. Hryciw, M. F. Fadden, and A. DaCosta

Case Study—A Landslide on Coastal Slope in Bellingham Bay **436**
X. Huang

Developing Resistance Factors for Design of Piles in Sand **444**
K. C. Foye, M. Prezzi, and R. Salgado

Quantitative Risk Analysis for Embankments, Dams, and Slopes

Probabilistic Slope Stability Analysis of a 300 m High Embankment Dam **452**
Qun Chen and Li-Ying Chang

Identification of Hazardous Loose Landslide Deposits and Scars Formed during the 2008 Wenchuan Earthquake **460**
H. F. Zhao and Limin Zhang

Bounding the Probability of Failure for Levee Systems **468**
Justin C. Hollenback and Robb E. S. Moss

Breaching of Changkai Levee in June 2010 in Jiangxi Province, China **476**
M. Peng and L. M. Zhang

Distinct Element Modelling for High Rock Slopes in Static and Dynamic Conditions: A Case Study **484**
Ganesh W. Rathod, A. K. Shrivastava, and K. S. Rao

Reliability Analysis of Stone Columns for Ground Improvement **493**
Jose A. Alonso and Rafael Jimenez

Earthquake Engineering and Soil Dynamics II

Application of SCPTU for Assessing Liquefaction Potential of the 1976 Tangshan Earthquake, China **501**
Guojun Cai, Songyu Liu, and Anand J. Puppala

Characterizing the Liquefaction Potential of the Pleistocene-Age Wando Formation in the Charleston Area, South Carolina **510**
T. Heidari, R. D. Andrus, and S. M. J. Moysey

Influence of r_d on Liquefaction Triggering Evaluation at Two Case History Sites **518**
John Liao and Jorge Meneses

Evaluating Bias of Liquefaction-Induced Settlement Methods for Performance-Based Design **526**

H. Hayati and R. E. S. Moss

Estimating CSRs for Evaluating Liquefaction That Are Consistent with Building Code Design Spectra **534**
Aaron S. Bradshaw and Russell A. Green

Potential Differences between Time Series and Random Vibration Theory Site Response **544**
Albert R. Kottke and Ellen M. Rathje

Geotechnical Assessment, Characterization, and Design for Risk Management II

Understanding Uncertainty: Assessment and Management of Geotechnical Risk in Tunnel Construction **552**
Thomas W. Pennington and Donald P. Richards

Communicating and Managing Risk in Geotechnical Engineering Practice **560**
Jessee A. Scarborough

Reliability Analysis of Deep Excavation Based on a Semi-Empirical Approach **568**
J. K. Park, G. Biscontin, and P. Gardoni

Jet-Grouting in Cohesive Soils for Ground Improvement in Hawaii **578**
John Y. L. Chen, Robin M. Lim, and Kyle Furuhashi

Risk Assessment of Success Dam, California: Evaluation of Operating Restrictions As an Interim Measure to Mitigate Earthquake Risk **586**
D. Bowles, M. Ruthford, and L. Anderson

Load and Resistance Factor Design (LRFD) for Foundation Systems

Some Observations on Reliability-Based Design of Rock Footings **600**
Widjojo A. Prakoso and Fred H. Kulhawy

A Practical LRFD Design Method for Deep Foundations Using Side Friction and End Bearing **608**
H. Klammler, M. McVay, Jeongsoo Ko, P. Lai, and R. Herrera

Reliability-Based Design of Shallow Foundations in Cohesionless Soils under Compression Loading: Serviceability Limit State **616**
Sami O. Akbas and Fred H. Kulhawy

Quantile Framework for Simplified Geotechnical Reliability-Based Design **624**
Jianye Ching and Kok-Kwang Phoon

Reliability Assessment of Eurocode 7 Spread Foundations Design Methodology **632**
Sónia H. Marques, A. Topa Gomes, and A. Abel Henriques

Deterministic and Probabilistic Seismic Analyses of a Slope-Footing System 640
Nancy Salloum, Dalia Youssef Abdel Massih, Abdul-Hamid Soubra, and Jacques Harb

Limit State Design in Geotechnical Engineering

A Comparative Study of Drilled Shaft Design Using LRFD and Expanded RBD 648
Yu Wang, Zijun Cao, and Fred H. Kulhawy

Limit States Design of Pile Foundations in Clay under Combined Action of Transient Uplift Loads and Frost Jacking 656
Konstantin Ashkinadze

Safety Margin in Design of Pile-Supported Structural Slabs for Frost Action 664
Konstantin Ashkinadze

Statistical Characterization and Stochastic Simulation of Load-Displacement Behavior of Shallow Footings 672
Marco Uzielli and Paul W. Mayne

Reliability Based Design of Base Heave Stability in Wide Excavations 680
Shih-Hsuan Wu, Chang-Yu Ou, and Jianye Ching

Probabilistic Analysis of Shallow Foundations on Rocks Obeying Hoek-Brown Failure Criterion 688
Nut Mao, Tamara Al-Bittar, and Abdul-Hamid Soubra

Risk and Reliability in Geoenvironmental Engineering

Influence of Aging on the Mechanical Behavior of Municipal Solid Waste 696
A. Nayebi, N. Shariatmadari, M. H. Hamzeie Tehrani, and P. Oskouie

Effect of 1D Infiltration Assumption on Stability of Spatially Variable Slope 704
Anastasia M. Santoso, Kok-Kwang Phoon, and Ser-Tong Quek

Old Sewer, Big Risks: Managing Risks during the Design and Construction of a 21-Story Building Adjacent to a Critical 100-Year-Old Sewer Structure 712
Damian R. Siebert, Joel S. Mooney, Richard Marks, Daniel Ocasio, and Kevin McKenna

Effect of Leachate Recirculation and Extent of Degradation on the Stability of Bioreactor Landfill Slopes 720
Amit Srivastava, G. L. Sivakumar Babu, Krishna R. Reddy, and Hanumanth S. Kulkarni

Sustainable Flood Risk Management: Lesson from Recent Cases 728
Xiong (Bill) Yu and Yuewen Huang

Life Cycle Approaches for Brownfields Redevelopment 736
Patricia M. Gallagher and Sabrina Spatari

Retaining Structures I

Strain Localization Effect on System Reliability Based Design of Bridge 744

Abutments under Earthquake Loading
B. Munwar Basha and G. L. Sivakumar Babu

Serviceability Considerations in the Design of Sheet Pile Walls for Risk Management **754**
Ömer Bilgin, Eman Mansour, and Mohamad Gabar

Reliability Based Performance Evaluation of Earth Retaining Structures **762**
Manojit Chakraborty, A. Murali Krishna, and Arunasis Chakraborty

Wall and Ground Responses in a Braced Excavation Considering Spatial Variability **770**
Zhe Luo, C. Hsein Juang, and Fu-Kuo Huang

Evaluation of LRFD Resistance Factors and Risk for Mechanically Stabilized Earth Walls **778**
S. Wasman, M. McVay, D. Bloomquist, M. Harrison, and P. Lai

Hazards/Risks I

(Sub)Global Rock Slope Stability: Using Rock Mass Indices to Characterize and Manage Rockfall Risk **787**
Brian Bruckno

Evaluation of the Susceptibility of Landslides and Debris Flows on Costa Rica's National Road Network: Analysis of a Segment of National Route 32 **795**
Diego A. Cordero Carballo

Spatial Prediction of Groundwater Depth to Trigger Liquefaction in St. Louis **804**
Jae-Won Chung and J. David Rogers

Study on Risk Assessment for an Individual Landslide **812**
Juan Du and Kun-Long Yin

Geohazard Interpretation of the Cagliari Slope (Southern Sardinia, Italy) **820**
William J. Johnson, Francesca Zolezzi, James Nicholls, Eric J. Parker, and Ennio Morgante

Delineation of Slope Profiles from Digital Elevation Models for Landslide Hazard Analysis **829**
Mesut Turel and J. David Frost

Earthquake Engineering and Soil Dynamics III

Establishing Confidence in Surface Wave Determined Soil Profiles **837**
P. Michaels

Surface Wave Benchmarking Exercise: Methodologies, Results, and Uncertainties **845**
B. R. Cox and C. M. Wood

Analysis of Surface Wave Benchmarking Data **853**

Don Zhao

An Assessment of Surface Wave Techniques at the Texas A&M National Geotechnical Experimentation Site **859**

Khiem T. Tran and Dennis R. Hiltunen

Analysis and Interpretation of the Texas A&M University Benchmark Data Using the Refraction Microtremor Technique **867**

A. Pancha and S. Pullammanappallil

Determination of the Dynamic Soil Characteristics at the NGES **875**

S. A. Badsar, M. Schevenels, and G. Degrande

Analysis of SASW, MASW, and Passive Surface Wave Data Collected at the National Geotechnical Experimentation Site at Texas A&M University **886**

A. J. Martin

Geotechnical Assessment, Characterization, and Design for Risk Management III

Active Risk Management in Geotechnical Engineering **894**

W. Allen Marr

Risk Assessment of Success Dam, California: Flood Related Potential Failure Modes **902**

Loren Anderson, Michael Ruthford, Vlad Perlea, David Serafini, Jack Montgomery, and David Bowles

Geotechnical Risk in the Peruvian Andes **910**

A. Carrillo-Gil and A. Carrillo-Acevedo

Quantified Risk Assessment of Shield Tunneling Effects on Urban Cement Concrete Pavement **915**

Q. F. Hu and H. W. Huang

Risk Assessment of Success Dam, California: Earthquake Induced Potential Failure Modes **923**

M. Ruthford, V. Perlea, D. Serafini, M. Beaty, L. Anderson, and D. Bowles

A Parametric Study on Factors Affecting Ground Vibrations during Pile Driving through Finite Element Simulations **931**

Mo Zhang and Mingjiang Tao

Retaining Structures II

Tunnel Face Support Pressure and Associated Risk **939**

Mahmoud Ahmed and Magued Iskander

Risk Analysis of Pile Pressing-In on an Adjacent Earth-Retaining Wall **948**

Amy D. D. Lu and Albert T. Yeung

Numerical Study on the Dynamic Behavior of Retaining Walls Backfilled with Shredded Tires 955
E. Huggins and N. Ravichandran

Probabilistic Analysis of the Deflection of Retaining Walls in Deep Excavation 963
Y. G. Tang

Risk Management with Performance-Based Geoengineering Monitoring: APM Tunnel Extension at Hartsfield-Jackson International Airport 971
Thomas Allen Tye and W. Allen Marr

Hazards/Risks II

Probability-Based Risk Assessment of Landslide/Slope Failure 979
Y. Y. Chi, Y. F. Lee, C. H. Juang, Y. L. Wu, and Y. P. Wu

Road Slopes Risk Assessment of the Northern Part of Gifu Prefecture, Japan 988
Yusuke Honjo, Yu Otake, Shuzi Moriguchi, and Takashi Hara

Managing Settlement Risk Due to Tunneling beneath Downtown Seattle 996
Michael A. Lach

Assessing the Probability of Occurrence of Earthquake-Induced Landslides Offshore the U.S. East Coast: A First-Order, Second Moment Approach 1004
Eugene C. Morgan and Laurie G. Baise

An Innovative Landslide Risk Assessment System: Application to Highway Embankments 1012
L. Pantelidis

Seismic Risk Assessment and Application in the Central United States 1020
Zhenming Wang

Earth Structures/Slopes

Implicit Expression Solution of Slope Reliability on Kinematical Element Method and Response Surface Method 1028
Ping Cao and Ke Zhang

Field Performance of a New Approach Slab System 1036
Qiming Chen and Murad Abu-Farsakh

External Stability of Geotubes Subjected to Wave Loading 1044
M. Khalilzad and M. A. Gabr

Probabilistic Assessment of Commercial Design Guides for Steep Reinforced Slopes: Implications for Design 1055
W. A. Kitch, R. B. Gilbert, and S. G. Wright

Using Computer Simulations to Take a Closer Look at Load and Resistance Factors for Designing Geosynthetic-Reinforced Walls 1063

Stanley M. Miller

Impact of Non-Analytical Factors in Geotechnical Risk Assessment of Levees **1073**
Mary Perlea and Edward Ketchum

Geotechnical Assessment, Characterization, and Design for Risk Management IV

Rockfall and Mitigation Evaluation with 3-D Discrete Element Modeling **1082**
R. Zhang and A. Rock

GeoRisk in the Design-Build Procurement Process **1090**
John Christos Daoulas

Owner Involvement—Choosing Risk Factors for Shallow Foundations **1098**
Roger A. Failmezger and Paul J. Bullock

Model Test Study of Soil Variation Impact on Shield Tunnel Segment Structure **1109**
Hongwei Huang, Dongming Zhang, Qunfang Hu, and Jie Zhang

Mitigating Risk and Managing Foundation Cost and Schedule on "Mega" Transmission Line Projects: Beginning with the End in Mind **1117**
K. Yamatani and A. Jahangir

Comparison Study on Computer Simulations for Bridge Scour Estimation **1125**
Xinbao Yu, Junliang Tao, and Xiong (Bill) Yu

Uncertainty Analysis

Updating Uncertainties in Friction Angles of Clean Sands **1133**
Jianye Ching, Jieru Chen, and Kok-Kwang Phoon

Constructing Joint Distributions of Multivariate Geotechnical Data **1141**
Jianye Ching, Kok-Kwang Phoon, and Wen-Chao Huang

Extension of CSRSM for the Parametric Study of the Face Stability of Pressurized Tunnels **1149**
Guilhem Mollon, Daniel Dias, and Abdul-Hamid Soubra

Beam on Spatially Random Elastic Foundation **1157**
S. Haldar and D. Basu

Teaching Reliability at the Undergraduate Level **1165**
Robb Eric S. Moss

This page intentionally left blank

Risk of Limit-Equilibrium Failure of Long Earth Slopes: How it Depends on Length

Erik Vanmarcke

Department of Civil and Environmental Engineering, Princeton University, Princeton, NJ; M. ASCE; PH (609) 751-0221; email: evm@princeton.edu

ABSTRACT

We compare two- and three-dimensional approaches to assessing the risk of limit-equilibrium failure of long earth slopes, embankments, dams or levees. The writer's earlier simplified three-dimensional stochastic slope stability model is extended by considering different types of spatial variation of the sliding resistance along the axis of the slope, including multi-scale and self-similar variation. Evaluating the probability $p_f(b)$ of a sliding failure involving failure-zone segments of different width b, the model predicts that slope failures extending over a very long or a very short segment are highly improbable, and quantifies the most likely width. This also enables comparison, highly relevant in practical applications, of slope reliability measures obtained based on 2-D and 3-D stability analyses. Using stochastic failure-threshold-crossing analysis, it is further shown that the probability $P_F(B)$ of a sliding failure anywhere along a long slope or embankment of given total length B grows linearly with the length, when $P_F(B) \ll 1$, and the mean rate of increase in this "system failure" risk per unit length is quantified.

INTRODUCTION

Many studies aimed at determining the risk of slope failure — by Wu and Kraft (1970), Yucemen et al. (1973), Alonso (1976), Matsuo (1976), Hachich and Vanmarcke (1983), Christian et al. (1994), Li and Lumb (1987), Griffiths and Fenton (2004), Low et al. (1998 & 2007), among others — work within the framework of conventional plane strain analysis of slope stability. In the first paper to treat the three-dimensional slope stability problem in a probabilistic framework (Vanmarcke 1977b), the sliding soil mass is modeled as a portion of a cylinder with finite length b bounded by vertical end sections. This 3-D stochastic methodology, initially applied to slopes in cohesive

soil (when the use of undrained strength is appropriate), was generalized in Vanmarcke (1980) to deal with slopes with more general (Mohr-Coulomb-type) strength characteristics under drained, undrained or partially drained conditions. The methodology permits treatment of fairly general shapes of failure surfaces, in part by representing effects attributable to the two end sections of the failure surface in a simplified manner. In this paper, we review and refine the basic 3-D stochastic methodology, rendering it capable of accommodating a wide range of models for the correlation structure of the random variation of the resistance-against-sliding along the slope axis.

2-D SLOPE STABILITY: PROBABILISTIC TREATMENT

Classical limit-equilibrium stability analysis (e.g., Fellenius 1936; Bishop 1955) considers a typical cross-section (in the present context, at any location x along the centerline of a long earthen slope or embankment or levee) and defines the (cross-sectional) safety factor F as the ratio of the resisting moment to the driving (or overturning) moment,

$$F = \frac{\text{Resisting Moment}}{\text{Driving Moment}} = \frac{M_R}{M_D}, \tag{1}$$

In a simple probabilistic treatment of the problem — easily extended, but without much altering this paper's main theses — the cross-sectional resisting moment M_R is treated as a random variable with mean $\overline{M}_R$, standard deviation $\widetilde{M}_R$, and coefficient of variation $V_{M_R} = \widetilde{M}_R/\overline{M}_R$. (Throughout the paper, $\overline{Z}$ and $\widetilde{Z}$ denote, respectively, the mean and the standard deviation of the random quantity Z). This requires consideration of the correlation structure of horizontal and vertical variation of shear strength within the cross-section. In static limit-equilibrium slope stability analysis, uncertainty about the driving moment is usually dwarfed by uncertainty about the resisting moment; it is reasonable to (initially) ignore the variability of M_D, and we assume $\widetilde{M}_D \approx 0$ in the probabilistic analysis presented below.

Mean and standard deviation of the safety factor. The mean of the (cross-sectional) safety factor F is then:

$$\overline{F} = \overline{M}_R/\overline{M}_D. \tag{2}$$

The standard deviation of of F equals the standard deviation of M_R times the reciprocal of the mean of M_D:

$$\widetilde{F} = \widetilde{M}_R/\overline{M}_D. \tag{3}$$

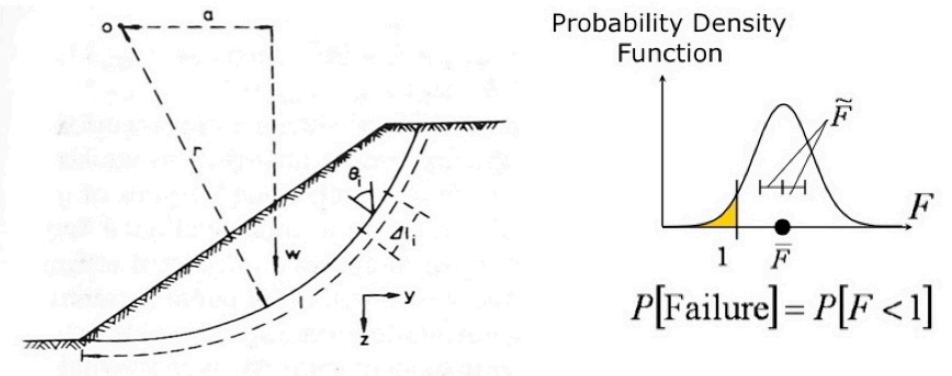

Figure 1: **Simple 2-D Model to Evaluate Slope Failure Risk. The Factor of Safety is $F = M_R/M_D$, and "Failure" Corresponds to $F < 1$.**

Note that the coefficient of variation $V_F = \widetilde{F}/\overline{F}$ is equal to $V_{M_R} = \widetilde{M}_R/\overline{M}_R$ if the driving moment is (or, as herein, is be assumed to be) deterministic.

Reliability Index and Probability of Failure. In the context of the 2-D stability analysis, the calculated probability of failure p_f corresponds to the area under the probability density function of the (cross-sectional) safety factor F at values less than one (see Fig. 1, on the right side):

$$p_f = \text{Prob}[F < 1]. \tag{4}$$

An indicator of slope safety is the reliability index β, defined in terms of the mean and the standard deviation (or the coefficient of variation) of the factor of safety, as follows:

$$\beta = \frac{\overline{F} - 1}{\widetilde{F}} = \frac{1}{V_F}\,\frac{\overline{F} - 1}{\overline{F}}. \tag{5}$$

It measures the distance between the mean safety factor $\overline{F}$ and its failure threshold, $F = 1$, in units of standard deviation of the safety factor, $\widetilde{F}$.

The failure probability p_f may be expressed in terms of β as follows:

$$\begin{aligned} p_f &= P[F < 1] = P[(F - \overline{F})/\widetilde{F} < \beta] \\ &= P[U < -\beta] = F_U(-\beta), \end{aligned} \tag{6}$$

in which $F_U(\cdot)$ is the cumulative probability distribution of the standardized safety factor, $U = (F - \overline{F})/\widetilde{F}$, which has zero mean and unit standard deviation. Either the normal (Gaussian) or lognormal distribution is commonly adopted to evaluate this "notional" probability — "notional", because the event the probability refers to, $F < 1$, defined in the context plane strain (2-D) analysis, is *not* a well-defined physically realizable event. This point is clarified in the next section, in which we explicitly consider the out-of-plane width of the soil mass involved in any real failure event.

The preceding analysis can be performed for any assumed circular or non-circular cross-sectional failure arc. One needs to search for the sliding-arc geometry, accounting for the material properties within the cross-section, that will yield the smallest value of the mean safety factor $\overline{F}$ or the reliability index β, or the largest value of failure probability p_f. (The reliability index β and failure probability p_f depend not only on $\overline{F}$, but also on the coefficient of variation and within-cross-section correlation structure of the shear strength. Owing to the nonlinearity between F and β, and between β and p_f, the various critical-arc geometries will likely differ, but not by much.

SIMPLIFIED 3-D SLOPE STABILITY: PROBABILISTIC TREATMENT

An analytically tractable and highly informative approach to probabilistic three-dimensional limit-equilibrium slope stability analysis rests on the assumption that the 3-D sliding mass has the same cross-sectional characteristics over a finite width b along the slope axis x, and has vertical cutoffs at both ends. If the cross-section through the sliding mass is a circular arc, as in Figures 1 and 2, the backside of 3-D failure surface will be cylindrical.

In the probabilistic treatment of the problem, the set of cross-sectional resisting moments $M_R(x)$ is seen as the realization of a weakly stationary one-dimensional random function of x, with mean $\overline{M}_R$, standard deviation $\widetilde{M}_R$, and a horizontal correlation structure that depends on separation distance (between cross-sections) measured along the slope axis. Specifically, the correlation structure of $M_R(x)$ can be described by a correlation function $\rho(\Delta x) \equiv \rho_{_{M_R}}(\Delta x)$, where Δx measures the horizontal distance (along the slope axis) between two cross-sections, or by the reduction factor $\Gamma(b) \equiv \Gamma_{_{M_R}}(b)$, which expresses how the standard deviation of $M_R(x)$ decreases under local averaging in function of the averaging-window size b.

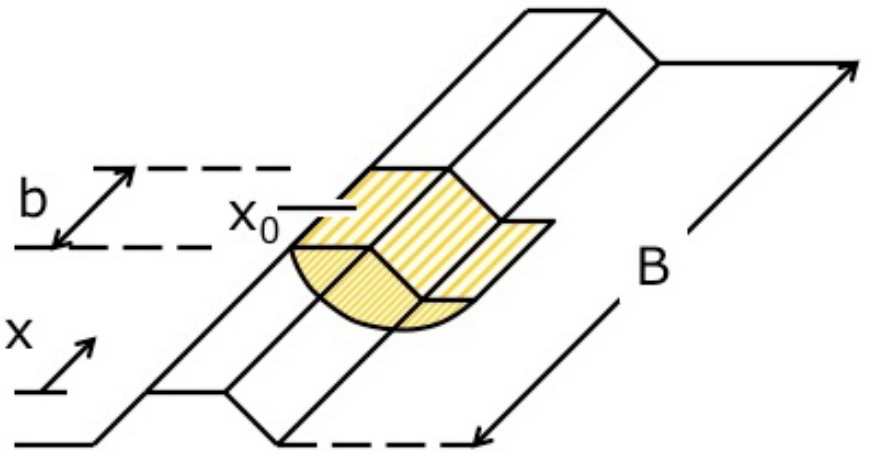

Figure 2: **Idealized 3-D Sliding Mass Model**

The scale of fluctuation of $M_R(x)$, the integral of $\rho(\Delta x)$ from $-\infty$ to $+\infty$, is denoted by $\delta \equiv \delta_{M_R}$. For common (single-scale) random process models, the reduction factor $\Gamma(b)$ will converge toward a simple asymptotic form as the ratio b/δ grows, namely $\Gamma(b) \approx (\delta/b)^{1/2}$, for $b \geq \delta$. This expression in fact provides an alternate definition for the scale of fluctuation (Vanmarcke 1977a & 1983). Also, to first approximation: $\Gamma(b) \approx 1$ for $0 \leq b \leq \delta$.

The function $\Gamma(b)$ is obtainable, in principle, from statistical analysis of weighted averages of shear strengths associated with individual cross-sections $M_R(x)$ at different locations x along the slope axis. A conceivable direct approach is to evaluate the actual cross-sectional resisting moments $M_R(x)$ from information (e.g., field and lab measurements) gathered at specific locations ($x_0, x_0 + \Delta x_0, x_0 + 2\Delta x_0$, etc.). This would provide a set of values of $M_R(x)$ from which one could estimate the mean $\overline{M}_R$, the standard deviation $\widetilde{M}_R$, and characteristics of the (horizontal) correlation structure. An indirect

approach, pursued in Vanmarcke (1980), is to derive these statistical parameters from data about the random variables (layer thicknesses, strength parameters, pore pressures) contributing to the uncertainty of $M_R(x)$.

Safety Factor in the 3-D Probabilistic Analysis. The factor of safety, in the three-dimensional formulation, now depends on the location of x of the center of the failure zone, and becomes itself a random function $F_b(x)$, with marginal statistics — its mean $\overline{F_b}$ and standard deviation $\widetilde{F_b}$ — dependent on the failure-zone width b. For a sliding mass located between $(x_0 - b/2)$ and $(x_0 + b/2)$, the safety factor $F_b(x_0)$ may be expressed as follows:

$$F_b(x_0) = \frac{\text{Resisting Moment}}{\text{Driving Moment}} = \frac{M_{R,b}(x_0) + R_e}{M_{O,b}(x_0)}, \tag{7}$$

in which b = width of the failure zone; $M_{R,b}(x_0)$ = the integral of the resisting moments $M_R(x)$ for cross-sections on the backside of the potential sliding mass; $M_{D,b}(x_0)$ = the total driving moment, i.e., an integral of the cross-sectional driving moments within the failure zone; and R_e = the contribution of the end sections of the failure zone to the resisting moment. The quantity $M_{R,b}(x_0)$ is the integral of the resisting moments of cross-sections located between the limits $x_1 = (x_0 - b/2)$ and $x_2 = (x_0 + b/2)$:

$$M_{R,b}(x_0) = \int_{x_1}^{x_2} M_R(x)dx. \tag{8}$$

Keeping the interval $b = |x_2 - x_1|$ fixed and moving it along the slope axis gives rise to a derived random function, $M_{R,b}(x)$, which is a 'moving integral' of the random process $M_R(x)$. The means of $M_{R,b}(x)$ and $M_{D,b}(x)$ are:

$$\overline{M}_{R,b} = b\,\overline{M}_R \qquad \text{and} \qquad \overline{M}_{D,b} = b\,\overline{M}_D. \tag{9}$$

If the values of $M_R(x)$ corresponding to different locations x were perfectly correlated, the standard deviation of $M_{R,b}(x_0)$ would be equal to $b\,\widetilde{M}_R$. However, the integration operation (in Eq. 8) will mitigate the impact of large local deviations of $M_R(x)$ from its mean $\overline{M}_R$,. This effect can be quantified in terms of the dimensionless reduction factor $\Gamma(b) \equiv \Gamma_{M_R}(b)$, as follows:

$$\widetilde{M}_{R,b} = b\,\widetilde{M}_R\,\Gamma(b), \tag{10}$$

in which $\Gamma(b)$, already mentioned earlier, by definition equals the square root of the "variance function" (Vanmarcke, 1977a & 1983), which expresses the

fractional reduction of the "point variance" (of stationary random processes) under local averaging, for different 'averaging-window sizes' b.

The end-section contribution, R_e, to the resisting moment can be calculated, for a given sliding-surface-end-section geometry (not necessarily the straight vertical cutoff shown in Fig. 2), by integrating contributions to the resisting moment from all points within the two end-sections. We denote its mean by $\overline{R}_e$, and introduce the quantity $d = \overline{R}_e/\overline{M}_R$, with the dimension of length, obtainable from deterministic stability analysis. The mean of the total resisting moment can then be expressed as a sum of two components:

$$\overline{M}_{R,b} + \overline{R}_e = b\,\overline{M}_R + d\,\overline{M}_R = (b+d)\,\overline{M}_R. \tag{11}$$

With reference to the cross-section shown on the left side of Fig. 1 (and the quantities defined in that figure), the distance d equals $2A/l$, where $A =$ the area of cross-section above the (circular) failure arc, and $l =$ the length of the arc. Since the shear strength throughout any cross-section is random, the resistance contribution R_e will also be random. However, the uncertainty in R_e has only a secondary effect on the results of the probabilistic stability analysis, especially at larger values of b of most practical interest in 3-D slope safety assessment, and it will not be explicitly treated herein.

Mean and standard deviation of the factor of safety. Treating the driving moment as deterministic or prescribed — extensions are considered later — the mean of the safety factor $F_b(x_0)$ can be expressed as follows:

$$\overline{F}_b = \frac{\overline{M}_R\,b + \overline{R}_e}{\overline{M}_D\,b} = \frac{\overline{M}_R(b+d)}{\overline{M}_D\,b} = \overline{F}\,(1+\frac{d}{b}), \tag{12}$$

where $\overline{F} = \overline{M}_R/\overline{M}_D$ is the 'plane strain' mean safety factor obtainable either directly from Eq. 2 or by taking $\overline{F}_b$ in Eq. 12 to its asymptotic limit,

$$\lim_{b\to\infty} \overline{F}_b = \overline{F} = \frac{\overline{M}_R}{\overline{M}_D}. \tag{13}$$

The quantity $(b+d)$ may be thought of as the "effective width" of the failure zone (for the purpose of computing the mean resisting moment), while d/b measures the relative importance of the end effects. Actually, end-sections having more realistic shapes — different from the idealized vertical cutoffs shown in Fig. 2 — can also be represented by the distance $d = \overline{R}_e/\overline{M}_R$, now more generally interpreted as the value, $b \equiv d$, for which $\overline{F_b} \equiv \overline{F}_d = 2\,\overline{F}$.

The standard deviation of the safety factor $F_b(x_0)$ equals the standard deviation of $M_{R,b}$ times the reciprocal of the mean of $M_{D,b}$. We may write::

$$\widetilde{F}_b \simeq \frac{b\,\widetilde{M}_R\,\Gamma(b)}{b\,\overline{M}_D} = \Gamma(b)\,\widetilde{F}, \tag{14}$$

where $\widetilde{F} = \widetilde{M}_R/\overline{M}_D$ is the standard deviation of the (2-D) cross-sectional safety factor. Note that $\widetilde{F}$ is not equal to the asymptotic value of $\widetilde{F}_b$ when $b \to \infty$. Instead, $\widetilde{F}_b \to 0$, since $\Gamma(b) \to 0$, as $b \to \infty$ (*unless* the scale $\delta \equiv \delta_{M_R}$ of the one-dimensional random process $M_R(x)$ is itself infinite).

The mean and the standard deviation of $F_b(x_0)$ depend on: the mean plane strain safety factor $\overline{F}$; the coefficient of variation $V_F = V_{M_R}$ of the resistance mobilized along the 'failure arc' within each cross-section; the parameter d, accounting for end effects, obtainable from deterministic (for circular arcs, 2-D) stability analysis; and the correlation structure, represented by $\Gamma(b) \equiv \Gamma_{M_R}(b)$, of the cross-sectional resisting moments along the slope axis.

Reliability Index as a Function of the Failure-Zone Width. The reliability index can again be expressed in terms of the mean and standard deviation of the factor of safety, both now dependent on b, as follows:

$$\beta_b = \frac{\overline{F}_b - 1}{\widetilde{F}_b}. \tag{15}$$

It measures the distance between the mean safety factor, $\overline{F}_b$, and its failure threshold, $F_b = 1$, in units of standard deviation of the safety factor, $\widetilde{F}_b$. Inserting the expressions for $\overline{F}_b$ and $\widetilde{F}_b$, and dividing by the cross-sectional (2-D) reliability index β, yields the following expression for the ratio of the 3-D reliability index to the 2-D reliability index, for $b > 0$ and $\overline{F} > 1$:

$$\frac{\beta_b}{\beta} = \{1 + \frac{d}{b}\,\frac{\overline{F}}{\overline{F} - 1}\}\,\frac{1}{\Gamma(b)}\,. \tag{16}$$

This equation indicates that two factors, marked by opposing trends, control the behavior of the reliability index β_b as a function of the width b of the failure zone. As b increases, the first factor (dependent on d/b and $\overline{F}$) decreases from very high positive values when $b \to 0$ to unity as $b \to \infty$. The second factor, $[\Gamma(b)]^{-1}$, presuming the scale $\delta \equiv \delta_{M_R}$ is finite, grows from a

unit value when $b \to 0$ to infinity as $b \to \infty$. Clearly, our interest focuses on the value $b_{critical} \equiv b_{cr}$ that minimizes the product of these two factors.

Before tackling the optimization problem, we can already draw some useful conclusions from Eq. 16, which expresses the ratio β_b/β of reliability indices (linked directly to the slope-failure probabilities) obtained by means of 3-D and 2-D analyses, respectively. The two factors on the right side of Eq. 16 are both *no less than one* for all possible values of the failure-zone width b. This means, first, that the reliability index, and the corresponding failure risk, calculated based on 2-D stochastic stability analysis is *always conservative* relative to that obtained from 3-D analysis. (The limiting case, $\beta_b/\beta \to 1$, is associated with $\delta \to \infty$ and $b \to \infty$, an unrealistic situation). Second, as will be demonstrated below, for any realistic values of the parameters, the 2-D analysis yields *over-conservative* results, i.e., estimates for the probability of a (localized) slope-failure event that *may be orders of magnitude too high*. Such conservatism (in risk estimation) defeats the purpose of risk assessment and the promise of risk-informed decision-making in geotechnical engineering.

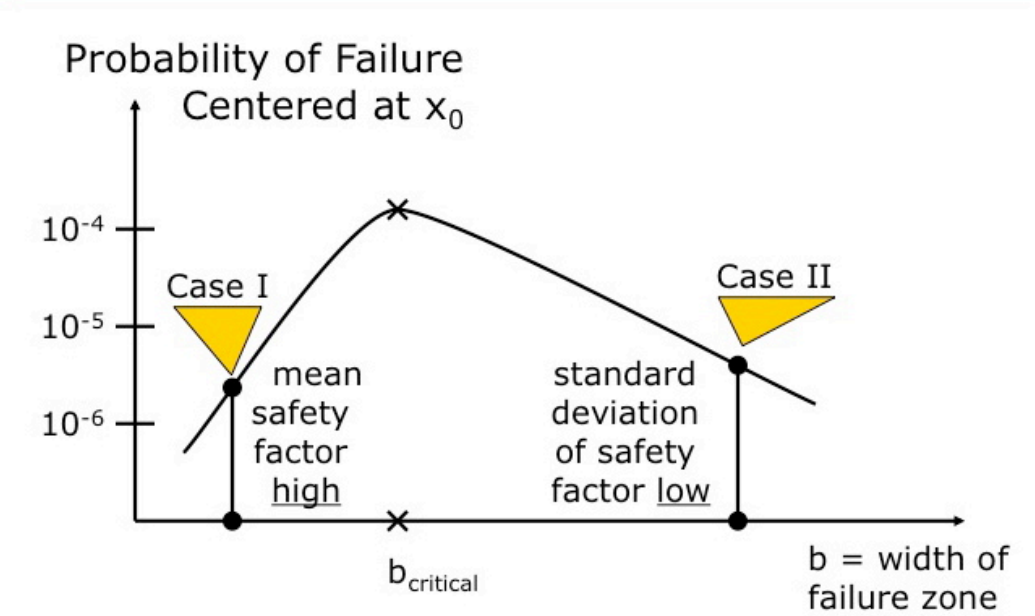

Figure 3: **Failure Probability vs. Failure-Zone Width**

Risk of Failure at any Specific Location. We now examine the probability of failure $p_f(b)$ involving a failure-zone segment of width b centered at any given location x along the slope (or embankment or levee) axis. Equal to the area under the probability density function of F_b for values below one, it can also be expressed in terms of the reliability index β_b, as follows:

$$\begin{aligned} p_f(b) &= P[F_b < 1] = P[(F_b - \overline{F}_b)/\widetilde{F}_b < \beta_b] \\ &= P[U < -\beta_b] = F_U(-\beta_b), \end{aligned} \tag{17}$$

where, again, $F_U(\cdot)$ is the cumulative probability distribution of the standardized variable $U = (F_b - \overline{F}_b)/\widetilde{F}_b$ which has zero mean and unit standard deviation. It is reasonable to assume, in light of the Central Limit Theorem, that the spatially averaged resisting moments $M_{R,b}$ (and hence the safety factor F_b itself) obey a Gaussian distribution. Actually, for the same reason — averaging of random-strength values along the failure arc — it makes sense to use the Gaussian distribution when calculating p_f by means of Eq. 6.

Consider the two main statistics – mean and standard deviation – of the safety factor F_b as a function of b. The mean $\overline{F}_b$ drops down to its plane strain level, while the spread of the distribution of the safety factor, measured by $\widetilde{F}_b$, is roughly constant at small b-values and then steadily decreases once b exceeds the scale of fluctuation $\delta = \delta_{M_R}$ of the one-dimensional random process $M_R(x)$. As indicated in Fig. 3, at low b-values ("Case I") the failure probability is very small (relative to its maximum at some "critical value" b_{cr}, evaluated in the next subsection) due to the high mean values of the safety factor F_b. At large b-values ("Case II") the failure probability is also very small (relatively) because the standard deviation of the safety factor F_b keeps decreasing while the mean approaches the asymptotic value $\overline{F}_{b\to\infty} \to \overline{F}$.

The following series approximation (Dwight 1961) for the Standard Gaussian cumulative distribution $F_U(\cdot)$ is useful at relatively large positive u-values:

$$F_U(-u) = (\sqrt{2\pi}u)^{-1} e^{-u^2/2}(1 - u^{-2} + 3u^{-4} - 16u^{-6} + ...). \tag{18}$$

(The error in this series expansion is less than the last term used.) Combining Eqs. 17 and 18, we can express the failure-event probability $p_f(b)$ as follows:

$$p_f(b) = F_U(-\beta_b) = g(\beta_b)\, e^{-\beta_b^2/2}. \tag{19}$$

The function $g(\beta_b)$ varies relatively slowly with β_b within the range of values of β_b likely to be of practical interest. For example, when $1.5 < \beta_b < 5$, the

function $g(\beta_b)$ varies only by a factor of three, while the exponential factor changes by five orders of magnitude. For practical reliability calculations, it makes sense to use $g(\beta_b) \approx (\sqrt{2\pi}\beta_b)^{-1}$, thereby in effect ignoring all but the first term in the above series approximation. (It is straightforward, as well, to refine the approximation by including additional terms of the series.) We use the above approximation in a subsequent section of the paper.

Critical Width of the Failure Zone. The minimum value of β_b can be found by setting the derivative of β_b/β (given by Eq. 16) with respect to b equal to zero, and solving for b. If and when the (standard-deviation-reduction) function $\Gamma(b)$ can be expressed as a power law, $\Gamma(b) \propto b^{-0.5}$, the b-value that minimizes β_b, denoted by b^*, can be expressed as follows:

$$b^* = \frac{\overline{F}\, d}{\overline{F} - 1}. \tag{20}$$

Note that the major influence on b^* is the plane strain mean safety factor, $\overline{F}$. The smaller the *mean safety margin*, i.e., the difference between $\overline{F}$ and the unit failure threshold $F = 1$, the larger the ratio b^*/d.

The power law, $\Gamma(b) \propto b^{-0.5}$, does not apply when b is less than δ, however. Instead, $\Gamma(b) \approx 1$ when $b \leq \delta$. In case δ exceeds b^* (as given by Eq. 20), the critical failure-zone width b_{cr} will be roughly equal to δ. In conclusion,

$$b_{cr} \approx \text{Max}\,\{\text{b}^*, \delta\}. \tag{21}$$

In words, the critical failure-zone width b_{cr}, defined as the value of b that minimizes β_b or maximizes $p_f(b)$, will be the larger of two quantities, namely b^* (as given by Eq. 20) and the scale of fluctuation $\delta \equiv \delta_{M_R}$.

Minimum Value of the Reliability Index β_b. Substituting Eq. 20 into Eq. 16 yields the quotient of the minimum 3-D reliability index β_{b^*} (applicable when $b^* \geq \delta$) and the 2-D reliability index β:

$$\frac{\beta_{b^*}}{\beta} = \frac{2}{\Gamma(b^*)} \approx 2\,(b^*/\delta)^{\,0.5}\,. \tag{22}$$

When b^* is less than δ, we need to go back to Eq. 16 and set $b = \delta$ to evaluate the minimum ratio of 3-D to 2-D reliability indices. Inserting $\Gamma(\delta) \approx 1$ yields:

$$\frac{\beta_\delta}{\beta} \approx 1 + \frac{d}{\delta}\,\frac{\overline{F}}{\overline{F} - 1}\,. \tag{23}$$

These two candidate expressions for the minimum ratio of reliability indices, Eqs. 22 and 23, give the same result, $\beta_b/\beta \approx 2$, when $b = b^* = \delta$, while for $\delta \geq b^*$, the minimum value of the ratio of reliability indices, given by Eq. 23, gradually decreases, from $\beta_\delta/\beta \approx 2$ (when $\delta \approx b^*$) to $\beta_\delta/\beta = 1$ as $\delta \to \infty$.

More Refined Analysis when the Scale δ is Very Large. Careful consideration of the correlation structure of one-dimensional random processes — the details are beyond the scope of this paper — suggests an alternative to the crude approximation, $\Gamma(b) \approx 1$ for $b \leq \delta$, that led to the estimate $b_{cr} \approx \delta$ in case $\delta \geq b^*$ (see Eq. 21). Under local averaging of a stationary one-dimensional random process such as $M_R(x)$, one always expects *some* degree of smoothing, and hence a reduction in the standard deviation, even when the averaging window b is less than the scale of fluctuation $\delta = \delta_{M_R}$. Consequently, a better model for $\Gamma(b)$, say, within the range $d \leq b \leq \delta$, is a simple (relatively slowly decaying) power law: $\Gamma(b) \approx (d/b)^\alpha$, with $0 < \alpha \leq 1/2$. Inserting this power-law approximation for $\Gamma(b)$ into Eq. 16, again setting the derivative of the ratio β_b/β equal to zero, and solving for b, yields the following expression for the critical failure-zone width: $b_{cr} = [(1-\alpha)/\alpha]\, b^*$, where b^* is as given by Eq. 20. When $\alpha = 0.5$, we have $[(1-\alpha)/\alpha] = 1$ and $b_{cr} = b^*$. The main conclusion is that the critical failure width, in case the scale δ is very large, is better predicted by $[(1-\alpha)/\alpha]\, b^*$ than by δ itself.

Multi-Scale and/or Self-Similar Correlation Structure. There is merit, in the context of modeling both short- and long-range patterns of spatial variation of cross-sectional resistances $M_R(x)$ at different locations x along the axis of long earth slopes, to consider a class of 'multi-scale' random processes tending to exhibit self-similar behavior as has been observed in many natural phenomena, both temporal and spatial (Hurst 1951; Mandelbrot 1965).

In general, a stationary multi-scale random process, $Z(x)$, may be thought of as a sum of statistically independent component processes $Z_i(x)$, $i = 0, 1, ..., n$, each one characterized by its scale of fluctuation δ_i and its fractional contribution $\widetilde{Z}_i^2//\widetilde{Z}^2$ to the overall or composite variance $\widetilde{Z}^2$. Visualize the discrete *scale spectrum* (Vanmarcke 2010) of the composite process $Z(x)$ — it would show the component fractional contributions $\widetilde{Z}_i^2/\widetilde{Z}^2$, which sum to one, plotted against the component scales δ_i. The composite or overall scale of fluctuation of $Z(x)$, it is easy to show (Vanmarcke 2010), is just a weighted sum of the component scales, the weights being the fractional contributions to the total variance. There are important sampling-and-estimation issues

related to such multi-scale models — for instance, there may be little or no data on the larger-scale fluctuations, or one may be choose to treat them as (deterministic) trends — but these are beyond the scope of this paper.

Our interest focuses on composite random process models for $M_R(x)$ having a *wide scale spectrum*, i.e., for which the ratio δ_n/δ_0 is very large, which implies slow correlation decay and behavior indicative (by analogy to temporal variation) of 'long memory' and persistence of variability of local means, regardless of the averaging length. Instead of the power law $\Gamma(b) \propto b^{-1/2}$, for large values of b, one expects slower decay, characterized by $\Gamma(b) \propto b^{-\alpha}$, where $0 < \alpha < 1/2$. Indeed, as mentioned in the preceding subsection, one expects (and observes) this kind of slow decay of $\Gamma(b)$ even for single-scale random processes, when b-values are less than the scale of fluctuation.

Note that the standard deviation of the *local integral*, instead of the local average, over a given distance b, will also follow a power law, but with coefficient $\alpha + 0.5$. The latter is quite closely related to the (so-called) Hurst coefficient "H" used to characterize self-similar or fractal random variation. Note, however, that the 'Hurst effect' involves more than just the question of how local integration of a random process affects its 'point variance' — the original Hurst statistic (used to assess long-term storage capacity of the reservoir behind the Aswan Dam on the Nile River) is, by definition, the 'range' between minimum and maximum values of local integrals of a random process (observed for a long time or over a long distance). Hence, the coefficients "H" and "$1 + \alpha$", while related, are not directly comparable.

3-D Failure Risk Analysis in the Multi-Scale Case. We now examine the implications of the power-law behavior of the standard-deviation-reduction function, $\Gamma(b) \propto b^{-\alpha}$, with coefficient α in the range $0 < \alpha \leq 0.5$, for the 3-D slope-failure-risk analysis. The upper-bound value $\alpha = 0.5$ implies "single-scale-process behavior" (i.e., no long-term persistence of correlation), while lesser (positive) values of α are indicative of multi-scale-process (and/or self-similar) behavior. The function $\Gamma(b)$ characterizing the cross-sectional resisting moments $M_R(x)$ may thus generally be expressed as

$$\Gamma(b) \equiv \Gamma_{M_R}(b) = (\delta_0/b)^{\alpha}, \quad b \geq \delta_0, \;\; 0 < \alpha \leq 0.5, \tag{24}$$

in which $\delta_0 = \delta_{0,M_R}$ may be interpreted as the *smallest* scale of fluctuation of a presumed multi-scale random process model for $M_R(x)$. Also, we may assume $\Gamma(b) \approx 1$ when $0 \leq b \leq \delta_0$. No upper bound on b needs to be set when

using the power law in Eq. 24, as there is presumably (for practical purposes) no limit on the largest scale of fluctuation δ_n of the underlying multi-scale random process. Note that in case $\alpha = 0.5$, the function $\Gamma(b) \equiv \Gamma_{M_R}(b)$ behaves as for a single-scale random process, with scale $\delta \equiv \delta_{M_R} = \delta_0$.

Inserting the power law for $\Gamma(b)$ into Eq. 16, again setting the derivative of the ratio β_b/β equal to zero, and solving for b, yields a result similar to Eq. 20 for the critical failure-zone width, expressed as a multiple of d:

$$\frac{b_{cr}}{d} = \frac{1-\alpha}{\alpha} \cdot \frac{\overline{F}}{\overline{F}-1}. \tag{25}$$

When $\alpha = 0.5$, and hence $[(1-\alpha)/\alpha] = 1$, Eq. 25 reduces to Eq. 20. However, in case $M_R(x)$ has a *wide scale spectrum* and/or exhibits self-similar behavior, the α-value may be, say, 0.25, corresponding to $[(1-\alpha)/\alpha] = 3$.

Finally, inserting the above expression for the ratio b_{cr}/d into Eq. 16 yields the quotient of the *minimum* 3-D (width-dependent) reliability index $\beta_{b_{cr}}$ and the 2-D (cross-sectional) reliability index β,

$$\frac{\beta_{b_{cr}}}{\beta} = \frac{1}{1-\alpha} \cdot \frac{1}{\Gamma(b_{cr})}\,, \tag{26}$$

for values of the power-law coefficient α in the range $0 < \alpha \leq 0.5$. Eq. 26 reduces to Eq. 22 when $\alpha = 0.5$, in which case $(1-\alpha)^{-1} = 2$.

Comparing 2-D and 3-D Stochastic Slope Stability Analyses. Based on the results presented above — for different assumptions, expressed through the function $\Gamma(b)$, about the correlation structure of the cross-sectional resisting moments along the axis of a long slope or embankment — we conclude that one should expect the ratio of 3-D to 2-D reliability indices, β_b/β, for the critical value $b = b_{cr}$ of the failure-zone width, *to be close to two*. The reasons for this rather high value of the ratio $\beta_{b_{cr}}/\beta$ are: (1) the added resistance against sliding due to the (3-D) end effects, and (2) the variance reduction associated with *real* finite-width slope-sliding events. In light of the high sensitivity of the failure probability to the reliability index — note that the dominant factors in the expressions for $p_f(b)$ and p_f are, respectively, $\exp\{-\beta_b^2/2\}$ and $\exp\{-\beta^2/2\}$ — there is a clear message about the danger of doing stochastic slope stability analysis only within a 2-D framework, namely *over-conservatism* in the form of *gross over-estimation of the failure risk*.

RISK OF FAILURE OF LONG SLOPES

A most important 'system reliability' aspect of the slope stability problem is the dependence of risk of failure on the total length B of an earth slope, embankment or levee. Long 'linear' earth slopes associated with dams, dikes and highways should not fail anywhere along the axis, as any local failure may have severe 'system-wide' consequences. This aspect of 3-D probabilistic slope stability analysis differs greatly from that considered above. We now envision slope-failure events occurring at random, more or less frequently, along the axis of a long slope, and the focus is on trying to evaluate the mean rate of occurrence (per unit length along the slope axis) of such events — each event is a 3-D slope failure characterized by a failure-zone width $b_{cr} \ll B$. For long slopes, the chance of one or more failures somewhere along the slope axis, and hence the probability of 'system failure', steadily increases with the overall length B of the slope. This 'systemic risk', $P_F(B)$, can easily exceed the probability p_f estimated based on 2-D (cross-sectional) stochastic slope stability analysis, even though the latter is prone to giving very conservative results compared to the 3-D local-failure-risk estimate $p_f(b)$.

An effective and elegant way to deal with this problem is by 'threshold-crossing analysis', in which the factor of safety $F_b(x)$ is viewed as a function of x, the position of the center of the failure zone along the embankment axis. We assume that the failure-zone width b is fixed, in particular, at the value $b = b_{cr}$ obtained in the preceding section. A slope failure will occur if the safety factor $F_b(x)$ crosses into the unsafe domain $F_b < 1$ at any location x between $b/2$ and $B - b/2$. The condition $F_b(x) \leq 1$ is equivalent to:

$$U_b(x) = \frac{F_b(x) - \overline{F}_b}{\widetilde{F}_b} < \frac{(1 - \overline{F}_b)}{\widetilde{F}_b} = -\beta_b. \tag{27}$$

For any given location x, the left side is a standardized random variable with zero mean and unit standard deviation. It may also be viewed as a random function, $U_b(x)$, characterizing the fluctuations of the cross-sectional resisting moments locally averaged over the failure-zone width b centered at different locations x. A slope-sliding event within the axial length interval b centered at x is equivalent to $U_b(x)$ being below the failure threshold $(-\beta_b)$.

The random function $U_b(x)$ will tend to be Gaussian (since the resisting moments $M_{R,b}$ are approximately Gaussian, in accordance with the Central

Limit Theorem), and the slope reliability — or its 'survival' probability — will have the following approximate form (Vanmarcke 1975):

$$P_S(B) = \begin{cases} [1 - p_f(b)]\ \exp\{-(B-b)\ \nu(\beta_b)\}, & B \geq b, \\ 1 - p_f(B), & B \leq b, \end{cases} \tag{28}$$

in which $p_f(\cdot)$ is the probability of failure at any specific location (analyzed in the preceding section), and $\nu(\beta_b)$ is the rate of decay of the 'system reliability' per unit length along the slope axis. The probability of slope failure, $P_F(B) = 1 - P_S(B)$, can usually (in practice) be more simply expressed as follows:

$$P_F(B) \simeq \begin{cases} p_f(b) + (B-b)\ \nu(\beta_b), & B \geq b, \\ p_f(B), & B \leq b. \end{cases} \tag{29}$$

The above approximation, for $B \geq b$, is obtained by assuming $\nu(\beta_b) \ll 1$ and replacing the exponential form e^{-u} by $(1-u)$ in Eq. 28. Of course, this works only if the resulting value for $P_F(B)$ remains well below one — otherwise, one must use the original expression, Eq. 28. The term linear in B, in Eq. 29, is expected to dominate the failure risk for long slopes:

$$P_F(B) \simeq B\ \nu(\beta_b), \tag{30}$$

in which $\nu(\beta_b)$ is the rate of increase of the system-failure risk per unit length of the slope. Again, the 'linear approximation' is suitable only if it yields (system-failure) probabilities well below one. Also, the idea, throughout this section, is that b is to be set equal to the critical failure-zone width b_{cr}.

Growth Rate of System Failure Risk per Unit Length. From the theory of stationary Gaussian random processes, applied here to the normalized-safety-factor function $U_b(x)$, the mean rate $\nu(\beta_b)$ of down-crossings (per unit length) of the normalized failure threshold $(-\beta_b)$ can be expressed using the classical formula of S.O. Rice (1944):

$$\nu(\beta_b) = r_b\ \exp\{-\beta_b^2/2\}, \tag{31}$$

in which r_b denotes the mean *zero-crossing* rate, namely the value of $\nu(\beta_b)$ when $\beta_b = 0$. Eq. 31 indicates that the mean spatial rate of local-slope-failure events decreases rapidly as the reliability index β_b grows.

For any value $b > 0$, owing to the local averaging of cross-sectional resisting moments $M_(x)$, the derived one-dimensional random processes $M_{R_b}(x)$ and

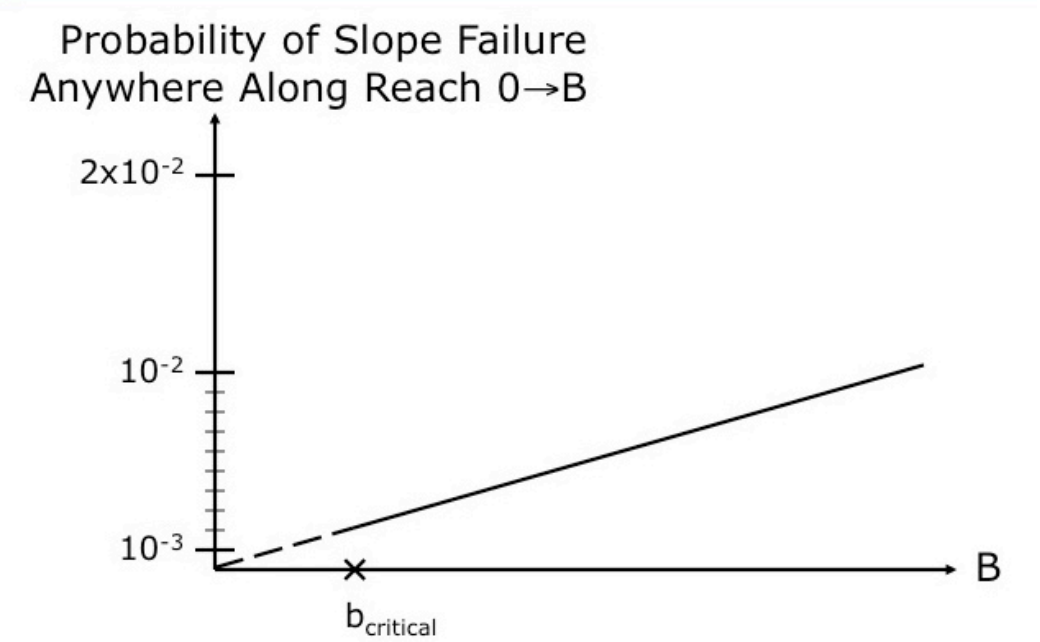

Figure 4: **Slope Failure Risk versus Length (when $P_F(B) \ll 1$)**

$F_b(x)$ (as well as the *normalized* safety-factor process $U_b(x)$) are sure to be "mean-square differentiable", that is, the variance of their derivative with respect to x is finite and can be reliably computed. An important related result is that the mean rate r_b can be expressed in terms of the correlation function $\rho(b)$ and the standard-deviation reduction factor $\Gamma(b)$ of the cross-sectional resisting moments $M_R(x)$, as follows (Vanmarcke 1983 & 2010):

$$r_b = \frac{1}{\pi\sqrt{2}} \frac{[1-\rho(b)]^{1/2}}{b\,\Gamma(b)}. \tag{32}$$

Combining Eqs. 31 and 32, and assuming $[1-\rho(b)] \approx 1$, amply justified by the fact that b is to be set equal to b_{cr}, yields

$$\nu(\beta_b) \approx [\pi\sqrt{2}\, b\, \Gamma(b)]^{-1}\ \exp\{-\beta_b^2/2\}. \tag{33}$$

We can now, in principle, evaluate $\nu(\beta_b)$ and $P_F(B)$ as a function of b for many different slip surfaces. A better choice is to adopt the "critical" cross-sectional failure arc (associated with $\overline{F}$ and found by deterministic analysis)

and replace b by the "critical failure-zone width" b_{cr}. This leads to the following estimate for the failure risk of a slope of length B, for $B \geq b_{cr}$:

$$P_F(B) \simeq \frac{B}{b_{cr}} \, (\pi\sqrt{2})^{-1} \, [\Gamma(b_{cr})]^{-1} \exp(-\beta_{b_{cr}}^2/2) \,, \tag{34}$$

presuming $P_F(B) \ll 1$. The predicted mean rate of growth of the slope-failure risk per unit length, namely the multiplier of B on the right side of Eq. 34, depends — indirectly, through b_{cr}, $\beta_{b_{cr}}$ and $\Gamma(b_{cr})$ — on the following: (1) the mean plane strain safety factor $\overline{F}$, obtainable from 2-D deterministic slope stability analysis; (2) the distance d, also obtainable from the deterministic analysis; and (3) the parameters expressing the variability and spatial correlation structure of the (one-dimensional) random process $M_R(x)$ of cross-sectional resisting moments, namely the coefficient of variation V_{M_R}, the scale of fluctuation $\delta = \delta_{M_R}$ and/or the power-law coefficient α.

The Concept of Equivalent Independent Segments. An interesting question, from a practical standpoint, concerns the validity of the concept of "equivalent independent segments", according to which one might try to estimate the failure probability $P_F(B)$, in case $P_F(B) \ll 1$, by adding (identical) segment-specific failure probabilities $p_f(b)$. A simple version of this would be to count the number of segments of width b_{cr} over the total length B, namely $N = B/b_{cr}$, and compare the prediction $P_F(B) \simeq N \, p_f(b_{cr})$ to the result obtained by threshold-crossing analysis, $P_F(B) \simeq B \, \nu(\beta_{b_{cr}})$. The values of the main quantities involved, $p_f(b)$ and $\nu(\beta_b)$ evaluated at $b = b_{cr}$, are dominated by the *same* exponential factor, $\exp(-\beta_b^2/2)$, which can vary by orders of magnitude. The question, more broadly, is whether there exists a stable-valued multiplier ϕ that can produce a "characteristic segment length" $\phi \, b_{cr}$, corresponding to a number $N' = B/(\phi \, b_{cr})$ of segments, such that the two estimates for the system-failure risk, $N' \, p_f(b)$ and $B \, \nu(\beta_b)$, for $b = b_{cr}$, agree across a wide range of possible values of the input variables. An approximate expression for ϕ, obtained by using Eqs. 19 and 34, is

$$\phi \approx \sqrt{\pi} \, \beta_{b_{cr}}^{-1} \, \Gamma(b_{cr}). \tag{35}$$

In case the critical failure-zone width, expressed (in Eq. 25) as $b_{cr} = b^* = [(1-\alpha)/\alpha][\overline{F}/(\overline{F}-1)]d$, exceeds δ, this surprisingly simple result is found:

$$\phi \approx \sqrt{\pi} \, \alpha \, V_F \, \frac{\delta}{d}. \tag{36}$$

For a set of conceivably-realistic values, $\alpha = 0.5$, $V_F = 0.1$ and $\delta = d$, Eq. 36 yields $\phi \approx 0.0886$. The implication, in this numerical example, is that a long-slope-failure-risk calculation based on the concept of "equivalent independent segments" — according to which the overall length B is divided into non-overlapping segments of size b_{cr}, and again presuming $P_F(B) \ll 1$ — would underestimate the failure risk of long slopes by quite a large factor, $1/\phi \approx 11.3$. The length b_{cr}, expressed a multiple of d, depends on α and the plane strain mean safety factor $\overline{F}$. For instance, taking $\overline{F} = 1.25$ and (again) $\alpha = 0.5$, yields $b_{cr} = 5\,d$. Therefore, if $d = \delta$ were chosen (instead of b_{cr}) as the characteristic–segment size, the slope-failure risk would still be underestimated, within the linear-in-B range, by a factor of more than two.

In conclusion, predicting the system-failure risk of long slopes by using the concept of "equivalent independent segments" yields unreliable results — and it is unnecessary in light of the availability of a more direct and fundamental approach to the problem: stochastic failure-threshold-crossing analysis.

Risk Assessment and Management of Long Earth Slopes. A most important 'system reliability' aspect of slope stability is the dependence of the systemic risk on the length of the embankment or levee. The failure risk grows nearly linearly with B, provided the calculated risk is well below one. An argument can be made that the estimate for $P_F(B)$ thus obtained constitutes a close lower bound to the slope failure probability: slip surfaces different from the critical surface as regards location, length or shape are not explicitly accounted for, but elements favoring the closeness of the bound are: (1) the strong correlation among failure events associated with adjacent, partially overlapping failure surfaces (and masses of soil); and (2) the decay of the failure probability for failure surfaces different from the critical one.

The relationship between the slope failure risk $P_F(B)$ and the length B can be used in making risk-informed design decisions (or, for existing structures, decisions about maintenance and upgrading). Specifically, the methodology enables one to determine the required plane strain mean safety factor $\overline{F}$ to achieve a prescribed system-reliability criterion, e.g., $P_F(B) = 10^{-3}$. The required value of $\overline{F}$ will depend on the length of the slope and on the variability and correlation structure of the cross-sectional resisting moments.

Any attempt to perform long-slope-failure-risk calculations based only on the 2-D (cross-sectional) reliability index β is bound to disappoint, because β is expected to fall well below the 3-D reliability index β_b, while calculated

risks are hyper-sensitive to the reliability index. Related, it is very important to distinguish clearly between 3-D probabilistic analyses that (1) assess the effect of the out-of-plane width b in single, local slope-failure events (leading to estimates for $p_f(b)$, in our notation), and (2) evaluate the risk of a failure event — one or more — occurring anywhere along the axis of a long slope (leading to estimates for $P_F(B)$, in our notation). The former yields a failure probability, $p_f(b)$, that is always less than the corresponding probability p_f obtained by 2-D analysis, while the latter yields a system failure probability $P_F(B)$ which, for large enough values of B, can easily exceed p_f. A recent paper on stochastic-finite-element-based estimation of 3-D slope reliability by Griffiths al. (2009) fails to make this distinction and reaches doubtful conclusions about how the results of 2-D and 3-D reliability analyses compare.

FURTHER OBSERVATIONS

(1) The probabilities $p_f(b)$ and $P_F(B)$ have been expressed in terms of the reliability index $\beta_b = (\overline{F}_b - 1)/\widetilde{F}_b$. Identical results are obtained when failure events are expressed in terms of the *safety margin*, namely the difference between the resisting moment and the driving moment, in case the latter is treated as deterministic, or is prescribed. Failure occurs if the safety margin $(M_R - M_D)$ turns negative or if the normalized safety margin becomes less than $(-\beta_b^{'})$, where $\beta_b^{'}$ is now defined as the quotient of the mean and the standard deviation of the safety margin. The two reliability indices, $\beta_b^{'}$ and β_b, are identical if there is no uncertainty in the driving moment.

(2) For long slopes, if the cross-sections vary (systematically, predictably) as a function of the location x along the axis, and/or if either the soil layer depths or the soil properties have known trends or discontinuities, the decay rate $\nu(\beta_b)$ will likewise become dependent on x. Extension of the preceding analysis is straightforward if a slope can be divided into relatively long 'nominally homogeneous' segments with lengths B_1, B_2, etc. For each segment the critical values of b and $\nu(\beta_b)$ need to be determined and the segment-specific failure probabilities may be added, provided the sum of the probabilities involved is small, to obtain the "system" failure probability.

(3) In the multi-scale model, the slow random fluctuations of local averages of the resisting moment $M_R(x)$ along the slope axis may be seen as a reducible source of uncertainty. By spacing boreholes (and determining the strength

profile) along the embankment axis at intervals Δx smaller than the scale(s) of fluctuation of the more slowly varying components, one may succeed in significantly reducing the fraction of the variance in the safety factor F_b attributable to the more slowly varying components. This is an example of how formal risk analysis can be used to evaluate, in quantitative terms, the (risk-reduction) benefits of geotechnical data acquisition.

(4) The probabilistic analysis has explicitly recognized only the true or inherent variability of the shear strength. The failure risk is expressed as a function of the reliability index, which in turn depends on the statistical parameters of the random variables contributing to the strength. The analysis assumes that these parameters are known, and essentially evaluates the *conditional* probability of failure given the parameter values. In reality, these values must be estimated on the basis of a limited geological information, imperfect field or laboratory strength measurements, and engineering judgment and experience. In principle, the procedure for incorporating such added uncertainty is straightforward: one obtains the value of $P_F(B)$ corresponding to each possible set of strength (and model) parameters, and then weighs these estimates according to their relative likelihood. Needless to say, the data base to accomplish this task is not yet available. In particular, for different soil types more pertinent information is needed about the variability and spatial correlation of soil properties such as shear strength.

(5) Random external loads may be treated in a similar way. These loads may be quite predictable (e.g., surcharges, hydrostatic loads) or highly unpredictable (e.g., earthquake loads). In either case, the analysis just presented may be used to obtain estimates of the *conditional* risk of slope failure given the external loading. These conditional probabilities must then be combined with the results of an assessment of the likelihood of occurrence of various load levels during the (intended) operational life of a (spatially extended) structure. Considering external loads such as floods and earthquakes will make the failure risk of slopes or levees dependent on both time and space. In the case of seismic loading, one needs to consider the likelihood of strong ground motion — dependent on the frequency of potentially damaging earthquakes in the region — as well as the characteristics of the ground motion, including its spatial variation, during an earthquake. Considering potential slope failures due to flooding caused by rainfall during tropical storms, different scenarios of potential global change (in tropical-storm frequency and intensity) will introduce long-term trends in slope failure risks.

CONCLUSIONS

This paper addressed the classical limit equilibrium slope stability problem within a three-dimensional and (analytical, closed-form) probabilistic framework. The methodology can be applied to safety assessment of slopes with rather general strength characteristics and drainage conditions, and can be adapted to any deterministic plane strain stability analysis method. Also, it can accommodate a wide range of models for the correlation structure of the cross-sectional sliding resistances along the slope axis, including those consistent with multi-scale and self-similar patterns of random variation.

The paper clearly demonstrates the importance, in fact the necessity, of accounting for the three-dimensional nature of the problem in extending conventional stability analysis into the realm of quantitative risk assessment. For long embankments, failure events involving either very long or very short failure zones are shown to be improbable. The existence of a most likely failure-zone width is revealed and a method to evaluate it is presented.

Based on a comparison of reliability indices — linked directly to calculated failure probabilities — obtained by means of 3-D and 2-D stochastic slope stability analysis, we reach these practically-significant conclusions. First, the reliability index derived based on 2-D (plane strain) slope stability analysis is always conservative relative to that obtained from 3-D analysis. Second, for any realistic parameter values, the 2-D analysis yields over-conservative results, i.e., estimates for the probability of a (localized) slope-failure event that may be orders of magnitude too high. Such conservatism (in risk estimation) defeats the purpose of risk assessment and the promise of risk-informed decision-making (for this class of problems) in geotechnical engineering.

An estimate is obtained for the probability $P_F(B)$ that a failure, often with system-wide consequences, will occur anywhere along the axis of (long) slope of given total length B. In the basic analysis, the cross-sectional properties, nominally identical, are modeled as randomly varying along the axis of the slope. The dominant contribution to $P_F(B)$, provided $P_F(B) \ll 1$, is found to be a term linear in B, and we evaluate the mean rate of local-slope-failure events per unit of length (along the slope axis). Extension of this analysis is straightforward if a long slope can be divided into 'nominally homogeneous' segments with lengths B_1, B_2, etc. The segment-specific failure probabilities may then be added, provided the sum of probabilities involved is small,

to obtain the "system" failure probability. These results have important implications in the design of cuts and slopes, and provides the basis for development of more rational reliability-based criteria for designing 'lifelines' such as highway or railway embankments, dams, dikes and levees.

The main source of uncertainty accounted for in the stochastic slope stability analysis is the spatial variation of cross-sectional resistances against sliding. If the results of the risk analysis are interpreted as conditional probabilities, however, the methodology provides the basis for more complete slope reliability assessment in which other (partially uncertain) information, mainly about loading and environmental conditions, can be incorporated.

ACKNOWLEDGMENT

The writer acknowledges partial support for this research under a project entitled Improved Hurricane Risk Assessment with Links to Earth System Models, funded through the Cooperative Institute for Climate Science (CICS) by the National Oceanographic and Atmospheric Administration (NOAA).

REFERENCES

Alonso, E.E. (1976). "Risk analysis of slopes and its application to slopes in Canadian sensitive clays." *Geotechnique*, 26(3): 453-472.

Bishop, A.W. (1955). "The use of the slip circle in the stability analysis of slopes." *J. Geotechnique*, 5(1), 7-17.

Christian, J.T., Ladd, C.C. and Baecher, G.B. (1994). "Reliability applied to slope stability analysis." *J. Geotech. Eng. ASCE*, 120(12), 2180-2207.

Dwight, H.B. (1961) *Tables of Integrals and Other Mathematical Data*, 4th Edition, MacMillan, New York

Fellenius, W. (1936). "Calculation of the stability of earth dams." *Trans. Congr. Large Dams, 2nd*, Washington, 4: 445.

Griffiths, D.V. and Fenton, G.A. (2004). "Probabilistic slope stability analysis by finite elements." *J. Geotech. Geoenviron. Eng.*, ASCE, 130(5), 507-518.

Griffiths, D.V., Huang, J. and Fenton, G.A. (2009). "On the reliability of earth slopes in three dimensions." *Proceedings of the Royal Society A*, 465(2110), 3145–3164.

Hachich, W. and Vanmarcke, E. (1983). "Probabilistic updating of pore pressure fields." *J. Geot. Eng. Div.*, ASCE, vol. 109, 373-385.

Hurst, H.E. (1951). "Long-term storage capacity of reservoirs." *Trans. Am. Soc. Civil. Eng.* 116, 770-799.

Lacasse, E.E. (1994). "Reliability and probabilistic methods." *Proc. 6th Int. Conf. Appl. Stat. Problems in Civil Eng.*, 225-227.

Lacasse, E.E. and and Nadim, F. (1996). "Uncertainties in characterizing soil properties." *ASCE Uncertainties'96 Conf. Proc.*, 49-75.

Li, K.S. and Lumb, P. (1987). "Probabilistic design of slopes." *Can. Geotech. J.*, 24(4), 520-535.

Low, B.K., Gilbert, R.B. and Wright, S.G. (1998). "Slope reliability analysis using generalized method of slices." *J. Geotech. Geoenviron. Eng.*, ASCE, 124(4), 350-362.

Low, B.K. , Lacasse, S. and Nadim, F. (2007) ''Slope reliability analysis accounting for spatial variation." *Georisk*, 1(4), 177-189.

Mandelbrot, B.B. (1965). "Une classe de processus homothetiques a soi: Application a la loi climatologique de H.E. Hurst." *C.R. Acad. Sci.*, Paris, 260, 3274-3277.

Matsuo, M. (1976). "Reliability in embankment design." Mass. Inst. Tech., Dept. Civil Eng., Report R76-33.

Rice, S.O. (1944). "Mathematical analysis of random noise." *Bell System Technical J.*, 32, 282.

Vanmarcke, E. (1975). "On the distribution of the first-passage time for normal stationary random processes." *J. Appl. Mech.*, 42: 215-220.

Vanmarcke, E. (1977a). "Probabilistic modeling of soil profiles." *J. Geotech. Eng. Div.*, ASCE, 103 (GT11) 1227-1246.

Vanmarcke, E. (1977b). "Reliability of earth slopes." *J. Geotech. Eng. Div.*, ASCE, 103 (GT11) 1247-1265.

Vanmarcke, E. (1980). "Probabilistic stability analysis of earth slopes." *Eng. Geol.*, 16: 29-50.

Vanmarcke, E. (2010). *Random Fields: Analysis and Synthesis*, 2nd Edition, World Scientific Publishing Company; 1st Edition, M.I.T. Press, 1983.

Wu, T.H. and Kraft, L.M. (1970). "Safety analysis of slopes." *J. Soil Mech. Found. Div.*, 96, 609-630.

Yucemen, W.S., Tang, W.H., and Ang, A.H.S. (1973). "A Probabilistic Study of Safety and Design of Earth Slopes." University of Illinois Research Report.

Development of a Risk-based Landslide Warning System

Wilson H. Tang[1] and L. M. Zhang[2]

[1] Professor Emeritus, The Hong Kong University of Science and Technology, Clear Water Bay, Hong Kong; e-mail: wtang@ust.hk
[2] Professor, The Hong Kong University of Science and Technology, Clear Water Bay, Hong Kong; e-mail: cezhangl@ust.hk

ABSTRACT

A risk-based, real-time landslide warning system is being developed for Provincial Road 303 near the epicenter of the 2008 Wenchuan Earthquake. The essence of the warning system is to warn the traffic or construction teams of the risks in different parts of the road caused by an imminent storm or ongoing rainfall event. The terrains along the road are divided into cells based on types of hazards (landslides, rockfalls, or debris flows) and geomorphic considerations. Digital elevation models for the cells have been constructed based on results of remote sensing and local engineering surveys. A rain-gauge network has been established to measure real time rainfall distributions over the cells, considering changes in elevation and wind direction. The occurrence probability of landslides in each cell in response to a recorded rainfall event is evaluated using standard reliability methods. Based on such failure probabilities, it is possible to produce a real-time risk map along the road. The warning levels for different cells are then determined separately by further considering their respective total potential loss of lives and expected mortality rate.

INTRODUCTION

The 2008 Wenchuan earthquake in China triggered over 45,000 landslides, rock avalanches and collapses (Xu et al. 2010). The debris of these landslides deposited on steep terrains. In normal weather conditions such deposits are in a quasi-stable condition. Upon severe storms, many of these loose deposits may loose stability, which then either fall down from high elevations or turn into torrential debris flows. Instability of the landslide scars may also be triggered by normal rainfall. In the summers of 2008, 2009, and 2010, numerous slides, debris flows and rock falls occurred and caused a large number of casualty and serious damage to properties. Multiple geohazards not only occurred at particular sites, but also developed over time as a disaster chain (Zhang 2009; Zhang et al. 2010). The term “landslide” is broadly used in this paper to represent any slide, debris flow or rockfall event.

The 45 km segment of Provincial Road 303 (PR303) between Yingxiu and Wolong in Sichuan Province, China, goes across the epicenter of the 2008 Wenchuan earthquake. Wolong is where the Great Panda National Reserve is located. About 40 km west of Wolong is another scenic spot, the 6251 m tall Four-Girl Mountain. The alignment of the road between Yinxiu and Wolong is primarily along the Yiziqi River. The river is bounded by terrains with elevations between 900 and 5100 m (Fig. 1). The terrains on both sides of the road are rather steep, between 40 and 84 degrees in many places as shown in Fig. 2. The valley depths along the road range from a few hundred meters to over 2000 m (Fig. 1).

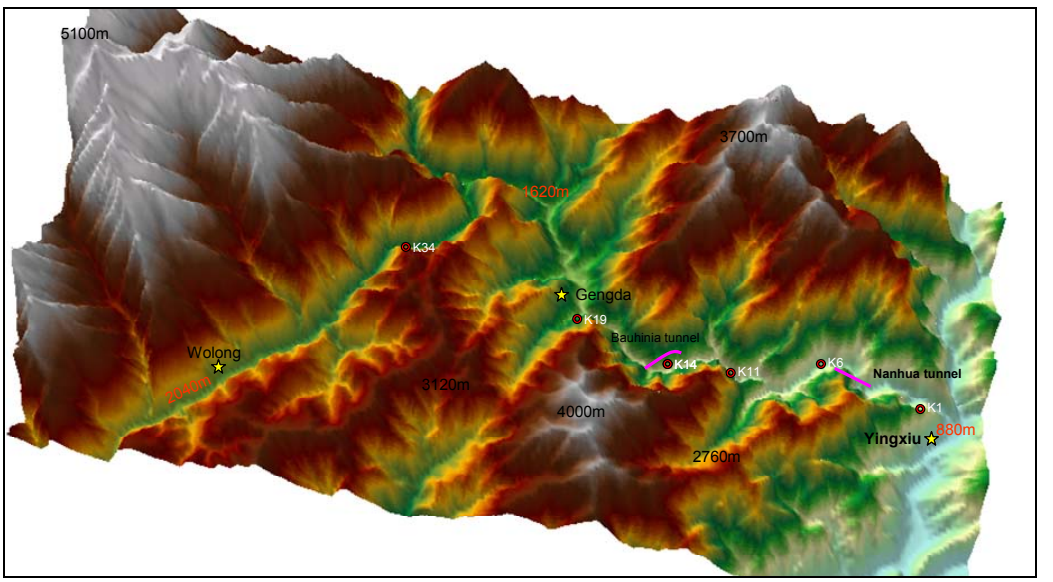

Figure 1. Topography of PR303 shortly after the 2008 Wenchuan earthquake.

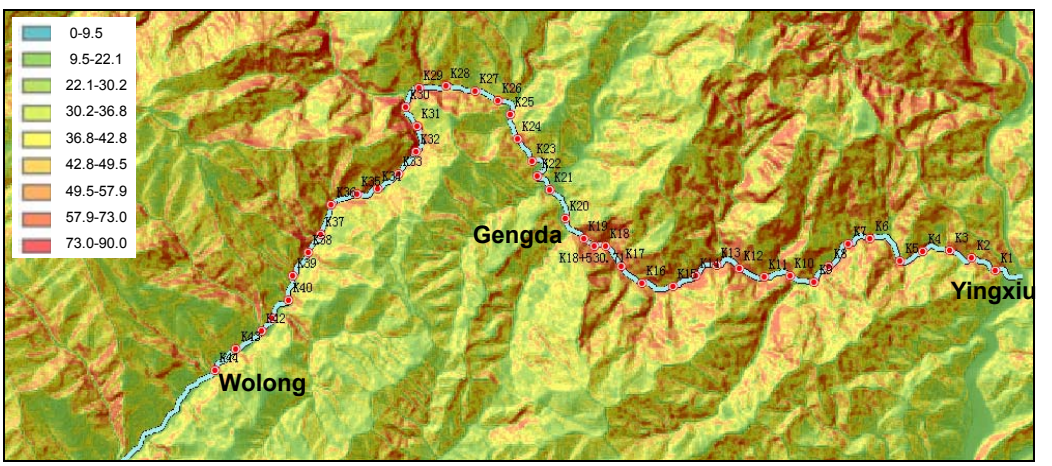

Figure 2. Gradient of the natural terrain along PR303.

This paper outlines a risk-based landslide warning system established for PR303. The geologic settings and some post-earthquake failure events along the road are described first. Then why a risk- and raingauge-based warning methodology is

adopted for the warning system is explained. Next, the basic components of the warning systems and the risk assessment procedure are described. Finally, the proposed warning criteria are delineated.

THE NEED FOR A LANDSLIDE WARNING SYSTEM

Post-earthquake failure events

Approximately 80% of the road between Yingxiu to Gengda (Fig. 2) was either buried by landslides or severely damaged during the earthquake. Much of the steep terrain is covered with loose landslide deposits and under numerous shattered rock slide scars, as shown in Fig. 3. According to a field investigation conducted shortly after the earthquake by Sichuan Provincial Highway Design Institute (2008), the road was affected directly by 72 rock avalanches/collapses, 68 rockfalls, 17 debris flows, and 4 landslides. Fig. 4 shows two scenarios of road damage. In Fig. 4(a), the majority of a segment of the road along the valley was buried by landslide deposits from the steep terrains. In Fig. 4(b), rocks fall from high elevations either during a rain event or after the end of a sunny day.

Figure 3. Distribution of slides and rockfalls between Yingxiu and Gengda.

Figure 4. PR303 shortly after the earthquake: (a) buried roadbed along the bottom of the valley; (b) boulder falls from high elevations.

Numerous landslides occurred in the summers of 2008, 2009, and 2010. Fig. 5 shows several landslide-induced rockfall scenarios at K13+500. A rockfall barrier was constructed in March 2010. It was completely destroyed by June 2010 after several rockfall events. A reinforced concrete open tunnel was constructed to replace the rockfall barrier. The open tunnel was buried by a 20,000 m^3 slide and penetrated by a large boulder on 6 July 2010.

Figure 5. Damage of rockfall barrier and a rockfall protection tunnel due to repeated rockfalls at K13+500 in 2010.

On 13-14 August 2010, a severe storm swept the study area, with 160 mm rainfall in 8 hours. This storm triggered about 35 failure events including debris flows, rockfalls, and slides. Four debris flows between milestones K2+700 and K7+100, in particular caused serious damage to PR303. For instance, the debris flow originating from the Xiaojiagou ravine had a volume of approximately 1 million m^3, and a run-out distance of 1800 m. The debris material buried the road between milestones K4+400 and K5+500 and the outlet of an important tunnel, and formed a debris lake. These four debris flows led to the damage of 6.2 km of road (4.6 km buried by the debris and 1.6 km submerged by the debris lake). The riverbed also rose by 21 m in some places due to the deposition of the debris flow materials. As a result of these debris flows and the rising riverbed, several kilometers of the newly-built road had to be abandoned and re-reconstruction had to be started.

Figure 6. Large debris flows at K4+400 - K5+500.

Need for a landslide warning system

The reconstruction of PR303 started in April 2009. Although effort has been made to strengthen some unsafe slopes at reachable elevations, many sources of hazards at high elevations have not been identified. In fact, numerous landslides occurred since the start of the highway construction as mentioned earlier. It is expected that similar landslide events will continue to occur after the commission of the re-constructed highway. The situation prompts the need for an effective landslide warning system to minimize potential loss of lives.

ADOPTION OF A RAINFALL- AND RISK-BASED WARNING SYSTEM

Warning of a particular type of landslide may be made based on

- Measurement of ground surface movements using optical surveys, fissurometers, tilt meters, GPS, terrestrial photogrammetry, ground-based radar interferometry, image analysis etc. (e.g., Gili et al. 2000; Chang and Lin 2007; Casagli et al. 2010);
- Measurement of underground movements using inclinometers, magnetic settlement transducers etc. (e.g, Yin et al. 2010);
- Measurement of movement/stress related physical quantities using distributed fiber optics, ground tremor sensors, geophones etc. (e.g., Kurihara 1997; Liu 1999);
- Measurement of triggering factors such as rainfall and groundwater, etc. (e.g., Campbell 1975; Apip et al. 2010; Baum and Godt 2010; Yin et al. 2010).

Measurements of surface and underground movements or movement/stress related physical quantities serve as good indicators for warning against the failure of a well defined slope. In fact, monitoring a few important slopes along a highway is the most frequently adopted method when such slopes are clearly identified. By measuring the movements at several indicating points on a slope or the stresses in slope supporting structural elements, it is possible to evaluate the stability of the slope at a particular time against pre-specified thresholds of the monitored quantities, and to predict the future performance of the slope based on the trends of movement/stress. Measurements of triggering factors such as rainfall, on the other hand, serve as

indicators for warning against failure of a large number of slopes.

In this project, the latter method, i.e., warning based on measurements of real-time rainfall, is adopted for the following four reasons:

- Dense distribution of hazards: Over 160 spots along the road under study were impacted by various slides, falls and debris flows in the past 2.5 years. It would be difficult to instrument and monitor all of them.
- Inaccessible hazards at up to 2000 m above the road: During the reconstruction of PR303, the contractors had cleared much of the dangerous boulders and quasi-stable loose deposits located in the belt about 100 m away from the road, and installed wire meshes on road-side rock cliffs. However, numerous loose deposits and landslide scars on the steep terrains a few hundreds to 2000 m above the road could not be stabilized due to access problems. In fact, these high-elevation hazards have been the main sources of damage in the past 2.5 years. It is not feasible to instrument substandard slopes at such high elevations.
- Sources of hazards not yet clearly identified: The great number of hazardous slopes in the steep terrains that may adversely affect the highway (Figs. 1-3) have not been clearly identified even using latest remote sensing technologies. Some injury or damage events occurred without knowing exactly where the falling materials came from. Randomly choosing a few places to monitor helps little to improve the general risk profile of the road.
- Sustainability of warning system: While large movements usually occur before a loose deposit detaches from the bedding material, sensitive instruments such as fiber optic sensors and inclinometers embedded in the soil slope will be destroyed once the slope fails. Replacement of sensors is costly. Noticing that slides and falls occurred at the same location repeatedly, the use of embedded sensors is less appealing in terms of both robustness and costs.

In contrast, warning methods that rely on the measurement of triggering factors such as rainfall, temperature, wind, etc., are more suitable for the conditions along PR303. In this project, a risk- and raingauge-based warning methodology is adopted. The anticipated advantages of this method are as follows:

- Accommodating a large number of slopes.
- Accommodating uncertain and inaccessible sources of hazards.
- Robustness and lower operational costs.

MODULES OF THE WARNING SYSTEM

Einstein and Sousa (2006) described essential elements of a warning system. The general principle of the proposed risk-based warning system for PR303 is shown in Fig. 7. The major steps in developing the risk-based warning system include:

- Divide the terrain along the road into several zones based on their topographic and geologic conditions and failure types (slides, debris flows, and rockfalls) occurred in the past 2.5 years;
- Install a real-time rain-gauge network and measure the rainfall distribution over the study area;
- Predict the likelihood of the occurrence of each type of rain-induced failure in

each zone;
- Assess the risk to the traffic and road facilities;
- Develop warning criteria for each zone based on recorded or forecasted rainfall, and issue warning messages through an integrated traffic safety system.

Accordingly, the entire warning system consists of five modules: an automatic rain gauge network, digital terrain models, geotechnical reliability analysis models, risk assessment models, and a warning-issuing system. These modules are described separately in the following sections.

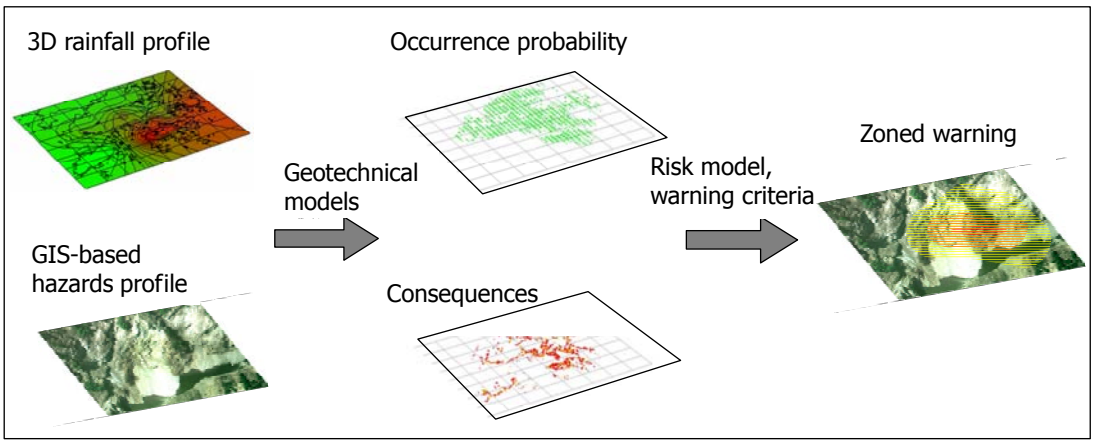

Figure 7. General principle of the proposed landslide warning system.

THREE-DIMENSIONAL AUTOMATIC RAINGAUGE NETWORK

Rainfall has been shown to be the primary trigger of various types of failures along the road after the 2008 Wenchuan earthquake. The rainfall amount in the study area is affected greatly by the climate and local topographic conditions. The elevation of the road varies from 880 m at Yingxiu to 1500 m at Gengda. The average yearly rainfall and temperature along this section vary in the rages of 1002 – 1265 mm and 15.2 - 15.9°C, respectively. The elevation of the road from Gengda to Wolong varies from 1500 m to 2040 m; the average yearly rainfall and temperature in this section decrease dramatically to 828 mm and 5.0°C, respectively. Considering the sensitivity of occurrence of slope failures to rainfall characteristics as will be discussed later in this paper, it is necessary to measure the variations of rainfall along the road. Hence, 20 rain gauges were installed along the road, spaced approximately at 3 km, as shown in Fig. 8.

The safety of a specific segment of road may be affected by hazards in a large terrain on both sides of the road. The influential terrain is here defined as the catchments from which any detached material may have an adverse impact on the road. For instance, the rockfalls at K34 were found to originate from the collapse of the scars approximately 700 m above the road; the debris flow at K5 was from the loose deposits distributed in terrains up to 1900 m above the road. Hence, it is equally important to measure, at a particular milestone, the variations of rainfall with terrain

elevation and wind direction. In this project, six rain gauges were installed in two cross sections of the road, 3 gauges each section, as shown in Fig. 8.

The single tipping bucket rain gauges are adopted (Fig. 9(a)). The gauge has an orifice diameter of 200 mm and rainfall resolution of 0.1 mm. It comes with an automatic data acquisition system powered by a storage battery and a 20 W solar panel. Rainfall data is transmitted to the control center using a General Packet Radio Service (GPRS) wireless communication network (Fig. 9(b)). The data is then processed at the control center. The sampling frequency is adjustable: every 5 minutes upon heavy rain and a longer period when there is no rain. Therefore, it is possible that the risk profile of the road be updated regularly.

Even though 20 rain gauges have been installed in the study area of approximately 100 km^2, the rainfall values at many locations are still not available and have to be extrapolated or interpolated based on the rainfall values at the 20 measurement locations. A Kriging method is developed for this purpose.

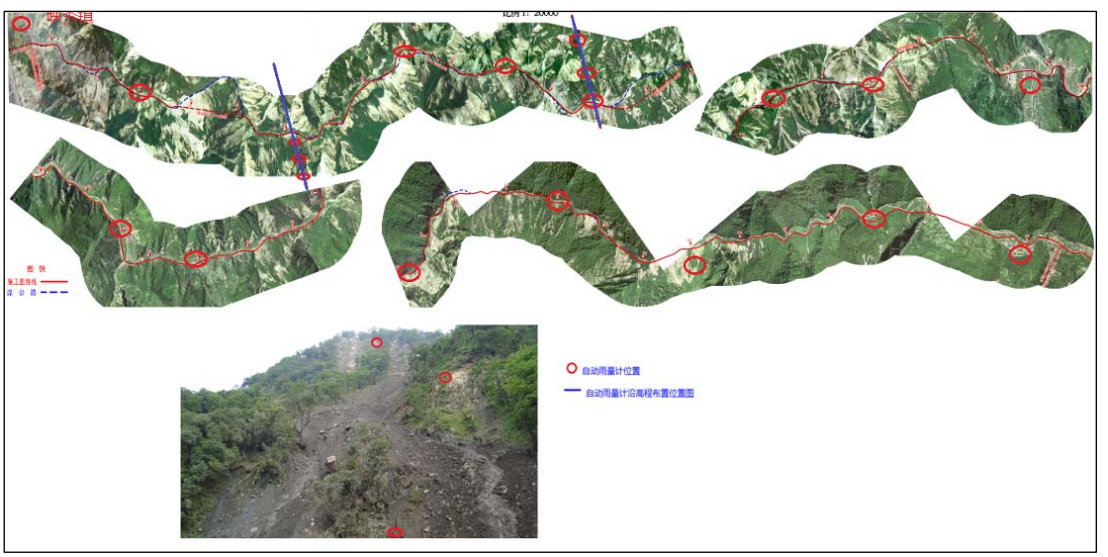

Figure 8. Three-dimensional automatic rain-gauge system.

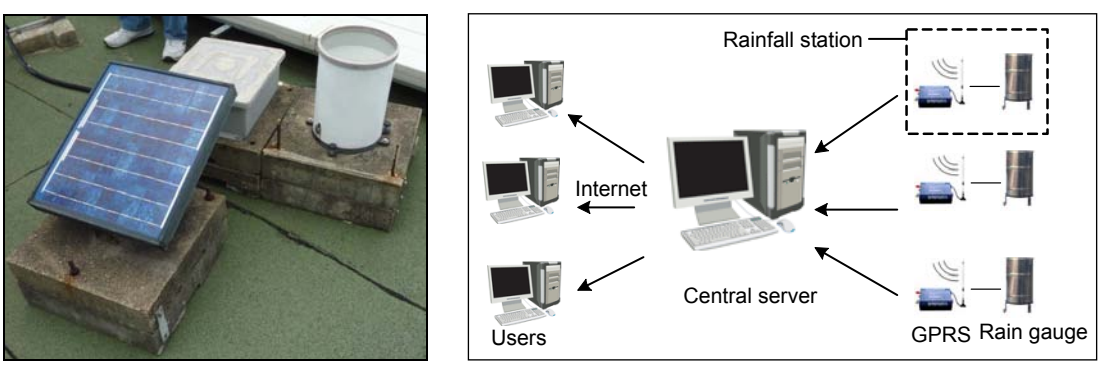

(a) (b)

Figure 9. (a) A GEO rain gauge; (b) transmission of rainfall data through a GPRS wireless communication system.

DIGITAL TERRAIN AND LITHOLOGY MODELS

The terrain models are created in a GIS framework. A three-dimensional digital elevation map (Fig. 1) is available with an elevation contour resolution of 2.0 m along a 400 m wide strip along the road, and 20 m away from the strip. To facilitate stability analysis and risk analysis, the information of the terrain has been separated into several layers: lithology, streams, roads, land use, highway facilities; and other facilities.

RELIABILITY MODELS

Statistical models

Risks caused by weather-related geohazards can be assessed based on landslide-rainfall correlations using statistical models. Statistical analyses can be performed at several levels based on the amount of information available: analysis of threshold rainfall; rainfall-landslide frequency correlations; and multi-variable analysis of landslide triggering factors.

Analysis of threshold rainfalls

Numerous researchers have established separate empirical relations to estimate threshold rainfalls that may trigger slides, rockfalls or debris flows (Jibson 1989; Bolley and Oliaro 1999, Chau et al. 2003; NOAA-USGS Debris-Flow Task Force 2005; Baum and Godt 2010). The threshold rainfall is usually expressed as a relation between rainfall intensity, I, and rainfall duration, D. A local I-D relation cannot be easily extrapolated to neighboring regions because the annual precipitation and rainfall distribution of one region may be different from those of another region. One way to overcome this shortage is to normalize the rain intensity by dividing the event rainfall intensity by the mean annual precipitation (e.g. Jibson 1989). The total event rainfall, defined as the amount of rainfall in a certain period beyond which landslides will occur, is sometimes used as a threshold (e.g. Corominas and Moya 1999; Baum and Godt 2010). Data of threshold rainfalls for a particular type of landslides in the Wenchuan Earthquake zone is rather limited.

The empirical relations are statistically valid and provide threshold rainfalls for issuing warning signals. However, the approach may not be applicable to specific slopes. In addition, it does not indicate the severity of hazards.

Rainfall-landslide frequency correlations

The Geotechnical Engineering Office of the Hong Kong Government compiled a Natural Terrain Landslide Inventory (King 1999). Based on the available data between 1985 and 2000, Evans (1997) and Ko (2005) investigated the correlations between rainfall and landslide frequency for natural terrain slopes. Maximum rolling 24-hour rainfall normalized by location-specific mean annual rainfall was adopted to represent the severity of the rainfall conditions at different locations. Both a year-based rainfall-natural terrain landslide correlation and storm-based correlation were established. The storm-based correlation enables the assessment of the probability of occurrence of different natural terrain landslide densities under different rainfall

scenarios, and are applicable to hazard identification, risk quantification and formulation of natural terrain landslide warning system. Such correlation can be used as a basis to develop risk-based warning criteria when the distribution of natural slopes in the entire territory is available. Finlay et al. (1997), Yu (2004) conducted similar analysis for man-made slopes in Hong Kong. Based on the comprehensive failure record Cheung and Tang (2005a, 2005b) established an increased failure rate with time. Such relation could be used to facilitate effective landslide hazard management.

Multi-variable analysis of landslide triggering index

To include local conditions, it is possible to relate a landslide index (or occurrence probability) for a particular type of landslide with several site-specific specific triggering factors in addition to the local rainfall. Several methods have been utilized to establish multi-variable correlations, such as logistic regression method (Dai and Lee 2001). Additional factors include geological conditions (rock minerals, topographic information, tectonic geology, engineering geology, hydrogeology, ravine density, and vegetation), hazard density, and human activities. Warning decision can be made based on the calculated landslide index. For instance, China Institute of Geo-environment Monitoring (2005) and China Meteorological Bureau use the occurrence probability from a multi-variable regression analysis as the basis for nation -wide geohazard warning. Warning is issued when the estimated occurrence probability is greater than 40%. The benefit of the practice is its ability to identify regions of high level hazards. The method is, however, not based on consequences.

Physical models

As the geological conditions and rainfall characteristics vary significantly along the road and landslide data in the past 2.5 years is limited, it is difficult to establish credible rainfall-landslide correlations for general uses. Therefore, physically-based models for assessing landslide risks are resorted to in this project. The road is under a multi-hazard environment; hence physical analyses for slides, rockfalls, and debris flows must be conducted separately. In the following sections, the assessment of risks of loose deposits along the road segment between K2 and K7 is illustrated.

Loose deposits between K2 and K7

The terrains along the 5-km long road segment between K2 and K7 are very steep as the bedrocks are generally hard rocks, primarily granite and granodiorite. The terrains are covered with numerous loose soil deposits formed by collapses during the earthquake. Using a GIS-based technique, 53 soil deposits can be identified as shown in Fig. 10. These deposits are distributed along four ravines; namely, Pubugou Ravine, Xiaojiagou Ravine, Hanhua Ravine and Wasigou Ravine. The area, average slope angle, scar and toe elevations of each of these soil deposits are listed in Table 1. These deposits, together with the soil deposits at the bottom of the valleys, are the main source of instability. Rockfalls occur when surface boulders lose support upon erosion of soil. Small to medium scale channelized debris flows occur when the deposits at the bottom of the valleys erode by surface runoff. Large scale debris flows occur when the overland deposits slide into the valleys during a severe storm. The probability of failure of each of the deposits in Table 1 and the associated risk will be evaluated.

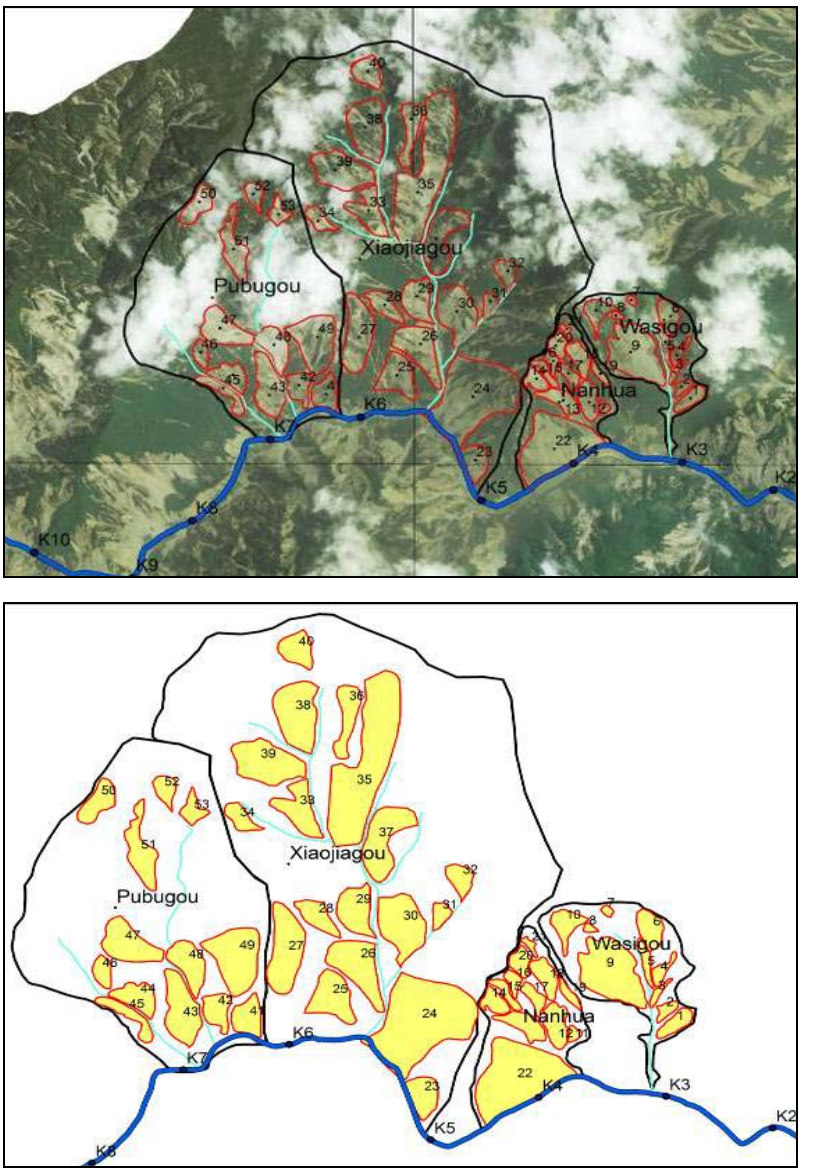

Figure 10. Distribution of 53 loose soil deposits between K2 and K7 along PR303.

Table 1. List of 53 loose soil deposits identified between K2 and K7 along PR303.

Deposit ID	Area (m^2)	Toe elevation (m)	Scar elevation (m)	Elevation difference (m)	Average slope angle (degree)	Distance between toe and road (m)
1	36353	1220	1570	350	33	1123
2	16479	1305	1540	235	26	1246
3	11919	1200	1575	375	31	1452
4	20472	1460	1750	290	29	1650
5	23025	1460	1800	340	6	1732
6	52000	1705	2060	355	27	2053
7	6263	2040	2150	110	28	2382
8	6070	2020	2130	110	27	2250

9	211690	1390	2010	620	24	1662
10	49522	1900	2240	340	27	2251
11	10367	1270	1375	105	32	636
12	56418	1265	1560	295	26	930
13	52914	1330	1685	355	24	1011
14	33082	1610	1850	240	20	1064
15	21598	1570	1880	310	28	1218
16	18035	1675	1900	225	29	1411
17	25924	1460	1780	320	26	1128
18	46010	1570	1930	360	20	1386
19	16568	1485	1710	225	34	1061
20	30589	1780	2095	315	23	1537
21	9155	1950	2130	180	19	1717
22	318104	1000	1450	450	29	883
23	70435	1100	1320	220	31	501
24	447089	1080	1760	680	24	1252
25	108174	1100	1490	390	19	778
26	139565	1180	1640	460	25	1415
27	161512	1400	2100	700	22	1374
28	57665	1630	2010	380	20	1899
29	92372	1375	1770	395	33	1905
30	154981	1295	1810	515	31	1892
31	24072	1500	1840	340	40	1831
32	41695	1760	2040	280	34	2382
33	95477	1870	2400	530	24	2879
34	39247	2280	2620	340	41	3457
35	434939	1745	2680	935	35	3645
36	74535	2270	2700	430	44	4633
37	150082	1600	2020	420	33	3220
38	159714	2200	2680	480	27	4357
39	156456	2165	2700	535	39	5119
40	64855	2700	3010	310	21	3147
41	61474	1100	1410	310	33	463
42	53325	1090	1380	290	25	725
43	127348	1140	1550	410	27	725
44	64940	1300	1620	320	28	1510
45	46834	1280	1650	370	30	708
46	32688	1640	1895	255	24	1778
47	113878	1600	2085	485	28	1844
48	83096	1240	1670	430	40	1292
49	171932	1200	1905	705	39	1133
50	63639	2780	3030	250	31	3327
51	96259	2100	2790	690	6	2909
52	34300	2620	2900	280	11	3622
53	32234	2460	2680	220	19	3520

Reliability of the soil deposits during rainfall infiltration

Numerous studies have been carried out to evaluate the stability of soil slopes under rainfall infiltration. Zhang et al. (2011) conducted a review of the literature on stability

analysis of rainfall-induced slope failures. The thicknesses of the soil deposits between K2 and K7 are typically shallow while their plan dimensions are large (Table 1). Therefore, these soil deposits may be assumed as infinite slopes for preliminary risk analysis purposes, as shown in Fig. 11. The loose fill material is assumed to be 3 m thick. The initial ground water table is assumed to be far below the original native ground surface. Transient seepage analysis was conducted to investigate the infiltration of rainfall during six levels of rain (Table 2). The initial pore-water pressure conditions were established assuming a steady state condition subject to a constant rate of rainfall equivalent to the average annual rainfall spread evenly over the year (=3.59×10^{-8} m/s). Fig. 12 shows the pore water pressure distributions in a 40° infinite slope subject to a sustained rain of 20 mm/hour in intensity. The initial pore-water pressure is approximately linearly distributed. During rainfall infiltration, the wetting front advances gradually but the pore-water pressures in the wetted zone are still negative. The groundwater table rises gradually and is close to the ground surface after 8 hours of rain.

Table 2. Classification of raining events (China National Standardization Commission 2008).

Class	Intensity	12-hour rainfall (mm)	24-hour rainfall (mm)
0	No rain	0	0
1	Light rain	0.1 – 4.9	0.1 - 9.9
2	Moderate rain	5.0 - 14.9	10.0 - 24.9
3	Heavy rain	15.0 - 29.9	25.0 - 49.9
4	Torrential rain	30.0 - 69.9	50.0 - 99.9
5	Large storm	70.0 - 139.9	100.0 - 249.9
6	Extreme storm	≥ 140.0	≥ 250.0

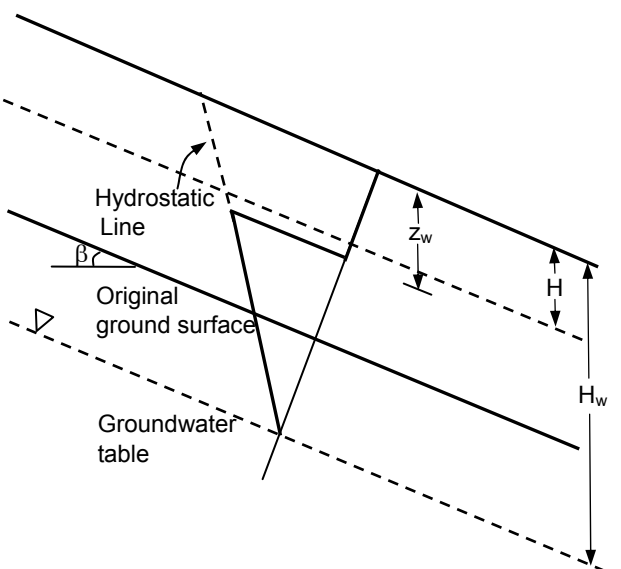

Figure 11. Stability of an infinite loose soil deposit.

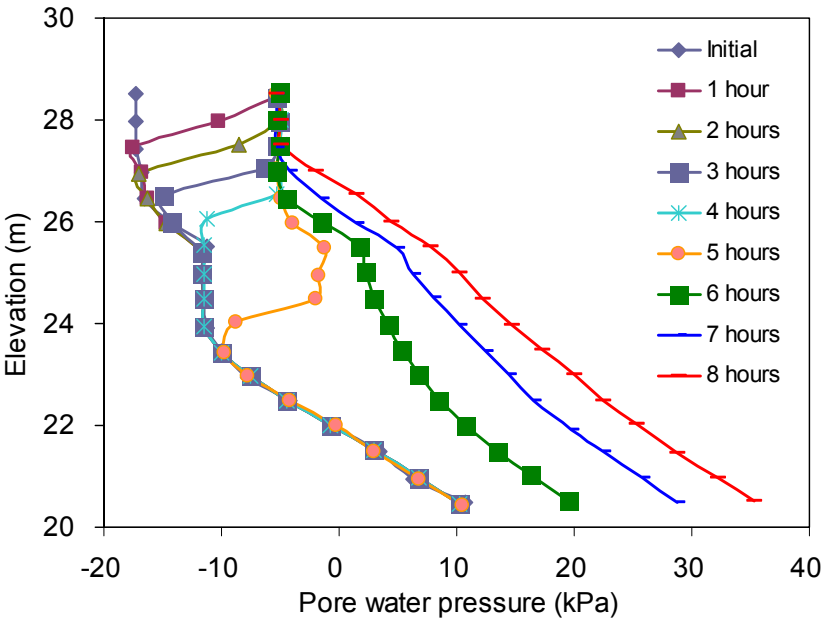

Figure 12. Change of pore-water pressures with time during rainfall infiltration in a 40° slope.

The factor of safety, Fs, of the infinite slope at the hydrostatic condition can be expressed as (Rahardjo et al. 1995)

$$Fs = \frac{c'}{\gamma_t H \sin\beta\cos\beta} + \frac{\tan\phi'}{\tan\beta} + \left(\frac{H_w}{H} - 1\right)\left(\frac{\gamma_w}{\gamma_{sat}}\right)\left(\frac{\tan\phi^b}{\tan\beta}\right) \quad (1)$$

where β = slope angle; H = depth of sliding; H_w = depth of groundwater table; c' and ϕ'= effective cohesion and friction angle of the soil, respectively; ϕ^b = friction angle related to the contribution of soil suction to the shear strength; γ_w and γ_{sat} = unit weight of water and total unit weight of saturated soil, respectively.

As rainwater infiltrates, the suction at shallow depths dissipates. When the wetting front is at a depth z_w from the ground surface (Fig. 11) and when the suction maintained within the wetted zone is ignored, the factor of safety of the slope along the sliding surface at the wetting front is

$$Fs = \frac{c'}{\gamma_t H \sin\beta\cos\beta} + \frac{\tan\phi'}{\tan\beta} \quad (2)$$

After the wetting front reaches the interface between the loose deposit and the native ground, positive pore-water pressures may build up in the loose deposit and the ground water table may rise above the interface. The factor of safety will then decrease as the groundwater table rises,

$$Fs = \frac{c'}{\gamma_t H \sin\beta\cos\beta} + \frac{\tan\phi'}{\tan\beta} - \frac{m\gamma_w \tan\phi'}{\gamma_{sat}\tan\beta} \quad (3)$$

where $m = (1 - H_w/H) > 0$.

The probability of failure of each of the deposits in Table 1 is calculated based on Equations (1)-(3) using Monte Carlo simulation (e.g. Malkawi 2000; Fenton and Griffith 2008). Two failure modes are considered: failure along the sliding surface at depth of the wetting front and failure along the interface between the new soil deposit and the native soil. The failure probability of the slope is taken as the greater of those for the two failure modes. The mean values of the cohesion and friction angle for the loose soil are 8 kPa and 32.7°, respectively, and their coefficients of variation are 0.32 and 0.14, respectively. Fig. 13(a) shows the variations of the probability of failure of a 3 m thick, 40° slope with time when subjected to the rains shown in Table 2. A sustained rain of 70 mm/12 hours (storm) is shown to be able to trigger the failure of such as slope and a large storm of 140 mm/12 hours is almost certain to trigger the failure of such slopes. Fig. 13(b) shows the effect of slope angle on the probability of failure of the slope under a rainfall intensity of 140 mm/12 hours. Slopes gentler than 30° are at a less critical condition. However slopes steeper than 40° may fail easily when subject to a severe storm.

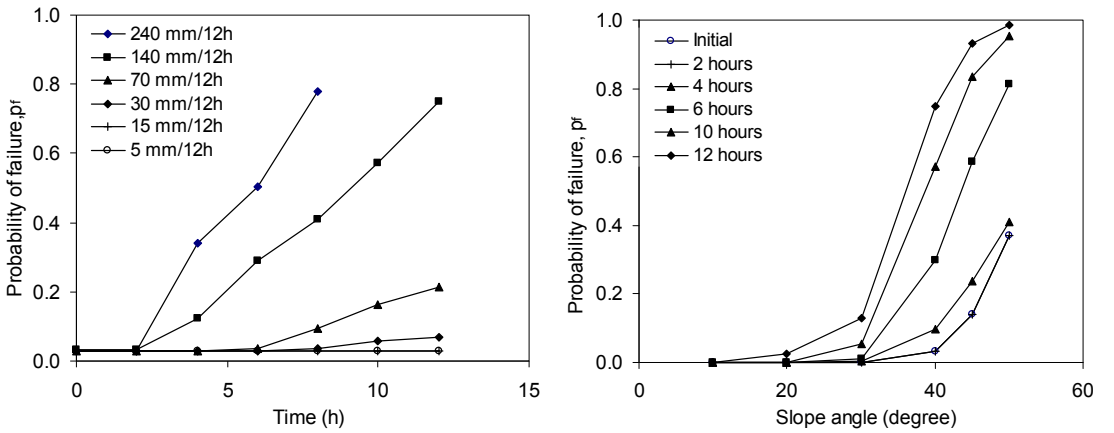

(a) (b)

Figure 13. (a) Variation of probability of failure of a 40° slope with rainfall time; (b) Effect of slope angle on probability of failure under a rainfall intensity of 140 mm/12 hours.

ASSESSING RISKS TO HUMAN LIVES

Assessment model

A generic framework for landslide risk assessment and management is summarized in Einstein (1997), Wong et al. (1997), Fell et al (2005), Ho et al. (2000), Ho and Ko (2009), Lacasse and Nadim (2009), and Tang et al. (2009). The human risks of the loose soil deposits distributed between K2 and K7 are evaluated to demonstrate the analysis of "cell risk". The element at risk is taken as the passengers traveling on the road who may be buried by the landslide debris should a landslide occur. The human risk, denoted by annual loss of life, R(LOL), is quantified by (Morgan et al. 1992):

$$R(LOL) = [P(L) \times P(T:L) \times P(S:T)] \times [V(D:T) \times E(n)] \quad (4)$$

where P(L), P(T:L) and P(S:T) are the annual probability of the landslide, the probability of the landslide reaching the highway and the probability that passengers are present at the locations impacted by the landslide (i.e., the temporal spatial probability of the element at risk), respectively; V(D:T) is the vulnerability of the person to the landslide event (i.e, the chance the person loses his/her life when he/she is impacted by the landslide); E(n) is the number of persons at risk.

Risks of all possible slides, rockfalls, and debris flows must be considered separately and combined in decision making. Only the assessment of the 53 loose soil deposits is illustrated in this paper.

Given a road segment, E(n) and P(T:L) rely on the run-out distance of the landslide under consideration. The run-out distance is often estimated using empirical relations. Many empirical relations are available in the literature (e.g., Corominas 1996; Fell et al. 2005). Here the relation proposed by Corominas (1996) is adopted:

$$\frac{H_D}{L_t} = AV^B \tag{5}$$

where H_D = elevation difference; L_t = travel distance; V= landslide material volume; A and B = coefficients. For example, based on the correlation between landslide volume and travel distance established for flow slides in loose fill slopes in Hong Kong, coefficients A and B can be determined as 0.719 and -0.08, respectively (Hunter and Fell 2003). These values are adopted in this analysis.

A reference run-out distance, ΔL, is used here to note the distance that the landslide debris runs out beyond the inside edge of the roadbed. A positive reference run-out distance indicates that the landslide debris buries the road and a negative reference run-out distance indicates that the landslide debris does not reach the road and hence has no direct effect on the road at time of the landslide.

The element at risk on the road during normal operation of the road can be estimated based on the design traffic flow: 1/6 vehicles per second at a design vehicle speed of 40 km/h, which is equivalent to 35 persons/km. The vulnerability given that a landslide reaches the car location *V(D:T)*, is taken as 1.0 considering that vehicles will be completely buried (Australian Geomechanics Society Sub-Committee on Landslide Risk Management 2000). Given the probability of failure, element at risk and vulnerability of each loose deposit, the human risk can be calculated using Eq. (2).

The risks are expressed in an F-N (number of fatality N – frequency of N or more fatalities per year) plot in Fig. 14 and an individual risk plot in Fig. 15. The F-N curves and the individual risk curve are plotted for six rainfall intensities (5 mm/12 hours, 30 mm/12 hours, 70 mm/12 hours, 140 mm/12 hours, 240 mm/12 hours). The frequencies of the four levels of rain are taken as 1.0, 1.0, 0.78, 0.28, 0.052, and 0.0062, respectively as found in Sichuan Hydrology Manual (Sichuan Provincial Central Hydrological Station 1979). Figs. 14 and 15 represent the risk profile shortly after the earthquake. Indeed the risk level is very high, which is not surprising referring to the landscape shown in Fig. 4. Three methods to mitigate the high risks would be to (1) change the highway alignment or use tunnels to avoid the hazardous slopes; (2) strengthen the high-risk slopes and construct rockfall barriers; and (3) implement a warning system to reduce the elements at risk in case of slope failures.

Landslide warning reduces the potential loss of lives by decreasing the elements at

risk. Therefore, the risk profiles shortly after the earthquake, after the completion of highway construction, and after the implementation of the warning and evacuation system must be compared to check the adequacy of engineering measures and justify any selected warning criteria.

WARNING CRITERIA AND IMPLEMENTATION

An effective way to minimize the loss of lives and properties is to warn the passengers and construction teams to evacuate from the road and close the road when catastrophic hazards are eminent. Since it is only feasible to control traffic at three locations along the study road, the warning exercise and associated risk assessment must be conducted for two road segments separately. For a specific road segment, once the current rainfall intensity is measured and the antecedent rainfall is known, the occurrence probability of the hazard can be calculated using the geotechnical models presented earlier and the corresponding consequence evaluated. Once the risk level exceeds specified criteria, warning should be issued and emergency management plan mobilized.

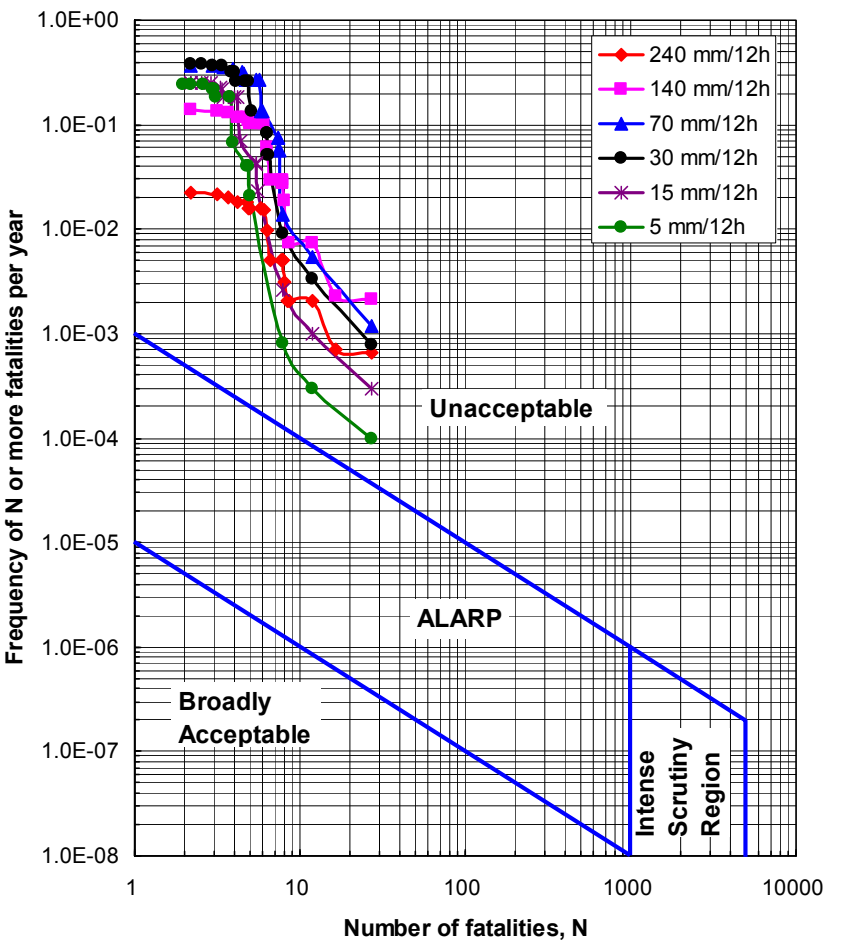

Figure 14. F-N curves for K2-K7 shortly after the earthquake at six rainfall levels.

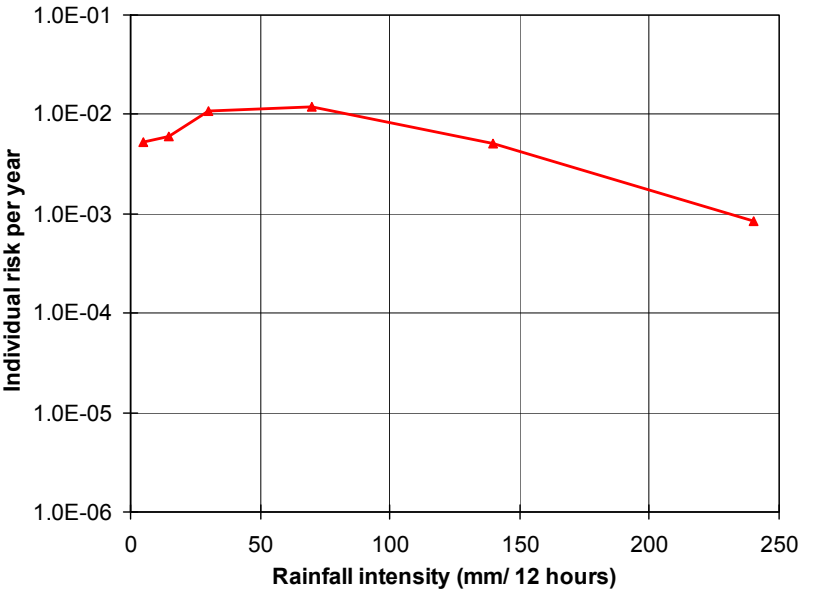

Figure 15. Individual risk for K2-K7 shortly after the earthquake.

Warning criteria

Warning criteria based on tolerable risks are preferred in this project though deterministic warning criteria based on intensity-duration relations and cumulative rainfall are available in the literature (e.g., Chleborad et al. 2008; Baum and Godt 2010). Tolerable risks have been a topic of intensive discussions (Finay and Fell 1997; Fell and Hartford 2007; Australian Geomechanics Society Sub-Committee on Landslide Risk Management 2000; Ho et al. 2000). Tolerable risk criteria are often expressed in terms of individual risk [e.g. an upper limit of 10^{-5} as in Hong Kong Government Planning Department (1994) and societal risk in an F-N plot (Fig. 14). Such criteria are considered suitable for describing the general risk profile in a statistical basis. Their suitability for landslide warning purposes, however, may be questionable. Events of serious consequences are often of a low occurrence frequency and therefore associated with a low annual risk. In making a warning decision when a storm event is certain, the conditional risk given the occurrence of the storm would be relevant. The conditional risk is the risk that may be caused by landslides induced by the storm even when it indeed happens. The conditional total loss of lives is calculated by

$$PLL_c = \sum_{i=1}^{n} p_{fi} V_i N_i \tag{6}$$

where n = number of slope features; p_{fi} = conditional probability of failure of slope *i* given a recorded storm event, which can be calculated using the slope stability and reliability analysis methods described earlier; V_i = vulnerability factor for slope *i*, which is taken as 1.0; and N_i = number of people at risk present in the area impacted by slope *i*, which is the number of passengers inside the segment of road potentially buried by the debris from the failure of the slope. The mortality rate (or the likelihood of casualty) is defined as the ratio of the total potential loss of lives and the total population within the part of road under study,

$$r_m = \frac{PLL_c}{N_p} = \frac{\sum_{i=1}^{n} p_{fi} V_i N_i}{N_p} \quad (7)$$

where N_p is the total population within the part of road under study.

We extend the risk matrix of Chinese Ministry of Housing and Urban-Rural Development (MOHURD) (2009) to landslide warning applications. Table 3 shows the proposed warning criteria based on both conditional potential total loss of lives, PLLc, and mortality rate. Five warning levels are defined in Table 3 based on these two parameters. Both parameters are essential in the warning criteria. Mortality rate, rather than occurrence probability, is used here because the occurrence of a storm event has already been detected by the rain-gauge network when making a warning decision. Given the same mortality rate, larger traffic flow over a given road section will imply a larger PLL_c. Warning should be issued and elements at risk evacuated when the expected PLL_c reaches a certain critical value. Similarly, given the same PLL_c, warning will be needed if the expected mortality rate is high or the individual risk is high, but might not be needed if the expected mortality rate is very low. The use of mortality rate reduces chances of false warning. For instance, several gentle soil deposits over a busy road segment could yield a very high PLL_c. However, given a storm, the conditional probability of failure of these deposits is rather low (Fig. 13(b)) if the slope angle is less than 20°. The use of PLL_c alone then could lead to frequent false warnings without landslides. On the other hand, when the deposits are very steep, these deposits are likely to fail during the storm. The morality rate and the conditional individual risk will be high. Warning decision can be made more promptly then using mortality rate as another decision parameter.

MOHURD (2009) developed a risk matrix for risk management of underground works of urban rail transit. The consequence is divided into five classes from catastrophic to very serious, serious, considerable, and negligible. The chances are divided into five classes from frequent to not credible. The classes of consequences for risk to property, human lives, project delays, environment, reputation have been defined. Table 4 shows the classes of human casualty or injury. Australian Geomechanics Society Sub-Committee on Landslide Risk Management (2000) also proposed a quantitative risk matrix for level of risk to property. The consequences to property are classified into five levels and the associated likelihood classified into six levels. A similar risk matrix for risk to human lives, however, was not available.

Table 3. Warning criteria based on total potential loss of lives and mortality rate

Mortality rate, r_m	Potential loss of lives (PLL_c) in one rain event				
	Negligible E	Considerable D	Serious C	Very serious B	Catastrophic A
0-0.01%	Level 1	Level 1	Level 2	Level 3	Level 4
0.01-0.1%	Level 1	Level 2	Level 3	Level 3	Level 4
0.1-1%	Level 1	Level 2	Level 3	Level 4	Level 5
1-10%	Level 2	Level 3	Level 4	Level 4	Level 5
10-100%	Level 2	Level 3	Level 4	Level 5	Level 5

Table 4. Classes of human casualty or injury for underground works of urban rail transit (after MOHURD 2009).

Class	Number of casualties (including missing) or injuries	Risk acceptance
A	Casualties > 10	Not allowed
B	Casualties = 3-9, or serious injuries > 10	Intolerable
C	Casualties = 1-2, or serious injuries = 2-9	Tolerable
D	Serious injury = 1, or moderate injuries = 2-10	Acceptable
E	Moderate injury = 1	Ignorable

Implementation

To facilitate instant decision making, systematic parametric studies have been conducted for the major potential hazards along the road, so that the warning level at possible combinations of antecedent rainfall and current rainfall has been stored in a tabular form. Fig. 16 shows the relationship between 12-hour rainfall and the potential loss of lives caused by the 53 loose deposits between K2 and K7. Both the potential loss of lives at given rainfall intensities (PLL_c) and the annual potential loss of lives are presented. The annual potential loss of lives in a given rain event is the PLL_c in that rain event times the annual frequency of the rain event. Note that the potential of life is not zero when there is no rain. The changes in risk are minimal when subjected to a light (<5 mm/12 hours), moderate (5 - 15 mm/12 hours), or heavy rain (15 – 30 mm/12 hours). However, the risk may increase substantially when subject to a storm heavier than 30 mm/12 hours. The analysis concurs with the observations made in the past three wet seasons.

Once a warning level is selected for the road segment based on measured rainfall intensity and Tables 3 and 4, a warning message will be shown on an electronic display board at the both ends of the road segment. Selected messages and suggested actions for risk management are summarized in Table 5. Once the risk level reaches critical level 4, the traffic, construction teams, and important equipment along the road should be advised to evacuate. The risk profile along the road should be frequently updated and reported to the highway maintenance authority and police authority. The road should be closed once a decision to issue Level 5 warning signal is made.

Table 5. Warning messages and suggested actions for risk mitigation.

Warning level	Warning messages	Suggested actions
Level 1	No message	Normal monitoring
Level 2	No message	Enhanced monitoring; safety staff alerted
Level 3	Landslides likely to occur at xx	Issuing warning message; safety staff alerted
Level 4	Landslides very likely to occur at location xx	Issuing warning message; traffic control; emergency team in action
Level 5	No entry; landslides occurring at location xx	Issuing warning message and road closure; evacuation and rescue.

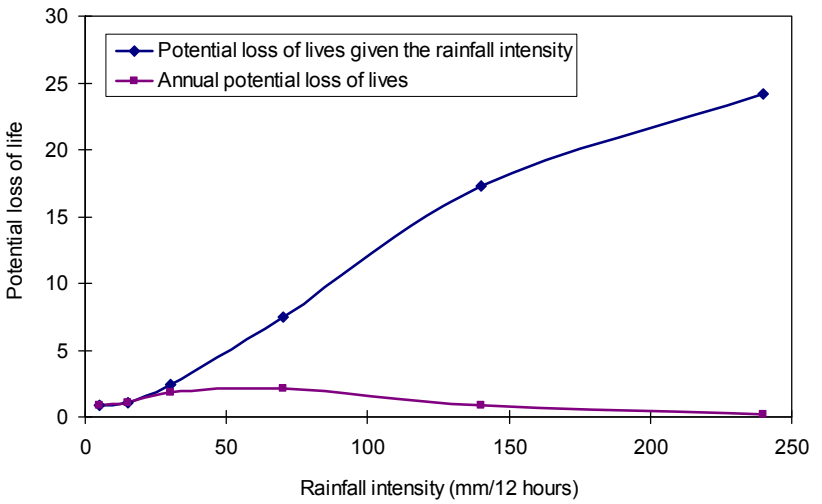

Figure 16. Relationship between 12-hour rainfall and potential loss of lives for K2-K7 at normal traffic flow condition.

SUMMARY

Provincial Road 303 near the epicenter of the 2008 Wenchuan Earthquake is subject to high risks from the failure of loose soil deposits at high elevations or debris flows originating from high elevations. A risk-based, real-time landslide warning system is being developed for this road. The aim of the warning system is to decrease the risk level by reducing the elements at risk in case of storms. The system consists of an automatic rain gauge network, digital terrain models, geotechnical reliability analysis models, risk assessment models, and a warning-issuing system. Since it is only feasible to control traffic at three locations along the study road, the warning exercise and associated risk assessment must be conducted for two road segments separately. The evaluation of the risk profiles for a 5 km road segment between K2 and K7 under several rainfall intensity values is illustrated in this paper. The road segment is under 53 large loose soil deposits located from a few meters to 1700 m above the road. The risk level of the road segment increases substantially and becomes intolerable when the rainfall intensity exceeds 30 mm/12 hours. Warning criteria based on total potential loss of lives and mortality rate are proposed in a matrix form. Five warning levels are defined in the matrix.

The proposed working framework can accommodate the use of various physically based landslide assessment models. The reliability of the warning system can be gradually enhanced when more failure and site information becomes available for updating the analysis models involved.

ACKNOWLEDGMENTS

The authors would like to express their sincere thank to their PhD students, Mr. M. Peng, Miss S. Zhang, Miss H. F. Zhao, and Mr. H. X. Chen for their hard work in

conducting the risk analysis. Technical inputs from Messrs. B. Xiang, X. F. Wang, H. Pan, and Q. Yuan of Sichuan Provincial Transportation and Communications Department are essential in conceiving the landslide warning system. The financial support from Sichuan Provincial Transportation and Communications Department and the Research Grants Council of the Hong Kong SAR (No. 622210) is acknowledged.

REFERENCES

Apip, A. Takara, K., Yamashiki, Y., Sassa, K., Ibrahim, A. B., and Fukuoka, H. (2010). "A distributed hydrological-geotechnical model using satellite-derived rainfall estimates for shallow landslide prediction system at a catchment scale". *Landslides*, 7(3), 237-258.

Australian Geomechanics Society Sub-Committee on Landslide Risk Management. (2000). "Landslide risk management concepts and guidelines". *Australian Geomechanics,* 35, 49-92.

Baum, R., and Godt, J. (2010). "Early warning of rainfall-induced shallow landslides and debris flows in the USA". *Landslides*, 7(3), 259-272.

Bolley, S., and Oliaro, P. (1999). "Analisi dei debris flows in alcuni bacini campione dell'Alta Val Susa". *Geoingegneria Ambientale e Mineraria*, Marzo, 69–74.

Campbell, R. H. (1975). "Soil slips, debris flows, and rainstorms in the Santa Monica Mountains and vicinity, southern California". In: US Geological Survey Professional Paper 851. Washington DC, U.S. Government Printing Office, 51 pp.

Casagli, N., Catani, F., Ventisette, C., and Luzi, G. (2010). "Monitoring, prediction and early warning using ground-based radar interferometry." *Landslides,* 7, 291-301.

Chang, S. Y., and Lin, C. P. (1997). "Debris flow detection using image processing techniques." *Debris-Flow Hazards Mitigation: Mechanics, Prediction, and Assessment*, Chen & Major (eds), Millpress, Netherlands, 549-560.

Chau, K. T., Wong, R. H. C., Liu, J., and Lee, C. F. (2003). "Rockfall hazard analysis for Hong Kong based on rockfall inventory". *Rock Mech. Rock Eng.,* 36(5), 384-408.

Cheung, R. W. M., and Tang, W. H. (2005a). "Reliability of deteriorating slopes." *J. Geotech. Geoenviron. Eng.,* 131(5), 589-597.

Cheung, R. W. M., and Tang, W. H. (2005b). "Realistic assessment of slope reliability for effective landslide hazard management." *Geotechnique*, 55(1), 85-94.

China Institute of Geo-Environment Monitoring. (2005). *Technical guidelines for geohazards forecasting and warning.* Beijing.

China Meteorological Administration. (2010). *Meteorological grading of geological hazards.* Beijing.

China National Standardization Commission. (2008). *Short-range weather forecast,* GB/T 21984-2008. Beijing.

China National Standardization Commission. (2009). *Code of risk management for underground works of urban rail transit, GB××—2009*. Beijing.

Chleborad, A. F., Baum, R. L., and Godt, J. W. (2008). "A prototype system for forecasting landslides in Seattle, Washington area". Engineering Geology and Landslides of the Seattle, Washington, area, Geological Society of America

Reviews in Engineering Geology, 103-120. doi:10.113-/2008.4020(06).
Corominas, J. (1996). "The angle of reach as a mobility index for small and large landslides." *Can. Geotech. J.,* 33, 260–271.
Corominas, J., and Moya, J. (1999). "Reconstructing recent landslide activity in relation to rainfall in the Llobregat River basin, Eastern Pyrenees, Spain." *Geomorphology,* 30, 79–93.
Dai, F. C., and Lee, C. F. (2001). "Frequency-volume relation and prediction of rainfall-induced landslides." *Engineering Geology*, 59, 253-266.
Einstein, H. H. (1997). "Landslide risk-Systematic approaches to assessment and management". *Landslide Risk Management, Proceedings of the Int. Workshop on Landslide Risk Assessment,* Honolulu, USA, 19-21 Feb. 1997, Cruden and Fell (eds), A.A. Balkema Publishers, Rotterdam, 15-24.
Einstein, H., and Sousa, R. (2006). "Warning system for natural threats." *Proc. 2006 ECI Conference on Geohazards*, Lillehammer, Norway, F. Nadim, R. Pottler, H. Einstein, H. Klapperich, and S. Kramer (eds), http://services.bepress.com/eci/geohazards/1.
Evans, N. C. (1997). *Preliminary assessment of the influence of rainfall on natural terrain landslide initiation*. Discussion Note No. DN 1/97, Geotechnical Engineering Office, Civil Engineering and Development Department, Hong Kong.
Fell, R., and Hartford, D. (1997). "Landslide risk management". *Landslide Risk Management, Proceedings of the Int. Workshop on Landslide Risk Assessment,* Honolulu, USA, 19-21 Feb. 1997, Cruden and Fell (eds), A.A. Balkema Publishers, Rotterdam, 51-109.
Fell, R., Ho, K. K. S., Lacasse, S., and Leroi, E. (2005). "A framework for landslide risk assessment and management." *Landslide Risk Management*, O. Hunger, R. Fell, R. Couture, & E. Eberhardt (eds), A.A. Balkema Publishers, Rotterdam, 3-25.
Fenton, G. A., and Griffith, D. V. (2008). *Risk assessment in geotechnical engineering*, John Wiley & Sons, New York.
Finlay, P. J., and Fell, F. 1997. "Landslides: risk perception and acceptance". *Can. Geotech. J.* 34: 169-188.
Finlay, P. J., Fell, R., and Maguire, P. K. (1997). "The relationship between the probability of landslide occurrence and rainfall". *Can. Geotech. J.,* 34(6), 811-824.
Gili, J. A., Corominas, J., and Rius, J. (2000). "Using global positioning system techniques in landslide monitoring". *Engineering Geology,* 55, 167-192.
Ho, K. K. S., and Ko, F. W. Y. (2009). "Application of quantified risk analysis in landslide risk management practice: Hong Kong experience". *Georisk*, 3(3), 134-146.
Ho, K., Leroi, E., and Roberds, B. (2000). "Quantitative risk assessment: application, myths and future direction". *Proceedings of GeoEng2000*, 19-24 Nov. 2000, Melbourne, Australia, in CD ROM.
Hong Kong Government Planning Department. (1994). *Potentially hazardous installations*. In Hong Kong Planning Standards and Guidelines. Hong Kong Government, Hong Kong.
Hunter, G., and Fell, R. (2003). "Travel distance angle for "rapid" landslides in constructed and natural soil slopes" *Can. Geotech. J.,* 40, 1123-1141.
Jibson, R. W. (1989). "Debris flow in southern Porto Rico". *Geological Society of*

America, Special Paper 236, 29–55.

King, J. P. (1999). *The natural terrain landslide study – Natural terrain landslide inventory.* GEO Report No. 74, Geotechnical Engineering Office, Civil Engineering and Development Department, Hong Kong.

Ko, F. W. Y. 2005. *Correlation between rainfall and natural terrain landslide occurrence in Hong Kong*. GEO Report No. 168, Geotechnical Engineering Office, Civil Engineering and Development Department, Hong Kong.

Kurihara, J., Takezawa, N., Yamakoshi, T., and Yanagimachi, T. (1997). "Study on method of setting threshold of ground vibration sensor for detecting debris flow". *Debris-Flow Hazards Mitigation: Mechanics, Prediction, and Assessment*, Chen & Major (eds), Millpress, Netherlands, 603-611.

Lacasse, S., and Nadim, F. (2009). "Landslide risk assessment and mitigation strategy." *Landslides – Disaster Risk Reduction*, K. Sassa, P. Canuti (eds.), Springer-Verlag Berlin Heidelberg, 31-61.

Liu, X. (1999). "Application of fiber optics sensing technology in geotechnical engineering." *Chinese J. of Rock Mechanics and Engineering*, 18(5), 588-591.

Malkawi. A. I. H., Hassan, W. F., and Abdulla, F. A. (2000). "Uncertainty and reliability analysis applied to slope stability." *Structural Safety*, 22, 161-187.

MOHURD. (2009). *Code of risk management for underground works of urban rail transit.* Ministry of Housing and Urban-Rural Development, Beijing.

Morgan, G. C., Rawlings, G. E., and Sobkowicz, J. C. (1992). "Evaluating total risk to communities from large debris flows". *Proceedings of the 1st Canadian Symposium on Geotechnique and Natural Hazards*, Vancouver, Canada, 225-236.

NOAA-USGS Debris-Flow Task Force. (2005). *NOAA-USGS debris-flow warning system, Final report. U*.S. Geological Surveys Circular 1283.

Rahardjo, H., Lim, T. T., Chang, M. F., and Fredlund, D. G. (1995). "Shear strength characteristics of a residual soil." *Can. Geotech. J.*, 32(1), 60-77.

Sichuan Provincial Central Hydrological Station (1979). *Sichuan hydrology manual*. Chengdu, Sichuan.

Sichuan Provincial Highway Design Institute (2008). *Investigation of geohazards along RP303 between Yingxiu and Wolong caused by Wenchuan Earthquake on 12 May 2008*. Chengdu, Sichuan, 58pp.

Tang, W. H., Zhang, J., and Zhang, L. M. (2009). "Characterizing geotechnical model uncertainty". *Proceedings of ICOSSAR'2009 (10th International Conference on Structural Safety and Reliability),* 13-17 Sept. 2009, Osaka, Japan. In CD Rom.

Wong, H. N., Ho, K. K. S., and Chan, Y. C. (1997). "Assessment of consequence of landslides." *Landslide Risk Management, Proceedings of the Int. Workshop on Landslide Risk Assessment,* Honolulu, USA, 19-21 Feb. 1997, Cruden and Fell (eds), A.A. Balkema Publishers, Rotterdam, 111-149.

Xu, C., Dai, F. C., Yao, X., Chen, J., Tu, X. B., Cao, Y. B., and Xiao, J. Z. (2010). "GIS based certainty factor analysis of landslide triggering factors in Wenchuan Earthquake." *Chinese Journal of Rock Mechanics and Engineering*, 29(Z1), 2972-2981 (in Chinese).

Yin, Y. P., Wang, H. D., Gao, Y. L., and Li, X. C. (2010). "Real-time monitoring and early warning of landslides at relocated Wushan Town, the Three Gorges Reservoir, China". *Landslides*, 7(3), 339-349.

Yu, Y. F. (2004). *Correlations between rainfall, landslide frequency and slope information for registered man-made slopes*. GEO Report No. 144, Geotechnical Engineering Office, Civil Engineering and Development Department, Hong Kong.

Zhang, L. L., Zhang, J., Zhang, L. M., and Tang, W. H. (2011). "Stability analysis of rainfall-induced slope failures: a review". *Geotechnical Engineering, Proceedings of the Institution of Civil Engineers*, in press.

Zhang, L. M. (2009). "Challenges in multi-hazard risk assessment and management: Geohazard chain in Beichuan Town caused by Great Wenchuan Earthquake". *Proc. 2nd International Symposium on Geotechnical Safety ands Risk (IS-Gifu 2009),* Honjo et al. (eds), Gifu, Japan, 11-12 June 2009, Taylor & Francis Group, London, 237-244.

Zhang, L. M., Peng, M., and Xu, Y. (2010). "Assessing risks of breaching of earth dams and natural landslide dams". *Proc. Indian Geotechnical Conference – 2010, GEOtrendz,* December 16–18, 2010, IGS Mumbai Chapter & IIT Bombay, Macmillan Publishers India Ltd., Mumbai, Vol. III, 81-92.

Unresolved Problems in Geotechnical Risk and Reliability

John T. Christian[1] and Gregory B. Baecher[2]

[1] Corresponding author. Consulting Engineer, 89 Kodiak Way, Ste. 2312, Waltham MA 04451, (781) 209-2799, christian2@rcn.com
[2] Glenn L. Martin Institute Professor of Engineering, University of Maryland, College Park, MD 20742.

ABSTRACT

The geotechnical engineering and research communities have made significant progress in understanding how concepts of probabilistically based reliability analysis interact with the unique features of the geotechnical environment and in developing procedures to apply probabilistic methods to practical geotechnical problems. This conference presents evidence of both the scope of current activities and the success of recent applications. However, many issues remain unresolved. This paper identifies ten problems, issues, or areas of activity in which major questions are still open. It is to be hoped that they will form the agenda for the next generation of research and development at the interface of two disciplines that address uncertainty every day – geotechnical engineering and reliability analysis.

INTRODUCTION

One of the major attractions of geotechnical engineering for civil engineering students has always been that it deals with a world in which many important matters are not well known or understood, a world in which cut-and-dried solutions seldom apply. At about the same time as the pioneers in geotechnical engineering were establishing the foundations of their discipline, another group of researchers were applying probabilistic concepts to develop rational ways to deal with uncertainty in what came to be reliability analysis. It is remarkable that there was little interaction between the geotechnical and reliability efforts.

However, in the 1970s the pioneering efforts of people such as T. H. Wu, Peter Lumb, Allin Cornell, and Robert Whitman showed that the reliability and geotechnical worlds really did have something to say to each other. Recent years have seen great advances in applying probabilistic reliability ideas to geotechnical problems, reflected both in increasing numbers of papers and in greater interest on the part of clients and practical engineers in expressing reliability in quantitative terms. The profession has learned a lot in the process, but it has also discovered that some issues remain stubbornly intractable. This paper identifies ten problems that have not been resolved satisfactorily – at least to the authors' satisfaction – and whose clarification would greatly benefit the practice of geotechnical engineering.

On August 8, 1900, speaking at the International Congress of Mathematicians at the Sorbonne, the great mathematician David Hilbert presented a set of ten important problems in mathematics. These were unsolved at the time, and some remain so today. Finding solutions to these problems strongly influenced the development of

mathematics throughout the 20thC. The complete list of 23 problems that Hilbert eventually proposed became available in English translation in the *Bulletin of the American Mathematical Society* (1902). It is interesting to consider a similar list of important and unresolved problems in the application of risk, reliability, and probabilistic methods to geotechnical engineering. Although there is no reason there could not be more or fewer important unresolved problems, ten is a convenient number. These problems range from statistically-informed guidance for practical site characterization, to dealing with correlated failure modes in systems risk assessments, to risk communication and active risk management

The subsequent sections contain brief statements of the unresolved problems and some comments on where the efforts to resolve them now stand. The available space and time are not adequate for a full discussion of any one problem, each of which could easily occupy a full professional paper. The order of presentation of the problems is independent of their relative importance or likelihood of successful solution. Also, these problems are not necessarily mutually independent; progress toward resolving one of them may affect the state of others.

TEN UNRESOLVED PROBLEMS

1. Why are failures less frequent than our reliability studies predict? The reliability studies carried out over the past few decades generally give probabilities of failure on the order of several percent or more for the usual range of uncertainties in soil properties and analytical tools. We do not observe this frequency of failures. Why not?

The typical coefficients of variation (standard deviation as a fraction of the mean) reported from soil engineering property testing are on the order of 20-30% (Phoon and Kulhawy 1996; Baecher and Christian 2003). Presuming a mean factor of safety of E[FS]=1.5, the corresponding reliability indices (β) are about 1.67 to 1.1, implying probabilities of failure in the vicinity of 0.1 for Normally distributed uncertainties. These are at least an order of magnitude larger than the observed frequency of adverse performance. They are two orders of magnitude larger than the frequency of all-modes failures of earth dams (Baecher *et al*. 1979).

One answer to this riddle is that the uncertainty in soil properties is being overestimated. If the coefficient of variation in the field is actually smaller than the value used to estimate the probability of failure, the probability of failure will be overestimated. However, extensive studies of the measured variability of soil properties in the laboratory and *in situ*, (e. g., Phoon and Kulhawy 1999a and 1999b) have shown that, although different properties have different variabilities, there does not seem to be much difference between the laboratory and the field.

A second answer is that we do not apply factors of safety to mean property values but to some conservative fraction of the mean. US Army Corps of Engineers practice, as an example, is to use a 1/3-rule in choosing engineering properties: the design property is taken at that value which is larger than 1/3 of the observations and smaller than 2/3 (USACE 2003). For Normally distributed data, that is approximately the mean less 0.4 standard deviations. This implies a reliability index with respect to the mean of 1.5 to 2.1, or corresponding probabilities of failure in the vicinity of

0.05. These are more in keeping with observed rates, but still too high. There is a tendency for engineers to be conservative in estimating soil properties, underestimating strength and overestimating compressibility, even when trying to identify the best estimates. It is hard to overcome the habits of years.

Another answer is that the variation we observe in test data includes both actual variations of *in situ* properties and measurement error (*i.e.,* noise). That measurement error can be large. In the post-Katrina risk analysis studies of the New Orleans levee system, the noise in undrained strength data was estimated to be about 75% of the total data variance (USACE 2009). This is hardly surprising, especially for a measurement as prone to disturbance and measure error as unconsolidated-undrained strength. The lesson to be learned from these empirical studies is that care must be exercised in assigning coefficients of variation to soil engineering properties, and that we likely over-estimate the uncertainties in soil properties, maybe by a great deal.

Finally, many analytical models used to calculated factors of safety and probabilities of failure are not accurate. Because slope stability analyses usually involve assuming general patterns of failure, the analyst may miss a critical mode, and there can be an unconservative bias. However, most analytical models used in geotechnical engineering are conservatively biased, the bearing capacity equations being an especially good example. A further complication is the large number of multiplied factors used to account for deviations from the basic case in, for example, bearing capacity and liquefaction analyses. It is far from clear that these factors apply across the full range of parameters or even that they should be combined by multiplication. Christian and Carrier (1978) demonstrated that, even in the relatively simple case of a foundation load on a linearly elastic, isotropic medium with only two factors, one for shape and one for embedment, multiplying the factors gave less accurate results than simply ignoring the embedment factor.

It is also possible that the actual rate of unsatisfactory performance may be under-reported. Unless the failure is spectacular, it is unlikely that every case of foundation failure, excessive settlement, slope distress, and so on is included in the data repositories for geotechnical facilities.

Resolution of some of the other issues in this list may have an impact on the understanding of the infrequency of failures. In any case, the credibility of reliability analysis requires that there be a demonstrable relation between observed behavior and behavior predicted by analytical models.

2. What is the actual variability of soil and rock properties? Several studies have been published on the variability of the properties of soils and rocks (*e. g.*, Phoon and Kulhawy 1999a 1999b). Sometimes the values in these publications are simply adopted into reliability calculations without further efforts to establish the variability for the particular project at hand. Despite the excellent work that has been done on this issue, it is not a closed matter, and more work needs to be done. In particular there needs to be more work on how much effort is required to improve the estimates for a particular site.

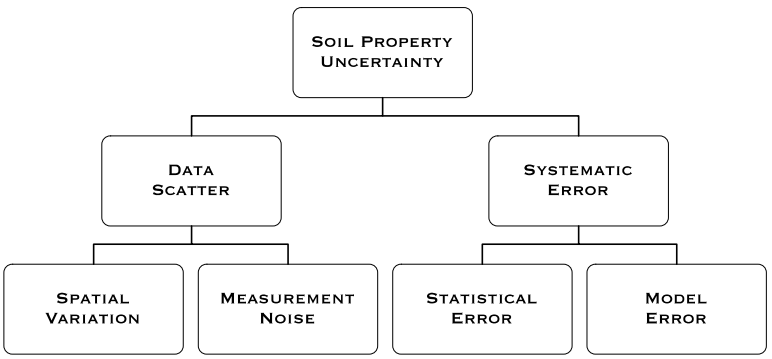

Figure 1. Contributions to soil engineering property uncertainty

This issue follows on the last concerning our over estimation of probabilities of failure. Variations in soil engineering data involve at least two things: (1) actual spatial variability from one point to another in the soil mass, and (2) noise introduced by our methods of measurement. The latter can be large. In addition, however, there are at least two bias (*i.e.,* systematic) errors that creep into our assessments: (3) statistical error due to limited numbers of observations, and (4) model error due to the approximate nature of our mathematical descriptions of the physics of soil behavior.

The systematic errors do not appear in the data scatter since they are biases on the mean. Yet, they affect our reliability calculations in profound ways, because they do not average out with scaling. For example, if we are told, "the probability of failure of a long embankment is 0.1," does this mean that, 10% of the length is expected to fail, or there is a 1-in-10 chance that the embankment fails in its entirety, or something between these two? The answer depends on the source of uncertainty underlying the probability. If the uncertainty derives entirely from spatial variation of strengths or loads, then the first statement is correct. If the uncertainty derives entirely from a systematic error, like the model used to predict stability, then the second statement is correct. But if the uncertainty derives from a mixture of sources, some spatial and some systematic, then the third statement is correct. The third is almost always the case in practice.

One can anticipate some of the general trends of variability in soil and rock. It is to be expected that the coefficient of variation would be larger for undrained strength than for friction angle, and even larger for the coefficient of hydraulic conductivity. The variances of properties of rocks are clearly dependent on the size of the test specimen—larger specimens have smaller variance—and this raises questions of how to extrapolate to field conditions. In other words, establishing the variability of a property requires different approaches for different properties, different materials, and different ways of testing.

One complication is that the uncertainty in properties may be larger than expected and may have unforeseen consequences. For example, although one would expect that the unit weight of soil in a fill would have a relatively low coefficient of variation, actual experience has shown that field measurements of density yield surprising ranges of values. Furthermore, the variance in the unit weight of fill can have a large effect on the uncertainty in the factor of safety in slope stability calculations.

A fundamental problem is the lack of data. Field exploration is expensive, so there are seldom enough data to support meaningful statistical analyses. Similarly, there is a tradition of basing conclusions in laboratory testing programs on small numbers of tests. It is quite common to encounter laboratory programs consisting of three or four consolidation tests or triaxial strength tests. These are not enough to support broad conclusions about the statistics of soil properties, and run afoul of Tversky and Khanaman's (1971) "law of small numbers" biases.

Phoon and Kulhawy developed their statistical results by scouring the literature to find enough data. However, this should not be the end of the matter. Others should be extending the available data, looking for more data, and refining the statistical studies. One hopeful development is that the ASCE now encourages authors of papers in the Journal of Geotechnical and Geoenvironmental Engineering to submit supplemental data, which become available when the electronic form of the paper is accessed.

3. The effects of spatial correlation and how to deal with them. Geological materials arrive at their present configurations by either an orderly construction process operated by humans or a geologic process that follows physical principles. Therefore, their physical properties exhibit spatial correlation to a greater or lesser extent. While there has been some success in describing spatial correlation by techniques such as auto-correlation and geostatistics, and spatially correlated random finite element methods have been employed to analyze their effects, the techniques for dealing with spatial correlation are difficult to implement, they are poorly understood by the practice, and their consequences are often ignored.

Fenton and Griffiths (2008) have used stochastic finite element methods to investigate the effects of spatial correlation in classical geotechnical problems such as flow through dams, slope stability, and settlement of shallow foundations. Their book summarizes research results that were previously published individually. The results show that correlation can have significant effects, even on problems that are thought to be well understood. Although Fenton and Griffith's work comprises by far the most extensive investigation of correlation effects, more limited studies by others have shown similar effects.

Engineers often deal with phenomena that are difficult to analyze by considering the limiting cases. For correlation effects, these are the cases of perfect correlation ($\delta = \infty$) and no correlation ($\delta = 0$). In the case of perfect correlation the values of the uncertain parameters are the same for all distances, and correlation effects need not be explicitly considered. In the uncorrelated case, random variations about the expected value average out in any analysis with fine enough discretization. For a problem such as settlement of shallow foundations or stability of a slope, for which the relevant properties are averaged over a broad extent, one would expect the cases of perfect correlation and no correlation to give the same expected results. However, intermediate values of correlation may give larger values of, say, relative settlement, and the maximum effect in some cases seems to occur for values of correlation coefficient approximately equal to the distance for which the difference in performance is sought. Where correlation effects are concerned, the conventional approach of consi-

dering limiting cases does not work, and the analysis of the actual correlation effects is difficult.

A further concern is that determining correlation patterns in the field is not easy. Auto-correlation methods and geostatistics require large amounts of data taken over a broad range of distances. In an actual project it is rarely feasible to collect the data using conventional exploration tools. Can the exploration techniques be improved to provide adequate descriptions of correlation? How can correlation best be described? Are there general patterns that can be used without the need for a full-blown exploration program for every project? How can correlation effects be conveniently incorporated in analyses without recourse to stochastic simulations in every case?

4. Scale effects in geotechnical reliability. Much of geotechnical engineering involves scaling properties from small laboratory samples or from field tests on limited volumes. We know that scaling to full scale properties is a statistical problem, but it has not been fully addressed or assimilated by the profession.

Some geotechnical problems are governed by average properties; others are dominated by the behavior of local seams or discontinuities. The settlement of a shallow foundation is an example of the former, and the stability of a rock slope is typical of the latter. Sometimes, as in the case of compaction testing, the properties of a small sample are reasonably comparable to those in the field, but often, as in the testing of rock samples, the behavior of a small sample is notably different from that of the rock mass. The combination of the relative importance of local discontinuities and different effects of sample size creates conditions in which scaling the properties of soils and rocks becomes a difficult and often poorly understood problem.

Geotechnical engineers and researchers have long recognized that scaling problems present difficulties. There has also been some progress in addressing them rationally. Unfortunately, many of the problems remain unresolved, and practitioners are often not aware of what progress has been made. This is an area in which progress in research could have important impact on practice.

For example, levee systems comprise constructed embankments or walls extending tens of miles across ground that is poorly characterized from an engineering perspective. Levees fail, if they do, at locations where loads are high with respect to strength, or where seepage resistance is low. If these critical locations are identified ahead of time, traditional methods can be used to analyze stability and calculate factors of safety or probabilities of failure. In such situations, the overall length of levee is immaterial, because the weakest spots have been identified and dealt with. The probability that the levee fails is that of these weakest spots.

The more common situation is that the full length of the levee system is not characterized with enough detail for the engineer to know unambiguously where the weakest spots are. In this case, any section of the levee system has some probability of experiencing higher than average loads or lower than average characteristics, and as a result, of being a “weak spot.” Since this unfortunate combination cannot be uniquely identified before a failure occurs—there is not enough information to do so—the longer the total length of levee, the greater the chance that such an unfortunate

combination exists somewhere, and thus the higher the probability of a failure somewhere.

This "probability of a failure somewhere" is the *probability of system failure*. Other things being equal, most people would agree that the longer the length of levee, the greater the chance of system failure. The probability of system failure is not a property of natural randomness in nature, but of the limited information available to the engineer with which to characterize the levee system, and consequently to know where the weakest link is and how weak it is.

For the purposes of reliability modeling, common failure modes can be categorized as one of three types with respect to the effect levee length has on the probability of system failure: (1) those depending on continuum properties of the levee structure or subsurface—examples are limiting equilibrium strength stability, or large high permeability zones in levee foundations; (2) those depending on unknown or undetected "flaws" in either the levee or subsurface—examples are buried channels, cracks in the levee structure, or animal burrows; and (3) those depending on known discrete features like through-going pipes, transitions between levee or wall sections, and gates.

The probability of failure for the first two categories is affected by the length of the levee. In both cases, longer levees, in principle, have higher probabilities of system failure, because the chance of encountering either a weak zone (category 1) or a flaw (category 2) increases with length. The probability of failure for the third category is unaffected by length, because critical locations are known.

In a seminal paper dealing with spatial variability, Vanmarcke (1977) showed that both the probable length of failure and the growth of systems failure probability with levee length could be related to the autocorrelation distance of soil strength properties. This leads to an equation for systems failure probability of the form,

$$P(one-or-more-failures) = 1-(1-p)^n \qquad (1)$$

in which n = the number of equivalent independent reaches, which depends on the characteristic length of correlation, and p = the probability of failure of the individual reach.

The difficulty with this formula is, that while theoretically elegant, it seems to strongly over-estimate the probability of systems failure in practice. For a practical case such as New Orleans or Sacramento, the probabilities calculated with this formula far exceed the observed rates of levee failure. Why? One interesting direction of study is better to understand the positive correlations among the uncertainties affecting each levee reach, and thus lowering the probability of a first-excursion failure.

5. Can we develop reliability models for internal erosion? Internal erosion or piping is a well-known phenomenon, especially in dam and levee construction, and it clearly involves a stochastic process of successive removal of material by the forces of flowing water. However, the practical design methods are deterministic, and we do not have adequate methods to detect its occurrence in existing structures.

About one-third of the failures of modern earth dams occur because of internal erosion, and, as a result, there has been a great deal of attention paid to this failure

mode and to how its probability of occurrence for a specific structure might be assigned. The major problem in rationally assigning these probabilities, however, is that we lack a physics-based engineering model for predicting internal erosion and consequent piping from first principles. The issue here is not one of applying probabilistic methods to a problem whose physics is well understood. It is a problem for which the basic mechanical processes have not been described adequately. Internal erosion or piping clearly involves a stochastic process of flowing water removing particles one by one from the erodible zone. However, the criteria used for design of inverted filters are expressed in terms of the grains sizes of the different layer and do not incorporate the thicknesses of the layers. Workers on dam safety recognize that current methods do a poor job of predicting the formation of a solution cavity or even of identifying it after it has developed.

Our current reliability model for internal erosion derives from pioneering work done at USBR in the 1990's (Von Thun 1996) and by Fell and his colleagues in Australia (Fell and Fry 2007). This work provides valuable insight into the causes and prediction of internal erosion. It decomposes the process of internal erosion into discrete steps: the initiation of erosion at a flaw, the subsequent progression of that erosion through the embankment, the continuation of the erosion to create a self-supported pipe, the failure of human intervention to prevent the development of a pipe, and finally the event of the pipe forming a breech (**Figure 2**).

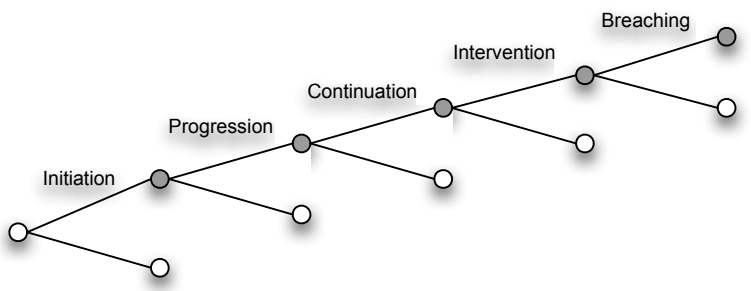

Figure 2. Event tree for internal erosion failure in an earth dam

The difficulty with this analytical approach is that the first three components of the event tree are essentially unobservable. The probability at each stage is subjectively assessed but there is no ground-truth by which to judge whether the resulting computed probability of piping failure makes sense. With no disrespect to the insightful work that has led to this reliability approach, the event tree analysis itself is a little like theology, but of course the present authors have nothing better to propose.

In view of the potentially catastrophic consequences of internal erosion, successful resolution of the probabilistic mechanics of internal erosion could have a major impact on the safety evaluation of existing facilities.

6. Connecting the observational method to Bayesian updating. Peck (1969) described the development of the observational method originally proposed by Terzaghi and provided several examples of its practical use. In a paper near the end of his life, Terzaghi (1961) wrote, "Soil engineering projects […] require a vast amount of effort and labor securing only roughly approximate values for the physical constants that

appear in the equations. The results of the computations are not more than working hypotheses, subject to confirmation or modification during construction. In the past, only two methods have been used for coping with the inevitable uncertainties: either adopt an excessively conservative factor of safety, or make assumptions in accordance with general, average experience. The first method is wasteful; the second is dangerous. A third method is provided that uses the experimental method. The elements of this method are 'learn-as-you-go:' Base the design on whatever information can be secured. Make a detailed inventory of all the possible differences between reality and the assumptions. Then compute, on the basis of the original assumptions, various quantities that can be measured in the field. On the basis of the results of such measurements, gradually close the gaps in knowledge, and if necessary modify the design during construction."

The observational method requires that information be collected as the project is carried out so that the design and construction strategy can be updated. It also requires that there be an initial plan for how to deal with changed conditions. Invoking the observational method to make the design more robust without making provisions for obtaining updated information and for changing the design in response is a prescription for unsatisfactory performance. In other words, the observational method requires rational consideration of the uncertainties in the parameters and a clear plan for dealing with events as they develop.

Bayesian thinking is essentially the same logic that Terzaghi describes, but based on mathematical logic, and as a result it is a powerful basis for inference. *Bayes' Rule* says that uncertainties expressed as probabilities can be modified (*i.e.,* updated) by observational information according to the conditional probability (*Likelihood*) of those observations were a certain hypothesis true or not,

$$P(hypothesis \mid data) \propto P(hypothesis)P(data \mid hypothesis) \qquad (2)$$

in which $P(hypothesis \mid data)$ is the updated probability based on having made certain observations, $P(hypothesis)$ is the probability before seeing the data, and $P(data \mid hypothesis)$ is the Likelihood of the data. Wu (1974), Einstein *et al.* (1976), and others long ago drew the connection between the observational method and Bayesian thinking, but the two approaches—one growing out of geotechnical practice and the other out of statistics—have yet to be functionally combined except in special cases such as Einstein's Tunnel Cost Model. Yet, the benefits could be substantial.

Bayesian thinking has permeated a range of fields from artificial intelligence to criminal forensics to the attribution of disputed authorship. It served as an important piece of Alan Turning's approach to cracking the German *Enigma* codes during World War II. Why haven't we used it to bring the observational method into the 21st century?

7. Risk communication and active risk management. We have developed methods for estimating the risk of various types of failure. We have not developed ways to communicate the risks to owners and the public, despite wide use of F-N diagrams. Nor do we have methods for managing and controlling the risks of our projects while projects are underway.

There are actually two types of risk communication involved: communication with the owners and communication with the public. In both cases the basic problem is that the engineer must convert technical knowledge of risk into language that can be understood by persons who are not conversant with the technology used to develop the estimates of the risk. However, the public (or publics) has a much wider range of concerns and agendas and has great difficulty dealing with risks posed by low probability events that have large consequences.

The F-N diagram (Figure 3) is now often used to communicate relative risks. It shows the annual probability of exceedance for different levels of damage and is especially useful for conveying relative risks. The IPET studies of the effects of Hurricane Katrina developed color-coded contour plots of expected levels of inundation with annual probabilities of 2%, 1%, and 0.2%.

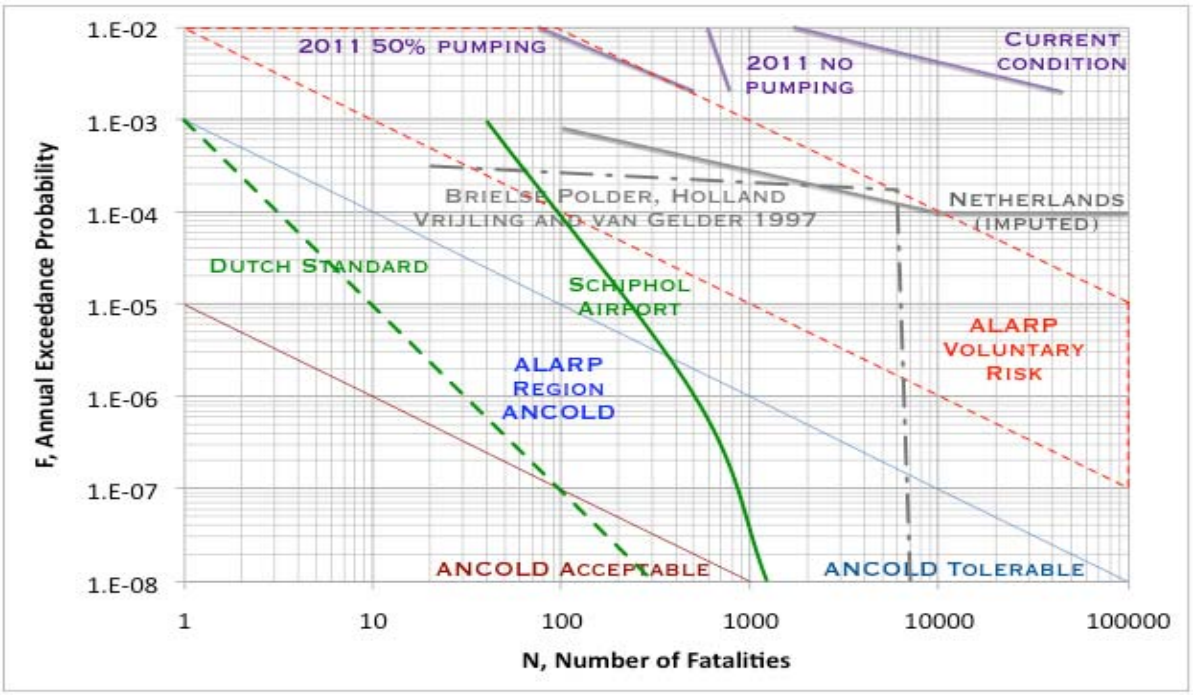

Figure 3. F-N plot for flooding risks, including ANCOLD criteria for dams.

Although computers now make it possible to prepare graphical descriptions of risk in formats that convey the essential information accurately both to owners and to the general public, the unthinking use of computerized graphics can also yield misleading and incomprehensible plots. It is now very easy to produce very bad graphics. Except for the F-N plot, we have not established standard ways to disply our results.

The underlying issue is that it is difficult for the public, owners, and even engineers to deal with and plan for extremely rare events that have severe consequences. How should resources be allocated? Which of many dire scenarios

should be taken seriously? We would like to achieve some sort of balance between events with different probabilties of occurrence and diferent consequences, but we can be sure that we have not yet achieved it.

8. Applying LRFD when properties are determined by effective stress. Load and Resistance Factor Design (LRFD) was originally developed as a rational way to qualify the contributions of different loadings in the analysis of steel and concrete structures. Resistance was and remains a single variable in those applications. The factors are applied primarily to the loads. LRFD has been applied with some success to develop design procedures for piles, which are essentially structural members embedded in the ground. The approach has been somewhat less satisfactory when applied to retaining structures, and even then effects such as strength dependent on normal stress and varying water pressures are often ignored. Attempts to apply the LRFD philosophy to general geotechnical problems including effective stress, uncertain water levels, uncertain failure modes, and other common geotechnical phenomena have often devolved into efforts to make the new design procedures give the same results as the old ones. Can a method that has revolutionized structural engineering be applied rationally to geotechnical engineering? If so, how?

A second issue is that it is relatively easy to explain how the various load combinations ought to be chosen to be consistent with their contributions to the probability of failure. It is much harder to explain how this procedure works when the loads and resistance interact, as they do in frictional materials. There is a danger that the factors become mysterious parameters with no physical justification and that the designers therefore lose track of what they are doing.

The idea that different safety factors ought to apply for different parameters or different loading conditions has a long history in geotechnical engineering. Taylor (1948) discussed the concept in the context of slope stability analysis. Also, codes have been developed in which load and resistance factors were developed to be generally consistent with previous geotechnical practice and structural design methods. However, it does not appear that the research community has developed an approach that is consistent with the principles of LRFD and with the physical principles of soil and rick mechanics.

9. Guidance to practitioners on exploration strategies. There is a large literature on sampling strategy, but it has had little impact on the way we do explorations for new projects. Part of the problem is that the results are not very useful unless they are combined with Bayesian updating. There is a need for serious study of what can be done in a realistic environment and for communicating these insights to practitioners.

Much of current sampling strategy evolved from military applications such as searching for mines. The first result of the theory is that one needs to do a lot of sampling to reduce the probability of error to an acceptable level. This is not a very useful result. Bayesian updating can be used to improve the situation.

However, we have not developed sampling strategies that are consistent with modern Bayesian methods and that are understood by people who must make decisions in the field about borings and sampling. To complicate matters, it is clear that

the appropriate strategies depend strongly on the geological settings and the nature of the facility to be built.

If a value of a soil property, such as shear strength, or of a field measurement, such as settlement, lies far from the previously observed general trend, what impact should this have on the design procedures? While there are statistical techniques for dealing with outliers, it is not clear how they can be applied in the actual practice of geotechnical engineering. This may be a modern extension and elaboration of Terzaghi's well-known emphasis on the importance of "minor geologic details."

10. Can we improve on "DeMorgan's Rule" for multiple failure modes? In situations such as dam safety the usual rules for calculating the failure probability of the system from the computed failure probabilities of the individual modes of performance often lead to results that seem unreasonably conservative. Current practice is to assume the extreme cases that the behaviors of the individual failure modes are either perfectly correlated or perfectly uncorrelated ("De Morgan's Rule"). Is this the best we can do? How can we improve on this approach?

In the situation where one does not know whether the failures of the modes are in fact probabilistically independent, the probability of system failure, presuming all the modes mutually independent, is an upper bound. The lower bound on the probability of system failure is given by the case of perfect dependence among all the probabilities $p_i = p_j = p$; that is, for the case in which, if one mode fails, they all fail, or if one mode does not fail, they all do not fail. In this case the probability of system failure is the same as any mode failing, p. Thus, the bounds on the probability of system failure are,

$$p \le P(\text{system failure}) \le 1-(1-p)^n \tag{3}$$

in which n = the number of modes. Ang and Tang (1984) have called these, the *unimodal bounds* on the probability of systems failure. They are sometimes also called, the *DeMorgan bounds*, after the logician Augustus DeMorgan (1806-1871). It should be noted that these bounds are very wide if n is large and p is small.

There has been considerable discussion over how to select a unique probability of system failure within these bounds, but no satistactory solution appears at hand. Bromwell, Dean, and Vick (2006) proposed taking the mid-point, but that is an arbitrary choice. Why the mid point? Why not the mid point of the logarithms of the probabilities? The nuclear safety industry adopts a simple "beta factor" or weighted average of the two bounds, typically about 25% of the independent case (Ali Mosleh, personnal communication, 2010).

The problem with this formulation is that the probability of system failure rises quickly with n. Note, this is almost identical to the "length effect" problem. If we are considering piping forming at the interface between core and foundation, there could be an essentially infinite number of possible channels, in which case $P \to 1$.

In practice, the uncertainties in the failure modes are likely not to be probabilistically independent, and thus DeMorgan's Law is only an upper bound, and may in fact be quite a distant upper bound, especially for large n, implying failure geometries that are spatially adjacent or even overlapping. The problem is that we don't have a good

way of estimating the degree of probabilistic dependence among the separate failure modes.

SUMMARY

The ten issues described above range from technical, mechanical problems that have defied solution to matters of communication between researchers, designers, and constructors. It is certainly not an exhaustive list, but we present it so that it will challenge the geotechnical reliability community in its efforts in the coming years. It will be interesting to return to these issues in the future to see how much progress we have made.

ACKNOWLEDGEMENTS

The authors are indebted to the helpful comments of many colleagues on an earlier draft of this paper, but especially to (in alphabetical order): J. Michael Duncan of Virginia Tech; W. Allen Marr of Geocomp Corporation; Therese McAllister of the National Institute of Standards and Technology; Thomas O'Rourke of Cornell University; Robert Patev of the US Army Corps of Engineers; and K.K. Phoon of the National University of Singapore.

REFERENCES

Ang, A. H. S., and W. H. Tang (1984) *Probability Concepts in Engineering Planning and Design, Vol. 2 – Decision, Risk, and Reliability*, New York, J. Wiley.

Baecher, G. B. and J. T. Christian (2003). *Reliability and Statistics in Geotechnical Engineering.* Chichester, West Sussex, England ; Hoboken, NJ, J. Wiley.

Bromwell, L.G., R. G. Dean, and S. G. Vick (2006) Report of Expert Review Panel Technical Evaluation of Herbert Hoover Dike Lake Okeechobee, Florida. Prepared for South Florida Water Management District. BCI Engineers and Scientists, Lakeland, Florida.

Christian, J. T., and W. D. Carrier III (1978) "Janbu, Bjerrum, and Kjaernsli's chart reinterpreted," *Canadian Geotechnical Journal*, 15(1), 123-128.

Einstein, H. H., D. A. Labreche, *et al*. (1976). "Decision analysis applied to rock tunnel exploration." *Engineering Geology*, 12(2), 143-161.

Fell, R. and J. J. Fry (2007). *Internal erosion of dams and their foundations*. London ; New York, Taylor & Francis.

Fenton, G. A., and D. V. Griffths (2008) *Risk Assessment in Geotechnical Engineering*, New York, J. Wiley.

Hilbert, D. (1902) "Mathematical problems." *Bulletin of the American Math.ematical Society*, 8(10), 437-479.

Hill, P., D. Bowles, *et al.* (2003). "Estimating overall risk of dam failure: Practical considerations in combining failure probabilitries." *ANCOLD 2003 Risk Workshop*. Hobart, Tasmania, Australian National Committee on Large Dams.

Peck, R. B. (1969) "Advantages and limitations of the observational method in applied soil mechanics." *Geotechnique*, 19(1), 171-187.

Phoon, K. K. and F. H. Kulhawy (1996). “On quantifying inherent soil variability.” *Uncertainty in the Geologic Environment*, Madison, WI, ASCE.

Phoon, K. K., and F. H. Kulhawy (1999a) “Characterization of geotechnical variability.” *Canadian Geotechnical Journal*, 35(4), 612-624.

Phoon, K. K., and F. H. Kulhawy (1999b). “Evaluation of geotechnical property variability.” *Canadian Geotechnical Journal*, 35(4), 625-639.

Tversky, A. and D. Kahneman (1971). “Belief in the law of small numbers,” *Psychological Bulletin, 76*(2): 105-110.

USACE (2003). Slope Stability. U. S. Army Corps of Engineers. Washington, USACE.

USACE (2009). Performance Evaluation of hte New Orleans and Southeast Louisiana Hurricane Protection System. Washington, U. S. Army Corps of Engineers. Volume VIII - Engineering and operaoinal risk and reliability alanysis.

Vanmarcke, E. (1977). "Probabilistic modeling of soil profiles." *Journal of the Geotechnical Engineering Division, ASCE* 103(11), 1227-1246.

Von Thun, J. L. (1996). “Understanding seepage and piping failures – the No.1 dam safety problem in the west.” *ASDSO Western Regional Conference*. Lake Tahoe, Nevada,, Association of State Dam Safety Officials.

Wu, T. H. (1974). "Uncertainty, Safety, and Decision in Soil Engineering." *Journal Geotechnical Engineering Division, ASCE,* 100(3), 329-348.

Learning to Live with Geohazards: From Research to Practice

Suzanne Lacasse and Farrokh Nadim

Norwegian Geotechnical Institute (NGI)/International Centre for Geohazards (ICG), P.O.Box 3930 Ullevaal Stadion, NO-0806 Oslo, Norway, Ph +47 22 02 30 00, Fax +47 22 23 04 48, e-mail: suzanne.lacasse@ngi.no, farrokh.nadim@ngi.no.

ABSTRACT

The paper summarizes key aspects in the assessment of geological hazard and risk and exemplifies these with applications in practice. Methods for estimating the risk, from simple qualitative approaches to more complex quantitative ones are presented. Risk frameworks are presented. Key components of risk management, such as the notion of acceptable and/or tolerable risk, risk mitigation, especially early warning systems, risk communication and multi-risk issues are addressed. Case studies on the stability of a rock slope in Western Norway, vulnerability assessment and risk management for landslides, the assessment of tsunami risk in a coastal town, risk mitigation to prevent quick clay landslides, the hazard and risk associated with a major dam breach, the implementation of early warning systems to prevent catastrophic consequences and risk communication with all categories stakeholders are provided. The paper also briefly describes three ongoing research projects in the 7th Framework Programme of the European Commission on risk assessment and management of geohazards.

INTRODUCTION

Geohazards represent a major threat to human life, constructed facilities, infra-structure and natural environment in many regions of the world. During this past decade 2000-2009, natural disasters caused nearly one million fatalities, affecting nearly 2.5 billion people across the globe.

In 2010 alone, 295,000 fatalities were recorded by Munich RE (2011) and the overall economic losses were more than double those of 2009, for approximately the same number of natural catastrophes. Table 1 presents the 2010 natural catastrophe data published by Munich RE NatCatSERVICE. Most of the increase is due to the in-crease in the exposed population. The frequency and/or severity of climate-driven natural hazards seem also to be rising. Some of the reasons for the increase are obvious, others less so. However, many lives could have been saved if more had been known about the risks associated with geohazards and risk mitigation measures had been implemented.

Table 1. Natural catastrophes in 2010 (Munich Re 2011)

Events and losses	2010	2009	Average 2000-2009	Average 1980-2009
Number of events	950	900	785	615
Overall losses (US$m)	130,000	60,000	110,000	95,000
Insured losses (US$m)	37,000	22,000	35,000	23,000
Number of fatalities	295,000	11,000	77,000	66,000

Developing countries are more severely affected by natural disasters than developed countries, especially in terms of lives lost (UNDP 2004, UNISDR 2009a and IFRC 2004). Table 2 shows the data compiled by IFRC (2001) for the decade 1991-2000.

Table 2. Natural disasters between 1991-2000 (IFRC 2001)

Countries	No. of disasters	No. of lives lost
Low and medium developed countries	1838	649,400
Highly developed countries	719	16,200

Of the total number of persons killed by natural disasters in this period, the highly developed countries accounted for 5 % of the casualties. In absolute numbers, the material damage and economic loss due to natural hazards in highly developed countries by far exceed those in developing nations. However, this reflects the grossly disproportionate values of fixed assets, rather than actual economic vulnerability.

Mitigation and prevention of the risk posed by natural hazards have not attracted widespread and effective public support in the past. However, the situation has changed dramatically during the past decade, and it is now generally accepted that a proactive approach to risk management is required to significantly reduce the loss of lives and material damage associated with natural hazards. The wide media attention on major natural disasters during the last decade has clearly changed people's mind in terms of acknowledging risk management as an alternative to emergency management. A milestone in recognition of the need for natural disaster risk reduction was the approval of the "Hyogo Framework for Action 2005-2015: Building the Resilience of Nations and Communities to Disasters" (ISDR 2005). This document, approved by 164 UN countries during the World Conference on Disaster Reduction in Kobe in January 2005, defines international working modes, responsibilities and priority actions for the coming 10 years.

While earthquakes, floods, tsunamis and storms receive wide attention in the news, landslides are not recorded as separate hazard by Munich Re. Nevertheless they occur frequently and can have dramatic consequences. The European statistics from the past 100 years (Table 3) indicate that the frequency of landslides in Europe (about 20 major events per year) is the highest among natural hazards, compared to floods, earthquakes and cyclones. However the number of fatalities and the quantity of material damage is far greater under earthquakes.

Table 3. Socio-economic impact of natural hazards in Europe (1900-2000).

Hazards	Lose of life	Natural damage
45 floods	10,000	105 B€
1700 landslides	16,000	200 B€
32 earthquakes	239,000	325 B€

It should be noted that landslides are also frequently triggered by floods and earthquakes and are not statistically recorded as landslides, but as floods and earthquakes, in the disaster databases.

In the 20th century, the economic losses from natural hazards were greatly underestimated, the awareness of hazards and risk was insufficient, and the mitigation and regulation to avoid damage and loss was inadequate. Since 2005, the awareness of the need for mitigation of natural hazards has greatly increased. On the other hand, since the 80's, hazard and risk assessment of the geo-component of a system has gained increased attention. The offshore, hydropower and mining industry were the pioneers in applying the tools of statistics, probability and risk assessment. Gradually, environmental concerns and natural hazards started implementing hazard and vulnerability assessment. Nowadays the notion of hazard and risk is a natural question in most foundation aspects and even project management.

This paper describes briefly the framework of risk management and illustrates its use with case studies of several of the steps of the analysis, including hazard, vulnerability and risk assessment with different approaches, and examples of risk mitigation and risk communication.

THE HAZARD IN RISK ASSESSMENT

The task of risk analysis professionals is about assessing hazard, vulnerability and risk in the context of safety. We all know, perhaps much more than the public affected by the risk, that the analysis of safety in facilities or on natural slopes with the potential for major accidents, is a very complex task and subject to major uncertainties. In our geo-analysis, we "run the risk" of not seeing "the forest for the trees", or the risk of not seeing "safety for the steps in the risk assessment". In addition, we "run the risk" of using the numbers in a complex analysis, for example an event tree analysis, to arrive at, even subconsciously, the answers one wants to achieve. Unbiased estimates, when data are lacking, are difficult to achieve, even for the most experienced professional.

It is essential that the assessment models for hazard and risk become more transparent and easier to perceive and use, without reducing the complexity of the models required for the assessment. There is today an increasing focus on hazard- and risk-informed decision-making. Therefore integrating deterministic and probabilistic analyses in a complementary manner, as recommended since the late 80's (e.g. Lacasse *et al.* 1989), will enable the user (with or without scientific background) to

concentrate on the analysis results rather than the more complex underlying information. Focus needs to remain on "safety". The complementary deterministic-probabilistic approach brings together the best of our profession and the required engineering judgment from the geo-practicians and the risk analysis proponents.

TERMINOLOGY

The terminology used in this paper is generally consistent with the recommendations of ISSMGE Glossary of Risk Assessment Terms (listed on TC304 web page: http://jyching.twbbs.org/issmge/home_2010.htm). The key terms used in the context of the paper are:

Danger (Threat): Natural phenomenon that could lead to damage, described by geometry, mechanical and other characteristics. Description of a threat involves no forecasting.

Hazard: Probability that a particular danger (threat) occurs within a given period of time.

Exposure: The circumstances of being exposed to a threat.

Risk: Measure of the probability and severity of an adverse effect to life, health, property, or the environment. Mathematically, risk is defined as Risk = Hazard × Potential worth of loss.

Vulnerability: The degree of loss to a given element or set of elements within the area affected by a hazard. It is expressed on a scale of 0 (no loss) to 1 (total loss).

In UNISDR terminology on Disaster Risk Reduction (2009), "disaster" is defined as "a serious disruption of the functioning of a community or a society causing widespread human, material, economic or environmental losses which exceed the ability of the affected community or society to cope using its own resources". The term "natural disaster" is slowly disappearing from the disaster risk management. Without the presence of humans, one is only dealing with natural processes; these become disasters only when they impact a community or a society.

RISK MANAGEMENT

Framework

Risk management broadly refers to coordinated activities to assess, direct and control the risk posed by geohazards to the society. It integrates the recognition and assessment of risk with the development of appropriate strategies for its mitigation. The risk management process is a systematic application of management policies, procedures and practices to the tasks of communicating, consulting, establishing the context, identifying, analyzing, evaluating, monitoring and implementing risk mitigation

measures (Draft ISO/ IEC 31010 Ed. 1.0: Risk Management - Risk Assessment Techniques).

Risk management frameworks have the common objective of answering the following questions (modified from Lee and Jones 2004):

- What are the dangers and their magnitude? [Danger Identification]
- How often can the dangers of a given magnitude occur? [Hazard Analysis]
- What are the elements at risk? [Elements at Risk Identification]
- What is the potential damage to the elements at risk? [Vulnerability Assessment]
- What is the probability of damage? [Risk Estimation]
- What is the significance of the estimated risk? [Risk Evaluation]
- What should be done? [Risk Management]

Figure 1 illustrates such an integrated process for the assessment and management of the risk associated with a landslide. The framework is iterative. It is often required to go back to an earlier step to reassess in light of new information. Figure 2 provides one example of a framework for risk management, as used in one of the Norwegian standards. The process starts with risk estimation (frequency and consequence analysis), continues with risk analysis, then risk assessment, and finally safety management and risk control.

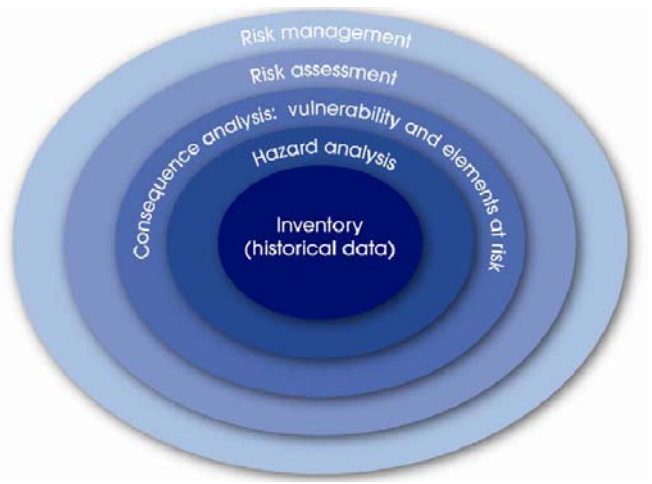

Figure 1. Integrated risk management process including risk assessment.

Fell *et al.* (2005) made a comprehensive overview of the state-of-the-art in landslide risk management. Several risk formulations have been proposed, and Düzgün and Lacasse (2005) list a large number of these. A large body of literature also exists on earthquake risk management. In the following sections, methodologies for answering one or more of the above questions are discussed.

The first step in any decision-making process for disaster risk reductions is a quantitative risk assessment. One typically assesses risk based on a number of plausible scenarios. For example, in the case of a landslide, the following steps would be used:

(1) define scenarios for triggering the landslide and evaluate their probability of occurrence; (2) compute the run-out distance, volume and extent of the landslide for each scenario; (3) estimate the losses for all elements at risk for each scenario; and (4) estimate the risk. Risk assessment is part of an integrated risk management process.

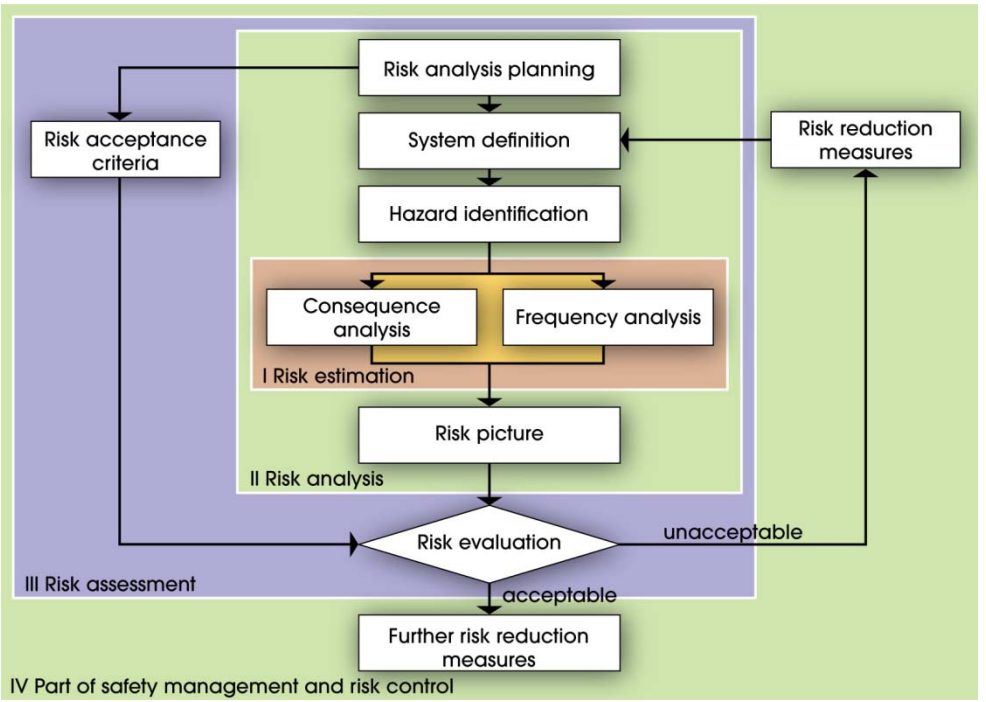

Figure 2. Example of risk management (NORSOK Standard Z-013 2001).

Acceptable and tolerable risk

One of the most difficult tasks in risk assessment/management is the selection of risk acceptance criteria. As guidance to what risk level a society is apparently willing to accept, one can use 'F-N curves'. The F-N curves relate the annual probability of causing N or more fatalities (F) to the number of fatalities, N. The term "N" can be replaced by other quantitative measure of consequences, such as costs. The curves can be used to express societal risk and to describe the safety levels of particular facilities. Figure 3 presents a family of F-N-curves. Man-made risks tend to have a steeper curve than natural hazards in the F-N diagram (Proske 2004). F-N curves give statistical observations and not the acceptable or tolerable thresholds.

Who should define acceptable and tolerable risk level? The potentially affected population, government, or the design engineer? Societal risk to life criteria reflect the reality that society is less tolerant of events in which a large number of lives are lost in a single event, than if the same number of lives is lost in a large number of separate events. Examples are public concern at the loss of large numbers of lives in airline crashes, compared to the much larger number of lives lost in road traffic accidents. Figure 4 presents an interim risk criterion recommendation for landslides

on natural hillsides in Hong Kong (GEO 1998). Acceptable risk refers to the level of risk requiring no further reduction. It is the level of risk society desires to achieve. Tolerable risk presents the risk level reached by compromise in order to gain certain benefits. A construction with a tolerable risk level requires no action/expenditure for risk reduction, but it would be desirable to control and reduce the risk if the economic and/or technological means for doing so are available.

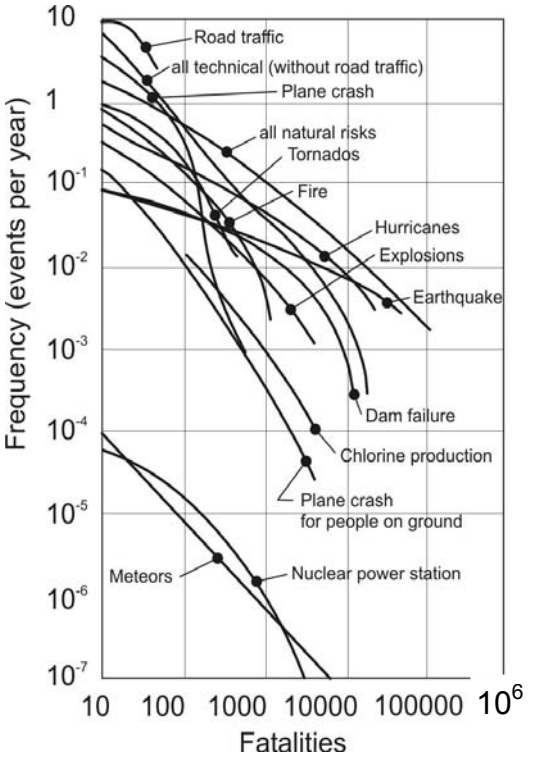

Figure 3. F-N curves (United States Nuclear Regulatory Commission 1975; Proske 2004).

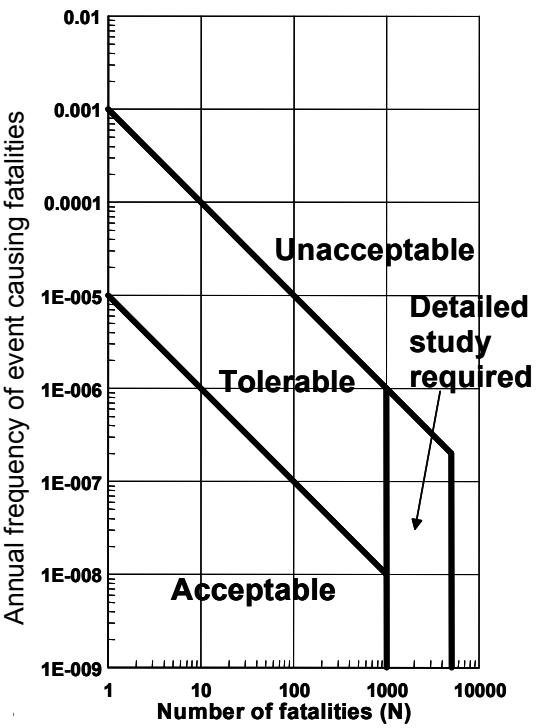

Figure 4. Hong Kong criteria (GEO 1998).

Risk acceptability depends on several factors such as voluntary vs. involuntary situation, controllability vs. uncontrollability, familiarity vs. unfamiliarity, short/long-term effects, existence of alternatives, type and nature of consequences, gained benefits, media coverage, availability of information, personal involvement, memory, and level of trust in regulatory bodies. Voluntary risk levels tend to be higher than involuntary risk levels. Once the risk is under personal control (e.g. driving a car), it is more acceptable than the risk controlled by other parties. For landslides, choosing to live close to a natural slope can be considered as a voluntary risk, while having a slope engineered close to one's dwelling is an involuntary risk as the decision of engineering the slope was taken by others. Societies that experience geohazards frequently may have a different risk acceptance level than those experiencing them rarely. Informed societies can have better preparedness for natural hazards.

Total risk is defined by the sum of specific risk. It is, however, difficult to evaluate its sum, since the units for expressing each specific risk differ. Individual risk has the unit of loss of life/year, while property loss has the unit of loss of property/year (e.g. USD/yr). Risk acceptance and tolerability have different perspectives: the individual's point of view (individual risk) and the society's point of view (societal risk).

Risk mitigation

The strategies for the mitigation of risks associated with geohazards can broadly be classified in six categories: 1) land use plans, 2) enforcement of building codes and good construction practice, 3) early warning systems, 4) community preparedness and public awareness campaigns, 5) measures to pool and transfer the risks and 6) physical measures and engineering works. The first five strategies are referred to as non-structural measures, which aim to reduce the consequences of geohazards; while the last strategy comprises active interventions such as construction of physical protection barriers, which aim to reduce the frequency and severity of the geohazards.

A mitigation strategy involves: 1) identification of possible disaster triggering scenarios, and the associated hazard level, 2) analysis of possible consequences for the different scenarios, 3) assessment of possible measures to reduce and/or eliminate the potential consequences of the danger, 4) recommendation of specific remedial measures and, if relevant, reconstruction and rehabilitation plans, and 5) transfer of knowledge and communication with authorities and society.

A recent report by The World Bank (2010) looked into the effectiveness of government policies and private actions in preventing disasters. The report looked at disasters primarily through an economic lens, and drew four main conclusions. First, a disaster exposes the cumulative implications of many earlier decisions, some taken individually, others collectively, and a few by default. Several factors usually contribute to any disaster, and effective prevention measures are not always "obvious". Second, disaster prevention and mitigation is often possible and cost-effective. Third, many risk mitigation measures – private and public – must work well together for effective prevention. Fourth, the exposure to hazards will rise in cities, but increased exposure does not necessarily increase the vulnerability.

In many situations, the most effective risk mitigation measure is an early warning system that gives sufficient time to move the elements at risk out of the harm's way. The remainder of this section focuses on issues related to early warning systems and highlights the challenges in their design.

Early warning systems

Early warning systems appear as an effective solution to reduce the vulnerability to geohazards. Two case studies will show the implementation of early warning. Figure 5 illustrates the components of an early warning system.

Monitoring and early warning systems are more than just the implementation of a technological/scientific solution. The human factors, social elements and information communication such as decision-making authorities (e.g. government agencies, local authorities, police/fire), form, content and perception of warnings issued, population response, emergency plans and their implementation and plans for reconstruction/recovery are also essential parts of the system. An early warning system without consideration of the social aspects could create a new type of emergency (e.g. evacuating a village because sensors indicate an imminent landslide, but without giving the village population any place to go, shelter or means to live). There can be failures in the technology and maintenance, but failures in communication and in response can be even more dramatic.

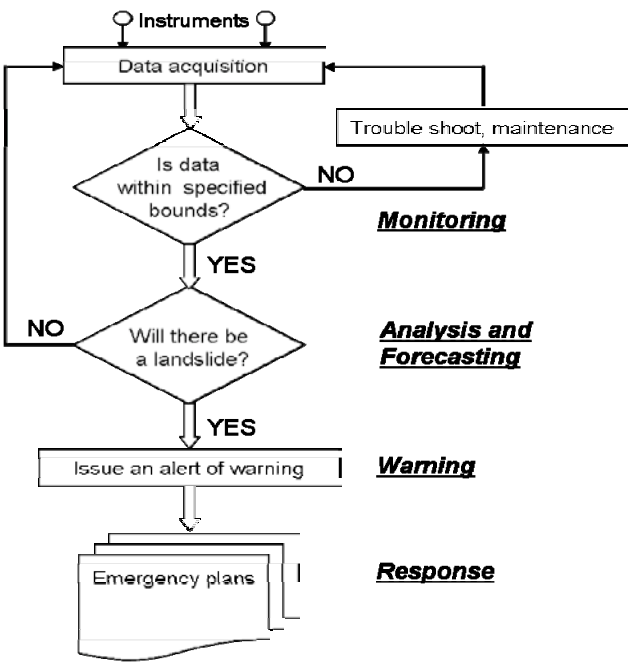

Figure 5. Typical early warning system (DiBiagio and Kjekstad 2007).

Technology

Technology and off-the-shelf solutions for the sensors and IT-system components of an early warning system are so accessible and diverse that the technology itself is probably not the limiting factor for most early warning systems. Types of available technology include:

- ordinary sensors (e.g. pressure, displacement, temperature)
- sensor systems (e.g. weather stations, survey stations, radar)
- communication technology (wire, radio, internet, mobile phone, satellite)
- data collection systems and data processing capabilities
- messaging services (sirens, telephone, sms, television)

The difficulty can often lie in practical issues, such as accessibility of a location for installation and maintenance of sensors and system components. Another issue is inclement weather, e.g. high winds, extreme temperatures, snow and rain, which may affect sensors or communication lines, damage cables or instruments and block radar reflectors. Installations may be remote, and to some degree it is necessary to rely on local inhabitants for operation and maintenance of the equipment.

Redundancy is necessary

Early warning systems are by definition critical systems, and as such it is absolutely necessary that the system remains in operation at all times, requiring a chain of functional components: monitoring of key parameters - raw data transmission - data processing, interpretation and modelling - decision making - issuing of warnings - reaction of protected population and emergency services. A breakdown at any point in this chain renders the system useless.

Good measurement solutions in critical systems often employ alternative measurement technologies (i.e. two different ways to measure a quantity) as well as redundancy in the sensors themselves. Data transmission, if possible, could be routed through multiple channels, e.g. via internet (full data set) and via radio (status indicator or reduced data). Similar considerations should be taken for the entire system, e.g. models for data interpretation, personnel, communication with the public and emergency systems.

Issuing an alarm requires a prediction

In order to issue an alarm, one must make a prediction of what is about to happen. Making a prediction requires an understanding of the physical process. Sufficient lead time must be available to be able to take an effective action. The system needs quantitative indicator parameters (e.g. rainfall, water levels, pressures, vibrations, movements or displacements). The main challenge in designing an early warning system is the reliable and effective specification of threshold values. This involves generally some form of forecasting based on past trends in the measurements. Engineering judgment is an important element in this process. The system must also be flexible so that the threshold parameters can be changed as more information becomes available on the performance of the monitoring system and the engineered facility.

False alarms – The little boy who cried wolf

The children's story about the little shepherd boy who cried "wolf" is the classic example of how false alarms can destroy credibility in a system. A population subject to a false alarm reacts the first, second, and maybe a third time, but quickly the alarm loses credibility. Initially an implicit trust exists between the affected population and the "experts", and an acknowledgment of the system exists. Lost trust can only be won back with difficulty.

Multi-risk and risk perception

Most inhabited areas are exposed to several natural and anthropogenic threats. Some of these threats are causally related with respect to their occurrence and their consequences. As a result, people can suffer losses not just from single events, but also from multiple events in combination. Classes of interactions include triggered events, cascading effects, and rapid increases of vulnerability during successive events. Planners, policy-makers and scientists, usually treat the hazards and risks related to such events separately from each other, neglecting the interdependencies among the different phenomena and the importance of risk comparability. The multi-risk approach – a joint analysis and quantification of all the anthropogenic and natural risks that could affect a territory – would provide the basis for sound environment management and land use planning, as well as competent emergency management before and during catastrophic events (Durham 2003). Multi-risk evaluation is a relatively new field, its theoretical framework is incomplete, and is fragmented across a number of disciplines.

In Europe, there is increasing research interest in the multi-risk perspective, where cascading hazards and time-dependent vulnerability are considered. Risk perception and risk communication are complex issues that are also under research scrutiny. Three European research projects addressing these issues are briefly described at the end of this paper.

TOOLS FOR RISK ASSESSMENT

Risk assessment, the starting point for risk management, may utilize a variety of formal and informal tools according to the context, access to data and technology level of uncertainties and stakeholders involved.

Deterministic and probabilistic approaches

The stability situation for natural and man-made slopes is often expressed in terms of factor of safety. The factor of safety is defined as the ratio of the characteristic resisting force to the characteristic load (driving force). The conventional approach does not address the uncertainty in load and resistance in a consistent manner. The ambiguous definition of "characteristic" values allows the engineer to implicitly account for uncertainties by choosing conservative values of load (high) and resistance parameters (low). The choices, however, are somewhat arbitrary. Slopes with nominally the same factor of safety could have significantly different safety margins because of the uncertainties and how they are dealt with. Duncan (2000) pointed out that "Through regulation or tradition, the same value of safety factor is often applied to conditions that involve widely varying degrees of uncertainty. This is not logical." As shown in Figure 6, a low safety factor does not necessarily correspond to a high probability of failure and vice versa. The relationship between the factor of safety and probability of failure depends on the uncertainties in load and resistance.

Probability theory and reliability analyses provide a rational framework for dealing with uncertainties and decision making under uncertainty. Depending on the level of sophistication, the analyses provide one or more of the following outputs:

- Probability of failure (or probability of unsatisfactory performance)
- Reliability index
- The most probable combination of parameters leading to failure
- Sensitivity of result to any change in parameters

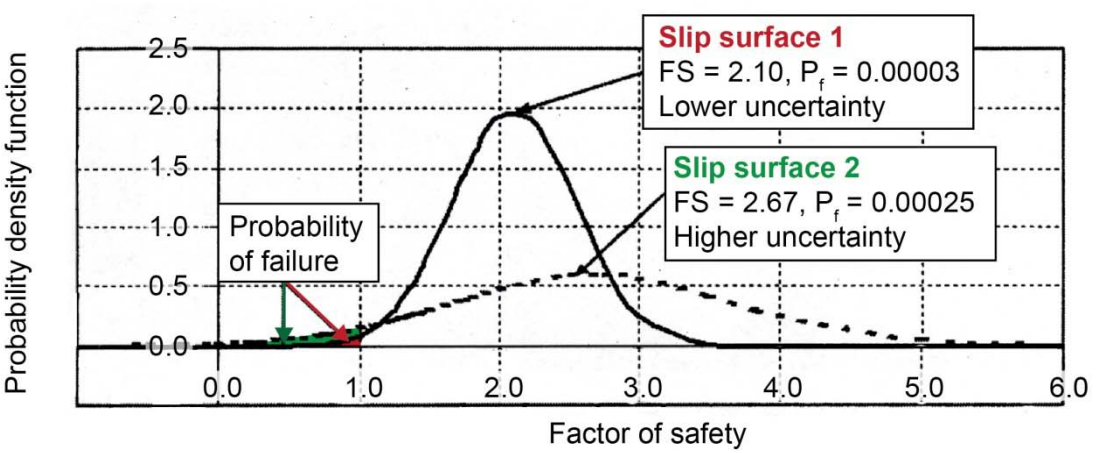

Figure 4. Factor of safety and probability of failure for two "critical" slip surfaces.

Christian *et al.* (1994) provided an example of the use of comparative probabilities. Three heights of dikes were proposed for the James Bay project: 6, 12, and 23 m. The first two are single stage dikes; the last was a composite dike built in stages. Table 4 gives the estimated factors of safety and probabilities of failure for the three alternatives. Although the factors of safety are similar, the probabilities of failure are quite different. The 23-m dike has a lower probability of failure, which is not reflected in the factor of safety.

One way to use these results in engineering design is to consider the desirable target probability of failure (Leroi *et al.* 2005). However, the computed failure probability is sometimes difficult to interpret as it is dominated by lack of knowledge. Therefore it is often more useful to compare probabilities of failure for different alternative courses of action than to rely on the absolute probability of failure.

Table 4. Probabilities of failure for James Bay Dikes (Christian *et al.* 1994).

Dike height, H	Factor of safety, F	Probability of failure, P_f
H = 6 m, single stage	1.6	$2.5 \cdot 10^{-2} = 0.0250$
H = 12 m, single stage	1.5	$4.7 \cdot 10^{-3} = 0.0047$
H = 23 m, multiple stage	1.5	$7.1 \cdot 10^{-4} = 0.0007$

Christian (2004) discussed the pros and cons of deterministic and probabilistic safety formats for the evaluation of the stability of existing slopes. The deterministic approach requires that a number of troublesome issues be addressed, including what is meant by the conventional factor of safety and how close is the slope to failure. Simple idealized examples and actual case studies show that slopes with high calculated factors of safety are not necessarily the safest.

Well-established reliability methods, such as the first-order second-moment approximation (FOSM), the first-order reliability method (FORM), Monte Carlo simulation and event tree analysis are useful techniques for determining the reliability of a design and for estimating the probability of failure. The reliability methods also reveal which parameters contribute most to the uncertainty in the stability. A simple prescription of a factor of safety to be achieved in all instances is not realistic and may lead to either overdesign or underdesign.

In the case of landslide events, hazard assessment for a specific slope usually involves a probabilistic analysis of the slope, while hazard assessment for a region generally requires the computation of frequency of the landslides. For regional analyses, data to be collected are in the form of maps related to geomorphology, geology, land-use/cover and triggers. For specific slopes, the required data for hazard analysis include slope geometry such as height, width, inclination of slope and potential failure plane, shape and length of failure plane etc., strength parameters data for possible trigger such as rainfall intensity, water level, severity of dynamic loads e.g. earthquake magnitude, acceleration and/or other characteristics. The probabilistic models used for a specific slope vary depending on the failure mechanism (e.g. flows, falls or slides) and the slope-forming material (e.g. soil or rock).

Analyses of specific slopes use deterministic (factor of safety, numerical analyses) and/or probabilistic methods, e.g. first order, second-moment (FOSM), first order reliability method (FORM), point estimate methods, and Monte Carlo Simulation (MCS) (Ang and Tang 1984). Recent trends combine different approaches for an improved model of the hazard(s). A prior uncertainty analysis is essential as it allows a rational calculation of total uncertainties associated with different sources of uncertainty (e.g. in parameters and models). The quantification and analysis of uncertainties play a critical role in the risk assessment. In the case of complex systems, the event tree approach is particularly useful.

Event tree analysis

The event tree approach (Vick 2002; Hartford and Baecher 2004; Ang and Tang 1984; Høeg 1996; and many others) is a technique to identify potential failure mechanisms and provides insight into how a series of events leading to non-performance might unfold. The probability of each event, given the occurrence of an initiating event, is quantified. As the number of events increases, the trees fan out like the branches of a tree. Each path in the event tree represents a specific sequence of events, resulting in a particular outcome. The events from a common node should be

defined such that they are mutually exclusive. Once each event in the tree is given a probability, the probability for each sequence of events is the multiplication of probabilities along the branches. The result is a set of frequency-outcome pairs (the outcome could be, e.g. "failure" or "no failure"). The total probability is the sum of all events leading to an outcome.

In an event tree analysis, engineering judgment and experience are needed in addition to the results of statistical and deterministic analyses. To achieve consistency in the evaluation of the probabilities (from one expert to the other and from one situation to another), a convention is often used to anchor the probabilities (Vick 2002; Hartford and Baecher 2004):

Verbal description of uncertainty	Event probability
Virtually impossible	0.001
Very unlikely	0.01
Unlikely	0.10
Completely uncertain	0.50
Likely	0.90
Very likely	0.99
Virtually certain	0.999

with the following definitions:

Virtually impossible:	Event that due to known physical conditions or processes can be ruled out with almost complete confidence.
Very unlikely:	The possibility cannot be entirely ruled out on the basis of physical or other reasons.
Unlikely:	Event is unlikely, but it could happen.
Completely uncertain:	There is no reason to believe that one outcome is any more or less likely than the other to occur.
Likely:	Event is likely, but it may not happen.
Very likely:	Event is highly likely, but may not happen, although one would be surprised if it did not happen.
Virtually certain:	event due to known physical conditions or processes that can be described and specified with almost complete confidence.

In a multi-disciplinary process such as the analysis of hazard and risk associated with natural hazards, a number of "experts", specialists and stakeholders are assembled and need to agree on the numbers set on the branches of the event tree. One needs then to achieve 'consensus'. Consensus derives from Latin, 'cum' meaning 'together with' and 'sentire' meaning to 'think' or 'feel'. Etymologically, 'consensus' therefore means to think or feel together'. In a decision-making process, consensus aims to be:

– inclusive: as many stakeholders as possible should be involved in the process;
– participatory: the process should solicit wide input and participation;

– cooperative: participants should strive to reach the best possible decision for the group rather than pursue a majority opinion, potentially to the detriment of a minority;
– egalitarian: all members of a consensus should be allowed, as much as possible, equal input into the process;
– solution-oriented: common agreement rather than differences should be emphasized, using compromise to reach decisions.

One can debate whether there is too much emphasis placed on engineering judgment in the event tree approach. However, all deterministic and probabilistic approaches involve some degree of engineering experience and judgment.

CASE STUDIES

Case Study 1: Hazard assessment and early warning - Åknes slope

Rock falls and rockslides are among the most dangerous natural hazards in Norway, mainly because of their tsunamigenic potential. The three most dramatic natural disasters in Norway in the 20th century were tsunamis triggered by massive rockslides into fjords or lakes (Loen in 1905 and 1936 and Tafjord in 1934), causing more than 170 fatalities (Bjerrum and Jørstad 1968; Anda and Blikra 1998). As public attention on natural hazards increases, the potential rockslides in the Storfjord region in western Norway have earned renewed focus. A massive rockslide at Åknes could be catastrophic as the rockslide-triggered tsunami is a threat to all the communities around the fjord. The Åknes/Tafjord project was initiated in 2005 by the municipalities, with funding from the Norwegian government, to investigate rockslides, establish monitoring systems and implement a warning system and evacuation plan to prevent fatalities, should a massive rockslide take place.

Åknes is a rock slope over a fjord arm on the west coast of Norway. The area is characterised by frequent rockslides, usually with volumes between 0.5 and 5 millions m^3. Massive slides have occurred in the region. Bathymetric surveys of the fjord bottom deposits show that numerous and gigantic rockslides have occurred many thousands of years ago. The Åknes/Tafjord project (www.aknes-tafjord.no) includes site investigations, monitoring, and an early warning system for the potentially unstable rock slopes at Åknes in Stranda County.

Experience from Norway and abroad shows that rockslide events are often preceded by warning signs such as increased displacement rate, micro-tremors and local sliding. Accelerating rate of displacement several weeks and even months before a major rockslide event is typical. Slope movements have been detected at Åknes down to 60 m depth. New borehole data suggest movements down to 100 m. Important uncertainties lie in the most likely failure depth and location, and whether the slide will occur as one large 30-60 millions m^3 sliding event or a succession of several 'small' slide events. Figure 7 presents the Åknes slope and two slide scenarios: Area I with

slide volume 10-15 millions m^3, and where the observed displacement is 6-10 cm/yr; Area II with slide volume 25-80 millions m^3, and where the observed displacement is 2-4 cm/yr. Water seeps ("springs") are seen emerging on the downstream slope (Kveldsvik *et al.* 2008). Figure 8 shows some of the displacements observed at the upper crack. The displacements appear to move linearly with time. The total annual displacements vary from less than 2 cm up to about 10 cm.

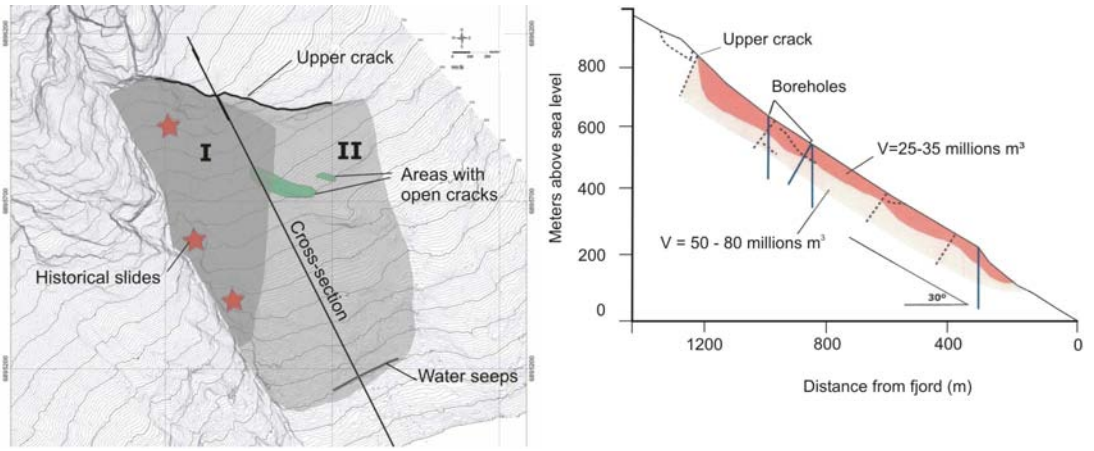

Figure 7. Sliding volume scenarios (modified from Blikra *et al.* 2007).

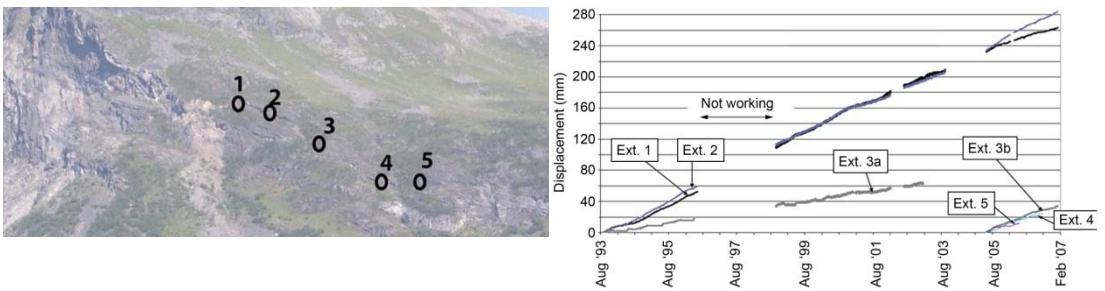

Figure 8. Displacements from extensometers 1, 2, 3, 4 and 5 at the top scarp at Åknes (Kristensen *et al.* 2010; Kveldsvik *et al.* 2006; 2008)

As part of the on-going hazard and risk assessment and validation of the early warning system, event trees were prepared by pooling the opinion of engineers, scientists and stakeholders. The objective was to reach consensus on the hazard and risk associated with a massive rockslide at Åknes (Lacasse *et al.* 2008).

The large variations in weather and atmospheric conditions in the fjord and mountain areas pose unusual challenges to the instrumentation. Snow avalanche and rock bursts occur often in the area to be monitored. Solar panels do not provide sufficient electricity, and energy has to be obtained from several sources to ensure a stable and reliable supply. Data communication is impaired during periods of adverse weather. An Emergency Preparedness Centre is located in Stranda. The monitoring system is equipped with:

Surface monitoring
- GPS-network with 8 antennas
- total station with 30 prisms
- ground-based radar with 10 reflectors
- 5 extensometers measuring crack opening
- geophones that measure vibrations
- 2 lasers measuring opening of the 2 largest cracks

Monitoring in borehole
- inclinometers measuring displacements
- piezometers measuring pore pressure
- temperature
- electrical resistivity of water

Meteorological station
- temperature
- precipitation and snow depth
- wind speed
- ground temperature
- radiation

Light Detection and Ranging (LiDAR) mapping and radar measurements were also done. Several independent systems were installed to ensure continuous operation at all times, and different communication systems were implemented to ensure continuous contact with the Emergency Preparedness Centre in Stranda.

Modelling of tsunami following rock slide

The tsunami wave propagation due to an Åknes rock slide was modelled numerically for two rock slide scenarios: slide volume of 8 million m^3 and 35 million m^3. Run-up values were estimated for 15 locations in the Storfjord region (Eidsvig and Harbitz 2005; Glimsdal and Harbitz 2006; Eidsvig *et al.* 2008). The results of the simulation for three locations are shown in Table 5. Preliminary results of tsunami modelling suggest an inundation height of up to 35 m at Hellesylt for rockslide volume of 35 million m^3 at Åknes. The modelling of the tsunami caused by the rockslide includes several uncertainties. To reduce the uncertainties, physical modelling is presently underway.

Table 5. Estimated run-up heights in the Storfjord region.

Location	Run-up heights 8 millions m^3	Run-up heights 35 millions m^3
Hellesylt	8-10 m	25-35 m
Geiranger	8-15 m	20-40 m
Stranda	1-3 m	3-6 m
Fjøra	1-2 m	5-7 m
Tafjord	3-5 m	12-18 m

Event tree analysis (ETA) for Åknes rock slope

The event trees were constructed by pooling the opinion of engineers, scientists and stakeholders. The objective was to reach consensus on the hazard, vulnerability and risk associated with a rockslide at Åknes and quantify the hazard (probability of a

rockslide and tsunami occurring) and the potential losses (human life and material and environmental damage). Different triggers for the rockslide were analysed.
The ETA was carried out over several days, where scientists and stakeholders with relevant competence to grasp the situation as a whole were assembled. The objectives of the analysis were also to examine the required parameters for an effective early warning system and suggest possible mitigation measures, e.g. drainage wells and drainage galleries.

The participant list below included the following stakeholders:

- manager for Åknes/Tafjord project
- mayor of community
- social scientist from community
- city planner from community
- policeman working on emergency plans and evacuation
- local politician
- representative from community office
- directorate for safety and emergency preparedness
- journalist/media
- officer from ministry of highways
- meteorologist
- physical geographer
- social geographer
- geologist
- engineering geologist
- rock mechanics specialist
- geotechnical engineer
- tsunami specialist
- instrumentation specialist
- earthquake engineer
- seismologist
- mathematician
- statistician
- risk analysis specialist

The following event trees were constructed:

- event tree, rockslide due to seismic trigger
- event tree, rockslide due to high pore pressure trigger
- event tree, rockslide due to weathering and creep trigger
- event tree, tsunami wave against Hellesylt
- event tree, consequences of tsunami
- event tree, optimum observations for early warning

Event trees were constructed for three triggers of rock slope instability: earthquake, high pore pressure and weathering creep and weakening of sliding plane. The event trees represent the judgment for the situation in October 2007 when the ETA was carried out. The trees set numbers for the probability of a slide within the next year, but the probability will change with time. The event trees should therefore be updated as new information becomes available.

Figure 9 (Lacasse *et al.* 2008) presents an example of the event tree for tsunami propagation, given that the rockslide has occurred. The numbers are given to illustrate the process, and are not to be used as estimates for the rock slope at Åknes. The steps for the tsunami event tree included: 1) rockslide is triggered; 2) slide is in one massive volume or in pieces; 3) volume of rockslide, V; 4) resulting run-up height on land. The failure probability is the summation of the failure probabilities in all the

branches of the tree which leads to failures. Table 6 lists the probability of run-up height amplitudes at one of the locations.

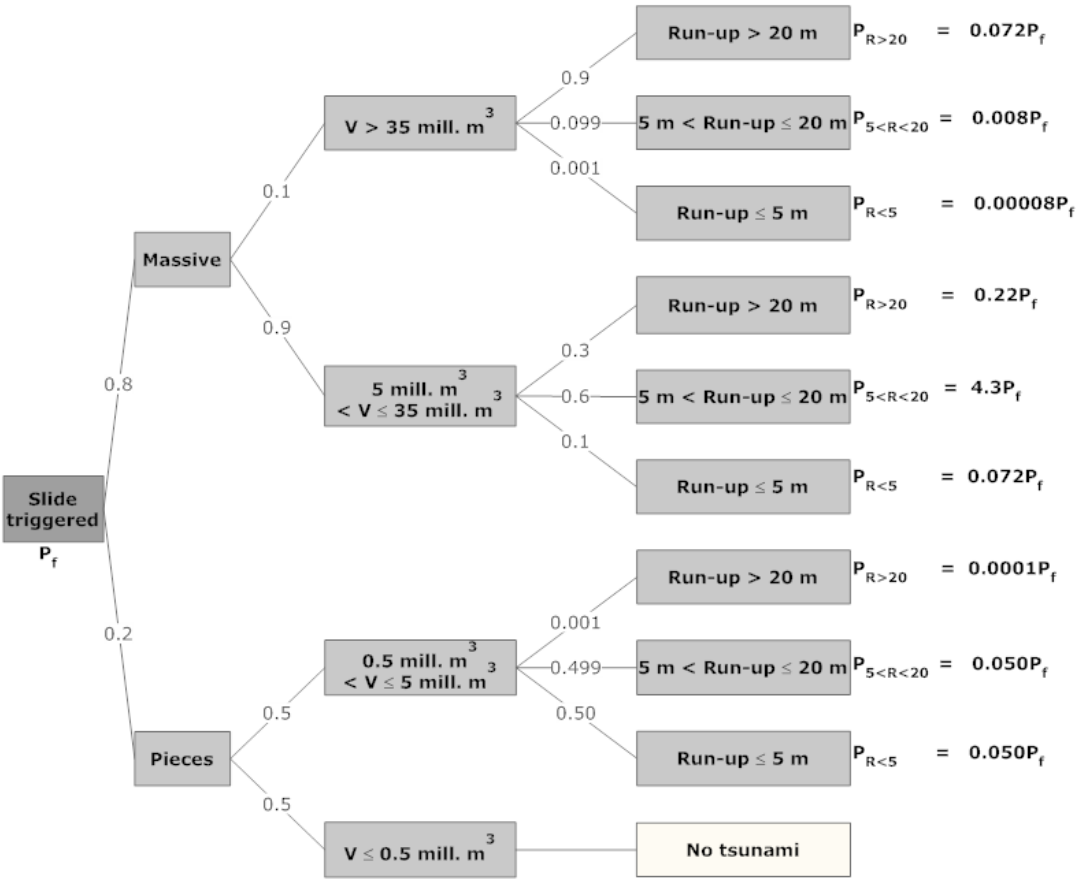

Figure 9. Event tree for tsunami propagation, once rock slide has occurred.

The magnitude of the consequences (loss of life and material property and environmental damage) depends on: warning time before tsunami hazard occurs, reliability of emergency preparedness plan, run-up height, local water level, local water flow velocity, availability of escape routes and distance to safe havens, time of the day, time of the year, training of professionals and public, unforeseen concurrent event etc. These factors form the steps of the event tree on consequences.

Table 6. Probability of run-up heights (Ruh) at Hellesylt, given that a rock slide of larger volume has occurred with $P_f = 10^{-3}$/yr.

$R \leq 5$ m	5 m < $R \leq 20$ m	$R > 20$ m
$P = 0.3P_f = 3 \times 10^{-4}$/yr	$P = 0.5\ P_f = 5 \times 10^{-4}$/yr	$P = 0.1\ P_f = 1 \times 10^{-4}$/yr

Early warning and emergency preparedness

The Åknes/Tafjord early warning and emergency preparedness system was implemented early 2008. As part of this system, the Emergency Preparedness Centre in Stranda is in operation continuously (24 hours, 7 days), and has guidelines for alert levels as a function of observed displacement rates on the extensometers. Figure 10

and Table 7 present an example of the alarm and response system. The system is in continuous evolution. The evaluation of the alarm status is done on the basis of an integrated interpretation of all measurements available, and their evolution over time (Blikra *et al.* 2007; Blikra 2008).

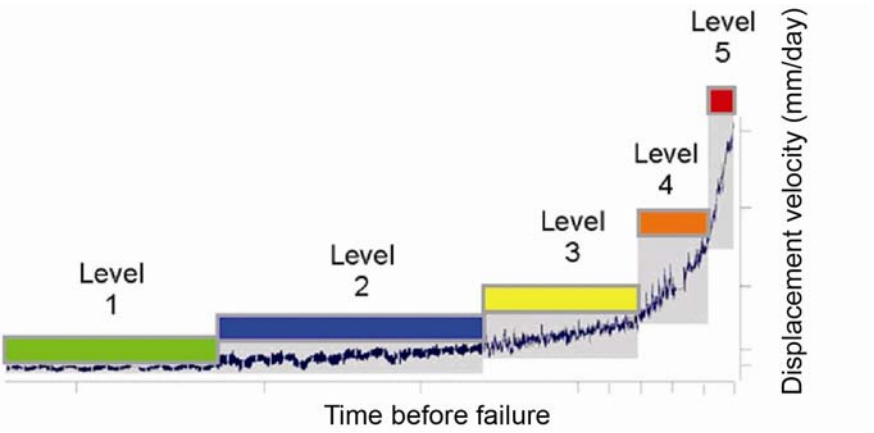

Figure 10. Alarm levels as function of displacement velocities.

Table 7. Sketch of alarm levels and response indicated in Figure 10.

Alarm level	Activities and alarms	Response
Level 1 Normal situation	Minor seasonal variations No alarm	EPC staff only Technical maintenance
Level 2 Awareness	Important seasonal fluctuations, on individual and multiple sensors Values < upper thresholds for Level 2	Increase frequency of data review, compare different sensors Call in geotechnical/geological/ monitoring expert
Level 3 Increase awareness	Increased displacement velocity ob, served on several individual sensors Values < upper thresholds for Level 3	Do continuous review and survey; geo-expert team at EPC full time Inform police and emergency/pre-paredness teams in municipalities
Level 4 High hazard	Accelerating displacement velocity observed on multiple sensors Values < upper thresholds for Level 4	Increase preparedness, continuous data analysis Alert municipalities to stand prepared for evacuation
Level 5 Critical situation	Continuous displacement acceleration Values > upper thresholds for Level 4	Evacuation

EPC = Emergency Preparedness Centre in Stranda

The event tree for the Åknes early warning system involved, among others, the following steps: 1) time needed for warning (t in weeks, days or hours, some triggers give more time than other); 2) technology (working, yes or no); 3) are signals picked up? (yes or no); 4) are signals correctly interpreted (human element, time available, delegation of authority, etc.)?; 5) warning parameter(s) to follow up before and during warning; 6) choice of threshold values. A number of factors are important:

- 4-5 weeks each year are the most critical because of climatic factors (snow-melt) combined with extreme precipitation; at that time, one should define an increased alarm level;
- life and range of operation of sensors should be checked continuously;
- any presence of large amount of water in the boreholes should be monitored;
- what is/are the most representative measurements for early warning;
- monitoring should be spread out, as failure may occur in other locations than crack;
- consider additional boreholes and other measurements;
- statistics of measured data should be built in system, with Bayesian updating;
- adapt warning curve (Figure 10) as more knowledge is acquired;
- consider whether police and other authorities should be on standby earlier than suggested in Table 7;
- be prepared with a new monitoring system to be set in operation quickly after a first slide that may have destroyed the instrumentation in place.

Case Study 2: Vulnerability assessment – Norwegian clay slopes

The zone assessed in this study is located in an urban area on the Southern coast of Norway, extending about 1 km along the banks of a river in the vicinity of a fjord. The quaternary geology indicates that the soils in the area are normally consolidated. Typical soil profiles display a 1.5 m to 3.5 m thick river sand layer at the surface, underlain by marine deposits, mainly consisting of silty clay and clayey silt with some fine sand layers with thickness 10 to 23 m. The clay deposits are exposed to river erosion. The sensitivity of the clay, based on fall cone test results, was measured as close to or over 100, indicating "quick clay" behaviour. Previous studies concluded that the pore pressure is probably not sensitive to variations in precipitation.

In terms of vulnerability, risk is expressed as:

$$R = H \cdot V \cdot W$$

where R is risk, H is hazard, V is vulnerability and W is the value of the elements at risk. Vulnerability has two perspectives. The social vulnerability, or the "capacity of a society to cope with hazardous events" and the physical vulnerability, or the "degree of expected loss in a system from a specific threat", quantified between 0 (no loss) and 1 (total loss). Vulnerable categories include people, structures, lifelines, infrastructure, vehicles, and the environment. The model in this case study addresses the physical vulnerability quantitatively.

The vulnerability is evaluated with the VIS formulation, or $V = I \cdot S$, where V is vulnerability, I the intensity of landslide and S the susceptibility of vulnerable elements.

The intensity (I) expresses the potential damage caused by a landslide for example, as a function of its kinematics (volume, depth and displacement), and its kinetics (velocity, momentum). The proposed model is

$$I = k_S \cdot [r_D \cdot I_D + r_G \cdot I_G]$$

where k_s = Spatial impact ratio
r_D = Dynamic relevance factor
r_G = Geometric relevance factor
I_D = Dynamic intensity component
I_G = Geometric intensity component

The components of landslide intensity are:

- The spatial impact ratio expresses how much the category of the elements at risk is affected spatially by a landslide, and is defined in the range [0,1]. In Figure 11, the spatial ratio k_s is A_i/A_t.
- The relevance factors are assigned by the user, specific to a landslide type and the vulnerable categories, and reflect the available knowledge (or belief) on the relevance of the dynamic and geometrical characteristics of the landslide in causing loss. The approach sets one constraint on the relative values of relevance factors, where the sum shall at all times be equal to unity ($r_D + r_G = 1$). Table 8 provides four examples of relevance factors.
- The dynamic intensity (I_K) expresses the destructive potential of a landslide's kinetic energy and momentum, and is defined in the range [0,1]. Figure 12 provides an example of dynamic intensity model for structures as a function of the slide velocity, C.

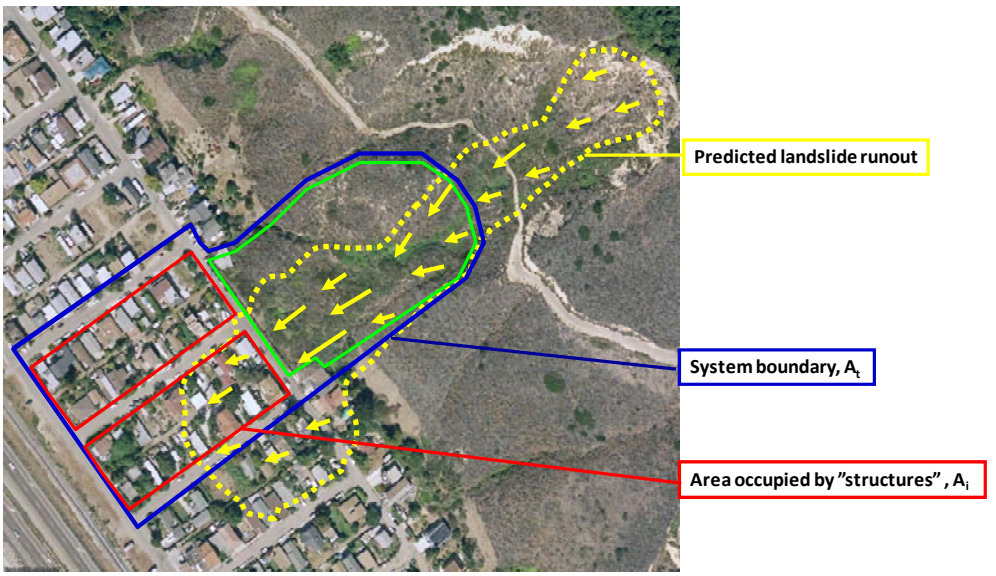

Figure 11. Illustration of spatial impact ratio.

Table 8. Examples of relevance factors.

Category	Landslide	r_D	r_G
Structures	Rapid	0.90	0.10
Structures	Slow	0.15	0.85
Persons	Rapid	0.75	0.25
Persons	Slow	1.00	0.00

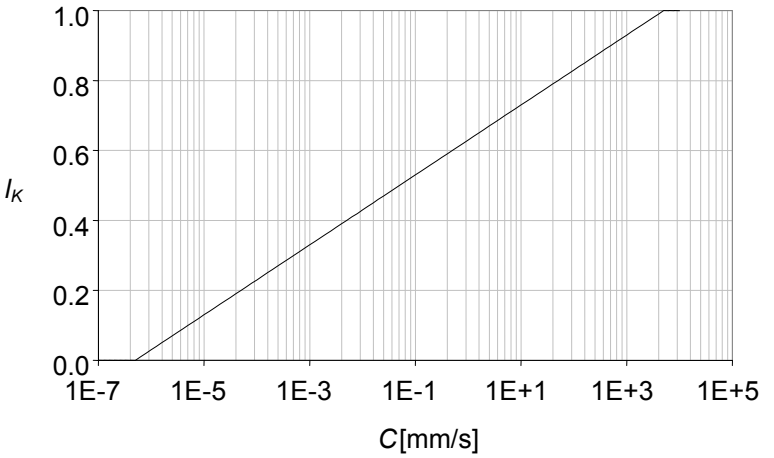

Figure 12. Example of dynamic intensity model for structures (based on Cruden and Varnes 1996).

– The geometric intensity (I_M) accounts for the dimensional properties of the sliding masses (e.g. depth, volume, displacement, area), and is defined in the range [0,1]. Figure 13 provides an example of geometric intensity model for structures. The intensity factor is a function of the absolute ground displacement, D_G, and the threshold value of D_G above which complete loss may be assumed, D_{Gt}.

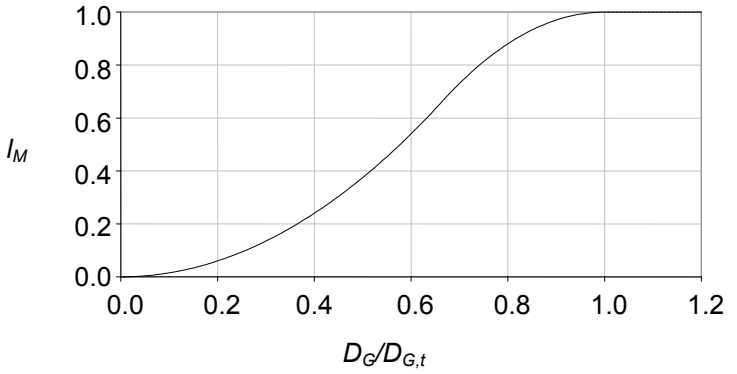

Figure 13. Example of geometrical intensity model for structures.

The susceptibility in the VIS model expresses the propensity of the vulnerable element to undergo loss, and depends on the physical characteristics (resistance and geometry) of the element. The susceptibility is independent of the landslide intensity. The susceptibility model is expressed as:

$$S = 1 - \prod_{i=1}^{n_s} (1 - \xi_i)$$

where the susceptibility factors (ξ_i) are category-specific and reflect the user's belief or knowledge on the susceptibility. The factors range between [0,1] and should be mutually independent (Kaynia *et al.* 2008).

Table 9 illustrates the approach for determining the susceptibility of structures and persons, and gives examples of the influence of factors such as population density, income and age. The susceptibility of structures (S_{STR}) depends on the structure type and the state of maintenance. The susceptibility of persons (S_{PSN}) depends on the population density, the income and the age. Figure 14 presents an additional example of the susceptibility of persons in structures, where S_{PST} is the susceptibility of persons for an average building and S_{STR} is the susceptibility of an average structure.

In an example application of the model for structures subjected to the landslide in Figure 11, the landslide intensity was calculated as 0.20, and the susceptibility was obtained as 0.54, giving a vulnerability of 0.11 (Figure 15). The vulnerability factor is low, due to the relatively low spatial impact ratio, Values would have been significantly higher for the same landslide if a smaller reference area, for example only half of the urban area, had been considered in Figure 11, because the spatial impact ratio would have been much higher (and close to 1). This limitation of the model should be considered and reference areas should be carefully considered in any analysis.

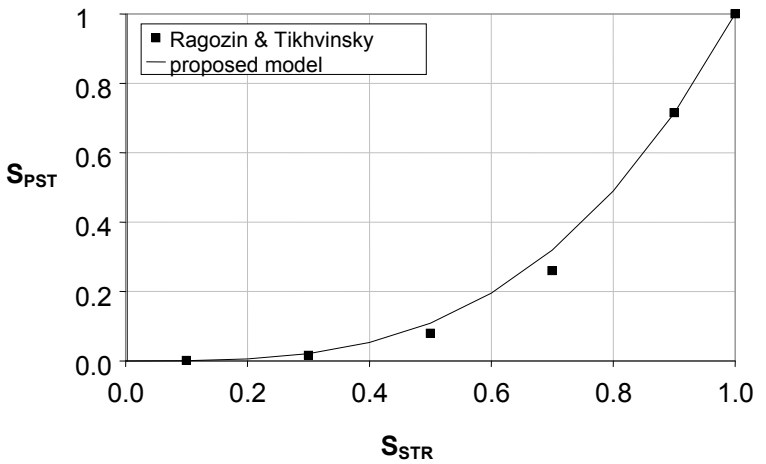

Figure 14. Example of susceptibility model for persons in structures.

The proposed approach allows a quantitative estimate of the vulnerability. It operates at the level of categories of elements at risk, which is an advantage, making the understanding of the estimates more accessible. The model is applicable to all types of landslides, and is allow the user to adopt specific own models if his/her experience goes beyond published material. However, as with all models, the numerical results need to be assessed with care, given the hypotheses done and the choice of the reference areas made.

Table 9. Susceptibility of structures and persons.

Structures

Proposed model: $S_{STR} = 1-(1-\xi_{STY})(1-\xi_{SMN})$

Structure type			State of maintenance	
Structure type	Resistance	x_{STY}	State of maintenance	E(x_{SMN})
Lightest simple structures	None	1.00	Very poor	0.50
Light structures	Very low	0.90	Poor	0.40
Rock masonry, concrete and timber	Low	0.70	Medium	0.25
Brick masonry, concrete structures	Medium	0.50	Good	0.10
Reinforced concrete structures	High	0.30	Very good	0.00
Reinforced structures	Very high	0.10		

Persons (outdoors and in vehicles)

Proposed model: $S_{PSN} = 1-(1-\xi_{PDN})(1-\xi_{GDP})(1-\xi_{AGE})$

Population density

$$\xi_{PDN} = \begin{cases} 0.1 \cdot D_P^{\,0.25} & D_P \le 10{,}000 \\ 1.00 & D_P > 10{,}000 \end{cases}$$

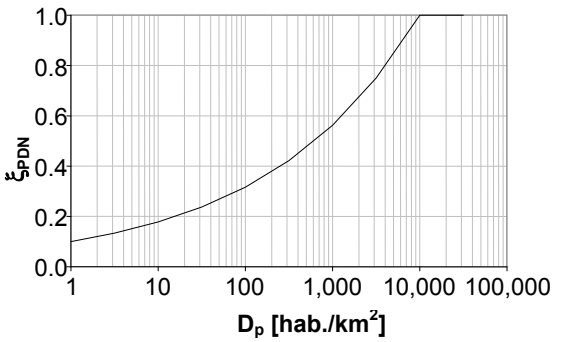

Income

$$\xi_{GDP} = \begin{cases} 0.95 - 0.90\left(\dfrac{GDP_c}{10{,}000}\right)^{1.4} & GDP_c \le 10{,}000 \\ 0.05 & GDP_c > 10{,}000 \end{cases}$$

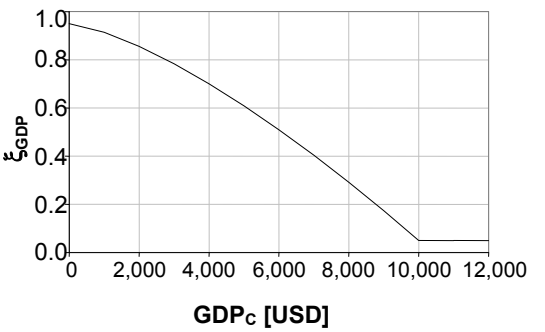

Age

Age (yrs)	x_{AGE}	Age (yrs)	x_{AGE}	Age (yrs)	x_{AGE}
0-5	1.00	20-50	0.00	65-70	0.70
5-10	0.90	50-55	0.10	70-75	0.90
10-15	0.70	55-60	0.30	> 75	0.95
15-20	0.30	60-65	0.50		

$V = I \cdot S = 0.20x0.54=0.11$

$C = 200$ m/s
$A_t = 2300$ m^2
$A_i = 512$ m^2

Intensity, I:
$k_s = 0.22$
$r_D = 1.00$
$r_G = 0.00$
$I_D = 0.89$
$I = 0.22\ (1.0x0.89)=0.20$

Susceptibility, S:
40 structures (5 light, 22 masonry, 13 reinforced concrete; 50% in poor state, 50% in good state)
$S = 0.54$

Figure 15. Example of vulnerability calculation.

Case Study 3: Risk assessment - 2004 tsunami in Indian Ocean

The 26 December 2004 Indian Ocean tsunami was the most destructive tsunami in modern times, causing over 250,000 casualties, and devastating large areas along the coastlines of Indonesia, Thailand, Malaysia, Myanmar, Sri Lanka, India, the Maldives and even some parts of the east African coast. The tsunami was generated by the magnitude 9.3 Sumatra-Andaman earthquake caused by propagating stress release on the subduction zone created by the steadily on-going northeast subduction of the Indo-Australian plate under the Burma/Sunda plate. The earthquake caused vertical seabed movements of up to 5 m over an area of 1200 km × 300 km.

Along the west coast of Thailand, the tsunami caused about 8,000 fatalities due to inundation levels of 5 to 12 m above the sea level at the most severely affected areas. In the aftermath of the Indian Ocean tsunami, the authorities in Thailand required the evaluation of future tsunami risk and practical guidelines for land use and rehabilitation of the exposed areas. From a risk management perspective, four important issues were focussed on (Nadim and Glade 2006):

1. Tsunamis with similar or even larger magnitudes have occurred in these areas long before humans settled. Thus tsunamis are part of the general "set" of natural processes operating in these regions and consequently, it is just a matter of time until the next tsunami will occur, and it may be of even greater magnitude.
2. It is essential to have a long-term view of the problem: the actions taken today will affect the exposure of future generations to tsunami risk.
3. If the present trends in population growth and development along the coastlines continue, the exposure along the coastlines to tsunami risk will increase.

Loss model and perception of risk

The most complete description of the possible losses (risk) is quantitatively in terms of a "probability distribution", which presents the relative likelihood of any particular loss value or the probability of losses being less than any particular value. Alternatively, the "expected value" (i.e., the probability weighted average value) of loss can be determined as a single measure of risk. The general scenario-based risk formulation was issued:

$$E[Loss] = \sum_{All\ S} \sum_{All\ \underline{C}} \underline{C} \cdot P[\underline{C} \mid S] \cdot P[S]$$

where $\underline{C}$ is a particular set of losses (of comprehensive and mutually exclusive set of possible losses), S is a particular scenario (of comprehensive and mutually exclusive discrete set of possible scenarios), P[S] is the probability of occurrence of scenario S, $P[\underline{C} \mid S]$ is the conditional probability of loss set $\underline{C}$ given that scenario S has occurred, and E[Loss] is the "expected value" of loss. "Loss" may refer to any undesirable consequence, such as loss of human life, economic loss, loss of reputation, etc., in terms of its direct and indirect effects (e.g. local damage of railway tracks and related interruption of industrial traffic), its affects on different social groups (e.g. individuals, community, insurance, government) as well as its short- and long-term influences on a society (e.g. fatalities could include all children of a community, the tourist industry might collapse). The focus of the study was on the loss of human life.

Calculation of the terms in the above equation is not trivial. Nadim and Glade (2006) argued that the hazard term in the above equation (i.e. P[S]) is not constant with time. Moreover, the expected number of fatalities depends on many factors, for example on which week-day and what time of the day the tsunami occurs, whether the tsunami occurs during high tide or low tide, whether or not an effective tsunami warning system is operative at the time of the tsunami, how the issued warning is communicated to the respective groups and individuals, public awareness on what to do if tsunami warning is issued, etc. An implicit assumption in the study is that an effective tsunami warning will be in place in Thailand and other countries around the Indian Ocean within a few years. Although various organizations and institutions work on the implementation of such an early warning system, this assumption may prove to be problematic.

The potentially affected population could be divided into three groups based on their temporal exposure to the tsunami danger, and their choice in exposing themselves to risk: 1) people who live in the exposed areas permanently, 2) tourists who only live in the exposed areas one or two weeks each year, and 3) locals who do not live in the exposed areas, but work there during the tourist season. The risk considerations for the 3 groups are not the same. What matters for the first group is the "real risk" (which might be impossible to quantify) which is taken deliberately or unconsciously, while the "perceived risk" influences heavily the behaviour of the second group, because their exposure to the "real risk" is much lower due to their limited temporal exposure. The number of people comprising the third group is

strongly correlated to the number of tourists, so for this group both the real risk and the perceived risk are important.

The actual risk and the perceived risk for the tsunami are likely to be quite different. The tsunami modelling studies done for the project showed that the most likely source for a tsunami on the west coast of Thailand is a major shallow earthquake on the northern section of the Sumatra-Andaman subduction zone. Considering that this section of the fault experienced a magnitude 9.3 earthquake in December 2004 and a magnitude 8.7 earthquake in March 2005 (Nias earthquake), it is not likely that a similar event would occur in the next few hundred years. One of the key conclusions of the study was that much of the energy stored on the fault is already released and it will take several hundred years before that segment of the fault has the potential of being the source of a magnitude 9+ earthquake again. Consequently the scientifically derived annual probability of a major tsunami event in western Thailand during the next fifty to hundred years is extremely low. However, the *perceived risk* of a tsunami in that area is much higher because of the event that did happen recently, and this is what really matters for various social groups, including the decision-makers and the tourist industry in Thailand. In addition, social groups were affected globally, as the fatalities included also Europeans, Americans, Japanese, etc., and were not limited to local population only – which is the case in most other extreme events such as earthquakes or floods. Consequently, there is a global involvement of a locally occurring event.

A rare event with extreme consequence

As the Indian Ocean tsunami of 26 December 2004 tragically demonstrated, a rare, extreme tsunami event might cause thousands of fatalities. When the probability of occurrence of an undesirable event (e.g. hazard) is extremely low and the consequences have the potential to be extremely high, the calculated risk in terms of expected human fatalities is highly uncertain. The calculated risk is essentially a zero times infinity problem. This implies that an outcome could change by several orders of magnitude due to very small variations in the initial assumptions. To a lesser degree, this issue is also a problem for estimating the risk posed by an extreme earthquake or landslide. An argument that is sometimes used to distinguish earthquakes or large landslides, which are relatively rare events, from other, more frequent natural hazards, such as storms, floods, etc., is that the latter often have a stronger place in societal memory. Tsunamis are on the same scale as extreme earthquakes, i.e. catastrophic tsunamis at a given location are extremely rare events.

The seismic hazard evaluation performed in the study concluded that within the next 50 to 100 years, the largest credible earthquake to be prepared for is a magnitude 8.5 event (Harbitz *et al.* 2006). The event could cause a tsunami which at the most gives an inundation level of 1.5 to 2.0 m above sea level. If the tsunami occurs at high tide, the inundation level could be 2.5 to 3.0 m above the mean sea level (Harbitz *et al.* 2006). After about 100 to 200 years, the potential for earthquakes greater than M 8.5 will increase gradually, and so does the potential for generating larger tsunamis than

that for the M 8.5 earthquake scenario (NGI 2006). The return period for the tsunami-generating M 8.5 event was estimated to be 200 to 800 years.

The estimate of the return period of a magnitude 9.3 earthquake, similar to the one that caused the tsunami on 26 December 2004, vary between 400 years using the subduction rate, and 1140 years using the seismicity statistics (Harbitz *et al.* 2006). A key issue regarding the return period is the timing of major earthquake events within the occurrence cycle. The evaluations suggested that an M 9+ earthquake in the Sumatra subduction zone with potential tsunami effects on Thailand will most likely not occur before at least 400 years after the 2004 megathrust earthquake. For the M 8 to 8.5 earthquakes the cyclicity is less predictable (i.e. the occurrence is more random within recurrence interval), but even for such events the probability of occurrence will be quite low for a long time after 2004, increasing gradually with time. In the long-term perspective (100–200 years), risk mitigation measures should protect the exposed population from a tsunami similar to the one that occurred on 26 December 2004, i.e. 5 to 12 m above the mean sea level. It should be noted, however, that the maximum tsunami wave heights along the west coast of Thailand and their spatial variation for a future m 9.3 earthquake may be quite different from those observed during the 26 December 2004 event. The possible range of characteristics of a future extreme tsunami event needs further investigation.

Is the tsunami risk in Thailand acceptable or tolerable?

A part of risk assessment and risk management is to deal with risk acceptance criteria. In the context of the present study, one of the key questions was "Is tsunami risk level in Thailand acceptable?" Here, it is important to recognize the difference between acceptable and tolerable risks defined earlier. This differentiation is often reflected through the use of the so-called 'F-N curves'. The F-N curves relate the annual probability of causing N or more fatalities (F) to the number of fatalities, N. This is the complementary cumulative distribution function. The term "N" can be replaced by any other quantitative measure of consequences, such as monetary measures. Such curves may be used to express societal risk criteria and to describe the safety levels of particular facilities.

The application of societal risk to life criteria is to reflect the reality that society is less tolerant of events in which a large number of lives are lost in a single event, than if the same number of lives is lost in a large number of separate events (e.g. Alexander 2000). Examples are public concern to the loss of large numbers of lives in airline crashes, compared to the many more lives lost in road traffic or small aircraft accidents (e.g. Alexander 2002).

The use of cumulative F-N curves to reflect this is not universal. An example which has been tried on an interim basis in Hong Kong to assist landslide risk management of natural hillside hazards was shown in Figure 4 (GEO 1998; Malone 2005). The criteria in Figure 4 were used to assess the tolerability of tsunami risk level in Thailand.

Based on the return period estimates for tsunami scenarios, the recommended design water levels, and the experience from the 26 December 2004 tsunami, the annual risk to human life from a tsunami on the west coast of Thailand, and the changes in this risk with time can be estimated. The Indian Ocean tsunami of 26 December 2004 caused very few casualties (none recorded in the available databases) in the coastal areas of Thailand where the inundation level was less than 3 m. The main reason is that the coastal areas in west Thailand reach a level of 4-5 m above mean level at a very short distance from the shoreline. Almost all the fatalities in Thailand occurred in areas where the inundation level was more than 5 m above the mean sea level. This is in contrast to the affected coastal regions in India and Sri Lanka where the elevation of 3 m above sea level is reached several hundred meters from the shoreline, and where many people died in areas where the inundation level was about 3 m.

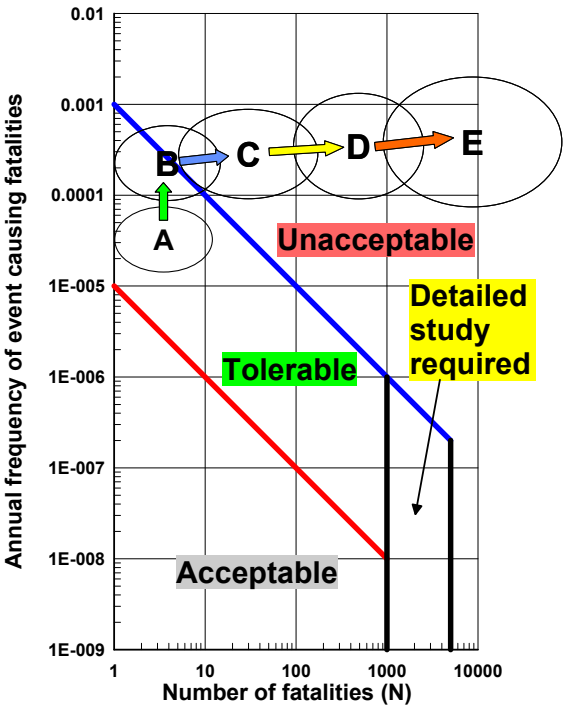

Zone	Time
A	today
B	50-100 yrs
C	150-200 yrs
D	250-300 yrs
E	26 Dec. 2004 and 400-500 yrs

Figure 15. Estimated tsunami risk in Thailand compared with GEO's 1998 tolerance criteria.

Figure 15 shows the estimated risk plotted on the societal risk acceptance criteria diagram for Hong Kong. Zone A represents the best estimate of the tsunami risk in Thailand for the next 50 to 100 years. This risk is associated with the occurrence of an M 8.5 earthquake at a critical location on the Sumatra-Andaman subduction zone. Zone E, which clearly represents an unacceptable situation, represents the situation prior to the tsunami of 26 December 2004 and also the long-term situation after several hundred years if no risk mitigation is done. Zones B, C and D give the best estimate of the risk in 50 to 100 years, 150-200 years and 250-300 years respectively. Figure 16 shows another version of the risk depicted on Figure 15 where the vertical axis represents risk in terms of the expected annual human fatalities (averaged over several hundred years) in Thailand due to a tsunami.

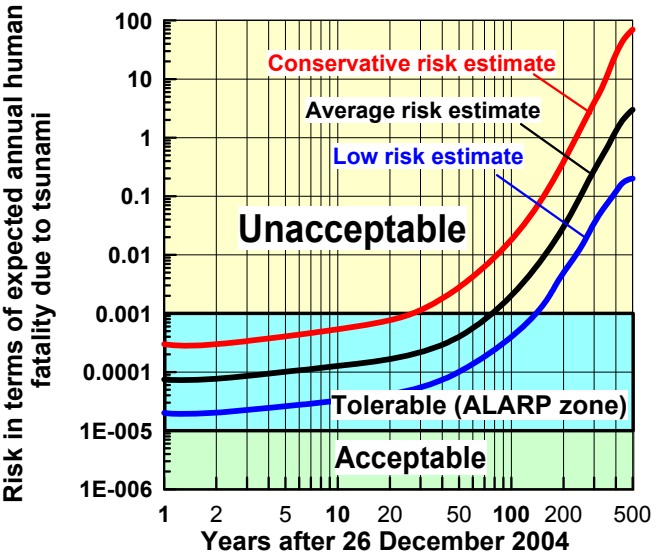

Figure 16. Risk levels associated with tsunami along the west coast of Thailand as implied by Figure 15 and averaged over several hundred years.

The main conclusion that can be drawn from the risk diagrams is that, as far as the tsunami risk in Thailand is concerned, the present day situation without risk mitigation measures is marginally acceptable and will remain so for one or two generations. However, a long-term strategy must be implemented to mitigate the tsunami risk by reducing the vulnerability and enhancing the coping potential of the exposed population to an event similar to the one that occurred on 26 December 2004.

Risk mitigation strategy for Thailand

Several mitigation measures were proposed to mitigate the risk associated with tsunamis on the coast of Thailand (Karlsrud *et al.* 2006). If no risk mitigation measures are planned and implemented in the reasonably near future, it is likely that the long term tsunami risk will be forgotten within the next 50 years or so, because no significant tsunamis are likely to occur within such a time frame. The collective memory of the society in relation to natural hazards with long return period has repeatedly been proven to be short. It is therefore recommended to already plan for implementation of mitigation measures that can reduce the exposure to, and consequences of, severe tsunamis for future generations.

In the short term perspective, steps could ensure a lasting long term awareness of the tsunami risk, for instance "monuments" constructed along the coast warning future generations about the tsunami risk. Such monuments can also be designed to act as part of the physical protection measures against tsunamis. One should also consider including tsunami risk in the school curriculum and textbooks and establishing a yearly national tsunami day. Specific plans for physical measures should be developed, and they could be implemented over time to reduce the tsunami risk.

To ensure the long term awareness, countries exposed to natural hazards are encouraged to centralize their efforts in dealing with warning against all kinds of natural hazards, such as tsunami, flooding, landslides, storm surges etc. On the pro-active level, countries should have stronger recourse than today to hazard mapping, and emergency preparedness (how to deal with a catastrophic event once it occurs).

Karlsrud *et al.* (2006) recommended specific mitigation measures for three typical areas along the west coast of Thailand: City of Patong on the Phuket Island, located on an alluvial fan at the base of a 4 km wide bay; Bang Niang tourist resort areas stretching for about 12 km north of Khao Lak in an area with long and wide beaches; Ban Nam Khem fishing village. Figure 17 illustrates two of the schemes developed.

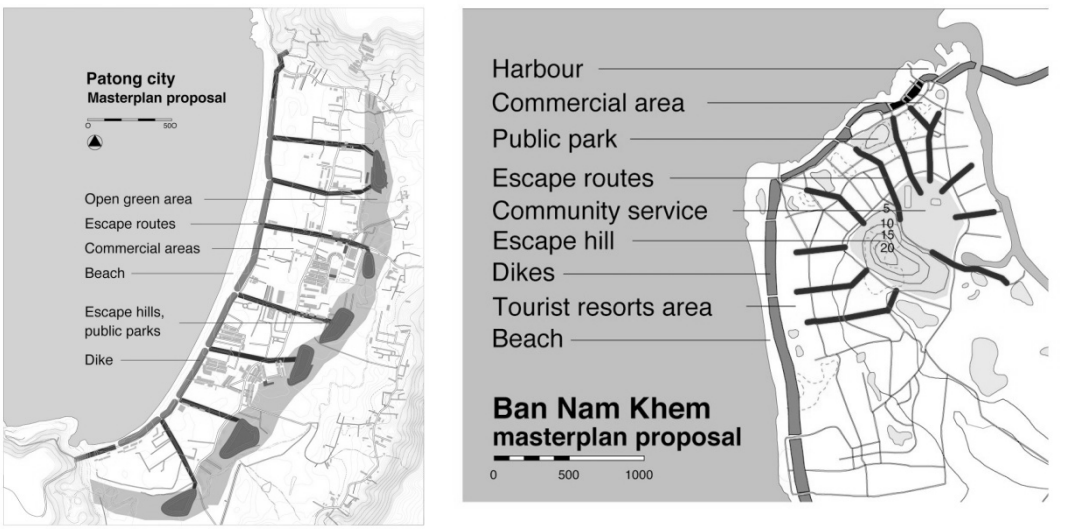

Figure 17. Examples of tsunami risk mitigation master plan.

On the left: Patong City with elevated green-belt areas approximately 400 m inland from the beach, serving as safe escape hills, and system of escape routes; car traffic is to be banned from escape routes. On the right: Ban Nam Khem fishing village with layout of protection dike around Ban Nam Khem with escape routes to safe high areas. The recommended mitigation measures for Thailand included the following main elements:

- Implementing new requirements for land-use planning and establishment of new building codes to reduce exposure to and/or consequences of future tsunamis.
- Establishing easily accessible and well-marked escape routes to areas that are safe from tsunami. Such safe areas may be artificially elevated land areas or buildings/ and structures accessible to all at all times, within a distance of about 500 m.
- Constructing artificial walls/dikes to limit the impact and inundation of tsunamis.
- Raising the ground level (vertical land reclamation) where buildings are to be constructed in the future. This may be a particularly attractive option for the development of tourist resort areas, for example on Ban Nam Khem fishing village.

- Ensuring that future buildings will not be damaged and that sleeping areas are safe (e.g. collapsible walls in the direction of the wave, sleeping quarters on second floor).
- Ensuring awareness for future generations.

The results of the project were disseminated through a number of workshops and seminars arranged with invited participants from the countries around the Indian Ocean. The report on the study is available for download at

www.ccop.or.th/download/pub/tsunami_final_report.pdf

Case Study 4: Risk mitigation - quick clay in Drammen

Risk zonation for quick clay

As part of work for The Norwegian Water Resources and Energy Directorate (NVE), Gregersen (2001) developed a simple method to classify and map the risk posed by potential quick clay slides. Potential slide areas are given "engineering scores" based on an evaluation of the geotechnical parameters, local conditions, persons or properties exposed and engineering judgement. Hazard classes are described as low, medium and high. Consequence classes are discussed as not severe, severe and highly severe. The resultant risk, based on engineering evaluation and experience, is divided in five risk classes (Lacasse *et al.* 2004).

Hazard classes

The hazard level depends on topography, geological and geotechnical conditions, and changes at the site. The evaluation of the hazard is done with the help of Table 10. The weight given to each hazard in Table 10 (or later, to consequence in Table 11) describes its importance relative to the stability of the slope. The hazard classes are:

Low: Favourable topography and soil conditions; extensive site investigations; no erosion; no earlier sliding; no planned changes, or changes will improve stability.

Medium: Less favourable topography and soil conditions; limited site investigations; active erosion; important earlier sliding in area; planned changes give little or no improvement of stability.

High: Unfavourable topography and soil characteristics; limited site investigations; active erosion; extensive earlier sliding in area; planned changes will reduce stability.

The zones with weighted score between 0 and 17 (up to 33% of maximum score) are mapped as "low hazard" and have low probability of failure by sliding. The zones with weighted score between 18 and 25 (up to 50% of maximum score) are mapped as "medium hazard" and have a higher, though not critical, probability of failure. The zones with weighted score between 26 and 51 are mapped as "high hazard" and have a relatively high probability of failure.

Table 10. Evaluation of hazard for slides in quick clay in Norway.

Hazard	Weight	Score for hazard			
		3	2	1	0
TOPOGRAPHY					
Earlier Sliding	1	Frequent	Some	Few	None
Height of slope, H [i)]	2	>30 m	20-30 m	15-20 m	<15 m
GEOTECHNICAL CHARACTERISTICS					
Overconsolidation ratio (OCR)	2	1.0-1.2	1.2-1.5	1.5-2.0	>2.0
Pore pressures [ii)]					
- In excess (kPa)	3	> + 30	10-30	0-10	Hydrostatic
- Under pressure (kPa)	-3	> - 50	-(20-50)	-(20-0)	Hydrostatic
Thickness of quick clay layer [iii)]	2	>H/2	H/2-H/4	<H/4	Thin layer
Sensitivity, St	1	>100	30-100	20-30	<20
NEW CONDITIONS					
Erosion [iv)]	3	Active/ sliding	Some	Little	None
Human activity					
- Worsening effect	3	Important	Some	Little	None
- Improving effect	-3	Important	Some	Little	None
TOTAL SCORE					
Maximum weighted score		51	34	16	0
% of max. weighted score		100%	67%	33%	0%

i) For the quick clays in the study, inclination was identical for all slopes (1:3), and slope inclination was not included as a variable. In a general study, slope inclination should be added in the list of hazards.

ii) Relative to hydrostatic pore pressure

iii) In general, the extent and location of the quick clay are also important.

iv) Erosion at the bottom of a slope reduces stability.

Table 11. Evaluation of consequence for slides in quick clay in Norway

Possible damage	Weight	Score for consequence			
		3	2	1	0
HUMAN LIFE AND HEALTH					
Number of dwellings[i])	4	> 5 Closely spaced	> 5 Widely spaced	≤ 5 Widely spaced	0
Persons, industry building	3	> 50	10-50	< 10	0
INFRASTRUCTURE					
Roads (traffic density)	2	High	Medium	Low	None
Railways (importance)	2	Main	Required	Level	None
Power lines	1	Main	Regional	Distrib. network	Local
PROPERTY					
Buildings, value[ii])	1	High	Significant	Limited	0
Consequence of flooding[iii])	2	Critical	Medium	Small	None
TOTAL SCORE					
Maximum weighted score		45	30	15	None
% of max. weighted score		100%	67%	33%	0%

i) Permanent residents, in both sliding area and within run-out distance.

ii) Normally no one on premises, but building(s) have historical or cultural value

iii) Slides may cause water blockage or even dam overflow, flooding may cause new slides; there should be time for evacuation; damage depends on a complex interaction of several factors.

Consequence classes

Consequences are commonly evaluated in terms of human life safety, environmental, financial and social effects. The evaluation of the consequences is done with the help of Table 11 with consequence classes:

Not severe: No or small danger for loss of human life, costly damage or consequences.

Severe: Danger for loss of life or property or important economical or social loss

Highly severe: High exposure of human life loss or large economical or social loss.

The zones with weighted score between 0 and 6 (13% of maximum score) are mapped as "not severe". In these zones, there would be very few or no permanent residents. The zones with weighted score between 7 and 22 (up to 50% of maximum score) are mapped as "severe". The zones with weighted score between 23 and 45 are mapped as "highly severe"; they would hold a large number of persons, either as residents or as persons on the premises temporarily.

Risk classes

The risk score to classify the mapped zones into a risk class is obtained from:

$$R_{WS} = H_{WS(\%)} \times C_{WS(\%)}$$

where R_{WS} = Weighted score for risk mapping

$H_{WS(\%)}$ = Hazard weighted score in %

$C_{WS(\%)}$ = Consequence weighted score in %

Table 12 gives the risk scores for the five risk classes used for quick clay slides in Norway. Figure 18 shows a risk mapping of the area Modum in Norway.

Table 12. Risk classes for slides in quick clay in Norway.

Risk Class	1 (lowest)	2	3	4	5 (highest)
Risk Weighted Score (RWS)	0-160	167-600	628-1900	1906-3200	3200-10,000
RWS (% of max RWS)	0-1.6%	1.6-6%	6.3-19%	19-32%	32-100%

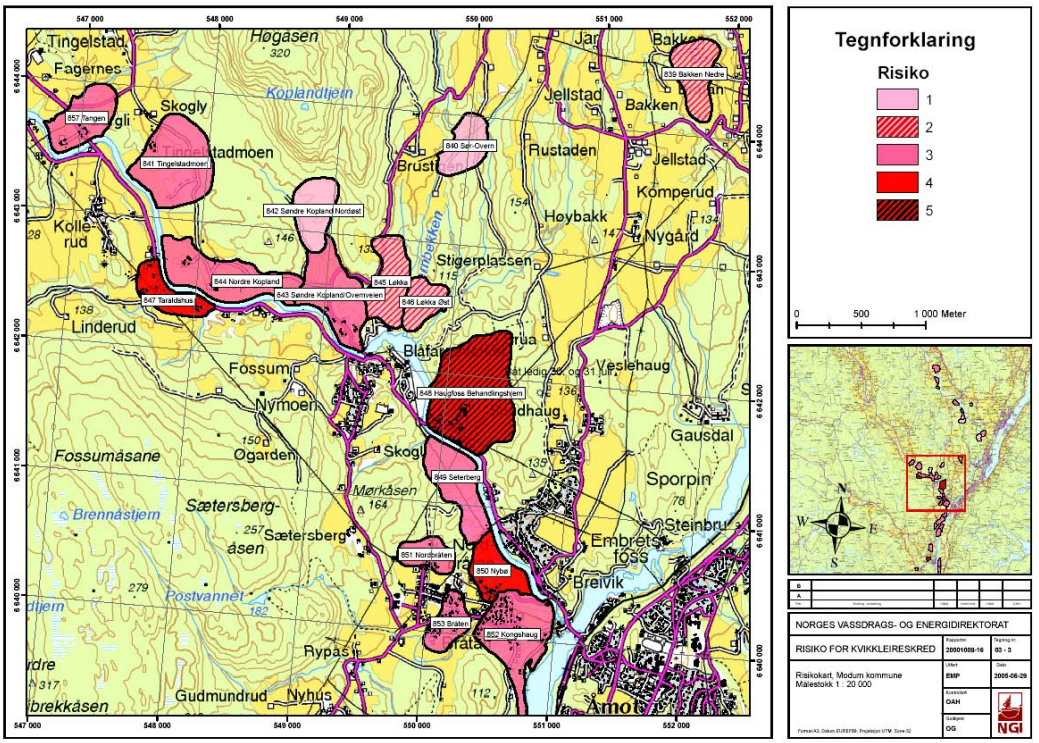

Figure 18. Quick clay risk map for Modum, Norway.

Decision on mitigation measures

To make decisions on the need for additional soil investigations, stability analyses or other remedial actions, Table 13 gives recommendations for quick clay areas in Norway.

Table 13. Activity matrix as a function of risk class.

Activity	Risk class			
	1-2	3	4	5
Soil investigations	None	Consider additional in situ tests and pore pressure measurements	Require additional in situ tests and pore pressure measurements	Require additional in situ tests, pore pressure measurements and laboratory tests
Stability analyses	None	None	Consider doing	Require
Remediation[i)]	None	None	Consider doing	Require

[1)] e.g. erosion protection, stabilizing berm, unloading, soil stabilization, moving of residents

The volume of the sliding material is probably the most important factor for the extent of the run-out zone. If several millions of cubic metre is involved, the run-out cannot be evaluated by simple dynamic or topographic models. This is especially important if large rivers are blocked and huge amounts of water are dammed with the possibility of generation of catastrophic flood waves downstream.

The city of Drammen, along the Drammensfjord and the Drammen River, is built on a deposit of soft clay. Stability analyses were done in an area close to the centre of the city, and indicated that some areas did not have satisfactory safety against a slope failure. Based on the results of the stability analyses and the factors of safety (FS) obtained, the area under study was divided into three zones (Gregersen 2005):

- Zone I FS satisfactory
- Zone II FS shall not be reduced
- Zone III FS too low, area must be stabilised.

In Zone III, a counter fill was immediately placed in the river to support the river bank, and the factor of safety checked again. The counter fill provided adequate stability (Gregersen 2008).

In Zone II, no immediate geo-action was taken, but a ban was placed on any new structural and foundation work without first ensuring increased stability. Figures 19 and 20 illustrate four cases (Gregersen 2008; Karlsrud 2008): (1) if an excavation is planned, it will have to be stabilised with anchored sheetpiling or with soil stabilisation, e.g. with chalk-cement piles; (2) new construction or new foundations cannot be done without first checking their effect on the stability down slope; for example, adding a floor to a dwelling may cause failure because of the added driving forces due to the additional loading, and new piling up slope will cause a driving force on the soil down slope.

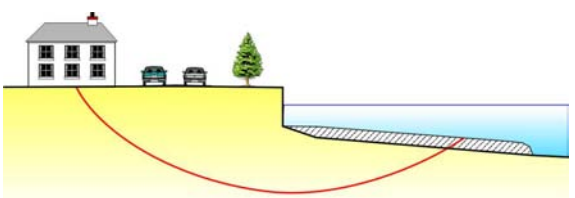

Figure 19. Mitigation in Zone III in Drammen.

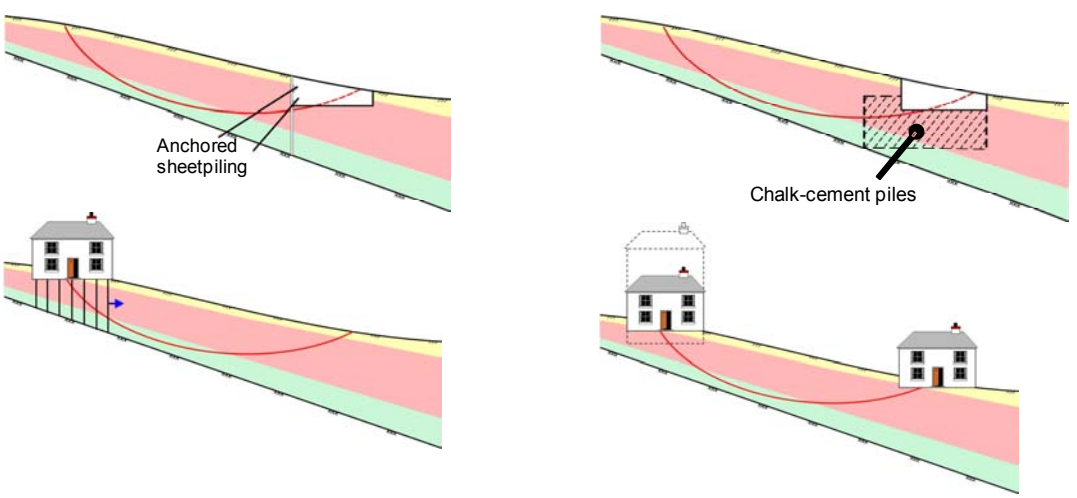

Figure 20. Hazard, mitigation and preventive measures in Zone II in Drammen (Gregersen 2008; Karlsrud 2008).

Case Study 5: Risk mitigation - Early Warning System for landslide dams

Lake Sarez is located in the Pamir Mountain Range in eastern Tajikistan. The lake was created in 1911 when an earthquake triggered a massive rock slide (volume: ~2 km^3) that blocked the Murgab river valley. A natural dam, Usoi Dam, was formed by the rockslide which retains the lake. The dam is at an altitude of 3200 meters. With a height of over 550 meters, it is by far the largest dam, natural or man-made, in the world.

Lake Sarez, impounded by this natural dam, is now about 60 km long and has a maximum depth of approximately 550 m and a volume of 17 km^3. The lake has never overtopped the dam but the current freeboard between the lake surface and the lowest point of the dam crest is only about 50 m. The lake level is currently increasing about 30 cm per year. If this natural dam were to fail, a worst-case scenario would be a catastrophic outburst flood endangering thousands of people in the Bartang, Panj, and Amu Darya valleys downstream.

There is another natural hazard at Lake Sarez, namely, a large active landslide on the right bank (Figure 21). If this unstable slope should fail and slide into the lake, it would generate a surface wave large enough to overtop the dam and cause a severe flooding downstream. Experts who studied the hazards agree that the most probable scenario at Lake Sarez is failure of the right bank slope and overtopping of the dam.

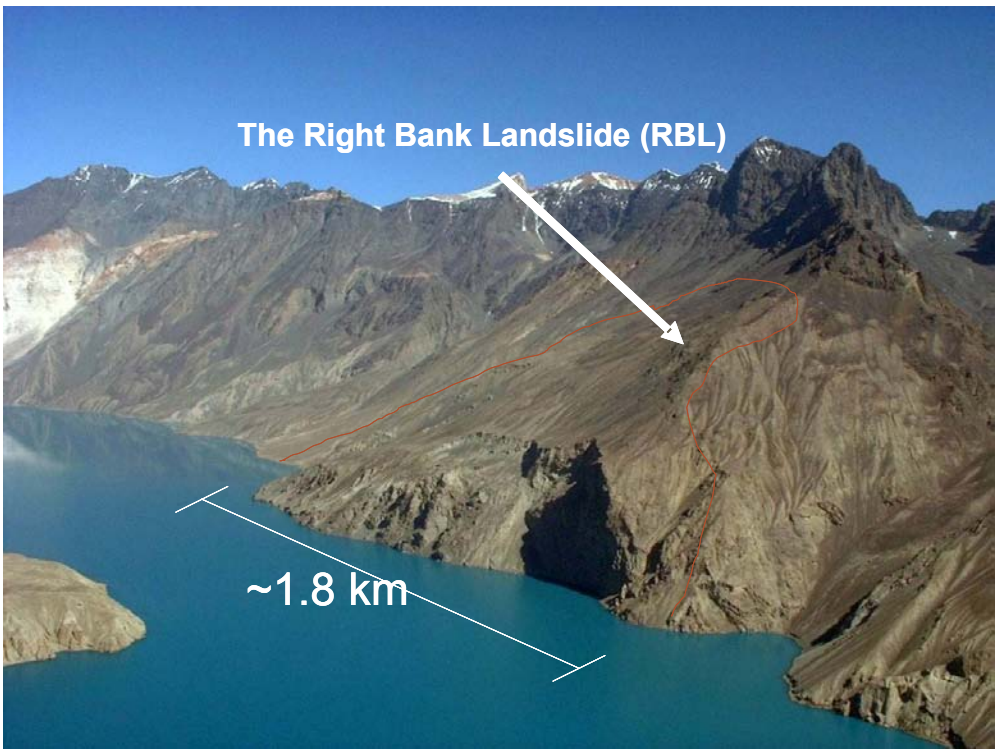

Figure 21. Active landslide on the right bank of Lake Sarez (Photo, State Secretariat for Economic Affairs, Switzerland).

In 2000, an international "Lake Sarez Risk Mitigation Project (LSRMP)" was launched under the auspices of the World Bank to deal with the risk elements posed by Usoi dam and Lake Sarez. The two main objectives of the project were to find long-term measures to minimize the hazard and to install an early warning system to alert the most vulnerable communities downstream. The early warning system for Lake Sarez has been in operation since 2005. The system has 9 remote monitoring units linked to a central data acquisition system at a local control centre near the dam. Data is transmitted via satellite to the main control centre in Dushanbe, Tajikistan's capital. Alerts and warning messages are sent from Dushanbe to 22 communities connected to the system. The local control centre is manned 24 hours per day, every day. The measurements included in the monitoring program are listed in Table 14.

At present, the warning system comprises three alarm levels. Each level is based on monitored data and/or visual observations. Threshold values for triggering alarms include both maximum measured values and rate of change with time. These are listed in Table 15. Alarm states and emergency warning plans are summarized in Table 17.

Table 14. Early warning system measurements at Lake Sarez (Stucky 2007).

Measurement	Methodology
Lake elevation	Pressure transducer in the lake
Detection of large surface wave	Pressure transducer in the lake
Seismic event	Strong motion accelerometers
Surface displacements	GPS
Flow in Murgab river downstream	Radar type level sensor
Turbidity in the outflow water	Turbidity meter
Flood conditions down stream	Level switches
Meteorological data	Complete weather station

Table 15. Threshold values for Level 1 and Level 3 alarm states (Stucky 2007).

Level	Source	Threshold value
1	Seismic acceleration	a > 0.05 g
	Lake level elevation	H > 3270 m above sea level
	Rate of change of lake level	dH/dt > 25 cm/day
	River flow downstream	Q > 300 m^3/s or Q < 10 m^3/s
	Manual alarm input	Unusual visual observation
3	Height of detected wave on lake	Wave height > 50 m
	Flood sensor	Q > 400 m^3/s
	River flow down stream	Q > 400 m^3/s or Q < 5 m^3/s
	Rate of change of river flow	dQ/dt > 15 m^3/s/h
	Manual alarm	Major event observed

At the start, some initial operational and maintenance were encountered, but these have been resolved underway. The principal problem has been insufficient power in some of the remote villages. The system satisfied the specified one-year error-free test program and has been formally turned over to the Ministry of Defence who now has responsibility for operation of the system. The plan is to keep the early warning

system in operation until 2020 which is the target date for completion of the mitigation works. The least expensive mitigation measure to reduce the risk is to permanently lower the lake level by about 120 m using a diversion tunnel around the landslide.

Table 16. Alarm states and emergency warning plan (DiBiagio and Kjekstad 2007).

Level 0 –Normal state		**Level 1 – Abnormal state but not critical**	
Definition	All systems operating properly No abnormal conditions detected	Definition	Abnormal situation due to a natural phenomenon or technical problem
Origin of warning	Early Warning System Local operating personnel	Origin of warning	Early warning system Local operating personnel
Destination of warning	Local control centre and Dushanbe	Destination of warning	Local control centre and Dushanbe
Action	Daily operation and maintenance	Action	Inspection, checking, repair and observation
Level 3 –Escape Signal		**Level 4 –Back to normal signal**	
Definition	Abnormal condition detected based on several sources	Definition	Normal conditions confirmed after a Level 3 alarm
Origin of warning	Early Warning System Local control centre or Dushanbe	Origin of warning	Dushanbe
Destination of warning	Local control centre and all villages downstream	Destination of warning	Local control centre and all villages
Action	People in villages evacuate to predefined safe areas	Action	Back to Level 0

Case Study 6: Risk of tailings dam break

The last example is a hazard and risk analysis to estimate the probability of non-performance of a tailings management facility at Roşia Montană in Romania (www.gabrielresources.com/prj-rosia.htm). The analyses established whether the dam provides acceptable safety against release of tailings and toxic water, and whether additional hazard reducing measures are needed. The project lies within the existing Roşia Montană mining district north-east of the town of Abrud in the Apuseni Mountains of Transylvania. The project will mitigate the consequences of the historic and future mining operation with the interception and containment of contaminated water currently entering the system, treatment of the contaminated waters and isolation and recovery of the waste rock piles within the project boundary. The operation of the project will generate tailings for approximately 17 years, producing tailings from the processing of a total of approximately 215 Mt of ore. The proposed mining and processing operation requires the construction and operation of a Tailings Management Facility (TMF) in the valley. The TMF includes a Starter Dam as a first stage of the Corna Dam, a Secondary Containment Dam (SCD), a tailings delivery system, a reclaim water system and a waste rock stockpile (Figure 22). The TMF is designed as a depository for the treated tailings residue. The Corna

Valley TMF site is to provide the required design storage capacity for the life of the mine, plus an additional contingency capacity

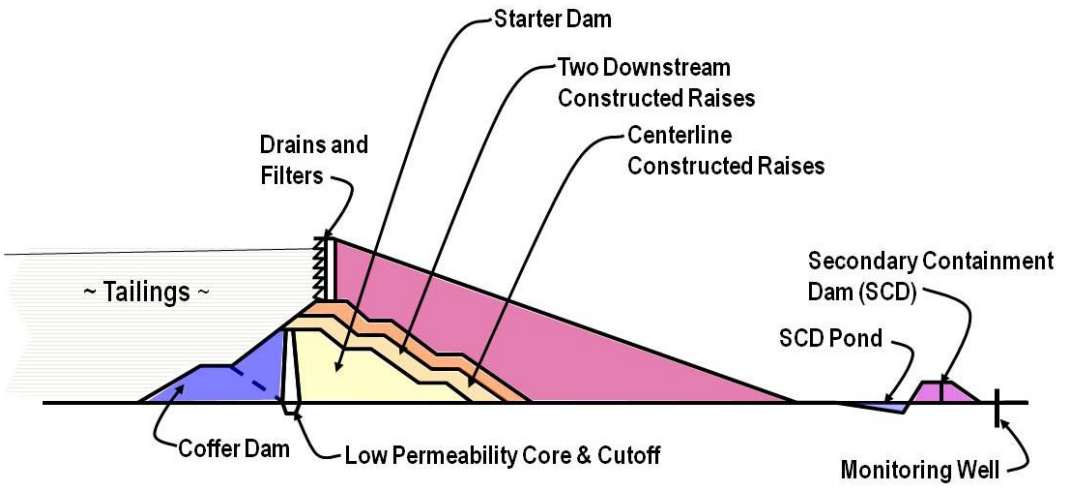

Figure 22. Cross-section of tailings dam in Romania (Corser, P. 2009. personal communication. MWH Americas, Inc. Bucharest, Romania).

To establish whether the dam provides acceptable safety against "uncontrolled" release of tailings and water during its life, an event tree approach was used to do the hazard analyses. This technique identified potential failure mechanisms and followed how a series of events leading to non-performance of a dam might unfold. The probability of each scenario, given a triggering event, was quantified.

The event tree hazard analyses considered the dam at different stages of its life and calculated the probability of non-performance. A non-satisfactory performance of the dam was defined as an uncontrolled release of tailings and water from the dam over a period of time. The release could be due to a breach of the crest of the dam or over-topping without breach of the dam. The analyses looked at critical scenarios, including all potential modes of non-performance for the Corna dam under extreme triggers such as a rare, unusually strong earthquake and extreme rainfall in a 24-hour period.

Design considerations

The most significant requirements that influenced the probabilities in the hazard analyses include:

- Operational freeboard at all times of one meter above storage elevation for maximum reclaim pond and 2 PMP (probable maximum flood) volumes; the freeboard leads to a storage volume capacity at all times of 2 PMP (equivalent to 5.5 millions m^3 volume), corresponding to a capacity of two 1/10,000-year rainfall occurring within the same 24 hours;
- Gentle slopes for the Starter Dam (≈2H:1V upstream and ≈2H:1V downstream);
- Gentle slopes for the Corna Dam slopes (3H:1V);
- Good quality rockfill for the Starter Dam construction and the final Corna Dam;

- "Well drained" tailings beach at the upstream face of the dam, where equipment can be moved for repairs, in case of movement or partial breach;
- Secondary Containment Dam (SCD) with about 50,000 m^3 containment capacity when the main dam is completed after 16 years;
- Diversion channels along the sides of the valley to divert excess rainfall runoff away from the TMF pond to minimise the risk of overtopping;
- Emergency spillway to control any excess water released;
- Comprehensive geotechnical monitoring system planned for safety surveillance;
- Careful control of construction by owner and contractor/engineer.

Event tree analysis

To establish whether the dam provides acceptable safety against "uncontrolled" release of tailings and water during its life, an event tree analysis was done, after a site visit by the members of the event tree team visited the site. A first-hand view of the site conditions and review of the available material is absolutely essential for this type of assessment. An event tree workshop was organised to develop the event trees and reach a consensus when quantifying the hazards. The analysis involved breaking down the complex system into its fundamental components, and determining the potential "failure" mechanisms leading to non-performance of the dam and the physical processes that could cause such mechanism.

The key factors considered in the analyses included: dam configuration (Starter dam, dam during construction (times 3 years, 9-12 years) and dam at completion (16 years); triggers, including earthquake shaking, extreme rainfall and/or snowmelt, natural terrain landslide in the valley and failure of the waste stockpile into the tailings reservoir.

Acts of war or sabotage, impact by meteorites or other extreme events of this type, with probability of occurrence less than 10^{-7} per year were not considered, as they would result in so low probabilities of non-performance that they are not realistic to consider.

The non-performance modes considered included:

1) Foundation failure, due to, e.g. excess pore pressures or weak layer in foundation leading to cracking, instability and breach of the dam.
2) Dam slope instability downstream or upstream, due to e.g., construction pore pressure in core of Starter Dam, excessive pore pressures caused by static or earthquake loads or instability due to inertia forces.
3) Unravelling of downstream toe and slope, due to e.g. overtopping or excessive leakage through or under the dam. This can be caused by a slide into reservoir, dam crest settlement due to deformations of the Starter Dam, piping, internal erosion and sinkhole formation, or excessive deformations (slumping) of the top vertical part of the Corna Dam during earthquake shaking.

4) Dam abutment failure followed by breach, due to e.g. slide close to and/or under part of the dam.
5) Liquefaction of the tailings.

Figure 23 presents some of the configurations and examples of the non-performance modes analysed. Overtopping without breach of the dam, including under-capacity or damage of the Secondary Containment Dam was also considered, not as a separate non-performance, but as one of the events in the sequence of events in the trees.

Different conditions can affect the probability of a hazard occurring or severity of a consequence, for example construction deficiencies or inadequate response of the field control team at the site when warning signals may appear. The analyses also looked into construction deficiencies, e.g. inadequate filters leading to uncontrolled internal erosion, inadequate drainage, very weak construction layers or zones in the embankment, inadequate types of material(s) in the embankment fill, or insufficient quality control and unforeseen construction schedule changes. These conditions were also integrated in the event trees as separate events during the course of the construction of the Starter Dam and Corna dam.

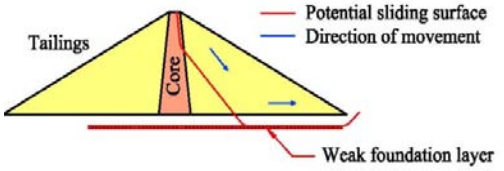

(a) Foundation failure

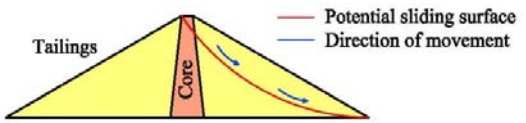

(b) Dam slope instability

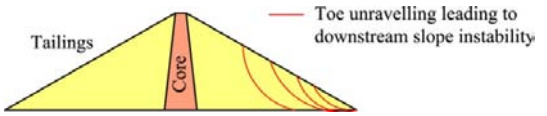

(c) Toe unravelling

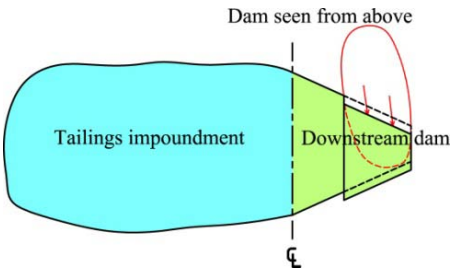

(d) Abutment failure of Starter Dam or Corna Dam

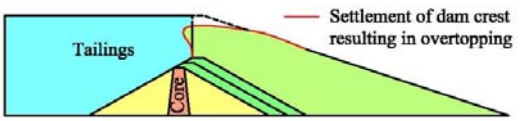

(e) Breach of completed Corna Dam due to settlement of crest

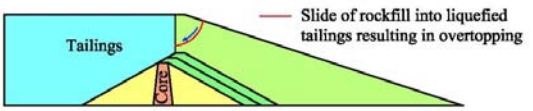

(f) Breach of completed Corna Dam due to liquefaction of tailings and to rockfill sliding into tailings.

Figure 23. Sketches showing examples of non-performance modes.

Probability of non-performance

At the event tree workshop, a discussion was first held to screen the most critical, and yet plausible, time in the life of the TMF to analyze, e.g. during construction of the Starter Dam, during the downstream construction stages, during the centreline construction of the final dam, and/or in the early years after completion of the final dam. A matrix of dam configuration and time was prepared, and the following modes were seen as most critical and susceptible to lead to the highest probabilities of non-performance. As part of the mode screening, the following considerations were subjected to a consensus decision: most critical times during life of the dam, extreme and critical precipitation (rainfall, flood and snowmelt), likelihood of failure of the waste stockpile, critical situations after construction of the dams, and geo-environmental considerations.

Table 17 presents the short version of the analyses prioritised. They are grouped by triggering event and by the dam "Configuration" analysed, the Starter Dam, the completed Corna Dam or an intermediate construction stage of the dam. Event trees were developed for each trigger, with each non-performance mechanism looked at separately. In some cases, two non-performance mechanisms were considered successively.

The total probability of non-performance is the sum of all contributing probabilities to the non-performance for each of the dam configurations. Table 18 summarizes the total probabilities for each configuration and trigger, and Table 19 presents the total probabilities for each configuration of the dam (all triggers included). The probabilities were presented as a function of the release of tailings and water associated with the non-performance of the Dam. The highest probability of non-performance was 1 x 10^{-6}/yr, or once in a million years.

The highest probabilities of non-performance were associated with earthquake shaking of the main dam and the static liquefaction of the tailings at time 9 to 12 years. The scenarios would result in some material damage and some contamination, but only in the vicinity downstream of the dam. For the Starter Dam, no reasonable expected scenario lead to a significant release of tailings and water because of the limited quantity of water available and the reserve capacity provided (2 PMP's). Internal erosion may cause, with a probability of once in a million year, a small escape of tailings and water. The escape would cause only modest contamination of the immediate vicinity downstream. Essentially all material released could be contained by the Secondary Containment Dam. The analyses showed the following:

- No sequence of plausible accidental events results in a probability of non-performance of the dam greater than once in a million years (or 10^{-6}/yr).
- The estimated probabilities of non-performance are lower than what is considered acceptable as design criteria for dams and other containment structures around the world and lower than probabilities of non-performance for most other engineered structures.

Table 17. Overview of event tree analyses.

Configuration	Time	Trigger	Non-performance mode
Starter Dam	1.5 yrs	Earthquake shaking	Foundation failure
Starter Dam	1.5 yrs	Earthquake shaking	Dam slope instability
Starter Dam	1.5 yrs	Earthquake shaking	Abutment failure
Starter Dam	1.5 yrs	Earthquake shaking	Toe unravelling
Completed dam	16 yrs	Earthquake shaking	Foundation failure
Completed dam	16 yrs	Earthquake shaking	Downstream slope instability and liquefaction
Completed dam	16 yrs	Earthquake shaking	Abutment failure
Starter Dam	1.5 yrs	Precipitation, flood, snowmelt	Foundation failure
Starter Dam	1.5 yrs	Precipitation, flood, snowmelt	Dam slope instability
Starter Dam	1.5 yrs	Precipitation, flood, snowmelt	Abutment failure
Starter Dam	1.5 yrs	Precipitation, flood, snowmelt	Internal erosion and toe unravelling
Starter Dam	1.5 yrs	Precipitation, flood, snowmelt	Operational delays
Starter Dam + 2 raises	4 yrs	Precipitation, flood, snowmelt	Operational delays
Starter Dam + 2 raises	4 yrs	---	Natural terrain slide in valley slope
Intermediate	9-12 yrs	---	Failure of waste stockpile
Completed Dam	16 yrs	---	Failure of waste stockpile
Starter dam	1.5 yrs	---	Internal erosion
Intermediate	9-12 yrs	---	Liquefaction of tailings

The factors that contribute to the low probability of non-performance include the use of good quality rockfill for the downstream surface of the dam, gentle downstream slopes for both the Starter and the main dam, dam capacity to store extreme precipitation and/or snowmelt events, spillway to release excess water in a controlled manner, the planned safety monitoring to warn of any early signs of unexpected performance and the proposed preparedness to remediate to any indication of unexpected behaviour.

The physical impact in terms of damage to the environment was also studied, if a breach in the dam should occur. The analysis suggested that the tailing would flow over a couple of 100 meters and that the tailings volume would be of limited volume. Studies of water model were also conducted, and the levels of pollution may be above surface water discharge standards for a limited period of time and in the immediate neighbourhood of the tailings dam, but only under the worst case conditions (low flow in the downstream river). However, monitoring, early warning and emergency procedures are to be implemented to contain damage to a minimum. The weather and flow conditions for this to occur combined with the probability of dam breach occurring at the same time resulted in the probability of occurrence would

reduce to 1 in 10 million years (Whitehead, P. (2009). Private communication. Aquatic Environments Research Centre, University of Reading).

Table 18. Total probabilities per volume released per trigger.

Configuration	Trigger/Event	P[Overtops Secondary containment dam]	
Starter Dam	Earthquake All non-performance modes	7.3 x 10^{-7}/yr	
Starter Dam	Precipitation All non-performance modes	4.7 x 10^{-8}/yr	
Starter Dam	Internal erosion	1.3 x 10^{-6}/yr	
Starter Dam	Precipitation Operation delays	2.0 x 10^{-7}/yr	
		P[Small release]	**P[Large release of water and tailings]**
Final Dam	Earthquake All non-performance modes	1.1x10^{-6}/yr	1.1 x 10^{-6}/yr
Final Dam	Failure of waste stockpile	2.4x10^{-7}/yr	1.7 x 10^{-7}/yr
Time= 4 yrs Dam	Precipitation Operation delays	5.5x10^{-7}/yr	5.5 x 10^{-7}/yr
Time = 4 yrs Corna Dam	Natural terrain slide in valley slopes	2.8x10^{-7}/yr	1.0 x 10^{-7}/yr
Starter Dam	Failure of Carnic waste stockpile	2.4x10^{-8}/yr	1.7 x 10^{-8}/yr
Time = 9-12 yrs Main Dam	Static liquefaction in tailings	5.2x10^{-6}/yr	1.3 x 10^{-6}/yr

Table 19. Total probabilities of non-performance per dam configuration.

Configuration	P[Non-performance]
Starter Dam (t= 1.5 yrs, internal erosion)	1.3 x 10^{-6} /yr
Completed Dam (t = 16 yrs)	1.3 x 10^{-6}/yr
Intermediate stage (t = 4 yrs)	6.5 x 10^{-7}/yr
Intermediate stage (t = 9-12 yrs)	1.3 x 10^{-6}/yr

RISK COMMUNICATION

Holding participatory workshops involving as many stakeholders as possible is an excellent way to communicate hazard and risk and to gauge perception. Several meetings of this type are usually needed. Two case studies in this paper used participatory processes to arrive at an estimate of the hazard and/or risk.

In this section, the authors wish to outline the creative and visionary efforts of the Geotechnical Engineering Office in Hong Kong (Department of Civil Engineering) to improve risk communication. In Hong Kong, frequent and disastrous slides may be triggered by heavy rainfall. Major landslides have caused fatalities in the past, so the Government of Hong Kong launched series of preventive actions that have reduced considerably the consequences of the slides that inevitably occur every year.

One key element among the preventive measures are the Hong Kong public education initiatives, that are complementary to the technical assistance and advisory services provided to slope owners, the erection of warning signs and the observation and repairing to slopes. The public education initiatives contribute to reducing the hazard of slope failure by reminding the slope owners to regularly maintain their slopes, and also help reduce the consequences of landslides by promoting personal precautionary measures during heavy rain.

The public education initiatives include: (1) "Slope and Home Safety" programme in collaboration with the Hong Kong Red Cross, with exhibitions, involving teenager students as safety ambassadors, visits to less fortunate residents, safety talks and assistance to elders; (2) television and radio announcements on the circumstances of recent landslides, targeted to the workers and the general public, and announcements of more general nature such as "No illegal dumping of waste on sloping ground"; (3) educational material for different curricula in the schools, roving exhibitions and school talks, and participation in scientific school fairs; and (4) commemorative videos, exhibition and even a fall "fiesta". The fiesta, in particular, is a public attraction with all the components of a town celebration with competitions, games, food and entertainment, each pertaining in some manner to the hazard and risk associated with natural hazards. It also turns out that public education initiatives are often far less expensive that engineering works.

RESEARCH UNDERWAY IN THE EUROPEAN COMMUNITY

SafeLand

SafeLand (www.safeland-fp7.eu) is a large-scale collaborative project under the European Commission's 7th Frame Programme. The 3-year project (2009-2012) has a total budget of near 9 M€ and involves 27 partners from 12 European countries. The project is coordinated by the International Centre for Geohazards (ICG) at NGI. The project, titled "Living with landslide risk in Europe: Assessment, effects of global change, and risk management strategies", aims at improving the methods for assessing and managing the landslide risk in Europe, both for today's situation and, in the future, including the effects of climate and demographic changes. SafeLand is to provide policy-makers, public administrators, researchers, scientists, educators and other stakeholders with an improved and harmonized framework and methodology for the assessment and quantification of landslide risk in Europe. It will evaluate the changes in risk pattern caused by climate change, human activity and policy change and provide guidelines for choosing the most appropriate risk management strategies, including risk mitigation and prevention measures.

SafeLand recognizes that risk management not only requires an integrated approach involving different specialists in the geosciences (engineers, geologists, geographers, geophysicists, meteorologists, …) to assess and quantify the risk, but also a close collaboration among social scientists, stakeholders and the geo-scientists to identify

the most appropriate risk mitigation measures. The scientific and technical objectives of the Risk Management part of SafeLand are two-fold: (1) carry out a state-of-the-art review, propose new mitigation and prevention measures, and produce a web-based toolbox of technically and economically appropriate (and innovative) prevention and mitigation measures based on experience and expert judgment throughout, and outside, Europe; and (2) develop and test a risk communication and stakeholder-led participatory process for choosing prevention and mitigation measures that are most appropriate from the technical, economic, environmental and social perspectives. The Risk Management part will be the culmination of the research in SafeLand and provide the tools required for dealing with landslide risk: a tested and documented framework with methodology and procedures for an effective implementation of landslide risk management.

During the first year of the SafeLand project, Risk Management studies have been performed along two axes: (1) preparation of a web-based toolbox for stakeholders with decision-making guidance based on a state-of-the-art study of existing physical mitigation measures, and (2) performing detailed case studies of the influence of political culture, organizational structures and economic context on implementation of landslide risk management tools. Scoping studies documenting the risks and the political history, legal frameworks, policy issues, institutional geography and views of stakeholders on current and future risks have been performed for Norway and Italy, and these will be followed by studies in France, Romania and India. These scoping studies are a key element for the development of a risk-communication and participatory stakeholder-led process for choosing the prevention and mitigation measures that are appropriate from technical, economic, environmental and social perspectives.

One of the objectives of the SafeLand project is to improve the profession's knowledge on the impact of human activities on increasing or decreasing the landslide hazard. Human-induced landslides may result from changes in slope caused by terracing for agriculture, cut-and-fill construction for highways, construction activity, mining operations, rapid draw-down of dams, changes in land cover such as deforestation, and changes in irrigation or surface runoff. However, in many situations the human activities have intentionally or unintentionally improved the slope stability and reduced landslide hazard. The anthropogenic factors could therefore play a positive role in reducing the landslide risk. During the first year of the project, an empirical model for assessing the changes in landslide frequency (hazard) as a function of changes in the demography and population density was developed. Calibration and validation of this model is currently underway.

MOVE

MOVE (www.move-fp7.eu) is a large-scale collaborative project under the European Commission's 7th Frame Programme. The 3-year project (2008-2011) has a total budget of near 2.7 M€ and involves 13 partners from 9 European countries. The project is coordinated by the University of Florence in Italy. MOVE will create

knowledge, frameworks and methods for the assessment of vulnerability to natural hazards in Europe. It will use indices and indicators to help improve societal and environmental resilience. Emphasis will be placed on clear, capable measurement and accounting for uncertainties. MOVE will identify gaps in existing methodologies. It will produce a conceptual framework that is independent of scale and hazard type. It analyse physical (technical), environmental, economic, social, cultural and institutional vulnerability. These will be measured for specific hazards and at different geographical scales. Floods, temperature extremes, droughts, landslides, earthquakes, wildfires and storms will be studied. Methodologies will be tested in case study regions on vulnerable elements and appropriate hazard types. Case studies will examine the availability and quality of existing data at sub-national (NUTS 3-5) and local scales. MOVE will evaluate statistical data (for cities, from EUROSTAT, etc.) and remote sensing information. The case studies will integrate methods of estimating potential economic damage and social vulnerability. The generic framework, data analysis and applicability tests will result in a standard approach to vulnerability assessment in Europe. Stakeholders will be consulted systematically to enable MOVE to draw attention to the practical value of its methodologies.

MATRIX

MATRIX is a large-scale collaborative project under the European Commission's 7th Frame Programme. The 3-year project (2010-2013) has a total budget of 4.3 M€ and involves 11 partners from 9 European countries, as well as one partner from Canada. The project is coordinated by GeoForschungsZentrum (GFZ) in Potsdam, Germany. MATRIX will tackle multiple natural hazards and risks in a common theoretical framework. It will integrate new methods for multi-type assessment, accounting for risk comparability, cascading hazards, and time-dependent vulnerability. MATRIX will identify the conditions under which the synoptic view provides significantly different and better results— or potentially worse results—than established methods for single-type hazard and risk analysis. Three test cases (Naples, Cologne and the French West Indies), and a "virtual city" will provide MATRIX with complex characteristic multi-hazard and multi-risk scenarios. The MATRIX IT-architecture for performing, analyzing and visualizing relevant scenarios will generate tools to support cost-effective mitigation and adaptation in multi-risk environments.

MATRIX will build extensively on the most recent research on single hazard and risk methodologies carried out (or ongoing) in many national and international research projects, particularly those supported by DG Research of the European Commission. The MATRIX consortium draws together a wide range of expertise related to many of the most important hazards for Europe (earthquakes, landslides, volcanic eruptions, tsunamis, wildfires, winter storms, and both fluvial and coastal floods), as well as expertise on risk governance and decision-making. The project has ten leading research institutions (nine European and one Canadian) as partners, and involves in addition end-user partners from industry, and from the European National Platforms for Disaster Reduction.

SUMMARY AND CONCLUSIONS

The paper presented a partial overview approach to evaluate hazard and risk and shows how research gradually moves into practice, sometimes by simplifying the approaches but most importantly by bringing forth examples of applications of the methodology. The paper presents six case studies from rock slope failure to tsunami threat and dam breach, looking into hazard, vulnerability and risk.

The tools of statistics, probability and risk can be intermixed, and the aim when doing such analyses, is obtaining the most realistic and representative estimate of hazard and risk.

Faced with natural hazards, society's only resource is to learn to live and cope with them. One can live with a threat provided the risk associated with it is acceptable or promises are made to reduce the risk to a tolerable level. After the recent natural catastrophes around the world, risk mitigation is gaining increasing interest and opens new challenges and new opportunities for our profession.

Emerging issues are accounting for multi-risk, climate and global changes and risk communication, especially bridging the gap between the technological and social aspect of hazard, vulnerability and risk.

REFERENCES

Alexander, D.E. (2000). "Confronting catastrophe." *Oxford University Press*, New York.

Alexander, D.E. (2002). "Principles of emergency planning and management." *Oxford University Press*, New York.

Anda, E. and Blikra, L. (1998). "Rock-avalanche hazard in Møre og Romsdal, Western Norway. 25 Years of Snow Avalanche Research." *Norwegian Geotechnical Institute, Publication No. 203*.

Ang, A.H-S. and Tang, W.H. (1984). "Probability Concepts in Engineering Planning and Design I & II." John Wiley & Sons, New York.

Bjerrum, L. and Jørstad, F. (1968). "Stability of Rock Slopes in Norway." *NGI Publication No. 79*.

Blikra, L.H. (2008). "The Åknes rockslide; monitoring, threshold values and early-warning" *10th International Symposium on Landslides and Engineered Slopes*, Xi'an, June 2008. China.

Blikra, L.H., Jogerud, K., Hole, J. and Bergeng, T. (2007). "Åknes/Tafjord prosjektet – Status og framdrift for overvåking og beredskap". *Report 01-2007*. www.aknes-tafjord.no, 30 p.

Christian, J.T. (2004). "Geotechnical Engineering reliability: how well do we know what we are doing?" *J. Geotechnical and Geoenvironmental Engineering,* 130(10):985-1003.

Christian, J.T., Ladd, C.C. and Baecher, G.B. (1994). "Reliability applied to slope stability analysis", *J. Geotech. Engrg., ASCE* 120(12): 2180-2207.

Coppersmith, K.J. and Youngs, R.R. (1986). "Capturing uncertainty in probabilistic seismic hazard assessment within intraplate tectonic environments." *Proc. Third US Natl. Conf. on Earthquake Engineering, Earthquake Engineering Research Institute*, Vol. 1, pp. 301-312.

Cornell, C.A. (1968). "Engineering seismic risk analysis." *Bull. Seism. Soc. Am* 58, pp 1583-1606.

Cruden, D.M. and Varnes, D.J. (1996). "Landslides Types and Processes." In: Turner A.K. & Schuster R.L. (Eds.) *Landslides: Investigation and Mitigation. Transportation Research Board Special Report* 247. National Academy Press, WA, 36-75

DiBiagio, E. and Kjekstad, O. (2007). "Early Warning, Instrumentation and Monitoring Landslides." *2nd Regional Training Course, RECLAIM II*, 29th January–3rd February 2007

Duncan, J.M. (2000). "Factors of safety and reliability in geotechnical engineering." *J. of Geotechnical and Geoenvironmental Engineering* 126(4): 307-316.

Düzgün, H.S.B. and Lacasse, S. (2005). "Vulnerability and acceptable risk in integrated risk assessment framework." International Conference on Landslide Risk Management. Vancouver 2005. 18th Annual Vancouver Geotechnical Symposium. Proceedings, pp. 505-515.

Eidsvig, U. and Harbitz, C. (2005). "Innledende numerisk analyser som følge av mulige skred fra Åkneset (Preliminary numerical analyses of tsunamis generated by a slide at Åknes)." *NGI Report 20031100-2*. Oslo, Norway. 100 p.

Eidsvig, U.K., Lacasse, S., Nadim, F. and Høeg, K. (2008). "Event tree analysis of hazard and risk associated with the Åknes rockslide." *ICG/NGI Report 20071653-1*. Oslo, Norway.

Fell, R., Ho, K.K.S., Lacasse, S. and Leroi, E. (2005). "A framework for landslide risk assessment and management – State of the Art Paper 1." *Landslide Risk Management*, Hungr, Fell, Couture and Eberhardt (eds), Taylor & Francis, London: 3-25.

GEO (Geotechnical Engineering Office) (1998). "Landslides and Boulder Falls from Natural Terrain: Interim Risk Guidelines." *GEO Report 75*, Gov. of Hong Kong SAR.

Glimsdal, S. and Harbitz, C. (2006). "Preliminary results using an improved tsunami model." *NGI Rpt 20051018-1*. Oslo, Norway. 70 p.

Gregersen, O. (2001). "Metode for klassifisering av faresoner, kvikkleire". *20001008-1, Norwegian Geotechnical Institute*, Oslo, Norway, 24 January 2000.

Gregersen, O. (2005). "Program for økt sikkerhet mot leirskred. Risiko for kvikkleireskred Bragernes, Drammen." *Report 2004 1343-1. Norwegian Geotechnical institute*, 26 January 2005

Gregersen, O. (2008). "Kartlegging av skredfarlige kvikkleireområder." *Paper for NGM-2008* (Northern Geotechnical Conference 3-5 September 2008). Sandefjord, Norway. 9 p.

Harbitz, C.B., Bungum, H., Løvholt, F., Lindholm, C.D., Glimsdal, S., Nadim, F., Pedersen, G. and Gauer, P. (2006). "Earthquake related tsunami hazard assessment along the western coast of Thailand." *Natural Hazards and Earth System Sciences*.

Hartford, D.N.D. and Baecher, G.B. (2004). "Risk and uncertainty in dam safety". Thomas Telford. London, UK. 391 p.

Høeg, K. (1996). "Performance evaluation, safety assessment and risk analysis of dams." *Hydropower and Dams*. 6, 3, Nov. 1996. 8 p.

IFRC (International Federation of Red Cross and Red Crescent Societies) (2001). *World Disaster Report, Focus on Reducing Risk.* Geneva, Switzerland, 239 pp.

IFRC (International Federation of Red Cross and Red Crescent Societies) (2004). *World Disaster Report*.

ISDR (International Strategy for Disaster Reduction) (2005). *Hyogo Framework for Action 2005-2015*, 21 pp.

Karlsrud, K. (2008). "Hazard and Risk Mapping for Landslides". *Paper for 33rd IGC* (International Geology Congress). (6-14 August 2009). Oslo.

Kaynia, A.M., Papathoma-Köhle, M., Neuhäuser, B., Ratzinger, K., Wenzel, H. and Medina-Cetina, Z. (2008). "Probabilistic assessment of vulnerability to landslide: Application to the village of Lichtenstein, Baden-Württemberg, Germany." *Engineering Geology,* Vol. 101, Issues 1-2, 23 September 2008, pp. 33-48.

Kristensen, L., Blikra, L.H. and Hole, J. (2010). "Åknes: State of instrumentation and data analysis." Åknes report 02 2010, 41 p

Kulkarni, R.B., Young, R.R. and Coppersmith, K.J. (1984). "Assessment of confidence intervals for results of seismic hazard analysis." *Proc. Eighth World Conf. on Earthquake Engineering*, San Francisco, Vol. 1, pp. 263-270.

Kveldsvik, V., Eiken, T, Ganerød, G.V., Grøneng, G. and Ragvin, N. (2006). "Evaluation of movement data and ground conditions for the Åknes rock slide"; South African Institute of Mining and Metallurgy, *Intern. Symp. on Stability of Rock Slopes in Open Pit Mining and Civil Engineering*. pp 279-299.

Kveldsvik, V., Einstein, H.H., Nilsen, B. and Blikra, L.H. (2008): "Numerical stability models of the 650,000 m^2 Åknes rock slope based on measured displacements and geotechnical data". *Rock Mechanics Rock Engineering*.

Lacasse, S. (2008). Report on Session 3: Innovation and Digital Technology. International Forum on Landslide Disaster Management, Hong Kong, Nov. 2007

Lacasse, S., Eidsvik, U., Nadim, F., Høeg, K. and Blikra, L.H. (2008). "Event Tree analysis of Åknes rock slide hazard." *IV Geohazards Québec, 4th Canadian Conf. on Geohazards*, pp. 551-557.

Lacasse, S. and Nadim, F. (2008). "Landslide Risk Management: Country Report For Norway". *2007 International Forum on Landslide Disaster Management. Proceedings Vol. II, GEO, Hong Kong, pp. 99-124.*

Lacasse, S., Nadim, F., Høeg, K. and Gregersen, O. (2004). "Risk Assessment in Geotechnical Engineering: The Importance of Engineering Judgement". *The Skempton Conference, Proc.* London UK. V 2, pp 856-867.

Lacasse, S., T.R. Guttormsen and A. Goulois (1989). "Bayesian updating of axial capacity of single pile". ICOSSAR'89, San Francisco, USA, pp. 287–294.

Lee, E.M. and Jones, D.K.C. (2004). *Landslide Risk Assessment*. Thomas Telford, London. 454 p.

Leroi, E., Bonnard, Ch., Fell, R., and McInnes, R. (2005): "Risk assessment and management – State of the Art Paper 6." Landslide Risk Management, Hungr, Fell, Couture and Eberhardt (eds), Taylor & Francis, London: 159-198.

Malone, A.W. (2005). "The story of quantified risk and its place in slope safety policy in Hong Kong." In: Glade, T., Anderson, M.G. and Crozier, M.J. (eds.): *Landslide hazard and risk*. Wiley, Chichester, 643-674.

McGuire, R. (2004). "Seismic Hazard and Risk Analysis." *EERI monograph* (MNO-10), ISBN: 0-943198-01-1, 221 p.

Munich RE (2011). www.munichre.com/app_pages/touch/naturalhazards/@res/pdf/NatCatNews/2011_01_03_munich_re_NatCatSERVICE_en.pdf?1

Nadim, F. and Glade, T. (2006). "On tsunami risk assessment for the west coast of Thailand." *ECI Conference: Geohazards - Technical, Economical and Social Risk Evaluation*, 18-21 June 2006, Lillehammer, Norway.

NGI (2006). "Tsunami risk reduction measures with focus on land use and rehabilitation." *Norwegian Geotechnical Institute report 20051267-1*, 14 January 2006.

NORSOK standard Z-013 (2001): "Risk and emergency preparedness analysis", rev. 2, www.standard.no

Proske, D. (2004). *Katalog der Risiken.* Eigenverlag Dresden. 372 p.

Ragozin, A.L. and Tikhvinsky, I.O. (2000). "Landslide hazard, vulnerability and risk assessment." In: E. Bromhead, N. Dixon and M.-L. Ibsen, Editors. Research, Theory and Practice. Proceedings on the 8th International Symposium on Landslides, *Cardiff, 26-30 June 2000, Landslides* (2000), pp. 1257-1262.

SSHAC (Senior Seismic Hazard Analysis Committee) (1997). "Recommendations for Probabilistic Seismic Hazard Analysis: Guidance on Uncertainty and Use of Experts." US Nuclear Regulatory. *Commission report CR-6372*, Washington DC.

Stucky (2007). "Lake Sarez Risk Mitigation Project - Component A. Final Report to Ministry of Emergencies and Civil Defence of the Republic of Tajikistan." Renens, Switzerland, 20 January 2007.

UNDP (United Nations Development Programme) (2004). "Reducing Disaster Risk – A Challenge for Development." *Bureau for Crisis Prevention and Recovery*, New York, 146 pp.

UNISDR (2009a). "Global assessment report on disaster risk reduction (GAR 2009)." ISBN/ISSN: 9789211320282, www.preventionweb.net/english/hyogo/gar/

UNISDR (2009b). "Terminology on Disaster Risk Reduction." www.unisdr.org/eng/library/UNISDR-terminology-2009-eng.pdf

United States Nuclear Regulatory Commission (1975).

Vick, S. (2002). "Degrees of Belief. Subjective Probability and Engineering Judgment." ASCE Press. 405 p.

www.gabrielresources.com/prj-rosia.htm

Åknes/Tafjord project webpage: www.aknes-tafjord.no.

GEO-RISKS IN THE BUSINESS ENVIRONMENT

William F. Brumund[1], Ph.D., F.ASCE, D.GE, P.E.

ABSTRACT: Companies are exposed to many geo-risks that arise from work done on engineering projects. Companies are also exposed to other geo-risks that are not specifically related to performance on a project. This paper considers risks that may arise from the characterization of the subsurface conditions and how engineers conceptualize and model these conditions and related uncertainties. The author considers one of the areas of greatest exposure to companies is incorrectly defining the mode(s) of deformation or failure (the conceptual model). In addition, significant risks may arise by doing calculations using models that have not been checked and verified or when the user does not understand the algorithms and model boundary conditions. Business risks can arise from large, long-term projects that may be greater than those on smaller, more limited assignments because of the expanded conditions within the scope of work. Business risks can also arise from events that are rare, have extreme impacts, and are unpredictable or extremely difficult to predict. Some risks associated with changing legal interpretations are noted and risks associated with working in different states, countries and from different offices are discussed. The limitations and business risks for companies that have project opportunities in OFAC counties is also discussed.

INTRODUCTION

Companies today are exposed to business risks that arise from work in the geotechnical, mining, and geo-environmental areas (business geo-risks) that may be different and more over-arching than risk issues normally associated with a specific project or task. Also, the business risks that can arise on large, long-term projects may be greater than those a company would normally be exposed to on a short-term assignment which has a more limited scope of work. There are also business risks that may arise from rare, extreme impact events that cannot be predicted and can only be evaluated retrospectively. This paper will consider some of the origins of the above three types of geo-risks, and offer some examples of how each type of risk might arise. In addition, some other risks and liabilities associated with the business of consulting will be discussed.

[1] Principal, Golder Associates, 9428 Baymeadows Road, Suite 400, Jacksonville, FL 32256-7979, bbrumund@golder.com

SITE CHARACTERIZATION, MODE OF FAILURE, AND ANALYTICAL TOOLS

In the past quarter of a century, the development of analytical tools and computing capability has been awesome. Today, engineers are able to analyze problems that could not have been analyzed, in detail, 25 years ago. For example, a transient unsaturated groundwater flow problem can be characterized using a nonlinear partial differential equation. Today this problem can be solved using commercial numerical codes on a computer. The solution to this problem would have been impractical before the development of computer models. In the past, much simpler approximations would have been used and engineers would have bracketed expected outcomes.

The advanced field data collection techniques available today enable professionals to acquire gigabytes of detailed geotechnical and environmental data. The ability to portray the variability of parameters within a geologic stratum or unit is easier and more detailed today than was possible a few decades ago. This variability in the data is often described through the use of probabilistic distributions. In theory, therefore, the current data acquisition and overall design practice should be much better than in the past because of the ability of design professionals to characterize the subsurface conditions more accurately and analyze complex problems more rigorously.

Unfortunately, however, the improved data acquisition methods and more sophisticated analytical techniques do not automatically result in a better conceptual formulation or understanding of the subsurface system, and may not result in better designs. The design professionals must understand the geomorphic history at a site and define the relevant stratagraphic units. Depending on the variability of parameters within a stratum, it may be appropriate to subdivide a stratum into layers or zones having similar parameters. There may be a need for this subdivision for one class of problems and not for another. For example, the subsurface model used, and the associated data needs, may be different for a contaminant hydrogeological assessment than might be needed for a slope stability assessment.

An important, and sometimes overlooked, element to characterizing subsurface is recognizing that it is generally not possible to know what the actual variability is with respect to stratigraphy or design parameters. Subsurface conditions and parameter variability may differ across space and time and may be significantly different than assumed or inferred from limited data; therefore, significant errors may be introduced into the models and analyses. Failing to recognize this uncertainty in models can create business risks related to the geo-practice. Therefore, it is critically important to recognize that uncertainty exists and account for it in reviewing the output from the analytical solutions.

After developing an accurate subsurface site characterization model, a careful assessment must be made of the possible modes of deformation or failure. When considering various mode(s), professionals must assess the kinematic possibility of the material deforming or failing in the manner assumed. Once the most probable mode(s) of deformation or failure is defined, then the professionals must decide how that mode of deformation or failure should be analyzed. An inaccurate definition of the mode(s) of deformation or failure is one of the major business risks that a company may be exposed to in the geotechnical or geo-environmental field. No matter how sophisticated the analysis, if the wrong mode of deformation, failure, or contaminant transport is analyzed, the results will mislead the professionals.

Detailed modeling and analyses should be done only after: 1) the best characterization of the subsurface is defined from an assessment of the geology, material types, and variability of material parameters, 2) the most realistic mode(s) of deformation or failure are determined, and 3) the most appropriate analytical techniques are selected. The fundamental aspects of the profession have not changed as a result of the development of computers and advanced analytical solutions.

Forty years ago (pre-computer and the dawn of digital calculators) when considering a geotechnical project, engineers and geologists developed their best characterization of the subsurface conditions and evaluated what the most realistic modes of deformation or failure might be. Engineers considered whether the mode(s) of deformation or failure were kinematically possible and realistic. If conditions warranted, a stratum might be subdivided into several layers and different parameters assigned to each layer. The design professionals developed their best estimate of the geotechnical parameters that would be used in their analyses for each stratum or layer. Judgment was used in the selection of design parameters; the parameters might not be the mean value of the test data for each layer. This approach was necessary because all the calculations were done by hand, were laborious, and were time consuming to perform. Based on thought and experience, the professionals developed a "sense" or "feel" for how the system would perform and what the expected results might be. Analyses were done to refine or verify the expected results. When computer software was developed to do limit equilibrium slope stability analyses using a method of slices analysis, many consulting firms would insist that the critical failure surface predicted using the computer model be redone manually so the designers could verify the computer output and gain an appreciation for the interaction of the forces and moments.

Where has all the insight and thought gone? In the author's opinion, geotechnical and environmental professionals today sometimes begin running the computer models without having carefully considered: 1) the geologic site characterization (i.e. the site conceptual model), 2) the most realistic mode(s) of deformation or failure, and 3) the applicable design parameters for each unit in the subsurface model. Professionals sometimes rush into initial modeling to "see what is happening" or to "find the answer," but the expected outcomes may not have been carefully considered

or estimated beforehand. As a result, design professionals may be misled by spreadsheet output or results from commercial computer programs.

Because of the ease of running computer analyses using a range of parameters for each stratum (e.g. the stratum variability), professionals may not consider characterizing a stratum using smaller substrata where the variability of the data within each substrata is smaller. Such an approach might be more realistic in determining where the critical failure surface might be located. Similarly, in environmental projects, subdividing a stratum into different layers, where the layers have different parameters (e.g. hydraulic conductivity), might be more realistic in assessing the movement of groundwater or transport of contaminants within the subsurface.

It is not unusual for professionals to tabulate and manage data on spreadsheets and then perform important analyses or calculations using this data in the same spreadsheet or workbook. New spreadsheets or workbooks are often created for each project or new assignment. It is not uncommon for work on these spreadsheets to be done without documenting on each worksheet the title of what is being calculated, a job number, a date, a file name, a tab name, or a record of the author of the work. In addition, many, if not most, of these *ad hoc* spreadsheets are not checked to ensure the calculations are done accurately for the assumed model or reviewed to ensure the proper parameters were input and implemented properly in the spreadsheet. Yet the results from these spreadsheets are often used as a basis for design and are included in engineering reports. Although it is easy to do data manipulation and reasonably sophisticated calculations with spreadsheet programs, unless the data entry and formulas are checked and verified, professionals can be misled by the results and a company can incur significant liability risks, in the form of negligence claims, by improperly using these tools.

Even when the conceptual model is reasonable, it is still possible to be misled by inappropriate application of the computer model. If the design professional doesn't fully understand the algorithms, understand how to use the computer code, and understand how to properly address the boundary conditions, the computer output may not yield results that are meaningful or realistic. The author considers that unless the professional has a sense of what the computer results should be, it may be difficult for the design professional to assess whether the computer results are reasonable. Independent rough, simple predictions of what the expected answer should be need to be done if at all possible. Improper computer modeling is another area of risk exposure for businesses. These risks may be in the form of negligence claims against the firm and, in some states, against the design professional personally.

There is a growing interest in the use of probability theory to represent model uncertainty and the distribution of possible parameter values in a given zone or at a specific point. This is nominally intended to represent the confidence in the model and the parameter values. This uncertainty reflects the professional's ignorance in what the real conditions are and is different from the variability or fluctuations (e.g.

in parameter values within a given stratum or layer) with time and space. If done correctly, the probabilistic representation of the model and input parameters can convey the professional's level of confidence in the analysis and model results. It can help the designers highlight which models and parameters have the greatest impact on a design, and by better defining the model and values of the parameters, the confidence in a design can be increased or a more cost effective design developed. However, like any analytical approach, uncertainty theory can be a mixed blessing. If improperly implemented, a probabilistic representation of the data in a layer may obscure a weak zone that can have a dominant impact on the failure mode or mask the impact a strong zone may have on performance.

The author is aware of analyses where data from different geologic formations that had different material parameters and variability were characterized as a single material. It was noted that the spatial variability could be reduced by gathering additional information, but there was no discussion of geomorphic history and material types in the analysis of the data. Advanced probabilistic analyses were improperly applied to the data as if it were from one unit. Such an approach should not be used to characterize different materials as a single unit whose parameters exhibited considerable variability. Just because it is possible to mathematically analyze a broad, diverse, data set does not mean such an analysis should be done if the engineering fundamentals do not support such an analysis.

Consider a case history where the primary consolidation in a thick layer of soft clay was calculated under a large embankment. The primary settlement predictions were conveyed to the owner. The owner, therefore, had an expectation of the magnitude of embankment settlement that would occur. The embankment settled more than double the predicted amount, and the settlement was asymmetric. Settlement plates were used to measure vertical settlement at various locations and slope inclinometers were used to detect lateral deformations in the soft clay. Substantial lateral deformation occurred in the soft clay due to undrained shear deformation. Although the instrumentation was specified by the design professional, no predictions were made of the anticipated time–settlement or time-lateral deformation behavior for the instrumentation. This is an example where the professional's conceptual deformation model was incomplete; since no predictions were made for the time response of each instrument, it was more difficult for the designers to recognize that the performance deviated substantially from their expectation until much later in the project. This example demonstrates the need for the professional to understand all the possible modes of deformation or failure and assess the possibility for each mode to occur. As stated earlier, not understanding and recognizing all the modes of deformation or failure is one of the largest risks that a company may have in terms of business geo-risks.

In another case history, a dam and reservoir system was upgraded by removing a saddle dike in the reservoir and constructing a fuse plug in the area to increase the ability of the reservoir to pass a larger design storm than the dam was originally designed to accommodate. Prematurely, the fuse plug was pressed into service and

breached as it was intended to do. What was unexpected was the erosion of the fuse plug outlet channel and the release of much more water from the reservoir than was anticipated. As a result, extensive downstream property and consequential damages occurred. Fortunately, there was no loss of life. This project is another example where all the potential failure modes were not adequately identified or considered at the design stage.

In summary, a company can incur significant business geo-risks on geotechnical, mining, and geo-environmental projects. Some of the areas, which if not done correctly, create these risks:

1) Incorrect development of the conceptual subsurface model
2) Incorrect or incomplete definition of the mode(s) of deformation or failure
3) Incorrect numerical modeling, including:
    a) Selecting analytical techniques that do not comport the mode(s) of deformation or failure
    b) Missing or not recognizing important details in the conceptual model and site data
    c) Incorrectly using computer models
    d) Using spreadsheets that have not been checked or undergone a thorough quality assurance review

The author considers that the sophisticated analytical tools available to designers today should not be used as a substitute for sound, prudent, engineering and geologic judgment. Reliance on modeling results, without thoughtful consideration of the geologic site characterization, appropriate design parameters, and expected outcomes, can create significant liabilities to a company in the form of negligence claims.

RISKS ON LARGE, LONG-TERM PROJECTS

Large, long-term, complex projects may create unforeseen liability issues for companies. Most companies are thrilled to win large, multi-year projects that can keep many dozens or hundreds of employees busy for years or decades. However, budget constraints, schedule issues, along with managerial, cultural, and political issues can influence design details and limit the extent of necessary critical and periodic technical reviews. During the evolution of these projects, the scope often changes and key professionals may retire or be rotated onto other project assignments. As a result, legacy issues and entrenched design logic may prevent a critical examination of all facets of a project design. The logic may have been sound in the past, but may not be appropriate for the current scope of work. Consider the following projects:

- 1984, Union Carbide pesticide plant in Bhopal, India, experienced a leak of methyl isocyanate gas (MIC). Water entered a tank of MIC and caused an exothermic reaction. In June 2010 several ex-employees were convicted of causing death by negligence.

- 1986, Chernobyl nuclear plant in the Ukraine failed during an unauthorized systems test. Automatic reactor shutdown systems were disabled and a test was run to see how long the turbines could run cooling water pumps without power.
- 1986, NASA Challenger exploded 73 seconds after takeoff. Failure was attributed to an "O" ring on a solid fuel rocket booster.
- 2010, BP Deepwater Horizon drilling platform in the Gulf of Mexico. Design operational decisions associated with completing the well led to its explosion.

The failures of all the above major projects were preventable. The projects had under gone detailed reviews, and complex monitoring systems were in place, but the unthinkable happened. There are also examples of large project failures in civil and mining projects. These projects may not have the same visibility as the above projects but the fundamentals of design, monitoring, maintenance, and project management are similar. Examples of these include:

- 1972, Buffalo Creek dam failure in West Virginia – a 40 to 60 foot high dam retaining coal mine waste failed after a period of heavy rain on February 26. The water level was reported to be near the crest of the dam. The failure resulted in the death of 125 people.
- 1976, Teton Dam in Idaho failed on June 5. The dam was designed by the US Bureau of Reclamation. The most probable cause of failure was a combination of collapse of permeable loess in the core, piping, and a fractured foundation under the dam. The failure resulted in the death of 11 people.
- 1977, Kelly Barnes Dam in Georgia failed on November 6, after several days of heavy rainfall. The original dam was constructed in 1899 and was modified and expanded in 1939. Overall, the dam was reported to be in poor condition and lacked a sufficient design. No specific cause of failure was identified but it included slope failure of the dam and the possible collapse of the low level spillway.

Companies can employ many strategies to help ensure that these large, long-term, complicated projects function effectively. Some of these include:

- Have a crystal clear approach to design, reviews, monitoring, and re-design.
- The design team and management must understand the design requirements and schedule.
- Avoid "group think." Direct reports do not like to deliver bad news to senior managers/leaders. As a result, leaders tend to get overly filtered reports. Effective leaders ask for and demand to hear the bad news.
- Stamp out complacency. All monitoring data must be analyzed as though it is the first set of monitoring results received. Monitoring data should be compared to the predicted response.
- Legacy issues have no place in the project team. A critical assessment must be done and redone to ensure that the current strategy and design approach is the best available at the time.

- Put in place an effective Review Board. This Review Board must have access to and review basic data, design assumptions, performance criteria, monitoring data, and have an independent look at the approach being used in the conduct of the project. For long-term projects, rotate members of the Review Board to help ensure that new ideas and a fresh look are being provided.

Companies pursuing large, long-term projects should recognize that the legal risks on these projects may be different and more complex than normally experienced on smaller, short-term assignments. As a result, different approaches must be used on the larger jobs. Although the default standard of care for firms working on these large projects is a negligence standard, the circumstances and conditions of the engagement normally implies the need for comprehensive technical reviews, enhanced QC/QA procedures, and other issues to help ensure the work product will function as intended. Careful attention to contract terms is critical on these large projects and the company must continually work to ensure that the expectations of all the parties are aligned throughout the project.

RARE, EXTREME IMPACT, EVENTS

Companies are also exposed to rare, extreme impact events in the course of business or on individual projects. In the book, *Black Swan* (Taleb, 2007), the author discusses what these rare, extreme events (Black Swans) are, and why they are not predictable in advance. These rare and extreme impact events can create major liabilities, and they may create significant, game changing opportunities. Taleb uses the example that if a Stone Age thinker was asked to develop a strategic plan for the future and did not envision the invention of the wheel, his forecast would be wrong. If you were preparing strategic forecasts in the 1970s and 1980s and did not anticipate the evolution of computers, email, and the internet, your estimates would have been incorrect. One of the purposes of a formal risk assessment is to try to identify rare events that might occur that would have serious consequences. Because of the low likelihood of occurrence, these events are often "screened out" in making project decisions. Professionals doing risks assessments must try to identify and evaluate the rare events, but it is not possible to identify the "Black Swans" as defined by Taleb.

Rare and extreme impact events can occur on engineering projects and in the business environment. Two simple examples are provided below that illustrate these "black swan" events.

The Ka Loko Dam in Kauai, Hawaii was constructed in the late 1880s on one side of an existing volcanic cone. The dam had a homogeneous section and had a maximum height of about 40 feet. An overflow spillway was constructed in the right abutment in about 1912 when the dam was raised. The Ka Loko reservoir provided water for irrigation of sugar cane fields in the area. By the early 1970s, the

commercial production of sugar cane ceased and the reservoir was no longer needed for commercial sugar cane production. Portions of the dam and reservoir were sold or transferred to private owners in the late 1980s.

Following about six weeks of heavy rain, on March 14, 2006, the Ka Loko Dam failed and water rushed downstream, over the Kuhio Highway, and in the process killed seven people. Figure 1 shows a view of the breach in the Ka Loko Dam from the rear of the reservoir taken in May 2006. Figure 2 shows the breach as seen from the right abutment.

Figure 1 - Breach from rear of the reservoir

Figure 2 - Breach as seen from the right abutment

In 1998, the then current owner of the dam had the overflow spillway filled with earthfill so the reservoir water level could be raised. The original location of the spillway was in the right abutment just to the right of the breach shown in Figure 1. After functioning for almost 120 years, the dam failed eight years after the overflow spillway was filled and made non-functional.

The author considers that filling in the spillway over 110 years after construction could not have been predicted and could not have been contemplated by the original designers. The original designers probably did not envision that the dam would even be in operation after 110 years. This act constituted a rare and extreme event (Black Swan) that had devastating impacts. Filling the spillway constituted a geotechnical event or geo-risk that had and is having significant business and financial consequences to all parties involved with this project.

Since these rare, extreme impact, unpredictable events (Black Swans) may occur, the author considers that the only way a firm can protect itself against the financial consequences of these events is by having adequate insurance. Since these events are unpredictable, no amount of training or technical qualifications of the employees can reduce the risk of these events occurring.

In another example, a firm had a construction monitoring assignment but failed to adhere to the agreed upon protocol for reporting its findings. Because of the failure

to follow the protocol, the firm was sued for breach of contract by the client and sued by a third party. The insurance company that provided the firm's professional indemnity insurance was the Reliance Insurance Company. The Reliance Insurance rating (Best rating) began to drop in 2000 and in September 2000 the firm cancelled the Reliance policy and obtained insurance with another insurance company. Reliance Insurance Company was ordered into liquidation on October 3, 2001; this was thirteen months after the firm canceled its policy with Reliance. On the above project, Reliance Insurance was notified of a potential claim several months before the policy was cancelled. Because all professional indemnity policies are written on a "claims made" basis, Reliance Insurance was the insurer responsible for this claim. Since the bulk of the legal costs and expenses on the above matter were incurred after Reliance Insurance was forced into liquidation, the firm had to fund all the legal fees, settlement costs, and a trial judgment without having timely reimbursements from its insurance company.

The Reliance Insurance Company was one of the largest property and casualty insurance companies to ever be forced into liquidation in the United States. The rare and extreme impact event in the above case was the combination of the insurance company being forced into liquidation, after the claim was reported, and not being able to pay what it was liable for under the insurance policy. This is another example of a commercial "black swan" in the consulting business.

OTHER BUSINESS RISKS

The business landscape in the consulting fields of geotechnical, mining, and the environmental areas is changing rapidly and these changes present new risks to companies and individual professionals. Some emerging business risks that companies must consider and evaluate are discussed in the following paragraphs.

Personal professional liability -- There are disturbing trends in the interpretation and enforcement of limitation of liability clauses in contracts, particularly on projects where there are only "economic losses." Economic losses are those where there is no personal injury, no third party claims, and the only damages are economic. Many consulting contracts, since the mid-1970s, include a limitation of liability clause. If there are claims that arise out of the contract that are only economic in nature, the aggrieved party's recourse is governed by the contract. In a Florida Supreme Court decision in 1999, Moransis v Heathman [744 So.2d 973 (Fla. 1999)], the court decided that the plaintiff could sue the consulting firm under the contract and sue the individual professionals who worked on that project even though they were employees of the consulting firm that had the contract for the work. The plaintiff was able to sue the professionals in tort for what normally would be a contract dispute.

Subsequently (June 2010), a Florida appellate court found that the limitation of liability clause in a contract between a design firm and its client cannot be applied to limit the liability of an individual professional that is an employee of the firm [Witt v.

La Gorce Country Club, Inc., 34 Fla.L Weekly D1161a]. Other states have adopted similar interpretations for economic loss matters. This trend creates another expanding business risk for companies and its employees. Most errors and omissions insurance policies obtained by a company cover the negligent acts of the firm and its employees acting on the firm's behalf. Although the employees sued may have insurance coverage under their employer's policy, this trend toward personal liability implies that insurance premiums may increase in the future because of the expanded risk exposure of the insurer.

Professional registration -- As businesses grow, there are opportunities to work for clients in other states or countries; also there may be opportunities to work with professionals in other offices in the same firm on projects. From a business standpoint, professionals and business leaders must ensure that the necessary registration requirements, both individual and corporate, are met before signing a contract or having professionals do design work on projects not in a "home" jurisdiction. For example, if a subject matter expert in a US office, who is registered in his home state, is asked to take the lead role for a design in another country, the registration requirements for that professional must be investigated. If the firm has a local company in the foreign country, can or should the subject matter expert sign a design report or drawings if the design is issued from the local office? Registration requirements, business practices, and contract validity and enforceability may depend on how situations like the above are addressed.

OFAC limitations -- Businesses must also be aware of OFAC limitations on international work. OFAC stands for Office of Foreign Asset Control, a department under the US Department of the Treasury; OFAC enforces economic and trade sanctions against targeted foreign countries. If a project opportunity arises in an OFAC listed country, depending on the sanction, US firms cannot work there and US based insurance companies will exclude coverage for any work done in that country. This can create significant business risks, legal and commercial, if companies elect to undertake assignments in OFAC listed countries.

SUMMARY

A number of different types of business risks have been presented that are typical for firms working in the geotechnical, mining, and geo-environmental areas (geo-risks). Addressing these business geo-risks is quite different than assessing geo-risks on a specific project or for a particular analytical solution. Successful companies must strive to ensure that all components of the geo-risk spectrum, both project risks and business risks, are understood and adequately addressed.

Some of the important issues to consider to help ensure that the broad spectrum of technical and business geo-risks are minimized include:

- Ensure that an adequate conceptual model is developed, including site characterization, for the specific requirements of the project. Ensure that uncertainty in the model is evaluated if appropriate.
- Ensure that proper deformation and failure mode(s) are identified.
- Ensure that analytical models used have been checked and have gone through a quality assurance process, the model assumptions are understood, and the analyst has experience in doing the analyses.
- Compare model results with more simple predictions to verify the results are reasonable. Make performance estimates before undertaking analytical modeling.
- Ensure that capable and well trained staff are assigned to each task. Ensure that all project personnel know what their scope of work is on each task.
- Audit projects to ensure compliance with company procedures.
- Ensure the technical work is checked and that project technical reviews are done.
- Establish "review boards" for projects as needed. Consider having both internal and external members. The review board members should be involved early in the project. These reviewers should know the scope of work, should approve the work plan elements established by the project team, should review basic data, analytical approach, and analytical results. Review board members should be consulted and have input into the important project decisions.
- On large, long-term projects, periodically review all important assumptions. Ensure the approach being used is reasonable and appropriate. Beware of complacency on the project. Carefully review all monitoring information. Have technical reviews done by professionals not previously involved with the project to get a "fresh" assessment. Carefully assess the technical reviews and evaluate whether changes in the project are warranted.
- Recognize that rare, extreme impact, unpredictable events can and do occur.
- Ensure that the company has an adequate insurance program for the company's needs. Evaluate "self insured retention" limits (deductible amount) and the policy ceiling limits. In considering ceiling limits, recognize that "black swan" events might occur.
- Research the financial health and stability of the firm's insurance company. Balance the insurer's financial health with the quoted premium when selecting an insurance provider.

REFERENCES

Taleb, N.N. (2007). *Black Swan*, Random House

The Practical Application of Risk Assessment to Dam Safety

Gregg A. Scott[1], P.E., F. ASCE

[1]Lead Civil Engineer, U.S. Army Corps of Engineers, 12300 W. Dakota Ave., Lakewood, CO 80228, (720) 398-7526, Gregg.A.Scott@usace.army.mil, (formerly with the Bureau of Reclamation, Denver, CO)

ABSTRACT

The Bureau of Reclamation (Reclamation) is responsible for about 370 high- and significant-hazard storage dams and dikes which form a major part of the water resources infrastructure for the western United States, including such icons as Hoover and Grand Coulee Dams. To better manage this inventory of ageing dams with limited resources, Reclamation began using comprehensive risk assessment as the primary tool for dam safety decision-making in the mid-1990's. This paper describes the basic building blocks used in Reclamation dam safety risk analyses and how they are assembled to assess risks. The results of such risk analyses are used to set priorities for additional study or risk reduction actions using Reclamation's public protection guidelines, which are also discussed.

INTRODUCTION

The vast majority of the more than 370 high- and significant-hazard dams in Reclamation's inventory are now more than 50 years old. In addition, population growth and local zoning regulations have resulted in significant development within the downstream flood plains over the past few decades. With limited resources available to manage this inventory, a rational approach was needed to make decisions and establish priorities within the dam safety program. Risk assessment has been used to fill that need since the mid-1990's.

From the outset, Reclamation recognized that procedures and data available for dam safety risk analysis, while quantitative, provide only approximate numerical results. Therefore, agency guidance on performing risk analysis strives to be advisory rather than prescriptive, allowing the risk analyst(s) to use the proper balance of engineering judgment, relative frequency data, and calculations in estimating risks. Thus, the numbers, while important, are less important than understanding and documenting what the major risk contributors are and why.

The basic building blocks used for risk analyses at the Bureau of Reclamation, each of which are discussed this paper, are as follows.

- Potential failure mode analysis
- Hazard analysis (load frequencies for seismic, flood, and reservoir loading)
- Risk categorization and screening

- Event trees and fault trees
- Incident and failure relative frequency data
- Probabilistic analyses and models
- Subjective probability and expert elicitation
- Fragility curves
- Consequence evaluation

Reclamation's dam safety public protection guidelines (Bureau of Reclamation, 2011) are used to assess the results of dam safety risk analyses. They provide guidance on how to (1) portray and evaluate the results of risk analyses, (2) assess the need for action, and (3) prioritize dam safety activities. These guidelines were never intended to be used as rigid decision-making criteria to declare a facility "safe" or "unsafe" based solely on a risk estimate. Since the numbers are approximate measures of risk, and since the risk guidelines are not rigid, additional reasoning is essential to justify the risk estimates and the recommended actions. This is referred to as the "dam safety case". Building the case with respect to Reclamation's public protection guidelines is also described in this paper. Additional details of the methods and procedures outlined in this paper can be found in Reclamation's training manual (Scott et al, 2010). Although this paper is focused on dam safety, the concepts and methods presented can be applied to a wide variety of issues.

PUBLIC PROTECTION GUIDELINES

Risk, by definition, includes consideration of both failure likelihood and the consequences of failure. This can be represented as a lot-log plot with annual failure probability on the vertical axis and consequences on the horizontal axis, as shown in Figure 1. Reclamation's public protection guidelines primarily address life safety consequences. In general, society is "risk averse" and Reclamation's guidelines reflect this concept. That is, as the consequences (e.g. number of fatalities) increases, society generally expects the likelihood of those consequences to decrease. For example, if 100 fatalities occur in individual car accidents across the country during a single day, most of the country will not hear about any of them. However, if an airliner goes down and 100 people perish all at once, the incident will make national and even international news. Thus, the risk guidelines established by Reclamation require decreasing likelihood of failure as the consequences increase, represented by a diagonal line with negative slope. The diagonal line shown in Figure 1 corresponds to an annualized life loss of 0.001 lives/year.

In addition to societal risk, Reclamation's guidelines indicate the annualized failure probability should be less than 1 in 10,000. This is intended to provide a minimum level of performance for any dam whose failure would release life-threatening flows, even if the consequences are small. This helps limit agency exposure to dam failure and ensure a low risk to the most exposed individual. This guideline is shown by horizontal line in Figure 1 at an annualized failure probability of 0.0001. Risks or failure probabilities exceeding the guideline values indicate increasing justification to take action, and those below the guideline values represent

decreasing justification to take action. In the case of new dams or major dam rehabilitation projects, the target guideline values are one order of magnitude lower, but cost must also be considered. It is difficult to estimate probabilities to very low values with any degree of certainty. Therefore, when the consequences are estimated to be very large and the failure probability very low, each case is examined to ensure the risks are "As Low As Reasonably Practicable (ALARP)". These guidelines are generally consistent with those established by other water resources organizations and ensure that dam failure represents a relatively insignificant portion of the total risk individuals are exposed to on a daily basis.

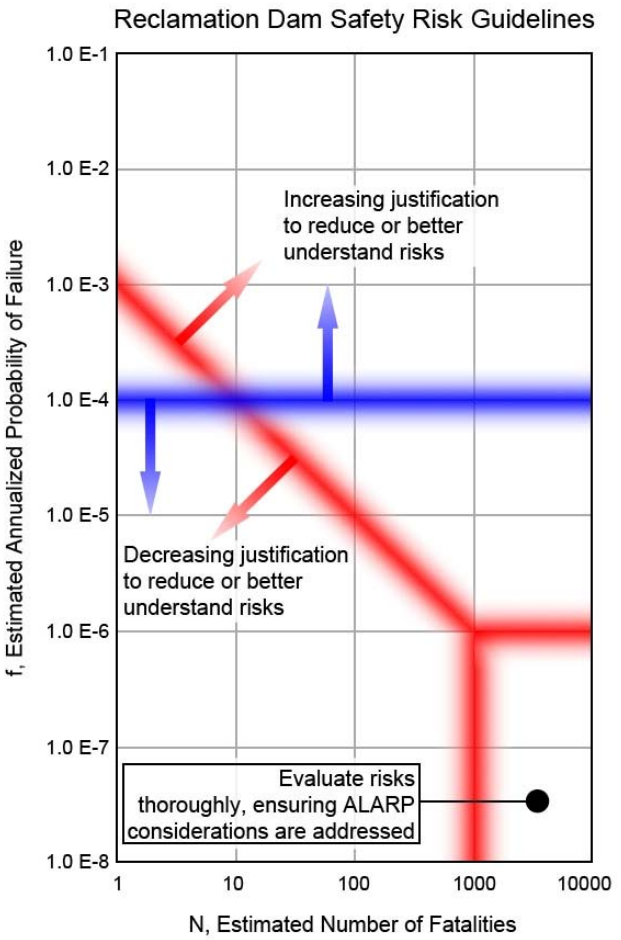

Figure 1. Reclamation's Public Protection Guidelines

HAZARD ANALYSIS

Risk analysis requires that all loadings to which dams or associated facilities are potentially subjected be expressed in probabilistic terms. This requires different types of hazard analyses than used for the deterministic Probable Maximum Flood (PMF) or Maximum Credible Earthquake (MCE) loadings. In addition, it often requires that the probability of various reservoir water surface elevations be estimated, as many potential failure modes are sensitive to this loading. The details

of these hazard analyses are not described here. Typically, the specialized services of flood hydrologists and seismologists are needed, although U.S. Geological Service websites provide information from which rough estimates for flood and earthquake frequencies can be made for most of the United States. Detailed reservoir operations data are needed to establish reservoir loading frequencies, although care must be taken to ensure that the data are representative of future operations. If a change has been made to the way in which a reservoir is operated, only those data consistent with that change should be used in the evaluation. Typically, hazard curves are generated, representing the annual exceedance probability of a particular loading parameter. These parameters might include reservoir elevation, peak flood inflows, flood volumes, peak horizontal ground acceleration, or spectral acceleration. If there is a particular need, other loading parameters, such as peak ground velocity, can also be evaluated in this manner. Figure 2 shows an example seismic hazard curve, along with uncertainty limits.

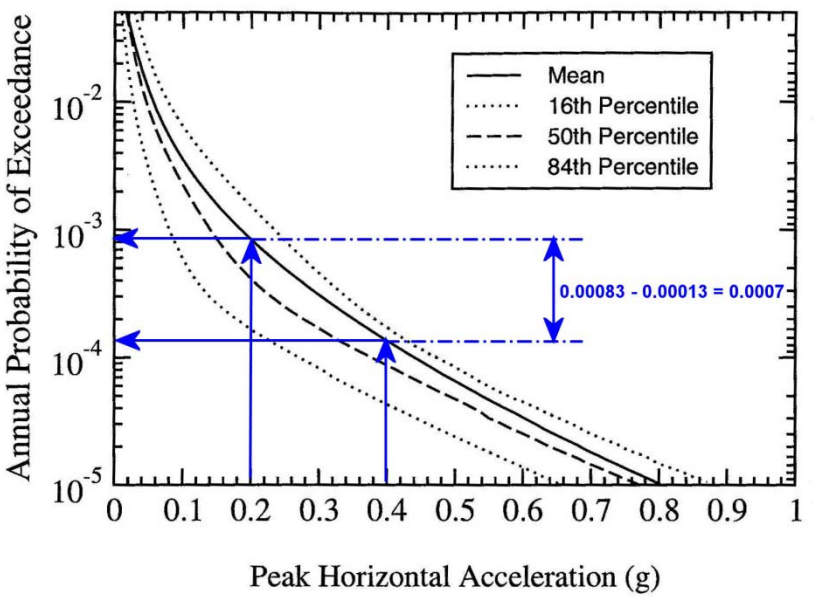

Figure 2. Seismic Hazard Curve

In some cases it is desired to estimate the annual probability that a loading will be within a certain range. This can be accomplished by subtracting the annual exceedance probability of the upper end of the load range from the annual exceedance probability of the lower end of the load range. For example, referring to Figure 2, the mean annual probability of peak ground acceleration between 0.2 g and 0.4 g is simply the annual exceedance probability at 0.4 g (0.00013) subtracted from the annual exceedance probability at 0.2 g (0.00083) or 0.0007.

POTENTIAL FAILURE MODE ANALYSIS

The first, and perhaps the most critical, step in a dam safety risk analysis involves identifying and fully describing potential failure modes based on an

evaluation of a dam's vulnerabilities. If this first step is not diligent and thorough, it doesn't matter what is done for the rest of the risk analysis; the results will have significantly less value, and may even lead to incorrect or unsubstantiated conclusions.

Identifying and Describing Potential Failure Modes. It is important to include, but also think beyond, traditional analyses when identifying potential failure modes. Dams are engineered systems, and significant thought must be put into the details surrounding the interactions between the various features of a particular facility. Some of the greatest risks for uncontrolled reservoir release may be due to operational problems or potential failure modes that do not lend themselves to standard engineering calculations.

An adequate job of identifying potential failure modes can be performed only after all relevant background information for a dam is diligently collected and thoroughly reviewed. This includes information related to geology, design, analysis, construction, flood and seismic loading, operations, and performance monitoring. Photographs, particularly those taken during construction or unusual events, are often vital to identifying vulnerabilities. It is essential that the records be reviewed by more than one person, as something might have been overlooked in previous reviews, and one person may pick up on critical information that another person might miss. A site visit, looking for clues to dam safety vulnerabilities and with a view toward potential failure modes, is also important.

Identifying potential failure modes is best done in a team setting, with a small diverse group of qualified people. Input from operating personnel is essential to the process. A facilitator guides team members in developing the potential failure modes, based on the team's understanding of the project vulnerabilities resulting from the data review and current field conditions. The potential failure modes must be described fully, from initiation to breach (or uncontrolled reservoir release). Three parts are included in the description:

- ***The initiator.*** This is the loading or physical condition that leads to initiation of the potential failure mode. For example, this could include increases in reservoir level due to flooding (perhaps exacerbated by a debris-plugged spillway), strong earthquake ground shaking, malfunction of a gate, or an increase in internal water pressures due to drain plugging.
- ***Failure progression.*** This includes the step-by-step process, or states of nature, that would be needed to lead to the breach or uncontrolled release of the reservoir. The location(s) where the dam is most vulnerable and the failure is most likely to develop should be highlighted. For example, this might include the path through which materials would be transported in a piping scenario, the location of overtopping in a flood, or anticipated failure surfaces in a sliding situation.
- ***The breach.*** The expected magnitude of the breach or uncontrolled release of the reservoir is also part of the description. This includes the breach mechanism, and how rapid and large the expected breach would be. Defining these breach characteristics aids in assessing the impacted areas and available

time to implement emergency actions, such as warnings and evacuations, to mitigate the potential consequences of failure.

The reasons for completely describing the potential failure modes are three-fold: (1) to ensure that the team and reviewers have a common understanding of what is being evaluated, (2) to ensure that someone reading or using the report well into the future will have a clear understanding of what the team was thinking, and (3) to enable development of an event tree or other means of estimating risks, if warranted. It is often helpful to also sketch the potential failure modes to help ensure there is a common understanding of each. These sketches should be based upon drawings or figures to scale so that the relative pressure heads, distances, and gradients are appropriately understood.

An example of a potential failure mode description, as initially written and then as edited to be more useful is listed below. This example will be used throughout the paper to illustrate key points of the dam safety risk assessment process. For an additional example, see Scott and Fiedler (2010).

- ***Unedited*** (Insufficient detail)**.** Sliding of the concrete dam foundation.
- ***Edited.*** As a result of high reservoir levels and continuing increase in uplift pressure in the right abutment of the arch dam due to inability to maintain the drainage system and large earthquake shaking (the initiator), sliding of large rock Block No. 3, formed by near vertical bedding plane partings, the continuous low angle joint seen downstream of the dam and in construction photographs crossing the foundation, and the high angle joint sets mapped in the reservoir area, initiates. The arch dam is unable to redistribute the loads around the unstable block and the block continues to slide, taking dam Blocks 1 through 7 with it. The dam fails during the shaking or enough movement of the block occurs to open joints and increase water pressures to the point where post-earthquake instability ensues (the step by step progression). Rapid brittle failure of this portion of the arch occurs, followed by partial collapse of the upper portion of the dam where arch action is lost due to removal of the abutment support. It is expected that most of the upper third of the dam would be lost (the breach characteristics).

Analyzing Potential Failure Modes. After the team has completely described a potential failure mode, it is then evaluated by listing the adverse factors that make the failure mode "more likely" and the favorable factors that make the failure mode "less likely". These factors are based on the team's understanding of the facility and background material. The factors must be thoroughly described in the documentation so that someone reading or using the report in the future will understand what the team was thinking. The facilitator guides the team through this process.

Consider the potential failure mode described above. A list of adverse and favorable factors might look like the following. Regular text shows how they might be initially captured, while text in italics indicates how they would be further clarified in the report.

Adverse or "More Likely" Factors

- A large potentially unstable foundation block is well defined *(see Figure 3)*. *Geologic mapping of the hard dolomitic limestone in the downstream right abutment shows continuous high angle bedding plane partings angled obliquely toward the channel from upstream to downstream forming continuous side plane boundaries. A continuous low angle joint can be observed in the downstream abutment, and construction photos indicate it traverses completely across the dam foundation forming the block base plane. Continuous high angle joints were mapped in the upstream reservoir area, capable of forming back release surfaces for the block.*

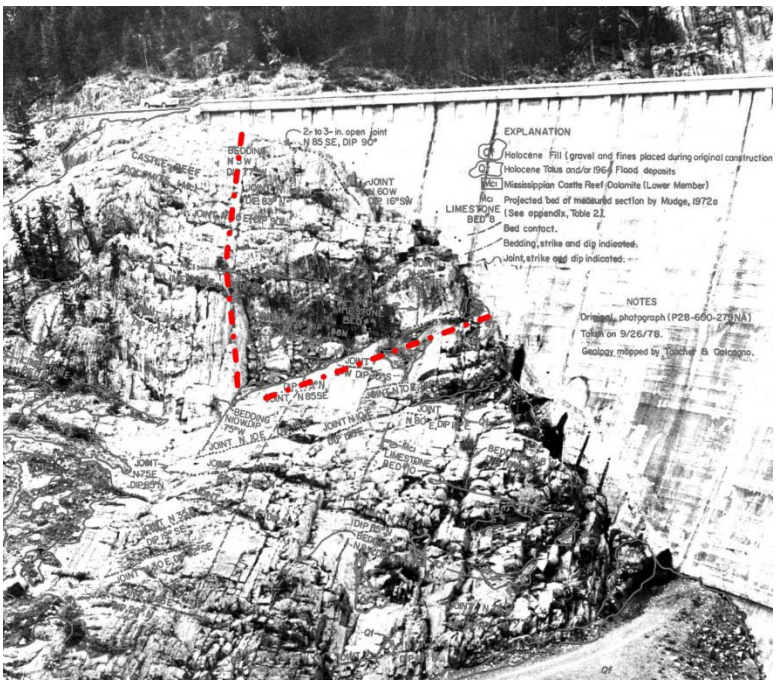

Figure 3. Photo Showing Right Abutment Block

- It is not possible to maintain the *foundation* drainage system. *The foundation drain holes were drilled from an upstream fillet and connected to the outfalls through piping with a series of right angle bends. It is not possible to maneuver drain cleaning equipment around these bends.*
- The piezometer levels are increasing. *Piezometers installed at the base of the dam indicate rising foundation water pressures. The pressures have risen 15 to 20m near the lower right abutment since 1942.*
- Water squirts up about 1m from rockbolt holes on the downstream right abutment. *These rockbolt holes are downstream of the right abutment rock block and squirt when the reservoir reaches high elevations, indicating high foundation water pressures downstream of the dam.*
- Analyses indicate Factors of Safety against sliding for the rock block drop below 1.0 for several excursions during earthquake ground motions

representative of a M6.5 earthquake, 0.5g peak ground acceleration, annual maximum arch thrust, and current uplift conditions.

Favorable or "Less Likely" Factors

- The *bedding plane parting* side planes provide resistance *since there is a component of the arch thrust acting normal to these discontinuities.*
- There has been no indication of foundation movement to date. *Although the collimation system is not set up to measure foundation movements on the right abutment, there is no indication of offset joints or concrete cracking in the area of the right abutment block.*
- Analyses indicate Factors of Safety exceeding 1.5 for currently estimated uplift conditions *and maximum annual static arch loading conditions with frictional strength only based on sliding tilt tests (45 degrees on the side bedding plane parting and 50 degrees on the rougher base plane joint, with no cohesion)*.

RISK SCREENING

Once all the adverse and favorable factors have been collected, each potential failure mode can be screened using a qualitative or semi-quantitative matrix approach. The intent of the screening is to identify the potential failure modes which contribute most to the risk, and screen out those that contribute very little to the risk. It can take substantial effort to estimate quantitative risks, and it is important to concentrate quantitative efforts on the most critical potential failure modes. Risk screening can be done any time there is a need to prioritize activities.

Risk screening involves placing each identified potential failure mode into broad categories of failure likelihood and consequences. It is important to calibrate (to the extent possible) the categories and descriptors to be meaningful within the context of risk guidelines, traditional analyses, failure mode assessment, and historical dam performance.

Failure Likelihood. Examination of historical dam failure rates indicates that dams fail at a rate of roughly 1 in 10,000 per dam year of operation, depending on the failure mode and age of the structure (Whitman (1984), Von Thun (1985), Hatem (1985), Foster et al (1998), Douglas et al (1998)). This forms the basis for evaluating failure likelihood for a given potential failure mode. For example, if the key factors affecting the potential failure mode are weighted toward adverse (more likely), the annual failure likelihood is probably greater than 10^{-4}. If weighted toward favorable (less likely), then the annual failure likelihood is probably less than 10^{-4}. Similarly, the estimated annual exceedance probability of a flood or earthquake that is likely to cause failure indicates the approximate likelihood of seismic or hydrologic failure. Although this does not account for risks associated with the entire range of loading, experience has shown that it is a reasonable approximation for screening purposes. The team can use the factors identified in analyzing the potential failure modes and the following likelihood categories and descriptors to categorize each one. In a

general sense, each category represents an "order of magnitude" range in failure likelihood.

- ***Very High.*** There is direct evidence or substantial indirect evidence to suggest it has occurred and/or is likely to occur. Or, a flood or an earthquake with an annual exceedance probability more frequent (greater) than 0.001 would likely trigger the potential failure mode.
- ***High.*** The fundamental condition or defect is known to exist, indirect evidence suggests it is plausible, and key evidence is weighted more heavily toward likely than unlikely. Or, a flood or an earthquake with an annual exceedance probability between 0.001 and 0.0001 would likely trigger the potential failure mode.
- ***Moderate.*** The fundamental condition or defect is known to exist, indirect evidence suggests it is plausible, and key evidence is weighted more heavily toward unlikely than likely. Or, a flood or an earthquake with an annual exceedance probability slightly more remote than 0.0001 would likely trigger the potential failure mode.
- ***Low.*** The possibility cannot be ruled out, but there is no compelling evidence to suggest it has occurred or that a condition or flaw exists that could lead to its development. Or, a flood or an earthquake with an annual exceedance probability much more remote than 0.0001 would likely trigger the potential failure mode.
- ***Remote.*** Several events must occur concurrently or in series to trigger failure. Most, if not all of the events are very unlikely; failure potential is negligible or non-credible.

Failure Consequences. Dam failure consequences can take many forms, including loss of project benefits, destruction of downstream property, life loss, environmental damage, and socio-economic impacts. Dam safety is typically concerned with public safety, and thus consequences for risk analysis typically focus on the potential for life loss, although other consequences are also considered in the decision process.

An evaluation of dam failure case histories indicates that the number of fatalities is primarily dependent on: (1) the population at risk (PAR) within the dam break inundation boundary, (2) the severity of the flooding, and (3) the amount of warning time the PAR has to evacuate the area (Graham, 1999). Other considerations include the degree to which the PAR understands what is about to descend upon them, and the availability and clarity of possible evacuation routes. The population at risk can be broadly categorized by transient activity (recreation, highways, etc.) and the size of communities and development within the inundation zone. The severity of flooding is a function of the potential destruction within the flood plain. The warning time is a function of when the warnings are issued and the time it takes for the flood wave to reach the population at risk. For example, with flood monitoring and forecasting, it may be possible to warn and evacuate the downstream population prior to dam overtopping. On the other hand, a sudden failure under normal operating conditions may catch the downstream population by surprise. Considering all of

these aspects of consequence evaluation, the following broad consequence categories can be defined.

- ***Level 0.*** No significant impacts to the downstream population other than temporary minor flooding of roads or land adjacent to the river. Or downstream discharge results from fuse plug operation or from an intended overtopping at a designated emergency release location, to help ensure discharge occurs from this designated location rather than causing failure of larger structures. Discharge from these locations results in an incremental spike in what is generally a high discharge flow level. It may also result in some minor increase in downstream damages over what would occur from passing the flood discharge through a conventional spillway.
- ***Level 1.*** Downstream discharge results in minor property and environmental damage. Damage is likely to recreation areas, roads, and bridges in low-lying areas. Direct loss of life is unlikely but possible. Costs of re-constructing the project features and the negative publicity associated with a dam failure would also be incurred.
- ***Level 2.*** Downstream discharge results in moderate property and environmental damage. Damage to permanently occupied structures, recreation areas, roadways, and bridges in low lying areas is likely. Some direct loss of life is likely, related primarily to difficulties in warning and evacuating recreationists/ travelers and small population centers. Costs associated with re-constructing the project features and negative publicity associated with a dam failure would also be incurred.
- ***Level 3.*** Downstream discharge results in extensive damage to permanently occupied structures, roadways and bridges throughout the inundation zone. Moderate direct loss of life is likely, related primarily to difficulties in warning and evacuating recreationists/ travelers, smaller population centers, and large population centers with significant warning time. Costs associated with re-constructing the project features and negative publicity associated with a dam failure would also be incurred.
- ***Level 4.*** Downstream discharge results in extensive damage to permanently occupied structures, roadways and bridges throughout the inundation zone. Direct loss of life could be high due to limited warning for large population centers and/or limited evacuation routes. Costs associated with re-constructing the project features and negative publicity associated with a dam failure would also be incurred.

In a general sense, each category represents an order of magnitude range in consequences, with loss of life likely in Categories 2 through 4. Although these categories are thought to be a reasonable breakdown for screening purposes, more detailed consequence evaluations will be discussed later.

Risk Matrix. A "risk matrix" can be established to portray the risk associated with the identified potential failure modes, with likelihood of failure on the vertical axis (using cell divisions corresponding to the likelihood categories previously defined)

and consequences on the horizontal axis (using cell divisions corresponding to the consequences categories previously described). Figure 4 illustrates the risk matrix relative to the risk guidelines previously described. A likelihood category and consequence category is assigned to each identified potential failure mode, and then they are plotted in the appropriate cell of the matrix. It is important that the justification and rationale for each assigned category be captured and documented. Potential failure modes with Remote likelihood and Level 0 consequences are not included in the matrix since they would be typically be ruled out either because the chances of failure or consequences were thought to be negligible.

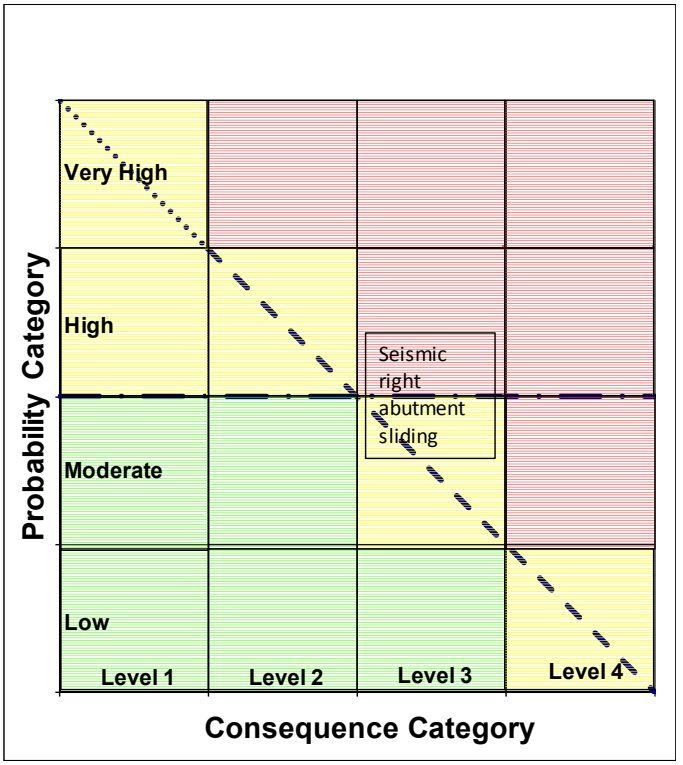

Figure 4. Risk Matrix

Risk increases going diagonally from the yellow cells toward the upper right hand corner of the matrix; hence there is increasing justification to take action to address the risks, and the urgency of addressing potential failure modes typically increases. Similarly, risks decrease moving diagonally from the yellow cells toward the lower left hand corner of the matrix, and the need and urgency to address them also typically decreases. The yellow cells represent the approximate boundary of established guidelines, and consideration should be given to addressing potential failure modes that plot in the yellow or red cells.

Confidence in the risk category ratings is considered to be an essential part of the risk assessment. If the confidence is low, performing a detailed quantitative risk analysis may help shed light on what additional information could increase confidence in the estimates. If risks are low, and confidence is high, then a detailed quantitative risk analysis probably cannot be justified. The following confidence

categorization scheme can be defined. (The confidence category names were selected to avoid confusion with the likelihood category names.)

- ***Good***. Confidence in the rating is high; it is unlikely that additional information would change the rating.
- ***Poor***. Confidence in the rating is low; additional information could very well result in a change to the rating.
- ***Medium***. In between Good and Poor.

For the example potential failure mode related to arch dam abutment stability previously described, the ratings (plotted on Figure 4) and rationale might look something like the following:

- ***Likelihood rating.*** Moderate to High; Available earthquake analyses suggest large earthquake ground motions with an exceedance probability slightly more remote (less) than 1/10,000 could trigger movement of the block under current water pressure conditions. It is unknown whether ground motions more frequent than 1/10,000 would also trigger block movement. Additional key evidence is weighted toward "more likely". Foundation water pressures continue to rise, reducing stability. The foundation drains cannot be cleaned due to numerous right angle bends in the embedded connecting piping. Evidence of high pressures in the abutment includes water squirting from rockbolt holes at high reservoir levels.
- ***Likelihood confidence rating.*** Good; the evidence is clear that water pressures are increasing and sufficient analyses have been performed to indicate potential behavior of the abutment block under increased seismic loading. It is unlikely that additional information would change the category. However, analyses at other ground motion levels and a detailed quantitative risk analysis may provide additional insights into remediation alternatives and better information from which to make a decision.
- ***Consequences rating.*** Level 3; although only the top portion of the dam would breach, it is expected that such a failure would be rapid and brittle, with a wall of water over 20-m-high initially traveling down the canyon. Most of the reservoir volume (over 10^8 m^3) is contained in the upper third of the reservoir. Approximately 80 people in the 40 km of valley between the dam and State Highway 52 (including those in 30 cabins, the Sunrise Resort, the Gold Gulch campground, and 6 ranches, all of which are located near the river) could be caught by surprise and the fatality rate is expected to be high in this reach. There are no towns or settlements for the next 50 km, then four smaller towns will be inundated before the flood hits a larger town about 150 km downstream, with over 10,000 people estimated at risk in these communities. The warning time in these downstream communities should keep the fatality rate low, although some fatalities would be expected, especially if failure occurred at night.
- ***Consequences Confidence Rating.*** Good; a high level reconnaissance was performed to evaluate the population at risk, and given the small warning time

and deep, rapid flooding near the dam, it is unlikely that additional information would change the rating. However, it would be valuable to further quantify the consequences if a quantitative risk analysis is performed.

In general, any potential failure mode with a poor confidence in one or both of the risk categories may be a candidate for additional quantitative risk analysis, since such an analysis may shed light on what specific information could lead to higher confidence. Similarly, potential failure modes plotting in the yellow or red cells would be candidates for quantitative risk analyses to verify that additional action should be taken, and to help guide what that action should be. Potential failure modes that fall into the green cells with a confidence rating of "Good", or which are assigned a Remote likelihood rating or Level 0 consequences rating would typically not be carried forward for detailed quantitative risk analysis.

Since Reclamation decided to initially develop quantitative risk estimates for all of its high and significant hazard dams, this approach has found use primarily with other agencies and organizations. In this regard, it should be noted that the process is particularly useful for initially addressing an inventory of dams. Potential failure modes for all of the dams in an inventory can be plotted on the matrix using different color schemes, and the location of a particular dam and potential failure mode on the matrix can be used to help prioritize activities.

EVENT TREES AND FAULT TREES

If a complete and thorough description of a potential failure mode is developed as previously described, it is usually a simple matter to break the failure mode into a series of steps, events, or states of nature that are necessary to lead to failure. These can be represented on an event tree. Event trees consist of a series of linked nodes and branches. Each node represents an uncertain event or condition. Each branch represents one possible outcome of the event or one possible state that a condition may assume. The event tree is constructed from left to right, starting with an initiating event and proceeding through potential failure mode development to dam breach and consequences. Figure 5 represents an event tree constructed to represent the seismic arch dam abutment failure mode previously described. Only one seismic load branch (1/10,000 to 1/25,000 annual exceedance probability) is constructed all the way through the tree for illustration purposes. The conditional failure probability branches following the load branch must be duplicated for all load ranges above the threshold load value (which will be discussed later). In this case the probability of failure is dependent on not only the earthquake loading level, but also the reservoir level at the time the earthquake hits. If several reservoir and earthquake levels were modeled in the tree, it would be extremely large. To simplify the evaluation, only one reservoir load range was included, chosen to represent loadings significant to the abutment block and at levels that would produce significant consequences if failure occurred.

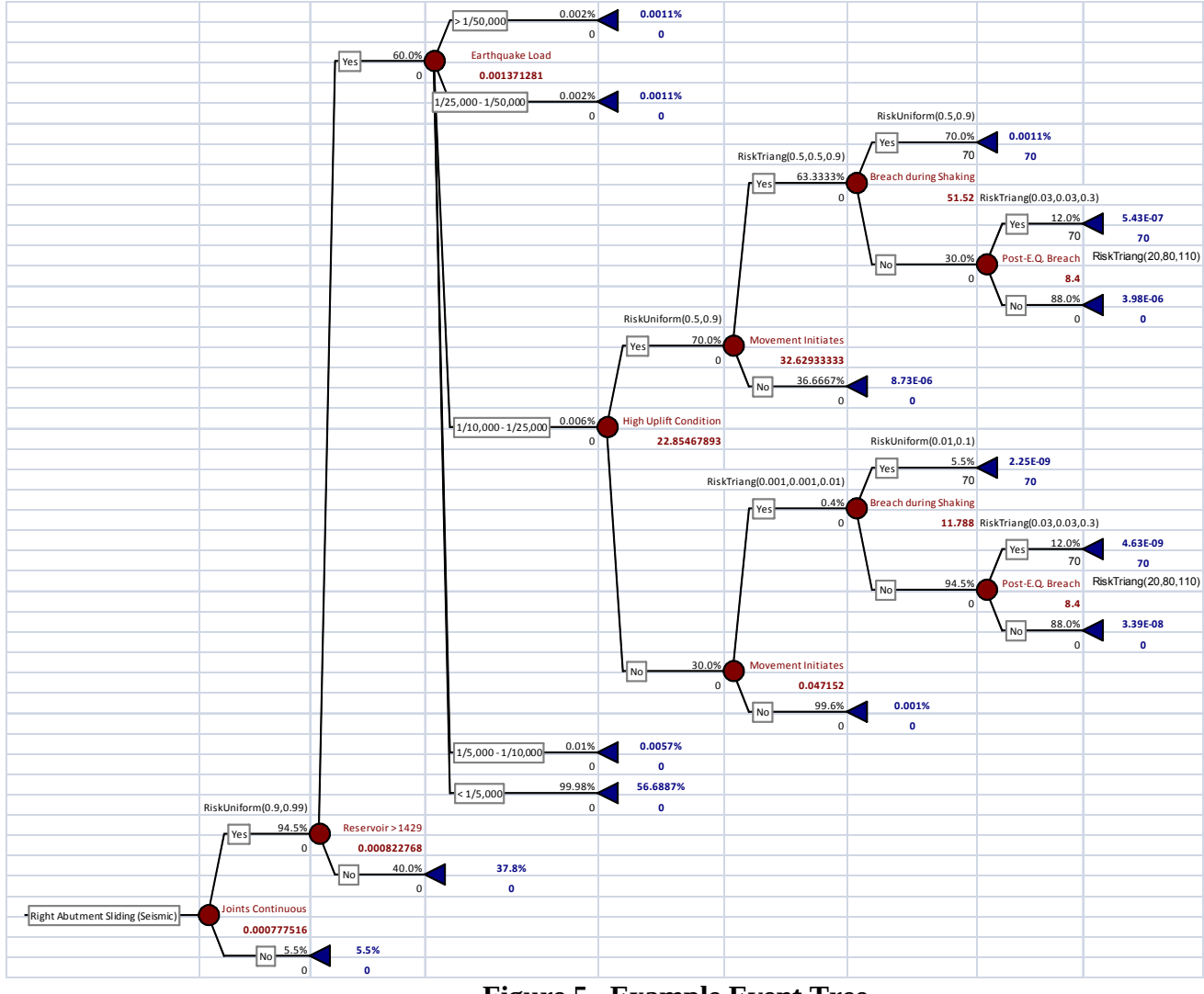

Figure 5. Example Event Tree

The likelihood of each branch on the event tree is evaluated, using results from numerical modeling with probability distributions as parameter inputs, statistical evaluations when sufficient frequency-based information exists, and/or subjective degree-of-belief estimates. The methods used to estimate probabilities depend on the available information, level of study, and question to be answered. These methods will be described in more detail later in this paper. When estimating the likelihood for each node in an event tree, it is assumed the condition represented by the previous branch is true.

Risk is defined as the product of the load probability, the failure probability given the load, and the consequences given that failure occurs. The loading is typically put into the event tree near the beginning of the tree. When the loads are represented with annual probabilities, the results are "annualized". It is useful to partition the loading into ranges, and evaluate the remainder of the tree for each load range. The probability estimates following the loading are referred to as "conditional" probabilities. That is, they are based on the condition that the specified loading has occurred.

The entire range of loading must be accounted for. In the case of reservoir elevation, only levels up to normal full pool were considered in combination with earthquake loading in the example event tree. The chance of a flood and earthquake occurring simultaneously was thought to be negligible. Selecting the appropriate load ranges is not a trivial matter. It is important to identify the threshold loading, below which failure probability is negligible. While simple in concept, the selected value(s) can have a significant effect on the annual failure probability, especially if adverse behavioral thresholds correspond to relatively likely events or conditions. Therefore, care is needed in making this selection. In Figure 5, the threshold ground motion was selected to be an earthquake with an annual exceedance probability less than 1/5,000. There would be negligible failure probability associated with this branch and it would be terminated at that point.

It is important to select enough load ranges such that the transitions in conditional failure probability are smoothly captured. On the other hand, too many load ranges can make interpreting the results more difficult. That is, it is more difficult to understand where the risks are coming from and why. Load range boundaries should be selected, to the extent possible, at loads where the structural response is expected to change. It is a good idea to examine the estimated conditional failure probability at the lower and upper ends of each load range. If they represent an extreme range, then the load range is probably too large. For example, if the estimated conditional failure probability is estimated to be 0.1 at the low end of a load range, and 0.99 at the high end of the range, then it would be appropriate to subdivide the tree into more load ranges. When estimating conditional probabilities for a load range, it is important to remember that most of the load range probability comes from the lower end of the range, and therefore estimating conditional failure probabilities representative of the high end of the load range must be avoided. For example, the load range (0.2 to 0.4g) probability shown in Figure 2 is dominated by the load probability at 0.2g. Estimating conditional failure probabilities for conditions or from analyses represented by 0.4g only should be avoided.

The probabilities for all potential outcomes associated with a given node must add to 1.0. The individual outcome probabilities are multiplied along each branch. The probability product at the right hand end of each branch that results in dam failure represents the annual failure probability for all the conditions that are realized along that particular branch. The summation of probabilities for all branches where failure is realized represents the total annualized failure probability for the potential failure mode. To calculate the annualized life loss (or other annualized consequences), the consequences associated with each end branch that results in failure is multiplied by the annual failure probability associated with that branch. Summation of these values is the total annualized consequences.

Fault trees start with an assumed failure condition and work backward to evaluate the causes. Probabilities can be assigned along the way. They are typically constructed from top down. Fault trees have the advantage of using what are referred to as "and gates" and "or gates". This gives additional flexibility in the evaluation of complex systems that may fail due to problems with only one critical component, or may require problems with several components before failure occurs. For this reason, they are typically used for mechanical and electrical systems related to gate reliability. Fault trees will not be described in detail here. For additional discussion of fault trees see Vick (2002).

FRAGILITY CURVES

Fragility curves are sometimes used to represent the probability of an adverse outcome as a function of some other parameter. For example, the probability of failure might be expressed as a function of reservoir level or earthquake load as a continuous curve. Fragility curves can also be used to represent a node on an event tree. They can be developed using numerical analyses or subjective probability. An advantage of using fragility curves in combination with hazard curves is that very small load range increments can be used in calculating risk (essentially the curves are multiplied together in a manner similar to an event tree), and thus the selection of the load range intervals becomes relatively unimportant. A disadvantage of using fragility curves is that it becomes more difficult to sort out what is controlling the risk (for example, whether it is from remote earthquakes with high conditional failure probabilities, or more frequent events with lower reservoir levels). This is particularly true if several curves are multiplied together representing various nodes on an event tree. Fragility curves often represent nonlinear failure probability as a function of some variable. This nonlinearity can lead to surprising results when the analysis straddles sharp changes in the slope of the curve, and often careful scrutiny of the risk analysis results is needed. Since the example case presented here was evaluated using an event tree and discrete ranges, fragility curves were not used. See Vick (2002) for additional discussion of fragility curves.

PROBABILISTIC ANALYSES AND MODELS

With the development of new computer analysis tools; now, if you can program a deterministic analysis into a spreadsheet, you can use it to perform

probabilistic analyses. This section describes the basic concepts of performing probabilistic analyses using a standard spreadsheet program (Microsoft ® Excel), and commercially available macro add-ins for probabilistic analysis (Palisade Corporation's @Risk). Other companies sell similar software (e.g. Lotus 1-2-3, and Crystal Ball by Decisioneering, Inc.). It should be noted that other commercially available engineering analysis programs have the capability to perform probabilistic analysis. However, care must be taken to assure that there is a complete understanding of what is being produced by these programs.

Consider for example the arch dam abutment potential failure mode previously discussed. A relatively simple safety factor (SF) calculation (SF = resisting force/driving force) will provide insights as to how likely the block is to move under maximum earthquake loading and how likely the block is to remain stable under post-earthquake conditions (assuming it did not fail during the shaking). The traditional deterministic safety factor approach provides some insight into failure probability. Reasonably conservative input values (shear strength, water pressures, unit weights, and arch loads) are used in the analyses, and if the resulting safety factor satisfies established criteria, the likelihood of failure is probably low. How low is another question, and safety factor by itself is not a good indication.

In the example arch dam abutment case, to examine the post-earthquake stability of the block (assuming it survived the earthquake shaking), the standard deterministic equations for calculating the three-dimensional safety factor against sliding (Hendron et al 1980) are programmed into a spreadsheet, but instead of defining the input parameters as single constant values, they are defined as distributions of values. Thus, instead of calculating a single value for the output safety factor, a distribution of safety factor is generated from numerous iterations using the Monte-Carlo approach, whereby each of the input distributions is sampled numerous times in a manner consistent with its shape. This output distribution is used to determine the probability of safety factor less than that representing unsatisfactory performance (typically 1.0). In many cases, the probability of safety factor less than 1.0 can be estimated by dividing the number of safety factors calculated to be less than 1.0 by the total number of safety factors calculated. Only when there are no safety factors calculated to be less than 1.0 is another approach needed, as described later.

When deciding on distributions to use for input variables, it is important to keep in mind that any value selected during the Monte-Carlo simulation has to be representative of what could reasonably be expected over the entire area it represents. For example, in the analysis performed for the arch dam abutment, the friction angle selected for any given block plane is applied to the entire plane, and not to localized variations along the plane. In some cases it may be appropriate to break the areas of concern into characteristic areas, and assign probability distributions to each area separately.

The dip, dip direction, and friction coefficients of the discontinuities forming the abutment block are uncertain. The orientation of the bedding is more regular and better defined than the other joints. Therefore, the dip and dip direction of the bedding were defined as a triangular distribution (low value, best estimate value, and high value) with the mean measured value representing the peak of the distribution,

plus and minus three degrees to define the maximum and minimum values. Similar distributions were defined for the other joint sets, except that one or two additional degrees were used to define the upper and lower limits.

In the case of friction angles, enough tilt tests were performed on large bedding joint specimens, that a mean and standard deviation (following approximately a normal distribution) could be defined from the results. However, a smaller standard deviation was actually used since it was thought many of the low and high strength samples would represent only localized areas of the plane and not the overall effective strength of the entire surface. Since the other joints appeared to be rougher, both the mean friction angle and standard deviation were increased by a few degrees compared to the bedding joints.

The weight of the block was varied using a uniform distribution (equally likely between lower and upper input values) considering reasonable variations in unit weight and block volume. The water forces are also uncertain, but for post-earthquake conditions it was assumed the joints opened sufficiently to generate full hydrostatic loading on the back release joint, varying linearly to the "daylight" trace of the side and base plane joints downstream. The post-earthquake thrust from the arch dam, although uncertain, was taken as constant for a high reservoir elevation, based on finite element structural analyses simulating post-earthquake conditions to the extent possible. The results of 10,000 iterations in terms of sliding safety factor are shown in Figure 6.

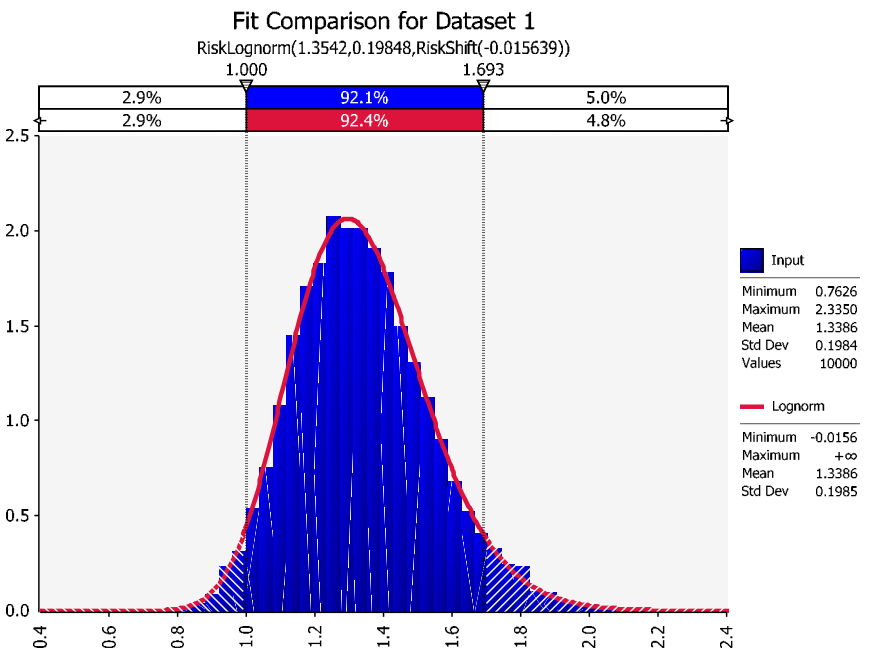

Figure 6. Output from Monte Carlo Simulation (horizontal axis is safety factor)

As can be seen, approximately 290 or 2.9 percent of the calculated safety factors were less than 1.0 (i.e. probability of SF < 1.0 = 0.029). As another method for estimating the probability of safety factor less than 1.0, the parameter "reliability

index" or β is introduced. This can be particularly useful when none or very few of the safety factors calculated during the Monte-Carlo simulation are less than 1.0 and it is desired to estimate the area under the "tail" of the safety factor distribution. The reliability index is defined as the "number of standard deviation units" between the mean value and value representing failure. If the results follow a normal distribution, the reliability index relative to a safety factor of 1.0, is simply $(SF_{AVG} - 1.0)/\sigma_F$, where SF_{AVG} is the mean safety factor and σ_F is the standard deviation of the safety factor distribution. There is a standard function in Microsoft Excel that allows one to calculate the probability of a safety factor less than the value representing unsatisfactory performance directly from the reliability index. For example, in this case the probability of SF < 1.0 = 1-NORMSDIST(β).

In many cases, the output safety factor may not follow a normal distribution, but rather a lognormal distribution. This can be examined using distribution fitting techniques available in most Monte-Carlo software. If safety factor follows a lognormal distribution more closely, the same method can be used to estimate the probability of SF<1.0. The only difference is that the reliability index is calculated with a different formula to convert it to standard normal space (Corps of Engineers, 2006), as follows:

$$\beta_{\log normal} = \frac{\ln\left(\frac{SF_{mean}}{\sqrt{1+V_{SF}^2}}\right)}{\sqrt{\ln\left(1+V_{SF}^2\right)}}$$

Where SF_{mean} is the average safety factor and V_{SF} is the coefficient of variation for the safety factor, equal to the standard deviation divided by the mean. In the example arch dam abutment case, the results follow a lognormal distribution quite well as shown in Figure 6. Using this equation produces a reliability index of 1.90 and a probability of SF<1.0 equal to 0.028. This is very close to the value estimated directly from the results described earlier.

It is unlikely that enough information exists to define the input distributions with extreme confidence. Therefore, a key component to performing a probabilistic analysis is examining which input distributions had the largest effect on the output safety factor distribution. For this, the @Risk program prints out a list of ranking coefficients. Those input distributions with the highest positive or negative ranking coefficients affect the results most. For the example arch dam results just described, the coefficients are shown in Table 1.

The larger the absolute value of the coefficient, the greater the effect of that parameter on the results. A negative ranking coefficient just means that the variable is negatively correlated with the result. That is, an increase in the parameter results in a decrease in the safety factor. It can be seen that the base plane friction angle affects the results the most followed by the side plane dip direction. The side plane friction angle and base plane dip also have a relatively significant effect on the results. For those parameters with the highest ranking coefficients, additional parametric studies would be appropriate to examine how a small change in the distribution affects the results. In some cases this may show a large change, indicating additional

information could increase confidence in the input parameters and reduce the risk estimates. For the example arch dam abutment case, if the mean value of the four most sensitive parameters is changed by two degrees in the negative direction, and the limits and standard deviations are increased by two degrees, the probability of SF<1.0 increases by about an order of magnitude to 32.8 percent. Additional information on these types of analyses can be found in Scott (2008).

Table 1. Sensitivity Rank Coefficients

Parameter	Spreadsheet Cell	Regression Coefficient
Joint set 3 dip direction (CW w/r N), Back	B22	0.058
Joint set 2 dip direction (CW w/r N), Side	B21	-0.527
Joint set 1 dip direction (CW w/r N), Base	B20	0.154
Dip of joint set 3 (degrees), Back	B17	0.019
Dip of joint set 2 (degrees), Side	B16	0.048
Dip of joint set 1 (degrees), Base	B15	-0.333
Estimated weight of the wedge	C9	0.044
f3, the Joint Set 3 friction angle, Back	B37	0
f2, the Joint Set 2 friction angle, Side	B36	0.367
f1, the Joint Set 1 friction angle, Base	B35	0.648

The values obtained from probabilistic stability analyses are typically used to estimate conditional probabilities for a node in an event tree. The issue previously discussed, where most of the load range probability is associated with the exceedance probability at the lower end of the range, can be addressed to a certain extent when performing Monte-Carlo analyses by setting up a distribution from which to sample the load for each iteration and then running the subsequent safety factor calculation at that load.

RELATIVE FREQUENCY DATA

For some events or issues, case history information exists from which to draw inferences about how often, and thus how likely, adverse events or dam performance occurs, typically expressed as a frequency per dam year of operation. The general rate of dam failures was discussed previously. However, to be meaningful in evaluating individual potential failure modes, events, or specific conditions, the data must be broken down into smaller relevant data sets. For example, it can be useful to examine the historical rate of the initiation of piping through various mechanisms. This has been done for Reclamation's inventory of dams (Engemoen and Redlinger, 2009). The dam in question (geometry, soil types, etc.) can then be compared to dams in the data base to draw conclusions as to the likelihood of piping initiation. Douglas et al (1998) and Foster et al (1998) have collected information on historical

failure rates of dams worldwide and correlated them with specific features or conditions. This information can be valuable in a more global sense. However, inferences from statistical evaluations break down when population or sample sizes are too small and when site-specific characteristics poorly match those of the population upon which the forecasting is based. Nevertheless, sometimes this is the best information from which to estimate probabilities.

In the case of our example arch dam abutment, there are no known cases of arch dam failure as a result of abutment instability under seismic loading or under static loading after five years of successful operation. Therefore, this type of evaluation would have limited applicability. About all that could be inferred is the upper limit of failure rate, assuming that one such a failure occurred in the near future, but this inference would generally be too conservative.

SUBJECTIVE PROBABILITY AND EXPERT ELICITATION

Many situations arise in the course of performing risk analyses for dams where sufficient statistical information is not available and models for calculating probabilities simply don't exist. In order to make quantitative risk estimates, it then becomes necessary to judge the likelihood of various events or conditions. In such cases probabilities are estimated or assigned using subjective "degree-of-belief". Subjective probability estimates are the ranges of values judged to be believable based upon the available evidence. They are typically estimated by elicitation in a team setting where the breadth of experience brought to the table by a group of individuals qualified to make the estimates is drawn out by a facilitator.

Reclamation has adopted a verbal mapping scheme for most subjective probability estimates, which often take the form of an event tree branch estimate. The mapping scheme adopted by Reclamation is based primarily on experiments reported by Reagan et al (1989), which are traceable to a known set of results. These experiments show that, within reasonable limits, people are pretty well calibrated and consistent relative to known probabilities, provided they use words that most people would adopt on their own and provided the likelihoods are not inordinately large or small. Vick (2002) has summarized those results. Reclamation has adapted this information, and uses the mapping scheme shown in Table 2, along with approximate results of the experiments for comparison.

A key finding of the experiments was that people's ability to judge likelihood does not extend very far out on either end of the probability scale (i.e. to more than a couple orders of magnitude as one approaches either zero or one), even when words like "almost impossible" or "almost certain" are used. This is likely due to the fact that most people's experience does not allow them to conceptualize likelihoods at these extreme probabilities. Despite the evidence to suggest that these are about the limits to which people are well calibrated, Reclamation adds one more order of magnitude to the upper and lower end of the scale, such that in special situations higher or lower numbers could be estimated. However, it is recognized that these numbers should rarely be used, and only in situations where an additional order of magnitude is needed. For example, a team can become calibrated to different levels of likelihood as events are discussed and probabilities are estimated. After frequent

assignments in the range of 0.01 to 0.05, an event is encountered that is perceived to have an even lower likelihood. Then it would be reasonable to assign a value as low as 0.001. It should be noted that this discussion applies to subjective probability estimates for which there are no relative frequency data or probabilistic analyses to support the estimate. In cases where these exist, lower estimates are often made when supported by the information.

Table 2. Verbal Descriptors and Associated Approximate Probabilities used by Reclamation (adapted from Vick, 2002)

Verbal Descriptor	Suggested Probability	Approximate Probability Range from Reagan et al
Virtually Impossible, due to known physical conditions or processes that can be described and specified with high confidence	0.001	0-0.05
Very Unlikely, although the possibility cannot be ruled out	0.01	0.01-0.15
Unlikely, considerably more unlikely than not	0.1	0.05-0.25
Neutral, with no reason to believe that one outcome is more or less likely than the other (when given two outcomes)	0.5	0.4-0.6
Likely, considerably more likely than not	0.9	0.6-0.92
Very Likely, but not completely certain	0.99	0.75-0.99
Virtually Certain, due to known physical processes and conditions that can be described and specified with high confidence	0.999	0.9-0.995

Estimating event tree branch probabilities using subjective expert elicitation is done similar to the procedure described for failure mode screening, by listing the adverse factors (factors that make the node more likely) and favorable factors (factors that make the node less likely) associated with each node. These factors are the evidence that is used to reach a range in likelihood estimates and build the case for the numbers that are generated. The process of collecting and listing the "adverse and favorable factors" by the facilitator typically generates significant discussion, which in turn provides a relative sense of the importance of each factor discussed. It is important for the facilitator to draw out the diverging opinions, as they could represent different views on the topic, and may represent the bounds for the estimates. Once the facilitator senses discussion has ended, the group is queried for a range of probability estimates using the verbal descriptors. These estimates should represent reasonable ranges, not necessarily the absolute minimum and maximum anyone can conceive of. The shape of the distribution should also be discussed. Is the probability estimate more likely to be somewhere in between the upper and lower values, in which case a triangular distribution might be appropriate, or is it equally likely anywhere in between, in which case a uniform distribution would be appropriate. In other cases, it may be appropriate to build a cumulative distribution

(e.g. likely less than = 90th percentile, likely greater than = 10th percentile, 50/50 = 50th percentile).

After the estimates or ranges of estimates are made, the rationale and justification for those estimates must be captured and documented. An attempt is made to reach consensus on a best estimate and a range of estimates. However, differences in opinion are beneficial to the process, and if consensus cannot be reached, the diverging views are documented along with their reasoning and the resulting estimates. The facilitator helps guide the process, on the lookout for biases or adverse group interactions along the way.

Biases can affect subjective probability estimates. These must be recognized, and to the extent possible, the risk analysis facilitator must strive to minimize their impacts on the estimates. Some of the more common are summarized briefly below (see also Vick, 2002).

- ***Overconfidence Bias.*** Perhaps the most pervasive bias is the tendency for engineers to be more confident than the evidence warrants. This usually leads to estimates that are closer to zero or to one than they really should be, and/or to distributions that are narrower than they should be. One way to help avoid this is to start with an exercise where estimators need to estimate the likelihood of known events, first on their own and then as a group. Often people will have trouble making these estimates individually, but will have more success as a group.
- ***Anchoring Bias.*** This is the tendency for estimates to not vary much from values that are initially presented to the group, either from relative frequency information or other sources. This is not mentioned to discourage presentation of relative frequency information, which is often useful to arrive at a reasonable estimate. However, if this information is presented, it should be as appropriate as possible to the problem being estimated and consideration should be given as to how the specific case might vary from the general population. Anchoring bias can be avoided to some extent by discussing potential extreme values before settling on a "best estimate".
- ***Motivational Bias.*** This results when one or more of the members making estimates have a vested interest in the outcome. For example, if the designer of the dam is in the room, that person may want to push the view that the dam is well designed and there should be no problems with it, and therefore will provide low failure probability estimates. Or perhaps an office needs work, and their representative is quick to push for higher failure probability estimates in the hopes that designs and modifications will soon follow. A facilitator can attempt to bring out opposing views when an opinion appears to be expressed from a motivational bias.
- ***Availability Bias.*** This results from over-emphasizing the most recent, most easily recalled, or most vivid evidence. For example, if the team just discussed a catastrophic failure case history, there could be a tendency for the team to assign a higher likelihood to that failure mechanism. This may be appropriate if relevant similar conditions exist between the failure case history and dam being studied, but may not be appropriate if the similarities are

questionable. A facilitator can try to point out the relevance of the latest information and counter it with an opposing view, if it is not thought to be representative of the issue at hand.

If the group selected to make the estimates has been chosen properly, people will enter the exercise with the appropriate expertise, an open mind, and a willingness to get to the best possible results. When this occurs, beneficial interactions take place, and additional ideas expand from those being discussed. Arguably, the group reaches a better conclusion than any of the individual members could have reached on their own. However, sometimes the group may stumble along one or more of the following lines. The facilitator must recognize when this is occurring, and try to direct the group toward a more positive direction.

- A dominant individual may overly influence the way the group goes by "bullying" everyone into thinking the way they do. It takes a fairly strong facilitator to deal with this, and usually requires emphasizing and bringing out the opposing point of view as well as drawing others into the conversation. Alternatively, an anonymous individual estimating procedure can be instituted to ensure everyone's input is received, but then the group must decide how an expected value and distribution will be selected from the results.
- People may not say what they really feel for fear of appearing unknowledgeable, and will tend to go along with the rest of the group even though they have important input. This requires the facilitator to draw out their opinions by directing questions specifically at these individuals.
- The group gets tired due to the rigors of the session, and people agree just in order to get it done. The facilitator is not immune to this trap. If it is obvious that proper attention is not being paid to something, it is important to stop, take a break, and discuss ways to invest proper time for the evaluation.

In the case of the example arch dam abutment instability potential failure mode previously described, three of the event tree nodes were estimated using subjective degree-of-belief methods: Joints Continuous, High Uplift Condition, and Breach during Shaking. To illustrate the process, only the "High Uplift Condition" node will be described here. For this node, the team was estimating the likelihood that the high water pressures represented by a pressure contour map developed by the rock mechanics analyst was truly representative of what exists in the abutment, or whether there was enough residual drainage in the system and natural jointing to be more typical of what one would expect of a drained abutment. The adverse and favorable factors related to this node are listed below. Note that some are the same as originally used in the failure mode screening, and that some of the factors provide opposing views on a given condition. This will often be the case, and the team must decide which of the factors are most convincing.

Adverse or "More Likely" Factors

- It is not possible to maintain the *foundation* drainage system. *The foundation drain holes were drilled from an upstream fillet and connected to the outfalls*

through piping with a series of right angle bends. It is not possible to maneuver drain cleaning equipment around these bends.

- The piezometer levels are increasing. *Piezometers installed at the base of the dam indicate rising foundation water pressures. The pressures have risen 15 to 20m near the lower right abutment since 1942.*
- Water squirts up about 1m from rockbolt holes on the downstream right abutment. *These rockbolt holes are downstream of the right abutment rock block and squirt when the reservoir reaches high elevations, indicating potentially high foundation water pressures well downstream of the dam.*

Favorable or "Less Likely" Factors

- The water pressure contours used in the analysis show levels above the ground surface *downstream of the dam in areas where no seepage appears.*
- The rockbolt holes that squirt water are downstream of the rock block. *The pressures under the block are not known; it may be that the water is connected to the rockbolt holes through a path that does not feed the block planes. It is not clear if the rockbolt holes squirted when the drainage system was new.*
- The piezometers that show increasing pressures are not in the vicinity of the rock block. *The closest piezometer is at the base of the right abutment; the block is in the upper right abutment. There are no piezometric measurements under the rock block.*

The team weighed the evidence and decided on a low estimate of neutral (0.5) and a high estimate of likely (0.9) for high water pressures existing in the abutment consistent with the analysis, with no reason to believe it is more likely anywhere within the range (i.e. a uniform distribution). The rationale is as follows: there is clear evidence that the original drainage system is deteriorating and cannot be maintained, and there is evidence that water pressures in the abutment could be high at higher reservoir elevations. Therefore, estimates on the likely side are warranted. The primary mitigating factor that keeps the estimates from being higher is the fact that there are no piezometric measurements to confirm the values used in the analysis, which may be at least locally on the conservative side.

CONSEQUENCE EVALUATION

Consequences associated with dam failure can take many forms, including economic, environmental, sociological, and life safety. Although all of these may enter into the decision process, dam safety risk analyses tend to focus on the potential for loss of life. In this regard, the methodology developed by Graham (1999) continues to be the primary means of estimating potential life safety consequences at the Bureau of Reclamation. Although there are some cases when quantifying the number of potential fatalities may not be desirable, the sad fact of the matter is that when dams fail, people often die, and this must be acknowledged. The methodology developed by Graham is based on case studies of historical dam failures and flash

floods. The data suggests that the level of life loss is dependent primarily on four factors:

- ***Population at Risk.*** The number of people who would be exposed to flooding from a dam break.
- ***Flood severity.*** Three categories of flood severity are considered: high, medium, and low. For high severity flooding, the area is wiped clean and the ultimate flood depths appear suddenly, for example as a result of rapid failure of a concrete dam in a narrow canyon. For medium severity flooding, houses are washed off their foundations, but the ultimate flood depths ramp up with time and mangled structures and trees remain for refuge. Houses and buildings are not washed off their foundations for low severity flooding and the smaller flood depths and velocities gradually rise to their peaks.
- ***Warning time.*** The more time people have to evacuate, the more effective the evacuation will be. The time it takes to detect failure and initiate warning is subtracted from the flood wave travel time (determined from the inundation mapping) to arrive at the warning time.
- ***Flood severity understanding.*** If people understand precisely what is about to descend upon them, they are more likely to evacuate in a timely manner and stay away, whereas they may not do so if their understanding of the situation is vague.

The flood plain downstream of a dam is typically divided into reaches representing different population centers. Dam break inundation maps are used to identify the population that would be flooded within each reach. A flood severity, warning time, and flood severity understanding is assigned to each population center based on the characteristics derived from the inundation study. A spreadsheet can be set up to use the results from Table 3 in estimating consequences. Possible distributions in population at risk (PAR), flood severities, warning times, and understandings can be included in the spreadsheet to account for additional uncertainty. For example, the potential for loss of life at night may be significantly different than during day time hours (due to differences in warning time and/or PAR), or during the summer when recreation use is at a peak versus times of the year when recreation use is minimal.

It should be noted that the case histories from which this method was developed included only small to moderately-sized population centers with limited warning time. The effects of evacuation are included in the fatality rates. It is recognized that additional consideration is required for large population centers with significant warning time. In these cases, an evaluation of evacuation routes and the potential for "grid-lock" must be undertaken, and appropriate fatality rates applied to the population that is unable to or does not evacuate. Models for numerically simulating consequences under such conditions are being developed at Utah State University and BC Hydro. However, these models are more complex and take time to learn and use. Regardless of the method used, it is recognized that estimating fatalities, which involves assessing complex human behavior, can only be very approximate. Therefore, typically a wide range in potential fatalities is considered.

The database used to develop the method includes no seismic failures. Following an earthquake large enough to fail a dam, the inundation area would likely be seriously damaged with major disruption to communication lines, evacuation routes, and availability of emergency personnel. Under these circumstances, the warning time and ability to evacuate could be reduced. However, the probability of the reservoir being full or at a high level during an earthquake should also be considered.

Table 3. Empirically-Based Fatality Rates (after Graham, 1999)

Flood Severity	Warning Time	Understanding	Fatality Rate	
			Suggested	Range
High	None	N/A	0.75	0.30 to 1.00
	15 to 60 min	Vague	Use above values – apply to number of people who remain in flood plain after evacuation.	
		Precise		
	> 60 min	Vague		
		Precise		
Medium	None	N/A	0.15	0.03 to 0.35
	15 to 60 min	Vague	0.04	0.01 to 0.08
		Precise	0.02	0.005 to 0.04
	> 60 min	Vague	0.03	0.005 to 0.06
		Precise	0.01	0.002 to 0.02
Low	None	N/A	0.01	0.0 to 0.02
	15 to 60 min	Vague	0.007	0.0 to 0.015
		Precise	0.002	0.0 to 0.004
	> 60 min	Vague	0.0003	0.0 to 0.0006
		Precise	0.0002	0.0 to 0.0004

For the example arch dam abutment failure mode, the consequence evaluation is summarized in the spreadsheet shown in Table 4. In this case, the flood severity was not considered to be constant for some of the population centers. For example, in Town 2, it was estimated that about 25 percent of the population at risk would be near the edge of the inundation boundary, where the flood severity would be low, while about 75 percent of the population at risk would be closer to the river where the flood severity would be medium. This concept could also be used to assign probabilities to other variables that affect the fatality rates. For example, the actual amount of warning time is uncertain, and various warning times could be evaluated by assigning probabilities to each considering daytime and night time conditions (as long as the probabilities add to 1.0 for each reach). Similarly, if there is uncertainty in the population at risk due to transient activity or other factors, various values with associated probabilities can be assigned. In the example, the exposure time associated with a campground in the reach from 5 to 47 km was factored into the population at risk before entering it into the table. In addition, because of the long sparsely populated reach from 5 to 47 km, the warning time category was considered to be about the same during both daytime and night time hours.

Table 4. Consequences for Example Problem

River km	Wave Travel Time (hrs)	Reach Description	Population at Risk	Flood Severity	Flood Severity Probability	Warning Time (hrs)	Warning Understanding	Fatality Rates			Fatalities		
								Low	Medium	High	Low	Medium	High
0 to 5	0.1	Dam to diversion dam	39	High	1	0	N/A	0.3	0.75	1	11.7	29.3	39
5 to 47	1	Diversion dam to state highway	38	High	0.9	0	N/A	0.3	0.75	1	10.3	25.7	34.2
			38	Medium	0.1			0.03	0.15	0.35	0.1	0.6	1.3
47 to 87	3	State highway to town 1	60	Medium	1	1 to 2	Vague	0.005	0.03	0.06	0.3	1.8	3.6
87 to 90	4	Town 1	301	Medium	0.9	2 to 3	Vague	0.005	0.03	0.06	1.4	8.1	16.3
			301	Low	0.1			0	0.0003	0.0006	0.0	0.0	0.0
90 to 109	5	Town 2	166	Medium	0.75	3 to 4	Precise	0.002	0.01	0.02	0.2	1.2	2.5
			166	Low	0.25			0	0.0002	0.0004	0.0	0.0	0.0
109 to 123	6	Town 3	368	Medium	0.5	4 to 5	Precise	0.002	0.01	0.02	0.4	1.8	3.7
			368	Low	0.5			0	0.0002	0.0004	0.0	0.0	0.1
123 to 133	7	Town 4	1864	Low	1	5 to 6	Precise	0	0.0002	0.0004	0.0	0.4	0.7
133 to 159	9.5	City	11743	Low	1	7.5 to 8.5	Precise	0	0.0002	0.0004	0.0	2.3	4.7
Total			**15452**								**24**	**71**	**106**

COMBINING RISKS

During risk analyses, estimates of risk are generated for individual potential failure modes. These estimates might include probability or risk values for different loading conditions, loading ranges, failure modes, spatial segments, or other situations. The risk associated with each potential failure mode is useful information. In addition, after all potential failure modes have been identified, described, and evaluated relative to the risk they pose, the results need to be combined and portrayed so that the total risk for the facility is understood.

It is important when combining risks from different potential failure modes for a given load range, that the joint "common cause" conditional failure probability be appropriately handled. For example, if the conditional failure probabilities for multiple potential failure modes for the same loading are large (e.g. they sum to greater than 1.0), they must be corrected so that the total conditional failure probability (when added) is equal to $1-(1-P_1)(1-P_2)\ldots(1-P_n)$, where $P_1, P_2 \ldots P_n$ are the uncorrected conditional failure probabilities. According to the unimodal bounds theorem, this equation results in the upper bound conditional failure probability, while the lower bound is simply the largest of the uncorrected individual conditional failure probabilities. When adjusting individual conditional probabilities, as a convenient and reasonable simplification, the reduction associated with the joint conditional failure probability is typically distributed proportionally to each of the potential failure modes. The individual probabilities are multiplied by the ratio of the corrected total failure probability to the sum of the uncorrected individual probabilities. For example, consider the following conditional probabilities for a given load range under earthquake loading:

- P(A|Earthquake) foundation sliding of concrete section = 0.7
- P(B|Earthquake) radial gate arm buckling = 0.5
- P(C|Earthquake) foundation liquefaction and freeboard loss = 0.5

The sum of these conditional failure probabilities is 170%, but the total conditional failure probability cannot exceed 100%. Using the unimodal bounds equation, P[No Failure] = (1 - P[A]) x (1 - P[B]) x (1 - P[C]) = (1 - .7) x (1 - .5) x (1 - .5) = (.3 x .5 x .5) = 0.075, and the system failure probability is 1 – 0.075 = 0.925. The individual conditional failure probabilities are normalized as follows:

- P[A|Earthquake] = (.925/1.7) * .7 = 0.381
- P[B|Earthquake] = (.925/1.7) * .5 = 0.272
- P[C|Earthquake] = (.925/1.7) * .5 = 0.272

Long structures pose particularly difficult problems when attempting to assess the risk to the downstream population. Conceptually, a dam which is 5,000-feet long would pose a higher risk than a structure with an identical cross-section but only 500-feet long. However, dividing a long structure into reaches, each "x-feet" long, and accumulating risk for each reach can be an arbitrary exercise. Therefore, Reclamation practice has been to divide long structures into segments based on

differences in geology (foundation conditions), construction (construction material, zoning, or cutoff conditions), and geometry (height, width, or other factors that could affect breach outflow).

Consideration must also be given to multiple structures forming a single reservoir. There is no "correct" means for combining these risks. However, from a practical standpoint Table 5 provides guidance on how this can be approached.

Table 5. Guidance for Combining Dam Safety Risks

Type of System	Type of Component Failure	Methods for Combining Component Failure Probabilities	Methods for Combining Component Failure Risks
Single dam and PAR	separate loading conditions (static, seismic, hydrologic)	account for correlations explicitly in event tree(s); add probabilities to determine total failure probability	add end-branch risks to determine expected loss of life from dam failure
Single dam and PAR	separate failure modes for any given loading condition	determine unimodal bounds; if bounds are narrow, add probabilities to determine failure probability over all such failure modes. Otherwise, retain probability bounds	similar consequences for each failure mode: determine bounds; add applicable end-branch risks if bounds are narrow. Otherwise, retain risk bounds.
			different consequences for each failure mode: add applicable end-branch risks to determine risk over all such failure modes
Single dam and PAR	separate segments of different height and breach conditions (all loading conditions)	determine unimodal bounds; if bounds are narrow, add probabilities to determine failure probability over all such segments. Otherwise, retain bounds	add segment risks to determine risk over all such segments
Single dam and PAR	separate segments with different foundation conditions (static and seismic loading conditions only)	same geologic origin or process: determine unimodal bounds; if bounds are narrow, add probabilities to determine failure probability over all such segments. Otherwise, retain probability bounds	same geologic origin or process: determine bounds; if bounds are narrow, add risks to determine risk over all such segments. Otherwise, retain risk bounds
		different geologic origin or process: add segment probabilities to determine failure probability over all such segments	different geologic origin or process: add segment risks to determine risk over all such segments
Multiple dams, same PAR	Determine probabilities of failure separately for each dam. For total risk, treat each dam as for a segment of a single dam.		

DEALING WITH UNCERTAINTY

The likelihood estimates for each event and each state of nature comprising an event tree model are uncertain. If probability distributions are input, Monte-Carlo simulation can be used to treat the uncertainty in these variables explicitly. Monte-Carlo simulation results are depicted in scatter-plots as shown in Figure 7, developed from the example event tree shown in Figure 5 (assuming the seismic hazard is lognormally distributed), where each point represents a single combination of possible values chosen from each variable's probability distribution. The mean (shown by the white circle) represents the 'expected value' of the risk estimates. The outlying points represent situations where extreme values are chosen from each variable's probability distribution. If the events within the tree are all independent, the likelihood that all are at extreme values at the same time is extremely unlikely. However, the likelihood of and extent to which the variation in results exceed the risk guidelines can be an important input to the decision process.

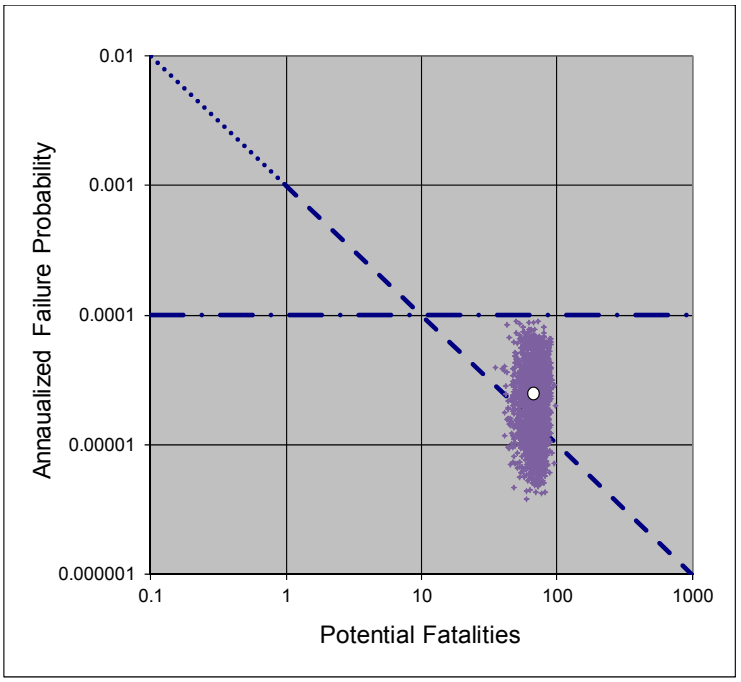

Figure 7 – Scatter Plot from Event Tree Monte-Carlo Analysis

Comparing Figure 7 with Figure 4 indicates that the risks are estimated to be slightly lower from the detailed quantitative risk analysis in comparison to the qualitative screening. Although the consequences category was a reasonable reflection of the detailed evaluation, the likelihood category was about half an order of magnitude higher. This is not untypical, as in general the team is focused on maximum loadings when making the qualitative likelihood category selection. Breaking the response down into smaller load increments often has the effect of reducing the failure probability. For this example, a detailed evaluation of the

complete event tree (not shown) indicates the following (listed here to give a flavor for the types of information that can and should be gleaned from such an exercise):

- No one seismic load range dominates the risk. The decrease in load probability roughly offsets the increase in conditional failure probability as the loading increases.
- The risk is dominated by the branches corresponding to high uplift pressures. If it could be assured that the abutment was well drained and the chance of high uplift pressures was negligible, the estimated mean annualized failure probability would drop from about 2.1×10^{-5} to 1.5×10^{-6}. (Note: event trees provide a useful tool to examine the effects of risk reduction actions that would alter the estimated probabilities for one or more branches.)
- In general, the risk is dominated by dam failure as a result of abutment block movement during seismic shaking. Even in cases where dam failure during seismic shaking was thought to be unlikely, the probability of post-seismic instability was even more unlikely. The exception was the seismic load range from 1/10,000 to 1/25,000 and drained conditions where the chance of failure during seismic shaking was estimated to be very low. (Note: the chance of failure was considered to be negligible for 1/5,000 to 1/10,000 ground motions and drained conditions.)
- The mean for this one potential failure mode exceeds the public protection societal risk guideline of 0.001 lives per year, plotting in the area of increasing justification to reduce or better understand the risks, although none of the simulation points exceeded the 0.0001 annualized failure probability threshold. It therefore follows that the total risk (sum of all potential failure modes) will also exceed the risk assessment guidelines

A key issue relates to the effects of uncertain input distributions on the risk results. As previously described, the sensitivity rank coefficients can be used to identify those distributions to which the results are most sensitive when performing Monte-Carlo analyses using event trees. Plausible upper and lower bound values for a sensitive variable can be chosen and held constant in a Monte-Carlo simulation while all other variables are allowed to vary according their full input distribution. When this test causes the scatter-plot mean to move significantly, there may be justification to obtain additional information. However, additional reasoning is then needed to convince the decision makers that the upper or lower bound values are plausible. Reasoning is also needed as to why the additional information being requested is likely to reduce the uncertainty and influence the decision.

BUILDING THE DAM SAFETY CASE

The risk estimates for dam safety related potential failure modes, regardless of the methods used to arrive at them, are only approximate. If performed diligently in a relatively consistent manner, they are useful in program management. However, Reclamation's public protection (risk assessment) guidelines are not intended as rigid decision criteria for declaring a dam "safe" solely on the basis of a risk estimate.

Therefore, additional reasoning, termed the dam safety case or simply "the case", is needed to convince the decision makers that (1) the interpretation of the condition of the structures and their ability to withstand future loading, (2) the risk estimates, and (3) the recommended actions are all coherent and make sense. Going through the process of developing the risk estimates, if done thoroughly and rigorously, will result in the "learning" needed to build the case. As part of the case, three elements must be addressed: (1) whether the estimated risk justifies action, (2) if so, the urgency of taking action, and (3) the confidence in the estimates and whether additional information is likely to change perception of the need and urgency to take action. All three components of the risk estimates must also be addressed: (1) the loadings, (2) the response of the structures to the loadings, and (3) the consequences.

The risk estimates and the dam safety case do not in themselves ensure the safety of a facility. The dam safety case becomes the basis for risk management in the effect it has on the activities related to operation and care of the facility. The understanding given to all those associated with a facility by a well-constructed dam safety case is intended to focus attention on technical aspects essential to the facility's integrity. The risk analysis methodology is designed to take apart and examine all the features of a dam and facility, and diagnose its particular vulnerabilities. This information must then be interpreted and synthesized into the case. The dam safety case should be carefully crafted so that all descriptions and terms are easy to understand by the prime audience, all arguments are cogent and coherently developed, all references are easily accessible, and all conclusions are fully supported and follow logically from the arguments.

The case is built from arguments, or claims and the evidence to support them, which can apply to individual nodes in an event or fault tree, potential failure modes in general, consequence evaluations, or recommendations. For example, an event tree is structured to present a number of claims in series, with each claim having a probability estimate based on the supporting evidence. The series structure is most convincing when each probability estimate in the string is well substantiated. Conversely, if even one claim in the string is highly uncertain, the case becomes much weaker. A claim that is particularly weak is a good candidate for a sensitivity study as previously described. Sometimes, two or more claims can be made, any one of which if highly convincing, would substantiate the dam safety case. Sometimes, several independent claims combine to justify the recommended action when none by itself can sway the argument. In this latter case, the greater the number of claims that can be substantiated, the stronger the case becomes.

When making the case, usually it is informative to demonstrate where the highest contributions to risk are coming from, and to highlight the strongest evidence to support why this makes sense. The potential failure modes that contribute most to the risk should be identified, and the reasons why this is believable enumerated. Sometimes the highest contributions come from a particular loading branch of the event tree, and it is useful to know whether this is due to lower conditional failure probabilities associated with frequent loadings, or higher conditional failure probabilities associated with infrequent loadings.

Potential Claims that Help Establish Belief in the Loading Conditions. Exceedance probabilities for storm peak inflows and volumes in comparison to the reservoir's storage and the spillway's discharge capacities provide understanding regarding behavioral thresholds to flooding. So does an interpretation of exceedance probabilities of peak horizontal acceleration levels or other seismic loading parameters where dam responses are likely to change. The nature of the storm (general rain, rain-on-snow, or thunderstorm) or earthquake source (random, subduction zone, or active seismogenic crustal fault) and which are dominating the hazard for various load ranges helps in understanding the nature of the uncertainty portrayed in the hazard curves. The type of empirical information used to generate the hazard curve (e.g. the historical flood record extends out approximately 150 years, and paleo-geologic information contributed to non-exceedance levels of 1/5,000) can provide a measure of confidence in the loadings.

In the case of our example dam, the claim is that the seismic hazard curve appropriately represents the probability of seismic loading at the site. The evidence to support this claim includes careful evaluation of potential seismic sources which include north- to northwest-striking Cenozoic normal faults with known or possible Quaternary displacement, and random or background seismicity on buried faults that lack surface expression. One nearby range-bounding fault shows clear evidence of late Quaternary displacements from observations of offset soil profiles, and the fault lengths and slip rates could be reasonably deduced from the exposures. Observations at other range-bounding faults were hampered by access problems, extensive vegetation, and obliteration of the record by erosion. However, even if they are treated the same as the fault with observed late Quaternary displacement, the inferred slip rates are low enough that the seismic hazard is clearly dominated by the background seismicity. The historic earthquake record in the vicinity of the dam is good, with instrumented recordings extending back to 1925. A total of 223 earthquakes were available for recurrence calculations, with two greater than M 6.5. Earthquake recurrence statistics show that the data follow a “maximum likelihood” fit quite well. Therefore, confidence in the predictive capability of the recurrence model is high.

Potential Claims that Help Establish Belief in the Dam's Response to Loading. Key evidence of exceptionally bad behavior from piezometers, structural measurement points or seepage weirs would be highly convincing of potentially adverse behavior. Factors that demonstrate poor design or faulty construction techniques are also important. The case should include mention of design details or features that indicate most-likely locations of vulnerabilities. Strong evidence from laboratory or in situ tests that show low strength is also helpful. Analysis results that indicate adverse behavior to loadings not yet experienced can be convincing if they are thoroughly calibrated and verified, are representative of the field conditions and provide relevant information for an identified potential failure mode. On the other hand, evidence of good structural performance based on monitoring, attention to sound design and construction details, positive analysis results related to the identified potential failure modes, and/or testing that indicates high strengths would also be important.

In the case of our example dam, several claims are made in evaluating the event tree in support of the overall claim that the chances of poor abutment performance under seismic loading are higher than we would like to see for the associated consequence level. The first claim is that the upper right portion of the dam is founded on a well defined foundation block, formed by continuous bedding plane partings and joints, with the probability of the joints being continuous enough to release the block estimated to be high (0.9 to 0.99). The evidence to support this claim includes the following: (1) a continuous open bedding plane parting forming the side plane of the block was mapped downstream of the dam, (2) a continuous open low angle joint forming the base plane of the block was mapped downstream, (3) a construction photograph indicates the base plane is continuous across the foundation contact to the upstream side of the dam, and (4) joints mapped upstream of the dam could connect to form a continuous release surface at the back of the block.

The second claim is that there is a good chance that high water pressures exist within the right abutment near the block. The evidence to support this claim includes the following discussion. The foundation drainage system cannot be cleaned or maintained as evidenced by the way in which it was constructed with numerous right angle bends between the drain holes and the outfalls. Although there are no direct measurements of abutment water pressures in the immediate vicinity of the right abutment block, evidence suggesting the foundation water pressures are increasing and may be high in the vicinity of the block (with an estimated probability from neutral to likely, 0.5 to 0.9) includes: (1) piezometric pressures measured at the base of the right abutment have increased by over 15 m since 1947, and (2) rock bolt holes immediately downstream of the block squirt water about 1 m into the air at high reservoir levels.

Given this information, detailed deterministic and probabilistic analyses were performed to estimate the probability of the remaining nodes under various earthquake load ranges and abutment water pressure conditions. Additional details of the analyses and results, why they are believable, and how they were weighted to arrive at probability estimates would also be provided in building the case.

Potential Claims that Help Establish Belief in the Life Loss Estimate. It is not sufficient to briefly describe the features inundated downstream and report a life loss number. A life loss estimate claim would be established by including pertinent facts regarding population centers categorized by downstream flood wave travel time and anticipated flood severity, listing key factors affecting the failure initiation and breach development time, and briefly commenting on ease of evacuation. Also important are the factors that would increase or decrease the life loss from the best estimate, what the range might be, and why the best estimate is more likely to fall at some point in the range. It is also useful to identify where most of the fatalities are likely to occur and why.

In the case of our example dam, the claim is that there would be multiple fatalities if this potential failure mode were to develop, most likely approaching 100. Evidence suggests the type of breach that would result from concrete arch dam abutment instability would be rapid and brittle, based on historical experience such as

the sudden failures of St. Francis Dam in southern California and Malpasset Dam in southern France. Given such a failure, a wall of water over 20 m high would travel down the canyon downstream of the dam. The approximately 80 people (on average) in this portion of the canyon in cabins, campgrounds, resorts, and ranches who reside primarily near the river and would be subjected to high severity flooding with no warning other than the seismic ground vibrations and sound of the rushing water. Nearly 80 percent of the total fatalities are estimated to occur in this reach. Once the flood wave exits the canyon, it would spread out and attenuate. Several small towns and a large town would be affected by the flooding, particularly those people nearest the river. Although fatalities are expected in these areas, the reduced flood severity and warning will keep them to about 20 percent of the total.

PRIORITIZING ACTIONS

As a general rule, as the probability of failure and risk increase, the justification and urgency to take action also increase. Similarly, as the probability of failure and risk decrease, the justification and urgency to take action also decrease. It is important to strive to develop consistent risk estimates through established methodology and review. However, it must be recognized that risk estimates are likely to come from a variety of sources. Complete consistency in the estimates cannot be expected. Therefore, it is important to consider other factors, such as those listed below, when prioritizing activities. All else being equal, the numbers can then be used as a prioritization tool.

- Direct evidence that failure is in progress and the dam is almost certain to fail if action is not taken quickly would be considered the highest priority.
- A case where both the probability of failure and the risk are high (exceeding risk assessment guidelines) would generally be more critical than a case where only one or the other is extremely high. Equal weight would be given to cases where one or the other (risk or failure probability) are in this category.
- A case where the high risk or failure probability is driven by a single potential failure mode would generally be more critical than a case where several potential failure modes must be accumulated to arrive at high risk.
- A case where the risk is driven by potential failure modes manifesting during normal operating conditions would typically take priority over cases where the risks stem primarily from flood or earthquake loadings.
- A case where the uncertainty band is relatively tight and the mean and median estimates are close to each other would take priority over a case where there is significant scatter in the data and the mean and median are far apart.
- A case where it is relatively easy and inexpensive to mitigate or confirm the risk would generally take priority over a case that is difficult and expensive to mitigate or confirm.

In the case of our example dam, the evidence was compelling that societal risks were in an area of increasing justification to reduce risks, and confidence in the

evaluation high enough that decision-makers were convinced to take action. A drain-drilling program was completed (see Figure 8). Piezometers installed in the vicinity of the abutment block planes confirmed that the pre-drainage abutment water pressures were elevated, and demonstrated the reduction achieved by the additional drainage. Based on the effectiveness of the drainage program, the annualized failure probability was considered to be reduced to that of a well-drained abutment (as examined by setting the probability of "High Uplift Condition" to zero in the event tree), resulting in a reduction in risk of just over an order of magnitude.

Fig. 8. Drilling Abutment Drains

CONSTRUCTION RISKS

When the risks associated with a dam are determined to be in the area of increasing justification to reduce risk, structural modifications may be necessary. In these cases, a decision may be needed to temporarily expose the public to even greater risks during the time that it takes to construct the modifications. It is important to balance costs with efforts to minimize these construction risks. It is also important for the decision makers to understand these risks and the cost trade-offs. Therefore, it is often necessary to characterize the risk during construction, and indicate how much it increases with respect to baseline pre-modification conditions, as well as the duration for which the increased exposure occurs. Conditions that can lead to increased risks during construction include:

- Excavations that lower the crest of the dam and increase its susceptibility to flood overtopping erosion failure.

- Excavations at the toe of a dam that increase its susceptibility to sliding instability by removing mass and allowing potential sliding surfaces to daylight in the excavation.
- Excavations that remove a portion of the downstream slope or foundation of an embankment leading to a shortened seepage path, a potential open and unfiltered exit for seepage, and increased susceptibility to piping.
- Full or partial replacement of structural features, such as spillways, that results in a temporary decrease in the hydraulic capacity or structural stability of a dam.

In cases where construction risks are elevated in comparison to existing risks, timing can be everything. That is, the reservoir water surface elevation may drive the risk during construction and the likelihood of reaching various elevations may vary during the year. Thus, it is important to adjust the construction schedule so that the high risk activities occur when the reservoir is likely to be lowest. In addition, shorter construction durations limit the risk exposure. In some cases it may be necessary to require lowering of the reservoir, or performing the work in small increments to accomplish the modifications without substantially increasing the risks.

A key component of many construction projects is a cofferdam to protect the work area from flooding. Design of cofferdams requires the same risk considerations as any other water retention structure. Consequences need to be considered. Will failure of the cofferdam result in release of the reservoir, or just flooding of the work area? The trade-offs in cost versus risk reduction need to be weighed.

In the case of our example arch dam, the risks associated with introducing drill water into the block potential sliding planes during drain or piezometer drilling and triggering a sliding situation were evaluated. However, given the currently relatively high static factors of safety and the localized effect of the drill water pressure injection, it was determined that the increase in risk during drain drilling was small, and would mostly occur at a time in the late spring when the reservoir was being drawn down for water supply. In addition, the drains would be drilled from a rock face lower on the abutment and it would not be possible to charge the rock joints with a significant column of water pressure.

CONCLUDING REMARKS

The Bureau of Reclamation has been using risk assessment to make dam safety decisions and prioritize the resulting actions for over 15 years. The aging infrastructure, increase in population growth downstream, and limited resources make this a reasonable and transparent method for risk management. Key to making the process effective is beginning with a detailed analysis of potential failure modes. If shortcuts are taken during this process, the results of the risk analysis could be unreliable and misleading. Once the potential failure modes are understood, a screening process can be used to identify those for which quantitative risk estimates are appropriate. A variety of tools are available for making the quantitative risk estimates, as described in this paper. The process of making the estimates affords the opportunity to learn about the dam and its vulnerabilities in more detail. It is

recognized that risk estimates and risk assessment guidelines are only approximate, and that it is essential to "build the case" for why the condition of the structures and their ability to withstand future loadings, the risk estimates, and the recommended actions are consistent and all make sense. If done diligently with an open mind, risk assessment can be a very effective tool for managing the risks associated with storing large amounts of water upstream of populated areas.

ACKNOWLEDGEMENTS

This paper represents experienced gained in performing and evaluating risk analyses and risk assessments for more than 15 years at the Bureau of Reclamation in Denver, Colorado. Over that time, many talented people contributed to developing the methods and procedures used by the organization, which are reflected in the write-up. A special thanks is extended to Bill Engemoen for his thorough and insightful review of this paper.

REFERENCES

Bureau of Reclamation (2011). "Dam safety public protection guidelines, a risk framework to support dam safety decision-making." U.S. Department of the Interior, Bureau of Reclamation, Denver, Colorado.

Corps of Engineers (2006). "Reliability analysis and risk assessment for seepage and slope stability failure modes for embankment dams." Engineering Technical Letter No. 1110-2-561, Department of the Army, U.S. Army Corps of Engineers, Washington, D.C.

Douglas, K.J., M. Spannagle, and R. Fell (1998). "Analysis of concrete and masonry dam incidents." UNICIV Report No. R-373, The University of New South Wales, Sydney, Australia.

Engemoen, W.O., and C.G. Redlinger (2009). "Internal Erosion Incidents at Bureau of Reclamation Dams." *Proceedings, U.S. Society on Dams Annual Meeting*, Nashville, TN: 731-745.

Foster, M.A., R. Fell, and M. Spannagle (1998). "Analysis of embankment dam incidents." UNICIV Report No. R-374, The University of New South Wales, Sydney, Australia.

Graham, W.J. (1999). "A procedure for estimating loss of life caused by dam failure." Report DSO-99-06, U.S. Department of the Interior, Bureau of Reclamation, Denver, Colorado, September, 1999.

Hatem, G.A. (1985). "Development of a data Base on dam failures in the U.S. – preliminary results." Thesis, Stanford University.

Hendron, A.J. Jr., E.J. Cording, and A.K. Aiyer (1980). "Analytical and graphical methods for the analysis of slopes in rock masses." NCG Technical Report No. 36, U.S. Army Nuclear Cratering Group, Livermore, California.

Reagan, R., F. Mosteller, and C. Youtz (1989). "Quantitative meanings of verbal probability expressions." *J. Applied Psychology*, Vol. 74 (3): 433-442.

Scott, G.A. (2007). "Probabilistic stability analysis – you can do it." *Proceedings, Association of State Dam Safety Officials Annual Conference*, Austin, Texas.

Scott, G.A. and others (2010). "Dam safety risk analysis, best practices training manual." Version 2.1, U.S. Department of the Interior, Bureau of Reclamation, Denver, Colorado.

Scott, G.A. and W.R. Fiedler (2010). "Shedding some light on this thing called risk assessment, part II – example risk analysis." *The Journal of Dam Safety*, Association of State Dam Safety Officials, Vol. 8 (3): 8-19.

Vick, S.G. (2002). *Degrees of belief – subjective probability and engineering judgment*. ASCE Press, Reston, Virginia.

Von Thun, J.L. (1985). "Application of statistical data from dam failures and accidents to risk-based decision analysis on existing dams." Bureau of Reclamation, Denver, Colorado.

Whitman, R.V. (1984). "Evaluating calculated risk in geotechnical engineering." *J. Geotechnical Engineering,* ASCE, Reston, Virginia, Vol. 110 (2): 145-188.

Random Field Model Parameters for Columbia River Silt

Armin W. Stuedlein[1], Ph.D., P.E., M. ASCE

[1] Assistant Professor, Oregon State University, 220 Owen Hall, Corvallis, OR, 97331

ABSTRACT Although some reliability-based design codes require the adjustment of resistance factors based on site variability, familiarity with methods to determine and model the inherent spatial variability of soil stratigraphy is not widespread. As a result, it is common for random field model parameters that have been reported in the literature to be used in lieu of site-specific parameters. However, few studies on the inherent variability of silt, if any, have been reported. To address this need, the uncertainty in select in-situ test data generated to support the planning and development of a 12 Ha industrial site overlying Columbia River Silt is characterized. Due to the high sampling frequency, random field model parameters were estimated for the corrected cone penetration resistance resulting from the cone penetration tests (CPTs). Stationarity of individual soil layers was achieved using linear trend removal and verified using the Modified Bartlett test statistic with fitted autocorrelation models. The coefficient of inherent variability and scale of fluctuation determined using fitted autocorrelation models are compared to values generated using less rigorous methods. The random field model parameters presented herein provides a set of random field parameters for modeling the vertical spatial variability of silt.

Keywords: CPTs, site investigation, soil properties, statistics, inherent variability

INTRODUCTION

Since 2007, all federally funded infrastructure projects in the United States require the use of reliability-based design (RBD) codes with adjustment of resistance factors based on site variability. However, methods to characterize and model the inherent variability of soil stratigraphy are not commonly implemented in routine design. One reason for the infrequent use of rigorous statistical models is the cost to obtain the volume of data required to adequately evaluate the covariance structure of a soil deposit (Fenton, 1999). Alternatively, geotechnical engineers may implement random field model (RFM) parameters reported in the literature (e.g., Phoon and Kulhawy, 1999) for similar sites to model the inherent variability of soils. This approach is reasonable for sites that share similar depositional and stress history with previously characterized geologic units, however, the diversity of existing geologic environments can provide a significant challenge. For example, very few random field studies in silt have been performed, if any, despite the broad global distribution of such deposits.

The objectives of this study are to present an interpretation of the characterization of the inherent spatial variability of Columbia River Silt, found within the Columbia River Valley, Oregon and Washington State. First, the geologic setting and subsurface characterization of the study site is described. Following a review of Random Field Theory and stationarity assessment methods, random field model parameters for the

mechanical response of the soil to cone penetration in the vertical direction are generated. The random field model parameters determined for Columbia River Silt will provide designers with a starting point for the evaluation of the inherent variability of silt at other sites.

LOCATION AND GEOLOGIC SETTING OF STUDY SITE

The project site was situated approximately 2 km northeast of the Columbia River in Longview, Washington, a port city located at the confluence of the Cowlitz and Columbia Rivers, 80 km east of the Pacific Ocean. The site is located in the Portland Basin, which formed in the early and middle Miocene; the region was inundated by periodic eruptions of the widely distributed Grande Ronde Basalt flood flows, which occurred between 16.5 and 6 Ma (Snavely et al., 1973). Sea level fluctuations and catastrophic floods associated with the glacial Lake Missoula subjected the region with alternating cycles of erosion and sedimentation in the Pleistocene (Trimble, 1963). Holocene soils, typically present to the depth of 30 m below the ground surface, consist of alluvial silt and fine sand deposits, characterized with local deposits of organic debris and silt (Evart, 2004). Pumice and mud-flow deposits are typically encountered at a depth of 17 to 20 m as a result of Holocene-era eruption of Mount St. Helens.

SUBSURFACE CHARACTERIZATION

The geotechnical services to support the development of a 12 Ha industrial site included explorations, in-situ testing, and sample retrieval for laboratory analyses. The in-situ test program consisted of four hollow stem auger borings for Standard Penetration Tests (SPT) and thin-walled tube samples, and eleven Cone Penetration Tests with pore pressure measurement (CPTu; designated P1 through P11). The CPTu data, borings, and sixteen test pits indicated a generally uniform groundwater depth of 0.3 to 0.6 m below the ground surface. In-situ testing revealed variable thicknesses of very soft silt to clayey silt (MH), very soft to soft sandy non-plastic silt (ML), and a fairly uniform medium dense, very silty sand (SM) pumice layer as described above. Thick, spatially variable lenses of clean to silty sand (SP-SM) were encountered in several piezocones. Figure 1 indicates a typical subsurface profile with SPT N values, corrected cone tip resistances, q_T, water contents, and Atterberg limits. The deposit of Columbia River Silt at the study site was separated into upper and lower layers by the pumice layer. The consistency of the silt typically increased linearly with depth as interpreted from q_T values, which ranged from 0.6 to 1.1 MPa and 1.2 to 2.1 MPa in the upper and lower

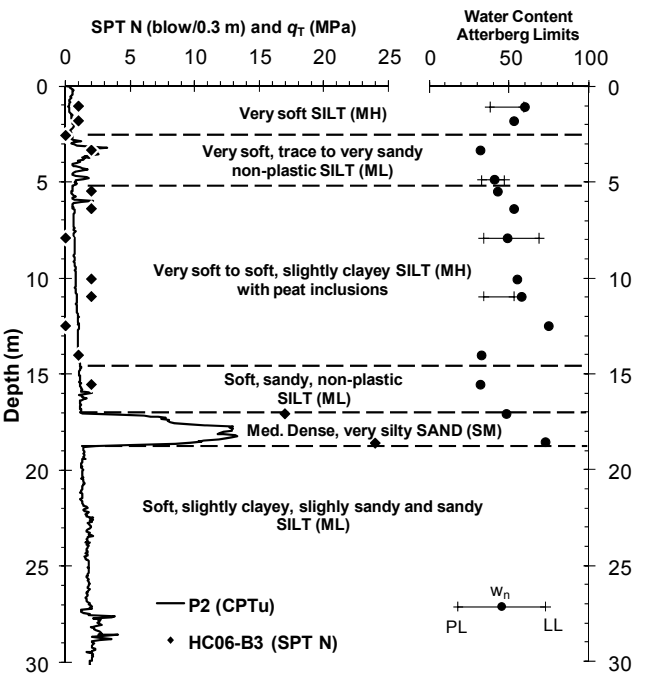

FIG. 1. Typical subsurface profile.

layers, respectively. Plastic indices (PI) typically ranged from 5 to 50, with liquidity indices (LI) representative of soft to very soft consistencies of 0.5 to 2.0. Incremental and constant rate of strain consolidation tests on specimens prepared from thin-walled tube samples indicated that plastic Columbia River Silt was moderately compressible, with average strain compression indices, $C_{c\varepsilon}$, of 0.15 with coefficient of variation (*COV*) of 8 percent. The surcharge program implemented to prestress a number of structure footprints resulted in consolidation settlements of up to 450 mm corresponding to surcharge heights of up to 4.5 m.

RANDOM FIELD THEORY

Random field theory (RFT) comprises a framework for the characterization of spatial variability because it may return statistical results suited to plan exploration and sampling strategies (e.g., Goldsworthy et al., 2007), generate inferences, and allow the incorporation of spatial variation in reliability models (Baecher and Christian, 2003). Since RFT incorporates location-specific dependence, it is a superior framework than regression analyses, which are based on classical statistics and the basic assumption that all observations in a soil deposit have an equal likelihood of being represented within a population sample and were uncorrelated. Although the deposition of a geologic unit is not random, the inherent variability of soil is commonly modeled using RFT (Baecher, 1999). For instance, a measurement of interest, *g(z)*, may be separated into a deterministic trend function, *t*(*z*), and a randomly fluctuating component, *w*(*z*), representing inherent soil variability, as:

$$g(z) = t(z) + w(z) \tag{1}$$

where *z* =depth (DeGroot and Baecher, 1993; Phoon and Kulhawy, 1999). A requirement for the evaluation of random fields is the conditioning of data as necessary to obtain weak stationarity (Lacasse and Nadim, 1996; Jaksa et al., 1997; Fenton, 1999; Phoon et al., 2003; Uzielli et al., 2005). An acceptable level of stationarity is characterized with: (1) a constant mean; and (2) the autocovariance being a singular function of separation distance between observations. This may be obtained by trend removal, differencing, and/or variance transformation (Jaksa, 1995). The subtraction of trends appears to be the most frequent method to attain stationary fields. Refer to Fenton (1999), Cafaro and Cherubini (2002), and Baecher and Christian (2003) for considerations in trend removal.

The inherent variability of a soil parameter can be characterized with the mean, the variance or *COV*, and the scale of fluctuation (VanMarcke, 1977, 1983). Phoon and Kulhawy (1999) recommend the use of the coefficient of inherent variability rather than the variance, defined as:

$$COV_W(z) = \frac{\sigma_W(z)}{t(z)} \tag{2}$$

where *t* = the mean trend value and σ_w = standard deviation of the fluctuating component. The scale of fluctuation, δ, or the distance within which soils demonstrate reasonably strong correlation, is the third parameter required to fully characterize a finite random field. Small values of δ represent quick fluctuations about the mean trend whereas large values of δ represent correlation over a long distance. The δ may be estimated using a number of methods, including: (1) expeditive method (VanMarcke, 1977), (2) variance

reduction function (VanMarcke, 1977); (3) intersection of the sample autocorrelation function (ACF) with the Bartlett's limit (Jaksa, 1995); and (4) autocorrelation model fitting (e.g., VanMarcke, 1978). The expeditive, variance reduction function, Bartlett's limit, and autocorrelation model fitting methods are referenced herein following Uzielli et al. (2005) as VXP, VRF, BLM, and AMF, respectively. The AMF method necessitates fitting of smooth autocorrelation models to the sample ACF using curve fitting measures (e.g., ordinary least squares). The autocorrelation models considered herein include the single exponential (SNX), binary noise (BIN), cosine exponential (CSX), second-order Markov (SMK), and squared exponential (SQX) models, due to their frequency of use in geotechnical applications (Jaksa et al., 1999; Phoon, et al., 2003; Uzielli et al., 2005). Table 1 provides the equation of each AMF and corresponding δ.

Table 1. Autocorrelation models and corresponding scale of fluctuation (Phoon et al, 2003); τ = lag distance.

Autocorrelation Model	Equation	Scale of Fluctuation δ
SNX	$\rho(\tau) = \exp(-\lambda\lvert\tau\rvert)$	$2/\lambda$
BIN	$\rho(\tau) = 1 - c\lvert\tau\rvert$ for $\lvert\tau\rvert \le 1/c$, 0 otherwise	$1/c$
CSX	$\rho(\tau) = \exp(-b\lvert\tau\rvert)\cos(b\tau)$	$1/b$
SMK	$\rho(\tau) = (1 + d\lvert\tau\rvert)\exp(-d\lvert\tau\rvert)$	$4/d$
SQX	$\rho(\tau) = \exp[-(a\tau)^2]$	$\sqrt{\pi}/a$

VERTICAL RANDOM FIELD MODEL PARAMETERS

Assessment of Stationarity

The generation of random field model parameters for use in RFT required the assessment and confirmation of stationary data. Prior to stationarity assessment, the Bartlett's test statistic, B_{stat} (Table 2), was calculated and plotted for each CPTu record to identify spikes in the B_{stat} and corresponding likely separation of statistically homogenous layers. The portion of the CPTu record corresponding to potentially stationary layers of Columbia River Silt were then fit with a linear trend to generate residuals for further stationarity assessment, the resulting ACF determined, autocorrelation models fitted, and δ and COV_W determined. Figure 2a provides a 5.1 m interval of Columbia River Silt identified in CPTu record P10. The residuals indicate relatively low variation in variance, with the exception of thin sandy silt lenses commonly found Columbia River Silt. Following construction of the sample autocorrelation functions for each considered CPTu segments, the autocorrelation models described in Table 1 were fit to each sample ACF. Figure 2b provides the resulting sample ACF and fitted autocorrelation models. Note that the portion of the sample ACF less than the Bartlett's limit, $r_B = \pm\ 1.96/\sqrt{n_d}$, is considered unreliable (Lumb,

Table 2. Modified Bartlett's test procedure (Phoon et al, 2003).

$$B_{stat} = \frac{2.303(m-1)}{C} \cdot \left[2 \cdot \log s^2 - \left(\log s_1^2 + \log s_2^2\right)\right]$$

where: $s^2 = \frac{s_1^2 + s_2^2}{2}$, s_1, s_2 = segment σ

$$C = 1 + \frac{1}{2 \cdot (m-1)}$$

m = number of points in segment

$$k = \frac{\delta}{\Delta z}$$

$$I_1 = \frac{n \cdot \Delta z}{\delta}\frac{n \cdot \Delta z}{k \cdot \Delta z} = \frac{n}{k}$$

$$I_2 = \frac{m \cdot \Delta z}{\delta}\frac{m \cdot \Delta z}{k \cdot \Delta z} = \frac{m}{k}$$

n = number of points in record

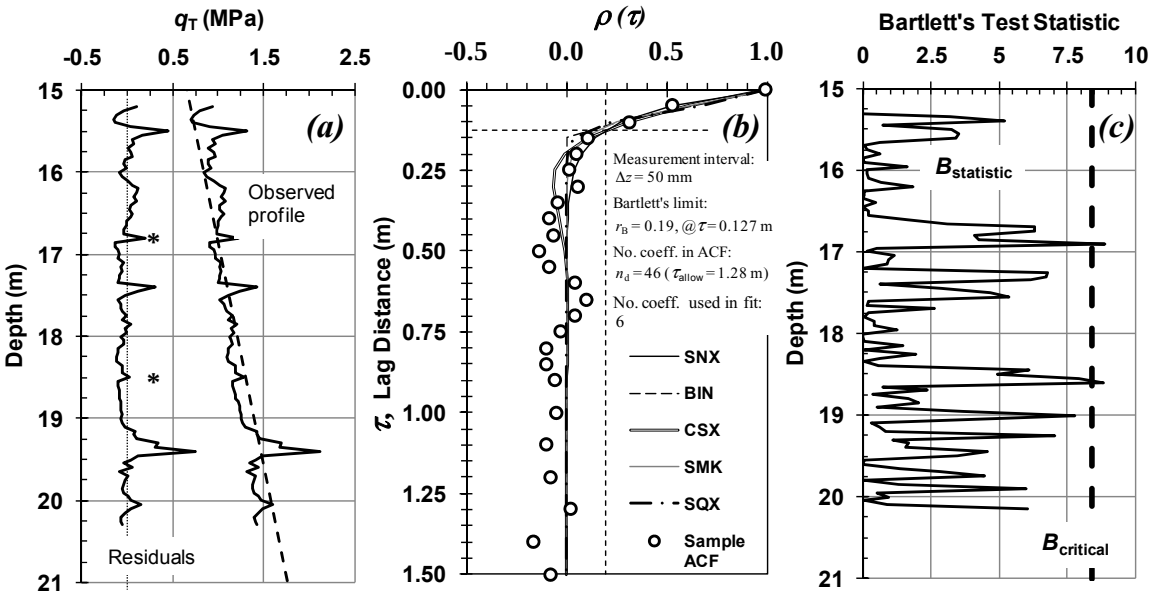

FIG. 2. Assessment of P10, Upper Silt Layer: (a) Observed and de-trended q_T data; (b) Sample autocorrelation function and fitted autocorrelation models; (c) Profile of Mod. Bartlett's test statistic.

1974); however, since the sampling interval, Δz, was equal to 50 mm (rather than the preferred Δz = 20 mm; ASTM D 5778-07), no portion of the sample ACF following the first crossing of zero autocorrelation was considered in the autocorrelation models fit and reported herein. The single exponential model (SNX) was found to best fit the sample ACFs for all Columbia River Silt records considered herein.

Stationarity was assessed by performing the Kendall's τ test and the modified Bartlett's test (Table 2). Factors k, I_1 and I_2, shown in Table 2, represent the normalized scale of fluctuation, sampling length, and segment length, respectively, and were generated by Phoon et al. (2003) to modify the Bartlett's test for use with RFT. Factor's I_1 and I_2 are dependent on the autocorrelation model used to simulate the sample autocorrelation function, and are used to calculate the critical value of the modified Bartlett's test, B_{crit}. B_{crit} is compared to the maximum value of B_{stat}, or B_{max}, to test for stationary data at the 5% confidence level. Refer to Phoon et al. (2003) for the formulations for autocorrelation model-specific B_{crit}. Phoon et al. (2003) recommend the use of $I_2 = 1$ for $k \geq 10$, and $I_2 = 2$ for $5 \leq k < 10$, to ensure that the variance calculations consider enough observations to be statistically meaningful. However, difficulties may arise when using large, though regionally typical, sampling intervals (e.g., Δz = 50 mm) in soils with short distance autocorrelation. In fact, it may be impossible to achieve $k > 5$ in soils with very rapid value fluctuations about the trend. Since this issue appeared to arise in the evaluation of Columbia River Silt, the small sample method (Lacasse and Nadim, 1996) was employed for determining the segment standard deviation, σ.

Figure 2c shows the resulting profile of the modified Bartlett's statistic for the record considered and the SNX autocorrelation model. Typically, when B_{stat} crosses the B_{crit} line, the record is considered statistically inhomogeneous, and the record is considered to have failed the Modified Bartlett's test (a "strict" interpretation). However, when neglecting local, minor spikes in B_{stat} corresponding to thin sandy silt partings that were not significant in extent per Phoon et al. (2003) and as indicated by asterisks in Fig. 2b,

inspection of the B_{stat} profile indicates a stationary random field (a "qualified" pass). Table 3 summarizes the values of vertical scale of fluctuation, δ_v, quality of AMF fit in terms of the coefficient of determination R^2, B_{crit}, B_{max}, and Kendall's τ statistics for each record considered. As indicated in the summary, due to the frequency of very thin sandy silt partings within Columbia River Silt, many records would have failed the Modified Bartlett's test statistic under a "strict" interpretation. Note that while fitting high order polynomials may have produced more uniform residuals, there is no physical justification for doing so when the evidence clearly points to a linear increase in q_T.

Table 3. Summary of stationarity testing.

	SNX Model		Modified Bartlett's Test				Kendall's Test	
Record	δ_v **(mm)**	R^2	B_{crit}	B_{max}	**Strict Pass / Fail**	**Qualified Pass / Fail**	$Z_{\tau,\kappa}$	**Pass / Fail**
Upper Silt Layer								
P1	139	0.917	8.17	9.18	Fail	Pass	1.17	Pass
P2	135	0.974	8.38	5.26	Pass	N/A	-2.95	Fail
P3	145	0.989	8.81	17.65	Fail	Pass	-0.18	Pass
P4	112	0.995	8.81	10.83	Fail	Pass	-2.01	Fail
P5	210	0.996	11.57	13.67	Fail	Pass	4.76	Fail
P6	321	0.816	16.10	26.37	Fail	Pass	-1.40	Pass
P8	458	0.907	21.19	24.00	Fail	Pass	-0.83	Pass
P9	367	0.892	17.92	22.14	Fail	Pass	-0.79	Pass
P10	153	0.994	8.43	8.88	Fail	Pass	-0.57	Pass
P11	117	0.973	7.60	12.50	Fail	Pass	-0.21	Pass
Lower Silt Layer								
P2	216	0.991	10.96	5.08	Pass	N/A	-0.09	Pass
P4	97	0.994	6.34	7.39	Fail	Pass	-0.42	Pass
P6	59	0.998	N/a	N/a	N/A	N/A	2.22	Fail
P9	444	0.900	20.66	18.20	Pass	N/A	-0.29	Pass
P10	449	0.966	21.08	41.39	Fail	Pass	0.07	Pass
P11	179	0.872	10.24	11.46	Fail	Pass	-0.21	Pass

The use of Kendall's τ test, a non-parametric test for statistical independence is advantageous due to its relative ease of use, and because independent data are by definition stationary. Uzielli et al. (2004, 2007) compared the power of the Kendall's test statistic to the Modified Bartlett's test on stress normalized CPT data for statistically homogeneous soil units. They determined that although the Kendall's test statistic was less discriminatory, the determination of stationarity was comparable to that deduced through use of the Modified Bartlett's test statistic. Figure 3 presents stress normalized corrected cone tip resistance and friction ratio of the Columbia River Silt CPT records on Robertson's (1990) chart. It is observed that of the 15 records available for comparison, all were found to pass the Modified Bartlett's test, whereas 12 passed Kendall's test. Although the number of records is too low to develop a broad conclusion,

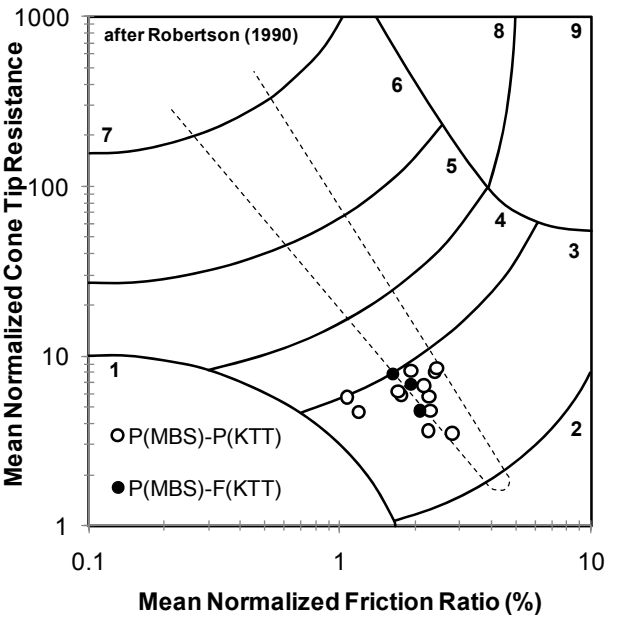

FIG. 3. Comparison of weak stationarity (P) or non-stationarity (F) by the Modified Bartlett's Test (MBS) and the Kendall's τ Test (KTT). Note: P6, lower layer, not shown due to inability to satisfy minimum requirements for the MBS.

it would appear that qualifying a pass in the Modified Bartlett's test to account for thin sand partings relaxes the severity of the test. With this in mind, the two tests for stationarity appear comparable. However, the use of a relaxed rejection criterion herein diverges from the approach reported in Uzielli et al. (2004, 2007), and may not readily allow the support of their findings. Further comparison of the Modified Bartlett's and Kendall's test for stationarity is warranted.

Vertical Random Field Parameters for Columbia River Silt

The random field model parameters deduced for the mechanical soil response to cone tip penetration, including the mean q_T, $COV_{W,v}$, SNX model and the associated δ_v are provided in Table 4 for the upper and lower Columbia River Silt layers. Since these values represent the first assessment for silt, no comparison to previously reported values can be made. In general, the upper Columbia River Silt layer may be represented by a mean q_T = 0.88 MPa, $COV_{W,v}$ = 18%, and δ_v = 190 mm, whereas the lower Columbia River Silt layer may be represented by a mean q_T = 1.51 MPa, $COV_{W,v}$ = 18%, and δ_v = 265 mm. Some variation in these layer-by-layer values is noted; for example, the COV in $COV_{W,v}$ is relatively large at 34 and 82% for the upper and lower layers, respectively. The comparison of δ_v developed with the VXP, VFR, and BLM procedures to the estimates of the Modified Bartlett's test (AMF method) is of interest due to the ease of their use. The δ_v calculated using the alternate methods, shown in Table 4, indicate that the AMF method provided comparable estimates of δ_v developed with less rigorous methods, and that no δ_v estimation method returned a value consistently greater than or less than another. Separately, the trend in corrected cone tip resistance is remarkably variable. Tests were typically performed within 100 to 150 m of one another, yet the *COV* in q_T trend is on the order of 55 to 60%. These variations in trend simply reflect the highly variable nature of seemingly uniform alluvial silt deposits.

SUMMARY AND CONCLUSIONS

This paper presents the development of random field model parameters for Columbia River Silt. The random field model parameters were found to represent a relatively high level of variability with short autocorrelation distances. Based on this study, the following conclusions regarding the random field modeling of corrected cone tip resistance are made:

1. The single exponential (SNX) ACF model was best suited for random field modeling of Columbia River Silt.
2. The vertical scale of fluctuation, δ_v, and vertical coefficient of inherent variability, $COV_{W,v}$, determined using autocorrelation model fitting (AMF) for the *upper silt layer* ranged from 112 to 367 mm and 10 to 25%, respectively, with mean δ_v and $COV_{W,v}$ equal to 190 mm and 18% respectively.
3. The δ_v and $COV_{W,v}$ determined using AMF for the *lower silt layer* ranged from 75 to 417 mm and 8 to 49%, respectively, with mean δ_v and $COV_{W,v}$ equal to 265 mm and 18% respectively.
4. Alternative and less rigorous estimation methods for δ_v generally produced similar estimates.
5. Alternate methods to estimate segment σ may be necessary in soils exhibiting short autocorrelation distances and explored with relatively large sampling intervals.

Table 4. Summary of random field parameters for Columbia River. Values of δ_v derived from the AMF method correspond to the SNX model.

CPTu Record	Mean q_T (MPa)	Trend in q_T (MPa/m)	$COV_{W,v}$ (%)	Record Length (m)	δ_v VRF (mm)	δ_v BLM (mm)	δ_v VXP (mm)	δ_v AMF (mm)
Upper Silt Layer								
P1	0.86	0.031	24.1	6.10	124	113	267	149
P2	0.91	0.065	9.5	10.95	190	106	291	135
P3	0.77	0.052	23.2	11.95	101	110	222	145
P4	0.61	0.048	22.2	14.00	99	151	311	112
P5	1.05	0.015	24.5	11.00	219	190	255	219
P6	0.86	0.032	14.6	13.15	406	850	318	321
P9	1.11	0.052	11.6	8.25	395	390	267	367
P10	1.16	0.128	11.0	5.10	136	127	272	153
P11	0.58	0.056	19.5	13.25	142	105	256	113
μ =	0.88	0.053	17.80	10.42	201	238	273	190
σ =	0.21	0.032	6.12	3.22	119	247	30	93
COV (%) =	23.3	59.7	34.4	30.9	59.3	103.7	10.9	48.9
Lower Silt Layer								
P2	1.75	0.001	8.2	5.20	150	183	224	216
P4	1.23	0.067	10.0	5.80	130	80	242	97
P6	1.45	0.052	20.2	7.45	75	52	248	59
P8	1.41	0.098	13.2	7.25	372	530	292	458
P9	1.41	0.049	8.9	5.75	417	560	280	444
P10	2.07	0.046	49.1	8.90	324	450	371	449
P11	1.25	0.055	13.4	7.60	251	108	315	132
μ =	1.51	0.052	17.57	6.85	246	280	282	265
σ =	0.30	0.029	14.48	1.31	131	224	50	180
COV (%) =	20.0	54.8	82.4	19.1	53.4	79.8	17.9	67.8
Aggregate Statistics								
μ =	1.16	0.053	17.70	8.86	221	257	277	223
σ =	0.40	0.029	10.19	3.09	122	230	39	138
COV (%) =	35.0	55.8	57.6	34.9	55.5	89.7	14.0	61.8

ACKNOWLEDGEMENTS

The author is grateful for permission by the owner and the geotechnical engineer of record, J. Jeffrey Wagner, P.E. of Hart Crowser, Inc., to use the data assessed herein. The author thanks the reviewers for their helpful comments.

REFERENCES

Baecher, G.B. (1999) Discussion of "Inaccuracies Associated with Estimation of Random Measurement Errors," *Journal of Geotechnical and Geoenvironmental Engineering*, ASCE, Vol. 125, No. 1, 79-81.

Baecher, G.B., and Christian, J.T., (2003) Reliability and Statistics in Geotechnical Engineering, John Wiley and Sons, London and New York.

Cafaro, F. and Cherubini, C. (2002) "Large Sample Spacing in Evaluation of Vertical Strength Variability of Clayey Soil," *Journal of Geotechnical and Geoenvironmental Engineering*, ASCE, Vol. 128, No. 7, 558-568.

DeGroot, D.J. and Baecher, G.B. (1993) "Estimating Autocovariancea of In-situ Soil Properties," Journal of Geotechnical and Geoenvironmental Engineering, ASCE, Vol. 119, No. 1, 147-166.

Evart, R.C. (2004) "Geologic Map of the Saint Helens Quadrangle, Columbia County, Oregon, and Clark and Cowlitz Counties, Washington," *Scientific Investigations Map 2834*, U.S. Geologic Survey, 23 pp.

Fenton, G.A. (1999) "Random Field Modeling of CPT Data," *Journal of Geotechnical and Geoenvironmental Engineering*, ASCE, Vol. 125, No. 6, 486-498.

Goldsworthy, J.S., Jaksa, M.B., Fenton, G.A., Kaggwa, W.S., Griffiths, D.V., and Poulos, H.G. (2007) "Effect of sample location on the reliability based design of pad foundations," *GeoRisk*, Taylor and Francis, Vol. 1, No. 3, 155-166.

Jaksa, M.B. (1995) "The Influence of Spatial Variability on the Geotechnical Design Properties of a Stiff, Overconsolidated Clay," *Ph.D. Thesis*, Faculty of Engineering, University of Adelaide.

Jaksa, M.B., Brooker, P.I., and Kaggwa, W.S. (1997) "Inaccuracies Associated with Estimation of Random Measurement Errors," *Journal of Geotechnical and Geoenvironmental Engineering*, ASCE, Vol. 123, No. 5, 393-401.

Lacasse, S., and Nadim, F. (1996) *"*Uncertainties in characterising soil properties,'' *Uncertainty in the geologic environment: from theory to practice*, GSP No. 58, ASCE, Reston, Va., 49–75.

Lumb, P. (1974) "Chapter 3: Applications of Statistics in Soil Mechanics," *Soil Mechanics - New Horizons*, Lee, I.K., Editor, American Elsevier, New York, 44-111.

Phoon, K.K. & Kulhawy, F.H. (1999) "Characterization of Geotechnical Variability," *Canadian Geotechnical Journal*., Vol. 36, No. 4, 612-624.

Phoon, K.K., Quek, S.T., An, P. (2003) "Identification of Statistically Homogenous Soil Layers Using Modified Bartlett Statistics," *Journal of Geotechnical and Geoenvironmental Engineering*, Vol. 129, No. 7, ASCE, Reston, Virginia. 649-659.

Robertson, P.K. (1990) "Soil Classification Using the Cone Penetration Test," *Canadian Geotechnical Journal*, Vol. 27, No. 1, 151-158.

Snavely, P.D., Jr., MacLeod, N.S., and Wagner, H.C. (1973) "Miocene tholeiitic basalts of coastal Oregon and Washington and their relations to coeval basalts of the Columbia Plateau," *Geological Society of America Bulletin*, Vol. 84, pp. 387–424.

Trimble, D.E. (1963) "Geology of Portland, Oregon and adjacent areas," *U.S. Geological Survey Bulletin 1119*, 119 pp.

Uzielli, M., Lacasse, S., Nadim, F., and Phoon, K.K. (2007) "Soil Variability Analysis for Geotechnical Practice," *Proceedings, Characterisation and Engineering Properties of Natural Soils*, Taylor and Francis, 1653-1752.

Uzielli, M., Vannucchi, G., and Phoon, K.K. (2004) "Assessment of Weak Stationarity Using Normalized Cone Tip Resistance," *Proceedings, 9th ASCE Specialty Conference on Probabilistic Mechanics and Structural Reliability*, Albuquerque, July 26-28, 2004 (CD-ROM).

Uzielli, M., Vannucchi, G., and Phoon, K.K. (2005) "Random field characterisation of stress-normalised cone penetration testing parameters," *Geotechnique*, Vol. 55, No. 1, 3-20.

VanMarcke, E.H. (1977) "Probabilistic Modeling of Soil Profiles," *Journal of the Geotechnical Engineering Division*, ASCE, Vol. 103, No. GT11, 1227-1246.

VanMarcke, E.H. (1978) "Probabilistic Characterization of Soil Profiles," *Site Characterization and Exploration*, Specialty Workshop, ASCE, Northwestern University, Evanston, Ill., 199-216.

Reliability-based design for allowable bearing capacity by considering differential settlement on highly fractured rock masses

Jianye Ching[1], Yu-Gang Hu [2], Zon-Yee Yang [3] and Jang-Quang Shiau [4]

[1] Associate Professor, Dept of Civil Engineering, National Taiwan University, Taipei, Taiwan. Tel: 886-2-33664328; Email: jyching@gmail.com
[2] Ph.D. Student, Dept of Civil Engineering, National Taiwan University, Taipei, Taiwan. Tel: 886-2-33663366#55034; Email: hu.yugang77@gmail.com
[3] Professor, Dept of Civil Engineering, Tamkang University, Taipei, Taiwan.
[4] Consulting Geotechnical Engineer, SJQ Geotechnical Professional Engineers Office, Taipei, Taiwan.

ABSTRACT

This study addresses the impact of spatial variability of rock masses on the differential settlement between two footings. A simple elastic perfectly plastic model based on the Hoek-Brown criterion and calibrated by a rock mass database is utilized to reproduce the spatial variation of the key rock mass properties in the finite element analyses and to simulate the deformation behavior of rock masses. With Monte Carlo simulations, stochastic samples of load-deformation curves of the two footings are obtained, which are further used to derive reliability-based allowable bearing stresses based on the design criteria of allowable angle of distortion. The analysis results show that the geological strength index (GSI) of rock masses and the uniaxial compressive strength of intact rock are the two dominant factors that affect the reliability-based design. Comparisons to the existing codes show that they are appropriate for poor to fair rock masses, conservative for good to very good rock masses and un-conservative for very poor rock masses.

INTRODUCTION

This study aims to build a random field model for the spatial variabilities of shear strength and deformability of highly fractured rock masses, and subsequently to conduct a preliminary analysis on differential settlements between two footings on rock masses. Efforts are made to quantify the magnitude of the variability in the deformation modulus and shear strength parameters, to quantify their scales of fluctuation, and to simulate the spatial variabilities by using random field models. Based on the results of Monte Carlo simulations, reliability-based design charts for allowable bearing capacity considering differential settlements will be developed.

Cherubini (2000) considered the ultimate bearing capacity on an idealized c-ϕ soil. Spatial variability and uncertainties of the shear strength are modeled by introducing a variance reduction factor that quantifies the degree of spatial averaging. Popescu et al. (2005) implemented full random field finite element analyses that explicitly consider spatial correlation for the similar purpose. Fenton and Griffiths (2002) considered strip footings over elastic media with uncertain

elastic constants to quantify differential settlement. Fenton and Griffiths (2005) considered total and differential elastic settlements under three-dimensional scenarios, modeled by three-dimensional random fields of elastic modulus.

RANDOM FIELD MODELS

Spatial variabilities of soil/rock properties can often be modeled as random fields. Among random field models, stationary lognormal random fields are widely used for soil/rock properties due to their simplicity and the fact that most soil/rock properties are non-negative. A stationary lognormal random field can be simulated by taking exponential of a stationary Gaussian random field, which can be in turn simulated by adding a desirable shift term to a zero-mean stationary Gaussian random field. However, in finite element analysis the properties of the elements are discrete; meaning a constant average value should be assigned to each element. A procedure, called the local average subdivision (LAS), for achieving the "local averaging" over each element was developed by Fenton and Vanmarcke (1990). Fenton and Griffiths (2003) further suggested that local averaging be conducted in the logarithm space of geotechnical parameters rather than in the original space.

CALIBRATION OF RANDOM FIELD MODELS FOR ROCK MASS PROPERTIES

For finite element analysis of differential settlement, the key parameters include the shear strengths and deformation moduli of the rock masses. Therefore, the calibrations for the random field models of the deformation modulus E_m of rock masses, the Hoek-Brown's constant m_i and the uniaxial compressive strength σ_{ci} are necessary. The GSI is a parameter based on engineering judgment for overall rock mass condition, rather than a precise physical parameter varying in space. In particular, GSI cannot be defined for a tiny volume (point) of rock mass. Hence, GSI cannot be modeled as a random field, which is a random function that can be defined for any given point. As a result, GSI will be treated as a variable rather than as a random field.

Deformation modulus. Hoek and Diederichs (2006) summarized the following GSI-based correlation equation between the deformation modulus and the disturbance factor based on a large database from China and Taiwan:

$$E_m\left(MPa\right) = 10^5\left(1 - D/2\right) / \left(1 + \exp\left(\frac{75 + 25D - GSI}{11}\right)\right) \tag{1}$$

where E_m is the deformation modulus of rock masses; D is the disturbance factor.

This database adopted by Hoek and Diederichs (2006) consists of more than 60 sites in China and Taiwan and more than 400 GSI vs. E_m data points, including more than 200 data points from sedimentary rock masses, more than 150 from igneous rock masses and more than 50 from metamorphic rock masses. The data points from this database are plotted in Figure 1 together with the above correlation equation with D = 0, 0.5 and 1.

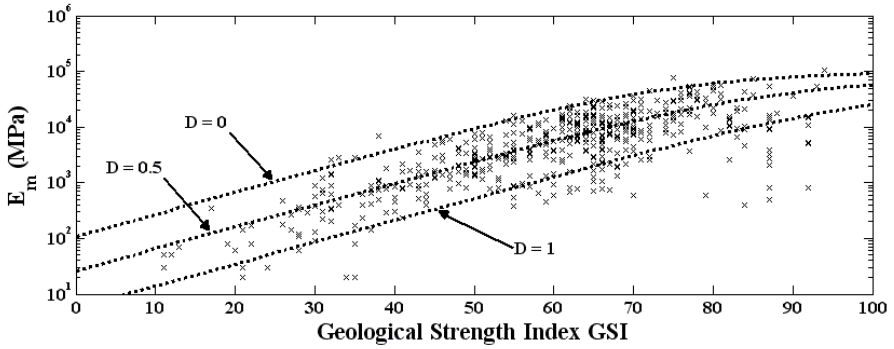

Figure 1 E_m vs GSI database from Taiwan and mainland China.

For the data points from a particular site, the correlation equation generally performs satisfactorily with a carefully chosen D value. In Figure 2, the data points from a site in China are plotted as a demonstration. For this site, D = 0.4726 obtains an optimal fit to the data points. The deviations of the actual data points to the D = 0.4726 line can be taken as the estimated coefficient of variation (c.o.v.) of the site-specific total uncertainty. In this case the c.o.v. = 0.348. This total uncertainty is a combined effect of (a) measurement errors of E_m, (b) transformation uncertainty of Eq. (1) and (c) spatial variability of E_m. The same curve fitting exercise is conducted for all sites in the database, and the resulting estimates for D and E_m c.o.v.s are plotted in Figure 3. It is clear that D values for most sites are within [0.2, 1.0], while the E_m c.o.v.s are within [0, 1.5].

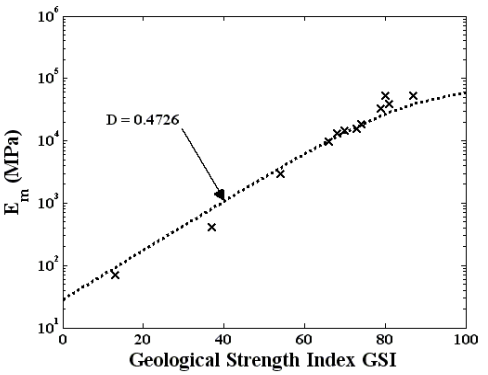

Figure 2 E_m vs GSI data points from a site in China.

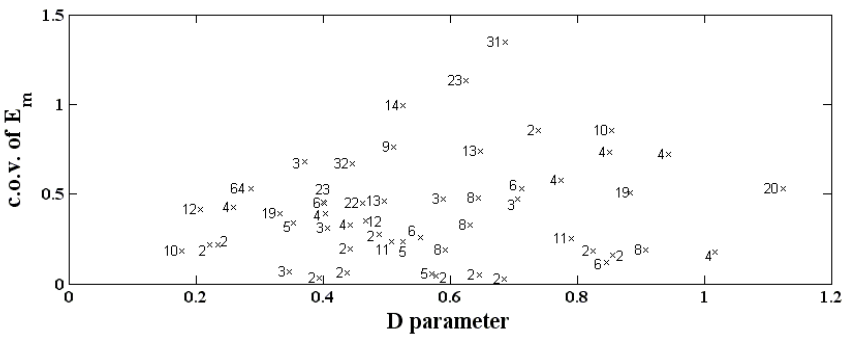

Figure 3 Estimates for D and c.o.v.s for all sites in China and Taiwan. The number next to each point indicates the number of data points at the site.

Uniaxial compressive strength and the Hoek-Brown constant. The mean value of σ_{ci} random field can be determined by uniaxial compressive tests on intact rock samples, which are routinely done in practice. Therefore, this mean value will be treated as a number to be determined from laboratory tests. For the c.o.v. of σ_{ci} random field, Gunsallus and Kulhawy (1984) compiled a database of σ_{ci} for eight sedimentary rock units in northeastern United States. Each unit contains between 2 and 19 uniaxial compressive test samples. The analysis showed that the c.o.v. of the total variability for σ_{ci} ranges widely from 7% to 59% and is on average 27%. In principle, besides the spatial variability, these total variabilities may also contain measurement errors. In this study, 30% is chosen to be the c.o.v. of the σ_{ci} random field.

Mohr-Coulomb parameters. The most up-to-date version of the Hoek-Brown criterion (Hoek et al. 2002) is used to convert the parameters (GSI, m_i, σ_{ci}) into the Mohr-Coulomb parameters (c, ϕ) in this study:

$$\sigma_{1f} = \sigma_3 + \sigma_{ci}\left(m_b \frac{\sigma_3}{\sigma_{ci}} + s\right)^a \tag{2}$$

where σ_3 is the confining pressure; σ_{1f} is the maximum principle stress at failure; m_b, s and a are model parameters depending on GSI and D:

$$m_b = m_i \exp\left(\frac{GSI-100}{28-14D}\right) \qquad s = \exp\left(\frac{GSI-100}{9-3D}\right) \qquad a = \frac{1}{2} + \frac{1}{6}\left[\exp\left(\frac{-GSI}{15}\right) - \exp\left(\frac{-20}{3}\right)\right] \tag{3}$$

where m_i is the Hoek-Brown constant, depending on rock type; D is the disturbance factor.

Hoek et al. (2002) provided the following equations to convert the Hoek-Brown parameters into the Mohr-Coulomb parameters:

$$\phi = \sin^{-1}\left[\frac{6a \cdot m_b\left(s + m_b\sigma_{3n}\right)^{a-1}}{2(1+a)(2+a) + 6a \cdot m_b\left(s + m_b\sigma_{3n}\right)^{a-1}}\right]; \quad \frac{c}{\sigma_{ci}} = \frac{\left[(1+2a)s + (1-a)m_b\sigma_{3n}\right]\left(s + m_b\sigma_{3n}\right)^{a-1}}{(1+a)(2+a)\left(1 + \frac{6a \cdot m_b\left(s + m_b\sigma_{3n}\right)^{a-1}}{(1+a)(2+a)}\right)^{1/2}} \tag{4}$$

where σ_{3n} is equal to the maximum σ_3 of interest divided by σ_{ci}. In this study, σ_{3n} is taken to be 0.25.

Scales of fluctuation. The scales of fluctuation (SOF) were assumed known. In reality, these scales are unknown, and in fact, it is quite difficult to estimate them. This is because the estimation of horizontal scales of fluctuation (δ_h) and vertical scales of fluctuation (δ_z) typically requires multiple data points in close proximity. While such data points may be readily available for soil properties, they are relatively rare for rock mass properties. Moreover, these SOFs are expected to vary with rock types since the formation of various types of rocks is quite different, hence the spatial correlation pattern should be also different. A possible solution for sedimentary rocks is to postulate that their SOFs are similar to those for the forming soils, hence they should more or less inherit the SOFs from the

soils. This study adopts the bounds for soils as the bounds of the SOFs of σ_{ci} random field: $3m \le \delta_h \le 80m$ and $0.1m \le \delta_z \le 6.2m$ [Ranges of SOFs for strength-related properties of soils, adopted from Phoon (1995)].

RANDOM FIELD FINITE ELEMENT ANALYSIS

Figure 4 shows the mesh employed in the finite element analyses (ABAQUS). Two strip footings are modeled as two rigid plates loaded at the surface of the rock masses. The footings are assumed to have rough bases.

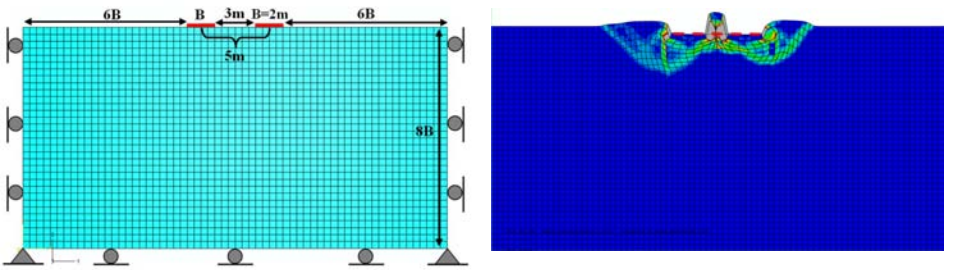

Figure 4 Finite Element Mesh: (Left-Hand) Un-deformed Shape; (Right-Hand) Deformed Shape (the Contour Quantifies the Plastic Strains).

A linearly elastic and perfectly plastic constitutive model is adopted to simulate the behavior of rock masses. Plane strain eight-node quadratic elements are used, and the large-deformation mode is turned on to accommodate nonlinearity induced by large deformation. Except the Poisson's ratio, ν, being fixed at 0.3, other parameters (including c, ϕ and E_m) for each element are randomly simulated according to the following steps. These steps require the GSI and (δ_h, δ_z) to be prescribed as certain values.

1. Randomly pick a sample (D_S, cov_S) from the points in Figure 3.
2. Based on the (D_S, cov_S) sample in Step 1 and the prescribed GSI, obtain the mean value and c.o.v. of the E_m random field. Together with the prescribed δ_h and δ_z, simulate the local average samples of E_m for all elements.
3. Based on the rock type, determine the mean value of m_i random field. The c.o.v. is taken to be 15%. Together with the prescribed δ_h and δ_z, independently simulate the local average samples of m_i for all elements.
4. Based on the prescribed mean value of σ_{ci}, its 30% c.o.v. and the prescribed δ_h and δ_z, independently simulate the local average samples of σ_{ci} for all elements.
5. Based on the D_S sample in Step 1, prescribed GSI and sampled m_i for all elements in Step 3, c/σ_{ci} and ϕ can be obtained for all elements by using Eq. (4). Multiplying c/σ_{ci} with the local average samples of σ_{ci} in Step 4 will yield the c parameters for all elements.

Doing the above steps once yields a set of local average samples (c, ϕ, E_m) for all elements in the finite element analysis. For each realization of c, ϕ and E_m random samples for all elements, the footings are subjected to vertical loads up to the point of non-convergence. The limiting bearing stress, q_L, corresponding to the limiting angle of distortion can be readily identified from the q versus d_a (angles of distortion) plot.

RELIABILITY-BASED DESIGN FOR DIFFERENTIAL SETTLEMENT OF STRIP FOOTINGS ON ROCK MASSES

For a set of prescribed GSI, mean value of σ_{ci}, δ_h and δ_z, 1000 sets of c, ϕ and E_m random field samples are drawn. For each set of random field samples, the aforementioned finite element analysis is taken to obtain a sample of load-deformation curve and hence a sample of limiting bearing stress q_L. These 1000 samples of q_L can then be used to develop the allowable bearing stress q_a vs failure probability P_F plot. Here, the term "failure" means "unable to meet the limiting angle of distortion criterion". The relation between P_F and q_a is as follows:

$$P_F(q_a) \approx \frac{1}{1000}\sum_{i=1}^{1000} \mathrm{I}\left(q_a > q_L^{(i)}\right) \tag{5}$$

where I(.) is the indicator function: 1 if the statement is true and 0 otherwise.

Main results. The sensitivity studies under four combinations of δ_h and δ_z and two mean values of m_i taken for simulations. The upper and lower bounds for the scales of fluctuation (i.e. 30m < δ_h < 80m and 0.1m < δ_z < 6.2m) are taken to make the four extreme combinations of δ_h and δ_z, while two mean values of m_i, 5 and 35, are attempted. In the results, δ_h and δ_z do not significantly affect q_a because the distance between foundations is much smaller than the SOF. The two plots in Figure 5 demonstrate the variation of q_a for P_F = 0.1, 0.01 and 0.001 (solid, dotted and dashed lines, respectively) with respect to GSI for limiting angle of distortion = 1/500 and for footing spacing = 5m. In the same plots, the ultimate bearing capacity q_u based on Hansen's formula (Hansen 1961), where c and ϕ are checked based on the mean values of m_i and σ_{ci}, are plotted as the thick solid lines. The footing spacing can in principle affect the angle of distortion, therefore a larger spacing of 10m is also attempted. The trend is similar and the effect of footing spacing is found to be not as significant as other influential factors. Therefore, only the plots for the spacing = 5m are presented for brevity. The mean value of σ_{ci} is taken to be 1 MPa for Figure 5.

Sensible trends are observed: q_a grows with increasing P_F, increasing GSI, increasing mean value of m_i, increasing mean value of σ_{ci} and increasing limiting angle of distortion. It is evident that GSI is the most important parameter that affects q_a. Although not as influential as GSI, the mean values of σ_{ci} and m_i (i.e. the shear strength of intact rock) have certain effect on q_a. The horizontal scale of fluctuation, δ_h, does not significantly affect q_a, while the vertical one δ_z has greater effect. It is found that q_a is always less than the ultimate bearing capacity q_u, but approaches q_u as GSI becomes large. Moreover, the difference between q_a and q_u is larger for large mean value of m_i, and vice versa. This implies that for rocks with large m_i (e.g. granite) exceedance of distortion angle dominates the design for small GSI, and the ultimate failure may dominate for large GSI. However, for rocks with small m_i (e.g. shale, claystone) the ultimate failure may dominate for a wider range of GSI. The recommended allowable bearing stresses for limiting angles of distortion of 1/500, 1/250 and 1/150 are developed in Table 1. The ranges in the recommended q_a incorporate the variation of q_a with respect to the various δ_h, δ_z and footing spacing of 5m and 10m.

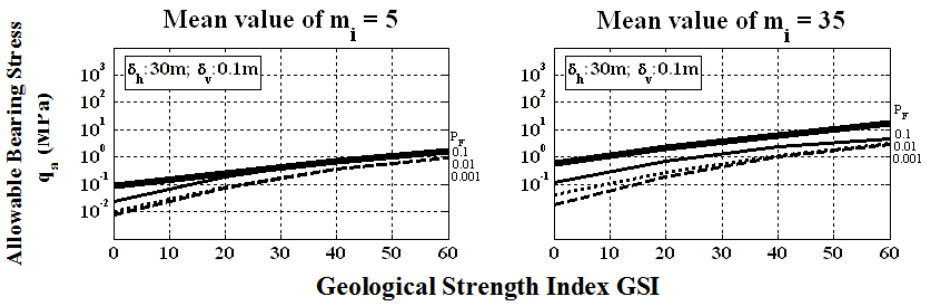

Figure 5 Allowable Bearing Stress q_a for P_F = 0.1, 0.01 and 0.001 (Solid, Dotted and Dashed Lines, Respectively) with Respect to GSI [Mean Value of σ_{ci} = 1MPa; Limiting Angle of Distortion = 1/500; Footing Spacing = 5m].

Table 1 Ranges for q_a (in MPa) Recommended by This Study

Limiting angle of distortion = 1/500									
Mean σ_{ci} (MPa)	P_F	Mean value of m_i = 5				Mean value of m_i = 35			
		GSI = 0	20	40	60	GSI = 0	20	40	60
1	0.1	0.02~0.05	0.17~0.22	**0.65~0.76**	**1.19~1.46**	0.06~0.13	**0.53~0.71**	**1.20~2.20**	**2.59~3.73**
	0.01	0.004~0.02	0.06~0.09	0.37~0.39	**0.86~0.89**	0.01~0.04	0.19~0.26	**0.91~1.23**	**1.23~3.24**
	0.001	0.002~0.01	0.03~0.08	0.30~0.36	**0.73~0.85**	0.003~0.02	0.12~0.19	**0.72~1.20**	**0.78~2.96**
10	0.1	0.02~0.06	**0.27~0.73**	**1.94~5.11**	7.86~10.48	0.04~0.11	**0.66~2.26**	**4.90~13.55**	16.26~25.68
	0.01	0.01~0.03	0.08~0.21	**0.74~1.63**	**4.67~6.55**	0.01~0.03	**0.20~0.90**	**1.90~6.97**	9.12~19.97
	0.001	0.003~0.01	0.04~0.08	**0.37~0.76**	**3.36~6.11**	0.005~0.01	**0.13~0.47**	**1.29~5.79**	**5.18~16.72**
100	0.1	0.02~0.08	**0.24~1.11**	**2.39~10.49**	20.12~70.07	0.04~0.15	**0.42~3.50**	**3.92~36.16**	33.3~165.5
	0.01	0.004~0.02	0.06~0.21	**0.74~2.45**	6.67~27.61	0.01~0.15	**0.11~1.10**	**1.45~13.71**	12.09~72.26
	0.001	0.001~0.01	0.02~0.08	**0.31~0.97**	**3.60~18.01**	0.001~0.02	**0.07~0.54**	**0.57~8.07**	7.07~52.29
Limiting angle of distortion = 1/250									
Mean σ_{ci} (MPa)	P_F	Mean value of m_i = 5				Mean value of m_i = 35			
		GSI = 0	20	40	60	GSI = 0	20	40	60
1	0.1	0.03~0.06	0.19~0.23	**0.67~0.71**	**1.22~1.46**	0.10~0.15	**0.65~0.76**	**1.94~2.40**	**2.59~4.74**
	0.01	0.004~0.02	0.07~0.10	**0.36~0.40**	**0.86~0.96**	0.02~0.05	0.26~0.29	**1.00~1.23**	**1.21~3.26**
	0.001	0.002~0.01	0.05~0.08	0.36~0.37	**0.70~0.91**	0.01~0.03	0.17~0.23	**0.83~1.14**	**0.77~2.87**
10	0.1	0.05~0.09	**0.51~1.00**	**2.92~5.11**	8.90~10.39	0.08~0.23	**1.19~3.00**	7.24~14.21	17.96~31.37
	0.01	0.01~0.03	0.17~0.34	**1.29~2.00**	**5.56~7.04**	0.02~0.07	**0.38~1.3**	**2.95~8.00**	9.38~20.81
	0.001	0.006~0.02	0.01~0.15	**0.70~1.13**	**4.58~6.82**	0.01~0.02	**0.24~0.80**	**2.11~8.00**	**5.39~19.54**
100	0.1	0.02~0.16	**0.43~2.27**	**5.14~17.97**	34.30~83.31	0.08~0.30	**0.84~6.34**	7.77~56.95	63.42~220.30
	0.01	0.004~0.03	**0.12~0.42**	**1.64~4.71**	12.69~46.93	0.01~0.05	**0.21~2.10**	**2.52~24.22**	23.67~107.20
	0.001	0.002~0.02	0.04~0.17	**0.69~2.10**	6.95~30.64	0.01~0.04	**0.12~1.06**	**1.33~15.69**	13.43~85.53
Limiting angle of distortion = 1/150									
Mean σ_{ci} (MPa)	P_F	Mean value of m_i = 5				Mean value of m_i = 35			
		GSI = 0	20	40	60	GSI = 0	20	40	60
1	0.1	0.03~0.06	0.19~0.26	**0.66~0.71**	**1.22~1.47**	0.13~0.17	**0.69~0.73**	**1.91~2.35**	**2.60~4.74**
	0.01	0.006~0.02	**0.08~0.10**	**0.33~0.40**	**0.85~0.97**	0.03~0.07	0.29~0.30	**1.00~1.16**	**1.21~3.29**
	0.001	0.003~0.01	0.06~0.09	**0.33~0.40**	**0.69~0.93**	0.01~0.04	0.22~0.27	**0.89~1.13**	**0.75~2.88**
10	0.1	0.07~0.14	**0.73~1.13**	**3.56~5.11**	8.79~10.24	**0.13~0.40**	**1.74~3.46**	9.05~14.36	18.36~30.80
	0.01	0.02~0.04	**0.26~0.45**	**1.73~2.25**	**5.08~6.92**	0.03~0.11	**0.57~1.52**	**3.80~7.87**	9.24~15.99
	0.001	0.01~0.03	0.13~0.22	**1.05~1.40**	**4.86~5.62**	0.02~0.03	**0.39~0.97**	**2.61~7.86**	**5.30~19.57**
100	0.1	0.02~0.28	**0.68~3.77**	9.08~25.25	48.05~91.51	**0.14~0.51**	**1.44~9.97**	12.79~77.08	95.45~233.00
	0.01	0.004~0.05	**0.18~0.74**	**2.93~7.56**	19.46~55.44	0.02~0.13	**0.36~3.13**	**4.21~33.04**	39.28~147.80
	0.001	0.002~0.04	0.07~0.29	**1.00~3.53**	11.17~43.66	0.01~0.07	**0.21~1.76**	**2.22~21.30**	22.52~98.18

Comparison to existing design codes. The allowable bearing stresses given in existing codes. With the exception of the Detroit code, q_a ranges from 0.4 to 5.8 MPa. The cells in Table 1 that overlap with the range of [0.4 MPa, 5.8 MPa] are boldfaced. This range is most consistent to the q_a recommended in the table for GSI = 40 with a wide range of mean values of σ_{ci} and m_i, for GSI = 20 with mean value of σ_{ci} of 10~100 MPa, and for GSI = 60 with mean value of σ_{ci} of 1~10 MPa. Goodman (1989) characterized the quality of rock masses as very poor for

GSI < 20, poor for 20 < GSI < 40, fair for 40 < GSI < 60, good for 60 < GSI < 80 and very good for GSI >80. Based on the above observations, the existing codes seem appropriate for poor to fair rock masses. They may be quite conservative for good to very good rock masses and un-conservative for very poor rock masses.

CONCLUSION

Differential settlement between footings located on rock masses is studied by using random field finite element analyses. The random field parameters are carefully calibrated by using database for mechanical properties of rock masses. Reliability-based allowable bearing stresses for several limiting angles of distortion are identified based on the simulations results for the random field finite element analyses. These recommended reliability-based allowable bearing stresses are presented as design charts and table. Comparisons between the recommended allowable stresses with those found in the existing codes show that the existing codes are appropriate for poor to fair rock masses, conservative for good to very good rock masses and un-conservative for very poor rock masses.

REFERENCES

Cherubini, C. (2000). Reliability evaluation of shallow foundation bearing capacity on c-ϕ soils. *Canadian Geotechnical Journal*, 37, 264-269.

Fenton, G.A. and Griffiths, D.V. (2002). Probabilistic foundation settlement on spatially random soil. ASCE *Journal of Geotechnical and Geoenvironmental Engineering*, 128(5), 381-390.

Fenton, G.A. and Griffiths, D.V. (2003). Bearing capacity prediction of spatially random c- soils. *Canadian Geotechnical Journal*, 40, 54-65.

Fenton, G.A. and Griffiths, D.V. (2005). Three-dimensional probabilistic foundation settlement, ASCE *Journal of Geotechnical and Geoenvironmental Engineering*, 131(2), 232-239.

Fenton, G.A. and Vanmarcke, E.H. (1990). Simulation of random fields via local average subdivision. ASCE *Journal of Engineering Mechanics*, 116(8), 1733-1749.

Goodman, R.E. (1989). *Introduction to Rock Mechanics*, 2nd Ed.. John Wiley & Sons, New York.

Hansen, J.B. (1961). A general formula for bearing capacity. *Bulletin No. 11*, Danish Technical Institute, Copenhagen, 38-46.

Hoek, E. and Brown, E.T. (1980). *Underground Excavations in Rock*. London, Institution of Mining and Metallurgy.

Hoek, E. and Diederichs, M.S. (2006). Empirical estimation of rock mass modulus. *International Journal of Rock Mechanics and Mining Science*, 43, 203-215.

Hoek, E., Carranza-Torres, C.T. and Corkum, B. (2002). Hoek-Brown failure criterion-2002 edition. *Proceedings of the Fifth North American Rock Mechanics Symposium*, Toronto, Canada.

Phoon, K.K. (1995). *Reliability-Based Design of Foundations for Transmission Line Structures*. Ph.D. Dissertation, Cornell University.

Popescu, R., Deodatis, G. and Nobahar, A. (2005). Effect of random heterogeneity of soil properties on bearing capacity. *Probabilistic Engineering Mechanics*, 20, 324-341.

Assessment of Levee Site Variability as a Function of the Number of Explorations

Christopher B. Groves[1], Hollie L. Ellis[2], and N. Kyle Tabor[3]

[1] Shannon & Wilson, Inc., 2043 Westport Center Drive, St. Louis, MO 63146, PH 314-699-9660, email cbg@shanwil.com
[2] Shannon & Wilson, Inc. 400 N 34th Street, Suite 100, PO Box 300303, Seattle, WA 98103-8600, email hle@shanwil.com
[3] Shannon & Wilson, Inc., 2043 Westport Center Drive, St. Louis, MO 63146, PH 314-699-9660, email nkt@shanwil.com

ABSTRACT

Alluvial site variability and the probability of a geotechnical levee failure are interrelated. The probability of a geotechnical levee failure generally increases with site variability. Highly variable sites are difficult to characterize, and the likelihood of encountering the worst conditions during a subsurface investigation is small. Increasing the number of borings increases the knowledge of the site but does not entirely eliminate the uncertainty. Variability of soil parameters have been addressed by estimating the mean and standard deviation of the various parameters and computing the uncertainty in the computed factor of safety based on a mean value analysis. This method estimates the uncertainty of the factor of safety based on the variability of the soil parameters, but does not address variability with regard to site stratigraphy, which has much more uncertainty. Groves et al. (2010) proposed a method to address the probability of a geotechnical levee failure based on the variability of soil stratigraphy.

INTRODUCTION

Purpose. Undiscovered conditions may be present between the borings which may lead to inadequate levee design, posing an unanticipated hazard to the people and properties protected by the levee. It is desirable to have a method of evaluating or assessing the information gathered during site exploration to quantify the potential hazard posed by the undiscovered conditions. For this study, we are most concerned with levee failures that occur due to site conditions that were undiscovered at the time of the design.

The purpose of this paper is to describe our approach to evaluating exploration and analytical results to estimate the uncertainty in site conditions that may be inferred from those results. The practical application of this approach is to provide a rational method of determining if further, more closely-spaced explorations or tests are needed.

Scope. Probabilistic methods have been used to quantify flood hazards and conditional probability of levee failure; but, as yet, it is difficult to quantify the probability that a levee reach can or cannot withstand a specific flood. Methods have been proposed to address variability in soil parameters, but no accepted method exists to address the spatial variability of site soils. The issue is not the proper friction angle of a sand deposit, it is whether the sand is continuous.

Seepage and stability analyses are often conducted in a deterministic manner to compute a factor of safety. The apparent thinking is that if a factor of safety of 1.4 is computed for the worst known conditions along the levee, the factor of safety at all locations must be greater than 1.0. This is independent of the number of borings.

We have proposed a method to estimate the probability of a potential failure. The method assumes that exploratory borings or cone penetration tests determine the subsurface conditions at one location with reasonable accuracy. A selected mode of failure is analyzed repeatedly for many borings or cone penetration tests in a given levee reach. The resulting factor of safety for levee stability is plotted on a cumulative probability curve.

This paper presents an evaluation of the confidence of the results based on the size of the data sample. The variability of the site conditions is based on the variability encountered in the exploratory borings or cone penetration test (CPT) holes along a reach where the subsurface conditions appear to be similar. We assume that the variability encountered in the explorations and tests is representative of the spatial variability of the site. For this study we computed the factor of safety for landside stability under steady state seepage conditions. Other modes of failure may be analyzed by the method proposed herein.

APPROACH

Our approach is to estimate site variability using traditional deterministic, limit equilibrium stability analysis methods to determine landside factors of safety (FOS). The key assumption of this approach is that the variability of the calculated FOS population reflects the combined spatial variability of the subsurface soils, variability of the embankment soils, variability of the levee geometry, and variability introduced by levee structural features (e.g. cutoff walls, berms, etc.). As described below, we estimate the site variability for actual levee conditions and for hypothetical uniform levee conditions to infer what portion of the total variability can be attributed to spatial variability of the subsurface soils.

The FOS population used in our study was determined from 40 CPT soundings taken along a 5-mile reach of levee from the California Central Valley Levee Evaluation Program. All CPT were obtained on a single geologic landform. The resulting population of FOS were analyzed using statistical methods to determine the probability of encountering a factor of safety of less than or equal to one in this population.

Other Assumptions. This approach assumes that CPT soundings adequately determine the physical properties of the soil at one location. Permeability values were selected based on the normalized soil behavior type determined from CPT soundings. Estimated hydraulic conductivity values were selected for each soil behavior type based on recommendations from Lunne et al. (1997). Soil layers were assumed to extend horizontally to both the riverside and landside of the levee embankment. The soil layers derived from the CPT data were taken as the actual soil conditions. The authors believe that our assumption is valid that the levee foundation identified in each boring or test is a relatively unbiased, random sample of the subsurface conditions.

Levee Geometry. Levee geometry has a significant effect on the landside stability of a levee. The focus of this study is to evaluate the variability of the foundation materials and not the effects of levee geometry. Therefore, this analysis was based on assumed uniform levee geometry. The uniform levee geometry was developed based on the median levee cross section within the levee reach. The purpose of using a uniform section was to eliminate the bias in the calculated FOS created by existing manmade cut-off walls, seepage berms, and variable levee crest widths and side slope angles.

Analysis Method. Underseepage and stability analyses were performed with Geo-Studio Suite 2007 which included SEEP/W and SLOPE/W. Underseepage analyses were performed to determine the steady-state pore pressures that were used in the stability analyses. It is understood that for many levees steady state seepage is not achieved for short duration floods.

STATISTICAL ANALYSIS

The statistical analysis consisted of an evaluation of the distribution of the population of FOS for each levee configuration (original geometry, modified geometry, and repair scenarios) and each river stage (as stated above); and determination of the probability of obtaining an FOS of less than or equal to one.

The distribution of the population of FOS values was evaluated by performing a goodness-of-fit test of normality on the data. This test is a method of determining if a data set can be approximated by a normal distribution. The test consists of ordering the data, calculating a cumulative probability based on a uniform distribution of the observed data, and calculating the inverse of the normal distribution for each of the calculated cumulative probabilities. The inverse normal distribution values are plotted against the data values and a least-squares linear regression is performed to determine the degree of correlation between these two sets of values. A high degree of correlation is an indication that the data set is approximately normally distributed. An example of a goodness-of-fit test for the original levee geometry case and a 200-year minus 2 feet river stage is shown in Figure 1. The normal approximation to the actual data set is shown in Figure 2.

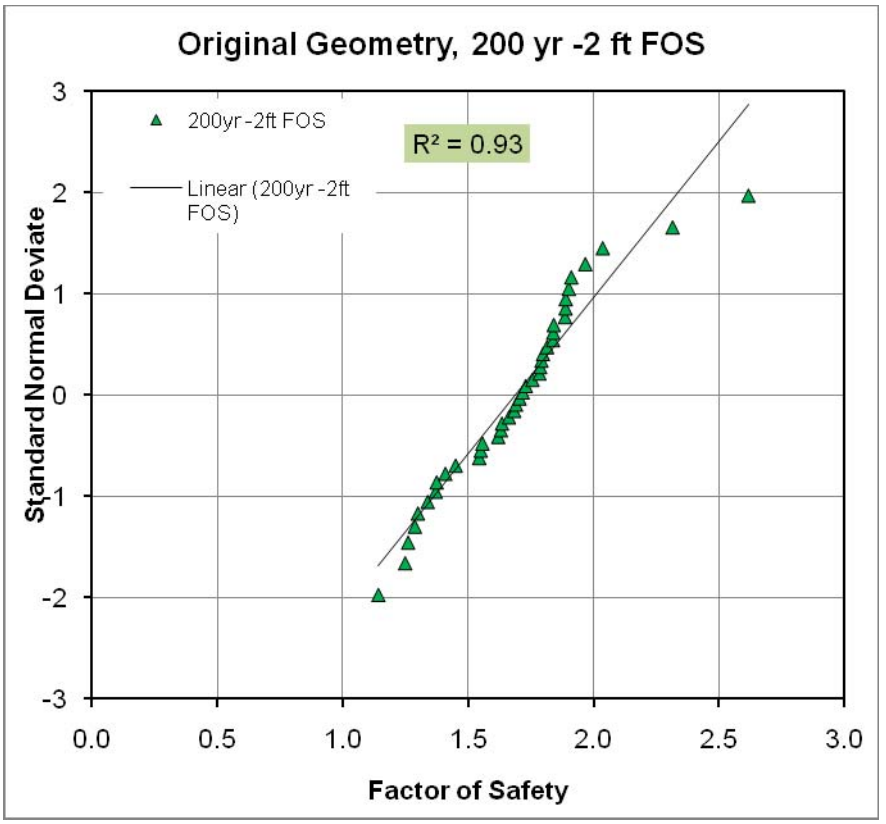

Figure 1. Normal approximation to data set.

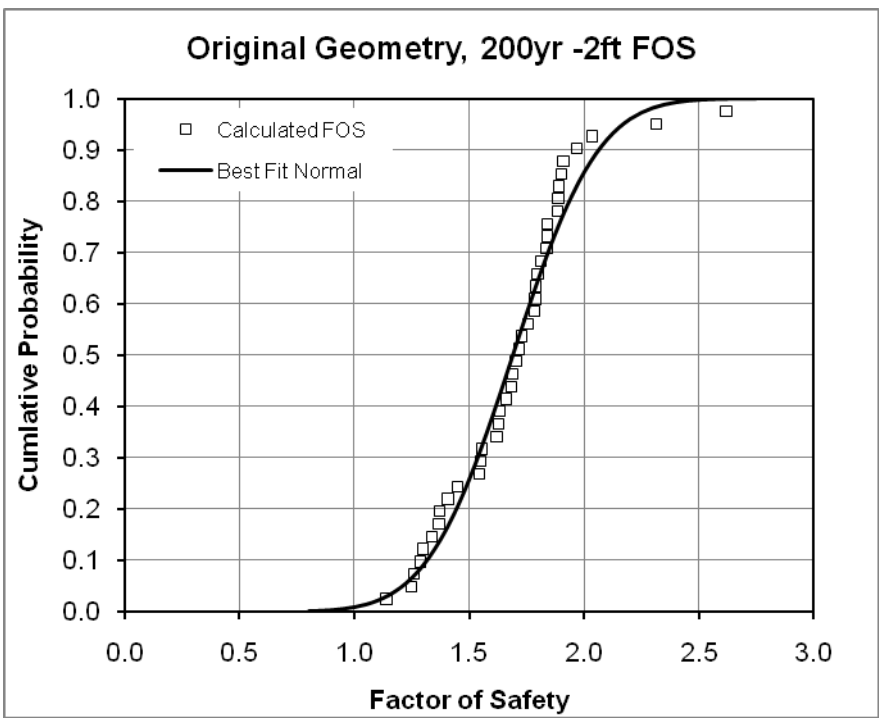

Figure 2. Goodness-of-fit test for normality.

The correlation coefficients for the goodness-of-fit tests ranged from 0.92 to 0.99 for the 20 cases (5 geometry scenarios X 4 river stages). The relatively high correlations indicate that the FOS populations can reasonably be further analyzed using the normal distribution. There is some departure from normality at the tails of the distribution, but, in our opinion, these departures do not substantially affect our analysis.

Once we conclude that the FOS populations are approximately normally distributed, it is a straightforward calculation to determine the probability of obtaining an FOS of one or less in each population. The probability of obtaining an FOS of one or less can also be seen graphically in Figure 2. In this figure, the uniform section has a probability of about 0.2 of having an FOS of one or less, whereas the repair options have probabilities of 0.01 or less.

Our research involved performing seepage and stability analysis for a given levee reach with 40 CPTs. Each probing was analyzed using the same methods to create a subsurface profile for each probing location. Seepage and stability analyses were performed to determine a FOS for each location. The FOS dataset was then analyzed statistically. The dataset was found to approximately follow a normal distribution with an average FOS of 1.62 and a standard deviation of 0.30. When plotting the cumulative probability distribution of the FOS, we observed that the probability of failure (P_f) was about 2.0%.

Results. In order to evaluate the adequacy of the number of borings, the original dataset of the 40 FOS was randomly sampled with sets of 20, 10, and 5. Subsets of data from the original dataset were randomly sampled 1000 times.

Table 1. The random sampling resulted in the following estimates of P_f:

Sample Size	40	20	10	5
Probability of Failure	2.0%	2.4%	2.5%	3.2%

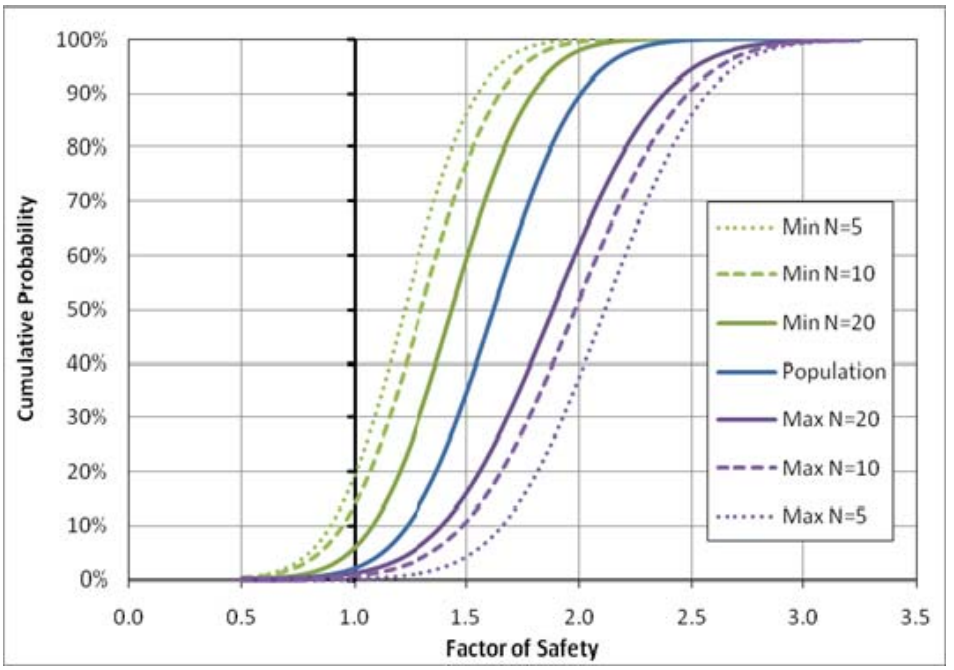

Figure 3. Cumulative probability distribution as a function of sample size.

The above figure shows the distributions for the cumulative probability distribution for our original data (Population) and sampled subsets for sample size of 20, 10, and 5. The minimum and maximum cumulative probability curves from each of the 1,000 samples of each subset are plotted to illustrate the potential range of results that could be obtained for each sample size. As the sample size of the randomly sampled data sets decreases, it can be seen that the potential range increases, with the consequence of greater uncertainty (lower confidence) in the estimate of P_f.

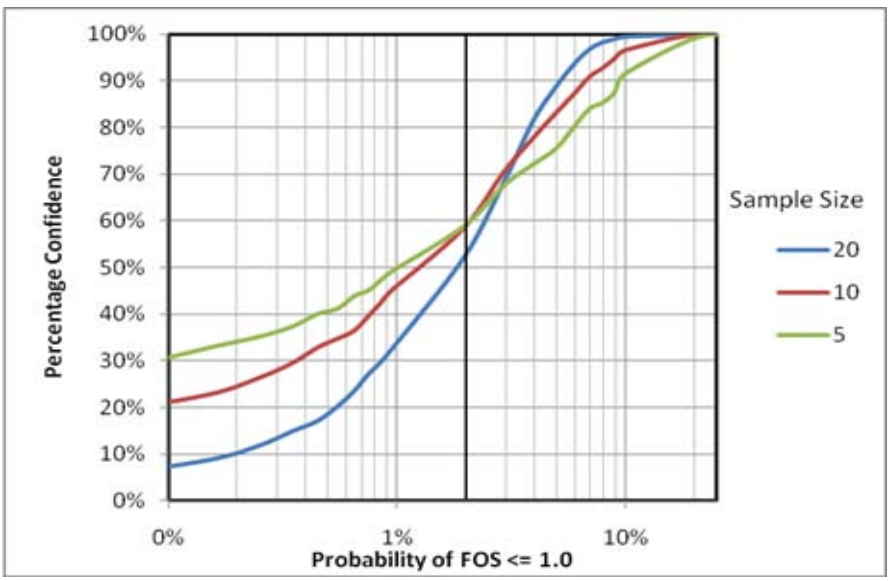

Figure 4. Percent confidence as a function of sample size.

Figure 4 shows the cumulative distribution function of P_f for each of the randomly sampled datasets. These curves show that, for a sample size of 5, there is about an 8% probability that P_f is greater than 10%, 50% probability that P_f is greater than 1%, and 70% probability that P_f is greater than 0.1%. For samples sizes of 10 and 20, the probabilities are approximately 4% - 53% -79% and 1% - 67% - 92%, respectively.

Table 2. The Confidence that P_f is greater than a certain percent

Sample size	**>10% P_f**	**>1% P_f**	**>0.1 %P_f**
5 samples	8 %	50 %	70 %
10 samples	4 %	53 %	79 %
20 samples	1 %	67 %	92 %

CONCLUSIONS

- A normal distribution appears to be adequate for this case (40 CPT soundings) when plotting factor of safety against cumulative probability. Correlation coefficients from 0.92 to 0.99 were consistently computed.
- If a levee alignment were to cross greatly different landforms, the correlation coefficient may be lower and some distribution other than normal may be encountered.
- The method indicates the relative confidence of a smaller sample size.
- While it is generally the case that increasing sample size leads to increased confidence in the results, this research illustrates the influence of sample size on the uncertainty and sensitivity of a P_f estimate.
- Any sample size can either under- or over-predict P_f. The key is that larger sample sizes provide greater confidence in the prediction, i.e. less uncertainty in either direction.

REFERENCES

Geo-Slope International, 2007, SLOPE/W v 7.13: Calgary, Alberta, Geo-Slope International.

Geo-Slope International, 2007, SEEP/W v 7.13: Calgary, Alberta, Geo-Slope International.

Groves, Christopher; Ellis, Hollie; and Tabor, N. K. (2010), Statistical evaluation of levee design data, *Advances in Analysis, Modeling and Design* (D. Fratta, A.J. Puppala, and B. Muhunthaneds.), GeoFlorida, Geotechnical Special Publication No. 199, ASCE, 1962-1971.

Lunne, Tom; Robertson, P. K.; and Powell, J. J. M., 1997, Cone penetration testing in geotechnical practice: London, England, Blackie Academic & Professional, 312 p.

Influence of Geotechnical Dataset on the Range of Influence of Undrained Shear Strength

Site Onyejekwe[1] and Louis Ge[2]

[1]Graduate Student, Department of Civil, Architectural, and Environmental Engineering, Missouri University of Science and Technology, Rolla, MO 65409. Email: sokbd@mst.edu

[2]Assistant Professor, Department of Civil, Architectural, and Environmental Engineering, Missouri University of Science and Technology, Rolla, MO 65409. Email: geyun@mst.edu

ABSTRACT

The knowledge of the spatial variability of geotechnical parameters, which can be described statistically by the mean, the variance, and the scale of fluctuation, is important in reliability-based design. Of particular importance is the scale of fluctuation. It can be used to compute the variance reduction factor, a factor of spatial averaging of geotechnical properties to reduce their point variance.

The most prevalent method of determining the scale of fluctuation uses datasets whose data points are at close and regular intervals, e.g. measurements from cone penetrometer soundings. Another method, when continuous measurements are not available, uses datasets that are widely spaced and at irregular intervals. Presented in this paper is a comparison of the range of influence of the undrained shear strengths at three different locations in Missouri determined from continuous and regularly spaced CPTu data and the non-continuous and irregularly spaced Shelby tube sampling data.

INTRODUCTION

Geotechnical performance is often governed by spatially averaged soil properties. The variability of soil properties averaged over a domain is less than that of their point properties (Vanmarcke, 1977). For instance, the variability of the average shear strength along the length of a pile will be less than its point value. This is known as the averaging effect in spatial variability. The spatial averaging effect results in a reduction in the variance used in reliability based design (RBD) in geotechnical engineering. Neglecting this spatial averaging effect normally leads to an overestimate of variability and therefore, a conservative design.

The spatial variability of a parameter can be described statistically by the mean, variance, and the scale of fluctuation, θ. The scale of fluctuation defines the distances over which a significant correlation of material property values exists (Vanmarcke, 1977). There are basically two approaches in analyzing the spatial variability of geotechnical parameters. One uses an autocorrelation function (ACF) from random field theory and time series analysis (Vanmarcke, 1977) and the other

uses the semivariogram function (SVF) from geostatistics proposed by Matheron (1963). With the ACF, the correlation length is determined while the range of influence, a, is determined with the SVF. Both a and the correlation length can be used to determine the scale of fluctuation.

Both approaches to spatial variability analysis have been used extensively in geotechnical engineering. They have been used primarily in connection with continuous data at close, regular and fixed intervals, mainly CPT data (Jaksa et al., 1997, 2000; Elkateb et al., 2003).

A considerable amount of data are required to establish a well-defined profile and compute the scale of fluctuation. The cone penetration test (CPT) provides sufficient data to establish a well-defined profile but is not frequently used in regular geotechnical projects. The standard penetration test (SPT), in which none to a few undisturbed samples for laboratory testing are obtained, does not provide sufficient data to establish a well-defined profile required for the computation of the scale of fluctuation.

The continuous Shelby tube sampling method, on the other hand, has the potential of providing sufficient data to establish a well-defined profile required for the computation of the scale of fluctuation. With this method, laboratory tests can be assigned at a closer spacing (closer than SPT) and direct measurements of geotechnical parameters can be obtained.

This paper reports an attempt of evaluating the range of influence determined from two different dataset types, namely the CPT soundings and laboratory tests on Shelby tube samples.

EXPLORATORY AND LABORATORY PROGRAM

Data for this paper were obtained principally from a very carefully planned field exploration and laboratory investigation program. Continuous Shelby tube sampling and cone penetrometer (with porewater pressure measurements) (CPTu) soundings were carried out in adjacent locations in Missouri along with a suite of laboratory tests on the Shelby tube samples. A special protocol, which largely followed the best practice in geotechnical exploration and testing (Ladd and DeGroot, 2003) was implemented during this program. Exploration at each location was completed within the two-week time frame suggested by Rethati (1988) for sampling (obtaining Shelby tube samples) and testing (CPTu) to be considered time-invariant.

The undrained shear strength, $S_{u(UU)}$ determined from the unconsolidated undrained triaxial test (UU) on each specimen taken from Warrensburg, St. Charles, and New Florence sites. The corresponding undrained shear strength from CPTu soundings taken at the immediate vicinity (about 2 to 3 feet) of each of the borehole locations was analyzed. The CPTu data were calibrated against laboratory test data so that both results are comparable. The bearing factor, N_{kt} values for the Warrensburg, St. Charles, and New Florence sites were 6, 19 and 15 respectively. The undrained shear strength, $S_{u(UU)}$ profile from laboratory tests and CPTu soundings are presented in Figure 2 for Warrensburg, St. Charles, and New Florence sites. The UU tests were conducted at about 2 to 3 feet intervals; hence, there is a paucity of data in this case compared to the CPTu data. The CPTu soundings were conducted with a 60° cone, a

rate of penetration of 0.79±0.2 inch/second, while data were acquired at 0.16 feet intervals. The CPTu profiles and the $S_{u(UU)}$ profiles are presented in Figure 1.

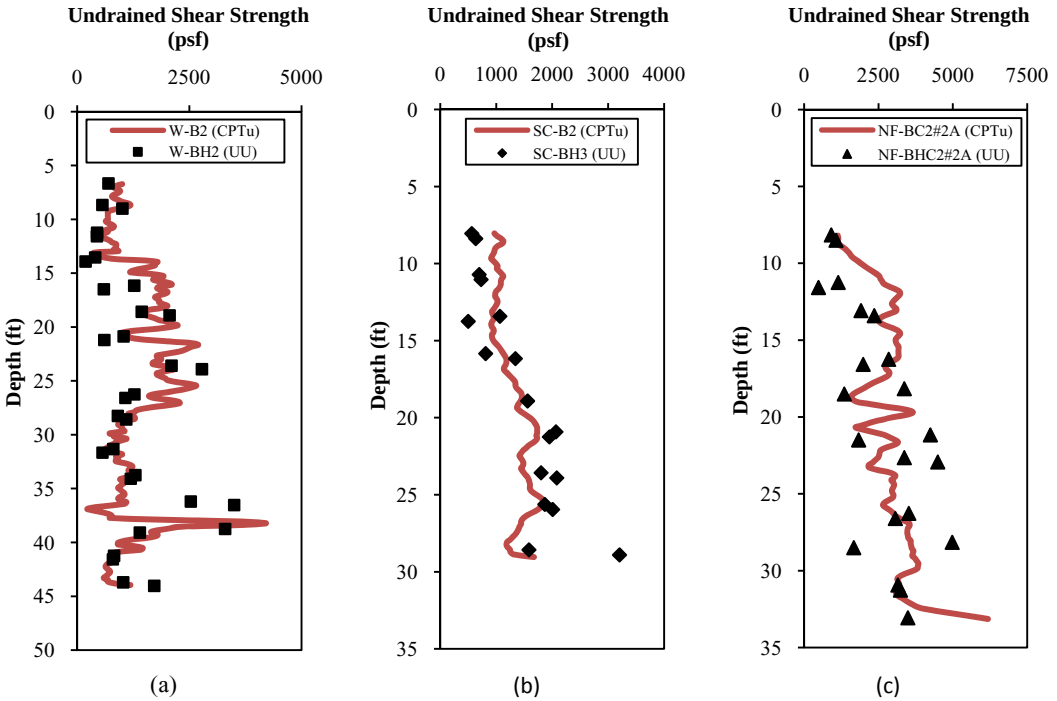

Figure 1. $Su_{(UU)}$ profile (a) Warrensburg (b) St. Charles (c) New Florence

Based on laboratory tests, the soil within the limits of the exploration depth at the different locations were classified according to the Unified Soil Classification System (USCS) as CL, CH, and CL for the Warrensburg, St. Charles, and New Florence sites respectively. This was verified with the soil behavior type from the CPT profiles. Consequently, these soil classifications were adopted for purposes of analyses.

The Warrensburg site (located in Western Plains geological region of Missouri) is generally composed of soft, silty soils overlying shale, sandstone, or limestone bedrock. The St. Charles site (located in Glaciated Plains geological region of Missouri) is an alluvial site located within the floodplain between the Mississippi and Missouri rivers near the confluence of those rivers. The subsurface is composed of approximately 35 feet of soft, fat clay overlying alluvial sands. The New Florence site (located in Glaciated Plains geological region of Missouri) is an "upland soil" site composed of relatively stiff clay overlying sandstone, limestone and/or shale bedrock.

ANALYSIS

The semivariogram function was used in this study since it does not require the stationarity of the mean and constant data spacing and the maximum number of lags allowable is $N/2$ (Kelkar and Perez, 2002); where N is total number of data points. Hence, although it is recommended that data be detrended to make them stationary, trends in data can be accepted, and a tolerance can be applied to the sampling interval (Journel and Huijbregts, 1978; Clark and Harper, 2000). The foregoing makes the

semivariogram function the more appropriate option for the analysis of the laboratory test data where there are fewer data.

The experimental semivariogram is characterized by three parameters (Jaksa et al, 1997): (a) the nugget effect, C_o, which is due to microvariabilities of the mineralization of the soil particles, and measurement errors; (b) the sill, C_1 (= C + C_o), which measures, on the average, the squared difference between data pairs; and (c) the range of influence (also range), a, which is the distance at which samples become independent of one another. A typical spherical theoretical semivariogram is presented in Figure 2.

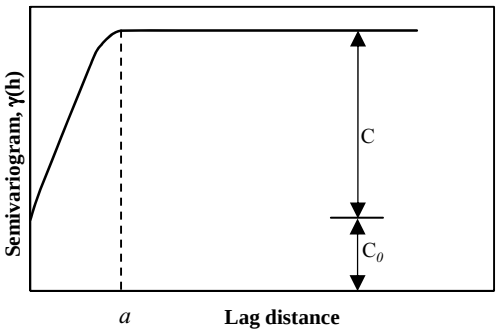

Figure 2. Typical spherical theoretical variogram

The range of influence, a, is related to the scale of fluctuation, θ, by means of various models. The relationship is such that the higher the range of influence, the higher the θ and vice versa. Hence, the range of influence will be considered primarily in this analysis.

The geostatistics software Vesper *version* 1.62 (Minasny et al., 2005) was used in this study. In the determination of the scale of fluctuation, a best-fit continuous theoretical semivariogram model is fitted to the experimental semivariogram through the least squares-method and the range of influence, *a,* is determined. There are many theoretical semivariogram models available including the nugget effect, spherical, exponential, Gaussian, and hole-effect models (McBratney and Webster, 1986; Meek 2001; Baecher and Christian, 2003). The spherical and the exponential models were used in this paper. The spherical model, shown in Figure 2, reaches a sill value at a lag distance equal to a. The exponential model reaches the sill value asymptotically. Hence, for practical purposes, the range of influence is the lag distance where the variogram reaches 95% of the sill value.

The scale of fluctuation, θ, is then evaluated analytically using equations stated in Cressie (1993) or by means of various models that relate the range of influence to the scale of fluctuation, θ. Original data was used in the variogram analysis for Warrensburg and New Florence while residuals from the removal of a linear trend were used for St. Charles. The removal of the best-fit linear trend from Warrensburg and New Florence data resulted, in both cases, in residuals with stronger trend present.

The lag distance for computing the experimental variogram is the distance interval at which data were acquired. Hence, for the laboratory data, the lag distance

was 2 feet while for the CPTu data, the lag distance was 0.16 feet. Also for the CPTu data, for the purposes of comparing the two datasets and evaluating the effect of lag distance on range of influence, two more determinations at lag distances of 1- and 2-feet were implemented. The lag tolerance (percentage of lags) represents the percentage of the lag distance considered in the determination of the semivariogram. For example, 50% lag tolerance on a lag distance of 10 feet has a tolerance of 5 – 15 feet. A lag tolerance of 50% was applied to the irregularly-spaced laboratory data so as to take every data point into account in the determination of the semivariogram, while for the regular CPTu data, a smaller the lag tolerance of 25% was applied. Also for the CPTu data, for the purposes of comparing the two datasets and evaluating the effect of lag tolerance on range of influence, two more determinations at lag tolerances of 50% and 0% were implemented. These variogram computation parameters are presented in Table 1.

Table 1. Variogram computation parameters

Variable	Laboratory		Field (CPTu)			
Lag Distance (ft)	2	0.16	1	1	2	2
Tolerance (%)	50	25	50	0	50	0

RESULTS

The results of the variogram analysis for the Warrensburg, St. Charles, and New Florence sites are presented in Figure 3; laboratory data and field data for (lag = 0.16 ft, tolerance = 25%), and (lag = 2 ft, tolerance = 50%) in Figures 3a – c, and 3d – f respectively. The variograms for other field data were omitted for purposes of clarity as they plotted very close to those for the field data in Figures 3d – f. A summary of parameters of the variograms are presented in Table 2. The variograms were fitted on the basis of the lowest root-mean-square error. In Figure 3, variograms for the laboratory and the field data are denoted by borehole identifiers W-BH-, SC-BH-, NF-BH- and W-B-, SC-B-, NF-B- for the Warrensburg, St. Charles, and New Florence sites respectively. For the field data, the borehole identifiers are followed by the lag distance. In both cases, the letter, V, stands for the theoretical variogram. Hence, W-B2-0.16-V means theoretical variogram for Warrensburg, Boring 2, 0.16 feet lag distance. In Table 3, the letter, *z*, after the lag distance stands for 0% tolerance.

In all cases, the sill (= variance) of the variograms of the field data plotted below that of the laboratory data. This can be attributed to the much larger number of field data which must have led to a reduced variance. For the exponential model (fitted to the Warrensburg data), the smaller slope at the origin for the field data resulted in higher values of range than that for the laboratory data. While for the spherical model (fitted to the St. Charles and the New Florence data), the smaller slope at the origin for the field data can result in higher or lower values of range depending on the distance at which the sill is reached. In this case, the values of the range are generally lower for the field data. The increase of the value of the range for Warrensburg field data is in the region of 200 to 300% of the laboratory data value. The decrease in the value of the range for the St. Charles and the New Florence field data are in the region of 30 to 40% and 5 to 30% respectively.

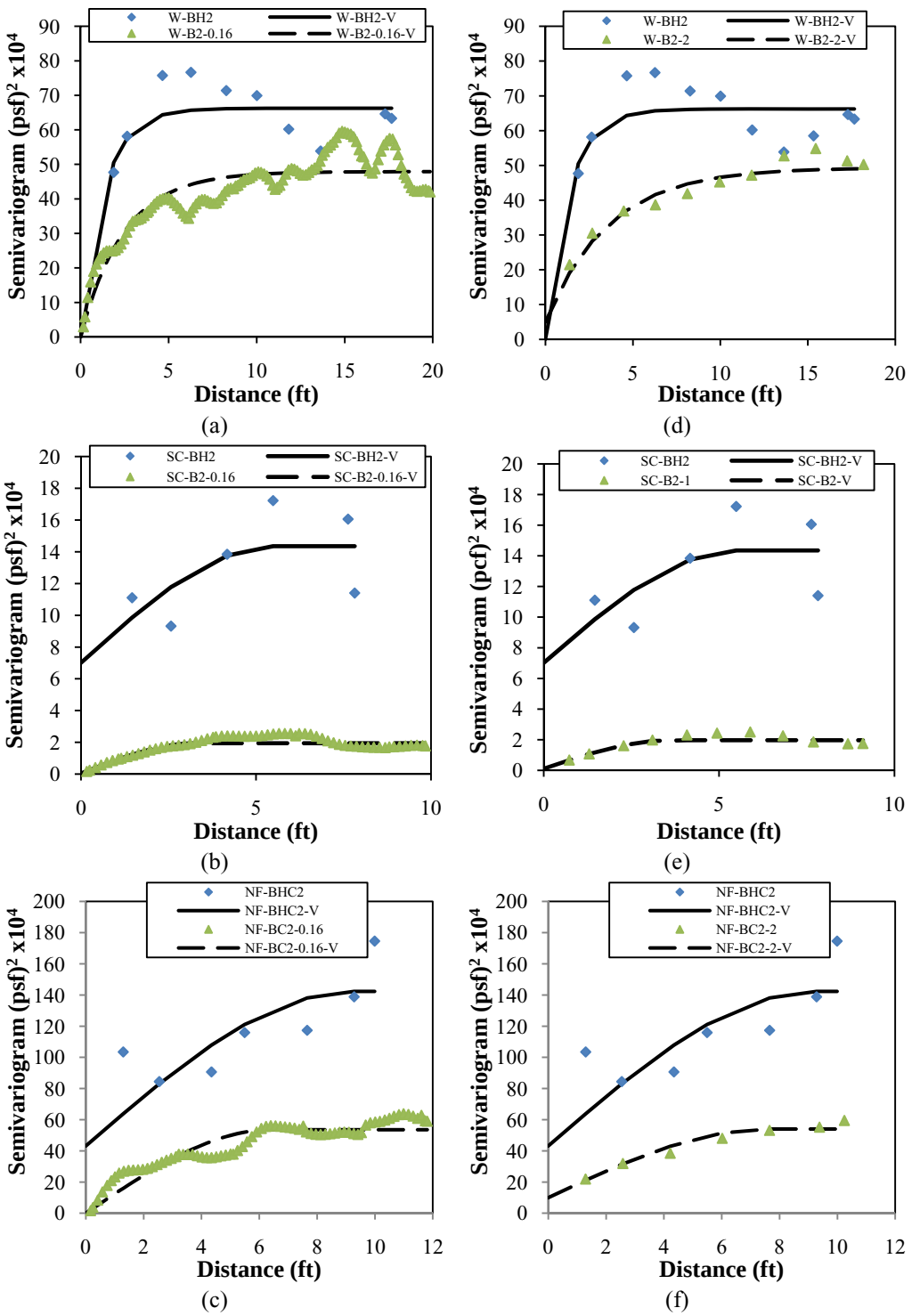

Figure 3. Semivariograms

Comparing the range of influence for both datasets at 50% tolerance and 2-foot lag distance, the range of influence for the field data was higher for Warrensburg (about 300%) and lower for St. Charles (about 30%), and the New Florence (about

20% times) sites. This follows the trend discussed in the paragraph above. The removal of tolerance (50% to 0%) from the field data led to a decrease in range for Warrensburg and St. Charles, and an increase for New Florence. The magnitude of the change in range both cases were small.

Table 2. Variogram parameters

Parameter	**W-BH2**	**W-B2-0.16**	**W-B2-1**	**W-B2-1*z***	**W-B2-2**	**W-B2-2*z***
Model	Exponential	Exponential	Exponential	Exponential	Exponential	Exponential
C_0 (psf)^2	0	595.8	50000	50000	50000	50000
C_1 (psf)^2	662494	478465	423764	420687	443733	445150
a (ft)	1.31	2.46	2.83	2.40	3.60	3.46
Parameter	**SC-BH2**	**SC-B-0.16**	**SC-B-1**	**SC-B-1*z***	**SC-B-2**	**SC-B-2*z***
Model	Spherical	Spherical	Spherical	Spherical	Spherical	Spherical
C_0 (psf)^2	70114	413.7	1085.6	845.1	1573	1336
C_1 (psf)^2	73387	19027	18557	18405	18540	18577
a (ft)	5.51	3.30	3.59	3.39	3.93	3.77
Parameter	**NF-BHC2**	**NF-BC2-0.16**	**NF-BC2-1**	**NF-BC2-1*z***	**NF-BC2-2**	**NF-BC2-2*z***
Model	Spherical	Spherical	Spherical	Spherical	Spherical	Spherical
C_0 (psf)^2	431284	0	108311	88255	99395	110863
C_1 (psf)^2	991779	535777	437002	479810	441028	462651
a (ft)	9.25	6.43	7.79	8.94	7.58	8.34
Notes: NF-BC2 = NF-BC2#2A; NF-BHC2 = NF-BHC2#2A						

CONCLUSION

In this paper, a comparison of the range of influence of the undrained shear strength profile, at three different locations (Warrensburg, St. Charles, and New Florence) in Missouri, determined following the geostatistics approach from the continuous, close and regularly-spaced CPTu data and the non continuous, widely-spaced and irregularly-spaced data from laboratory tests on specimens from continuous Shelby tube sampling. Based on the analyses presented in this paper, the following conclusions were reached.

- There are differences in the range of influence computed using the two different datasets of interest. These differences, in terms of increase or decrease, follow no particular pattern but may be dependent on the type of variogram model employed.
- For the exponential model in which the semivariogram reaches the sill asymptotically and the range of influence is the lag distance where the semivariogram reaches the 95% of the sill value, the combination of a lower slope at origin and lower sill resulted in a higher range of influence for the field test data.
- For the spherical model in which the semivariogram reaches the sill value at lag distance of *a*, which is the range of influence, the combination of a lower slope at origin and lower sill resulted in a lower range of influence for the field test data.

It is not possible to draw broad conclusions on the basis of the limited studies reported herein. Considering both number of data and the quality of profile obtained, the range of influence (hence the scale of fluctuation) I best determined using CPTu data. However the use of CPTu is not prevalent in industry. Hence, it is important that that the relationship between the range of influence from CPTu data and the range of influence from other more prevalent sampling and testing methods as amended is

determined. The development of this relationship will be of particular importance to practitioners who do not have other types of data (not CPTu) and want to employ the spatial averaging effect in reliability-based design. Hence, further studies on this subject involving more boreholes and more semivariogram models are recommended.

REFERENCES

Baecher, G. B., and Christian, J. T. (2003). Reliability and Statistics in Geotechnical Engineering. Chichester, UK: Wiley.

Box, G. E. P., Jenkins, G. M., and Reinsel, G. C. (1994). Time Series Analysis: Forecasting and Control. Upper Saddle River, NJ: Prentice Hall

Clark, I. and Harper, W. V. (2000). Practical Geostatistics 2000. Alloa, Scotland: Geostokos.

Cressie, N. A. C. (1993). Statistics for Spatial Data. New York: Wiley.

Elkateb, T., Chalaturnyk, R., and Robertson, P. K. (2003). An Overview of Soil Heterogeneity: Quantification and Implications on Geotechnical Field Problems. Canadian Geotechnical Journal, 40: 1-15.

Jaksa, M. B., Brooker, P. I. and Kaggwa, W. S. (1997). Inaccuracies Associated with Estimating Random Measurement Errors. Journal of Geotechnical and Geoenvironmental Engineering (ASCE), Vol. 123, No. 5, pp. 393-401. New York: ASCE.

Jaksa, M. B., Kaggwa, W. S., and Brooker, P. I. (2000). Experimental evaluation of of the scale of fluctuation of a stiff clay. In R. E. Melchers, and M. G. Stewart (eds.), Proceedings of the 8th International Conference on Applications of Statistics and Probability to Soil and Structural engineering, Sydney, December 12-15, 1999, pp. 415-422. Rotterdam: Balkema.

Journel, A. G., and Huijbregts, CH. J. (1978). Mining Geostatistics. London: Academic Press.

Kelkar, M., and Perez, G. (2002). Applied Geostatistics for Reservoir Characterization. Richardson, Texas: Society for Petroleum Engineers.

Ladd, C.C. and DeGroot, D.J. (2003). Recommended Practice for Soft Ground Site Characterization. The Arthur Casagrande Lecture, Proceedings of the 12th Panamerican Conference on Soil Mechanics and Geotechnical Engineering, Boston, MA, Vol. 1, pp. 3-57. Essen, Germany : Verlag

Matheron, G. (1963). Principles of Geostatistics. Economic Geology, Vol. 58, pp. 1246 – 1266.

McBratney, A. B., and Webster, R. (1986). Choosing functions for semi-variograms of soil properties and fitting them to sample estimates. European Journal of Soil Science, 37: 617-639. Oxford: Wiley-Blackwell.

Meek, D. W. (2001). A Semiparametric Method for Estimating the Scale of Fluctuation. Computer and Geosciences, 27: 1243-1249.

Minasny, B., McBratney, A.B., and Whelan, B.M. (2005). VESPER version 1.62. Australian Centre for Precision Agriculture, The University of Sydney, NSW 2006. *http://www.usyd.edu.au/su/agric/acpa*. (Assessed 08/16/2010).

Rethati, L. (1988). Probabilistic Solutions in Geotechnics. Amsterdam: Elsevier.

Vanmarcke, E. H. (1977). Probabilistic Modeling of Soil Profiles. Journal of Geotechnical Engineering (ASCE), Vol. 103, No. 11, pp. 1227 – 1246.

RELIABILITY BASED APPROACH TO QUANTIFY MONTMORILLONITE MINERAL IN EXPANSIVE CLAYS

Bhaskar Chittoori[1] and Anand J. Puppala[2]

[1]Faculty Associate-Research, Department of Civil Engineering, The University of Texas at Arlington, Box. 19308, Arlington, Texas 76019; PH (817) 272-5738; sinu@uta.edu.
[2]Professor, Department of Civil Engineering, The University of Texas at Arlington, Box. 19308, Arlington, Texas 76019; PH (817) 272-5821; anand@uta.edu.

ABSTRACT

Clay mineral quantification is an under explored area in geotechnical engineering. This is primarily due to the complexity and expensive nature of the current quantification methods. Simpler prediction models using chemical properties of the soil such as Cation Exchange Capacity (CEC), Specific Surface Area (SSA) and Total Potassium (TP) have been developed to successfully predict the percentage and dominant clay minerals in a soil. The reliability of predictions of these models still needs to be addressed. Hence, in this paper, the reliability of one such method in predicting the percentage of clay mineral Montmorillonite is evaluated. There are two objectives for this reliability analysis: one is to calculate the percentage contribution of the chemical parameters (CEC, SSA and TP) towards the prediction of Montmorillonite in the soil, and the second is to determine the probability of prediction failure which is defined as the prediction being +/- 10% of the original mineral amount. First Order Second Moment (FOSM) method is used in this analysis with a slight modification in the parameter variation. For this purpose, a total of twenty natural soils and their chemical properties are used to obtain the mean and standard deviation of CEC, SSA and TP values. Two artificially mixed soil specimens with known percentages of mineral Montmorillonite are later used for validating and assessing the probability of mineralogy prediction failures.

INTRODUCTION

One of the shortcomings of the current chemical stabilization techniques is the lack of understanding of the complex interactions between the mineralogy of the soil and the additives used for soil stabilization. Due to the above, several premature failures of pavements on stabilized sub-soils and poor long-term performance of them have prompted a research to incorporate both clay mineralogy aspects into the pavement design practices and then address durability issues in the original design. However, incorporating clay mineralogy into the stabilization is not an easy task due to costs involved in quantifying the clay minerals in the soil.

To reduce these costs and obtain approximate, if not exact, quantitative clay mineral information, Chittoori (2008) developed a simple method based on chemical properties of the soil to obtain the approximate percentages of the clay minerals Illite, Kaolinte and Montmorillonite. In particular, this study established a statistical equation based on regression analysis to obtain the percentage of Montmorillonite in the clay fraction of the soil using chemical species measurements such as cation exchange capacity (CEC) and specific surface area (SSA). However, the reliability of such equations is often questioned due to the uncertainties such as soil variability, operator variability and other measurement errors involved in geotechnical engineering. The main focus of this paper is to verify the reliability of one such

equation using the First Order Second Moment (FOSM) method outlined by Christian et al. (1994). Christian et al. (1994) applied FOSM method to assess the uncertainty in the factor of safety of a slope, there by arriving at reliability index which indicated the safety of the structure.

BACKGROUND AND NEED FOR RELIABILITY BASED APPROACH

The term "uncertainty" is very familiar to a geotechnical engineer. Uncertainty in geotechnical engineering is due to any of several reasons: the inherent variability of different soil properties that are being tested, operator dependence of various geotechnical tests, lack of knowledge of the geology of the soil and others (Baecher and Christian, 2003). Factor of Safety (FOS) based design, which is well-known in geotechnical engineering, does not always address these uncertainties, hence, the failures in various structures such as roads, buildings, bridges, and dams which are built on them. Many researchers like Harr (1987) and Ang and Tang (2007) have identified various risk factors involved in civil engineering and detailed methods to quantify these uncertainties. Also, researchers including Christian et al. (1994), Duncan (2000), Christian (2004) and Fenton et al. (2005) have tried to incorporate reliability-based design in various geotechnical analyses. New design methodologies such Load and Resistance Factor Design (LRFD) are being introduced which account for these uncertainties in some form.

As per Duncan (2000), a simple reliability analysis can be used along with routine geotechnical engineering practices to provide a means of evaluating the combined effects of uncertainties in the parameters involved in the calculations. They also offer a useful supplement to conventional analyses that can make the analysis more reliable and confident.

Montmorillonite is an expansive mineral and belongs to the group of 2:1 layer silicate minerals. The basic structural unit is a layer consisting of two inward-pointing tetrahedral sheets with a central alumina octahedral sheet. The bonds between layers are weak and have excellent cleavage, allowing water and other molecules to enter between the layers causing expansion (Grim, 1953). Montmorillonite has a very small particle size, which is responsible for the very high specific surface area values ranging from 600 m^2/g to 800 m^2/g. The range of CEC values for Montmorillonite is from 47 to 162 meq/g as reported by Borchardt (1989). This mineral is responsible for the swelling and shrinking in the soil during moisture changes. Soils containing Montmorillonites are more prone to landslides, as they retain more water and drain more slowly than soils with Kaolinite or soils with small amount of clay (Mitchell and Soga, 2005). Hence, quantification of mineral Montmorillonite is very critical for geotechnical engineering purposes. However, there has been very little focus on its quantification mainly due to the complexity and expensive nature of the current mineral quantification methods such as X-ray diffraction studies, scanning electron microscopy or differential thermal analysis.

In a research study conducted by Chittoori (2008), chemical properties such as Cation Exchange Capacity (CEC) and Specific Surface Area (SSA) were measured and used to quantify mineral Montmorillonite in the soil. A total of 20 natural soils and 6 artificial soils with known %Montmorillonite (%M) content were used in this study. Regression analysis of measurements was conducted to obtain a statistical equation to predict the amount of Montmorillonite in a soil. The equation uses CEC and SSA of soils as attributes. Equation 1 has an R^2 value of 0.92 and is presented below. The reliability of this equation in providing accurate predictions has not been verified and the risk involved in using such equation is not quantified.

$$\%M = -2.9 + (0.18 * CEC) + (0.12 * SSA) \quad (1)$$

In the present research, an attempt is made to incorporate the reliability-based analysis in the %M predictions of this equation. In order to verify the reliability of the above equation to predict %M from chemical properties of soil such as CEC and SSA, the FOSM method outlined in Christian et al. (1994) is closely followed. In order to use this method in the current research, a performance variable needs to be defined. The prediction error, P is used to define the performance variable which is equivalent to the difference between the actual and the measured percentages of %M in a soil.

$$P = \%M_a - \%M_P \quad (2)$$

Where P = Prediction error, $\%M_a$ = Actual percentage Montmorillonite and $\%M_p$ = Predicted percentage Montmorillonite

Ideally the value of P should be equal to zero for a perfect model prediction, however this is not always possible in the real world problems. Hence, a prediction margin of ±5% is accepted as a safe estimate of the %M in a given soil. Now, the performance variable P can be described as

$$P = M (CEC, SSA) + e \quad (3)$$

Where M (CEC, SSA) is a model depending on the soil chemical properties CEC and SSA and e is the modeling error that describes the deviation of the model from the real world. The uncertainty in prediction can be estimated by the variance in P and the variances in all the parameters contributing to P.

$$V[P] \approx V [M (CEC, SSA)] + V[e] \quad (4)$$

This can be expanded in Taylor series and truncated to the first order for simplicity and can be expressed as follows

$$V[P] \approx \sum_{CEC=x}^{y} \frac{\partial M}{\partial CEC} \sum_{SSA=a}^{b} \frac{\partial M}{\partial SSA} C[CEC, SSA] + V[e] \quad (5)$$

Where $C[CEC, SSA]$ is the covariance of the parameters CEC and SSA contributing towards P

Equation 5 can be divided by conventional differentiation techniques or by simple divided differences approximation to the partial derivatives. In this research, Equation 5 is solved by divided difference approach, similar to the steps used by Christian et al. (1994).

EXPERIMENTAL DATA

In order to explain the procedure involved in estimating the uncertainty in the prediction capabilities of the proposed statistical model to obtain % Montmorillonite (%M) in a given soil, two artificial mixes of soils with known %M are prepared. The percentages of Montmorillonite are chosen so that one soil is dominant in Montmorillonite and the other is not. Soil A1 (Montmorillonite dominant) had a %M of 70% and A2 with a %M of 30%. The mixes were prepared with an intention to represent the two extremes of the realm: one with high %M and one with low %M. The remaining portion of the artificial mixes consisted of either Quartz or Kaolintie which are known to have very low CEC (1 to 5 meq/100g) and SSA (10 to 30 m^2/g)

values and would not interfere the CEC and SSA determination of the entire mix. To assess the mean and standard deviation of the CEC and SSA values for these soils, several mixes (3 each) were prepared with same %M as soils A1 and A2, (i.e. three different mixes with %M value of 70% and three different mixes with %M value of 30%). Triplicate tests were performed on each of the mixed samples to yield more numbers for mean (μ) and standard deviation (SD) determination. The authors understand that the data points to obtain the mean and SD are very limited; however, for illustrating the method used, the given data should be sufficient. Further studies are being conducted to elaborate the method. Table 1 presents the μ and SD values for both the soil mixes along with the %M values.

Table 1 Mean and Standard deviation values for the two artificial mixes

Soil Name	CEC, meq/100g		SSA, m^2/g		%M
	μ	SD	μ	SD	
A1	98	18	542	80	70
A2	69	18	255	41	30

Equation (1) is used to calculate the amount of Montmorillonite and the results are presented in Table 3 alongside the actual mixed %M and the prediction error, P. It can be observed from the table that the prediction error is within the accepted safe estimate value of ±10%.

Table 2 Mean and Standard deviation values for the two artificial mixes

Soil Name	%M		Absolute P (%)
	Actual	Predicted	
A1	70	79.81	9.81
A2	30	39.91	9.91

PROCEDURE FOR QUANTIFYING UNCERTAINITY

The procedure to quantify uncertainty in predicting %M in a given soil is given as follows based on the process postulated by Christian et al. (1994):

1. Identify all the variables that contribute to the prediction of %M. In this case, the variables are CEC and SSA.
2. Determine the best estimate or the mean value for each variable and obtain the best estimate of $\%M_P$ using Equation (1) for these values.
3. Calculate the mean expected value for Prediction Error, P using $\%M_P$ and $\%M_a$; this value being the E[P].
4. Estimate the uncertainty or the variance in these variables (CEC and SSA).
5. Perform sensitivity analysis by estimating the change in prediction error when the variables are changed. This is performed in the current research by varying the CEC and SSA by ±1times their corresponding standard deviation. Further, the parameters are also varied as a percentage of the mean values to arrive at an optimum value for the variation.
6. Variance in P is calculated using (5).
7. Also, the reliability index, β is calculated using the following equation

$$\beta = \frac{E[P]-1.0}{E[P]*Cov[P]} \quad (6)$$

Where E[P] = expected value of P

Cov[P] = Coefficient of variation of P given as,

$$Cov[P] = \frac{\sigma[P]}{E[P]} \quad (7)$$

where σ[P] = standard deviation of P

The above detailed procedure is performed on the two selected artificial soils A1 (high Montmorillonite soil) and A2 (low Montmorillonite soil) of the present research, and the calculations involved for A2 soil are presented in Table 3 below. In this table, it should be noted that the values in column 5 are the values of CEC and SSA varied as either a percentage of μ or the number times of SD. In the present case, the values are varied as 1% of their corresponding mean values. Also, the values in column 6 are the prediction errors with the range of CEC and SSA values used in Equation (1).

It can be noted from the table that the percentage contribution of SSA is higher than that of CEC for this soil. Similar results are observed in the case of soil S2 as well. Hence, it can be concluded that SSA of soil has a higher influence on %M in the clay fraction of the soil than CEC. From the above table, partial derivative V[P] is used to obtain the coefficient of variance for P which is required to obtain the reliability index and probability of prediction failure. These results are presented in Table 4.

Table 3 Typical calculations involved in the realiability analysis for A2 soil

Parameter	μ	SD	Variance	Value in Analysis	PE (%)	Difference in PE (ΔP)	Δx	ΔP/Δx	Partial V[P] = (ΔP/Δx)²*Variance	% Contribution
CEC	69	18.0	324.00	69.69	10.2742	0.2484	1.4	0.1800	10.4976	30.25
				68.31	10.0258					
SSA	253	41.0	1681.00	257.55	10.4560	0.6120	5.1	0.1200	24.2064	69.75
				252.45	9.8440					

Note: μ = Mean; SD = Standard deviation; PE = prediction error;

Table 4 Typical calculations to determine β and p(F) for A2 soil

Parameter	Formula used	Value obtained
Variance of PE	V[P] = ∑(ΔP/Δx)	**34.704**
Standard Deviation of PE	σ[P] = (V[P])^2	**5.891**
Expected Value of PE	E[P] = PE for mean values of CEC and SSA	**9.910**
Coeff. of Variation of PE	cov[P] = (σ[P]/ E[P])*100	**58.04**
Reliability Index	β = (E[P] – 1.0)/ σ[P]	**1.512**
Probability of Prediction Failure	p(F) = Standard normal distribution with mean E[P] and SD σ[P]	**6.02E-02**

DISCUSSION

An analysis is conducted to recommend an optimum value, by which the parameters (CEC and SSA in this case) are to be varied in order to estimate the partial derivative of $\Delta P/\Delta x$ in Table 3 using Taylor's First Order approximation. For this, the CEC and SSA values are varied as 0.01, 0.1 1 and 10% of their corresponding mean values and 1, 2 and 3 times of their corresponding SD values. Figure 1 presents the variation of reliability index when the parameters CEC and SSA are varied as a percentage of their mean value. It can be observed from the figure that soil A2 had a better reliability index than soil A1 for all parameters' variations. Hence, it should be noted that the given equation has a better reliability on soils with lower percentages of Montmorillonite. Also, the reliability index for soil A1 remained constant for all % changes of mean and increased with % change in SD variations, while soil A2 showed a constant reliability index for all the parameter variations except for 3xSD variation. Based on this analysis, it is recommended that the parameters be varied as 1% of mean or 1 times standard deviation as it is recommended to vary the parameters by an optimum amount that is not too small and not too large.

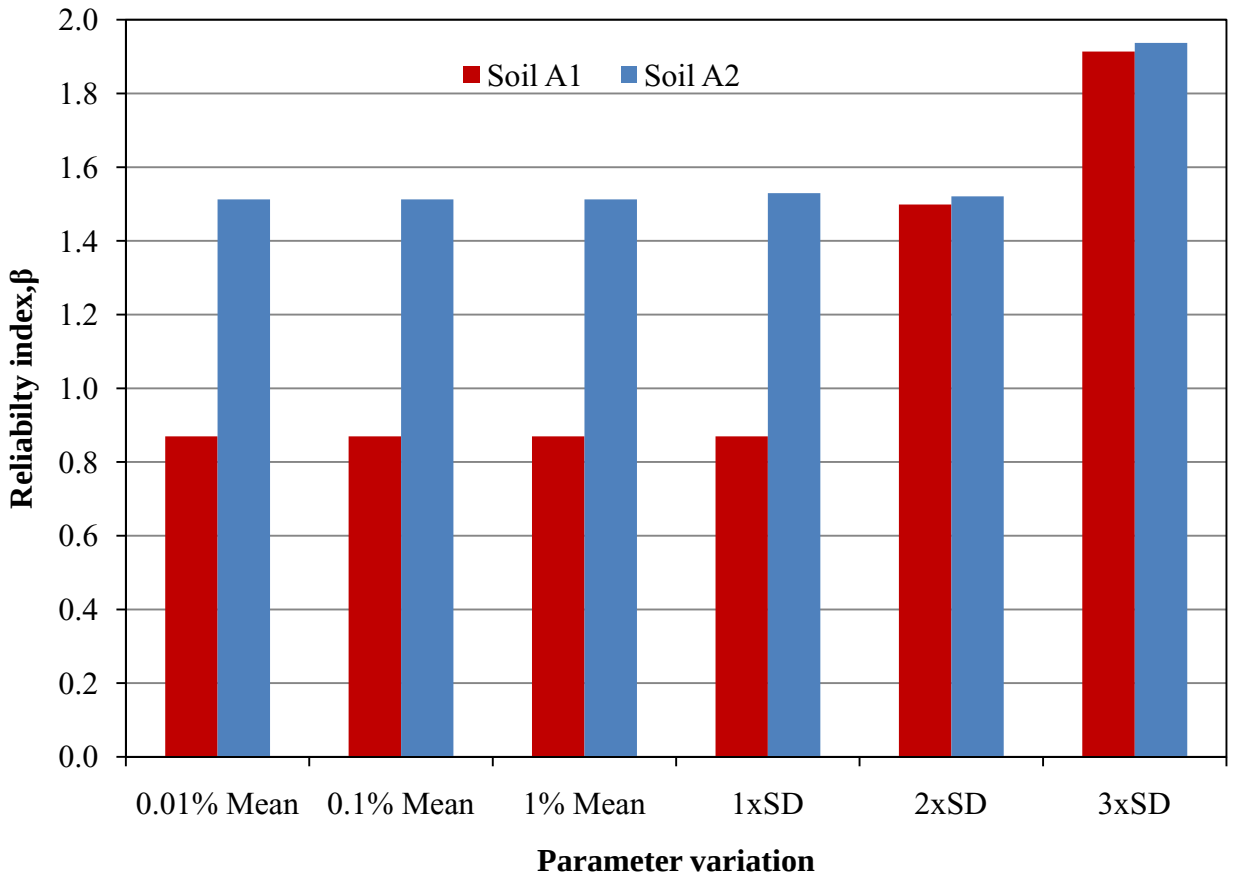

Figure 1 Realiability index values for different types of parameter variations

Figure 2 presents the variation of probability of prediction failure with a reliability index. In this figure, results for both soils A1 and A2 are included. The reliability index value of 1.0 is recommended for a very low risk analysis; i.e. for a less sensitive structure. Based on the

analysis, the reliability of percentage montmorillonite as predicted by equation (1) is low for soil A1 and acceptable for soil A2.

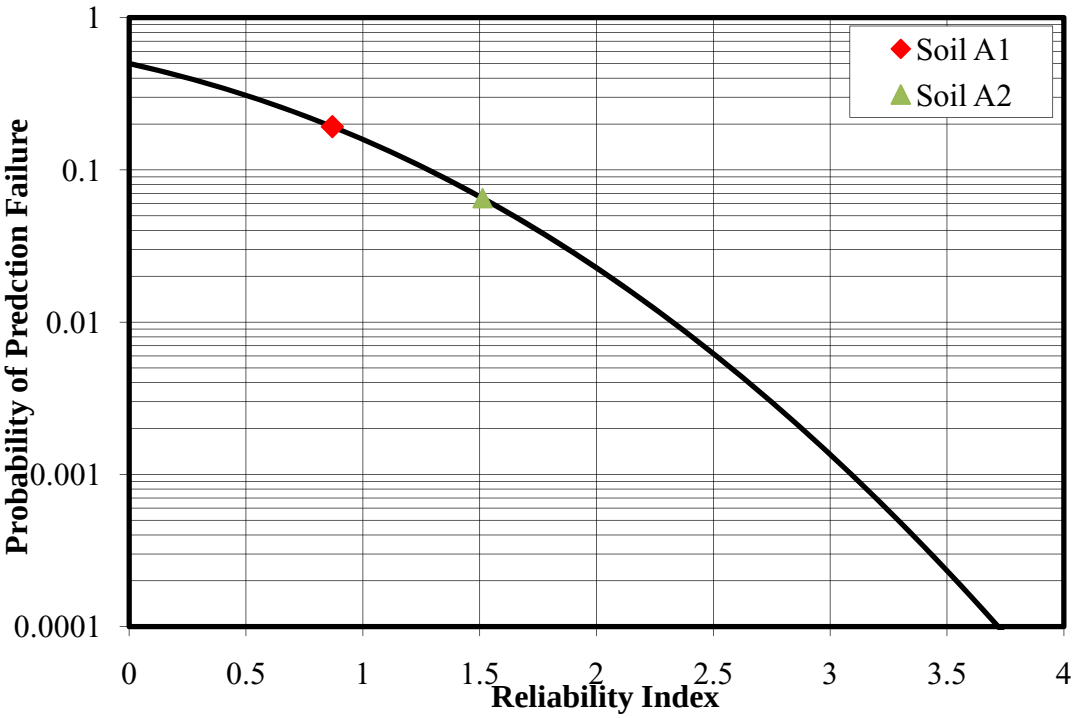

Figure 2 Variation of reliability index with probability of prediction failure for soils A1 and A2 (parameters varied by 1% of mean)

SUMMARY

Reliability analysis was performed for statistical equation recommended for the prediction of mineral Montmorillonite by Chittoori (2008). First Order Second Moment method was followed to conduct the reliability analysis. Analysis was conducted to recommend an optimum value for varying the parameters for this method, and it is recommended that the parameters be varied by 1% of its mean value or 1 times it standard deviation. It was observed that the percentage contribution of SSA is higher than that of CEC.

It was observed that the Equation 1 has an acceptable reliability of %M predictions for soils with low %M and low reliability for soils with high %M. This low probability of accuracy for high %M content still does not affect the current state of analysis. This is because though the probability of prediction failure is high (0.19 in the case of soil A1), the predictions already made for such soils indicate that these soils are problematic for engineering characterization. This means that the predictions could have an error of +/- 20%, but their predictions magnitudes already exceed threshold levels of %M levels that are considered problematic for these soils.

Further studies with more soil samples are still required, which will lead to modifications of the prediction models. The usage of the equation is still recommended, as long as there is a clear understanding of its limitations in the prediction capabilities of %M in soils. This analysis will elevate the use of clay mineralogy in particular %M information in the present geotechnical practice, which would lead to more reliable interpretations of soil behaviors.

REFERENCES

Ang, A. H. S. and Tang, W. H. (2007). *Probabilistic concepts in engineering: Emphasis on applications to civil and environmental engineering*, John Wiley and Sons Inc.

Baecher, G. and Christian, J. T. (2003). *Reliability and statistics in geotechnical engineering*, John Wiley and Sons, London and New York.

Borchardt, G. (1989). "Smectites.", In J.B. Dixon and S.B. Weed, eds., Minerals in Soil Environments, 2nd ed., Madison, WI: Soil Science Society of America.

Chittoori, B. C. S. (2008). "Clay mineralogy effects on long-term performance of chemically treated expansive clays." Doctoral Dissertation, The University of Texas at Arlington, TX, 326 pages.

Christian, J. T., Ladd, C. C and Baecher, G. B. (1994). "Reliability applied to slope stability analysis." ASCE, *Journal of Geotechnical Engineering*. 120 (12), 2180-2207.

Christian, J. T. (2004). "Geotechnical engineering reliability: How well do we know what we are doing?." ASCE, *Journal of Geotechnical and Geoenvironmental Engineering,* 130(10), 985-1003.

Duncan, M. J. (2000). "Factor of safety and reliability in geotechnical engineering." ASCE *Journal of Geotechnical and Geoenvironmental Engineering*. 126 (4), 307-316.

Fenton, G. A., Griffiths, D. V. and Williams, M. B. (2005). "Reliability of traditional retaining wall design." *Geotechnique*. 55(1), 55-62.

Grim, R. E. (1953). "Clay Mineralogy." McGraw Hill Book Company, New York.

Harr, M. E. (1987). *Reliability based design in Civil engineering* McGraw Hill Book Company, New York.

Mitchell, J. K., and Soga, K. (2005). *Fundamentals of Soil Behavior*. 3rd ed., John Wiley & Sons Inc, New York.

Subset Simulation and its Application to a Spatially Random Soil

Ashraf Ahmed[1] and Abdul-Hamid Soubra, M.ASCE[2]

[1] PhD student, University of Nantes, GeM, UMR CNRS 6183, Bd. de l'université, BP 152, 44603 Saint-Nazaire cedex, France, Tel: 0033240905106,
Fax: 0033240905109, E-mail: Ashraf.Ahmed@univ nantes.fr
[2] Corresponding author, Professor, University of Nantes, GeM, UMR CNRS 6183, Bd. de l'université, BP 152, 44603 Saint-Nazaire cedex, France,
Tel: 0033240905108, Fax: 0033240905109, E-mail: Abed.Soubra@univ-nantes.fr

ABSTRACT

The failure probability of a footing resting on a spatially random soil is currently computed using Monte Carlo simulation (MCS) methodology. This approach is well known to be very time-consuming especially for computing small failure probabilities. One alternative to MCS is the subset simulation approach. This approach is used in this paper to perform a probabilistic analysis at the serviceability limit state of a strip footing resting on a soil with a spatially varying Young modulus. The random field was discretized using Karhunen-Loeve expansion. The probabilistic numerical results have shown that the failure probability calculated by subset simulation is very close to that computed by MCS methodology but with a significant reduction in the number of simulations.

INTRODUCTION

The failure probability of geotechnical problems modeled by random fields is generally calculated using Monte Carlo simulation (MCS) methodology. This method is very expensive for the computation of a small failure probability. Au and Beck (2001) proposed an efficient approach (called subset simulation) to calculate the small failure probabilities. Except Au et al. (2010) and Santoso et al. (2010) who applied this approach to the random field problems, the subset simulation method was mainly applied in literature to problems where the uncertainties of the different parameters were modeled by random variables. These authors have considered only one-dimensional random field problems. It should be noted that Au et al. (2010) have discretized the random field into a finite number of random variables equal to the number of elements of the deterministic model. Thus the random dimension depends on the number of elements of the deterministic model. In this paper, the subset simulation method was proposed to calculate the failure probability in case of a two-dimensional random field discretized by K-L expansion. As will be explained hereafter, the random dimension in the present work does not depend on the number of elements of the deterministic model but on the size M of the K-L expansion. The proposed procedure was applied to perform a probabilistic analysis at the serviceability limit state (SLS) of a shallow strip footing subjected to a central vertical load (P_V). The uncertain random field considered in the analysis is the soil Young modulus (E). The footing vertical displacement was used to represent the

system response. The deterministic model used to compute the system response is based on numerical simulations using the commercial software FLAC^{3D}.

KARHNUEN-LOEVE EXPANSION

Consider a random process H(X, θ) where X denotes the spatial coordinates and θ indicates the random nature of the corresponding quantity. If μ is the mean of the process, then the process can be expanded as follows Spanos and Ghanem (1989):

$$\mathrm{H}(\mathrm{X},\theta) = \mu + \sum_{i=1}^{\infty} \sqrt{\lambda_i}\,\phi_i(X)\,\xi_i(\theta) \qquad (1)$$

where λ_i and ϕ_i are the eigenvalues and eigenfunctions of the covariance function $C(X_1, X_2)$ and $\xi(\theta)$ is a vector of standard uncorrelated random variables. The series expansion in Equation (1) is referred to as the K-L expansion. For practical implementation, the approximate random process is defined by truncating the series in Equation (1) to a finite number of terms M. The choice of the number of terms M depends on the desired accuracy of the problem being treated.

SUBSET SIMULATION

Subset simulation was proposed by Au and Beck (2001) to compute the small failure probabilities. The basic idea of subset simulation can be described as follows: Consider a failure region F defined by the condition G<0 where G is the performance function and let (s_1, …, s_k, ..., s_{Nt}) be N_t samples located in the space of the uncertain variables. It is possible to divide the failure region F into a number of nested failure regions F_1, …, F_j, ..., F_m of increasing size where $F_1 \supset .. \supset F_j \supset .. \supset F_m = F$ (Fig. 1).

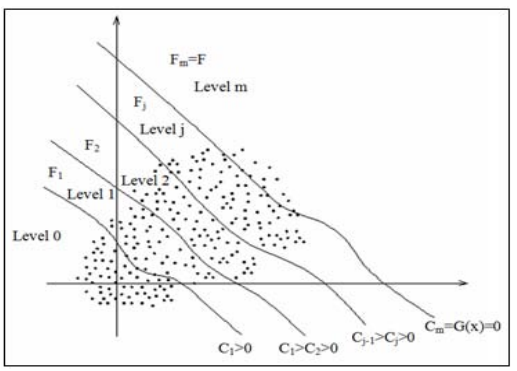

Figure 1. Nested Failure domain

An intermediate failure region F_j can be defined by $G_j<C_j$ where $C_j>0$. Thus, there is a decreasing sequence of positive numbers C_1, …, C_j, ..., C_m corresponding respectively to F_1, …, F_j,…, F_m where $C_1>\ldots>C_j>\ldots> C_m=0$. The N_t samples (s_1, …, s_k, ..., s_{Nt}) will be divided into groups where each group contains a given number N_s

of samples (s_1, …, s_k, ..., s_{Ns}). The failure probability corresponding to an intermediate failure region F_j is calculated as follows:

$$P(F_j) = \sum_{k=1}^{Ns} I_{F_j}(s_k) \quad (2)$$

I_{F_j} =1 if $s \in F_j$ and I_{F_j} =0 otherwise. The conditional failure probability $P(F)=P(F_m)$ can be calculated from the previous nested sequence of conditional failure regions as follows:

$$P(F)=P(F_m)=P(F_m|F_{m-1})xP(F_{m-1}|F_{m-2})xP(F_{m-2}|F_{m-3})x \ ... \ xP(F_2|F_1)xP(F_1) \quad (3)$$

IMPLEMENTATION OF SUBSET SIMULATION ALGORITHM IN THE CASE OF A SPATIALLY VARYING SOIL PROPERTY

As mentioned previously, this paper aims at employing the subset simulation methodology for the computation of the failure probability in the case of a spatially varying soil property. In order to achieve this objective, K-L expansion described before is used to discretize the random field. Therefore, the random field is transformed into a finite number of random variables $\{\xi_i\}_{i=1,...,M}$. Due to this transformation, the use of subset simulation becomes an easy task. The algorithm of subset simulation in case of a spatially varying soil property can thus be described by the following steps:

1- Choose the number M of terms of K-L expansion. This number must be sufficient to rigorously represent the target random field.
2- Generate a vector $\{\xi_1, \ldots, \xi_k, \ldots, \xi_M\}$ by direct Monte Carlo simulation with the target probability density function P_t. Notice that P_t is normal in our case.
3- Use the K-L expansion to obtain the first realisation of the random field. Then, use the deterministic model to calculate the corresponding response.
4- Repeat steps 2 and 3 to obtain N_s realisations and their corresponding responses. Then, evaluate the corresponding values of the performance function to obtain the vector $\mathbf{G}_0=\{g_1, \ldots, g_k, \ldots, g_{Ns}\}$.
5- Propose an intermediate failure probability $P(F_j)$ and evaluate the first failure threshold C_1 which corresponds to the failure region F_1 where C_1 is equal to the $[(N_s x P(F_j))+1]^{th}$ value in the increasing list of elements of the vector $\mathbf{G}_0$. This ensures that the value of $P(F_1)$ wi equal to the proposed value of $P(F_j)$.
6- Among the N_s realisations, there are $[N_s x P(F_j)]$ ones whose values of the performance function is less than C_1 (i.e. they are located in the failure region F_1). The corresponding vectors $\{\xi_1, \ldots, \xi_k, \ldots, \xi_M\}$ of these realisations are used as 'seeds' to generate an additional $[(1-P(F_j))N_s]$ vectors of $\{\xi_1, \ldots, \xi_k, \ldots, \xi_M\}$ using Markov chain method based on Metropolis-Hasting algorithm. These new vectors are used to obtain the random field realisations of level 1 using K-L expansion. The corresponding responses are evaluated using the deterministic model and the corresponding vector of performance function $\mathbf{G}_1=\{g_1, \ldots, g_k, \ldots, g_{Ns}\}$ is computed.

7- Evaluate the second failure threshold C_2 as the $[(N_s x P(F_j))+1]^{th}$ value in the increasing list of the vector $\mathbf{G}_1$.
8- Repeat steps 6-7 until reaching the value of the last failure threshold (i.e. $C_m=0$). For the last failure threshold, thowing equation may be used:

$$P(\mathrm{F_m}\left|F_{m-1}\right.) = \sum_{k=1}^{Ns} I_{F_m}(s_k) \tag{4}$$

Where I_{F_m} =1 if the performance function g_k corresponding to the sample s_k is negative and I_{F_m} =0 otherwise.
9- Finally, the failure probability P(F) is evaluated according to Equation (3).

EXAMPLE PROBLEM

In this section, the proposed procedure for the computation of the failure probability is illustrated through an example problem. In this example, the failure probability at SLS (i.e. the probability of exceeding a tolerable vertical displacement) of a strip footing resting on a soil having spatially varying Young modulus and subjected to a central vertical load (P_v) is calculated. The Young modulus was considered as a log-normal random field with mean value μ=60MPa and coefficient of variation COV=15%. An exponential covariance function was used in this paper. The random field was discretized using K-L expansion. Although an isotropic random field is often assumed in theature; in this paper, different values of the horizontal and vertical autocorrelation distances were studied and analyzed. The performance function used to calculate the failure probability is defined as follows:

$$G=v_{max}-v \tag{5}$$

where v_{max} is a prescribed tolerable vertical displacement and v is the footing vertical displacement due to the applied load. The deterministic model used to calculate the footing vertical displacement (v) is based on the commercial numerical code $FLAC^{3D}$. Due to the non-symmetrical footing movement created by the soil heterogeneity, the entire soil domain shown in Fig. 2 was considered to calculate the footing displacement. The values of the parameters of the soil, footing and interface are given in Table (1).

It should be mentioned here that a normal PDF was used as a target probability distribution P_t. However, a uniform PDF was used as a proposal probability distribution P_p. Notice also that the intermediate failure probability $P(F_i)$ was chosen equal to 0.1. Notice finally that v_{max} was assumed equal to 4cm and P_v was taken equal to 1000kN/m throughout the paper. As mentioned before, the accuracy of the approximated random field depends on the number M of terms of the K-L expansion. For the most critical configurations of the autocorrelation distances used in this paper [(L_x=10m and L_y=0.5m), (L_x=5m and L_y=1m)], the eigenvalue vanishes when the number of terms is $M \approx 100$ terms. As a conclusion, the number

of terms will be set to M=100 terms for all the probabilistic calculations presented in this paper.

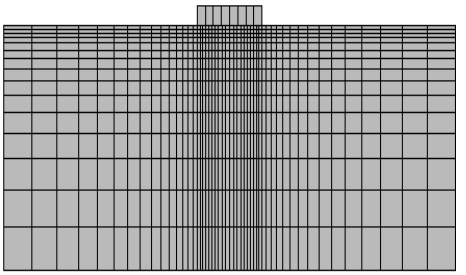

Figure 2. Soil domain and mesh used in the numerical simulation

Table 1. Shear Strength and Elastic Properties of Soil, Footing, and Interface

Variable	Soil	Footing	Interface
c	20kPa	N/A	20kPa
φ	30°	N/A	30°
ψ_s=2/3 φ	20°	N/A	20°
E	60MPa	25GPa	N/A
ν	0.3	0.4	N/A
K_n	N/A	N/A	1GPa
K_s	N/A	N/A	1GPa

Comparison between subset simulation and MCS methodologies

In this section, the failure probabilities calculated at each level of the subset simulation were compared to those obtained by MCS. To perform this comparison, a random field with L_x=10m and L_y=1m (called hereafter the reference case) was considered. For each level j of the subset simulation, the corresponding failure threshold C_j was calculated and presented in Table (2) for different values of the number of realisations N_s.

Table 2. Evolution of the performance function with the different levels of the subset simulation and with the number of realisations (N_s) at each level

Performance function C_j	Number of realisations at each level (N_s)				
for each level j	50	100	150	200	250
C_1	0.0086	0.0077	0.0080	0.0076	0.0076
C_2	0.0058	0.0048	0.0050	0.0041	0.0040
C_3	0.0044	0.0015	0.0019	0.0011	0.0011
C_4	0.0017	0	0	0	0
C_5	0	-	-	-	-

This table indicates that the failure threshold decreases with the successive levels until reaching zero at the last level. This means that the realisations generated by the proposed procedure successfully progress towards the limit state surface G=0 which indicates the validity of the proposed procedure. Notice that the value of the failure threshold remains almost constant for $N_s \geq 200$. This means that 200 realisations at each level are sufficient to calculate the failure probability. To confirm the validity of the present approach, a comparison with MCS was carried out. The number of realisations N of MCS should be adequate for a rigorous calculation of the failure probability. The accuracy of MCS can be estimated by calculating the coefficient of variation of the failure probability as follows:

$$COV_{P_f} = \sqrt{(1-P_f)/NP_f} \quad (6)$$

Using this equation, the coefficient of variation of the failure probability was calculated and presented in Fig. 3. It was found to decrease with the increase of the number of realisations. It reaches an asymptote when the number N of realisations is equal to 20,000. Hence, 20,000 realisations were used to calculate the failure probabilities by MCS. The comparison between the subset simulation method (using 4 levels with N_s=200, i.e. 800 realisations) and the MCS method is presented in Fig. 4.

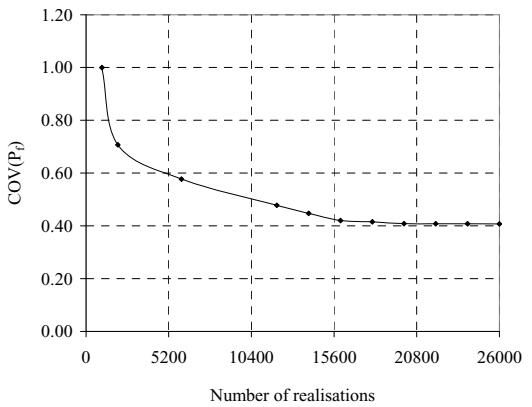

Figure 3. Effect of number of realisations of MCS on COV(P_f)

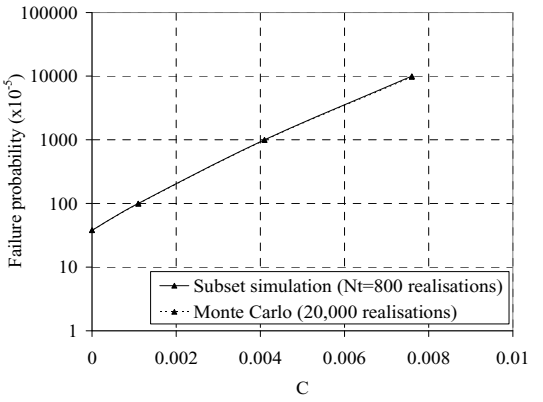

Figure 4. Comparison between P_f obtainedat at each level of subset simulation and that computed by MCS

Notice that to calculate the failure probability at level j using MCS, the performance function should be set equal to C_j. In this case, the failure region is defined as $G \leq C_j$ and the safety region is defined as $G > C_j$. The failure probability can then be calculated as:

$$P(F_i) = \sum_{k=1}^{N} I_F(s_k) \quad (7)$$

where $I_F = 1$ if s_k is located in the failure region F_j and $I_F = 0$ otherwise. Fig. 4 shows that for the case where N_s=200 realisations, the failure probabilities calculated by subset simulation were found to be very close to those computed by MCS. For smaller values of N_s, there is some discrepancy between both approaches (results not shown in this paper). From Fig. 4, one can conclude that the 20,000 realisations required by MCS methodology can be reduced to only 800 realisations by applying the proposed procedure based on subset simulation methodology.

Parametric study

In order to investigate the effect of the anisotropy of the random field, the failure probability was plotted against the vertical and horizontal autocorrelation distance in Figs. 5 and 6 respectively for the prescribed footing breadth. (i.e. B=2m).

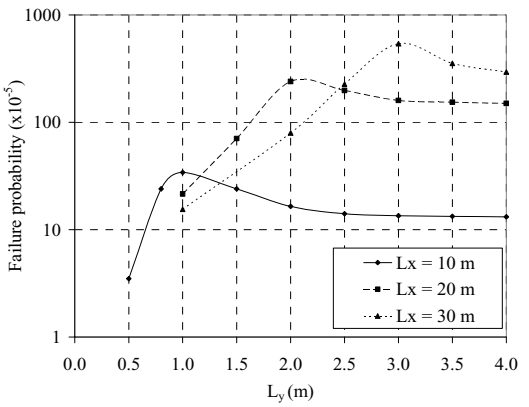

Figure 5. Effect of L_y on the failure probability for different values of L_x

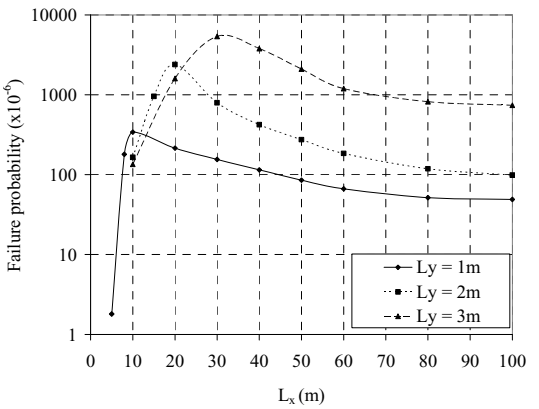

Figure 6. Effect of L_x on the failure probability for different values of L_y

Both figures show that the failure probability presents a maximum when the ratio of L_x to L_y is equal to 10 for B=2m. This observation can be explained as follows: The small value of the autocorrelation distance (L_x or L_y) induces a large soil heterogeneity which results in a large variety (i.e. a great number of high and small values) of the Young modulus beneath the footing. This variety leads to small footing displacement and consequently to small failure probability. The small footing displacement occurs because the rigid footing is prevented to settle due to the presence of a high number of small strong zones beneath this footing; the high number of small weak zones being of little effect in this case; the increase in the autocorrelation distance increases the footing displacement and consequently the failure probability. On the other hand, when the autocorrelation distance is very large in either the vertical or the horizontal direction, the problem becomes similar to that of the one-dimensional random field for which the failure probability is smaller than that of the two-dimensional isotropic case. For medium autocorrelation distances, the soil contains a number of strong zones adjacent to a number of weak zones whose areas are greater than those corresponding to the case of the one-dimensional random field. The soil movement can easily develop throughout the weak zones. As a result, the failure probability increases in such cases with respect to the case of the one-dimensional random field. The values of the autocorrelation distance corresponding

to the maximum can be used to define a conservative design case for probabilistic analysis when rigorous information about the autocorrelation distance is not available. Notice finally that for the same ratio of L_x/L_y but greater values of L_x and L_y, the maximum failure probability was found to be higher. This is due to the simultaneous increase of the autocorrelation distances in both the vertical and the horizontal directions which makes the failure probability tend to that of the homogeneous soil. The numerical results of Figs 5 and 6 also indicate that the failure probability is more sensitive to the vertical autocorrelation distance. This is because the rate of change in the failure probability (i.e. rate of increase or decrease) when increasing the vertical autocorrelation distance by a certain percentage is larger than that when increasing the horizontal autocorrelation distance by the same percentage.

CONCLUSION

This paper presents an alternative procedure to Monte Carlo Simulation (MCS) methodology for the computation of the failure probability of a strip footing resting on a soil with spatially varying properties. This procedure is based on the subset simulation approach. The proposed procedure was applied to calculate the failure probability at the serviceability limit state of a strip footing resting on a soil with a spatially varying Young modulus and subjected to a central vertical load. The random field was discretized into a finite number of random variables using K-L expansion. The vertical displacement of the footing center was used to represent the system response. The deterministic model used to compute the system response is based on numerical simulations using the commercial software FLAC^{3D}. The failure probability calculated by the proposed procedure was compared to that computed by MCS methodology and was found to be very close with a significant decrease in the number of calls of the deterministic model. For the case of a non-isotropic random field, the failure probability presents a maximum value. The maximum was obtained at a fixed value of $L_x/L_y=10$ for a footing breadth equal to 2. Notice however that for the same ratio of L_x/L_y but greater values of L_x and L_y, the maximum failure probability was found to be higher. It has also been shown that the failure probability is more sensitive to the vertical autocorrelation distance than the horizontal one.

REFERENCES

Au, S. K., and Beck, J. L. (2001). “Estimation of small failure probabilities in high dimentions by subset simulation.” *J. Prob. Engrg. Mech.,* 16,263-277.

Au, S. K., Cao, Z. J., Wang, Y. (2010). “Implementing advanced Monte Carlo simulation under spreadsheet environment.” *J. Structural Safety,*32(5),281-292.

Santoso, A. M., Phoon, K. K., Quek, S. T. (2010). “Modified Metropolis-Hasting algorithm with reduced chain-correlation for efficient subset simulation.” *J. Prob. Engrg. Mech.,* doi:10.1016/j.probengmech.2010.08.007.

Spanos, P. D., and Ghanem, R. (1989). “Stochastic Finite Element Expansion for Random Media.” *J. Engrg. Mech.,* 115(5),1035-1053.

Probabilistic Analysis of Basal Heave in Deep Excavation

Y. G. Tang[1] and Gordon T. C. Kung[2]

[1]Department of Architecture, Hwa-Hsia Institute of Technology, Taipei 23568, Taiwan; PH (886-2)8941-5133; FAX (886-2)2941-5730; email: tang@cc.hwh.edu.tw
[2]Sustainable Environment Research Center, National Cheng Kung University, No. 500, Sec. 3, Anming Rd., Annan District, Tainan 70955, TAIWAN; PH (886-6) 384-0136 ext. 210; FAX (886-6) 384-0960; email: tckung@mail.ncku.edu.tw

ABSTRACT

The deterministic model using the factor of safety against basal heave (FS) defined as the ratio of soil resistance over mobilized force is usually used to evaluate the failure of basal heave in excavation. However, such deterministic method cannot deal with model and parameter uncertainty. In this study, one excavation case, in which the basal heave failure has occurred, is employed to study its probability of failure. The uncertainty of undrained shear strength of soil is considered in the analysis based on laboratory tests presented in past studies. The Monte Carlo simulation is then used to perform the probabilistic analysis of basal heave. Results show that the probability of failure for basal heave computed based on the original design and UU test results can be as large as 40% when FS equals to 1.0 and COV of undrained shear strength is equal to 0.2. The probabilistic analysis of basal heave can provide valuable information to advance the excavation design.

INTRODUCTION

Excavation for the construction of buildings and infrastructure in urban areas is often a challenge due to the complicated construction environment. A successful excavation requires stability of the excavation and maintenance of the integrity of the adjacent structures. In the analysis of stability of a braced excavation, the basal heave problem has received much attention from geotechnical engineers especially the excavation site is located in a city with thick soft clay layers such as Singapore, Shanghai, and Taipei. In practice, the basal heave analysis in the design of a new excavation case must meet the requirement of the design code in each of countries. However, some excavation case histories, in which the basal heave failure has occurred and been reported occasionally, reflect that it may be desirable to examine the existing analysis methods through the concept of probability.

Over the past decade, few references (e.g., Kung et al. 2007; Schuster et al. 2009) have successfully incorporated the concept of probabilistic analysis into the analysis of excavation-induced wall deflection, ground movements, and damage potential to a building adjacent to an excavation. In this paper, the methodology of probabilistic analysis is incorporated into the method for analyzing basal heave proposed by the Taiwan building code. The probabilistic analysis on the basal heave can be performed with the Monte Carlo simulation method. The excavation case history of basal heave failure presented by Hsieh et al. (2008) is employed herein to

conduct the probabilistic analysis. The analysis results are then used to discuss the applicability of probability analysis in the basal heave analysis of excavation and some conclusions are drawn.

METHOD OF BASAL HEAVE ANALYSIS

The method of basal heave analysis in the Taiwan building code is adopted to conduct the probabilistic analysis of an excavation case in the present study. Specifically, the formula of basal heave analysis in the Taiwan building code (TGS, 2001), in which a circular failure surface centered at the lowest strut (see Figure 1) is assumed, is very similar to that proposed by Terzaghi (1943). The factor of safety (*FS*) against basal heave is defined by the ratio of the resisting moment (M_r) to the driving moment (M_d) of the lowest strut as follows:

$$FS = \frac{M_r}{M_d} = \frac{R\int_0^{\frac{\pi}{2}+\alpha} s_u (Rd\theta)}{(W+q)R/2} \geq 1.2 \tag{1}$$

where s_u is the undrained shear strength of clay; R is the radius of the failure arc; W is the total weight of the soil; q is the surcharge above the excavation surface within a R wide area outside the retaining construction; θ is the angle between the failure surface and the horizontal direction; α is the angle of failure arc in excavation zone and can be obtained by $\alpha = \cos^{-1}(h/R)$ where h is the distance from the lowest strut to the excavation surface.

EXCAVATION CASE HISTORY

An excavation case history, in which the basal heave failure has been recorded and re-analyzed by Hsieh et al. (2008), is employed to conduct the probabilistic analysis of basal heave in the present study. The dimension of the excavation case is about 100 m long and 26 m wide. A diaphragm wall, 24 m in depth and 0.7 m in thickness, was used as a retaining wall. The final excavation depth was 13.45 m. Figure 2 shows the stratigraphy and construction sequences. The excavation case is located at the backfill zone of a deserted watercourse. The level ranging from GL –10.7 to –44.7 m was the soft silty clay (CL). The groundwater level was approximately at GL –2.8 m. Hsieh et al. (2008) indicated that the basal heave failure occurred about 2.5 hours after the final stage of excavation had been completed (at GL –13.45 m). The entire internal bracing system collapsed in this event of basal heave failure.

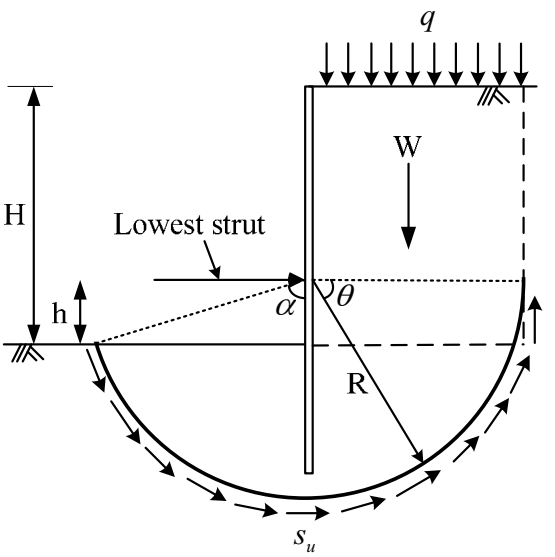

Figure 1. **Method of basal heave analysis in the Taiwan building code**

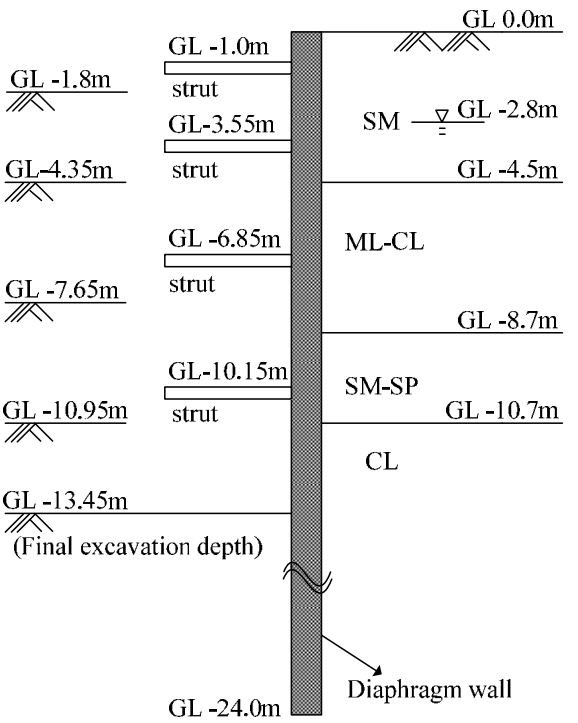

Figure 2. **Construction sequences of the excavation case**

According to the definition of formula of basal heave failure (see Eq. 1 and Figure 1), the undrained shear strength of silty clay between GL –10.7 and –44.7 m has the predominant effect on the analysis of basal heave failure. Hsieh et al. (2008) conducted three kinds of tests, including the field vane shear test, the triaxial unconsolidated undrained (UU) test, and the K_0-consolidated undrained axial

compression test. Their study concluded that the undrained shear strength determined by the triaxial unconsolidated undrained test is suitable for the isotropic basal heave analysis using the Taiwan building code, whereas the FS calculated from the triaxial K_0-consolidated undrained axial compression test tends to be higher and therefore not suitable for basal heave analysis. The FS obtained from the field vane shear test tends to be irregular. Therefore, only the undrained shear strength determined by the UU test is adopted to conduct the probabilistic analysis in the present study.

Figure 3 reveals the results of UU tests on the undisturbed samples taken from the layer at depths from -10.7m to -30m in this excavation site. The undrained shear strength of clay at various depths must be determined for the calculation of factor of safety against basal heave. Due to the limited results of UU tests, those data points are used to determine a simplified profile of undrained shear strength with depth for the intended probabilistic analysis of basal heave in the following section. In addition, the in-situ measurements show that the pore-water pressure obtained with electronic piezometers is nearly hydrostatic. For simplicity, other basic soil properties for this silty clay layer are not shown herein and can be referred to Hsieh et al. (2008).

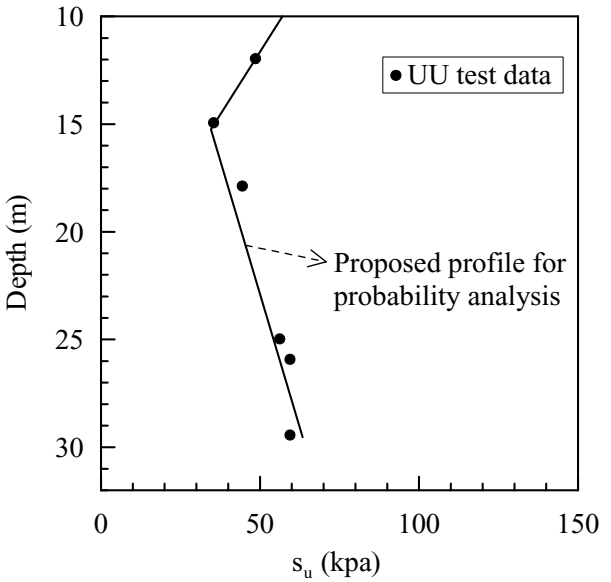

Figure 3. **Variation of undrained shear strength of clay layer with depth**

PROBABILISTIC ANALYSIS FOR BASAL HEAVE

As expressed in Equation 1, five parameters are required in the analysis of basal heave, that is, R, W, α, q and s_u. The former four parameters can be precisely determined (fixed values) provided the excavation design is completed. Therefore, only the uncertainty of the latest parameter (s_u) must be provided for the probabilistic analysis of basal heave. According to past studies (e.g., Phoon 1999), the coefficient of variation (COV) for undrained shear strength of clay varies within a wide range. For instance, Phoon (1999) indicated that the COV values of medium clay would fall in the range from 0.11 to 0.49. The mean value of COV is 0.22. The UU test has been extensively conducted in Taipei silty clay over the past decades. It may be difficult to

determine the COV value of undrained shear strength of the Taipei clay based only on the six data points of UU tests, as shown in Figure 3. This study collected the results of UU tests presented in several previous studies (e.g., Huang et al. 1987; Moh et al. 1989) to preliminarily estimate the value of COV. The computation results reveal that the COV of undrained shear strength of the Taipei clay is approximately equal to 0.2-0.3, which is similar to that presented by Phoon (1999).

The profile of undrained shear strength of clay proposed in Figure 3 as well as the assumption of normal distribution with COV=0.1, 0.2, 0.3, 0.4, and 0.5 are incorporated together into the probabilistic analysis of basal heave failure using the Monte Carlo simulation method. Figure 4 shows the analysis results for various COV scenarios. The relative frequency is adopted to draw the histogram for various factor of safety in this figure. The mean value of factor of safety against basal heave computed with various COV values is around 1.05±0.01. The standard deviation of factor of safety against basal heave increases with the increase of COV value. Also shown in this figure are the best-fit normal distribution curves for each of COV scenarios. This result is expectable due to the normal distribution assumption for the input soil parameter, s_u.

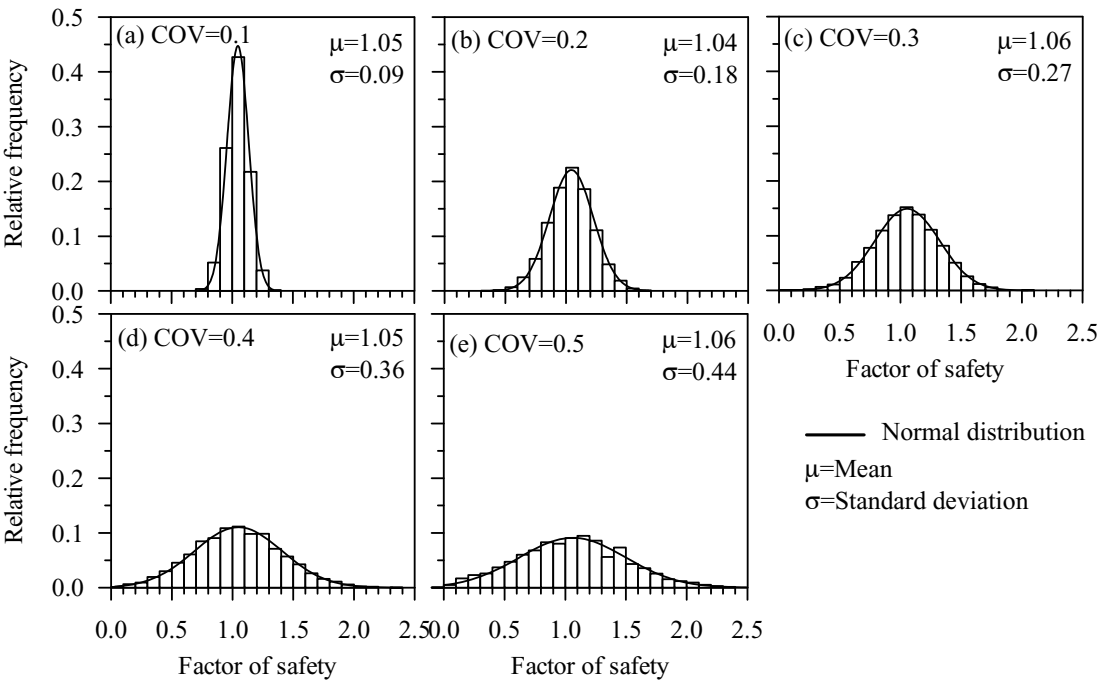

Figure 4. Histogram and distribution of factor of safety against basal heave computed based on UU tests

Based on the best-fit normal distribution curves shown in Figure 4, it is feasible and simple to conduct the probabilistic analysis of basal heave failure provided the definition of factor of safety against basal heave is given. In theory, the basal heave failure can be defined as the factor of safety is equal to 1.0 (see Figure 5). Another possible definition is the requirement of the design code. In this study, FS=1.2 proposed by the Taiwan building code for the excavation design is also

employed as a criterion to compute the probability of failure although it may not necessarily reflect the real failure situation.

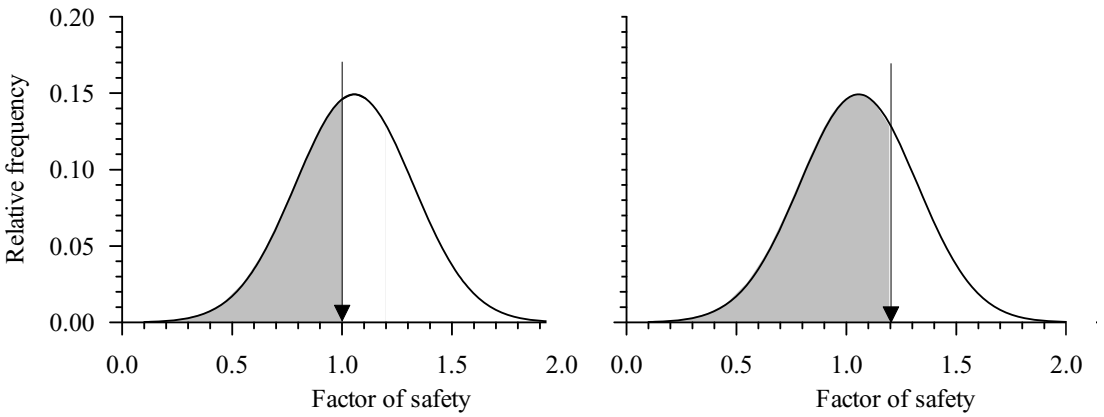

(a) based on failure definition in theory (b) based on requirement of design code

Figure 5. Definitions of probability of basal heave failure

Figure 6 reveals the results of probabilistic analysis for basal heave failure. For the definition of FS=1.0, the probability of failure would increase with the increase of COV. However, for the scenario of FS=1.2, the opposite trend, that probability of failure decreases with the increase of COV, can be obtained. Note that it is not appropriate to conclude that the excavation design is relatively safe when higher COV of undrained shear strength is given. As shown in Figure 6, the accuracy in estimating the probability of failure against basal heave with two scenarios (FS=1.0 and FS=1.2) would be significantly reduced with the increase of COV.

As shown in Figure 6, when COV is equal to 0.2, the estimated probability of failure is approximately equal to 0.8 with FS=1.2 and 0.4 with FS=1.0, respectively. These results reflect that the probability that the original excavation design would not meet the requirement of the Taiwan building code based on the results of re-investigation of soil properties in this case is as high as 80%, while the probability of basal heave failure is about 40%, which is considered really high. Compared with the original analysis of basal heave in this case, the undrained shear strength of clay adopted in the original analysis is relatively higher than that determined by the UU tests conducted by Hsieh et al. (2008).

As shown in Figure 4, the factor of safety against basal heave calculated by the deterministic analysis (Equation 1) is 1.05 greater than 1.0. It may be concluded that the design of excavation is safe in theory although the factor of safety is lower than the requirement of the design code. However, the probability of failure is about 40% in this case. Use of probabilistic analysis can provide more information to engineers to judge the rationality of engineering design. Also, this result reflects that it is very crucial to make every effort to conduct the high-quality test and determine the appropriate soil parameters, irrespective of use of deterministic analysis or probabilistic analysis.

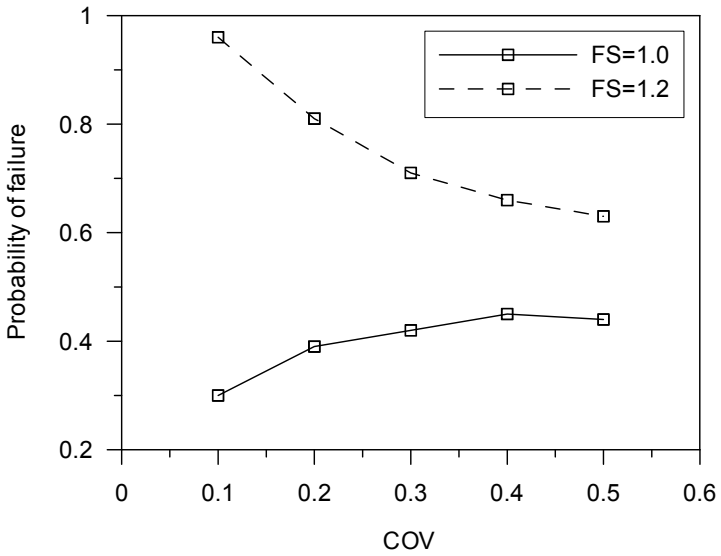

Figure 6. **Probability of basal heave failure and probability of less than FS = 1.2**

CONCLUSIONS

This study conducted the probabilistic analysis on an excavation case in Taipei, in which the basal heave has occurred, based on the UU test results presented by Hsieh et al. (2008) as well as the Taiwan building code. According to the results of probabilistic analysis, the mean value of factor of safety is 1.05±0.01. For the scenario of COV=0.2, the probability of basal heave failure is approximately equal to 40%. If we take the requirement of the design code (FS=1.2) as a criterion to calculate the probability of basal heave failure, the probability of failure would reach as high as 80%. Note that use of FS=1.2 to calculate the probability of failure does not represent a real "failure" condition. These results reflect that there is a probability of 80% that the original excavation design would not meet the requirement of the Taiwan building code based on the results of re-investigation of soil properties in this case. Use of probabilistic analysis can provide more information to engineers to judge the rationality of engineering design.

ACKNOWLEDGEMENTS

The study on which this paper is based was supported by the National Science Council, Taiwan through Grant NSC 98-2221-E146-006. This financial support is greatly appreciated. The opinions expressed in this paper do not necessarily reflect the views and policies of the National Science Council, Taiwan.

REFERENCES

Hsieh, P. G., Ou, C. Y., and Liu, H. T. (2008). "Basal heave analysis of excavations with consideration of anisotropic undrained strength of clay." *Canadian Geotechnical Journal*, 45, 788-799.

Huang, C. T., Lin, Y. K., Kao, T. C., and Moh, Z. C. (1987). "Geotechnical Engineering Mapping of the Taipei City," *9th Southeast Asian Geotechnical Conference*, Bangkok, Thailand, 3-109-3-120.

Kung, T. C. (2003). *Surface settlement induced by excavation with consideration of small strain behavior of Taipei silty clay*, Ph.D. Dissertation, National Taiwan University of Science and Technology, Taipei, Taiwan.

Kung, G. T. C., Juang, C. H., Hsiao, E. C. L., and Hashash, Y. M. A. (2007). "Simplified model for predicting wall deflection and ground surface settlement caused by braced excavation in clays." *Journal of Geotechnical and Geoenvironmental Engineering*, ASCE, 133(6), 731-747.

Moh, Z. C., Chin, C. T., Liu, C. J., and Woo, S. M. (1989). "Engineering Correlations for Soil Deposits in Taipei," *Journal of the Chinese Institute of Engineers*, 12(3), 271-283.

Phoon, K. K. (1999). "Characterizaton of Geotechnicial variability," *Canadian Geotechnical Journal*, 36, 612-624.

Schuster, M., Kung, G. T. C., Juang, C. H., and Hashash, Y. M. A. (2009). "Simplified model for evaluating damage potential of buildings adjacent to a braced excavation." *Journal of Geotechnical and Environmental Engineering*, ASCE, 135(12), 1823-1835.

Taiwan Geotechnical Society. (2001). *Design specifications for the foundation of buildings.* Taiwan Geotechnical Society, Taipei, Taiwan.

Terzaghi, K. (1943). *Theoretical soil mechanics*. John Wiley & Sons Inc., New York.

Influence of the Scale of Fluctuation of the Friction Angle on the Face Stability of a Pressurized Tunnel in Sands

M. Guilhem Mollon[1], Kok-Kwang Phoon[2], F.ASCE, Daniel Dias[3], and Abdul-Hamid Soubra[4], M.ASCE

[1]LGCIE, INSA Lyon, Université de Lyon, Domaine scientifique de la Doua, Bât JCA Coulomb, 20 Avenue Albert Einstein, 69621 Villeurbanne, France ; guilhem.mollon@insa-lyon.fr
[2]Civil Engineering Department, National University of Singapore, Singapore; Block E1A, #07-03, 1 Engineering Drive 2, Singapore 117576; cvepkk@nus.edu.sg
[3]LGCIE, INSA Lyon, Université de Lyon, Domaine scientifique de la Doua, Bât JCA Coulomb, 20 Avenue Albert EINSTEIN, 69621 Villeurbanne, France ; daniel.dias@insa-lyon.fr
[4]GeM, Université de Nantes, Boulevard de l'université, BP 152, 44603 Saint-Nazaire cedex, France ; abed.soubra@univ-nantes.fr

ABSTRACT

The present paper makes use of a 2D limit analysis mechanism developped in Mollon et al. 2011 to study the influence of the scale of fluctuation of the friction angle in a soil mass on the critical collapse pressure of a pressurized tunnel face. The variability of the soil is simulated by random fields in the framework of the Karhunen-Loeve Expansion method, with various scales of fluctuation. A Monte-Carlo sampling scheme is used to examine the probabilistic impact of this variability as well as possible emergent behaviours that may be qualitatively different from well known behaviours associated with homogeneous sand. Probabilistic results show that L/D ratio (i.e. autocorrelation length of the friction angle random field, over tunnel diameter D) has an important influence on the dispersion of the critical collapse pressure. For a small to moderate value of this scale of fluctuation with respect to the tunnel diameter, it appears that there are several critical positions of the failure mechanism, whereas such phenomenon is unlikely for large values of L/D.

INTRODUCTION

The estimation of the fluid pressure that has to be applied to a tunnel face to maintain its stability is of major interest in real tunnelling projects. This paper aims at investigating the impact of the scale of fluctuation of the friction angle of sands on the collapse of a pressurized tunnel face. This is done by using a 2D analytical collapse mechanism defined in the framework of the kinematical theorem of limit analysis. This mechanism was extensively presented and validated in homogeneous and heterogeneous sands in a previous study (Mollon et al. 2011), and appeared to provide a reasonable estimate of the critical collapse pressure and of the shape of failure in a spatially varying sand, at a moderate time cost. Extensive stochastic simulations of heterogeneous sands are used herein to evaluate the role of the scale of fluctuation of the soil friction angle and its impact on the face stability.

The collapse mechanism is a rotational rigid block as shown in Fig. 1. It moves with a cylindrical velocity field about point O. The geometrical construction of this mechanism is based on a spatial discretization of a lower and an upper slip lines, emerging respectively from two points A and B belonging to the tunnel face. The

failure mechanism is defined by four geometrical parameters as shown in Fig. 1a: R and β are related to point O (centre of rotation), and H and R_m are related to the position of the two points A and B. The discretization process (Fig. 1b) uses a large number of radial lines meeting in O (two successive lines are separated by angle δα). Thus, the two slip lines AE and BE are divided into a large number of small segments, which respect locally the normality condition related to the kinematical theorem (i.e. each segment of the slip lines makes an angle φ with the velocity vector, φ being dependant on the coordinates (x, y) of the point considered). The general assumptions of this mechanism and its generation are detailed in Mollon et al. [2011]. For each set of the four geometrical parameters, the kinematical theorem of limit analysis allows one to obtain a value of the collapse pressure σ_c. The optimal value of this pressure is obtained by maximization with respect to the four geometrical parameters. A tunnel with a diameter D=10m is adopted as an illustrative example in this study along with a soil unit weight equal to 18kN/m^3.

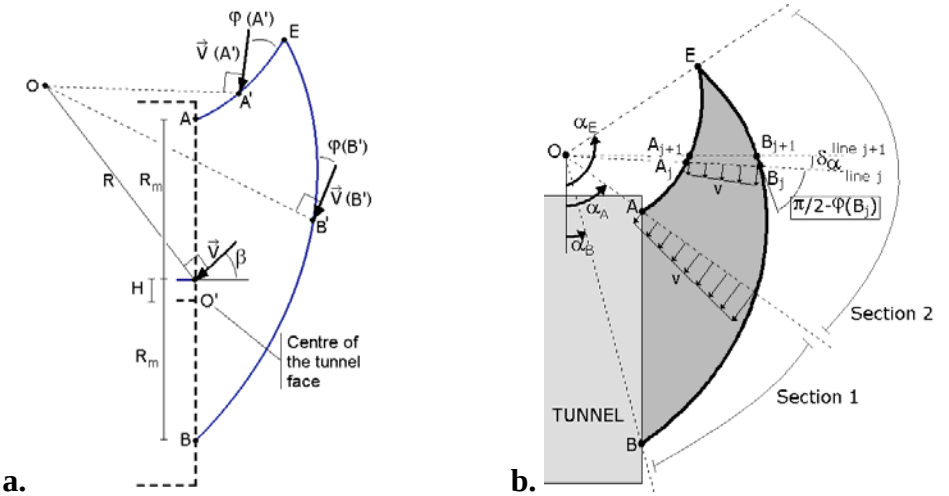

Figure 1. a. General description of the collapse mechanism; b. Discretization scheme

SIMULATION OF RANDOM FIELDS

The spatial variability of the sand is modelled here by random fields, which are simulated using the well known Karhunen-Loeve (KL) expansion. In this preliminary attempt to investigate the impact of the spatial variability of the friction angle on the collapse of a tunnel face, only two-dimensional lognormal fields with a mean μ_{log}=30° and a standard deviation σ_{log}=3° (i.e. a coefficient of variation of 10%) are used. The simulation of such a field requires an underlying normal field with a mean μ_{normal} and a standard deviation σ_{normal} which are deduced from the target mean and standard deviation μ_{log} and σ_{log} (Sudret and Der Kiureghian [2000]). An exponential autocorrelation function is chosen for this underlying normal field:

$$\rho(A,B) = \exp\left(-\frac{|x_A - x_B|}{L_x} - \frac{|y_A - y_B|}{L_y}\right) \quad (1)$$

It can be demonstrated that, as long as the COV remains low (which is true in the present case), the autocorrelation function of the lognormal field is not far from the one of the underlying field. The detailed method of simulating the underlying normal field can be found elsewhere (Sudret and Der Kiureghian [2000], Phoon et al. [2005]). Only isotropic random fields with $L_x=L_y=L$ are used in this study. Several L/D values are studied here, as well as the two limit cases L/D=0 and L/D=∞. An infinite autocorrelation length corresponds to a homogeneous field, and can be modelled by only one random variable. On the other hand, an autocorrelation length equal to zero corresponds to a non-correlated field, i.e. a soil in which the value of φ at each point is totally uncorrelated with the ones of surrounding points. Notice that the KL expansion is not able to generate such a field, and another approach is used here. The soil mass is divided into a very large number of square pixels with a size of 1cm (i.e. D/1000 for a tunnel diameter of 10m), and each pixel is assigned a random value of φ respecting the lognormal distribution given previously. This process is believed to provide a reasonable approximation to an uncorrelated field.

RESPONSE SURFACES

The response surfaces obtained for some realizations of the random field corresponding to various L/D values are provided in Fig. 2. These surfaces are represented by lines of equal value of the collapse pressure σ_c in the plane of the two geometrical parameters β and R of the mechanism (note that, for this figure, a full face failure was considered, i.e. H=0m and R_m=5m). The solid lines denote an interval of 1kPa. The dotted lines denote a more refined interval of 0.2kPa. The most probable collapse mechanism is the one for which the value of σ_c is maximal. For homogeneous fields (L/D=∞), Fig. 2 shows that the response surface is very regular and that the maximum is unique. It can therefore be found very easily with a classical optimisation tool. In heterogeneous soils, however, the response surface is much more complex. In the case L/D=1, its shape is slightly modified and leads to two very close local maximums, which correspond to two collapse mechanisms with a quasi-similar shape. When L/D=0.1, the response surface becomes much more distorted, and leads to two different maximums with very different values of the parameters β and R. However, one of these two maximums has a much larger value of σ_c and probably leads to the preferential failure mechanism. For the two cases L/D=1 and L/D=0.1, the surface remains quite smooth, and optimisation algorithms are able to find the global maximum without difficulty. On the contrary, the case L/D=0 shows a very complex response surface, with a large number of local maximums. Optimisation algorithms are not able to provide the exact location of the global maximum of such a surface, but provide a correct estimate of the maximal value of σ_c because this surface is quite flat at its top. In other words, there are a large number of fairly distinctively different mechanisms (different β and R) producing very similar σ_c. It is not possible to identify the most likely failure mechanism – it appears rather indeterminate.

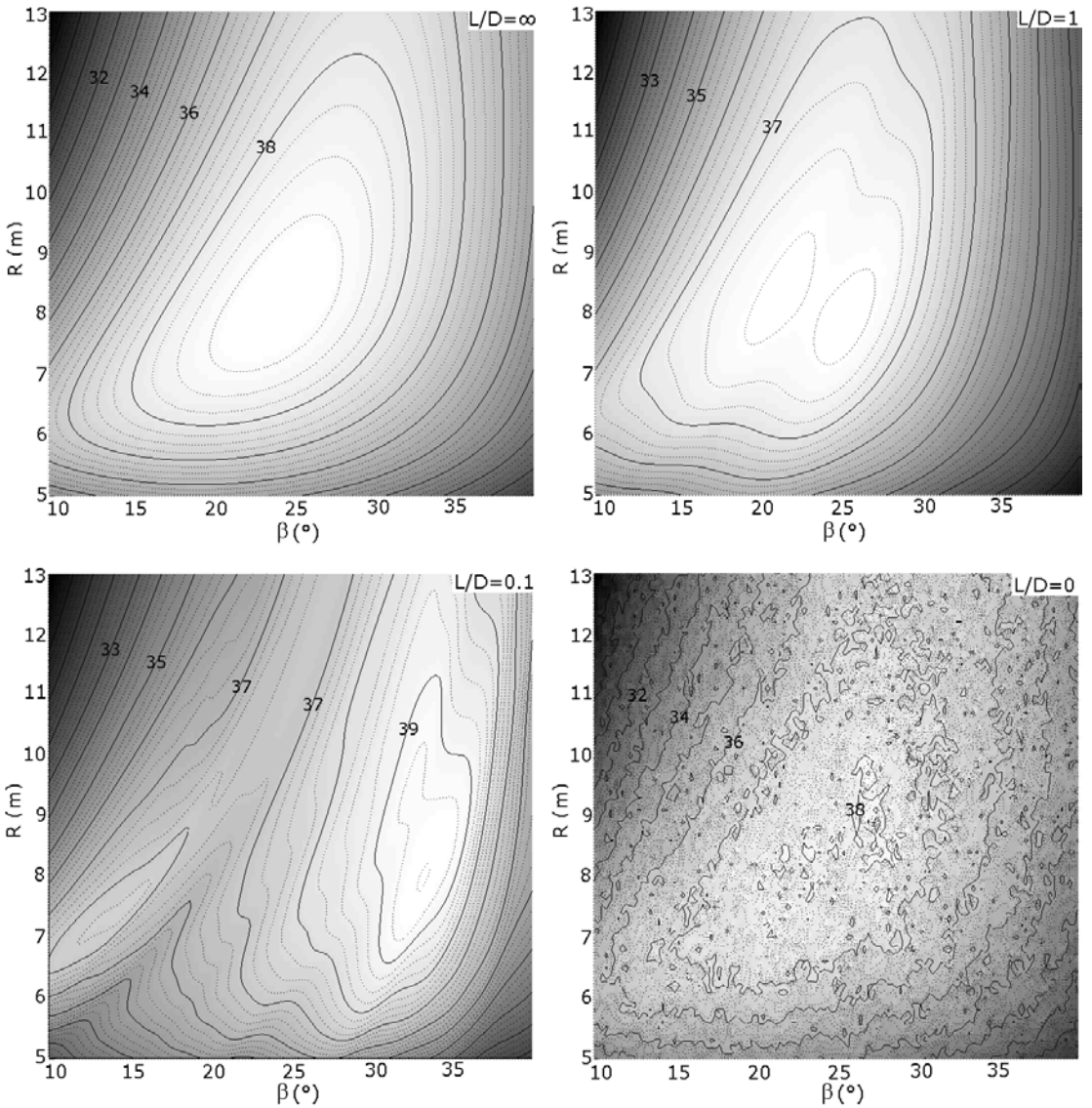

Figure 2. Response surfaces (in kPa) for several values of L/D

MONTE-CARLO SAMPLING

Several values of L/D ranging from 0.05 to 2 are considered, as well as the two limit cases L/D=0 and L/D=∞. For each case, a Monte-Carlo simulation is carried out using 10,000 samples. For each sample, the value of the global maximum σ_c is stored, as well as the corresponding parameters β, R, H, and R_m (except for the case L/D=0, for which the location of the global maximum is indeterminate as may be seen from Fig. 2). Moreover, when a local maximum appears, the collapse pressure and the corresponding parameters are stored as well. It was found that, for all the values of L/D and for the range of the samples examined, the parameters H and R_m of the global and local maximums were always equal to 0m and 5m respectively, which means that the spatial variability of φ in a sand is not able to trigger collapses involving only a part of the tunnel face. Thus, only full-face failures are considered here, and the only varying parameters (β and R) are those related to the position of point O which represents the centre of rotation of the failure mechanism.

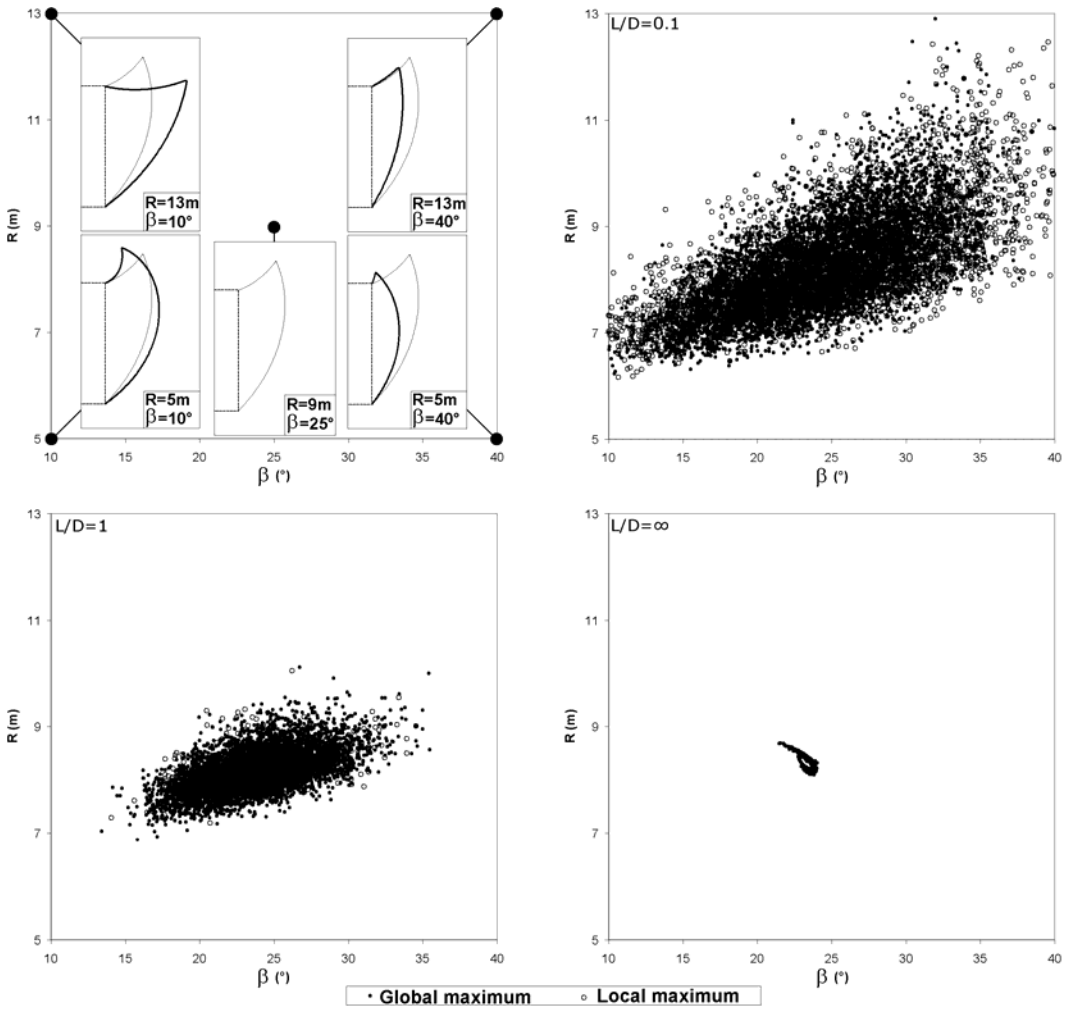

Figure 3. Positions of the global and local maximums of σ_c as obtained from the 10,000 samples for various values of L/D

The positions in the (β, R) plane of the global and local maximums as obtained from the different samples are plotted in Fig. 3. It clearly appears that a small value of L/D leads to a large cloud of maximums and thus to various collapse shapes. On the contrary, a large value of L/D leads to a small variability for the parameters β and R, and thus to a quite "standard" collapse mechanism. Notice that Fig. 3 also shows the critical positions of the failure mechanism for different values of β and R.

Fig. 4a shows the evolution of the coefficients of variation (COV) of β, R, and σ_c with L/D. The observation of Fig. 3 concerning the variability of β and R is confirmed by the values of the COV of β and R given in Fig. 4a. Indeed, the COV of the two parameters β and R are equal to 21% and 12% respectively for a very small scale of fluctuation (L/D=0.05), and decrease to very small values (1% and 0.5% respectively) for a very large scale of fluctuation (L/D=∞). On the other hand, the COV of σ_c increases with L/D, from 4% (for L/D=0.05) to 16% (for L/D=∞). The simple assumption L/D=∞ is therefore conservative in terms of the variability of σ_c. It is interesting that L/D=∞ produces almost the same mechanism but exhibits a large variability in σ_c. On the contrary, L/D=0 produces a large variety of failure mechanisms, but exhibits almost the same σ_c. At first glance, these results seem rather

counter-intuitive. However, the fact that a smaller variability of σ_c was obtained for small L/D values may be explained as follows: for a very small autocorrelation distance, the zone involved by the possible failure mechanism will have average values of the friction angle close to the mean value of the random field because of the large number of high and small values of the friction angle. This leads to close values of the collapse pressure and thus to a smaller variability in this pressure. On the other hand, the fact that a great variability in β and R was obtained for a small autocorrelation distance may be related to the fact that several paths of the failure mechanism would be possible due to the quick changes in the values of the friction angle in this case.

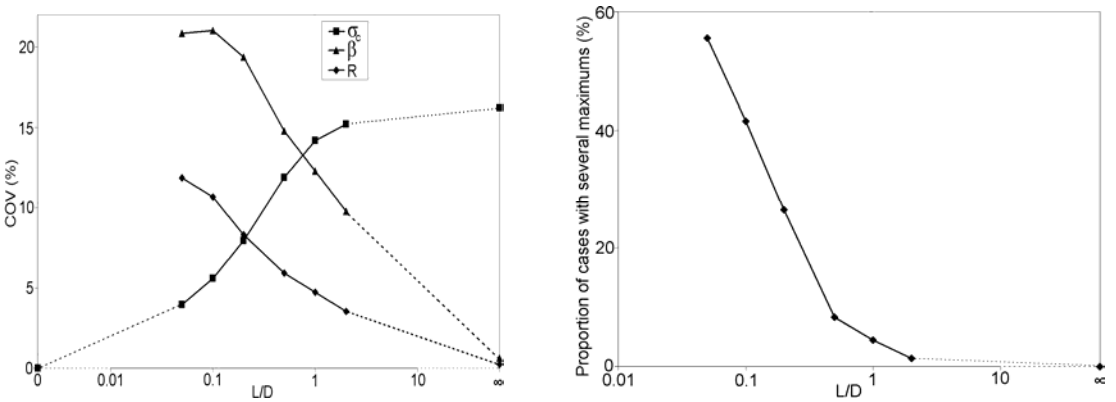

Figure 4. a. Influence of L/D on COV of σ_c, β_c, and R_c; b. Influence of L/D on the proportion of realizations leading to several maximums

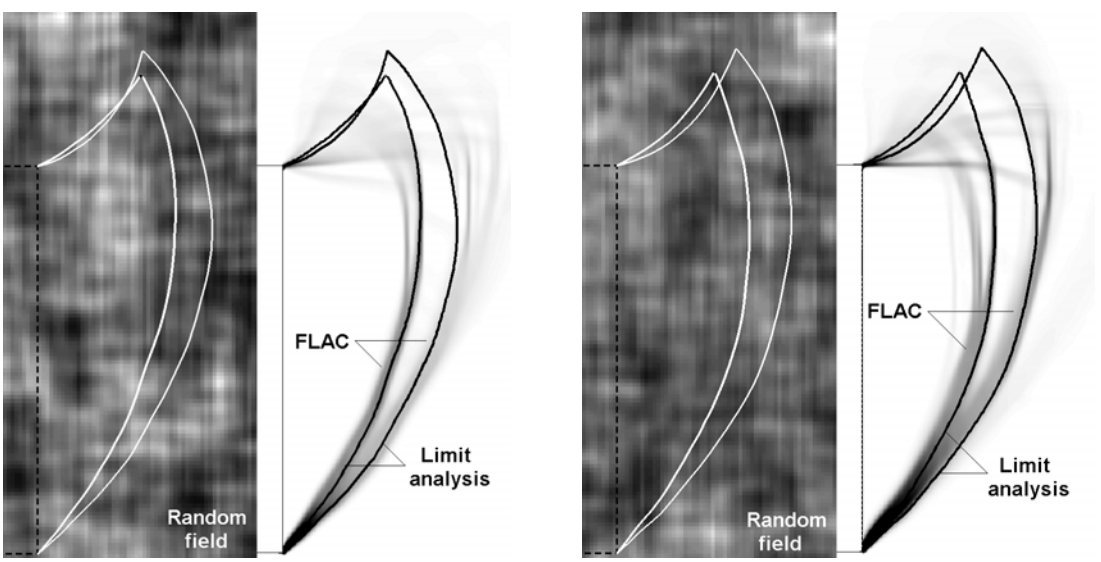

Figure 5. Comparison between limit analysis and FLAC for two examples of realizations leading to multiple failures.

Fig. 4b shows the impact of L/D on the proportion of samples leading to several maximums. For L/D=∞, this proportion is zero because homogeneous soils always lead to very regular response surfaces (Fig. 2). However, it appears that this proportion increases when L/D decreases and can reach 55% for L/D=0.05. When several maximums exist, the global maximum may have a much larger value of σ_c

than the local one. In such a case, one can assume that the local maximum has a limited importance and that the global maximum is the one corresponding to the real failure. However, Monte-Carlo results show that 3.8% of the samples for L/D=1 leads to two maximums with a relative difference smaller than 1% in terms of σ_c. For L/D=0.1, this proportion reaches 18.5%. In such a case, when two maximums have very close values of σ_c, it is very difficult to discern which mechanism or a combined mechanism will be realized in reality. On Fig. 5, one can observe the collapse mechanisms obtained for two samples exhibiting such a "multiple" failure, for L/D=0.1. Two failure mechanisms corresponding to the two close maximums of σ_c are plotted for each sample. In order to verify the obtained failure patterns, the software FLAC is used to set up a numerical model (Fig. 6a). FLAC is a commercial program based on a lagrangian finite differences resolution scheme. The critical collapse pressure σ_c is found by a bisection method described in Mollon et al. 2011, and the failure pattern is obtained by applying σ_c-0.3kPa to the tunnel face. The advantage of the FLAC model when compared to the proposed limit analysis model is that it does not imply any assumption of the failure velocity field. It is therefore a convenient verification tool, despite its expensive computational cost. The failure patterns obtained by FLAC are provided as well in Fig. 5, and show a good agreement with the limit analysis results. The spatial variability of φ in sands is therefore able to trigger qualitatively different and more complex failure mechanisms involving several concurrent slip-lines, which do not appear in homogeneous soils.

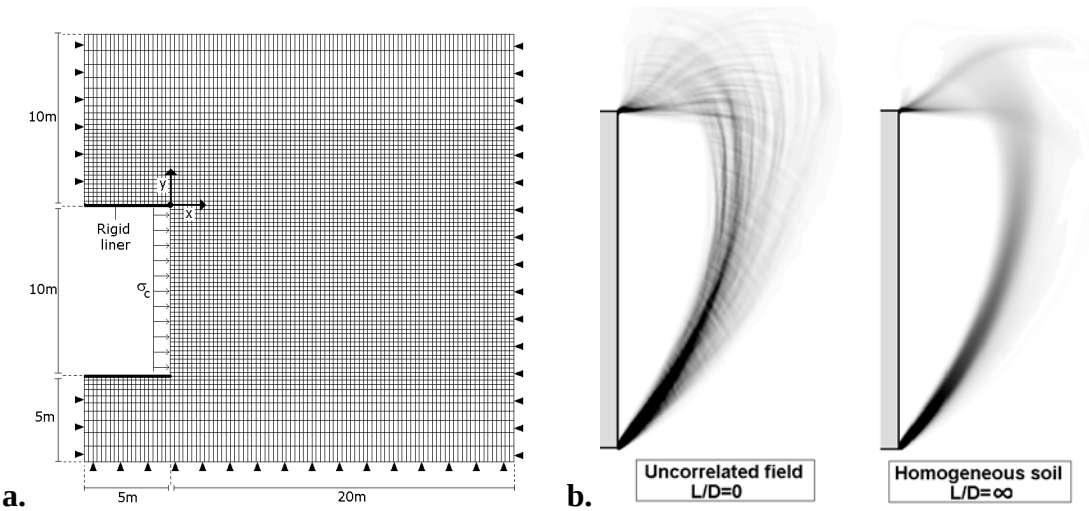

Figure 6. a. Flac Model; b. Failure shapes for the two limit cases

STUDY OF THE LIMIT CASE L/D=0

When observing the response surface of the limit case L/D=0 (Fig. 2), it is difficult to assess if the number of maximums is very large (if one considers all the irregularities of the response surface as local maximums) or if there is only one maximum (if one considers that those irregularities are irrelevant and that the surface has to be smoothed). The large number of local maximums would lead to a large number of concurrent collapse mechanisms. On the other hand, the irregularities of the surface could potentially be interpreted as numerical artifacts/noises superposed to an "actual" smooth surface, which would lead to a single mechanism and a failure

close to the ones observed in homogeneous soils. On Fig. 6b, one can observe the failure shapes obtained by the FLAC model for the two limit cases L/D=0 and L/D=∞. According to these results, it seems that the numerous local maximums observed on the response surface of the case L/D=0 are physically meaningful, since the failure apparently involves a large number of slip lines. Thus, FLAC and limit analysis results seem to be consistent. However, it could mean that both approaches are wrong in the sense that the approximate method of representing an uncorrelated field used in this study may be inadequate. In such a case, a smoothing process applied to the response surface may be acceptable, and the maximum may be unique. This would imply the existence of a "critical" autocorrelation length, for which the proportion of multiple failures would be maximum at an intermediate autocorrelation length between the two limits, L/D=0 and L/D=∞. Nevertheless, the existence of very small autocorrelation lengths may be academic because these scales of fluctuation are usually smoothed by the common geotechnical experimental laboratory or field devices, which deal with meso-scale samples and meso-scale averaged parameters. The physical interpretation of classical parameters such as the friction angle at very small scales is currently tenuous. These important issues are left for further studies.

CONCLUSION

A two-dimensional limit analysis mechanism is used in this paper to study the impact of the spatial variability of the friction angle of sands on the stability of a pressurized tunnel face. A Monte-Carlo method is used to carry out the stochastic simulations, and evaluate the impact of the autocorrelation length of the random field. It appears that the heterogeneities of the sand are not able to trigger partial failures (i.e. failures involving only a part of the tunnel face). A small autocorrelation length (with respect to the tunnel diameter) leads to a wide variety of collapse mechanisms, but reduces the dispersion of the critical collapse pressure. On the contrary, a large autocorrelation length leads to quite "standard" unique failure mechanism, but increases the coefficient of variation of the collapse pressure. The assumption of a homogeneous soil with a large autocorrelation distance is therefore conservative in terms of the variability of the critical collapse pressure. Moreover, it appears that small autocorrelation lengths are able to trigger multiple failures. This emerging phenomenon could not appear in homogeneous soils, and emphasises the practical interest of stability studies involving spatially variable soils.

REFERENCES

Mollon, G., Phoon, K.-K., Dias, D., and Soubra, A.-H. (2011), "Validation of a new 2D failure mechanism for the stability analysis of a pressurized tunnel face in a spatially varying sand", *J. of Engrg. Mech,* ASCE, in press.

Phoon, K.K., Huang, H.W., and Quek, S.T. (2005). "Simulation of strongly non-Gaussian processes using Karhunen-Loeve expansion." *Prob. Engrg. Mech.*, 20 (2), 188-198.

Sudret, B, and Der Kiureghian, A. (2000). "Stochastic finite element methods and reliability, a state of the art", Report n°UCB/SEMM-2000/08, November 2000, Dpt. of Civil and Environmental Engineering, Berkeley, California.

Probabilistic Finite Element Analysis of a Raft Foundation Supported by Drilled Shafts in Karst

D.V. Griffiths[1], D. Dotson[2] and J. Huang[1]

[1]Division of Engineering, Colorado School of Mines, Golden CO 80401; PH (303) 499 8507; email: d.v.griffiths@mines.edu
[2]Chief Designer Geo-Structural Design Group, AMEC, Nashville, TN 37211; PH (615) 333 0630 ; email: don.dotson@amec.com

ABSTRACT

The paper describes probabilistic analyses performed as part of a large expansion to an existing cement manufacturing plant. A raft supported by drilled shafts was proposed for the project, but during installation, significant slurry and concrete loss began to occur indicating numerous voids existed in what was previously considered competent limestone bedrock. Since the possibility of voids, especially at the shaft tip, could serious reduce the shaft capacity, a probabilistic Monte Carlo 3D finite element simulation was proposed for the most heavily loaded raft foundation. The purpose of the simulation was to determine the probability of adverse performance, giving guidance as to whether any remedial measures (e.g., additional structural elements or thickened raft) might be required.

INTRODUCTION

This paper details analysis and results obtained from 3D finite element deterministic and probabilistic studies of a heavily loaded area of a factory expansion project.

The foundation for a large expansion to a manufacturing facility was under construction. The proposed foundation described in this paper was to consist of a reinforced concrete raft foundation, 9.5 feet thick, supported by 5 ft diameter shafts founded in competent rock as shown in plan-view in Figure 1. During construction of the shafts, karst was discovered when large quantities of drilling slurry were lost during drilling of some of the rock sockets. A subsequent, detailed subsurface investigation of the rock beneath the remainder of the shafts to be constructed, revealed that 35% of the exploratory borings contained randomly distributed voids that were expected to significantly undermine the tip resistance of some of the shafts. Little was known about the locations of the karst voids underlying shafts that had been successfully constructed, so a probabilistic approach was adopted to determine the effect of the voids on the performance of the raft.

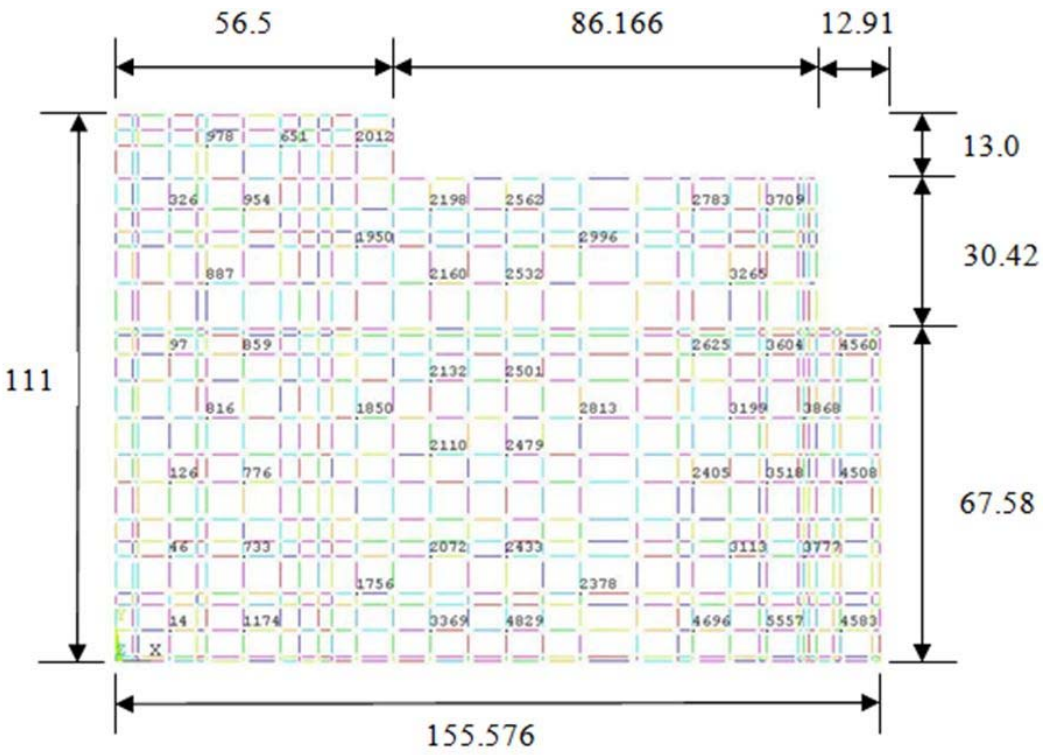

Figure 1. Plan view of finite element mesh for raft showing the numbered locations of shafts (dimensions in ft).

The analyses were performed using the software suite described by Smith and Griffiths (2008) which can be downloaded from the authors web site at `www.mines.edu/~vgriffit/4th_ed` In particular, Program 5.4 from that system, which models 3D elastic solids using 20-node hexahedral elements, was modified to include vertical springs to represent the supporting shafts. The springs were assigned one of two possible stiffness values. A shaft founded on competent rock was assigned twice the stiffness of a shaft founded in a void. The rationale for this 2:1 ratio was that results from an O-test performed on a shaft in competent rock, which indicated a similar stiffness contribution from the tip and the sides as shown in Figure 2. A conservative value of about 89,000 kip/ft was selected as the spring stiffness for a shaft in competent rock.

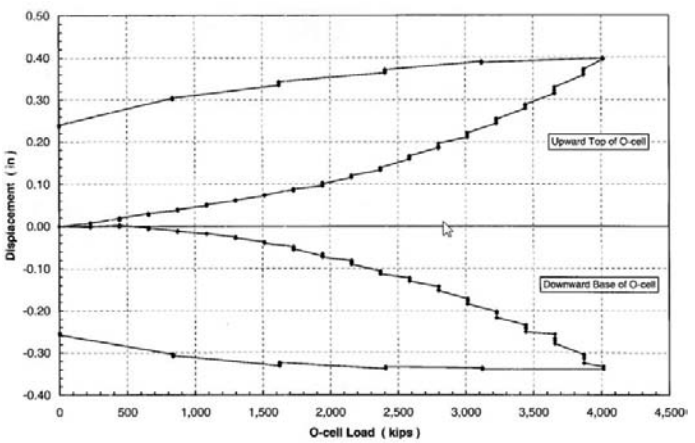

Figure 2. Results of O-test performed on a shaft founded in competent rock.

FOUNDATION ANALYSES

Referring to Figure 1, the nodes signified by a small dot and a number indicate the plan locations of the 49 shafts situated below the raft. The thickness of the raft was 9.5 ft, and two rows of elements were included in the depth direction. The full model consisted of 1210 20-node hexahedral elements and 7084 nodes. Reduced Gaussian integration (8 sampling points per element) was used to generate the stiffness matrix of the raft after which the shaft spring stiffnesses were added to the appropriate diagonal terms of the matrix. The properties used for the analysis are given in Table 1.

Table 1. Data for raft/shaft foundations.

Young's modulus of slab	453,600.0 kip/ft^2
Poisson's ratio of the slab	0.17
Likelihood of tip hitting a void	35%
Shaft stiffness (tip in competent rock)	89,000 kip/ft
Shaft stiffness (tip in void)	44,500 kip/ft
Total vertical load on the raft	47,870 kip

LOADING

Vertical forces were applied at numerous locations on the slab as shown in Figure 3, in addition to two moments to model wind loading on the superstructure. The figure also shows the location of two fixed boundary nodes to eliminate horizontal movement and rotation of the raft about a vertical axis.

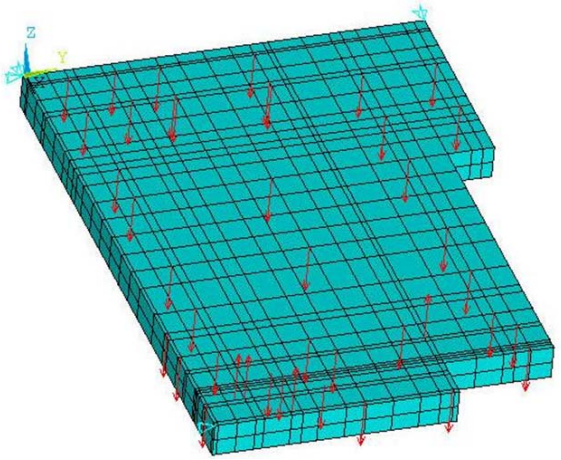

Figure 3. Finite element mesh for raft showing applied loads and fixed nodes.

DETERMINISTIC ANALYSES

Two deterministic analyses were initially performed; one in which shafts were assigned stiffness corresponding to intact rock (89,000 kip/ft) and one in

which all shafts were assigned stiffness corresponding voids (44,500 kip/ft). These analyses established lower and upper bounds on raft displacements.

Results. With all springs set to 89,000 kip/ft a maximum vertical displacement of 0.0275 ft (0.33 in) was obtained in close agreement with an independent analysis using the package STAAD that gave 0.32 in. The maximum in-plane moments back-figured from the stresses across the slab sections were $M_x = 575$ kip ft/ft and $M_y = 1301$ kip ft/ft. The corresponding displacement with all springs set to 44,500 kip/ft was 0.0455 ft (0.55 in) with essentially the same maximum moments.

STOCHASTIC ANALYSES

Probabilistic analysis of foundation settlement is a rapidly growing area of interest to engineers and academics (e.g. Baecher and Ingra 1981, Beacher and Christian 2003, Brzakała and Puła 1996).

The stochastic analyses described in this paper used a standard normal distribution to assign a reduced stiffness of 44,500 kip/ft to 35% of the shafts and the full stiffness of 89,000 kip/ft to 65% of the shafts. There are 49 shafts and the loads were the same as in the deterministic analyses. The analysis with stochastic spring stiffnesses was repeated 1600 times using Monte-Carlo simulations. With the assumption of independence between shafts (i.e. one shaft encountering a void would not change the likelihood of one of its neighbors also encountering a void), the analysis is a Bernoulli process with a mean of $49 \times 0.35 = 17$ and a standard deviation of $\sqrt{49 \times 0.35 \times (1 - 0.35)} = 3.34$ as shown in the histogram of Figure 4.

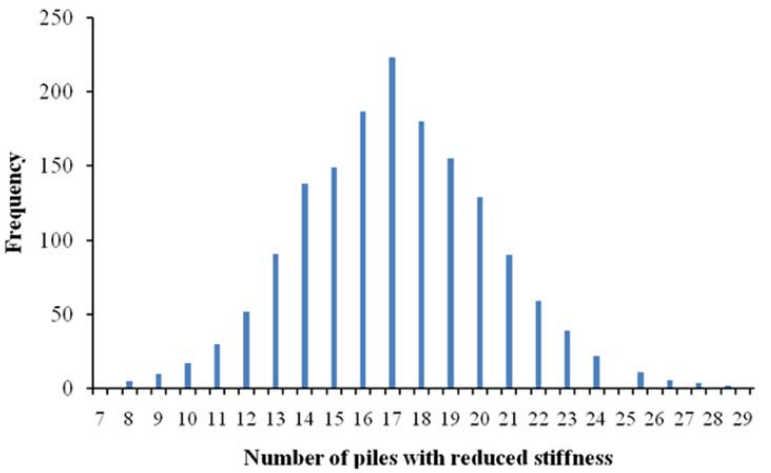

Figure 4. Histogram of number of shafts with reduced stiffness under raft Following 1600 Monte-Carlo simulations.

From each simulation, the maximum vertical displacement and the maximum in-plane moments in the slab in two directions were recorded. Following the suite of Monte-Carlo simulations, histograms of these quantities were plotted and their means and standard deviations computed.

Maximum Vertical Displacement. Figure 5 shows a histogram of the maximum vertical displacement. In the vast majority of simulations it occurred at the same place as in the deterministic analysis. A summary of statistical results for the maximum displacement following 1600 Monte-Carlo simulations is given in Table 2.

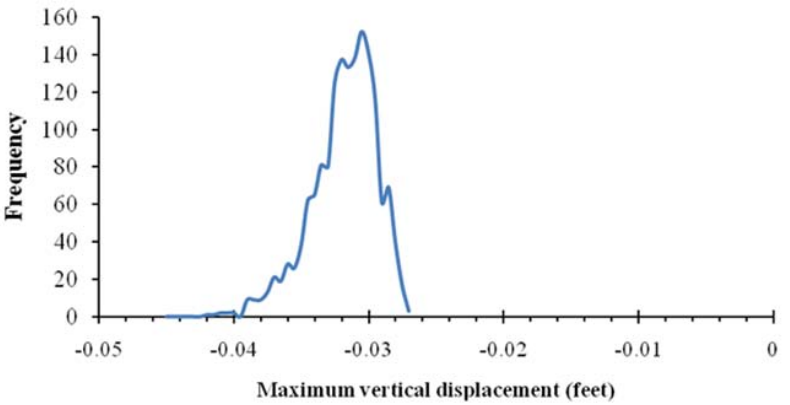

Figure 5. Histogram of the maximum vertical displacement in the raft following 1600 Monte-Carlo simulations.

Table 2. Statistical output for the maximum vertical displacement in the raft.

Mean	$\mu_{\delta(\max)} = 0.0321$ ft (0.385 in)
Standard deviation	$\sigma_{\delta(\max)} = 0.0024$ ft (0.029 in)
Minimum	$\delta_{(\min)} = 0.0273$ ft (0.327 in)
Maximum	$\delta_{(\max)} = 0.0423$ ft (0.507 in)

It can be noted that the coefficient of variation of the maximum displacement is $v_{\delta(\max)} = \sigma_{\delta(\max)} / \mu_{\delta(\max)} = 0.07$, or 7% which is quite low, presumably due in part to the stiff 9.5 ft thick reinforced concrete raft.

Moments. Figures 6 and 7 show histograms of the maximum moments in the raft following 1600 Monte-Carlo simulations.

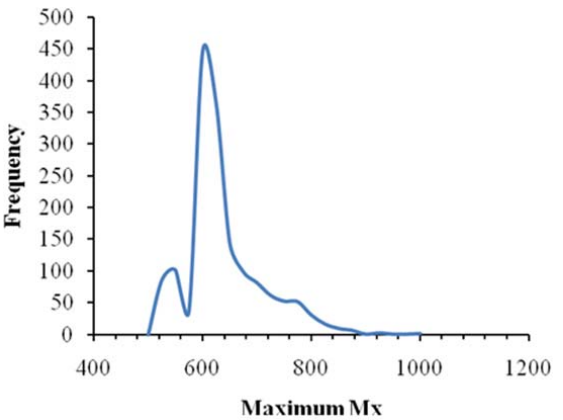

Figure 6. Histogram of the maximum M_x moment in the raft following 1600 Monte-Carlo simulations (moments in kip ft/ft)

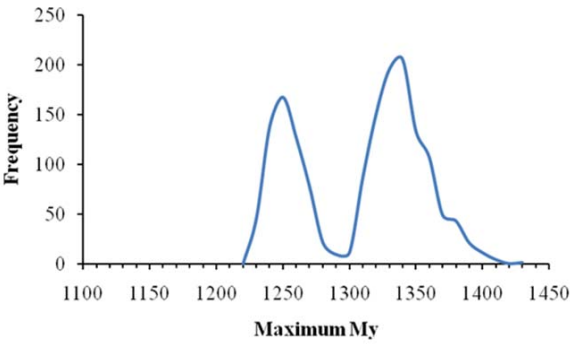

Figure 7. Histogram of the maximum M_y moment in the raft following 1600 Monte-Carlo simulations (moments in kip ft/ft).

A summary of statistical results for the maximum M_x and M_y moments in the raft following 1600 Monte-Carlo simulations is given in Table 3.

Table 3. Statistical output for the maximum M_x and M_y moments in the raft.

Mean	$\mu_{M_{x(\max)}} = 626$ kip ft/ft	$\mu_{M_{y(\max)}} = 1304$ kip ft/ft
Standard deviation	$\sigma_{M_{x(\max)}} = 72$ kip ft/ft	$\sigma_{M_{y(\max)}} = 46$ kip ft/ft
Minimum	$M_{x(\max)\max} = 978$ kip ft/ft	$M_{y(\max)\max} = 1422$ kip ft/ft
Maximum	$M_{x(\max)\min} = 509$ kip ft/ft	$M_{y(\max)\min} = 1224$ kip ft/ft

It can be noted that the coefficients of variation of the maximum moments are given as $v_{M_{x(\max)}} = \sigma_{M_{x(\max)}} / \mu_{M_{x(\max)}} = 0.12$ and $v_{M_{y(\max)}} = \sigma_{M_{y(\max)}} / \mu_{M_{y(\max)}} = 0.04$

While the variability of $M_{x(max)}$ is relatively higher than $M_{y(max)}$, it can still be concluded that the level of variability of the maximum moment in both directions is low, with a worst-case coefficient of variation of about 12%.

The histogram of $M_{y(max)}$ shown in Figure 7 displays an unusual bi-modal distribution which might warrant further investigation. At this stage the bi-modal behavior is thought to be due to a nearby critical underlying shaft that causes the moment to switch between the two values depending on whether its stiffness is high or low.

CONCLUDING REMARKS

Deterministic and stochastic analyses have been performed on the raft foundation of a factory expansion project. The motivation for the analyses was that randomly located voids in the underlying karst could lead to significantly reduced shaft resistance. Monte-Carlo simulations were performed with the assumption that 35% of shafts had no tip resistance and would have side resistance only.

An initial deterministic analysis gave very close agreement for the maximum displacement with previously obtained results using the STAAD package. Stochastic analyses on the raft with randomly reduced shaft stiffness gave a quite low coefficient of variation of the maximum displacement of about

7%. The coefficients of variation of the maximum in-plane moments were somewhat higher with a maximum of 12% for the moment about the x-direction.

Subsequent analyses could be performed using these values to estimate the probability of threshold displacements or moments being exceeded. The low variations observed for these quantities however suggest that this might be of marginal value, since relatively small safety margins would lead to extremely low probabilities of unacceptable performance. Ultimately, based on the probabilistic analyses described in this paper, it was concluded that poor performance of the raft foundation was unlikely and that the project could continue without extensive mitigation measures such as grouting of the underlying karst or installation of additional drilled shafts.

ACKNOWLEDGEMENTS

The authors wish to acknowledge the support of NSF grant CMMI-0970122 on “GOALI: Probabilistic Geomechanical Analysis in the Exploitation of Unconventional Resources" and KGHM Cuprum, Wrocław, Poland through the Framework 7 EU project on “Industrial Risk Reduction” (IRIS).

REFERENCES

Baecher, G.B. and Ingra, T.S. (1981). “Stochastic FEM in settlement predictions. *J.Geotech. Engng-ASCE*, 107, 449–463.

Baecher, G.B. and Christian, J.T. (2003). “Reliability and Statistics in Geotechnical Engineering”, John Wiley & Sons, Hoboken, NJ.

Brzakała,W. and Puła, W. (1996), “A probabilistic analysis of foundation settlements.”, *Comput. Geot*., 18(4), 291-309.

Fenton, G.A. and Griffiths, D.V. (2008), “Risk Assessment in Geotechnical Engineering”, John Wiley & Sons, Hoboken, NJ.

Smith, I.M. and Griffiths, D.V. (2004), “Programming the Finite Element Method”, John Wiley & Sons, Chichester, UK. Reprinted (2006, 2008)

PROBABILISTIC SLOPE STABILITY ANALYSIS AS A SUPPLEMENT TO A DETERMINISTIC STUDY

Dayal, Nishant, P.E., A.M. ASCE[1] , Prieto, A. Rafael, Ph.D., A.M. ASCE[2], Lewis, J. Paul, P.E., A.M. ASCE[3], Scherer, R. David, P.E., A.M. ASCE[4]

ABSTRACT: The project involved a landslide and the subsequent remediation. The landslide measured approximately 800 ft along the head scarp and 400 ft from head to toe, with an average movement of about 20 ft. The geotechnical investigation included 44 borings, 13 inclinometers, and 12 piezometers. An extensive laboratory testing program provided detailed information about the geotechnical soil properties of the landslide area. The remediation was designed and constructed at a cost of nearly 3 million dollars. The design followed conventional allowable stress design methods and a long term factor of safety against sliding of 1.3.

This paper presents an academic exercise on the stability of the final slope template following a basic probabilistic approach. The purpose of this study is to complement the deterministic design and generate information about this type of analysis applied to real world cases. The paper encourages engineers to perform probabilistic analysis in addition to deterministic analysis to complement the factor of safety.

The results of the soils characterization are compared and complemented with available literature information. A Monte Carlo technique is used to simulate scenarios based on the variability of the soil parameters and establish the probability distribution of the factor of safety against sliding. The probabilistic analysis provides a better understanding of the risk associated to the factor of safety, and shows that the internal friction angle of the colluvial soil has the most influence on the computed factor of safety in this case.

[1] Geotechnical Engineer, Gannett Fleming, Inc., 207 Senate Ave., Camp Hill, PA 17011; ndayal@gfnet.com
[2] Geotechnical Designer, Gannett Fleming, Inc., 207 Senate Ave., Camp Hill, PA 17011; rprieto@gfnet.com
[3] Geotechnical Practice Manager and Vice President, Gannett Fleming, Inc., 207 Senate Ave., Camp Hill, PA 17011; plewis@gfnet.com
[4] Senior Geotechnical Engineer, Gannett Fleming, Inc., 207 Senate Ave., Camp Hill, PA 17011; dscherer@gfnet.com

INTRODUCTION

Probabilistic methods were introduced in slope stability evaluation by Wu and Kraft (1970). Geotechnical engineers continue to slowly introduce this valuable tool as clients begin to request it.

Engineers deal with uncertainties associated with soil parameters in different ways (Christian, 2004). A proper site characterization based on subsurface investigation and engineering judgment normally precedes a design process. These observational and investigative efforts provide engineers with parameters with spatial and temporal variability. A different design factor of safety is used for different load cases but the factor of safety has often the same value without considering the different degrees of uncertainties associated with different slopes (Duncan, 2000).

This paper utilizes simple calculations and SLOPE/W software to evaluate the probability of meeting the design criteria of a remediated slope, and compares the results to the deterministic value of factor of safety calculated as part of the original design.

MATERIALS AND METHODS

The following describes the parameters and procedures used to evaluate the slope stability for the long term condition. However, a similar procedure can be applied to evaluate short term condition or any other load case.

Deterministic Method

Forty-four borings were drilled at the site to investigate and design the rehabilitation of the landslide. The overburden generally consists of reddish brown sand and gravel with silt and clay (SM and GM). The original soils are described as colluvium and glacial till. The SPT-N values recorded in the borings indicate generally medium dense to very dense soils. Results of the laboratory tests conducted to obtain the design shear strength parameters for long term conditions are listed in Table 1, and Figure 1 illustrates the reconstructed slope.

Table 1: Final Design Soil Strength Parameters

Soil	Saturated Unit Weight (pcf/ kN/m^3)	Effective Friction Angle (deg)	Cohesion (psf/ kN/m^2)
Fill	140/22	32	0
Residual	140/22	29	0
Colluvial	140/22	29	0
Bedrock	Impenetrable		

A traditional deterministic slope stability analysis was carried out yielding a factor of safety of 1.3 using SLOPE/W software from Geo-Slope (2007) and Spencer's

method. The required minimum factor of safety against sliding required by the client was 1.3. Hence, the design met the client design criterion for long term stability.

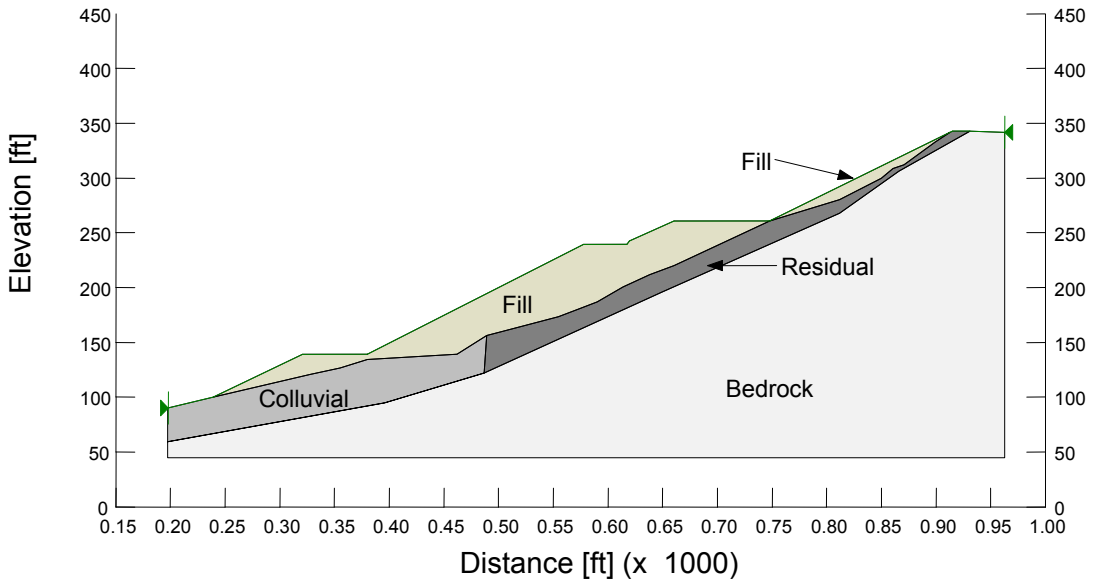

FIG: 1 - Reconstructed Slope

Probabilistic Method

Table 2 compares soil parameters' statistical data for obtained from laboratory tests and published data. The coefficient of variation obtained from laboratory data falls within the range of coefficient of variation published in the literature. In the absence of sufficient information to calculate the standard deviation, the mean value obtained from laboratory test results and the coefficient of variation obtained from published literature may be used to estimate the standard deviation.

Table 2: Comparison of Published Data and Data Obtained from Laboratory Testing

Soil Parameter	From Design Information			Duncan (2000)		Phoon & Kulhawy (1999)
	Mean Value	Standard Deviation	COV (%)	Standard Deviation	COV (%)	COV (%)
All Soils - Unit Weight	140 pcf (22 kN/m^3)	6.07 pcf (0.95 kN/m^3)	5.1	4.2 - 9.8	3 - 7	< 10
Fill - Effective Friction Angle	32 deg	3.01 deg	9.4	0.64 - 4.16	2 - 13	5 - 15
Residual soil - Effective Friction Angle	29 deg	3.49 deg	12.6			
Colluvial soil - Effective Friction Angle	29 deg	4.03 deg	12.9			

A Monte Carlo simulation technique was used to generate 50,000 probable scenarios, and it was necessary to establish a credible range of values for each soil parameter. This study followed the three-sigma rule (Dai and Wang, 1992) for all parameters, which assumes a probability of 99.73% that the true field value lies within this range, and the results are listed on Table 3. The three-sigma rule can result in unrealistically wide ranges and additional limits are often established based on subsurface investigation and engineering experience. In order to facilitate the interpretation of the results, the ranges obtained from three-sigma rule were not modified in this exercise.

Table 3: Range of Soil Parameters Based on the Three-Sigma Rule

Soil Parameter	Mean Value (μ)	Standard Deviation (σ)	μ-3σ	μ+3σ
All Soils - Unit Weight	140 pcf (22kN/m^3)	6.07 pcf (0.95 kN/m^3)	121.79 pcf (19.12 kN/m^3)	158.21 pcf (24.84 kN/m^3)
Fill - Effective Friction Angle	32 deg	3.01 deg	22.97 deg	41.03 deg
Residual soil - Effective Friction Angle	29 deg	3.49 deg	18.53 deg	39.47 deg
Colluvial Soil- Effective Friction Angle	29 deg	4.03 deg	16.91 deg	41.09 deg

Random numbers within these ranges are uniformly distributed. In addition, the probabilistic analysis is carried out by using the same critical surface obtained from the mean values for all randomly generated simulations. This highlights the importance of proper soil profile characterization.

RESULTS

Figure 2 shows the results of the slope stability analysis for the case using the mean values of all soil parameters. As expected, the factor of safety corresponds to the same value obtained on the original design of the slope remediation, FS = 1.3.

The most relevant results from the probabilistic slope stability analysis are shown in Figure 3, each curve obtained by varying a single soil parameter to observe its effect on the long term factor of safety against sliding. The probability versus factor of safety for each soil parameter and also when all soil parameters are considered together is shown in Figure 3. The graph shows that the probability of the factor of safety being less than 1.3 for this remediated slope is nearly 44.5%. In other words, the results of the simulation indicate that the remediated slope has 55.5% probability of having a factor of safety greater than 1.3.

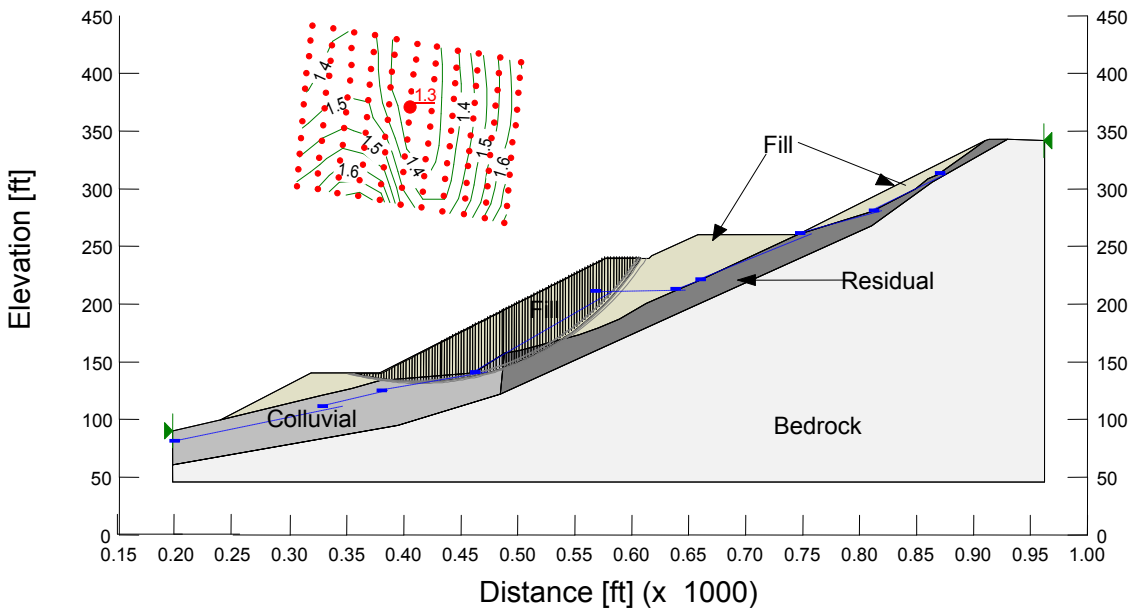

FIG. 2 - Critical Failure Surface Using Mean Values, FS = 1.3

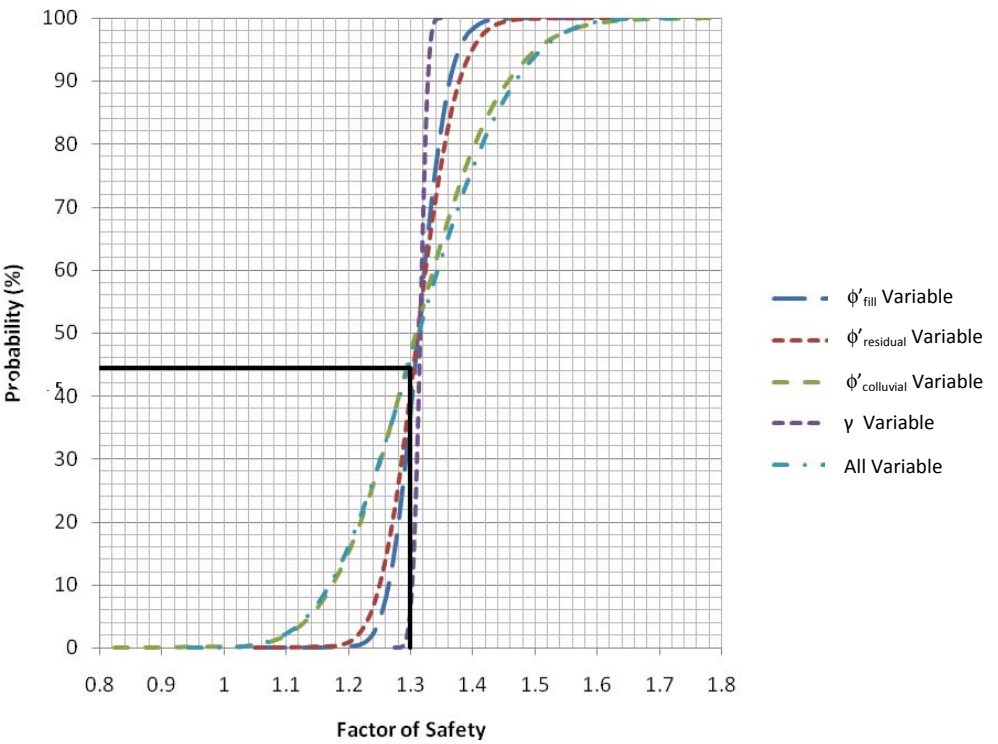

FIG 3 - Probability vs. Factor of Safety

It is important to understand that probability of success (probability that the system is stable), and probability of meeting the design criteria are arguably not the same results. The probability of success in this case, is the probability that the slope has a factor of safety greater than unity, P(FS>1.0)=99.97% for all varying soil parameters, while probability of meeting the design criteria for this particular case is P(FS>1.3)=55.5%. This basic comparison between P(FS>1.0) and P(FS>1.3), (i.e. probability of failure and probability of meeting the design criterion) shows the benefits of adding probabilistic analyses to traditional slope stability evaluations.

Silva, Lambe, and Marr (2008, Figure 1) classify earth structures in four categories ranging from best to poorly engineered and assigns annual probability of failure to various factor of safety based on expert judgment. The plot yields a value of 5×10^{-3} for the annual probability of failure for this slope based on a design factor of safety of 1.3 and Category II earth structure.

Variable unit weight for all soils – The standard deviation of the factor of safety is 0.023. The probability that the slope has a factor of safety greater than 1.3 is 92.8% when varying the unit weight and considering all other soil parameters constant at their mean values.

Variable angle of internal friction for fill – The variability in the friction angle of fill results in a standard deviation of 0.174 for its factor of safety. In this case, there is a 62.0% probability that the slope has a factor of safety greater than 1.3.

Variable angle of internal friction for the residual soil – The standard deviation of the factor of safety is 0.174. In this case, there is a probability of 59.0% that the slope has a factor of safety greater than 1.3.

Variable angle of internal friction for the colluvial soil – The standard deviation of the factors of safety is 0.347. The colluvial soil shows considerable influence on the factor of safety. There is a 53.0% probability that the factor of safety is greater than 1.3 when including the variability of the internal friction of the colluvial soil. Hence, the colluvial soil friction angle has the most influence on the factor of safety for this particular case.

The probabilistic slope stability evaluation including uncertainties of all soil parameters shows a standard deviation of the factor of safety of 0.232. Note that, as expected, the inclusion of all variable parameters drastically increases the variability of the factor of safety. As discussed earlier, the probability of the slope having a factor of safety greater than 1.3 is 55.5%.

CONCLUSIONS

A probabilistic slope stability analysis is recommended to complement the deterministic analysis. Although it is advisable, it is not always mandatory to have a high volume of information to carry out a probabilistic analysis. Standard deviations

can be obtained from a combination of mean values from laboratory data and published literature. One major advantage of this additional analysis is that it provides additional understanding of the design factor of safety. A high factor of safety never corresponds to a 100% safe structure; instead, it has a certain degree of uncertainty associated with it which can be quantified by means of the probabilistic analysis.

Soil parameters, geometry, and ground water level will have different impact on the computed factor of safety. Experienced engineers normally hypothesize about which parameters are the most important for traditional slope stability analysis, and probabilistic analysis help confirm or deny such hypothesis and the risk associated with their decisions. The stability of the slope considered in this study is most sensitive to the friction angle of colluvial soils and least sensitive to the unit weight.

REFERENCES

Baecher, G. B., and Christian, J. T. (2003). *Reliability and statistics in geotechnical engineering*, Jon Wiley & Sons, West Sussex, England.

Christian, J. T. (1994). "Geotechnical engineering reliability: How well do we know what we are doing?" *J. Geotech. and Geoenvir. Engrg.*, ASCE, 130(10), 985-1003.

Dai, S. H., and Wang, M. O. (1992). *Reliability analysis in engineering applications*, Van Nostrand Reinhold, New York

Duncan, J. M. (2000). "Factors of safety and reliability in geotechnical engineering." *J. Geotech. and Geoenvir. Engrg*., ASCE, 126(4), 307-316.

Geo-Slope International, Inc. (2007). *Geostudio 2007 (Version 7.16, Build 4840)*, Calgary, Alberta, Canada.

Phoon, K. K., and Kulhawy, F. H. (1999). "Characterization of geotechnical variability" *Canadian Geotechnical Journal*, 36(4), 612-624.

Silva, F., Lambe, T. W. and Marr, W. A. (2008), "Probability and risk of slope failure." *J. of Geotech. and Geoenvir. Engrg*, ASCE, 134(12), 1691-1699.

Wu, T. H., and Kraft, L. M. (1970). "Safety analysis of slopes." *J. Soil Mech. and Found. Div*., ASCE, 96(2), 609-630.

Liquefaction Probability by Probabilistic Version of Robertson and Wride Model

Chih-Sheng Ku[1], C. Hsein Juang[2], Jianye Ching[3] and Der-Her Lee[4]

[1] Associate Professor, Dept of Civil and Ecological Engineering, I-Shou University, No. 1, Section 1, Syuecheng Road, Dashu District, Kaohsiung city, 840, Taiwan; email: csku@isu.edu.tw
[2] Professor, Dept of Civil Engineering, Clemson University, Clemson, SC 29634; also affiliated with National Central University, Jhongli, Tauyuan, 320, Taiwan
[3]Associate Professor, Dept of Civil Engineering, National Taiwan University, Taiwan
[4]Professor, Dept of Civil Engineering, National Cheng-Kung University, Taiwan

ABSTRACT:

The Robertson and Wride (RW) method is perhaps the most widely used cone penetration test (CPT)-based simplified method for soil liquefaction evaluation. This method is a deterministic model, which expresses the liquefaction potential in terms of factor of safety. In many occasions, there is a need to express the liquefaction potential in terms of liquefaction probability. A probabilistic version of the Robertson and Wride model that is linked to the deterministic solution provides an incentive for the practicing engineer to adopt the probabilistic approach. In this paper a probabilistic version of the RW model is developed. Examples that demonstrate the use of the probabilistic RW model are presented along with a discussion of the treatment of parameter uncertainties in the liquefaction evaluation.

INTRODUCTION

The most widely used method for liquefaction potential evaluation in geotechnical practice in the North America and throughout much of the world is the simplified procedure pioneered by Seed and Idriss (1971). The simplified procedure was developed based on field observations and field and laboratory tests with a strong theoretical basis. Recent updates of the simplified procedure (e.g., Seed et al., 1985; Youd et al., 2001; Idriss and Boulanger, 2006) relied almost entirely on case histories of liquefaction/no-liquefaction. These case histories were collected from sites on level

to gently sloping ground, underlain by Holocene alluvial or fluvial sediments at shallow depths (< 15 m). In a case history, the occurrence of liquefaction was primarily identified with surface manifestations such as lateral spread, ground settlement, and sand boils. Because the simplified method was "calibrated" based on such case histories, the "occurrence of liquefaction" should be interpreted accordingly, that is, the emphasis is on the surface manifestations.

In this paper, the focus is on the evaluation of liquefaction potential using the cyclic stress-based, simplified method that utilizes CPT. The most widely used CPT-based simplified method in geotechnical practice is the one proposed by Robertson and Wride (1998), and recent updates of this method by Robertson (2009). The Robertson and Wride (RW) method is a *deterministic* method, in which the liquefaction potential is measured as factor of safety (F_S) defined as the ratio of cyclic resistance ratio (CRR) over cyclic stress ratio (CSR).

In many situations, it is desirable to express the liquefaction potential in terms of the *probability of liquefaction* (P_L), rather than the factor of safety (F_S). Examples of such situations include: mapping liquefaction potential in a district (or a city or county) where it is easier to interpret the liquefaction potential in terms of the probability rather than the safety factor; post-event investigations (or back analysis of case histories) where the conservative bias that is typically found in the existing deterministic models becomes undesirable as it may complicate the assessment; and the performance-based earthquake engineering where the unbiased probability at the component level is required. Thus, the goal of this paper is to develop a simple probabilistic model that is linked directly to the deterministic RW model.

DATABASE

The database adopted for developing the probabilistic RW model consists of 152 cases taken from Robertson (2009) and additional 13 cases taken from a recent report by Moss et al. (2009). The 152 cases were derived by Robertson (2009) through re-screening of the cases previously compiled and evaluated by Moss (2003). The original database by Moss (2003), also available in Moss et al. (2006), included 182 case history results (146 liquefied cases and 36 non-liquefied cases). However, 30 cases (23 liquefied cases and 7 non-liquefied cases) were described as 'Class C' data that were case histories where the CPT results were obtained using either "non-standard or mechanical cone" or with "no friction sleeve data available." The Class C data are clearly less reliable than the rest of the data. Thus, these data were excluded from the database of Robertson (2009), which consists of only 152 cases (116 liquefied cases and 36 non-liquefied cases).

It is noted that Robertson's re-evaluation of the cases from Moss et al. (2006) resulted in different classification of some sites. As pointed out by Robertson (2009), taking *average* in situ test values, as was done by Moss et al. (2006), involves considerable subjective judgment, which can be misleading in interbedded soils and may not adequately represent the various individual soil layers. The re-evaluation was critical in some key sites including those at Whiskey Springs (1983 Borah Peak earthquake), Balboa Blvd. and Malden St. (1994 Northridge, USA), and Kornbloom (1982

Westmorland, USA). Robertson (2009) concluded that these sites were incorrectly classified when using only the Moss et al. (2006) average parameter values.
The other 13 cases (9 liquefied cases and 4 non-liquefied cases) in the adopted database are taken from a report by Moss et al. (2009), which documented the results of a recent field update of the liquefied and non-liquefied sites in the Tangshen, China earthquake. Thus, the new database adopted in the present paper consists of a total of 165 cases (125 liquefied cases and 40 non-liquefied cases).

PROBABISTIC VERSION OF ROBERTSON METHOD

The developed mapping function allows for a simple estimate of P_L based on the computed F_S. This mapping function will be developed using the principle of maximum likelihood. The goal of the present analysis is to express P_L as a function of the safety factor of liquefaction. The latter is denoted by

$$F_S = CRR(q_{t1N,cs})/CSR \quad (1)$$

where $CRR(q_{t1N,cs})$ is determined using the RW method:

$$\mathrm{CRR}\left(q_{t1N,cs}\right) = \begin{Bmatrix} 0.08 + 93\left(q_{t1N,cs}/1000\right)^3, & \text{for } q_{t1N,cs} > 50 \\ 0.05 + 0.833\left(q_{t1N,cs}/1000\right), & \text{for } q_{t1N,cs} \le 50 \end{Bmatrix} \quad (2)$$

Only the basic idea for the maximum likelihood estimation will be herein presented. The actual F_S of each case is modeled as the predicted F_S (Eq. 1) is multiplied by a random model factor with unknown mean and COV. If the distribution type, mean, and COV of the model factor are given, P_L for each case can be calculated. The likelihood is simply the product of the P_L's for all liquefied cases and the $(1-P_L)$'s for all non-liquefied cases. The distribution type, mean, and COV that maximize this likelihood are therefore the maximum likelihood estimates. The resulting P_L equation is

$$P_L = 1 - \Phi\left[\frac{0.102 + \ln(F_s)}{0.276}\right] = 1 - \Phi\left[\frac{0.102 + \ln(CRR) - \ln(CSR)}{0.276}\right] \quad (3)$$

where Φ is the standard normal cumulative distribution function.
Equation (3) is essentially a P_L-F_S mapping function. Figure 1 shows a plot of this mapping function. The liquefaction probability P_L is seen here as a function of F_S, or alternatively, as a function of CSR and $q_{t1N,cs}$ (because CRR is a function of $q_{t1N,cs}$). It is noted that when $F_S = 1$, Eq. (3) yields $P_L = 0.356$, indicating that the *deterministic* RW method is generally conservative. Recall that F_S of 1.2 is recommended by the Building Seismic Safety Council (1997) for seismic design of ordinary structures against liquefaction. If a safety factor of $F_S = 1.2$ is adopted for the RW method, P_L is reduced to 0.15 according to Eq. (3). This probability ($P_L = 0.15$) is in the likelihood class of "almost certain will not liquefy" (Chen and Juang, 2000). The probability of 0.15 is also adopted by Moss et al. (2006) as the basis for deriving their deterministic

boundary curve. Thus, the developed probabilistic version of the RW method is reasonable and consistent with the current state of practice.

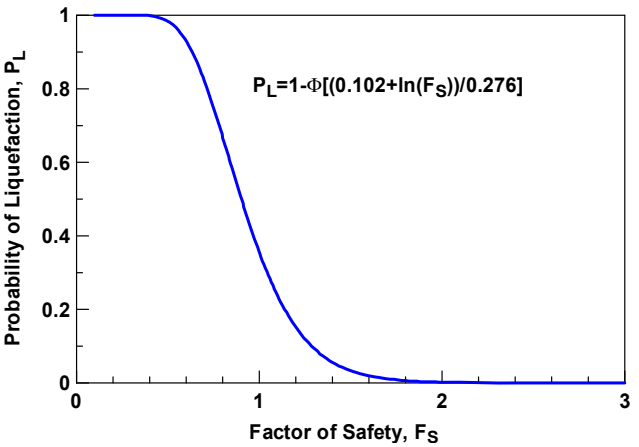

Figure 1. The P_L-F_S mapping function specific to the RW method

APPLICATION TO A FUTURE CASE

Equation 3 is readily applicable to evaluating P_L in a future case with a given set of seismic and in situ test parameters. If the uncertainty in the input parameters is significant, an effort should be made to characterize this uncertainty. Each uncertain parameter, which is treated as a random variable accordingly, may be characterized with a mean and a standard deviation (and the distribution type if possible). To consider the parameter uncertainty in a given case, Monte Carlo simulation analysis, in lieu of Eq. (3), may be conducted with a given "limit state" (such as the boundary curve of the RW method) to estimate P_L. Alternatively, we can treat the *nominal* probability computed from Eq. (3) as the mean of this probability. We can then try to estimate the variation of the computed probability caused by the uncertainty in the input parameters, in terms of ±1 standard deviation bound of this probability. This information on the variation of the computed probability, as a way of dealing with the uncertainty of the input parameters, enables us to make a better informed design decision.

According to Eq. (3), P_L is a function of ln(CSR) and ln(CRR), and the latter is in turn a function of $q_{t1N,cs}$. The uncertainty in $q_{t1N,cs}$ must be characterized in a site investigation. The methods for site characterization can range from simple, traditional approach of considering the variation in some selected "critical" cross-sections based on engineering judgment to the more sophisticated mathematical approaches such as three-dimensional characterization using artificial neural networks (Juang et al., 2001). Similarly, the uncertainty in CSR is caused by the uncertainty in the estimated a_{max} (peak ground surface acceleration) and M_w (moment magnitude) for the given site and the uncertainty in the component models of CSR, such as r_d (depth-dependent shear stress reduction factor, MSF (magnitude scaling factor), and K_σ (overburden correction factor for cyclic stress ratio). In this paper, we assume that the mean and standard deviation of $q_{t1N,cs}$, denoted by $\mu_{qt1N,cs}$ and $\sigma_{qt1N,cs}$, respectively,

as well as the mean and standard deviation of CSR, denoted as μ_{CSR} and σ_{CSR}, respectively, can be obtained. We further define the COV of $q_{t1N,cs}$ to be $\delta_{qt1N,cs} = \sigma_{qt1N,cs}/\mu_{qt1N,cs}$ and the COV of CSR to be $\delta_{CSR} = \sigma_{CSR}/\mu_{CSR}$.

Because of the uncertainties in CSR and $q_{t1N,cs}$, the terms ln(CSR) and ln(CRR) in Eq. (3) should be treated as random variables; accordingly, there is a need to determine the mean and standard deviation of ln(CSR) and ln(CRR). The mean and standard deviation of ln(CSR), denoted as $\mu_{\ln(CSR)}$ and $\sigma_{\ln(CSR)}$, respectively, may be estimated by the first order analysis (Juang et al., 2009):

$$\mu_{\ln(CSR)} \approx \ln\left[\mu_{CSR}\right] \quad \sigma^2_{\ln(CSR)} \approx \left[\frac{\partial \ln CSR}{\partial CSR}\right]^2 \sigma^2_{CSR} = \frac{\sigma^2_{CSR}}{\mu^2_{CSR}} = \delta^2_{CSR} \tag{4}$$

Similarly, the mean and standard deviation of ln(CRR), denoted as $\mu_{\ln(CRR)}$ and $\sigma_{\ln(CRR)}$, respectively, may be estimated by the first order analysis (Juang et al., 2009):

$$\mu_{\ln(CRR)} \approx \ln\left[CRR_{q_{t1N,cs}}\right] \tag{5}$$

$$\sigma^2_{\ln(CRR)} \approx \left[\frac{\partial \ln CRR(q_{t1N,cs})}{\partial q_{t1N,cs}}\right]^2 \qquad \sigma^2_{q_{t1N,cs}} \approx \left[\frac{\ln\left(CRR(\mu_{q_{t1N,cs}} + \sigma_{q_{t1N,cs}}\right) - \ln\left(CRR(\mu_{q_{t1N,cs}} - \sigma_{q_{t1N,cs}}\right)}{2}\right]^2 \tag{6}$$

The variation (or uncertainty) of the computed P_L caused by the variation of ln(CSR) and ln(CRR) may be expressed in an interval estimate of P_L, referred to herein as the "one sigma bound" interval. The lower bound and the upper bound of this interval, denoted as P_L^- and P_L^+, respectively, are obtained by varying the two parameters, ln(CSR) and ln(CRR), within ±1 standard deviation of their mean. With the knowledge of $\mu_{\ln(CSR)}$, $\sigma_{\ln(CSR)}$, $\mu_{\ln(CRR)}$ and $\sigma_{\ln(CRR)}$, the lower and upper bounds of the "one sigma bound" interval of P_L can be determined as follows (derived from Eq. 3):

$$P_L^{\pm} = 1 - \Phi\left[\frac{0.102 + \left(\mu_{\ln(CRR)} - \mu_{\ln(CSR)}\right) \mp \sqrt{\sigma^2_{\ln(CRR)} + \sigma^2_{\ln(CSR)}}}{0.276}\right] \tag{7}$$

When a future case is analyzed assuming no parameter uncertainty (i.e., $\sigma_{\ln(CSR)} = \sigma_{\ln(CRR)} = 0$), Eq. (7) will yield $P_L^- = P_L^+ = P_L$. In such scenario, Eq. (7) is reduced to Eq. (3). When the parameter uncertainty has to be considered but the variation in the input parameter is limited to ±1 standard deviation from the mean, the lower and upper bounds of the "one sigma bound" interval of P_L can be computed with Eq. (7).

Example applications of the proposed model: As an example, case McGowan 136 in the 1989 Loma Prieta earthquake is considered. No liquefaction was observed at this site in the 1989 event. At the depth of 2.75 m, σ'_v = 42.92 kPa, σ_v = 46.36 kPa, a_{max} = 0.26g, and M_w = 7.0; based on these data, CSR is computed based on the formulation which yields CSR = 0.151. Based on the measured CPT parameters, the

following parameters are derived: $q_{t1N} = 55.07$, $I_c = 2.13$, and thus, $q_{t1N,cs} = 83.08$. By means of the RW method (Eq. 2), CRR = 0.133 and thus F_S = CRR/CSR = 0.88. By definition of the factor of safety, liquefaction is implied in this case since $F_S < 1$. This "prediction" before the event would have been considered incorrect since field observation indicating no liquefaction. However, as noted previously, the RW method is generally conservative, which implies that $F_S = 1$ is not an unbiased boundary (or limit state). Exactly how this should affect the interpretation of the results of the back analysis of a case history is not clear. This, again, suggests that the deterministic models, which yield a factor of safety, may not be an unbiased (and effective) tool for back analysis of case histories or for post-event investigation. The deterministic models are, however, appropriate for a forward analysis of a future case, in which a conservative bias is generally preferred.

Assume that the computed $q_{t1N,cs}$ and CSR values are representative of the soil of concern at this site, P_L can be computed with Eq. (3), which does not require the knowledge of parameter uncertainty. The analysis using Eq. (3) yields $P_L = 0.53$. According to the likelihood classes proposed by Chen and Juang (2000), "liquefaction or no liquefaction is equally likely to occur" given this probability. This probability-based assessment offers a reasonable interpretation of the given data and can explain the field observation of "no liquefaction" better than the deterministic solution does.

The next example is to illustrate the application of the proposed probabilistic model, including the consideration of the input parameter uncertainty. Let us consider the case Marine Lab UC-7 in the 1989 Loma Prieta earthquake. Liquefaction was observed at this site in the 1989 event. At the depth of 8.7 m, $\sigma'_v = 86.75$ kPa, $\sigma_v = 148.55$ kPa, $a_{max} = 0.25g$, and $M_w = 7.0$; based on these data, CSR is determined to be 0.168. Based on the measured CPT parameters, the following parameters are derived: $q_{t1N} = 46.41$, $I_c = 2.20$, and thus, $q_{t1N,cs} = 79.5$. By means of the RW method (Eq. 2), CRR = 0.127 and thus F_S = CRR/CSR = 0.76. Liquefaction is implied since $F_S < 1$, which would have been considered a correct prediction since field observation indicating liquefaction.

Assume that the computed $q_{t1N,cs}$ and CSR values are representative (or the mean) of the soil of concern, and without considering the parameter uncertainty, P_L can be computed with Eq. (3), which yields $P_L = 0.74$. This probability falls in the likelihood class of "very likely to liquefy" according to Chen and Juang. Thus, this "prediction" would have been considered reasonable since the field observation indicating liquefaction. Nevertheless, it would be interesting to see how much this probability is affected by the parameter uncertainty and how the changes may be interpreted.

It is helpful to note that the computed probability reflects the given state of information (especially the degrees of parameter uncertainty), and thus, different probabilities can be obtained for the same case with different states of information. These probabilities are all meaningful with respect to their assumed states of information before the event, although the probability can only be 0 or 1 after the event.

Let us first assume that in this case CSR is "fixed" ($\delta_{CSR} = 0$) and $q_{t1N,cs}$ is random with a coefficient of variation $\delta_{qt1N,cs} = 0.05$. In other words, $\sigma_{CSR} = 0$ and $\sigma_{qt1N,cs} = 3.98$. Based on Eqs. (4) through (6), the following are obtained: $\mu_{\ln(CRR)} = -2.066$, $\sigma_{\ln(CRR)} = 0.055$, $\mu_{\ln(CSR)} = -1.784$, and $\sigma_{\ln(CSR)} = 0$. By applying Eq. (7), the lower and

upper bounds are determined to be: $P_L^- = 0.672$ and $P_L^+ = 0.801$. Thus, the "one sigma bound" interval of P_L is approximately in the range of $P_L = 0.67 – 0.80$.

Next, assume that CSR is also random with $\delta_{CSR}= 0.1$, in addition to a 5% coefficient of variation in $q_{t1N,cs}$. Again, based on Eqs. (4) through (6), the following are obtained: $\mu_{ln(CRR)} = –2.066$, and $\sigma_{ln(CRR)} = 0.055$, $\mu_{ln(CSR)} = –1.784$, $\sigma_{ln(CSR)} = 0.1$. By applying Eq. (7), the lower and upper bounds are determined to be: $P_L^- = 0.594$ and $P_L^+= 0.857$. Thus, the one-sigma-bound range is $P_L = 0.59 – 0.86$.

Repeating the above analysis with $\delta_{CSR} = 0.2$ and everything else remaining the same, the following results are obtained: $P_L^- = 0.460$ and $P_L^+ = 0.920$. Thus, the one-sigma-bound range is: $P_L = 0.46 – 0.92$. Finally, repeating the above analysis with $\delta_{CSR} = 0.3$ will yield the one-sigma-bound range of the probability, $P_L = 0.33 – 0.96$.

All of the results presented previously, suggests a very high likelihood of liquefaction (in some scenario, the one-sigma-bound probability can be as high as 0.96). Furthermore, it is observed that as the degree of uncertainty in the input parameters increases, the one-sigma-bound range of P_L becomes wider, which indicates a greater uncertainty in the computed probability. The results also show that for the same F_S value ($F_S = 0.76$ in this case), the computed P_L can vary significantly given different states of information (or degrees of uncertainty). Thus, the factor of safety is unable to account for the effect of the parameter uncertainty because that for a given case, it is always a constant. On the other hand, an accurate estimate of P_L requires an accurate characterization of the parameter uncertainty, and even with the most accurate characterization of this uncertainty, the probability is not a constant; rather, it should be expressed at least as a one-sigma-bound interval. The one-sigma-bound interval allows for making a better informed decision.

It is important for the engineer to reduce the uncertainty of the input parameters through a site investigation program that is appropriate for a given project. In case that the uncertainties in the input parameter cannot be eliminated, these uncertainties must be estimated and considered explicitly in the analysis so that the variation (in terms of one-sigma bounds) of the computed P_L can be assessed. The added information (about the variation of the computed probability) would enable a more informed design decision to be made.

CONCLUSIONS

1. The probabilistic RW model has a unique feature not available in the existing models-- a simple equation is created by which the variation of the computed liquefaction probability caused by the parameter uncertainty can be estimated.
2. Examples presented in this paper somehow confirm the effectiveness and simplicity of the proposed probabilistic RW model.
3. The results presented in this paper show that the variation in the computed P_L increases as the degree of uncertainty in the input parameters increases.
4. The computed liquefaction probability reflects the state of information (or degree of uncertainty in the input parameters). Different probabilities can exist for different states of information. Before the seismic event, these probabilities are all meaningful with respect to their corresponding states of information.

REFERENCES

Ang, A.H.S., Tang, W.H. (2007). *Probability concepts in engineering: Emphasis on applications to Civil and Environmental engineering.* 2nd edition, John Wiley & Sons Inc.

BSSC (1997). *NEHRP recommended provisions for seismic regulations for new buildings and other structures.* 1997 edition, Part 2, Commentary, Building Seismic Safety Council, Washington, DC.

Chen, C.J., Juang, C.H. (2000). Calibration of SPT- and CPT-based liquefaction evaluation methods. *Innovations and Applications in Geotechnical Site Characterization*, GSP 97, ASCE, 49 – 64.

Idriss, I.M., Boulanger, R.W. (2006). "Semi-empirical procedures for evaluating liquefaction potential during earthquakes." *Soil Dynamic and Earthquake Engineering,* 26 (2-4), 115-130.

Juang, C.H., Fang, S.Y., Tang, W.H., Khor, E.H., Kung, G.T.C., Zhang, J. (2009). "Evaluating model uncertainty of an SPT-based simplified method for reliability analysis for probability of liquefaction." *Soils and Foundations*, 49 (1), 147-152.

Juang, C.H., Jiang, T., and Christopher, R. (2001). "Three-dimensional site characterization – neural network approach." *Geotechnique*, 51(9), 799-809.

Moss, R.E.S. (2003). *CPT-based probabilistic assessment of seismic soil liquefaction initiation*. Doctor of Philosophy dissertation, Univ. of California, Berkeley, CA.

Moss, R.E.S., Seed, R.B., Kayen, R.E., Stewart, J.P., Der Kiureghian, A., Cetin, K.O. (2006). "CPT-based probabilistic and deterministic assessment of in situ seismic soil liquefaction potential." *Journal of Geotechnical and Geoenvironmental Engineering,* 132 (8), 1032-1051.

Moss, R.E.S., Kayen, R.E., Tong, L., Songyu, L., Cai, G., and Wu, J. (2009). "*Reinvestigation of Liquefaction and Nonliquefaction Case Histories from the 1976 Tangshan Earthquake*." PEER Report No. 2009/102, August.

Robertson, P.K. (2009). Performance based earthquake design using the CPT. Proceedings, *IS-Tokyo 2009*, June 2009, Tokyo, Japan, pp. 3-20.

Robertson, P.K., Wride, C.E. (1998). "Evaluating cyclic liquefaction potential using the cone penetration test." *Canadian Geotechnical Journal,* 35 (3), 442-459.

Seed, H.B., Idriss, I.M. (1971). "Simplified procedure for evaluating soil liquefaction potential." *Journal of Soil Mechanics and Foundation Division,* 97 (SM9), 1249-1273.

Seed, H.B., Tokimatsu, K., Harder, L.F., Chung, R.M. (1985). "The influence of SPT procedures in soil liquefaction resistance evaluation." *Journal of Geotechnical Engineering,* 111 (12), 1425 – 1445.

Youd, T. L., Idriss, I. M., Andrus, R.D., Arango, I., Castro, G., Christian, J.T., Dobry, R., Liam Finn, W.D., Harder, L.F., Jr., Hynes, M.E., Ishihara, K., Koester, J.P., Laio, S.S.C., Marcuson, W.F., III, Martin, G.R., Mitchell, J.K., Moriwaki, Y., Power, M.S., Robertson, P.K., Seed, R.B., Stokoe, K.H., II. (2001). "Liquefaction resistance of soils: summary report from the 1996 NCEER and 1998 NCEER/NSF workshops on evaluation of liquefaction resistance of soils." *Journal of Geotechnical and Geoenvironmental Engineering,* 127 (10), 817-833.

Design Criteria for the Differential Settlement of Landfill Foundations Modeled Using Random Fields

K. C. Foye, Ph.D., P.E., M. ASCE[1] and X. Zhao, Ph.D., P.E.[2]

[1]CTI and Associates, Inc., Wixom, MI; PH (248) 486-5100; email: kfoye@cticompanies.com
[2]CTI and Associates, Inc., Wixom, MI; PH (248) 486-5100; email: xzhao@cticompanies.com

ABSTRACT

The long-term functionality of composite landfill final cover systems and composite floor liner systems depends on the distortions imposed on these systems by differential settlement. The evaluation of differential settlement is particularly challenging for final cover systems, because of the heterogeneity of waste, and for floor liners over highly variable subgrades (e.g. existing waste, mine spoil, etc.). Deterministic approaches to landfill settlement prediction are not able to capture the spatial variability in the waste mass and subgrade properties which control differential settlement. An alternative, probabilistic solution is to use random fields to model the waste and subgrade properties. This paper discusses the application of a random field model to the design of landfill final cover and floor liner systems. The paper suggests an approach to select acceptable probabilistic criteria for design.

INTRODUCTION

Landfill engineers widely recognize that the slope of landfill baseliners and leachate collection systems must be selected to ensure drainage of leachate from the liner system throughout the life of the facility. Accordingly, the prediction of baseliner settlement is a necessary activity in assessing potential designs. Designers also recognize that differential settlements, not absolute values of settlement are the most pertinent to this problem. In particular, the creation of local depressions in baseliner and final cover systems for landfills prevents them from draining properly and minimizing advective gradients through the liner system (Qian et al. 2002). Therefore, designs of these systems must be engineered to limit the negative impact of these differential settlements.

Settlement of embankment subgrades (including landfill foundations) is largely due to compression of the materials beneath the embankment. This compression is a function of the compressibility of the materials and the loads imposed on them. Differential settlements therefore arise from differences in loading or differences in compressibility. Engineers assess differences in loading directly through consideration of the design embankment geometry and composition. In contrast, a complete assessment of differences in subgrade compressibility is limited by the costs of sampling and testing. The existence of local variations in

compressibility is recognized by engineers, but is excluded mathematically from most settlement analyses. This problem is exacerbated in the case of embankments founded on waste materials, which exhibit greater heterogeneity than soils.

Foye and Soong (2010) introduced a methodology to simulate the differential settlement of landfill floor liners above existing waste using random fields in conjunction with a simple isolated column settlement model. In this methodology, random fields are generated to simulate the variation of the subgrade compressibility. The columnar settlement model, using the random field compressibility values as input, computes the settlement at discrete points along the floor drainage flowline. This calculation results in a post-settlement flowline elevation profile. The post-settlement slope between the discrete points is calculated. Finally, the frequency of occurrence of various post-settlement slopes is counted. This process is repeated for multiple realizations of the random field in order to generate a large population of post-settlement slopes.

For the simulation methodology described above to be useful as a design tool, three issues must be addressed: 1) a representative model of solid waste compressibility is needed, 2) an appropriate model of spatial correlation is needed to generate the random fields, and 3) a probabilistic design criterion that is compatible with the simulation method is needed. Foye et al. (2007) addressed the first issue by considering available models and fitting them to field measurements of landfill settlement. Foye and Soong (2010) devised an interim solution to the second issue, following the example of Fenton et al. (1996) in treating similar problems with random fields. This paper suggests a solution to the third issue by presenting a technique where probabilistic design criteria can be inferred from existing design practice.

CALCULATION METHODOLOGY

The analysis discussed in this paper is concerned with differential settlement along the flowlines of leachate collection pipes at the bottom of landfills. In the development of the proposed probabilistic design criteria selection technique, the following analysis methods were used to model settlement along these flowlines.

Isolated Column Compression Model. The settlement of the landfill floor is computed at several discrete points along the design flowline. Foye et al. (2010) proposed an analysis methodology where the settlement at each of these discrete points is modeled as the compression of an isolated column. In the case of a landfill floor founded on existing waste, a settlement model for solid waste is needed. Following the discussion by Foye et al. (2007), the compression of solid waste can be modeled as the sum of the following two equations:

$$\Delta h_c = C_c' h_0 \log \frac{\sigma_i}{\sigma_0} \tag{1}$$

$$\Delta h_B = E_{DG}\left(1 - e^{-dt}\right) h_0 \tag{2}$$

where Δh_c is the settlement due to mechanical compression, C'_c is the compression index, h_0 is the pre-settlement thickness of the waste, σ_i is the vertical stress acting on

the waste at time t after waste placement, σ_0 is the initial vertical stress acting on the waste, Δh_B is the settlement due to biological degradation, E_{DG} is a coefficient representing the maximum biological settlement, and d is the biological degradation rate coefficient. Foye et al. (2007) found mean values of C'_c, E_{DG}, and d based on field measurements of landfill settlement. The variability of these coefficients was also described in terms of the error between calculated values of settlement using Eq. (1) and Eq. (2) and measured values of $\Delta h_c + \Delta h_B$. Accordingly, mean values of C'_c, E_{DG}, and d are used to calculate the expected value $E[\Delta h_{c,u} + \Delta h_{B,u}]$ at each flowline point u. Simulations of $\Delta h_{c,u} + \Delta h_{B,u}$ accounting for the variability of C'_c, E_{DG}, and d are then calculated

$$\Delta h_{c,u} + \Delta h_{B,u} = (1 + COVz_u)E\left[\Delta h_{c,u} + \Delta h_{B,u}\right] \tag{3}$$

where z_u is a realization of standard normal ("unit normal") random variable Z at point u, generated according to the random field procedure below, and COV is the coefficient of variation of $\Delta h_c + \Delta h_B$.

Random Field Generation. In this paper, random fields are generated using Local Average Subdivision, following the procedure developed by Fenton (1990). Random values are selected according to a normal distribution. Similarly to Fenton et al. (1996), the spatial correlation is modeled using the following correlation function:

$$\rho(\tau) = \exp\left(-\frac{2|\tau|}{\theta}\right) \tag{4}$$

where ρ is the correlation coefficient, $|\tau|$ is the absolute distance between two points being modeled ("the lag distance"), and θ is the scale of fluctuation. Scale of fluctuation θ can be understood as the distance at which field values are no longer significantly correlated.

Because this paper considers differential settlement along leachate collection pipe flowlines, a 1-dimensional random field simulation is used to model the heterogeneity of compressibility beneath each flowline. This approach contrasts with the 2-dimensional random fields used by Foye and Soong (2010) and Fenton et al. (1996) in their respective finite element models. The 1-dimensional approach is used to facilitate a simple spreadsheet implementation for design calculations and to create post-settlement profiles that are readily interpreted. Foye and Soong (2010) proposed an interim technique to determine values of θ to generate 1-dimensional random fields for the columnar settlement model. Based on this technique, $\theta/h_0 = 256$ was proposed as a viable definition for use in conjunction with the columnar settlement analyses.

Post-Settlement Slope Calculation. The effect of differential settlement is to change the slope of the landfill floor between the analysis points. The post-settlement slope between points u and u+1 along the flowline is calculated as

$$s_{i,u} = \frac{\left[y_{0,u+1} - \left(\Delta h_{c,u+1} + \Delta h_{B,u+1}\right)\right] - \left[y_{0,u} - \left(\Delta h_{c,u} + \Delta h_{B,u}\right)\right]}{x_{u+1} - x_u} \tag{5}$$

where y_0 is the initial elevation at each point and x is the distance from the end of the flowline to each point. In this paper, many random field realizations of $\Delta h_c + \Delta h_B$ are

generated for each point. The number of slope values s_i that pass or fail the minimum post-settlement slope are counted for all points and all simulations. If the percent of counted slopes that pass the minimum slope is acceptable, the design floor grade is accepted. The following section discusses an approach to develop a criterion for the acceptable frequency of passing slopes.

CANDIDATE DESIGN CRITERION

A probabilistic design criterion is needed to assess the effectiveness of a proposed landfill floor design using the random field model approach. According to the analysis methodology outlined above, many random field realizations of the post-settlement flowline profile are generated. The frequencies of post-settlement slopes calculated in all realizations are plotted in a histogram and the percentage of slopes passing the minimum slope is computed. The probabilistic criterion needed is the acceptable percentage of passing slopes. This paper proposes to find a probabilistic acceptance criterion for new floor designs using the following steps:

1. Use the random field analysis technique to analyze an existing design believed to perform acceptably.
2. Calculate the percentage of calculated slopes meeting the minimum performance standard.
3. Using the same analysis technique, compare this percentage to the percentage calculated for the new design.

Step 1. Use Random Fields to Analyze an Existing Design. The random field, columnar settlement analysis described above was first applied to an existing landfill baseliner constructed over a natural clay foundation. The existing design was deemed appropriate by the design engineer and approved by the regulatory authority. The baseliner's central flowline was designed with a 1.30% slope towards the leachate sump with the goal of achieving a minimum post-settlement slope of 1.00% according to a deterministic analysis. Table 1 summarizes the relevant parameters used in the settlement analyses. These values are taken directly from the calculations and measurements supporting the approved design. As shown in Table 1, the thickness of waste to be placed above the landfill floor and the thickness of the underlying clay varied across the site. Values of σ_i and h_0 at each calculation point were therefore selected according to the appropriate waste and clay thickness, respectively, for each point according to the design plans.

Figure 1 presents example pre- and post-settlement profiles for a single realization of a random field, columnar settlement analysis. Two post settlement profiles are shown to illustrate the effect of calculating post-settlement slopes with two different values of $x_{u+1} - x_u$ (referred to below as calculation interval). Longer calculation intervals tend to overlook local peaks and valleys, creating a smoother appearance to the profile.

Table 1. Analysis Parameters for Existing Landfill Baseliner Design

Property	Value	Standard Deviation[1] (coefficient of variation)
Compression Index [$C_C = (1+e_0)C'_c$]	0.29	0.103 (36%)
Recompression Index	0.058	0.0206 (36%)
Initial Void Ratio (e_0)	0.59	-
In-Situ Clay Unit Weight (kN/m^3)	20.4	-
Waste Unit Weight (kN/m^3)	10.2	-
Clay Foundation Thickness (m)	2.7 – 5.1	-
Waste Thickness (m)	22 – 83	-

1) SD calculated from site-specific data, COV = 30% is typical (Baecher and Christian 2003)

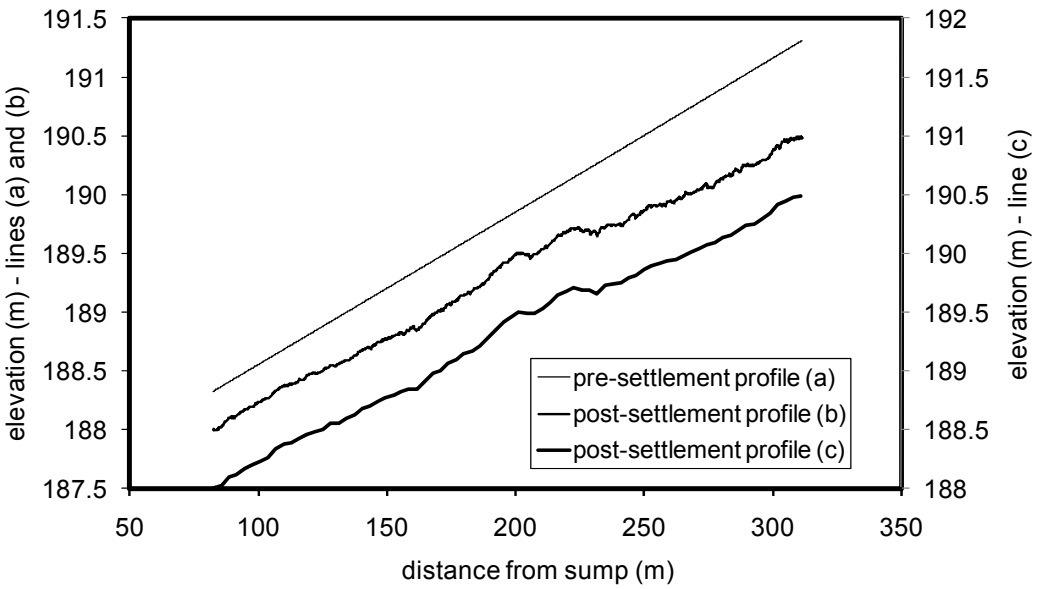

Figure 1. Typical Liner Profiles Calculated for Existing Design on Clay Foundation – (a) pre-settlement profile, (b) post-settlement profile calculated every 0.15 m, and (c) post-settlement profile calculated every 3 m.

Step 2. Calculate the Percentage of the Modeled Floor Meeting the Minimum Performance Standard. In this step, the multiple realizations generated in Step 1 to simulate the post-settlement liner profile for the existing, acceptable design case are examined. The frequency of occurrence of different post-settlement slopes along each segment of the profiles is counted and corresponding histograms generated. Figures 2 and 3 show the resulting histograms for two different calculation intervals. As expected from the appearance of the 0.15-m interval profile in Figure 1, the histogram shown in Figure 2 has captured the relatively extreme changes in slope over the shorter intervals compared to the histogram in Figure 3. Because comparable measures of performance are needed between the existing design (Steps 1 and 2) and the proposed design (Step 3), the difference between Figures 2 and 3 highlights the need to identify a calculation interval that is appropriate for comparison

between Steps 2 and 3. A calculation interval of 3 m was selected for this paper since it represents a relatively small survey interval for the construction of landfill floors.

Figure 2 suggests that a 35% occurrence of slopes less than 0% (no positive drainage at the local scale) over the entire simulation set is acceptable when slopes are calculated at 0.15m intervals using this technique. Figure 3 suggests that a 9% occurrence of slopes less than 0% over the entire simulation set is acceptable for 3-m calculation intervals.

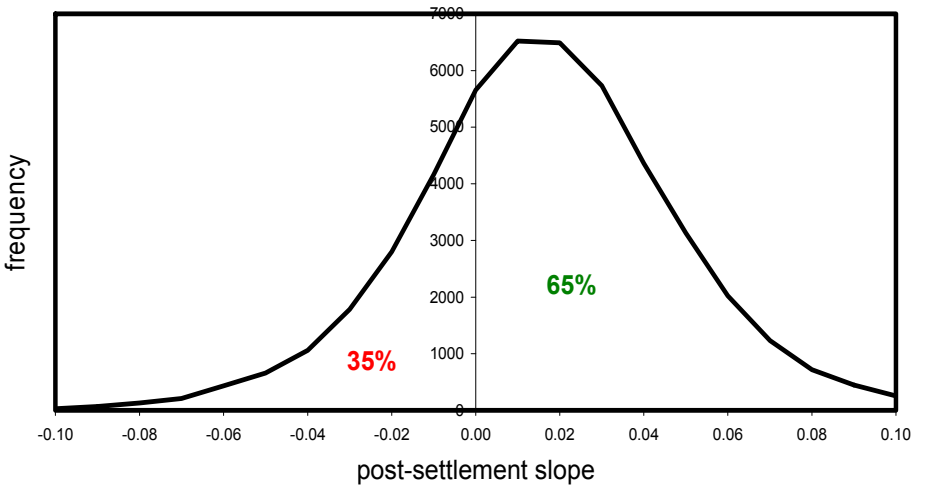

Figure 2. Histogram of the Post-Settlement slopes, calculated at 0.15-m intervals for waste placed on clay subgrade using random field analysis technique. Aggregated results from multiple simulations are shown.

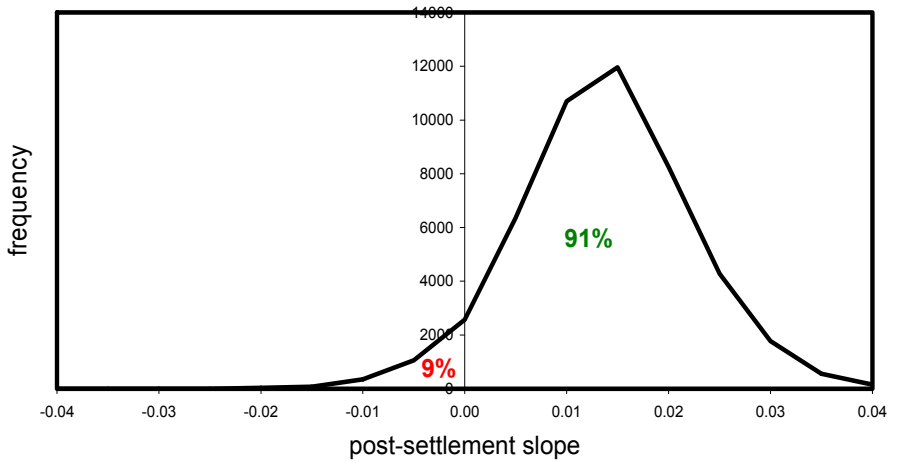

Figure 3. Histogram of the Post-Settlement slopes, calculated at 3-m intervals for waste placed on clay subgrade using random field analysis technique. Aggregated results from multiple simulations are shown.

Step 3. Compare Results with Analysis of Candidate Design. In this step, the design criterion from Step 2 for a 3-m calculation interval is applied to the design of a new landfill floor founded on existing solid waste. The settlement analysis parameters related to this design are summarized in Table 2.

Figure 4 shows the resulting histogram of post-settlement slopes calculated using the random field, columnar settlement analysis technique described above. The initial design slope used to generate the results shown in Figure 4 was optimized to 7.00% in order to produce a post-settlement slope<0% frequency less than or equal to 9%, based on the findings in Step 2. Due to the waste properties, the dispersion of the resulting post-settlement slopes is greater for waste foundations than for clay. Accordingly, the minimum required initial design slope is also greater.

Table 2. Analysis Parameters for Candidate Liner Design Over Existing Waste

Property	Value	Standard Deviation
C'_c	0.22[1]	note 3
E_{DG}	0.193[2]	note 3
d (day^{-1})	0.00867[2]	note 3
In-Place Waste Unit Weight (kN/m^3)	11.0	-
Future Waste Unit Weight (kN/m^3)	10.2	-
In-Place Waste Thickness (m)	6.1 – 36.6	-
Future Waste Thickness (m)	26.8 – 41.5	-

1) value from Qian et al. (2002)
2) value from Foye et al. (2007)
3) since available data describes variability in terms of calculated settlement, coefficient of variation for total settlement = 0.19, adapted from Foye et al. (2007)

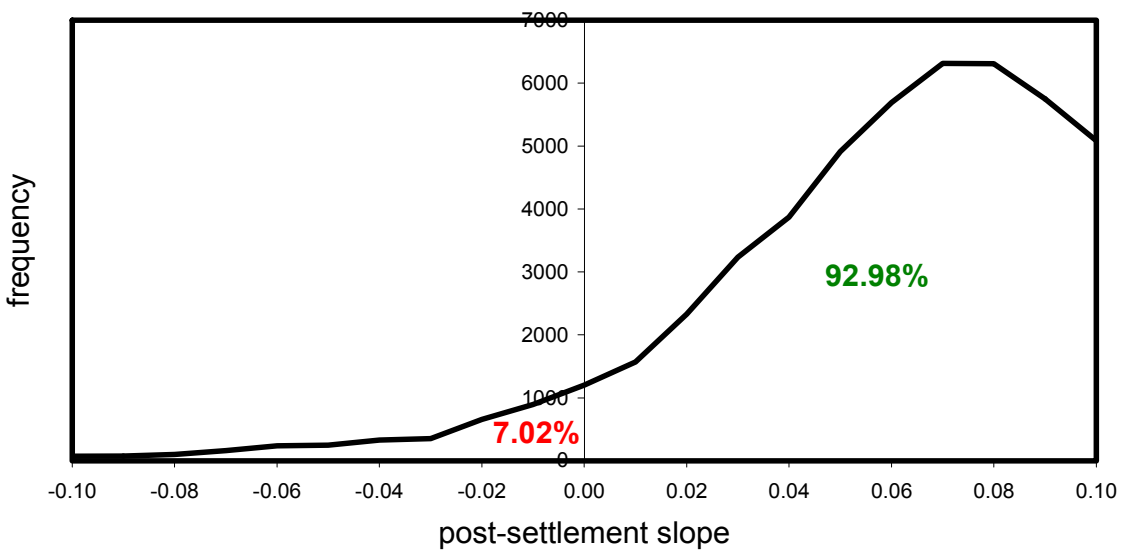

Figure 4. Histogram of the Post-Settlement slopes, calculated at 3-m intervals, for waste placed on a waste subgrade. Aggregated results from multiple simulations are shown. The results for an optimized initial design slope of 7.00% are shown.

CONCLUSION

Random fields are ideally suited to problems of differential settlement modeling of highly heterogeneous foundations, such as waste. Random fields model unobserved or unmeasurable variables affecting the spatial distribution of a design parameter, such as compressibility. When used for design, the use of these models prompts the need for probabilistic design criteria.

This paper presented an example where an analysis of an existing, accepted landfill baseliner design founded on clay was used to establish the probabilistic design criteria for the design of a composite liner system over waste. These results highlight how the proposed analysis method is sensitive to the calculation interval. Accordingly, the same probabilistic design criteria cannot be applied to different calculation intervals or methods of analysis. Therefore, parallel analyses of proposed and reference design cases, similar to the examples presented in this paper, are needed so that the analyst can confidently make a relevant comparison and draw relevant conclusions about the level of performance provided by new designs.

Considering the inherent spatial variability in waste and earth materials and the need for engineers to apply sound quantitative practices to engineering analysis, it is important to apply the available probabilistic techniques to problems of differential settlement. This paper has outlined one method to implement probability-based differential settlement analyses for the design of landfills and other embankments. The design criteria development technique presented in this paper is one tool to bridge the gap from deterministic practice to probabilistic practice. Following this approach, it is possible to build a body of experience with these methods and consider new design problems with confidence.

REFERENES

Baecher, G. B. and Christian, J. T. (2003). *Reliability and Statistics in Geotechnical Engineering*. Wiley, Hoboken, NJ, 605 p.

Fenton, G. A. (1990). Simulation and Analysis of Random Fields. *Ph.D. Dissertation*, Dept. of Civil Engineering and Operations Research, Princeton University, 174 p.

Fenton, G. A., Paice, G. M., and Griffiths, D. V. (1996). "Probabilistic Analysis of Foundation Settlement." *Uncertainty in the Geologic Environment: from Theory to Practice*, GSP No. 58, ASCE, Reston,VA, 651-665.

Foye, K. C. and Soong, T. (2010) *"*Simulating Differential Settlement of Landfill Foundations using Random Fields*" GeoFlorida 2010: Advances in Analysis, Modeling & Design*, GSP No. 199, ASCE, Reston, VA, 2042-2051.

Foye, K. C., Zhao, X., Voice, T. C., and Hashsham. S. A. (2007) *"*Settlement Monitoring for Bioreactor Landfill Airspace Management*." 7th FMGM 2007: Proceedings of the Seventh International Symposium on Field Measurements in Geomechanics*, GSP No. 175 (CD-ROM), ASCE, Reston, VA.

Qian, X., Koerner, R. M., and Gray, D. H. (2002). *Geotechnical Aspects of Landfill Design and Construction*. Prentice Hall, Upper Saddle River, NJ, 717 p.

Bayesian Updating of Load Settlement Curves for Footings on Cohesionless Soil

Shadi S. Najjar[1], A.M. ASCE and Michel Saad[2]

[1]Assistant Professor, Dep. of Civil and Env. Eng'g., American University of Beirut, PO.Box 11-0236 Riad Solh 1107-2020; PH(961)3108853; email: sn06@aub.edu.lb.
[2]Graduate Student, Dep. of Civil and Env. Eng'g., American University of Beirut, PO.Box 11-0236 Riad Solh 1107-2020; PH(961)319652; email: mws17@aub.edu.lb.

ABSTRACT

The design of spread footings on cohesionless soils is generally governed by serviceability requirements. Recent studies have investigated the use of normalized load-settlement curves to model the behavior of footings at all levels of displacement using databases of load tests. An investigation of available databases with complete load-settlement curves indicates that more than 85% of available data corresponds to plate load tests or footings that are smaller than 1.0m in width. There is a need to confirm the applicability of these curves to footings with widths ranging from 1.0m to 10.0 m. The main objective of this paper is to update available normalized load-settlement curves using point measurements of settlement and load from full scale footings. The updating process was conducted using the first-order, second-moment Bayesian method (FSBM) which allows for determining updated load-settlement curves and quantifying the uncertainty associated with these curves to facilitate their use in practical reliability-based design of footings on cohesionless soils.

INTRODUCTION AND BACKGROUND

The efficient design of shallow foundations on granular soil is governed by the accuracy and reliability of current settlement prediction models. Most traditional methods of settlement prediction for footings on granular soil do not address the expected nonlinearity in the load-settlement behavior. As a result, recent efforts in this field have attempted to study the overall load-settlement behavior of a foundation under load using various analytical and empirical models (Lutenegger and Adams 2003, Briaud 2007, Elfass et al. 2007) or using the observed behavior of well-documented footing tests which allow for an assessment of the overall generalized load-settlement behavior of footings (Akbas and Kulhawy 2009a). Akbas and Kulhawy (2009a) assembled a database comprised of 167 axial compression tests with complete load-settlement curves for footings on soils ranging from silt to gravel. The database was used to evaluate the normalized load-settlement behavior of footings in cohesionless soils. The normalization was conducted by dividing the settlement (s) by the footing width (B) and the force (Q) by the interpreted failure load (Q_{L2}), which is defined as the failure threshold which corresponds to the beginning of the final linear portion of the load-settlement curve (Akbas and Kulhawy 2009a). The normalization was conducted to achieve a common load-settlement behavior for all the tests in the database.

To achieve this objective, Akbas and Kulhawy (2009a) approximated the normalized load-settlement curves measured for each load test in the database using a hyperbolic fitting model with two fitting parameters, *a* and *b* such that:

$$Q/Q_{L2} = \frac{s/B}{a(s/B)+b} \quad (1)$$

The parameters *a* and *b* were calculated using least square regression. For the 125 cases analyzed (42 out of 167 test cases were not included in the analysis since the load tests in these cases were terminated at small settlements), results indicated averages and coefficients of variation of 0.7 and 0.22 (for parameter *a*) and 1.77 and 0.54 (for parameter *b*), respectively. These values were reduced to 0.69 and 0.21 (for parameter *a*) and to 1.68 and 0.38 (for parameter *b*) when the results were averaged for each site and when the sites with residual or cemented soils were excluded. The resulting mean normalized load-settlement curve (*a=0.69* and *b=1.68)* and the 125 load-settlement curves are presented on Fig. 1. The curves indicate that the load-settlement relationship exhibits significant scatter about the mean relationship.

Despite the fact that the derived normalized hyperbolic load-settlement curve shown on Fig. 1 constitutes the first rigorous attempt for modeling the full load-settlement behavior of footings on cohesionless soil, a closer look at the actual data indicates that only 22 out of 167 test cases involve footings that have widths that are greater than 1.0m, and only 14 footings with widths greater than 1.0m were used to derive the load-settlement relationship on Fig. 1. There is a need for validating and updating this relationship with test cases involving footings of practical field scale. There is a wealth of data in the literature on point measurements of settlement and load for such footings. The paper aims at utilizing the First Order Second Moment Bayesian approach (FSBM) to update the current normalized load-settlement relationship which is mainly derived from footings with widths that are smaller than 1.0m, using point measurements of settlement and load from full scale footings.

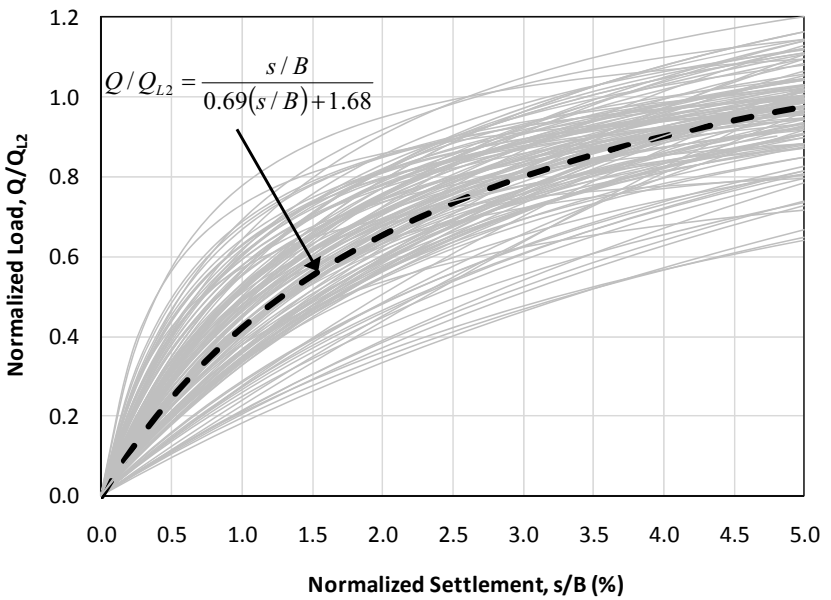

Figure 1. Best-fit and average hyperbolic normalized load-settlement curves for 125 load tests reported in Akbas and Kulhawy (2009a).

DATABASE OF POINT MEASUREMENTS OF SETTLEMENTS AND LOADS FOR FOOTINGS ON COHESIONLESS SOIL

Akbas (2007) compiled a database of 426 cases involving point measurements of settlements and loads for shallow foundations on granular soils. Since the database included 116 test cases that were extracted from the old database (Akbas and Kulhawy 2009a), these test cases were excluded from the analysis, resulting in a net number of original tests of 310. These point measurements of settlement and load were not used in the calibration of the model proposed by Akbas and Kulhawy (2009a). Thirty five tests involved footings with widths that are less than 1m, 204 tests with widths between 1m and 10m, and 51 tests with widths greater than 10m. To utilize the database collected by Akbas (2007) in the assessment/updating of the normalized load settlement relationship proposed in Fig. 1, the point measurements had to be normalized with respect to B and Q_{L2}. This posed a problem since the value of Q_{L2} was not available for the point measurements. However, Akbas and Kulhawy (2009b) proposed a relationship between Q_{L2} and the conventional ultimate bearing capacity (Q_{tcp}) of the foundation. This relationship suggested that Q_{L2} could be estimated by Q_{tcp} for footings with widths greater than 1.0m. For footings with widths that are smaller than 1.0m, they proposed a relationship between Q_{L2} and Q_{tcp} which takes into consideration the effect of the footing width (B). This relationship could be used to evaluate Q_{L2} for each of the 310 tests mentioned above. Since the accurate estimation of Q_{tcp} involves knowledge about soil properties that were not presented in Akbas (2007), the ratio of Q/Q_{L2} was back-calculated from tabulated settlement predictions obtained and presented in Akbas (2007) using the model proposed in Fig. 1. The back-calculated ratio of Q/Q_{L2} coupled with the ratio of the measured settlement to the footing width (s/B) constituted one point (among 310 points) to be used in the evaluation/updating process of the hyperbolic model presented in Fig. 1.

The 310 normalized data points are plotted in Fig. 2a together with the original mean load-settlement relationship proposed by Akbas and Kulhawy (2009a). In Fig. 2b, all the cases with a B that is less 1.0m are excluded. The data presented in Figs. 2a and 2b indicates that the hyperbolic model seems to provide an acceptable prediction of the point measurements. However, a closer look at the ratio of predicted to measured Q/Q_{L2} for the available tests indicates that on average, the hyperbolic model tends to overestimate the normalized load for a given normalized settlement. The mean value of the ratio of predicted to measured Q/Q_{L2} is equal to 1.33 with an associated coefficient of variation of 0.47. If only footings with widths greater than 1.0 are included, the mean ratio of the predicted to measured Q/Q_{L2} increases slightly to a value of 1.36. The difference in the two mean values, although small, is related to the fact that the hyperbolic model was derived from footings with widths that are generally smaller than 1.0m. An analysis of the data with footing widths smaller than 1.0m (35 test cases only) confirms the above argument since the ratio of predicted to measured Q/Q_{L2} for these small footings/plates was found to have a reduced mean value of only 1.10 and a corresponding reduced coefficient of variation of 0.38. Since only 35 footings with widths smaller than 1.0 are included in the database, their effect on Figs. 2a and 2b was not pronounced and was limited to increasing the mean ratio of predicted to measured Q/Q_{L2} from 1.33 to 1.36.

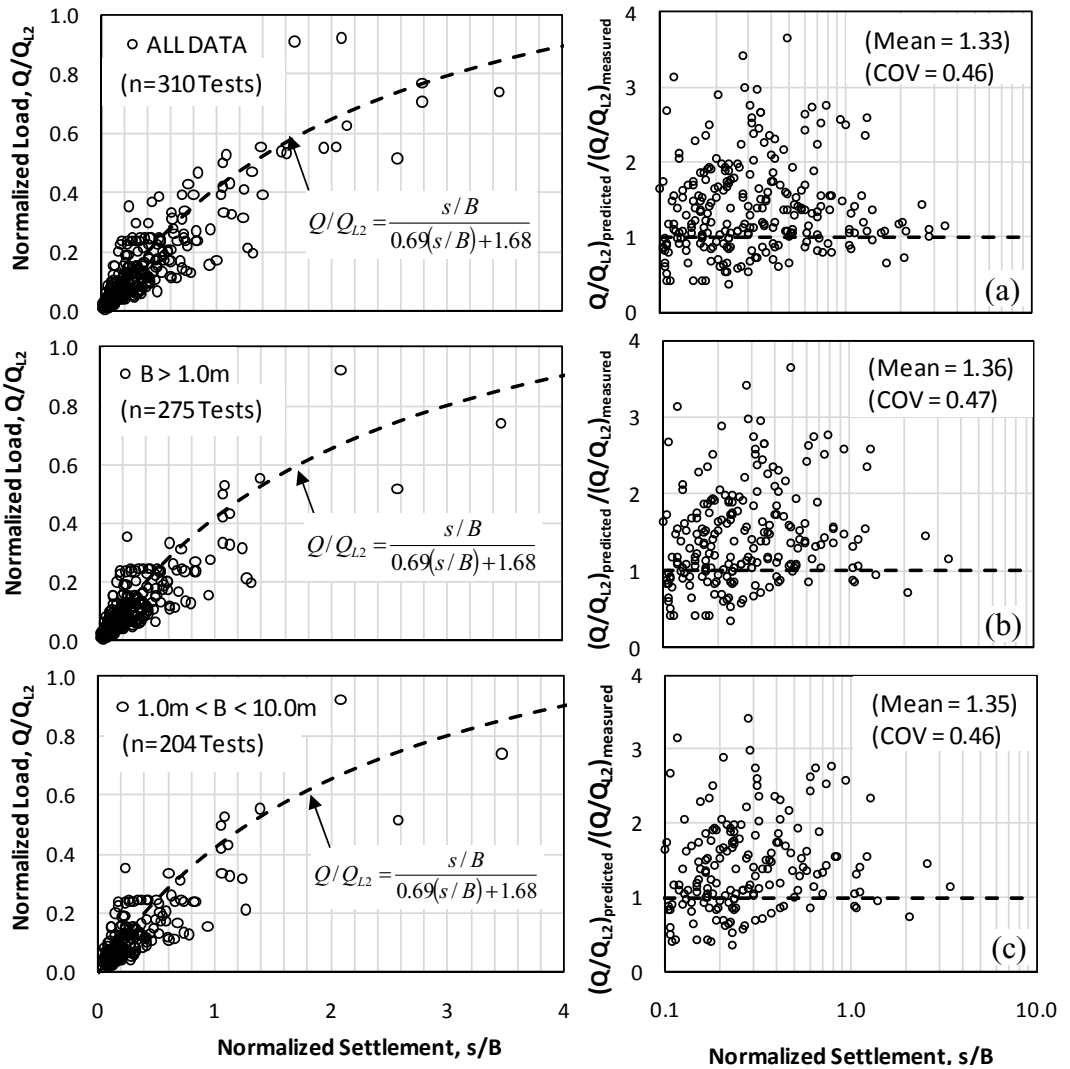

Figure 2. Normalized point measurements of load and settlement for different footing widths (Data from Akbas 2007).

The above discussion indicates that the hyperbolic model could be updated using data from full scale footings with widths that are in the range of 1m to 10m. The normalized point measurements for such footings (204 test cases) were plotted on Fig. 2c. The statistics of the ratio of predicted to measured Q/Q_{L2} for these footings were found to be similar to the case with B>1m indicating similar behavior. It is worth noting that although the mean ratio of predicted to measured Q/Q_{L2} is in the order of 1.33 to 1.36, this ratio increases if only the cases with s/B between 0.4% and 2.0% are included in the analysis. This range represents settlements that are expected for full scale footings with widths ranging from 2.0m to 7.0m and allowable settlements that are in the range of 2.5cm to 5.0cm. If only such cases are taken into consideration, the mean ratio of the predicted to measured Q/Q_{L2} increases to a value of 1.43 for the case involving all footing widths, and to 1.56 and 1.58 for the cases involving footings with B greater than 1.0m and B between 1.0m and 10.0m, respectively. These results further reinforce the need for updating the curve proposed in Fig. 1 using data for footings with widths that are greater than 1.0m.

PROBABILISTIC HYPERBOLIC LOAD-SETTLEMENT MODEL

The hyperbolic model in Equation 1 could be represented probabilistically by considering that the normalized force Q/Q_{L2} for a given normalized displacement s/B is a random variable with a mean and a standard deviation that are represented by:

$$\mu_{Q/Q_{L2}} = \frac{s/B}{\Phi_1(s/B)+\Phi_2} \qquad \text{and} \qquad \sigma_{Q/Q_{L2}} = e^{\Phi_3}\mu_{Q/Q_{L2}} \tag{2}$$

Where Φ_1, Φ_2 are the parameters of the hyperbolic model and $e^{\Phi 3}$ reflects the coefficient of variation in the value of Q/Q_{L2}. The exponential term is used to ensure that the coefficient of variation is a positive quantity. In the probabilistic model, the parameters (Φ_1, Φ_2 and Φ_3) were assumed to be random numbers that are defined by their means, variances, and covariances. The prior estimates of the means and variances of Φ_1 and Φ_2 were adopted from the statistics proposed by Akbas and Kulhawy (2009a) ($\mu_{\Phi 1}$=0.69, $cov_{\Phi 1}$=0.21; $\mu_{\Phi 2}$=1.68, $cov_{\Phi 2}$=0.38). An analysis of the 125 pairs of Φ_1 and Φ_2 indicated that the two parameters are negatively correlated with a correlation coefficient ρ of -0.71. This estimate was used as a prior estimate of the correlation coefficient between Φ_1 and Φ_2. As a prior estimate, the parameter Φ_3 was assumed to have a mean of -1.0 and a coefficient of variation of 0.3. This translates into a mean value of $e^{\Phi 3}$ of about 0.36 and a coefficient of variation in $e^{\Phi 3}$ of about 0.3. The sensitivity of the problem to the statistics of Φ_3 will be evaluated in later sections of this paper. Since there is no physical reason for Φ_3 to be correlated to either Φ_1 or Φ_2, it was assumed that Φ_3 was statistically independent from Φ_1 and Φ_2.

FIRST ORDER – SECOND MOMENT BAYESIAN METHOD (FSBM)

The FSBM proposed by Gilbert (1999) was used to calibrate the probabilistic hyperbolic model using normalized point measurements of settlement and load derived from full scale footings. The FSBM uses Bayes' theorem (Eq. 3) to update the probability distribution of the model parameters for a given set of data.

$$f_{\vec{\Phi}|\vec{\varepsilon}}\left(\vec{\Phi}\middle|\vec{\varepsilon}\right) = L\left(\vec{\varepsilon}\middle|\vec{\Phi}\right) f_{\vec{\Phi}}\left(\vec{\Phi}\right) \Big/ \int_{-\infty}^{+\infty}\ldots\int_{-\infty}^{+\infty} L\left(\vec{\varepsilon}\middle|\vec{\Phi}\right) f_{\vec{\Phi}}\left(\vec{\Phi}\right) d\Phi_1 \ldots d\Phi_n \tag{3}$$

where $f_{\vec{\Phi}|\vec{\varepsilon}}\left(\vec{\Phi}\middle|\vec{\varepsilon}\right)$ and $f_{\vec{\Phi}}\left(\vec{\Phi}\right)$ are the updated (given the new data $\vec{\varepsilon}$) and prior joint distributions of the model parameters $\vec{\Phi}$, $L\left(\vec{\varepsilon}\middle|\vec{\Phi}\right)$ is the likelihood function, and $\int_{-\infty}^{+\infty}\ldots\int_{-\infty}^{+\infty} L\left(\vec{\varepsilon}\middle|\vec{\Phi}\right) f_{\vec{\Phi}}\left(\vec{\Phi}\right) d\Phi_1 \ldots d\Phi_n$ is a normalizing constant. The first (updated mean vector $\vec{\mu}_{\vec{\Phi}|\vec{\varepsilon}}$) and second (updated covariance matrix $C_{\vec{\Phi}|\vec{\varepsilon}}$) moments of the calibrated model parameters are derived from a second-order approximation of Eq. 3 by approximating the natural logarithm of the likelihood function with a second-order Taylor series. The expansion point $\vec{\Phi}^*$ which maximizes the natural logarithm of the likelihood function is then obtained and used to calculate approximations for the updated mean vector $\vec{\mu}_{\vec{\Phi}|\vec{\varepsilon}}$ and the updated covariance matrix $C_{\vec{\Phi}|\vec{\varepsilon}}$ (Gilbert 1999).

UPDATED PROBABILISTIC HYPERBOLIC LOAD-SETTLEMENT MODEL

The updating process of the hyperbolic relationship presented in Fig. 1 was conducted using two sets of data. The first set involves the 310 cases representing all the foundations in the Akbas (2007) database (Cases I, II, and III), while the second set (Cases IV and V) was restricted to the 204 load cases with footing widths that range from 1.0m to 10.0m. The prior means, coefficients of variation, and correlation coefficients of the model parameters are presented in Table 1. The prior mean value of Φ_3 was taken as -0.2, -0.5, and -1.0, representing coefficients of variation in Q/Q_{L2} of 0.82, 0.60, and 0.37, respectively. The sensitivity of the results of the updating process to these values was analyzed. The updated model parameters for the different scenarios are presented in Table 1 for comparison.

For Cases I, II, and III, results indicated that the updated mean values of Φ_1 and Φ_2 were equal to 1.30 and 1.60, respectively (compared to 0.69 and 1.68 for the prior case) and were insensitive to the prior values of the mean of Φ_3. When only footings with widths ranging from 1.0m to 10.0m were analyzed, the updated mean values of Φ_1 and Φ_2 ranged from 1.23 to 1.24 and 1.63 to 1.66, respectively. For both sets of data, results in Table 1 indicate that the updating process resulted in updated mean model parameters Φ_1 and Φ_2 that are different than the prior means. This difference is illustrated graphically on Fig. 3, which shows the updated mean normalized load-settlement curves for the two updating scenarios, with the point measurements corresponding to the case with 1.0m<B<10.0m. As expected, the updated curves are lower than the original curve proposed by Akbas and Kulhawy (2009a). For the practical range of normalized settlements (0.5% < s/B < 2.0%), the updated curves provide a better fit to the measured data. For larger settlements (s/B > 2%), the lack of enough data makes the assessment of the behavior relatively vague. As such, there is a need for gathering more information of load and settlement in this high settlement range for practical footings on granular soil.

Table 1: Results of the Bayesian Updating Process for Different Prior Scenarios

	Updating Using All Data (310 Tests)						Updating Using Footings with 1.0m<B<10.0m (204 Tests)			
	Case I		Case II		Case III		Case IV		Case V	
Model Parameters	Prior	Updated	Prior	Updated	Prior	Updated	Prior	Updated	Prior	Updated
$\mu_{\Phi1}$	0.69	1.30	0.69	1.30	0.69	1.31	0.69	1.23	0.69	1.24
$cov_{\Phi1}$	0.21	0.05	0.21	0.05	0.21	0.05	0.21	0.07	0.21	0.07
$\mu_{\Phi2}$	1.68	1.60	1.68	1.60	1.68	1.63	1.68	1.63	1.68	1.66
$cov_{\Phi2}$	0.38	0.02	0.38	0.02	0.38	0.02	0.38	0.03	0.38	0.02
$\mu_{\Phi3}$	**-1.0**	-0.75	**-0.5**	-0.73	**-0.2**	-0.57	**-0.5**	-0.70	**-0.2**	-0.51
$cov_{\Phi3}$	0.30	0.06	0.30	0.06	0.30	0.06	0.30	0.07	0.30	0.08
$\rho_{\Phi1, \Phi2}$	-0.71	-0.54	-0.71	-0.54	-0.71	-0.54	-0.71	-0.52	-0.71	-0.53
$\rho_{\Phi1, \Phi3}$	0	0.04	0	0.04	0	0.04	0	0.03	0	0.03
$\rho_{\Phi2, \Phi3}$	0	0.21	0	0.21	0	0.18	0	0.22	0	0.18

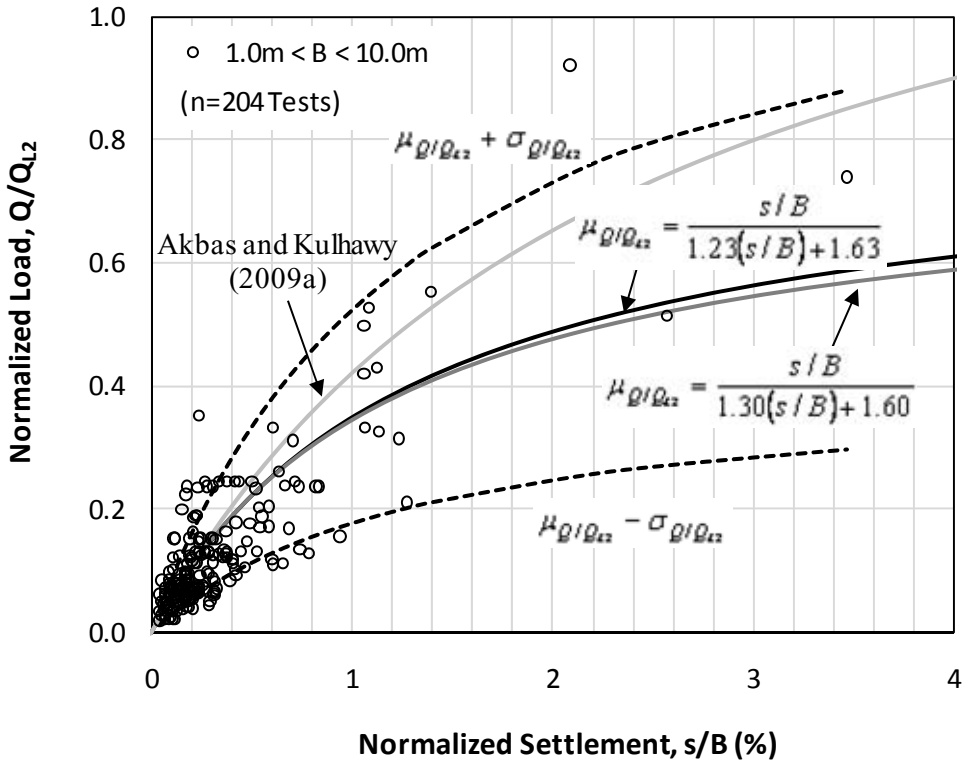

Figure 3. Prior and updated mean normalized load-settlement relationships.

The parameters that affect uncertainty in the load-settlement relationships are the coefficients of variation in Φ_1 and Φ_2 in addition to the mean and coefficient of variation of Φ_3, which could be combined using a first order approximation (Gilbert 1999) to produce an estimate of the overall uncertainty. Results in Table 1 indicate that the updated coefficients of variation for Φ_1 and Φ_2 are small ($0.05<cov_{\Phi 1}<0.07$ and $0.02<cov_{\Phi 2}<0.03$) compared to their prior estimates. This is related to the formulation of the probabilistic hyperbolic model which models separately the mean and the standard deviation of Q/Q_{L2} for a given s/B. In the model proposed by Akbas and Kulhawy (2009a), the uncertainty in the load-settlement relationship is solely expressed by the uncertainty in Φ_1 and Φ_2 resulting in relatively large values for the coefficients of variation of Φ_1 and Φ_2. In the probabilistic model presented in this paper, the main uncertainty is expressed by Φ_3 which governs the coefficient of variation of Q/Q_{L2} for a given s/B. The updated mean of Φ_3 ranged from -0.57 (for prior estimate of -0.2) to -0.75 (for prior estimate of -1.0 and -0.5), and the coefficient of variation of Φ_3 was about 0.06. The upper bound of -0.57 in the updated mean of Φ_3 corresponds to a coefficient of variation of 0.57 in the predicted value of Q/Q_{L2}, while the lower bound of -0.75 represents a coefficient of variation of 0.47. From a practical perspective, it is very unlikely that the prior estimate of the mean of Φ_3 is as low as -0.2 (cov of Q/Q_{L2} of 0.82). As a result, the updated value of the mean of Φ_3 corresponding to the case with a mean prior estimate of -0.5 will be adopted in this paper to predict curves representing plus and minus one standard deviations about the mean relationship. These curves represent uncertainty in Q/Q_{L2} and are plotted on Fig. 3 for the case involving footings with widths ranging from 1.0m to 10.0m.

CONCLUSIONS

The following conclusions can be drawn based on the analysis conducted:

1. For a given settlement, the normalized hyperbolic load-settlement relationship proposed by Akbas and Kulhawy (2009a) slightly overpredicted the point measurements of load obtained from full-scale footings, with the mean value of the ratio of predicted to measured Q/Q_{L2} being in the range of 1.33 to 1.36.
2. For normalized settlements that are more representative of practical footings designed at typical allowable settlements ($0.4\% < s/B < 2\%$), the predictions of the Akbas and Kulhawy (2009a) model become more unconservative, with a mean ratio of predicted to measured Q/Q_{L2} being in the range of 1.56 to 1.58.
3. The updating of the hyperbolic load-settlement curve with point measurements from full-scale footings using the First Order Second Moment Bayesian approach indicated that the updated curve exhibited a softer response in comparison to the original curve especially at normalized displacements that are greater than 0.5%.
4. The uncertainty in the updated hyperbolic model was also assessed using the Bayesian updating process and indicated a coefficient of variation in the order of 0.5 in the estimated Q/Q_{L2} for a given normalized displacement s/B.

ACKNOWLEDGMENTS

The authors would like to acknowledge the University Research Board (URB) at the American University of Beirut for funding this research study.

REFERENCES

Akbas, S.O. (2007). *"Deterministic and probabilistic assessment of settlements of shallow foundations in cohesionless soils."* Ph.D. thesis, Cornell Univ., Ithaca.

Akbas, S.O. and Kulhawy, F.H. (2009a). "Axial compression of footings in cohesionless soils.I: load-settlement behavior." *Journal of Geotechnical and Geoenvironmental Engineering*, 135(11), 1562-1574.

Akbas, S.O. and Kulhawy, F.H. (2009b). "Axial compression of footings in cohesionless soils.II: bearing capacity." *Journal of Geotechnical and Geoenvironmental Engineering*, 135(11), 1575-1582.

Briaud, J.L. (2007). "Spread footings in sand: Load settlement curve approach." *J. Geotech. Geoenviron. Eng.*, 133(8), 905-920.

Elfass, S., Norris, G., and Vimalaraj, P. (2007). "A simple bearing capacity equation." *Proc., Geo-Denver 2007: New Peaks in Geotechnics (GSP 171)*, H. W. Olsen, ed., ASCE, Reston, Va., 1-10.

Gilbert, R.B. (1999). ''First-order second-moment Bayesian method for data analysis in decision making.'' Geotechnical Engineering Center, Dept. of Civil Engineering, Univ. of Texas at Austin, Tex.

Lutenegger, A.J. and Adams, M.T. (1998). "Bearing capacity of footings on compacted sand." *Proc., 4th Int. Conf. on Case Histories in Geotechnical Engineering*, St. Louis, Mo., 1216-1224.

Stochastic vs. Deterministic Analysis of Consolidation Problem in Natural Alluvial Deposits

Pouya Pishgah Gilani[1] and Reza Jamshidi Chenari[2]

[1]MSc student , Department of Civil Engineering, Guilan University, Iran.
Email: pouya.pishgah@gmail.com
[2]Assistant Professor, Department of Civil Engineering, Guilan University, Iran.
Email: jamshidi_reza@guilan.ac.ir

ABSTRACT

The soil permeability, k play important role in the consolidation of natural alluvial deposits which are unavoidably heterogeneous. The spatial variation of consolidation parameters can be decomposed conveniently into a smoothly varying trend function and a fluctuating component. Deterministic trends of permeability and volume compressibility coefficient are de-trended from in-situ tests and the residual component is assumed to represent stochastic behaviour. This paper focuses on the combined effect of deterministic and stochastic variability of consolidation parameters which are so-called inherent variability, on the consolidation behaviour of natural deposits. Both coupled and uncoupled formulations are considered in this study and the aim is to show the importance of different components of inherent variability of consolidation parameters when they are embodied in an integrated analysis in comparison to when they are taken into account individually.

INTRODUCTION

It is well known that taking the coefficient of consolidation c_v as a constant is a major shortcoming of conventional consolidation theory (Duncan, 1993). To overcome this shortcoming, many studies were conducted on the 1-D nonlinear consolidation problem, in which the coefficient of permeability, k and the volume compressibility, m_v were shown to vary with effective stress and void ratio (Davis and Raymond, 1965; Li et al.,1999; Xie et al.,2002). Both m_v and k_v play important roles in the consolidation of heterogeneous soil but they cannot embodied into a single c_v (see, e.g., Lee et al. 1992; Pyrah 1996). Meanwhile the problem of 1-D consolidation of non-homogeneous soil was studied assuming that k and m_v vary with depth (Schiffman and Gibson 1964).

There have been a few studies that used stochastic approaches to investigate coupled consolidation and settlement problems. Freeze (1977) dealt with one-dimensional consolidation by taking account of the cross correlation between the m_v and the k, which were chosen randomly from probability density functions. Hong (1992) studied 1D consolidation by treating c_v as a random variable. Badaoui et al. (2007) investigated 1D consolidation by the thin layer method combined with Monte

Carlo simulations. More recently, Huang et al. (2010) investigated the coupled Biot consolidation theory by using random field theory (see. e.g., Griffiths and Fenton 1993; Fenton and Griffiths 2008).

This paper focuses on the comparison between the deterministic computation (based on a linear trend) and the combined rigorous approach which takes into account simultaneously both the linear trend and the fluctuations. This will efficiently demonstrate the interest of considering a stochastic approach based on a spatially varying soil property which respect to a classical deterministic approach only on a smoothly varying trend function.

RANDOM FIELD MODEL FOR INHERENT SOIL VARIABILITY

Inherent variability results primarily from the natural geologic processes that produced and continually modify the soil mass in situ (Kulhawy 1992). In principle, spatial variation of a soil deposit can be characterised in detail, but only with a great number of observations, which normally are not available. Thus, for engineering purposes a simplification is introduced – a model – with which this spatial variation, illustrated in Figure 1, can be decomposed conveniently into a smooth deterministic trend, $t(z)$ and fluctuating component, $w(z)$ as follows (Phoon et al. 1995) :

$$\xi(z) = t(z) + w(z)$$

in which $\xi =$ in situ soil property and z = depth. The inherent soil variability can be represented by the fluctuating component, if w(z) is modelled as a homogeneous random field, as suggested by Vanmarcke (1983). The fluctuating component is characterised as a random variable of zero-mean and non-zero variance.

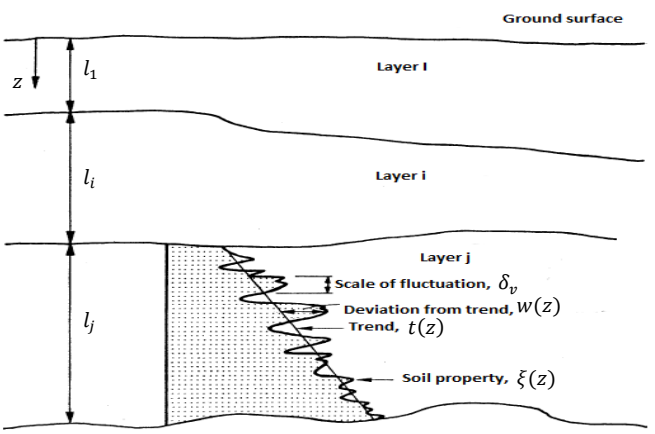

Figure 1. Inherent soil variability (Phoon et al. 1995)

DETERMINISTIC VARIATION OF PERMEABILITY

Consolidation and permeability characteristics are important to quantify stress/strain relations and the time-dependent behaviour of soils. It is often observed

that increasing stress in a soil causes a permeability decrease as porosity (and void ratio) decreases. Several relationships have been proposed to mathematically account for changing permeabilities with changing stress (Terzaghi et al. 1996 ; Tavenas et al. 1983).Vaughan (1989) proposed that the permeability, varies exponentially with the mean effective stress, $\acute{\sigma}$:

$$k = k_0 \exp(-B\acute{\sigma})$$

Where k_0 is the permeability at zero mean effective stress and B is a user-specified material property.

Regarding to the above relationship, permeability is a function of effective stress. Generally the deeper a soil is buried, the greater increase of effective stress under the pressure of overburden, and the lower is its permeability. Concerning natural processes, all soil properties in situ vary vertically, and trend analysis is considered with distinguishing deterministic trend for k. In this paper a linearly depth-decreasing trend was assumed to represent the deterministic trend of permeability profiles with depth.

STOCHASTIC VARIATION OF PERMEABILITY

The stochastic component of permeability can be modelled by taking a proper distribution type which best fits to the real statistical distribution. Different distributions like normal, log-normal, etc have been used in literature. Among all, the normal and log-normal distributions are more widely used in comparison to others. The choice of a lognormal distribution is motivated by the fact that most geotechnical parameters are strictly non-negative, a property of the lognormal distribution (but not the normal) while still having a simple relationship with the normal distribution. However if someone watches to prevent negative values to appear the normal (Gaussian) distribution is probably the most important distribution in use today. This is largely because sums of random variables tend to a normal distribution. Truncation of the probable negative portion of a normally distributed data for permeability which is believed by authors to be insignificant, by utilizing the absolute values of the data will preclude the negative values to appear while maintaining the original PDF with no major change. For permeability which inherits zero cut off value like other geotechnical parameters, if one consider a normal distribution with the mean and COV of 1 and 40 respectively (representing wide inherent variation), the probability for the coefficient of permeability to become negative is less than 0.62% which seems trivial and unimportant. The statistical variations of most soil properties follow normal distributions. Many natural “additive” type phenomena, or phenomena involving many accumulating factors, therefore tend to have normal distributions. In the coupled example of this paper the soil permeability was assumed to have normal distribution for the fluctuating component representing stochastic behaviour. Two different coefficients of variation of 20% and 40% were chosen for comparison purpose. Coupled and uncoupled approaches are adopted here to highlight the difference between deterministic and stochastic analysis results. For this aim and for simplicity sinusoidal variation was

chosen to represent the stochastic component of the permeability in uncoupled analyses. Also uncorrelated truncated normally distribution data generation scheme was used in coupled analyses for comparison purpose only.

UNCOUPLED CONSOLIDATION PROBLEM

A simple uncoupled (Terzaghi) approach was adopted in order to show the effect of different components of inherent variation of permeability on the average degree of consolidation. m_v was held constant while k was assumed to bear a linear depth-decreasing trend along with a sinusoidal fluctuating component which is believed to represent stochastic behaviour. By assuming a depth-constant initial pore pressure profile (u_i), the un-coupled equation for isochrones will be :

$$u_z = \sum_{m=0}^{\infty} \frac{2u_0}{M} \sin\left(\frac{Mz}{H}\right) \exp\left(-M^2 T_V\right)$$

The average degree of consolidation for different analyses namely linearly varying, sinusoidal fluctuation and the general property (combined) was calculated by introducing the linear and sinusoidal variation into the T_V formulation, separately and also in combined fashion and are depicted in Figure 2. The superposition of the results for individual components is also provided in Figure 2 (Pishgah and Jamshidi 2010).

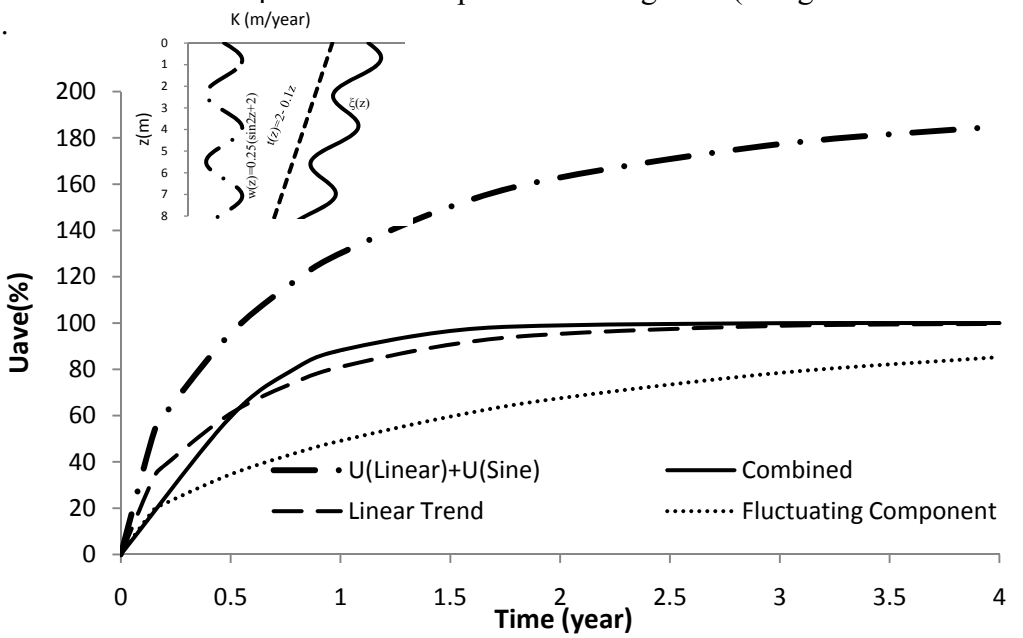

Figure 2. Average degree of consolidation versus time for inherent soil variability-uncoupled (Pishgah and Jamshidi 2010)

COUPLED CONSOLIDATION PROBLEM

For the coupled consolidation analysis in present study, commercially available finite difference code, FLAC 4.0 (Itasca 2002) is used for the numerical modelling of spatially variable and linearly varying soil properties. The RDEV

keyword was used which returns normally distributed permeability values using a function form Press et al. (2002). The inbuilt VAR function enables to define a linear variation in the property over the given range to represent deterministic variation. A FISH function was developed in order to determine and plot average degree of consolidation for various analyses.

A one-dimensional consolidation problem will be analyzed in this paper. A saturated layer of soil thickness of $H = 20\ m$ and large horizontal dimension rests on a rigid, impervious base. A constant surface load, $p_y = 100\ kPa$, is applied on the layer, and the initial state of the problem corresponds to undrained equilibrium with a uniform pore pressure, $p_0 = 100\ kPa$. The soil matrix is homogeneous and behaves elastically, and the isotropic Darcy's transport law applies. With time, the fluid drains through the layer surface, transferring the load from the fluid to the soil matrix. The problem is one dimensional (uniaxial strain conditions) and a slice of unit width is considered in the numerical simulation to model the coupled process of fluid and mechanical response.

The FLAC model grid for this problem is a column of 20 zones aligned with y axis. The base of the column is fixed, and lateral displacements are restricted. A mechanical pressure, p_y , is applied at the top of the column. The pore pressure is initialized to a uniform value of $p_0 = p_y$ throughout the model. Drainage is allowed by fixing and initialising the pore pressure at zero at the top of the model. The properties for this example are illustrated in Table 1.

Table 1. Input Model Properties (coupled example)

Property	Value
Drained bulk modulus, K	$5 \times 10^8\ Pa$
Shear modulus, G	$2 \times 10^8\ Pa$
Water bulk modulus, K_w	$2 \times 10^9\ Pa$
Biot coefficient, α	1.0
Porosity , n	0.3

A linearly depth decreasing trend from the surface to the base varies from 2×10^{-4} to $10^{-4}\ \frac{cm}{s}$ assuming to represent deterministic trend. In this study, the stochastic analyses of the permeability were performed by conducting 100 realizations and analyses accordingly. By adding the values of permeabilities obtained from each stochastic simulation with deterministic values of corresponding depth, the summation were considered for combined analyses.

Permeability is one of the most variable soil properties and its coefficient of variation is generally very high. The values of COV were considered as 20% and 40% chosen for comparison only. Although the real variation of permeability found

in literature, sometimes inherits quite large values, the mean value which is assumed for stochastic analyses is: —.

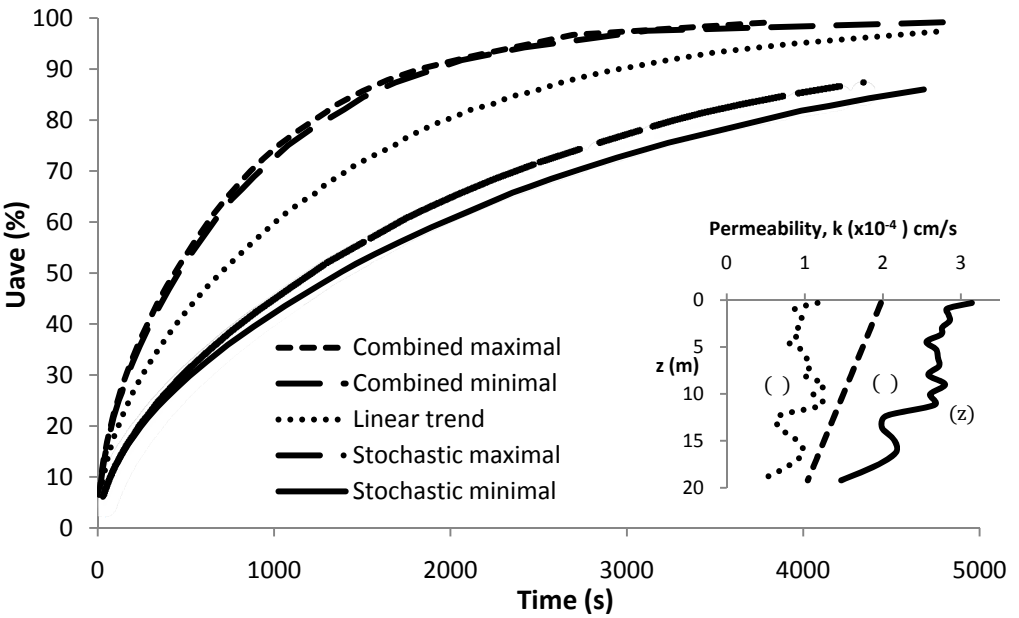

Figure 3. Average degree of consolidation versus time for inherent soil variability with coefficient of variation of 20 % for input permeability

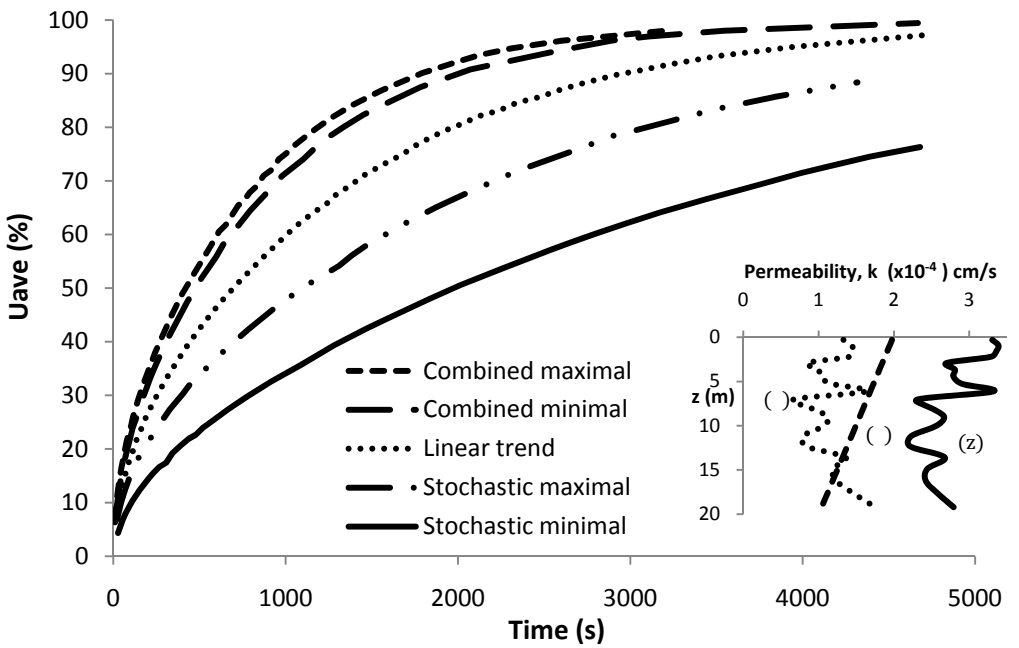

Figure 4. Average degree of consolidation versus time for inherent soil variability with coefficient of variation of 40 % for input permeability

Table 2. Settlement results (Coupled)

Coefficient of Variation of Permeability	Deterministic (mm)	Stochastic (mm)	Combined (mm)	Superposed (mm)
20 %	2.501	δ_{mean}= 2.291 (COV_{δ} = 14 %)	δ_{mean}= 2.557 (COV_{δ}= 1.5 %)	4.792
40 %	2.501	δ_{mean}= 2.173 (COV_{δ} = 68 %)	δ_{mean}= 2.556 (COV_{δ}= 1.7 %)	4.674

The maximum settlement results, δ accumulated on top of the layer were calculated in the analyses. For stochastic and combined analyses, the average settlement of 100 analyses, δ_{mean} and its coefficient of variation, COV_{δ} are reported in Table 2, also provided the superposition of the results of analysis for individual components. It can be seen that the results of combined and superposed analyses are not consistent. It means that it does not make sense to perform the deterministic and stochastic analysis individually and superpose them to achieve combined effects because it will overestimate the settlement. Figures 3 and 4 show the average degree of consolidation versus time for different analyses, as discussed above. It can be seen that the increase of the coefficient of variation of permeability, will cause a distinctive increase of the space between maximal and minimal for stochastic analyses, while there is no such effect observed for the combined analyses.

CONCLUSION

For both coupled and uncoupled consolidation analyses presented in this study, it was demonstrated numerically and graphically that it is essential to take different components of inherent variability of permeability into account simultaneously in each individual analysis. As governing equation for consolidation is not linear, the superposition of involved parameters proves to be invalid and always combined consideration of deterministic and stochastic components of permeability is needed to be conducted. Settlement results of coupled analysis also confirm the differences between combined and individual results. The effect of increasing the COV of permeability on the COV of stochastic settlement is more prominent in comparison to the COV of combined settlement in the example presented above. It appears that the contribution of deterministic component of permeability is more significant than the stochastic portion when comparing the combined average settlement to that of deterministic. In light of the information provided herewith, it is therefore important to take into account different components of inherent variability of permeability simultaneously with more emphasis on the deterministic trend.

REFERENCES

Badaoui, M., Nour, A., Slimani, A., and Berrah, M. K. (2007). "Condolidation statistics investigation via thin layer method analysis." *Transp. Porous Media*, 67, 69-91.

Davis, E. H., Raymond, C. P. (1965). "A non-linear theory of consolidation." *Geotechnique*, 15(2):161-173.

Duncan, J. M. (1993). "Limitations of conventional analysis of consolidation settlement." *Journal of Geotechnical Engineering ASCE,*119(9), 1333-1359.

Fenton, G. A., and Griffiths, D. V. (2008). "Risk assessment in geotechnical engineering." Wiley, New York.

FLAC 4.00. (2002). "Reference Manual." Itasca Consulting Group, Inc.Minneapolis.

Freeze, R. A. (1977). "Probabilistic one-dimensional consolidation." *J. Geotech. Engrg. Div.*, 103(GT7),725-741.

Griffiths, D. V., and Fenton, G. A. (1993). "Seepage beneath water retaining structures founded on spatially random soil." *Geotechnique*, 43(4), 577-587.

Hong, H. P. (1992). "One-dimensional consolidation with uncertain properties."*Can. Geotech. J.*, 29, 161-165.

Huang, J., Griffiths, D.V. and Fenton, G.A. (2010). "Probabilistic analysis of coupled soil consolidation." ASCE Journal of Geotechnical and Geoenvironmental Engineering, Vol. 136, No. 3, 417-430

Kulhawy, F. H., Brigisson, B. and Grigoriu, M. D. (1992). "Reliability-based foundation design for transmission line structures: transformation models for in situ tests." Report EL-5507(4), Electric Power Research Institute, Palo Alto, California

Lee, P. K. K., Xie, K. H., and Cheung, Y. K. (1992). "A study on one-dimensional consolidation of layered systems."*Int. J. Numer. Analyt.Meth.Geomech*., 16(11), 815-831.

Li, B.H., Xie, K.H., Ying, H.W., Zeng, G.X. (1999). "Semi-analytical solution of 1-D nonlinear consolidation considering the initial effective stress distribution." *Chinese Journal of Civil Enigineering*, 32(6):47-52 (in chinese)

Phoon, K-K., Kulhawy, F.H., and Grigoriu, M. D. (1995). "Reliability based design of foundations for transmission line structures."*Electric Power Research Institute*, Palo Alto, Report TR-105000.

Pishgah Gilani, P., Jamshidi Chenari, R. (Accepted Sep.2010). "Discussion of "Probabilistic Analysis of Coupled Soil Consolidation" by Jinsong Huang, D.V. Griffiths and Gordon A. Fenton", *ASCE Journal of Geotechnical and Geoenvironmental Engineering*.

Press, W.H.M., Teukolsky, S.A., Vetteling, W.T., Flannery, B.P. (2002). *Numerical Recipes in C++: The Art of Scientific Computing.* Second edition.Cambridge University Press.

Pyrah, I.C. (1996). "One-dimensional consolidation of layered soils."*Geotechnique*. 46(3), 555-560.

Rowe, P.W. (1972). "The relevance of soil fabric to site investigation practice." *Geotechnique*, 46(3), 555-560.

Schiffman, R.L., Gibson, R.E. (1964). "Consolidation of non-homogeneous clay layers." *Journal of the Soil Mechanics and Foundations Division*, *ASCE*, 4043: 1-30.

Tavenas, F., Jean, P. Leblond, P. and Leroueil, S. (1983). "The permeability of natural soft clays.II Permeability characteristics." *Canadian Geotechnical Journal,* 20, 645-550.

Terzaghi, K., Peck, R.B. and Mersi, G. (1996). *Soil mechanics in engineering practice,* 3rd ed., Wiley, New York.

Vanmarcke, EH. (1983). *Random fields; analysis and synthesis,* MIT Press, Cambridge.

Vaughan, P.R. (1989). "Non-linearity in seepage problems-theory and field observation." Del Mello Volume, Edgard Blucher Ltda.,Sau Paulo, Brasil, 501-516.

Xie, K.H., Wen, J.B., Hu, H.Y. (2002). "A study on one-dimensional consolidation of double-layered soil." *Computers and Geotechnics*, 29, 151-168.

Bearing Capacity of Strip Footings on Spatially Random Soils Using Sparse Polynomial Chaos Expansion

Tamara Al-Bittar[1] and Abdul-Hamid Soubra[2], M.ASCE

[1] PhD student, University of Nantes, GeM, UMR CNRS 6183, Bd. de l'université, BP 152, 44603 Saint-Nazaire cedex, France; E-mail: Tamara.Al-Bittar@univ-nantes.fr
[2] Professor, University of Nantes, GeM, UMR CNRS 6183, Bd. de l'université, BP 152, 44603 Saint-Nazaire cedex, France; E-mail: Abed.Soubra@univ-nantes.fr

ABSTRACT

In this paper, a numerical model that considers the spatial variability of the soil properties is presented to compute the probability density function (PDF) of the ultimate bearing capacity of strip footings resting on spatially random soils. An efficient uncertainty propagation methodology was employed in this paper. This methodology makes use of a sparse polynomial chaos expansion (SPCE) for the system response. The probabilistic numerical results have shown that (i) the autocorrelation distance has significant effect on the PDF of the bearing capacity, (ii) the probabilistic mean value of the bearing capacity presents a minimum for a given value of the ratio of the horizontal and vertical autocorrelation distances, (iii) the coefficient of variation of the cohesion parameter has a more significant influence than that of the friction angle on the variability of the response and finally (iv) the negative correlation between the soil shear strength parameters decreases the response variability.

INTRODUCTION

In this paper, the probability density function (PDF) of the ultimate bearing capacity of a shallow strip foundation resting on a spatially varying soil is computed using the sparse polynomial chaos expansion (SPCE) methodology. The deterministic model is based on numerical simulations using FLAC^{3D} software. The soil cohesion and friction angle are considered as two anisotropic non-Gaussian cross-correlated random fields. The methodology proposed by Vořechovsky (2008) is used to generate the two random fields. The adaptive algorithm suggested by Blatman and Sudret (2010) to build up a SPCE is used to obtain a meta-model (i.e. an approximate analytical expression) of the ultimate bearing capacity. Finally, this meta-model is employed to perform the probabilistic analysis using Monte Carlo simulation technique. The paper is organized as follows: The first two sections aim at presenting the method used to generate the two random fields and the SPCE methodology employed to determine the analytical expression of the system response. They are followed by a presentation and a discussion of the probabilistic numerical results.

METHOD OF GENERATION OF ANISOTROPIC CROSS-CORRELATED NON-GAUSSIAN RANDOM FIELDS

Let us consider two anisotropic non-Gaussian cross-correlated random fields $Z_i^{NG}(x, y)\,(i = c, \varphi)$ described by: (i) constant means and standard deviations (μ_i, σ_i; $i = c, \varphi$), (ii) non-Gaussian marginal cumulative distribution functions G_i ($i = c, \varphi$), (iii) a target cross-correlation matrix C^{NG} and (iv) a common square exponential autocorrelation function ρ_Z^{NG} [(x, y), (x', y')] which gives the values of the correlation function between two arbitrary points (x, y) and (x', y'). This autocorrelation function is given as follows:

$$\rho_z^{NG}[(x, y), (x', y')] = \exp\left(-\left(\frac{x - x'}{a_x} \right)^2 - \left(\frac{y - y'}{a_y} \right)^2 \right) \quad (1)$$

where a_x and a_y are the autocorrelation distances along x and y respectively. The Expansion Optimal Linear Estimation method (EOLE) and its extension to cover the case of correlated non-Gaussian random fields are used herein to generate the two random fields of c and φ. Notice that EOLE was first proposed by Li and Der kiureghian (1993) for the case of uncorrelated Gaussian fields, and then extended by Vořechovsky (2008) to cover the case of correlated non-Gaussian fields. In this method, one should first define a stochastic grid composed of q grid points (or nodes) $\{(x_1, y_1), ..., (x_q, y_q)\}$ for which the values of the field are assembled in a vector $\chi = \{Z(x_1, y_1), ..., Z(x_q, y_q)\}$. Then, one should determine the correlation matrix for which each element $\left(\Sigma_{\chi;\chi}\right)_{i,j}^{NG}$ is calculated as follows:

$$\left(\Sigma_{\chi;\chi}\right)_{i,j}^{NG} = \rho_z^{NG}\left[(x_i, y_i), (x_j, y_j)\right] \quad (2)$$

The common non-Gaussian autocorrelation matrix $\Sigma_{\chi;\chi}^{NG}$ and the target non-Gaussian cross-correlation matrix C^{NG} should be transformed into the Gaussian space using Nataf model [Nataf (1962)] since the discretization of the random fields using EOLE is done in the Gaussian space. As a result, one obtains two Gaussian autocorrelation matrices $\Sigma_{\chi;\chi}^{c}$ and $\Sigma_{\chi;\chi}^{\varphi}$, and a Gaussian cross-correlation matrix C that can be used to discretize the two random fields as follows:

$$\tilde{Z}_i(x, y) = \mu_i + \sigma_i \sum_{j=1}^{N} \frac{\kappa_{i,j}^{D}}{\sqrt{\lambda_j^i}} . \phi_j^i . \Sigma_{Z(x,y);\chi}^i \qquad i = c, \varphi \quad (3)$$

where $(\kappa_{i,j}^{D}; i = c, \varphi)$ are two cross-correlated blocks of independent standard normal random variables obtained using the Gaussian cross-correlation matrix C between the two fields [for more details, the reader may refer to Vořechovsky (2008)]. Notice finally that $(\lambda_j^i, \phi_j^i; i = c, \varphi)$ in equation (3) are the eigenvalues and eigenvectors of the two Gaussian autocorrelation matrices $\Sigma_{\chi;\chi}^{c}$ and $\Sigma_{\chi;\chi}^{\varphi}$ respectively, and $\Sigma_{Z(x,y);\chi}$ is the correlation vector between the random vector χ and the value of the field at an

arbitrary point (x, y). Once the two Gaussian random fields are obtained, they should be transformed into the non-Gaussian space by applying the following formula:

$$\tilde{Z}_i^{NG}(x, y) = G_i^{-1}\left\{\Phi\left[\tilde{Z}_i(x, y)\right]\right\} \qquad i = c, \varphi \tag{4}$$

where $\Phi(.)$ is the standard normal cumulative density function.

SPARSE POLYNOMIAL CHAOS EXPANSION (SPCE) METHODOLOGY

The polynomial chaos expansion (PCE) methodology aims at replacing a complex deterministic model (i.e. finite element/finite difference numerical model) whose input parameters are modeled by random variables by a meta-model which allows one to calculate the system response using an approximate simple analytical equation [Huang et al. (2009), Blatman and Sudret (2010)]. The coefficients of the PCE are computed herein using a regression approach.

For a deterministic numerical model with M input uncertain parameters, the uncertain parameters should first be represented by independent standard random variables $\{\xi_i\}_{i=1,\ldots,M}$ gathered in a random vector ξ. The random response Γ of our mechanical model can then be expressed by a PCE of order p fixed by the user as follows:

$$\Gamma_{PCE}(\xi) = \sum_{\beta=0}^{\infty} a_\beta \Psi_\beta(\xi) \cong \sum_{\beta=0}^{P-1} a_\beta \Psi_\beta(\xi) \tag{5}$$

Where P is the number of terms retained in the truncation scheme, a_β are the unknown PCE coefficients to be computed and Ψ_β are multivariate (or multidimensional) Hermite polynomials which are orthonormal with respect to the joint probability distribution function of the standard normal random vector ξ. These multivariate polynomials can be obtained from the product of the one-dimensional Hermite polynomials [Huang et al. (2009)] as follows:

$$\Psi_\beta = \prod_{i=1}^{M} H_{\alpha_i}(\xi) \tag{6}$$

where $H_{\alpha_i}(.)$ is the α_i-th one-dimensional Hermite polynomial and α_i are a sequence of M non-negative integers $\{\alpha_1, \ldots, \alpha_M\}$. In practice, one should truncate the PCE representation by retaining only the multivariate polynomials of degree less than or equal to the PCE order p. For this reason, a classical truncation scheme based on the determination of the first order norm is generally adopted in the literature. This first order norm is defined as follows: $\|\alpha\|_1 = \sum_{i=1}^{M} \alpha_i$. The classical truncation scheme suggests that the first order norm should be less than or equal to the order p of the PCE. Using this method of truncation, the number P of the unknown PCE coefficients is given by $P = \frac{(M+p)!}{M!\,p!}$. Thus, the number P of the PCE coefficients increases dramatically with the number M of the random variables and the order p of the PCE. To overcome such a problem, Blatman and Sudret (2010) have shown that the number of significant terms in a PCE is relatively small since the multidimensional

polynomials Ψ_β corresponding to high-order interaction (i.e. those resulting from the multiplication of the H_{α_i} with increasing α_i values) are associated with very small values for the coefficients a_β. Thus, a truncation strategy based on this observation was developed by Blatman and Sudret (2010) in which the multidimensional polynomials Ψ_β corresponding to high-order interaction were penalized. This was performed by considering the hyperbolic truncation scheme that considers the q-norm instead of the first order norm. The q-norm is given by $\|\alpha\|_q = \left(\sum_{i=1}^{M} \alpha_i^q \right)^{1/q}$ where q is a coefficient ($0<q<1$). The hyperbolic truncation scheme suggests that the q-norm should be less than or equal to the order p of the PCE. In this formula, q can be chosen arbitrarily. Blatman and Sudret (2010) have shown that sufficient accuracy is obtained for $q \geq 0.5$. Below this value, we may risk to reject some significant terms.

The proposed methodology leads to a sparse polynomial chaos expansion SPCE that contains a small number of unknown coefficients which can be calculated from a reduced number of calls of the deterministic model. This is of particular interest in the present case of random fields which involve a significant number of random variables. This strategy will be used in this paper to build up a SPCE of the system response.

The iterative procedure suggested by Blatman and Sudret (2010) for building up a SPCE can be described as follows:

1. Prescribe a target accuracy R^2_{TARGET}, a coefficient q for the hyperbolic truncation scheme, and a maximal order p that the SPCE can reach. In this paper, a target accuracy $R^2_{TARGET} = 0.999$, a coefficient q=0.7, and a maximal order p=5 were used.
2. Consider a set of K realizations (in our case K=200) of the standard normal random vector ξ, called experimental design (ED) and collect the corresponding model evaluations in the vector Γ. Consider also an empty matrix A.
3. Initialization (p=0): add to A the Ψ_0 term corresponding to p=0 and which result from the multiplication of the $H_{\alpha i}$ where all the α_i (i=0, 1, …, M) are equal to zero.
4. Enrichment of the PCE basis (p = p+1): Two sub steps are performed within this step as follows:
   - Forward step: Add to A one by one the different Ψ_β (which have not been considered before) that have a q-norm satisfying $p-1 \leq \|\alpha\|_q \leq p$ and for which a significant increase in the coefficient of determination R^2 is obtained.
   - Backward step: Discard from A the Ψ_β terms [with a q-norm strictly less than p (i.e. $\|\alpha\|_q < p$)] that lead to a negligible decrease in the coefficient of determination R^2.

One should note that the coefficient of determination R^2 is used to check the goodness of fit of the SPCE [Blatman and Sudret (2010)]. The value $R^2=1$ indicates a perfect fit of the true model response Γ, whereas $R^2=0$ indicates a nonlinear relationship between the true model Γ and the SPCE model Γ_{SPCE}.

5. Go to step 4 to perform an enrichment of the (ED) by adding some realizations of the vector ξ (in our case a block of 100 new realizations is added), if the regression problem is ill-posed. Otherwise go to step 6.
6. Stop if either the target accuracy R^2_{TARGET} is achieved or if p reached the order fixed by the user, otherwise go to step 4.

Once the unknown coefficients of the SPCE are determined, the PDF of the ultimate bearing capacity can be estimated. This can be done by simulating a large number of realizations (using Monte Carlo technique) of the standard normal variables on the meta-model.

NUMERICAL RESULTS

The aim of this section is to present the probabilistic results. It should be remembered here that the system response involves the ultimate bearing capacity of a rough rigid strip footing subjected to a symmetrical vertical load. The footing is placed on a weightless spatially varying frictional and cohesive (c, φ) soil with no surcharge loading on the ground surface. The friction angle φ is assumed to follow a beta distribution, and the cohesion c is assumed to be lognormally distributed. The mean values and coefficients of variation of the two random fields are given as follows: $\mu_c = 20kPa, Cov_c = 25\%$; $\mu_\varphi = 30^0, Cov_\varphi = 10\%$. The deterministic model is based on numerical simulations using the finite difference code FLAC^{3D}. The adopted soil domain considered in the analysis is 15m wide by 6m deep. It should be noted that the size of a given element in the mesh depends on the autocorrelation distances of the soil properties. Der Kiureghian and Ke (1988) have suggested that the length of the smallest element in a given direction (horizontal or vertical) should not exceed 0.5 times the autocorrelation distance in that direction. For the boundary conditions, the horizontal movement on the vertical boundaries of the grid is restrained, while the base of the grid is not allowed to move in both the horizontal and the vertical directions. The rough strip footing of 2m width and 0.5m height is assumed to be weightless and it is supposed to follow an elastic linear material. As shown in Fig. 1, the spatial variability of the soil properties can produce (for a given realization) a non-symmetrical mechanism with a footing rotation although the footing is subjected to a symmetrical vertical load.

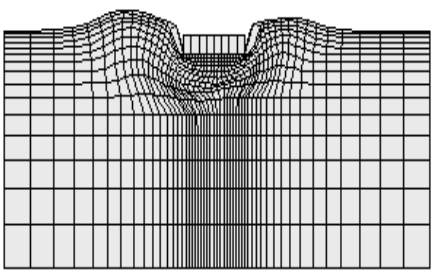

Figure 1. Deformed mesh

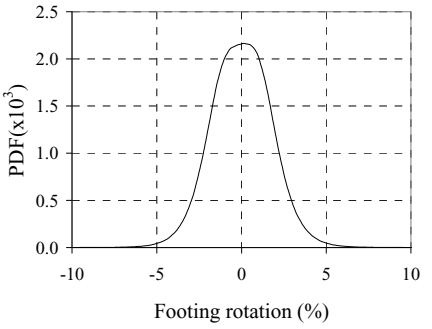

Figure 2. PDF of the footing rotation

Figure 2 presents the PDF of the footing rotation for a reference case considered in this paper for which a_x=10m, a_y=1m, and r(c, φ)=-0.5 where r(c, φ) is

the cross-correlation coefficient between the two random fields. This figure shows that the footing rotation of a single realization is not null, but the mean value of all rotations for the whole realizations is null. The standard deviation is found to be equal to $1.6e^{-4}$. In the following sections, one examines the effect of the different probabilistic governing parameters of the two random fields on the PDF of the ultimate bearing capacity of the foundation.

Effect of the autocorrelation distances a_x and a_y

Figure 3 presents the PDF of the ultimate bearing capacity for different values of a_y (a_y=0.5, 0.8, 1, 2, 5, 8m) when a_x=10m and r(c, φ)=-0.5.This figure shows that the PDF is less spread out when the vertical autocorrelation distance a_y decreases. The variability of the ultimate bearing capacity decreases with the increase in the soil heterogeneity since the zone involved by the possible failure surface will have average values of the shear strength parameters close to the mean values of the two fields because of the large number of high and small values of the shear strength parameters. This leads to close values of the ultimate bearing capacity and thus to a smaller variability in the ultimate bearing capacity. Fig. 4 shows that the probabilistic mean value of the ultimate bearing capacity presents a minimum.

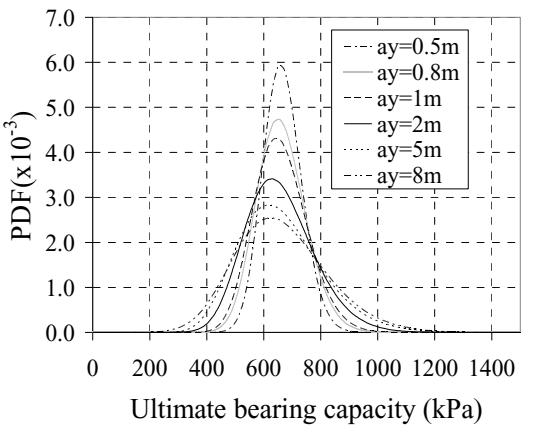

Figure 3. Influence of a_y on the PDF of the bearing capacity in the case where r(c, φ)=-0.5 and a_x=10m

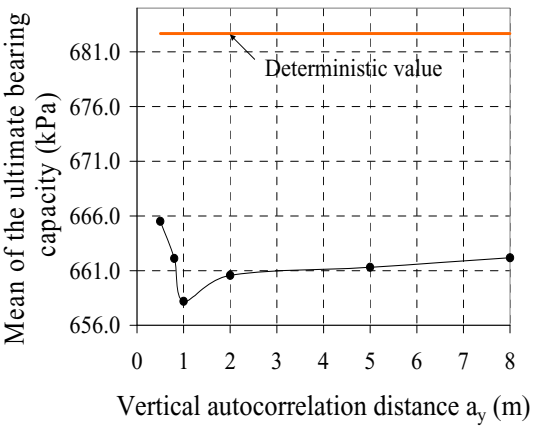

Figure 4. Influence of a_y on the probabilistic mean in the case where r(c, φ)=-0.5 and a_x=10m

This minimum was obtained when a_y=1m, i.e. when the ratio between the horizontal and the vertical autocorrelation distances is equal to 10 for B=2m. When a_y decreases from 8m to 1m, one can notice that the mean ultimate bearing capacity decreases. This can be explained by the fact that increasing the soil heterogeneity introduces weakness zones, thus leading to smaller bearing capacity. The increase in the ultimate bearing capacity for values of a_y smaller than 1m may be explained by the fact that as the autocorrelation distance decreases, the weakest path becomes increasingly tortuous and its length is also longer. As a result, the failure mechanisms will start to look for shorter path cutting through higher values of the shear strength parameters.
Figure 5 presents the PDF of the ultimate bearing capacity for different values of a_x (a_x=2, 4, 10, 20, 30, 50m) when a_y=1m and r(c, φ)=-0.5. The same observations made

before remain valid in the present case. Notice that beyond a value of a_x=20m, the horizontal autocorrelation distance have a small effect on the variability of the ultimate bearing capacity. The minimum probabilistic mean value of the ultimate bearing capacity was obtained at the same ratio a_x/a_y found before [see Fig. 6].

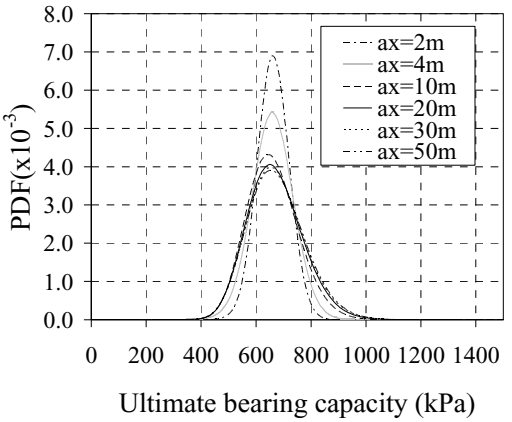

Figure 5. Influence of a_x on the PDF of the bearing capacity in the case where r(c, φ)=-0.5 and a_y=1m

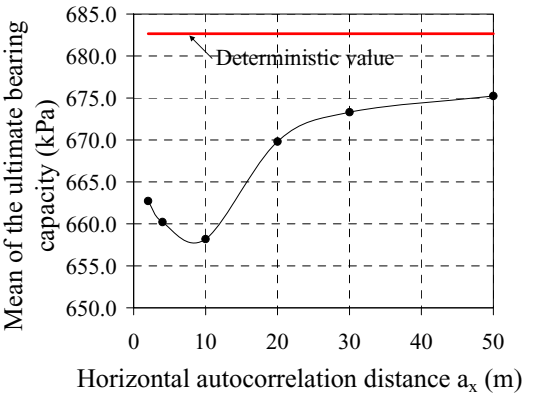

Figure 6. Influence of a_x on the probabilistic mean in the case where r(c, φ)=-0.5 and a_y=1m

Effect of the cross-correlation coefficient and the coefficients of variation of the random fields

Figure 7 presents the PDF of the ultimate bearing capacity for negatively cross-correlated r(c, φ)=-0.5 and uncorrelated r(c, φ)=0 random fields when a_x=10m and a_y=1m. This figure shows that the PDF is less spread out in the case of a negative correlation between the two random fields.

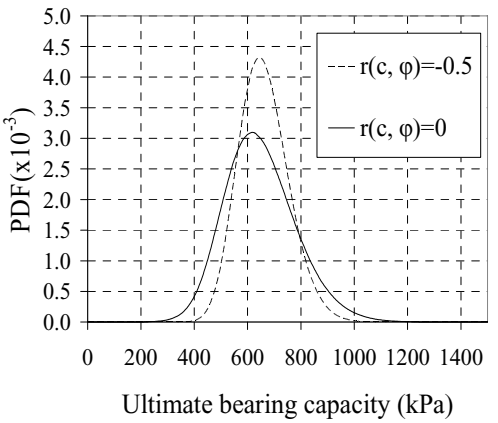

Figure 7. Influence of r(c, φ) on the PDF of the bearing capacity in the case where a_x=10m and a_y=1m

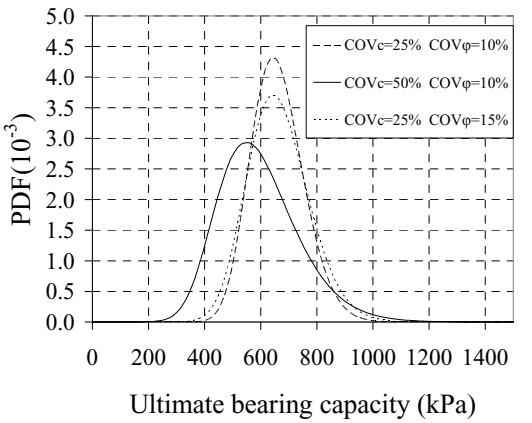

Figure 8. Influence of COV of c and φ on the PDF of the bearing capacity in the case where a_x=10m and a_y=1m

The negative correlation decreases the variability of the response because the increase of one parameter value implies a decrease in the value of the other parameter. Thus, the total shear strength slightly varies. This leads to a reduced variation in the

ultimate bearing capacity. It should be mentioned that the probabilistic mean value of the ultimate bearing capacity slightly increases when a negative correlation between the two random fields exists.

Figure 8 presents the PDF of the ultimate bearing capacity for three configurations of the coefficients of variation. Notice that for the three cases, the cross-correlation coefficient and the autocorrelation distances are those of the reference case where r(c, φ)=-0.5, a_x=10m, and a_y=1m. Fig.8 shows that the PDF becomes more spread out when the coefficients of variation increase. The coefficient of variation of the cohesion parameter was found to have a more significant influence than that of φ on the variability of the system response.

CONCLUSIONS

The effect of the spatial variability of anisotropic cross-correlated non-Gaussian shear strength parameters on the ultimate bearing capacity of a strip footing was studied. The deterministic model was based on numerical simulations using the finite difference code FLAC^{3D}. An efficient uncertainty propagation methodology was employed in this paper. This methodology makes use of a non-intrusive approach to build up a sparse polynomial chaos expansion (SPCE) for the system response. This methodology allows one to compute the system response by an analytical expression and then determine the PDF of the system response by simulating a large number of realizations using the Monte Carlo technique. The main conclusions can be summarized as follows: (i) the spatial variability of soil properties produces a non-symmetrical mechanism with a footing rotation although the footing is subjected to a symmetrical vertical load, but the mean value of all rotations for the whole realizations is null; (ii) the probabilistic mean of the ultimate bearing capacity presents a minimum for a given ratio of the horizontal and vertical autocorrelation distances; (iii) the negative correlation between the soil shear strength parameters decreases the response variability; (iv) the variability of the cohesion parameter has a more significant influence than that of the friction angle on the statistical moments of ultimate bearing capacity.

REFERENCES

Blatman, G., Sudret, B. (2010). "An adaptive algorithm to build up sparse polynomial chaos expansions for stochastic finite element analysis." *Prob Eng Mech*, 25, 183-197.

Huang, S.P., Liang, B., Phoon, K.K. (2009). "Geotechnical probabilistic analysis by collocation-based stochastic response surface method." *Georisk*, 3(2), 75-86.

Li, C. C., Der Kiureghian, A. (1993). "Optimal discretization of random fields." *J Eng Mech*, 119, 1136-54.

Nataf, A. (1962). "Détermination des distributions de probabilités dont les marges sont données." *CR Acad Sci*, 225, 42-3.

Vořechovsky, M. (2008). "Simulation of simply cross correlated random fields by series expansion methods." *Structural Safety*, 30, 337-363.

Der Kiureghian, A. Ke, JB. (1988). "The stochastic finite element method in structural reliability." *Probabilistic Engineering Mechanics*, 3, 83-91.

Spatial Variability of Aperture in a Rough-Walled Crack in Surface Soil

J. H. Li[1], Z. F. Wang[2], and L. M. Zhang[3]

[1]Assistant Professor, Department of Civil and Environmental Engineering, Harbin Institute of Technology Shenzhen Graduate School, Shenzhen, PH (86) 2603-3506; FAX (86) 2603-3509; email: huithrough@yahoo.com.cn
[2]Research Assistant, Department of Civil and Environmental Engineering, Harbin Institute of Technology Shenzhen Graduate School, Shenzhen.
[3]Professor, Department of Civil and Environmental Engineering, the Hong Kong University of Science and Technology, Hong Kong.

ABSTRACT

The presence of cracks can increases the potential failure of clay liners and soil slopes because the cracks can provide preferential flow paths and increase the hydraulic conductivity. The hydraulic conductivity of cracked soil is significantly affected by the crack aperture, which is difficult to quantify because of its highly variable properties. The objective of this paper is to characterize the probability distribution and spatial variability of a rough-walled crack in surface soil. First, a digital imaging method was used to log cracks in the field. Then the edges of the crack were extracted using a live-wire algorithm and used to calculate the crack aperture. Finally, the probability distribution and statistical properties for crack aperture was studied. Results show that the crack aperture follows a normal distribution. The average aperture is 1.137 mm and the standard deviation is 0.225 mm. The autocorrelation function of crack aperture can be modeled by an exponential structure.

INTRODUCTION

Cracks are common in clay liners, slopes, and dams. The presence of cracks can provide preferential pathways for water infiltration. Such preferential flows may significantly increase the hydraulic conductivity and the pore water pressures in soils. As a result, the strength of the soils will be reduced and the failure chance of the slope and dam will increase (Baker 1981). In addition, the preferential flow in clay liners can increase the underground contaminant solute transport (Albretcht and Benson 2001).

A key parameter to analyze the preferential flow is the hydraulic conductivity of a crack, which is dependent on the aperture of the crack. The saturated hydraulic conductivity is often described by the cubic law, in which the rate of flow is proportional to the cubic power of the crack aperture. The cubic law is only valid when water flows through a smooth planar crack (Snow 1969). However, the crack surfaces are always rough and the crack apertures vary with location. Persoff and Pruess (1995) made a replica of a natural rock fracture to model water flow through a rough fracture.

The apertures of a rough-walled crack are often described statistically. The randomness of a crack in rock was widely studied using linear profilometer scans (e.g., Gentier 1986), two-dimensional imaging from replicas of the pore space made by injection of Wood's metal or epoxy resins (Gentier et al. 1989), and application of fluid drops of known volume (Hakami 1988). These methods, however, cannot be used to study soil cracks because soil cracks are prone to be disturbed.

In this paper the probability distribution and spatial variability of the apertures of a rough-walled crack were analyzed based on a field survey. First, a digital imaging method was used to log cracks in the field. Then the edges of the cracks were extracted continuously from the digital images using live-wire algorithm. The aperture of the crack at any location can be obtained from the continuous edges. Finally, the probability distribution for the crack aperture was proposed. The mean, standard deviation, and autocorrelation function of the crack aperture were analyzed. The scope of the paper is limited to the investigation of surface cracks. The crack depth is not considered in this paper. The findings reported in this paper are mainly based on the observations made in the field tests.

THE SURVEY SITE

The survey site is located at the foot of Huangshan Slope, which is beside Nanxu Avenue in Zhenjiang, China. The average annual rainfall at the survey site is 1088 mm. The average annual duration of sunshine is 2001 h. The survey site was excavated and backfilled in 2002. The slope of the survey site, 1:3–1:5, is relatively gentle.

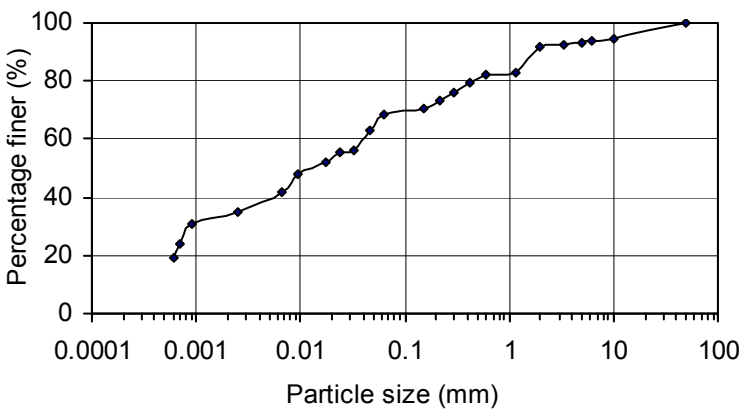

Figure 1. Particle size distribution of the silty clay.

The particle size distribution of the shallow soil was measured based on BS1377 and is shown in Fig. 1. The predominant particles are silt (34%) and clay (35%), with some sand (23%) and gravel (8%). Typical geotechnical properties of the soil, including dry unit weight, saturated water content, liquid limit, plastic limit, shrinkage limit, and expansive index are given in Table 1. The minerals of the soil are mainly illite and montmorillonite. The soil is classified as a silty clay with a medium expansivity in accordance with the criteria in ASTM standard D4829-03. An expansive soil exhibits significant swelling and shrinking upon wetting and drying. Consequently, densely populated cracks develop at shallow depths.

Table 1. Properties of the Silty Clay at the Survey Site.

Soil property	Values	Remark
Dry unit weight (kN/m^3)	16.7	
Saturated water content (%)	30.0	
Liquid limit (%)	40.4	
Plastic limit (%)	15.6	
Shrinkage index	13.0	
Expansive index	56	ASTM standard D 4829-03

MEASUREMENT OF CRACK APERTURES

A digital imaging method was used to log the cracks on the soil surface. A snapshot was taken with minimized distortion by fixing the camera on a tripod and using a scale placed on the plot as a reference. The camera had pixels of 2560 by 1920. The resolution of the snapshot was the ratio between the picture size and the effective pixels, which was about 0.068 mm. Figure 2 shows a picture of the cracks on the soil surface. This picture was taken when the water content of the soil was 13%. The development of cracks was very slow and the crack aperture was almost unchanged when the water content was below 13%.

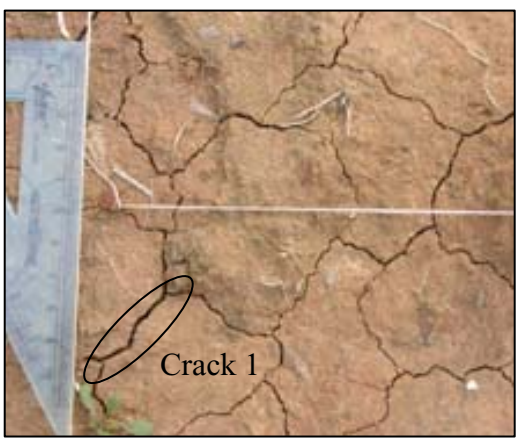

Figure 2. Image of surface cracks.

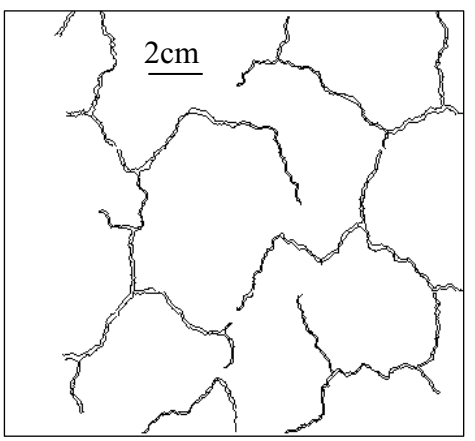

Figure 3. Continuous crack edges.

Li and Zhang (2010) measured the crack apertures manually from a digital image. They measured three aperture values along a crack but did not obtain the spatial variability of cracks. In this paper the edges of a crack was first extracted from the digital image continuously. The crack aperture at any location can be obtained from the crack edges.

A live-wire algorithm can be used to extract crack edges (Chodorowski et al. 2005). In this method, a gradient magnitude and a gradient direction of the color vector are calculated for the color image field. The weighted sum of the gradient

magnitude, gradient direction, Laplacian zero crossing-edge detection, and Canny edge detection gives a cost function. The path that has a minimal value of the cost function between any two points is the optimal boundary. The Laplacian zero crossing-edge detection and Canny edge detection can be implemented using the edge detection functions from MATLAB's Image Processing Toolbox. The live-wire algorithm is a semi-automatic method. A point on a boundary of a crack is first assigned to specify a start point. Then another point on the boundary is chosen and the edge between the two points is calculated. The edge of a crack can be accurately extracted by assign several points on the boundary. The live-wire method has the advantages of good accuracy, continuity and repeatability, and allowing user's participation. The edges of a crack in Fig. 2 were extracted using the live-wire method and shown in Fig. 3.

The crack aperture can be obtained using the extracted continuous edges. The crack aperture at a certain point is defined as the minimal distance between the two edges of a crack at that point. A set of points was chosen to calculate the apertures of the crack. First, a start point was assigned. Then a circle was drawn through the start point. The next point was the intersection between the circle and the edge. A set of points was chosen following this procedure. The crack aperture can be calculated for this set of points. The calculated crack aperture for crack 1 in Fig. 2 is shown in Fig. 4.

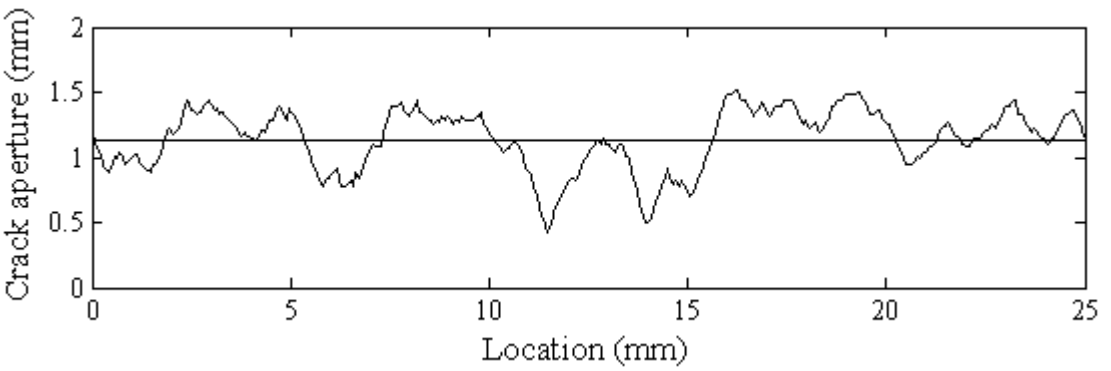

Figure 4. Aperture values of a crack.

STATISTICAL ANALYSIS OF CRACK APERTURE

Statistical distribution of crack aperture. The obtained crack aperture values can be used to determine the probability distribution of the crack aperture for a rough-walled crack. If the number of crack aperture values along a crack is too small, the assumed probability distribution for the crack parameters may not be valid. A minimum number of crack aperture values is required to ensure a reasonable level of accuracy for the probability distribution. If a maximum error of m times the standard deviation, $m\sigma$, is allowed on the mean value of the parameters with a probability of at least $(1-\alpha)$, the minimal number of crack aperture values required to represent the assigned probability distribution is (Desu and Raghavarao 1990):

$$n = \left(\frac{z_{\alpha/2}}{m} \right)^2 + 1 \tag{1}$$

where $z_{\alpha/2}$ is the value of the standard normal variate at a cumulative probability level (1-α/2); σ is the standard deviation of the mean value of crack aperture; and m is a factor to define the maximum allowable error in the mean value.

If a maximum error of 0.1σ is allowed on the mean value of aperture with a probability of at least 95%, the required minimal number of crack aperture values is 386. In this study, there are 408 aperture values along the crack. The number of crack aperture values is sufficient to represent the assigned probability distribution.

Figure 5 shows the histogram for the aperture values along crack 1 (as shown in Fig. 2). The average aperture is 1.137 mm and the standard deviation is 0.225 mm. Many researchers (Gentier 1986; Hakami 1988) found that fracture apertures in rocks followed a skewed distribution well approximated by a lognormal distribution. In this paper, a lognormal distribution with parameters λ = 0.0525 and ζ = 0.191 and a normal distribution with μ = 1.0758 and σ = 0.206 are used to model the probability distribution of the crack aperture. The assumed distributions are also shown in Fig. 5.

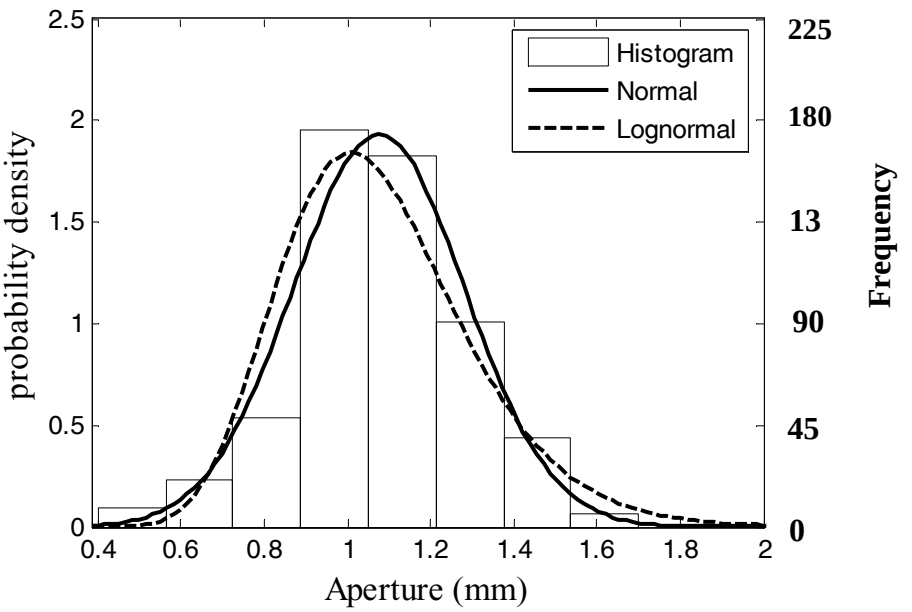

Figure 5. Histograms and distribution for the crack aperture.

A chi-square test is used to test the log-normal distribution. The chi-square test is a widely used goodness-of-fit test (Ang and Tang 2007). The test compares the observed frequencies n_1, n_2,..., n_k of k values (or in k intervals) of the variate with the corresponding theoretical frequencies e_1, e_2,..., e_k calculated from the assumed theoretical distribution model. If the assumed distribution yields

$$\sum_{i=1}^{k} \frac{(n_i - e_i)^2}{e_i} < c_{1-a,f} \tag{2}$$

in which $c_{1-\alpha,f}$ is the critical value of the chi-square distribution at a cumulative

probability of (1-α), the assumed theoretical distribution is an acceptable model at significance level α. For the crack apertures in this paper, the critical value is 26.1 at a significance level of 0.001. The observed difference is 19.4 for the assumed lognormal distribution and 16.2 for the assumed normal distribution. Both distributions pass the chi-square test at a significance level of 0.001. The observed difference for the normal distribution is smaller than that for the lognormal distribution, which indicates that the normal distribution may be more appropriate to describe the spatial variability of crack aperture.

Spatial variability of crack aperture. Random field theory was used to analyze the spatial variability of the crack aperture. The aperture of a rough-walled crack varies with locations and can be divided into two parts (Baecher and Christian 2003):

$$z(x) = t(x) + u(x) \tag{3}$$

where x is the location; $z(x)$ is the aperture of a crack at location x; $t(x)$ is the value of the trend at x; and $u(x)$ is the residual variation. The trend can be characterized by an equation or a constant. The residual indicates the variability about the trend. The remaining spatial structure of variation in the residuals can be described by spatial correlation, usually called autocorrelation because it refers to correlations of an individual variable with itself over space. Autocorrelation is the property that describes the residuals off the trend. Mathematically, the autocorrelation function is

$$\rho(\lambda) = \frac{1}{Var[z(x)]} E[u(x_i)u(x_{i+\lambda})] \tag{4}$$

where $\rho(\lambda)$ is the correlation coefficient; λ is the separation distance between the two residual variables ; $Var[z(x)]$ is the variance of the residuals; and $E[u(x_i)u(x_{i+\lambda})]$ is the covariance of the residuals for the two variables spaced at separation distance λ. Autocorrelation function is introduced to indicate the spatial correlation of the crack aperture. The autocorrelation function can be in the form of linear, exponential or power functions. The exponential correlation structure is often used in geotechnical engineering and in the following form:

$$\rho(\lambda) = e^{-\lambda / a} \tag{5}$$

In this paper the trend of aperture is almost horizontal as shown in Fig. 4. Therefore, the trend can be assumed to be a constant and equal to the mean value of aperture. The residual variation of the crack aperture is shown in Fig. 6. The correlation coefficient is calculated for different separation distances and shown in Fig. 7.

An exponential function can be used to model the autocorrelation of the crack aperture as shown in Fig. 7. When the separation distance is 0 mm the correlation coefficient is 1.0. This is reasonable because the residuals of the two variables spaced at separation distance 0 mm vary exactly the same. The correlation coefficient is high when the separation distance is small. This means that the crack apertures at close separation exhibit a high degree of correlation. For example, those separated by 0.136 mm have a correlation coefficient of 0.969. As the separation distance increases the correlation coefficient goes down. When the separation distance is large enough the correlation coefficient approaches zero. This means the crack apertures for two points far away with each other are unrelated. The correlation coefficient is

oscillating when the separation distance becomes large in Fig. 7. The reason may be that the sample size is too small to calculate a representative correlation coefficient. The minimum sample size to calculate the correlation coefficient is about 350 according to Figure 7. The minimum number required to describe the spatial correlation is smaller than the minimum sample size required describing the probability distribution, which is 386 in this paper.

The scale of fluctuation can be obtained according to the variance reduction method (Baecher and Christian 2003). The scale of fluctuation is 2.525 mm when the autocorrelation function follows the exponential structure as shown in Figure 7.

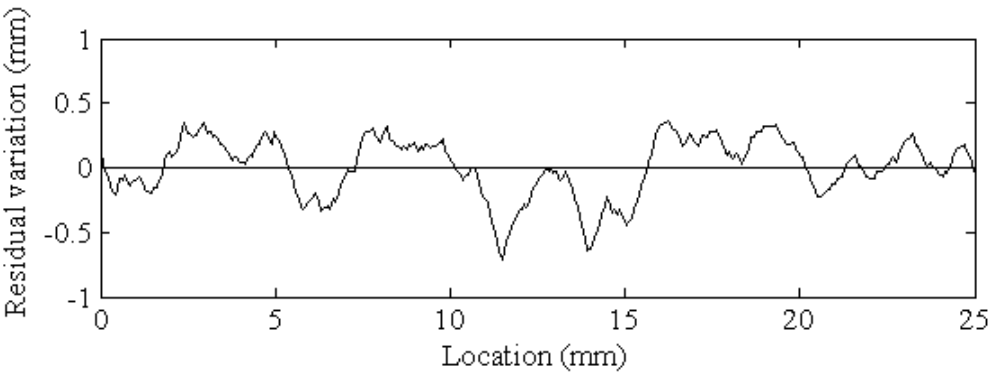

Figure 6. Variation of the residuals of crack aperture.

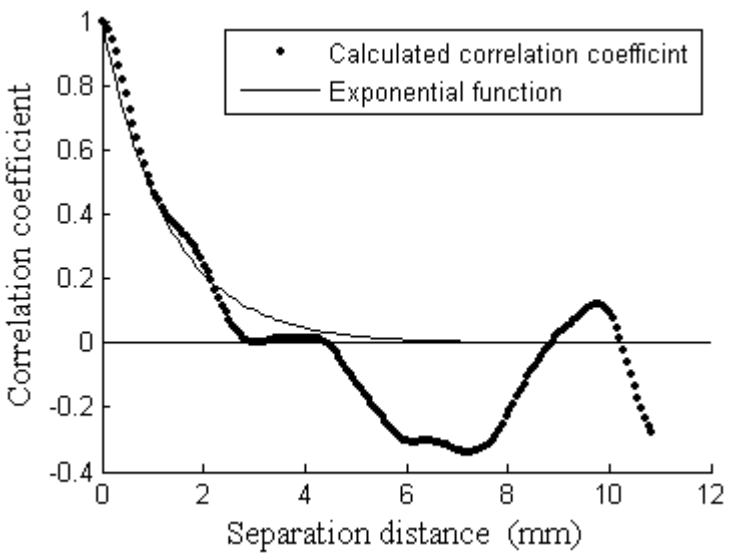

Figure 7. Autocorrelation function of crack aperture.

CONCLUSIONS AND DISCUSSION

The probability distribution and spatial variability of a rough-walled crack in surface soil were studied in this paper. The aperture of a rough crack followed a normal distribution. The average crack aperture is 1.137 mm and the standard deviation is 0.225 mm. The trend of crack aperture can be modeled by a constant which is equal to the mean value. The autocorrelation function of crack aperture can

be modeled by an exponential structure and the scale of fluctuation is 2.525 mm.

The crack aperture may increase with increasing in water content and clay content in the soil. This paper considered the cracks when the water content below the shrinkage limit. The methods used to describe the statistical properties of the crack in this paper can be applied to the similar problems although the results may vary from case to case.

ACKNOWLEDGEMENTS

This research was supported by the Natural Science Foundation of China (Project No. 51009043) and Natural Scientific Research Innovation Foundation in Harbin Institute of Technology (HIT.NSRIF.2009141).

REFERENCES

Albretcht, B. A., and Benson, C. H. (2001). "Effect of desiccation on compacted natural clays." *Journal of Geotechnical and Geoenvironmental Enginneering*, 127(1), 67-75.

Ang, A. H. S., and Tang, W. H. (2007). *Probability concepts in engineering: emphasis on applications in civil and environmental engineering.* New York: John Wiley& Sons.

Baker, R. (1981). "Tensile strength, tension cracks, and stability of slopes." *Soils and Foundations*, 21(2), 1-17.

Chodorowski, A., Mattsson, U. Langille, M., and Hamarneh, G. (2005). "Color Lesion Boundary Detection Using Live Wire." *Medical Imaging 2005: Proc. of SPIE*, Bellingham, Vol. 5747: 1589~1596.

Desu, M. M., and Raghavarao, D. (1990). *Sample size methodology*. San Diego: Academic Press, Inc.

Gentier, S. (1986). *Morphologie et comportement hydromecanique d'une fracture naturelle dans un granite sous contrainte normale*. Ph.D. thesis, Univ. d'Orleans, Orleans, France.

Gentier, S., Billaux, D., and van Vliet, L. (1989) "Laboratory testing of the voids of a fracture." *Int. J. Rock Mech. Rock. Eng.*, 22, 149-157.

Baecher, G. B., and Christian, J. T. (2003). *Reliability and Statistics in Geotechnical Engineering* .John Wiley & Sons Ltd, England.

Hakami, E. (1988). *Water flow in single rock joints.* Licentiate thesis, Lulea Univ. of Technol., Lulea, Sweden.

Li, J. H., and Zhang, L. M. (2010). "Geometric parameters and REV of a crack network in soil." *Computers and Geotechnics*, 37(4), 466-475.

Persoff, P., and Pruess, K. (1995). "Two-phase flow visualization and relative permeability measurement in natural rough-walled rock fractures." *Water Resour. Res.*, 31(5), 1175-1186.

Snow, D.T. (1969). "Anisotropic permeability of fractured media." *Water Resour. Res.*, 5(6): 1273–1289.

Parameter Estimation and Uncertainty Analysis Incorporating Engineering Judgment by Bayesian Inversion

C.P. Lin[1] and Y.C. Hung[2]

[1] Department of Civil Engineering, National Chiao Tung University, 1001 Ta-Hsueh Rd, Hsinchu, Taiwan; PH +886-3-513-1574; FAX +886-3-571-6257; email: cplin@mail.nctu.edu.tw
[2] Department of Civil Engineering, National Chiao Tung University, 1001 Ta-Hsueh Rd, Hsinchu, Taiwan; PH +886-3-513-1574; FAX +886-3-571-6257; email: hij@nqu.edu.tw

ABSTRACT

In parameter estimation, geotechnical engineers are accustomed to provide their best estimates with engineering judgments. But the bounds or indication of the significance of their estimates are seldom given. It is difficult to routinely implement reliability-based design if gauging uncertainties of engineers' estimates is not mandatory or does not become a usual practice. The objective of this paper is to advocate the importance of gauging uncertainty in the course of parameter estimation. A framework for parameter estimation and uncertainty analysis incorporating engineering judgment is illustrated based on Bayesian inversion. The data uncertainty is considered by additive noise model and the degree of confidence of engineering judgment is accounted for by the prior information in the Bayesian paradigm. The information contained in the posterior distribution resulting from the Bayes theorem is interpreted by optimal estimator, uncertainty of estimation, and resolution operator. The advantages of Bayesian inversion over commonly-used least square method are illustrated by some simple examples.

INTRODUCTION

Reliability analysis is essentially related to propagation of uncertainty from design parameters through the design model. Quantitative interpretation of reliability or risk requires information on the uncertainty of design parameters. For reliability analyses, it is necessary to estimate the mean and standard deviation for key parameters (Whitman 2000). In parameter estimation, geotechnical engineers are accustomed to provide their best estimates often times with engineering judgments. But the bounds or indication of the significance of their estimates are seldom given. It is difficult to routinely implement reliability-based design if gauging uncertainties of engineers' estimates is not mandatory or does not become a usual practice.

Geotechnical testing is in general an error-prone process. The error may be in the form of a bias (systematic error) or data scatter consisting of random testing errors and innate variability (real spatial variation) (Christian et al. 1994). The spatial variability and its consequence on reliability analysis can be dealt with by random field model, such as the classical work of Vanmarcke (1977). This paper focuses only on the measurement error. Sometimes a transformation model is needed to relate the

direct measurement from a geotechnical test to an appropriate design property (Phoon and Kulhawy 1999a, 1999b). The estimation of transformation parameter and its uncertainty can be seen as another "measurement" problem and dealt with by the same mathematical approach.

Simple measurement systems involve direct measurement of interested parameters. But more often, the interested quantities have to be inferred from the measurable quantities and the model describing the relationship between the interested quantities and measurable quantities, especially in non-destructive testing, back-calculation, and transformation model. These problems are generally treated as inverse problems. Symbolically, the data and model parameters are related as

$$\boldsymbol{d}_{obs} = g(\boldsymbol{m}) \qquad [1]$$

in which data is denoted by vector $\boldsymbol{d}_{obs}$, model parameters are denoted by vector $\boldsymbol{m}$, and $g(.)$ represents the model. As defined above, the data and model parameters are in some way related and can be denoted by Equation [1]. No claims are made either that the equation $g(\boldsymbol{m}) = \boldsymbol{d}_{obs}$ contains enough information to specify the model parameters uniquely or that they are even consistent. One of the purposes of inverse theory is to answer these kinds of questions and to provide means of dealing with the problems that they imply. Linear algebraic methods are classical approaches used to study the inversion based on a forward model. Several useful concepts were developed such as concept of non-uniqueness and concepts of data and model resolutions. Menke (1989) and Santamarina and Fratta (1998) provide detailed description of these methods. These methods do not account for the data error explicitly and cannot analyze the inverse problem in a truly nonlinear manner. One other approach to study the inverse problem is to use a statistical framework. The statistical framework can be further categorized into two parts: classical statistics and Bayesian statistics. Tarantola (1987) formulated the inverse problem on a strong theoretical information theory in the Bayesian paradigm and show how different state of information can be combined to describe an answer to the inverse problem. The objective of this paper is to advocate the importance of gauging uncertainty in the course of parameter estimation. A framework for parameter estimation and uncertainty analysis incorporating engineering judgment is illustrated based on Bayesian inversion.

FRAMEWORK OF BAYESIAN INVERSION

The first step to describe the inverse problem is to construct the forward problem. The coordinates of the model space ($\boldsymbol{m}$) are basically composed of the desired unknown parameters. The data space ($\boldsymbol{d}$) and forward model ($g(.)$) usually depend on how the experiments are set up. For instance, consider the example in which one is to estimate the coefficients, c and $\tan\phi$ of Mohr Coulomb failure criteria by various experimental setups.

$$\text{(a)}\begin{bmatrix}\tau_1\\ \tau_2\end{bmatrix}=\begin{bmatrix}1 & 50\\ 1 & 100\end{bmatrix}\begin{bmatrix}c\\ \tan\phi\end{bmatrix} \quad \text{(b)}\begin{bmatrix}\tau_1\\ \tau_2\\ \tau_3\\ \tau_4\end{bmatrix}=\begin{bmatrix}1 & 50\\ 1 & 75\\ 1 & 100\\ 1 & 125\end{bmatrix}\begin{bmatrix}c\\ \tan\phi\end{bmatrix} \quad \text{(c)}\begin{bmatrix}\tau_1\\ \tau_2\\ \tau_3\\ \tau_4\end{bmatrix}=\begin{bmatrix}1 & 50\\ 1 & 50\\ 1 & 100\\ 1 & 100\end{bmatrix}\begin{bmatrix}c\\ \tan\phi\end{bmatrix} \qquad [2]$$

Apparently, there is more than one way to setup the experiment to infer the model parameters. One of the questions that the inverse analysis tries to answer is which one of these experimental setups is the best.

Equation [1] or [2] represents a perfect relationship between data and model parameters. However, all the measured data are subject to noise that leads to uncertainty. One way to deal with the uncertainty is to use the additive noise model (Tarantola 1987). In the forward model some assumptions have been made in order to make the solution possible. In addition to model error, we can also add the measurement error to Equation [1] to account for the noise in the measurement. So Equation [1] becomes

$$\boldsymbol{D}_{obs} = g(\boldsymbol{M}) + \boldsymbol{\Delta}_m + \boldsymbol{\Delta}_d = g(\boldsymbol{M}) + \boldsymbol{\Delta} \quad [3]$$

in which $\boldsymbol{\Delta}$ is the total noise (sum of model error $\boldsymbol{\Delta}_m$ and measurement error $\boldsymbol{\Delta}_d$). Note that capital letters are used to denote data and noise in Equation [3] to be consistent with the notation of probability theory, a capital letter is used to denote a random variable and lower case is used to denote the deterministic variable or values taken by random variables. Bayesian statistics takes the viewpoint that the most general way of describing a state of information over a parameter set is by defining a probability density over the corresponding parameter space. In this sense, model parameters are considered as random variables like noise $\boldsymbol{\Delta}$ and data $\boldsymbol{D}_{obs}$.

Using Bayesian interpretation, $\boldsymbol{M}$ and $\boldsymbol{D}_{obs}$ become jointly distributed random variables having joint density $p(\boldsymbol{d}_{obs},\boldsymbol{m})$. Before the experiment or the observation of $\boldsymbol{D}_{obs}$ is made, the model parameters are unknown. Regardless of the ignorance of the model parameters, we have some idea (prior information) about $\boldsymbol{M}$ (i.e. the range and distribution of $\boldsymbol{M}$). After conducting the experiments or making the observations, the ignorance (very weak prior information) can be improved and model parameters can be better estimated. Hence, when using Bayesian statistics concept to solve the inverse problem, the appropriate question to ask is: given a priori information on some model parameters ($p(\boldsymbol{m})$), and given a stochastic system (uncertain physical law, $g(\boldsymbol{M})+\boldsymbol{\Delta}$) that relates some observable parameters to the model parameters, how should the priori information be modified to improve the knowledge about the model parameters based upon some observations? Following the property of conditional probability and total probability law, Bayes theorem states that the posterior probability (probability distribution of model parameters conditioned on a certain observation) is

$$p(\boldsymbol{m} \mid \boldsymbol{d}_{obs}) = \frac{p(\boldsymbol{d}_{obs} \mid \boldsymbol{m})p(\boldsymbol{m})}{p(\boldsymbol{d}_{obs})} = \frac{p(\boldsymbol{d}_{obs} \mid \boldsymbol{m})p(\boldsymbol{m})}{\int_{\Lambda} p(\boldsymbol{d}_{obs} \mid \boldsymbol{m})p(\boldsymbol{m})d\boldsymbol{m}} \quad [4]$$

If the prior information $p(\boldsymbol{m})$ and statistical model of $\boldsymbol{\Delta}$ can be answered with reasonable assumptions, the probability distribution of the model parameters after considering the data observations can be calculated by Equation [4], which leads very naturally to the analysis of error and to tests of the significance of answers even for highly nonlinear problems.

Using the Bayesian statistical model, the solution of inverse problems and the analysis of error can be performed in a fully nonlinear way (but perhaps with a prohibitively large amount of computing time). In fact Equation [4] is the solution to

the inverse problem. The most general way of studying the information obtained on the parameter values is by a direct study of the probability density $p(\boldsymbol{m}/\boldsymbol{d}_{obs})$. But there is no way to display it in a multidimensional space if the number of model parameters is greater than two. One of the most comprehensive understandings is obtained by calculating the marginal probability distribution of a particular model parameter. But it involves intensive computation of multidimensional integration. The meaning of "solving" an inverse problem depends on the type of practical application. Often times, we are interested in obtaining the "best" estimate in some sense. The sense of optimality is defined as the minimum of a certain error cost. It has been shown, for example in Poor (1988), that by using different cost functions, the optimal estimator becomes the mean, medium and maximum of the posterior probability distribution, respectively. Among these optimal estimators the Maximum A Posterior (MAP) estimator is the most popular because efficient optimization scheme can be used.

$$\hat{\boldsymbol{m}}_{MAP} = \arg\min_{\boldsymbol{m}} p(\boldsymbol{m}/\boldsymbol{d}_{obs}) \qquad [5]$$

When the solution of the inverse problem is given as an optimal estimator, it is necessary to discuss the uncertainty. The most common and convenient way to represent the uncertainty is to calculate the covariance of the posterior distribution as

$$C_{M/D_{obs}} = \int_{\Lambda} (\boldsymbol{m}-\hat{\boldsymbol{m}})(\boldsymbol{m}-\hat{\boldsymbol{m}})^T p(\boldsymbol{m}/\boldsymbol{d}_{obs}) d\boldsymbol{m} \qquad [6]$$

GAUSSIAN PROBLEMS

Assuming Gaussian distributions for the prior and data error leads to the easiest computations. A multi-variable Gaussian distribution is defined as

$$p(\boldsymbol{x}) = \frac{1}{\sqrt{(2\pi)^N |C_x|}} \exp\left\{-\frac{1}{2}(\boldsymbol{x}-\mu_x)^T C_x^{-1}(\boldsymbol{x}-\mu_x)\right\} \qquad [7]$$

and denoted as $N(\boldsymbol{\mu}_{\boldsymbol{x}}, C_x)$, in which $\boldsymbol{\mu}_{\boldsymbol{x}}$ is the mean vector and C_x is the covariance matrix. Assuming Gaussian distribution for prior model $\boldsymbol{M}$ and noise $\boldsymbol{\Delta}$ (i.e. $\boldsymbol{M}\sim N(\boldsymbol{m}_p, C_M)$, and $\Delta\sim N(0,C_\Delta)$), the posterior probability density (Equation [4]) becomes

$$p(\boldsymbol{m}|\boldsymbol{d}_{obs}) = \frac{1}{p(\boldsymbol{d}_{obs})(2\pi)^N \sqrt{|C_\Delta||C_M|}} \cdot \exp\left\{-\frac{1}{2}\left[(\boldsymbol{d}_{obs}-g(\boldsymbol{m}))^T C_\Delta^{-1}(\boldsymbol{d}_{obs}-g(\boldsymbol{m})) + (\boldsymbol{m}-\boldsymbol{m}_p)^T C_M^{-1}(\boldsymbol{m}-\boldsymbol{m}_p)\right]\right\} \qquad [8]$$

Note that when calculating MAP estimator for Equation [8], it is not necessary to calculate $p(\boldsymbol{d}_{obs})$ since it is not a function of $\boldsymbol{m}$. In fact, maximizing Equation [8] is equivalent to minimizing the term in exponential. Equation [5] becomes

$$\hat{\boldsymbol{m}}_{MAP} = \arg\min_{\boldsymbol{m}}\left\{(\boldsymbol{d}_{obs}-g(\boldsymbol{m}))^T C_\Delta^{-1}(\boldsymbol{d}_{obs}-g(\boldsymbol{m})) + (\boldsymbol{m}-\boldsymbol{m}_p)^T C_M^{-1}(\boldsymbol{m}-\boldsymbol{m}_p)\right\} \qquad [9]$$

For linear Gaussian problems, the covariance of the posterior distribution (Equation [6]) and the resolution operator defining the relation between estimated

model parameter and true model parameter can be analytically obtained using principles of multivariate Gaussian distribution. Non-linear problems can be approximated by the linearized problem (Tarantola 1987). Let $\hat{\boldsymbol{m}}_{MAP}$ be the MAP estimator obtained by solving Equation [9]. The model can be approximated by first order Taylor's series approximation.

$$g(\boldsymbol{m}) \cong g(\hat{\boldsymbol{m}}_{MAP}) + \left[\frac{\partial g}{\partial m}\right]_{\hat{\boldsymbol{m}}_{MAP}} (\boldsymbol{m} - \boldsymbol{m}_{MAP}) = g(\hat{\boldsymbol{m}}_{\mathbf{MAP}}) + A_{MAP}(\boldsymbol{m} - \hat{\boldsymbol{m}}_{MAP}) \quad [10]$$

where $A_{MAP} = \left[\frac{\partial g}{\partial m}\right]_{\hat{m}_{MAP}}$ is the sensitivity operator evaluated at $\boldsymbol{m} = \hat{\boldsymbol{m}}_{\boldsymbol{MAP}}$. It is typically evaluated using finite difference scheme. Using Equation [10], the posterior probability density (Equation [8]) can be approximated by a Gaussian distribution

$$p(\boldsymbol{m} / \boldsymbol{d}_{\boldsymbol{obs}}) \cong const \cdot \exp\left\{-\frac{1}{2}(\boldsymbol{m} - \hat{\boldsymbol{m}}_{\boldsymbol{MAP}}) C_{M_{est}}{}^{-1} (\boldsymbol{m} - \hat{\boldsymbol{m}}_{\boldsymbol{MAP}})\right\} \quad [11]$$

in which C_{Mest} is the linearized model covariance

$$C_{M_{est}} = \left(A_{MAP}{}^{T} C_{\boldsymbol{\Delta}} A_{MAP} + C_M{}^{-1}\right)^{-1} \quad [12]$$

And the linearized resolution matrix can be written as

$$R \cong I - C_{M_{est}} C_M{}^{-1} \quad [13]$$

If the resolution operator is equal to identity, then model estimator is equal to the true model parameters plus some error due to data uncertainty and the uncertainty of the estimation becomes zero (i.e. C_{Mest} becomes zero matrix). In such case, the model is said to be perfectly resolved. Any prior information is transformed to the best estimation with zero uncertainty. The farther the resolution operator is from identity, the worse the resolution. The resolution operator acts as a filter. The true model and the prior judgment are filtered by the resolution operator to calculate the estimated model. We cannot see the real world. We can only see a filtered version. However, the resolution operator tells us the structure of the problem. As the resolution operator gets farther from identity, the model becomes more poorly resolved and the engineering judgment plays more roles in the estimation of model parameters.

SIMPLE EXAMPLES

Simple examples are given to help visualizing the probability space and understanding the Bayesian statistics. A linear Gaussian example is first given to show the effects of prior information on the solutions of the inverse problems and the interpretation of the variance and resolution operator. Consider the simplest 1-D linear problem, $D=AM+\Delta$, where $M \sim N(m_p, \sigma_M^2)$ and $\Delta \sim N(0, \sigma_\Delta^2)$. The joint distribution $p(M,D)$ is shown in Figure 1a. Visually, the posterior distribution is the curve obtained by normalizing the intersection of the vertical plane $d=d_{obs}$ and the joint probability as shown in Figure 1b. Assuming different values of A and prior information, the

estimated parameter M, the associated standard deviation, and resolution operator are listed in Table 1. Also listed in Table 1 is the conventional least square solution for comparison. The standard deviation of the estimations indicates the significance of the estimated without knowing the true solutions, while the resolution operator reflects the structure of the inverse problem. Stronger prior information (i.e. σ_M is small) reduces uncertainty of estimation, but may also result in bias in estimation when the prior model is prejudiced (i.e. m_p is away from m_{true}), as schematically illustrated in Figure 2. However, we can be aware of the cases where the estimation is sensitive to prior judgment by looking at the resolution operator. For example, for A=0.5, the resolution R=0.5 (<<1) and the Bayesian estimation will be erroneous if the prior model is very unrealistic; but for A=2.0, the resolution R=0.94 (≅1) the estimation is relatively insensitive to the unrealistic prior model. It is important to note that there is a tradeoff between the resolution and variance. When making stronger prior judgment, the variance decreases but the resolution also decreases. Therefore, never making strong judgment if you don't know much about the model parameters.

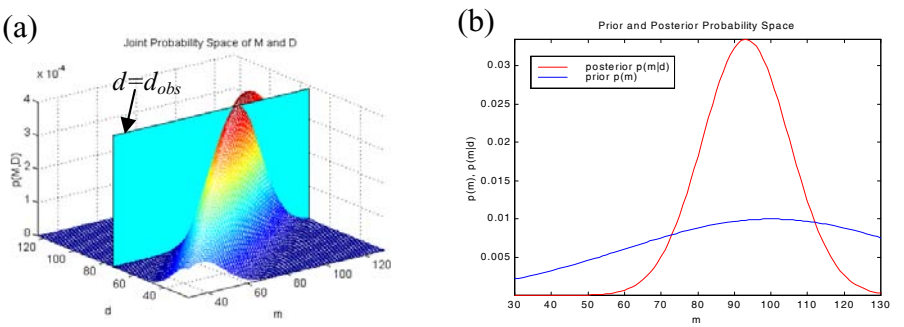

Figure 1. (a) The joint distribution; (b) the prior and posterior distribution of a 1-D linear Gaussian problem.

In the following example, the nature of nonlinearity and what it implies in the inverse analysis are discussed. Consider a simple 1-D non-linear problem, $g(M)=\sqrt{M}$, $M\sim N(60, 40^2)$, and $\Delta\sim N(0, 5^2)$. The conditional probability of D_{obs} conditioned on M is $p(d_{obs}/m)\sim N(g(m),\sigma_\Delta^2)$ and the joint probability $p(m,d_{obs})$ can be calculated *as* $p(m,d_{obs}) = p(d_{obs}/m)\ p(m)$. The joint probability space is plotted in Figure 3a and the posterior distribution and its linearized approximation are shown in Figure 3b. The posterior distribution suggests that this is a well-posed nonlinear problem since the posterior distribution is uni-modal and close to its linearized approximation. The optimization scheme will converge to the MAP estimate and the approximated uncertainty analysis can be done using the results of the Linear Guassian problem. Similarly the joint probability space, posterior probability and its linearized Guassian approximation are shown in Figure 3c and 3d for $g(M)=0.0009M^3-0.1336M^2+5.4398M-9.1459$. This is an ill-posed nonlinear problem in which the posterior is multi-modal and the linearized approximation of uncertainty analysis is less satisfactory. For highly ill-posed nonlinear problems, care has to be taken to obtain global optimum for the MAP estimator and the rigorous uncertainty analysis needs to be done in a truly nonlinear way using numerical integration. Introducing the prior information in the Bayesian framework reduces the non-uniqueness caused by the nonlinearity or under-determinate system. Therefore, the optimal estimator and the uncertain analysis

still provide meaningful data interpretation for highly ill-posed nonlinear or under-determinate problems using the Bayesian framework.

Table 1. Case study of the 1-D linear Gaussian problem. (Assuming m_{true}=80; σ_d=10)

A	d_{obs}	Case 1: Ignorance m_p=100; σ_M=40			Case 2: Prejudice m_p=100; σ_M=20			Case 3: Ignorant prejudice m_p=100; σ_M=20			$\hat{m}_{LS}$
		$\hat{m}_{MAP}$	$\sigma_{\hat{M}}$	R	$\hat{m}_{MAP}$	$\sigma_{\hat{M}}$	R	$\hat{m}_{MAP}$	$\sigma_{\hat{M}}$	R	
0.5	d_{true}-σ_d	68	17.89	0.8	80	14.14	0.5	90	14.14	0.5	60
	d_{true}+σ_d	100	17.89	0.8	100	14.14	0.5	110	14.14	0.5	100
1.0	d_{true}-σ_d	71.76	9.70	0.94	76	8.94	0.8	80	8.94	0.8	70
	d_{true}+σ_d	90.59	9.70	0.94	92	8.94	0.8	96	8.94	0.8	90
2.0	d_{true}-σ_d	75.38	4.96	0.98	76.5	4.85	0.94	77.65	4.85	0.94	75
	d_{true}+σ_d	85.23	4.96	0.98	85.9	4.85	0.94	87.06	4.85	0.94	85

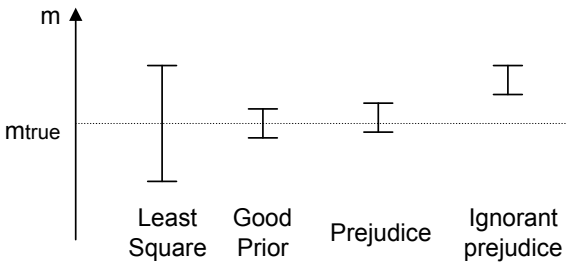

Figure 2. Effect of prior information on the estimation of model parameter.

When discussing the construction of model and data space, three examples are given for the problem of determining the soil shear strength parameters in Equation [2]. Intuitively case (b) should be the best setup. A more scientific method for selection of the optimal setup can be based on the concept of model resolution operator. The best experimental setup is the one with a resolution matrix closest to identity matrix. Assume prior value and standard deviation are respectively 50 and 25 for cohesion and tan(30) and tan(5) for friction angle. And the standard deviation of shear strength measurement is 2. The resolution matrix for each case are calculated as

$$\text{(a) } R=\begin{bmatrix}0.9739 & 13.2809\\ 0.0003 & 0.8224\end{bmatrix} \quad \text{(b) } R=\begin{bmatrix}0.9843 & 7.0304\\ 0.0002 & 0.9195\end{bmatrix} \quad \text{(c) } R=\begin{bmatrix}0.9856 & 7.3924\\ 0.0002 & 0.9013\end{bmatrix}. \qquad [14]$$

This result suggests that indeed case (b) is a better setup than (c) and (c) is a better setup than (a). Bayesian framework allows us to take into account of what we know about the data error and prior information to make the best design to our best knowledge.

CONCLUSION

The Bayesian formulation provides a nice framework for inverse problems in both parameter estimation and uncertainty analysis. The engineering judgment can be naturally blended in for by the prior information in the Bayesian paradigm. The

advantages of Bayesian inversion over commonly-used least square method are illustrated by some simple examples with emphasis on the effect and role of engineering judgment. It is shown that Bayesian framework also provides a straight forward means for design of experiment.

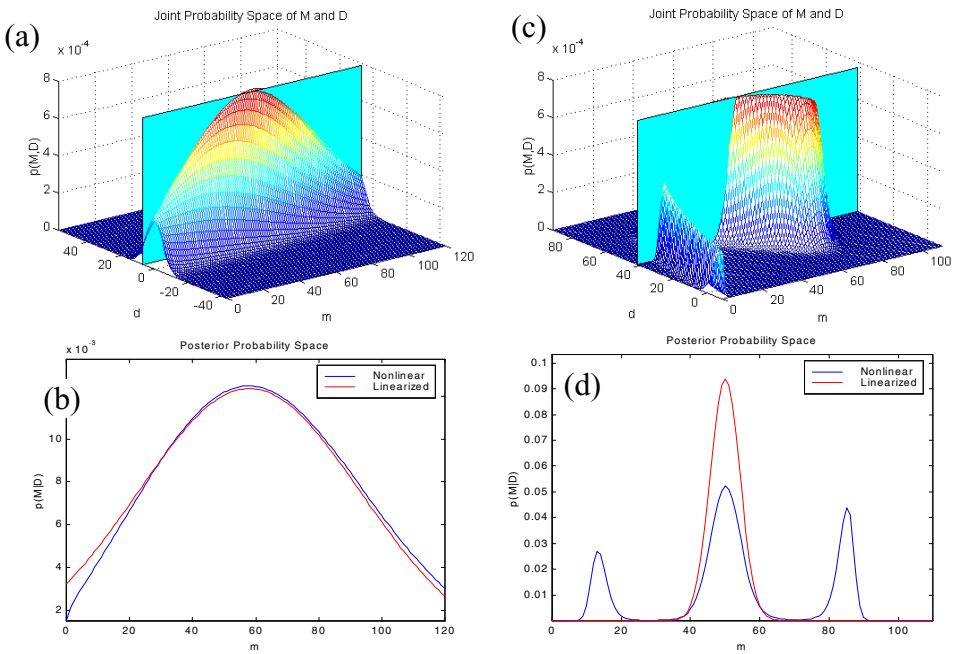

Figure 3. Joint probability space of an well-posed 1-D non-linear problem(a,b) and an ill-posed 1-D non-linear problems(c,d).

REFERENCES

Christian, J. T., Ladd, C. C., and Baecher, G. B. (1994), "Reliability applied to slope stability analysis," J. Geotech. Engrg., ASCE, 120(12), 2180-2207.

Menke,W. (1989), Geophysical data Analysis: Discrete Inverse Theory, Academic Press.

Phoon, K. K. and Kulhawy, F. H. (1999a), "Characterization of geotechnical variability," Can. Geotech. J., 36, 612-624.

Phoon, K. K. and Kulhawy, F. H. (1999b), "Evaluation of geotechnical variability," Can. Geotech. J., 36, 625-639.

Poor, H. V., 1988, An Introduction to Signal Detection and Estimation, Springer-Verlag, New York.

Santamarina, C. and Fratta, D. (1998), Introduction to Discrete Signals and Inverse Problems in Civil Engineering, ASCE Press, 327 pp.

Tarantola, A., 1987,Inverse Problem Theory, Elsevier, Amsterdam.

Vanmarcke, E. H. (1977), "Probabilistic modeling of soil profile," J. of Geotech. Engrg., 103(11), 1227-1246.

Whitman, R. V. (2000), "Organizing and evaluating uncertainty in geotechnical engineering," J. of Geotech. and Geoenvironmental Engrg, 126 (7), 583-593.

Site Response Effects on Partially Ergodic PSHA

G. A. Montalva[1], A.M. ASCE and A. Rodriguez-Marek[2], M. ASCE

[1]Assistant Professor, Civil Engineering Department, University of Concepción -Chile, Edmundo Larenas s/n Concepción Chile. Email: gmontalva@udec.cl Ph:+56-41-220-4446
[2]Associate Professor, Charles E. Via, Jr. Department of Civil & Environmental Engineering, Virginia Tech, 214 Patton Hall, Blacksburg, VA 24061. Email:adrianrm@vt.edu

ABSTRACT

Near surface materials play an important role in modifying seismic waves, hence the uncertainty in their properties is significant to the surface ground motion uncertainty. A partially non-ergodic approach that removes the uncertainty associated with site response from the ergodic ground motion prediction equation, and then accounts for the epistemic site response uncertainty within a particular site is presented. Probabilistic seismic hazard analyses (PSHA) results show that for better characterized sites the uncertainty on surface ground motion can be drastically reduced with respect to the ergodic prediction. This effect is stressed when long return periods are examined. The presented approach also produces a reduction on the ground motion prediction bias due to the site-specific modeling of site response.

INTRODUCTION

Probabilistic seismic hazard analysis (PSHA) is the preferred tool used to deal with the uncertainty involved in predicting earthquake intensities. This uncertainty is due to our limited understanding of earthquake phenomena and to the random nature of the seismic process. This paper presents a methodology to consider partially ergodic PSHA as an alternative to the typical (i.e. fully ergodic) PSHA analyses. This relaxation of the ergodic assumption allows for the consideration of local site effects without double counting its uncertainty.

Ground Motion Prediction Equations and Ergodicity: A traditional PSHA uses ground motion prediction equations (GMPE) that are developed with surface data. Because there is not enough data to constrain statistical models to specific regions, faults, or sites, parameterizations are used to account for path effects (typically divided into distance and a site terms), and source effects. Ground motion uncertainty is computed assuming that the ground motion uncertainty at a site is the same as the uncertainty computed from a large data set that includes ground motions from different sources and sites, this is referred to as the *ergodic assumption* (Anderson and Brune, 1999).

While a fully non-ergodic approach would minimize the uncertainty in the prediction of ground motion intensities, the limitation for such a model is the lack of data. In the absence of non-ergodic models, ergodic models such as the Next Generation Attenuation Relationships (Abrahamson et al. 2008) are generally used. These GMPE are developed with a large database that includes site-to-site variability. For the case where site-specific seismic hazard analyses are computed using site response analyses and including site response uncertainty (that comes from uncertainty in soil properties and behavior) a "double counting" of uncertainty results, at least for part of the uncertainty due to site response.

EVIDENCE AGAINST AN ERGODIC ASSUMPTION

To assess the effects of a non-ergodic, or partially ergodic, GMPE and therefore PSHA with reduced uncertainty, sites that have recorded a significant number of events, ideally from the same source (i.e. fault or fault section), are required. A set of ground motions that satisfies these requirements are the ground motion records from the KiK-net (Kiban-Kyoshin, 2010) network. The main results shown on this paper are based on the study of this database. However, other publications, such as Lin et al. (2010), Chen and Tsai (2002), Atkinson (2006), and Bindi et al. (2000), have analyzed the cases for Taiwan, Southern California, and Italy. Table 1 presents the comparison of single-site residual standard deviations versus standard deviations of the residuals from a fully ergodic GMPE obtained from the KiK-net database. These standard deviations are computed for residuals of the logarithm of the pseudo-spectral accelerations. Similar results are observed in other regions (Rodriguez-Marek et al. 2010).

Table 1. Single-site versus Ergodic Standard Deviations.

Period (sec)	Single-site σ	Ergodic σ
PGA	0.6725	0.8181
0.06	0.6655	0.8248
0.1	0.6800	0.8939
0.3	0.6582	0.8537
1	0.6122	0.7558
1.36	0.6095	0.7472

As shown on Table 1, the differences in the standard deviations for the ergodic and non-ergodic cases are significant. The residuals for the non-ergodic case are the true deviations from the mean estimate, when repeatable site effects at each site are accounted for, and when used on a PSHA exercise result in a much lower hazard (Montalva, 2010). Hence site specific information helps shift some of the total uncertainty (from an ergodic model) to a deterministic value. However, these measures of the uncertainty are only available at the ground motion station sites. An important consideration is whether there are fundamental grounds to use lower than the ergodic sigma values for sites that have not recorded enough ground motions to

constrain the repeatable site effects, or that simply don't have a ground motion station. The authors believe that reducing epistemic uncertainty (i.e. sigma) is possible when more knowledge (e.g. site investigation) is incorporated into the prediction of the site-specific ground motion; if no additional information or understanding is available then the use of ergodic sigmas would be unavoidable from a theoretical point of view.

PARTIALLY NON-ERGODIC GMPE'S

The KiK-net database is particular in that it has recordings both at surface and at depth, which allow for empirical (and of course analytical) consideration of site effects. This makes possible the development of GMPE's for the surface, at depth, and a combined GMPE that uses ground motion records from surface and borehole simultaneously. These three models are explained in detail in Montalva (2010); only the main characteristics are briefly described herein. The selection of the functional form was based on its ability to be constrained by data (some models require intensive seismological modeling, along with recorded data, to constrain their model parameters). The selected functional form is the one proposed by Boore and Atkinson (2008), and the general form is given by,

$$y = \mu + \delta W_{es} + \delta B_e \quad (1)$$

where, μ is the median estimate of the logarithm of the ground motion intensity (pseudo-acceleration), δW_{es} is the within event residual, and δB_e is the between events residual. The median model is composed of a magnitude term, a distance term, and a site term. The within event residual can be partitioned into a site-to-site residual (δS2S) and a within site residual (δWS_{es}) as shown in the equations below.

$$\mu = F_m + F_d + F_{site} \quad (2)$$

$$\delta W_{es} = \delta S2S + \delta WS_{es} \quad (3)$$

Figure 1 shows the comparison of the total standard deviation for the ergodic model (i.e. the standard deviation of $\delta = \delta W_{es} + \delta B_e$) and for the non-ergodic or single-site (i.e. the standard deviation of $\delta WS_{es} + \delta B_e$). Notably, if the between event uncertainty is removed, the standard deviation for the single-site case are remarkably similar for very different regions of the world (see Lin et al., 2010; Rodriguez-Marek et al., 2010). The difference between the two sets of curves on Figure 1 is the site-to-site variability which we can consider epistemic uncertainty as it can be reduced with increased site investigation.

The relaxation of the ergodic assumption is possible by acknowledging the fact that δS2S is epistemic, then the site-to-site residual at the ground surface (superscript G) can be divided into site-to-site residual at the borehole (superscript B) and a site amplification residual.

$$\delta S2S^G = \delta S2S^B + \delta S2S^{AMP} \quad (4)$$

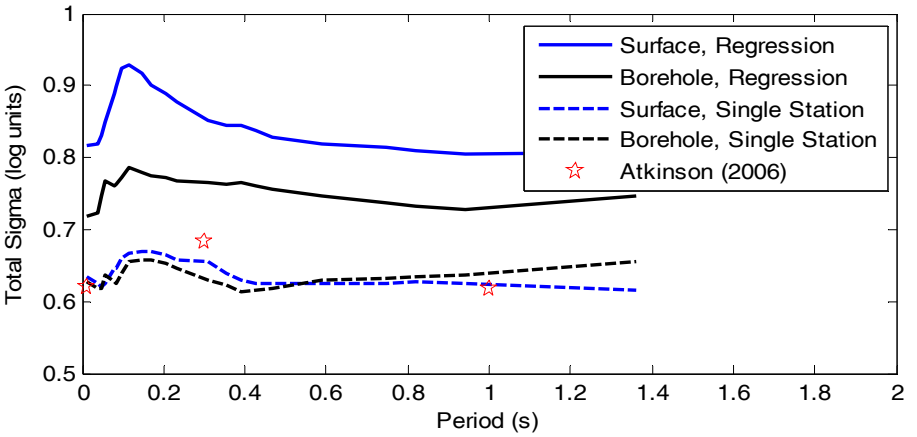

Figure 1. Comparison of total standard deviation for ergodic and non-ergodic GMPE's for surface and borehole. Results from Atkinson (2006) are shown for reference.

The partition of $\delta S2S^{G}$ allows for the use of the ergodic GMPE *at the borehole* (or at depth), which has lower variability than the surface regression, and the use of site response analyses to compute $\delta S2S^{AMP}$. The latter gives the possibility to lower variability by conducting thorough site investigation and site response analyses, and to reduce the site-to-site bias of the ergodic GMPE for the surface (i.e. μ^{G}).

EFFECTS ON HAZARD CALCULATIONS

To illustrate the effects of a PSHA conducted using the ergodic versus the partially ergodic model herein proposed, an example PSHA is studied. The seismicity affecting a fictitious sample site is defined as follows,

- Areal Source of seismicity of 100 by 100 kilometers.
- Activity rate of 0.38, for Mw between 4 and 7
- Truncated exponential Mw distribution (with parameter $\lambda = 0.8$).

The average shear-wave velocity (Vs30) of the site is set to 400 (m/s) and the Bazzurro and Cornell (2004) methodology is used to compute the nonlinear site response. Two types of scenarios were studied within the same base case, the first assuming the site is perfectly characterized, and the second one assuming uncertain Vs30 with a 10% coefficient of variation. For the case of no uncertainty on the site profile, the hazard was calculated for a range of return periods. Where the hazard is expressed as the mean annual rate of exceedance of the pseudo-acceleration (Sa) at a period of 0.1 seconds in units of "g" (gravity). This results are presented in Figure 2, were the ergodic PSHA is also shown for comparison.

To include the epistemic uncertainty on site response, uncertainties on the site's Vs30 and on the profile itself were considered. The latter one was considered when calculating the Bazzurro and Cornell parameters, the uncertainty on the site's Vs30 was included within a logic tree framework. Then different hazard curves were calculated for each Vs30 value. Note that the Bazzurro and Cornell nonlinear site

response parameters are calculated separately for each Vs30 realization. Figure 3 shows the calculated hazard curves for 5 different Vs30 values.

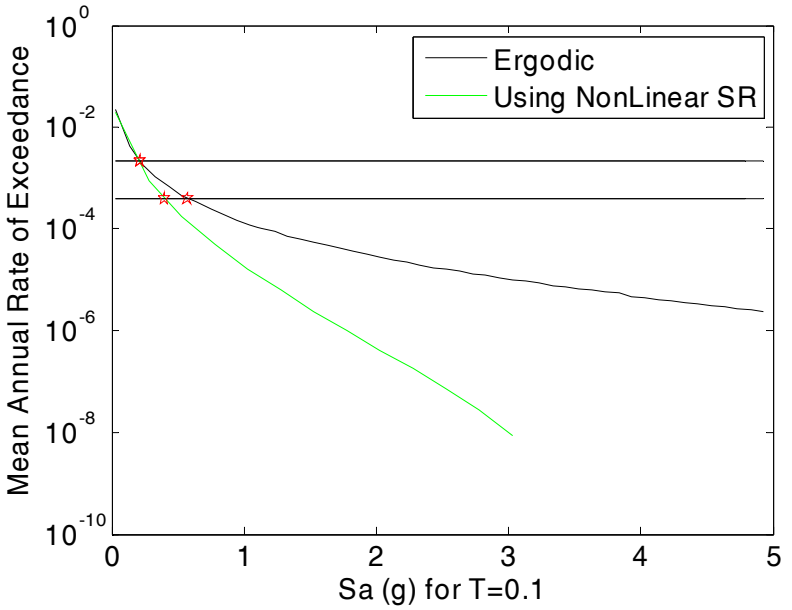

Figure 2. Hazard curve for the case of no epistemic uncertainty on site response.

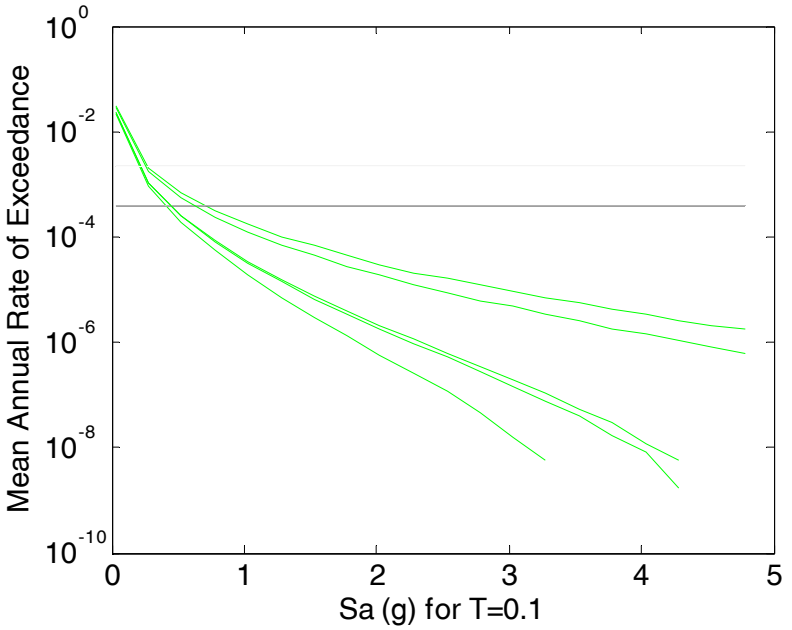

Figure 3. Hazard curves for different site scenarios (i.e. uncertainty on site characteristics)

Each hazard curve in Figure 3 corresponds to one value of Vs30 that comes from the 10% coefficient of variation assumption (a detailed study of the uncertainty in Vs30 measurements can be found in Moss 2008). Since Vs30 uncertainty is

assumed to be epistemic, each hazard curve in Figure 3 has a weight for the computation of the mean hazard that reflects how far from the median estimate it is. The median Vs30 value was taken to be the same 400 (m/s). The mean hazard curve obtained for the case of uncertain Vs profile is compared to the cases without uncertainty and the ergodic model in Figure 4. Note all these hazard calculations are done using the GMPE's developed with the KiK-net database (Montalva, 2010).

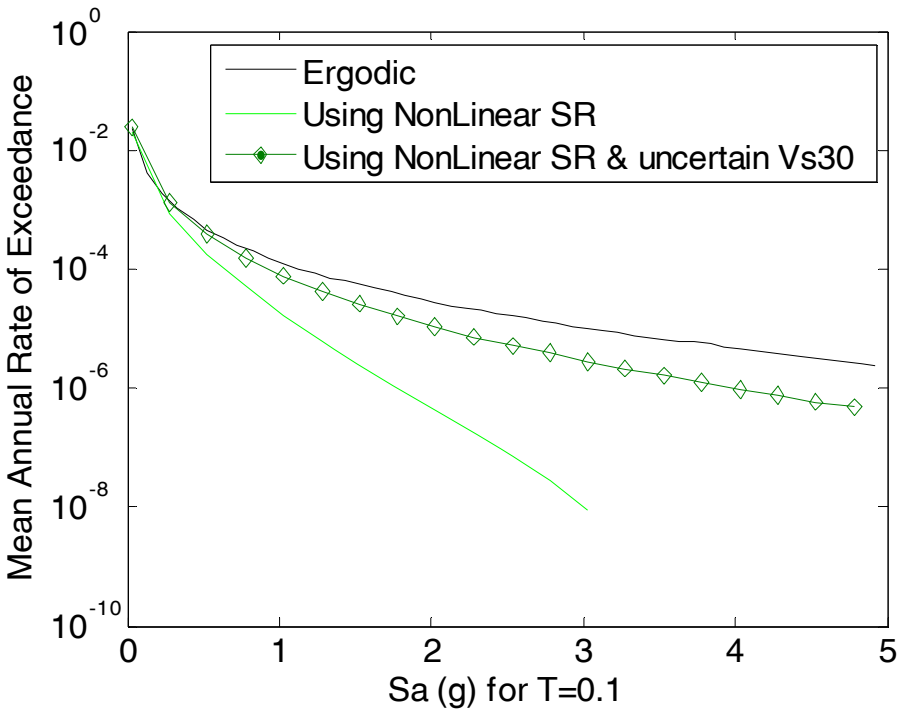

Figure 4. Hazard curves for the sample scenario, comparing ergodic, partially-ergodic, and partially-ergodic plus site uncertainty cases.

CONCLUSIONS

The main contribution of this work is the procedure for computing partially ergodic site-specific PSHA. The authors believe the methodology to be realistic, in the sense that does not use the high standard deviations drawn from ergodic regressions that are not seen on specific sites (i.e. ground motion stations). We acknowledge that we cannot directly use the median ground motion estimate for specific sites and single-site standard deviation unless we have an instrument at the site of interest.

In addition it is shown that site conditions and the degree of certainty on them, is extremely relevant to hazard calculations. Note that the 10% coefficient of variation assumed in the example is a conservative value, typical SASW uncertainty is in the order of 6%. This fact could be used as ground for seismic codes to reward thorough site investigations, because of the lower uncertainty on the expected behavior of those structures.

ACKNOWLEDGMENTS

This research was supported by the U. S. Geological Survey (USGS), Department of Interior, under USGS award numbers 08HQGR0086 and G10AP00029. The views and conclusions contained in this document are those of the authors and should not be interpreted as necessarily representing the official policies, either expressed or implied, of the U. S. Government.

REFERENCES

Abrahamson, N., Atkinson, G., Boore, D., Bozorgnia, Y., Campbell, K., Chiou, B., Idriss, I. M., Silva, W., Youngs, R. (2008). "Comparisons of the NGA ground-motion relations." *Earthquake Spectra*, 24(1), 45–66.

Anderson, J. G. and Brune, J. (1999). "Probabilistic seismic hazard analysis without the ergodic assumption." *Seism. Res. Lett.*, 70, 19-28.

Atkinson, G. M. (2006). Single-Station Sigma. *Bulletin of the Seismological Society of America*, 96(2), 446–455.

Chen Y.-H., Tsai, C.-C. P., 2002. A stable algorithm for regression analyses using the random effects model. *Bulletin of the Seismological Society of America* Vol. 92 (1), 1984-1991.

Bazzurro P., Cornell, C. A., 2004. Ground-Motion Amplification in Nonlinear Soil Sites with Uncertain Properties. *Bulletin of the Seismological Society of America* 94 (6), 2090–2109.

Bindi D., Luzi L., and Pacor F. (2009)."Interevent and Interstation Variability Computed for the Italian Accelerometric Archive (ITACA)." *Bulletin of the Seismological Society of America* Vol. 99 (4), 2471–2488.

Boore, D. M., Atkinson, G. M. (2008). "Ground-motion prediction equations for the average horizontal component of pga, pgv, and 5%-damped psa at spectral periods between 0.01 s and 10.0 s." *Earthquake Spectra* Vol. 24 (1), 99–138.

Kiban-Kyoshin, N. (2010). "Database." available from http://www.kik.bosai.go.jp/, last accessed on May 2010.

Lin, P., Abrahamson, N.,Walling, M., Lee, C.-T., Chiou, B., Cheng, C. (2010). "Repeatable path effects on the standard deviation for empirical ground motion models." To be submitted.

Montalva, G.A. (2010). "Site-Specific Seismic Hazard Analyses." Ph.D. dissertation. Washington State University, Pullman, WA, USA.

Moss, R. E. S. (2008). "Quantifying Measurement Uncertainty of Thirty-Meter Shear-Wave Velocity." *Bulletin of the Seismological Society of America* Vol. 98 (3), 1399–1411.

Rodriguez-Marek A., Montalva G. A., Cotton F, and Bonilla F. (2011). "Analysis of Single-Station Standard Deviation Using the KiK-net data" Accepted January 2011 for publication on *Bulletin of the Seismological Society of America.*

A Case Study of Alternative Site Response Explanatory Variables in Parkfield, California

E. M. Thompson[1], L. G. Baise[2], Robert E. Kayen[3], Eugene C. Morgan[2], and James Kaklamanos[2]

[1]Tufts University, Department of Civil and Environmental Engineering, 200 College Ave, Medford, MA 02155, USA; email: eric.thompson@tufts.edu
[2]Tufts University, Department of Civil and Environmental Engineering, 200 College Ave, Medford, MA 02155, USA
[3]U.S. Geological Survey, MS999, 345 Middlefield Road Menlo Park, CA 94025, USA

ABSTRACT

The combination of densely-spaced strong-motion stations in Parkfield, California, and spectral analysis of surface waves (SASW) profiles provides an ideal dataset for assessing the accuracy of different site response explanatory variables. We judge accuracy in terms of spatial coverage and correlation with observations. The performance of the alternative models is period-dependent, but generally we observe that: (1) where a profile is available, the square-root-of-impedance method outperforms V_{S30} (average S-wave velocity to 30 m depth), and (2) where a profile is unavailable, the topographic-slope method outperforms surficial geology. The fundamental site frequency is a valuable site response explanatory variable, though less valuable than V_{S30}. However, given the expense and difficulty of obtaining reliable estimates of V_{S30} and the relative ease with which the fundamental site frequency can be computed, the fundamental site frequency may prove to be a valuable site response explanatory variable for many applications.

INTRODUCTION

Empirical ground motion prediction equations (GMPEs) include terms to model the earthquake source, path, and site. This paper is concerned with how the site effects are included in GMPEs. Since GMPEs are generally the result of regression analysis (e.g., Joyner and Boore, 1993), we refer to the GMPE term or terms that represent site effects as the site response explanatory variable(s). The most common site response explanatory variable is the 30 m S-wave velocity (V_{S30}). Three of the five Next Generation Attenuation (NGA) GMPE developers used an additional site response variable based on the depth to a specific S-wave velocity (V_S): Abrahamson and Silva (2008) and Chiou and Youngs (2008) define the soil depth parameter as the minimum depth at which V_S reaches 1.0 km/sec ($Z_{1.0}$) and Campbell and Bozorgnia (2008) define the soil depth parameter as the minimum depth at which V_S reaches 2.5 km/sec ($Z_{2.5}$).

Douglas et al. (2009) discuss the importance of accounting for the accuracy of the different ways that V_{S30} can be estimated. They point out that only 35% of the records in the NGA database have measured values of V_{S30}, while the rest are inferred

through correlations with surficial geology. Moss (2008) showed that estimates of V_{S30} from correlations with geologic units are much less accurate than downhole or noninvasive measurements. In this paper, we indicate the estimation method of an estimate of V_{S30} with the superscript: we write the V_{S30} estimated from correlations with geologic units as V_{S30}^{geo}.

The value of a site response variable cannot be judged solely by the reliability of the measurement. The accuracy with which any variable can predict site response is a combination of how well that variable correlates with site response (i.e., model uncertainty) and the accuracy with which that variable can be estimated at a specific location (i.e., estimation uncertainty). In this context, estimation uncertainty refers to the difference in the accuracy with which V_{S30}^{geo} predicts site response compared to other estimates of V_{S30}. In contrast, model uncertainty refers to the decision to use V_{S30} as the site response explanatory variable in the GMPE, as opposed to other possibilities, such as $Z_{1.0}$ or a combination of both.

Additionally, a site response explanatory variable should be judged by spatial coverage. The reason that V_{S30}^{geo} is needed is because downhole or noninvasive measurements of V_{S30} are not available at most strong motion stations. For seismic hazard maps, V_{S30} is generally not known for a large percentage of the map. This motivated Wald and Allen (2007) to develop correlations of V_{S30} with topographic slope derived from satellite data that can be estimated with uniform precision at any location on Earth (updated by Allen and Wald, 2009). We refer to the magnitude of the topographic slope computed using the Wald and Allen method as δ and the estimates of V_{S30} as V_{S30}^{δ}.

Thompson et al. (2010) collected 52 noninvasive velocity profiles at strong motion station in the Parkfield region of California. These data provide a valuable opportunity to assess the accuracy of different site response explanatory variables because these densely spaced velocity profiles are generally associated with strong motion stations. We begin by describing the data that we use in this study; this includes the velocity profiles and the ground motions used to assess the different explanatory variables. We then define the different site response explanatory variables that we include in this paper and how we compute the observed site response from recorded ground motions and the data selection criteria. Using the observed data, we then quantify the accuracy with which the different explanatory variables perform in terms of the correlation to observed amplifications.

DATA

Velocity Profiles and Ground Motion Selection. The 52 velocity profiles collected by Thompson et al. (2010) at strong motion stations are shown in Figure 1. Additionally, we show the epicenter of the 2004 M 6.0 Parkfield earthquake, but we do not include the records from this earthquake in our analysis to avoid the complication of nonlinear and finite fault effects which could be important because epicentral distance to these stations is so small. Instead, we analyze motions from the 1983 M 6.36 Coalinga earthquake. Of the 52 stations with measured velocity profiles

in the Parkfield region, 36 recorded the Coalinga earthquake. Figure 1 also shows the Jennings (1958) geologic units, which define V_{S30}^{geo}.

METHODS

Site Response Explanatory Variables. We have already discussed some of the site response explanatory variables in the Introduction (V_{S30}^{geo}, V_{S30}^{δ}). The velocity surveys by Thompson et al. (2010) employed the spectral analysis of surface waves (SASW), and so we refer to the V_{S30} estimated from an SASW V_S profile as V_{S30}^{SASW}. Additionally, we compute the fundamental site frequency (f_0) using the procedure described by Zhao et al., (2006).

The SASW V_S profiles include information that should be pertinent for site response besides the single value of V_{S30}. Thus, we investigate alternative data reduction methods to simplify the information in the V_S profile to a single value that can be used as a site response explanatory variable in the GMPE regression analysis.

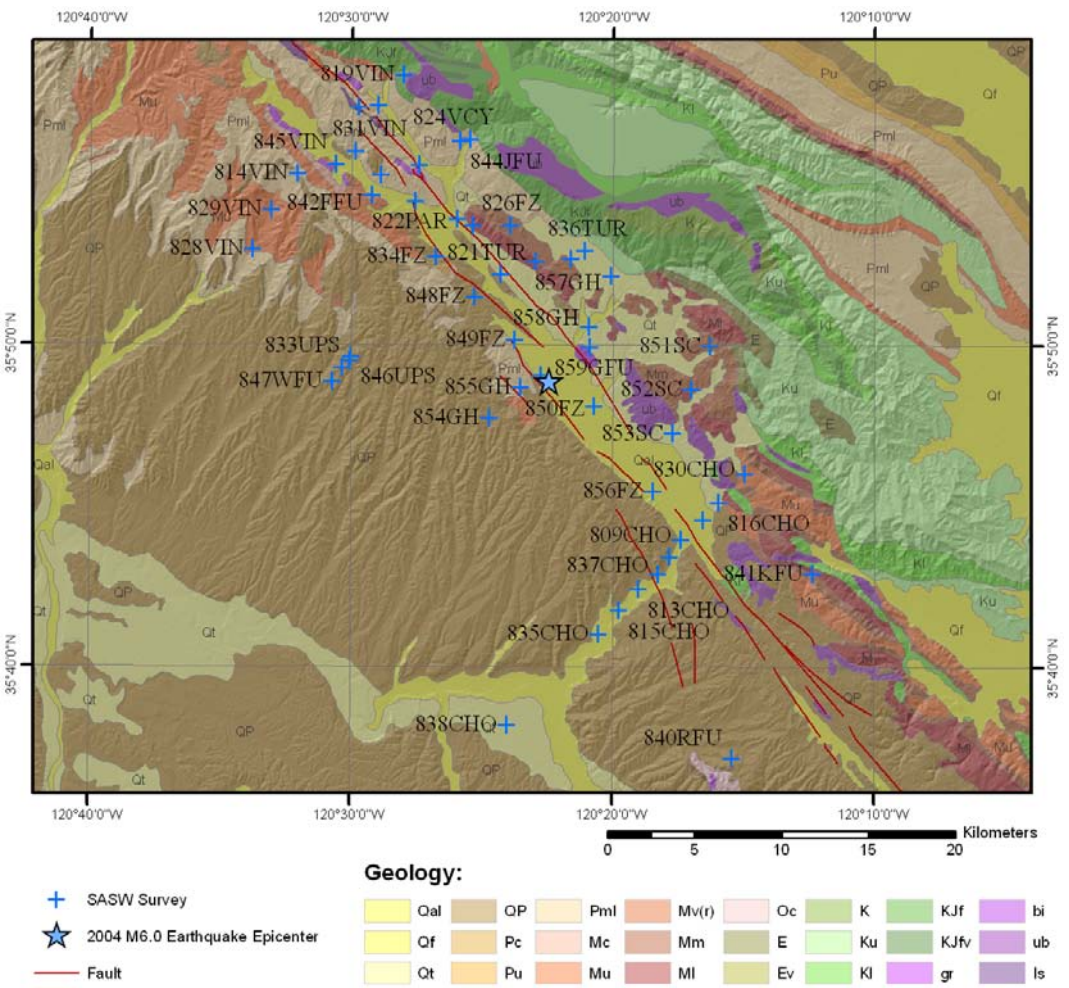

Figure 1. Vicinity map for the 52 Parkfield strong motion stations with measured velocity profiles analyzed in this paper.

This includes the square-root-of-impedance method (SRI) and the one-dimensional plane SH-wave computation (SH1D). Unlike various V_{S30} estimates and f_0, both of these alternative methods are period-dependent and thus have the potential to provide a more accurate estimate of the site response amplification.

The SRI method of estimating the site response amplifications (described by Joyner et al., 1981) computes the amplification that a seismic wave will experience as it travels between two materials with different impedances, where the impedance is defined as the product of density and velocity: $\rho \times V$. The key assumption of this method is that the seismic energy is completely transmitted across the material interfaces. The SRI method ignores the effects of seismic reflections and refractions that will occur within a stack of laterally constant layers. Joyner et al. (1981) found that the impedance effect, as opposed to the effects of reflections and refractions, is the dominant process that contributes to site amplification. We refer to the amplifications predicted by the SRI method as $a^{SRI}(T)$.

Accounting for the effect of reflections and refractions could potentially provide a more realistic model of site response amplification than $a^{SRI}(T)$. We accomplish this by assuming vertically incident plane SH-wave (the horizontally polarized component of the S wave) propagation through a laterally homogeneous medium (SH1D). We compute the amplifications using the Thomson-Haskell method (Thomson, 1950; Haskell, 1953) and denote the predicted amplifications as $a^{SH1D}(T)$.

Empirical Site Response Amplifications. We define the site response amplification in terms of the pseudospectral acceleration (PSA), which is a function of the fundamental period (T) of a single-degree-of-freedom system (SDOF): the site response amplification is

$$\ln[a(T)] = \ln[\mathrm{PSA}(T)] - \ln[\mathrm{PSA}^r(T)], \quad (1)$$

where $\mathrm{PSA}^r(T)$ is the PSA at the reference site and $\mathrm{PSA}(T)$ is the PSA at the location of interest (all of the PSA values in this article assume 5% viscous damping). In order to assess site response explanatory variables within the GMPE framework, we define PSA^r as the PSA computed from an existing GMPE for the reference rock condition. This approach assumes that the GMPE accurately accounts for the path and source effects. We are comfortable with this assumption for this application because it is unlikely that the unaccounted-for source and path variability will create spurious correlations with any of the site response explanatory variables that we consider in this article. Uncorrelated variability may reduce the degree of correlation between the site response explanatory variables and the site response amplification values, but will not favor one variable over another. For this paper, we use the Boore and Atkinson (2008) GMPE, though the choice is arbitrary.

RESULTS

We compare the goodness-of-fit of the recorded site response amplifications to the various site response explanatory variables using Pearson's product moment correlation coefficient (r). This is the most widely used measure of linear association between two variables. The larger the absolute value of r, the better a site response explanatory variable will perform in a regression analysis. The standard form of most GMPEs regress the logarithm of PSA against the logarithm of the site response explanatory variable (typically V_{S30}) because both of these variables are assumed to be lognormally distributed. Thus, it is appropriate for us to compute r from the $\ln[a(T)]$ and the natural logarithm of the site response explanatory variable.

Figure 2 plots the site response amplifications against the six different site response explanatory variables that we consider in this paper: (a) $\ln[f_0]$, (b) $\ln[\delta]$, (c) $\ln[V_{S30}^{geo}]$, (d) $\ln[V_{S30}^{SASW}]$, (e) $\ln[a^{SRI}(T)]$, and (f) $\ln[a^{SH1D}(T)]$. Note that we choose to

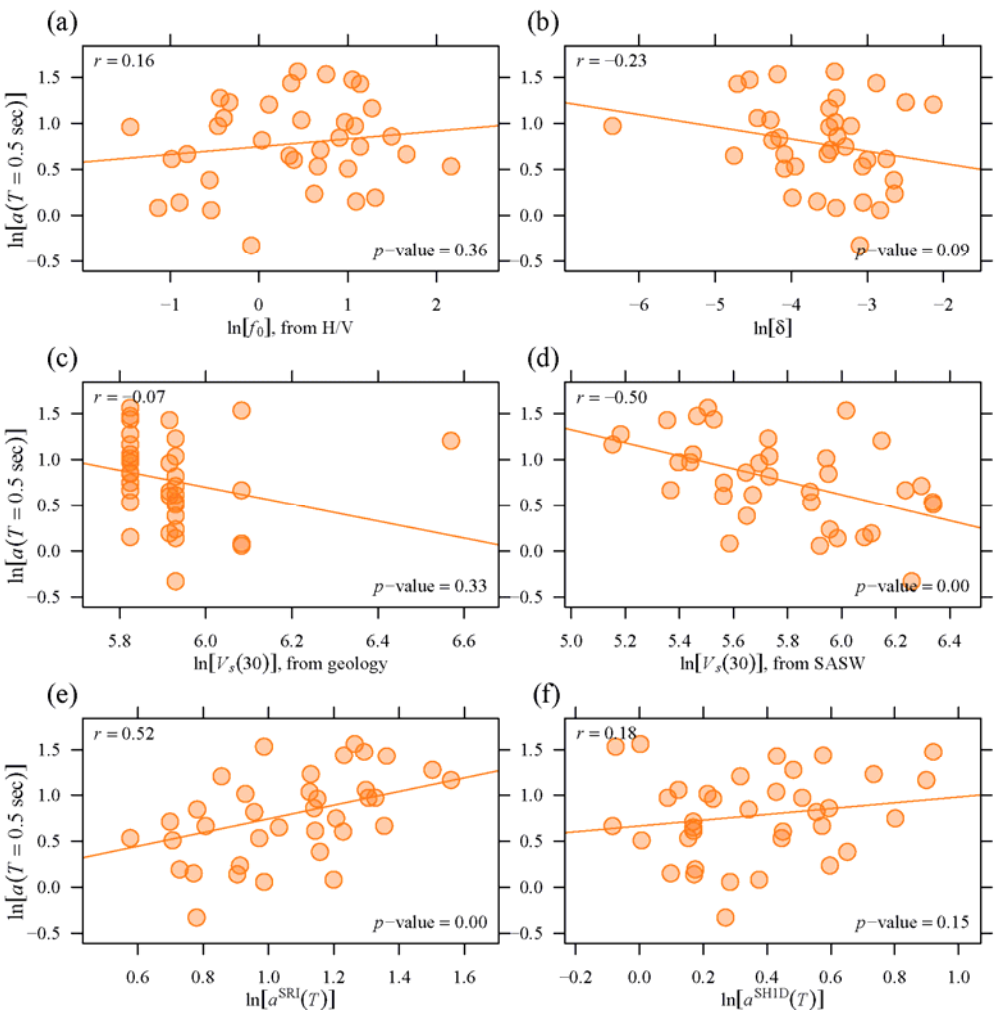

Figure 2. Correlations of ln[$a(T$=0.2 sec)] with (a) ln[f_0], (b) ln[δ], (c) ln[V_{S30}^{geo}], (d) ln[V_{S30}^{SASW}], (e) ln[$a^{SRI}(T)$], and (f) ln[$a^{SH1D}(T)$].

use $\ln[\delta]$ rather than $\ln[V_{S30}^{\delta}]$. We feel that a fair assessment of the topographic slope method would allow the full range in variability of δ. The value of r is reported in the top-left corner of each subfigure, and the *p*-value for the null hypothesis that $r = 0$ is reported in the bottom-right corner. This figure illustrates that none of the site response variables exhibit a strong correlation, but the best site response variable for the 0.5 sec amplification is $\ln[a^{SRI}(T)]$ with $r = 0.52$, slightly larger than the correlation for $\ln[V_{S30}^{SASW}]$. Surprisingly, the correlation for $\ln[a^{SH1D}(T)]$ is substantially smaller than for either $\ln[a^{SRI}(T)]$ or $\ln[V_{S30}^{SASW}]$, though it is the most complex explanatory variable to compute. At a 5% confidence level, the correlation that we observe between the amplifications and $\ln[f_0]$, $\ln[\delta]$, $\ln[V_{S30}^{geo}]$, and $\ln[a^{SH1D}(T)]$ are not significant, though $\ln[\delta]$ would be significant at the 10% confidence level. These observations, however, are based only on a single period, and we should consider a wide range of periods in comparing the performance of the different explanatory variables.

Table 1 provides the r values for the six different explanatory variables at periods from 0.05 to 10 sec. Table 1 reveals clear trends in the performance of the different explanatory variables as a function of period. Site response is positively correlated with f_0 at small periods and negatively correlated with f_0 at larger periods. Because of this gradual transition, r is not statistically significant for intermediate periods (as indicated by *p*-values not reported here). In contrast, $|r|$ for all of the explanatory variables that are based on the velocity profiles are greater at larger periods (with the exception of the small values at T = 10 sec). The period-dependence of the correlation of $\ln[\delta]$ and $\ln[V_{S30}^{geo}]$ is less clear. The performance of $\ln[\delta]$ is relatively constant with respect to period except that the performance is particularly poor for $T \geq 1.0$ sec, while $\ln[V_{S30}^{geo}]$ performs best at T = 0.75 sec but does not exhibit a clear performance trend.

The ability of the SRI method to capture the period dependence of site response amplifications gives it an important advantage over V_{S30}. The values of r in Table 1 confirm

Table 1. Correlation coefficients for the different site response explanatory variables for different periods.

T (sec)	$\ln[f_0]$	$\ln[\delta]$	$\ln[V_{S30}^{geo}]$	$\ln[V_{S30}^{SASW}]$	$\ln[a^{SRI}(T)]$	$\ln[a^{SH1D}(T)]$
0.05	0.33	-0.26	-0.15	-0.39	0.36	-0.11
0.10	0.42	-0.22	-0.13	-0.26	0.29	-0.05
0.20	0.42	-0.25	-0.07	-0.25	0.30	0.03
0.40	0.39	-0.29	-0.07	-0.33	0.35	0.08
0.50	0.16	-0.23	-0.07	-0.50	0.52	0.18
0.75	0.05	-0.28	-0.29	-0.70	0.70	0.32
1.00	-0.09	-0.07	-0.19	-0.59	0.60	0.26
2.00	-0.39	0.13	0.04	-0.46	0.52	0.17
4.00	-0.40	0.04	-0.08	-0.54	0.63	0.36
5.00	-0.33	0.02	-0.07	-0.51	0.59	0.31
7.50	-0.40	0.04	-0.08	-0.54	0.63	0.36
10.00	-0.01	0.19	0.19	-0.14	0.23	0.04

this expectation: the $|r|$ for both methods are identical at T = 0.75 sec, and the SRI method performs better than V_{S30} as the period diverges from this value (with an exception at T = 0.05 sec). We expect the substantial decrease in r for $a^{SRI}(T)$ at T = 10 sec because the V_S profiles do not extend to depths where $a^{SRI}(T)$ can be computed, and so the $a^{SRI}(T)$ for the largest possible T is used. Collecting profiles that extend to greater depths will improve the performance of the SRI method at larger periods unless two- or three-dimensional wave propagation effects are the source of the misfit.

Although δ and V_{S30}^{geo} do not correlate particularly well with the site response amplifications in Parkfield, these explanatory variables have the most extensive spatial coverage and thus are valuable for site response mapping and estimating the site response where no V_S profile is available. Of these two, we see that δ performs significantly better than V_{S30}^{geo} for $T \leq 0.5$ sec. At larger periods, both of these explanatory variables do not exhibit significant correlations. The observation that topographic slope performs better than surficial geology for the Parkfield data set combined with the ease with which δ can be computed at any location across the globe suggests the topographic slope method may be an attractive alternative to V_{S30}^{geo} when no other estimate is available. Further work is required to determine if this result is true in general, or only applicable to Parkfield.

SUMMARY

The Parkfield strong motion stations and velocity profiles provide a valuable case study for comparing the performance of alternative site response explanatory variables. These data show that the SRI method provides a valuable improvement over V_{S30}, and that the topographic slope performs is at least as good of a predictor of site response as surficial geology. These conclusions, however, must be qualified by noting that the sample size is limited (only amplification 36 observations) and the samples are limited to one earthquake (1983 Coalinga earthquake). Future work should expand the sample size by using more earthquake and more strong motion stations.

ACKNOWLEDGEMENTS

This research is funded by National Earthquake Hazards Reduction Program (NEHRP) Award #G09AP00062.

REFERENCES

Abrahamson, N., and Silva, W. (2008). “Summary of the Abrahamson and Silva NGA ground motion relations.” *Earthquake Spectra*, 24(1), 67–97.

Allen, T. I., and Wald, D. J. (2009). “On the Use of High-Resolution Topographic Data as a Proxy for Seismic Site Conditions (VS30).” *Bull. Seism. Soc. Am.*, 99(2A), 935–943.

Boore, D. M., and Atkinson, G. M. (2008). "Ground-motion prediction equations for the average horizontal component of PGA, PGV, and 5%-damped PSA at spectral periods between 0.01 s and 10.0 s." *Earthquake Spectra*, 24(1), 99–138.

Campbell, K., and Bozorgnia, Y. (2008). "NGA ground motion model for the geometric mean horizontal component of PGA, PGV, PGD and 5% damped linear elastic response spectra for periods ranging from 0.01 to 10 s." *Earthquake Spectra*, 24(1), 139–71.

Chiou, B. S.-J., and Youngs, R. R. (2008). "An NGA model for the average horizontal component of peak ground motion and response spectra." *Earthquake Spectra*, 24(1), 173–215.

Douglas, J., Gehl, P., Bonilla, L. F., Scotti, O., Regnier, J., Duval, A.-M., and Bertrand, E. (2009). "Making the most of available site information for empirical ground-motion prediction." *Bull. Seism. Soc. Am.*, 99(3), 1502–1520.

Haskell, N. A. (1953). "The dispersion of surface waves on multilayered media." *Bull. Seism. Soc. Am.*, 72, 17–34.

Jennings, C. W. (1958). "Geologic atlas of California, San Luis Obispo sheet." Calif. Div. Mines Geol. Geologic Atlas Map GAM 018, scale 1:250,000.

Joyner, W. B., Boore, D. M. (1993). "Methods for regression analysis of strong-motion data." *Bull. Seism. Soc. Am.*, 83(2), 469-487.

Joyner, W. B., Warrick, R. E., and Fumal, T. E. (1981). "The effect of quaternary alluvium on strong ground motion in the Coyote Lake, California, Earthquake of 1979." *Bull. Seism. Soc. Am.*, 71(4), 1333–1349.

Thompson, E. M., Kayen, R. E., Carkin, B., and Tanaka, H. (2010). "Surface wave site characterization at 52 strong motion recording stations affected by the Parkfield M6.0 Earthquake of 28 September 2010." U.S. Geol. Surv. Open-File Rept. 2010-1168.

Thomson, W. T. (1950). "Transmission of elastic waves through a stratified solid." *Journal of Applied Physics*, 21, 89–93.

Moss, R. E. S. (2008). "Quantifying measurement uncertainty of thirty-meter shear-wave velocity." *Bull. Seism. Soc. Am.*, 98(3), 1399–1411.

Wald, D. J., and Allen, T. I. (2007). "Topographic slope as a proxy for seismic site conditions and amplification." *Bull. Seism. Soc. Am.*, 97(5), 1379–1395.

Wills, C. J., and Clahan, K. B. (2006). "Developing a map of geologically defined site-condition categories for California." *Bull. Seism. Soc. Am.*, 96(4), 1483–1501.

Zhao, J., Irikura, K., Zhang, J., Fukushima, Y., Somerville, P., Asano, A., Ohno, Y., Oouchi, T., Takahashi, T., and Ogawa, H. (2006). "An empirical site-classification method for strong-motion stations in Japan using H/V response spectral ratio." *Bull. Seism. Soc. Am.*, 96(3), 914–25.

Estimating Repair Cost and Downtime Due to Earthquake-Induced Damage at Container Ports

L.M. Ivey[1], G.J. Rix[2], S.D. Werner[3], and A. L. Erera[4]

[1]Graduate Research Assistant, School of Civil and Environmental Engineering, Georgia Institute of Technology, Atlanta, GA 30332-0355; PH: (404) 894-2282; email: lindsay.ivey@gatech.edu
[2]Professor, School of Civil and Environmental Engineering, Georgia Institute of Technology, Atlanta, GA 30332-0355; PH: (404) 894-2292; email: glenn.rix@ce.gatech.edu
[3]President, Seismic Systems & Engineering Consultants, 8601 Skyline Boulevard, Oakland, CA 94611; PH: (510) 531-7489; email: sdwerner@ix.netcom.com
[4]Associate Professor, School of Industrial and Systems Engineering, Georgia Institute of Technology, Atlanta, GA 30332-0355; PH: (404)385-0358; email: alan.erera@isye.gatech.edu

ABSTRACT

Ports play a critical role in transportation infrastructure, but are vulnerable to seismic hazards. Current risk management practices focus on the effect of seismic hazards on individual port structures. However, damage and downtime of these structures has an impact on the overall port system's ship handling operations and the economic impacts that result from extended earthquake-induced disruption. The following paper overviews the concepts and methods developed for the seismic risk management of a port-wide system of berths. In particular, the use of spatially correlated ground motion intensity measures to estimate damage to pile-supported marginal wharves and container cranes via fragility relationships developed by project team members. Additionally, the repair costs and downtimes determined via repair models for both types of structures. Finally, the impact on ship handling operations calculated via logistical models of the port system. The paper also discusses how the results from such an analysis might be used by port decision makers to make more informed decisions in design, retrofit, operational, and other seismic risk management options.

INTRODUCTION

In the modern world, ports play an important role in the shipping industry and the world economy. However, numerous ports world-wide, including several in the U.S. along the west coast, are vulnerable to seismic hazards (Figure 1). Historical examples such as the 1995 Kobe earthquake or the 2010 Haiti earthquake demonstrate that port components are susceptible to earthquake damage. Furthermore, when damage to individual structures such as wharves and cranes occurs, it affects port operations by disrupting shipping. Repair of physical port damage can be costly, but loss of shipping revenue due to downtime can have an even

greater cost. In 1995 after the M6.9 Hyogoken-Nanbu earthquake, the Port of Kobe suffered extensive liquefaction, wharf, and crane damage. The direct losses associated with replacing damage facilities amounted to approximately $5.5 billion dollars. However, the indirect losses from business interruptions, although much harder to quantify were much greater. Chang (2000) noted, "Once shippers were forced to invest in setting up operations elsewhere while Kobe was repairing its earthquake damage, they seemed in many cases not to have returned." The overall impact of the earthquake reduced in rank what was once the 6th largest container port in the world to the 55th largest port in 2007 (AAPA 2009), 12 years after the earthquake.

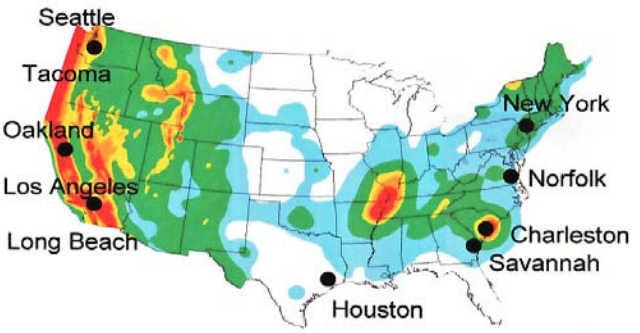

Figure 1. Several of the largest container ports in the U.S. are seismically at risk since they are located in areas of high seismic hazard.

OBJECTIVE

Current seismic design guidelines meant to protect ports focus on the performance of individual components within the port, and not on the functionality of the port as a system and the effects on operations. Therefore, the aim of the research conducted within the scope of this project includes performing risk analyses of the port system as a whole, generating results that address system-wide performance, instead of performance of individual components. System-wide results offer more valuable information to those in the port responsible for making seismic risk decisions, by defining performance using monetary losses instead of arbitrarily defined earthquake motions.

Container ports are a network of components that work concurrently as a large system. At the whole, the port's function is to transfer cargo to and from container ships. However, this activity can be done at one of several port terminals, which can be composed of one or more berths. Thus, a berth is the basic operational unit of a port, and each berth contains several components that work together to transfer cargo (Figure 2): pile-supported wharves and container cranes.

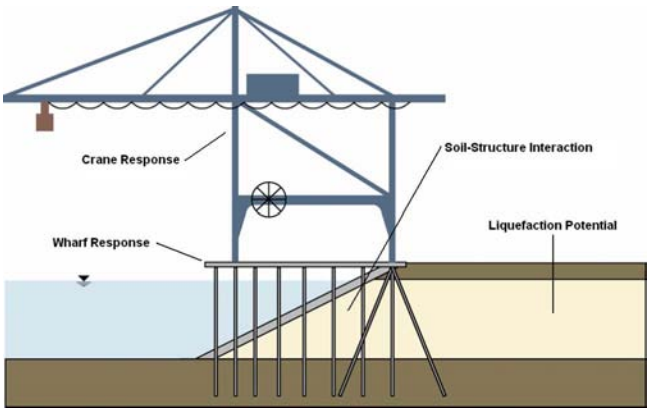

Figure 2. Typical Container Berth

The response to earthquake excitation for each of these components (Figure 2) varies. Consequently, estimating earthquake-induced losses is complicated by uncertainties in the structural response of the components, uncertainties in seismic hazard, and uncertainties in operational matters. Therefore, the most robust way to account for these varied uncertainties is via probabilistic risk analysis. For the container port system, that analysis is represented by the following equation:

$$\lambda_T(l) = \sum_{i=1}^{N} \upsilon_i \left[\int_{RRIM} \int G_{\vec{L}|\vec{RR}} f_{\vec{RR}|\vec{IM}} f_{\vec{IM}|M=m_i,R=r_i} \right] \qquad (1)$$

Equation 1 solves for the mean rate of exceedance of losses occurring within the port system. Specifically, $\lambda_T(l)$ is the mean rate of exceedance of losses for a portfolio of terminal facilities $T = [T_1, T_2, ..., T_j]$; N is the number of seismic source zones used in analysis; ν_i is the mean rate of occurrence of earthquakes larger than a minimum magnitude originating in source zone *i*; $G_{\vec{L}|\vec{RR}}$ is the complementary cumulative distribution function of the losses conditional on the repair requirements at each terminal; $f_{\vec{RR}|\vec{IM}}$ is the probability density function of the repair requirements at each terminal conditional on the intensity measures; and $f_{\vec{IM}|M=m_i,R=r_i}$ is the probability density function of ground motion intensity conditional on earthquake *i* with specific values of magnitude and distance. As Equation 1 is quite complex, its particulars will be further explained in the following sections.

SEISMIC HAZARD

The first step in calculating the mean rate of exceedance of losses requires the estimation of the intensity of the ground motions at the port components. This seismic hazard analysis is contained within the $f_{\vec{IM}|M=m_i,R=r_i}$ term of Equation 1, which is the probability density function of ground motion intensity conditional on an earthquake's magnitude (*m*) and distance (*r*) from source zone *i*. The earthquakes used are randomly sampled through a Monte Carlo simulation from the California Earthquake Rupture Forecast (Field et al. 2009). This earthquake rupture forecast

lists the possible earthquake ruptures above some minimum magnitude and its probability of occurrence within Californian faults. Due to the nature of Monte Carlo simulation and the occurrence rate of likely earthquakes, the simulation is likely to produce a large number of small magnitude earthquakes and a small number of large magnitude earthquakes. However, large magnitude earthquakes are of more interest within the risk analysis since they are more likely to produce damage. Stratified sampling (Jayaram and Baker 2010) would allow for the preferential sampling of large events while ensuring that simulated events remain stochastically representative. However, for years that an earthquake does occur, the intensity measure at the terminal site will be calculated in order to find the component response.

Spatially Distributed Network. It is important to remember that unlike a singular structure, such as a building, the port lies over an area. Earthquake motions in one terminal as compared to another terminal will not be identical, but they will be correlated. To account for the spatial distribution within the port, two techniques are used. First, the mean rate of exceedance of losses is calculated for multiple terminal facilities ($T = [T_1, T_2, ..., T_j]$), and aggregated at the end. Second, spatial distribution or the correlation of ground motions between the terminals is accounted for in the seismic hazard calculation. For a given earthquake *k*, a ground motion prediction equation (GMPE) is used to estimate firm-site ground motion intensity measures at each terminal within the port. The basic form of these GMPEs is:

$$\ln\left(Y_{jk}\right) = \ln\left(\bar{Y}_{jk}\right) + \varepsilon_{jk} + \eta_k \tag{2}$$

where Y_{jk} is the ground motion intensity measure of interest at terminal *j* due to earthquake *k*, $\bar{Y}_{jk}$ is the median value of the intensity measure obtained from the GMPE, ε_{jk} is the intra-event residual, and η_k is the inter-event residual. For a portfolio of sites separated by only a few kilometers (e.g., terminals within a port), the intra-event residuals are correlated (Jayaram and Baker 2008; Jayaram and Baker 2009). Correlation at short periods (< 2 seconds), however depends on the similarity of geologic conditions between sites. For a port, the geologic conditions between the terminals are fairly similar, and it is expected that V_s30 at the sites would show clustering. The actual calculation of the intra-event residual uses semivariograms defined by the separation h between sites u and u'.

The ground motion prediction equation is applied to every simulated earthquake in order to estimate intensity measures. For this study, PGV is calculated for wharf fragility and SA and SA at 5% damping is calculated for crane fragility. Figure 3 shows the mean annual rate of exceedance for a simulation of earthquakes to which the GMPE was applied:

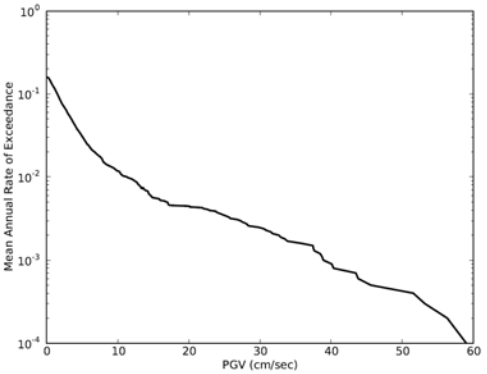

Figure 3. Mean Rate of Exceedance Curve (PGV)

COMPONENT FRAGILITY

The middle term of the bracketed section of equation 1 ($f_{\overrightarrow{RR}|\overrightarrow{IM}}$) calculates the component response to the intensity measures from the earthquake, and the repair requirements necessary to fix the resulting damage. More simply, $f_{\overrightarrow{RR}|\overrightarrow{IM}}$ represents the fragility relationship of the port components. Within the context of this project, these relationships were calculated using both physical and numerical modeling.

Wharf. For the wharf, a series of 2D have been created and 3D models will be created. The current version consists of 2D non-linear analytical models using OPENSEES (Shafieezadeh et al. 2009). The 2D model uses 63 earthquake motions to develop fragility curves for the port components by modeling the response of the underground portion of the pile using a soil-structure interaction technique involving macroelements (Varun 2010), the response of the pile-deck connection, and quantifying lateral movement of the wharf to/from the crane rails. Results of the 2D model showed that the most common response of the wharf was a relative movement of the entire wharf seaside, away from the crane rail. Pile damage was apparent in 6 of the 63 earthquakes.

Estimating Repair Costs and Downtime. With the guidance of port officials and those within the industry, repair costs and downtimes were estimated for the most likely port damage states. Even among the likely states, the wharf still has numerous potential damage states and it is not possible to show them all in limited space. As an example, repair costs and downtime estimations for the relative movement of the wharf and crane rail are shown in Table 2.

Table 2. Repair Model Summary for Relative Movement of Crane Rail

Damage State	Repair Cost, $		Downtime Days
	Without Contingencies	With Contingencies	
< 6" of relative movement	$148,200	$272,700	30 days
≥ 6" of relative movement			
- Repairs include new structural connection	$1,846,300	$3,397,200	6 months
- Repairs exclude new structural connection	$1,226,300	$2,256,400	3 months

Crane. The crane modeling was conducted using a finite element analysis technique (Kosbab 2010). Several simplified analysis were conducted to determine the most vulnerable aspects of the crane, and then the modeling conducted to develop the fragility analyses was done two dimensionally. Using the same database of 63 earthquakes as the wharf analysis, it was found that for cranes, earthquake responses were classified into one of four damage states:

1.) Derailment – Derailment occurs when the lateral loads are large enough to reduce the axial reaction of one crane leg to zero, causing the leg to be displaced from the wharf-mounted crane rail. Derailment must be repaired by using mobile cranes or jacking systems to reposition the derailed crane back onto the crane rails.
2.) Immediate Use – In this damage state the crane suffers minor structural damage but is still available for use post-earthquake. Specific damage includes frame buckling or torsional movement.
3.) Structural Damage – In this damage state, the crane suffers enough significant structural damage that it can not be used immediately, but has not collapsed. Specific damage includes severe portal deformation and local buckling.
4.) Complete Collapse – In this state structural damage to the crane is so severe that the structure collapses; repairs are usually not possible, and replacement is the only option. Since most container cranes are made by the same company, purchases are semi-custom and replacement can take one year or more.

Each of these damage states is represented in the fragility curves created for the cranes (Figure 4):

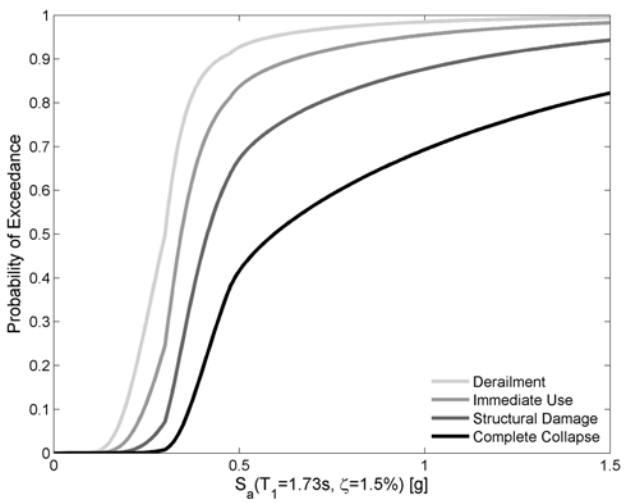

Figure 4. Fragility curves for a Light-Duty, 50-ft gauge crane

Estimating Repair Costs and Downtime. Using the previous four damage states, through discussions with crane manufacturers, the following costs and downtime estimates were prepared (Table 3):

Table 3. Repair Costs and Downtimes for Cranes from (Kosbab 2010)

Damage State	Cost ($)	COV	Downtime (Days)	COV
Derailment	50,000	0.3	6	0.3
Immediate Use	300,000	0.5	10	0.5
Structural Damage	500,000	0.5	60	0.5
Complete Collapse	7,000,000	0.3	330	0.3

Mean Rate of Exceedance for Repair Costs and Downtime. Total cost and downtime are calculated for each wharf segment, and then segments can be aggregated to get the total cost per terminal (Figure 5). However, the wharf segment remains the basic unit of measure because the effect of downtime must be further analyzed within an operations model.

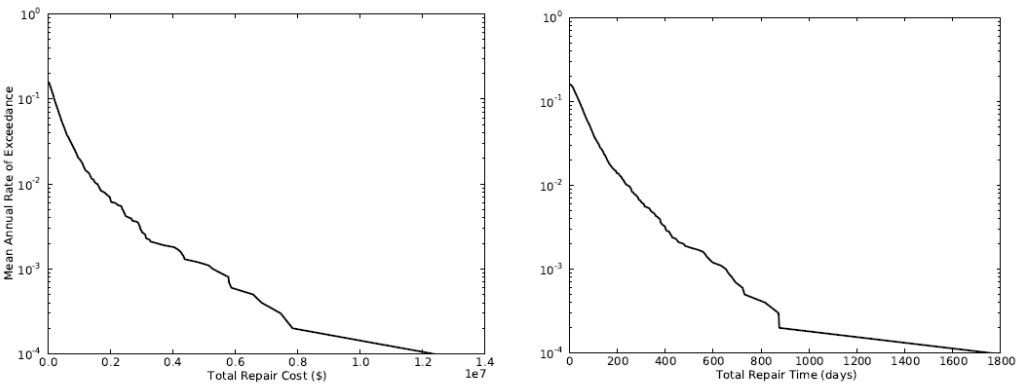

Figure 5. Mean rate of Exceedance Curves for Total Repair Cost and Time

OPERATIONS MODELING

To this point, Equation 1 has taken likely earthquake motions and applied those to the port components to calculate damage and subsequent repair requirements. To fully calculate the loss associated with the earthquake motion, the first term of Equation 1, ($G_{DV|RR}$), takes the repair requirements and calculates the losses associated with them. As seen in the previous section, monetary loss from physical damage is easy to calculate. However, in the case of a port, downtime is also considered "damage". When port components are rendered unusable post-earthquake, the facilities available for use decrease. In turn, the throughput of cargo into / out of the port also decreases. Decreased throughput amounts to monetary business interruption losses caused by the physical port damage. However, as port repairs advance, the decrease in throughput also decreases. As a result, operations modeling will be required to calculate the monetary business interruption loss due to downtime over the repair period of the port (Ak 2008).

CONCLUSIONS

At this point in the project, the operations' modeling has yet to be integrated into the framework. However, once it has, equation 1 can be fully realized and the total losses

(physical and business interruption) from an earthquake in the walkthrough table can be calculated. Calculation of losses as a means to evaluate port performance offers a myriad of applications that can provide port stakeholders with the means to make more informed seismic risk decisions. Within the scope of this project, the framework will be used to:

- Perform benefit-cost analyses on alternative seismic design and mitigation strategies.
- Plan for port emergency response operations.
- Calibrate current seismic design to determine whether they satisfy seismic design requirements.

ACKNOWLEDGEMENTS

This material is based on work supported by the National Science Foundation under Grant Nos. CMS-0530478 and CMS-0402490. Any opinions, findings, and conclusions or recommendations expressed in this material are those of the authors and do not necessarily reflect the views of the National Science Foundation.

REFERENCES

AAPA. (2009). "Port Industry Statistics." American Association of Port Authorities.

Ak, A. (2008). "Berth and Quay Crane Scheduling: Problems, Models, and Solution Methods," Georgia Institute of Technology, Atlanta, GA.

Chang, S. E. (2000) "Transportation performance, disaster vulnerability, and long-term effects of earthquakes." *Second EuroConference on Global Change and Catastrophe Risk Management*, Laxenberg, Austria.

Field, E. H., Dawson, T. E., Felzer, K. R., Frankel, A. D., Gupta, V., Jordan, T., Parsons, T., Peterson, M., Stein, R., Weldon, R., and Wills, C. (2009). "Uniform California Earthquake Rupture Forecast, Version 2 (UCERF2)." *Bulletin of the Seismological Society of America*, 99(4), 2053-107.

Jayaram, N., and Baker, J. W. (2008). "Statistical Tests of the Joint Distribution of Spectral Acceleration Values." *Bulletin of the Seismological Society of America*, 98(5), 2231-2243.

Jayaram, N., and Baker, J. W. (2009). "Correlation model for spatially distributed ground-motion intensities." *Earthquake Engineering and Structural Dynamics*.

Jayaram, N., and Baker, J. W. (2010). "Efficient Sampling and data reduction techniques for probabilistic seismic lifeline risk assessment." *Earthquake Engineering and Structural Dynamics*, 39, 1109-1131.

Kosbab, B. (2010). "Seismic Performance Evaluation of Port Container Cranes Allowed to Uplift," Georgia Institute of Technology, Atlanta, GA.

Shafieezadeh, A., DesRoches, R. D., Werner, S. D., and Rix, G. J. (2009). "Seismic Response of Pile-Supported Container Wharves." Technical Council on Lifeline Earthquake Engineering (TCLEE) Conference 2009, Oakland, CA.

Varun, V. (2010). "A non-linear dynamic macroelement for soil structure interaction analyses of piles in liquefiable sites," PhD Thesis. Georgia Institute of Technology, Atlanta, GA.

Effect of Fabric Anisotropy on Seismic Response of Strip Foundations

Bo Li[1], Xiangwu Zeng[2], and Hao Yu[3]

[1]Dept. of Civil Engineering, Wenzhou University, Zhejiang, China 325000, PH (86) 577-88191373; FAX (86) 577-86697753; email: autumnlibo@gmail.com
[2]Dept. of Civil Engineering, Case Western Reserve University, Cleveland, OH 44106, PH (216) 392-2923; FAX (216) 368-5229; email: xxz16@case.edu
[3]Dept. of Civil Engineering, Case Western Reserve University, Cleveland, OH 44106, PH (216) 785-1150; FAX (216) 368-5229; email: hxy88@case.edu

ABSTRACT

Failure of strip foundations induced by earthquake has been widely observed in the field. Fabric anisotropy of sand due to the deposition history and pattern may affect the response of strip foundations in seismic bearing capacity and settlement. In this study, eight earthquake centrifuge tests were performed on models of a strip foundation to study the seismic response of strip foundation with base layer deposited by different angles. A special rigid container was designed and used to prepare models with different directions of soil deposition. It was found that fabric anisotropy greatly influenced the response of the ground and structure in displacement, acceleration, and excess pore pressure. It shows that conventional design method should consider the influence of deposition history and pattern, which significantly affected the seismic bearing capacity and settlement of strip foundations.

INTRODUCTION

The definition of "fabric anisotropy" was introduced by Oda (1981). Two types of fabric anisotropy can be observed in uniform sand which was deposited under the action of gravitational force; they are: (i) anisotropy by the preferential alignment of non-spherical particles parallel to the horizontal direction; and (ii) anisotropy by the concentration of the unit vector, **n**, in the vertical direction. Both types of anisotropy are possible in a naturally deposited sand of non-spherical particles. Fabric anisotropy has considerable influence on the strength, bearing capacity, and liquefaction resistance of sand. Recently, the effect of fabric anisotropy on granular materials was investigated experimentally (Oda, 1979, 1981, Mitchell et al., 1978, Tatsuoka et al., 1986, Li et al., 2010).

To study the effect of fabric anisotropy on the seismic response of a strip foundation, a special centrifuge container was designed and manufactured. Eight centrifuge tests were conducted on a strip foundation model with 0°, 45° and 90° deposition angles. Three tests were conducted on dry soils while another three on saturated soils. In addition, one dry and one saturated test were repeated to check the repeatability of results.

TEST PROGRAM

Soil Used in the Tests. Toyoura sand was used in the model tests, which has been widely used in the laboratory to study the effect of fabric anisotropy. The index properties of the sand and grain size distribution curve are shown in Figure 1.

Scaled Strip Foundation. The scaled foundation model was made of aluminum, of which the geometry is shown in Figure 2. The mass of the prototype was 28 tons. The pressure induced by the strip foundation on the ground was 25 kPa.

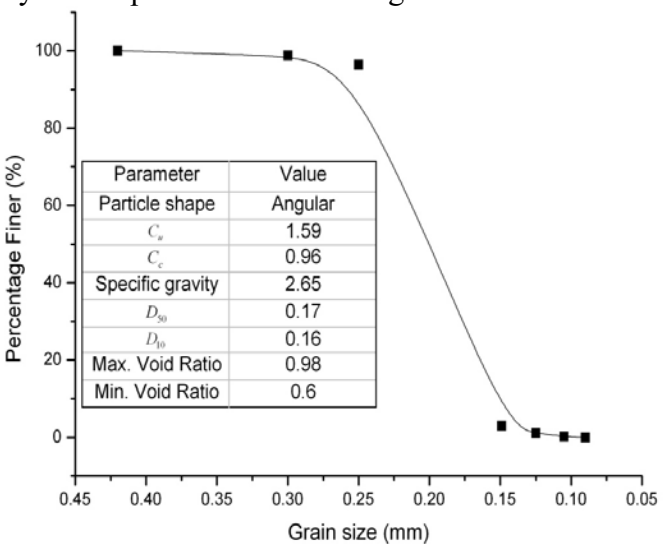

Figure1. Particle size distribution curve of Toyoura sand.

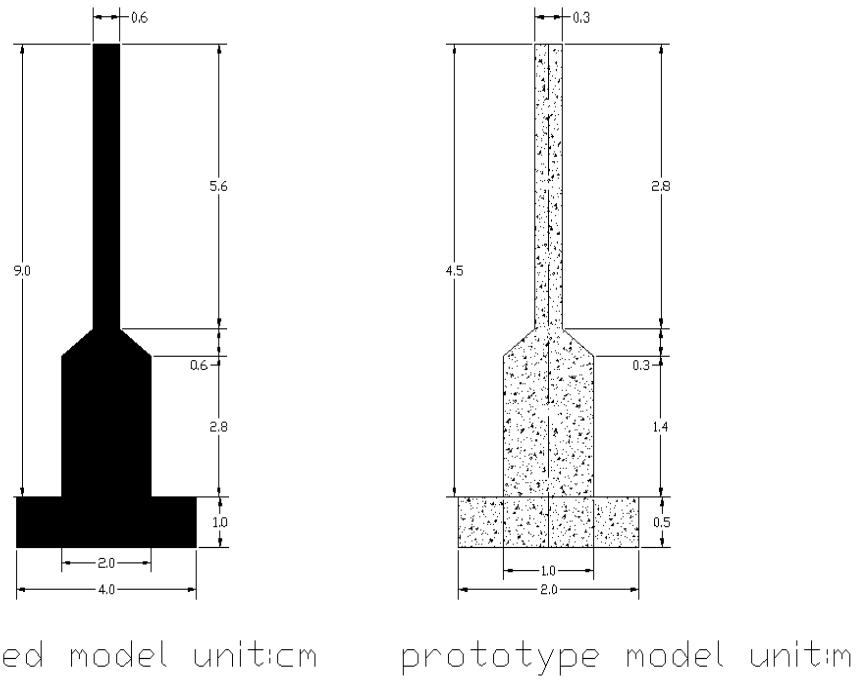

Figure 2. Geometry of the scaled model and the corresponding prototype.

Testing Facility and Model Container. The centrifuge tests reported here were conducted on the geotechnical centrifuge at Case Western Reserve University that has an effective radius of 1.37 m. The centrifuge payload capacity is 20 g-ton with a maximum acceleration of 200g for static tests and 100g for dynamics tests. The rigid box used in this test consists of 5 removable rectangular aluminum plates. The internal dimensions of the box are 53.3 cm (length) $\times$ 24.1 cm (width) $\times$ 17.7 cm (height). The centrifuge is equipped with a hydraulic shaker designed by the TEAM Corporation. The direction of shaking is perpendicular to the vector of rotation of the centrifuge. Before conducting the model tests a calibration test was performed on the box so as to simulate the earthquake that would have the desired amplitude and frequency. In theory a hydraulic shaker should be able to generate a specified earthquake. The earthquake simulated by the shaker was recorded by an accelerometer fixed on the shake table.

For the special model preparation method, a rigid model container made of aluminum was designed and manufactured for this project. As stated by Kawai and Kanatani (1998), to minimize the shear distortion, the container was design to be as rigid as possible. The container had removable end walls and removable cover so that they can be taken out during model preparation. This makes it possible to prepare the model in any specific deposition angle. The models with 45° deposition angle are illustrated in Figure 3.

Model Preparation Procedures. The details of the model preparation method can be found in Li et al. (2010). During the model preparation process, the transducers were installed at given locations near the centerline of model in the longitudinal direction. Four pore pressure transducers were located on both sides of the strip foundation. Accelerometers were used to record input motion, soil acceleration response in Rankine active zone (CDE), transition zone (BCD) and passive zone (ABC) which can be determined before test as shown in Figure 4, and the response of the strip foundation in horizontal and vertical directions. The definition of Rankine active, transition and passive zones could be found in Das (2006). In the meantime, the horizontal displacement of the building and settlement of ground were measured by LVDTs (linear variable differential transformer). The test configuration and schematic section of a model is shown in Figure 4. For the saturated model, carbon dioxide was used to replace the air in the void of the soil. Then de-aired water was introduced in the model under a vacuum condition to achieve high degree of saturation for the model.

SELECTED RESULTS

After a centrifuge model was ready, the profile of the model was measured. In each model test, the model was spun up to a centrifugal acceleration of 50g gradually. The model was allowed to stay at 50g for at least 5 minutes to allow for excess pore water pressure to dissipate fully. The input motion used is shown in Figure 5 and the test condition was summarized in Table 3. After the test, the model was spun down gradually. The profile of the model was measured again.

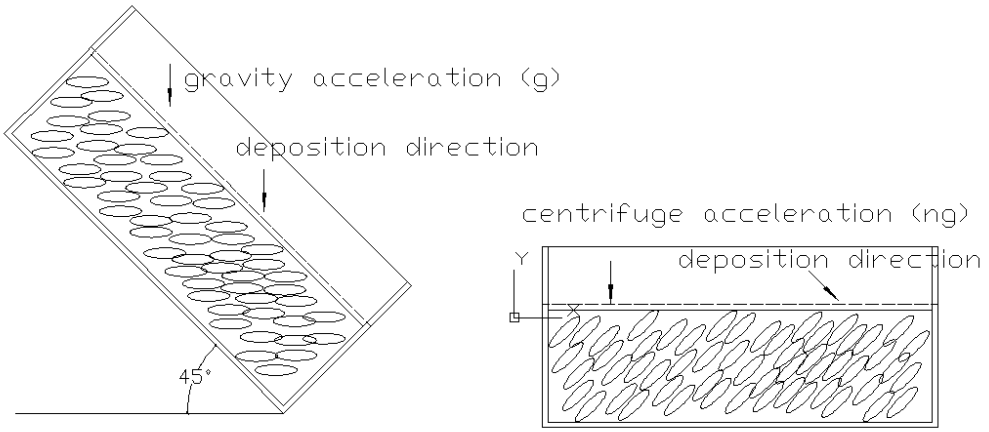

Figure 3. Sketch of centrifuge models.

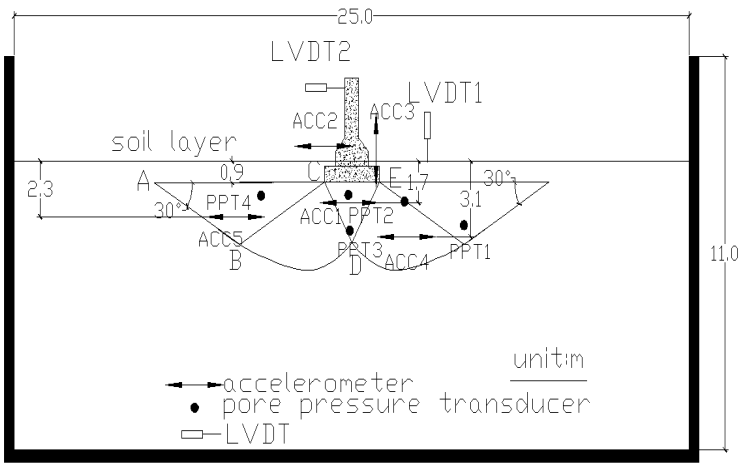

Figure 4. Sketch of a centrifuge model (ACC: accelerometer; PPT: pore pressure transducer; LVDT: displacement transducer).

Effect of Fabric Anisotropy on Acceleration in the Model. Due to the limited space of the paper, the results of only a few selected tests were shown here. The recorded acceleration time histories at the location of ACC2, which was fixed to the strip foundation just above the ground surface are shown in Figure 6. In the dry tests the acceleration showed symmetric response and great similarity to the input motion and there was little difference between the models prepared by different deposition angles. However, in the saturated tests (Figure 6a), the model prepared by 0° deposition angle exhibited great similarity to the input motion while the cases of 45°and 90° showed difference from the input motion, as both exhibited tendency of acceleration amplification near the end of input motion. From the analysis of signal correlation, the correlation coefficient between case of 0° and 90° deposition angles was 0.8, indicating some dis-similarity (Table 1), which agreed with the observation shown in Figure 6a. The number shown in main diagonal of the table was the results when the same test was repeated. Since the coefficient of correlation was high,

repeatability of results was very good. The theory and procedures for a correlation analysis was described by Rangarao et al. (2005). Thus it can be seen that the fabric anisotropy of the soil did not affect the acceleration response of the strip foundation significantly. The response of ACC4 which was located in the transition zone is illustrated in the Figure 6b. It showed significant differences between these models. From Table 2 the correlation coefficient decreased from 0.90 in a repeated test to 0.44 for the model prepared with 90° deposition angle. Similar results were observed in tests on retaining wall models (Li et al., 2010). It can be concluded that the effect of fabric anisotropy on acceleration in or near the passive earth pressure zone was more significant than that in the active earth pressure zone.

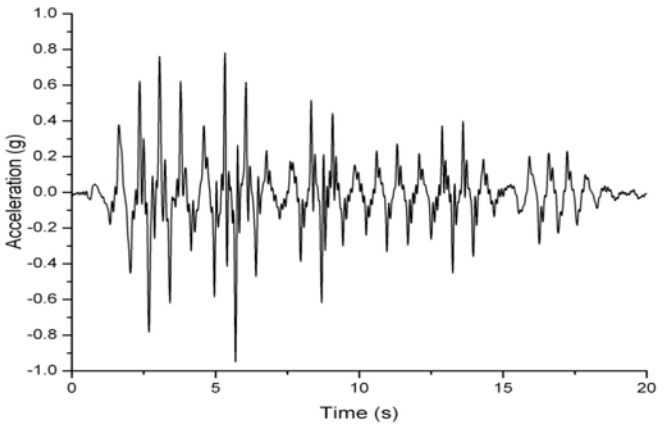

Figure 5. Typical input acceleration.

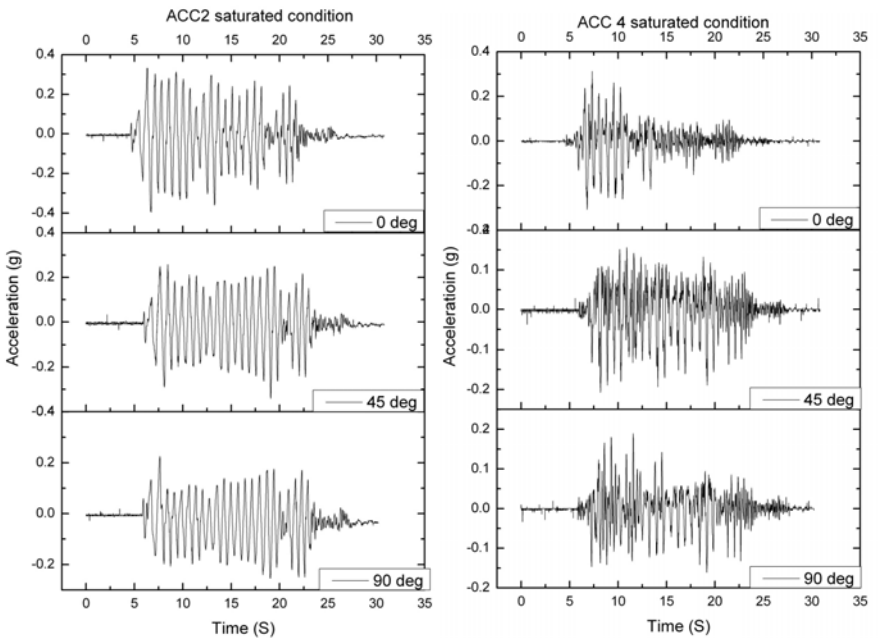

(a) ACC2 (b) ACC4

Figure 6. Recorded time histories of ACC2 and ACC4 in saturated condition.

Table 1. Normalized correlation of acceleration by ACC 2 in saturated tests.

Model types(ACC2)	0˚	45˚	90˚
0˚	—	0.86	0.8
45˚	0.86	0.97	0.91
90˚	0.8	0.91	—

Table 2. Normalized correlation of acceleration by ACC 4 in saturated tests.

Model types(ACC4)	0˚	45˚	90˚
0˚	—	0.54	0.44
45˚	0.54	0.9	0.63
90˚	0.44	0.63	—

Effect of Fabric Anisotropy on Displacement. LVDT 1 measured the horizontal displacement near the top of the strip foundation. As shown in Figure 7, it is clear that model prepared by 90° deposition angle had the largest dynamic and residual displacements (7.9 cm and 5.4 cm, respectively) and model prepared by 0° had the smallest dynamic and residual displacements (7.0 cm and 2.2 cm, respectively). In saturated tests (Figure 7b), the tendency was significantly amplified. The model prepared by 90° deposition angle recorded displacement that was almost out of bound of the LVDT. It also provided a possible explanation why some buildings failed but some did not even at the same location, a phenomenon widely observed in Niigata Earthquake (Mitchell et al., 1978). Figure 8 shows the relationship between rotational displacement and base acceleration of the strip foundation, which could easily identify the development of rotational displacement and the seriousness of damage. In the dry test, the rotational displacement was still in the safe range; however, in the saturated test, the rotational displacement for the model prepared by 90° deposition angle increased rapidly (Figure 8b). It could be concluded that the fabric anisotropy of sand played an important role, which itself was related to the deposition history and pattern in the field. The results of the tests were summarized in Table 3. The cross-sectional views of the saturated models before and after earthquake tests are shown in Figure 9. The solid lines shown in Figure 9 illustrate the conceptual force chain. Clearly, the model prepared by 90° deposition angle had the largest ground settlement and the model of 0° had the smallest in both dry and saturated conditions. This supports the conclusion that the seismic settlement of foundations on granular soil is not totally attributable to the soil density (Richard et al. 1993).

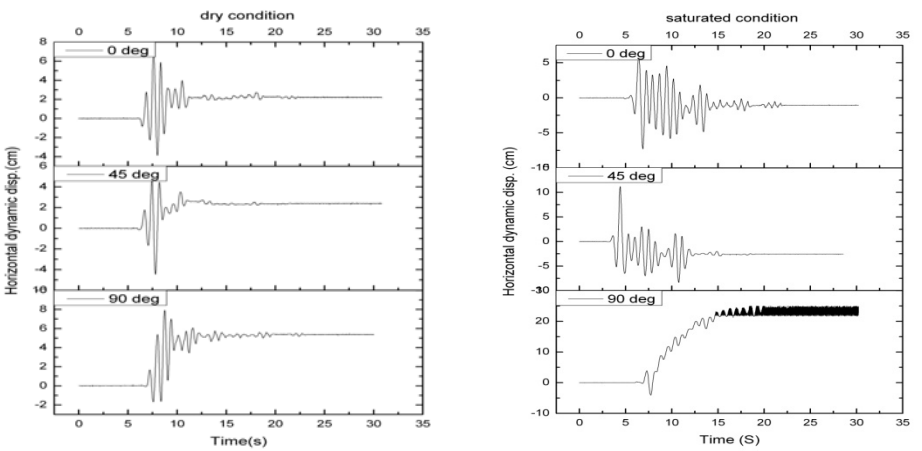

Figure 7. Recorded time histories of horizontal dynamic displacement.

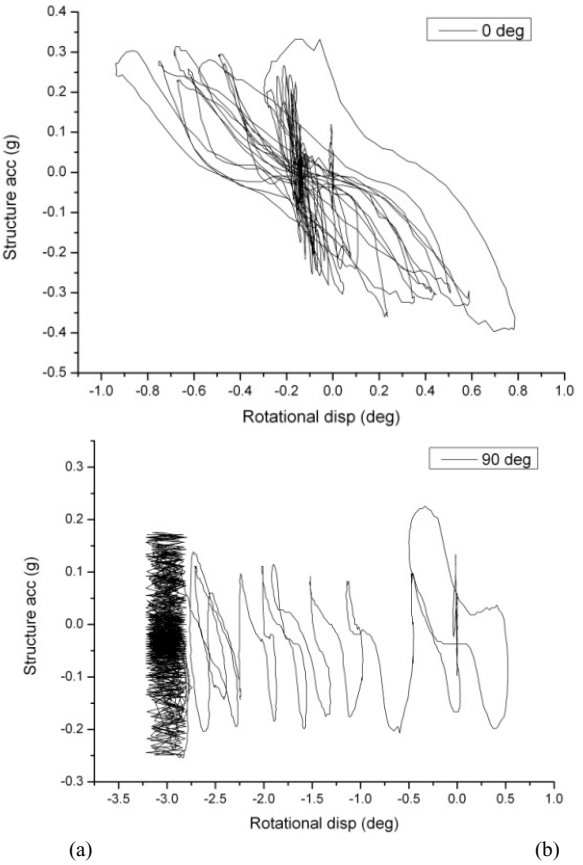

Figure 8. Correlation between base acceleration and rotation angle in saturated tests.

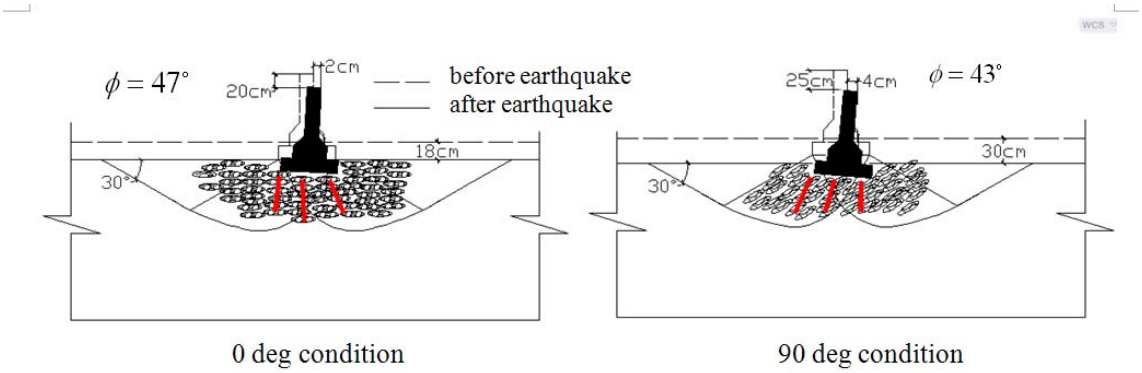

Figure 9. Cross-sectional view before and after earthquake in saturated tests.

Effect of Fabric Anisotropy on Pore Water Pressure. For the three saturated tests, the recordings of PPT 2 and PPT 3 were presented here (Figure 10) to show the influence of fabric anisotropy. As shown in Figure 4, PPT 2 and PPT 3 were located just underneath the strip foundation with different depth. From the recording of PPT2 and PPT3, all the models showed the cyclic variations and the model prepared with 90° deposition angle had more cyclic variation with lower frequencies. This observation also indicated the rotational displacement of the strip foundation in these tests. It was worthy of noting that the dissipation of pore pressure of in the model

prepared by 0° deposition angle was more rapid than the model of 90° at both locations. It indicates that ground with 0° deposition angle exhibited higher liquefaction resistance. Furthermore, the longer time it took for the dissipation of pore pressure, the larger displacement of the ground would be. This also implied that case of 90° would have the largest horizontal displacement and settlement, just as observed in the tests.

Table 3. Test Conditions and Result Summary.

Test No.	Inclination angle (deg)	Dry/Sat	Relative density (%)	Max. disp. (cm)	Min. Disp. (cm)	Residual disp. (cm)	Settlement of soil (cm)
1	0	Sat	35	6.9	-6.2	-1.0	19.5
2	45	Sat	38	11.2	-8.2	-2.6	25.0
3	90	Sat	35	28	-4	28.0	45.0
4	0	Dry	35	7.0	-3.6	2.2	2.5
5	45	Dry	34	4.8	-4.3	2.4	6.6
6	90	Dry	37	7.9	-1.6	-5.4	7.7

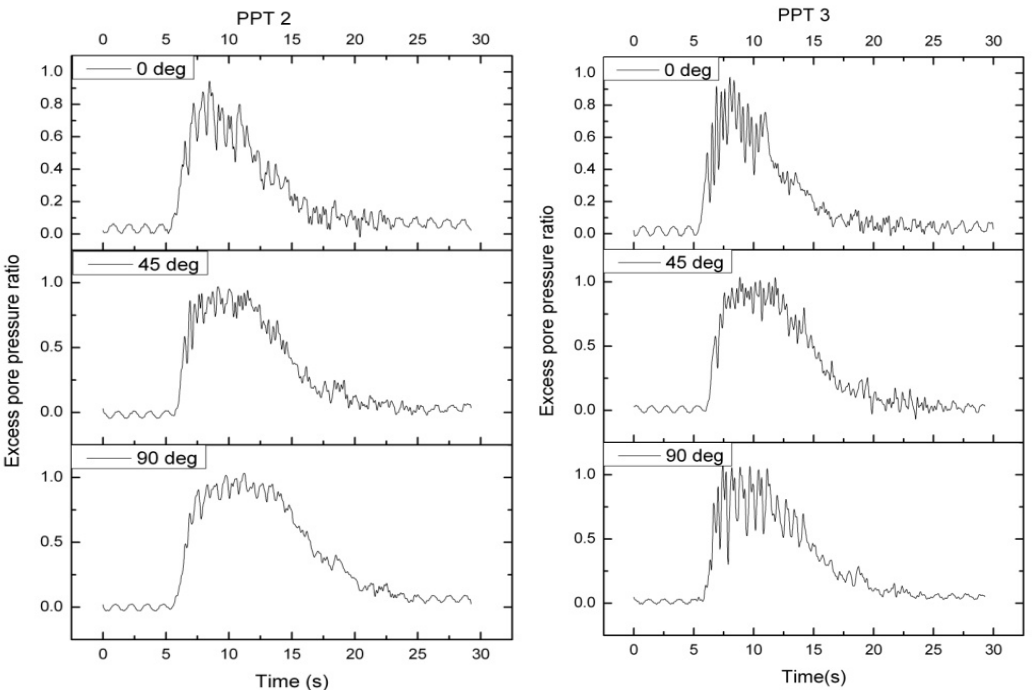

Figure 10. Recorded time histories of pore pressure in saturated condition.

DISCUSSIONS

In the analysis of acceleration response, the similarity defined by signal correlation was used to compare the differences in response between different models. As shown in the cross-sectional views of the models (Figure 9), the friction angles of the soils under the strip foundation would be different (Oda, 1979). This study showed that the fabric anisotropy had much effect on the response of strip foundation. Thus it is recommended that the design methods and parameters used should take into account the influence of fabric anisotropy of the soil in the ground.

Here microscopically the concept of force chains were introduced to explain why there was the largest settlement in case of model prepared by 90° deposition angle. The chains were illustrated by red solid lines in Figure 9. Before the earthquakes, the ground consolidation was completed in all cases and a stable force chain existed. However, the pattern of force chain was different. For the case of the model with 90° deposition angle, the force chains were in transient equilibrium since the long axis of particles were paralleled with gravity, which was an unstable situation in nature. When the earthquake came, it created a large disturbance. The force chains would collapse and resulted in the largest displacement in both dry and saturated conditions. Probably, the existence of water would aggravate the collapse of force chains. Furthermore, the saturated condition was more complicated because of the interaction between fabric anisotropy and excess pore pressure. After the earthquake, the particle of in the model with 90° deposition angle changed to horizontal direction, of which the final internal microstructure would be similar to that of the model prepared with 0° deposition angle. Of course, this assumption of force chain collapse needs further verification by micromechanics or numerical methods such as discrete element method. From Table 3, the horizontal displacement and ground settlement of saturated case was much more severe. In this study, the bearing pressure of the strip foundation was only 25 kPa, which represents a light structure. The mass inertia was not large during the earthquake. Therefore, for a heavy block building with high length-width ratio, the mass inertia could amplify the effect of fabric anisotropy.

In the centrifuge tests reported above, the friction angle variation resulted from different deposition angles as proposed by Oda (1979) probably led to the totally different response of the geotechnical structure.

SUMMARY AND CONCLUSIONS

Centrifuge tests were conducted to study the effect of fabric anisotropy of Toyoura sand on the seismic response of a strip foundation. The acceleration time histories, excess pore water pressure, and the horizontal displacement of the strip foundation and settlement of the ground in cases of 0°, 45° and 90° of soil deposition angles and with both dry and saturated ground were investigated.

The results of the tests reported here show:

(1) The differences in experimental results between the tests with different deposition angles clearly indicated the influence of fabric anisotropy on the seismic response of a strip foundation, which was a new phenomenon observed in such details.

(2) The fabric anisotropy was more emphasized in passive area which could be shown in acceleration response and displacement. The effect of anisotropic shear strength of granular material should not be neglected in considering stability problem in engineering design. In areas with high seismicity, the deposition history and pattern should be investigated in the design phase.

(3) Toyoura sand with angular platy particle shape has a strong fabric anisotropy which should be considered as a significant parameter in engineering design. Thus, the effects of particle shape and roughness and the resulting fabric anisotropy need to be further studied.

(4) It is indicated that ground prepared by different angle showed the different liquefaction resistance.

For future research, the liquefaction resistance of level ground prepared by different deposition angles will be tested in the centrifuge. It will provide a clear picture about the effect of fabric anisotropy on liquefaction potential and the evolution of force chains during ground vibration.

ACKNOWLEDGMENT

The first author would like to acknowledge the support provided by the Saada Family Graduate Fellowship for the work reported here.

REFERENCES

Das, M. B. (2006). *Principles of foundation engineering* Six Edition (Thomson, Canada).

Kawai, T., and Kanatani, M. (1998). "Seismic performance of a caisson type seawall with an armored embankment." *Proceedings, Centrifuge 98*, 351-358.

Li, B., Zeng, X. and Ming, H. Y. (2010). "Seismic Response of Retaining Wall with Anisotropic backfills." *Earth Retention Conference 3*, ASCE, 688-695.

Mitchell, J. K., Frank, J. G. and Willem, C.B. (1978). "Fabric analysis of undisturbed sands from Niigata, Japan." Technical report No. S-78-11, University of California, Berkeley.

Oda, M. (1972). "Initial fabrics and their relation to mechanical properties of granular material." *Soil and Foundations*, 12(1), 17-36.

Oda, M. (1979). "Effect of strength anisotropy on bearing capacity of shallow footing in a dense sand." *Soils and Foundations*, 19 (3), 15-28.

Oda, M. (1981). "Anisotropy strength of cohesionless sands." *Journal of the Geotechnical Engineering Division*, ASCE, 107 (9), 1219-1231.

Rangarao, Kaluri V. and Mallik, R.K. (2005). *Digital signal processing-a practitioner's approach*, John Wiley & Sons, New York.

Richard, R. Jr., Elms D. G. and Budhu, M. (1993). "Seismic bearing capacity and settlements of foundation." *Journal of Geotechnical Engineering*, 119 (4), 662-674.

Tatsuoka, F., Sakamoto, M., Kawamura, T. and Fukushima, S. (1986). "Strength and deformation characteristics of sand in plane strain compression at extremely low pressures." *Soils and Foundations*, 26 (1), 65-84.

Seismic Response of Reinforced Soil Retaining Walls: Is PGA-Based Design Adequate?

J.B.Varnier[1] and K. Hatami[2*]

[1]Graduate Research Assistant, School of Civil Engineering and Environmental Science, University of Oklahoma, 202 W. Boyd St., Room 303, Norman, OK 73019; email: jbvarnier@ou.edu
[2]Assistant Professor, School of Civil Engineering and Environmental Science, University of Oklahoma, 202 W. Boyd St., Room 450B, Norman, OK 73019, PH (405) 325-3674; FAX (405) 325-4217; email: kianoosh@ou.edu
*Corresponding Author

ABSTRACT

Current seismic design approaches for reinforced soil retaining walls and slopes are primarily based on the peak ground acceleration (PGA) and neglect other important ground motion characteristics. As a continuation of an earlier study, dynamic response of a segmental (modular block) retaining wall subjected to different ground motions is investigated. A numerical simulation approach is used to examine the influence of ground motion characteristics other than the PGA on the seismic response of the reinforced soil wall. A total of 19 recorded ground motions and 2 variable-amplitude harmonic waves were used as the input acceleration. All input motions were scaled to a PGA value of 0.15g in order to isolate the influence of other strong ground motion parameters including predominant frequency, duration and intensity. Results of the study demonstrate the extent to which input ground motions with the same PGA values can result in different wall responses. It is concluded that current seismic design guidelines for reinforced soil structures need to be revised to include important influences of other ground motion characteristics in order to enhance the safety and economy of these structures.

INTRODUCTION

There are currently several design guidelines available for MSE walls under static loading conditions (AASHTO 2009, FHWA 2009, NCMA 2009). Reinforced soil retaining walls have generally shown satisfactory performances under seismic loading when compared to conventional gravity retaining walls (e.g. Tatsuoka et al. 1995, Bathurst et al. 2002). At the same time, more large earthquakes are recorded around the world and national seismic hazard maps (e.g. USGS 2008, NBCC 2010) are continuously modified to accommodate the most recent major seismic events and to reflect updated seismic hazard levels. Consequently, increasing numbers of reinforced soil retaining walls are constructed in seismically active areas and will be subjected to significant ground motions.

One of the most common approaches for seismic design of reinforced soil retaining walls is to use the Mononabe-Okabe theory and a selected peak ground

acceleration to determine the lateral earth force behind the reinforced soil wall (Bathurst et al. 2002). Reinforcement load is usually determined based on calculated distribution of lateral earth pressure using the tributary area approach (e.g. Bathurst et al. 2002, FHWA 2009, AASHTO 2009). These methods are limited to sites where the peak ground acceleration is not expected to exceed 0.29g. For greater accelerations, sliding block displacement methods have been proposed for reinforced soil walls (e.g. Cai and Bathurst 1996). A recent National Cooperative Highway Research Program report (NCHRP 2008) recommends the use of Newmark's sliding block method to determine the maximum wall displacement under seismic loading. In the original Newmark's method, the reinforced soil mass is assumed as a rigid body, which may not be a reasonable assumption for taller walls. Moreover, displacement methods are limited to internal and external sliding mechanisms of the reinforced mass and do not address other important internal failure mechanisms such as reinforcement over-stressing or pullout.

Due to the shortcomings of the limit-equilibrium methods described above, numerical methods that allow the entire response of a structure to be simulated hold promise as an effective tool to help develop new seismic design guidelines for reinforced soil retaining wall structures. These tools can be used to determine factors of safety against collapse and examine the serviceability of these structures under site-specific seismic loading conditions. Seismic analysis of MSE walls using numerical simulation has been the subject of several past studies (Bathurst and Hatami 2001). A survey of recent studies in this area is given by Hatami and Varnier (2011). In almost all the studies surveyed by the authors, the focus of the work has been on the influence of the MSE wall design (i.e. size, geometry, reinforcement/backfill properties and boundary conditions) on its predicted seismic performance using sample input ground motions. Limited work has been done to investigate the influence of input ground motion characteristics on the seismic performance of MSE walls. Hatami and Bathurst (2001) carried out numerical simulations on a typical modular block (segmental) wall model using six different recorded motions and two harmonic accelerations. They normalized the peak ground acceleration of all input motions to 0.15g and demonstrated that the wall response can still be significantly different due to influences of ground motion frequency characteristics and duration. They also concluded that the random nature of recorded ground motions results in smaller wall response as compared to the response to single-frequency harmonic excitations.

The present paper extends an earlier work by Hatami and Bathurst (2001) and examines the response of a wider range of input ground motion records. The influences of ground motion parameters including their frequency content and intensity on the predicted responses of an MSE wall model are discussed.

NUMERICAL MODELS

The numerical simulations were carried out using the program FLAC 5.0 (Itasca 2005). Figure 1 depicts the FLAC model of a segmental retaining wall used in this study. The wall backfill during construction was simulated using the hyperbolic

model proposed by Duncan et al. (1980) with the properties given in Table 1 representing a compacted sand backfill. The reinforcement layers were assumed to have negligible slippage within the backfill and their tensile modulus was assumed as J = 1000 kN/m. After the wall was constructed, it was subjected to different horizontal accelerograms listed in Table 2. These accelerograms were simultaneously applied to the backfill foundation and far-end boundary based on the assumption that the acceleration was uniform over the backfill depth at a sufficient distance from the wall facing.

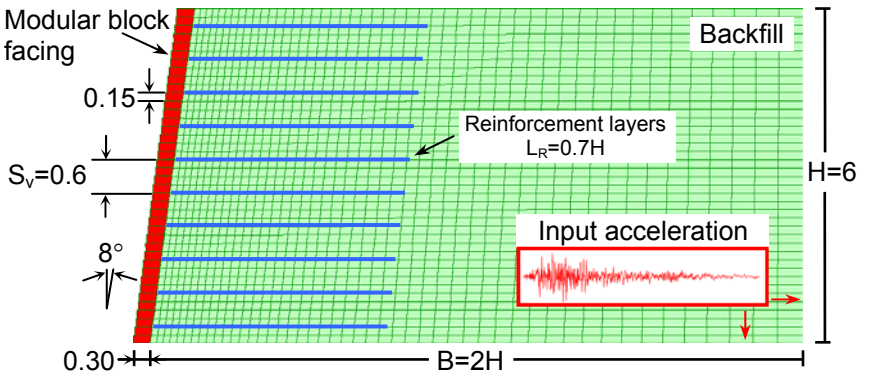

Figure 1. Discretized model of a 6 m-high segmental (modular block) retaining wall at end of construction (Dimensions are in meters).

The numerical model of the type used in this study has been validated against the results of shaking table tests of 1.2 m-high model reinforced soil walls (e.g. El-Emam et al. 2001). Before applying input accelerations to the wall model, its fundamental frequency was determined to be f_1 = 3 Hz based on its free vibration response.

A mass-proportional damping ratio equal to 10% (ξ = 0.1) was assumed for the wall model. However, the Mohr-Coulomb model used for the backfill and the friction between the wall components (i.e. blocks/blocks, blocks/soil and soil/reinforcement) produce additional damping in the system.

The recorded ground motions given in Table 2 were chosen from a database of accelerograms that is classified according to their PGA/PGV ratios (Naumoski et al. 1988, 1993). PGA and PGV denote the peak ground acceleration in g (i.e. acceleration of gravity) and the peak ground velocity of the recorded ground motion in m/s, respectively. The categories VH, NH, NI, NL and NVL in Table 2 stand for Very High, New High, New Intermediate, New Low and, New Very Low PGA/PGV ratios, respectively.

Table 1. Backfill properties

Backfill unit weight, γ	20.4 kN/m^3
Stiffness Properties	
Young's Modulus, E	-
Bulk modulus, K	-
Shear Modulus, G	-
Elastic modulus number, K_e	2000
Bulk modulus number, K_b	2000
Elastic modulus exponent, n	0.25
Bulk modulus exponent, m	0.25
Failure ratio, R_f	0.73
Poisson's ratio, ν	0.2
Strength Properties	
Peak friction angle, Φ	46 °
Cohesion, c	0
Dilatation angle, ψ	6 °

Table 2. Properties of earthquake records used in the current study

Record			No. of data points	Duration				Intensity (1)				Frequency		Soil Cond.
No.	Naumoski et al.			t	t_T	t_d	t_d*	PGA(1)	PGV(1)	PGV_n(2)	I_{MA}(2)	f_g	PGA/ PGV	
	1998	1993		sec	sec	sec	sec	g	m/s	m/s	m^3/s^{-5}	Hz	g.s/m	
1	H2	NH2	2202	0.02	44.04	6.74	2.90	0.434	0.255	0.088	0.047	2.87	1.70	Rock
2	H3	NH3	1993	0.02	39.86	3.24	1.60	0.105	0.046	0.066	0.082	6.98	2.28	Rock
3	H4	NH4	2039	0.02	40.78	5.70	2.98	0.085	0.051	0.090	0.113	3.54	1.67	Stiff Soil
4	H5	NH5	2548	0.02	50.96	2.24	1.72	0.146	0.072	0.074	0.048	2.48	2.03	Rock
5	H7	NH7	612	0.02	12.24	3.52	2.66	0.084	0.044	0.079	0.114	5.27	1.91	Rock
6	H9	NH(3)	1851	0.02	37.02	12.60	6.34	0.146	0.085	0.087	0.117	4.93	1.72	Rock
7	H11	VH(3)	853	0.02	17.06	4.40	2.34	0.151	0.059	0.059	0.058	7.18	2.56	Stiff Soil
8	H12	NH13	1400	0.02	28.00	5.82	4.16	0.146	0.06	0.062	0.067	2.91	2.43	Stiff Soil
9	H14	VH15	578	0.02	11.56	5.44	4.00	0.042	0.016	0.057	0.078	6.45	2.63	Rock
10	I3	NI3	2719	0.02	54.38	30.54	19.76	0.156	0.157	0.151	0.242	1.37	0.99	Rock
11	I6	NI6	3259	0.02	65.18	11.98	6.60	0.15	0.149	0.149	0.188	1.90	1.01	Rock
12	I12	NI11	3000	0.02	60.00	28.06	19.20	0.078	0.068	0.131	0.229	0.73	1.15	Stiff Soil
13	I14	NI13	6001	0.01	60.01	14.80	10.90	0.105	0.116	0.166	0.174	1.55	0.91	Rock
14	L4	NVL5	1264	0.02	25.28	11.66	9.58	0.101	0.193	0.287	0.265	0.90	0.52	Stiff Soil
15	L6	NL2	2088	0.02	41.76	15.06	9.58	0.129	0.186	0.216	0.157	3.39	0.69	Stiff Soil
16	L9	NL3	2865	0.02	57.30	15.86	10.52	0.119	0.173	0.218	0.147	0.37	0.69	Rock
17	L10	NL(3)	4107	0.02	82.14	17.64	12.20	0.106	0.17	0.241	*0.260*	0.45	0.62	Stiff Soil
18	L12	NL15	4350	0.02	87.00	40.16	35.78	0.205	0.275	0.201	0.239	0.69	0.75	Stiff Soil
19	L14	NL6	3841	0.01	38.41	23.59	21.95	0.052	0.074	0.213	0.208	0.85	0.70	Rock
20	S1		400	0.025	10.00	2.15	2.025	0.15	0.08	0.080	0.300	3	1.88	-
21	S2		480	0.013	6.00	2.15	2.100	0.15	0.04	0.040	0.299	6	3.75	-

Notes: (1) The original PGA and PGV values correspond to the records before they were scaled to PGA = 0.15g; (2) Peak Ground Velocity, PGV_n, and modified Arias Intensity, I_{MA}, are reported for the scaled records; (3) H9, H11, and L10 do not appear in the classification reported by Naumoski et al. (1993). They were classified in the New High, Very High, and the New Low categories, respectively, based on their PGA/PGV ratios.

The two sinusoidal input motions are defined by $\ddot{u}_g(t) = \sqrt{\beta e^{-\alpha t} t^{\zeta}} \sin(2\pi f_g t)$ (Itasca 2005), where t is time, f_g is the frequency of base acceleration, and α, β and ζ are constants equal to 5.5, 31 and 12, respectively. All input ground motions were scaled to PGA = 0.15g in order to examine the influences of other ground motion characteristics on the wall response. In the intensity section of Table 2, PGV_n is the peak ground velocity of the record after scaling to PGA = 0.15g. The new duration, t_d*, and the modified Arias Intensity, I_{MA}, are defined as:

$$t_d^* = \int_0^{t_T} \ddot{u}_g^4(t)dt \quad ; \quad I_{MA}(\xi) = \frac{\cos^{-1}(\xi)}{g\sqrt{1-\xi^2}} \int_0^{t_T} \ddot{u}_g^4(t)dt$$

The numerical simulations were carried out using the T_d*, which is equal to t_d* increased by half a second at the beginning and at the end of shaking in order to include a quiet zone (Hatami and Varnier 2011).

RESPONSE OF THE RETAINING WALL TO GROUND MOTION

The responses of the segmental retaining wall model to the input ground motions are investigated in terms of its facing lateral displacement, lateral earth pressure and reinforcement load.

Wall lateral displacement. Figure 2 shows the histories of facing lateral displacement at the top of the wall subjected to a selection of input motions listed in Table 2. To avoid clutter in the figure, results are shown for only two records in each PGA/PGV category and the harmonic waves. The selected records resulted in the smallest and largest magnitudes of wall lateral displacement at end of shaking within each category.

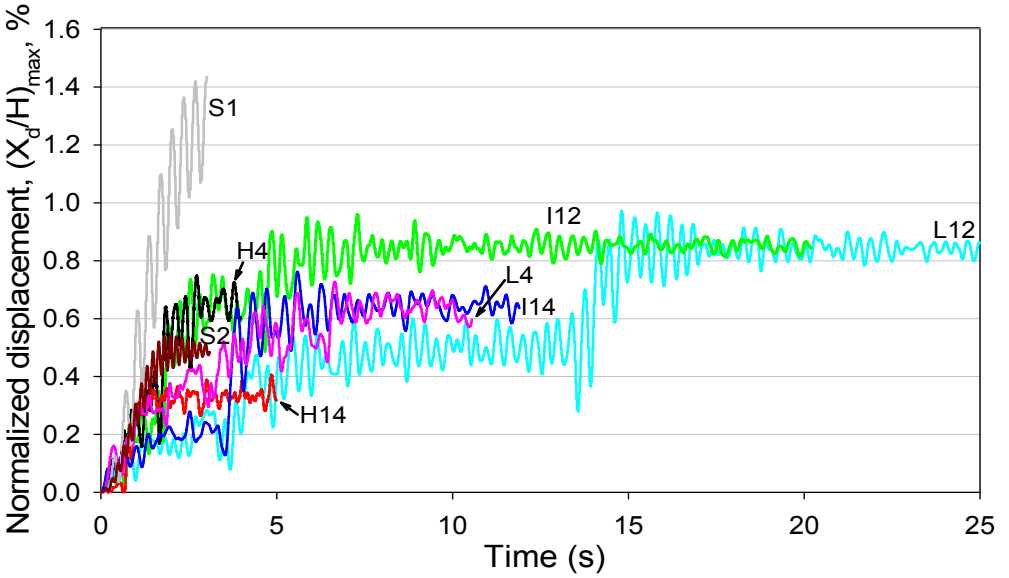

Figure 2. History of predicted facing lateral displacement at the top of the 6 m-high wall subjected to selected input ground motions (all scaled to PGA = 0.15g).

Results shown in Figure 2 clearly indicate that input ground motions with the same PGA but otherwise different characteristics can produce significantly different wall response results. For instance, in the High PGA/PGV category, constructive influences of greater I_{MA} (45%), PGV_n (58%), and closer frequency ratio to unity of Record H4 ($f_{r_H4} = f_g/f_1 = 1.12$ vs. $f_{r_H14} = 2.13$) resulted in significantly greater (i.e. approximately twice as large) wall displacement response as compared to that of Record H14. Meanwhile, the strong ground motion duration of Record H4 is smaller than that of Record H14. Similarly, input wave S1 with $f_{r_S1} = f_{g_S2}/f_1 = 0.99$ and a high PGV_n value resulted in significantly greater wall response as compared to that of input wave S2 with $f_{r_S2} = 1.98$ and a lower PGV_n. Overall, Intermediate and Low PGA/PGV records resulted in higher wall displacements as a consequence of their greater intensity and velocity (energy) characteristics.

Reinforcement load and lateral earth pressure. Figure 3 shows end-of-shaking (EOS) distributions of (a) maximum reinforcement load and (b) connection load in the 6 m-high wall subjected to all recorded motions listed in Table 2. Figure 4 shows distributions of corresponding lateral earth pressures over the height of the wall. The magnitudes of static, incremental seismic and total lateral earth pressure are shown in Figures 4a, 4b and 4c, respectively. Theoretical distributions of horizontal active

(Coulomb) and at-rest lateral earth pressure at end of construction are also plotted in Figure 4a. Distributions of incremental seismic lateral earth pressure according to NCMA (2009) are plotted in Figure 4b. The corresponding total lateral earth pressures are plotted in Figure 4c. The range bars in Figures 3 and 4 show the maximum, minimum and the mean values of the reinforcement load and the lateral earth pressure at selected elevations (i.e. top and bottom reinforcement layers, 2/3 and 1/3 of the wall height). The range bars are shown at slight offsets from the target elevations in order to make them easier to follow.

Results shown in Figure 3 indicate that maximum reinforcement and connection loads occur near the middle of the wall height (i.e., H/2) independently of the input ground motion. Significantly lower reinforcement and connection loads are observed at the top of the wall as a consequence of the lower lateral earth pressure and at the bottom of the wall due to the influence of the foundation. The load distributions shown in Figure 3 are consistent with those reported by Bathurst and Hatami (1998) (for models with fixed toe conditions) and Ling et al. (2005).

Furthermore, results shown in Figure 3 and Figure 4 indicate a clear dependence of the wall lateral earth pressure and reinforcement load response on the ground motion characteristics apart from their PGA value. Specifically in these figures, seismic earth pressure responses of the wall when subjected to input ground motions in different PGA/PGV categories are convincingly different from one another. The reinforcement load and lateral earth pressure are both greater for records with Intermediate and Low PGA/PGV ratios as compared to those due to the High PGA/PGV ratio category. In the case of Intermediate PGA/PGV category, the constructive effect of the proximity between the ground motion and wall frequencies and greater input energy of the records has resulted in the greatest wall response among the PGA/PGV categories for the 6 m-high wall model examined.

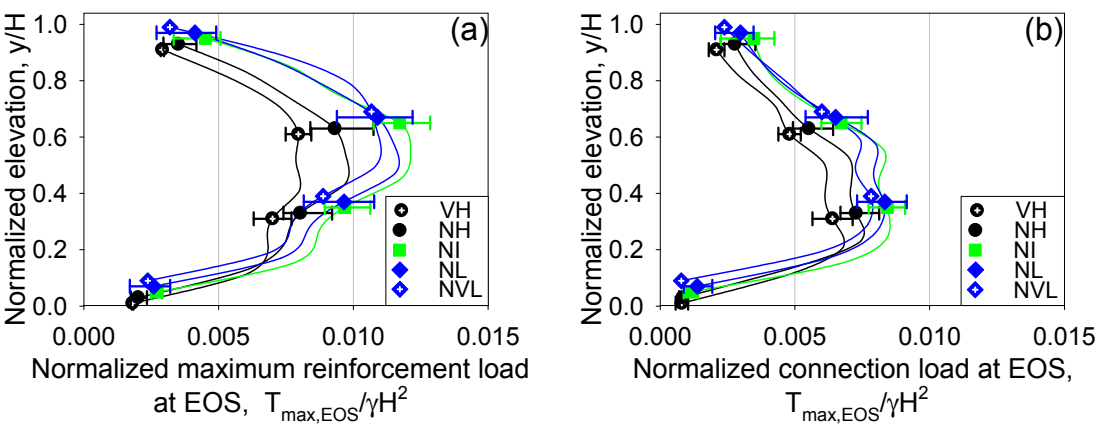

Figure 3. Distribution of (a) maximum reinforcement load and (b) connection load in the 6 m-high wall at end of shaking subjected to recorded ground motions listed in Table 2.

Results shown in Figure 4a indicate that the lateral earth pressure behind the facing of the 6 m-high segmental wall approaches an active state at the end of

construction prior to shaking. Results shown in Figure 4b indicate that both the distribution and magnitudes of the incremental (seismic) lateral earth pressure behind the wall facing can be significantly different (and in the case shown, greater) than those proposed in the current design approaches (e.g. NCMA 2009). Similarly, total lateral earth pressures resulting from all input ground motions examined are different from the design values as shown in Figure 4c regardless of their PGA/PGV category. The design values especially underestimate the predicted lateral earth pressure toward the bottom of the wall.

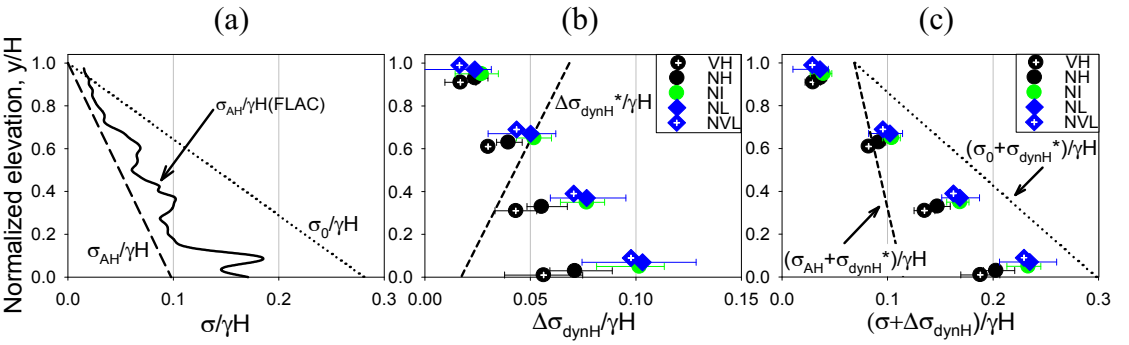

* Based on NCMA (2009)

Figure 4. Distributions of the normalized lateral earth pressure behind the facing column for the 6 m-high wall: (a) Static component, (b) Incremental seismic component, and (c) Total pressure distribution

CONCLUSIONS

Results of this study show that seismic response of reinforced soil walls is a function of several ground motion characteristics including their intensity and frequency content. Therefore, using a single-valued peak ground acceleration could lead to inaccurate prediction of the wall response and hence a potentially unsafe design. Responses of reinforced soil walls to ground motions in different PGA/PGV ratio categories were found to be markedly different. Therefore, PGA/PGV ratio of the ground motion could be considered as a possible input parameter for the design of reinforced soil walls.

REFERENCES

AASHTO (2009). LRFD Bridge Design Specifications, 4th Edition, (Interim to 2007 Edition), Washington, D.C.

Bathurst R.J. and Hatami K. (1998). "Seismic response analysis of a geosynthetic-reinforced soil retaining wall." *Geosynthetics International*, 5(1-2), 127-166.

Bathurst R.J. and Hatami K. (2001). "Review of numerical modeling of geosynthetic reinforced-soil walls". *10th International Conf. on Computer Methods and Advances in Geomechanics*, Tucson, AZ, USA, January 2001, 2, 1223-1232.

Bathurst R.J., Hatami K. and Alfaro M.C. (2002). "Geosynthetic-reinforced soil walls and slopes-Seismic aspects." In Shukla, S.K., ed., Geosynthetics and their Applications, Thomas Telford, 327-392.

Cai Z. and Bathurst R.J. (1996). "Seismic-induced permanent displacement of geosynthetic reinforced segmental retaining walls." *Can. Geo. J.*, 31, 937-955.

Duncan J.M., Byrne P., Wong K.S. and Mabry P. (1980). "Strength stress-strain and bulk modulus parameters for finite-element analysis of stresses and movements in soil masses." Report UCB/GT/80-01, UC Berkeley, CA, USA.

El-Emam M.M., Bathurst R.J., Hatami K. and Mashhour M.M. (2001). "Shaking table and numerical modelling of reinforced soil walls." *International Symposium on Earth Reinforcement*, Fukuoka, Kyushu, Japan, 329-334.

FHWA (2009). "Design and construction of mechanically stabilized earth walls and reinforced soil slopes", Pub. No. FHWA-NHI-10-024, FHWA GEC 011, v. 1.

Hatami K and Bathurst RJ, (2001). "Investigation of seismic response of reinforced-soil retaining walls." *4th International Conference on Recent Advances in Geotechnical Earthquake Engineering and Soil Dynamics*, March 2001, San Diego, CA, USA, Paper no. 7.18.

Hatami K. and Varnier J.B. (2011). "Influence of ground motion characteristics on seismic response of MSE walls." *Soil Dynamics and Earthquake Engineering*, (In Review).

Itasca Consulting Group (2005). "FLAC - Fast Lagrangian Analysis of Continua." Version 5.0, Itasca Consulting Group, Minneapolis, MN, USA.

Ling H.I., Liu H. and Mohri Y. (2005). "Parametric studies on the behavior of reinforced soil retaining walls under earthquake loading." *Journal of Engineering Mechanics*, ASCE 131(10): 1056-1065

National Cooperative Highway Research Program, Report 611, Seismic Analysis and Design of Retaining Walls, Buried Structures, Slopes, and Embankements (2008). Transportation Research Board, Waschington, D.C.

Naumoski, N., Tso, W.K. and Heidebrecht, A.C. (1988). "A selection of representative strong motion earthquake records having different A/V ratios." EERG Report 88-01, McMaster University, Hamilton, Ontario, Canada.

Naumoski, N., Tso, W.K. and Heidebrecht, A.C. (1993). "Representative ensembles of strong motion earthquake records." EERG Report 93-01, McMaster University, Hamilton, Ontario, Canada.

NBCC (2010). "National building code of Canada 2010", http://www.nrc-cnrc.gc.ca/eng/ibp/irc/codes/codes-guides.html.

NCMA (2009). Design Manual for Segmental Retaining Walls, 3rd Edition.

Tatsuoka F., Koseki J. and Tateyama M. [1995]. "Performance of geogrid-reinforced soil retaining walls during the Great Hanshin-Awaji Earthquake, January 17, 1995." *Proceedings of the First International Conference on Earth quake Geotechnical Engineering*, IS-Tokyo '95: 55–62.

USGS (2008). http://earthquake.usgs.gov/hazards/products/

Performance Based Assessment of Dynamic Soil-Structure Interaction Effects on Seismic Response of Building Frames

Behzad Fatahi[1], Hamid Reza Tabatabaiefar[2], Bijan Samali[3]

[1]Lecturer of Geotechnical Engineering (PhD, CPEng), Centre for Built Infrastructure Research, University of Technology Sydney (UTS), NSW, 2007, Australia: Phone: +612 9514 7883; Email: behzad.fatahi@uts.edu.au

[2]PhD Candidate, Centre for Built Infrastructure Research, University of Technology Sydney (UTS), NSW, 2007, Australia: Phone: +612 431966224; Email: SeyedHamidReza.Tabatabaiefar@eng.uts.edu.au

[3]Professor of Structural Engineering (PhD, MIEAust), Centre for Built Infrastructure Research, University of Technology Sydney (UTS), NSW, 2007, Australia: Phone: +612 9514 9942; Email: bijan.samali@uts.edu.au

ABSTRACT

Soil–Structure Interaction (SSI) has progressed rapidly in the second half of 20th century stimulated mainly by requirements of the nuclear power and offshore industries to improve the seismic safety. In this study, a fifteen storey moment resisting building frame is selected in conjunction with three different soil deposits with shear wave velocity less than 600m/s. The design sections are defined after applying dynamic nonlinear time history analysis based on inelastic design procedure using elastic-perfectly plastic behaviour of structural elements. These frames are modelled and analysed employing Finite Difference approach using FLAC 2D software under two different boundary conditions, namely fixed-base (no soil-structure interaction), and considering soil-structure interaction. Fully nonlinear dynamic analyses under the influence of different earthquake records are conducted and the results of inelastic behaviour of the structural model are compared. Variations of the shear modulus ratio with the shear strain are included in the nonlinear dynamic analysis. The results indicate that the inter-storey drifts of the structural model resting on soil types De and Ee (according to the Australian standard) substantially increase when soil-structure interaction is considered for the above mentioned soil types. Performance levels of the structures change from life safe to near collapse when dynamic soil-structure interaction is incorporated. Therefore, the conventional inelastic design procedure excluding SSI is no longer adequate to guarantee the structural safety for the building frames resting on soft soil deposits. Design engineers need to address the effects of dynamic SSI precisely in their design especially for construction projects on soft soils.

INTRODUCTION

Recent improvements in seismological source modelling, analysis of travel path effects, and characterization of local site effects on strong shaking have led to significant advances in both code-based and more advanced procedures for evaluating seismic demand for structural design. However, a missing link has been an improved and empirically verified treatment of soil-structure interaction (SSI). *Soil-Structure*

Interaction (SSI) refers to the process, in which, the response of the soil influences the motion of the structure and response of the structure influences the motion of the soil.

The seismic excitation experienced by structures is a function of the earthquake source, travel path effects, local site effects, and soil-structure interaction (SSI) effects. The result of the first three of these factors is a ‘‘free-field’’ ground motion. Structural response to free-field motion is influenced by SSI. In particular, accelerations within structures are affected by the flexibility of foundation support and variations between foundation and free-field motions. Consequently, an accurate assessment of inertial forces and displacements in structures can require a rational treatment of SSI effects.

The importance of SSI both for static and dynamic loads has been well established and the related literature spans at least 30 years of computational and analytical approaches to solving soil–structure interaction problems. Since 1990s, great effort has been made for substituting the classical methods of design by the new ones based on the concept of performance-based seismic design. Also, the necessity of estimating the vulnerability of existing structures and assessing reliable methods for their retrofit have greatly attracted the attention of engineering community in most seismic zones throughout the world. To have a better judgment on the structural performance, a comprehensive study with the ability of predicting the level of damage to the structure due to the design earthquake should be conducted. Several researchers (e.g. Veletsos and Meek, 1974; Kobayashi et al., 1986; Gazetas and Mylonakis, 1998; Wolf and Deeks, 2004; Galal and Naimi, 2008) studied structural behaviour of un-braced structures subjected to earthquake under the influence of soil-structure interaction. Examples are given by Gazetas and Mylonakis (1998) including evidence that some structures founded on soft soils are vulnerable to SSI. According to available literature, generally when the shear wave velocity of the supporting soil is less than 600 m/s, the effects of soil-structure interaction on the seismic response of structural systems, particularly for moment resisting building frames, are significant. Thus, for ordinary building structures, the necessity of a better insight into the physical phenomena involved in SSI problems has been heightened. In this study, SSI effects are investigated on the performance level of a fifteen storey moment resisting building on various soil types including soil types Ce, De, and Ee according to Australian standards (See Table 2).

PERFORMANCE-BASED ENGINEERING ASSESSMENT

Practising civil engineers usually use inelastic analysis methods for the seismic evaluation and design of existing and new buildings. The main objective of inelastic seismic analysis is to predict the expected behaviour of the structure against future probable earthquakes more precisely. This has become increasingly important with the emergence of performance-based engineering (PBE) as a technique for seismic evaluation and design using performance level prediction for safety and risk assessment

(ATC-40, 1996). Since structural damage implies inelastic behaviour, traditional design and analysis procedures based on linear elastic techniques can only predict the performance level implicitly. By contrast, the objective of inelastic seismic analysis method is to directly estimate the magnitude of inelastic deformations and distortions (performance level). *Performance levels* describe the state of structures after being subjected to a certain hazard level and are classified as: fully operational, operational, life safe, near collapse, or collapse (Vision 2000, 1995; FEMA 273/274, 1997). Overall lateral deflection, ductility demand, and inter-storey drifts are the most commonly used damage parameters. The above mentioned five qualitative performance levels are related to the corresponding quantitative maximum inter-storey drifts (as a damage parameter) of: <0·2%, <0·5%, <1·5%, <2·5%, and >2·5%, respectively.

CHARASTRISTICS OF THE EMPLOYED MODELS

In this study, a fifteen storey concrete moment resisting building frame resting on a shallow foundation (4 meters in width and 12 meters in length) is selected in conjunction with three soil types with the shear wave velocity less that 600m/s comprising one cohesionless and two cohesive sample, representing classes Ce, De and Ee, according to classification criteria listed in Section 4 of AS 1170.4 (Earthquake action in Australia). As it is a plane strain problem, shallow foundation width has been taken into account to calculate moment of inertia of the footing.

Structural sections are designed according to AS3600-2001 (Australian Standard for Concrete Structures) after undertaking inelastic dynamic analysis under influence of four different earthquake ground motions, as a fixed base model. The characteristics of the earthquake ground motions are tabulated in Table 1. Performance level of the structural model is considered as life safe level in this design indicating the maximum inter-storey drifts of the model being less than 1.5%.

Table 1. Earthquake ground motions used in this study

Earthquake	Country	Year	PGA (g)	Mw (R)
Northridge	USA	1994	0.843	6.7
Kobe	Japan	1995	0.833	6.8
El Centro	USA	1940	0.349	6.9
Hachinohe	Japan	1968	0.229	7.5

Characteristics of the utilised soils are shown in Table 2. The subsoil properties have been extracted from actual in-situ and laboratory tests (Rahvar 2005, 2006a, 2006b). Therefore, these parameters have merit over the assumed parameters which may not be completely conforming to reality. It is assumed that watertable is well below the ground surface. The shear wave velocity, shown in Table 2, has been obtained from down-hole test, which is a low strain in-situ test. This test generates a cyclic shear strain of about 10^{-4} percent where the resulting shear modulus is called G_{max}. In the

event of an earthquake, the cyclic shear strain amplitude increases and the shear strain modulus and damping ratio which both vary with the cyclic shear strain amplitude, change relatively. Vucetic and Dobry (1991) for cohesive soils and Seed and Idriss (1986) for cohesionless soils represented ready to use charts indicating the variations of the shear modulus ratio with the shear strain in nonlinear dynamic analysis as well as material damping ratio versus cyclic shear strain, adopted in this study.

Table 2. Geotechnical characteristics of the utilised soils in this study

Soil Type (AS1170)	Shear wave velocity Vs (m/s)	Unified classification	Shear Modulus *Gmax* (kPa)	Poisson Ratio	SPT	Plastic Index (PI)	C' (kPa)	ϕ' (Degree)	Reference
Ce	600	GM	623409	0.28	N>50	-	5	40	Rahvar (2005)
De	320	CL	177304	0.39	30	20	20	19	Rahvar (2006a)
Ee	150	CL	33100	0.40	6	15	20	12	Rahvar (2006b)

DYNAMIC ANALYSIS OF SOIL-STRUCTURE INTERACTION

Several efforts have been made in recent years in the development of analytical methods for assessing the response of structures and supporting soil media under seismic loading conditions. There are two main analytical procedures for dynamic analysis of soil-structure systems under seismic loads, equivalent-linear and fully nonlinear methods. According to Byrne et al. (2006), the equivalent-linear method is not appropriate to be used in dynamic soil-structure interaction analysis as it does not capture directly any nonlinear effects because it assumes linearity during the solution process. In addition, strain-dependent modulus and damping functions are only taken into account in an average sense, in order to approximate some effects of nonlinearity (e.g. damping and material softening). Byrne et al. (2006) concluded that the most appropriate method for dynamic analysis of soil-structure system is *fully nonlinear method.* The method correctly represents the physics associated with the problem and follows any stress-strain relation in a realistic way. Considering the mentioned priorities and capabilities of the fully nonlinear method for dynamic analysis of soil-structure systems, this method is used in this study in order to attain rigorous and more reliable results. Using fully nonlinear method for dynamic analysis, enable us to apply Vucetic & Dobry (1991) and Seed and Idriss (1986) charts directly to the model and take soil nonlinearity into account in an accurate and realistic way. Direct Method is employed in this study and Finite Difference software, FLAC2D, is utilised to model the soil-structure system and to solve the equations for the complex geometries. On the other hand, inelastic seismic analysis and design method is employed in this study to directly estimate the performance level of the structural system. In the inelastic analysis and design of a structure, the ultimate load of the structure as a whole is regarded as the

design criterion. This method is rapid and provides a rational approach for the analysis of the structure. It also provides striking economy as regards the weight of structural material since the sections required by this method are smaller in size than those required by the method of elastic analysis. The plastic moment is used to determine the plastic behaviour of the column–beam element.

NUMERICAL SIMULATION OF SOIL - STRUCTURE SYSTEM

In this study, fully nonlinear time history dynamic analysis has been employed using FLAC 2D to define inelastic seismic response of the concrete moment resisting frame under the influence of SSI. Dynamic analysis is carried out for two different systems: (i) fixed-base structure on the rigid ground (Figure 1), and (ii) structure considering subsoil using direct method of SSI analysis as the flexible base model (Figure 2). The following aspects have been incorporated in the dynamic time history analysis of the study:

- Fully nonlinear behaviour of the subsoil including material nonlinearity (relationship between soil stiffness and material damping ratio versus cyclic shear strain proposed by Vucetic and Dobry (1991) and Seed and Idriss (1986)) and geometric nonlinearity (large strains)
- Inelastic (elastic-perfectly plastic) behaviour of structural system (according to ATC-40, 1996) and geometric nonlinearity of the structure (large displacements)
- Cracked sections for the reinforced concrete section by using cracked section coefficients according to Section 10.11.1 of ACI318.2002

The soil-structure model (Figure 2) comprises beam elements to model structural elements, two dimensional plane strain grid elements to model soil medium, fixed boundaries to model the rigid bed rock, absorbent boundaries (viscous boundaries) to avoid reflective waves produced by soil lateral boundaries, and interface elements to simulate frictional contact and probable slip due to seismic excitation. According to Rayhani and Naggar (2008), horizontal distance between soil boundaries is assumed to be five times the structure width, and the bedrock depth is assumed to be 30 m. It should be noted that input of an earthquake motion into FLAC is typically done using either a "rigid base" or a "compliant base." For a rigid base, a time history of acceleration is specified for grid points along the base of the mesh. While simple to use, a potential drawback of a rigid base is that the motion at the base of the model is completely prescribed. In reality, the bedrock acts like a fixed displacement boundary reflecting downward-propagating waves back into the model. In this study, similar to Mejia and Dawson (2006), the bedrock boundary condition has been assumed as rigid. Four different earthquake ground motions (Table 1) are applied to both systems in two different ways. In the case of modelling soil and structure simultaneously using direct method (flexible base), the earthquake records are applied to the combination of soil and structure directly at the bed rock level, while for modelling the structure as the fixed base (without soil), the earthquake records are applied to the base of the structural models.

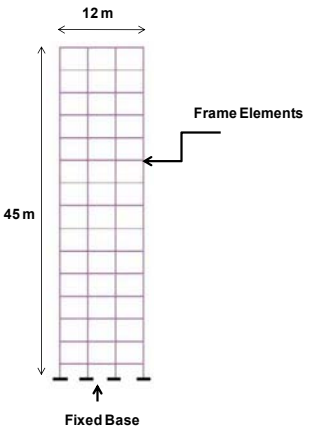

Figure 1. Fixed-base model

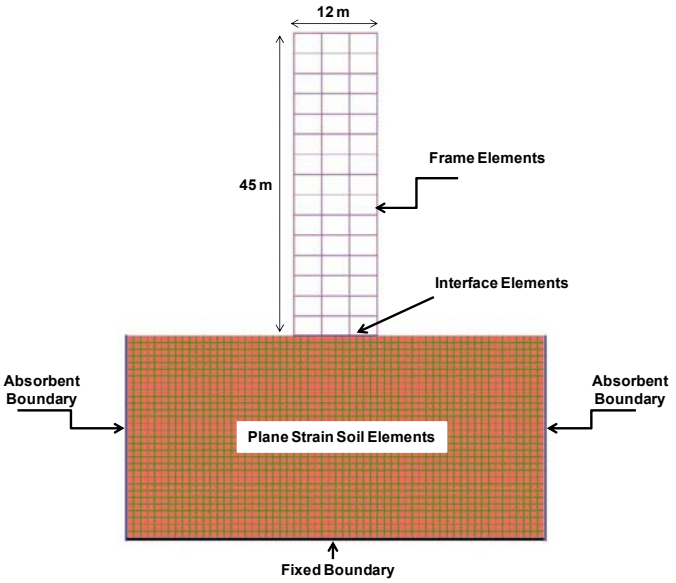

Figure 2. Components of the Soil-Structure model in FLAC

RESULTS AND DISCUSSIONS

The results of the inelastic analyses including the base shear and the inter-storey drifts are determined and compared for the fixed-base and flexible-based models resting on the three different types of soil, so as to clarify the effects of subsoil rigidity on inelastic seismic response of moment resisting frames and their performance levels. According to the results summarised in Table 3, the ratio of base shear of the flexible-base models ($\tilde{V}$) to that of fixed-base (V) in all models are less than one. Therefore, base shear of the structures modelled with soil as flexible-base are always less than the base shear of structures modelled as fixed base. These results have good conformity to Section 5.6.2 of NEHRP-2003 regulations, as in this section, reduction in base shear due to SSI is predicted.

Table3. Base shear ratio of flexible-base to fixed-base models

Earthquake	Fixed-base model	Soil Type Ce		Soil Type De		Soil Type Ee	
	V (kN)	$\tilde{V}$ (kN)	$\tilde{V} / V$	$\tilde{V}$ (kN)	$\tilde{V} / V$	$\tilde{V}$ (kN)	$\tilde{V} / V$
Northridge	441	432	0.979	316	0.716	203	0.461
Kobe	550	533	0.969	391	0.710	258	0.469
Hachinohe	167	158	0.946	123	0.736	63	0.377
El Centro	194	178	0.917	133	0.686	72	0.371

Comparing the inter-storey drifts of fixed-base and flexible-base models resting on soil classes Ce, De, and Ee (Figures 3-6), it is observed that the inter-storey drifts of the flexible base model resting on soil class Ce do not differ much from that of the fixed-base model. As a result, the performance level of the model resting on soil class Ce remains in life safe level.

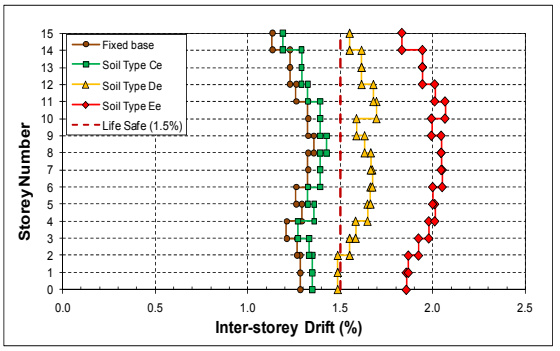

Figure 3. Inelastic inter-story drifts for the fixed base and flexible base models (Northridge earthquake, 1994)

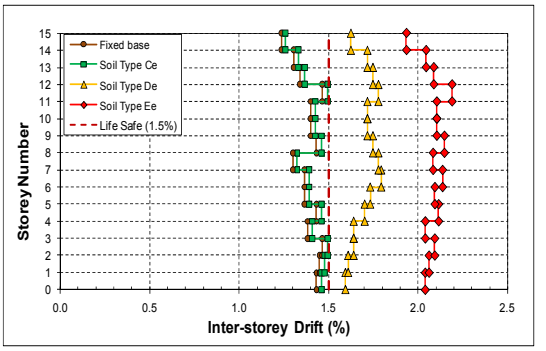

Figure 4. Inelastic inter-story drifts for the fixed base and flexible base models (Kobe earthquake, 1995)

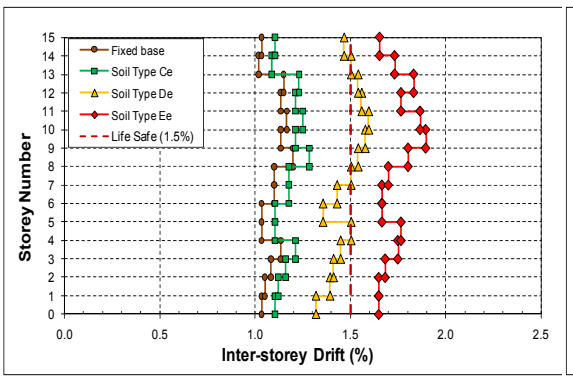

Figure 5. Inelastic inter-story drifts for the fixed base and flexible base models (El Centro earthquake, 1940)

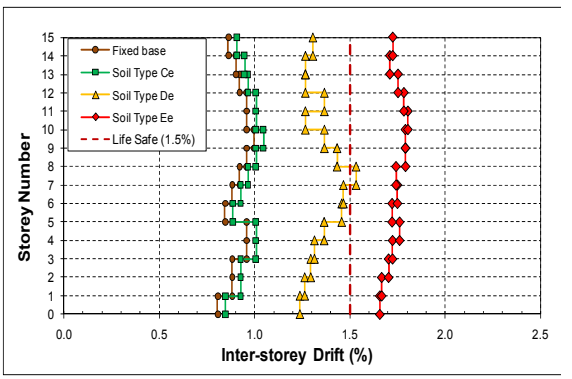

Figure 6. Inelastic inter-story drifts for the fixed base and flexible base models (Hachinohe earthquake, 1968)

However, inter-storey drifts of the flexible base model resting on soil class De increases to more than 1.5% by incorporating dynamic SSI. Thus, performance level of the model resting on soil De changes from life safe level to near collapse level. The situation is more critical for the model on soil class Ee as the performance level of the model substantially increases from life safe to near collapse level as in Figures 3 and 4 the inter-storey drifts exceed. Such a significance change in the inter-storey drifts and subsequently performance level of the model resting on soils De and Ee (especially for soil class Ee) is absolutely dangerous and safety threatening.

CONCLUSION

According to the results of the numerical investigation conducted in this study for the 15 storey concrete moment resisting building frame resting on soil classes Ce, De and Ee, it is observed that performance level of the model resting on soil class Ce does not change substantially and remains in life safe level. Therefore, the effects of soil-structure interaction for inelastic seismic design of moment resisting buildings founded

on soil type Ce is negligible, while performance level of the model resting on soil classes De and Ee substantially increase (especially for soil class Ee) from life safe to near collapse. As a result, considering SSI effects in inelastic seismic design of concrete moment resisting building frame resting on soil classes De and Ee is vital. In brief, the conventional inelastic design procedure excluding SSI is not adequate to guarantee the structural safety for the moment resisting building frames resting on soil classes De and Ee. It is highly recommended to practicing engineers working in high earthquake risk zones, to consider SSI influences in dynamic analysis and design of the above mentioned structures to ensure structures perform safely.

REFERENCES

AS1170.4 (2007). "Earthquake action in Australia". *Standards Australia*, NSW, Australia.

AS3600. (2001). "Concrete Structures". *Standards Australia,* NSW, Australia.

Byrne, P. M., and Wijewickreme, D. (2006). "Liquefaction Resistance and Post-Liquefaction Response of Soils for Seismic Design of Buildings in Greater Vancouver", *59th Canadian Geotechnical Conference,* 1267-1278.

Dutta, C.H., Bhattacharya, K., and Roy, R. (2004). "Response of low-rise buildings under seismic ground excitation incorporating soil-structure interaction", *Soil Dynamic and Earthquake Engineering*, 24(9), 893-914.

FEMA 273/274, (1997). "NEHRP Guidelines for the Seismic Rehabilitation for Buildings". Emergency Management Agency, Washington, D.C.

Galal, K. and Naimi, M. (2008). "Effect of conditions on the Response of Reinforced Concrete Tall Structures to Near Fault Earthquakes", *Struct.Design tall Spec.build,* 17(3), 541-562.

Gazetas, G. and Mylonakis, G. (1998). "Seismic soil-structure interaction: new evidence and emerging issues", *Geotech. Earthquake Eng. and Soil Dynamics,* 10(2), 1119-1174.

Mejia, L. H., and E. M. Dawson. (2006). "Earthquake Deconvolution for FLAC", Proceedings of the 4th International FLAC Symposium, Madrid, Spain, pp. 211-219.

Rahvar. (2005). "Geotechnical and Geophysical Investigations and Foundation Design Report of Musalla Construction Site in Tehran", P. O. Rahvar Pty Ltd., Vol. 1, Tehran, 1-64.

Rahvar. (2006a). "Geotechnical Investigations and Foundation Design Report of Kooh-e-Noor Commercial Building", P. O. Rahvar Pty Ltd., Final Report, Tehran, Iran, 1-69.

Rahvar. (2006b). "Geotechnical Investigations and Foundation Design Report of Mahshahr Train Station", P. O. Rahvar Pty Ltd., Iran Railways Authority, Mahshahr, Iran, 1-42.

Rayhani, M.H. and El Naggar, M.H. (2008). "Numerical Modelling of Seismic Response of Rigid Foundation on Soft Soil", *International Journal of Geomechanics* 8(6), 336-346.

Seed, H. B., and Idriss, I.M., (1969). "Influence of Soil Conditions on Ground Motion During Earthquakes", *J. Soil Mech. Found. Div. ASCE*, 95(2), 99-137.

Veletsos, A.S. and Meek, J. W. (1974). "Dynamic Behaviour of Building-Foundation system", *Journal of Earthquake Engineering and Structural Dynamics*, 3(2), 121-38.

Vucetic, M. and Dobry, R. (1991). "Effects of Soil Plasticity on Cyclic Response", *Journal of Geotechnical Engineering*, 117(1), 89-10.

Vision 2000 Committee. (1995). "*Performance Based Seismic Engineering of Buildings. Structural Engineers Association of California (SEAOC)*", Sacramento, CA.

Effects of Slenderness Ratio on Seismic Behavior of Vertical Micropiles

Gholamreza Saghaee [1] and Reza Noorzad [2]

[1]Département de Génie Civil, Faculté de Génie, Université de Sherbrooke, J1K2R1, Sherbrooke, Québec, Canada; G.Saghaee@usherbrooka.ca
[2]Faculty of Civil Engineering, Nooshirvani University of Technology, Babol, Mazandaran, Iran; rnoorzad@nit.ac.ir

ABSTRACT:

Micropiles are piles with diameter less than 300 millimeters. Because of the small diameter and long length, they may have different behaviour than piles. Since micropiles are used with various length in seismic retrofitting of existing structure; in this study seismic analyses have been performed on two dimensional plain-strain models of vertical micropiles by means of the finite element code PLAXIS to assess the effects of micropile slenderness ratio (D/L) on seismic behavior of vertical micropiles. The results of the analyses showed that the axial force; the shear force and the bending moment decreased by decreasing slenderness ratio. The results show that slender micropiles have good performance under seismic loading.

Keywords: Micropiles, Finite element, Seismic analysis, Length, Interface.

INTRODUCTION

Micropiles are generally defined as piles with the diameter less than 300 millimeters which are constructed by boring holes in the ground, placing reinforcements and filling the void spaces by means of grouting. Substantial advantages in using micropiles have resulted in an increasing applicability of this technology in foundation retrofitting. Some of the advantages associated with micropiles are: minimal disturbance in earth, low excavation volume, simplicity in construction of inclined micropiles, possibility of construction under low overhead space conditions in retrofitting of existing foundations.

Micropiles, which may be regarded as frictional piles showed satisfactory seismic performance during recent earthquakes. Behaviour of the micropiles has not been given yet the needed attention in the literature, and there is an obvious need for further evaluation of seismic performance of these structures. In the lack of comprehensive full-scale performance data, numerical assessment seems to be one of the most suitable alternatives to study the seismic behaviour of micropiles.

This study seeks to evaluate the effect of micropile length on seismic behaviour of micropiles. Commercial finite element code PLAXIS has been used in performing of the dynamic analyses.

NUMERICAL MODELING

The finite element code used in the analyses is capable of modeling two dimensional plain strain and axisymetric conditions. Following the modeling procedure used by Sivakumar et al. (2004) which used plain strain conditions and referring to the studies were conducted by Anandarajah (1990) which showed that two dimensional modeling of soil-structure interactions (SSI) problems agree well with centrifuge model results. In this study, two dimensional plain strain conditions have been selected for the modeling. This procedure has been supported by other researches such as the modeling of grouted soil-cement columns by Omine et al. (1999). The Schematic model configuration and the finite element mesh that have been used in the analyses are shown in figure 1.a and 1.b. To take in to account the micropile cap in the numerical analysis and to eliminate the discontinuity error; the zone above the ground level is meshed.

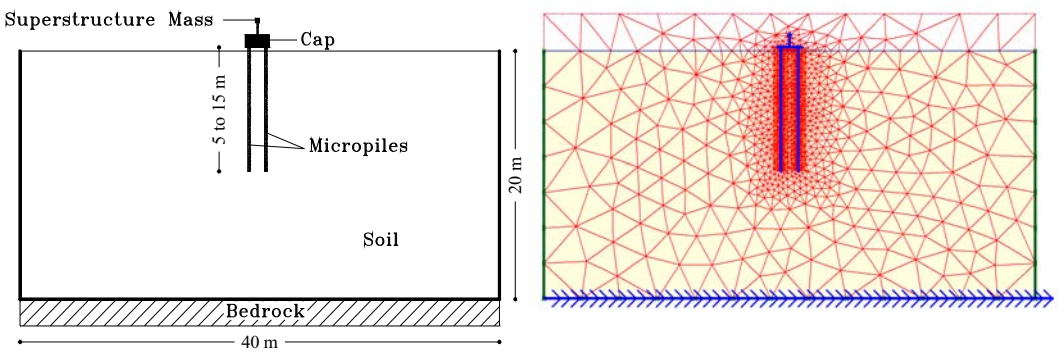

(a) **(b)**

Figure1. a) Schematic model configuration, b) Finite element mesh.

Referring to the literature, the distance from the pile to the vertical boundaries was suggested as 50 times the pile diameter and a length equal to the pile length was suggested for the distance from the pile tip to the bottom of the model (Neves et al. 2001). For the models used in this study, the model depth was selected equal to 20 meters, and due to the use of dynamic boundary conditions at the vertical boundaries, the model length was selected as 40 meters. The distance between micropiles and the cap connection was taken as 1.4 meters.

The soil used in the analyses was Seine River Sand (SRS) which is alluvial deposits of Seine River with a gradation curve shown in figure 2. Mohr-Coulomb elasto-plastic model has been used for the sand. The physical and mechanical properties of the SRS are given in table 1. Two vertical micropiles of the B type (according to FHWA micropile classification) with a diameter of 20 centimeters and CTS-TITAN103/78 steel reinforcements were considered in each model. Table 2 lists parameters which are used for the micropiles.

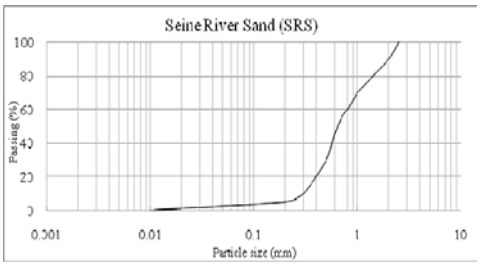

Figure2. Gradation curve of Seine River Sand (SRS)

Table 1. Soil properties used in numerical analysis

Soil	γ (KN/m^3)	E (Mpa)	ν	ϕ (Deg)*	C (Mpa)	ψ (Deg)*
Seine River Sand (SRS)	17.7	74	0.31	40	0	8.4

In this study only vertical micropiles are investigated. Micropiles were modeled by beam elements. This type of element with elastic behavior is available in PLAXIS. Beam elements in the finite element model have three degrees of freedom in each node; two transitional degrees of freedom (U_x and U_y) and one rotational degree of freedom (rotation in the x-y plane: φ_z). Since 15 node elements were used to simulate the soil, beam elements were modeled using 5 node elements. Beam elements are based on Mindlin's beam theory (Bath, 1982). This theory enables deformation in shear in the same manner as in bending. Furthermore, elements are allowed to undergo deformation under axial load. Bending moments and axial forces are derived from stresses in stress points. The five node beam element consists of four Gauss stress points.

One of the important considerations in SSI problems is the soil-structure interface which in this case is the micropile-soil interface (Wehnert and Vermeer, 2004). In order to correctly model this, interface elements were utilized to model the soil-micropile contact surface. In the construction of B-type micropiles, pressure grouting is performed after placing the grout under self weight. Grouting yields a cross section similar to the one shown in figure 3 (Astenbroich, 2001). This figure shows the cross section of a micropile with TITAN-IBO reinforcement which was used in this study. It can be seen in the figure 3 that structural bearing section is actually the combination of the grout and the reinforcement. There are cemented soil and densyfied ground Adjacent to the grout.

Table 2. Properties of the micropile's cross-section which is used in the numerical analysis

Reinforcement Type	D_m (m)	W(Kg/m)	ν	EA (KN)	EI (KN.m^2)
TITAN-IBO (103/78)	0.2	100.41	0.2	1401528	2597.59

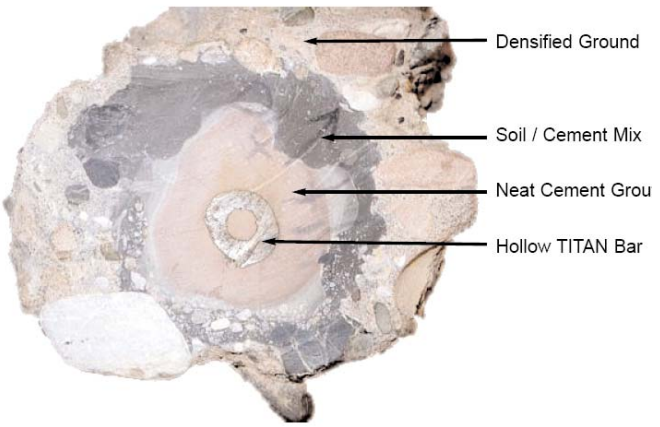

Figure 3. Cross section of exhumed TITAN/IBO Micropiles

The ribbed reinforcement provides adequate bond between grout and the reinforcement. This is why no reports have been given of failure of grout-reinforcement bond (FHWA, 2000). The grout-reinforcement bond strength is not dominant in the bearing capacity of micropiles compared to bond strength of soil-micropile interface. Therefore, it can be neglected in the modeling (Bruce et al. 1985). Thus, the soil-micropile interface may be modeled as cemented soil formed as a result of pressure grouting.

In the present study, the interface parameters are actually those of the sand in the vicinity of the micropile which has improved properties as a result of pressure grouting. Properties of the cemented sand were derived from published data by Dano et al. (2004) who derived these parameters for the Mohr-Coulomb model. They also showed that the Mohr-Coulomb model can be used to model effectively cemented sand. Since grouting adds tensile strength to soil, the tensile strength of cemented sand was employed for interface element in order to enable gapping possibility in the interface. This tensile strength (R_{cut}) was calculated from Equation 1 and was implemented as tensile failure in PLAXIS. In this equation C' and φ' are Cohesion and friction angle respectively. Table 3 lists properties of the interface element.

Table 3. Soil-Micropiles interface element properties used in numerical analysis

Interface Element	γ (KN/m^3)	E (Mpa)	ν	ϕ (Deg*)	C (Mpa)	ψ (Deg*)	R_{cut} (Mpa)
Grouted Seine River Sand (SRS)	201	180	0.31	42	0.18	21.4	0.16

*Degree

$$R_{cut} = \frac{2C' \times Cos\,\phi'}{1 + Sin\,\phi'} \qquad (1)$$

In order to take into account the effect of inertial forces due to superstructure on seismic behavior of micropiles in the numerical modeling; a single degree of freedom (SDOF) superstructure was modeled using a concentrated mass which is located on a zero mass column connected rigidly to the micropile cap. The natural frequency of the SDOF was assumed to be same as natural frequency of a ten-story building with average story height of 3 meters. The natural period of a ten story building can be obtained from the empirical relation $T=0.05H^{3/4}$ (Kramer, 2007). Based on this equation, the natural frequency of the ten-story superstructure is equal to $f_0= f_{SDOF}=1.56$ Hz. Length of the column supporting the superstructure was taken as one meter. The SDOF superstructure mass was proportional to micropiles length. The equal uniform skin shear stress was assumed for all different length. According to this assumption superstructure mass was determined as 8.8, 20 and 31.2 tons for micropiles with 5, 10 and 15 meters length respectively. Micropile cap was modeled as a concrete slab with one meter thickness. Micropiles were connected fixedly to the concrete cap.

Acceleration time history of 01/16/1995 Kobe earthquake at Takarazu station, 090 components was used as seismic loading at the base of the model. Figure 4 shows time histories of the acceleration, velocity and displacement of Kobe earthquake.

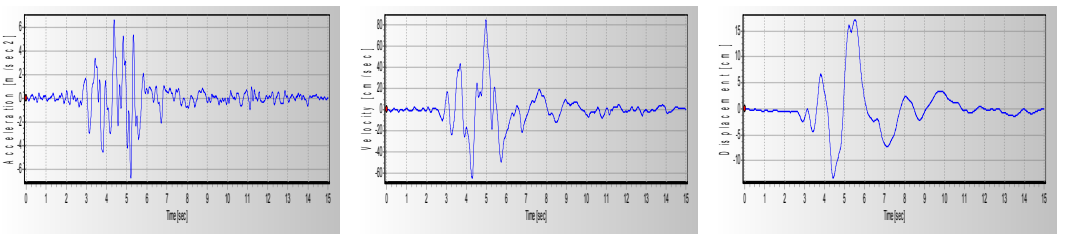

a)Acceleration b) Velocity c)Displacement

Figure 4. Time histories of Kobe earthquake.

The sides and bottom of the model vertical and horizontal boundaries were assigned respectively. Under static conditions, nodes on the vertical boundaries were fixed in the horizontal direction and nodes on the horizontal boundary were fixed in both vertical and horizontal directions. Under dynamic conditions, these boundaries were removed and absorbent boundaries based on formulation given by Lysmer and Kuhlemeyer (1969) were employed for the vertical boundaries, while bedrock was assumed to exist at the horizontal boundary level.

Rayleigh damping was used to model energy dissipation in the material. Damping ratios of 10% and 2% were used for the SRS and the micropile, respectively. These ratios were chosen based on the study has been conducted by Sadek and Shahrour (2004).

DYNAMIC ANALYSIS

Three different lengths were selected to study the effects of micropile slenderness ratio on micropiles seismic response. In this research Slenderness ratio is defined as D/L that D is micropile's diameter and L is the micropile's length. Theses lengths are 5, 10 and 15 meters. Figure 1.a shows an example of finite element model has been employed to perform dynamic analyses. The

amount of superstructure mass has direct effect on micropile internal forces and seismic responses, so to eliminate this effect, all internal forces and response values are divided by superstructure mass. It is called internal force ratio such as the axial force ratio, the shear force ratio and the bending moment ratio.

Figures 5.a and 5.b show the profile of axial force ratio envelope in micropiles due to seismic loading versus X/L for different lengths. Where X is the distance from micropile's head and L is the micropile's length. These profiles approximately indicate that maximum axial force ratio happen at cap-micropile connection level. Micropile tip bearing capacity increased with decreasing the micropile length. Figure 5.c shows the maximum axial force ratio of left and right micropile. It is shown in this figure that increasing the micropile length results in a decrease in the maximum axial force ratio.

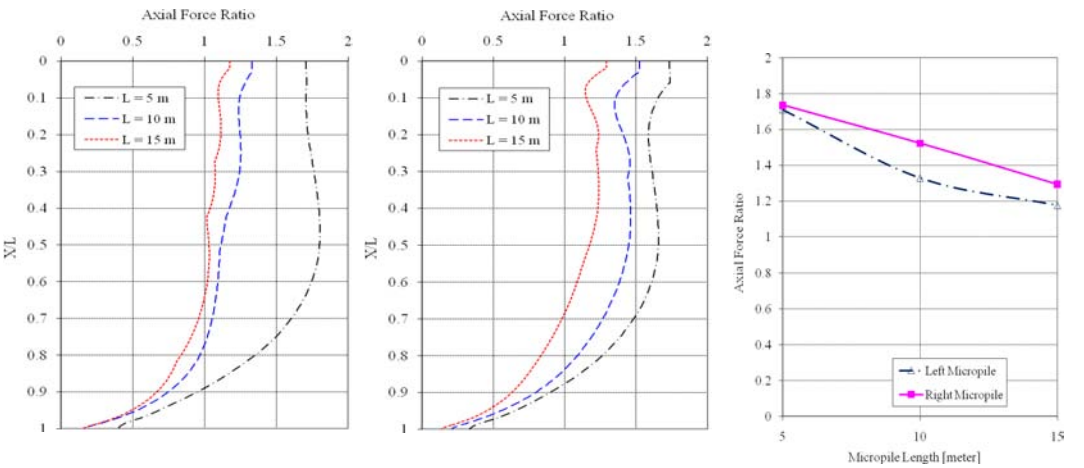

(a) **(b)** **(c)**

Figure 5. a) The envelope of the axial force ratio of the left micropile, b) The envelope of the axial force ratio of the right micropile, c) The m**aximum axial force ratio of the left and right micropiles in different lengths**

The profiles of the shear force ratio envelopes in micropiles under earthquake loading are shown in figures 6.a and 6.b. These profiles show the maximum shear force ratio happens at the micropile cap connection level.

The occurrence of the maximum shear force at the micropile-cap connection level indicates that the inertial forces have a noticeable effect on seismic response of micropiles. A significant point in the graphs 6.a and 6.b is for 10 and 15 meters micropiles. The shear force ratio in depth X/L>0.5 reaches approximately constant value and the shear force ratio increase intensively along the micropile for X/L values below 0.2. It should be noticed that shear force ratio for 5 meters micropile in depth X/L>0.5 is severely larger than two other lengths.

The maximum shear force ratios of the left and right micropiles with different length are given in figure 6.c It can be seen that increasing the micropile length results in a decrease in maximum shear force ratio. The maximum shear force ratio in 15 meters micropiles is averagely 35% of the 5 meters micropiles.

The envelopes of bending moment ratio along micropile under seismic loading are given in figures 7.a and 7.b. According to these figures the maximum bending moment ratio happens at the cap connection level.

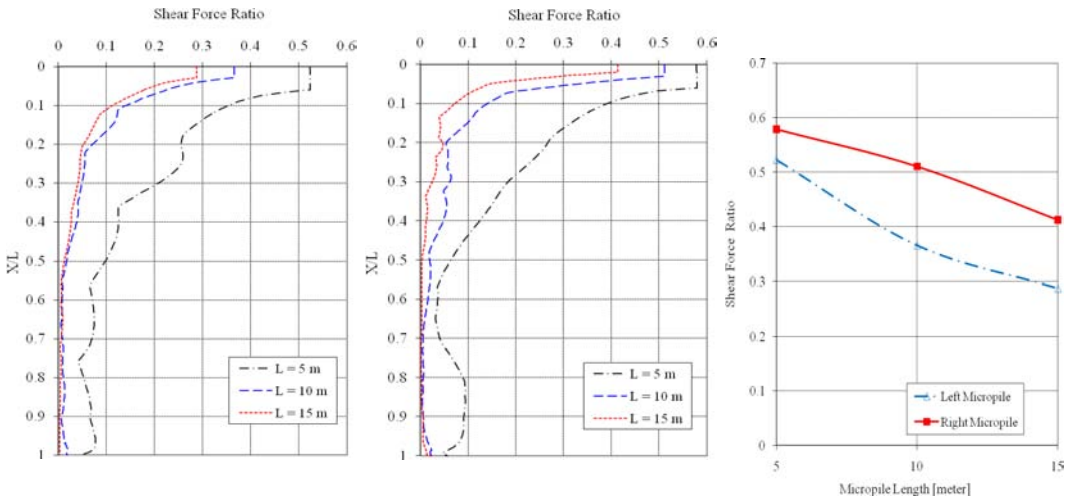

(a) (b) (c)

Figure 6. a) The envelope of the shear force ratio of the left micropile b) The envelope of the shear force ratio of right micropile c) The ma**ximum shear force ratio of the left and right micropiles in different lengths**

Figure 7.c shows the maximum bending moment ratio of left and right micropiles during earthquake loading in different length. It can be seen that the maximum bending moment ratio reduced by use of longer (slender) micropiles. Varying the micropile length from 5 meters to 15 meters decreases the maximum bending moment ratio by a factor of 50%. This reduction may be caused by

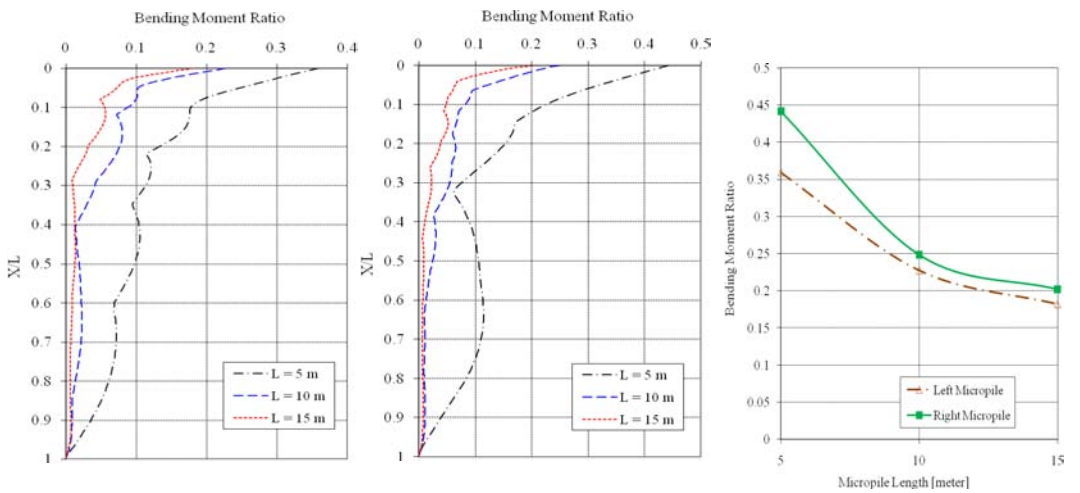

(a) (b) (c)

Figure 7. a) Envelope of bending moment ratio of left micropile b) Envelope of bending moment ratio of right micropile c) Maximum bending moment ratio of left and right micropiles in different lengths.

changing in the micropile structural stiffness in higher slenderness ratio where micropiles operate more flexible. It can be seen that the bending moment at the micropile tip is almost zero in all cases. It means that there is no fixity at the micropile tip in this Seine river sand

Figure 8.a shows the horizontal cap acceleration response ratio due to seismic loading for 5, 10 and 15 meters micropiles. The trend related to time history of horizontal cap acceleration response is almost the same for all selected length but generally maximum cap acceleration response ratio is smaller in the case of micropiles with higher slenderness ratio. By increasing the micropile slenderness ratio, the maximum acceleration response ratio decreases. The amount of deduction in 15 meters micropile is about 30% of the case of 5 meters micropiles.

Figure 8.b shows the horizontal cap displacement response ratio for selected micropiles. The maximum cap horizontal displacement response ratio is smaller in micropiles with higher slenderness ratio. By decreasing the micropile slenderness ratio the maximum horizontal cap displacement response ratio increases. The amount of increase for 5 meters micropile is about 3 of the 15 meters micropiles.

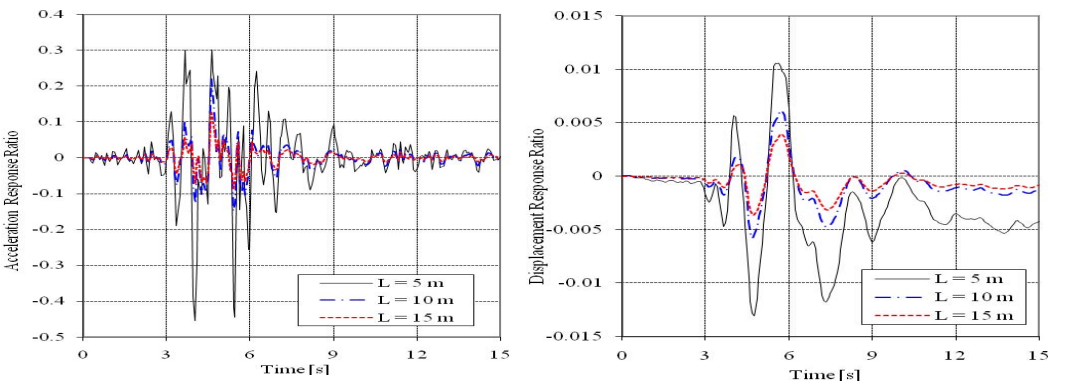

(a) **(b)**

Figure 8. a) The time history of horizontal cap acceleration response ratio for different micropiles length, b) The time history of horizontal cap displacement response ratio for different micropiles length.

CONCLUSION

This paper provides useful insight in to the effect of micropile slenderness ratio on seismic behaviour of vertical micropiles. The results show that using slender micropile in equal side bearing capacity condition, cause decrease in all internal forces and the cap responses induced by earthquake. As a result of this study, it can be suggested that use of more slender micropiles is more suitable in seismic zones.

REFERENCES

Anandarajah, A. (2000). "Fully coupled analysis of a single pile founded in liquefiable sands." *Proceedings of Sessions of Geo-Denver 2000 – Computer Simulation of Earthquake Effects.,* Geotechnical Special Publication, ASCE. 110,117- 131.

Astenbroich, H. (2001). "Micropile reinforcement systems and corrosion protection." *Presented at the ADSC Micropile Seminar,*Charlotte, NC, Nov.2001.

Bruce,D.A., Ingle,J.L. and Jones,M.R. (1985). "Recent examples of underpinning using minipiles." *Proceeding of 2nd International Conference on Structural Faults and Repairs*, London, April 30 - May 2: 13-28.

Dano, C., Hicher, P.Y. and Tailliez, S. (2004). "Engineering properties of grouted sands." *Geotechnical and Geoenviromental Engineering*. ASCE. March: 328-338.

FHWA, (2000). "Micropile design and construction guidelines." *US department of transportation, Federal Highway Administration, priority technologies program, implementational manual*: SA-97-070.

Kramer, S.L. (2007). "Geotechnical earthquake engineering." A.C.E. international publication.ISBN.B131707180.

Lysmer, J. and Kuhlmeyer, R.L. (1969). "Finite dynamic model for infinite media." *Journal of the Engneering Mechanics*. ASCE. Div:859-877.

Mitchell, D., Tinawi, R., and Sexsmith, R.G. (1991). "Performance of bridges in the 1989 Loma Prieta earthquake." *Lessons for Canadian designers. Canadian Journal of Civil Engineering* .18:4: 711-734.

Neves, M., Mestat, Ph., Frank, R. and Degny, E. (2001). "Research on the behavior of bored piles II", *Finite element modeling*. BL-231-055-GB.

Omine, K., Ochiai, H. and Bolton, M.D. (1999). "Homogenization method for numerical analysis of improved ground with cement-treated columns." *Proceedings of the International Conference on Dry Mix Methods for Deep Soil Stabilization*, ISBN 9058091082:161-168.

Sadek, M. and Shahrour, I. (2004). "Three dimensional finite element analysis of the seismic behavior of inclined micropiles." *Soil Dynamics and Earthquake Engineering*. 24:473-485.

Sivakumar Babu, G.L., Srinivasa Murthy, B.R., Murthy, D.S.N. and Nataraj, M.S. (2004). "Bearing capacity improvement using micropiles a case study". ,*Geotechnical Special Publication*, ASCE, 124.692-699.

Wehnert, M. and Vermeer, P.A. (2004). "Numerical analysis of load tests on bored piles." *Proceeding of NUMOG9th*, Ottawa, Canada 1-6.

Multichannel Analysis of Surface Waves (MASW) at the National Geotechnical Engineering Site at Texas A&M University (NGES/TAMU)

R. T. Williams[1] and D. Penumadu[2]

[1]Department of Civil and Environmental Engineering, 223 Perkins Hall, University of Tennessee, Knoxville, TN 37996-2010; PH (865) 332-1705; FAX (865) 974-2669; email: rick@utk.edu
[2] Department of Civil and Environmental Engineering, 223 Perkins Hall, University of Tennessee, Knoxville, TN 37996-2010; PH (865) 974-2503; FAX (865) 974-2669; email: dpenumad@utk.edu

ABSTRACT

We analyzed only the portion of the NGES/TAMU data set suitable for MASW, with a sledge hammer as the source. Lateral variations in Vs are obvious from inspection of the raw data. We selected 4 non-overlapping intervals for analysis, chosen for maximum lateral uniformity within an interval. Analysis of the data led to four dispersion curves, which were inverted to yield 1-D Vs profiles. We present alternative profiles based on different starting models for the inversion, to illustrate the degree on non-uniqueness in the results. The new contributions include the analysis of the MASW data using SurfSeis©, a program that is commercially available from the Kansas Geological Survey, and in parallel using shareware programs from the Seismic Un*x and CPS software packages. This software is freely distributed to the scientific community by the Colorado School of Mines, and St. Louis University, respectively. Here they were combined and adapted for MASW

INTRODUCTION

Multichannel analysis of surface waves (MASW) (Park et al. 1999; Xia et al. 1999) has emerged as a valuable technique for non-invasive seismic testing to evaluate shear-wave velocity (a proxy for shear stiffness) of the soil above bedrock during geotechnical site characterization (Penumadu and Park 2005; Long and Donahue 2007). The method involves analysis of the phase velocity dispersion of Rayleigh waves propagating horizontally, along the ground surface, in order to determine shear wave velocity in the underlying soil. Shear wave velocity (*Vs*) is typically presented in 1-D (*Vs* versus depth) or 2-D (the variation of *Vs* along a depth profile) format. The fundamental framework of MASW is based on the multichannel recording technologies used for seismic exploration (e.g. Telford et al. 1976; Dobrin and Savit 1988), combined with surface wave dispersion methods that originated in the analysis of earthquake data (e.g. Dorman and Ewing 1962).

Numerous case studies of MASW applications have been published. The Kansas Geological Survey has been particularly active, having undertaken numerous geophysical, geological, environmental, and geotechnical engineering projects. Park et al. (1998) and Ivanov et al. (2003) used the method to detect underground anomalies. Miller et al. (1999) used MASW to map weak spots in bedrock. Three-dimensional shear velocity mapping was accomplished using MASW at a military

weapons test site in Arizona (Miller et al. 2003). MASW was used to evaluate the effectiveness of a compaction operation conducted as a soil remediation tool at a construction site (Park and Miller 2003). Ivanov et al. (2006) used MASW to delineate a shallow fault zone and dipping bedrock layers.

Boore and Asten (2008) summarized the many methods that exist for non-invasively obtaining estimates of subsurface shear wave velocities using either active or passive seismic sources. Invasive methods that involve a borehole or seismic cone penetration tests (SCPTu) (De Reister 1971) also exist. Blind comparisons are important for assessing the strengths and weaknesses of the various methods, but few blind comparisons have been reported where multiple non-invasive methods were used. The word "blind" means that the measurements and interpretations for one method, here the MASW method, are performed independently of any other method.

The present MASW study builds upon the blind comparisons that were sponsored by the U. S. Geological Survey (USGS), where the measurements were made mainly at the Coyote Creek Outdoor Classroom (CCOC) (SCVWD 2010) or nearby in the adjacent William Street Park (WSP). The CCOC measurements included both non-invasive and invasive (borehole logs) data (Asten and Boore 2005). Subsequently, Boore (2006) and Boore and Asten (2008) were somewhat critical of the CCOC/WSP test site, on the grounds that it was an easy site, without strong gradients of velocity with depth. They concluded that it would be of great interest to repeat this blind interpretation exercise at other locations with different subsurface velocity variations.

NGES/TAMU TEST SITE

The data for the current blind test was collected at the National Geotechnical Experimentation Site (NGES) at Texas A&M University (TAMU). The TAMU site is well documented. Briaud (1995) described two regions within the NGES, broadly termed "clay" and "sand." A seismic data set was collected using multiple field techniques and made available to the community for interpretation, but investigators were not told whether the seismic data are from the clay region or the sand region. The data consists of raw field files collected from two-sensor (SASW) and multi-sensor (MASW) arrays using a variety of both active and passive seismic sources. Here subsets of this global set of seismic traces were selected for 1-D MASW analysis (Figure 1). MASW in 2-D is generally more desirable, but here 2-D was not possible because only five source positions at relatively wide spacing were available for each geophone deployment.

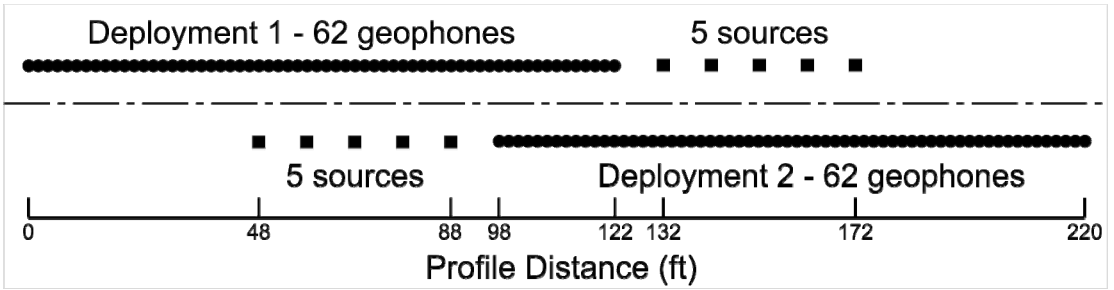

Figure 1. Geophone deployments and source positions. The field measurements were made using English units (ft) rather than SI units, and the data were analyzed in English units.

DATA ANALYSIS

The essence of MASW is the accurate determination of a phase velocity dispersion curve. The dispersion curve is obtained by interpretation of a dispersion image, and is subsequently inverted in terms of a 1-D model of soil layers, where the principal parameter in each layer is *Vs* (Park et al. 1999). Here we focus on the selection of the seismic traces to include in the computation of the dispersion images. As the 1-D model that results from the inversion does not allow for lateral variations in *Vs* it is important to select traces that cover a horizontal interval where the strata are as uniform as possible.

Inspection of the field records (Figures 2 & 3) reveals obvious lateral changes in the subsurface velocities. Considering geophone deployment 1 (Fig. 1), an abrupt change in the apparent slopes of the seismic arrivals can be seen in the vicinity of profile distance 70 ft in Figure 2. In the two intervals from 0 – 68 ft and from 72 – 122 ft, the apparent slopes are more nearly uniform. The first interval spans ~35 seismic traces, the second interval ~26 traces. The traces included in a dispersion image should include one or the other of these two intervals, but not both. Thus, the data from deployment 1 are divided for analysis into two subsets, leading to two dispersion images, which may yield different results for *Vs* in the soil layers. Here, two dispersion images and two corresponding *Vs* models were obtained from deployment 1 data, and a further two *Vs* models were obtained from the deployment 2 data.

The seismic data (e.g. Figure 2) are transformed to dispersion images according to the following procedure. (1) A tau-p transform is applied to the seismic traces, which changes the distance (geophone offset) axis to ray parameter p. (2) As the geophones are arrayed horizontally along the surface, the slowness S is the "horizontal slowness" of Aki and Richards (2002, p. 407), which is the same as the ray parameter p in the tau-p transform. Thus the p axis from the tau-p transform can be inverted to change the variable from the ray parameter p to phase velocity C. (3) A Fourier transform is applied, which changes the time axis to frequency. (4) Finally, the modulus of the complex Fourier transform is taken. The result is a dispersion image, as in Figure 4, where the axes are frequency and phase velocity, and the gray (or color) scale represents the amplitude of the seismic wave.

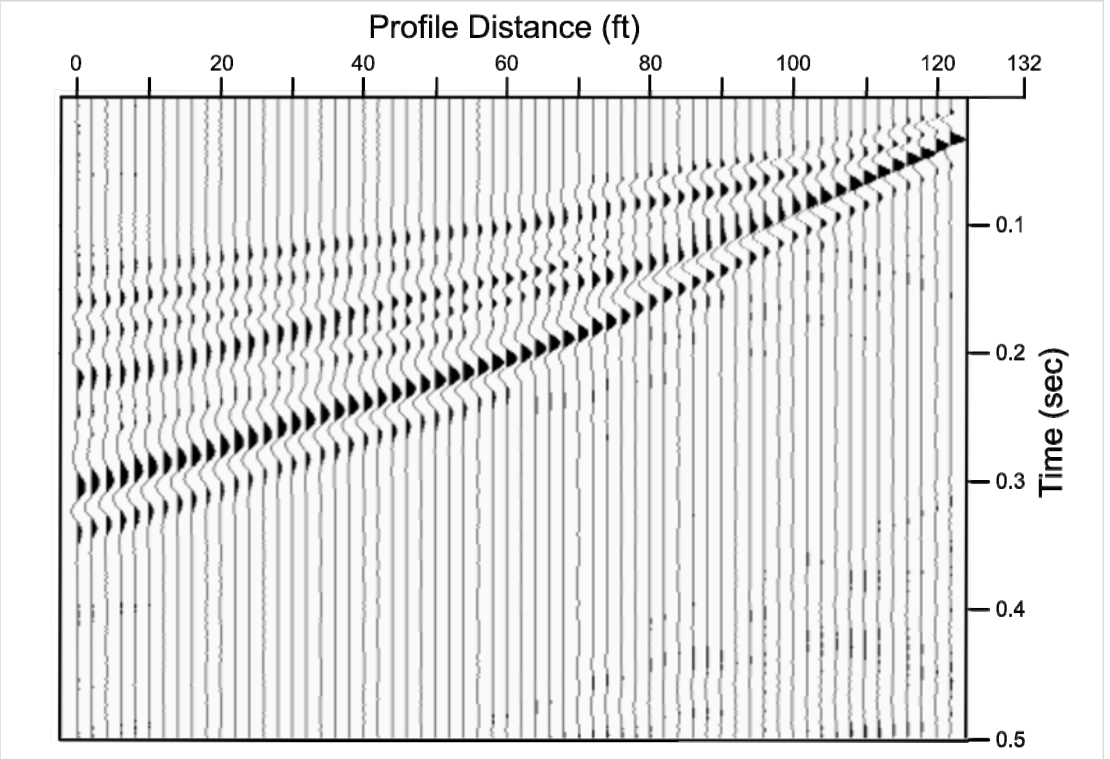

Figure 2. Seismic data example from deployment 1. Geophones were located at 0 to 122. The source was at 132 (Fig. 1).

The dispersion images were computed using both SurfSeis© (KGS 2006) and Seismic Un*X (Cohen and Stockwell 2010). The tau-p transform method described earlier was implemented using Seismic Un*x program modules. SurfSeis© is a program commercially available from the Kansas Geological Survey that is widely used by practitioners of the MASW method. The source code for SurfSeis© is proprietary, but workshop notes (KGS 2004, Appendix Chapter 3) include a detailed mathematical description of the algorithm, and state that the procedure is equivalent to a slant-stack in the frequency domain. The slant-stack is in-turn equivalent to a tau-p transform (Tatham 1989). Modifications to the data processing sequence outlined above may be helpful for some data sets, for example the tau-p transform may be replaced by a Radon transform.

The upper panel (Fig. 4A) is the tau-p transform result based on the data exactly as it appears in Figure 2. The lower panel (Fig. 4B) is the slant-stack in the frequency domain combined with spectral balancing to try to recover additional information at the lowest frequencies. Figure 4 was produced entirely using Seismic Un*x, but the dispersion image in panel B was also obtained in a parallel analysis using SurfSeis©. Although we used both SurfSeis© and Seismic Un*x to obtain dispersion images with equal results, we judge SurfSeis© to be far more user friendly.

Dispersion curves were interpreted from the dispersion images, and inverted to obtain 1-D Vs profiles. Inversion of the dispersion curves was carried out using both SurfSeis© and Computer Programs in Seismology (CPS) (Hermann 2002)

software. The CPS software has a lengthy history in earthquake and crustal structure studies, and has previously been used for MASW inversions (Stephenson et al. 2005).

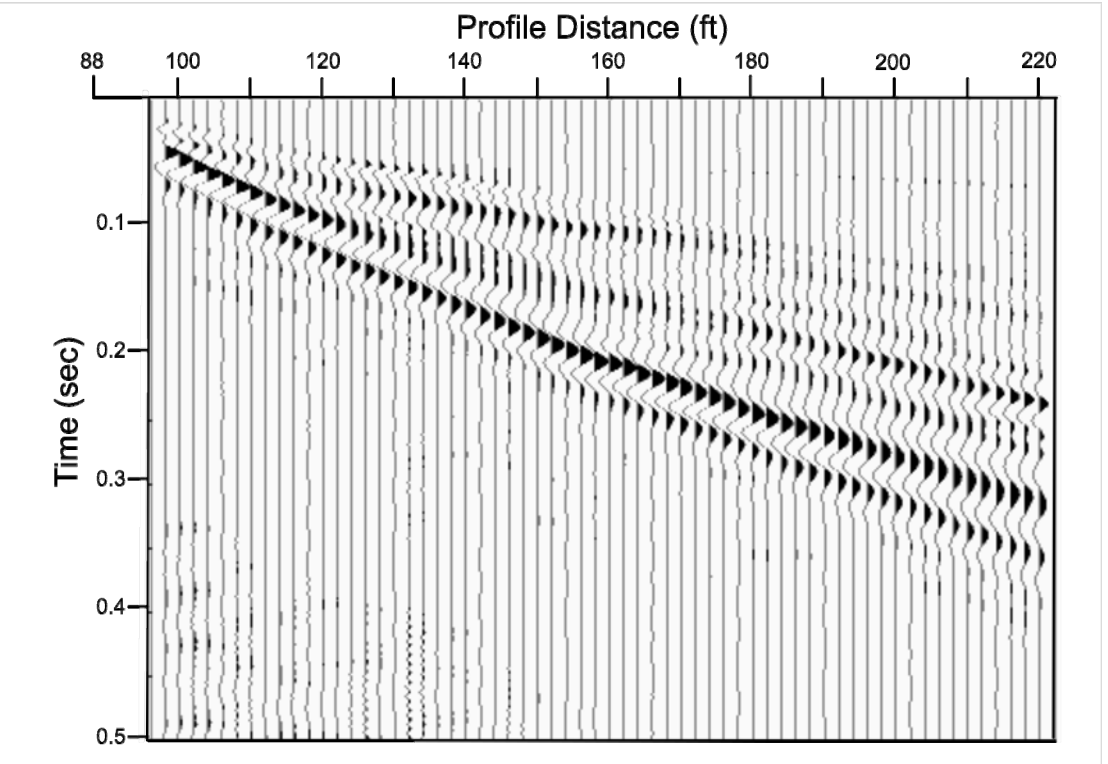

Figure 3. Deployment 2 data example. Geophones were located at 98 to 220. The source was at 88 (Fig. 1).

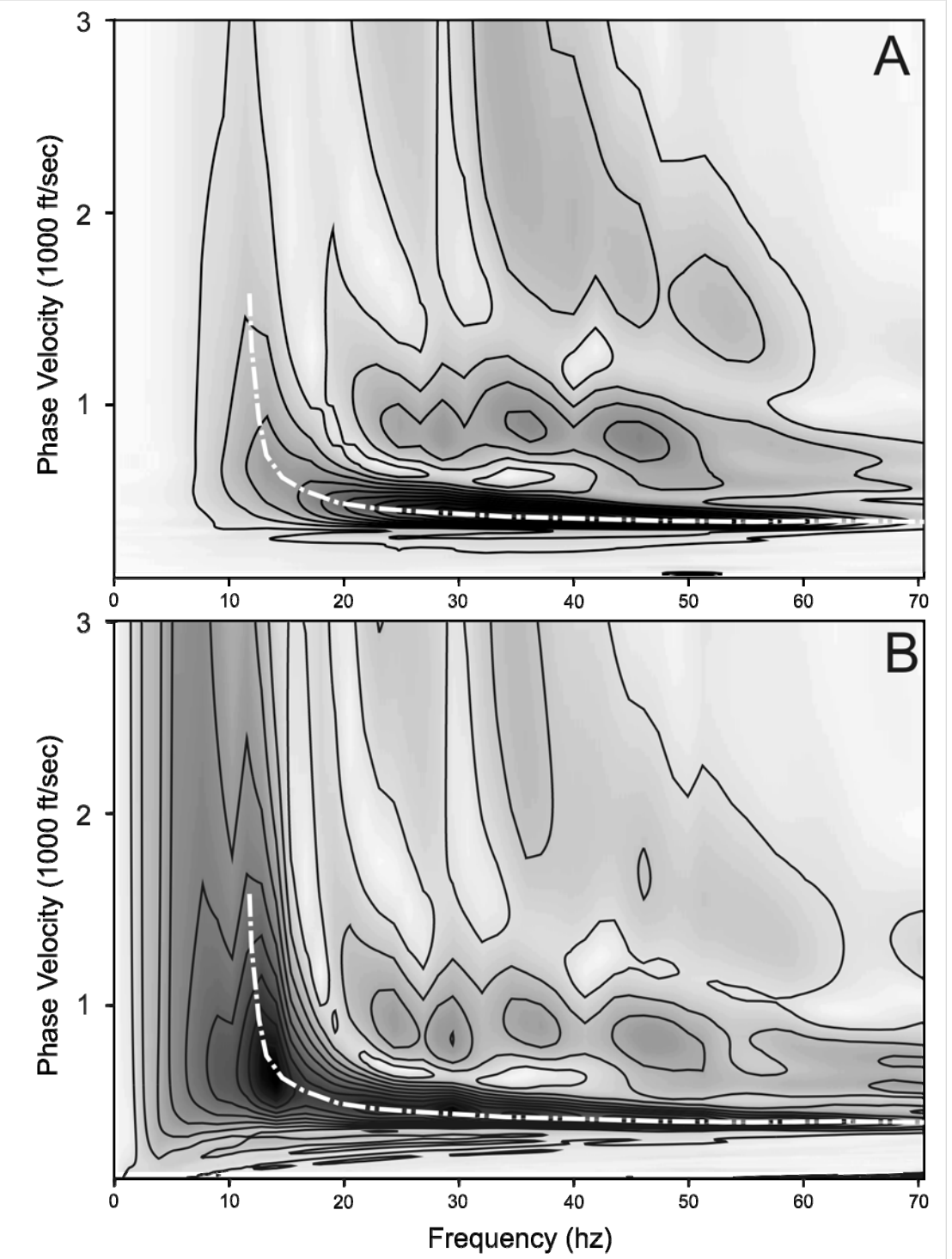

Figure 4. Example dispersion image. The geophones were at 72 - 122. The source was located at 132 (Fig. 2). Upper panel (A) is the tau-p transform result based on the data as exactly as it appears in Figure 2. Lower panel (B) is the slant-stack in the frequency domain combined with spectral balancing to try to

recover additional information at the lowest frequencies. Dashed white line is a dispersion curve that is inverted to obtain *Vs* versus depth.

RESULTS AND DISCUSSION

The two 1-D velocity models that were obtained by inversion of the two best dispersion curves are presented in Figure 5. The curves are labeled according to the midpoints of the respective geophone spreads (refer to Fig. 1 for locations). According to Briaud (1995) the site is underlain by 3 or 4 approximately uniform layers of sand and/or clay, above shale (or hard clay) bedrock. The shale bedrock lies at a depth of approximately 12.5 m. Numerous other inversions were performed, but it is beyond both the scope and length of this report to present those results and discuss them fully.

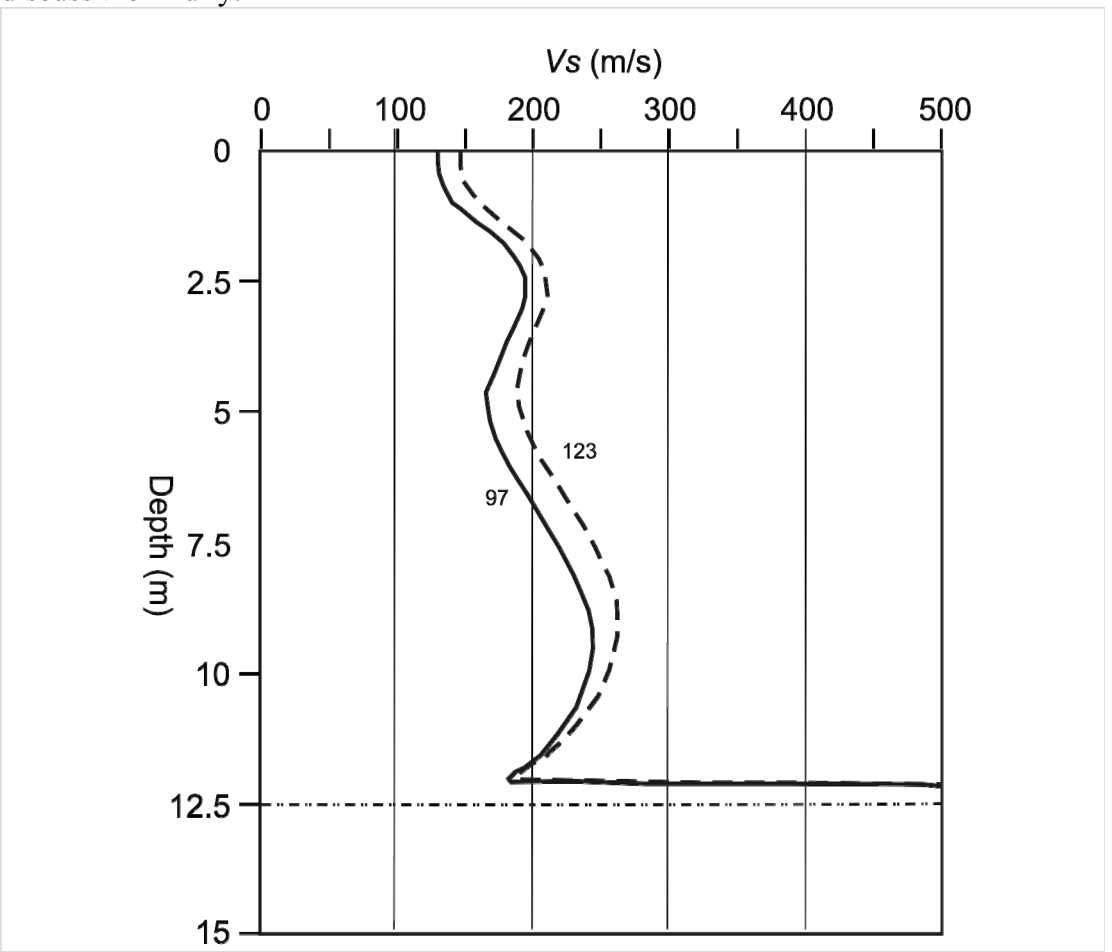

Figure 5. Inversion results from the two best subsets of the MASW data. Numbers on the curves denote the midpoints of the two geophone spreads.

At the outset, participants in this blind test were not informed about the nature of the stratigraphy under the seismic profile. A literature search revealed Briaud's (1995) description of the site, but the question remained as to whether the MASW

data were from the clay region or the sand region. The results presented in Figure 5 indicate that the answer is the clay region.

Concerning depth to shale bedrock, it was poorly constrained in all of the inversions. The 12.5 m depth was adopted *a priori* based on Briaud's description of the stratigraphy. The overlying soil was represented in the inversions by 32 uniform layers, which gives the inversion results on overall smooth appearance, which probably is not justified. Still the results suggest a thin (~0.5 m) low-velocity surface layer, which is underlain by three subsurface layers, two of higher velocity and a lower velocity layer sandwiched in between at a depth of ~5 m. That pattern is consistent with Briaud's description of the clay region, with a sand layer in the clay at 6 m depth.

Overall, this was not a good MASW data set, because the sources were mostly located too far from the geophones. The two best dispersion images were obtained from the source points nearest the two geophone deployments, at an offset distance of 10 ft. Longer offset distances could be advantageous for other methods, for example seismic refraction, but the focus here was on MASW and dispersion of the fundamental mode Rayleigh wave.

REFERENCES

Aki, K., and Richards, P. G. (2002). *Quantitative Seismology, 2nd edition*, University Science Books, Sausalito, California.

Asten, M. W., and Boore, D. M. (Editors). (2005). *Blind Comparisons of Shear-Wave Velocities at Closely Spaced Sites in San Jose, California*, United States Geological Survey Open-File Report 2005-1169, http://pubs.usgs.gov/of/2005/1169/>(Oct. 25, 2010).

Boore, D. M. (2006). "Determining subsurface shear-wave velocities: A review." in Bard, P.-Y., Chaljub, E., Conrou, C., Cotton, F., and Gueguen, P. (Editors) *Third International Symposium on the Effects of Surface Geology on Seismic Motion*, Grenoble, France, 30 August - 1 September 2006, Laboratoire Central des Ponts et Chauss'ees, 67-85.

Boore, D. M., and Asten, M. W. (2008). "Comparisons of shear-wave slowness in the Santa Clara Valley, California, using blind interpretations of data from invasive and non-invasive methods." *Bull. Seism. Soc. Am.*, 98, 1983-2003.

Briaud, J. L. (1995) *The National Geotechnical Experimentation Sites at Texas A&M University: Clay and Sand A Summary*, Report No. TAMU-NGES-007, Dept. of Civil Engineering, Texas A&M Univ., College Station, Texas.

Cohen, J. K. and Stockwell, Jr. J. W. (2010). *CWP/SU: Seismic Un*x Release No. 42: An Open Source Software Package for Seismic Research and Processing*, Center for Wave Phenomena, Colorado School of Mines, http://www.cwp.mines.edu/cwpcodes/>(Oct. 25, 2010).

De Reister, J. (1971) "Electric Penetrometer for Site Investigations." *Journal of SMFE Division*, ASCE, 97(SM-2), 457-472.

Dobrin, M. B, and Savit, C. H. (1988). *Introduction to Geophysical Prospecting*, McGraw-Hill, New York.

Dorman, J., and Ewing, M. (1962). "Numerical inversion of seismic surface wave dispersion data and crust-mantle structure in the New York–Pennsylvania area." *Journal of Geophysical Research*, 67, 5227–5241.

Hermann, R. B. (2002). *Computer Programs in Seismology: An Overview of Synthetic Seismogram Computation, Version 3.30*, Saint Louis University, 186 pages, http://www.eas.slu.edu/People/RBHerrmann/ComputerPrograms.html>(Oct. 25, 2010).

Ivanov, J., Miller, R. D., Lacombe, P., Johnson, C. D., and Lane Jr., J. W. (2006). "Delineating a shallow fault zone and dipping bedrock strata using multi-channel analysis of surface waves with a land streamer." *Geophysics*, 71(5), A39-A42.

Kansas Geological Survey (KGS). (2004). *MASW/SurfSeis© Workshop*, Kansas Geological Survey, Lawrence, KS.

Kansas Geological Survey (KGS). (2006). *SurfSeis© Version 2.05*, Kansas Geological Survey, Lawrence, KS.

Long, M., and Donohue, S. (2007). "In situ shear wave velocity from multi-channel analysis of surface waves (MASW) tests at eight Norwegian research sites." *Canadian Geotechnical Journal*, 44(5), 533-544.

Miller, R. D., Anderson T. S., Ivanov, J., Davis, J. C., Olea, R., Park, C. B., Steeples, D. W., Moran, M. L., and Xia, J. (2003). "3-D characterization of seismic properties at the Smart Weapons Test Range." *Society of Exploration Geophysicists Expanded Abstracts*, 22, 1195-1198.

Park, C. B., Miller, R. D., and Xia, J. (1999). "Multi-channel analysis of surface waves." *Geophysics*, 64(3), 800-808.

Park, C. B., Xia, J., and Miller, R. D. (1998). "Imaging dispersion curves of surface waves on multi-channel record." *Society of Exploration Geophysicists Expanded Abstracts*, 17, 1377-1380.

Penumadu, D., and Park, C. B. (2005). "Multi-channel analysis of surface wave method (MASW) for geotechnical site characterization." *American Society of Civil Engineers Geotechnical Special Publication*, Issue 130, 956-967.

Santa Clara Valley Water District (SCVWD). (2010). *Coyote Creek Outdoor Classroom,* http://www.valleywater.org/Programs/CoyoteCreekOutdoorClassroom.aspx> (Oct. 25, 2010).

Stephenson W. J., Williams, R. A., Odum, J. K., and Worley, D. M. (2005) "Comparison of ReMi, and MASW shear-wave velocity techniques with the CCOC borehole to 100 m, Santa Clara Valley." in Asten, M. W., and Boore, D. M., eds., *Blind Comparisons of Shear-Wave Velocities at Closely Spaced Sites in San Jose, California*, United States Geological Survey Open-File Report 2005-1169, http://pubs.usgs.gov/of/2005/1169/>(Oct. 25, 2010).

Tatham, R. H. (1989). "Tau-*p* filtering." in Stoffa, P. L, ed. *Tau-p: A Plane Wave Approach to the Analysis of Seismic Data,* Kluwer Academic Publishers, The Netherlands, 35-70.

Telford, W. M., Geldart, L. P. Sheriff, R. E., and Keys, D. A. (1976). *Applied Geophysics*, Cambridge University Press, Cambridge, England.

Xia, J., Miller, R. D., and Park, C. B. (1999) "Estimation of near-surface shear-wave velocity by inversion of Rayleigh waves." *Geophysics,* 64(3), 691-700.

Probabilistic Compressible Soil Thickness from Field Settlement Data

Sangho Lee[1] Ph.D., P.E., M.ASCE and Masud Alam[1], Ph.D., P.E., M.ASCE

[1]GESTRA Engineering, Inc., 1626 W. Fond Du Lac Ave. Milwaukee, WI 53205; PH (414)933-7444, FAX (414)933-7844; emails: slee@gestrainc.com and malam@gestrinc.com

ABSTRACT

Field data from settlement plates was monitored to trace the primary consolidation process of compressible soil induced by preloading fill. Hyperbolic regression method was applied to monitor the degree of consolidation of site soil. Layer thickness of compressible soil has been calculated from the measured consolidation time t_{60} or t_{90}, associated with a site average value of coefficient of consolidation. Time factor corresponding to target degree of consolidation is known a function of coefficient of consolidation, consolidation time and layer thickness (drainage length). The probability function of the compressible soil layer thickness could be evaluated from a statistical assessment of coefficient of consolidation on the site soils using joint probability density calculation.

INTRODUCTION

The field settlement observation is usually conducted by monitoring elevation changes of settlement plates under the preloading fill. From the data set of the settlement plate elevation change versus time, degree of consolidation of underlying compressible soil can be estimated, and remaining time to achieve ultimate consolidation can be also predicted using a hyperbolic regression method (Tan and Chew, 1996). This regression method only allows estimating of consolidation time (from t_{60} to t_{90}), but not the compressible soil layer thickness, which is only measurable from direct soil investigations. Settlement behavior observed in preloading site is related to time rate compressibility of soil (i.e., coefficient of consolidation) and thickness of the compressible soil layer. The soil compressibility can be estimated from laboratory test (i.e., one dimensional consolidation test) on limited undisturbed samples from isolated soil boring locations (for preliminary and/or confirmation purpose). Preloading points showing higher settlement amounts cannot be concluded to have larger compressible soil thickness without supplementary lab test on the soil property. It will cost significant time and budget to investigate soil compressibility from direct soil borings for every settlement plate location. Stochastic approach enables to compensate each shortcoming of limited data coverage of direct soil investigation and limited discerning ability of preloading data. Probability function of compressible soil thickness will help estimate a range of foundation settlement, anticipated from final design load. If further remedial action is necessitated after preloading, it can be used for estimation of soil volume for excavation below subgrade (EBS) or for pile length estimations.

PROJECT DESCRIPTION

A new industrial facility is proposed in the redevelopment area on Menomonee River estuary in the city of Milwaukee, WI. General geologic condition of river estuary consists of very compressible native organic soils and underlying dense sandy till material. Six soil borings were completed for preloading plan to identify the overall soil condition of the project site. For utilization of the undeveloped area as a new industrial park, engineered clayey fill had been placed on top of pre-exising sandy fill above the organic soil in 2005. Consolidation tests indicated the organic soil samples (9% to 32% in organic content) are slightly overly consolidated or normally consolidated (i.e., between 1.0 and 1.5 in over consolidation ratio). The deeper organic soils (i.e., below 30 feet from surface ground) are considered to follow a virgin compression line despite no available consolidation data on them, since high void ratio (50% to 133% in moisture content) was observed from all deep organic soils. Primary virgin compression index of compressible soil ranged from 0.15 to 0.68 to render an average value, 0.34. Primary recompression index of organic soil ranged 0.02 to 0.08 to render an averaged value, 0.03. Void ratio and moisture content ranges of Shelby tube compressible soil samples were from 0.7 to 2.0 and from 28% to 63% respectively. Secondary consolidation parameters were also obtained from the consolidation curves. Secondary compression indices of organic soils were estimated to be 0.003 to 0.01. Site soil profile known from preliminary soil borings is summarized in Table 1.

Table 1: Project Site Soil Condition* (before preloading)

Soil Profile	Layer thickness (feet)	Depth to layer bottom (feet)	Notes
Top soil	0.7-1.0	0.7-1.0	Removed before preloading
Engineered Clayey Fill	12.5-14.3	13.2-15.0	Very stiff to hard consistency
Non-engineered Sandy Fill	3.5-9.0	18.5-23.5	Very loose to medium dense relative density
Compressible Organic soil	3.5- 25.0	22.5-44.0	Alternative organic silt and elastic silt
Sandy/silty glacial till	>10.0	N/A	Dense to very dense

*Based on preliminary six soil borings

It was assumed at preloading design stage that the overall distributed load from the new facility will reach 500 pounds per square feet. Thus, initial preloading fill was planned and placed up to 10 feet of fill height from existing ground. After two month of preloading, the planned facility distributed load was changed into 800 psf, which necessitated addition of 7 feet of fill material, total of 17 foot tall preloading fill. The additional fill placement was selectively performed at the preloading area exhibiting significant settlement process. Total preloading time was over 5 months but actual

preloading period analyzed in this research was approximately 3 months after additional fill placement.

From December, 2009 to May, 2010, the vertical displacements of 16 settlement gauges, installed in the preloading area were continuously monitored on weekly basis. Individual settlement data were analyzed using the hyperbolic regression method (Tan and Chew, 1996) to identify consolidation progress at each settlement plate location. The linear relationship between time elapse divided by settlement amount and settlement time enables to decide t_{60} and t_{90} (Fig. 1).

The observed settlement induced from the preloading fill varied from 1.6 inches to 15.5 inches. A local area at center of preloading site showed very large settlement, in excess of 10 inches. This area was still showing below 90% consolidation at the end of preloading, thus additional compressible fill material or soil can exist in this area. Along the western limit of the preloading area, relatively small settlement (less than 2 inches) was also observed.

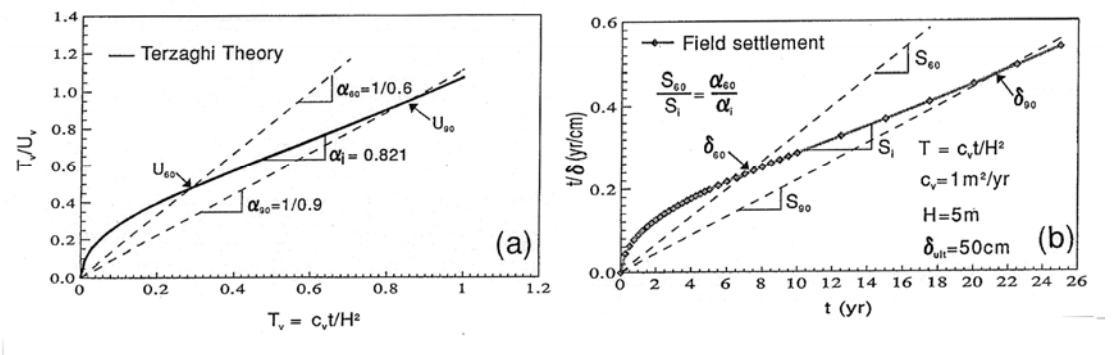

Figure 1 Hyperbolic Regressions of (a) Terzaghi theory and (b) field settlement data (Tan and Chew, 1996)

After preloading, three (3) confirmation soil borings were completed along the center of proposed building footprint. Consolidation tests on confirmation samples also indicate that over-consolidation ratio (OCR) of the organic silt at 25 feet below the future site grade increased to between 1.5 and 2.4, after removal of pre-loading fill.

METHODOLOGY

Stochastic approach enables to take into account variance of design parameters along with the mean values both of which can be estimated from a soil investigation program including field and laboratory tests. Consolidation times assessed from preloading data can be combined with soil compressibility (i.e., coefficient of consolidation) measured from laboratory tests to assess the probability function of compressible soil thickness. Field data (t_{60} or t_{90}) from the 16 settlement plate monitoring present better data coverage of preloading area, and more indicative to actual soil compressions than soil borings, from which discrete delineations of compressible soils are difficult. Information of data distributional shape (normal or uniform distribution) can be assessed from statistical analyses (mean, standard deviation, minimum and maximum values) on the field and laboratory data.

Uniform distribution can be applied for lab or field data with no indication of centralized distribution pattern, so called "truly random distribution". Only minimum and maximum values of data set will determine the distribution shape. Probability function will be a monotonic increasing linear shape, varying from zero to one. Probability density function (PDF) can be assessed by taking inverse of difference between the maximum and minimum values. No correlation can exist between two data sets other than fully independent ($\gamma = 0$) or fully dependent ($\gamma = -1$ or 1).

Normal distribution can be applied for presentation of lab or field data with indication of a centralized distribution pattern. Mean and standard deviation of data set will decide the distribution shape of PDF. Bell shaped Gaussian distribution function has no distribution limits. Thus inclusion of negative random variable with no physical meaning is inevitable in generation of the PDF, which is a demerit of using normal distribution model. An advantage of normal distribution model is allowing consideration of correlation between data sets in joint PDF generation. Joint normal density with each mean and standard deviation of two data sets can be presented with following formula.

$$f(x,y) = \frac{1}{(2\pi\sigma_x\sigma_y\sqrt{1-\gamma^2})} Exp[-\frac{1}{2(1-\gamma^2)}(\frac{(x-\eta_x)}{\sigma_x^2} + \frac{(y-\eta_y)}{\sigma_y^2} - 2\gamma\frac{(x-\eta_x)(y-\eta_y)}{\sigma_x\sigma_y})] \quad \textbf{(1)}$$

Where f(x,y) is joint normal density function of random variables x and y

η_x and η_y are the mean values of data sets x and y

σ_x and σ_y are the standard deviations of data sets x and y

γ is correlation factor between data sets x and y ($-1 < \gamma < 1$)

Distributional shapes of joint PDF for uniform and normal distributions are depicted in Fig. 2.

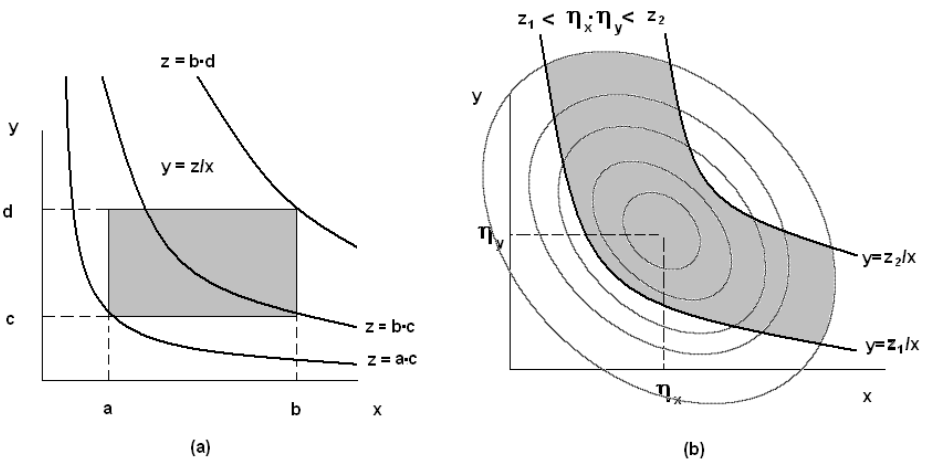

Figure 2 Calculation Procedures of Joint Probability Density Function of (a) Uniform and (b) Normal Distributions for Random Variables **x**, **y** and **z** where **z = x·y**

Most preloading sites allow assumption of one-dimensional excess pore pressure dissipation through upper and/or lower permeable layer except for end sides of preloading fill since preloading fill area is generally predominant compared to compressible soil layer thickness. Therefore, the layer thickness of compressible soil can be estimated using Terzaghi's consolidation theory.

$$H_{dr}^2 = \frac{C_v t}{T_v} \qquad \text{after Terzaghi, 1925} \qquad \textbf{(2)}$$

Where T_v is a time factor (0.286 for 60% consolidation, 0.848 for 90% consolidation)
t is consolidation time from field measurement (t_{60} or t_{90})
C_v is coefficient of consolidation of compressible soil measured from lab test.
H_{dr} is drainage length of compressible soil

PDF of squared drainage length (H_{dr}^2) can be obtained from joint probability density function of coefficient of consolidation and consolidation time, data sets of which are collected from laboratory tests and field measurements, respectively.

PDF of layer thickness (H_{dr} or $2H_{dr}$) can be derived from the PDF of squared drainage length with following relationship.

$$f_y(y) = 2yf_x(y^2)U(y) \qquad \text{after Papoulis, 1991} \qquad \textbf{(3)}$$

Where y is random variable, drainage length, and x is random variable, squared drainage length ($y = x^{0.5}$)
$f_y(y)$ is PDF of drainage length (H_{dr})
$f_x(x)$ or $f_x(y^2)$ is PDF of squared drainage length (H_{dr}^2)
$U(y)$ is unit step function (1 if $y \geq 0$ or 0 if $y < 0$)

ANALYSIS AND RESULT

The 60% consolidation time (t_{60}) was used for estimation of compressible layer thickness since all settlement data did not show over 90% consolidation after preloading. The data distribution of t_{60} shown in Fig. 3 (a) indicates the PDF of consolidation time is closer to uniform distribution than normal distribution. The 60% consolidation times at three locations presented outlier values exceeding 40 days, deviated from the consolidation times of other locations, thus these three data will not be included in the PDF generation of t_{60}. Data set of coefficient of consolidation (C_v) was collected from the one dimensional consolidation tests on five Shelby tube samples of compressible organic soils. Coefficient of consolidation was estimated from early loading stages (i.e., 0.25, 0.5, 1 , 2 and 4 ksf) since those loading levels are considered similar to overburden stress range applied on compressible soil during preloading. No conspicuous difference of C_v values was notable between over-consolidated and normally consolidated soils. Large C_v range, 10 to 100 times greater than general clay soil values is considered presenting characteristic of organic soil. The data distribution of C_v shown in Fig. 3 (b) indicates the PDF of coefficient of consolidation is closer to normal distribution (skewness=1.7; kurtosis=2.8).

Correlation between coefficient of consolidation, C_v and consolidation time, t_{60} was estimated from the 5 boring locations, which indicated apparent negative relationship (a correlation factor of -0.7), in correspondence with a fact that the consolidation time should be reduced as the value of coefficient of consolidation increase. Therefore, probability function of compressible soil thickness is expected to exist between two extreme cases- joint normal distribution with a negative correlation and joint uniform distributions, mutually independent between C_v and t_{60}.

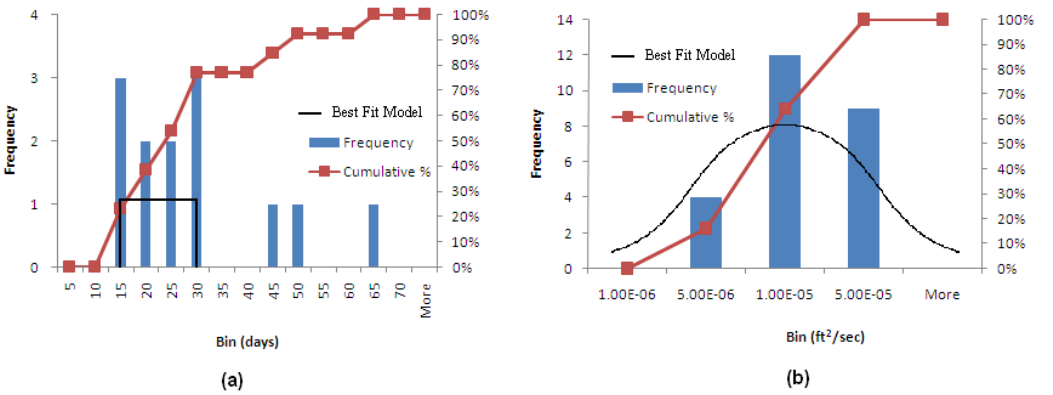

Figure 3 Data Distribution Patterns of (a) 60% Consolidation Time from 13 Settlement Gauges during Preloading and (b) Coefficient of Consolidation (C_v) for Organic Soils from 5 Boring Locations

Joint Uniform distribution Approach

Minimum and maximum values of coefficient of consolidation were estimated each 0.21 ft^2/day and 3.09 ft^2/day. Minimum and maximum values of consolidation time, t_{60} were estimated each 13 days and 28 days excluding three outlier values. Probability function of squared drainage length, H_{dr}^2, presented with coefficient of consolidation (C_v), multiplied by consolidation time, t_{60} and divided by 0.286, can be calculated as shown in Fig. 2 (a). Assessed PDF of H_{dr}^2 can be converted into PDF of H_{dr} as shown in Fig. 4 (a) and (b) using Equation (3).

Joint Normal distribution Approach

Mean and standard deviation values of coefficient of consolidation were estimated each 0.89 ft^2/day and 0.7 ft^2/day. Mean and standard deviation values of consolidation time, t_{60} were each 20.1 days and 6.0 days excluding three outlier values. Joint normal distribution function of squared drainage length, H_{dr}^2 can be calculated using following formula and as shown in Fig. 2 (b) with a negative correlation factor of -0.7.

$$F(z) = \int_0^{\infty} \int_0^{z/x} f(x,y)dydx \quad \textbf{(4)}$$

Where f(x,y) is PDF of Equation (1)
z is a random variable presenting H_{dr}^2

Percentage of model error from production of negative random variable of x and y in joint normal density function can be calculated by following formula.

$$Error(\%) = \int_{-\infty}^{0}\int_{-\infty}^{0} f(x,y)dydx \quad \textbf{(5)}$$

Similar to joint uniform distribution, assessed PDF of H_{dr}^2 can be converted into PDF of H_{dr} as shown in Fig. 5 (a) and (b).

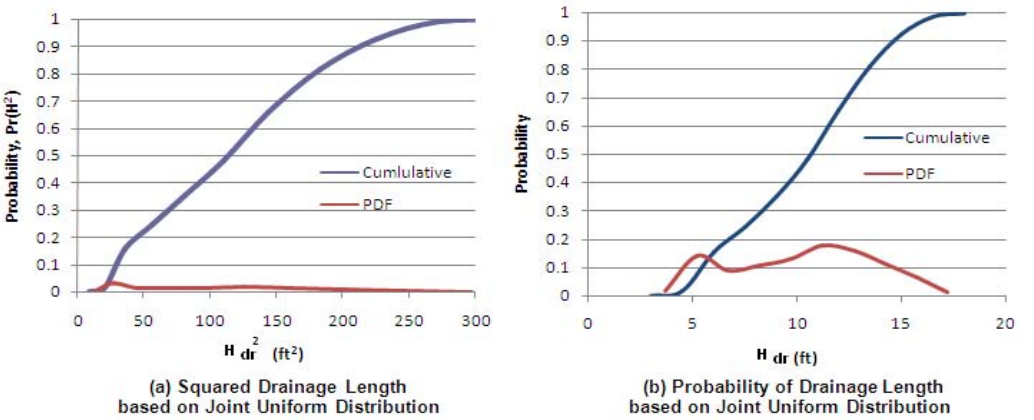

Figure 4 Probability Function of Drainage Length for Joint Uniform Distribution with Non-correlation between C_v and t_{60}

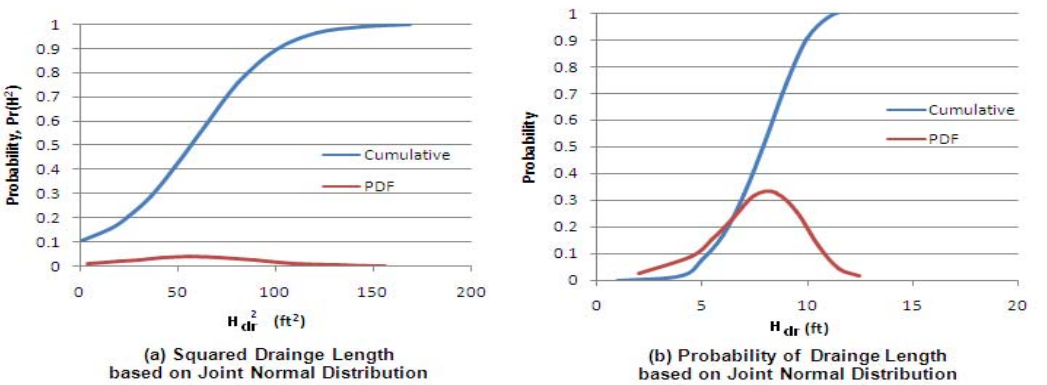

Figure 5 Probability Function of Drainage Length for Joint Normal Distribution with a Correlation Factor of -0.7 between C_v and t_{60}

From the site soil observations, double drainage is considered more appropriate for compressible layer drain condition since sandy fill and sandy till material overlies and underlies the compressible soil at each top and bottom. Fig. 6 shows comparison of probability function and PDF of estimated compressible soil layer thickness (2 H_{dr}), each based on uniform distribution and normal distribution. Model error of joint normal distribution was calculated to be 10.4 %, thus up to10 % of calculated layer thickness should not be convinced.

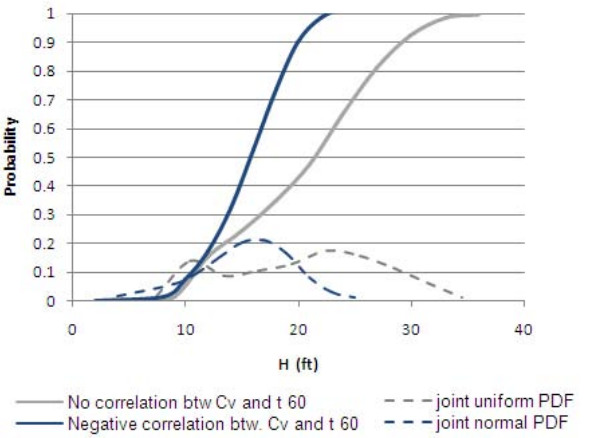

Figure 6 Results of Compressible Soil Thickness (H) Probability Function

CONCLUSION

Probability of compressible soil thickness could be estimated with data sets of consolidation time, estimated from preloading data and coefficient of consolidation, measured from one-dimensional consolidation tests. The data sets of consolidation time and coefficient of consolidation were characterized with a best fit probability density function. For the practicality of simplified approach, joint uniform and normal distributions were only considered to present the field and lab test data sets. From the project site, apparent negative co-relationship was observed between consolidation times and coefficients of consolidation, thus analysis result using joint normal distribution function is considered more appropriate to represent thickness of compressible soil layer below future site grade. Maximum likelihood of compressible soil layer thickness was estimated to be 18 to 22 feet for the organic soil, each estimated based on joint normal distribution and joint uniform distribution. The existence of organic soil layer with over 30 feet thickness was estimated less than 10% of entire project area. Those estimates are only confined to native organic soils in preloading area, excluding additional weak/soft fill or soil layers exhibiting local presidency.

REFERENCES

Papoulis, A. (1991) *Probability, Random Variable, and Stochastic Process*, 3rd Ed., WBC/McGraw-Hill, New York

Tan, S. and Chew, S. (1996) "Comparison of Hyperbolic and Asaoka Observational Method of Monitoring Consolidation with Vertical Drains", *Soil and Foundation*, Japanese Geotechnical Society, Vol. 36 (3), 31-42.

Terzaghi, K. (1925) *Erdbaumechanik auf Bodenphysikalischer Grundlager*, Deuticke, Viena

A Novel Application of Risk Analysis Methods to Evaluate the Future Viability of Two Large Concrete Stormwater Detention Tanks

[1]M. Eddleston, and [2] P. J. Mason

[1] MWH, Dominion House, Temple Court, Birchwood, Warrington, UK ;
PH 00441925845176; malcolm.eddleston@uk.mwhglobal.com.
[2] MWH, Terriers House, 201 Amersham Road, High Wycombe, UK;
PH 00441494557538; Peter.J.Mason@uk.mwhglobal.com

ABSTRACT

Many aspects of geotechnical design, such as the analysis of slopes using slip circles and the evaluation of imposed earth pressure, whether active, passive or at-rest, can be made fairly precisely. These lend themselves to the application of safety factors for use in design. However, problems involving groundwater flows and seepage often require an understanding of the security of the structure with respect to resistance to soil erosion. Such evaluations are complex and necessitate the use of quantitative risk analysis methodologies to provide an estimation of failure probabilities involving groups of experienced engineers providing subjective judgement through elicitation panel methods.

The paper describes the application of the Quantitative Risk Analysis (QRA) approach using event trees to assess the piping failure risk around two massive submerged, underground, concrete storage tanks in the UK. This process highlighted the most significant risks, their potential mitigation and the likelihood of the risks actually occurring in terms of a "Probability of Failure" within a particular time scale.

INTRODUCTION

Two Wastewater Storage Tanks were constructed in 1999 in North West England, UK to provide 60,000m3 of stormwater storage to prevent unsatisfactory stormwater overflow discharges during each annual Bathing Water Season. The asset comprises two very large diameter (36m) and deep (40m) buried tanks constructed as circular diaphragm walls with an interconnecting tunnel and associated infrastructure, See Figure 1.

NEED FOR A QUANTITATIVE RISK ASSESSMENT (QRA)

Since 2001 groundwater has been reported flowing into one of the tanks, Tank 2 around the joint between the base and a corbel ring beam which transfers loads from the base to the walls as shown in Figure 2.

Investigation and monitoring of these inflows has been undertaken and due to the local geology consisting of Triassic Mudstone and Halite Beds it was considered

that inflows into Tank 2 were likely to have initiated potential solution and the possibility failure mechanisms including fines loss, gypsum dissolution and halite (rock salt) dissolution.

Figure 1 Aerial View of the Detention Tanks

Figure 2 – Ingress into the Tank

There is a possibility that these mechanisms could lead to structural damage to the asset, including the interconnecting tunnel and Tank 2 base, as well as the surrounding infrastructure. It is likely that the consequences of such a failure would be significant and include the asset being out of use. Suggestions for permanent works to reduce risk to the asset include ground stabilisation grouting and a new corbel ring beam to counter uplift forces on the base

Due to the uncertainties attached to the failure mechanisms the client recognised need to be able to prioritise the risks and have a better understanding of their urgency before funding can be sought for either investigative, permanent or temporary works.

To do this it was recommended that Quantitative Risk Assessment (QRA) be undertaken for the asset, to be based, where appropriate, on a recognised methodology. An approach similar to one used on embankment dams was proposed. This 'Toolbox' methodology is based on the guidance document 'Risk Analysis for Dam Safety: A Unified Method for Estimating Probabilities of Failure of Embankment Dams by Internal Erosion and Piping, 2008' which has been jointly developed by the U.S. Bureau of Reclamation, US Army Corps of Engineers, The University of New South Wales and URS (Fell R., 2008).

AIM OF THE QUANTITATIVE RISK ASSESSMENT

It was intended that the QRA would:

- Identify and document all significant potential modes of failure in a logical manner.
- Form a consensus of opinion as to the most significant risks
- Assess the need and potential for improved evidence and investigations
- Identify and quantify the probability of each failure mode based on the evidence presented

- Form a consensus of opinion with regard to the effectiveness of mitigation methods and the best way to proceed
- Indicate the likelihood of risks occurring within a timeframe, albeit in a highly subjective manner

It was recognised that the results and conclusions of the QRA represent the best efforts of the team to form a consensus of opinion, to quantify the likelihood of failure events and draw conclusions which are of use to the asset owner.

QRA METHODOLOGY

Event Trees. The methodology adopted is based on the use of Event Trees which:

- represent progressions of events that could result in adverse consequences
- consist of a series of linked nodes and braches, each node representing an uncertain event or condition
- provide a graphical representation of the logic structure for the progression of each failure mode and a template for the assignment of event probabilities and calculation of risk
- identify where the greatest potential risks are
- foster common knowledge and understanding of failure modes, and synergetic discussion of various issues associated with failure modes

For the purposes of the QRA a failure event was be considered to be a progression of events which could lead to any or all of the following:

1. Death or serious injury.
2. The asset can no longer be used for its intended purpose without major remediation.
3. Significant damage to infrastructure external to the asset, including third party assets.

An event tree is constructed from left to right, starting with some initiator event and proceeding through events describing the response of the structure to each level of the initiator. These event sequences are developed all the way to a recognised failure mechanism. In the case of the Dam “Toolbox” standard event node descriptors have been used. These are Initiation, Continuation, Progression, Intervention and Failure.

Following consideration and trial runs the standard event tree node descriptors in Table 1 were developed for the QRA. These enable a clear and logical methodology to be followed, which is appropriate to all event trees. By considering one initiation node at a time and exploring the different routes to failure associated with it, it was considered to be possible to create a reasonably comprehensive list of potential failure events.

Table 1 . Description of Event Tree Nodes Developed for Bloomfield Road Storage Tanks QRA

	Event Tree Node Descriptor	Definition
1	Initiation	Consideration of the effect of a flow path on a particular stratum within the zone of influence of part of the asset, e.g. flow from the Sands & Gravels through the base / corbel joint causing fines loss around the tunnel.
2	Continuation	Consideration of the probability that the initiated effect (1) will stop of its own accord, i.e. without mitigation.
3	Progression	The series of events which need to occur for failure to happen e.g. describing how fines loss can eventually cause tunnel collapse.

Risk Estimating Team (RET). An important part of the Toolbox application on the dams is the use of a Risk Estimating Team (RET) formed from a consistent group of suitably qualified and experienced experts. This concept is appropriate for Bloomfield Road Tanks for which the responsibility of the RET is to agree the event trees and score the probabilities for each event node following discussion, consideration and challenging of the evidence and conclusions drawn to date. For the purposes of Bloomfield Road Tanks QRA the RET should:

- be small enough so as to be conducive to detailed and comprehensive discussions
- have sufficient knowledge and experience to be able to draw independent and, as far as is reasonably practical, correct conclusions from the evidence presented
- contain sufficient engineering expertise to be able to consider all parts of the asset in question, e.g. structural, geotechnical etc

Probability Scoring. Probability is defined in the Toolbox method (Fell R., 2008) as "a measure of the degree of certainty. This measure has a value between zero (impossibility) and 1.0 (certainty). It is an estimate of the … likelihood of the occurrence of the uncertain future event. There are two main interpretations:

1. Statistical – frequency or fraction – the outcome of a repetitive experiment of some kind and is in principle measurable by doing the experiment.
2. Subjective probability (degree of belief) – Quantified measure of belief, judgment, or confidence in the likelihood of an outcome, obtained by considering all available information honestly, fairly and with a minimum of bias. Subjective probability is affected by the state of understanding of a process, judgement regarding an evaluation, or the quality and quantity of information. It may change over time as the state of knowledge changes.

Due to the nature of the evidence available and the unique situation of the Bloomfield Road Tanks asset, this QRA will be almost entirely based on subjective probability.

Where there is not a basis (i.e. appropriate statistical information) for estimating statistical probability the Toolbox method uses verbal descriptors to assign response probabilities relative to the scale of verbal descriptors as shown in Table 2 (Fell R., 2008).

Table 2 Probability Mapping Scheme (Fell R., 2008)

Verbal Descriptors	Descriptor Probability
Virtually Certain	0.999
Very Likely	0.99
Likely	0.9
Neutral	0.5
Unlikely	0.1
Very Unlikely	0.01
Virtually Impossible	0.001

The total probability of a particular event occurring is simply the product of the scores allocated to each node of its event tree. To prevent abortive effort a virtually impossible score of 0.001 was allocated by the RET as ‘de-minimus’ in the workshop records.

QRA WORKSHOP

It is essential that prior to assigning a probability score to a particular event node the RET are all given the opportunity to comprehend, challenge and discuss the same evidence. Where possible this should be done with all the RET present, ideally in a workshop event. To improve its effectiveness the workshop should include a facilitator and recorder. The Toolbox approach (ref. Fell R., 2008) recommends that “the group (RET)... ‘brainstorms’ any and all information that is pertinent to the event node being discussed. Each piece of information is listed on a flip chart in either a ‘factors leading to a higher probability’ or ‘factors leading to a lower probability’ column depending on whether the information can be used as evidence to support or oppose belief in the event. The terms ‘factors leading to a higher probability’ and ‘factors leading to a lower probability’ are used in terms of the event node, as described, actually happening. The purpose of this step in the process is to display all the information that will be used in making the estimate for all team members to see and discuss. The team members can judge for themselves the

importance of the information being listed as they make their estimates". The factors and evidence considered on the flip chart notes must be recorded for reference in the workshop notes. Figure 3 summarises the workshop process.

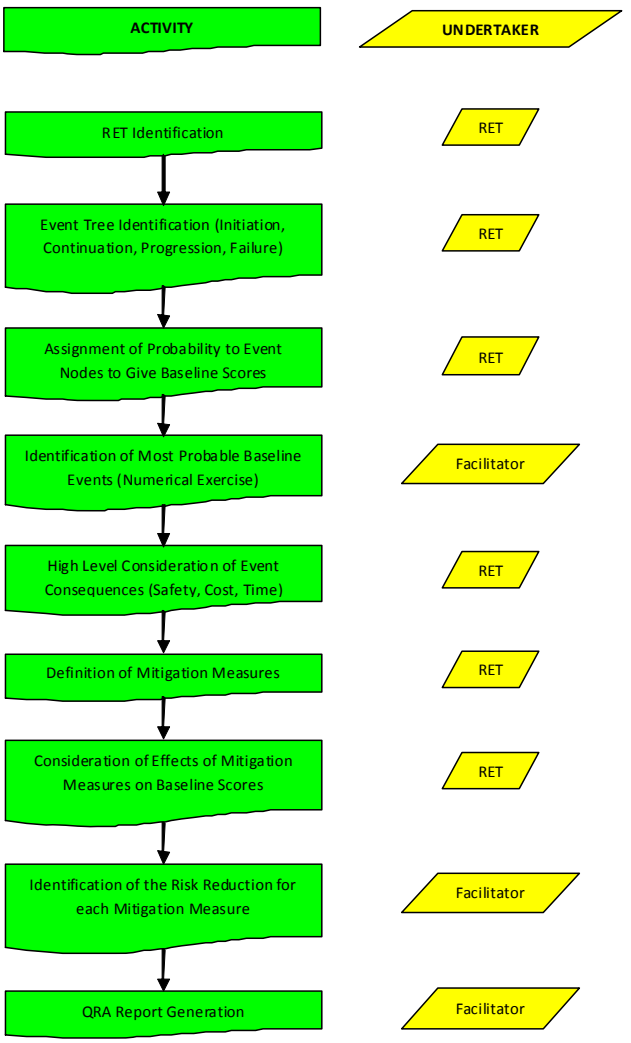

Figure 3 Summary of the Workshop Process

The following consequences will be of concern to asset owner and were estimated by the RET:

- Likelihood of injury / death (low, medium, high) as a result of failure;
- Immediate consequences of failure, e.g. tanks full, loss of mechanical and electrical equipment etc;
- Possible remedial works necessary to bring asset back into use and the associated cost;
- Possible duration for which the asset cannot be used;

- Possible impact on surrounding infrastructure for example the car park, road and sewer.

TOLERABILITY OF RISK USING THE QRA METHOD

In order to assess whether levels of risk are tolerable to UU, users of the Toolbox method on UU dams have adopted guidance from the HSE document r2p2, 2001. This outlines the HSE's tolerability of risk (TOR) framework in which risk is split into ranges as follows:

- Broadly acceptable – 'Risks falling into this region are generally regarded as insignificant and adequately controlled' (HSE, 2001)
- Unacceptable – 'a particular risk falling into that region is regarded as unacceptable whatever the level of benefits associated with the activity' (HSE, 2001)
- The zone between the unacceptable and broadly acceptable regions is the tolerable region. Risks in that region are typical of the risks from activities that people are prepared to tolerate in order to secure benefits.

An individual risk of death of one in a million per annum should be used as a guideline for the boundary between the broadly acceptable and tolerable regions' (HSE, 2001). For members of the public who have a risk imposed on them 'in the wider interest of society' this limit (between tolerable and acceptable) is judged to be\ 1 in 10 000 per annum.' (HSE, 2001)

CONCLUSIONS

The RET undertook a comprehensive QRA covering 97 potential failure events. Of these 25 were identified as having unacceptable or tolerable (ALARP) probabilities of occurrence, based on tolerability limits suggested by the HSE for per annum events involving fatalities. As it is not anticipated that any failure events have a high risk of causing fatalities these tolerability limits for probability may have to be amended by UU to be applied meaningfully for this specific asset. Within the most probable 25 failure events, 8 modes of failure have been identified. Within each mode events are differentiated by assumptions regarding groundwater pressure and timeframe. These modes are listed below, in order of the most probable events:

1. Gypsum Dissolution (Mudstone) Allowing Base Movement
2. Fines Loss from the Mudstone Allowing Base Movement
3. Chemical Attack of Corbel Ring Beam Shear Connectors Allowing Base Movement
4. Gypsum Dissolution (Mudstone) Allowing Tunnel Failure
5. Fines Loss from Sands and Gravels through Tunnel / D-wall Joint Allowing Tunnel Failure

6. Fines Loss from Sands and Gravels beneath Toe of D-wall and Through Base Joint Allowing Tunnel Failure

7. Halite Dissolution Allowing Base Movement

8. Halite Dissolution Allowing Tunnel Failure

In terms of immediacy the first seven modes were deemed to be unacceptable in the immediate (2 year) timeframe. Although the eighth is within the tolerable range in the immediate timeframe it cannot be deemed as acceptable until reasonably practicable measures, or mitigations, have been applied to reduce the risk (ALARP principle). The RET considered and priced, at a very high level, 4 mitigation options:

1. Bulk grouting of mudstone plug/halite, new corbel ring beam and new tunnel headwalls

2. Bulk grouting to consolidate connecting tunnel supporting stratum and new tunnel headwalls

3. Combination of mitigations 1 and 2

4. Mechanical seal to corbel/base joint

According to the reduction in probabilities calculated the most effective mitigation measure is Mitigation 3 which improves all probabilities to within the acceptable or tolerable (ALARP) range. Mitigation 4 is the next most effective mitigation measure however the design and costs for this option could not be determined as part of this exercise.

To conclude, the QRA exercise has been successful in achieving a credible consensus of opinion as to risks affecting the asset, considering the limited evidence available and subjective nature of the interpretation. The QRA also provides a consensus opinion of the relative effectiveness of mitigation measures, as determined by a reduction in probability. It has also created a logical and comprehensive framework for assessing possible failure events that can be used in the future as improved evidence becomes available.

REFERENCES

Fell, R., Foster, M., Davidson, R., Cyganiewicz, J., Sills, G. & Vroman, N. (2008). A Unified Method for Estimating Probabilities of Failure of Embankment Dams by Internal Erosion and Piping. *UNICIV Report R 446, The School of Civil and Environmental Engineering, the University of New South Wales, Sydney, Australia* 2052.ISBN:85841 413 9

Health and Safety Executive (2001), *Reducing risks protecting people (R2P2) – HSE's decision-making process*, HSE Books.

Risk Management for Large-Scale Foundation Design and Construction in Challenging Karst Geology

John I. Yao,[1*], P.E., M. ASCE and Emad Farouz,[2] P.E., M. ASCE

[1]Jacobs Associates, 234 East Colorado Boulevard, Suite 400, Pasadena, CA 91101; PH (626) 737-6522; FAX (626) 737-6530; e-mail: yao@jacobssf.com
[2]CH2M HILL, 15010 Conference Center Drive, Suite 200, Chantilly, VA 20151; PH (703) 376-5100; FAX (703) 376-5600; e-mail: emad.farouz@ch2m.com

ABSTRACT

A 173,700 square foot (16,100 m^2) facility consisting of maintenance hangar and shop facilities to allow isochronal maintenance of the C-5 Galaxy aircraft was recently completed in Martinsburg, West Virginia for the West Virginia Air National Guard. Nearly 200 drilled shafts ranging from 36 to 78 inches (914 to 1,981 mm) in diameter were designed and constructed to support significant downward and uplift design loads. The geology of the project site consisted of shale, and limestone with random karst features that included solution channels and voids measuring over 6 feet (1.8 m) vertically. These geologic features posed significant risks and challenges for the design and construction of the foundations for the aircraft hangar and shop facilities. This paper presents the methods applied to manage the risks associated with the karst geology at the site. Topics include selection of the foundation system; design approach and communication of design intent through the contract documents; and methods applied during construction, such as systematic probing and pile integrity testing, to ensure the drilled shafts were constructed to satisfy the design requirements.

INTRODUCTION

On December 4, 2006, the first of the massive C-5 Galaxy aircraft assigned for the 167th Airlift Wing arrived at the Eastern West Virginia Regional Airport (Shepherd Field) in Martinsburg, West Virginia. The Lockheed C-5 Galaxy is a military transport aircraft designed to provide strategic heavy airlift over intercontinental distances and to carry outsize and oversize cargo. The C-5 Galaxy, shown in Figure 1, has been operated by the United States Air Force (USAF) since 1969 and is one of the largest airplanes in the world. The USAF had decided to locate one of three regional isochronal inspection sites at the air base in Martinsburg. As many as 33 of the C-5 airplanes will transit through the air base for periodic inspection each year as part of a comprehensive maintenance program designed to keep the Air Force's largest aircraft flying well into the future (Cadle, 2007a,b).

[*] This author's involvement in the project discussed in this paper was during his previous employment with CH2M HILL.

Figure 1. C-5 Galaxy Aircraft.

In order to accommodate the C-5, an upgrade of the base facilities at Martinsburg was required. One of the projects in the upgrade involved the design and construction of a new 80,700 square foot (7,500 m^2) hangar bay (Maintenance Hangar) and 93,000 square feet (8,640 m^2) of associated shops and administration functions to allow isochronal maintenance of the C-5 aircraft. The shops are collectively housed within a Maintenance Mall located adjacent to the Maintenance Hangar. Figure 2 shows the plan of the C-5 Maintenance Hangar and Mall.

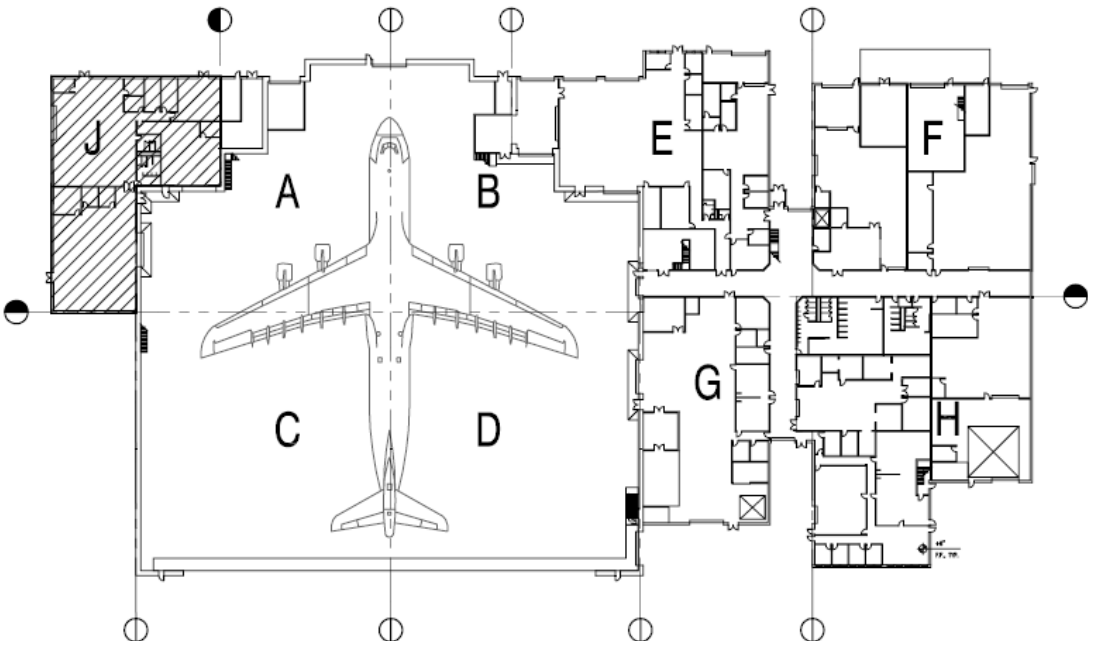

Figure 2. Plan of the C-5 Maintenance Hangar and Mall.

In Figure 2, the Maintenance Hangar consists of areas A, B, C, and D. The Maintenance Mall consists of areas E, F, G, and H. Area J (not discussed in this paper) was not constructed at the same time as the Maintenance Hangar and Mall.

SITE AND SUBSURFACE CONDITIONS

The site for the Maintenance Hangar and Mall was relatively flat. Differences in the elevations of the ground surface across the site were generally less than 10 feet (3 m). The geotechnical investigations found medium- to high-plasticity clayey silt or silty clay underlain by bedrock consisting of either shale or limestone. The shale was encountered only under the northwest part of the footprint of the Maintenance Hangar. The investigations also revealed the following subsurface conditions that had significant impact on foundation design of the structures:

- The depth to the top of shale bedrock was relatively consistent, ranging from 3.5 feet (1.1 m) to approximately 11 feet (3.4 m). However, the top of rock profile varied considerably and was highly erratic for the part of the site underlain by limestone. The top of limestone bedrock ranged from 5 feet (1.5 m) to over 40 feet (12 m) deep and could vary by 30 feet (9.1 m) within a horizontal distance of less than 15 feet (4.6 m). In fact, the drilling of one of the test borings had to be terminated because the augers kicked off the surface of the rock, which indicated a very steep top of rock profile in the area where the boring was drilled.
- Because of the karst nature of the limestone, the quality of the limestone bedrock varied significantly and irregularly from location to location, both horizontally and vertically. The Rock Quality Designation (RQD) for the core runs ranged from very poor (0–25%) to excellent (90–100%), but was generally poor (25–50%). The unconfined compressive strengths of the limestone samples tested ranged from 2,440 to 10,820 psi (16.8 to 74.6 MPa), but were typically between 4,000 and 7,000 psi (27.6 and 48.3 MPa).
- There was abundant evidence of karst features (including soil seams/layers, solution channels, and voids without any filling material) within the limestone bedrock. These random features could be a few inches (tens of millimeters) to 6 feet (1.8 m) in thickness based on results of rock coring and air-track probes.

The highly erratic top of rock profile and the random karst features posed risks and challenges to the design and construction of the heavily loaded foundations of the C-5 Maintenance Hangar and Mall.

FOUNDATION DESIGN

The C-5 Maintenance Hangar and Mall structures are supported by columns at nearly 200 locations. The downward design loads at each support location ranged from 60 to 1,600 kips (27 to 726 metric tons), and at some locations uplift design loads ranging from 16 to nearly 600 kips (7.3 to nearly 272 metric tons) were anticipated. Most of the higher design loads are associated with the supports for the Maintenance Hangar because, although the structure has a slightly smaller floor space than the Maintenance Mall, the Maintenance Hangar has significantly fewer columns in order to provide an open bay for the gigantic C-5 aircraft.

Since the soils at the site were determined to be unsuitable as the bearing stratum for the Maintenance Hangar and Mall, the foundations had to bear on competent rock below the overburden. As discussed, shale bedrock under the northwest part of the footprint of the Maintenance Hangar was found to be relatively shallow. As long as the foundation was not subjected to an uplift load at a location, the overburden soil could be removed and a footing bearing on competent shale constructed to support the column load. However, under most of the project area where limestone was present, erratic top of rock profile and random karst features existed. Thus, the selected foundation system had to meet the following criteria:

1. The system must be capable of accommodating a wide range of bearing depths at the different support locations.
2. The system can be adjusted relatively easily during installation if an adjustment in the bearing depth estimated during the design becomes necessary in the field.
3. Preferably, at support locations with both downward and uplift loads, the system also resist the uplift load and keep the installation process simple without introducing new components or procedures that could potentially complicate the construction.

A foundation system consisting of drilled shafts was found to satisfy all three criteria. A drilled shaft could be drilled and installed to any depth anticipated on this project in order to reach competent rock. Additionally, a drilled shaft could be designed to resist uplift load by side friction if sufficient length of the drilled shaft was installed in competent rock. Table 1 summarizes the five drilled shaft designs or types that cover all of the support locations for the Maintenance Hangar and Mall. These drilled shafts were reinforced with steel cages consisting of vertical bars and ties at 1 foot (0.3 m) spacing.

Table 1. Drilled shaft designs.

Type	Diameter	Minimum Socket Diameter in Competent Rock	Minimum Socket Length in Competent Rock
DP-1	4’-0” (1.22 m)	3’-6” (1.07 m)	1’-0” (0.30 m)
DP-2	4’-0” (1.22 m)	3’-6” (1.07 m)	2’-0” (0.61 m)
DP-3	6’-6” (1.98 m)	6’-0” (1.83 m)	5’-0” (1.52 m)
DP-4	6’-6” (1.98 m)	6’-0” (1.83 m)	8’-0” (2.44 m)
DP-5	3’-0” (0.91 m)	2’-6” (0.76 m)	1’-0” (0.30 m)

“Competent rock” shall be defined as the minimum socket length plus 2 drilled shaft diameters below the bottom of drilled shaft. Voids, soil seams, or solution channels shall not be present in competent rock. In the case of uneven or sloping rock profile, competent rock shall be measured from the lowest point of the rock within the area of the drilled shaft. Competent rock shall be determined by the Engineer.

All drilled shafts must be installed to competent rock by the minimum socket length indicated in Table 1. Drilled shafts that needed to resist uplift had socket lengths ranging from 2 to 8 feet (0.61 to 2.44 m). A drilled shaft type (i.e., DP-1, DP-2, etc.) was assigned to each support location, depending on the magnitude of the design load

and whether or not an uplift force needed to be resisted at that particular location. Estimated bottom elevations of the drilled shafts were also indicated in the construction contract documents so that the bidders could price the foundation work. The actual bottom elevations of the drilled shafts would be determined in the field based on a systemic procedure established in the construction contract documents and discussed later in this paper.

MANAGING THE RISKS OF KARST GEOLOGY

The karst geology posed two major risks to the drilled shaft foundation system. First, there was the risk of bearing the bottom of the drilled shaft on what could appear to be competent limestone bedrock, but actually has a significant karst feature such as a large void, soil seams, or solution channel immediately under the rock. Another risk for those drilled shafts that needed to resist uplift during the design life of the structures was insufficient socket length in competent rock. For example, a drilled shaft could extend the minimum socket length (see Table 1) below the top of rock, but still would not mobilize sufficient side friction to resist the design uplift load due to the presence of one or more karst features in between the top of the rock and the bottom of the drilled shaft. In order to manage these risks, the following strategies were implemented for the construction of the C-5 Maintenance Hangar and Mall foundations:

- The term "competent rock," as defined in the Table 1 footnote, was indicated in the construction contract documents. A clear definition was necessary in order to avoid different interpretations of the term by different individuals during the construction.
- At each drilled shaft location, prior to constructing the drilled shaft, three 1.5-inch (38-mm) minimum diameter test probes were required to be drilled to a depth below the estimated bottom elevation of the drilled shaft (indicated in the construction contract documents) equal to twice the drilled shaft diameter. If a void, soil seams, or solution channel was detected, the depth of the test probes was to be extended. The test probe length below the bottom elevation of the drilled shaft must be twice the diameter of the drilled shaft. The probe holes were to be filled by grout upon completion of testing.
- A qualified geotechnical engineer representing the Engineer was responsible for determining when competent rock was reached at each drilled shaft location. The result of the test probes show that no voids, soil seams, or solution channels existed below the bottom of the drilled shaft and that the socket length in competent rock satisfied the minimum required for the drilled shaft type specified for that location (see Table 1).
- With the exceptions of drilled shaft types DP-3 and DP-4 (see Table 1), the actual bottom of most drilled shafts be shallower or deeper than the estimated bottom elevation of the drilled shaft indicated in the construction contract documents, as long as the aforementioned requirements were met. Drilled shaft types DP-3 and DP-4 were designed to support significant downward and uplift loads, so they were subjected to more stringent (or from a risk

management perspective, more conservative) requirements. These larger-diameter drilled shafts must meet the aforementioned requirements, and the bottom of the drilled shafts extend to at least the estimated bottom elevations, even if all requirements could be met at a shallower depth.

The above strategies were the primary methods for managing the risks of the karst geology at the site. An additional tool used as a secondary verification that no significant karst features existed immediately below the drilled shafts was the pile integrity test (PIT). The PIT, also called Sonic Testing or Pulse Echo, is a low strain impact integrity testing typically used to detect the presence and location of potentially significant defects in the installed drilled shaft such as cracks, necking, and soil inclusions or voids. The equipment and technique are well established based on ASTM D5882. In the case of this project, the PIT would likely be able to detect major karst feature if it had existed below the bottom of a drilled shaft that was subjected to the test.

CONSTRUCTION

A test program was conducted prior to allowing installation of drilled shafts at all locations. Ten test drilled shafts were initially constructed at production locations selected by the Engineer in order to verify that the Contractor's installation methods could successfully and consistently produce drilled shafts that met the requirements of the specifications. A test boring was drilled within 3 feet (0.91 meter) of each test drilled shaft before the drilled shaft was installed to identify the depth of competent rock, and to help the geotechnical engineer and the Contractor prepare for conditions that would be encountered during drilled shaft construction. After successful completion of all test drilled shafts, including verification by the PIT, drilled shaft installations at other locations were allowed to begin.

During the construction of the drilled shafts for the C-5 Maintenance Hangar and Mall, significant karst features were observed. Figure 3 and Figure 4 are photos taken looking down into the drilled holes. Figure 3 shows limestone "floaters" (white in color) embedded within the soil (brown in color). Figure 4 shows the limestone on the left side of the drilled hole and soil on the right side of the hole.

Figure 3. Limestone "floaters" embedded in soil.

Figure 4. Limestone on left side of the drilled hole only.

Despite the presence of significant karst features, as shown in the figures, the drilled shaft foundations were completed through the successful application of the procedures indicated in the construction contract documents. Additionally, the total construction cost of the drilled shaft foundations was within 3 percent of the Engineer's estimate.

CONCLUSIONS

The successful completion of the C-5 Maintenance Hangar and Mall in Martinsburg, West Virginia, demonstrated that risks posed by significant karst features can be managed with a thorough understanding of the subsurface conditions at the project site and application of carefully developed risk-management strategies. The following conclusions are made by the authors from the design and construction of this project:

- The design of large-scale foundation in karst geology should consider constructability, particularly the ease by which the foundation system can be adjusted during construction in order to achieve adequate bearing (or uplift resistance) in competent rock.
- The risk management strategies need to be carefully developed for the anticipated subsurface conditions. It is important to present these strategies through the construction contract documents in a manner that is clear, concise, and easy to understand.
- The geotechnical engineer or engineering geologist in the field responsible for determining when competent rock is reached has a critical role in managing the risks posed by karst geology. He or she should be highly qualified and familiar with karst geological conditions.
- In spite of the small difference in the total construction cost and the Engineer's estimate for the foundations on this project, it may be difficult to accurately estimate the construction cost (i.e., the total length of the drilled shaft required) due to the random nature of the karst features. Adequate owner contingency for construction is recommended.

REFERENCES

Cadle, Mike (2007a). "C-5 Era Begins in Martinsburg as 167th Airlift Wing Takes Delivery of First Galaxy Aircraft." *Mountaineer Defender,* Spring 2007:6.

Cadle, Mike (2007b). "More Jobs Coming to Martinsburg Air Base." *Mountaineer Defender,* Spring 2007:6.

Effect of Spatial Variability and Model Uncertainty on the Design of Sockets in Weak Carbonate Rocks

Khaled H. Charif[1] M. ASCE and Shadi Najjar[2], A.M. ASCE

[1]Lead Geotechnical Engineer, Fugro Middle East, P.O. Box 2863, Dubai, United Arab Emirates, PH (971) 502509832; email: k.charif@fugroME.com
[2]Assistant Professor, Department of Civil and Environmental Engineering, American University of Beirut, PO.Box 11-0236 Riad El-Solh 1107-2020; PH (961) 3108853; email: shadi.najjar@aub.edu.lb

ABSTRACT

This paper provides a framework for studying the combined effect of model uncertainties and uncertainties due to spatial variability on the side friction of drilled shafts in weak carbonate rocks. High quality site investigation data for a site in Dubai-UAE is used to characterize the spatial variability of weak carbonate rocks. Reliability assessments using Monte Carlo simulations indicated that uncertainty due to spatial variability has a notable effect on the reliability index with the effect being related to the pile length. In addition, the calculated reliability indices were found to be strongly affected by whether the median or the 10^{th} percentile UCS value was used in the deterministic design.

INTRODUCTION AND BACKGROUND

The side friction of drilled shafts in weak carbonate rocks is generally computed using data from unconfined compressive strength (UCS) and rock quality designation (RQD). The method proposed by O'Neill and Reese (1999) is one of the commonly used methods for predicting side friction in these rocks. Recent analyses of instrumented pile load tests (Charif et al. 2010) for shafts in weak carbonate rocks indicated that predictions of side friction exhibited significant scatter when compared to actual back calculated side friction values. Based on the results of ten instrumented load tests conducted on shafts with diameters ranging from 0.6m to 1.5m and lengths ranging from 14m to 32m at seven sites across Dubai-UAE, Charif et al. (2010) evaluated the model uncertainty associated with the O'Neill and Reese (1999) model. The model uncertainty was reflected by the average (bias) and coefficient of variation (COV) of the ratio (λ) of predicted to measured skin friction, which were found to be equal to 1.17 and 0.49, respectively. The calculated COV could be considered to be relatively large reflecting uncertainty in the predictions of skin friction in soft rock.

In addition to the model uncertainty, the design of sockets in weak carbonate rocks is affected by vertical and lateral spatial variability in the UCS and RQD values. Spatial variability is generally modeled by the mean, standard deviation, and the spatial correlation structure of the relevant rock property and constitutes an additional source of uncertainty in predicting the side friction. There is very limited

data available in the literature on the spatial variability of weak carbonate rocks. Miller and Luark (1993), Tan et al. (2000), Mark et al. (2003), and Klammler et al. (2010) evaluated the vertical and/or horizontal correlation distances of the UCS of siltstone, sandstone, shale, and limestone layers for applications involving mining, slope stability, and foundation design. In these studies, autocorrelation and semi-variogram functions were used to evaluate the correlation lengths.

Based on the knowledge of the authors, there has been no attempt to study the combined effect of model uncertainties and uncertainties associated with spatial variability in applications involving the design of weak carbonate rocks. As a result, the main two objectives of this paper are to (1) evaluate the spatial variability of the UCS and the RQD for an 80-m thick deposit of weak rock in a typical site in Dubai, and (2) assess the reliability of designs obtained using conventional factors of safety using a Monte Carlo framework that combines model uncertainties with uncertainties due to spatial variability of rock properties.

SPATIAL VARIABILITY OF UCS AND RQD

Location, geology, and site characterization. The site under consideration is located at the Dubai waterfront and has a surface area of about 10,000 m^2. The geology is represented by an area of carbonate sedimentation. At the site, surfacial deposits consisting of sand dunes and evaporates together with marine sands and silts overlie interbedded carbonate rocks, consisting mainly of siltstones, sandstones, and calcisiltites. A geotechnical investigation was conducted at the site as part of the foundation design for a proposed tower structure. The investigation included drilling 9 boreholes up to maximum depths of 200m. The ground investigation was undertaken by Fugro Middle East using the PQ triple tube drilling technique. Immediately upon extraction, the cores were logged, photographed and samples were extracted for laboratory testing. It should be noted that for the purpose of this study, only the UCS data and RQD data corresponding to depths between 20m and 100m will be analyzed to limit the length of the paper. A plan showing the location of the boreholes is presented in Fig. 1.

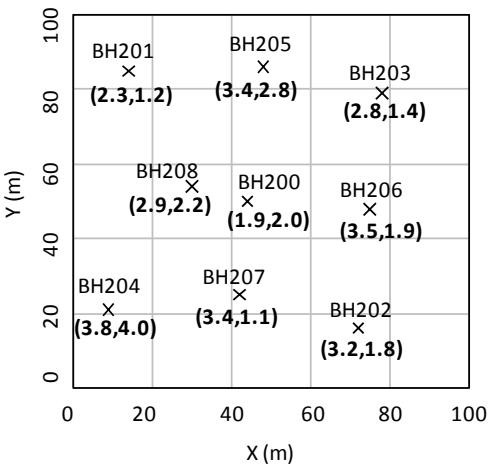

Figure 1. Borehole layout plan (numbers in parenthesis represent the mean and standard deviation of the UCS for depths between 20m and 100m).

Spatial variability of UCS data. The variation of the UCS with depth as obtained from 132 tests on cores obtained from the nine boreholes are presented in Fig. 2a. The mean value of the 132 data points is 2.94 MPa and the standard deviation is 2.21 MPa leading to a coefficient of variation of 0.75 in the point estimate of the UCS of the rock at the site. The variation of the mean UCS between boreholes is shown in Fig. 1 and indicates minimum and maximum average UCS values of 1.9 MPa and 3.8 MPa respectively. The data on Fig. 1 and on Fig. 2a do not indicate the presence of a spatial trend in the vertical direction or spatial clustering in the horizontal direction. As a result, the available data are pooled together and the resulting histogram is shown in Fig. 3a with theoretical fits of normal and lognormal probability density functions. The discrete cumulative distribution function (CDF) of the data in addition to the theoretical normal and lognormal CDFs are presented in Fig. 3b for comparison. Results on Fig. 3 indicate clearly that the lognormal distribution provides a realistic representation of the observed data, unlike the normal distribution which fails at providing an acceptable model to the tails of the observed UCS data range.

The spatial variability of the UCS of the rock is characterized by the mean, the standard deviation, and the spatial correlation structure, which is represented by autocorrelation functions or by semi-variograms. To simplify the spatial variability analysis, it is assumed that the soil is spatially statistically homogeneous and that the UCS results from the different boreholes represent a set of independent realizations of the same 1D random process (Fenton 1999). In other terms, it is assumed that the random process representing the variation of UCS with depth has the same joint distribution at any horizontal location. Based on the above, the analysis of the correlation structure will be limited to the vertical direction. It should be noted however that the results obtained from such an analysis may lead to a slight underestimation of the variability of statistical estimates since an entire shaft may be located in a zone of either high or low strength (Fenton 1999 and Klammler 2010).

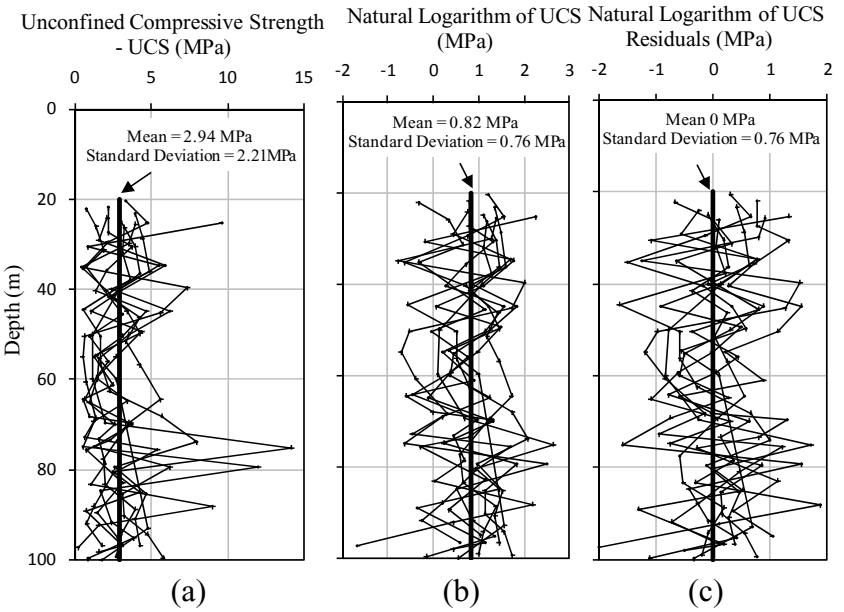

Figure 2. Variation of UCS data and UCS residuals with depth.

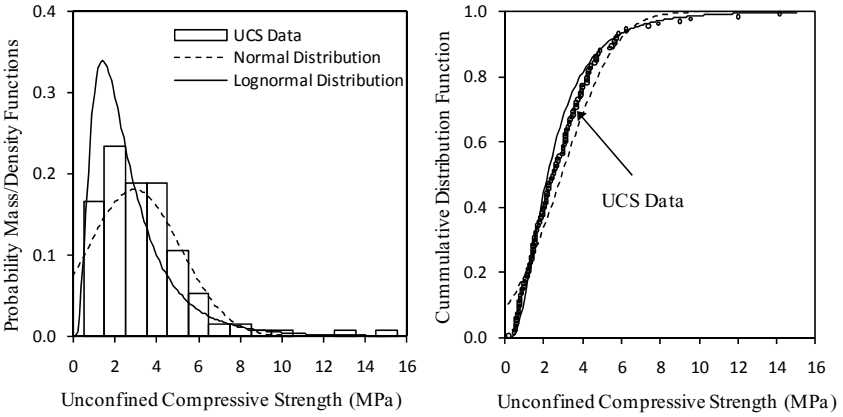

Figure 3. Theoretical normal and lognormal fits to the observed data

The vertical correlation structure of the UCS could be defined by a correlation distance or a scale of fluctuation. Since the UCS data follows a lognormal distribution reasonably well, the spatial variability analysis was conducted using the natural logarithm of the UCS data (Fig. 2b) which exhibited reasonable stationarity. Thus, the analysis of spatial correlation was conducted using the residuals of the logarithm of the UCS (Fig. 2c), which were used to calculate the vertical sample correlation and the experimental semi-variogram functions for the UCS data (Fig. 4). Details on how to evaluate these functions are presented elsewhere (Fenton 1999). Results on Fig. 4 indicate that even at the minimum vertical sampling interval considered (about 3m), the correlation function and the semi-variogram did not indicate any notable correlation between the UCS data points. The computed correlation coefficients fall within the Bartlett's limits which specify the boundaries for which the correlations are assumed to be statistically insignificant. On the other hand, the normalized semi-variogram exhibited values that are close to 1.0 even at a lag distance of 3m, indicating that the vertical correlation distance for the UCS samples at this particular site is less than 3.0m. This result is expected since both Miller and Luark (1993) and Klammler et al. (2010) evaluated vertical ranges of influence or correlation lengths of 0.55m and 1.5m to 3.0m, for siltstone and Florida limestone respectively.

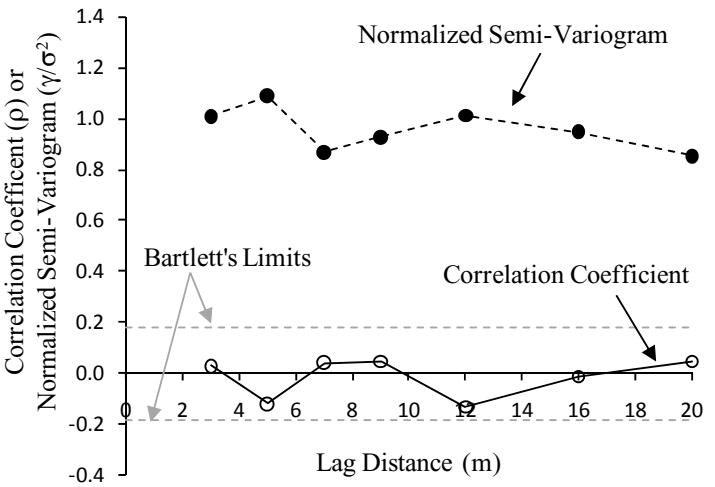

Figure 4. Correlation coefficient and normalized semi-variogram for UCS data

Spatial variability of RQD data. The variation of the RQD data with depth as obtained from 445 data points is presented in Fig. 5a and indicate a mean RQD of 93.4% and a standard deviation of 17.3% leading to a COV of 0.185 in the point estimate of the RQD at the site. Since the RQD has an upper bound of 100%, both the normal and lognormal distributions failed at providing a realistic fit of the RQD data (Fig. 5b). As a result, a more flexible probability model that incorporates a 3rd order Hermite polynomial (Najjar 2005) was used to represent the uncertainty in the RQD data (Fig. 5b). The average vertical experimental semi-variogram function for the RQD data is presented in Fig. 6. The semi-variogram indicates a range of influence of 10 to 15m. This is the range of lag distances over which the normalized semi-variogram values are less than 1.0. Based on the knowledge of the authors, the semi-variogram shown on Fig. 6 represents the first attempt to model the correlation structure of RQD in rocks. As a result, the resulting range of influence (correlation length) cannot be compared with any published data in the literature.

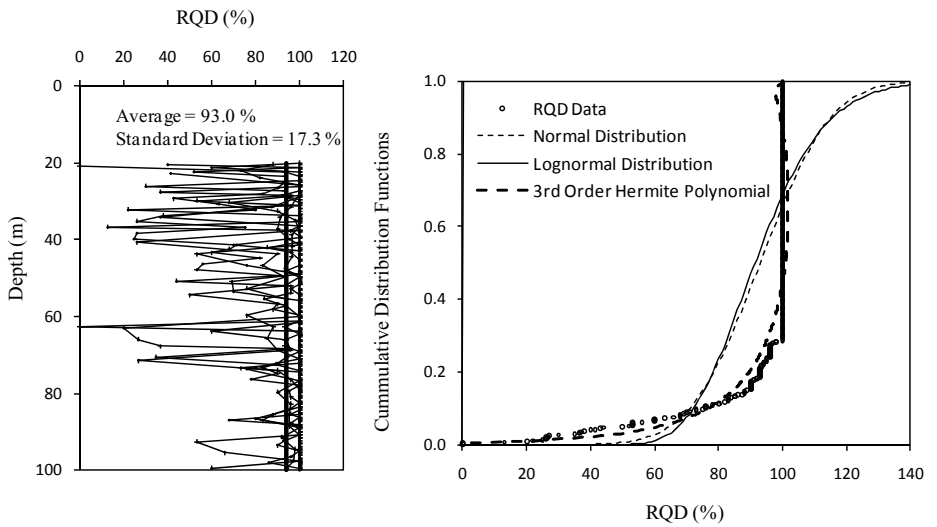

Figure 5. (a) Variation of RQD with depth and (b) theoretical CDFs for RQD

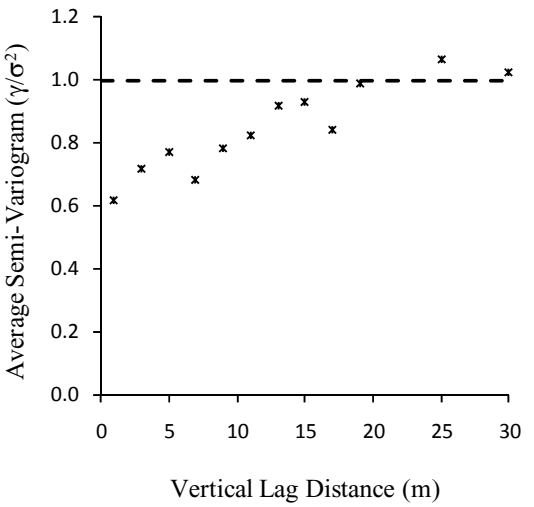

Figure 6. Average normalized semi-variogram for RQD Data

RESULTS OF THE RELIABILITY ANALYSIS

A Monte Carlo analysis consisting of 600,000 realizations was conducted to evaluate the probability of failure (reliability index). The design equation proposed by O'Neill and Reese (1999) for evaluating skin resistance for shafts in soft rock is:

$$Q_{side} = \left(\frac{\alpha \varphi q_{u,ave}}{\lambda} \right) \pi D L \quad (1)$$

where Q_{side} is the side shear, $q_{u,ave}$ is the average UCS along the shaft, α and φ are model parameters, λ is the ratio of predicted to measured skin friction, and D and L are the shaft diameter and length. The factor λ was modeled by a lognormal distribution with a mean of 1.17 and a COV of 0.49 while the load was assumed to follow a lognormal distribution with a COV of 0.15. Since the rock properties are averaged properties along the shaft length, the variances of the average properties ($q_{u,ave}$ and RQD_{ave}) were computed from the variances of the point using the reduction factor $\Gamma^2(L,\delta)$ which depends on the scale of fluctuation (δ) and the shaft length (L):

$$Var(q_{u,ave}) = \Gamma^2(L,\delta) Var(q_u) \text{ and } Var(RQD_{ave}) = \Gamma^2(L,\delta) Var(RQD) \quad (2)$$

$\Gamma^2(L,\delta)$ was taken to be 1.0 for L less than or equal to δ and δ/L for L greater than δ. The reduced variances were used to represent the uncertainty in the average UCS and RQD using δ values of 3m (conservative estimate for UCS) and 15m for the RQD.

The Monte Carlo framework was used to evaluate the reliability index for current deterministic design procedures for a typical factor of safety of 3.0. The design load was varied from 300 tons to 2400 tons and shaft lengths were calculated for diameters ranging from 0.6m to 1.5m. The reliability index for each design scenario was then evaluated using the Monte Carlo analysis. Two design cases were considered. In the first case, the 50th percentile UCS was used in the deterministic analysis to compute the pile length, while in the second case, a more conservative but common approach which involves using the 10th percentile UCS value was adopted.

Results of the reliability-based design analysis for the two design approaches are presented in Figs. 7 and 8. The results reflect three interesting observations: (1) for a given design load, the reliability indices increase consistently as the diameter decreases, (2) for a given pile diameter, the reliability indices increase as the design load increases, and (3) the reliability indices range between 2.0 and 2.4 for the case where the median UCS value is used in the design, and between 2.8 and 3.2 when the 10th percentile UCS is used instead. The first two observations are related to the reduction in the variance of the average UCS and RQD values as the length of the shaft increases. This effect is illustrated in Fig. 8 which shows an increase in the reliability index as the pile length increases. The effect of averaging is the greatest for the initial part of the curve. At larger lengths, the rate of variance reduction decreases and the increase in β levels off. This is amplified by the fact that at larger lengths, uncertainty in the model governs the reliability since uncertainty due to spatial variability is reduced by variance reduction. This observation is important and indicates that for a given reliability index, shafts with smaller diameters and larger lengths could be more economical than larger diameter piles with smaller lengths.

With regards to the magnitude of the reliability indices, results indicate that for the design approach which is based on the median UCS value, the calculated reliability indices are all less than 2.5, which is the minimum reliability index that could be considered to be acceptable for individual foundations by many design codes. The second design approach which utilizes the 10th percentile UCS resulted in reliability indices that are larger than 2.8, indicating a more acceptable design. It should be noted however that the results presented in Figs. 7 and 8 are based on the model uncertainty statistics obtained for the O'Neill and Reese (1999) model based on a limited number of instrumented pile load tests. These statistics should be confirmed in the future using larger databases of load tests.

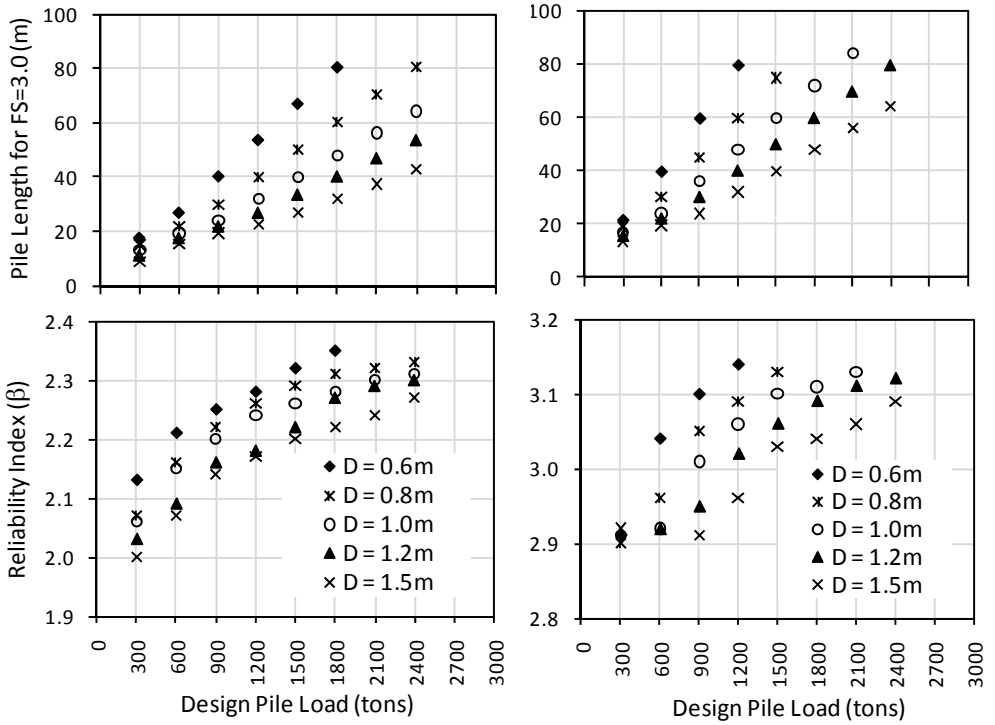

(a) Design using Median UCS (b) Design using 10th Percentile UCS

Figure 7. Variation of pile length and reliability index with design load

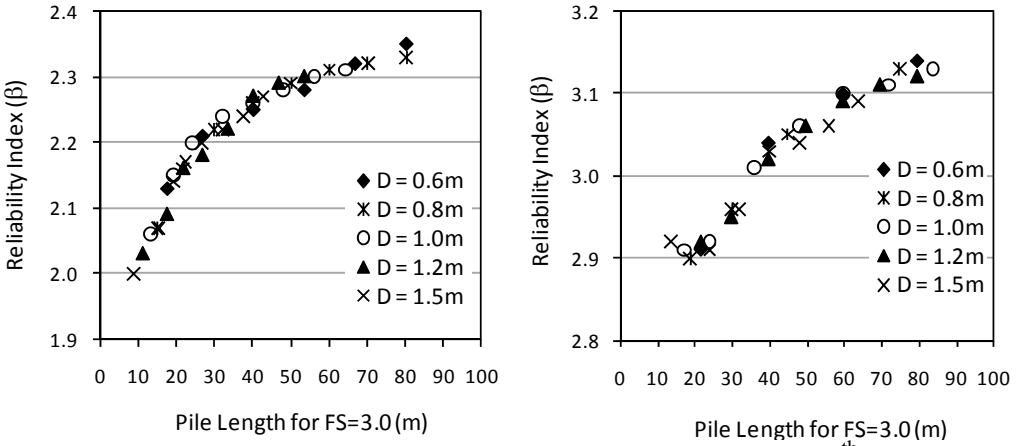

(a) Design using Median UCS (b) Design using 10th Percentile UCS

Figure 8. Variation of reliability index with shaft length

CONCLUSIONS

The following can be drawn with regards to the effect of model uncertainty and spatial variability on the design of shafts in weak carbonate rocks:

1. The distance over which UCS values for soft rocks could be assumed to be correlated is less than 3.0m, while the distance for RQD values is about 10m.
2. For a design factor of safety of 3.0, model uncertainties and uncertainties due to spatial variability result in reliability indices between 2.0 and 2.4 for designs obtained using the O'Neill and Reese (1999) model using the median UCS value, and 2.8 to 3.2 if the 10^{th} percentile UCS value is used instead.
3. The variance reduction due to spatial averaging of soil properties along the pile shaft has a significant effect on the calculated reliability index which was found to be larger for longer piles designed at the same factor of safety.

ACKNOWLEDGMENTS

The authors would like to acknowledge the University Research Board at the American University of Beirut for funding this work. Many thanks are also extended to Melanie Bier and Bryan Dimaano of Fugro Middle East, Dubai for their support. The assistance of Myra Fakhoury Charif of Schlumberger is also much recognized.

REFERENCES

Charif, K.H., Najjar, S.S., and Sadek, S. (2010). "Side friction along drilled shafts in weak carbonate rocks." *The Art of Foundation Engineering Practice,* Geotechnical Special Publication No. 198, ASCE.

Fenton, G.A. (1999). "Random field modeling of CPT data." *Journal of Geotechnical and Geoenvironmental Engineering*, ASCE, 125(6): 486-498.

Klammler, H., McVay, M., Horhota, D., and Lai, P. (2010). "Influence of spatially variable side friction on single drilled shaft resistance and LRFD resistance factors." *Journal of Geotechnical and Geoenvironmental Engineering*, ASCE, 136(8): 1114-1123.

Mark, C., McWilliams, L., Pappas, D. and Rusnak, J. (2004). "Spatial trends in rock strength - can they be determined from coreholes?" *Proc. of the 23rd International Conference on Ground Control in Mining. Morgantown, WV: West Virginia University,* 177-182.

Miller, S.M. and Luark R.D. (1993). "Spatial simulation of rock strength properties using a Markov-Bayes method." *Int. J. Rock Mech. Min. Sci. & Geomech.*30(7): 1631-1637.

Najjar, S.S. (2005). "*The importance of lower-bound capacities in geotechnical reliability reliability assessments*." Dissertation, Univ. of Texas at Austin, Texas.

O'Neill, M.W, and Reese, L.C. (1999). "Drilled shafts: construction procedures and design methods." *Report No. FHWA-IF-99-025, Federal Highway Administration*, Washington D.C. USA.

Tan, W., Wang, J., and Cai, M. (2000). "Spatial variability of rock strength and its impact on slope stability." *Electronic Journal of Geotechnical Engineering,* 5.

CPT-Based Probabilistic Characterization of Effective Friction Angle of Sand

Zijun Cao[1], Yu Wang[2], M.ASCE, and Siu-Kui Au[3] A.M.ASCE

[1]Department of Building and Construction, City University of Hong Kong, Hong Kong; PH (852) 3442-6492; email: zijuncao3@student.cityu.edu.hk
[2]Department of Building and Construction, City University of Hong Kong, Hong Kong; PH (852) 3442-7605; FAX (852) 3442-0427; email: yuwang@cityu.edu.hk
[3]Department of Building and Construction, City University of Hong Kong, Hong Kong; PH (852) 3442-2769; FAX (852) 3442-0427; email: siukuiau@cityu.edu.hk

ABSTRACT

Recent development and implementation of reliability-based design codes around the world underscore the needs of probabilistic characterization of soil properties. A Bayesian approach is presented in this paper to characterize probabilistically the effective friction angle ϕ' of sand using CPT data. The Bayesian framework is developed in conjunction with random field theory to model the inherent spatial variability and regression model to relate CPT measurements with ϕ'. The likelihood function and posterior distributions of uncertain parameters are derived. A sensitivity study is carried out to explore the effects of prior mean, variance, and correlation length on posterior mean.

INTRODUCTION

Over the last two decades, several reliability-based design (RBD) codes have been developed and implemented around the world, including the United States (e.g., Phoon et al. 1995, Paikowsky et al. 2010), Canada (e.g., Becker 1996), Europe (e.g., Orr and Farrell 1999), and Japan (e.g., Honjo and Kusakabe 2002). As these RBD codes use probability theory to deal rationally with geotechnical-related uncertainties that arise in geologic site interpretations, geotechnical properties, computational models, etc, their applications in turn call for the needs of probabilistic characterization of geo-material properties. Such probabilistic characterization has been a challenging task, at least partly, due to the inherent spatial variability of geo-materials and the fact that only a small portion of geo-materials are examined during site characterization. This is particularly crucial for projects with medium or relatively small sizes, in which the number of tests are usually too small to generate meaningful statistics for the probabilistic characterization.

This paper presents a Bayesian approach to characterize probabilistically the effective friction angle ϕ' of sand using cone penetration tests (CPT). The Bayesian framework and its key elements (e.g., prior information, likelihood function, and posterior information) are described. A sensitivity study then is carried out to explore the effect of prior information.

BAYESIAN FRAMEWORK

Probabilistic characterization of the effective friction angle ϕ' of sand is formulated in this paper as a Bayesian updating process (Wang et al. 2010). Starting from the Bayes' Theorem, Eq(1) can be derived for updating probability distribution parameters (i.e., mean μ, standard deviation σ, and correlation length λ) of a random variable ϕ' given CPT test data $\underline{\xi}$ as (e.g., Ang and Tang 2007)

$$p(\mu,\sigma,\lambda \mid \underline{\xi}) = k\ p(\underline{\xi} \mid \mu,\sigma,\lambda)\, p(\mu,\sigma,\lambda) \tag{1}$$

where $p(\mu,\sigma,\lambda \mid \underline{\xi})$ = the posterior distribution given data $\underline{\xi}$; $k = 1/\,p(\underline{\xi})$ = a normalizing constant that does not depend on μ, σ, and λ; $p(\underline{\xi} \mid \mu,\sigma,\lambda)$ = likelihood function that reflects model fit with the data; and $p(\mu,\sigma,\lambda)$ = prior distribution that reflects available information about the parameters in the absence of data (i.e., before CPT tests). In general, geotechnical site characterization is a multi-step process which utilizes both available prior information and project-specific information from test borings, in-situ testing, and/or laboratory testing. Prior information include, but are not limited to, maps and surveys, local experience, visual observations, and published reports and studies. After collection and consolidation of the prior information, project-specific information is obtained from further tests of the sites. Consider CPT, for example. A cylindrical steel probe is pushed into the ground, and the resistance to probe penetration is measured and related to soil properties of interest (e.g., ϕ') using regression equations.

Bayesian approach has been applied to geotechnical engineering, such as characterization of model uncertainty (e.g., Gilbert and Tang 1995, Zhang et al. 2009, Najjar and Gilbert 2009), calibration of estimated liquefaction probability (e.g., Juang et al. 1999), and updating of geotechnical parameters (e.g., Miranda et al. 2009). Computational complexity has been recognized as one key limitation of the Bayesian approach (e.g., Zhang et al. 2009). An asymptotic approximation is used in this paper to by-pass the computational complexity. The Bayesian approach in this work also considers the inherent spatial variability of soil, as described in the next section.

LIKELIHOOD FUNCTION

The inherent spatial variability of ϕ' within a single homogeneous stratum of sand is modeled by a one-dimensional homogeneous Gaussian random field, ϕ'(D), in which D is the depth and ϕ' is a random variable with mean μ and standard deviation σ (Vanmarcke 1983). The correlation structure of ϕ' is assumed to be an exponential covariance function (Fenton 1999)

$$COV[\phi'(D_1),\phi'(D_2)] = \sigma^2 \exp(-\frac{2 \mid d_{1,2} \mid}{\lambda}) \tag{2}$$

where λ = correlation length and $d_{1,2} = \left|D_1 - D_2\right|$ = the distance between depths D_1 and D_2. Let $\underline{\phi}' = [\phi'(D_1),\phi'(D_2),...,\phi'(D_n)]^T$ be a vector of effective friction angles at

depths $D_1, D_2, ..., D_n$, respectively. In the context of random field, $\underline{\phi'}$ can be expressed as a sequence of independent and identically distributed random variables

$$\underline{\phi'} = \mu \underline{1} + \sigma \underline{L}^T \underline{Z} \tag{3}$$

where $\underline{1} = [1,...,1]^T$, $\underline{Z} = [Z_1,...,Z_n]^T$ = a standard Gaussian vector with independent components, and $\underline{L}$ = a n-by-n upper-triangular matrix obtained by Cholesky decomposition of the correlation matrix $\underline{R}$. The (i, j) entry of $\underline{R}$ is given by

$$\underline{R}(i,j) = \exp(-\frac{2 \mid d_{i,j} \mid}{\lambda}) \tag{4}$$

The ϕ' of the tested soil is frequently estimated from CPT using a regression between ϕ' and the resistance, q_c, measured at the tip of the cone. Consider, for example, an empirical model developed by Kulhawy and Mayne (1990)

$$\xi = \ln q = a\phi' + b + \sigma_m \varepsilon \tag{5}$$

where $q = (q_c / p_a) / (\sigma'_{v0} / p_a)^{0.5}$ = the normalized cone tip resistance; σ'_{v0} and p_a = vertical effective stress and standard atmospheric pressure (i.e., 100 kPa), respectively; $a = 0.209$, $b = -3.684$, $\sigma_m = 0.586$, and ε = a standard Gaussian random variable. The last term $\sigma_m \varepsilon$ represents a modeling error associated with the regression equation.

Let $\underline{\xi} = [\xi_1,...,\xi_n]^T$ be a vector of $\ln q$ data at depths $D_1, D_2, ..., D_n$. Using Eqs(3) & (5) gives $\underline{\xi} = (a\mu + b)\underline{1} + (a\sigma \underline{L}^T \underline{Z} + \sigma_m \underline{\varepsilon})$. When the inherent spatial variability is assumed to be independent of model uncertainty (i.e., $\underline{Z}$ and $\underline{\varepsilon}$ are independent), $\underline{\xi}$ is a Gaussian vector with mean $(a\mu + b)\underline{1}$ and covariance matrix $\underline{C} = a^2\sigma^2 \underline{R} + \sigma_m{}^2 \underline{I}$, where $\underline{I}$ = a n-by-n identity matrix.

Within a Bayesian framework, the likelihood function is thus given by

$$p(\underline{\xi} \mid \mu, \sigma, \lambda) = (2\pi)^{-n/2} \mid \det \underline{C} \mid^{-1/2} \exp\{-\frac{1}{2}[\underline{\xi} - (a\mu + b)\underline{1}]^T \underline{C}^{-1} [\underline{\xi} - (a\mu + b)\underline{1}]\} \tag{6}$$

The prior distribution $p(\mu, \sigma, \lambda)$ is assumed to be a Gaussian distribution with mean (μ_0, σ_0, and λ_0) and standard deviation (ω_μ, ω_σ, and ω_λ)

$$p(\mu, \sigma, \lambda) = \frac{1}{(2\pi)^{3/2} \omega_\mu \omega_\sigma \omega_\lambda} \exp\{-\frac{1}{2\omega_\mu{}^2}(\mu - \mu_0)^2 - \frac{1}{2\omega_\sigma{}^2}(\sigma - \sigma_0)^2 - \frac{1}{2\omega_\lambda{}^2}(\lambda - \lambda_0)^2\} \tag{7}$$

With the likelihood function and prior distribution given by Eqs(6) & (7), the posterior probability distribution function (PDF) can be obtained from Eq(1), as described in the next section.

POSTERIOR INFORMATION

The posterior PDF in Eq(1) is a joint distribution among μ, σ, and λ. To

obtain the posterior marginal PDF for μ, integration on Eq(1) over σ and λ is needed (and similar for the other two parameters). Since the integrand is complicated, analytical integration is often infeasible. Numerical integration may be performed using a two-dimensional grid on the space of σ and λ for the posterior PDF of μ, but it must be performed repeatedly for a number of μ values so as to yield information about the whole marginal distribution. Such computational complexity has been recognized as one key limitation of the Bayesian approach in literature (e.g., Zhang et al. 2009). To overcome such limitation, Wang et al. (2010) used an asymptotic technique to approximate the integral, which is essentially a Gaussian approximation of the posterior PDF (Bleistein and Handelsman 1986). By this approximation, the posterior PDF for the model parameters is a joint Gaussian PDF with mean vector equal to the most probable value (MPV) of the posterior PDF. The MPV, denoted by (μ^*, σ^*, λ^*), maximizes the $p(\mu,\sigma,\lambda|\underline{\xi})$. Under this approximation, the determination of the posterior mean for μ, σ, and λ reduces to finding the MPV by numerically minimizing the function $-\ln p(\mu,\sigma,\lambda|\underline{\xi})$ in the three dimensional space of (μ, σ, λ). In addition, the covariance matrix $\underline{G}$ of the Gaussian PDF that approximates $p(\mu,\sigma,\lambda|\underline{\xi})$ is given by the inverse of the Hessian matrix of $f=-\ln p(\mu,\sigma,\lambda|\underline{\xi})$ evaluated at the MPV. The main diagonal terms of $\underline{G}$ give the posterior variance of μ, σ, and λ while the off-diagonal terms give their covariance, i.e., $s_\mu^{\,2}=\underline{G}(1,1)$, $s_\sigma^{\,2}=\underline{G}(2,2)$ and $s_\lambda^{\,2}=\underline{G}(3,3)$.

Implementation of the asymptotic technique contains two key elements: minimization of $f(\mu,\sigma,\lambda)=-\ln p(\mu,\sigma,\lambda|\underline{\xi})$ on their three-dimensional space to obtain μ^*, σ^*, λ^* and calculation of the inverse of the Hessian matrix of $f=-\ln p(\mu,\sigma,\lambda|\underline{\xi})$ evaluated at μ^*, σ^*, λ^* to obtain $s_\mu^{\,2}, s_\sigma^{\,2}, s_\lambda^{\,2}$. The minimization can be readily implemented by conventional optimization algorithm, e.g., the function "fminsearch" in MATLAB (Mathworks 2010). The differentiation of $f=-\ln p(\mu,\sigma,\lambda|\underline{\xi})$ for constructing the Hessian matrix can be evaluated numerically in MATLAB using finite difference. Wang et al. (2010) applied the Bayesian approach to characterize probabilistically ϕ' at the sand site of the National Geotechnical Experimental Site (NGES) at Texas A&M University (Briaud 1997). The Bayesian approach was shown to give probabilistic characterization that is consistent with the statistical information compiled from tests that have been carried out extensively in this NGES site.

EFFECT OF PRIOR INFORMATION

Prior information is a key element in the Bayesian framework, as shown in Eq(1). Its effect on the posterior information is explored through a series of sensitivity study described in this section. The sensitivity study is performed together with a set of CPT data that aims to characterize a ϕ' random field with μ = 32°, σ = 1.92°, and λ = 1 m. As shown in Figure 1, normalized tip resistance (q) from CPT tests are simulated from ground surface to a depth of 10 m at a spatial interval of

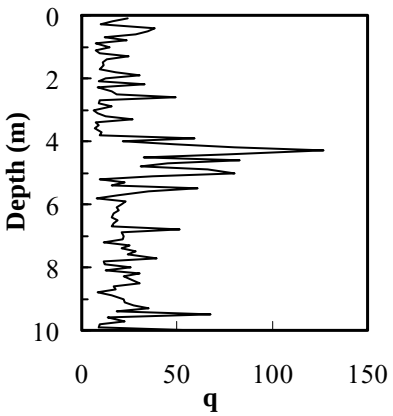

Figure 1. CPT data: normalized cone tip resistance, q, versus depth relationship.

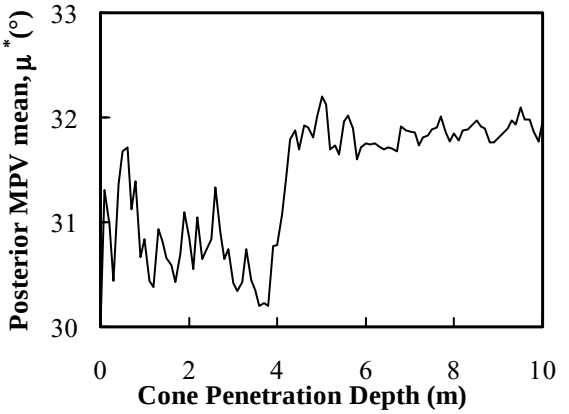

Figure 2. Posterior mean of sand effective friction angle.

Table 1. Range of parameters in sensitivity studies on prior information.

Parameter	Nominal Case	Absolute Range	Relative Range
μ_0 (°)	30	16 - 64	0.5μ - 2μ
ω_μ (°)	6	3.2 - 64	$0.2\mu_0$ - μ_0
σ_0 (°)	6	0.384 - 7.68	0.2σ - 4σ
ω_σ (°)	1.2	0.077 - 7.68	$0.2\sigma_0$ - σ_0
λ_0 (m)	1.5	0.1 - 2	0.1λ - 2λ
ω_λ (m)	0.3	0.02 - 2	$0.2\lambda_0$ - λ_0

Note: the true soil property: $\mu = 32°$, $\sigma = 1.92°$, and $\lambda = 1$ m

0.1 m using the aforementioned random field and regression models [i.e., Eqs(2) - (5)].

As a nominal case in the sensitivity study, prior information is taken as: $\mu_0 = 30°$, $\sigma_0 = 6°$, $\lambda_0 = 1.5$ m and $\omega_\mu = 6°$, $\omega_\sigma = 1.2°$, $\omega_\lambda = 0.3$ m. Figure 2 shows a variation of posterior mean μ^* of ϕ' as a function of cone penetration depth. For a given cone penetration depth, Bayesian updating is performed with the CPT soundings up to the given penetration depth. Figure 2 therefore depicts an evolution of μ^* as more and more CPT data is incorporated. When cone penetration depth is zero, no data, except prior information, is available to characterize ϕ' and therefore the curves always start with its prior mean. As the cone penetration depth increases, more CPT test results are incorporated and they gradually influence the posterior μ^*. The posterior μ^* in the figure gradually increases from prior $\mu_0 = 30°$ to about 32°, which is the true μ value of the ϕ' random field.

Effects of prior mean, variance, and correlation length on posterior mean are explored together with the 10-m CPT data shown in Figure 1. Table 1 summarizes the range of parameters in the sensitivity study. The following ranges are considered: μ_0 from 0.5μ to 2μ (i.e., 16° to 64°), σ_0 from 0.2σ to 4σ (i.e., 0.38° to 7.68°), λ_0 from 0.1λ to 2λ (i.e., 0.1 m to 2 m), ω_μ from $0.2\mu_0$ to μ_0, ω_σ from $0.2\sigma_0$ to σ_0, and ω_λ from $0.2\lambda_0$ to λ_0. Note that prior information contains both mean and standard deviations. The mean values represent their respective best estimates, and the standard deviations reflect their associated uncertainties or confident levels.

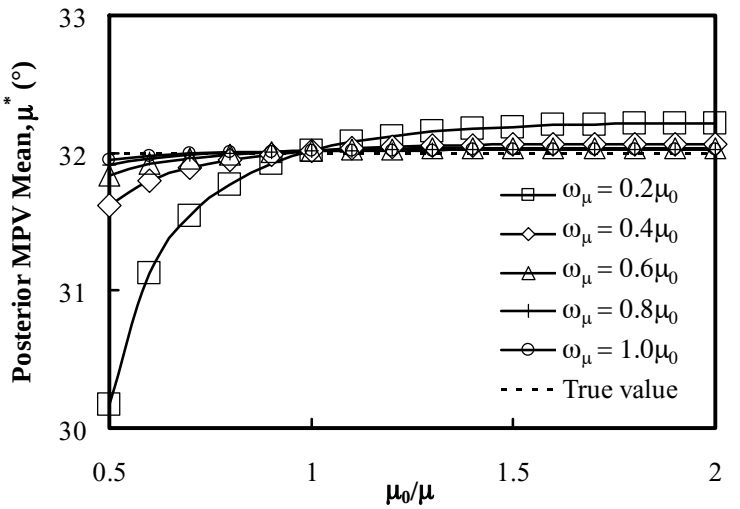

Figure 3. Effect of prior mean on posterior mean μ^*.

Effect of Prior Mean. Figure 3 summarizes results of the sensitivity study on prior mean in a plot of μ_0/μ versus posterior μ^*. For a wide range of μ_0 values (i.e., from 16° to 64° or μ_0/μ from 0.5 to 2 for the true μ = 32°), the posterior μ^* plots closely to the true μ value of 32°. In addition, the figure includes posterior μ^* for the ω_μ value varying from $0.2\mu_0$ to $1.0\mu_0$. When ω_μ is relatively large (i.e., uninformative or unconfident with μ_0), μ_0 only has a minimal influence on the posterior μ^*. However, as ω_μ decreases and the confident level gradually increases, the posterior μ^* gradually deviates from the true μ value of 32° and the influence of μ_0 on μ^* increases. The Bayesian approach properly accounts for prior mean that varies from very informative and consistent with the CPT data to uninformative and inconsistent with the CPT data.

Effects of Prior Variance and Correlation Length. Similar sensitivity studies are carried out for prior variance and correlation length, as summarized in Table 1. Figure 4 shows effect of prior variance on posterior μ^* in a σ_0/σ versus μ^* plot. For a wide range of σ_0 and ω_σ values, the posterior μ^* are virtually identical to the true μ value of 32°. Similar results are also obtained for a wide range of λ_0 and ω_λ values, as shown in Figure 5. The results imply that the effects of prior variance and correlation length are minimal in this example.

SUMMARY AND CONCLUSIONS

This paper presented a Bayesian approach to characterize probabilistically the effective friction angle ϕ' of sand using CPT data. The Bayesian framework was developed in conjunction with random field theory to model the inherent spatial variability and regression model to relate CPT measurements with ϕ'. The likelihood function and posterior distributions of uncertain parameters were derived. An approximate method was used to by-pass multi-dimensional integration involved in obtaining the marginal distributions of posterior distributions. A sensitivity study was carried out to explore the effects of prior mean, variance, and correlation length. It was shown that the Bayesian approach properly accounts for prior mean that varies

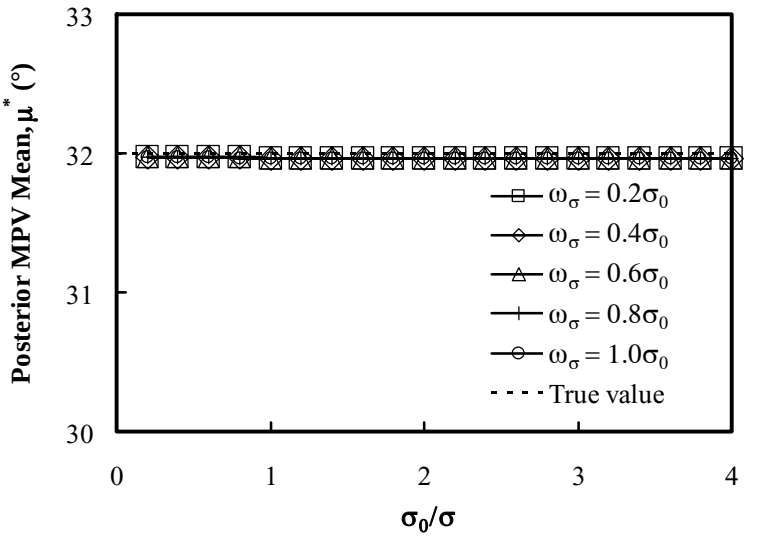

Figure 4. Effect of prior variance on posterior mean μ^*.

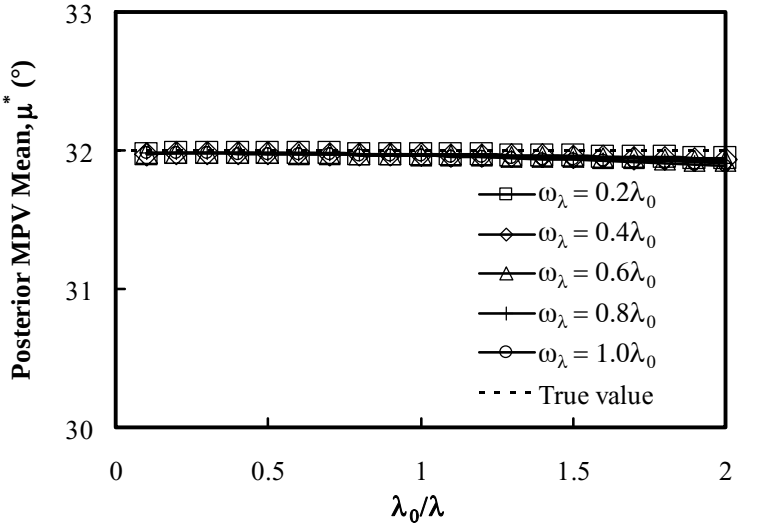

Figure 5. Effect of prior correlation length on posterior mean μ^*.

from very informative and consistent with the CPT data to uninformative and inconsistent with the CPT data. On the other hand, the effects of prior variance and correlation length on posterior mean are relatively minor.

ACKNOWLEDGMENTS

This paper is supported by a general research grant 9041484 (CityU 110109) from the Research Grants Council of the Hong Kong Special Administrative Region, China. The financial supports are gratefully acknowledged.

REFERENCES

Ang, A. H.-S. and Tang, W. H. (2007). *Probability Concepts in Engineering: Emphasis on Applications to Civil and Environmental Engineering*. Wiley, New York.

Becker, D. E. (1996). "Limit state design for foundations – part II: Development for national building code of Canada." *Can. Geotech. J.*, 33(6), 984-1007.

Bleisten, N. and Handelsman, R. (1986). *Asymptotic Expansions of Integrals*, Dover, New York.

Briaud, J. L. (1997). *The national geotechnical experimentation sites at Texas A&M University: clay and sand*. Report, NGES-TAMU-007-September 1997, Texas A&M University, 38p.

Fenton, G. (1999). "Random field modeling of CPT data." *J. Geotech. and Geoenvir. Eng.*, 125(6), 486-498.

Gilbert, R. B. and Tang, W. H., (1995). "Model uncertainty in offshore geotechnical reliability." *Proc. 27th Offshore Technology Conf.*, Houston, TX, 557–567.

Honjo, Y. and Kusakabe, O. (2002). "Proposal of a comprehensive foundation design code: Geo-code 21 ver.2." *Proc. International Workshop on Foundation Design Codes and Soil Investigation in View of International Harmonization and Performance Based Design*, Tokyo, 95-103.

Juang, C. H., Rosowsky, D. V., and Tang, W. H. (1999). "Reliability-based method for assessing liquefaction potential of soils." *J. Geotech. and Geoenvir. Eng.*, 125(8), 684–689.

Kulhawy, F. H. and Mayne, P. W. (1990). Manual on estimating soil properties for foundation design. *Report EL 6800*, Electric Power Research Inst., Palo Alto, 1990, 306p.

Mathworks Inc. (2010). MATLAB – the language of technical computing, <http://www.mathworks.com/products/matlab/> (March 9, 2009).

Miranda, T., Gomes Correia, A. and Ribeiro e Sousa, L. (2009). "Bayesian methodology for updating geomechanical parameters and uncertainty quantification." *International Journal of Rock Mechanics & Mining Sciences*, 46, 1144-1153.

Najjar, S. S. and Gilbert, R. B. (2009). "Importance of lower-bound capacities in the design of deep foundations." *J. Geotech. and Geoenvir. Eng.*, 135 (7), 890-900.

Orr, T. L. L. and Farrell, E. R. (1999). *Geotechnical Design to Eurocode 7*, Springer.

Paikowsky, S. G., Canniff, M. C., Lesny, K., Kisse, A., Amatya, S., and Muganga, R. (2010). "LRFD design and construction of shallow foundations for highway bridge structures." *NCHRP Report 651,* Transportation Research Board, Washington, DC

Phoon, K. K., Kulhawy, F. H. and Grigoriu, M. D. (1995). "Reliability-based design of foundations for transmission line structures." *TR-105000*, Electric Power Research Institute, Palo Alto, CA.

Vanmarcke, E. H. (1983). *Random Fields: Analysis and Synthesis*, Cambridge, MIT Press.

Wang, Y., Au, S. K., and Cao, Z. J. (2010). "Bayesian approach for probabilistic characterization of sand friction angles." *Engineering Geology,* 114(3-4), 354-363.

Zhang, J., Zhang, L. M., and Tang, W. H. (2009). "Bayesian framework for characterizing geotechnical model uncertainty." *J. Geotech. and Geoenvir. Eng.*, 135 (7), 932-940.

Prediction of Embankment Settlement from PCPT Measurements: a Case Study at Courtableau Bridge

Xinbao Yu[1] and Murad Abu-Farsakh[2], P.E.

[1]Louisiana Transportation Research Center, Louisiana State University, Baton Rouge, LA 70808
[2]Louisiana Transportation Research Center, Louisiana State University, Baton Rouge, LA 70808; PH (225) 767-9147; email: cefars@lsu.edu.

ABSTRACT

An accurate prediction of embankment settlement on saturated fine-grained soils is crucial to the proper design of approach slabs for bridges and to the mitigation of the bump problem. The traditional method based on laboratory test, i.e. Odometer test generally tends to miss-estimate both the magnitude and time rate of consolidation settlement. Piezocone penetration test (PCPT) has the merit of providing continuous profile of soil properties and gained wide popularity. The Louisiana Transportation Research Center (LTRC) investigated the use of PCPT and dissipation tests to predict magnitude and time-rate of embankment settlement. In this study, the data obtained at Courtableau Bridge site were used to evaluate the validity of the proposed settlement prediction methods. The predicted settlement using laboratory data, Sanglerat method, and the proposed method was compared with field measurements using horizontal inclinometers.

INTRODUCTION

A reasonable estimate of the consolidation settlement of embankments on soft soil deposits requires better and more accurate evaluation of the consolidation parameters of the subsurface soils. In situ tests, such as the piezocone penetration test (PCPT), can provide more accurate and reliable results than laboratory tests in evaluating the actual strength and consolidation properties of the soil under in-situ stress and drainage conditions. The PCPT has gained wide popularity and acceptance for subsurface investigation and soil characterization. The piezocone penetrometer is capable of measuring the profile of cone tip resistance, q_c, sleeve friction, f_s, and porewater pressure, u, at different locations. These measurements can be effectively used for soil identification and evaluation of different soil properties such as the consolidation characteristics of soils.

Continuous efforts have been made in Louisiana to improve the accuracy of prediction the embankment settlement using PCPT measurements (Abu-Farsakh 2004; Abu-Faraskh et al. 2007). New empirical calibration equations of constrained modulus and coefficient of consolidation were proposed in these studies. The research team at Louisiana Transportation Research Center (LTRC) has selected the Courtableau Bridge site to verify the proposed PCPT based method for prediction of

embankment settlement. In this paper, the subgrade soil properties were evaluated using both laboratory testing and in situ PCPT penetration and dissipation tests. Horizontal inclinometers were installed on both embankment sides of the bridge; and readings were taken at specified time intervals during and after construction. Predicted settlements by both the laboratory and PCPT methods were compared with the measured settlement to evaluate the performance of each method.

BACKGROUND

The magnitude of total consolidation settlement (S_c) of fine-grained soil can be estimated utilizing the constrained modulus (M) predicted from PCPT measured data using the following equation:

$$S_c = \sum H_i \frac{\Delta\sigma_i}{M_{avi}} \quad (1)$$

where, H_i is the thickness of the soil layer i, σ is the induced stress in the mid of layer i, M_{avi} is the average constrained modulus for a stress range from initial in situ vertical stress to the vertical stress after the completion of embankment fills (Senneset et al. 1988; Senneset et al. 1989).

Constrained Modulus, *M*

Several correlations have been proposed to estimate the constrained modulus from either the cone tip resistance (q_c) or the corrected cone tip resistance (q_t) (Abu-Farsakh 2004). The general relationship for M can be expressed as follows:

$M = \alpha \,.\, q_c$ or $M = \alpha \,.\, q_t$ (3)

Some of the popular correlation equations of constrained modulus are summarized in Table 1. Sanglerat (1972) presented a comprehensive array of α values for different soil types with different cone tip resistance values. Senneset (1988) presented a correlation based on corrected tip resistance (q_t) for silty soils. Senneset et al. (1989) presented a correlation based the tip resistance corrected by in situ soil vertical stress (σ_{vo}) for clayey soils. Abu-Farsakh (2004) and Abu-Farsakh et al. (2007) evaluated the aforementioned correlation equations based on test data on Louisiana soils and proposed two correlation equations as shown in Table 1.

Table 1. Correlation Equations of Constrained Modulus

Model	Equation
Sanglerat (1972)	$\alpha \,.\, q_c$, table of α provided in the reference
Senneset et al. (1988)	$2q_t$ for $q_t \leq 2.5$ MPa $4q_t$ for $2.5 < q_t < 5$ MPa Silty soil
Senneset et al.(1989)	$\alpha_p \,.\, q_n = \alpha_p \,.\, (q_t - \sigma_{vo})$ Pre-consolidation clay $\alpha_n \,.\, q_n = \alpha_n \,.\, (q_t - \sigma_{vo})$ Normal consolidation clay
Kulhawy and Mayne (1990)	$8.25(q_t - \sigma_{vo})$
Abu-Farsakh (2004) and Abu-Farsakh et al. (2007)	$3.15\, q_t$ $3.58\,(q_t - \sigma_{vo})$

Coefficient of Consolidation

The piezocone dissipation tests can provide the estimation of in situ coefficient of consolidation of subsurface soils. Dissipation test consists of stopping the cone penetration at certain depth and recording the dissipation of excess pore pressure (Δu) with time. The excess pore pressure is defined as the difference between the penetration pore pressure (u) and the static equilibrium pore pressure (u_o).

In this study, the Teh and Houlsby (1991) method was used to estimate the horizontal coefficient of consolidation of the soil near the cone tip as shown in Eq. (4).

$$c_h(piezo) = (T_{50}^* r_o^2 \sqrt{I_r}) / t_{50} \quad (4)$$

where, T_{50}^* is a modified time factor at 50% dissipation (T_{50}^*= 0.118 for the u_1 piezocone and 0.245 for the u_2 piezocone), $I_r = G/s_u$ is the rigidity index, G is the shear modulus, and s_u is the undrained shear strength. The shear modulus at 50% of yield stress (G_{50}) is usually used, which represents an average value of stress levels. UU tests and k_o-CU tests on retrieved soil samples were performed to determine unstrained shear strength s_u and shear modulus G at 50% yield stress respectively. The determined s_u and G were used to determine the rigidity index I_r.In this study, the $c_h(piezo)$ was converted to the c_h of normal soil following the procedure by Levadoux and Baligh (1986). Then, a ratio of k_h to k_v of 1.2 was used to calculate the vertical coefficient of consolidation of normal soil.

COURTABLEAU BRIDGE SITE

LADOTD decided to replace the old Bayou Courtableau Bridge located in St. Landry parish on LA route 103 about 8 miles north of Port Barre. The new bridge was built with precast prestressed concrete girders supported by pile bents sitting on square reinforced concrete driven piles.

A comprehensive field and laboratory testing program was conducted to investigate the soil properties of the study site, which included moisture content, density, Atterberg limits, particle size analysis, 1-D consolidation tests, UU tests, k_o-CU tests, and piezocone penetration and dissipation tests. The 1-D consolidation test results along with soil strata from soil boring log are presented in Figure 1. The first column of the plots shows the soil strata obtained from the boring log of the bridge site; the second column presents the moisture content, liquid limit, and plastic limit results of Shelby tube samples obtained from the site; the undrained shear strength from UU test is shown in the next column; the constrained modulus and coefficient of consolidation at the in-situ stress level determined from laboratory 1-D consolidation tests are shown in the following two columns, respectively; the last column plots the profile of OCR. These parameters were used in the calculation of embankment settlement in the later section. One CPT test was conducted on each embankment site of the bridge to profile the subgrade soils for settlement estimation. The profiles of CPT test results (q_t, f_s, and R_f) and the corresponding CPT soil classification using Zhang and Tumay (1999) CPT classification method are presented in Figure 2. As

shown by the CPT soil classification, the subgrade soil mainly consists of clayey silt in the upper 60 ft. below ground surface. Compared to the west embankment site, the east site is a little sandier. Several dissipation tests were conducted at each side of the bridge as shown in Figure 3 to obtain the consolidation parameters used for settlement estimation. The depths for the PCPT dissipation tests at the west side embankment are 1.96, 2.64, 3.83, 7.56, 9.55, 13.88, 16.15, and 18.15 m below the old pavement surface.

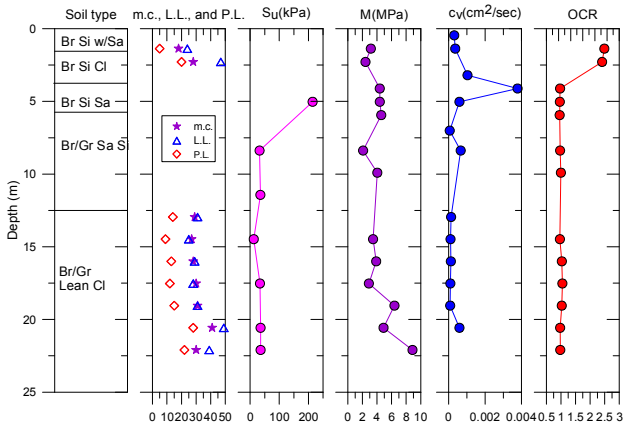

Figure 1. Profile of soil properties of east side subgrade.

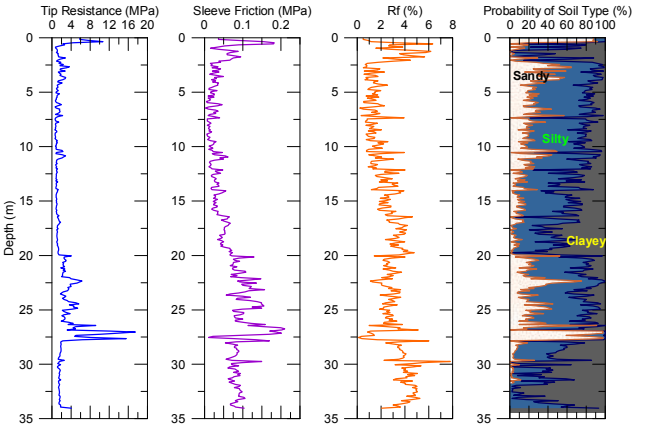

Figure 2. PCPT profiles and soil classification for Courtableau Bridge east site.

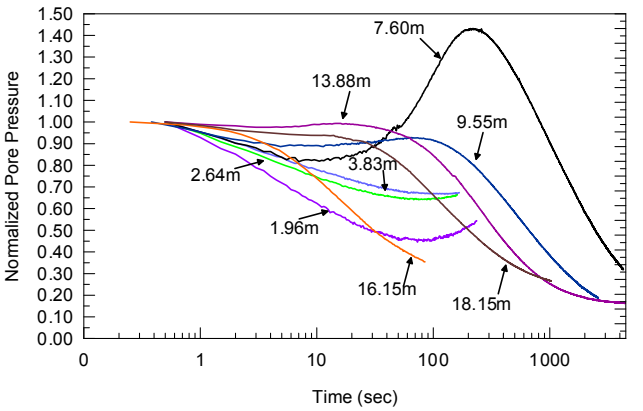

Figure 3. Dissipation test for Courtableau Bridge east site.

Installation of Horizontal Inclinometer

The newly constructed east embankment has a height of 8 ft. above the existing pavement and a width of 120 ft.; while the newly constructed west embankment has a height of 6 ft. above the existing pavement and a width of 110 ft. One horizontal inclinometer was installed at each embankment side underneath the middle of the approach slab to monitor the profile of consolidation settlement of subgrade soil along the embankment cross section. The installation plan of the inclinometers is shown in Figure 4. A 2 ft.-wide and 2 ft.-deep trench as shown in Figure 5 was dug after the completion of the first lift of embankment fill. The return pipe with a diameter of 3.34 in. (85 mm) and casing were also aligned on the bottom of the trench. The trench was then backfilled and manually compacted with a hand compactor. In this study, a digital horizontal inclinometer system manufactured by RST instruments Ltd. was used, which consists of inclinometer casing, a horizontal probe, control cable, and a readout unit. Each end of the inclinometer casing extended about 10 ft. beyond the embankment and was fastened to two wooden posts inserted deep into the natural ground to provide stable reference points for future survey. A first survey was conducted immediately after the trench was compacted to obtain the baseline survey plus to check the function of the casing. The inclinometer probe was pulled through the casing twice with the probe in forward and backward position at 2 ft. interval, i.e. the length of probe. The two readings can eliminate possible errors of the instrument and provide accurate measurement of settlement profile. The inclinometer readings were taken at specified time intervals until 6 months after the complete of the construction.

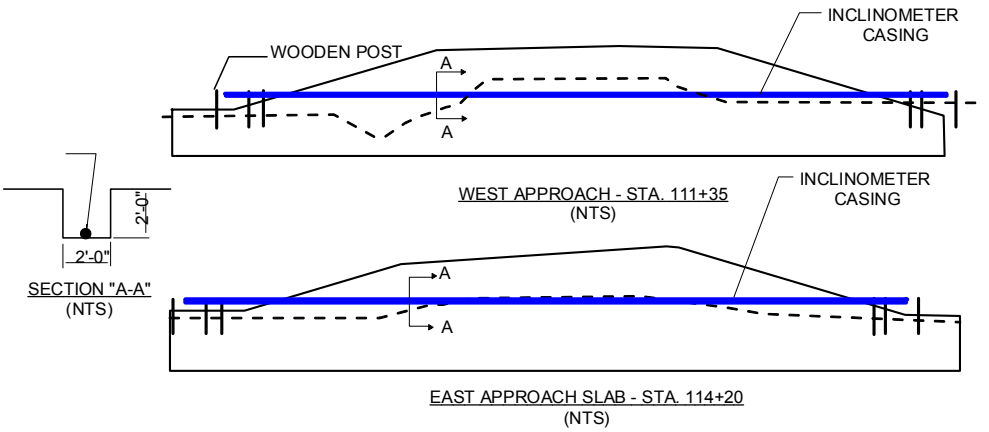

Figure 4. Installation plan of the horizontal inclinometers.

RESULTS AND ANALYSES

Constrained Modulus and Coefficient of Consolidation

The PCPT data obtained on each embankment site were used to estimate the constrained modulus, M, using the Sanglerat method and Abu-Farsakh (2004) correlation (M=3.15q_t), with q_t representing the average q_t value of the soil layer. The PCPT estimated constrained modulus along with those obtained from 1-D

consolidation tests are depicted in Figure 6a. The figure shows that both Sanglerat and Abu-Farsakh methods have close estimation of the in situ constrained moduli, which are generally larger than the laboratory measured values, especially in the upper 15 ft.

Figure 5. Installation of horizontal inclinometer casing and return pipe

The vertical coefficients of consolidation, c_v, were obtained using the Teh and Houlsby (1991) interpretation method from dissipation test results as described by Equations 4-6. The Rigidity indices were determined using laboratory UU and k_o-CU test results. Coefficient of consolidation is difficult to determine accurately in nature. The PCPT estimated vertical coefficients of consolidation generally agree well with laboratory measured values (Figure 6b).

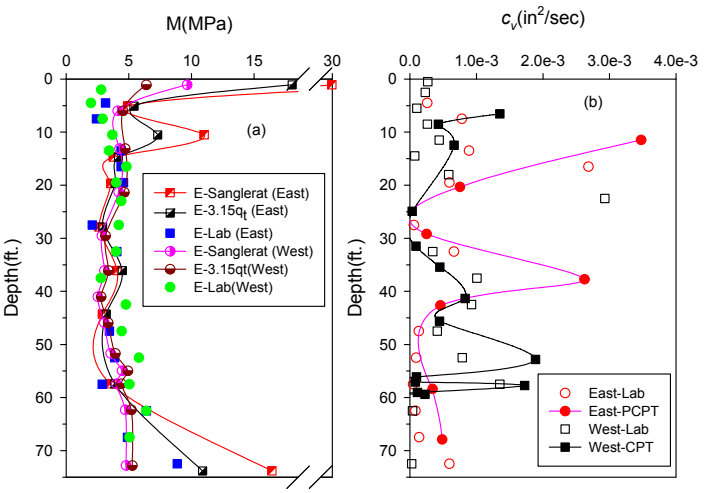

(a) Constrained modulus (b) Coefficient of Consolidation

Figure 6. Comparison of constrained modulus and coefficient of consolidation.

Settlement and Settlement Rate Prediction

The settlement calculation of Courtableau Bridge embankments was performed based on results of laboratory tests on retrieved in-situ samples and the PCPT field tests. The embankment additional surcharge was obtained as the height

difference between the new embankment and the existing embankment as indicated in Figure 4. Stress induced by the applied embankment surcharge ($\Delta\sigma$) is calculated using a MatLAB coded based on the concept of vertical stress distribution due to embankment loading (Poulos and Davis 1974). The 1-D consolidation test results conducted in the laboratory were used for settlement calculation as indicated by "-Lab" shown in Figures 7 and 8. The subgrade soil properties and the PCPT and the dissipation test results were presented earlier. The constrained modulus and vertical coefficient of consolidation shown in Figure 6 were also used for settlement calculations. The PCPT-predicted settlements (using Sanglerat and Abu-Farsakh correlations of *M*) were compared with the laboratory-calculated settlement and the field-measured settlement from the horizontal inclinometers as shown in Figures 7 and 8. The figures show that the proposed PCPT interpretation method predicted the total consolidation settlement better than the Sanglerat PCPT method and the laboratory method. The settlement predicted from laboratory tests results in the largest settlement. The Sanglerat method resulted settlements are slightly larger than the settlement obtained by Abu-Farsakh method.

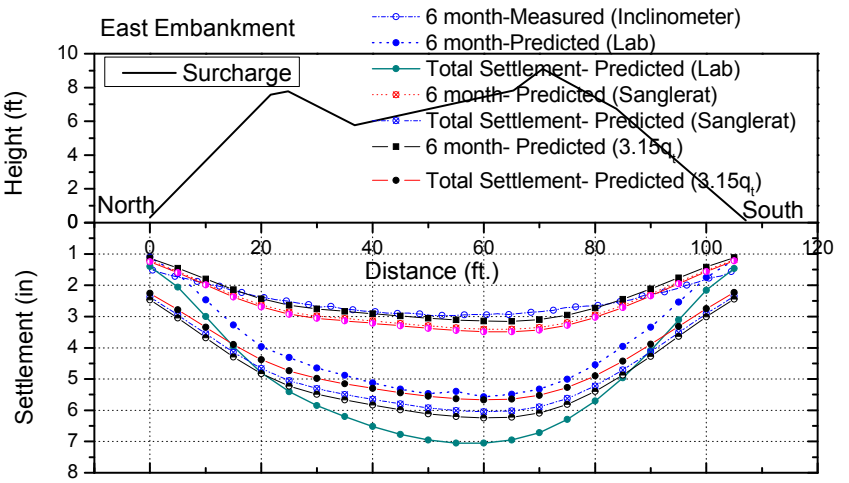

Figure 7. Comparison of settlement prediction at east embankment.

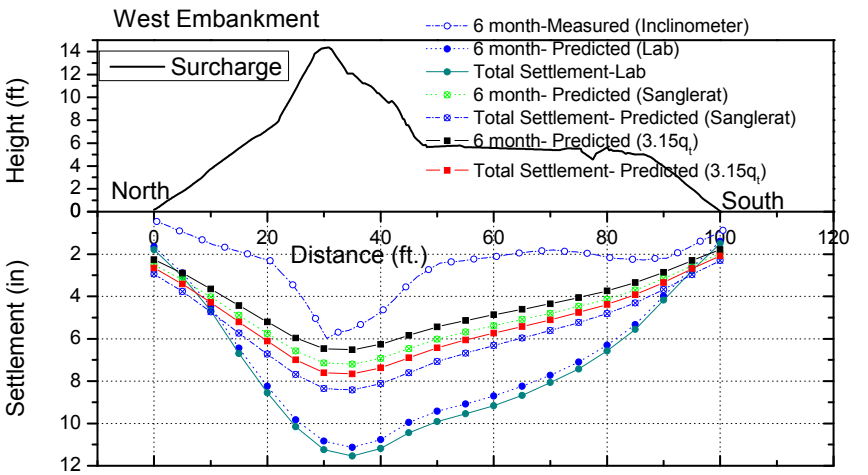

Figure 8. Comparison of settlement prediction at west embankment.

The accurate prediction of the rate of embankment settlement is very important to geotechnical engineers for better planning the extent of preloading period needed to overcome majority of settlement. The rates of consolidation settlement underneath the center of embankments predicted from the laboratory parameters and the PCPT dissipation tests using Teh and Houlsby (1988) interpretation method are presented in Figures 9a and 9b for the east and west embankments, respectively. The figures indicated that although the predicted magnitudes of settlement from laboratory and PCPT methods vary from the actual field measurements, the PCPT estimated rate of consolidation settlement from dissipation tests matches fairly well with the field monitoring.

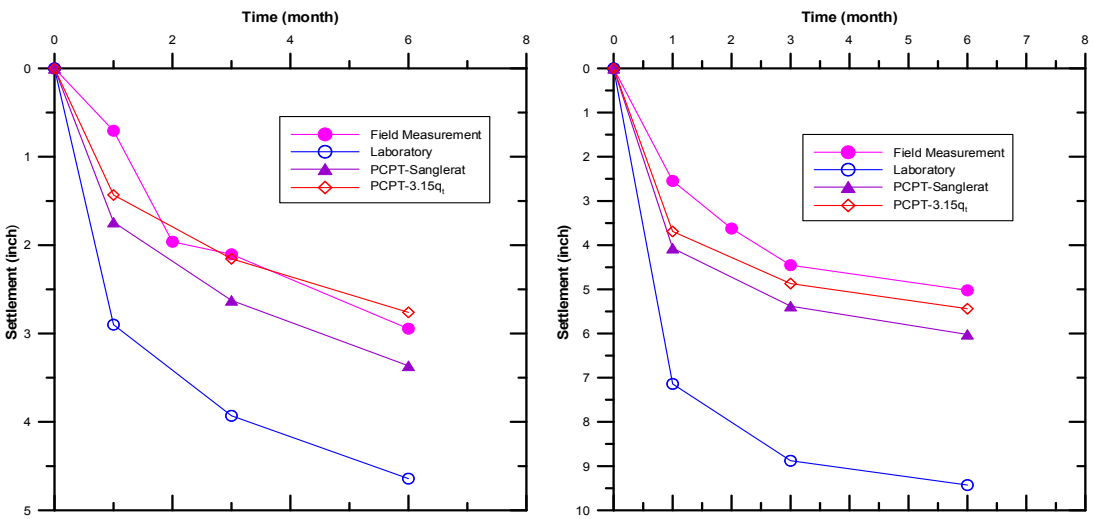

(a) East Embankment **(b) West Embankment**

Figure9. Rate of consolidation settlement.

Reliability of Settlement Prediction

The reliability of settlement prediction using PCPT is determined by the calibration equations for constrained modulus and coefficient of consolidation. These calibration equations are empirical and greatly depend on calibration database. The empirical equations used in this paper were developed from 7 embankment sites and verified with 3 embankment sites all located in Louisiana (Abu-Farsakh 2004). LADOTD decided to continue the verification process until enough reliability is achieved for LADOTD engineers to use this method confidently. The work presented in this paper is part of continue verification effort. When applying the recommended calibration equations in locations other than Louisiana, engineers should take cautions to check the accuracy.

CONCLUSION

This paper evaluated the capability of the PCPT method for predicting the embankment settlement due to the consolidation of underlying saturated fine-grained soils. The embankment construction site at the Courtableau Bridge was selected to verify the PCPT-based settlement prediction methods developed in a previous study

(Abu-Farsakh 2004). A comprehensive laboratory and field testing program was conducted to calculate and verify the magnitude and rate of embankment settlement. Field measurements from horizontal inclinometers were compared with consolidation settlements estimated using the PCPT and laboratory derived parameters

The results showed that the PCPT and dissipation data were able to reasonably estimate the magnitude and rate of consolidation settlement. The PCPT settlement prediction method using Abu-Farsakh correlations of constrained modulus (M=3.15q_t) has better performance than Sanglerat PCPT method and the laboratory calculation in estimating the magnitude of consolidation settlement of Courtableau embankments. The estimation of rate of settlement from PCPT dissipation tests using Teh and Houlsby interpretation method agrees fairly well with field measurements.

ACKNOWLEDGMENT

This research project is funded by the Louisiana Department of Transportation and Development (State Project No. 736-00-0781) and the Louisiana Transportation Research Center (LTRC Project No. 00-3GT). The authors greatly acknowledge the help and support of Zhongjie Zhang, Mark Morvant, Gavin Gautreau, and Khalil Hanief at LTRC.

REFERENCES

Abu-Faraskh, M. Y., Zhang, Z., and Gautreau, G. (2007). "Evaluating the Deformation Modulus of Cohesive Soils from PCPT for Consolidation Settlement Estimation." *Journal of the Transportation Research Board*. 2004: 49-59.

Abu-Farsakh, M. Y. (2004). *Evaluation of Consolidation Characteristics of Cohesive Soils from Piezocone Penetration Tests*. Louisiana Transportation Research Center Baton Rouge, LA, Report: 386, pp. 106.

Kulhawy, F. H., and Mayne, P. H. (1990). *Manual on Esitmating Soil Properties for Foundation Design*, Electric Power Research Institue, EPRI.

Levadoux, J. N., and Baligh, M. M. (1986). "Consolidation after Undrained Piezocone Penetration. II: Prediction." *Journal of Geotechinal Engineering*. 112(7): 707-726.

Poulos, H. G., and Davis, E. H. (1974). *Elastic Solutions for Soil and Rock Mechanics*. New York, John Wiley and Sons,Inc.

Sanglerat, G. (1972). *The Penetration and Soil Exploration*. Amsterdam, Elsevier.

Senneset, K., Sandven, R., and Janbu, N. (1989). "The Evaluation of Soil Parameters from Piezocone Tests." *Transportation Research Record*(1235): 24-37.

Senneset, K., Sandven, R., Lunne, T., By, T., and Amundsen, T. (1988). *Piezocone Tests in Silty Soils*. Proceedings of the International Symposium on Penetration Testing, ISOPT-1, Rotterdam, Balkema Pub.

Teh, C. I., and Houlsby, G. T. (1991). "An Analytical Study of the Cone Penetration Test in Clay." *Geotechinque*. 41(1): 17-34.

Zhang, Z., and Tumay, M. T. (1999). "Statistical to Fuzzy Approach Toward CPT Soil Classification." *Journal of Geotechinal and Environmental Engineering*. 125(3): 179-186.

Geochemical and Geotechnical Features of Terra Rossa in Karst Areas of Southern Appalachians

A. Nandi[1] and J. Moore[2]

[1,2] Department of Geosciences; East Tennessee State University; 100 CR Drive; Johnson City, TN 37614; Ph. 423-439-6086; Email: nandi@etsu.edu.

ABSTRACT

A sequence of siliceous dolomite and magnesian limestone, known as Knox group rock are prevalent in karst landforms of Southern Appalachians. Thick blanket of clay-rich red soils (terra rossa) are common along fractures, cavities, and between bedding planes of these calcareous, cavernous rocks. The red soil causes serious environmental and geotechnical hazards, hence proper understanding of the soil's pedology, geochemistry and engineering behavior can lead to better site characterization for safer development. Twenty four terra rossa samples were collected and laboratory analysis was performed such as: geochemistry (mineral content using X-Ray diffraction, and geotechnical characterization (grain size distribution, porosity, hydraulic conductivity, and shrink-swell potential). The soil profile above Knox rock exhibits distinct vertical variation in geochemical and geotechnical characteristics. The soils are well drained in the upper horizon and exhibit slight reduction in porosity and hydraulic conductivity with depth. The analysis indicate that these soils overall are good foundation materials, however proper drainage should be installed to prevent foundation damage, soil erosion and landslides in slopes.

INTRODUCTION

Carbonate (limestone and dolostone) enriched bedrock comprises approximately 20%, of the total land area of the contiguous United States (Moore, 1976). Terra rossa, a red clay rich soil, is the weathered product of carbonate which forms up to several meters thick and kilometers across the earth's surface. The soil has characteristic bright red color due to iron bearing minerals like hematite, goethite, ferrihydrite, siderite, magnetite, etc. (Torrent *et al.,* 1980; Schwertmann, 1988; Boero and Schwertmann, 1989). In recent years due to expanding development more terra rossa are exposed and are used as construction/foundation material. The environmental and engineering hazards associated with karst derived terra rossa are becoming increasingly serious, such as soil instability, iron leaching in ground water, variable drainage characteristics, bearing capacity and settlement failure, increased shrink swell potential, and variable degree of compaction.

The pedogenesis of terra rossa and relationship to underlying carbonates is a long-standing problem and two different theories are found in literature with respect to its parent material and origin. The most extensively accepted theory is that terra rossa has developed from insoluble residue of carbonate rocks (Moresi and Mongelli, 1988; Durn, 2003). However, other authors have highlighted that terra rossa could not have been formed entirely from insoluble residue of carbonate rocks. Research indicate the source of terra rossa might be debris, derived from erosion of clastic sedimentary rocks, wind-borne material from vicinity, and transported on lower lying limestone (Drumm and Yang, 2005). Although the origin of terra rossa is widely studied, only some work has been done on their geotechnical behavior. The understanding of geotechnical behavior of terra rossa has focused on their pedogenesis, climatic processes, and hydrogeology (Reeder and Crawford, 1989). The mineralogy of terra rossa is underexplored in the literature. Ubiquitous presence of variable minerals can also govern the geotechnical properties of this red soil. During the formation of terra rossa, iron oxide, and aluminum oxide coat and attach on the fine grained clay particles leading to a change in soil geotechnical properties such as: drainage, texture, porosity, hydraulic conductivity, and micro-structures. This paper discusses the properties and performance of terra rossa as an earth material used as foundation and/or construction material.

FIELD STUDY AREA

The study area is located in eastern Tennessee, a landscape characterized by karst topography. The karst is developed in soluble carbonate bedrock know as Knox group. Knox group rock is a 2,500 to 3,500 ft thick, Ordovician to Cambrian aged, siliceous dolomite and magnesian limestone sequence (Moore, 1976). The rock is folded and faulted into long NE–SW trending pattern due to the Appalachian Orogeny (Figure 1a). Through differential erosion, Knox group of rock have developed into the Valley and Ridge topography (Moore, 1976). The weathering of Knox carbonate rock produces a residual clay rich terra rossa (Figure 1b). This soil is about 50 to 100 ft thick in eastern Tennessee. The soil profile exhibit uneven vertical zoning, and can be divided in four basic horizons. The top horizon (O) is concentrated with high biological activity and disintegrated organic matter, which overlies the E horizon, consisted of dark orange to reddish brown fine to coarse grained granular sand. The third layer is designated as zone of accumulation or B horizon, made up of lighter brown colored fine grained massive clay. Below this horizon, a prominent saprolite zone of partially altered carbonate is present, which grades to the parent carbonate bedrock. The boundary between saprolite and carbonate bedrock is often indistinguishable. Overall, the interface between the bedrock and the terra rossa is typically irregular and found as pinnacles of rock protruding into the soil. From each soil profile horizon a total of twenty four grab samples were collected from a terra rossa test pit (Figure 2) and were analyzed on the basis of geochemical and geotechnical properties. Small plastic hollow cubes of known volume were used to collect undisturbed samples for measuring the field unit weight of the samples.

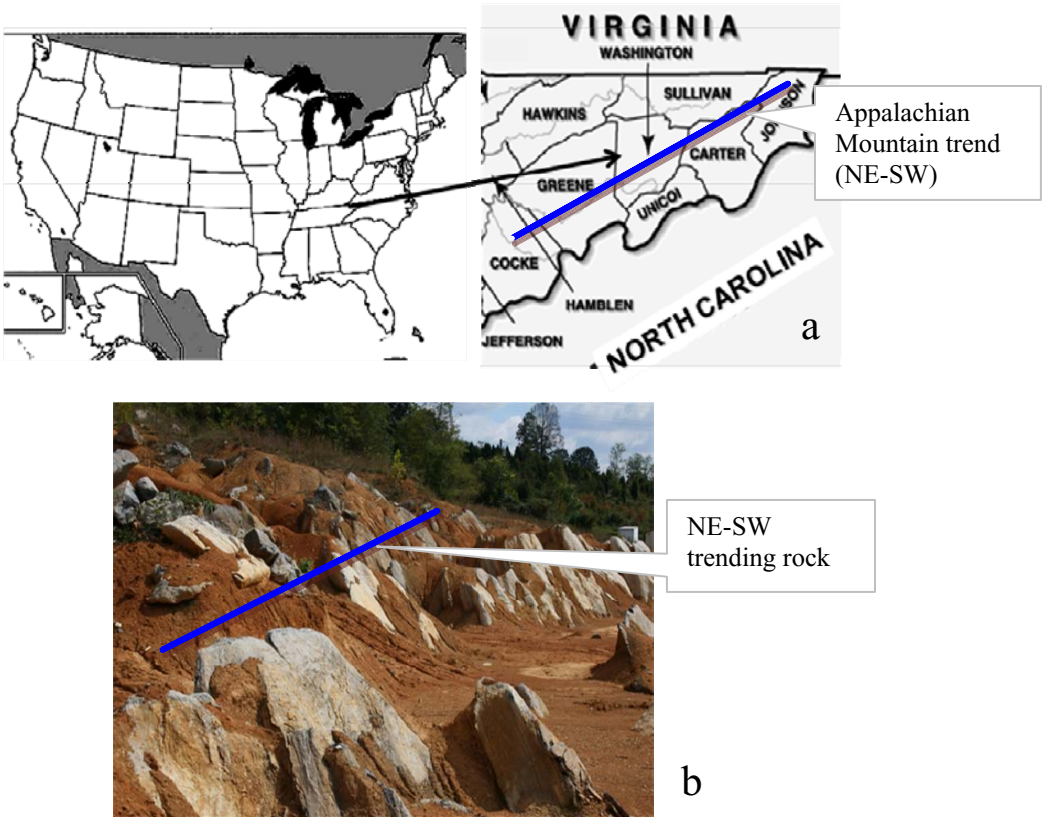

Figure 1. Location map showing the trend of the Appalachian Mountains (a). The terra rossa developed on the NE-SW trending Knox limestone; the pinnacles of the limestone are common in the area (b).

GEOCHEMICAL TESTING

The geochemical properties of the terra rossa were studied using X-ray diffraction (XRD) analysis. XRD was performed on powdered soil samples in order to assess the whole rock mineralogy. Samples were analyzed at Appalachian State University on a Shimadzu XRD 6000 diffractometer run at 40.0 kV and 30.0 mA. The data were collected from 05° to 50° 2-theta with a continuous scan of 2.0°/min and 0.02° sampling pitch. XRD peaks (reported as degrees 2-theta) were converted to d-spacings (in Å) using Bragg's Law.

GEOTECHNICAL TESTING

The geotechnical properties of the Knox derived terra rossa were studied in terms of moisture content, grain size distribution (GSD), shrink and swell potential, unit weight, porosity and hydraulic conductivity. The moisture content of the soil samples were measured using ASTM D 4643 method (ASTM, 1996). In this procedure, the soil is dried to remove all free moisture and the weight of moisture is measured consequently. The GSD was performed using sieve analysis on the terra rossa samples to determine the gradation (distribution of clastic particles, by size)

within a given sample. GSD analysis was performed following ASTM test number D422 (ASTM, 1996). Sieve analysis was then performed using screen sizes of 15.0, 4.75, 2.0, 0.85, 0.25, 0.106, and 0.075 mm. Cumulative grain size distribution curves were constructed based on the percent weight of material retained by each sieve. Free and differential swell test were performed in the terra rossa samples using water and kerosene as solvent of the clay minerals. The degree of expansiveness was calculated from initial and final volume of the soil in a period of 24 hours. The unit weight of the soil was calculated using small cube of undisturbed samples. Porosity of the soil samples were calculated using water saturation method. The hydraulic conductivity was calculated using constant head permeameter according to ASTM D 2434 method. Field unit weights were maintained while sample preparation for porosity and hydraulic conductivity tests.

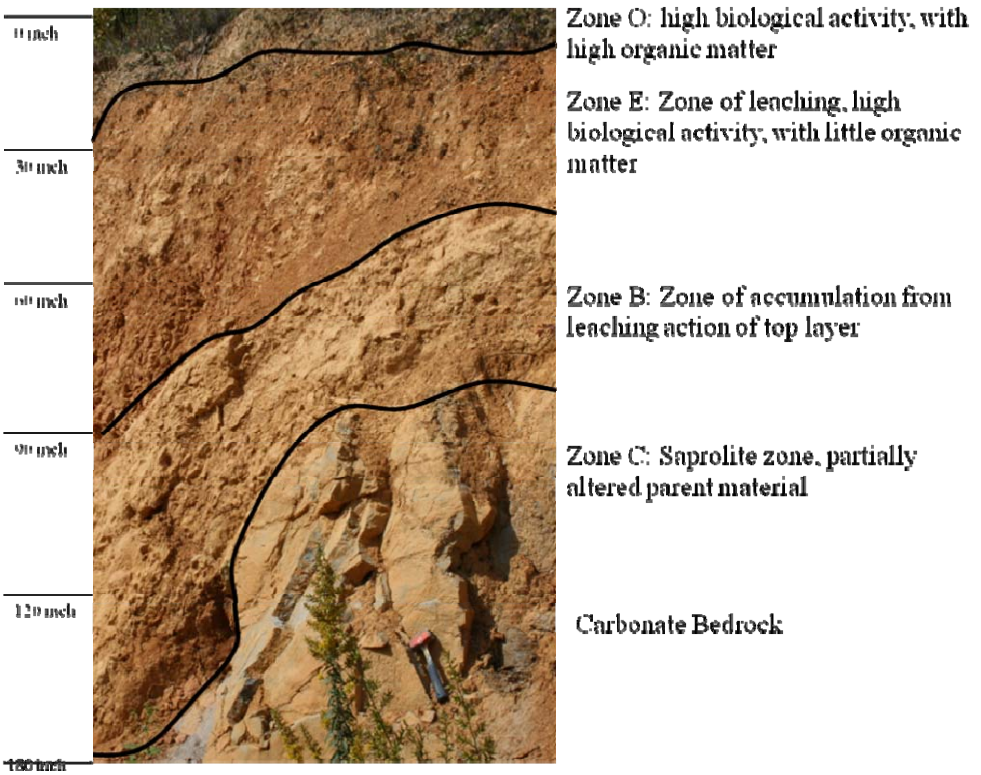

Figure 2. Soil profile of the test pit.

GEOCHEMICAL AND GEOTECHNICAL PROPERTIES

The XRD analysis of zone E, B and the bedrock indicated vertical zoning in mineral association. Quartz was found to be the most dominant phase in the E horizon. There is an indication of presence of ferrihydrite and amorphous hematite, which transforms into goethite in lower depth. The dominant mineral phases in B horizon are chlorite, illite, and quartz. Like B horizon, the saprolite area (C horizon) had a similar mineral assemblage. In this zone goethite was found along with some relic calcite from the underlying bedrock. Illite clay was not present in the saprolite zone. The predominant mineral in the limestone bedrock is calcite (Figure 3).

The moisture content of Knox derived terra rossa ranged from 24.48% to 32.12% (Table 1). B horizon indicated increased moisture content than E and C horizon. An obvious difference in grain size distribution was observed in the E horizon in contrast to B and C horizon. The E horizon has dominant coarser particles like sands and gravels. While the B and C horizons contain increased amount of finer particles like clay and silt (Figure 4).

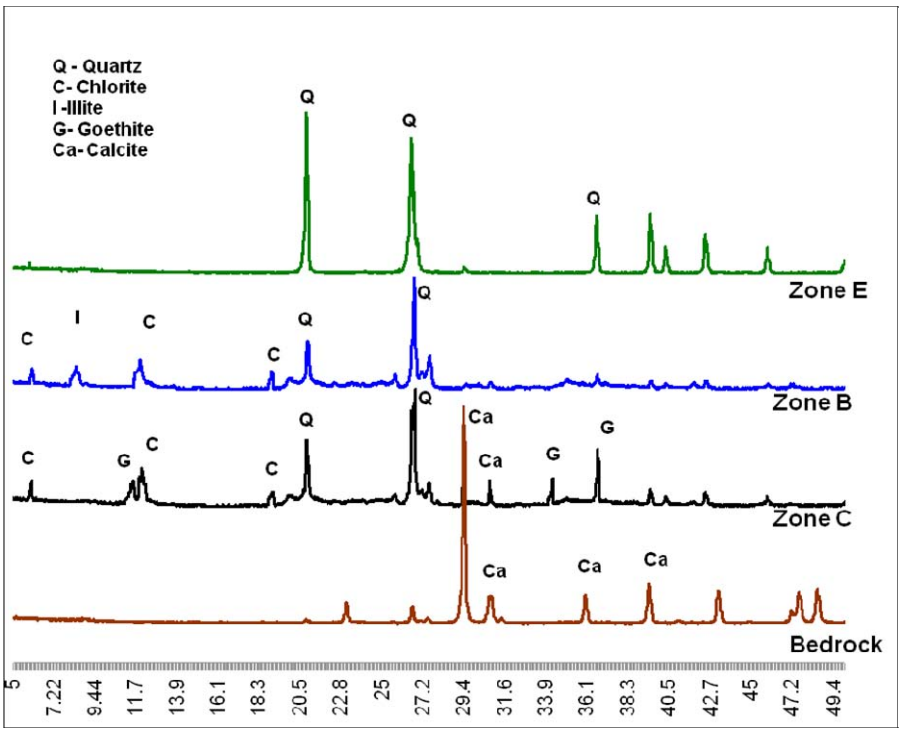

Figure 3. XRD analysis of the representative samples from different horizons of the soil profile.

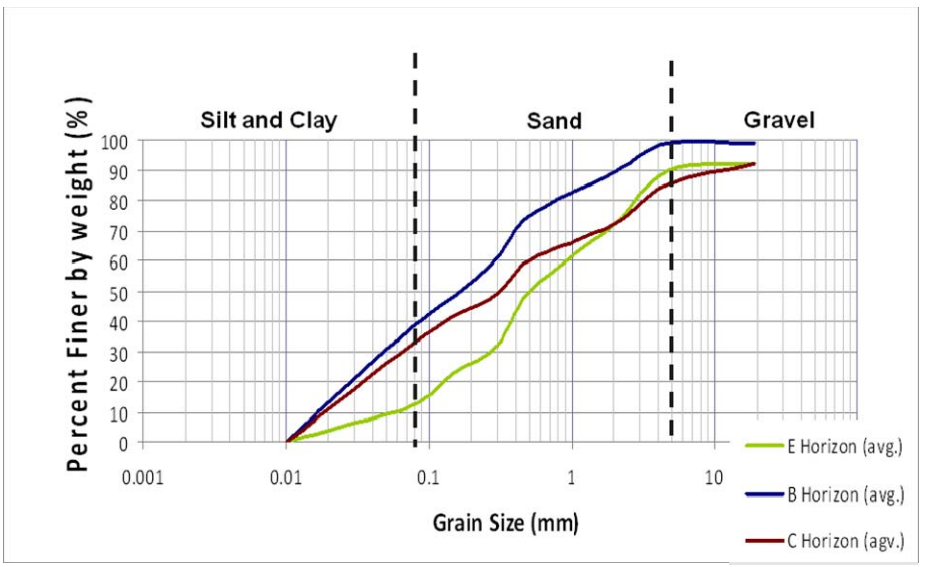

Figure 4. Average grain size distribution plot of the test samples.

Table 1. Summary table of the geochemical and geotechnical properties of the soil.

Horizon	Mineralogy	Moisture Content	Avg. Grain size distribution	Degree of expansiveness %	Porosity %	Hydraulic conductivity m/day
E	Quartz, Hematite, Ferrihydrite (?)	24.48% to 29.75%	Gravel: 10% sand: 88 % Silt and clay:12%	0%	36.4% - 45.3%	8.73 – 15.70
B	Quartz, Chlorite, Illite, Goethite, Halloysite	30.38% to 32.12%	Gravel 1% Sand:61 % Silt and clay:38%	0-10%	31.6% - 38.4%	5.41-9.31
C	Quartz, Chlorite, Goethite, Halloysite Calcite	25.35% to 31.22%	Gravel: 15% Sand 5 3% Silt and clay:32%	0-10%	35.5% - 46.1%	5.66 – 9.43

The degree of expansiveness of the entire soil profile indicates almost negligible swelling. Only very little swelling was observed in the clay rich B and D horizons (0 % to 10%). The porosity of the soil profile indicated consistent result with grain size distribution analysis and moisture content. Increased porosity was associated with coarser grain size in the E and D horizon. The hydraulic conductivity of the terra rossa soil was associated with porosity, degree of compaction, and presence of clay minerals. Hydraulic conductivity of the top E horizon was found to be more permeable than B and C horizons.

DISCUSSION

This paper accentuates the relationship between the intrinsic geochemical and geotechnical properties of Knox carbonate derived terra rossa, which is a common foundation and/or construction material in eastern Tennessee. On the basis of visual interpretation, geochemical and geotechnical characterization, the terra rossa soil profile was zoned as E horizon (zone of leaching), B horizon (zone of accumulation), C horizon (saprolite zone), and limestone bedrock. In the subsequent section, each soil horizon will be discussed separately in light of the measured properties.

E Horizon: Almost exclusive presence of quartz and abundance of sand and gravel in this horizon is in compliance with the zone of leaching, where the quartz rich coarser sand and gravel particles act as drainage layer. Fine grained silt and clay can seep through E horizon and gather in the underlying layer of the soil profile. Along with quartz, hematite and ferrihydrite are very common is top layers of terra rossa. Iron (Fe) is present in its highest oxidation state +3, and precipitates as hematite

(Fe_2O_3) and ferrihydrite (Fe_2O_3•0.5(H_2O)) which gives the bright red and brown color of the soil. Both minerals exhibit amorphous structures, and are not detectable by X-Ray diffraction studies. Their presence was confirmed by SEM-EDX studies. Due to absence of clay minerals in this horizon, the degree of expansiveness is negligible. Both porosity and hydraulic conductivity of E horizon soil were high, indicating a well drained soil horizon. The moisture content of the soil was fairly low, indicating the pores were partially filled with moisture.

B Horizon: Along with quartz, this horizon indicated occurrence of various non-swelling clay minerals, such as chlorite, illite, and halloysite. Presence of goethite confirmed the Fe enrichment in the soil. Ferrihydrite transforms into goethite at higher pH condition. Probably the higher pH can be accounted by the underlying carbonate bedrock. This horizon had higher concentration of silt and clay, and relatively low porosity and hydraulic conductivity than the overlying E horizon. The presence of abundant clay minerals, lower porosity and hydraulic conductivity indicate that B horizon is a poorly drained soil layer, which accumulate higher amount of moisture. The degree of expansiveness is still negligible as the clays are non-swelling type.

C Horizon: This layer exhibit analogous geochemical property with the overlying B horizon. The only difference exists with noticeable presence of calcite. The gravel percentage has increased. This is be explained by the presence of relic carbonate rocks in the saprolite zone. Porosity of this layer was high, where as the hydraulic conductivity did not reveal any significant difference from the B horizon. The higher porosity might be due to higher gravel sized carbonate particles. However the pores are not all interconnected, which is indicated by lower hydraulic conductivity of the layer. The moisture content has varied from moderately low to high. The presence of clay minerals might have influenced the moisture content of the soil.

In warm and humid environment chemical weathering and leaching of iron oxide have significant effect on the soil pedogenesis. The iron oxides tend to form thin layer of colloidal film. The thin film coat and attach on the clay particles and during dry period the colloidal iron oxides changes irreversible to hematite and goethite. This tendency of iron oxide increases the aggregation and particle cementation, leading to a change in certain engineering properties of soil. The aggregation and particle cementation change the cohesive clays to more granular type, which in turn modifies the shear strength parameters by decreasing the cohesion and increasing the internal friction of the soil particles. The cementation overall reduces the porosity, hydraulic conductivity and microstructures and hence modifies the drainage character.

CONCLUSION

A thick blanket of clay-rich terra rossa is widespread along fractures, cavities, and between bedding planes of carbonate rich Knox group rocks in eastern Tennessee. The soil thickness varies from 50 to 100 ft in different locations. This soil is very fertile due to the presence of high nutrient and mineral content, and

increased moisture content. The soil is commonly used as foundation material for civil structures. The geochemical and geotechnical analysis of the soil indicated a well-drained soil horizon on the top layer. Presence of abundant non-swelling clays, and reduced hydraulic conductivity in the lower horizons however reduces the drainage potential. Although the study eliminates the potential for structural damage due to swelling, but the likely change shear strength parameter can be critical in geotechnical design projects. Additionally precipitation of iron oxide can reduce the drainage characteristics of the soil. This eventually builds up the hydrostatic pressure, and might be detrimental to civil structures, if proper drainage is not installed.

REFERENCES

ASTM, (1996), Annual Book of ASTM Standards, Section 4, Construction, Vol. 4.08 Soil and Rock (I): D420-D4914 ASTM, West Conshohocken, Pa.

Boero, V. and Schwertmann, U. (1989) "Iron oxide mineralogy of terra rossa and its genetic implications": *Geoderma* 44, 319-327.

Drumm, E. C and Yang, M. Z. (2005), "Preliminary screening of residual soil stability in karst terrain": *Environmental Engineering Geoscience*, 11(1), 29–42.

Durn, G. (2003). "Terra rossa in the Mediterranean region: parent materials, composition and origin." *Geologia Croatatica*. 56:83–100.

Moore, H. L., (1976) "Drainage problems in carbonate terrain of East Tennessee". In *Proceedings of 27th Annual Highway Geology Symposium*: Orlando, FL, pp. 112–131.

Moresi, M., and Mongelli, G. (1988). "The relation between the terra rossa and the carbonate-free residue of the underlying limestones and dolostones of Apulia, Italy." *Clay Mineralogy*. 23:439–446.

Reeder, P. P. and Crawford, N. C., (1989) "Potential groundwater contamination of an urban karst aquifer—Bowling Green, Kentucky". In Beck, B. (Editor), *Engineering and Environmental Impacts of Sinkholes and Karst, Proceedings of the 3rd Multidisciplinary Conference on Sinkholes and the Engineering and Environmental Impacts of Karst:* Orlando, FL, October 2–4, pp. 197–206.

Schwertmann, U. (1988) "Some properties of soil and synthetic iron oxides": in *Iron in Soils and Clay Minerals, Nato Advanced Study Institute,* J. W. Stucki, B. A. Goodman, and U. Schwertmann, eds., Reidel Publishing Company, Dordrecht, Holland, 203-250.

Torrent, J., Schwertmann, U., and Schulze, D. G. (1980) "Iron oxide mineralogy of some soils of two river terrace sequences in Spain" *Geoderma*, 23, 191-208.

Characterizing Spatial Variability of Cone Penetration Testing through Geostatistical Evaluation

Saftner, D.A.[1], S.M. ASCE, Green, R.A.[2], M. ASCE, P.E., Hryciw, R.D.[3], M. ASCE, Fadden, M.F.[1], S.M. ASCE, and DaCosta, A.[1], S.M. ASCE

[1]PhD Candidate, Department of Civil and Environmental Engineering, University of Michigan, Ann Arbor, MI 48109; email: dsaftner@umich.edu, fadden@umich.edu, adacost@umich.edu

[2]Associate Professor, Department of Civil and Environmental Engineering, Virginia Tech, Blacksburg, VA 24061; email: rugreen@vt.edu

[3]Professor, Department of Civil and Environmental Engineering, University of Michigan, Ann Arbor, MI 48109; email: romanh@umich.edu

ABSTRACT

Geostatistical methods are used to quantify the spatial variability in cone penetration test (CPT) tip resistance at a site in southwest Indiana. Spatial variability of soil properties affects all geotechnical projects. Geostatistical tools provide a method to both predict the properties at unsampled locations and to quantify their uncertainty. Universal kriging is a geostatistical method that accounts for a variable mean, such as a varying mean tip resistance in different soil layers, when making predictions. In this paper, universal kriging is applied to a database of CPT results. Because CPT tip resistance shows greater variability with depth than with lateral distance, a method of accounting for greater correlation between measurements in the lateral direction than with depth is presented. Finally, cross-validation, or the removal of measured points from the database and use of the model to predict the known results, is used to validate the geostatistical model.

INTRODUCTION

The objective of this paper is to quantify spatial variability of CPT results at a site using geostatistical methods. In many site characterization projects, it is important to quantify variability and lessen the impact of its uncertainty on the project. One method of accomplishing this is through geostatistics. Geostatistics was first developed for work in the mining industry in the 1950s. The basic assumption is that the closer measurements are made to a location of interest the more useful they are in helping to predict properties at the location of interest. Using a method called kriging, one can estimate a property's value and error bound that accounts for the spatial distribution of the known data set (Chiles and Delfiner, 1999).

First, the site conditions at a sand and gravel quarry in Griffin, IN are described. Extensive CPT soundings were performed at the site. In the next section

the kriging process is described. Finally, the results of the geostatistical analysis are presented and the model is verified through cross validation.

SITE CHARACTERISTICS

The Griffin sand and gravel quarry is located in southwest Indiana, 25 miles northwest of Evansville. The site stratigraphy consists of five principle soil layers. Starting at the surface, they are: a clay layer, a loose sand layer, a dense sand layer, a loose gravelly sand layer, and a gravelly sand layer that increases in density with depth, to the extent that penetration testing, rotary drilling, and dredging are not feasible. The thickness of the clay, loose sand, dense sand, and loose gravelly sand layers are typically 1.5 m, 2.5 m, 6 m, and 4 m, respectively. While the transition between the clay and loose sand layer occurs between depths of 1 m and 1.6 m, the boundaries between the various sand layers are fairly consistent, within 20 cm of the depths listed above. These layers reflect the geologic history in the area. The dense sand and loose gravelly sand layers are Pleistocene glacial outwash. They were deposited by the Trafalger ice sheet. The loose sand layer is early Holocene fluvial sand (Fraser et al., 1997). Below the clay layer, the soil becomes coarser with depth, transitioning from a poorly graded sand (SP by the Unified Soil Classification System) in the loose sand layer to a poorly graded sand with gravel (SP with >15% gravel) in the loose gravelly sand layer. While the ground water table fluctuates with seasonal rainfall and the nearby Wabash River's level, at times reaching the surface, it is typically 3 m below the surface. The *in situ* testing plan, shown in Figure 1, was designed to characterize a portion of the site. Figure 1 shows the relative locations of CPT-9, 11, and 15 through 20. Example results from CPT-19 are shown in Figure 2.

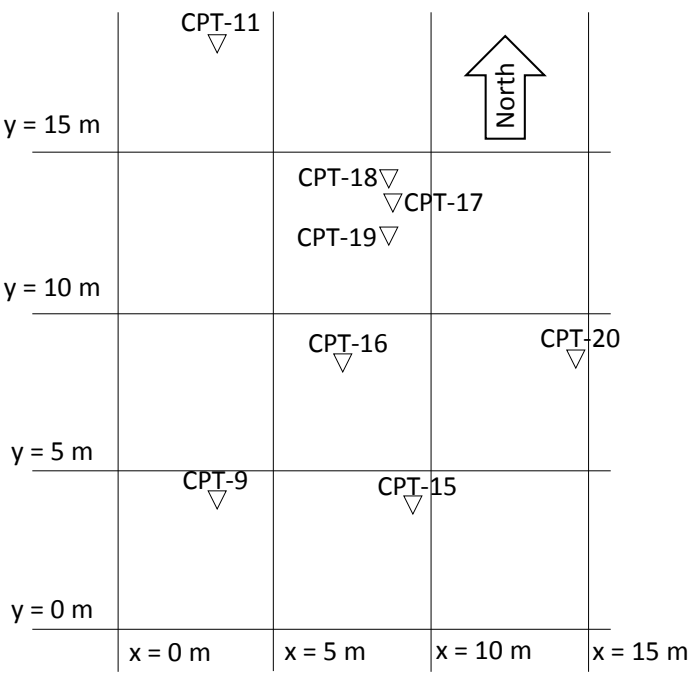

Figure 1. *In situ* testing plan.

KRIGING

Data Preparation To prepare the data for statistical analysis, several steps were taken. First, the CPT tip resistance was normalized for effective stress using Equation 1.

$$q_{c1N} = \frac{q_c/\sigma_{atm}}{\sqrt{\sigma'/\sigma_{atm}}} \quad (1)$$

where q_{c1N} is normalized tip resistance, q_c is measured tip resistance, σ' is effective stress, and σ_{atm} is atmospheric pressure. This method of normalizing tip resistance for effective stress is recommended by Robertson and Wride (1998).

CPT locations were defined using the grid shown in Figure 1. The y-coordinate describes N-S distance and the x-coordinate describes E-W distance. The depths where the soil transitions from one layer to another were also determined through interpretation of the CPT results.

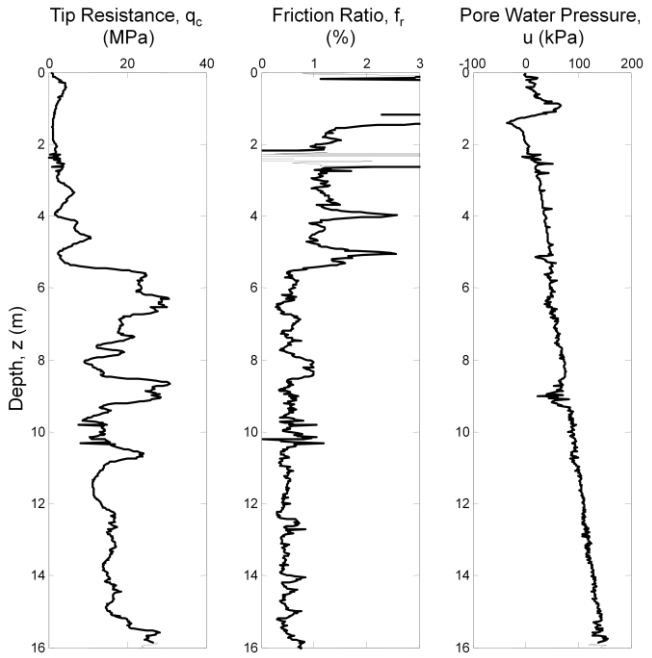

Figure 2. Typical CPT results from CPT-19.

Variogram Development The next step in the kriging process is the development of raw, experimental, and theoretical variograms. The raw variogram forms the basis from which one derives the theoretical variogram. Each data point is compared to every other point. Both the distance between the points, h, and raw variance, γ(h), are calculated. The raw variance is half of the square of the difference between two measurements. The experimental variogram separates the raw variogram into bins and averages all of the entries in that bin. The selection of bin size is important because if the bin size is too small, the experimental variogram will display too much variability to fit a theoretical variogram. However, if the bin size is too large, the experimental variogram will not contain enough information to determine the best theoretical variogram. In this paper, the bin size of 0.25 m was determined by trial and error.

A theoretical variogram is fit to the experimental variogram. While there are several statistical methods of ensuring that a theoretical variogram fits an experimental variogram, the theoretical variograms in this paper were fit visually, using a physical understanding of the system. Certain variograms models fit geologic data better than other models (Chiles and Delfiner, 1999). A sensitivity analysis

showed that a range of reasonable theoretical variograms fit to the experimental variogram did not significantly affect the results of the analysis.

Two theoretical variograms were developed for this paper. The first, used in ordinary kriging, assumed a global constant mean. Therefore, each of the normalized tip resistance values was compared to the other values. The second, used in universal kriging, accounted for different mean values of normalized tip resistance in the different soil layers by first subtracting the arithmetic mean from the layer and developing a raw, experimental, and theoretical variogram based on the residual values. The raw, experimental, and theoretical variogram developed for universal kriging is shown in Figure 3. The model used in this paper, an exponential model with a nugget, is defined in Table 1. The details of both theoretical variograms are shown in Table 2.

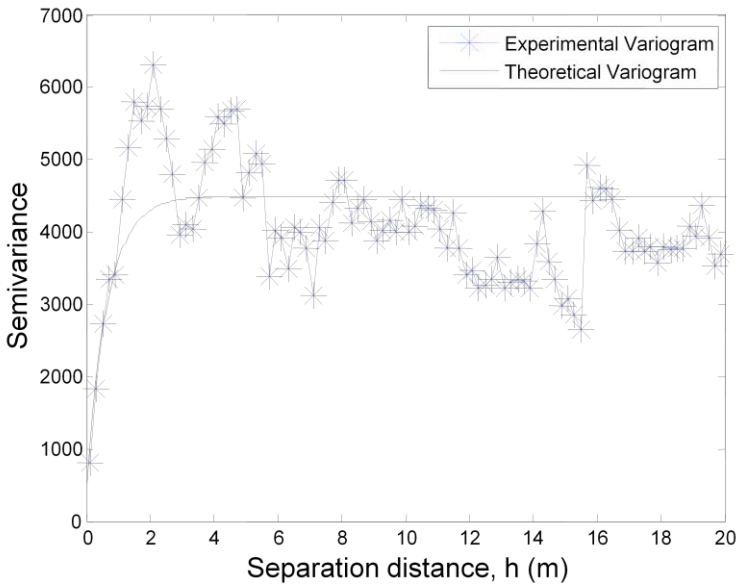

Figure 3. Raw, experimental, and theoretical variogram from the residual normalized tip resistance data.

Table 1. Definition of variogram and covariance functions.

Model	Variogram function	Covariance Function
Exponential with a nugget	$\gamma(h) = \begin{cases} b\left(1 - \exp\left(\frac{-h}{a}\right)\right) + c, h > 0 \\ b\left(1 - \exp\left(\frac{-h}{a}\right)\right), h = 0 \end{cases}$	$C(h) = \begin{cases} b * \exp\left(\frac{-h}{a}\right), h > 0 \\ b * \exp\left(\frac{-h}{a}\right) + c, h = 0 \end{cases}$

Table 2. Theoretical variograms used in ordinary and universal kriging models.

	Correlation Length, a (m)	Partial Sill, b	
Ordinary Kriging	6	10,000	
Universal Kriging	2	4,000	500

Using the theoretical variogram, one can determine the variance and covariance between the estimates made for a location of interest and all known data points. The covariance values make up the $\underline{\underline{\Sigma}}$ matrix. The $\underline{\underline{\Sigma}}$ matrix, expressed in Equation 2, is an n x n matrix determined using the covariance model and the distances between each of the measured observations, where n is the number of measured observations in the database. The equation used to calculate covariance from an exponential model with a nugget is shown in Equation 3.

$$\underline{\underline{\Sigma}} = \begin{bmatrix} C(h_{11}) & \dots & C(h_{1n}) \\ \vdots & \ddots & \vdots \\ C(h_{n1}) & \dots & C(h_{nn}) \end{bmatrix} \tag{2}$$

$$C(h) = b * \exp\left(\frac{-h}{a}\right) + c \tag{3}$$

Ordinary kriging Ordinary kriging is the most general form of kriging, and all other types of kriging are simply adaptations of this method. The formulation for ordinary kriging assumes there is a global spatial mean. Estimations were solved using the point estimate form presented in Equations 4 through 6.

$$\begin{bmatrix} \underline{\underline{\Sigma}} & \underline{F} \\ \underline{F^T} & 0 \end{bmatrix} \begin{bmatrix} \underline{\lambda} \\ -\nu \end{bmatrix} = \begin{bmatrix} \underline{\sigma_0} \\ 1 \end{bmatrix} \tag{4}$$

$$\underline{\sigma_0} = \begin{bmatrix} C(h_{10}) \\ C(h_{20}) \\ \vdots \\ C(h_{n0}) \end{bmatrix} \tag{5}$$

$$\underline{F} = [1 \quad \cdots \quad 1] \tag{6}$$

where $\underline{\lambda}$ is a set of weighting factors, and ν is the LaGrange multiplier. $\underline{\sigma_0}$ is calculated from the covariance between the estimated and measured data points. Each column in the $\underline{F}$ vector corresponds to a measurement location. This formulation ensures that the sum of all $\underline{\lambda}$ terms is one, guaranteeing an unbiased estimate. At each point the CPT measurement is estimated with the variance shown in Equation 7.

$$\sigma_{OK}^2 = C(0) - \underline{\lambda^T}\,\underline{\sigma_0} + \nu \tag{7}$$

Universal kriging The formulation for universal kriging is similar to ordinary kriging but accounts for the fact that there is not a global spatial mean. Estimations were solved using the point estimate form presented in Equations 8 and 9.

$$\begin{bmatrix} \underline{\underline{\Sigma}} & \underline{\underline{F}} \\ \underline{\underline{F}}^T & \underline{\underline{0}} \end{bmatrix} \begin{bmatrix} \underline{\lambda} \\ -\underline{\nu} \end{bmatrix} = \begin{bmatrix} \underline{\sigma_0} \\ \underline{f_0}^T \end{bmatrix} \tag{8}$$

$$\underline{f_0} = [1 \quad 0 \quad 0 \quad 0] \tag{9}$$

Each row in the $\underline{\underline{F}}$ matrix is based on the layer of the estimation location. The first row is the clay layer, the next row represents the loose sand layer, and so on. If the estimation location is in the clay layer, for example, the value in the first column would be one, with all other columns equal to zero. The $\underline{f_0}$ vector changes at each estimation point, corresponding to the layer. The example shown in Equation 9 corresponds to when the estimation point is located in the clay layer. At each point, the CPT measurement is estimated with the variance shown in Equation 10.

$$\sigma_{UK}^2 = C(0) - \underline{\lambda}^T \underline{\sigma_0} + \underline{f_0}\,\nu \tag{10}$$

Anisotropy Because soil properties vary more with depth than with lateral distance, it is necessary to account for anisotropy. The arithmetic mean of each layer was subtracted from each measurement in the corresponding layer, leaving only the residuals. The residuals were then used to create two variograms. The first uses only depth. Results from one CPT were not compared to other CPTs. The second variogram was built using lateral distance at a given depth. For example, the raw variogram was constructed using all the measurements at a depth of 3.10 m, 7.28 m, etc. The theoretical variograms that were fit to these two raw and experimental variograms were both exponential models with a nugget. The theoretical variograms only differed in the correlation length, with horizontal distance yielding a correlation length of 8 m compared to 1 m with vertical distance.

The ratio of the correlation lengths, equal to 8, is the scale factor. The data was transformed with all depth measurements multiplied by the scale factor, causing distance with depth to have the same correlation as lateral distance. The transformed data was the input into the universal kriging analysis. The transformed depth data was returned to measured values before plotting the predictions.

RESULTS OF GEOSTATISTICAL MODEL

Results of an initial model using ordinary kriging are shown in Figure 4. This figure shows predicted normalized tip resistance on an E-W plane located at the 10 m line shown in Figure 1. The areas depicted in white show CPTs conducted within 3 m of the plane. At locations far from measured values, predictions from ordinary kriging trend toward the mean value of normalized tip resistance, roughly 155. The mean value, however, is not a good indicator of normalized tip resistance in specific layers. Therefore, the universal kriging model was developed.

Results of the universal kriging model along the same E-W plane are presented in Figure 5. The universal kriging prediction mirrors the known layering at the site, even at prediction points far from measured values. The uncertainty, also

shown in Figure 5, still varies with proximity to measurement, but is significantly less than the uncertainty in the ordinary kriging model.

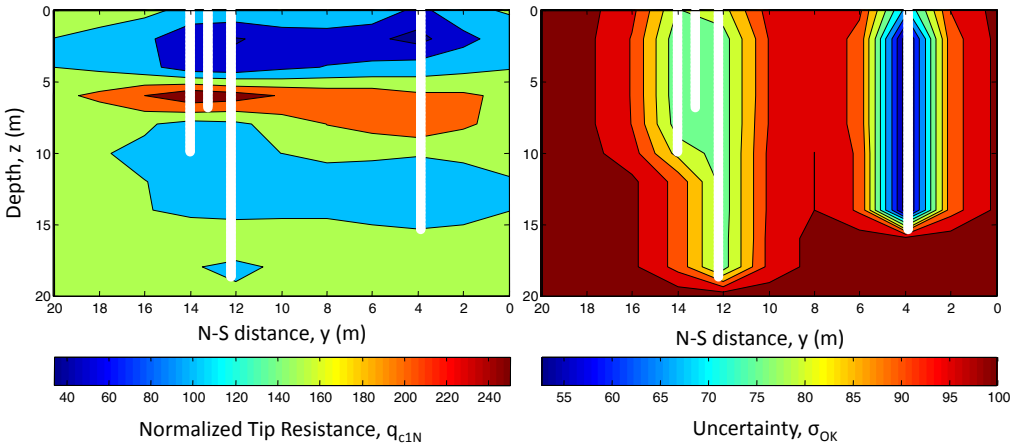

Figure 4. Results of ordinary kriging analysis along x = 10 m.

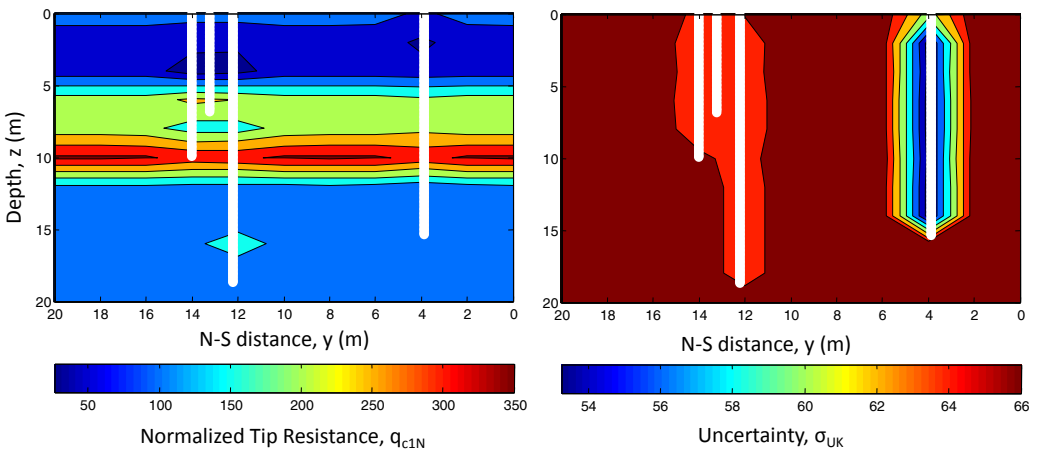

Figure 5. Results of universal kriging analysis along x = 10 m.

A simple comparison of these models shows that universal kriging is superior to ordinary kriging in this application. However, this does not demonstrate that the universal kriging model accurately predicts the normalized tip resistance at a given location. To that end, a cross-validation study was conduction where a CPT was removed from the data base and the model prediction at the test's location was compared to measured values. Figure 6 compares predicted to measured results at the location of CPT-18. The model predicts the measured results within one standard deviation throughout the depth of the test. This exercise was repeated with CPT-16 because it was far from other CPTs. The model again predicted the measured results within one standard deviation. However, when predicting values far from measurements, the model tends toward the mean of each layer. Despite predictions mirroring the mean values for each soil layer, smaller uncertainty from these predictions represent an improvement over ordinary kriging and standard statistical analysis.

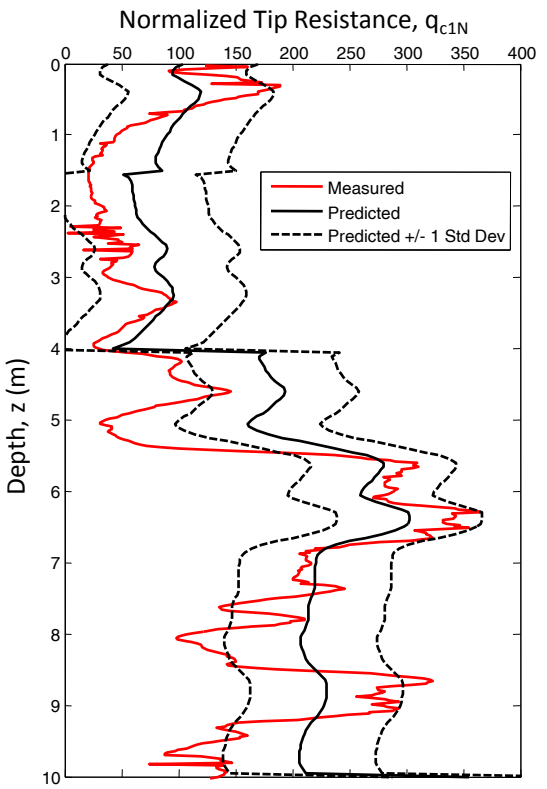

Figure 6. Results of cross-validation at CPT-16.

CONCLUSIONS

Universal kriging provides an excellent method of predicting tip resistance across a testing site. Improvements that came from using universal kriging versus ordinary kriging include lower uncertainties and a prediction that more clearly mirrors what is known about the site. Predictions made within a distance less than or equal to the model's correlation length from measured points reflect the variability naturally present in soil layers. However, predictions made far from measured points tend toward to mean of the soil layer. In cases where predictions are required far from measured points, the reduced uncertainty of universal kriging compared to ordinary kriging and standard statistical methods is the major advantage of this method.

ACKNOWLEDGMENTS

Support for the research presented herein came in part from the NSF NEESR-II grant CMMI 0530378. Dr. Anna Michalak's guidance and suggestions while teaching a course on geostatistics were instrumental to this work. Mulzer Crushed Stone, Inc. donated the use of its quarry and the expertise of its employees. Mr. Jan Pantolin and Dr. Yongsub Jung provided valuable assistance conducting *in situ* testing. This support and assistance is gratefully acknowledged.

REFERENCES

Chiles, J.P. and Delfiner, P., 1999. *Geostatistics: Modeling Spatial Uncertainty*, Wiley, New York.

Fraser, G.S., Thompson, T.A., Olyphant, G.A., Furer, L., and Bennett, S.W. (1997). "Geomorphic Response to Tectonically-Induced Ground Deformation in the Wabast Valley." *Seismological Research Letters*, 68(4), 662-674.

Robertson, P.K. and Wride, C.E., 1998. "Evaluating Cyclic Liquefaction Potential Using the Cone Penetration Test." *Canadian Geotechnical Journal*, 35, 442-459.

Case Study - A Landslide on Coastal Slope in Bellingham Bay

X. Huang[1]

[1]Austin X. Huang, Ph.D., P.E., L.G., F.ASCE, Merit Engineering, Inc., 2715 Meridian Street, Bellingham, WA 98225-2410, USA; PH (360) 738-6083; FAX (360) 738-1499; email: austin@meritengineering.com

ABSTRACT

The subject slope discussed in this paper runs east-west about 0.4 kilometers, is ~18 meter tall and roughly 25° to 40°, and leads down to the beach of Bellingham Bay, in Bellingham, Washington, USA. In the spring of 2009, after a period of excessive wet weather, a part of the slope (~50 meter long) experienced failure. Emergency response was called for to repair the failure section and slope stability analysis was executed for the remaining of the slope and slope was regraded for a safer slope with installation of curtain drain and placement of cast-in-place piles in the upcoming agenda. Field test borings were drilled to about 28 meters depth and soils were analyzed for pertinent engineering properties for slope stability analysis. STABLE program of University of Wisconsin-Madison was used for the analysis and building setback was recommended, which has an acceptable factor of safety (FS) under static and seismic conditions.

SITE RECONNAISSANCE

The subject site is located at the north shore of Bellingham Bay in Bellingham, Washington as shown in Figure 1. In March 2009, a failure occurred along the slope after a major storm event. 50 meters of total ~180 meters coastal slope failed. In May 2009 an initial site reconnaissance was conducted and site conditions have been documented.

Slope Conditions. Vegetation on the slope surface consisted of grass at the top, becoming forested toward the beach below. Thick underbrush began approximately half way down the slope. Trees included Alders and Maples and ranged from seedlings to ~0.5 meter diameter. Curved and tilted trees were observed on the slope, suggesting soil creep. The upper half of the slope had been de-vegetated of native forest as well as steepened with loamy sandy fill and grass.

A scarp of failure spanned ~50 meter along the crest of the slope with a typical cross section as shown in Figure 2. The scarp appeared to be characteristic of circular failure with vertical cut to ~11 meter tall. Debris from the failure covered the ground from the scarp base to the flat area below. Trees and underbrush were also toppled by this failure.

Exposed on the scarp plane was an upper layer of brown sand with gravel that

is likely uncontrolled fill, ~3.0 meter thick. Plastic wrapping, bricks and construction debris were observed throughout this layer. Two pipes ~0.15 meter in diameter were observed coming out of the scarp. Below the sand layer a soft gray clay layer was observed that continued below the exposure of the scarp. The clay appeared saturated with perched water sitting atop. Seepage was observed above the clay, at the bottom of the upper sand layer. Tension cracks near the scarp edge above the failure area, as well as along the edge of the slope ~30 meter to the east of the failure were documented.

Figure 1. Approximate Site Location Map.

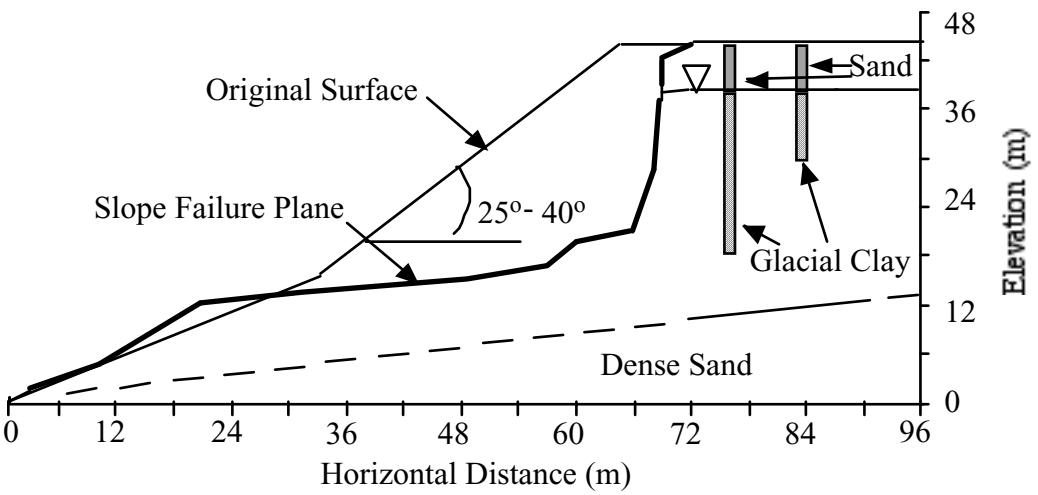

Figure 2. A cross-section of failure slope.

Surface and Groundwater Conditions. During the site reconnaissance in May 2009, surface water above the subject slope was observed. The weather that week had been rainy and it rained during the first half of the day. A large puddle of water covered the surface ~6 meter wide from near the west boundary of the failure to the East ~30 meter. The puddle nearly extended to the edge of the failure.

Water was also discovered seeping out of the face of the scarp at a height of 3-4.6 meters from the base of the upper sandy layer, above the clay layer. Evidence of soil channel erosion due to surface and stormwater runoff was observed as well. Nearby slope sections on adjacent properties also exhibited seepage, with concentrated small waterfalls in a few spots. A storm water drain pipe ~0.3 meter diameter exited the slope ~15 meters to the East of the scarp. From the pipe, water flowed to the bay as a creek.

After the slope failure, storm water was averted from the area directly behind the failure area to control erosion. The basin north of the scarp was also rerouted to the east basin to control erosion within the failure area.

SITE INVESTIGATION

Subsurface Investigation. Subsurface soil and groundwater conditions were investigated by conducting eleven geotechnical test borings to a maximum depth of 26.4 meters. Test borings were located along the slope in six cross-sections as shown schematically in Figure 3.

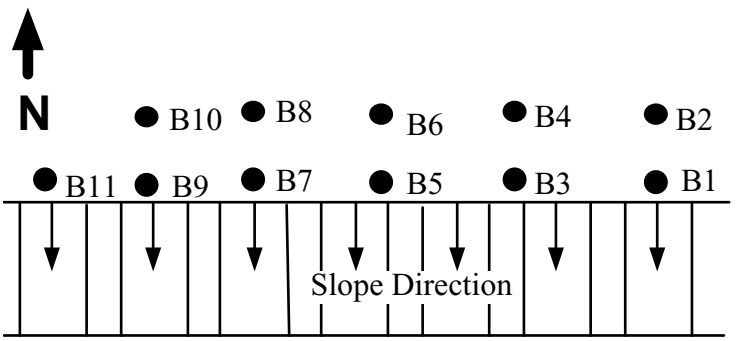

Figure 3. Schematic Test Boring Plan.

Soil profile from test borings are presented in Table 1. Subsurface soils at the site consist of:

a. Sand with Pebbles, Fill (SM)
b. Silty Gray Clay (CL)
c. Silty Sand with Gravel (SM)

a. Sand with Pebbles, Fill (SM)

To a depth of ~2.5 to ~5 meters in test borings is a layer of tannish brown to gray sand with pebbles. The near surface sand was typically medium to coarse and browner in color. By ~3 meters the sand graded to fine to medium and became more gray in color. The consistency of this sand layer was loose to

moderately dense and was moist to wet, becoming saturated with depth.

b. Soft Gray Clay (CL)

Soft gray clay was present in all test borings below the sand layer. The clay was typically saturated, soft and included silt and occasionally thin lenses of fine sand. The unit was observed to the depth of ~17 to ~18 meters. Penetrometer readings were generally ~24 kPa of unconfined compressive strength. The clay was characteristically sticky but easily malleable.

c. Silty Sand with Gravel (SM)

Encountered at ~17m depth was gray, dense, moist to wet fine sand with silt. The layer was observed to the end of drilling, 16m in borings B-5 and B-9. Observed beginning at ~17m depth were interbeds ~25- 75 mm thick fine sand. The layer is interpreted to be laterally extensive throughout the area.

Table 1. Soil Profiles from Test Borings (Depth from Surface, meters)

Soils From Top to Bottom	B1	B2	B3	B4	B5	B6	B7	B8	B9	B10	B11	N^
Fill: Sand	2.7	2.7	3.0	5.0	4.3	3.0	3.0	3.0	3.4	3.0	2.4	1.5
Soft Clay	15*	12*	17	9*	18	9*	18	9*	18	9*	9*	4
Dense Sand	-	-	18#	-	24#	-	20#	-	24#	-	-	30
Boring Depth	15	12	18	9	24	9	20	9	24	9	9	

Notes: * Test boring terminates in the soft clay layer.
Test boring terminates in the dense sand layer.
^ N is average value of Standard Penetration Test (SPT). SPT consists of driving a split-barrel sampler of 38 mm ID (*Inside Diameter*) and 51 mm OD (*Outside Diameter*) 0.46 m into ground using a 63.5 kg hammer with 0.76 m of free fall. The number of blows for last 0.3 m of penetration is obtained as blow count, N, which is correlated with the strength properties of soil.

Geologic Background. The project area is located in the Puget Lowlands of Whatcom County, dominated by various glacial outwash deposits from stades during the Frasier Glaciation of the Pleistocene Epoch (Easterbrook, 1976). Frasier units combine to be over ~60 m depth . The Soft Gray Clay and Silty Sand with Gravel units observed in test borings are likely stratified drift deposits from rivers, lakes, or marine deposits including floating ice into sea water and may correlate with several units within the Everson or Sumas stades of glaciation from ~12,000 to ~10,000 years ago. Beach deposits observed on site are mapped as terrace deposits of the Sumas Stade.

ENGINEERING PROPERTIES OF SOILS

Values for soil unit weights (γ) were used based on soil classification and

literature values from Hoek and Bray (1981). The value for cohesion (c) of the clay soil was estimated using the correlation between **c** and **N** (SPT test from geotechnical borings) and verified by similar values provided by Hoek and Bray (1981). The values for friction angles (ϕ) were back-calculated using the STABLE computer model (a computer program developed by University of Wisconsin). Atterberg Limit Tests and moisture content tests were conducted on representative clayey samples. The clay is confirmed to be non-sensitive clay with moisture contents near liquidity limits due to historical saturation.

Hoek and Bray (1981) specify the friction angle of soft glacial clay to be 27° to 32° and the cohesion to be 35 to 70 kPa. Hoek and Bray (1981) specify the friction angle of similar sandy soils to be 38° to 46° and cohesionless. The analysis is considered somewhat conservative due to selecting the lower bound parameters of estimated literature soil strength properties. Further, the soil strength parameters including cohesion (c) and friction angles of the soils have been obtained by back-calculation of the failed slope. The analysis, therefore, should produce more practical results because the parameters have been verified through multiple sources.

TABLE 2. Basic Engineering Properties for the Materials on Site

Soil	Depth (m)	Cohesion (kPa)	Friction Angle, ϕ	Dry Unit Weight (kN/m^3)	Wet Unit Weight (kN/m^3)
Sand	~3.7	0	30^o	17	21
Soft Clay	~18.3	35	29^o	14	17
Dense Sand	>24.4	0	38^o	17	21

SLOPE STABILITY ANALYSIS

Slope stability conditions were evaluated by using a STABLE computer model as well as by using calculations derived from literature Hoek and Bray (1981). Soil parameters were based on field tests, laboratory soil index tests, soil classification, and literature values. The existing slope is apparently not having an acceptable factor of safety as indicated by the slope failure. Therefore, the analysis was for providing a guidance for remediation measure to increase the factor of safety of the current slope.

Slope Failure Mode. Modes of slope failure are best categorized according to controlling geological structures. Slope failures may be controlled by geological structures such as joints, faults, bedding planes and layers of weak geologic materials. However, these failure modes can be reasonably ruled out since the slope consists only of soils with no bedrock controls.

The failure surface was observed while on site, characterized as a circular failure through multiple soil layers as illustrated in Figure 4. Soil slope failures are found to fail typically in a circular mode according to Hoek and Bray (1981). Among the more elaborate forms of analysis, the Bishop, Janbu, and Spencer methods of slices are most widely used. The Bishop and Janbu methods are more applicable for

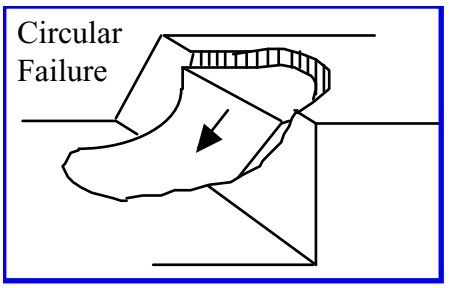

Figure 4. Illustration of the site slope failure mode.

circular failure while the Spencer model gives better results for irregular failure shapes.

Slope Stability Analysis using STABLE. Theoretically, a slope is stable if the Factor of Safety (FS) is greater than 1.0. However, in practical scenarios a minimum FS of greater than 1.0 is always adopted to account for uncertainties that may arise from either parameter estimations or approximations of conditions imposed by the analytical model which may not be perfectly applicable to the project site. A minimum FS of 1.5 is suggested for critical slopes adjacent to haul roads or important installations that are required to remain stable for long periods of time under static conditions (Hoek and Bray, 1981, Dunn *et al*, 1980) and is widely adopted in civil engineering practice.

In the analysis of the subject slope, the Janbu method of slices was employed, which yields more accurate results at this site over the Bishop model. The Bishop model is best suited for uniform soils while the Janbu model is more suitable for more complex soil horizons, similar to those present at the subject slope. Based on the parameters described in the previous sections, the STABLE program outputs a cross-section showing the most critical potential failure surface of the cross-section and the corresponding FS value for the surface. The analysis was approached in a somewhat conservative fashion, meaning the engineering properties of the soils were more indicative of the weaker soil conditions at the site.

To calibrate the STABLE model, two cross-sections were employed:

1) topographic information prior to the slope failure and
2) post-failure topography, shown in Figure 2.

Groundwater was modeled to be present to the surface based on site testing and conservative interpretation of site conditions during failure. Using these topography profiles, soil properties was calculated as presented in Table 2, such that the FS was ~ 1.0 for the failure occurrence at the prescribed failure surface. This method simulated the failure within the STABLE model, thereby verifying derived soil parameters.

Slope Stability Analysis for Site Remediation. The existing slope does not have an acceptable factor of safety as indicated by the failure. Therefore, a major task for the site is to design a remedial plan to increase the FS of the site slope.

Following the recommendation, a groundwater interceptor trench was installed along the slope, at about 9 m back from the slope's crest. The interceptor trench was installed to a depth of ~3.7 m, about 0.6 m into the Soft Gray Clay layer. Water from

the interceptor trench exits via a 0.9 m diameter tight-line pipe below the base of the slope near the beach and running water was observed throughout the site visits.

Slope stability analysis was conducted on the slope with the slope height (~18 m), the soil conditions as described in Tables 1 and 2, and the lowered groundwater conditions as the result of the interceptor trench installation. In the analysis, various slope angles were assumed simulating cut to the slope.

In the analysis, seismic loading conditions of the subject slope was considered by employing a horizontal earthquake coefficient of 0.20g for an earthquake magnitude of 6.5, typical of a near crustal event in northwest Washington, USA (ICC, 2003). This value is selected to be a conservative estimate of peak ground acceleration for glacial clay soils based on available literature. Typically, minimum FS values employed for seismic conditions are ~75% of target static value (FS ≈ 1.125).

CONCLUSIONS AND DISCUSSION

The slope failure described above was interpreted due to oversteepeness due to on-site fill activities and may have been mostly influenced and triggered by increased water flow and runoff onto the slope area. Surface water ran off from the property freely before the failure and the slope failure occurred right during a major storm event.

Following the recommendation, an interceptor trench has been installed along the slope at ~9 m behind the crest of the slope to the depth ~3.7 m, which is 0.6 m into the clay below the sand. Groundwater condition has since been tremendously improved in the slope. An additional interceptor trench will be installed 1.5 m back from the slope crest and 0.6 m deep, to catch surface water from flowing onto the top of the slope. Catch basins and the associated storm water system will transport water sufficiently away from the slope or past the toe of the slope such that slope erosion does not occur.

The failure slope area was cleaned and repaired by installing layers of fill soils consisting of mix of import sands with the on-site sandy and clayey soils. The fill soils were compacted into place and built into a slope of ~26°. The remaining on-site slope has been cut to reduce the slope angle to ~26° as recommended.

The analysis has indicated that the site slope should be scaled back to ~26° angle, which is approximately 2:1 (horizontal to vertical) slope, in order to increase the FS of the slope to 1.5 under static condition. This slope angle is consistent with those mostly common used in construction of embankment. However, the FS of the slope under the design seismic event will not satisfy the design requirement and a major earthquake may cause slope failure. The analysis indicates that by reducing the slope angle alone to increase the FS of the slope to the design standard under seismic loading, the slope angle needs to be scaled down to ~13°, which is practically not feasible. In order to raise the FS of the slope under the design seismic event, a slope shoring system was designed using vertical piles to provide lateral support. Cast in place piles were recommended to increase the FS to an acceptable level under both seismic and static conditions along the entire slope. The piles should be 0.9 m diameter, spaced 7.5 m apart on center, and installed 9.0 m into the dense Silty Sand with Gravel (SM) layer at depth, approximately 26 m in overall length as shown in

Figure 5. Piles should be placed ~6 m south of the slope crest or as far as possible, to be determined by the reach of the equipment from the top of the slope.

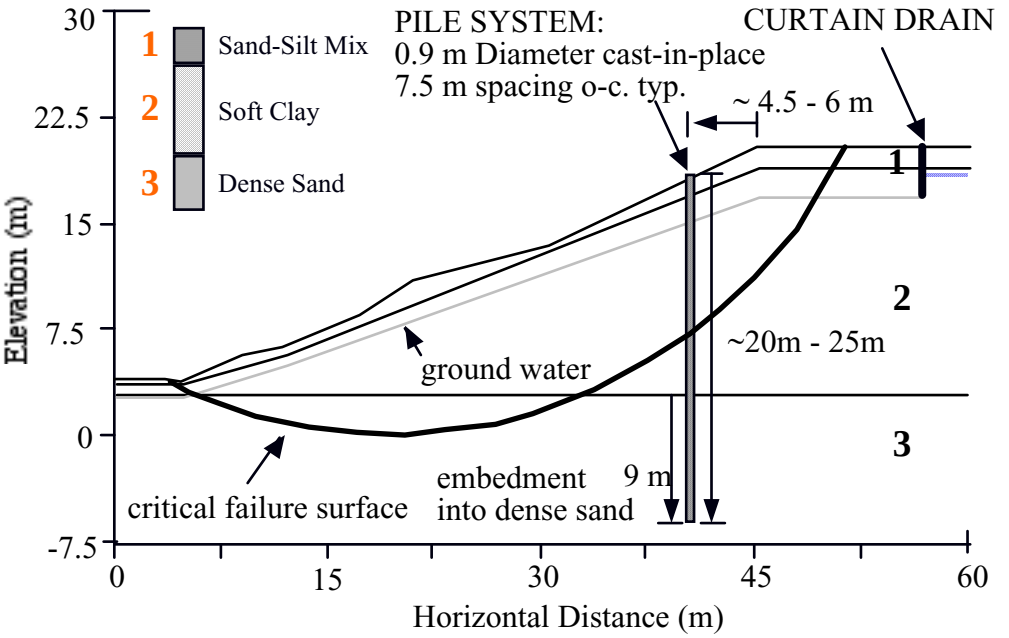

Figure 5. Schematic Drawing - Proposed Slope Improvement.

ACKNOWLEDGMENT

The case study presented in this paper is based on the Geotechnical Engineering Report by Merit Engineering, Inc. in 2009.

REFERENCES

Dunn, I.S., Anderson, L.R., and Kiefer, F.W. (1980). "*Fundamentals of Geotechnical Analysis.*" John Wiley & Sons, Inc., USA.

Easterbrook, Don (1976). "*Map Showing Engineering Characteristics of Geologic Materials, Western Whatcom County, Washington.*" Department of the Interior, United States Geological Survey.

Hoek, E. and Bray, J.W. (1981). "*Rock Slope Engineering*" Stephen Austin and Sons Limited, Hertford, London.

International Code Council (ICC). (2003). *International Building Code 2003*, Country Club Hills, Illinois, USA.

Merit Engineering, Inc. (2009). "*Slope Stability Report*" Merit Engineering, Inc., Bellingham, Washington, USA.

University of Wisconsin-Madison (2008). *STABLE* a computer software for slope stability analysis, Department of Civil and Environmental Engineering.

Developing Resistance Factors for Design of Piles in Sand

K. C. Foye, Ph.D., P.E., M. ASCE[1], M. Prezzi, Ph.D., A.M. ASCE[2], and R. Salgado, Ph.D., P.E., M. ASCE[3]

[1]CTI and Associates, Inc., Wixom, MI; PH (248) 486-5100; email: kfoye@cticompanies.com
[2]School of Civil Engineering, Purdue University, West Lafayette, IN, PH (765) 494-5034 email: mprezzi@purdue.edu
[3]School of Civil Engineering, Purdue University, West Lafayette, IN, PH (765) 494-5030 email: rodrigo@ecn.purdue.edu

ABSTRACT

Load and resistance factor design (LRFD) of foundations is an emerging design philosophy in the United States. Reliability analyses are the preferred tools to establish resistance factors, but the needed probabilistic information regarding design method uncertainty is difficult to obtain. This paper illustrates an approach to uncertainty assessment that seeks to isolate the various sources of uncertainty. Using this approach, reliability analysis is used to develop resistance factors for the design of driven pipe piles in sand. The resistance factor results are used to highlight some of the differences between design methods that are exposed by the proposed uncertainty assessment technique. This approach is key to helping engineers manage risk and assess the relative value of differing degrees and types of design knowledge.

INTRODUCTION

Load and resistance factor design (LRFD), a specific format for limit states design (LSD), is a design framework that indirectly addresses the uncertainty in the methods of calculating a foundation's capacity (resistance) and estimating the demands (load) placed upon it. This indirect assessment affords the engineer a tool to manage risk in design decisions. LRFD factors for use in design practice can be determined through a number of methods, including calibration to customary factors of safety and probabilistic reliability analysis. This reliability analysis requires a probabilistic characterization of foundation analysis method uncertainty. For pile design, this characterization can include consideration of pile load test databases or studies of the individual contributing sources of uncertainty. This paper focuses on some interesting outcomes from applying a detailed analysis of the contributing sources of uncertainty.

Basic LRFD Formulation for Piles. In terms of LSD, pile foundations are typically designed against an ultimate limit state (ULS). The basic LRFD inequality for ULS checks is

$$(RF)R_n \geq \sum (LF)_i Q_i \quad (1)$$

where RF is a resistance factor, R_n is the nominal design resistance, and $(LF)_i$ is a load factor for a particular load type Q_i. Accordingly, $(RF)R_n$ is a limit state value of resistance. In pile design, both base and shaft resistance contribute to the overall load-carrying capacity of the pile. These two contributions suggest two possible LRFD inequalities:

$$(RF)(R_s + R_b) \geq \sum (LF)_i Q_i \quad (2)$$

$$(RF)_s R_s + (RF)_b R_b \geq \sum (LF)_i Q_i \quad (3)$$

where R_s and R_b are the shaft and base resistances, respectively, and $(RF)_s$ and $(RF)_b$ are the shaft and base resistance factors, respectively. Although shaft and base resistance depend on many of the same soil properties, they develop by different physical processes and are computed separately using equations with differing degrees of uncertainty. Therefore, it is more useful to apply $(RF)_s$ and $(RF)_b$ as separate resistance factors, as in Eq. (3).

Probabilistic Framework to Develop LRFD Factors. When using probability to develop LRFD factors, values of RF and LF are selected such that the resulting factored load $\Sigma(LF)_i Q_i$ and resistance $(RF)R_n$ satisfying Eq. (1) lead to designs with an acceptable probability of failure. The reliability index is a number that expresses the probability of failure (i.e., of achieving a limit state) relative to the uncertainty of the design variables. The simplest, first-order second-moment definition of reliability index β when the problem can be reduced to a single design variable X is

$$\beta = \frac{\mu_X - x_{LS}}{\sigma_X} \quad (4)$$

where μ_X is the mean (often, the design value) of X, x_{LS} is the limit state value of X, and σ_X is the standard deviation of X. For multi-variable equations, computing β involves an optimization process. In this paper, the spreadsheet solution method proposed by Low and Tang (1997) is used. Obtaining values of RF and LF for use in design therefore becomes a further process of optimization where β is fixed and RF and LF are computed for a range of design scenarios to obtain the most conservative values (lowest RF and highest LF). An assessment of the design method uncertainty (e.g., σ_X in Eq. 4) is needed to perform this optimization.

One technique to quantify the uncertainty in design methods is to examine databases of predicted versus measured pile performance (e.g., Paikowsky 2004). An advantage of this technique is that a relatively large amount of data can be assembled on which to perform statistics. A disadvantage of this technique is that the method cannot discriminate between the various sources of uncertainty contributing to the observed scatter between predictions and measurements.

An alternative approach, adapted from Ellingwood (1980) in Foye et al. (2006a,b), is to identify the different sources of uncertainty separately, assign probabilistic models to each, then combine them in the final analysis. This approach is conceptually illustrated in Figure 1. Each contributing source of uncertainty results in increased overall uncertainty as their contributions are aggregated. Aggregation is accomplished by the following integration: $p_Y(y) = \int_{-\infty}^{\infty} p_{Y|X}(y|x) p_X(x) dx$, where

$p_Y(y)$ is the probability density function (PDF) representing the aggregated uncertainty of an output variable (e.g., a soil property), $p_X(x)$ is the PDF representing the uncertainty of an input variable (e.g., an in-situ test value), and $p_{Y/X}(y/x)$ is the conditional PDF representing the uncertainty of a design equation (e.g., the relationship between the in-situ test value and a soil property value). PDFs for each variable are fit to laboratory and/or field test data. Thus, this approach requires data quantifying the uncertainty for each input variable and design equation. In terms of Figure 1, the conceptual difference between the database approach and the component approach is that the database approach only allows an examination of the final, actual versus predicted data (lower-left graph), whereas the component approach allows an explicit quantification of the individual analysis steps (all graphs) and their impact on the final, aggregated uncertainty.

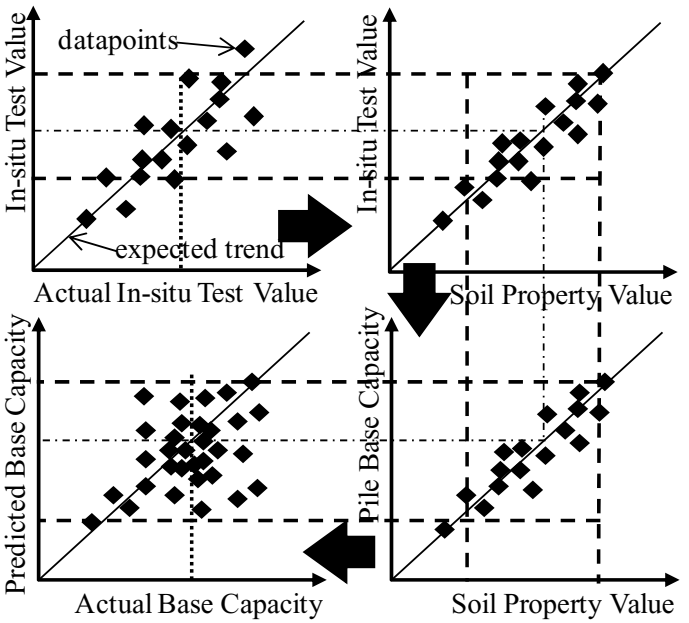

Figure 1. Conceptual representation of accounting for individual sources of uncertainty (clockwise from upper left): measurement, property correlation, capacity model, and final, aggregated uncertainty. The dashed line bounds qualitatively express the cumulative uncertainty at each step in pile capacity analysis. The alternating broken line represents the expected value.

EXAMPLE RESISTANCE FACTORS FOR PIPE PILES IN SAND

Pile design methods are either direct or property-based (Salgado 2008). Direct design methods rely on direct correlations between in-situ tests performed prior to pile installation and measured pile capacity following driving. Thus, direct design methods omit the uncertainty from soil property correlations (upper right in Figure 1). Property-based design methods compute pile capacity using various soil parameters as input. These parameters are computed from in-situ and/or laboratory tests performed on the soil prior to pile installation.

Property-based design methods present a greater challenge to designers because the underlying analyses typically fail to capture the physics of the problem

and, in addition, the design variables in these methods are more difficult to obtain reliably in the field. This condition results, at present, in property-based design methods that are significantly less reliable than comparable direct design methods.

Direct Estimation of Pile Shaft Capacity. The shaft capacity of a pile is computed by summing the contributions of imaginary segments along the length of the pile. The total shaft capacity is thus expressed as:

$$R_s = \sum_{i=1}^{n} q_{sLi} A_{si} \tag{5}$$

where q_{sLi} is the unit shaft resistance (force/unit area) for each segment i and A_{si} is the shaft area for that segment. Segment shaft area A_{si} is computed as $A_{si} = a_s \mathrm{d}L$, where a_s is the perimeter of the cross section and dL is the segment length. Based on results by Lee et al. (2003) for open-ended piles, q_{sL} from Eq. (5) is defined as

$$q_{sL} = \left(\frac{q_{sL}}{q_c} \right) q_c = 0.002 q_c \tag{6}$$

Design equation (6) represents the model relationship between pre-driving CPT measurements and post-driving pile shaft resistance for open-ended pipe piles. To assess the uncertainty in this model relationship, the calibration chamber data from Paik and Salgado (2003) for shaft resistance were considered. The probabilistic model of this uncertainty was also aggregated with the uncertainty introduced by the equations used to estimate q_c within the calibration chamber. The corresponding *RF* value, determined for $\beta = 3.0$, was computed as 0.41 when used in conjunction with ASCE-7 (ASCE 2000 load factors). This value is repeated in Table 1 for comparison with other results below.

Table 1. Resistance Factors (*RF*) for design of driven open-ended (OE) pipe piles in sand using results from the CPT or SPT. Values of *RF* are given for use with ASCE-7 and AASHTO load factors. *FS* indicates an approximate value of WSD safety factor corresponding to the resistance factors given.

Design Method	*RF* using ASCE-7 *LF*s	*RF* using AASHTO *LF*s	representative *FS*
Direct Design – CPT			
OE pipe shaft (Eq. 6)	0.41	0.45	3.7
OE pipe base (Eq. 9)	0.54	0.59	2.8
Property-Based Design – CPT			
OE pipe shaft (Eq. 11)	0.47	0.50	3.7
OE pipe base (Eq. 14)	0.42	0.45	3.5
Property-Based Design – SPT			
OE pipe shaft (Eq. 11)	0.42	0.45	4.0
OE pipe base (Eq. 14)	0.40	0.42	3.7

Direct Estimation of Pile Base Capacity. The base capacity of a pile is computed by

$$R_b = q_{b,10\%} A_b \tag{7}$$

where A_b is the gross pile base area,

$$A_b = \pi\left(\frac{d_0}{2}\right)^2 \tag{8}$$

and d_o is the outside diameter of the pipe pile base. For open-ended piles, $q_{b,10\%}$ from Eq. (7) is defined as

$$q_{b,10\%} = \left(\frac{q_{b,10\%}}{q_c}\right) q_c \tag{9}$$

where

$$\frac{q_{b,10\%}}{q_c} = -0.00443 IFR(\%) + 0.557 \tag{10}$$

IFR is the incremental filling ratio, a measure of the state of plugging of the pile at any point during driving (Paik et al. 2003). Lee et al. (2003) provide guidance on estimating values of *IFR* when field measurements are not available. The $q_{b,10\%}/q_c$ relationship (Eq. 10) was developed by Lee et al. (2003) based on calibration chamber test results of $q_{b,10\%}$. The uncertainty of this relationship was assessed similarly to the method discussed for shaft capacity.

Property-Based Estimation of Shaft Capacity. For open-ended piles q_{sL} from Eq. (5) is computed from

$$q_{sL} = \frac{K_s}{K_0}\tan\left(\frac{\delta_c}{\phi_c}\phi_c\right)\left(K_0\sigma'_v\right) \tag{11}$$

where K_s/K_0 is the ratio of the coefficient of lateral earth pressure after pile installation to the coefficient of lateral earth pressure at rest K_0, δ_c/ϕ_c is the ratio of interface friction angle δ_c to critical-state friction angle ϕ_c, and $(K_0\sigma'_v)$ represents the initial horizontal effective stress at the depth of the pile segment considered. The ratio K_s/K_0 is computed with

$$\frac{K_s}{K_0} = \beta\left(7.2 - 4.8 PLR\right) \tag{12}$$

where

$$\beta = 0.00018 D_R^2(\%) - 0.0089 D_R(\%) + 0.329 \tag{13}$$

with $20\% < D_R < 90\%$. *PLR* is the plug length ratio ($0 \le PLR \le 1$), defined as the ratio of plug length to pile penetration length, and $D_R(\%)$ is the relative density, expressed as a percent.

The prediction of unit shaft resistance, q_{sL}, represented by Eq. (12), contains uncertainties from three sources: 1) the increase in lateral earth pressure due to pile driving and pile loading expressed by K_s/K_0, 2) the coefficient of interface friction $\tan(\delta_c)$, and 3) the pre-driving lateral earth pressure ($\sigma'_h = K_0\sigma'_v$).

The combined uncertainty in the ratio K_s/K_0, defined by Eq. (12), is due to the variable uncertainties of D_R and *PLR* and to the model uncertainty present in the results of Paik and Salgado (2003). Foye et al. (2006a) examined the uncertainty of relative density determined from the CPT. The uncertainty in the K_s/K_0 model relationship was deduced directly from the scatter in the results of Paik and Salgado (2003) since D_R, σ'_h, and degree of plugging were closely controlled or measured.

The uncertainty of *PLR* predictions was assessed by considering the recommendations by Lee et al. (2003) and the data presented by Paik and Salgado (2003). Given that the sand around the pile can be described as loose, medium-dense, or dense, the designer will be able to estimate *PLR* to within ±0.15 of the actual value when aided by prototype pile driving results. The least biased probability density function to describe the uncertainty in this estimate is a uniform distribution with bounds ±0.15 of the expected value. Without the benefit of such results, *PLR* may be completely unknown. The most extreme expression of this uncertainty is a uniform distribution with bounds *PLR* = 0 and *PLR* = 1. The consequences of this difference in knowledge of *PLR* are explored below.

The uncertainty of δ_c was assessed by considering ϕ_c and the ratio δ_c/ϕ_c. Uncertainty in critical state friction angle ϕ_c was obtained from results reported by Bolton (1986). Uncertainty in the ratio δ_c/ϕ_c was assessed by considering the results of high-quality, direct-interface shear tests by Lehane et al. (1993), Jardine and Chow (1998), and Rao et al. (1998).

Property-Based Estimation of Base Capacity. For open-ended piles $q_{b,10\%}$ was found by Paik and Salgado (2003) to be related to the relative density, D_R(%), and the effective lateral earth pressure, σ'_h,as

$$q_{b,10\%} = \alpha\left(326 - 295\frac{IFR(\%)}{100}\right)\sigma'_h \tag{14}$$

where

$$\alpha = 0.0112 D_R(\%) - 0.0141 \tag{15}$$

with 20% < D_R < 90%. The prediction of unit base resistance q_b for open-ended pipe piles, represented by Eq. (13), contains uncertainties from two sources: 1) uncertainty in the $q_{b,10\%}/\sigma'_h$ relationship and 2) uncertainty in the initial lateral earth pressure σ'_h. As seen in Eq. (14), $q_{b,10\%}/\sigma'_h$ also depends on D_R. The uncertainty of these relationships was assessed using the same methodology discussed for pile shaft resistance. Uncertainty modeling of *IFR* is the same as that applied to *PLR*.

RESISTANCE FACTORS AS INDICATORS OF UNCERTAINTY

Table 1 summarizes the resistance factors determined for each of the presented pile design methods when reliability index β = 3.0. Resistance factors are presented for use in conjunction with both the ASCE-7 (ASCE 2000) load factors and the AASHTO (AASHTO 1998) load factors. Lower resistance factors are expected for design methods with greater uncertainty. Direct design methods are expected to have less uncertainty than property-based methods. This expectation is met by the *RF* results for open-ended pipe pile base resistance. Also, in-situ test methods that introduce greater uncertainty are expected to produce lower *RF* values. This expectation is confirmed by the relative values of *RF* obtained for CPT- and SPT-based methods.

Table 2 illustrates the effect of different degrees of confidence in *IFR* estimates on the reliability of the direct design of open-ended pipe pile base resistance (Eq. 9). Since parallel analysis of the effect of estimates of *PLR* on shaft resistance

has similar results, this discussion is limited to *IFR* and base resistance. Two cases are considered; 1) when *IFR* is unknown, it can assume any value between 0 and 100% with equal likelihood (uniform distribution) and 2) when *IFR* is estimated from prototype pile test results and it is modeled as uniformly distributed within ±15% of the estimated value. For both cases, Table 2 includes the calculated results for the *RF* value required to achieve reliability index $\beta = 3.0$, the value of β for $RF = 0.54$ as obtained in Table 1, and the probability of failure P_f if $RF = 0.54$.

Table 2. Resistance factors *RF* for β = 3.0, reliability indices β for *RF* = 0.54, and probabilities of failure P_f for ULS design checks of OE pipe pile base resistance using the Paik et al. (2003) method (Eq 9).

IFR determination	*RF* for $\beta = 3.0$	β if $RF = 0.54$	P_f if $RF = 0.54$
completely unknown	0.26	1.44	7.44%
estimated from prototype	0.54	3.00	0.131%

According to Table 2, if a pile is designed using $RF = 0.54$ without measuring *IFR* for a test pile (the completely unknown case), $P_f = 7.44\%$. If a test pile is used and *IFR* measured, the same $RF = 0.54$ value will lead to $P_f = 0.131\%$, a considerable difference in risk to the project. It is clearly unacceptable to have a 7.44% probability of failure. Also, designing piles twice as conservatively as may be necessary is a waste, as is indicated by the ratio of *RF* values for $\beta = 3.0$. Therefore, this example shows how the difference in *RF* values is an indirect indicator of relative risk. Also, the difference in *RF* values highlights, in this specific case, the value of measuring *IFR*, and, more generally, the value of obtaining information about design variables at costs that are comparatively small.

The following sequence is suggested by these results: 1) design the piles following a conservative estimate of *IFR* (higher values), 2) measure *IFR* during the installation of test piles at the site, and 3) revise the design as needed to reflect the site conditions. This technique allows information to be introduced and used to improve the estimated reliability or economy of the project.

CONCLUSIONS

In this paper, we computed resistance factors appropriate for use in the direct and property-based design of driven pipe piles in sands. Resistance factors are a useful quantitative tool to express the relative uncertainty of load capacity of different pile types and pile design methods. Property-based design methods tend to have higher uncertainty (lower *RF*) but apply to general cases. Direct design methods tend to have lower uncertainty (higher *RF*) but apply only to cases resembling the specific piles and soils of the source direct design database.

By systematically disassembling the design equations and considering the uncertainty associated with each design variable or relationship separately, we quantified the various sources of uncertainty for each method. Using this technique, we identified where the sources of uncertainty are different between design methods.

Finally, we presented an example showing the difference in resistance factors obtained when *IFR* is measured or unknown. This example illustrated the ability of

resistance factors to convey the design value of this additional information. Conversely, the impact on the reliability or risk of the design by omitting this information can be similarly assessed.

REFERENCES

American Society of Civil Engineers (ASCE) (2000). *Minimum design loads for buildings and other structures*, ASCE 7-2000, ASCE, Reston, Virginia.

AASHTO (1998). *LRFD Bridge Design Specifications, 2nd ed*. American Association of State Highway and Transportation Officials, Washington D.C.

Bolton, M. D. (1986). "The Strength and Dilatancy of Sands." *Geotechnique*, 36, 65-78.

Ellingwood, B., Galambos, T. V., MacGregor, J. G., and Cornell, C. A. (1980). *Development of a probability based load criterion for American National Standard A58 - Building Code Requirements for Minimum Design Loads in Buildings and other Structures*, National Bureau of Standards, Washington, D.C.

Foye, K. C., Salgado, R., and Scott, B. (2006a). "Assessment of Variable Uncertainties for Reliability-Based Design of Foundations." *Journal of Geotechnical and Geoenvironmental Engineering*, ASCE, 132(9), 1197-1207.

Foye, K. C., Salgado, R., and Scott, B. (2006b). "Resistance Factors for Use in Shallow Foundation LRFD." *Journal of Geotechnical and Geoenvironmental Engineering*, ASCE, 132(9), 1208-1218.

Jardine, R. and Chow, F. C., (1998). *Research into the Behaviour of Displacement Piles for Offshore Foundations*, OTO 98 833, Health and Safety Executive.

Lee, J., Salgado, R., and Paik, K. (2003). "Estimation of Load Capacity of Pipe Piles in Sand Based on Cone Penetration Test Results." *Journal of Geotechnical and Geoenvironmental Engineering*, ASCE, 129(6), 391-403.

Lehane, B. M., Jardine, R. J., Bond, A. J., and Frank, R. (1993). "Mechanisms of Shaft Friction in Sand from Instrumented Pile Tests." *Journal of Geotechnical Engineering*, ASCE, 119(1), 19-35.

Low, B. K., and Tang, W. H. (1997). "Efficient Reliability Evaluation Using Spreadsheet." *Journal of Engineering Mechanics*, ASCE, 123(7), 749-752.

Paik, K. and Salgado, R. (2003). "Determination of Bearing Capacity of Open-Ended Piles in Sand." *Journal of Geotechnical and Geoenvironmental Engineering*, ASCE, 129(1), 46-57.

Paik, K., Salgado, R., Lee, J., and Kim, B. (2003). "Behavior of Open- and Closed-Ended Piles Driven Into Sands." *Journal of Geotechnical and Geoenvironmental Engineering*, ASCE, 129(4), 296-306.

Paikowsky, S. G. (2004). *Load and Resistance Factor Design for Deep Foundations*, NCHRP Report 507, Transportation Research Board, Washington, D.C.

Rao, K. S., Allam, M. M., and Robinson, R. G. (1998). "Interfacial Friction Between Sands and Solid Surfaces." *Proc. ICE, Geotechnical Engineering*, 131, 75-82.

Salgado, R. (2008). *The Engineering of Foundations*. McGraw-Hill.

Probabilistic Slope Stability Analysis of a 300 m High Embankment Dam

Qun Chen[1] and Li-Ying Chang[2]

[1]Professor, State Key Laboratory of Hydraulics and Mountain River Engineering, College of Hydraulic and Hydropower Engineering, Sichuan University, P.O. Box 610065, Chengdu, Sichuan, China; PH (086) 85403351; email: chenqun@scu.edu.cn
[2]Doctoral student, State Key Laboratory of Hydraulics and Mountain River Engineering, College of Hydraulic and Hydropower Engineering, Sichuan University, P.O. Box 610065, Chengdu, Sichuan, China; PH (086) 85403351; email: togive@126.com

ABSTRACT

Based on the statistical properties of material parameters of 314 m high Shuangjiangkou gravel-clay core rockfill dam, the probabilistic slope stability analyses for the critical slip surface of the dam slope are performed using the Monte-Carlo method. The uncertainty of the shear strength and the spatial variation of the soils and the fluctuation of the phreatic line in the dam are considered in analysis. The factor of safety and the reliability index of the dam slope under different construction and reservoir impounding stages are investigated. The results show that the reliability index of the dam slope with a larger factor of safety is not always bigger than that with a smaller factor of safety. Therefore, for the evaluation of the stability of the embankment dam slopes, the assessment of dam safety will be more scientific and reasonable if the uncertainty of property parameters of the soils can be considered.

INTRODUCTION

Currently, the factor of safety of sliding resistance determined by the limit equilibrium method based on the determinate property parameters of soils is used to evaluate the stability of the dam slopes in China. However, the property parameters of practical soils are random variables with certain changeable range, so the probabilistic slope stability analysis should be used for safety evaluation of dam slopes.

The risk and probabilistic methods have been used for the analysis of slope stability for many years (Alonso 1976; Bergadon and Anderson 1985; Li and Lumb 1987; Christian et al. 1994; Gui et al. 2000; El-Ramly et al. 2003). In recent years, some researchers started to use probabilistic methods to analyze dam slope stability. The reliability and probability theories were developed for assessing the reliability index and the corresponding probability of failure of multi-layered embankment dams and slopes (Liang et al 1999). The reliability of high earth-rock filled dams on complex foundations was studied using the Monte-Carlo method (Zhou et al. 1998).

Impact of the statistical characteristic variables of shear strength parameters on the reliability index (Luan et al. 2004) and probability of instability (Chen et al. 2008) of the dam slope were investigated. The soils and rockfills vary in space, the spatia1 variability of the soils should be considered in the probabilistic analysis. However, the spatial correlation of the dam material was not considered in these probabilistic studies.

Based on the statistical properties of material parameters of 314 m high Shuangjiangkou gravel-clay core rockfill dam, the probabilistic slope stability analyses for the critical slip surface of the dam slope have been performed using the Monte-Carlo method. The uncertainty of the shear strength and the spatial variation of the soil, the fluctuation of the phreatic line in the dam have been considered in analysis. The factor of safety and the reliability index of the dam slope under different construction and reservoir impounding stages have been investigated. Furthermore, the influence of the autocorrelation distance of the dam soils on the reliability index was investigated.

ANALYSIS METHOD

In this paper, the seepage in the dam during reservoir impounding has been calculated using the saturate-unsaturated seepage theory. The seepage analysis software SEEP/W (Geo-Slope International Ltd. 2007a) has been used to study the steady-state seepage in the dam.

The critical slip surface is determined based on the mean values of the input parameters using a limit equilibrium method. Probabilistic analysis is performed on the critical slip surface, considering the variability of the input parameters using the Monte-Carlo method. The software SLOPE/W (Geo-Slope International Ltd. 2007b) is used to assess the dam slope stability including probabilitic analysis. Morgenstern-Price's analysis method (Morgenstern and Price 1965) is used for slope stability analysis.

A random number generation function to do the random sampling is used in the Monte-Carlo method. Each random number N has the same distribution as the input parameter. Then the parameter P needed for every deterministic analysis can be calculated by the following formula:

$$P = \mu + N\sigma \tag{1}$$

where, μ is the mean value and σ is the standard deviation of the parameter. The effective cohesion, c', and effective internal friction angle, φ', are considered as random variables in the probabilitic analysis and can be calculated using Equation (1). The trial number used in the Monte-Carlo method is 500000 in this study.

The reliability index is a parameter to indicate the reliability of the slope stability. If the mean and the standard deviation of the factors of safety are μ_F and σ_F, respectively, the reliability index β can be expressed as:

$$\beta = \frac{\mu_F - 1.0}{\sigma_F} \tag{2}$$

The spatial variability along the slip surface was considered by sampling the properties at a specified distance, that is, autocorrelation distance, along the slip surface (Geo-Slope International Ltd. 2007b).

ANALYSIS CASES AND PARAMETERS

The 314 m high Shuangjiangkou gravel-clay core rockfill dam, located on the Dadu River in the southwest of China, will be the highest embankment dam in the world. The main zones in the embankment, shown in Figure 1, are the gravelly clay core, the double layer filter, the transition, the rockfill shell and the kentledge. The core is founded on hard granite through a concrete base slab with a grouting gallery. There is a 96 m deep grout curtain below the concrete base slab in the bedrock. The rockfill shell is founded on three overburden layers above the granite. The overburden layers consist of boulder cobble gravel on the top (overburden 3), sandy cobble gravel (overburden 2) in the middle and cobble gravel with boulder (overburden 1) at the bottom. The rockfill section has an upstream slope of 2.0H:1.0V with a berm at elevation 2330.00 m and a downstream slope of 1.9H:1.0V. The elevations of the crest and the base of the dam are 2510.00 m and 2196.00 m, respectively. The crest is 8 m wide. The top width and bottom width of the core are 4 m and 128 m, respectively.

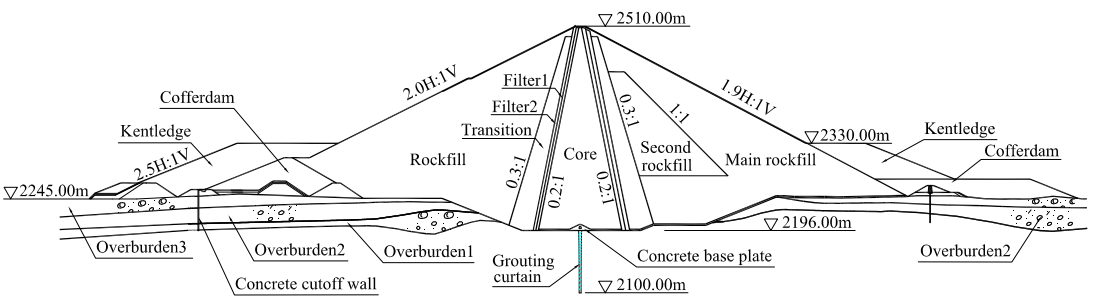

Figure 1. Maximum profile of the Shuangjiangkou dam

The probabilistic slope stability analyses for the maximum profile (Figure 1) of the dam were conducted in three conditions including completion of construction of the dam, reservoir impounding to dead water level and to normal water level. On each condition, firstly, the variation of the shear strength was considered, then, the spatial variation of the soils and the fluctuation of the phreatic line were added separately. These analysis cases are listed in Table 1. The fluctuation of the phreatic line was only considered for upstream slope of the dam because the phreatic line behind the core is very low and it has no impact on the stability of downstream slope. In cases 7 and 8, the variation of shear strength and fluctuation of the phreatic line are considered. Besides the cases in Table 1, the influence of the autocorrelation distance of the dam soils on the reliability index was investigated.

The strength and hydraulic properties of the material of the dam and the foundation were obtained based on test results. The shear strength parameters including the internal friction angle and the cohesion were considered as random variables. It was assumed that they all follow the normal distribution. Their standard deviations were obtained based on the investigation of the shear strength uncertainty for the materials of Shuangjiangkou dam and other similar dams (Wu 2008). The saturated coefficients of permeability, strength parameters and their standard deviations of the soils are listed in Table 2. The permeability functions estimated from soil-water characteristic and grain size distribution curves (Fredlund et al. 1994 and Fredlund et al. 1997) of the dam soils used in analyses are shown in Figure 2.

Table 1. Analysis cases in different conditions

Case	slope	Analysis conditions	
1	Upstream	End of construction, variation of shear strength	
2	Downstream		
3	Upstream	End of construction, variation of shear strength and spatial variation (autocorrelation distance=10 m)	
4	Downstream		
5	Upstream	Normal water lever, variation of shear strength	
6	Upstream	Dead water lever, variation of shear strength	
7	Upstream	Normal water lever	Fluctuant height=2m
8	Upstream	Dead water lever	Fluctuant height=5m

Table 2. Material parameters used in analyses

Material	Unit weight γ: kN/m^3	Saturated conductivity k_{sat}: m/d	Cohesion c: kPa		Friction angle φ: °	
			Mean	Standard deviation	Mean	Standard deviation
Overburden 1	20.6	25.9	17	3.0	39	2.20
Overburden 2	20.3	17.3	10	3.0	37	2.20
Overburden 3	20.5	43.2	16	3.0	37	2.20
Cofferdam	20.7	86.4	0		35	2.20
Core	21.1	0.00605	35	5.0	31	2.20
Filter 1	20.0	4.32	0		41.7	2.17
Filter 2	20.2	6.91	0		43.7	2.59
Transition	20.9	25.9	0		45.3	2.31
Upstream rockfill	21.5	86.4	0		40.8	2.26
Downstream main rockfill	21.1	86.4	0		47.7	2.95
Downstream second rockfill	20.9	40.0	0		45.7	2.95

RESULTS AND DISCUSSION

The probabilistic slope stability analysis results of the cases in Table 1 are listed in Table 3. The results are only related to the property of the upstream or downstream rockfill because the critical slip surface is very shallow and only through

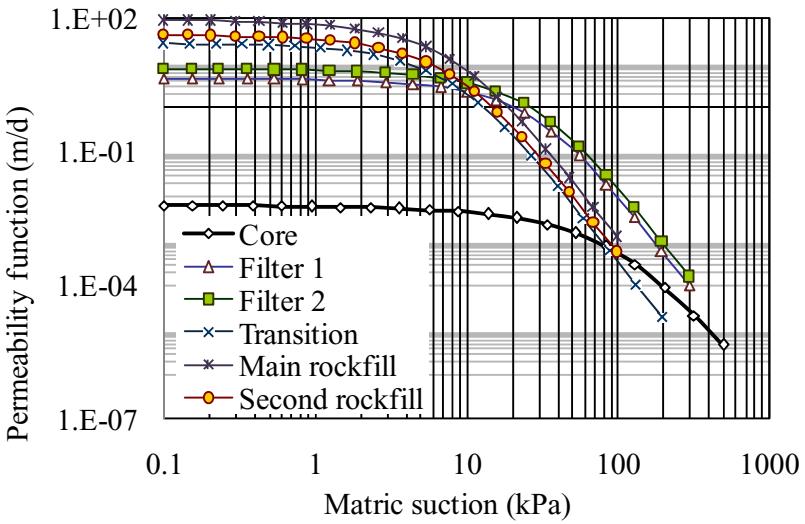

Figure 2. The permeability functions of the dam soils

Table 3. Probabilistic slope stability analysis results of the cases in Table 1

Case	Factor of safety		Reliability index
	Mean	Standard deviation	
1	1.770	0.143	5.395
2	2.112	0.222	5.012
3	1.770	0.031	24.504
4	2.112	0.045	24.764
5	3.742	0.211	12.970
6	1.790	0.144	5.484
7	3.739	0.244	11.225
8	1.779	0.152	5.144

Comparing case 2 with case 1, it is found that the reliability index of the upstream slope is bigger than that of the downstream slope because the standard deviation of the upstream rockfill is less than that of the downstream rockfill, which causes the standard deviation of the factor of safety of the downstream slope is bigger and its reliability index is less. This illustrates that the reliability index of the dam slope with a larger factor of safety is not always bigger than that with a smaller factor of safety.

Because the reliability index increases with the increase in the mean of the

factor of safety but decreases with the increase in the standard deviation of it, the reliability index can be less or bigger if both the mean and the standard deviation of the factor of safety is bigger. For example, the reliability index in case 2 is less than it in case 1, nevertheless it in case 4 is a little bigger than it in case 3.

When the spatial variation of the dam soils is considered (cases 3 and 4), the means of the factors of safety remains unchanged but the standard deviations of the factors of safety decrease (comparing case 3 with case 1 or case 4 with case 2) both for the upstream slope (cases 1 and 3) and the downstream slope (cases 2 and 4). This results in the increase of the reliability index of the dam slopes.

If the fluctuation of the phreatic line in the dam is included (cases 7 and 8), the means of the factors of safety decrease a little and the standard deviations of the factors of safety increase (comparing case 7 with case 5 or case 8 with case 6) both for the normal water level (cases 5 and 7) and dead water level (cases 6 and 8) conditions. Therefore, the reliability indexes of the dam slopes decrease.

Figure 3 shows the mean of the factor of safety and the reliability index change with the autocorrelation distance in dam soils. Both for the upstream slope (Figure 3(a)) and the downstream slope (Figure 3(b)), the means of the factors of safety almost unchange for the different autocorrelation distances. However, the reliability index decreases nonlinearly with the increase in the autocorrelation distance. When the autocorrelation distance is small, the reliability index decreases evidently; when it is bigger than a critical value, it will have no effect on the reliability index. Based on the investigation of the size of the critical slip surface, it is found that the critical value of the autocorrelation distance is nearly equal to the chordal length of the critical slip surface of the slope. Furthermore, the unchanged reliability index for the autocorrelation distance bigger than the critical value is equal to the reliability index in the case of no consideration of the autocorrelation distance.

For different autocorrelation distances, the reliability indexes of the upstream slope and the downstream slope are close agreement though the mean of the factor of safety of the upstream slope is lower than that of the downstream slope. It is because that the bigger standard deviation of the shear strength of the downstream rockfill results in the bigger standard deviation of the factor of safety though the mean of the shear strength of the downstream slope is bigger.

CONCLUSIONS

The probabilistic slope stability analyses were performed for the 314 high Shuangjiangkou gravel-clay core rockfill dam. The uncertainty of the shear strength and the spatial variation of the soils and the fluctuation of the phreatic line are considered in analysis.

The results show that the mean and the standard deviation of the factor of safety increase with the increase in the mean and the standard deviation of the shear strength of the dam soils, respectively. The reliability index of the dam slope with a larger factor of safety is not always bigger than that with a smaller factor of safety. A bigger standard deviation of the shear strength of the dam soil results in a bigger standard deviation of the factor of safety and a less reliability index. So, the uncertainty of the shear strength of the soils should be considered in evaluation of the

stability of the embankment dam slopes.

The mean of the factor of safety decreases a little and the reliability index of the dam slope also decreases on the conditions of considering the fluctuation of the phreatic line in the dam. The mean of the factor of safety remains unchanged but the reliability index of the dam slope increases if the spatial variation of the dam soils is considered.

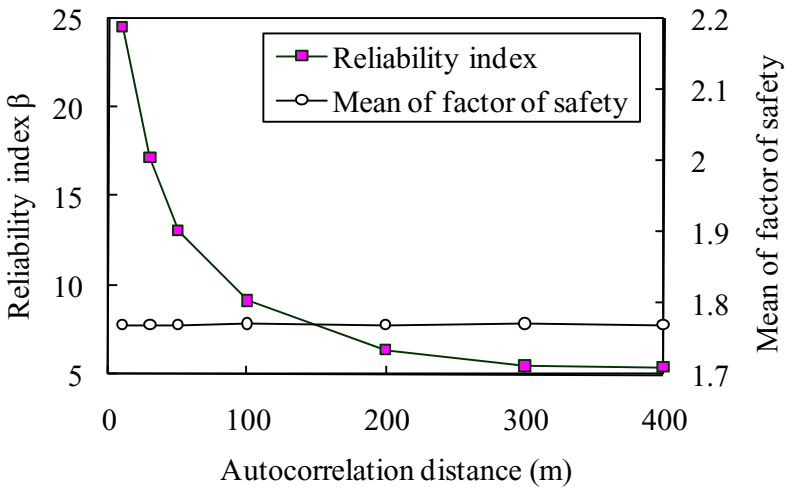

(a) Upstream slope

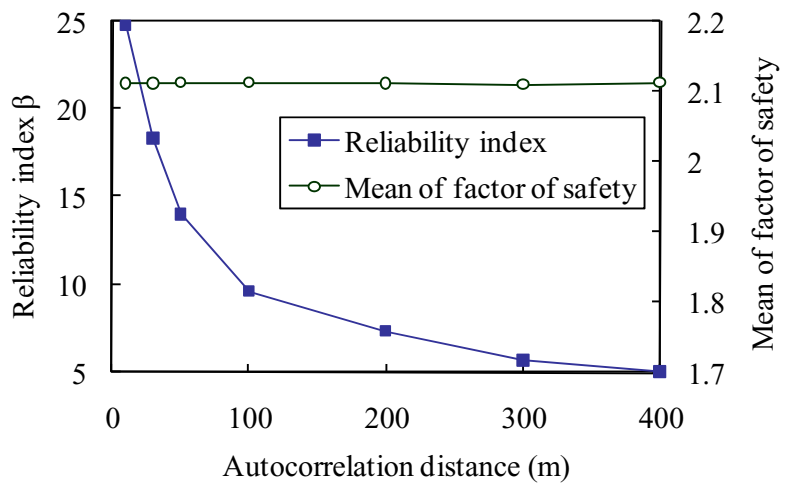

(b) Downstream slope

Figure 3. The mean of the factor of safety and the reliability index change with the autocorrelation distance

The mean of the factor of safety is almost changeless for the different autocorrelation distances. However, the reliability index decreases nonlinearly with the increase in the autocorrelation distance. It will decrease to a constant value when the autocorrelation distance bigger than chordal length of the slip surface.

REFERENCES

Alonso, E. E. (1976). "Risk analysis of slopes and its application to slopes in canadian sensitive clays." *Geotechnique*, 26 (3), 453-472.

Bergadon, D. T., and Anderson, L. R. (1985). "Stochastic analysis of pore pressure uncertainty for the probabilistic assessment of the safety of earth slopes." *Soils Found*., 25 (2), 87-105.

Chen, Q., Tang, M., and Zhu, F-Q. (2008). "Influence of uncertainty of strength parameters on the instability probability of the embankment dam slope." *Chinese J. Geotechnical Engrg*., 30 (11), 1594-1599. (in Chinese)

Christian, J. T., Ladd, C. C., and Baecher, G. B. (1994). "Reliability applied to slope stability analysis." *J. Geotechnical Engrg.* , 120 (12), 2180-2207.

El-Ramly, H., Morgenstern, N. R. and Cruden D. M. (2003). "Probabilistic stability analysis of a tailings dyke on presheared clay-shale." *Can. Geotech. J.*, 40(1), 192-208.

Fredlund, D. G., Xing, A., and Huang, S. (1994). Predicting the permeability function of unsaturated soils using soil-water characteristic curve. *Can. Geotech. J.*, 31(4): 533-546.

Fredlund, M. D., Fredlund, D. G., and Wilson, G. W. (1997). Prediction of the soil-water characteristic curve from grain-size distribution and volume-mass properties. In Proceedings of the 3rd Brazilian Symposium on Unsaturated Soils, Rio de Janeiro, 22-25 April, 1: 13-23.

Geo-Slope International Ltd. (2007a). Seepage Modeling with SEEP/W 2007. An Engineering Methodology, Second Edition.

Geo-Slope International Ltd. (2007b). Stability Modeling with SLOPE/W 2007. An Engineering Methodology, Second Edition.

Gui, S., Zhang, R., Turner J. P., and Xue, X. (2000). "Probabilistic slope stability analysis with stochastic soil hydraulic conductivity." *J. Geotechnical and Geoenvironmental Engrg.*, 126 (1), 1-9.

Li, K. S., and Lumb, P. (1987). "Probabilistic design of slopes." *Can. Geotech. J.*, 24 (4), 520-535.

Liang, R. Y., Nusier, O. K., and Malkawi, A. H. (1999). "Reliability based approach for evaluating the slope stability of embankment dams." *Engineering Geology*, 54(3), 271-285.

Luan, M-T., Xin, J-X., and Zhao, S-C. (2004). "Reliability analysis of concrete-faced rockfill dam's slope stability and its application." *Journal of Dalian University of Technology*, 42(5), 467-471. (in Chinese)

Morgenstern, N. R., and Price, V. E. (1965). "The Analysis of the Stability of General Slip Surfaces." *Geotechnique*, 15(1), 79-93.

Wu, Z-Y. (1965). "Research on the reliability analysis methodology of nonlinear strength slope stability of high rockfill dam and the safety factor criterion." Ph. D Thesis, Sichuan University, Chengdu, China. (in Chinese)

Zhou, J-P.， Peng, X-Z., and Zhao, S-R. (1998). "Stability reliability of earth-rock filled high dams on complex foundations." Journal of Southwest Jiaotong University, 33(5): 544-549. (in Chinese)

Identification of hazardous loose landslide deposits and scars formed during the 2008 Wenchuan earthquake

H. F. Zhao[1] and Limin Zhang[2], M. ASCE

[1]Research Assistant, Dept. of Civil and Environmental Engineering, The Hong Kong University of Science and Technology, HKSAR, China; email: hfzhao@ust.hk
[2]Professor, Dept. of Civil and Environmental Engineering, The Hong Kong University of Science and Technology, HKSAR, China; email: cezhangl@ust.hk

ABSTRACT

The Wenchuan earthquake triggered many landslides along Province Road 303 (PR303) in Sichuan Province. These landslide deposits pose hazards to the safety of the traffic and road facilities under rainfall conditions. Some of the slopes are hard to access as the terrains are steep and high. How to identify the hazards is a challenge to engineers. In this paper, a method for hazards identification is demonstrated for a segment of PR303 between milestones K34+00 m and K34+200 m. This method consists of three steps. First, identify all possible hazard sources based on field surveys and aerial photographs. Second, analyze past failure events to single out the most likely sources of hazards. Finally, apply numerical reliability analysis to ascertain the sources of hazards. Results of the case study show that the proposed method is effective for hazards identification in inaccessible terrains.

INTRODUCTION

PR303 in Sichuan Province is an important road to several national scenic parks. The Wenchuan earthquake triggered 61 slope failures, 63 rock avalanches and 19 debris flows along a 45 km segment of the road. Over 80% of the road between Yingxiu (the epicenter) and Wolong (the Grand Panda National Park) was damaged or buried by landslide deposits. Landslide deposits formed during the earthquake are densely populated on the steep terrains. Under rainfall infiltration, such deposits may lose stability and hence pose hazards to the safety of the traffic and road facilities.

Hazards identification is the basis for reconstruction of PR303. Some areas along PR303 are inaccessible as the terrains are very steep and high. It is unlikely to identify the sources of hazards through field reconnaissance alone. In this paper, a method for hazards identification is demonstrated on a large earthquake-induced landslide between milestones K34+00 m and K34+200 m. In this method,

preliminary field surveys, past failure events, and numerical simulations are combined to identify and ascertain sources of risk near K34.

GEOGRAPHIC AND GEOLOGICAL SETTINGS NEAR K34

Many slides and boulder fall events occurred at K34 in the past two years after the Wenchuan earthquake. The geomorphic and geologic features of the K34 landslide site are illustrated in a 1:2000 digital elevation map with a resolution of 2 m (Fig. 1) and an aerial photograph (Fig. 2). The K34 terrain is typically steep. The slope angles of the landslide area range from 35^{o} to 40^{o} and the depth of valley is nearly 1500 m. As the terrain is very steep and valley is very deep, it is unlikely to climb the mountains to conduct detailed surveys and identify the risk sources.

The geology of the landslide area comprises mainly of slate and sandy slate of the Triassic Xikang group, crystalline rock and phyllite of the Permo-carboniferous group and the Devonian period. A cross section along the main run-out axis is generated based on the digital elevation map and shown in Fig. 3b. Based on preliminary field surveys and aerial photographs, the sources of hazards near K34 are divided into three parts; namely, the landslide debris on the bottom, the deposits on a terrace and the top-fissured landslide scars. The bottom landslide deposit has a volume of approximately 40,000 m^3, which buried the road. The landslide debris is stable and a temporary road was built through the debris. Some fissured landslides scars are found 500–700 m above the road (Fig. 2) through survey from the opposite side of the valley. A terrace covered by gravelly soils with boulders is also identified 300-500 m above the road. The grain size of the deposit ranges from clays to boulders (Fig. 2). The thickness of the deposits is about 5 m - 12 m. Fig. 3a shows a photo of the bottom part of the slope, with the run-out axis marked. The fissured scars and the terrace are not visible from the road elevation.

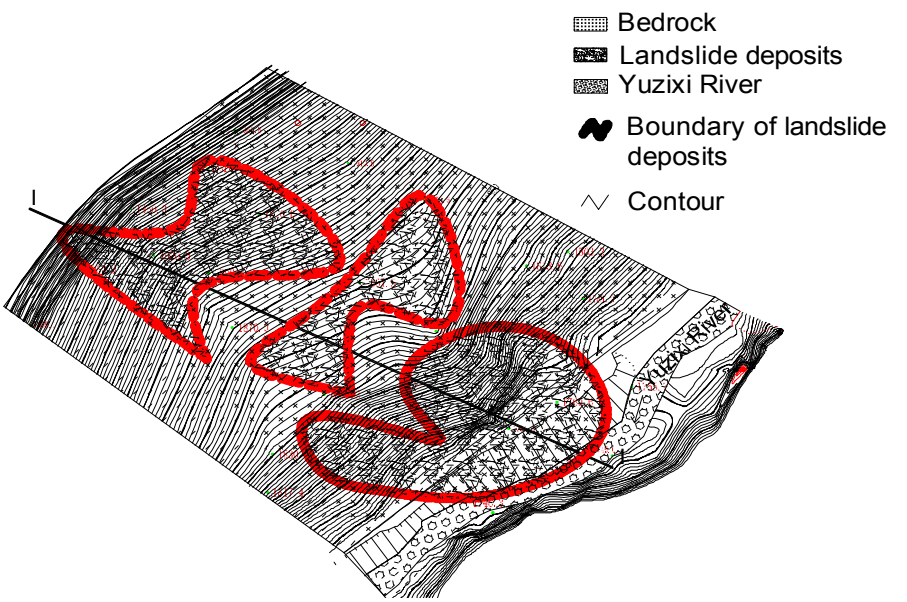

Figure 1. Digital elevation map of the terrain near K34 (1:2000).

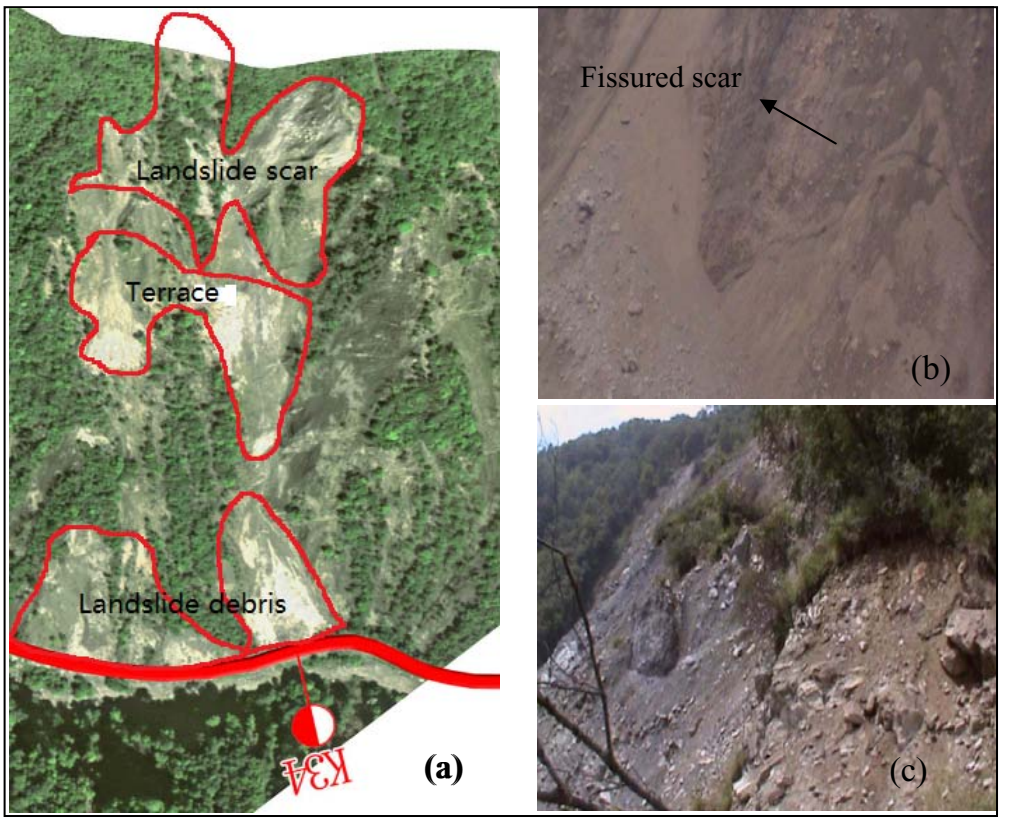

Figure 2. Photographs showing (a) the location of landslides, (b) the fissure scars, and (c) the landslide deposits.

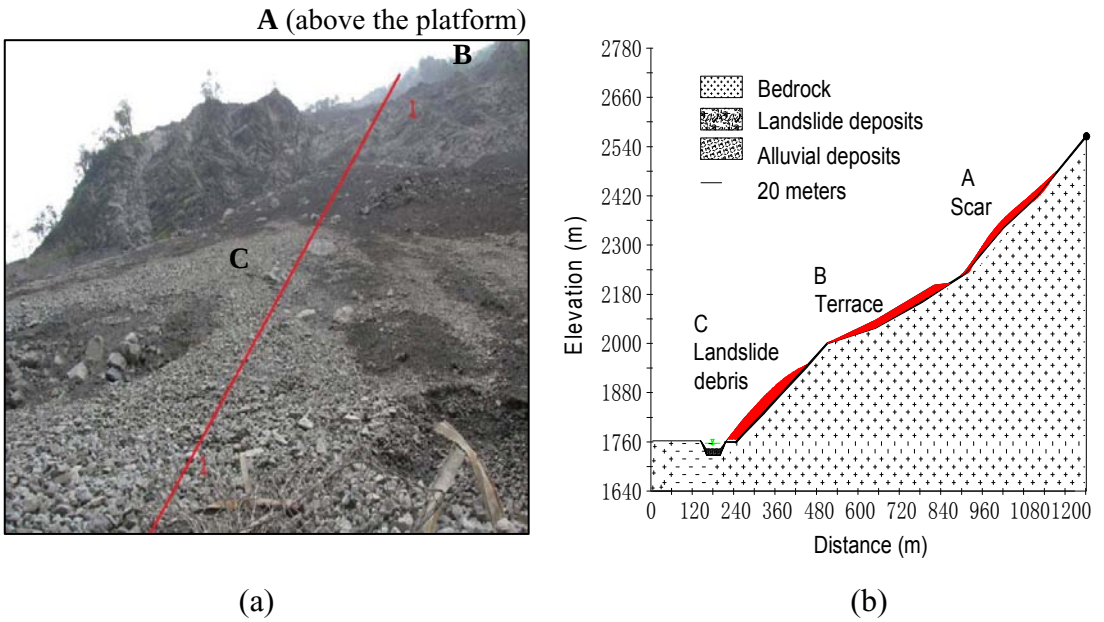

(a) (b)

Figure 3. Geomorphology and geology of the landslide site: (a) photo; (b) cross-section I-I.

INVENTORY OF FAILURES OCCURRED IN 2009-2010

Repeated slides occurred at K34, which caused one fatality and more than 10 shutdowns of the road. We obtained some information of failure events and landslide damage from the Sichuan Provincial Department of Transportation. Additional information was obtained through our field surveys along the road and by interviewing the contractors. Table 1 summarizes our findings; some photos of the failure events are shown in Fig. 4.

Table 1. List of slide and boulder-fall events at K34.

Time of failure	Type of damage
01 May 2009	Buried a car, temporarily interrupted the road
08 July 2009	Buried a truck and a car, temporarily interrupted the road
18 July 2009	A man on motorbike was killed by flying boulders
22 July 2009	Buried a truck, damaged equipment and interrupted the road
30 Aug. 2009-03 Sept. 2009	Interrupted the road and formed a landslide dam
26 May 2010	Hurt 4 contactors and destroyed 3 engineering trucks
28 May 2009-12 June 2010	Interrupted the road 6 times, damaged boulder protection fences
14 June 2010	Buried the road; destroyed the boulder protection fences

Figure 4. Failure events at K34.

IDENTIFICATION OF SOURCES OF RISK AT K34

Identification of potential sources of boulder falls based on the inventory. Once the Soil/rock detaches from a scar at a very high elevation, the most important factor controlling its falling trajectory is the slope geometry. The historical data in Table 1 provides a good indication of the sources of boulders on the terrain.

Following detachment, the landslide material proceeded at a high velocity, flying and bouncing as it traveled down (Fig. 5c). A field survey was conducted after the 3 Sept. 2009 boulder-fall event. Photos taken from the opposite side of the slopes are shown in Fig. 5. Evidence has been found that the boulder falls were initiated at

the scars. First, a fresh trace is observed on the scar after the rockfall occurred (Fig. 5a). Second, deposits of fine rock fragments are found on the terrace (Fig. 5b), which are considered as segregated materials of the collapsed rocks from the scars. It is noted that, during a granular flow event, coarse particles selectively move faster and to the surface while fine materials move slower and to the bottom.

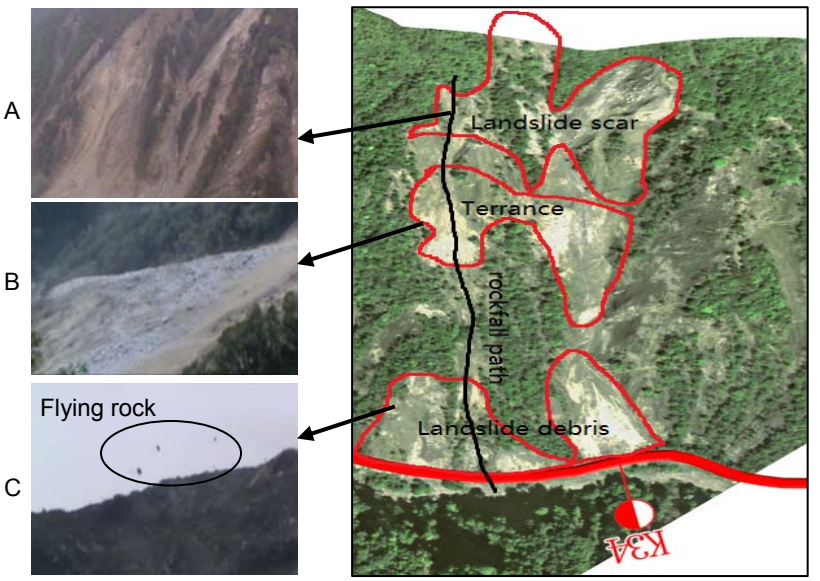

Figure 5. Rockfall events on 30 August and 3 September 2009: (a) A fresh trace on the scar; (b) Loose deposit on the terrace; (c) Flying and bouncing rocks.

Numerical simulation. Infiltration plays an important role in triggering of slope failures. With rainfall infiltration, the initially negative pore-water pressures in the slope will increase and the shear strength of the slope soil will decrease gradually. The slope may fail finally when the shear strength is insufficient to maintain the equilibrium of the soil.

Numerical analysis is conducted to simulate the event happened on 30 August - 3 September 2009 and to confirm the likely sources of risk. All of possible hazards are modeled. A finite element program Seep/W (GeoSlope International, 2001) is used to simulate the pore-water pressure responses due to rainfall infiltration and Slope/W is used to calculate the factor of safety of the slopes.

Based on the digital elevation model, the inclination angles of the bottom landslide debris, the terrace, and the fissured scar are 40 °, 24 ° and 42°, respectively. A tension crack is simulated on the top of the fissured scar. The crack is modeled as a special kind of "soil", which is much more permeable than intact soil, with its permeability being two orders of magnitude larger than the permeability of the intact soil. The assumed permeability functions and soil water characteristic curve for the soil matrix and the crack, which are required in the simulation of rainfall infiltration into the terrains, are portrayed in Fig. 6. The shear strength of unsaturated slope soils is described by the extended Mohr-Column equation (Fredlund et al. 1978):

$$\tau = \mathrm{c'} + (\sigma - u_a)\tan\phi' + (u_a - u_w)\tan\phi^b \qquad (1)$$

where τ is the shear stress on the failure plane at failure; c' is the effective cohesion; ϕ' is the effective angle of internal friction; ϕ^b is the angle indicating the rate of increase in shear strength with respect to matrix suction.

The design ϕ' values for soil matrix provided by Sichuan Provincial Highway Design Institute (2009) are used in the simulations, while other parameters are assumed. The parameters for the soil matrix and the crack are shown in Table 2. The presence of the crack reduces the soil strength. The rainfall data on 19-20 August 2010 reported by Weather China for Wenchuan County is used as a reference, as shown in Fig. 6. The rainfall on 30 August - 3 September 2009 is not available.

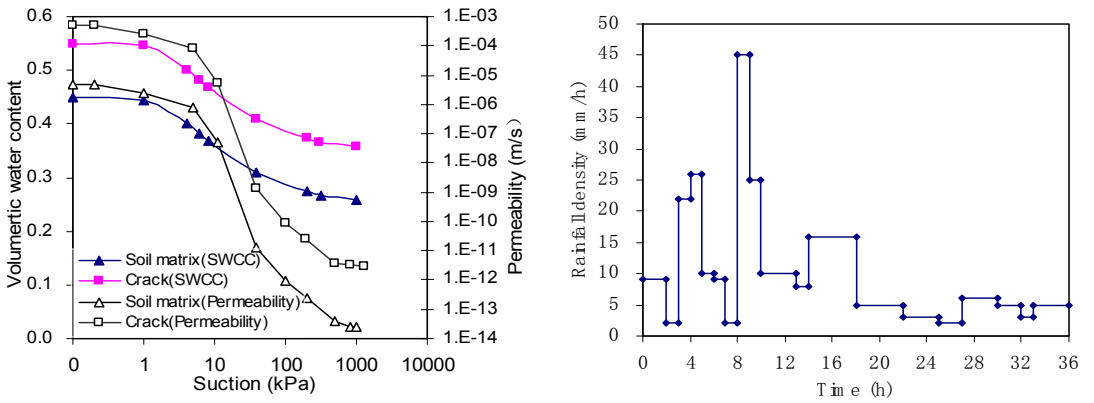

Figure 6. Soil property functions and rainfall data.

Table 2. Soil parameters used in Slope/W.

	Soil matrix		Crack	
	Mean value	Standard deviation	Mean value	Standard deviation
γ (kN/m^3)	21	3	16	3
ϕ' (degree)	30	1	0	1
c (kPa)	2	2	0	2
ϕ^b (degree)	10	1	6	1

Fig. 7 shows the pore-water pressure contours in the terrace and fissured scar at the end of the rainfall event. During water infiltration, the wetting front moves from the slope surface towards deeper locations. For the terrace, the perched water table does not reach the initial ground water table. The soil between the perched water table and the ground water table is still unsaturated after 36 hours of rainfall. For the fissured scar, the infiltrated water first passes through the crack and accumulates at the bottom of the crack. Then the water penetrates to the soil matrix that surrounds the crack. All the soils of the slope are saturated after 36 hours. Fig. 8 shows the potential slip surfaces and Fig. 9 shows the decrease of factor of safety with time. At the end of the rainfall event, the FOS is 1.14 for the bottom landslide debris, 1.46 for the terrace, and 0.65 for the fissured scar. Hence, when subject to the same heavy rainfall, the fissured scar appears to be less stable than the deposit on the terrace. The primary source of risk at K34 is the fissured scars at very high elevations.

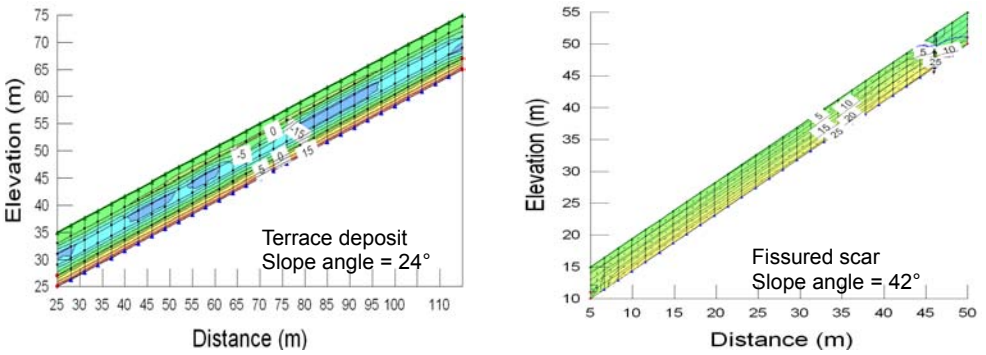

Figure7. Pore-water pressure contours (kPa) in the slopes.

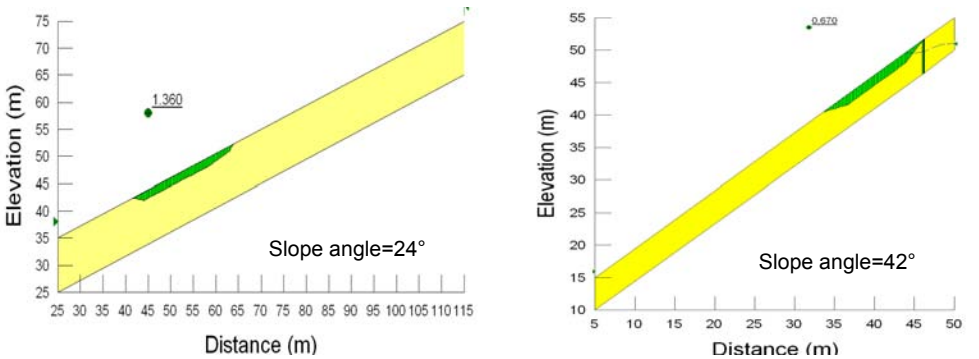

Figure 8. Factors of safety of the terrace deposit and fissured scar.

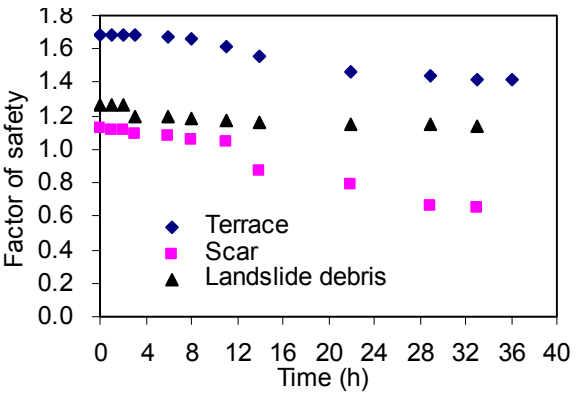

Figure 9. Decrease of factor of safety with rainfall infiltration time.

RELIABILITY ANALYSIS

Reliability of the fissured scar and the deposit on the terrace is analyzed focusing on the uncertainties in the shear strength parameters. All the parameters are assumed to be normally distributed, and the mean and standard deviation of each parameter are shown in Table 2. Parameters ϕ and c are negatively correlated with an assumed coefficient of correlation of $\rho = -0.5$. The Monte Carlo simulation method is used in the reliability analysis (Tobutt, 1982). 10000 sets of soil properties are generated. The probability distributions of the factor of safety are shown in Fig. 10. The

reliability index is obtained to indict the probability of failure. The reliability index is 4.1 for the terrace deposit and -5.1 for the fissured scar. This supports the observation that the fissured scar is deemed to fail upon a heavy rainfall.

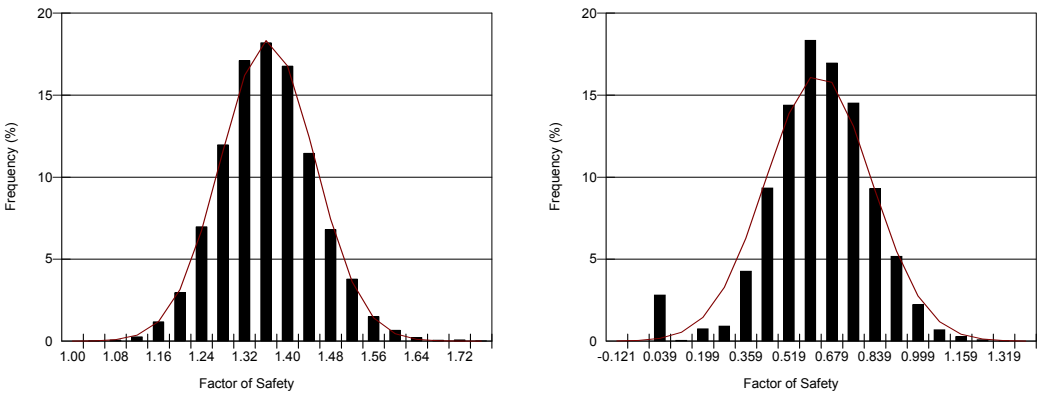

Figure 10. Histograms of the factor of safety using Monte-Carlo simulation.

SUMMARY

A methodology for identifying sources of hazards is presented and demonstrated with a case study at K34 on PR303. This method consists of three steps: identify the all possible hazard sources based on field surveys and aerial photographs; use historic failure events to single out most likely sources of hazards; and finally apply numerical analysis to ascertain the sources of hazards. The results of the detailed case study at K34 show that fissured scars at about 700 m above the road are the main source of repeated rock falls. The proposed method can be used to identify hazards in areas difficult to access. Reliability analysis of the fissured scar further confirms the findings from the field surveys and deterministic analyses.

ACKNOWLEDGEMENTS

The financial support from Sichuan Provincial Department of Transportation and the Research Grants Council of Hong Kong (Grant No. 622210) is acknowledged.

REFERENCES

Fredlund, D. G., Morgenstern, N. R., and Widger, R. A.(1978). “The shear strength of unsaturated soils.” *Can. Geotech. J.*, 15, 313-321.

Geo-slope Ltd. (2001a). *Seep/W for finite element seepage analysis, user's guide*. Geo-slope Ltd, Calgary, Canada.

Geo-slope Ltd. (2001b). *Slope/W for slope stability analysis, user's guide*. Geo-slope Ltd, Calgary, Canada.

Sichuan Provincial Highway Design Institute (2009). *Geological investigation for reconstruction of PR303 between Yingxiu and Wolong.* Chengdu, China.

Tobutt, D. C. (1982). “Monte Carlo Simulation methods for slope stability.” *Computers & Geosciences,* 8 (2), 199-208.

Bounding the Probability of Failure for Levee Systems

Justin C. Hollenback[1] and Robb E. S. Moss[2]

[1]Graduate Researcher, Department of Civil and Environmental Engineering, University of California Berkeley, CA 94720, jhollenback@berkeley.edu
[2]Assistant Professor, Department of Civil and Environmental Engineering, California Polytechnic State University, San Luis Obispo, CA 93407, rmoss@calpoly.edu

ABSTRACT

An exact solution for the probability of failure of large complex infrastructure systems is rarely obtainable; however the probability of failure can often be bounded. An example of this type of system is the levee system in the California Bay Delta. Large levee systems often consist of many components arranged in series and parallel sub-systems. There is the problem of defining component (or reach) length, and therefore the total number of components in the system where component length is dependent on failure mode. Methods of bounding probability of failure based on uni-, bi-, and tri-modal component probability of failure are discussed. The bounds are highly sensitive to the total number of components in the system. Characterization of spatial variability using semi-variograms is used to define component length for various failure modes. Combining the statistically defined component length with system probability of failure bounds allow for a more accurate estimate of failure probability. Demonstration of these methods and results for specific levee systems in the California Bay Delta are shown in this paper.

INTRODUCTION

Society is dependent on a wide variety of complex systems (e.g., water and power distribution). As time progresses the likelihood that a system will be exposed to hazards increases. In general, a system's ability to survive exposures decrease; a system tends to fatigue and degrade with time. Also with time a system can become increasingly complex. When a complex system is due for repair and improvements, constraints on logistics, resources, and funding make it nearly impossible for the entire system to be repaired at once. Thus, repair on specific components need to be prioritized so critical components get repaired first. This situation lends itself to the implementation of risk analysis; risk being the product of failure probability for a component and consequences of that failure, where failure probability is usually annualized and consequences are in terms of cost, lives lost, etc. The benefit of using risk to make critical decisions is in its ability to bring both the likelihood of component failure and the detrimental effects of component failure into one metric.

Our research focuses on levee systems, specifically the California Bay Delta and its use as a water distribution hub. The Bay Delta consists of a network of channels confined by a system of more than 1700 km of levees. These levees protect a collection of 65 islands and tracts, many of which have landside elevations below sea level. This means levees surrounding these islands hold back water year round,

even during dry periods. Roughly 25% of urban water used in the state is diverted through the Bay Delta. Approximately two thirds of the state's population relies on the Bay Delta for some portion of their drinking water and nearly 3 million acres of farmland depend on the Bay Delta for some quantity of irrigation water. The Bay Delta is currently in a fragile state. A major earthquake in the bay area could result in the failure of hundreds of kilometers of levees. This would, among other things, result in saltwater contamination of fresh water in the delta, rendering it useless as a fresh water distribution hub for a period of months, possibly years (URS, 2008).

Calculating the probability of failure for large complex systems, like the Bay Delta levees, is non-trivial and exact solutions are often unattainable for practical purposes. Bounding the probability of failure is a reasonable alternative to exact solutions. Probability of failure, exact solution or bounded, is sensitive to the number of components present in the system. Currently, the number of components in a levee system is not robustly defined. Here we review procedures for bounding the probability of failure for systems and present a method for statistically defining the number of components in a levee system.

BOUNDS ON PROBABILITY OF FAILURE FOR LARGE SYSTEMS

In civil engineering complex systems are generally composed of two types of idealized two-state sub-systems, parallel and series. A two-state system is either in survival state or failure state. Parallel systems, or redundant systems, are in failure state if all components fail. Series systems, or non-redundant systems, are in failure state if one or more components fail. Levees are predominantly series systems; if one section of a levee fails the system has failed. However, the state of any system depends on the definition of failure. Consider the Bay Delta's function of protecting land against flooding; if any section of levee on any island fails the system has failed. For its function as a water distribution hub, saltwater contamination of fresh water that flows through the Bay Delta would constitute failure. There exist scenarios that would require multiple islands to fail in order for saltwater contamination to occur. The behavior of the Bay Delta as a system in such a scenario isn't purely series or parallel, but a combination of both. Here, parallel sub-systems need to be grouped so that the system is a series of parallel sub-systems, or cut sets (Figure 1). By decomposing the system in this way the probability of failure of the cut sets can be estimated and the remaining system can be treated as purely series.

It is a seemingly difficult task to accurately calculate the probability of failure for a single levee reach. Simply defining the length of a single reach is not straightforward. For a complex levee system, even if the assumed number of components and their respective failure probability estimates are accurate, calculating the probability of failure is non-trivial. We will demonstrate that even if the system is entirely parallel or series, quantifying the probability of failure is no small task.

Series Systems. Let us first consider series levee systems (e.g. an island in the Bay Delta). Let event E_i, denote the failure of the i^{th} component. As stated before, failure of a series system is achieved if at least one component fails. The probability of failure of a series system is the union of all component failure probabilities. In set theory notion the probability of failure of a series system of n components is:

$$P(Faiure\,System_{series}) = P(\bigcup_{i=1}^{n} E_i) \qquad 1$$

The exact solution to the probability of the union of *n* events can be obtained using the inclusion exclusion rule, equation 2.

$$P(\bigcup_{i=1}^{n} E_i) = \sum_{i=1}^{n} P(E_i) - \sum_{i<j}^{n} P(E_i E_j) + \sum_{i<j<k}^{n} P(E_i E_j E_k) ... (-1)^n P(E_i E_j ... E_n) \qquad 2$$

The inclusion exclusion rule requires knowledge of all individual event probabilities and knowledge of probabilities of intersections of all possible combinations of events. If failure of each event, E_i, is statistically independent from all other events the probability of all intersections simplify to the product of their individual event probabilities. If failures are mutually exclusive (i.e. events cannot occur simultaneously) all intersection terms dropout. Unfortunately when dealing with levee systems rarely, if ever, are individual component failures statistically independent or mutually exclusive. Mutual exclusiveness of failures is obviously not a realistic assumption. One component failure doesn't rule out the possibility of another. Lack of statistical independence stems from inherent characteristics of levees: materials that levees are built on and with are spatially correlated, as are loads applied to levees (flooding, seismic, etc).

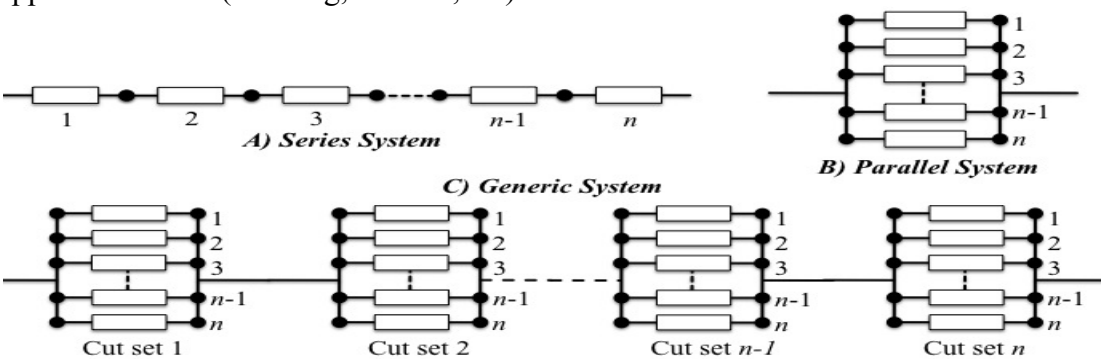

Figure 1: Schematic of different kinds of systems or sub systems.

The exact solution of the union of events lacks practical application. Since no simplifying assumptions apply to levee systems, alternatives are necessary. Bounding the probability of system failure can be a useful tool. Bounds on probability of failure make use of information that is reasonably obtainable, such as uni-, bi-, and tri-component probabilities of failure. Take an arbitrary system of *n* components for example. Uni-component probability of failure is that of any individual component, E_i, bi-component probability of failure is the joint probability of failure of any two components E_iE_j, and similarly tri-component probability of failure is the joint probability of failure of any three components $E_iE_jE_k$. For series systems the narrowest possible uni-component probability bounds are:

$$\max_i P_i \le P(\bigcup_{i=1}^{n} E_i) \le \min(1, \sum_{i=1}^{n} P_i) \qquad 3$$

These bounds were derived by Boole (1854) and proven to be the narrowest possible by Fréchet (1935). For large component probability of failure and large number of components (e.g. $P(E_i) > 0.05$ and $n > 20$) the upper bound will reduce to 1. Having

an upper bound of 1 for probability failure gives no insight to a specific system. For most practical applications these bounds are too wide. Narrower bounds can be achieved by utilizing higher-order component failure probabilities.

$$P_1 + \sum_{i=2}^{n} \max\left(0, P_i - \sum_{j=1}^{i-1} P_{ij}\right) \le P\left(\bigcup_{i=1}^{n} E_i\right) \le P_1 + \sum_{i=2}^{n}\left(P_i - \max_{j<i} P_{ij}\right) \quad 4$$

The bounds in equation 4 incorporate both uni-component and bi-component failure probabilities. These bounds were developed through work done by Kounias (1968), Hunter (1976), and Ditlevsen (1979). They have gained wide use (e.g., Song and Der Kiureghian 2003), unfortunately they are dependent on the ordering of bi-component failures. Often, the order that maximizes the lower bound doesn't necessarily minimize the upper bound. Additionally these bounds have not been proven to be the narrowest possible for the information used. With that said, these bounds do offer narrower bounds than equation 3 (Table 1).

Zhang (1993) took the theoretical bounds in 4 and generalized them for still higher-order component failure probabilities. Below, in equation 5, are bounds that utilize tri-component failure probabilities. Bounds that used quad-component failure probabilities were also developed but are not shown here.

$$P(\bigcup_{i=1}^{n} E_i) \ge P_1 + P_2 - P_{12} + \sum_{i=3}^{n} \max\left(0, P_i - \sum_{j=1}^{i-1} P_{ij} + \max_{k\in(1,2,\ldots,i-1)} \sum_{j=1, j\neq k}^{i-1} P_{ijk}\right)$$

$$P(\bigcup_{i=1}^{n} E_i) \le P_1 + P_2 - P_{12} + \sum_{i=3}^{n} [P_i - \max_{k\in\{2,3,\ldots,i-1\}, j<k} (P_{ik} + P_{ij} - P_{ijk})] \quad 5$$

Like equation 4 the tri-component bounds also depend on ordering of joint component failures. These bounds are still narrower (Table 1) than the bi-component bounds. It should be apparent that achieving narrower bounds increases computational effort significantly.

Parallel Systems. The exact solution for the failure probability of a parallel system is the intersection of the failure of all its components. Let event E_i be the failure of the i^{th} component. Using set theory notation the probability of failure for a parallel system of n components shown in equation 6. If individual events are statistically independent from one another than this simplifies to equation 7.

$$P(Failure\,System_{parallel}) = P(\bigcap_{i=1}^{n} E_i) \quad 6$$

$$P(Failure\ System_{parallel}) = P\prod_{i=1}^{n} P(E_i) \quad 7$$

This results from the fact that the probability of the intersection of statistically independent events is the product of the individual event probabilities (Benjamin and Cornell, 1970). If the events are not statistically independent and the system has a large number of components (e.g., >4) then the probability of their joint occurrence can be difficult and impractical to quantify. As stated earlier, individual component failures in levee systems are rarely statistically independent. In addition, depending on how reach length is defined, the number of components in a levee system can be relatively large. Boole (1854) derived uni-component bounds on the probability of failure of a parallel system:

$$\max(0, \sum_{i=1}^{n} P_i - (n-1)) \le P(\bigcap_{i=1}^{n} E_i) \le \min P_i \qquad 8$$

These are the narrowest bounds possible if the only available information is uni-component failure probabilities (Fréchet, 1935). Examining the left side of this inequality for low uni-component probabilities of failure and large n (e.g., $P(E_i) < 0.05$ and $n > 20$) the lower bound will often be 0. A lower bound of 0 for the failure probability of a system is hardly useful. For most practical applications Boole's uni-component bounds for parallel systems are too wide. There exist no theoretical higher order bounds for parallel systems (Song and Der Kiureghian 2003). However, using De Morgan's Rule (equation 9) higher order bounds can be developed:

$$P(Failure\ System_{parallel}) = 1 - P(\overline{\bigcap_{i=1}^{n} E_i}) = 1 - P(\bigcup_{i=1}^{n} \overline{E_i}) \qquad 9$$

SPATIAL VARIABILITY AND REACH LENGTH IN LEVEE SYSTEMS

It is worth noting here that all of the exact solutions and bounds presented above are sensitive to the number of components present in the system. Intuitively, this is expected. Increasing the number of components in a series systems leads to more opportunities for failure. Additional components in parallel systems increases redundancy, which reduces chances of failure. In any case, defining the number of components in a robust repeatable manner is important to the integrity of a probability of failure analysis. Generally in large levee systems, the number of components, or reaches, is inconsistently defined. Either through subjective examination of soil properties and levee geometries (URS, 2008)or with an arbitrary, predetermined, reach length that is not specific to a project or depositional environment (van Manen and Brinkhuis, 2005). Neither of these methods are ideal when considering sensitivity of failure probability estimates to the number of components. Here, we attempt to statistically define the number of components in a levee system based on geotechnical properties that control the probability of failure (e.g., strength, permeability, etc.). Since properties that control failures depend on the failure mode (e.g., seepage failure controlled by permeability, stability failure controlled by strength), reach length should be defined for each failure mode of concern. This concept will make the task of defining levee sections less arbitrary and subjective, and more robust.

Spatial variability is prevalent in geotechnical properties. For example, normalized tip resistance in a layer of sand will vary with depth, or permeability of a sandy layer will vary laterally. A semi-variogram is a tool used to quantify spatial variability. This study utilizes this tool to estimate lateral spatial variability of properties of interest to define levee reach length, and thus number of components in a levee system. Semi-variograms are used prominently in petroleum and mining exploration and have found favor in geotechnical engineering because of their applicability, and ease of use (e.g., Thompson et al. 2007). Semi-variograms are graphical tools that display how much data varies as a function of separation distance. They are used for continuous types of data such as, shear strength, grain size, permeability, etc. Conceptually, they are based on the idea that data collected at two

relatively close locations is more likely to be similar than data collected at two relatively far away locations.

Semi-variograms plot semi-variance versus separation distance and can generated as experimental semi-variograms (equation 10) or model semi-variograms (equation 11). Experimental semi-variograms are constructed from data pairs, z_i and z_j, sampled at discrete separation distances, h_{ij}. Model semi-variograms are continuous functions that describe spatial structure observed in the experimental semi-variogram for all distances, h. Experimental semi-variograms need to be constructed from data that exhibits first and second order stationarity. First order stationarity implies that the mean of the sample data doesn't vary with location. Second order stationarity implies that semi-variance is only dependent on separation distance and not absolute location. Functions used for model semi-variograms must be positive definite. There are several reasons for this requirement; the one most relevant to this study is that this maintains positive variance between points (necessary for variance cannot be less than zero).

$$\hat{\gamma}(\vec{h}) = \frac{1}{2N(\vec{h})} \sum_{all\, i,j,\vec{h}_{ij} \approx \vec{h}} [z_i - z_j]^2 \qquad 10$$

$$\gamma(\vec{h}) = \frac{1}{2} E\{[Z(\vec{x}) - Z(\vec{x} + \vec{h})]\} \qquad 11$$

Figure 2 shows an example of a model semi-variogram. Inspection of the model semi-variogram reveals some general characteristics. At small separation distances the semi-variance is small and increases as separation distance increases. At zero separation distance there is a small offset in the semi-variance. This is known as the nugget effect and is generally attributed to measurement error. There are two categories of model semi-variograms: transitional models, and non-transitional models. In a transitional model, as h increases, semi-variance either, asymptotically approaches a plateau, known as the sill, or reaches a plateau and remains constant. In theory, the sill of a transitional model equals the sample variance of the data set (Clark, 2001). The separation distance at which the sill is reached is referred to as the range. For transitional models that are asymptotic (e.g., the exponential model) the range is defined as the separation distance at which 95% of the sill is achieved. The model in figure 2 is an example of an asymptotic transitional model. In non-transitional models semi-variance continues to increase with separation distance and does not plateau. Generally speaking, non-transitional models imply that the data used are not stationary on some level.

The range of the model semi-variogram is used to define the reach length of a levee. Range defines the distance at which maximum statistical independence of data is achieved (i.e., distance where correlation is minimized). Data that is separated by distances larger than the range no longer have any *spatial* correlation. This is not to say that data is not correlated. Rather, correlation is no longer influenced by separation distance. However, for data that is spaced at distances less than the range, correlation is dependent on separation distance. In this case, estimates of how data are related are refined with information provided by the model semi-variogram.

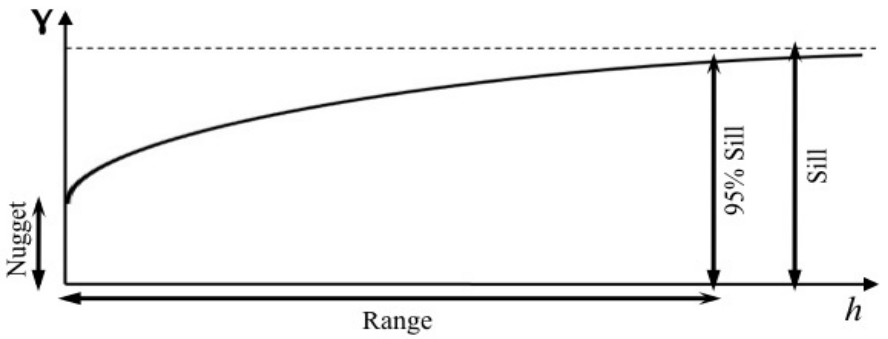

Figure 2: Conceptual diagram of a model semi-variogram. This is a generic, asymptotic transitional model with the sill, range, and nugget labeled.

Example. Consider a single 20 km long levee. If liquefaction of a sandy layer in the levee foundation is of concern a model semi-variogram could be constructed of tip resistance data in the critical layer. Assume the model reveals a reach length of 800 m (i.e., 25 components). For the simplicity of the example the following assumptions are made: if liquefaction is triggered in a component it will fail, CSR is a deterministic value and a constant of 0.15, CRR for all components follows a joint lognormal distribution with identical marginal distributions with mean = 0.25 and c.o.v. = 0.25, CRR for components follow a Dennet-Sobel (1995) class correlation matrix. The various bounds on the probability of failure of our example system were calculated using these assumptions and a Dunnet-Sobel (1955) one-dimensional integral to calculate the bi- and tri-component probabilities of failure (P_{ij} and P_{ijk}). Results are presented in Table 1. The calculations were repeated for two additional cases in which a model semi-variogram reveals reach lengths of 2000 m and 400 m. This demonstrates sensitivity of bounds to number of components.

Table 1: Sensitivity of number of components and order of probability bounds.

Components	N=10		N=25		N=50	
Bound	**Lower**	**Upper**	**Lower**	**Upper**	**Lower**	**Upper**
Uni	0.0255	0.2550	0.0255	0.6374	0.0255	1
Bi	0.0570	0.2112	0.0570	0.5207	0.0570	1
Tri	0.0913	0.1861	0.0913	0.4486	0.0913	0.886

CLOSING REMARKS

A conceptual framework of system reliability for levee systems has been discussed. Though bounding the probability of failure is more accessible than an exact solution, in most cases formulas to calculate bounds are still computationally nontrivial and require higher-order failure probabilities (Song and Der Kiureghian, 2003). Higher mode component failure probabilities need to be defined in a manner consistent with the spatial variability. Conceptually, this is straightforward for bi-component failure probabilities, however, that is not the case for higher-order probabilities. In addition most failure modes depend on more than one variable while semi-variograms are determined from only one variable. Experimental semi-variograms can be constructed from data of the property thought to be most critical. Alternatively, experimental semi-variograms can be constructed for all properties effecting failure and the property with the shortest range could control reach length.

ACKNOWLEDGEMENTS

This material is based on work supported by the U.S. Department of Homeland Security under Grant Award Number 2008-ST-061-ND0001. Administration of this grant is conducted through the Department of Homeland Security Center of Excellence for Natural Disasters, Coastal Infrastructure and Emergency Management (DIEM). The views and conclusions contained in this document are those of the authors and should not be interpreted as necessarily representing the official policies, either expressed or implied, of the U.S. Department of Homeland Security.

REFERENCES

Benjamin, J.R., and Cornell, C.A., (1970). Probability, Statistics, and Decision for Civil Engineers. McGraw-Hill

Boole, G. (1854). Laws of thought, American Reprint of 1854 ed., Dover, New York.

Clark I. (2001). Practical Geostatistics. Geostokos Limited.

Ditlevsen, O. (1979). ‘‘Narrow reliability bounds for structural systems.’’ Journal of Structural Mechanics, 7(4), 453–472.

Dunnett, C. W., and Sobel, M. (1955). “Approximations to the probability integral and certain percentage points of a multivariate analogue of Student’s t-distribution.” Biometrika, 42, 258–260.

Fréchet, M. (1935) ‘‘Généralizations du théorème des probabilitéstotales.’’ Fundamental Mathematics, 25, 379–387.

Hunter, D. (1976). ‘‘An upper bound for the probability of a union.’’ Journal of Applied Probability, 13, 597–603.

Issaks, E. H., and Srivastava, R. M. (1989). An Introduction to Applied Geostatistics. Oxford University Press.

Kounias, E. G. (1968). ‘‘Bounds for the probability of a union, with applications.’’ Annuls of Mathematical Statistics, 39(6), 2154–2158.

Moss, R.E.S., Hollenback, J.C., and Ng, J. (2010). “Spatial Variability of Levees as Measured Using the CPT.” Proc. CPT’10, Huntington Beach, CA, May.

Song, J., and DerKiureghian, A. (2003). “Bounds on System Reliability by Linear Programming.” Journal of Engineering Mechanics, 129.6: 627-636.

Thompson, E. M., Baise, L. G., and Kayen, R. E. (2007). "Spatial correlation of shear-wave velocity in the San Francisco Bay Area sediments." Soil Dynamics and Earthquake Engineering, 27, 144-152.

URS. (2008). Delta Risk Management Strategy (DRMS) Phase 1, Risk Analysis Report. Prepared by URS Corporation/Jack R. Benjamin and Associates, Inc., for California Department of Water Resources, December

vanManen, S. E., and Brinkhuis, M. (2005). “Quantitative flood risk assessment for Polders.” Reliability Engineering & System Safety. 90: 229-237.

Zhang, Y. C. (1993). ‘‘High-order reliability bounds for series systems and application to structural systems.’’ Computers & Structures, 46(2), 381– 386.

Breaching of Changkai Levee in June 2010 in Jiangxi Province, China

M. Peng[1] and L. M. Zhang[2]

[1]Research Assistant, Dept. of Civil and Environmental Engineering, The Hong Kong University of Science and Technology, HKSAR, China; email: pengming@ust.hk
[2]Professor, Dept. of Civil and Environmental Engineering, The Hong Kong University of Science and Technology, HKSAR, China; email: cezhangl@ust.hk

ABSTRACT

A heavy storm caused catastrophic floods in the summer of 2010 throughout southern China. Fu River, the second largest river in Jiangxi Province, with a length of 312 km and a drainage area of 15,800 km^2, experienced a 50-year return flood. A 347 m long segment of levee, Changkai Levee, breached on the evening of 21 June 2010 and 65,000 out of 100,000 residents in four towns were besieged by the breaching inflow. The breach was later blocked in 58 hours. This paper first introduces the process of the levee breach and studies the associated failure mechanisms. The main reasons for the failure are the low design standard (i.e. the design criterion is 20-year return flood while the actual flood reached the 50-year return level), erodible sandy soil conditions in the levee, and the scour of levee by the rapid water flow nearly vertical to the levee. Subsequently the procedures of rescuing the residents and blocking the breach are described. Finally why so many residents were besieged but no casualty was caused is explained.

INTRODUCTION

The precipitation in southern China was extremely large in May and June 2010, causing hundreds of fatalities and billions of economic losses. Jiangxi Province in southeast China faced the most serious flood season in 60 years. The precipitation during 1 April and 31 June 2010 was 1043 mm, exceeding 14% of that in another catastrophic flood season in 1998 (911 mm) (He, 2010). The precipitation map in the period of June 18 to 21 is shown in Figure 1a (National meteorological center of CMA, 2010).

Fu River, the second largest river in Jiangxi Province, with a length of 312 km and a drainage area of 15,800 km^2, experienced a 50-year return flood in June 2010. Changkai Levee in Fuzhou City (Figure 1a) protects 67.1 thousand hectares of farmland and 144.3 thousand people (Xu and Li, 2010). The levee, built gradually

from 1936, had breached at least four times since its first completion: in 1949 (with 39 breaches 8399 m in total length), 1952, 1973, and 1982 (with breaches 237 m in length). It was overtopped again on 23 June 1998, but the breach was under control with great pain (Han, 2010). The poor levee was subject to a more severe situation in the summer of 2010. The river water level in Linchuan, the center of Fuzhou City, reached 42.61 m at 4:00 am on 21 June, exceeding the warning level by 1.31 m. The corresponding flow rate was 8050 m^3/s, exceeding 25% of the largest discharge (6460 m^3 in 1998) ever recorded since 1952 (SFDH, 2010).

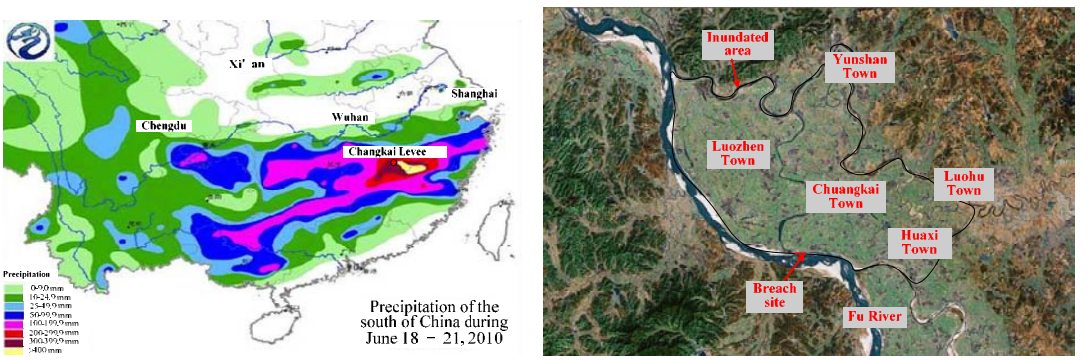

a) b)

Figure 1. Breach location and inundated area: a) breach location in precipitation map (National meteorological center of CMA, 2010); b) inundated area (based on Google Map and Bian, 2010).

This paper introduces the process and mechanisms of the levee breaching and the procedures of rescuing the residents and blocking the breach. The causes of breaching and the reasons that so many residents were besieged but no casualty was caused are also explained.

BREACHING

The segment of Changkai Levee in Hejia Village has a height of around 5.5 m, a crest width of around 10 m (Yahoo China, 2010). The levee was built with sandy silt that was of very high erodibility according to the classification of Briaud (2008). The foundation of the levee, consisting of gravel with sandy silt (Figure 2), has a bimodal (gap-graded) grain-size distribution. Piping could occur if subjected to a high hydraulic gradient (Skempton and Brogan, 1994). Piping was here defined as the progressive removal of soil particles from a mass by percolating water, leading to the development of channels (ASTM, 2002). Some signs of piping were found as early as 19 June 2010. At 2:00 am 20 June, a pipe about 0.2 m in diameter was found by an inspector, which was blocked with contingency materials by 30 people in two hours (China News, 2010).

The water level was only 0.5 m to the levee crest in the evening of 20 June. Due to the high hydraulic gradient (around 0.2 m/m) and the poorly graded foundation materials, several pipes formed at the bottom of the levee almost at the same time. The pipes developed rapidly and connected together. Soon, soils on top of these pipes collapsed and were washed away by the surge. The collapse turned the

piping failure event into an overtopping event (Xu and Zhang, 2009). The process followed closely the four phases presented by Wan and Fell (2004): initiation and then continuation of erosion, progression to form a pipe, and formation of a breach. The highly erodible sandy silt made the breach develop rapidly. Only within several minutes, the combined pipe became a large breach as wide as 12 m at 18:30 on 21 June (China News, 2010). The breach became 20 m wide at 18:45 (China News, 2010), and around 100 m wide at 23:40. The breach ceased to develop by 7:30 am on June 22, with the final width being 347 m (Yu and Lin, 2010). The billowy water from the Fu River finally inundated four towns in an area of 100 km^2 (Bian, 2010), as shown in Figure 1b.

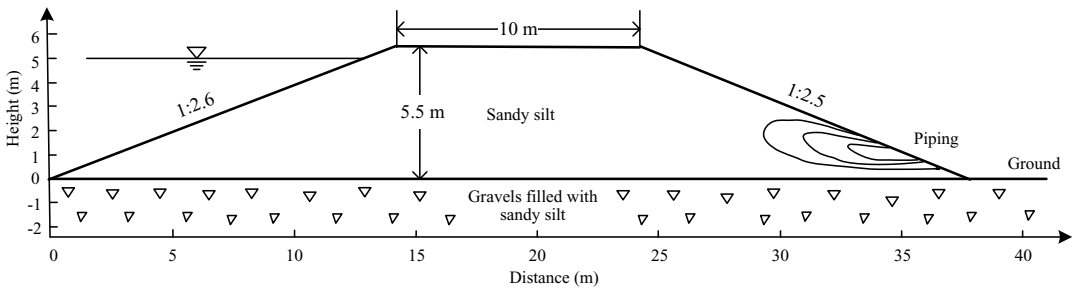

Figure 2. Cross section of Changkai Levee.

The main causes of the levee failure are the extremely heavy storm, the low design flood standard, the poor sandy soil conditions in the levee, and the scour of levee by the rapid water flow nearly vertical to the levee:

1. The precipitation was extremely large, which caused the water level in Fu River to exceed the warning level by 1.31 m. The flood was at a 50-year return level. The design of the levee, however, was just for 20-year return events.
2. The foundation of the levee, consisting of gravel with sandy silt, has a bimodal (gap-graded) grain-size distribution; piping could develop easily if subjected to a high hydraulic gradient (Skempton and Brogan, 1994). The levee, built with sandy silt, is of very high erodibility (Briaud, 2008), which allowed a rapid development of the breach.
3. As shown in Figure 1b, the Fu River makes a turn at the breaching site. The scour of levee by the rapid water flow nearly vertical to the levee was serious. The water level on the breaching side was higher than that on the opposite side.

PEOPLE AT RISK

Both the local government and the villagers did correctly evaluate the breaching risk beforehand. Several rumors, indicating that the levee already broke upstream of the river, were disseminated among the villagers one day before the failure. Very soon, the villagers received clarification that the levee was “safe.” Even though, 35 thousand villagers evacuated spontaneously before the levee broke. The remaining people watched the levee situations closely; some of them moved their properties to

the second floor or higher in their houses.

The order of evacuation was not issued until it was clear that the beaching process could not be under control. The local government then warned the people by shouting, hitting gongs, sending text messages via mobile phones, using loudspeakers on police vehicles and so on. However, it was slightly too late: 65 thousand out of the 100 thousand residents in the inundated area were besieged in the dreadful evening. Most of them took shelters on the second storey or higher in their own houses, surrounded by floodwater with an average depth of 1-2 m. The reasons that so many people were besieged are as follows:

1. The sudden break of the levee allowed little time for warning and evacuation.
2. No early warning and evacuation orders were issued long before the break, though the floodwater level exceeded the warning level by 1.3 m.
3. Some residents believed the levee was sufficiently safe as it was fortified annually. Meanwhile, a large team kept inspecting the levee and, if necessary, took repair actions.
4. Some residents stayed to take care of their properties. They believed they could take shelter on the second or upper floors in their buildings in case of levee failure.

RESCUE

Thanks to the experience of fighting against floods in the previous years and the influence of rumors, 35 thousand people evacuated from the threatened area spontaneously. The rest took refuge on the second or higher floors in their buildings. Just 0.5 hour after the breach of the levee on 21 June, the Fuzhou City government was mobilized to prepare the rescue: building temporary roads on the levee, transporting boats to the levee, arranging shelters for the refugees and so on. At around 20:00 on the day of breach, the government of Jiangxi Province dispatched 2000 firefighters, police officers and soldiers equipped with rescue facilities to the levee-breaching site. In the early morning of 22 June, the central government dispatched 1000 more soldiers to the site. By 8:00 am on 22 June, more than 10 thousand people, including firefighters, police officers, soldiers, and volunteers from the villagers, took part in the rescue with more than 430 boats. Approximately 33 thousand of victims had been evacuated or rescued by that time (Liu et al., 2010).

The rescue in the morning was very efficient; 20 thousand more victims were rescued from 8:00 to 11:00 am on 22 June (Liu et al., 2010). After that, the rescue slowed down, as the remaining victims, unlike the people who lived in the town centre, were distributed sparsely in an area of 100 km^2. Besides, as the water depth became shallower near the boundaries of the flooded area, the boats were more likely to be trapped and the propeller was likely to be stuck by trees or debris. By 14:00, another 3 thousand people were rescued. The rescued population increased to 93 thousand at 17:00 on 22 June, and 95 thousand at 7:00 am on 23 June (Chen, and Guo, 2010). All the 100 thousand people were evacuated or rescued by 19:00 on 23 June, two days after the breaching of the Changkai Levee, without any fatality. The number of rescuing people reached 15 thousand at the peak time, with more than

1300 boats mobilized. Premier Wen Jiabao spoke highly of the rescue when he visited the levee-breaching site on 24 June (Xu and Li, 2010).

Table 1 compares predicted fatality numbers using three existing models and the actual fatality. These are empirical models for estimating dam-break caused loss of life with parameters of population at risk, warning time and so on. The results could be references although in difference kind of floods (levee and dam break). Out of the predicted results, the minimum number of fatality is as large as 39. However, there was no death actually. The reasons for the deviation are:

1. The villagers had experienced several flood threats from levee breaks, and they kept alert in the flood season every year.
2. Rumors of levee failures made the residents better prepared and watch the levee situation more closely before the breach. In addition, they were warned by the government shortly before the arrival of the flood.
3. Nearly all the houses in the flood area were two- or multi-storey buildings. Most of the besieged people took refuge on the second or higher floors inside their buildings.
4. The rescue was timely and efficient, and the shelter facilities for the victims were prepared. Particularly the health and medical conditions were acceptable. The rescue work strengthened the confidence of the besieged people and minimized risky behavior to escape.
5. The breach occurred in the early evening in the summer, when the flood was still visible and most of the people were at home for dinner. These made the sheltering in their homes very efficient.

Table 1. Comparison of estimated and actual fatalities.

Population at risk	Warning time	Estimated fatalities using existing models			Actual death
		Brown and Graham, 1988	DeKay and McClelland, 1993	Graham, 1999	
100,000	≤ 15 min	50,000	39	70	0
		Warning time less than 15 minutes	Warning time = 15 minutes, low flood force	No warning and low flood severity	

BLOCKAGE OF THE BREACH

The flood inundated an area as large as 100 km^2, submerging all the pathways to the breach site except the Fuyin Highway. The 2458 km long Fuyin Highway connects the capital cities of Fujian Province and Ningxia Autonomous Region. The highway was still in operation after the breach of Changkai Levee, which became the only safe “island” for sheltering and traffic. A blocking plan was worked out to ship blocking materials from the opposite side of the Fu River through Fuyin Highway, which is not inundated. As shown in Figure 3(a), a temporary road was constructed from the highway to the levee, which ensures the transportation of soil and rock for blocking the 347 m wide breach. The blockage was primarily planned to be conducted from the downstream and to be completed in 6 days (Xu and Li, 2010). The plan was accelerated by blocking from both directions after a road from the

upstream was constructed [shown in Figure 3(b)].

(a) **(b)**

Figure 3. Blocking the Changkai Levee breach: (a) blocking plan (based on Google Map); (b) blocking construction (taken by Zhang Wu in Xinhua News).

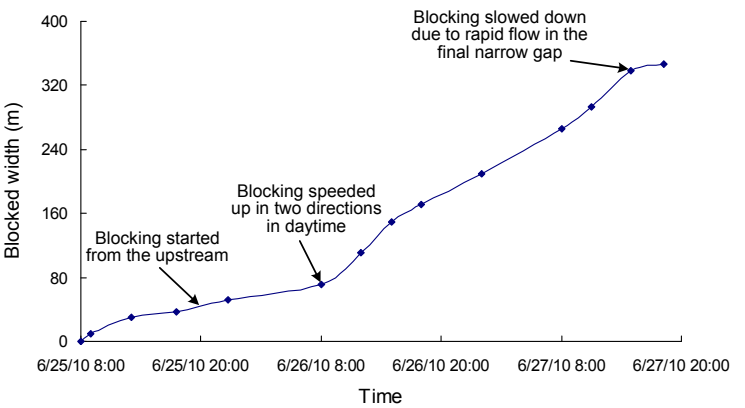

Figure 4. The timeline of blocking the breach.

The blockage started at 8:00 on 25 June after the completion of constructing a road on the 10 m wide levee. It did not go smoothly in the early stage, as shown in Figure 4. The main reasons were that the temporary road on the crest of the levee was too muddy for the traffic and the water flow through the breach was rapid. Considering that the efficiency could be even lower at night due to the lack of lighting, the 6-day plan might not be achievable. To accelerate the blocking process, several actions were taken: improving the temporary road by placing a layer of gravel and rocks; decreasing the outflow rate from a reservoir upstream; and initiating another working platform from the upstream of the levee as shown in Figure 3(b). The blocking from the upstream started at around 20:00 on 25 June. The effect was not obvious until the next morning. The blocked width was as large as 101.1 m from 8:00 to 18:00 on 26 June, almost three times what had been completed in the first 10 hours (shown in Figure 4). The work slowed down after 15:00 on 27 June when the breach was narrowed down to several meters. This last breach took more than three hours to close with the help of steel cages filled with rocks. The entire blocking work was finished at 18:17 on 27 June, less than 2.5 days since the start and around 6 days after the levee failure (Lou et al., 2010).

SUMMARY

An extremely heavy storm caused a 50-year return flood in the second largest river in Jiangxi Province, Fu River. Changkai Levee, which protects 67.1 thousand hectare of farmland and 144.3 thousand people, broke at 18:30 on 21 June 2010. Sixty five thousand residents were besieged by the billowy water from the 347 m wide breach. After a two-day rescue, all the besieged people were rescued at 19:00 on 23 June, without any casualty. The levee breach was blocked in 58 hours, more than 3 days ahead of schedule.

This paper introduces the process of the levee break and studies the mechanisms of the levee failure. The main reasons for the levee break are the extreme flood, the low design flood standard, the highly erodible sandy soil conditions in the levee, and the scour of the levee by the flow nearly vertical to the levee. Many people were besieged in the flood due to insufficient warning and evacuation. The firefighters, police officers, and solders conducted rescue immediately and blocked the breach at high efficiency. The timely rescue activities and the provision of proper shelters were the main reasons for the zero-casualty outcome.

ACKNOWLEDGEMENTS

The authors would like to acknowledge the support from the Research Grants Council of the Hong Kong SAR (Grant No. 622207), Ministry of Science and Technology of China (2009BAK56B05), and the National Science Foundation of China (Grant No. 50828901).

REFERENCES

ASTM. (2002). “Standard terminology relating to soil, rock, and contained fluids.” *ASTM D 653-02a*, ASTM, West Conshohocken, Pa.

Bian, Y. (2010). “The revelation of forest fire monitor – insight from weather satellites.” *China Weather*, http://www.weather.com.cn/index/zjzx/07/652664_5.shtml>(Jul. 3, 2010) (in Chinese).

Briaud, J. L. (2008). “Case histories in soil and rock erosion: Woodrow Wilson Bridge, Brazos River meander, normandy cliffs, and New Orleans levees.” *Journal of Geotechnical and Geoenvironmental Engineering*, 134(10), 1425-1447.

Brown, C. A., Graham W. J. (1988). “Assessing the threat to life from dam failure.” *Water Resources Bulletin*, 24(6), 1303-1309.

Chen J. H., and Guo, M. Y. (2010). “The 3rd day after Changkai Levee broke in Jiangxi: 95 thousand people had been evacuated safely.” *Xinhua News*, Reproduced by www.gov.cn, http://www.gov.cn/jrzg/2010-06/23/content_1634922.htm>(Jun. 23, 2010) (in Chinese).

China News. (2010). “The villagers behind Changkai Levee in Jiangxi received messages for clarifying levee-break ‘rumors’ one day before the breach.”

http://www.chinanews.com.cn/gn/2010/07-01/2374797.shtml>(Jul. 1, 2010) (in Chinese).

DeKay, M. L., McClelland, G. H.(1993). "Predicting loss of life in cases of dam failure and flash flood." *Risk Analysis*, 13(2), 193-205.

Google Map, *Fuzhou.* http://ditu.google.cn/.

Graham, W. J. (1999). *A procedure for estimating loss of life caused by dam failure.* U.S. Bureau of Reclamation, Dam Safety Office, Report no. DSO-99-06. 44 p.

Han, Y. (2010). "Break of Changkai Levee, a foreseeable disaster." *Economy & Nation Weekly.* Reproduced by Sohu.com. http://business.sohu.com/20100706/n273320981.shtml>(Jul. 6, 2010) (in Chinese).

He, N. B. (2010). "The average precipitation in the flood season in 2010 exceeds that in 1998." *Xinhua News*, reproduced by China Daily, http://www.chinadaily.com.cn/micro-reading/china/2010-07-30/content_635352.html>(Jul. 30, 2010) (in Chinese).

Liu, J., Hu, J. W., Guo, M. Y., and Lin Y. X. (2010). "When the levee broke - records of the rescue against the flood caused by Changkai Levee break in Fuzhou, Jiangxi Province." *Xinhua News*, http://www.gov.cn/jrzg/2010-06/22/content_1633976.htm>(Jun. 22, 2010) (in Chinese).

Luo, Z., W., Xu, Y. H., and Liu, Y. (2010). "Armed Police Hydropower Troop completed the Changkai Levee blocking three days ahead of schedule." *People's Armed Police*, reproduced by Xinhua News, http://news.xinhuanet.com/mil/2010-06/28/content_13761835.htm>(Jun. 28, 2010) (in Chinese).

National meteorological center of CMA (2010). The precipitation of the south of China, reproduced by China.com.cn, http://www.china.com.cn/news/2010-06/22/content_20317004.htm>(Jun. 22, 2010) (in Chinese).

SFDH (Office of State Flood Control and Drought Relief Headquarters) (2010). "Flood situations in major Chinese rivers in June 2010." http://sfdh.chinawater.com.cn/xhqxx/20100803/201008030025.htm>(Jul.1, 2010) (in Chinese).

Skempton, A. W., and Brogan, J. M. (1994). "Experiments on piping in sandy gravels." *Geotechnique*, 44(3), 449-460.

Wan, C. F., and Fell, R. (2004). "Investigation of rate of erosion of soils in embankment dams." *Journal of Geotechnical and Geoenvironmental Engineering*, 130(4), 373–380.

Xu, J. P., and Li, B. (2010). "On-the-spot record of the journey of Jiabao Wen to Fuzhou for visiting the victims and guiding the flood fighting work." *People's Daily*, http://politics.people.com.cn/GB/1024/11965550.html>(Jun. 25, 2010) (in Chinese).

Xu, Y., and Zhang, L. M. (2009). "Breaching parameters for earth and rockfill dams." *Journal of Geotechnical and Geoenvironmental Engineering*, 135(12), 1957-1970.

Yahoo China. (2010). "Changkai Levee break – three myths." *Focal Point*, Phase 97, http://news.cn.yahoo.com/jdgz/changkaidi.html>(Jun. 28, 2010) (in Chinese).

Yu, X. Z., and Lin Y. X. (2010). "The blocking of Changkai Levee breach completed ahead of schedule." *Xinhua News*, http://news.xinhuanet.com/society/2010-06/27/c_12269312.htm>(Jun. 27, 2010) (in Chinese).

Distinct Element Modelling for High Rock Slopes in Static and Dynamic Conditions: A Case Study

Ganesh W. Rathod[1], A. K. Shrivastava[2] and K. S. Rao[1]
[1]Department of Civil Engineering, Indian Institute of Technology Delhi, Hauz Khas, New Delhi, PIN-110016, India
[2]Department of Civil Engineering, Delhi Technological University, Delhi, PIN- 110042, India

ABSTRACT: The Static and dynamic rock slope stability analyses of the left and right abutments of the proposed Chenab (J & K, India) railway bridge were performed using the distinct element code UDEC for a 359 m high rock slope. The analyses have been carried out in three stages for predicting the behaviour of the rock slope. First, an initial static loading is applied in the numerical model. Second, weathering and interlocking conditions are modelled. Third, a dynamic loading is applied to simulate dynamic earthquake conditions. Various monitoring points were installed in the model for critical observations. The displacements and velocity values observed confirms the stability of the rock slope. The study provides an illustration of how the geo-mechanical properties of a rock mass can be integrated in a discontinuum rock slope model. This model has helped to better understand the dynamics of the rockslide when subjected to static and dynamic loads.

INTRODUCTION

Stability of jointed rock mass slope depends on geometry of slope, rock mass characteristics and shear strength behaviour of the joints (Souley and Homand, 1996). Since a rock mass is not a continuum, its behaviour is dominated by discontinuities such as joints, bedding planes and faults. In general, the presence or absence of discontinuities has a profound influence on the stability of rock slopes; the behaviour of these features plays a critical part in a stability evaluation (Shen and Barton 1997, Hoek et al. 2000). Detailed information on various numerical modelling techniques for rock slopes is available in Hudson and Feng (2007). The analyses described in this paper were conducted using the two-dimensional UDEC code first introduced by Cundall (1971). Bhasin and Kaynia (2004) and Kveldsvik et al. (2009) simulated the static and dynamic loading conditions in UDEC for high rock slopes of height 800m. Stability analysis of natural slopes of left and right abutments under different pier, arch and seismic loads using UDEC is carried out along the central section (alignment) for both left and right abutments. This paper presents the results of the investigations on the stability of both slope profiles of left and right abutments of the proposed Chenab Bridge using universal distinct element methods in different loading conditions.

THE PROJECT

The proposed railway line between Katra and Qazigund of Northern Railways crosses the River Chenab, which is a tributary to the Chenab River near Reasi. A railway bridge is proposed to construct between Chainage 50.4 and Chainage 51.715 Km. The Chenab bridge alignment is N120^{o}E towards the left abutment to N300^{o} towards the right abutment and the Chenab River flows

in SW direction. The Chenab bridge, once it is constructed, it would be the Highest Bridge in the World at height of 359 m from the river bed level and the abutments of the proposed bridge are shown in Fig. 1(a). The 1,263m long bridge consists of 950 m span steel arch over the river, in tandem with a 313m long viaduct upto Salal road 'B' station. This bridge consists of total 18 piers resting on ground. Among them 4 piers designated as P_{10}, P_{20}, P_{30}, P_{40} are on left abutment and the other 14 piers from P_{50} to P_{180} are resting on right abutment and sloping at 50-60^o.The loads exerted by these piers would affect the stability of the slopes. Apart from this, as the site falls under seismic zone V as per seismic zonation map of India (BIS: 1893, Part 1: 2002), the seismic loads are also to be considered in the analysis.

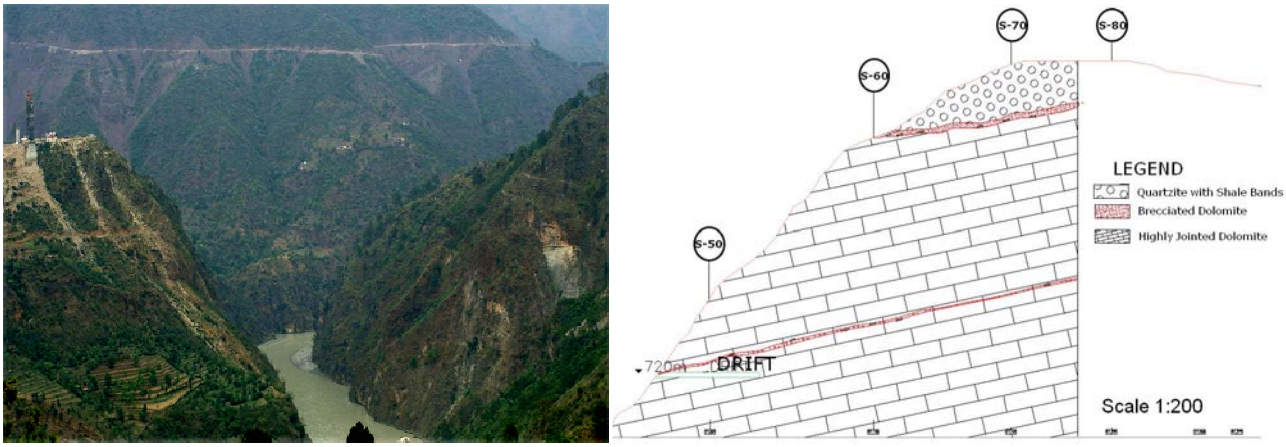

(a) **(b)**

Figure 1. (a) Abutments of Proposed Chenab Bridge (b) Geological Cross Section

FIELD OBSERVATIONS

The authors visited the different locations of construction site and gathered several geological and structural field observations. The sites where several direct shear and plate load tests were conducted in the drifts were also visited and specific observations were made on the failed rock mass. A special visit was also made to the riverbed in order to observe the geological nature of strata between toe and below the proposed arch foundation on both the abutments. Figure 1(b) shows the geological cross section along bridge axis for right abutment. Figure 2 illustrate the strata on left and right abutments.

GEOLOGICAL AND STRUCTURAL FEATURES

The railway alignment passes through the Shiwaliks and Pre-Tertiary rocks overlain by unconsolidated sediments of recent to sub-recent periods. The primary lithological units are dolomitic limestone with different degree of fracturing and occasssional weathering. Cherty, bouldery, brecciated and massive dolomite or dolomitic limestones of Sirban formations are mostly present in the area. The top layers are moderate to highly weathered but invariably the dolomite is fractured resulting into blocky mass. Mapping with reference to the alignment on the left and right abutments yielded that the strata are characterized by prominent sub-horizontal foliation joint and

(a) **(b)**

Figure 2. Strata on Abutment of Chenab (a) Left Abutment (b) Right Abutment

two sub-vertical joints which are very pronounced sets. Few random joint sets are also present occasionally. The attitude of the formations of the left and the right abutments are shown in Table 1.

Table 1. Characteristics of Major Discontinuities Set on the Left and Right Abutments

	Left Abutment			Right Abutment		
Feature	**Strike**	**Dip Amount**	**Dip Direction**	**Strike**	**Dip Amount**	**Dip Direction**
Rail Line Alignment	$N120^0$-$N300^0$			$N120^0$-$N300^0$		
Foliation Joint	$N140^0$-$N320^0$	21^0	$N050^0$	$N145^0$ -$N325^0$	28^0	$N050^0$
Joint Set ($J_{1)}$	$N150^0$-$N330^0$	65^0	$N240^0$	$N150^0$-$N330^0$	65^0	$N240^0$
Joint Set (J_2)	$N075^0$-$N255^0$	80^0	$N165^0$	$N075^0$-$N255^0$	80^0	$N165^0$

Foliation planes and other joint sets are very clear in the drifts made in the left and right abutments at expected arch foundation levels. Presence of minor shear zones was noticed and the fracturing was more in the right abutment. The overburden is very less at the right abutment than the left. General dip of the minor shear fractures is towards slope direction. Brownish staining is noticed at some locations on the joint surfaces. The drifts that were excavated through drill and blast are stable without any support.

GEOTECHNICAL CHARACTERIZATION

The stratigraphy of rock and discontinuity pattern on either side of abutment is more or less similar. Open pits at the proposed pier locations and the drifts on either abutment have also provided vital information about the rock mass condition. Several plate load tests and insitu direct shear tests and laboratory studies were also conducted by different agencies for ascertaining the rock mass, intact rock and joint properties. The available results were pooled together and a major exercise was conducted to obtain a more realistic and representative engineering behaviour for intact, rockmass and rock joints. Though, there is no unique value for a property and vary from location to location, the most appropriate values from the reported information and literature are chosen for the analysis. The geotechnical characteristics adopted for the left and the right abutments in this study are presented in Table 2.

Table 1. Representative Geotechnical Characteristics of Chenab Intact Dolomite

Sr. No.	Property	Value
1	Water Absorption, %	0.46
2	Density, g/cc	2.762
3	Sp. Gravity	2.81
4	Porosity, %	1.30
5	Sonic Wave Velocity Dry, km/sec Sat., km/sec	 4.60 4.68
6	UCS (Dry), MPa	160.50
7	UCS (Sat.) MPa	115.25
8	σ_t, MPa	16.86
9	Point Load Index, MPa	14.12
10	E_t (50), MPa	4.41×10^4
11	ν	0.22
12	c, MPa	22.50
13	ϕ, Degree	58^0
14	Deere Miller Classification (Deere and Miller, 1966)	CM/BM*
15	V_p, m/sec	6350
16	V_s, m/sec	3580
17	Hoek-Brown Constant 'm'	40

* M- Average Modulus Ratio, B- Strong Strength Class, C- Medium Strength Class

SEISMICITY OF THE AREA

Seismic activity in the region around the Chenab bridge site is mainly associated with Main Boundary Thurst and Main Central Thrust. Historical recordings reveal that the area is seismically very active and the site lies in seismic zone V as per the seismic zoning map of India (BIS: 1893, Part 1: 2002). Site specific design earthquake parameters for the Chenab bridge site were estimated by Basu (2004) based on regional and local geology, earthquake occurrences in the region around the site, and the seismotectonic setup of the area. The maximum ground acceleration considered for dynamic analysis is 0.31g (MCE) and 0.16g (DBE).

STABILITY ANALYSIS

For all but very weak rock materials, the analysis of rock slope stability is fundamentally a two-part process. The first step is to analyse the structure of the site to determine if the orientation of the discontinuities could result in instability of the slope under investigation. If so, the second step requires either a limit-equilibrium stability analysis or numerical modelling. Since the height of slope is high and the site falls under very active seismic belt, it was decided to analyse the slope numerically to investigate the stability of slope which comprises of rock mass that could potentially slide under static and dynamic forces.

NUMERICAL MODELLING

The distinct element method (UDEC) simulates the progressive failure of slopes using an iterative calculation procedure (Bhasin and Kaynia, 2004). The discontinuities in the numerical model are considered as planar features oriented normal to the plane of analysis. Mohr-Coulomb model was adopted the present study. Figures 3 and 4 show the jointed slope models for left and right abutments respectively. The explicit solution algorithm in UDEC permits either dynamic or static analysis (Itasca Manual, 2004). For dynamic calculations, user-specified velocity or stress waves can be input directly to the model either as an exterior boundary condition or interior excitation to the model.

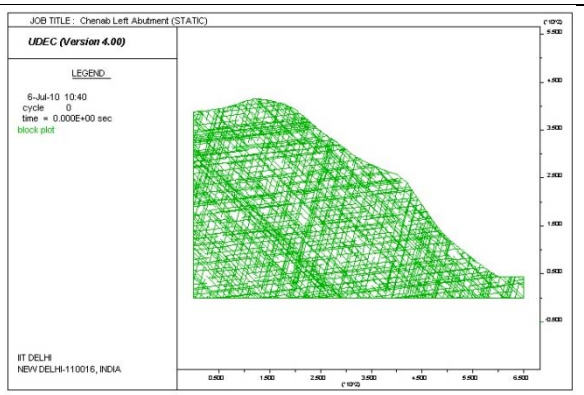

Fig. 3. UDEC Model for Left Abutment

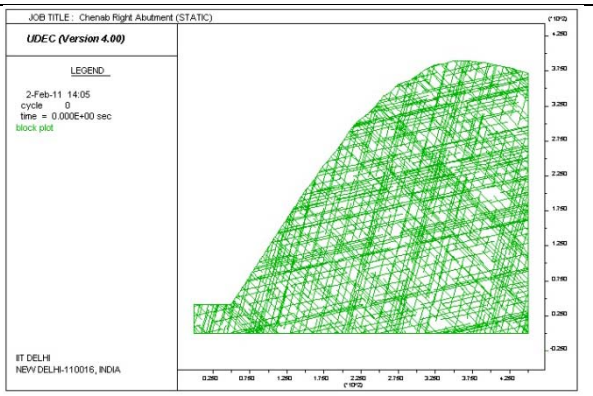

Fig. 4. UDEC Model for Right Abutment

LOADING CONDITIONS

Static Loading

This case simulates the prevailing rock conditions at the site where the rock mass is observed to be stable. Initially, the jointed rock slope model was equilibrated under gravity. All the blocks in the jointed model were discretised into deformable triangular finite difference zones where the motion of the block is calculated at the grid point of the triangular elements.

Dynamic Loading

In this case, dynamic excitation is applied to the rock slope to simulate earthquake conditions. The analysis starts from the end of static analysis with the calculated in situ stresses. A simple harmonic acceleration with well defined characteristics was used as input. A sinusoidal shear wave was applied to the model base and allowed to propagate upwards. The sinusoidal shear wave was applied for a period of 5 seconds and it's magnitude was estimated as

$$V_{\max} = \frac{a_{\max}}{\omega} = \frac{a_{\max}}{2\pi f}$$

Where, a_{max} is the peak ground acceleration, V_{max} is the ground motion velocity, f is the frequency in Hz and $\omega=2\pi f$ is the angular frequency

CASES CONSIDERED FOR THE ANALYSIS

Left Abutment (Katra Side)

All four joint sets are considered. The depth of foundation is assumed as 10 m. The six Monitoring Points (MP) 1 to 6 were installed in the model at a depth of 10 m i.e. at foundation level and six (7 to 12) MP installed at ground level. Total four cases i.e. CL11, CL12, CL13 and CL14 were analyzed for the left abutment and the details are given Table 3.

Right Abutment (Reasi Side)

The total of seven MP used in the model, out of which two were installed at ground level and rest at foundation level at a depth of 10 m. Total four cases i.e. CR11, CR12, CR13 and CR14 were analyzed for the right abutment.

RESULTS AND DISCUSSION

The numerical analysis was carried out for different cases considering various loading conditions, rock properties and presence of joint sets. Based on the observed velocities, displacements and stresses at monitoring points, the stability of the slopes was evaluated and results are given in Table 3. The cases with pier and seismic loads are considered to be the most critical and are discussed here.

Table 2. Factor of Safety Values Obtained for Different Cases

Sr. No.	Side	Case Notation	Rock Type	Joint Spacing, m	Pier Loads	Seismic Loads	Factor of Safety
1	LEFT	CL 11	Jointed Rock	20	--	--	**1.94**
2		CL 12	Jointed Rock	20	Yes	--	**1.91**
3		CL 13	Jointed Rock	20	--	Yes	**Safe**
4		CL 14	Jointed Rock	20	Yes	Yes	**Safe**
5	RIGHT	CR 11	Jointed Rock	20	--	--	**1.95**
6		CR 12	Jointed Rock	20	Yes	--	**1.90**
7		CR 13	Jointed Rock	20	--	Yes	**Safe**
8		CR 14	Jointed Rock	20	Yes	Yes	**Safe**

Left Abutment: Jointed Rock with Pier and Seismic Loads (Case CL14)

This is the dynamic loading case with all pier loads and the results are shown in Fig. 5. The X & Y velocities are approaching to zero for all points except the point no. 12. The X displacements at point 2 is 50 cm which is the highest value calculated in the model. The Y displacements at all monitoring points varies between 10 to 30 cm and shows the upward movement of blocks at point 4 and 9. The XX and YY stresses at P40 are calculated as -0.18×10^7 Pa and 1×10^7 Pa respectively. The maximum shear displacement of 30cm is observed at point 3. The shear stresses at points 1, 2, 3, 4, 5 and 6 are calculated for this dynamic case and found to be zero at the end of analysis. However there are locations where nominal shear stresses developed in the slope. The shear velocities observed are approaching to zero confirms a stable state of the slope. The shear stresses and displacement values are very low which indicates that there is no movement of blocks and the slope is stable. The strength/stress ratios (localized FoS) calculated using Mohr – Coulomb and Hoek and Brown approaches in terms of contours in the slope. The minimum ratio observed from both methods is around two. It is also very common that movement of random blocks on the surface

due to delineation of joints and no surface cover. However, stability of left abutment will further improve if one considers the horizontal loads.

Right Abutment: Jointed Rock with Pier and Seismic Loads (Case CR14)

This is the dynamic loading case with all pier loads. The X and Y velocities are approaching to zero for all points. The X displacements at point 2 is 50cm which is the highest value calculated in the model. The results for this case are shown in Fig. 6. The Y displacements at all monitoring points varies between -20 to 70 cm and shows the upward movement of blocks at point 4. The XX and YY stresses at P50 are calculated as 2 x 10^6 Pa and 0.8 x 10^7 Pa respectively. The maximum shear displacement of 35cm is observed at point 5. The shear stresses at points 1, 2, 3, 4, 5, 6, and 7 are calculated for this dynamic case and found to be zero at the end of analysis. However there are locations where nominal shear stresses developed in the slope. The shear velocities observed are approaching to zero confirms a stable state of the slope. The shear stresses and displacement values are very less which indicates that there is no movement of blocks and the slope is stable. The strength/stress ratios (localized FoS) calculated using Mohr - Coulomb and Hoek and Brown approaches in terms of contours in the slope. The minimum ratio observed from both methods is around two. It is also very common that movement of random blocks on the surface due to delineation of joints and no surface cover. However, stability of left abutment will further improve if one considers the horizontal loads.

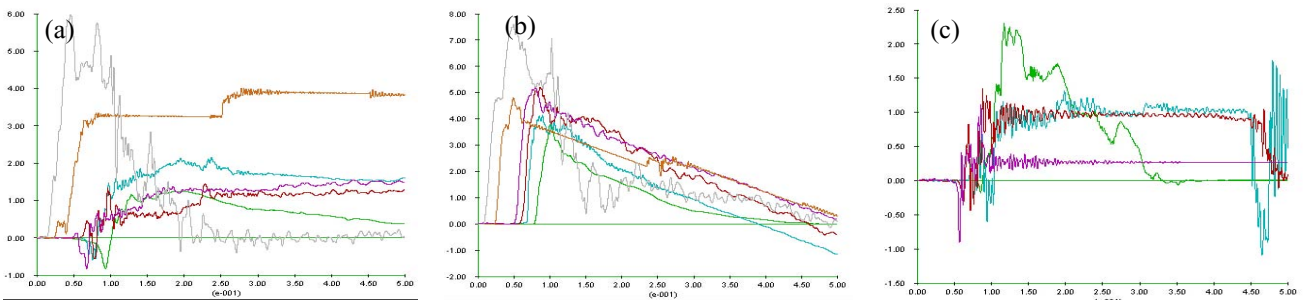

Figure 5. UDEC Results for Case AL14 a) X- Velocity b) Y- Velocity c) Shear Velocity

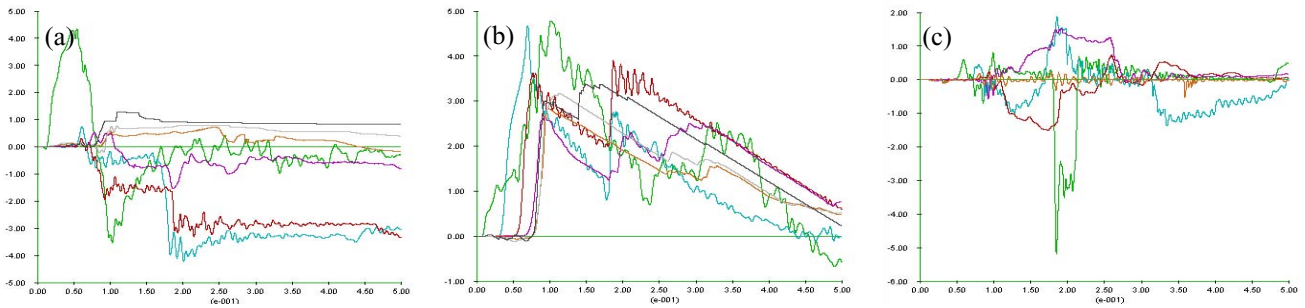

Figure 6. UDEC Results for Case AR14 a) X-Velocity b) Y-Velocity c) Shear Velocity

CONCLUSIONS

The vertical dimensions of left and right abutment considered in modelling are 418 m and 390 m respectively. And the corresponding horizontal dimensions are 650 m and 450 m. A numerical analysis is carried out for both abutments using UDEC considering joint sets and stiffness characteristics. Both static and dynamic analysis is carried out considering different loading conditions. The dynamic cases for both the abutments were considered to be the most critical. The shear displacements, shear velocities, shear stresses, XX and YY stresses at all monitoring points for both left and right abutments, show that the slopes are stable in static and dynamic conditions. The stability of the abutments will further improve when horizontal loads considered in the analysis. UDEC analysis revealed left and right slopes are stable with respective factor of safety under different loading conditions. A critical observation is attempted at P_1 and P_{10} arch foundation. The shear displacements, shear velocities and shear stresses at all monitoring points for both left and right abutments are within the acceptable limits and shows that the slopes are stable in static and dynamic conditions.

ACKNOWLEDGEMENTS

Authors greatfully acknowledge the help received from Konkan Railway Corp. Ltd. India, Northern Railway India and Scott Wilson UK during different stages of the study.

REFERENCES

Basu, S. (2004). “Site-specific design earthquake parameters for Chenab Bridge, J & K." Indian Institute of Technolgy Roorkee, India, Report No. EQ:2004-13.

Bhasin, R., and Kaynia, A. M. (2004). “Static and dynamic simulation of a 700-m high rock slope in western Norway.” *Engineering Geology* **71**, 213-226.

BIS: 1893–2002. Part 1: 2002 “Bureau of Indian Standards, Criteria for Earthquake Resistant Design of Structures, General Provisions and Buildings.”

Cundall, P. A. (1971). “A computer model for simulating progressive large scale movements in blocky rock system.” *Int. Proc. Symp. ISRM,* Nancy, France, Vol. I, Paper 11-8, 128-132.

Deere, D.U., and Miller, R.P. (1966) “Engineering classification and index properties for intact rocks.” Tech. Report No. AFNL-TR- 65-116, Air Force Weapons Lab., New Mexico.

Hoek E., Read J., Karzulovic A., and Chen, Z. Y. (2000). “Rock slopes in civil and mining engg.” *Intl. Conf. on Geotech & Geo Engg.*, 19-24 Nov, 2000, Melbourne, 1-17.

Hudson, J. A., and Feng, X. T. (2007). “Updated flowcharts for rock mechanics modelling and rock engineering design.” *Int. J of Rock Mech and Min Sci,* **44**, 174-195.

Itasca Manual (2004). “Dynamic analysis.” User’s guide UDEC version 4.0.

Kveldsvik, V., Kaynia, A. M., Nadim, F., Bhasin, R., Nilsen Bjørn and Einstein, H. H. (2009). “Dynamic distinct-element analysis of the 800 m high Åknes rock slope.” *Int. J of Rock Mech and Min Sci,* **46**, 686-698.

Shen, B., and Barton, N. (1997). “The disturbed zone around tunnels in jointed rock masses.” *Int. J of Rock Mech and Min Sci,* **34**, 117-125.

Souley, M., and Homand, F. (1996). "Stability of jointed rock masses evaluated by UDEC with an extended Saeb-Amadei constitutive law." *Int. J of Rock Mech Min Sci Geomech Abstr,* **33**, 233-244.

Reliability analysis of stone columns for ground improvement

Jose A. Alonso[1] and Rafael Jimenez[2], F. ASCE.

[1]Dragados, S.A.; Dirección Técnica (Edificio 3 Planta 1); Avda Camino de Santiago 50; 28050 Madrid; Spain. Email: jaalonsop@dragados.com

[2]Technical University of Madrid; ETSI Caminos, Canales y Puertos; C/ Profesor Aranguren s/n; 28040 Madrid; Spain; Email: rafael.jimenez@upm.es

ABSTRACT: Stone columns are commonly employed for ground improvement in geotechnical projects. This paper studies the problem of stone column settlement in the context of uncertainty and, in particular, the amount of deferred settlements that will occur after a specified time. An improved theoretical solution to the coupled column compression/consolidation problem that considers the influence of the radial deformation and yielding of the column on the (radial only) consolidation analysis is employed. In addition, reliability methods are used to consider the effects that uncertainty and variability have on computed settlement estimates and, hence, on the probability of failure. Uncertainties and variabilities considered include those related to column "as-built" properties and also those related to soil properties. Reliability is estimated using First Order Reliability Methods, and simulation methods are employed to double-check the validity of the results. Results indicate that uncertainties could have a significant effect on the reliability of stone column designs.

INTRODUCTION

Stone columns are commonly employed for ground improvement in geotechnical projects. Their main purposes are (i) to increase the shear resistance of cohesive and non-cohesive soils (hence increasing bearing capacity); (ii) to increase their stiffness (hence reducing settlements); and (iii) to increase the permeability of the soil mass, therefore speeding up consolidation of cohesive soils or reducing the liquefaction susceptibility of granular soils (see e.g., Hughes et al., 1975; Priebe, 1995, 1998; Phear and Harris, 2008).

Traditionally, stone column design has been mainly empirical and led by contractor experience (Charles, 2002). Although a wide body of knowledge has been compiled during the last few decades that makes the basic mechanisms of column behavior to be reasonably well understood (Castro and Sagaseta, 2009), Priebe's semi-empirical method is still commonly used for settlement design of stone columns in Europe (Priebe, 1995).

In this paper, we study the problem of settlements (i.e., amount and velocity) of

stone columns in the context of uncertainty and, in particular, the amount of deferred settlements that will occur after a specified time. This is a typical geotechnical problem in which, given uncertain parameters and for a given target probability, we aim to limit the total settlement that will affect a structure (or parts of a structure) to be constructed after a specified waiting (pre-loading) time, at the same time that we try to minimize costs associated to the waiting period.

To that end, we employ an improved theoretical solution to the coupled problem of column compression/consolidation that considers the influence of the radial deformation and yielding of the column on the (radial only) consolidation analysis (Castro and Sagaseta, 2009). In addition, we use reliability methods to consider the effects that uncertainties —as well as variability of geotechnical and material properties— have on our computed settlement estimates and, hence, on the probability of failure of our geotechnical design. That is, we compute the probability that the structure will suffer (after the specified time) settlements that are larger than one (acceptable) threshold. Uncertainties and variabilities considered include those related to column "as-built" properties, such as diameter and stiffness; and also to soil's properties, such as permeability and stiffness (which are themselves modified by the degree of soil densification achieved around the column during installation). The effects of uncertainties on the reliability of the design are quantified by means of First Order reliability methods (FORM), and simulation methods are employed to double-check the validity of the results.

SETTLEMENT OF STONE COLUMNS

Stone columns are a specific type of vibro compaction techniques, in which stone aggregates are added by means of special depth vibrators (Priebe, 1995); they reduce settlements because they act as rigid inclusions within the (softer) soil.

Although stone columns can be used with granular soils, they have been traditionally used with soft cohesive soils with more than approximately 15% fines content (silt and clay); note, however, that the new generation of more powerful vibrators developed in conjunction with improved construction techniques has enabled soils with "significantly higher" fines contents (up to, say, 45% total fines with up to 5% particles smaller than 5μm) to be treated using vibro compaction hence avoiding the need for stone aggregates (Slocombe et al., 2000). In any case, it is clear that, with their extensive use in projects with soft cohesive soils, the behavior of stone columns will often be heavily influenced by the presence of fines and, in particular, by the delayed (consolidation-like) deformations typically associated with them.

Castro and Sagaseta (2009) have recently presented an improved analytical model to consider the influence of the vertical and horizontal deformation of the column on settlements associated to the (radial only) consolidation of the soil mass, in which they consider that the soil behaves elastically and that the stone column has an elasto-plastic behavior (with friction angles ϕs and ϕc, and plastic dilatancy ψc). (In the following, subscript *c* indicates column and subscript s indicates soil.) Consolidation

is computed using "equivalent consolidation coefficients" (elastic and plastic), and the evolution of surface settlement versus time is obtained analytically by integration of the equation of radial consolidation. They also show that their model produces values of the stress concentration factor (i.e., SCF = σc/σs) that agree well with empirical observations. Further details of the analytical model, as well as solved examples of application, can be found in the original paper (Castro and Sagaseta, 2009).

UNCERTAINTY CHARACTERIZATION

Multiple sources of uncertainty can be considered in practical geotechnical engineering, including geometrical uncertainties, uncertainties on soil properties and other material properties, as well as model uncertainties. In this analysis, however, we only consider uncertainties (and variabilities) associated to the soft soils in which stone columns are constructed, as well as uncertainties associated to the geometry and the mechanical behavior of actual stone columns.

Table 1 summarizes the parameters that define the statistical distributions of the random variables employed to characterize uncertainties considered in this work. E_s and E_c are the Young´s Modulus of soil and column; C_r is the coefficient of radial consolidation of the soil; d_c is the diameter of the stone column; ϕs and ϕc are the friction angles of soil and column; and ψc is the angle of plastic dilation of stone columns. (Note that the soil is considered as elastic.) As an initial simplification, we have considered that such random variables are defined by uncorrelated normal distributions, although the computational methods employed in the subsequent reliability analysis (see below) can also handle the more general case of correlated and non-normal random variables (see e.g., Low, 2007). Ranges of variability are defined (as expressed by their coefficients of variation, or cov's) following the suggestions of the Spanish Recommendations for the Design of Maritime and Harbour Works (Puertos del Estado, 2005).

Table 1. Parameters of statistical distributions employed for uncertainty characterization

(a) Geotechnical properties

Property	Mean	Coef Var	Std Dev
E_s [kPa]	2000	0.3	600
C_r [m^2/day]	8.64E-03	0.5	4.32E-03
$\tan\phi_s'$	0.44	0.07	0.03

(b) Stone column properties

Property	Mean	Coef Var	Std Dev
d_c [m]	0.7	0.1 & 0.2	0.07 & 0.14
E_c [kPa]	30000	0.3	9000
$\tan\phi_c'$	0.84	0.07	0.06
$\tan\psi_c$	0.18	0.07	0.01

The reader should note that ranges of variability of geotechnical properties (Table 1(a)) are actually *site dependent*, so that values presented herein can only be considered as reasonable estimates. In that sense, for instance, Hong and Shang (1998) (see also Zhou et al., 1999) present a review of cov's for the vertical coefficient of consolidation of real soils, δCr, with values that range between 0.12 for

Mexico City clay and 0.69 for Pisa clay. They also suggest that the coefficient of variation of the horizontal coefficient of consolidation should be higher, and they use values of 0.5 and 0.75 in their sensitivity analyses (Hong and Shang, 1998). Similarly, Zhou *et al.* (1999) consider a δ_{Cr} of 0.5 with different types of statistical distributions. Additional suggestions for characterization of geotechnical variability have been published elsewhere (see e.g., Phoon and Kulhawy, 1999; Uzielli et al., 2007).

The uncertainty characterization of stone column properties (and, in particular, of stone column diameters, dc), however, has not been studied in such detail in the literature. Magnan et al. (2005) presents empirical evidence that suggests that column diameter depends (probably among other factors) on the strength of the soil, on the type of construction (e.g., dry vs. wet methods), on the energy transmitted to the soil by the vibrator, and on the sequence of construction. Similarly, Slocombe *et al.* (2000) present empirical evidence that suggests that the construction method (*e.g.,* top-feed vs. bottom-feed) and the quality of workmanship during treatment have a significant influence on the quality of the column and, in particular, in ensuring that the required column diameter is being achieved.

To illustrate the importance of variability in the diameter of stone columns, we consider two values of the coefficient of variation of column diameter dc ($\delta_{dc} = 0.1$ and $\delta_{dc} = 0.2$; see Table 1(b)). Note, however, that such values have been selected for illustrative purposes only, and that they do not intend to represent real cases. (The authors are currently conducting research to characterize variability of stone column diameters in real cases.)

RELIABILITY ANALYSIS

We use reliability methods to quantify the influence that uncertainties characterized above have on the probability of failure. To that end, we define a limit state function (LSF) to express the condition that the remaining settlement after a specified time (t) is less than a specified threshold ($\Delta s_{,adm} = 10$ cm in this case). That is, we have:

$$g(\cdot) = \Delta s_{adm} - (s_\infty - s_t) \quad (1)$$

where s_t is the settlement at time t and s_∞ is the final settlement once consolidation is completed ($t = \infty$). (Note that the LSF is defined following the usual convention in the reliability literature that $g(\cdot) \leq 0$ in the failure domain.) In this case, we also have that s_∞ is a function of soil's and column's random properties (i.e., $s_\infty \equiv s_\infty(Es, \tan\phi s, dc, Ec, \tan\phi c, \tan\psi c)$), and that s_t is a function of the same variables in addition to variables that control the speed of consolidation, such as the radial coefficient of consolidation, C_r. The actual formulas to compute s_t and s_∞ settlements depend on the state of the column (elastic, partially plastic, or completely plastic) and, for the sake of space, they are not reproduced herein. (The interested reader is referred to the original publication for details.)

Then, the problem is to compute the probability of failure Pf (or, alternatively, the reliability index $\beta = -\Phi^{-1}(P_f)$) of the LSF defined in (1). Such probability of failure

can be *approximated* using a First Order Reliability Method (FORM) or using simulation methods such as Monte Carlo (MC). We use the simple ellipsoid approach proposed by Low (1997) to compute FORM estimates of Pf. Such method, that can be easily implemented into a spreadsheet, is based on the solution of the constrained optimization problem of *minimizing* $\beta = \sqrt{\sum_i (x_i^* - \mu_i)^2 / \sigma_i^2}$ *subjected* to the condition that g(·) ≤ 0. ($\sum_i$ indicates summation over all random variables considered, x^*_i are the values of such random variables at the minimum solution —the so called "design point"—, and μ_i and σ_i^2 are the means and variances of each random variable.) MC methods approximate the probability of failure as $P_f \approx \frac{1}{N_s}\sum_{i=1}^{Ns} I(x_i)$, where N_s is the number of simulations and $I(x_i)$ is a Boolean function indicating whether the vector of randomly generated input parameters x_i produces (or not) failure of the system. (I = 1 indicates failure.)

FORM methods can also be used to compute sensitivity coefficients as $\alpha_i = -(x_i^* - \mu_i)/\beta\sigma_i$. Such sensitivity coefficients are useful for practical engineering, as they allow the designer to identify which random variables have a stronger influence on the reliability results, so that they should concentrate the characterization efforts (Jimenez-Rodriguez et al., 2006).

Figure 1 shows an example of our computed reliability estimates. In particular, Figure 1(a) shows the probability of failure for different design times; it is observed that, as expected, it decreases with time or, in other words, as consolidation proceeds. (The difference between FORM and MC results is probably due to the errors introduced when the non-linear LSF is linearized to compute FORM reliability estimates.) Also, note that (everything else being equal) Pf tends to be higher for cases in which the variability of column diameters is higher. Similarly, Figure 1(b) shows the relative importance of random variables (as given by the squares of the corresponding components of the sensitivity vector, α_i^2) on the computed reliability results for the case of δdc = 0.1. (Results for δdc = 0.2 show a similar trend and, for the sake of space, they have not been reproduced herein.)

Results show that the coefficient of radial consolidation has the highest influence on the reliability results—therefore agreeing with the conclusions of previous research on reliability of wick drain design (see e.g., Hong and Shang, 1998)—, and that column diameter and soil deformability are also important parameters. In addition, they suggest that the relative importance of the random variables considered change with time, so that the relative importance of Cr increases with time while the relative importance of dc and Es decrease with time.

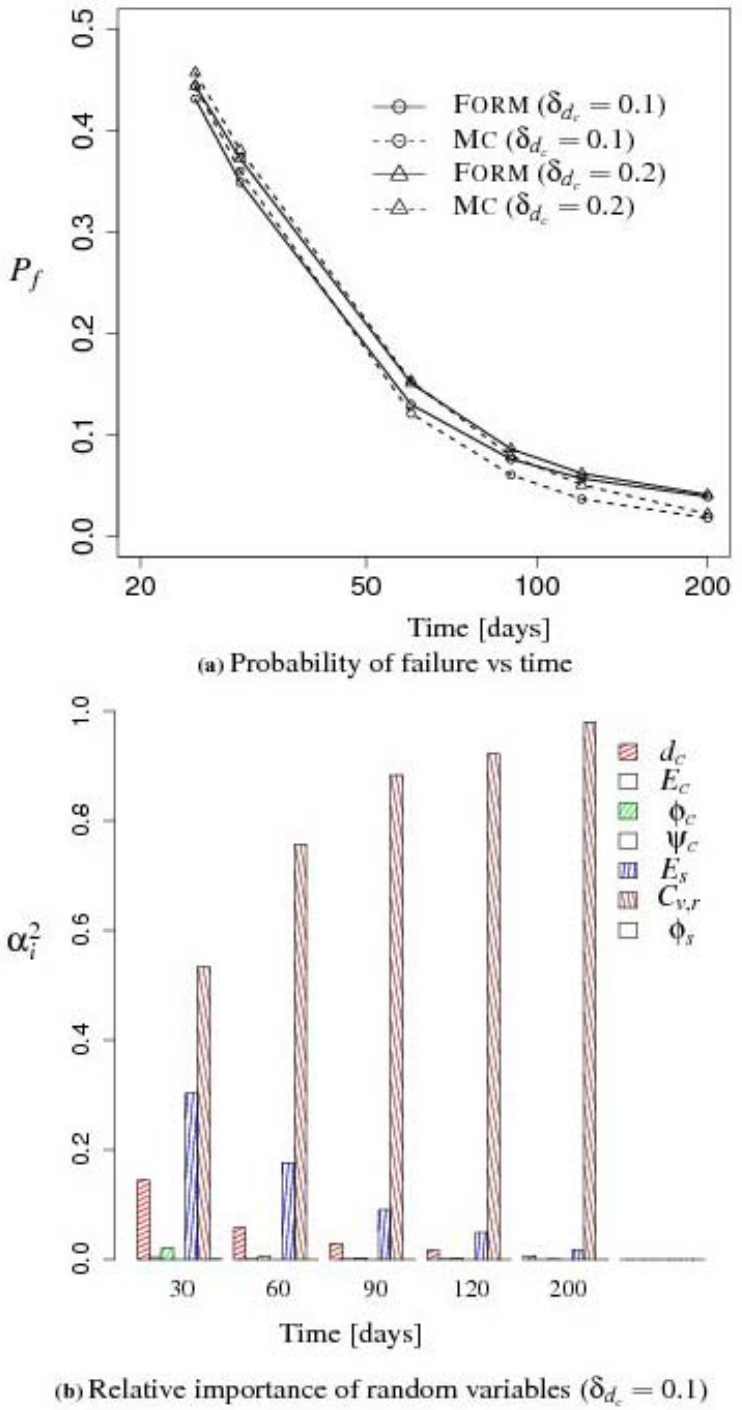

(a) Probability of failure vs time

(b) Relative importance of random variables ($\delta_{d_c} = 0.1$)

FIG. 1. Evolution of computed reliability results as a function of time

CONCLUSIONS

We present an example of application of reliability methods to the analysis of the problem of consolidation in stone column design and, in particular, to the typical geotechnical problem of designing stone columns so that the remaining settlement after a specified waiting period is below a given threshold. Settlements are computed using an improved analytical method that considers the coupling between column compression and consolidation, and FORM estimates are computed using a simple spreadsheet implementation of the ellipsoid reliability approach. We also compute the sensitivity results to illustrate the relative importance of the random variables considered.

Results indicate that, as expected, the reliability of the design increases as consolidation proceeds. In addition, we show that the use of such reliability methods allows us to quantitatively consider the influence of uncertainties in practical design cases; such analysis is not possible in typical deterministic methods for stone column design. We also obtain that, in this case, the coefficient of consolidation has the highest influence of the reliability results, and that column diameter and soil deformability are other important parameters. In addition, we find that the influence of the different random variables depends on the time considered. In this sense, the importance of construction method and workmanship is highlighted by the observation that probabilities of failure tend to be higher when the variability of stone column diameters is higher, and also by the observation that α_{dc}^2 is relatively more important for "short" times. This suggests that control of column diameter can be crucial when time is "expensive" and it is important to construct "early". Finally, it is observed that the importance of the radial coefficient of consolidation increases as time increases, hence suggesting that stone column construction method and quality of workmanship are probably less important if time is "cheap" and we can wait for consolidation to occur.

ACKNOWLEDGMENTS

Nicolás Burbano (Geocisa) and Goran Vukotic (Keller Terra) provided data, explanations, and expert advice. Their support is gratefully acknowledged.

REFERENCES

Castro, J., Sagaseta, C. (2009). "Consolidation around stone columns. influence of column deformation". *International Journal for Numerical and Analytical Methods in Geomechanics*, Vol. 33: 851-877.

Charles, J. A. (2002). Ground improvement: the interaction of engineering science and experience-based technology. *Geotechnique*, Vol 52. (7): 527-532.

Hong, H. P., Shang, J. Q. (1998). "Probabilistic analysis of consolidation with prefabricated vertical drains for soil improvement". *Canadian Geotechnical Journal*, Vol. 35: 666-677.

Hughes, J. M. O., Withers, N. J., Greenwood, D. A. (1975). "A field trial of the reinforcing effect a stone column in soil". *Geotechnique*, Vol 25 (1): 31-44.

Jimenez-Rodriguez, R., Sitar, N., Chacón, J. (2006). "System reliability approach to rock slope stability". *International Journal of Rock Mechanics and Mining Sciences*, Vol 43(6): 847-859.

Low, B. K. (1997). "Reliability analysis of rock wedges". *Journal of Geotechnical and Geoenvironmental Engineering*, Vol 123(6): 498-505.

Low, B. K. (2007). "Reliability analysis of rock slopes involving correlated nonnormals". *International Journal of Rock Mechanics and Mining Sciences*, Vol 44: 922-935.

Magnan, J. P., Droniuc, N., Canepa, Y., Dhouib, A. (2005). "Réflexions sur la conception des colonnes ballastées". In: *Proceedings of 16th International Conference of Soils Mechanics and Foundation Engineering*. Osaka, vol. 3, 1377-1380.

Phear, A. G., Harris, S. J. (2008). "Contributions to Géotechnique 1948-2008: Ground improvement". *Geotechnique*, Vol 58(5): 399-404.

Phoon, K. K., Kulhawy, F. H. (1999). "Characterization of geotechnical variability." *Canadian Geotechnical Journal*, Vol 36: 612-624.

Priebe, H. J. (1995). "The design of vibro replacement". *Ground Engineering*, (GT 07-13 E).

Priebe, H. J. (1998). "Vibro replacement to prevent earthquake induced liquefaction". *Ground Engineering*, 30-33.

Puertos del Estado (ed.) (2005). "*ROM 0.5-05.* Geotechnical *recommendations for the Design of Maritime and Harbour works*". Ministerio de Fomento, Madrid.

Slocombe, B. C., Bell, A. L., Baez, J. I. (2000). "The densification of granular soils using vibro methods". *Geotechnique*, Vol 50 (6): 715-725.

Uzielli, M., Lacasse, S., Nadim, F., Phoon, K. K. (2007). "Soil variability analysis for geotechnical practice". In: Tan, T. S., Phoon, K. K., Hight, D. W., Leroueil, S. (eds.), *Characterisation and Engineering Properties of Natural Soils*. Taylor & Francis Group, London, 1653-1752.

Zhou, W., Hong, H. P., Shang, J. Q. (1999). "Probabilistic design method of prefabricated vertical drains for soil improvement". *Journal of Geotechnical and Geoenvironmental Engineering*, Vol 125: 659-664.

Application of SCPTU for Assessing Liquefaction Potential of the 1976 Tangshan Earthquake, China

Guojun Cai[1], Songyu Liu[1] and Anand J. Puppala[2]

[1]Institute of Geotechnical Engineering, Southeast University, Nanjing 210096，China; email: focuscai@163.com; Tel: 86-25-83795086
[2]Department of Civil Engineering, The University of Texas at Arlington, Arlington, Texas 76019; email: anand@uta.edu; Tel: 817-272-5821

ABSTRACT

Recent findings related to the application of the shear wave velocity for the evaluation of liquefaction potential are first reviewed. Some sites were characterized using this in situ device and the results of these investigations are presented in this paper. Seismic piezocone penetration tests provided the in situ shear wave velocities of the subsurface sediments in Tangshan region, China, which were used to evaluate the liquefaction potentials of these soils. Two empirical methods based on normalized shear wave velocity are studied, which showed that the correlation between shear wave velocity data and liquefaction resistance was in better agreement with the boundary curve approach developed by the earlier studies. The correlation of q_c/G_0-$CRR_{7.5}$ can assess correctly liquefaction potential of Tangshan sites.

INTRODUCTION

A promising alternative, or supplement, to the penetration-based approaches is provided by the direct in situ measurements of small-strain shear-wave velocity V_S via seismic methods. The use of V_S as an index of liquefaction resistance is considered sound since both V_S and liquefaction resistance parameters are similarly influenced by the same factors such as void ratio, state of stress, stress history, and geologic age. Some advantages of using seismic shear wave velocity, V_S measurements are presented below (Dobry et al. 1981; Stokoe et al. 1988): (1) need no soil sample; (2) measurements can also be performed on small laboratory specimens, allowing direct comparisons between laboratory and field behavior; (3) V_S is a basic mechanical property of soil materials, directly related to small-strain shear modulus G_0 by:

$$G_0 = \rho V_s^2 \tag{1}$$

where ρ = mass density of soil; (4) G_0, or V_S , is normally a required property in earthquake site response and (5) V_S can be easily measured by the seismic tests, such as the downhole (DH) test, crosshole (CH) test and the spectral-analysis-of-surface-waves (SASW) technique at sites.

Three concerns when using V_S to evaluate liquefaction resistance are that (1) no samples are routinely obtained as part of the testing procedure for soil characterization and identification of non-liquefiable materials; (2) thin and low V_S strata may not be

detected if the seismic measurement interval is too large (Boulanger et al. 1997); and (3) measurements are made at small strains, whereas pore-water pressure buildup and liquefaction are medium- to high-strain phenomena (Jamiolkowski and Lo Presti 1990; Roy et al. 1996). The third concern can be significant for cemented soils, because small-strain measurements are highly sensitive to weak interparticle bonding that is eliminated at medium and high strains (Puppala et al., 1995).

The main focus of this research was to address the application of SCPTU method to evaluate liquefaction potentials of Tangshan city subsoils. Previous records of a major disaster occurred in 1976 were available and these records were used for comparting with SCPTU assessments. This paper summarizes the results from this analysis. A field performance data from Tangshan earthquake and in situ V_S measurements from 21 sites were utilized in the analysis.

LITERATURE REVIEW

Cyclic Stress Ratio (*CSR*)

The cyclic stress ratio, τ_{av}/σ'_{v0}, at a particular depth can be expressed as (Seed and Idriss 1971):

$$CSR_{7.5} = \frac{\tau_{av}}{\sigma'_{v0}} = 0.65\left(\frac{\sigma_{v0}}{\sigma'_{v0}}\right)\left(\frac{a_{\max}}{g}\right)(r_d)/MSF \quad (2)$$

where τ_{av} = average equivalent uniform cyclic shear stress caused by the earthquake and is assumed to be 0.65 of the maximum induced stress; σ'_{v0} = initial effective vertical (overburden) stress at the depth in question; σ_{v0} = total overburden stress at the same depth; a_{max} = peak horizontal ground surface acceleration; g = acceleration of gravity (=9.81 cm/s^2) ; and r_d = stress reduction coefficient. *MSF* = magnitude scaling factor, that is, the *CSR* is adjusted to an earthquake magnitude of 7.5 through the use of the magnitude scaling factor (*MSF*). The *MSF* can be quantified by $MSF = (M_w/7.5)^{-2.56}$ (Andrus and Stokoe, 1997). M_w = moment magnitude.

For routine practice and noncritical projects, the following equations may be used to estimate average values of r_d (Liao and Whitman 1986)

$$r_d = 1.0 - 0.00765z \quad \text{for} \quad z \leq 9.15 \text{ m} \quad (3a)$$

$$r_d = 1.174 - 0.0267z \quad \text{for} \quad 9.15 < z \leq 23 \text{ m} \quad (3b)$$

where z = depth below ground surface in meters.

Cyclic Resistance Ratio *(CRR)*

Andrus and Stokoe (1997, 2000) developed liquefaction resistance criteria from field measurements of shear velocity V_s. The use of V_s as a field index of liquefaction resistance is regarded as a sound practice since both V_s and *CRR* are similarly influenced

by void ratio, effective confining stresses, stress history, and geologic age (Hardin and Drnevich 1972). Dobry (1981) derived a relationship between *CSR* and overburden stress-corrected shear-wave velocity V_{S1} as follows:

$$\gamma_{av} = \frac{\tau_{av}}{(G)_{\gamma_{av}}} \tag{4}$$

where γ_{av} = average peak shear strain during a cyclic stress controlled test of uniform cyclic shear stress τ_{av}; and $(G)_{\gamma_{av}}$ = secant shear modulus at γ_{av} during the same cyclic test. By combining (1) and (4), the following CSR relationship is obtained:

$$CSR = \frac{\tau_{av}}{\sigma_{v0}^{'}} = f(\gamma_{av}) V_{s1}^2 \tag{5}$$

where $f(\gamma_{av})$ = function of γ_{av}; V_{s1} = overburden stress-corrected shear-wave velocity. Andrus and Stokoe (1997) proposed the following relationship between *CRR* and V_{s1}:

$$CRR = \left\{ a\left(\frac{V_{s1}}{100}\right)^2 + b\left(\frac{1}{V_{s1}^* - V_{s1}} - \frac{1}{V_{s1}^*}\right) \right\} MSF \tag{6}$$

where V_{s1}^* = limiting upper value of V_{S1} for cyclic liquefaction occurrence; *a* and *b* = curve fitting parameters.

q_c/G_0-$CRR_{7.5}$ Correlations

Existing approaches for assessing liquefaction potential are primarily based on correlations between a single index measurement, e.g., q_{c1} or V_{s1}, and a measure of liquefaction resistance, $CRR_{7.5}$. Since the strain level representative of q_{c1} or V_{s1} differs from that representing cyclic liquefaction of cohesionless soils, these index measurements do not relate precisely to the $CRR_{7.5}$ obtained from laboratory testing of high-quality soil samples. Theoretical analysis indicate that for cohesionless soils q_c/G_0 relates to plastic shear strength parameters, the friction and dilation angles, which in turn closely relate to liquefaction resistance. Roy (2008) developed a relationship between q_c/G_0 and $CRR_{7.5}$ based on the laboratory and in situ test data from 24 sites. It can be seen from Figure 1 that there are two distinct relationships between q_c/G_0 and $CRR_{7.5}$; one for Holocene soils and one for Pleistocene soils. These relationships are independent of fines content and grain compressibility.

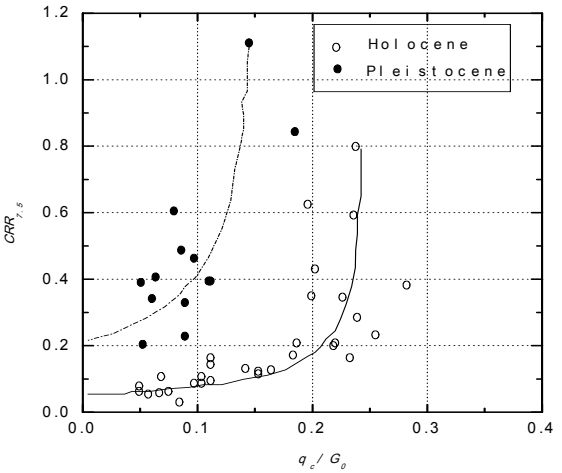

Figure 1. Relationship between q_c/G_0 and $CRR_{7.5}$ (Roy, 2008)

LIQUEFACTION ASSESSMENT STUDIES

Laboratory research has shown that shear wave velocity is a function of void ratio and effective confining stress (Hardin and Drnevich 1972). The shear wave velocity will increase with increasing depth for a sand of constant void ratio. Hence, the correlation between V_s and *CSR* should be based on shear wave velocity normalized with respect to an effective overburden stress. In terms of the traditional procedures for correcting CPT tip resistances to account for overburden stress, one can correct V_S to a reference overburden stress by the following equation (Robertson et al. 1992):

$$V_{s1} = V_s C_{v-s1} = V_s \left(\frac{P_a}{\sigma'_{v0}} \right)^{0.25} \quad (7)$$

where V_{S1} = overburden stress-corrected shear-wave velocity; $C_{v\text{-}s1}$ = factor to correct measured shear-wave velocity for overburden pressure; P_a = reference stress of 100 kPa or about atmospheric pressure (1 TSF). In applying the correction as shown in Eq. 7, it is implicitly assumed that the V_S is measured with both particle motion and wave propagation polarized along principal stress directions and one of those directions is kept vertical as suggested by Stokoe et al. (1985).

Based on laboratory testing of shear-wave velocity and cyclic triaxial tests, Tokimatsu and Uchida (1990) proposed another normalization approach of shear wave velocity.

$$V_{s1-M} = V_s C_{v-s1-M} = V_s \left(\frac{P_a}{\sigma'_m} \right)^{0.33} \quad (8)$$

$$\sigma'_m = \frac{\sigma'_{v0} + 2\sigma'_{h0}}{3} = \frac{1 + 2K_0}{3} \sigma'_{v0} \quad (9)$$

where $C_{v\text{-}s1\text{-}M}$ = factor to correct measured shear-wave velocity for mean effective stress; σ'_m = mean effective stress; K_0 = earth pressure coefficient at rest.

There is a small difference in the normalization of V_s. Normalization with σ'_m is considered more appropriate than the normalization with σ'_{v0} (Hardin and Drnevich, 1972). However, the estimation of σ'_m requires some knowledge of in situ K_o state which is not always known. The $V_{s1\text{-}M}$ values calculated using the Tokimatsu and Uchida (1990) method are 15-25% larger than the values calculated using the Robertson et al. (1992) method at Moss Landing area during the 1989 Loma Prieta earthquake. Boulanger et al. (1997) showed that the resulting data from Loma Prieta earthquake are in better agreement with the boundary curve method proposed by Robertson et al. (1992), than with the boundary curve proposed by Tokimatsu and Uchida (1990). In the present research, Tokimatsu and Uchida (1990) method was followed since K_o state was estimated using laboratory studies on in situ samples.

Tangshan SCPTU site details

Shear wave velocity measurements have been performed at many liquefaction and non-liquefaction sites. The occurrence of liquefaction was based on the appearance of surface evidence, such as boiling, ground cracks and fissures, and ground settlement. Seismic piezocone penetration testing was carried out at 21 sites in 2007, as shown in Figure 2. Typical SCPTU results in this study are presented in Figure 3, which shows the soil profile at one of these sites in terms of cone tip resistance, sleeve friction, friction ratio and pore water pressure. The friction ratio is the ratio of the sleeve friction to the cone bearing and is expressed in percent.

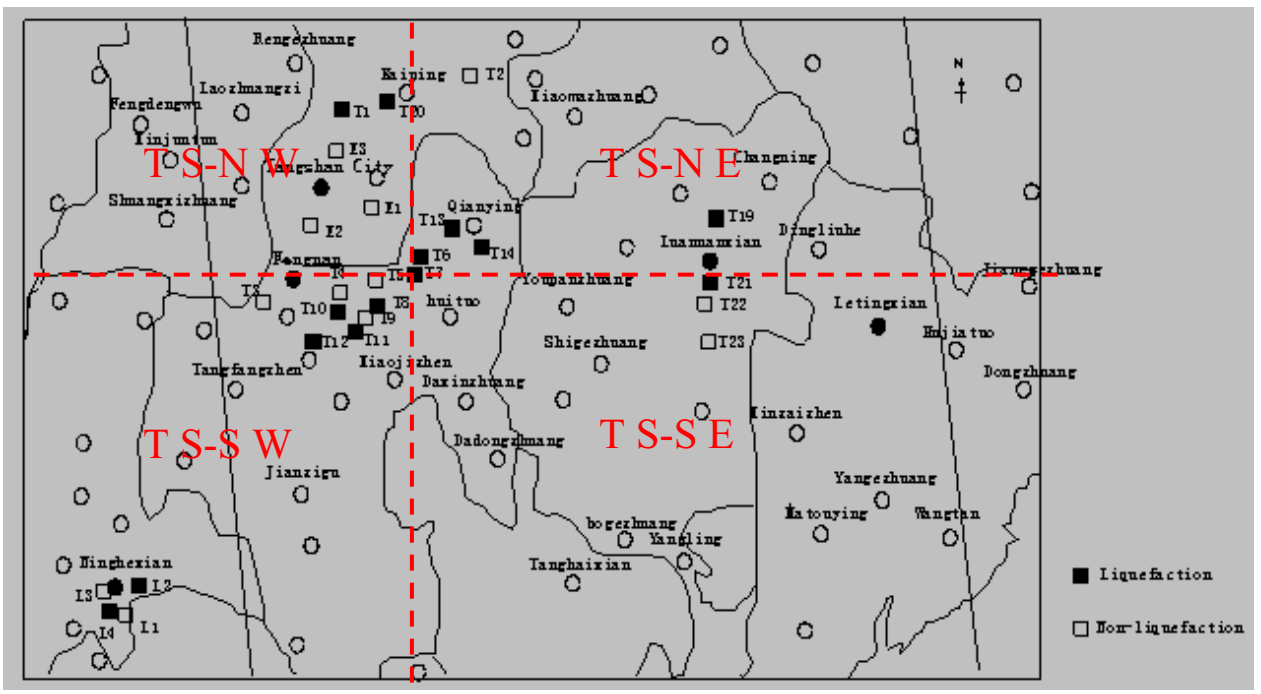

Figure 2. Regional map showing locations of investigated sites and location plan, Tangshan area, Hebei Province, China

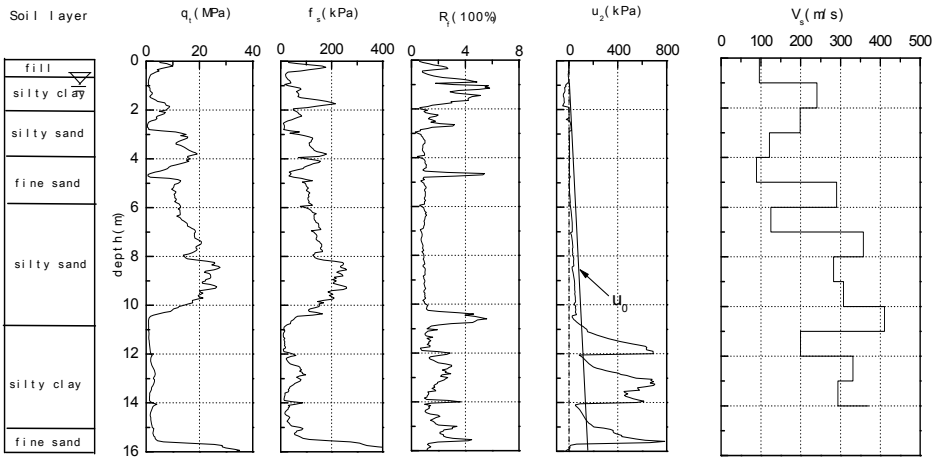

Figure 3. Typical seismic CPTU profiles in Tangshan

Liquefaction assessment and discussion

Values of V_{s1}, $V_{s1\text{-}M}$ and *CSR* were calculated for each measurement depth within the critical layer and then averaged. In the calculations, each site was assumed to be level ground. Values of $C_{V\text{-}s1}$ used to correct measured shear-wave velocities ranged from 1.30 to 0.92 for most of the data. And values of $C_{V\text{-}s1\text{-}M}$ ranged from 1.68 to 1.07 for most of the data. The potential of liquefaction was first assessed by comparing the cyclic stress ratio induced by a design earthquake with the critical cyclic stress ratio or cyclic resistance ratio determined from shear wave velocity measurements from SCPTU. These results are compared to the boundary curves proposed by Andrus and Stokoe (2000) in Figure 4 (a) and Tokimatsu and Uchida (1990) in Figure 4 (b). The correlation proposed by Andrus and Stokoe (2000) requires V_{s1}, while the correlation proposed by Tokimatsu and Uchida (1990) requires $V_{s1\text{-}M}$. It can be seen from Figure 4 that the resulting data are in better agreement with the boundary curve proposed by Andrus and Stokoe (2000) than with the boundary curve proposed by Tokimatsu and Uchida (1990).

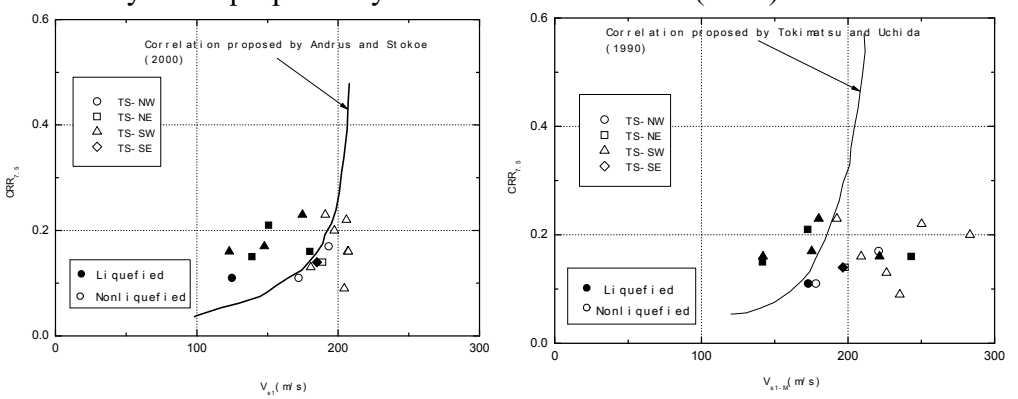

(a) (b)

Figure 4. Critical combinations of cyclic stress or resistance ratio and normalized shear wave velocity

Relationship of q_c/G_0-$CRR_{7.5}$ to assess liquefaction potential

To assess liquefaction resistance of Tangshan earthquake, values of $CSR_{7.5}$ from the 21 sites that did or did not liquefy in the earthquake are plotted against q_c/G_0 for the critical layers in Figure 5 together with the q_c/G_0 −$CRR_{7.5}$ relationships developed by Roy (2008). It can be seen from the Figure 5 that the liquefaction assessment of the procedure based on q_c/G_0 is satisfactory for Tangshan sites. The fact that q_c/G_0−$CRR_{7.5}$ relationships account for soil compressibility and geologic age, could be viewed as an advantage over many of the existing methods that require soil grain compressibility input in addition to q_c or V_s measurements. However, the proposed correlation for assessing liquefaction susceptibility requires independent measurement of q_c and G_0, necessitating a more detailed testing program compared with the minimum requirements for the alternative correlations based on decoupled use of q_c or V_s.

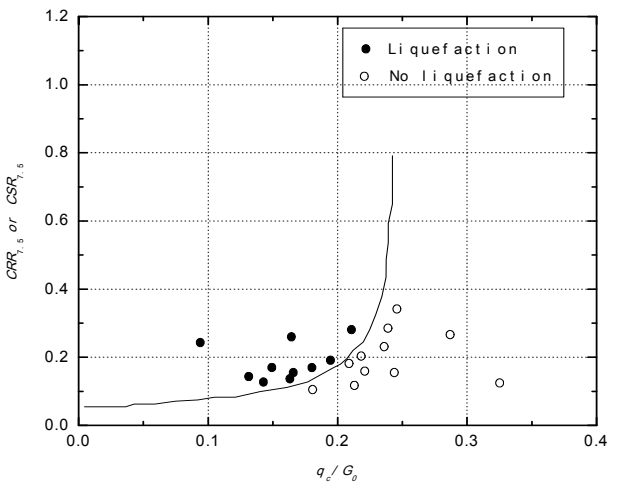

Figure 5. Relationship between q_c/G_0 and $CRR_{7.5}$ (Roy, 2008)

CONCLUSIONS

Comprehensive re-investigations using the SCPTU were made in liquefaction and non-liquefaction case histories from the 1976 Tangshan earthquake with the aid to assess the existing correlations between liquefaction resistance and shear wave velocity for sandy soils. Existing approaches for assessing liquefaction potential are primarily based on correlations between a single index measurement, e.g., q_{c1} or V_{s1}, and a measure of liquefaction resistance, $CRR_{7.5}$. Since the strain level representative of q_{c1} or V_{s1} differs from that representing cyclic liquefaction of cohesionless soils, these index measurements do not relate precisely to the $CRR_{7.5}$ obtained from laboratory testing of high-quality soil samples. For cohesionless soils q_c/G_0 relates to plastic shear strength parameters, the friction and dilation angles, which in turn closely relate to liquefaction resistance. Roy (2008) proposed that the q_c/G_0 could be related to $CRR_{7.5}$. The set of shear wave velocity data was in better agreement with the boundary curve by Andrus and Stokoe (2000) than with that by Tokimatsu and Uchida (1990). The correlation of q_c/G_0-$CRR_{7.5}$ can evaluate correctly liquefaction potential of Tangshan sites.

ACKNOWLEDGEMENTS

This research was supported by the National Natural Science Foundation of China (NSFC) (Grant No. 40702047), the Excellent Doctoral Dissertation Foundation of Southeast University, China (Grant No. YBJJ0714) and the Jiangsu Transportation Research Foundation (Grant No. 8821006021). The first author received financial support from the China Scholarship Council to attend the University of Texas at Arlington as a visiting research scholar.

REFERENCES

Andrus, R.D., and Stokoe, K.H. II. (1997). Liquefaction resistance based on shear wave velocity. In Proceedings of the National Center for Earthquake Engineering Research (NCEER) Workshop on Evaluation of Liquefaction Resistance of Soils, Technical Report NCEER-97-0022, Edited by T.L.Youd and I.M. Idriss. National Center for Earthquake Engineering Research, Buffalo, 89–128.

Andrus, R D., and Stokoe, K.H. II. (2000). Liquefaction resistance of soils from shear-wave velocity. *Journal of Geotechnical and Geoenvironmental Engineering*, 126(11), 1015–1025.

Boulanger, R.W., Mejia, L.H., and Idriss, I.M. (1997). Liquefaction at Moss Landing during Loma Prieta earthquake. *Journal of Geotechnical and Geoenvironmental Engineering*, 123(5), 453–467.

Dobry, R., Stokoe, K.H. II, Ladd, R.S., and Youd, T.L. (1981). Liquefaction susceptibility from S-wave velocity. In Proceedings of the ASCE National Convention, In Situ Tests to Evaluate Liquefaction Susceptibility, ASCE, New York.

Hardin, B.O., and Drnevich, V.P. (1972). Shear modulus and damping in soils: design equations and curves. *Journal of Geotechnical Engineering*, 98(7), 667–692.

Jamiolkowski, M., and Lo Presti, D. C. F. (1990). Correlation between liquefaction resistance and shear wave velocity. *Soils and Foundations*, 32(2), 145–148.

Liao, S.S.C., and Whitman, R.V. (1986). Catalogue of liquefaction and non-liquefaction occurrences during earthquakes. In Research Report. Department of Civil Engineering, Massachusetts Institute of Technology, Cambridge, Massachusetts.

Liu, H.X., Housner, G.W., Xie, L.L., and He, D.X. (2002). The great Tangshan earthquake of 1976, Earthquake Engineering Research Library, Cal Tech, Pasadena.

Puppala, A.J., Acar, Y.B. and Tumay, M.T. (1995). Cone penetration in very weakly cemented sand. *Journal of Geotechnical Engineering*, 121(8), 589–600.

Robertson, P.K., Woeller, D.J., and Finn, W.D.L. (1992). Seismic cone penetration test for evaluating liquefaction potential under cyclic loading. *Canadian Geotechnical Journal*, 29(6), 686–695.

Roy, D., Campanella, R. G., Byrne, P. M., and Hughes, J. M. O. (1996). ‘‘Strain level and uncertainty of liquefaction related index tests.’’ *Uncertainty in the geologic environment: From theory to practice*, Geotech. Spec. Publ. No. 58, Vol. 2, C. D. Shackelford, P. P. Nelson, and M. J. S. Roth, eds., ASCE, New York, 1149–1162.

Roy, D. (2008). Coupled use of cone tip resistance and small strain shear modulus to

assess liquefaction potential. *Journal of Geotechnical and Geoenvironmental Engineering*, 134(4), 519–530.

Seed, H.B., and Idriss, I.M. (1971). Simplified procedure for evaluating soil liquefaction potential. *Journal of Geotechnical Engineering*, 97(9), 1249–1273.

Stokoe, K. H., II, Lee, S. H. H., and Knox, D. P. (1985). Shear moduli measurements under true triaxial stresses. Proc., Adv. in the Art of Testing Soil Under Cyclic Conditions, ASCE, New York, 166–185.

Stokoe, K.H., II, Roesset, J.M., Bierschwale, J.G., and Aouad, M. (1988). Liquefaction potential of sands from shear wave velocity. *Proceedings of the 9th World Conference on Earthquake Engineering*, 3, 213–218.

Tokimatsu, K., and Uchida, A. (1990). Correlation between liquefaction resistance and shear wave velocity. *Soils and Foundations*, 30(2), 33–42.

Characterizing the Liquefaction Potential of the Pleistocene-age Wando Formation in the Charleston Area, South Carolina

T. Heidari[1], R. D. Andrus[2], and S. M. J. Moysey[3]

[1]Department of Civil Engineering, Clemson University, Clemson, SC 29631-0911; PH (864) 952-9246; FAX (864) 656-2670; email: theidar@clemson.edu
[2]Department of Civil Engineering, Clemson University, Clemson, SC 29631-0911; PH (864) 656-0488; FAX (864) 656-2670; email: randrus@clemson.edu
[3]Department of Environmental Engineering & Earth Sciences, Clemson University, Clemson, SC 29634-0919; PH (864) 656-5019; FAX (864) 656-1041; email: smoysey@clemson.edu

ABSTRACT

Liquefaction potential of the younger sand facies of the 100,000-year-old Wando Formation (Qws) near Charleston, South Carolina, is characterized using forty-two seismic cone soundings in this paper. Liquefaction potential is expressed in terms of the liquefaction potential index (LPI) and corrected for the influence of diagenetic processes using the ratio of measured shear wave velocity to estimated shear wave velocity. Locations of the cone soundings lie 12-32 km from the Woodstock fault, the probable source of the 1886 Charleston earthquake. It is found that values of LPI, computed assuming a single value of peak ground acceleration, are independent of the distance to fault, indicating uniform liquefaction susceptibility for Qws. Liquefaction probability curves are developed considering the influence of depth to the groundwater table and depth to the non-liquefiable Cooper Marl.

INTRODUCTION

The 1886 Charleston earthquake, with a moment magnitude of about 7, is the largest historic seismic event to have occurred in the eastern United States (Bollinger 1977). The probable source of the 1886 earthquake is the Woodstock fault zone. As illustrated in Figure 1, the Woodstock fault has been characterized as a right-lateral strike slip fault with an anti-dilatational compressional left step near Middleton Place (Durá-Gómez and Talwani 2009). A major cause of damage during the 1886 Charleston earthquake was liquefaction-induced ground failure (Dutton 1889).

Most of the study area is covered by a blanket of Quaternary (< 1.8 million years) sand and clay that obscures underlying Tertiary stratigraphic units (Weems and Lewis 2002). The younger sand facies of the 100,000-year-old Wando Formation (Qws) form the higher natural ground near the coast. The Cooper Group is a major Tertiary marine deposit that underlies the entire area and extends to depths > 100 m below mean sea level. The Cooper Group is locally known as the Cooper Marl, and consists of calcareous silts and clays.

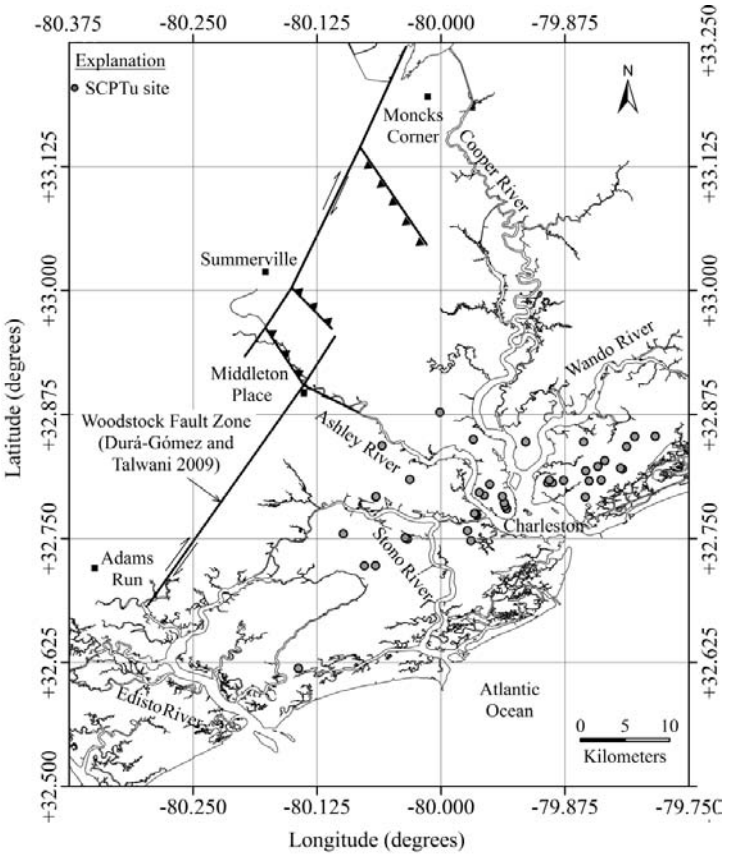

Figure 1. Map of the Greater Charleston area showing the Woodstock fault zone (Durá-Gómez and Talwani 2009) and the locations of SCPTu sites.

The primary objective of this study is to characterize the liquefaction potential of Qws surficial deposits. This paper extends the characterization of Qws deposits presented in Hayati and Andrus (2009) and Heidari and Andrus (2010) to include an analysis of the influence of depth to the groundwater table and depth to the Cooper Marl on liquefaction potential based on seismic cone penetration tests with pore pressure measurements (SCPTu). Locations of forty-two SCPTu sites considered in this study are plotted in Figure 1. Details of each SCPTu are given in Heidari (2011).

LIQUEFACTION POTENTIAL

The liquefaction potential index (LPI) is defined as (Iwasaki et al. 1978):

$$\mathrm{LPI} = \int_0^{20} F w(z) dz \tag{1}$$

where F = a function of factor of safety against liquefaction (FS) defined as $F = 1 - FS$ for $FS \le 1$ and $F = 0$ for $FS > 1$; z = depth in meters; and $w(z) = 10 - 0.5z$ is a depth-weighting factor given by Iwasaki et al. The LPI values calculated using Equation 1 could theoretically range from 0 to 100. LPI weighs factor of safety and thickness of potentially liquefiable layers according to the proximity of layers to the ground surface.

To screen out clay-rich layers not susceptible to liquefaction before LPI calculation, the cone penetration test-based criterion proposed by Robertson and Wride (1998) is used. According to their criterion, a layer with soil behavior type index (I_c) more than 2.6 is too plastic to be susceptible to liquefaction. This criterion is applied to layers in the Quaternary deposits. Although I_c is often < 2.6 in the Cooper Marl, the Cooper Marl is considered non-susceptible to liquefaction (Li et al. 2007; Hayati and Andrus 2008).

SCPTu profiles are considered acceptable for LPI analysis if the cone soundings extend to depths ≥ 20 m, extend into the Cooper Marl, or extend within two meters above the Cooper Marl based on available geologic maps. If SCPTu soundings are less than 20 m and extend within two meters above the Marl, the missing portion of the profile above the Marl is assumed to be the same as in the last two meters of the measured profile.

The factor of safety is defined as the cyclic resistance ratio divided by the cyclic stress ratio. The cyclic stress ratio (CSR) represents the seismic loading on the soil and can be expressed as (modified from Seed and Idriss 1971):

$$\mathrm{CSR} = 0.65\left(\frac{a_{\max}}{g}\right)\left(\frac{\sigma_v}{\sigma_v'}\right)(r_d) / (\mathrm{MSF}) \tag{2}$$

where a_{max} = peak horizontal acceleration at the ground surface; g = acceleration of gravity; σ_v and σ_v' = total and effective vertical overburden stresses, respectively; r_d = stress reduction coefficient; and MSF = magnitude scaling factor that accounts for the effects of shaking duration. The procedures recommended by Youd et al. (2001) to calculate each variable in Equation 2 are followed in this study. MSF is computed using $\mathrm{MSF} = 10^{2.24} / M_w^{2.56}$ where M_w = moment magnitude.

Cyclic resistance ratio (CRR) represents the resistance of the soil to liquefaction. For computing CRR from cone measurements, the following relationship developed by Robertson and Wride (1998) and recommended by Youd et al. (2001) is used:

$$\text{If } (q_{t1N})_{CS} < 50, \quad \mathrm{CRR} = 0.833\left(\frac{(q_{t1N})_{CS}}{1000}\right) + 0.05 \tag{3a}$$

$$\text{If } 50 \le (q_{t1N})_{CS} < 160, \ \mathrm{CRR} = 93\left(\frac{(q_{t1N})_{CS}}{1000}\right)^3 + 0.08 \tag{3b}$$

where $(q_{t1N})_{cs}$ = equivalent clean-sand cone tip resistance normalized to 100 kPa.

Because Equation 3 is based on fairly young sand deposits or deposits that liquefied in the recent past, the following correction is applied to the computed CRR:

$$\mathrm{CRR}_k = \mathrm{CRR} \times K_{DR} \tag{4}$$

where $\mathrm{CRR_k}$ = deposit resistance-corrected CRR, and K_{DR} = correction factor to capture the influence of diagenetic processes on CRR. The correction factor K_{DR} can be estimated using the following relationship (Hayati and Andrus 2009):

$$K_{DR} = 1.08\mathrm{MEVR} - 0.08 \tag{5}$$

where MEVR is the measured shear wave velocity corrected for overburden stress and fine content divided by the estimated velocity from cone penetration resistance defined by Andrus et al. (2004):

$$(V_{s1})_{cs} = 62.6\left[(\overline{q}_{t1N})_{cs}\right]^{0.231} \quad (6)$$

where $(V_{s1})_{cs}$ = equivalent clean-sand value of stress-corrected shear wave velocity in m/s, and $(\overline{q}_{t1N})_{cs}$ = average of $(q_{t1N})_{cs}$ over the 1-m test interval corresponding to the measured shear wave velocity. It should be noted that Equations 5 and 6 were derived using data from sandy soils (with $I_c < 2.25$) and diagenesis may be different in fine-grained soils. Therefore, both equations should be used cautiously in soils with $2.25 < I_c < 2.6$. It is also recommended that Equation 5 be used only for MEVR > 1, because Equation 3 is based on sites where MEVR is generally around 1.0.

LIQUEFACTION POTENTIAL BASED ON A SCENARIO EARTHQUAKE

The scenario shaking assumed for the initial LPI calculations is defined by M_w of 6.9 and a_{max} of 0.25g. These values are used for an evaluation of the influence of distance to the Woodstock fault, depth to top of the Cooper Marl, and depth to the groundwater table on LPI within the original forty-two SCPTu profiles. Although a_{max} changes as a function of distance from the fault for a given M_w, using a constant value of a_{max} allows the assessment of whether liquefaction susceptibility of Qws deposits close to the fault have been affected by previous earthquakes. The effects of varying M_w and a_{max} on LPI will be addressed latter in this paper by developing liquefaction probability curves as a function of a_{max}/MSF.

Presented in Figure 2 are variations of LPI values with distance to the Woodstock fault (*D*), depth to top of the Cooper Marl (*C*), and depth to the groundwater table (*W*). A regression analysis between LPI values and *D* indicated that there is no statistically significant correlation (coefficient of determination, $R^2 < 0.1$) between the LPI values and the site-to-fault distance, and the apparent trend suggested by the data in Figure 2(a) is opposite to what would be expected. On the other hand, R^2 is greater than 0.1 between the LPI values and *C* or *W*. The plotted LPI values indicate a slight increase with increasing *C* values (see Figure 2(b)), and a slight decrease with increasing *W* values (see Figure 2(c)). These trends are consistent with the definition of LPI.

To further evaluate the significance of the two predictor variables (*C* and *W*), the following regression equation is applied to the LPI data:

$$\text{LPI} = \beta_0 + \beta_1 C + \beta_2 W \quad (7)$$

where *C* and *W* in meters. From regression analysis, $\beta_0 = 3.60 \pm 4.35$ (95% confidence interval), $\beta_1 = 0.39 \pm 0.26$, and $\beta_2 = -2.36 \pm 1.70$. The coefficient of multiple regression and the standard deviation of the residuals (or error) associated with this regression are 0.29 and 3.82, respectively. The probability that the current result would have been found if the coefficient was equal to 0 for the estimated coefficient of β_1 and β_2 are 0.004 and 0.008, respectively, further indicating that LPIs for sites located within 12-32 km of the fault are significantly related to *C* and *W*.

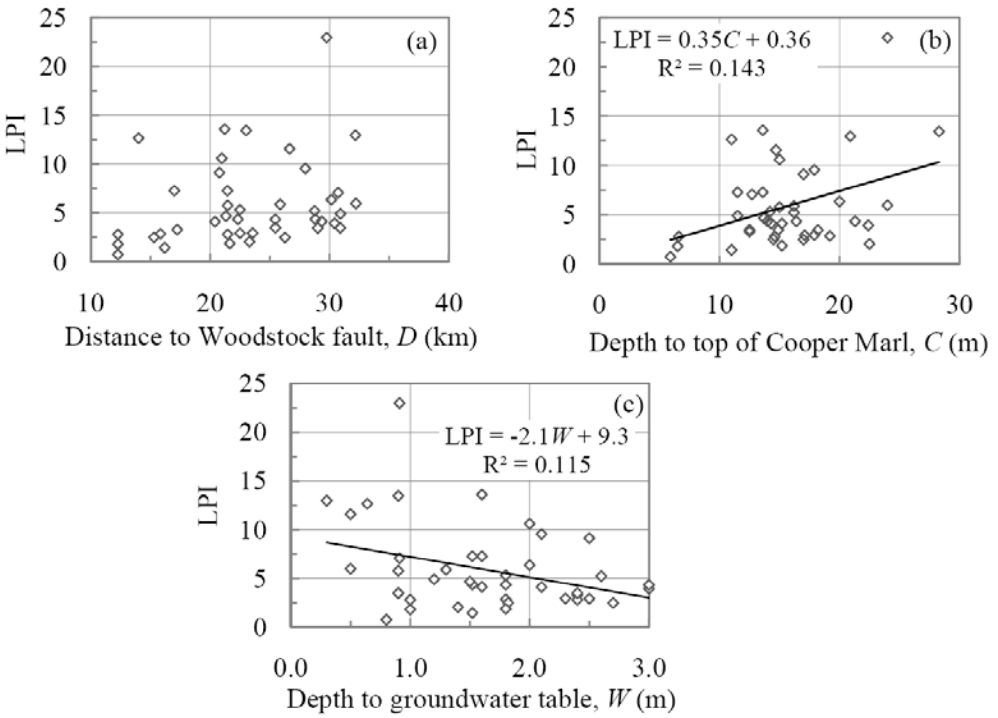

Figure 2. Variation of K_{DR}-corrected LPI with (a) distance to the Woodstock fault, (b) depth to top of the Cooper Marl, and (c) depth to the groundwater table for 42 SCPTu sites assuming M_w = 6.9 and a_{max} = 0.25g.

LIQUEFACTION PROBABILITY CURVES

The methodology proposed by Holzer et al. (2006, 2011), and Rix and Romero-Hudok (2007) is followed to develop liquefaction potential probability curves for any value of a_{max}/MSF. Considering LPI of 5 as the threshold for sand boil generation (Toprak and Holzer 2003), the probability of LPI $\geq$ 5 is derived from complementary cumulative distribution of LPI values for various values of a_{max} and M_w. The probability of LPI $\geq$ 5 is estimated as a function of a_{max} for a specific earthquake magnitude by repeating the calculation for 0.1, 0.15, 0.2, 0.25, 0.3, 0.4, and 0.5g. Repeating the calculation for $5.0 \leq M_w \leq 7.5$ in 0.5 magnitude increments, the probability of LPI $\geq$ 5 as a function of a_{max}/MSF is obtained.

Shown in Figure 3 are liquefaction probability curves developed for the Qws surficial deposits considering the influence of depth to top of the Cooper Marl and depth to the groundwater table. The probability of LPI $\geq$ 5 for a given a_{max}/MSF is derived assuming that the LPI values are log-normally distributed (denoted by circles in Figure 3) except when LPI values for some sites are calculated zero and the assumption that LPI values are from a log-normally distributed population is not correct. The probability of LPI $\geq$ 5 for the set of LPI analysis with LPI values of zero is computed using the experimental cumulative distribution of LPI values (denoted by triangles in Figure 3).

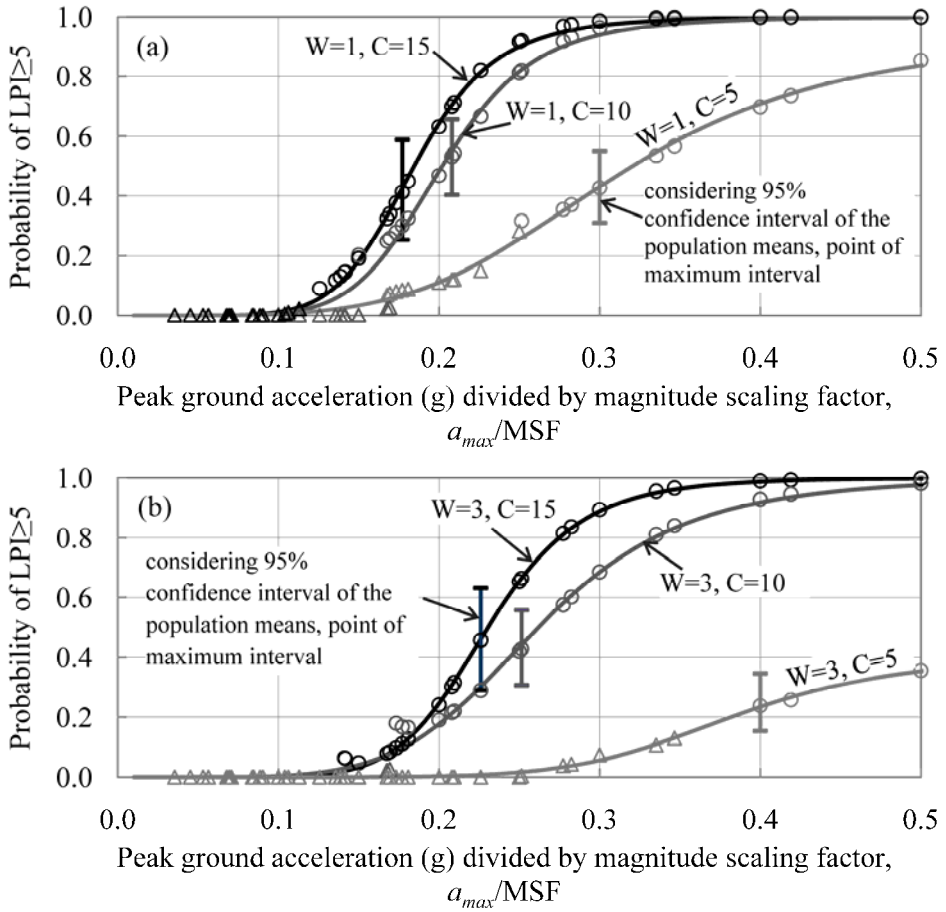

Figure 3. Liquefaction probability curves assuming depths to the groundwater table of (a) 1 m and (b) 3 m, and depth to top of Cooper Marl of 5, 10, and 15 m for Qws surficial deposits in the Charleston area. Note that the circles in the figure represent probability based on lognormal distribution, and the triangles represent probability based on experimental cumulative distribution.

The following equation is fitted to the calculated points plotted in Figure 3 representing the probability of LPI ≥ 5 as a function of a_{max}/MSF:

$$P_{LPI\geq 5} = \frac{\mathrm{a}}{\mathrm{b} + \left(\frac{a_{max}/\mathrm{MSF}}{\mathrm{c}}\right)^{\mathrm{d}}} \tag{8}$$

where a, b, c and d are curve fitting coefficients. The probability curves developed assuming depth to top of the Cooper Marl at 5, 10, and 15 m, are based on 42, 39 and 22 SCPTu sites, respectively. The curves for *C*=10-15 m are in general agreement with curves derived by Holzer et al. (2011) for South Carolina Pleistocene beach sands. Presented in Table 1 are the coefficients of Equation 8 for each set of LPI analyses.

Table 1. Coefficients of the Fitted Curves for Each Set of LPI Analysis

Depth to groundwater table (m)	Depth to top of Cooper Marl (m)	a	b	c	d
1	5	29.337	31.493	0.664	-4.529
1	10	30.560	30.559	0.330	-6.984
1	15	30.559	30.559	0.296	-7.241
3	5	17.585	44.121	0.631	-7.511
3	10	30.472	30.457	0.477	-5.704
3	15	30.611	30.610	0.356	-7.891

The 95% confidence interval of the probability of LPI $\geq$ 5 for the location with the largest confidence interval is shown along with each curve in Figure 3. The interval is derived from the lognormal cumulative distribution function assuming a population mean equal to the upper and lower limits of the 95% confidence interval of the sample mean.

CONCLUSION

The liquefaction potential of areas covered by Qws in the Charleston area was characterized in terms of LPI. LPI values were computed for forty-two SCPTu profiles after screening out layers not susceptible to liquefaction and correcting CRR for the influence of diagenetic processes using MEVR. Liquefaction probability curves are developed considering the influence of depth to the groundwater table and depth to the non-liquefiable Cooper Marl. These curves can be used for mapping liquefaction potential of Qws deposits near Charleston that are more than 12 km from the Woodstock fault. Liquefaction potential maps are useful tools for planners, engineers, and scientists working to mitigate damage during future earthquakes.

ACKNOWLEDGEMENTS

This research was supported by the United States Geological Survey (USGS), Department of the Interior, under Grant No. 08HQGR0085. The support of the USGS is greatly appreciated. The writers also thank the many individuals who assisted with data collection, in particular, William M. Camp of S&ME and William B. Wright and Thomas J. Casey of WPC. We are also indebted to Peter G. Chirico of USGS for providing the digital geologic map of the study area.

REFERENCES

Andrus, R. D., Piratheepan, P., Ellis, B. S., Zhang, J., and Juang, C. H. (2004). "Comparing liquefaction evaluation methods using penetration-V_S relationships." *Soil Dynamics and Earthquake Eng.,* 24(9-10), 713-721.

Bollinger, G. (1977). "Reinterpretation of the intensity data for the 1886 Charleston, South Carolina, earthquake." *Studies Related to the Charleston, South Carolina,*

Earthquake of 1886: A Preliminary Rep., D. W. Rankin, ed., USGS Professional Paper, 1028, 17–32.

Durá-Gómez, I., and Talwani, P. (2009). "Finding faults in the Charleston area, South Carolina: 1. Seismological data." *Seismological Res. Letters,* 80(5), 883-900.

Dutton, C. E. (1889). "The Charleston earthquake of August 31, 1886." *USGS Ninth Annual Rep. 1887-1888*, U.S. Geological Survey, Washington, D.C., 203-528.

Hayati, H., and Andrus, R. D. (2008). "Liquefaction potential map of Charleston, South Carolina based on the 1886 earthquake." *J. Geotech. and Geoenviron. Eng.,* 134(6), 815-828.

Hayati, H., and Andrus, R. D. (2009). "Updated liquefaction resistance correction factors for aged sands." *J. Geotech. and Geoenviron. Eng.,* 135(11), 1683-1692.

Heidari, T., (2011). "Characterizing liquefaction potential of Pleistocene soil deposits in the Charleston Area, South Carolina." *Ph.D. Dissertation*, Clemson University, Clemson, SC.

Heidari, T., and Andrus, R. D. (2010). "Mapping liquefaction potential of aged soil deposits in Mount Pleasant, South Carolina." *Eng. Geology,* 112(1-4), 1-12.

Holzer, T. L., Bennett, M. J., Noce, T. E., Padovani, A. C., and Tinsley III, J. C. (2006). "Liquefaction hazard mapping with LPI in the Greater Oakland, California, area." *Earthquake Spectra,* 22(3), 693-708.

Holzer, T. L., Noce, T. E., and Bennett, M. J. (2011). "Liquefaction probability curves for surficial geologic deposits." *Environ. & Eng. Geoscience*, Vol. XVII, No. 1, 1-21.

Iwasaki, T., Tatsuoka, F., Tokida, K.-I., and Yasuda, S. (1978). "A practical method for assessing soil liquefaction potential based on case studies at various sites in Japan." *Proc., 2nd Int. Conf. on Microzonation*, San Francisco, National Science Foundation, Washington, D.C., 885-896.

Li, D. K., Juang, C. H., Andrus, R. D., and Camp, W. M. (2007). "Index properties-based criteria for liquefaction susceptibility of clayey soils: a critical assessment." *J. Geotech. and Geoenviron. Eng.,* 133(1), 110-115.

Rix, G. J., and Romero-Hudock, S. (2007). "Liquefaction potential mapping in Memphis and Shelby County, Tennessee." *Rep. to USGS,* Denver, CO, available at http://earthquake.usgs.gov/regional/ceus/products/download/Memphis_LPI.pdf.

Robertson, P. K., and Wride, C. E. (1998). "Evaluating cyclic liquefaction potential using the cone penetration test." *Canadian Geotech. J.,* 35(3), 442-459.

Seed, H. B., and Idriss, I. M. (1971). "Simplified procedure for evaluating soil liquefaction potential." *J. Soil Mech. and Found. Div.,* 97(9), 1249-1273.

Toprak, S., and Holzer, T. L. (2003). "Liquefaction potential index: Field assessment." *J. Geotech. and Geoenviron. Eng.,* 129(4), 315-322.

Weems, R. E., and Lewis, W. C. (2002). "Structural and tectonic setting of the Charleston, South Carolina, region: Evidence from the Tertiary stratigraphic record." *GSA Bulletin,* 114(1), 24-42.

Youd, T. L., et al. (2001). "Liquefaction resistance of soils: Summary report from the 1996 NCEER and 1998 NCEER/ NSF workshops on evaluation of liquefaction resistance of soils." *J. Geotech. and Geoenviron. Eng.,* 127(10), 817-833.

INFLUENCE OF r_d ON LIQUEFACTION TRIGGERING EVALUATION AT TWO CASE HISTORY SITES

John Liao[1], Ph.D., P.E., and Jorge Meneses[2], Ph.D., P.E.

[1]Kleinfelder, Oakland, CA 94612; PH (510) 628-9000; FAX (510) 628-9009; email: jliao@kleinfelder.com
[2]Kleinfelder, San Diego, CA 92122; PH (858) 320-2000; FAX (858) 320-2001; email: jmeneses@kleinfelder.com

ABSTRACT

Soil liquefaction has been a major cause of damage to numerous structures during past earthquakes. Uncertainties associated with liquefaction evaluation arise not only from earthquakes themselves but also from how evaluation procedures handle ground motions parameters. Over the past decade, one of the significant advances on procedures of liquefaction triggering evaluation is the development of new equations for the shear stress reduction coefficient (r_d) for estimating earthquake-induced cyclic shear stresses. This paper presents: a) results of liquefaction triggering evaluations of two unique case histories of liquefiable sites where earthquake records were obtained at different depths; and b) comparison between using simplified r_d values from three liquefaction evaluation procedures and r_d values calculated by site-response-analysis (SRA) for the two sites. Comparison and assessment of relative conservatism of three liquefaction evaluation procedures are made between using the simplified r_d values and SRA back-calculated r_d values. Influences of r_d on liquefaction triggering evaluation of liquefiable sites are discussed.

INTRODUCTION

Soil liquefaction has been a major cause of damage to numerous structures during past earthquakes. Uncertainties associated with liquefaction evaluation arise not only from earthquakes themselves but also from how evaluation procedures handle ground motions parameters. Over the past decade, one of the significant advances on procedures of liquefaction triggering evaluation is the development of new equations for the shear stress reduction coefficient (r_d) in which more parameters are included to attempt to reduce the uncertainty associated with estimating earthquake-induced cyclic shear stresses.

Seed and Idriss (1971) proposed a mean and range of depth-dependent r_d values for estimating earthquake-induced cyclic shear stresses (CSR) based

on a few site response analyses for site conditions consisting of uniform profiles of 30-m deep sand directly underlain by rock. Because this equation was adopted by the Youd et al. (2001) procedure, it will be referred to as the Youd et al. procedure hereinafter. Idriss (1999) developed a new empirical equation for estimating magnitude- and depth-dependent r_d based on as many as several hundred site response analyses. In the new equation, moment magnitude is primarily used as a proxy for frequency content. Seed et al (2003) developed r_d equations based on their results of a total of 2153 site response analyses (i.e., 2153 r_d profiles) for a broad range of site conditions and for a broad range of shaking characteristics. Their equations are expressed as a function of (1) depth, (2) shaking intensity (peak ground acceleration), (3), site stiffness ($V_{s,12m}$), and (4) frequency content (magnitude) for the SPT-based procedure. Note that factor $V_{s,12m}$ is removed for the CPT-based procedures (Moss et al., 2006).

With these different r_d equations, one immediate question would be: How do they impact liquefaction triggering evaluation? This study attempts to answer this question and provides insights into the influence of r_d on liquefaction triggering evaluation for two particular sites.

SELECTED LIQUEFACTION CASE HISTORIES

A number of liquefaction case histories were reviewed and two were selected for this study, the Wildlife Liquefaction Array (WLA) site and the Port Island Downhole Array (PIDA) site. One of the important reasons to select the two sites is that de-convoluting of ground surface motion to obtain motions at different depths below the ground surface for the SRA is not needed due to available downhole acceleration time histories. Site subsurface conditions and instrumentation plans are not introduced here due to the limited space. Detailed descriptions are provided by Bennett et al. (1984) for the WLA site and by Elgamal et al. (1996) for the PIDA site.

SITE RESPONSE ANALYSES

SRAs were performed using the program SHAKE2000 (GeoMotions, 2009) for both sites. The recorded downhole ground motion was directly applied to the SHAKE2000 model as a within input motion. Figure 1 shows the comparisons of predicted and recorded ground surface motions at the WLA site at the top and at the PIDA site at the bottom. Youd and Carter (2003) reported liquefaction initiated at about 13 seconds at the WLA site and at about 10 seconds at the PIDA site, which are also observed in Figure 1.

LIQUEFACTION TRIGGERING EVALUATION

Triggering evaluations were performed using the CPT-based and the SPT-based procedures developed by Youd et al (2001), Cetin et al. (2004) and Moss et al. (2006) and Idriss and Boulanger (2008) (hereinafter, to be referred to as the Youd, Seed (for Cetin et al. (2004) and Moss et al. (2006), and IB procedures, respectively) for the WLA site. Unfortunately, no CPT-based triggering evaluation could be performed at the PIDA site due to the lack of available CPT data. Therefore, only r_d values are derived based on the Seed CPT-based procedure as presented in Figure 3. Table 1 presents parameters used to evaluate liquefaction triggering potential at each site. Note that the WLA site and the PIDA site have measured $V_{s,12m}$ values of 130 m/s and 192 m/s, respectively.

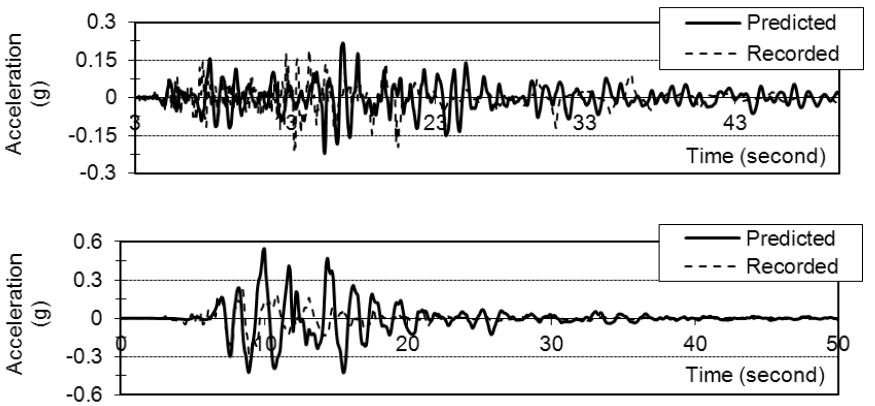

Figure 1. Predicted and recorded acceleration time histories at ground surface at WLA site (top) from 1987 Superstition Hills Earthquake (M = 6.6) and at PIDA site (bottom) from 1995 Kobe Earthquake (M = 7.2)

Table 1. Parameters for Liquefaction Triggering Evaluation

Site	Peak ground acceleration (g)	Moment magnitude	Ground water depth (m)	for the Seed procedure	
				P_L (%) for FOS calc.	$V_{s,12m}$ (m/s)
WLA	0.23	6.6	1.5	15	130
PIDA	0.54	7.2	4	15	192

RESULTS OF LIQUEFACTION TRIGGERING EVALUATION

Figure 2 shows comparisons of calculated r_d values at the WLA site. From depths of about 2.7 to 6.7 m below the ground surface, the Youd and IB procedures predicted larger r_d values than those computed from either the SRA or the Seed SPT- and CPT-based procedures. The Seed SPT-based procedure consistently computed smaller r_d values than those computed in the SRA. The Seed CPT-based procedure predicted similar r_d values to the SRA at depths ranging from about 2.7 to 5.2 m, but predicted significantly larger r_d values at depths greater than about 5.2 m. Figure 2 also shows a general divergence in

the computed r_d values with depth between the Youd and the IB procedures. The difference in predicted r_d values between the Seed SPT- and CPT-based procedures appears to result from the influence of $V_{s,12m}$. Figure 3 presents comparisons of predicted r_d values at the PIDA site. Similar to the WLA site, the Seed SPT-based procedure consistently predicted smaller r_d values than the other evaluated procedures at all depths. The IB and the Youd procedures predicted larger r_d values than those produced from SRA except at depths less than about 5 m while the Seed CPT-based procedure predicted much smaller r_d values than those from SRA. Overall, the predicted r_d values from the Seed SPT- and CPT-based procedures appear to provide a very similar trend to the r_d values computed with depth from SRA. Figures 2 and 3 also show that the IB and Youd procedures generally tend to predict greater r_d values than those predicted from the SRA.

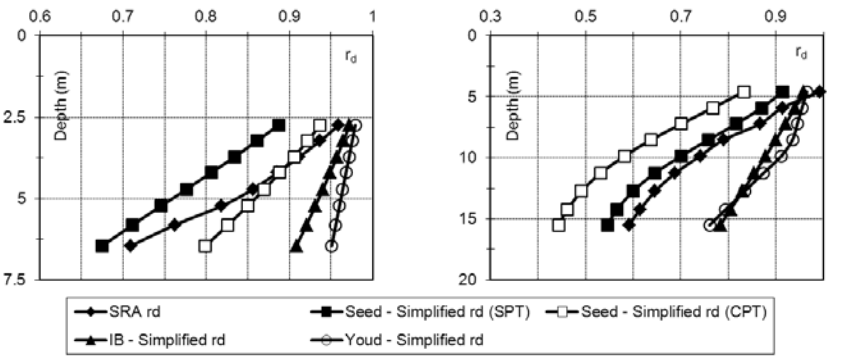

Figure 2. Comparisons of r_d values at WLA site

Figure 3. Comparisons of r_d values at PIDA site

Figure 4 shows comparisons of predicted factors of safety (FOS) using SPT-based procedures at the WLA site. The IB and Youd procedures both predicted smaller FOS values when using the simplified r_d values than when using SRA back-calculated r_d values, suggesting that the IB and Youd procedures are less conservative when they are used with SRA back-calculated r_d values than when they are used in conjunction with simplified r_d values. The Seed procedure predicted larger FOS values using simplified r_d values than using SRA back-calculated r_d values. Compared to the IB and the Youd procedures, the Seed procedure consistently predicted smaller FOS values over depths. It is also seen that the Seed procedure predicted a relatively constant difference in FOS values with depth between using simplified r_d values and SRA back-calculated r_d values. Such a difference for the IB and Youd procedures, however, appears to increase with depth.

Figure 5 presents comparisons of FOS using CPT-based procedures at the WLA site. The three procedures predicted smaller FOS using simplified r_d values, suggesting that these procedures are less conservative than when they are used in conjunction with SRA back-calculated r_d values. Figure 5 also shows that the differences in FOS values between using simplified r_d values and using SRA back-calculated r_d values are relatively smaller for each of the three procedures than those presented in Figure 4 (i.e. SPT-based procedures for the WLA site), particularly at greater depths.

Figure 6 illustrates comparisons of predicted FOS values using the SPT-based procedures at the PIDA site. The Seed procedure predicted the smallest FOS values while the IB procedure predicted larger FOS values. As in Figure 4, it is also seen that the Seed procedure predicted a relatively constant difference in FOS values with depth between using simplified r_d values and SRA back-calculated r_d values. Such a difference for the IB and Youd procedures increases with depth. Figure 6 again indicates that the IB and Youd procedures are less conservative when they are used with SRA back-calculated r_d values than when they are used in conjunction with simplified r_d values. The Seed procedure is more conservative when they are used with SRA back-calculated r_d values than when they are used in conjunction with simplified r_d values.

INFLUENCE OF $V_{s,12m}$ ON LIQUEFACTION TRIGGERING EVALUATION

In routine engineering practice the $V_{s,12m}$ parameter (weighted shear wave velocity in the upper 12 meters) is typically indirectly estimated from other soil properties (e.g., blow counts). SPT-blowcount based correlations generally provide significantly scattered $V_{s,12m}$ values, and the range of estimated $V_{s,12m}$ values using different correlations is significantly broad (DeJong, 2007). In this study, correlations by Imai and Tonouchi (1982), Seed et al. (1983), and Sisman (1995) were used to estimate $V_{s,12m}$ values for each site. The Imai and Tonouchi correlation estimated a $V_{s,12m}$ of 170 m/s for the WLA site and 175 m/s for the PIDA site. The Seed et al. correlation estimated a $V_{s,12m}$ of 130 m/s for the WLA site and 145 m/s for the PIDA site. The Sisman correlation estimated a $V_{s,12m}$ of 76 m/s for the WLA site and 85 m/s for the PIDA site. Figure 7 shows influences of $V_{s,12m}$ on liquefaction triggering evaluation using the Seed SPT-based procedure. Predicted FOS values varied by as much as 100% when $V_{s,12m}$ changed from 170 m/s to 76 m/s. Figure 7 also presents FOS values predicted by the IB and Youd procedures using the simplified r_d values. As can be seen at the WLA site, the Seed procedure predicted smaller FOS than the IB and Youd procedures regardless of $V_{s,12m}$ values. At the PIDA site, however, the Seed procedure predicted FOS greater than the IB and Youd procedures for a $V_{s,12m}$ of 85 m/s.

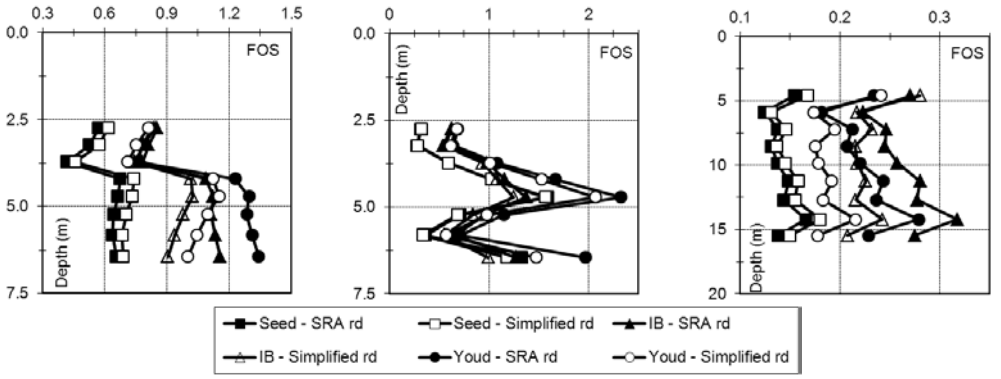

Figure 4. Comparisons of Calculated FOS (SPT-based Procedures) at the WLA Site

Figure 5. Comparisons of Calculated FOS (CPT-based Procedures) at the WLA Site

Figure 6. Comparisons of Calculated FOS (SPT-based Procedures) at the PIDA Site

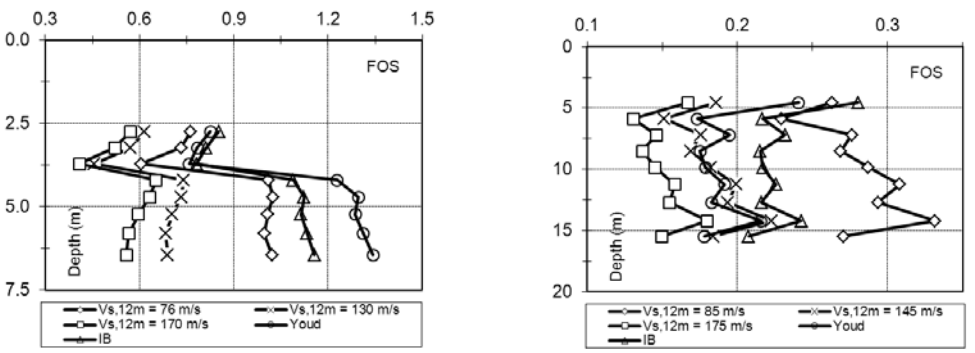

Figure 7. Influence of $V_{s,12m}$ on Liquefaction Triggering Evaluation using the Seed SPT-based Procedure: (left: WLA site; right: PIDA site)

CONCLUSIONS

Uncertainties associated with assessment of liquefaction risk arise not only from earthquakes themselves but also from how evaluation procedures treat ground motions parameters. The influence of r_d on liquefaction triggering evaluation of two unique case histories where earthquake records were obtained at different depths is investigated in this study. Based on the results of our studies, the following preliminary conclusions are drawn for these two sites regarding the relative conservatism of three liquefaction procedures between when using simplified r_d values and SRA back-calculated r_d values:

- The Seed SPT-based procedure is more conservative using SRA back-calculated r_d values than using simplified r_d values. However, the IB and the Youd SPT-based procedures are generally less conservative using SRA back-calculated r_d values than using simplified r_d values.
- The Seed (i.e., both SPT-and CPT-based) procedures is likely to predict more conservative results compared to the other two. The IB SPT-based procedure could be less conservative compared to the Seed and the Youd procedures.
- The difference in predicted FOS values between using simplified r_d and SRA back-calculated r_d values is generally smaller and more consistent for the Seed procedure than for the other two procedures.
- For the Seed et al. SPT-based procedure, the influence of $V_{s,12m}$ could be significant on triggering analyses, depending on whether $V_{s,12m}$ is measured or correlated and which correlation is used. In general, smaller values of $V_{s,12m}$ result in greater computed FOS values.

It is noteworthy that these two case histories are used to illustrate the relative conservatism of three liquefaction procedures between using simplified r_d values and SRA back-calculated r_d values. Generalizations of the conclusions about r_d should be cautious because results of the SRA are sensitive to input motion characteristics.

ACKNOWLEDGEMENT

The writers are grateful to University of California, San Diego Prof. A. Elgamal for providing ground motion array data at PIDA site.

REFERENCES

Bennett, M. J., McLaughlin, P. V., Sarmiento, J., and Youd, T. L. (1984) *Geotechnical investigation of liquefaction sites, Imperial Valley, California*, U.S. Geological Survey Open File Report, 84 – 252, 103p.

Cetin, K. O., Seed, R. B., Kiureghian, A. D., Tokimatsu, K., Harder, L. F., Kayen, R. E., Moss, R. E. S., (2004) "Standard Penetration Test-Based Probabilistic and Deterministic Assessment of Seismic Soil Liquefaction Potential." *Journal of Geotechnical and Geoenvironmental Engineering*, ASCE, 130 (12), 1314 - 1340.

DeJong, J. T. (2007) *Site characterization – guidelines for estimating Vs based on in-situ tests, stage 1 – interim report*, Department of Civil and Environmental Engineering, University of California, Davis.

Elgamal, A. –W., Zeghal, M., and Parra, E. (1996) "Liquefaction of reclaimed island in Kobe, Japan." *Journal of the Soil Mechanics and Foundations Division*, ASCE, 122 (1), 39 – 49.

GeoMotions. (2009) *SHAKE2000 – A computer program for the 1-D analysis of geotechnical earthquake engineering problems, User's Manual*, Lacey, Washington.

Holzer T. L., Youd, T. L., and Hanks, T. C. (1989) "Dynamics of Liquefaction during the Superstition Hills Earthquake (M = 6.5) of November 24, 1987." *Science*, 244, 56 – 59.

Idriss, I. M. (1999) "An update to the Seed-Idriss simplified procedure for evaluating liquefaction potential." *Proceedings of TRB Workshop on New Approaches to Liquefaction*, Publication No. FHWA-RD-99-165, Federal Highway Administration.

Idriss, I. M., and Boulanger, R. W. (2008) *Soil liquefaction during earthquakes*, Earthquake Engineering Research Institute MNO-12, Oakland, California.

Imai, T., and Tonouchi, K. (1982) "Correlation of N-value with S-wave velocity and shear modulus." *Proceedings of the 2nd European Symposium of penetration testing*, Amsterdam, 57 – 72.

Moss, R. E. S., Seed, R. B., Kayen, R. E., Stewart, J. P., Der Kiureghian, A., and Cetin, K. O. (2006) "CPT-based probabilistic and deterministic assessment of in situ seismic soil liquefaction potential." *Journal of Geotechnical and Geoenvironmental Engineering*, 132 (8), 1032 - 1051.

Seed, H. B., and Idriss, I. M. (1971) "Simplified procedure for evaluating liquefaction potential." *Journal of the Soil Mechanics and Foundations Division*, ASCE, 97 (9), 1249 – 1274.

Seed, H. B., Idriss, I. M., and Arango, I. (1983) "Evaluation of liquefaction potential using field performance data." *Journal of Geotechnical Engineering*, 109 (3), 458 – 482.

Sisman, H. (1995). *The relation between seismic wave velocities and SPT, pressuremeter tests*, MSc Thesis, Ankara University (in Turkish).

Youd, T. L., and Carter, B. (2003) *Influence of soil softening and liquefaction on response spectra for bridge design*, Utah Department of Transportation, Report No. UT-03.07, Salt lake City, Utah.

Youd, T. L., Idriss, I. M., Andrus, R. D., Arango, I., Castro, G., Christian, J. T., Dobry, R., Liam Finn, W. D., Jr. Harder, L. F., Hynes, M. E., Ishihara, K., Koester, J. P., Liao, S. S. C., Marcuson III, W. F., Martin, G. R., Mitchell, J. K., Moriwaki, Y., Power, M. S., Robertson, P. K., Seed, R. B., Stokoe II, K. H. (2001) ''Liquefaction resistance of soils: summary report from the 1996 NCEER and 1998 NCEER/NSF workshops on evaluation of liquefaction resistance of soils.'' *Journal of Geotechnical and Geoenvironmental Engineering*, 127 (10), 817–833.

Youd, T. L., and Wieczorek, G. F. (1984) *Liquefaction during the 1981 and previous earthquakes near Westmorland, California*, U.S. geological Survey Open-File Report No. 84 – 680.

Evaluating bias of liquefaction-induced settlement methods for performance-based design

H. Hayati[1], and R. E. S. Moss[2]

[1]Post Doctoral Researcher, Department of Civil and Environmental Engineering, California Polytechnic State University, San Luis Obispo, CA, 93407; PH (805) 756-1370; email: hhayati@calpoly.edu
[2]Asst. Prof., Department of Civil and Environmental Engineering, California Polytechnic State University, San Luis Obispo, CA, 93407; PH (805) 756-6427; email:rmoss@calpoly.edu

ABSTRACT

Liquefaction-induced ground settlement can control the foundation design in seismic areas. SPT and CPT-based semi-empirical methods to estimate such settlements primarily use post-liquefaction volumetric strain as measured in cyclic triaxial or simple shear tests. While a good understanding of laboratory measured post-liquefaction volumetric strain has evolved within the past two decades, predicted settlements show a significant scatter from observed settlements. A database of ground performance data from past earthquakes, including cases with observed ground settlements and cases with no ground settlement, has been complied for the purpose of this study. A good number of cases in this settlement database have been investigated for first time. Cases with significant lateral spreading or excessively large settlements were excluded in order to focus on the small to medium settlement range where performance-based design is feasible. This data shows that the semi-empirical methods consistently overestimate ground settlements for the practical settlement range of less than 0.2 m. The total error of settlement prediction model is presented in a probabilistic manner.

INTRODUCTION

Current standard of practice for prediction of liquefaction-induced settlement is based on semi-empirical methods. Most semi-empirical methods rely on both laboratory testing and field case histories. These methods typically include summation of volumetric strain caused by post-liquefaction reconsolidation with depth. The basic assumption is that liquefaction-induced settlement occurs as a result of post-liquefaction reconsolidation. Excess pore water pressure built up during undrained seismic loading will be followed by consolidation under *in situ* effective stress. Settlement can be developed even in partially liquefied soils when excess pore water pressure does not exceed *in situ* effective stress.

Performance of semi-empirical methods has been evaluated in several past studies using real settlement case history data. Regardless of what volume strain model being employed, predicted settlements show a significant scatter from observed

settlements. It is hypothesized that this scatter, currently lumped into a random error, can be broken down at least in part into systematic errors. A summary of suggested volume strain models and previous data compilation efforts are presented in this paper. Also presented in this paper is a database of ground performance during past earthquakes compiled for the purpose of this research. Cases investigated for this database were carefully screened to exclude sites with significant lateral spreading, excessive large settlements, or sites where settlement recordings were ambiguous or under contention. Also, sites with no liquefaction ground failure are included. These cases are used to estimate liquefaction-induced settlements corresponding to different probabilities of exceedance.

PREVIOUS STUDIES

Undrained cyclic laboratory tests including cyclic triaxial, torsional and simple shear tests under uni- and multi-directional conditions have been employed to quantify volumetric strains (e.g., Lee and Albaisa 1974, Yoshimi et al. 1975, Nagase and Ishihara 1988, Shamoto et al. 1996, Wu and Seed. 2004, and Cetin et al. 2009). These laboratory tests cover a wide range of relative densities, sand types, lateral strain and loading conditions. Two variables are typically required to read volume strain from a compatible chart; relative density (or equivalent SPT blow count) and seismic demand. Zhang et al. (2002) extended the SPT-based procedure proposed by Ishihara and Yoshimine (1992) to CPT measurements. A good discussion of test conditions and results of previous studies is presented in Shamoto et al. (1996) and Wu and Seed (2004).

Based on above studies, a good understanding of reconsolidation volume strains has evolved during past decades. However, estimation of settlement from volume strains has been performed in disparate ways. The common methods include: summation of volume strain with depth, weighted summation of volume strain with depth, and critical layer summation in which the critical liquefiable layer(s) are selected and volume strain is integrated over those specific layers. Most semi-empirical procedures in literature use strain summation with depth.

Based on cyclic simple shear tests, Wu and Seed (2004) proposed a procedure for level ground sites even where significant horizontal displacement was reported. To account for settlement induced by deviator deformations, they suggested adding 15% of estimated lateral spreading displacement to calculated settlement to obtain the total settlement. Wu and Seed (2004) evaluated the performance of the proposed procedure along with some other semi-empirical procedures in predicting the settlement of 57 case histories with known observed settlements during the past 7 earthquakes. Most of the predicted settlements fall between 0.5 and 2 times the observed settlements. Wu and Seed's (2004) procedure provides the least bias and standard error with respect to others.

Cetin et al. (2009) presented probabilistically based post-cyclic volumetric strain curves with corresponding standard error term. The procedure based on these set of charts is similar to rest of procedures other than it involves applying a weight factor to capture the larger contribution of soils in shallower depth in total settlement. The weight factor is a linear function versus depth, is equal to one at surface and becomes

zero at depth of 18m. Cetin et al. (2009) compiled a database of 49 ground settlement case histories from seven different earthquakes to check the performance of the proposed model along with some other models. Although the database included cases from level ground sites, a significant fraction of data came from sites with significant lateral displacement exceeding 0.5 m. The comparison of models reveals that the Cetin et al. (2009) procedure for settlement predictions provides the best fit for observed values. It appears that applying the depth weight factor reduces the scatter of data.

DATABASE

As discussed above several studies (e.g., Wu and Seed 2004, Cetin et al. 2009) have evaluated performance of existing semi-empirical methods for estimation of liquefaction-induced settlements. While applying a weight factor to volumetric strain was shown to slightly reduce the scatter of predicted settlements from observed values (Cetin et al. 2009) the scatter is still significant. In addition, there are some biases in the selection of settlement case histories in previous studies which raises doubts regarding performance of the prediction models. These include:

1) neglecting non-liquefaction sites when developing the methods,
2) including sites with significant lateral spreading in the vertical settlement database, and
3) not differentiating between large and small settlements which likely are induced by different mechanisms.

Whereas liquefaction triggering curves have been developed using a regression of both liquefied and non-liquefied cases, existing semi-empirical procedures to estimate liquefaction-induced settlement have been solely based on liquefied sites. All previous studies have only focused on how well current models predict observed settlement, and no study has attempted to answer how well settlement is predicted for no liquefaction cases. This has led to a conservative bias in settlement estimations.

The settlement mechanism at sites with large lateral displacements is likely different because void ratio approaches critical void ratio in order to produce such large displacements. Settlement at these sites cannot be explained solely by volumetric strains. Also, physical phenomena driving excessively large settlements is likely different than reconsolidation volumetric settlements. To investigate these biases, a database of liquefaction–induced ground settlement cases and no liquefaction cases was compiled for the purpose of this study. The following criteria were used to select settlement cases:

A. Level-ground site condition (slopes less than gradient5% or qualitatively described as a level ground site).
B. No lateral displacement exceeding the smaller of; half the vertical settlement or 0.1 m. SPT or CPT profiles versus depth are in close proximity (within a few meters) to where settlement observation/no-observation was made. If multiple SPT/CPT at a site are within a similar geologic unit, the average settlement obtained by all SPT/CPTs are assumed representative of that unit.
C. No vertical displacement exceeding 0.2 m.
D. One data point is assigned per site unless different geologic conditions or significantly different ground performance was observed. Thus, it was

required to have a consistent observation of ground performance for each case. (For example, in Charleston peninsula, SC, three data points were assigned for three zones of high, moderate and low liquefaction potential).

The resulting database is composed of 24 liquefaction-induced settlement or no liquefaction cases from 8 different earthquakes. A summary of cases are presented in Table 1. Current database includes 16 cases that were investigated for the first time. It also includes cases compiled by Wu and Seed (2004) and Cetin et al. (2009), but excludes the ones with significant lateral displacement or excessive settlement. Some of the cases investigated in previous studies were combined into single cases here as they belong to the same site with a similar geologic conditions and performance behavior.

Table 1: Settlement cases compiled for this study.

Earthquake, M_w	Site and location	References
1886 Charleston, 7.1	Zones of high, moderate and low liquefaction potential, Charleston, SC	Hayati and Andrus (2008)
	Clemson Research and Education Center, Near Charleston, SC, USA	Hayati (2009)
1964, Niigata, 7.5	Agano River, Niigata, Japan	Ishihara and Yoshimine (1992), Cetin et al. (2009)
1968 Tokachioki, 7.9	Paper manufacturing plant, P1,P4, P6, Hachinohe, Japan	Ohsaki (1970), Tokimatsu and Seed (1987), Cetin (2000)
1978 Miagiken-Oki, 7.4	Arahama sewage plant,Watari town, Japan	Tahno and Yasuda (1981), Cetin (2000)
1987 Edgecumbe, 6.5	Whakatane Board Mill- Saw Mill; Brady Farm (BDY004), Bay of Plenty, New Zealand	Christensen (1995)
1989 Loma Prieta, 6.9	Lower eastern part, Western part, Central part, Marina District, CA	Bennett (1990), Bardet and Kapuskar (1991), Zhang et al. (2002)
	Zone 1, Zone 2, Treasure Island[1], CA, USA	Power et al. (1998), Hryciw (1991), Zhang et al. (2002)
	Downtown Santa Cruz, CA, USA	Hryciw (1991)
	MBARI-Technology building, Moss Landing, Monterey Bay, CA, USA	Boulanger et al. (1997)
	Island Dike, Alameda Bay Farm, CA, USA	Kayen et al. (1992)
	Richmond Marine Terminal No.3, Port of Richmond, CA	Kayen et al. (1992)
1994 Northridge,6.7	North of crack, South of crack, Simi Valley, CA	Abdel-Haq et al. (1998)
1999 Kocaeli, 7.4	Site C3[2], Adapazari, Turkey	Bray et al. (2000), [3]
1999 Chi-Chi, 7.6	Yuanlin city area,Wufeng city area,YL-C19 , YL-C2 (Yuanlin), DN-1 (Dounan), Taiwan	Juang et al. (2005), [4]

[1] Settlement observation were made at location away from Island perimeter with negligible lateral spreading movements
[2] Sand boils, settlements, and lateral spreading were observed in the area and around adjacent buildings, however, building C3 did not undergo under any settlement , neither were sand boils were observed around it.
[3] <http://peer.berkeley.edu/publications/turkey/adapazari/index.html>
[4] <http://www.ces.clemson.edu/chichi/TW-LIQ>

Data pairs of computed and observed settlements are plotted in Figure 1 along with 1:1, 1:2, and 2:1 lines. Settlement calculations were made using Ishihara and Yoshimine (1992) volume strain charts and by summation of strain with depth. Settlement calculations for Marina District and Treasure Island were adopted from Zhang et al. (2002). Settlement calculations for Simi Valley were adopted from Abdel-Haq and Hryciw (1998). Settlement calculations for Agano River site in Niigata were adopted from Ishihara and Yoshimine (1992).These results show that for settlements under 0.2 m, the predictions consistently overestimate the actual settlement. In particular, settlement is predicted for the no liquefaction cases.

This data can be used for deterministic and probabilistic design purposes. The computed settlement model based on using Ishihara and Yoshimine (1992) for volume strain charts and integrating strain with depth is considered to be associated with systematic and random errors, as expressed by following equation:

$$S_{ci} = S_{oi} + \varepsilon_0 + \varepsilon_{1i} \quad (1)$$

Where S_{ci} is the i^{th} computed settlement, S_{oi} is the i^{th} observed settlement, ε_0 is the systematic error, and ε_{1i} is the random error in i^{th} observation. Based on 24 data points presented in Figure 1, the mean and standard deviation of $S_c - S_o$, are 10.5 cm and 7.9 cm respectively. This mean value represents the systematic error or model bias (ε_0), but considering the large coefficient of variation, care should be exercised when using this for deterministic approaches.

Quantifying the probability distribution of S_c–S_o values enables computing settlement for different probabilities of exceedance. Considering that the S_c–S_o values are positive and skewed, a lognormal distribution was fit to the data. The probability plot in Figure 2 shows that the lognormal distribution provides a reasonable fit. Listed in Table 2 are S_c–S_o values corresponding to different probabilities of exceedance. For example, probability of S_c–S_o exceeding 1.5 cm is 95%. This means the probability of S_c–S_o < 1.5 cm, or S_c–1.5 cm < S_o, is 5%. Thus, to obtain settlement with 5% probability of exceedance, 1.5 cm should be subtracted from computed settlement. Note: these corrections are appropriate for computed settlements based on integration of volume strain (Ishihara and Yoshimine, 1992) versus depth.

These results contradict the previous settlement studies in which computed settlement used to fall within 0.5 to 2 times of the observed settlements, that is, a significant random error with no obvious bias. The contradiction comes about due to including data from no liquefaction sites and separating large settlement from small and medium settlement; this we believe is dictated by the different physical mechanisms driving the two settlement categories. For small to medium settlements under 0.2 m, reconsolidation is most likely the major driving cause. Settlement overestimation in this range can be explained by considering the non-linear behavior of liquefied layers on site response. Soil liquefaction causes stiffness degradation and higher attenuation that is not captured with an equivalent linear total stress site response analysis. This effect reduces ground accelerations to values smaller than those computed using simplified procedures in liquefaction analysis.

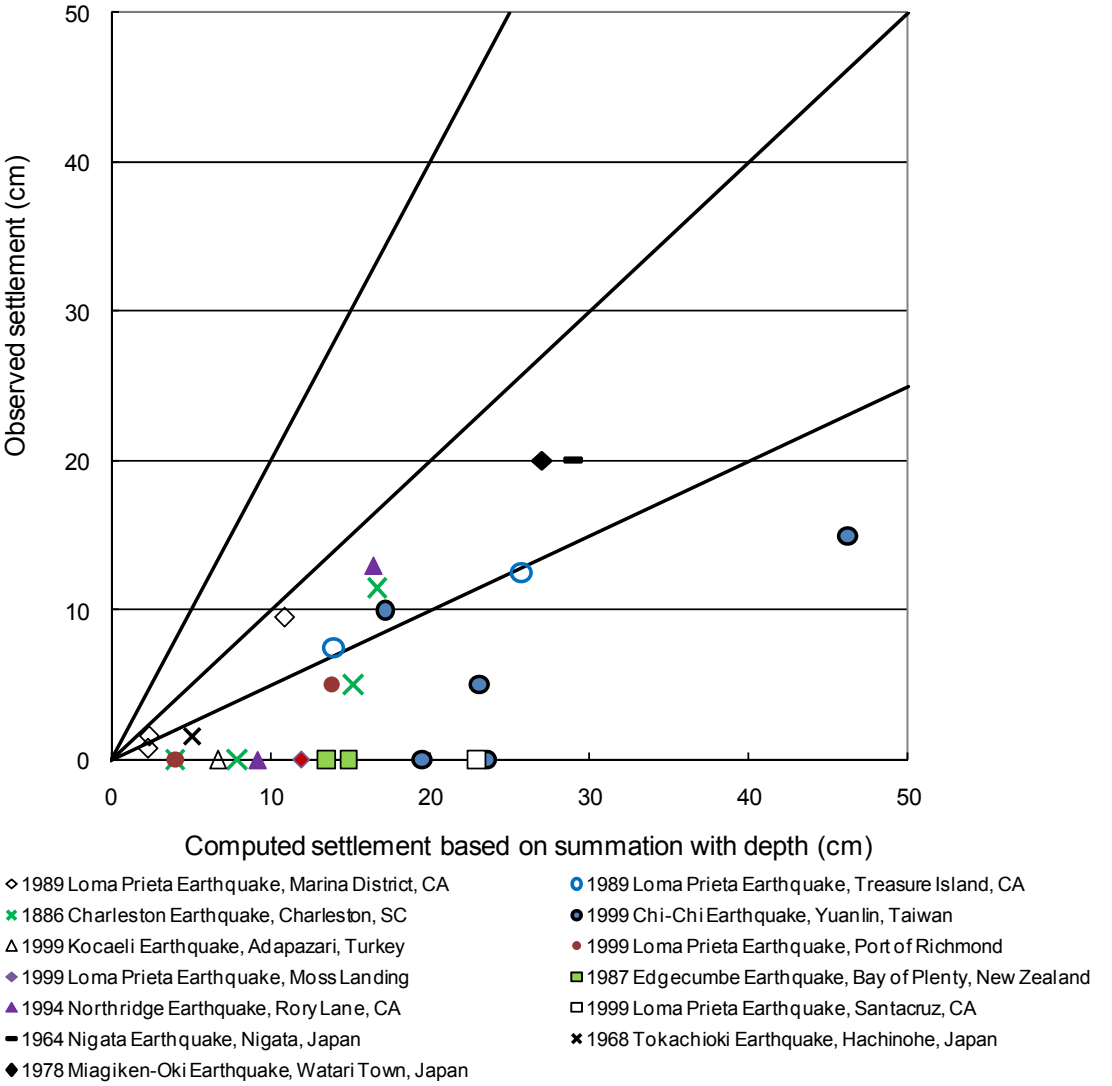

Figure 1. Shown are the 24 observed cases versus computed settlement.

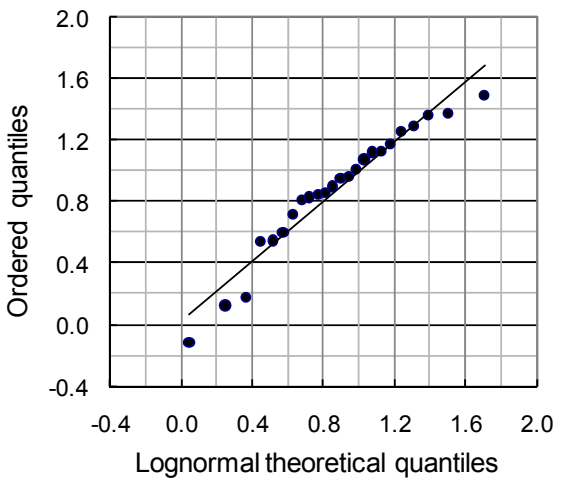

Figure 2. Lognormal probability plot for S_c - S_o values, S_c and S_o in cm.

Table 2: Probability of settlement exceedance

Probability of exceedance	$S_c - S_o$ (cm, Lognormal)
99	+0.8
95	+1.5
90	+2.2
75	+3.9
50	+7.5

CONCLUSIONS

Current practice for prediction of liquefaction-induced settlement is primarily based on summation of volumetric strain caused by post-liquefaction reconsolidation with depth. While reconsolidation volumetric strain has been carefully measured in laboratory tests, predicted settlements show significant scatter from observed settlements. A database of ground performance from past earthquakes, compiled for the purpose of this research, reveals that small to moderate (< 0.2 m) settlements are consistently overestimated. Presented is the total error of predicted settlement corresponding to different probabilities of exceedance. These results show there is a significant bias in liquefaction-induced settlement predictions when following existing methods.

REFRENCES

Abdel-Haq, A., and Hryciw, R.D. (1998). "Ground settlement in Simi Valley following the Northridge earthquake," *Journal of Geotechnical and Geoenvironmental Engineering*, 124(1), 80-89.

Bardet, J.P., and Kapuskar, M. (1991). "Site investigation of the Marina District of San Francisco in September 1990," *Report to NSF*, USC.

Bennett, M.J. (1990). "Ground deformation and liquefaction of soil in the Marina District. Chapter D of Effects of the Loma Prieta Earthquake on the Marina District, San Francisco, California," *U.S.G.S. Open-File Report 90–253*, U.S. Geological Survey, Reston, VA, D1–D36.

Boulanger, R. W., Mejia, L. H., and Idriss, I. M. (1997)."Liquefaction at Moss Landing during Loma Prieta Earthquake."*Journal of Geotechnical and Geoenvironmental Engineering*, 123(5), 453–467.

Bray, J. D., Stewart, J. P. (2000). "Damage patterns and foundation performance in Adapazari", in Kocaeli, Turkey Earthquake of August 17, 1999," *Reconnaissance Report, Earthquake Spectra*, 16 (Suppl. A), 163-189.

Cetin, K. O. (2000). "Reliability-based assessment of seismic soil liquefaction initiation hazard," *Ph. D. Dissertation*, University of California, Berkeley, CA.

Cetin, K. O., Bilge, H. T., Wu, J., Kammerer, A. M., and Seed, R. B. (2009). "Probabilistic Model for the Assessment of Cyclically Induced Reconsolidation Volumetric Settlements," *Journal of Geotechnical and Geoenvironmental Engineering*, 135(3), 387-398.

Christensen, S. A. (1995). "Liquefaction of cohesionless soils in the March 2, 1987 Edgecumbe Earthquake, Bay of Plenty, New Zealand, and other earthquakes," *Research report*, Department of Civil Engineering, University of Canterbury, Christchurch, New Zealand.

Hayati, H. (2009). "Characterizing liquefaction resistance of aged sand deposits," *Ph.D. Dissertation*, Clemson University, Clemson, SC.

Hayati, H., and Andrus, R. D. (2008a). "Liquefaction potential map of Charleston, South Carolina based on the 1886 earthquake," *Journal of Geotechnical and Geoenvironmental Engineering,* 134(6), 815-828.

Hryciw, R.D. (1991). "Post Loma Prieta earthquake CPT, DMT and shear wave velocity investigations of liquefaction sites in Santa Cruz and on Treasure Island," *Final Report to the U.S.G.S.*, Reston, VA.Award No. 14–08–0001-G1865.

Ishihara, K., Yoshimine, M., (1992)."Evaluation of settlements in sand deposits following liquefaction during earthquakes," *Soils and Foundations*, 32(1), 173–188.

Juang, C. H., Yuan, H., Li, D. K., Yang, S. H., Christopher. R. A. (2005). "Estimating severity of liquefaction-induced damage near foundation," *Soil Dynamics and Earthquake Engineering*, 25(5), 403-411.

Kayen, R. E., Mitchell, J. K., Seed, R. B. , Lodge, A., Nishio, S., Coutinho, R. (1992). "Evaluation of SPT-, CPT-, and shear wave-based methods for liquefaction potential assessment using Loma Prieta data," *Proc.4thU.S.-Japan workshop on earthquake resistant design of lifeline facilities and countermeasures against soil liquefaction*, NCEER, May 27-29, 1992, Honolulu, HI.

Lee, K. L., and Albaisa, A. (1974). "Earthquake induced settlements in saturated sands," *Journal of Geotechnical Division*, 100(GT4), 387–406.

Nagase, H. and Ishihara, K. (1988)."Liquefaction-induced compaction and settlement of sand during earthquakes," *Soils and Foundations*, 28(1), 66-76.

Ohsaki, Y. (1970). "Effects of sand compaction on liquefaction during Tokachioki earthquake," *Soils and Foundations*," 10(2), 112-128.

Power, M. S., Egan, J. A., Shewbridge, S. E., Backer, J., and Faris, J. R. (1998)."Analysis of liquefaction-induced damage on Treasure Island. The Loma Prieta, California, Earthquake of October 17, 1989," *U.S.G.S.Prof.Paper 1551-B*, U.S. Geological Survey, Reston, VA. B87-B120.

Shamoto, Y., Sato, M., Zhang, J. M., (1996)."Simplified estimation of earthquake-induced settlements in saturated sand deposits," *Soils and Foundations*, 36(1), 39-50.

Tahno, I., and Yasuda, S. (1981). "Liquefaction of ground during the 1978 Miyagiken-Oki earthquake," *Soils and Foundations*, 21(3), 18-34.

Tokimatsu, K., Seed, H. B., (1987). "Evaluation of settlements in sands due to earthquake shaking," *Journal of Geotechnical Engineering*, 113(8), 861-878.

Wu, J. and Seed, R.B., (2004). "Estimation of liquefaction-induced ground settlement [casestudies],"*Proc,5th International Conference on Case Histories in Geotechnical Engineering*, Paper No. 3.09, New York, NY.

Yoshimi.Y, Kuwabara, F., and Tokimatsu, K. (1975)."One-dimensional volume change characteristics of sands under very low confining stresses," *Soils and Foundations*, 15(3), 51-60.

Zhang, G., Robertson, P. K., and Brachman, R. W. I. (2002). "Estimating liquefaction-induced ground settlements from CPT for level ground," *Canadian Geotechnical Journal*, 39(5), 1168–1180.

Estimating CSRs for Evaluating Liquefaction that are Consistent with Building Code Design Spectra

Aaron S. Bradshaw[1], Ph.D., P.E. and Russell A. Green[2], Ph.D., P.E.

[1]Assistant Professor, Department of Civil and Envionmental Engineering, University of Rhode Island, Kingston, RI 02881; PH (401) 874-2680; bradshaw@egr.uri.edu
[2]Associate Professor, Department of Civil and Environmental Engineering, Virginia Tech, Blacksburg, VA 24061; PH (540) 231-9826; rugreen@vt.edu

ABSTRACT

This paper presents a new method for estimating the Cyclic Stress Ratio (CSR) for evaluating liquefaction that is consistent with building code design spectra and thus considers all possible earthquake scenarios that impact the site. Many of the current building codes such as the International Building Code include seismic design spectra that are based on probabilistic seismic hazard analysis (PSHA) data. This means that the design spectrum for a given site is not the result of one earthquake scenario, but rather reflects the contributions from a range of earthquakes of various magnitudes and site-to-source distances that could impact the site. Therefore, to be consistent with current codes the analysis of liquefaction potential of the foundation soils at a particular site should consider all potential earthquake scenarios. In this way the risk assumed in the analysis of the foundation soils is commensurate with the level of risk assumed in the design of the overlying structure. The new method is outlined using an example from a site located in Providence, Rhode Island.

INTRODUCTION

Liquefaction potential is commonly evaluated in engineering practice using the simplified procedure, the state-of-practice implementation of which is summarized in Youd et al. (2001). In this procedure, the factor of safety against liquefaction for level ground is estimated at any depth in the soil profile from the following equation:

$$FS = \frac{CRR \cdot K_\sigma}{CSR_{M7.5}} \tag{1}$$

where CRR = Cyclic Resistance Ratio, $CSR_{M7.5}$ = Cyclic Stress Ratio adjusted to a magnitude (M) 7.5 earthquake, and K_σ = factor that adjusts CRR to 1 atm effective vertical confining stress. The CRR describes the resistance of the soil to liquefy and is typically estimated from semi-empirical correlations related to Standard Penetration Test (SPT) blow counts, Cone Penetration Test (CPT) resistance, or *in situ* shear wave velocity. The CSR describes the cyclic loading on the soil from the earthquake

and is defined by the following expression:

$$CSR_{M7.5} = 0.65 \cdot \frac{\tau_{\max}}{\sigma'_{v0}} \cdot \frac{1}{MSF} \quad (2)$$

where: τ_{max} = maximum shear stress estimated at a specified depth; σ'_{v0} = initial effective overburden stress at a specified depth; and *MSF* = magnitude scaling factor.

Equation 2 requires estimation of the maximum shear stress and earthquake magnitude. Site response analyses can be performed to evaluate the maximum shear stress within the soil profile for a given magnitude event. However, this requires the selection of acceleration time histories that are representative of the magnitude and site-to-source distance of the design level event(s). There is still debate among the geotechnical engineering community as to how these records should be selected and/or scaled, and a discussion of these techniques is beyond the scope of this paper. Rather, this paper presents a new method for calculating *CSR* that is consistent with the building code design spectrum at the site of interest and thus considers all possible earthquake scenarios that impact the site. The method is illustrated using an example for a site located in Providence, Rhode Island. First, a description of the study site is given, followed by a detailed outline of the analysis procedure. The analysis results are subsequently presented along with conclusions.

DESCRIPTION OF THE STUDY SITE

A site investigation program was completed at the study site that included rotary wash borings with Standard Penetration Tests (SPT) as well as Seismic Cone Penetration Tests (SCPT). A donut hammer was used to perform the SPT, which provided a measured efficiency of 37%. A representative profile of the soil conditions at the study site including measured SPT blow counts (*N*), cone tip resistance corrected for pore pressure effects (q_t), and shear wave velocity (V_S) is shown in Figure 1. The site consists of approximately 4 to 10 m (13.1 to 32.8 ft) of sand and gravel fill underlain by a thick layer of non-plastic silt. The water table was encountered at a depth of about 1.6 m. The silt was deposited as glacial lake sediments during the last glacial retreat and is therefore characterized by seasonal varves. Grain size analyses of bulk samples indicate that the silt is composed of about 95% fines (<0.075 mm) and is non-plastic and thus classified as ML according to the Unified Soil Classification System (USCS). Previous geotechnical explorations (GZA, 1998) indicate that the silt is underlain by a very thin layer of till overlying bedrock. The depth to bedrock at the site ranges from about 36 to 61 m (120 to 200 ft) below the ground surface and the rock consists of a sandstone conglomerate.

ANALYSIS PROCEDURE

The proposed method for evaluation of *CSR* at a site involves four steps including: (1) determining the building code design spectrum for the site, (2) selecting ground motion time histories, (3) determining the amplitude scaling factors,

and (4) performing site response analyses and *CSR* calculations. The details of each step are outlined below.

Step 1: Determining the Building Code Design Spectrum for the Site. To evaluate *CSR* it is necessary to establish the seismic design motions for the site. For the design of new buildings, the 2000 Edition of the National Earthquake Hazard Reduction Program Provisions (BSSC 2000) constructs its design spectrum using 0.2 and 1.0 s 5% damped, spectral accelerations having a 2% probability of exceedance in 50 years (i.e., motions having ~2,500 year return period). This approach has also been adopted by the 2006 International Building Code (IBC) (ICC 2006). In 2002, the United States Geological Survey (USGS) issued the seismic hazard maps for rock motions that accompany the 2006 IBC codes.

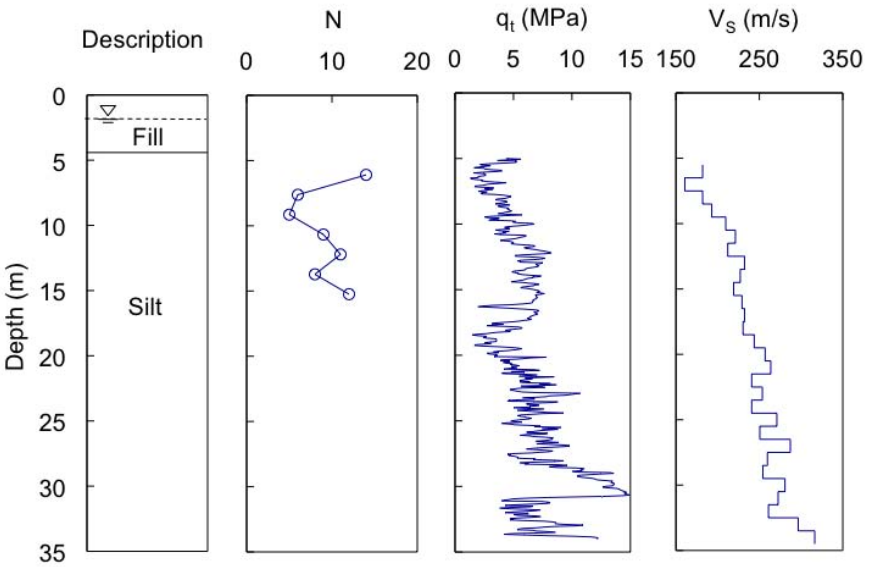

Figure 1. Representative geotechnical profile obtained from the site investigation.

The building code design spectrum for a firm rock condition (Site Class B) at the Providence site is shown in Figure 2, where the 0.2 and 1.0 second spectral accelerations (SA_{uhs}) having a 2% probability of exceedance in 50 years are shown as blue dots. It is important to emphasize that the building code design spectrum is not a response spectrum from an individual earthquake motion. Rather, it represents the combined effect of all possible seismic sources of engineering interest in the vicinity of the site, usually within a few hundred kilometers.

The deaggregation of the probabilistically determined spectral accelerations provides a breakdown of the percent contribution to the spectral acceleration by earthquake magnitude (M) and site-to-source distance (R). In active tectonic regions such as the western US, major faults are clearly identifiable and typically dominate the seismic hazard of the region. On the contrary, in the northeastern US, few faults have been identified and thus the seismic sources are typically represented as areal source zones that potentially encompass multiple unidentified and uncharacterized faults. The deaggregation of the ~2500 yr, 5% damped, 0.2 and 1.0 s spectral

accelerations (Site Class B) at the site (Figure 2) is shown in Table 1. The columns of the table can be used to identify the events that contribute the most to the seismic hazard at a particular oscillator period.

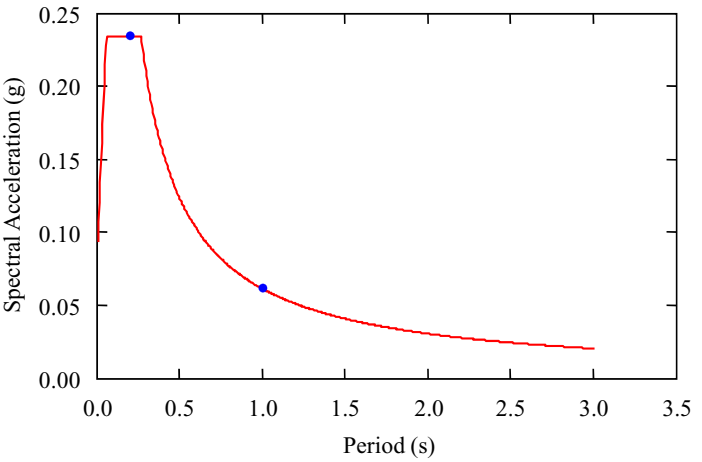

Figure 2. Building Code Design Spectrum (Site Class B) for the study site obtained (BSSC 2000).

Table 1. Seismic deaggregation for the 2,500-year rock motions at the study site, compiled from data obtained from USGS (2010).

M	R (km)	Contribution to Hazard, *C(T)* (%)	
		T=0.2 s	T=1.0 s
4.5 to 6	0 to 50	34.3	7.9
4.5 to 6	>50	9.6	4.4
6 to 7	0 to 10	0.0	0.0
6 to 7	10 to 50	11.3	8.8
6 to 7	50 to 100	10.1	8.7
6 to 7	>100	13.8	28.6
>7	0 to 10	0.0	0.0
>7	10 to 50	3.3	3.2
>7	50 to 100	4.8	4.7
>7	>100	12.2	32.9

As is characteristic of the results of probabilistic seismic hazard analyses in the northeastern US, the shorter period spectral accelerations are largely influenced by near-field (< 50 km), small magnitude (M4.5-6) events. In contrast, longer period spectral accelerations are more influenced by far-field (>100 km), large magnitude (M7+) events. As shown by Table 1, for 0.2 s, the largest contribution at the Providence site comes from local earthquakes having M<6 and occurring at site-to-source distances of less than 50 km. However, the distribution changes as the period increases from 0.2 to 1.0 s, where the largest contributions come from M6-7 and M>7 earthquakes occurring at a site-to-source distances of >100 km. These larger events originate from the Charlevoix Seismic Zone, which is located on the St. Lawrence River about 100 km downstream from Quebec City.

Step 2: Select Ground Motion Time Histories. Ground motion time histories are necessary to perform the site response analyses. The motions should be representative of the rock outcrop motions that are anticipated at the site. Although there has been a history of earthquakes in the Northeast, there are limited recorded ground motions from earthquakes of engineering interest (i.e., M ≥ 4.5) in the region. Perhaps the only sizable events for which motions were recorded were the 1988 M5.9 Saguenay earthquake and aftershocks, which occurred just south of Chicoutimi, Quebec, Canada in a relatively aseismic region 75 km north of the Charlevoix Seismic Zone.

In lieu of recorded intra-plate earthquake motions, "scaled" records from a database compiled by McGuire et al. (2001) were used in this study. McGuire et al. scaled actual motions recorded in active seismic regions (i.e., inter-plate motions) using response spectral transfer functions that related active seismic region motions to stable continental region motions (i.e., intra-plate motions). The transfer functions were based on a single-corner, point source model (e.g., McGuire et al., 2001; Boore, 1983; Silva and Lee, 1987). The authors prefer to use "scaled" motions over purely synthetic ones because the scaled motions preserve many of the characteristics of the original recorded motions to include the distribution of energy over the time of shaking. An example of a scaled time history is shown in Figure 3a for a magnitude 5.4 event at a site-to-source distance of 31 km.

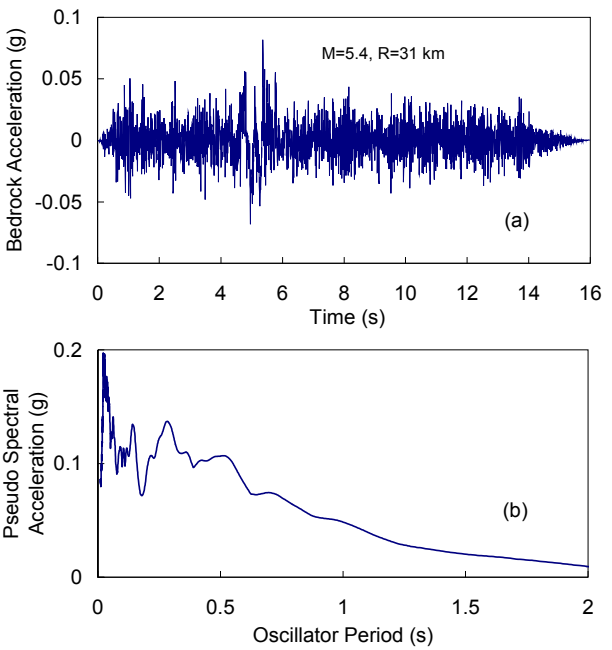

Figure 3. Example of (a) rock outcrop time history and (b) corresponding response spectrum used in determining the *CSR*.

McGuire et al. (2001) binned the scaled rock motions according to magnitude and site-to-source distance. In general, motions recorded on profiles having an average shear wave velocity of the upper 30 m (V_{s30m}) greater than 360 m/sec were

classified as "rock motions." This criterion includes NEHRP Site Classes A, B, and C (BSSC 2000). McGuire et al. subdivided the motions into 10 M-R bins, each containing at least 30 records. The bins were: (1) M 5-6, R= 0-50 km; (2) M 5-6, R= 50-100 km; (3) M 6-7, R= 0-10 km; (4) M 6-7, R= 10-50 km; (5) M 6-7, R= 50-100 km; (6) M 6-7, R= 100-200 km; (7) M 7+, R= 0-10 km; (8) M 7+, R= 10-50 km; (9) M 7+, R= 50-100 km; (10) M 7+, R= 100-200 km. Note that M is defined using the moment magnitude scale and R as the closest distance to the fault.

Step 3: Determine Amplitude Scaling Factors. The building code design spectrum shown in Figure 2 represents the contribution of all possible earthquake scenarios and forms the basis of the design spectrum specified in the NEHRP provisions and IBC. Therefore, rather than assuming *a priori* which events control the liquefaction hazard (e.g., modal events) as is done in a deterministic approach, the $CSR_{M7.5}$ in this study is computed in a manner consistent with the design spectrum. Therefore, the ground motion time histories selected from the database must be scaled a second time to adjust the amplitudes to be consistent with the building code design spectrum.

To determine the scaling factors, five records from each of the ten magnitude/site-to-source distance bins shown in Table 1 were selected from the time history database for a total of fifty records. The 5% damped pseudo acceleration response spectra were computed for each of the fifty time histories, an example of which is shown in Figure 3b. For each set of five records within a given M and R bin, the median values of the 0.2 and 1.0 s pseudo spectral accelerations (SA_{median}) were calculated assuming a lognormal distribution, which is consistent with many of the ground motion predictive equations. The median values are listed in Table 2.

Table 2. Median values of pseudo spectral acceleration for the selected time histories used in this study.

M	R (km)	$SA_{median}(T)$ (g)	
		T=0.2 s	T=1 s
4.5 to 6	0 to 50	0.19	0.01
4.5 to 6	>50	0.13	0.01
6 to 7	0 to 10	0.82	0.19
6 to 7	10 to 50	0.22	0.05
6 to 7	50 to 100	0.09	0.03
6 to 7	>100	0.11	0.03
>7	0 to 10	1.40	0.43
>7	10 to 50	0.53	0.08
>7	50 to 100	0.26	0.06
>7	>100	0.09	0.05

The deaggregation values in Table 1 were used as the basis to compute a weighted average (SA_{avg}) of the median spectral accelerations for each of the seven periods using the following equation:

$$SA_{avg}(T) = \sum_{i=1}^{10} C_i(T) \cdot SA_{median\ i}(T) \quad (3)$$

where C_i (T) = the percent contribution to the seismic hazard for the *i*th M-R bin at period T (Table 1), and $SA_{median\ i}$ (T) = median pseudo spectral acceleration for the *i*th M-R bin at period T. Amplitude scaling factors were then computed for 0.2 and 1.0 s using the following equation:

$$Amplitude\ Scaling\ Factor(T) = \frac{SA_{uhs}(T)}{SA_{avg}(T)} \quad (4)$$

where $SA_{uhs}(T)$ = pseudo spectral acceleration of the uniform hazard spectrum at period T (Figure 2), and SA_{avg} is given by Equation 3. The amplitude scaling factors are listed in Table 3. The amplitudes of the fifty time histories were then scaled using these factors at 0.2 and 1.0 s, and the motions were used in the site response analyses discussed in the next step.

Table 3. Amplitude scaling factors calculated for the Providence site.

Period (s)	0.2	1.0
Scaling Factor	1.41	1.58

Step 4: Perform Site Response Analyses and *CSR* Calculations

Site response analyses were performed using a modified version of SHAKE91 (Idriss and Sun 1992) to determine the maximum cyclic shear stress induced in the profile at various depths. The time histories were applied as outcrop motions at bedrock, which is at a depth of 49 m below the ground surface on average at the Providence site. The small strain shear modulus was estimated from the shear wave velocity data obtained using the seismic cone (Figure 1) and estimated bulk density values. Shear modulus and damping properties as a function of strain were estimated at various depths using empirical relationships developed by Ishibashi and Zhang (1993).

One hundred site response analyses were performed (i.e., 2 amplitude scale factors × 10 M&R bins × 5 time histories per bin = 100 analyses) and $CSR_{M7.5}$ profiles were computed for each using Equation 2. Figure 4 was used to estimate the magnitude scaling factor for each time history. Assuming log normal distributions, the medians of the $CSR_{M7.5}$ profiles from the site response analyses were then computed for the motions scaled to 0.2 and 1.0 s spectral accelerations.

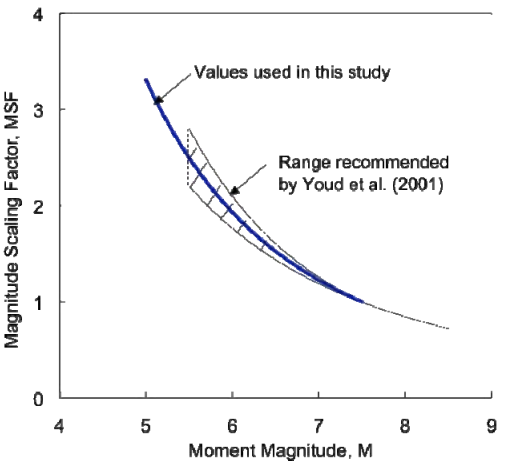

Figure 4. Magnitude scaling factor used in this study.

ANALYSIS RESULTS

The results of the analysis at the Providence site are shown in Figure 5 as profiles of $CSR_{M7.5}$ plotted with depth for the motions scaled to the 0.2 and 1.0 s spectral accelerations. The median values are shown at each period along with their respective standard deviations (σ). As shown in the figure, the $CSR_{M7.5}$ for the motions scaled to the 1.0 s spectral accelerations is higher than that for motions scaled to 0.2 s spectral accelerations. This implies that for this site longer period motions induce larger shear stresses in the profile than the higher frequency motions. Accordingly, the $CSR_{M7.5}$ for the motions scaled to the 1.0 s spectral accelerations should be used to evaluate the liquefaction potential at the site.

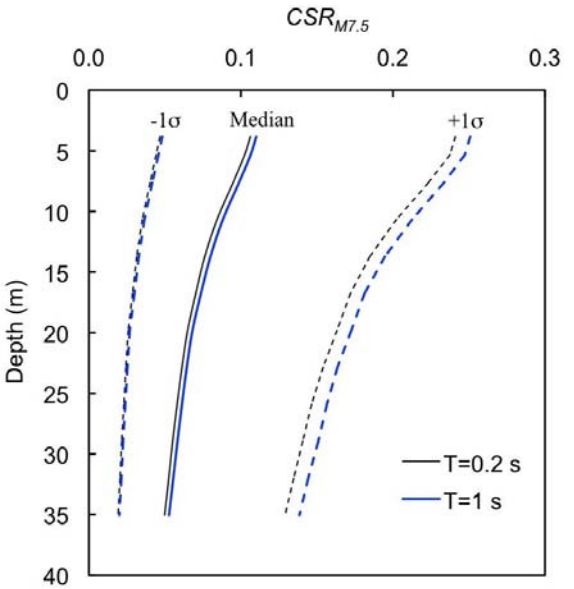

Figure 5. $CSR_{M7.5}$ profiles obtained from motions scaled to the 0.2 and 1.0 s spectral accelerations having a 2% probability of exceedance in 50 yrs.

SUMMARY AND CONCLUSIONS

A new method was presented for determining $CSR_{M7.5}$ that is consistent with the building code design spectrum at a given site. The method involved scaling bedrock time histories that are representative of the M and R earthquake scenarios identified in the deaggregation matrices for 0.2 and 1.0 s 5% damped spectral accelerations having an ~2500 yr return period. The amplitudes of the time histories were scaled to the 0.2 and 1.0 s spectral accelerations using a weighting scheme that is based on the percentages that the M and R earthquake scenarios contribute to the overall seismic hazard at the site, as determined from the deaggregation matrices. Site response analyses were performed to calculate *CSR* profiles for each scaled time history. Finally, the medians of the $CSR_{M7.5}$ profiles were calculated for the motions scaled to the 0.2 and 1.0 s spectral accelerations. For the site analyzed, the highest $CSR_{M7.5}$ profile occurred for the motions scaled to the 1.0 s spectral accelerations, implying that the longer period motions induce larger shear stresses in the profile than higher frequency motions. Accordingly, the $CSR_{M7.5}$ for T = 1.0 s should be used to evaluate liquefaction potential at this site. The advantage of the proposed method is that it considers the contributions of possible seismic hazards to a site and yields a $CSR_{M7.5}$ profile that is consistent with the building code design spectrum.

ACKNOWLEDGEMENTS

The participation of R. Green in this study was funded in part by NSF Grant Nos. CMMI 0962952 and 1030564. This support is gratefully acknowledged. However, any opinions, findings, and conclusions or recommendations expressed in this paper are those of the authors and do not necessarily reflect the views of the National Science Foundation.

REFERENCES

Boore D.M. (1983). "Stochastic simulation of high-frequency ground motions based on seismological models of the radiated spectra." *Bulletin of the Seismological Society of America*, 73(6), 1856-1894.

Bradshaw, A.S., Green, R.A., and Baxter, C.D.P. (2007). “Evaluation of Liquefaction Potential at a Silt Site in Rhode Island.” Civil Engineering Practice: Journal of the Boston Society of Civil Engineers Section, 22(1), 5-18.

Building Seismic Safety Council (BSSC) (2000). 2000 Edition, NEHRP Recommended Provisions for Seismic Regulations for New Building and Other Structures.

GZA (1998). Civic Center Interchange Modifications, Providence, Rhode Island. Report to the Rhode Island Department of Transportation by GZA GeoEnvironmental, Inc.

Idriss, I.M., and Sun, J.I. (1992). SHAKE91: A Computer Program for Conducting Equivalent Linear Seismic Response Analyses of a Horizontally Layered Soil

Deposits. Department of Civil and Environmental Engineering, University of California, Davis.

International Code Council (ICC) (2006). 2006 International Building Code.

Ishibashi, I., and Zhang, X. (1993). "Unified dynamic shear moduli and damping ratios of sand and clay." Soils and Foundations, 33(1), 182-191.

Kramer, S.L. (1996). Geotechnical Earthquake Engineering. Prentice Hall, New Jersey. P. 261.

McGuire, R.K., W.J. Silva, and C.J. Costantino (2001). Technical Basis for Revision of Regulatory Guidance on Design Ground Motions: Hazard- and Risk-consistent Ground Motion Spectra Guidelines. NUREG/CR-6728, US Nuclear Regulatory Commission, Washington, DC.

Silva W.J., and Lee, K. (1987). WES RASCAL Code for Synthesizing Earthquake Ground Motions. Report 24 State-of-the-Art for Assessing Earthquake Hazards in the United States, Miscellaneous Paper S-73-1, US Army Engineer Waterways Experiment Station, Vicksburg, MS.

United States Geological Survey (USGS) (2009). USGS Earthquake Hazards Program, Interactive Deaggregation, http://eqint.cr.usgs.gov/deaggint/.

Youd, T.L., Idriss, I.M., Andrus, R.D., Arango, I., Castro, G., Christian, J.T., Dobry, R., Finn, W.D.L., Harder, L.F., Hynes, M.E., Ishihara, K., Koester, J.P., Liao, S.S.C., Marcuson, W.F., III, Martin, G.R., Mitchell, J.K., Moriwaki, Y., Power, M.S., Robertson, P.K., Seed, R.B., and Stokoe, K.H., III. (2001). "Liquefaction Resistance of Soils: Summary Report from the 1996 NCEER and 1998 NCEER/NSF Workshops on Evaluation of Liquefaction Resistance of Soils." Journal of Geotechnical and Geoenvironmental Engineering, 127(10), 817-833.

Potential Differences between Time Series and Random Vibration Theory Site Response

Albert R. Kottke[1] and Ellen M. Rathje[2]

[1]Pacific Earthquake Engineering Research Center, University of California, Berkeley;
PH (612) 281-2259; Email: albert.kottke@gmail.com
[2]Department of Civil, Architectural, and Environmental Engineering, University of Texas, Austin;
Email: e.rathje@mail.utexas.edu

ABSTRACT

Response spectra at the surface of two sites are computed with equivalent-linear site response methods using time series and random vibration theory (RVT) input motions. The results indicate a potential for significant differences between the expected response spectrum computed using RVT and time series methods. Even under linear-elastic conditions (i.e., constant properties), the RVT method computes higher peaks and lower troughs in the ratio between the surface response spectrum and the input response spectrum when compared to the time series analyses. The differences between the RVT and time series analysis are dependent on the site characteristics. The implication of this study is that the results of an RVT site response analysis cannot be assumed to be representative of a time-series site response analysis.

INTRODUCTION

Site specific ground motions used in the assessment of seismic performance are computed using site response analyses that simulate the nonlinear response of the soil to earthquake ground shaking. In an analysis, the expected input motion is first estimated using a ground motion prediction equation and then characterized using either time series or random vibration theory (RVT). The use of RVT removes the time consuming process of selecting and scaling/modifying time series, and permits a statistically stable estimate of the expected surface response spectrum to be computed in one analysis – instead of the multiple time series analyses required due to motion-to-motion variability. While the RVT approach offers many advantages over the time series approach, there are few published validations of RVT based site response.

In the following study, linear and equivalent-linear site response simulations are conducted at three sites using simulated time series and RVT input motions. The relative differences in the spectral ratios are compared and factors governing the differences are identified.

RANDOM VIBRATION THEORY

Random vibration theory characterizes a motion by the amplitude of the Fourier amplitude spectrum (FAS) and the ground motion duration. No information regarding the phase of the motion is known, thus the complete time series cannot be computed. Instead, RVT allows for calculation of the expected peak value in the time domain using a combination of Parseval's theorem and extreme value statistics. Parseval's is used to relate the FAS to the root-mean-squared acceleration (a_{rms}) of the ground motion as follows:

$$a_{rms} = \sqrt{\frac{2}{T_{rms}} \int_0^\infty |X(f)|^2 \, df} = \sqrt{\frac{m_0}{T_{rms}}}$$

where T_{rms} is the duration of the time series motion, and $|X(f)|$ is the amplitude of the FAS at a frequency of f. A more simplified notion uses the zero-th moment (m_0), where the n-th moment is defined as:

$$m_n = 2 \int_0^\infty (2\pi f)^n |X(f)|^2 \, df$$

The peak acceleration (a_{max}) is related to a_{rms} by the peak factor ($PF = a_{max} / a_{rms}$). Cartwright and Longuet-Higgins (1956) derived an integral expression for the expected value of the peak factor in terms of the number of extrema (N_e) and the bandwidth (ξ) of the time series (Boore 2003):

$$E[PF] = \sqrt{2} \int_0^\infty (1 - (1 - \xi e^{-z^2})^{N_e}) \, dz$$

where N_e and ξ are based on the spectral moments (m_0, m_2, and m_4) of the FAS and the ground motion duration (T_{gm}):

$$\xi = \sqrt{\frac{m_2^2}{m_0 m_4}} \quad N_e = \frac{T_{gm}}{\pi} \sqrt{\frac{m_4}{m_2}}$$

The duration used in the calculation of the a_{rms} differs from the duration used in the calculation of N_e. When computing an oscillator response, Boore and Joyner (1984) recommend that the T_{rms} duration be increased to account for the extended duration.

ANALYTICAL MODELING

Site Profiles Analyzed. Site response simulations were performed for three sites: Turkey Flat (TF) near Parkfield, CA; Sylmar County Hospital (SCH) in Southern CA; and the Calvert Cliffs (CC) on the coast of Chesapeake Bay in MD. The TF site characteristics were based on data collected by Real et al. (2006). The velocity profile for the SCH site was based on the measurements made by Gibbs et al. (1999), but modified slightly to reduce the potential for large strains in the low-velocity surface (i.e., the shear-wave velocity of the surface layer was increased from 200 to 250 m/s). The CC site profile was based on data presented in the UniStar Nuclear Services (2007) Final Safety Analysis Report. Equivalent-linear analyses were performed using the SCH and CC sites. For these analyses, nonlinear curves were computed using the Darendeli (2001) empirical model and the reported index properties. The three different velocity profiles, shown in Figure 1, have similar velocities but different depths to bedrock. The site frequency, defined by the quarter wavelength ($f_s = 4H/\overline{V_s}$, where H is the height of the soil column and $\overline{V_s}$ is the time-averaged shear-wave velocity), corresponding to the TF, SCH, and CC sites are 4.8, 1.2 and 0.2 Hz, respectively.

Input Motions. The methods that are commonly used to define a ground motion for site response analysis include: scaled recorded motions, spectrally matched motions,

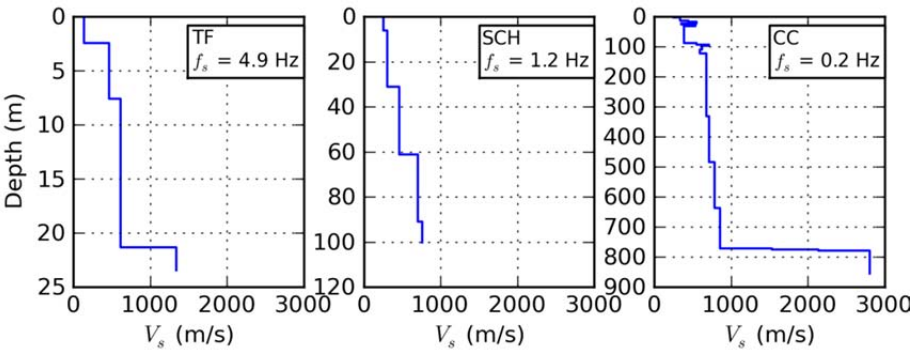

Figure 1. Shear-wave velocity (V_s) profiles for the TF (left), SCH (center), and CC (right) sites.

and synthetically generated motions. To minimize differences between the time series and RVT input motions, stochastically simulated time series were selected for these comparisons. The stochastic method computes an FAS based on seismological models that incorporate the effects of the source and the path. The RVT input motion is defined using the computed FAS and duration. The time series are simulated by using the program SMSIM which uses the same computed FAS to modify a windowed time series of white noise (Boore, 2003). Using these techniques, an RVT and 100 time series input motions were simulated for a magnitude 6.5 earthquake at a distance of 20 km. The peak ground acceleration (PGA) for this event was 0.17 g. Additionally, the motions were scaled up to PGA of 0.40 g by applying a scale factor of 2.35 so that a range of input intensities could be examined.

RESULTS

The stochastically simulated motions were propagated through the TF, SCH, and CC sites; first assuming the response of the soil is linear-elastic (LE) with 5% damping. The analyses were compared using the spectral ratio, which is defined as the ratio of the surface response spectrum to the input response spectrum. The relative difference between the time series and RVT analyses at a frequency f ($\delta_{SR}(f)$) is defined as follows:

$$\delta_{SR}(f) = \frac{S_{SR,RVT}(f) - \tilde{S}_{SR,TS}(f)}{\tilde{S}_{SR,TS}(f)}$$

where $S_{SR,RVT}$ is the spectral ratio computed using RVT and $\tilde{S}_{SR,TS}$ is the geometric mean of spectral ratios computed using the time series simulations.

Linear Elastic Analyses. The results of the TF site for the time series and RVT analyses are shown in Figure 2. The relative difference of the spectral ratio (δ_{SR}) between the RVT and median time series motions is less than 5% at most frequencies, with the largest differences (~8%) at frequencies of strong amplification (7.7 and 14 Hz). Similar results are observed in the response calculated for the SCH site (Figure 3) with the maximum relative difference of approximately 6% occurring at the site frequency (1.7 Hz). In the response of the CC site the RVT analysis is again relatively high at the site frequency (0.3 Hz), but the relative difference of 25% is more significant than for the other two sites (Figure 3). In addition to being relatively high at the site fre-

quency, the relative difference of RVT for the CC site is -12% at a frequency of 0.5 Hz. The spectral ratios for the CC site indicate a tendency for the RVT analysis to exaggerate the influence of the site and produce a response with higher peaks and lower troughs.

The results of the LE analyses indicate that the difference between RVT site response analysis relative to time-series analysis is dependent on the site characteristics. The site characteristics are reflected in the site transfer function used in the wave propagation analysis. The LE transfer functions for the three sites are shown in Figure 3 and these transfer functions were used for both the time series and the RVT analyses. Figure 3 shows that the transfer function of the TF site has a strong narrow peak at 14 Hz; the SCH site has a less strong, but wide, peak at 1.7 Hz; and the CC site has several strong, narrow peaks at frequencies below 1 Hz and its largest peak is at 0.2 Hz. Differences in the spectral ratios computed by RVT and time-series analysis are a result of differences in the shape of the FAS of the simulated time series and of the RVT input motion relative to these transfer functions.

Figure 4 shows the input FAS for the time series with the largest and smallest spectral ratios at a frequency of 1.7 Hz (the approximate site frequency) for the SCH

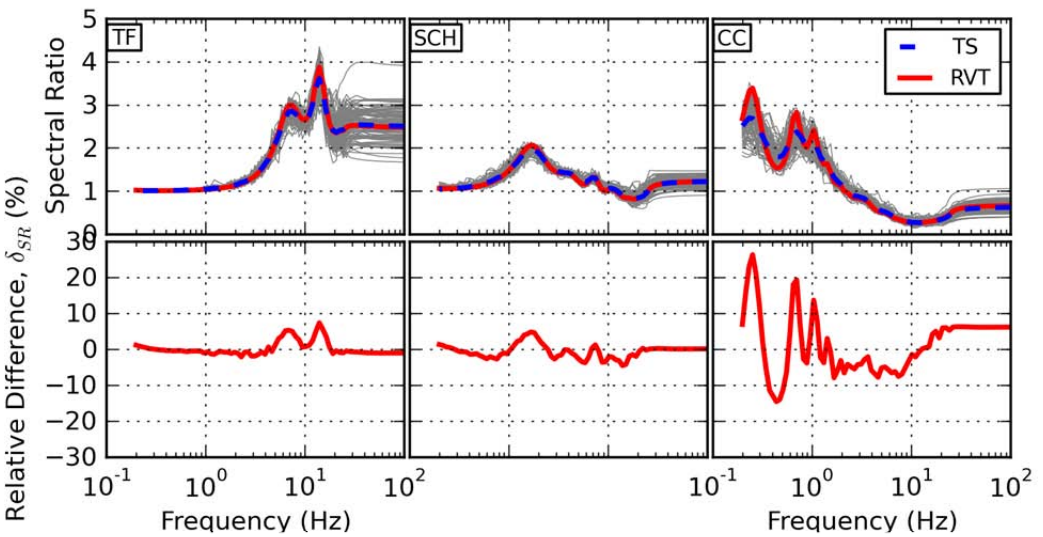

Figure 2. The spectral ratio (top row) computed with linear-elastic analyses for the RVT and time series methods and the associated relative difference (bottom row) for the TF (left column), SCH (center column), and CC (right column) sites.

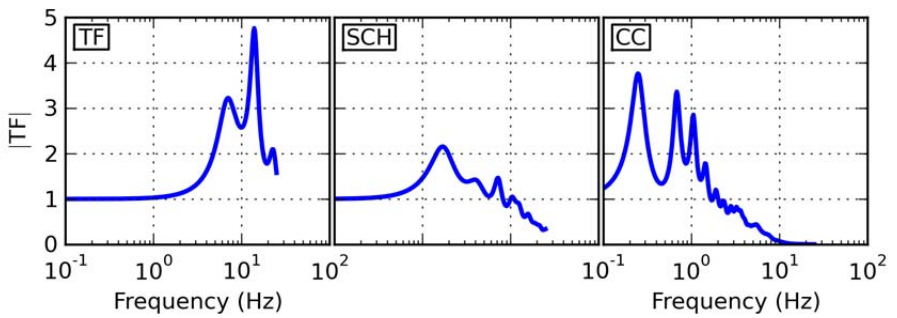

Figure 3. Amplitude of the linear-elastic transfer functions for the TF (left), SCH (center), and CC (right) sites.

site. Also shown is the input FAS for the RVT analysis. The time series with the smallest spectral ratio (*SR*(1.7 Hz)=1.72) shows a deficiency in motion at or near the frequency of the peak in the transfer function, while the time series with the largest spectral ratio (*SR*(1.7 Hz)=2.13) contains larger amplitudes around the same frequency. Additionally, the time series FAS display peaks and valleys within the frequency range of the peak of the transfer function. On the other hand, the RVT input motion contains no peaks and valleys in its FAS and varies smoothly. Because RVT varies smoothly and does not have any valleys or peaks within the width of the peak of the transfer function, it propagates the full strength of the transfer function to the surface and predicts a larger spectral ratio. As all time-series motions will have some irregularities in the FAS across the peak in the transfer function, the median spectral ratio from a suite of time-series analyses will never be as large as that calculated by RVT.

The effect of the smooth RVT input motion is magnified when the peak in the transfer function is multiplied by only a small number of frequencies of the input time series. The frequency increment at which the FAS is defined is constant for a given time series, and therefore the effect is magnified when the natural frequency of the site is low. Additionally, the effect will be magnified when the width of the transfer function is very narrow or when there is significant amplification in the transfer function.

For the CC site, the input FAS for the time series with the largest and smallest spectral ratios at a frequency of 0.3 Hz (the approximate site frequency) are shown in Figure 4 along with the LE transfer function and the input FAS for RVT. The first mode amplification for the CC site occurs at a lower frequency and over a narrower frequency range than the first mode amplification for the SCH site; thus, there is more difference between the spectral ratios from the time series analysis and RVT for the CC site (approximately 25% relative difference, see Figure 3). Additionally, there is more variability in the spectral ratios at the site frequency within the time series anal-

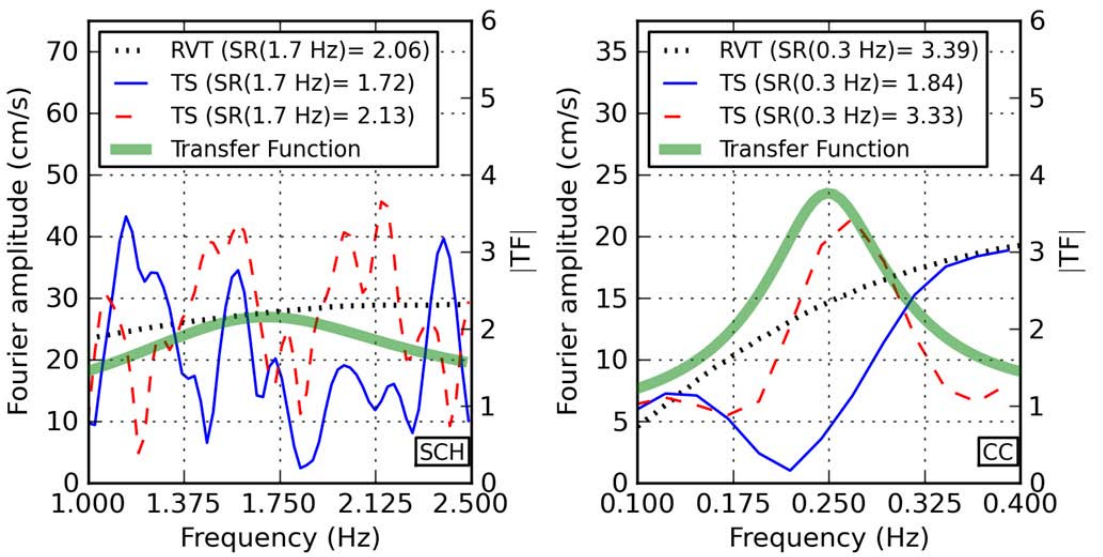

Figure 4. The input FAS for the time series with the largest and smallest spectral ratios for the SCH (left) and CC (right) sites, along with the input FAS of the RVT analysis and the LE transfer function.

ysis for CC site, with the maximum spectral ratio being 81% larger than the minimum spectral ratio. For SCH site, the maximum spectral ratio is only 23% larger than the minimum spectral ratio.

Equivalent-Linear Analyses. Equivalent-linear analyses were performed to investigate how the relative difference changes with input intensity and induced strain level. The input motions were propagated through the SCH site at two different intensity levels (0.17 and 0.40 g). Figure 5 shows the site response results for both the RVT and time-series analysis for a median input PGA of 0.17 g. In general, the results show good agreement between the time series and RVT analyses. However, the relative difference in the RVT analysis has increased compared to the LE analysis (Figure 2), with the maximum relative difference at the site frequency now approaching 10%. At frequencies with no site amplification (i.e., troughs in the transfer function, such as at 2.3, 4.5, and 7.3 Hz), there is a consistent under prediction of the spectral ratio. These trends are even stronger when the intensity of the input motions increases to 0.40 g (Figure 5), where the relative difference at the site frequency exceeds 10%. These analyses show that as the intensity of the input motion increases, the relative difference at the site frequency increases and it shifts to lower frequencies due to the reduction in the site frequency associated with softening of the site.

To explain the increase in the relative difference with increase in intensity level, it is important to understand how the median response from the time series analyses are influenced by the different strain levels induced by each individual motion. Consider the two stochastic motions shown in Figure 6. Motion #68 tends to strain the site less than the median, which makes the peak in the spectral ratio occur at a higher frequency (i.e., stiffer site). Motion #7 induces strains in the site larger than the median, causing the peak in the spectral ratio to be shifted towards lower frequencies. At the frequency of approximately 1.1 Hz (roughly the average degraded site

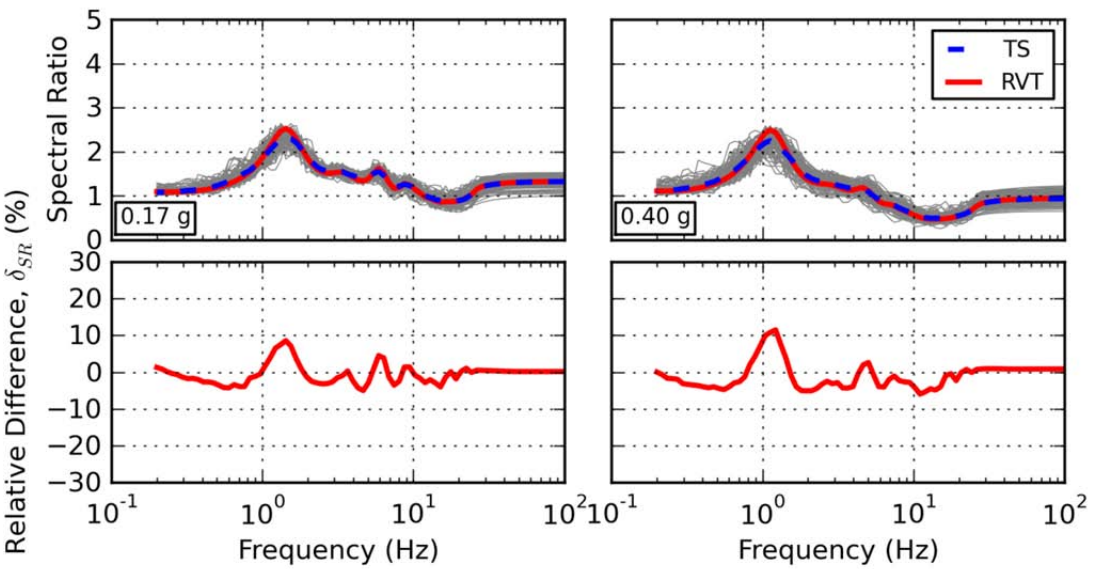

Figure 5. The spectral ratio (top row) and relative difference (bottom row) for the SCH site computed with EQL site response at input PGA of 0.17 (left column) and 0.40 g (right column).

frequency), these two motions both have spectral ratios less than the median of all of the motions, and thus motions that strain a site more than or less than the median produce smaller spectral ratios at the average site frequency. Motions that induce strains similar to the median response have the largest spectral ratio at the average site frequency. When all of the motions within the suite are averaged together, the effect of these differences is to pull down the median spectral response at the site frequency. At frequencies away from the peak spectral ratio, the motions #68 and #7 balance each other out (i.e., one is larger than the median and the other is smaller) such that the median of the time-series analyses is similar to RVT.

The relative difference of the EQL RVT analysis and the EQL time-series analysis for the CC site (Figure 7) shows slightly different trends than were observed for the SCH site. The low site frequency of approximately 0.3 Hz along with high bedrock shear-wave velocity of this Eastern US site (Figure 1) accentuates the rela-

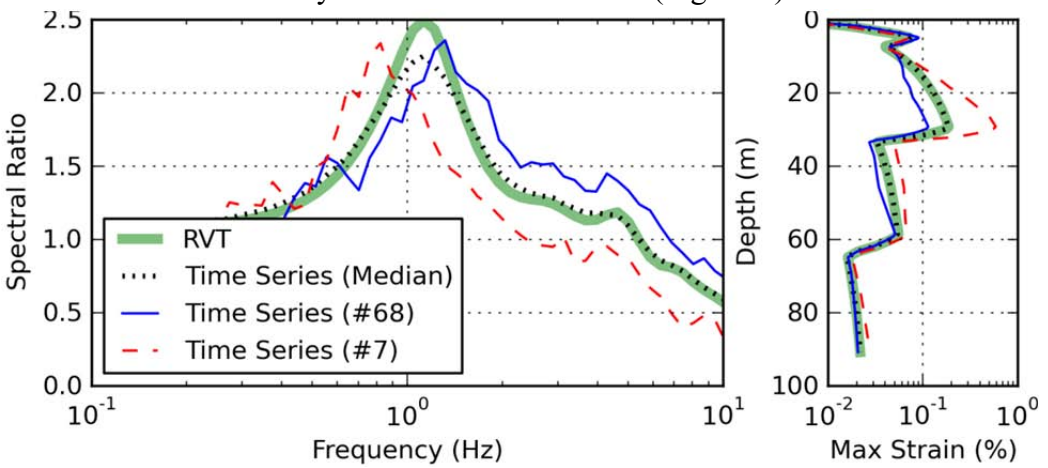

Figure 6. The spectral ratio and strain profile for two time series that induce varying levels of strain.

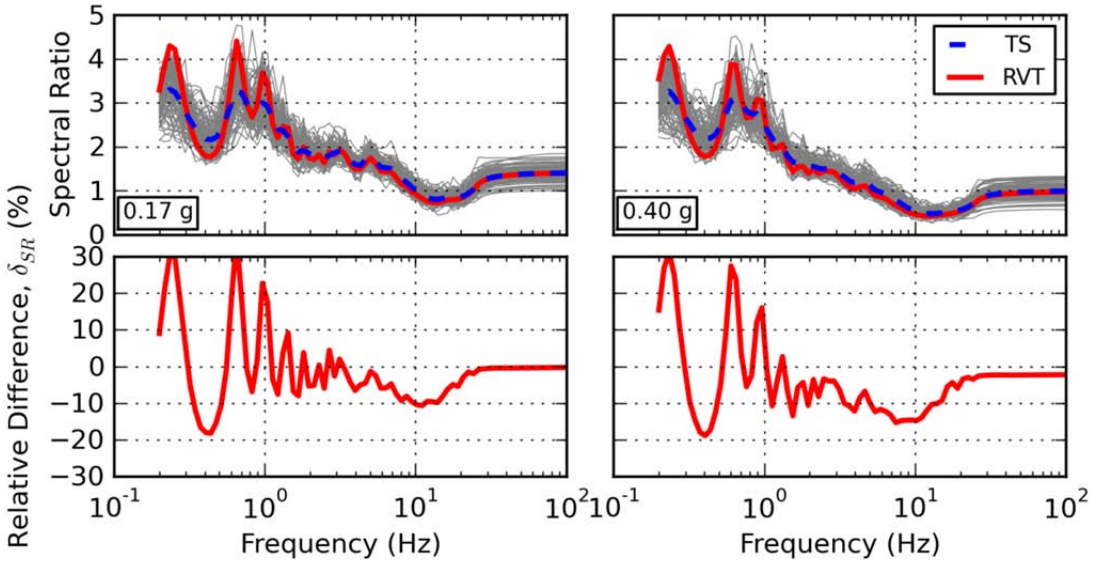

Figure 7. The spectral ratio (top row) and relative difference (bottom row) for the CC site computed with EQL site response at input PGA of 0.17 (left column) and 0.40 g (right column).

tive difference of the RVT spectral ratio at frequencies associated with peaks in the transfer function. This relative difference is as large as 25%. Additionally, the relative difference becomes increasingly negative at high frequencies and becomes increasingly negative as the input intensity increases.

SUMMARY

The analyses presented in this study demonstrate the time series and RVT site produce different estimates of the site response quantified by the spectral ratio. The difference in the site response computed using RVT analysis is affected by the characteristics of both the site and the input motions. The smooth shape of the RVT input FAS is more sensitive to the site transfer function than the irregular FAS of a time series, which results in larger amplification at the frequencies associated with peaks in the transfer function and less amplification at frequencies associated with troughs in the transfer function for RVT analyses. These differences are more significant for sites with low natural frequencies because the site amplification transfer function tends to be narrower and the number of points in the FAS affected by the amplification is smaller. Also important is the amplitude of the transfer function which increases for sites with large bedrock shear-wave velocity or other strong velocity contrasts. The relative difference of RVT at the site frequency increases with increasing intensity because the RVT analysis does not take into account how individual motions strain a site differently.

Financial support for this research was provided by the Nuclear Regulatory Commission.

REFERENCES

Boore, D. (2003). “Simulation of ground motion using the stochastic method.” *Pure and Applied Geophysics*, 160(3-4), 635-676.

Boore, D. and Joyner, W. (1984). “A note on the use of random vibration theory to predict peak amplitudes of transient signals.” *Bulletin of the Seismological Society of America*, 74(5), 2035-2039.

Cartwright D. and Longuet-Higgins M. (1956). “The statistical distribution of the maxima of a random function.” In *Proc. of the Royal Society of London. Series A, Mathematical and Physical Sciences*, 237(1209):212{232, 1956.

Gibbs J., Tinsley J., Boore D., and Joyner, W. (1999). *Seismic velocities and geological conditions at twelve sites subjected to strong ground motion in the 1994 Northridge, California, earthquake: a revision of OFR 96-740*. USGS OFR 99-446, U.S. Department of the Interior, U.S. Geological Survey, 1999.

Darendeli, M. (2001). *Development of a new family of normalized modulus reduction and material damping curves*. PhD thesis, The University of Texas, Austin, TX.

Real C., Shakal A., and Tucker, B. (2006). “Overview of the Turkey Flat ground motion prediction experiment.” *In Proc. SMIP06 Seminar on Utilization of Strong-Motion Data*, 117-136.

UniStar Nuclear Services. (2007). *Calvert Cliffs Nuclear Power Plant Unit 3, Combined License Application*, Part 2: Final Safety Analysis Report, Rev. 6.

Understanding Uncertainty: Assessment and Management of Geotechnical Risk in Tunnel Construction

Thomas W. Pennington[1] M. ASCE, P.E. and Donald P. Richards[2] F. ASCE, P.E.

[1] Professional Associate, Parsons Brinckerhoff, Inc., One Penn Plaza, New York, NY 10119, penningtont@pbworld.com
[2] Senior Professional Associate, Parsons Brinckerhoff, Inc., 555 17th Street, Suite 500, Denver, CO 80202, richardsdo@pbworld.com

ABSTRACT

Risk management is fast becoming routine in civil engineering as owners, engineers, and contractors recognize the benefit of capturing, assessing, and planning for risks on their projects. Recent experience has shown that risk management techniques employed on tunnel projects can help reduce unexpected cost impacts and delays. However, capturing these risks and accurately predicting their impact is not a simple task as the nature of the ground is difficult to predict and this uncertainty can often have the greatest influence on the success of the project. This paper discusses some of these techniques in detail and addresses how they can be used to help mitigate the most common cause of cost overruns and delays on tunnel projects, the ground and its behavior during construction. Details from case histories are presented to illustrate the influence that geotechnical risks can have on tunnel projects and the techniques implemented to mitigate these risks are outlined.

BACKGROUND

Unlike conventional surface construction, tunnel construction takes place in an unknown environment where ground conditions are difficult to predict prior to construction. Tunnel engineers are consistently faced with the difficult task of investigating geotechnical conditions along the project alignment, understanding and predicting ground behavior during construction, and planning for changing, and sometimes unforeseen, ground conditions. For many tunnel projects, this is a task that requires careful examination by experienced professionals and substantial investment (much more than traditional civil engineering projects).

It is not uncommon for the construction means and methods for a tunnel project to account for over one-half of the project cost. This is largely due to the significant investment required for large and highly specialized equipment, i.e., tunnel boring machines (TBMs), and the need for experienced labor to operate this equipment. Decisions related to the contractor's means and methods are of great importance to the financial success of the project, but also intimately dependent on the nature of the ground and the related geotechnical risks contained therein.

RISK MANAGEMENT IN TUNNELING

The design of the tunnel structure is inexorably tied to the methods and details of construction. The selection of excavation technique must be compatible with the full range of anticipated ground conditions and at the limits of the technique supplemental measures must be provided to facilitate a safe and stable excavation. Also the initial ground support for a tunnel must match the method of excavation and the installation of any ground improvements that may be required, along with the requirements of the ground and groundwater conditions. The most commonly encountered geotechnical risks for tunnels are:

- Excessive or unexpected groundwater inflow
- Unstable ground or unanticipated ground behavior
- Limited response capability due to confined working environment
- Poor judgment or error in design
- Incompatible selection of means and methods
- Poor on-site management and communication

Control of these and other risks requires acknowledgement of the risk, an assessment of probability of occurrence, and provisions for remedial measures to avoid the risk or methods of recovery in the event the risk event occurs. The risk management plan must capture these risks and include provisions for remedial measures to be implemented during construction.

RISK ASSESSMENT STRATEGIES

As with most projects, the planning and design phases include an evaluation of alternatives and how these alternatives will meet the needs of the project. During these phases, the risk management process should identify and disclose all geotechnical risks that must be considered the design and preparation of contract. Risks associated with different construction methods can be compared. If necessary, say if the ground conditions are particularly poor along a section of the alignment, detailed analyses may be performed to compare alternative mitigation measures so that the impacts of alternate construction methods are thoroughly considered. Risks may be addressed in several ways, as indicated below:

- Design of features that will reduce or eliminate the identified risk
- Selection of alignment to avoid adverse ground that increases tunneling risk
- Specification of minimum requirements to methods of tunneling and shaft construction that will minimize the identified risk
- Inclusion of contract provisions, including payment provisions, that will reduce contingencies in the construction contract bid price
- Inclusion of certain risk allocation components or contingencies in the contract documents
- Inclusion of unit price items in the contract payment provisions to

accommodate most likely differing site conditions

The origin and the effect of geotechnical risks can be classified for an orderly discussion. The origin of risks can be any of the following:

- Soil and groundwater conditions, including contaminated ground conditions, faults, intrusions, and buried valleys, differing from those anticipated
- Behavior of soil and groundwater different from that ordinarily expected or compared to conditions presented in the contract
- Misinterpretation of soil and groundwater conditions leading to the choice of inappropriate construction methods or equipment
- Mishandling of otherwise appropriate methods and equipment chosen by the contractor
- Unanticipated obstructions, natural or manmade, in the ground

The above list is certainly not exhaustive, but it covers the most common types of geotechnical risks in underground construction. By nature, geotechnical risks sometimes defy definition and the most onerous risks are those that were not anticipated by designer, contractor, owner, or by anyone else. The goal of the designer is to anticipate, as well as possible, the potential risks, to weigh their probability and effects, and to plan for handling the risk to the degree appropriate. Necessarily, this requires considerable judgment and applied experience. Allocating these risks in a contract also requires consideration of the contracting method, relationship between the contractor and the owner, the degree of control of the risk desired by the owner, and consideration of risk sharing between contract parties.

Decision aid tools. Where the risk of poor ground conditions or adverse ground behavior is judged to have a significant impact on a project's cost or schedule, decision aids can be used to provide a quick evaluation of geotechnical risks and their potential impact on a project. As discussed previously, significant risks to tunnel projects are often the compatibility of the contractor's means and methods with the anticipated range of ground and groundwater conditions along the full length of the tunnel alignment, presence of fault zones or weakness zones, and ground water inflows.

Selection of equipment that is ill-suited to the geotechnical conditions along a tunnel can have costly ramifications and is often a function of a multitude of variables (and not always technical in nature). In soft ground, selection of an appropriate closed-face TBM can be governed by grain size distribution of the soil, presence of highly permeable sand/gravel zones, and impacts to nearby infrastructure. Excavation of tunnels in rock will often need to consider the potential for uncontrollable and high groundwater inflows, presence of gas or contaminated groundwater, and the effectiveness of treating areas of poor ground ahead of the advancing excavation. Generalized flow charts for selection of hard rock and soft ground sub-aqueous tunnel excavation methods are provided in Figure 1.

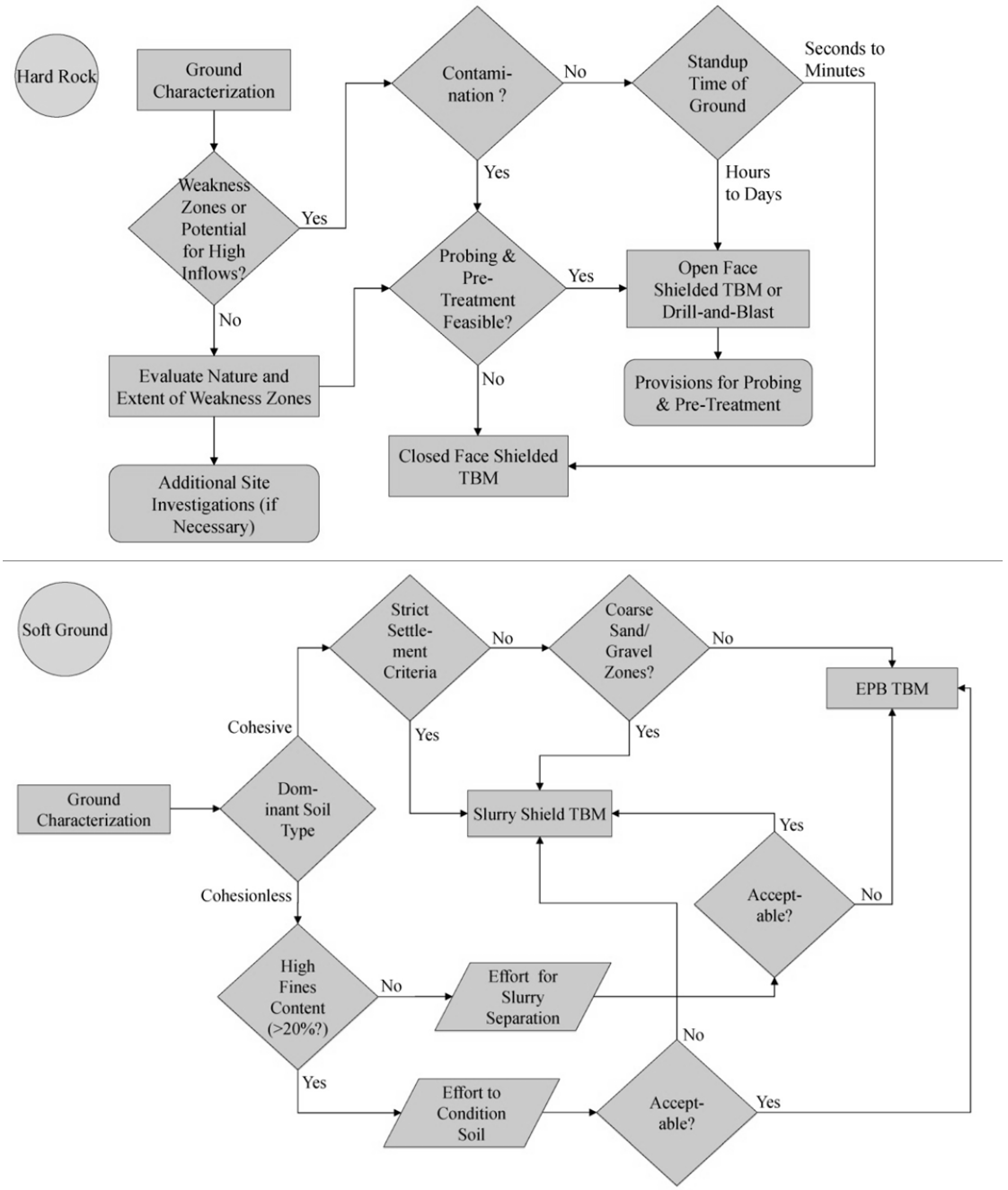

Figure 1. Flow Diagrams for Evaluating Tunnel Excavation Techniques in Hard Rock and Soft Ground

An example of a risk assessment model for groundwater inflow into a tunnel is presented in Figure 2. This decision tree illustrates in a rather simple format the probability of types of potential groundwater inflows (anticipated vs. unanticipated) and relative cost impacts on construction methodology, mechanical (TBM) and manual (drill-and-blast) tunnel excavation. The model also provides an evaluation of

the impact costs of managing groundwater inflow during pre-construction and post-excavation scenarios.

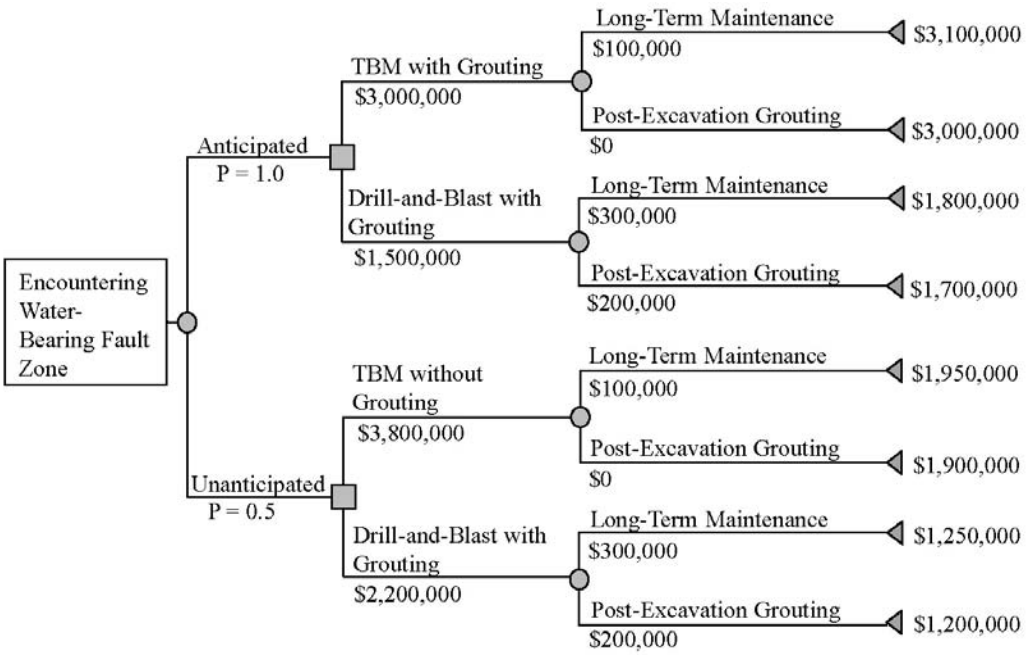

Excavation Method	Remediation	Cost
TBM	Long-term leak maintenance	3,100,000 + 1,950,000 = **$5,050,000**
	Post excavation grouting	3,000,000 + 1,900,000 = **$4,900,000**
Drill-and-Blast	Long-term leak maintenance	1,800,000 + 1,250,000 = **$3,050,000**
	Post excavation grouting	1,700,000 + 1,200,000 = **$2,900,000**

Figure 2. Decision Tree for Evaluating Cost of Groundwater Inflow Control for TBM and Drill-and-Blast Excavations

CASE HISTORIES

In tunnel construction, as with many construction projects, the risk of failure is always present. However, often the greatest risks are those related to geotechnical, or subsurface, risks and the related impact on or from the contractor's means and methods. Tunnels are built entirely in ground that will be variable and the equipment used and techniques employed must be compatible with this ground, or potentially significant cost increases and/or schedule increases may occur. The following sections present several recent case histories where understanding the risks associated with unknown or uncertain conditions have either benefited the project or resulted in delays and additional costs to the project.

Weak rocks and fault zones. Tunnel "F" of the Strategic Sewage Disposal System (SSDS) extends from Tsing Yi Island to Stone Cutters Island near the Kowloon side of Hong Kong Harbor in China. This tunnel is further described as a case study by McLearie et al. (2001) and Barton (2006). The tunnel extends for a distance of about

2.9 kilometers and up to 145 meters below sea level, a portion of which passes beneath the world's second largest container port. During the planning and design stages, contract consultants failed to adequately characterize a large fault zone within the limits of the tunnel alignment, the Tolo Channel Fault Zone. This zone was not explored or investigated in sufficient detail in large part due to difficulties in performing site investigations within the channel.

Tunnel excavation was carried out by an open face, main beam-type TBM. During initial tunneling three faults were crossed, ranging in length from about 15 to 275 meters in length (see Figure 3). Excavation through these zones lasted between 4 and 10 months and required extensive pre-treatment, primarily in the form of pre-excavation grouting from the within the tunnel excavation. As a result, significant delays to the project were incurred as a result of the reduced tunneling productivity, with advance rates about one tenth of the rate anticipated by the contract consultants.

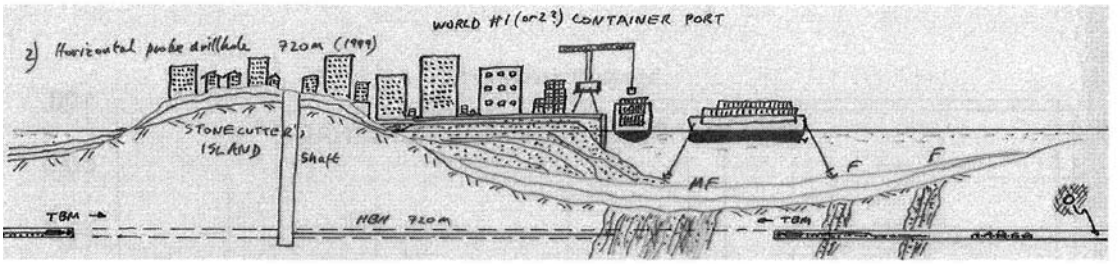

Figure 3. Schematic Indicating Tunnel Excavation through Fault Zones

Part of the difficulty in mining through the fault zones with a TBM was the limitations imposed by the confined working environment within the TBM itself. Probe hole drilling from within the TBM was extremely limited since holes had to be positioned through openings in the cutterhead, which were few, and there was only room for two rock drills to operate within the TBM. Pre-treatment within a tunnel is often most efficient during drill-and-blast type operations, as grout holes can be drilled more frequently for each excavation round and can also be placed at more effective grouting locations.

This project provides a valuable lesson for proper equipment selection, since in retrospect the reduced tunneling productivity for this project can be partially attributed to the decision to utilize a TBM. If drill-and-blast excavation was selected, perhaps better progress through the fault zones might have been achieved. This would have also provided a more flexible working environment and would have provided a more efficient pre-treatment of the ground and pre-support measures.

Compatibility with means and methods. The Bjorøy Road Tunnel near Bergen, Norway is 2 kilometers in length and was excavated using drill-and-blast techniques under as much as 79 meters of hydrostatic head. Difficulty was experienced during construction due to an unanticipated fault encountered (Holter et al., 1996). The fault zone had a total thickness of only 3.6 meters, but comprised extremely poor ground conditions, including breccia, clay, sand, coal fragments and flowing ground (see Figure 4). This feature went undetected prior to construction, primarily due to pre-construction investigations that were limited in scope.

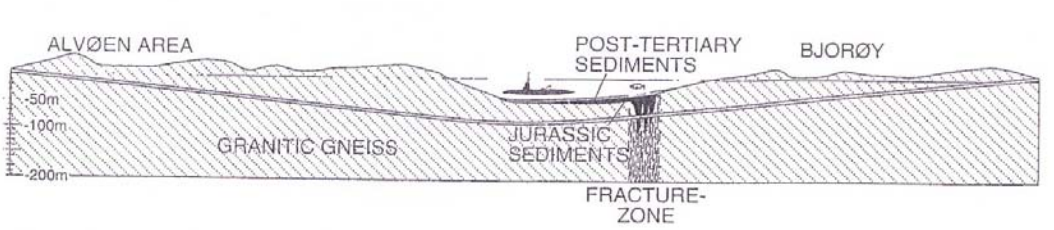

Figure 4. Profile of the Bjorøy Road Tunnel

Rock cover at the location of the fault was about 300 meters. The fault was originally detected during probing ahead of the excavation, at a distance of about 7.6 to 9 meters ahead of the face, when hundreds of cubic feet of sand and water blew into the excavation through the two-inch probe hole. It was quickly determined that significant pre-treatment would be required to advance the tunnel through this zone. Several methods of treatment were considered with the intent to provide a groundwater cutoff and to stabilize the ground. After much deliberation, an intensive consolidation grouting program was specified to improve stability of the soils and provide the necessary groundwater cut-off.

One of the major challenges of the pre-excavation grouting program was determining the layout and sequencing of grout holes to provide the grouting coverage needed to reduce instabilities and groundwater inflows. Due to the highly variable and uncertain nature of the fault zone, with its wide variations in rock quality and presence of clay-filled discontinuities, rock mass grouting was completed in two stages. The first stage was directed at sealing open joints and channels where high groundwater inflows occurred. The second stage involved grouting the finer joints of the rock, under high pressure, to provide a nearly watertight excavation.

Advance of the tunnel through the fault zone was slower than originally anticipated but ultimately successful. Following pre-treatment, groundwater inflow into the tunnel was minimal, despite additional occurrences of water-bearing joints at full hydrostatic pressure. These areas were also treated with pre-injection grouting to provide groundwater cut-off. This project highlights the need for construction operations to be flexible in the face of adverse ground conditions. Some tunnels, due to their remoteness or access restrictions are not capable of fully characterizing potentially difficult ground conditions.

Ground and groundwater control. Assessing ground and groundwater inflow and the need for control measures is often critical for tunnels and any underground excavation, as the presence of groundwater, often under high pressure, can severely disrupt excavations if not prepared for or mitigated in advance. For tunnels in rock, accurately predicting the location and magnitude of inflows is difficult as these are often controlled by geologic structures. Significant inflows can be encountered in singular features like an open rock joint that connects to an overlying aquifer with near infinite recharge (which can be the case for tunnels in tropical climates where residual soils provide a significant source of groundwater).

Singapore's Deep Tunnel Sewerage System (DTSS) was constructed to facilitate wastewater transport, treatment and disposal on the island of Singapore. The tunnels were constructed by multiple tunnel boring machines (TBMs) and included

concrete segment ground support. Contracts T-05 and T-06 were excavated through granite with the rock quality ranging from excellent to very poor (completely decomposed). Portions of the tunnel passed also through lengths of soil-like materials and mixed face conditions (hard rock and soil-like material simultaneously encountered in the excavation). On both of these contracts, earth pressure balance (EPB) TBMs were used and were configured as hard rock machines to excavate the granite. In addition to using pressurized face excavation technology (EPB) as a means to control ground and groundwater, other control measures such as probe drilling were introduced to reduce risks of unforeseen ground conditions. During construction, some delays were incurred due to frequent TBM maintenance and difficulties in accessing the cutterhead in up to 5 bars of water pressure (Marshall and Flanagan, 2007). However, there were no serious ground loss issues and tunneling performance was judged to be largely successful.

CONCLUSIONS

Tunnels represent some of the most demanding civil engineering projects due to the inherent uncertainty of the ground and the requirement to accurately predict ground behavior in advance of construction, and related risk consequences in construction. Overcoming these challenges is a significant task, but this challenge can often be overcome through the framework of a risk management program. Ultimately risk management employs judgment and experience as well as a good understanding of geotechnical conditions. Detailed analyses, whether based on statistical analysis or engineering judgment, should always be tempered with actual experience, field observations, and an evaluation of unforeseen and uncertain risk events. Geotechnical risks in tunnel projects are rarely eliminated during the planning and design process. Fortunately there are a wide range of techniques available to tunnel engineers to assist in evaluating, managing and potentially mitigating these risks.

REFERENCES

Barton, N., (2006). “Fault zones and TBM.” *Geotechnical Risk in Rock Tunnels*, Taylor & Francis, London.

Holter, K.G., E. Johansen, and A. Hegrenæs, (1996). “Tunnelling Through a Sandzone: Ground treatment experiences from the Bjorøy Subsea Road Tunnel.” *Proceedings of the North American Tunneling Conference,* ed. by L. Ozdemir, American Underground Construction Association, Littleton, Colorado.

Marshall, R.H., and R.F. Flanagan, (2007). “Singapore’s Deep Tunnel Sewerage System – Experiences and Challenges,” *Proceedings of the Rapid Excavation and Tunneling Conference*, ed. by M.T. Taylor and J.W. Townsend, Society of Mining, Metallurgy, and Exploration, Littleton, Colorado.

McLearie, D.D., W. Foreman, W.H. Hansmire, and E.K.H. Tong, (2001). “Hong Kong Strategic Sewage Disposal Scheme Stage 1 Deep Tunnels.” *Proceedings of the Rapid Excavation and Tunneling Conference*, ed. by W.H. Hansmire and I.M. Gowring, Society of Mining, Metallurgy, and Exploration, Littleton, Colorado.

Communicating and Managing Risk in Geotechnical Engineering Practice

Jessee A. Scarborough[1], PE, Member ASCE

[1] Senior Geotechnical Engineer with Bhate Geosciences Corporation; 5217 5th Avenue South, Birmingham, Alabama, USA 35212; Phone: (205) 591-7062; Fax: (205) 591-7184; E-mail: jscarborough@bhate-geo.com

ABSTRACT

The practice of geotechnical engineering is said to be as much art as science. Dealing with uncertainty, and communicating uncertainty and risk to clients is fundamental to the business of a geotechnical engineering consultant, and is emphatically not a science. Yet, a consistent framework for dealing successfully with geotechnical risk can be identified. This paper will examine six areas of geotechnical risk commonly encountered in the Southeastern United States. The six areas include: (1) sites with uncontrolled fill, (2) sites with highly plastic soils, (3) the occurrence of rock, (4) sinkhole occurrence, (5) deep foundations, and (6) mechanically stabilized earth (MSE) retaining walls. Geotechnical risk occurs in all portions of a project life-cycle (e.g., design, construction, and operation) and is not limited to the spatial variation of engineering properties. The paper briefly discusses each of the six topics to show a consistent framework for handling geotechnical risk.

INTRODUCTION

The practice of geotechnical engineering is said to be as much art as science. Science is the creation of rational principles through the formulation and testing of hypotheses based on observational evidence. Engineering is the application of rational principles to solve practical problems. Geotechnical engineering is engineering on or with earthen materials. Art is the aesthetic, the emotional, the unquantifiable. The art in geotechnical engineering is the gestalt created by the fusion of known and unknown. The geotechnical project report is the *Masterwork, the Mona Lisa*. Yet because it is practical, we desire rational guidance for its creation.

A four-step framework can be used for communicating risk and uncertainty: (1) Identify the uncertainty, (2) Evaluate the risk(s) associated with the uncertainty, (3) Communicate the risk and uncertainty, and (4) Recommend a solution. Craft your report to fit both the project and the owner. Don't just identify problems, provide solutions.

The underlying premise of this paper is dealing with uncertainty, and communicating uncertainty and risk to clients is fundamental to geotechnical engineering practice. Six project situations, commonly encountered in the Southeastern US, are examined as examples of how risk and uncertainty can be communicated and managed. The six include:

(1) sites with uncontrolled fill
(2) sites with highly plastic soils
(3) the occurrence of rock
(4) sinkhole occurrence
(5) deep foundation construction
(6) MSE retaining wall design

Without exception, the information available from other sources on each of these six topics is very broad. A detailed discussion is beyond the scope of this paper. This paper provides a brief vignette or summary with specific emphasis on an element of uncertainty or risk unique to each area, and focuses on the need to clearly communicate risk and uncertainty for geotechnical projects. Both positive and negative examples are provided.

SITES WITH UNCONTROLLED FILL

Dealing with construction on a site with uncontrolled fill is a difficult task for a geotechnical engineer. On non-filled sites, an evaluation of the site's geologic history can help guide the evaluation of the soil's engineering properties and deal with the hidden, but expected spatial variation in soil types and properties. On a site with uncontrolled fill, the geotechnical engineer has no natural clues for guidance. The fill properties will vary widely and without rhyme or reason. Buried debris or other deleterious materials, not encountered by borings, may well be present and can exert a tremendous influence the performance of the fill.

Building on sites with uncontrolled fill is an exercise in evaluating known costs versus largely unknown risks. A very common risk is the potential for larger than normal settlement of a building due to the presence and poor performance of the fill in the subsurface. In general, higher cost construction methods for site preparation or foundation construction will reduce the risk of poor building performance. The owner must make cost-risk decisions about construction with the knowledge the risk is his/hers, as are the decisions to reduce risk. While the geotechnical engineer and the design-team should make recommendations (not just list options) to the owner for building on the site, ultimately, the owner owns both the building and the risk. The owner may receive cost savings during construction, but in return, incurs a higher risk of unacceptable building performance. Table 1 shows an idealized grading of options for site preparation and foundation construction from lower cost-higher risk to higher cost-lower risk.

Table 1. General summary of cost-risk options for building on uncontrolled fill

Relative Cost	Actions taken for site preparation or foundation construction	Relative Risk
Lower cost	• Build on the site with no action taken to reduce settlement risk	Higher risk
↓	• Limited undercutting and replacement of fill soils only under footings	↑
↓	• Undercut and replacement of fill soils to a limited depth under the entire building area	↑
↓	• Ground improvement in portions of the building and fill area	↑
↓	• Use a deep foundation system to transfer structural loads to a natural material below the fill	↑
Higher cost	• Remove and replace all fill below the proposed building	Lower risk

Step 1 – Identify uncertainty: Presence of uncontrolled fill with a large and unknown variation in engineering properties
Step 2 – Evaluate risk(s): Larger than normal settlements are very likely
Step 3 – Communicate: Present a grading of options, and obtain an understanding of the owner's cost and risk preference
Step 4 – Recommend: Make a specific recommendation, don't just list options and cost estimates.

SITES WITH HIGHLY PLASTIC SOILS

The presence or absence of highly plastic soils is very much within the classic paradigm of the spatial variation of soil properties. In the Valley and Ridge physiographic province, the soils are predominantly residual, and often clayey. The soils are formed from the weathering of rocks laid down in the regional pattern, tilted bedding becoming relatively thin bands of rocks and soils at the ground surface; each band with similar properties. Understanding the geology is an important natural clue in understanding the distribution of soils on sites within the Valley and Ridge. Detecting the presence of highly plastic soils begins with the first site visit.

Highly plastic soils are a potential problem due to their predilection for shrink-swell behavior. Moreover, clayey soils also offer significant challenges during earthwork due to their affinity for moisture. This behavior arises from the chemical make up and structure of clay minerals. While a detailed discussion of clay chemistry is not possible in this paper, some specific guidance for identifying these problem soils can be provided. Atterberg limits are the classic index test used to identify highly plastic soils. Table 2 shows Atterberg limits associated with higher swell potential.

Table 2. Classification of Potential Swell Based on Atterberg Limits (after TM 5-818-7)

Classification of Potential Swell	Swell Potential percent (S_p)	Liquid Limit (LL) Percent	Plasticity Index (PI) percent
Low	< 0.5	< 50	< 25
Marginal	0.5 to 1.5	50 to 60	25 to 35
High	> 1.5	> 60	> 35

Yet not all highly plastic soils have significant shrink-swell behavior, especially in the Valley and Ridge. An additional index test is useful to identify potential shrink-swell behavior. The results of a hydrometer test provides a grain-size distribution for the fines, the silt and clay fraction of the soil. The fraction of clay size material is important. The ratio of the plasticity index to the fraction of clay size material is known as *activity*. An activity ratio greater than one indicates the potential for swell, with higher ratios having greater swell potential.

For relatively small to modest projects, undercutting of highly plastic soils and their replacement with low plasticity soils is often an adequate response. The depth of undercutting will vary, but is typically 2 to 4 feet. With larger projects, mixing of lime with the soil can change the clay chemistry reducing the soil's affinity for moisture. All projects should include provisions for the control of storm water, thus reducing the availability of water to subgrade soils.

Step 1 – Identify uncertainty: Use laboratory index tests to identify/confirm the presence of highly plastic soils.
Step 2 – Evaluate risk(s): The historical behavior of similar sites in the geologic setting is important. What existing evidence of shrink-swell behavior is in evidence at the site?
Step 3 – Communicate: Provide background, cite test results, and try to delineate the areal extent of potential problem areas.
Step 4 – Recommend: Make specific, directed recommendations to deal with the potential shrink-swell problem.

THE OCCURRENCE OF ROCK – ROCK SLOPE CONSTRUCTION

A recent project near Birmingham, Alabama was evaluated by a neighborhood geotechnical firm. The construction of a shopping center was proposed on a 100 acre site. The site was located on the southerly face of a NE-SW trending ridgeline. Extensive cut and fill were anticipated, up to about 80 feet high/deep. Based on published geologic mapping, the initial geotechnical project report identified the presence of an unfavorable dip in the soon to be exposed rock cut slope. The report went on to note slope instability was most likely at locations where the seepage of water was also present on/in the slope. The report recommended an inclination for the rock slope and adjacent soil slope. Seemingly as an afterthought, the report identified rock bolts and anchors as a measure to increase stability of the rock slope.

Figure 1 shows a sketch of the rock and soil slope as-recommended and as-constructed. Figure 1 also shows the location of sliding block slope failure that formed at the transition from rock to soil slope.

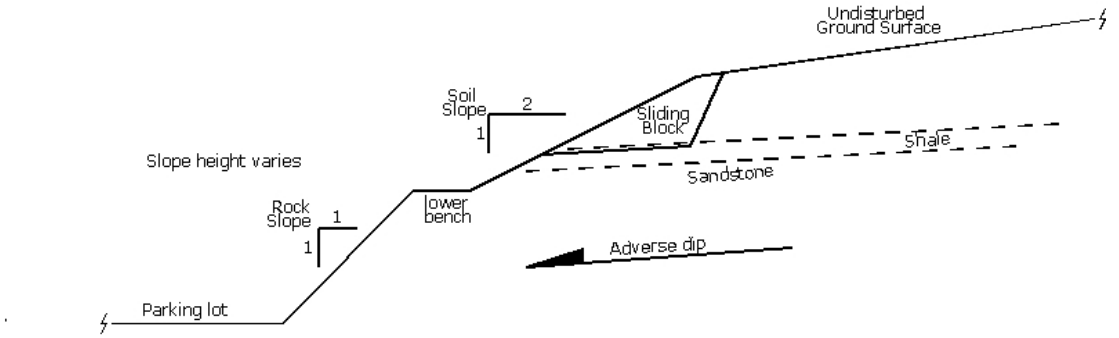

Figure 1. Cross-section sketch of slope and of the slope failure

The landslide occurred late in construction and involved about 14,000 cubic meters (18,000 cubic yards) of earthen material. The slide seemed to be correlated with the presence of both a weathered shale seam about 4 to 5 feet thick and with seepage on top of the shale seam.

It is very likely that the initial geotechnical consultant was not negligent, their report likely met the stardard-of-care in providing their recommendations. However, their report did not provide a good service to their client. The report identified a risk, described some uncertainty, and provided a recommendation. However, they did not clearly communicate what steps needed to be taken during construction to identify and reduce the potential for slope instability. The owner spent about $700,000 to repair the landslide. It is likely a somewhat lesser amount would have been spent in prevention of the instability. On-the-other-hand, it is also possible the slope failure would have occurred in the interim.

Step 1 – Identify uncertainty: Use geologic maps to help identify the adverse dip in the proposed rock cut slope.
Step 2 – Evaluate risk(s): The historical behavior of similar sites in the geologic setting is important. The presence of *weak* layers is a known bad actor in similar instabilities.
Step 3 – Communicate: Provide background, cite the historical behavior, and emphasize the need for observation and evaluation of the cut slope during construction.
Step 4 – Recommend: Provide strongly worded recommendations on the progress of the rock slope construction. Make specific, directed recommendations to deal with the potential slope instability, not just the generic rock bolts and anchors can be used to stabilize the slope if needed.

SINKHOLE OCCURRENCE

A park was recently constructed near downtown Birmingham, Alabama. The plan for the park included lakes as scenic water features. To reduce operational costs, the original park plan included pumping from the subsurface to maintain water levels in the lakes. The original geotechnical consultant recommended the use of a Bentonite based clay liner to reduce leakage from the lakes. During construction, as shown in Figure 2, a series of dropouts (sinkholes) occurred in one of the lakes. Concurrent with the sinkholes, the subsurface pumps became blocked with mud, which clearly suggested a link between the pumping and the sinkhole formation.

Sinkholes are hydro-geologic features that form due to erosion of soil above karst rock. Karst rock is rock soluble by water, such as the limestone/dolomite underlying the park site. The solutioning/weathering of the rock typically occurs in geologic time. The effect of this weathering is the creation of voids, such as open joints/bedding, in the rock that permit the flow of water. In near time, the flowing water erodes soils, and enough erosion in a specific location results in a sinkhole. Sinkholes are often expressed as a drop-out at the ground surface. Man's activity can be a trigger for sinkhole formation (Newton, 1976), such as the pumping from the subsurface at this site.

The sinkholes were repaired using concrete plugs at the soil-rock interface, replacement and thickening of the clayey lake liner, and the shutdown of the subsurface pumping operations. To-date, the repairs have been successful.

Figure 2. Sinkholes in the bottom of the drained lake

Step 1 – Identify uncertainty: The karst geologic setting was known to be susceptible to sinkholes.
Step 2 – Evaluate risk(s): The original assessment of the site identified sinkholes as a risk, but did not connect the pumping operations with increased risk of sinkhole occurrence.
Step 3 – Communicate: Talk to your clients, additional discussion of the site and the proposed operations plan might well have connected the dots between pumping of the ground water and sinkholes.
Step 4 – Recommend: Make specific recommendations targeting the client's needs and the risks on the project.

CONSTRUCTION OF DRILLED SHAFTS

During the 1960-70's drilled shaft foundations acquired a poor reputation in Birmingham, Alabama. Cost/pricing issues and construction difficulties (i.e., change orders) contributed to this. In the late 1970's, local contractors, architects, and engineers worked together to develop what became known as the *Birmingham Limestone Specification* (Bhate, 2010). This specification allows drilled shafts to be fairly bid, built, and paid for. Current Deep Foundation Institute (ADSC/DFI) documents have the same effect. Figure 3 shows a typical drilled shaft construction site.

Figure 3. Drilled shaft construction site

Engineers, architects, and construction managers inexperienced with drilled shaft construction or with conditions in karst rock can contribute to poor project performance by using inadequate construction specifications. Take, for example, a recent project in central Alabama. Drilled shaft bearing was specified and bid in the project plans based on auger refusal. The pinnacled nature of the bedrock, and the likelihood of weathered seams in the rock were not taken into account. A unit price for rock excavation was required, but did not affect the contractor's base bid. The contract was let with a $600k budget for drilled shaft construction. Work began, and the construction manager let work proceed as rock excavation costs mounted. The foundation contractor submitted change orders that brought the foundation cost to more than five million dollars. A reasonable fee based on a well-crafted specification and the actual work performed would likely have had a foundation budget around two million dollars, likely without significant cost overruns.

Step 1 – Identify uncertainty: A karst geologic setting has an irregular rock surface. Moreover, weathering of the rock results in soil filled seams and voids in the rock.
Step 2 – Evaluate risk(s): Past experience has shown significant cost overruns can occur when constructing drilled shafts in a karst area.
Step 3 – Communicate: Project specifications should realistically portray construction with consideration for actual site conditions and methods of construction. Well crafted specifications reduce the potential for poor cost performance.
Step 4 – Recommend: The geotechnical engineer should review project specification prior to bidding. The geotechnical report should recommend this review take place. Follow up communication after publishing the report should occur, and should push for such a review.

DESIGN AND CONSTRUCTION OF MSE WALLS

While published statistics of failures are not available, in the author's experience, mechanically stabilized earth (MSE) walls experience a higher frequency of failure than any other designed structure.

Scarborough (2005) described the failure of two MSE walls and identified issues contributing to the failures in the design and construction process. These issues included (but were not limited to): (1) analyses of global stability are an important factor in the design process, and (2) identification of drainage and utility issues prior to construction. The design guidance published by the National Concrete Masonry Association (NCMA, 2007) was identified as contributing to these omissions in the design process.

One way to force retaining wall designers to include global stability in the design is for the walls be constructed on a turn-key, design-build basis where the wall designer is solely responsible for the wall design. This, even to the point, where separate exploratory borings and laboratory testing, to support the needed analyses, are performed by the retaining wall designer.

In 2010, the NCMA published updated design guidelines (NCMA, 2010). The updated guidelines exacerbate this issue, recommending the retaining wall designer not be required to perform global stability analyses. The updated guidelines make the geotechnical engineer responsible not only for global stability, but also responsible for coordination to make sure the retaining wall design is complete. Moreover, the updated NCMA guidelines recommend MSE walls not be built under a design-build contract.

The writer rejects these positions and asserts that a failure to consider mass/compound/global stability in the design of a MSE retaining wall is a violation of not only what should be the accepted standard of care for their design, but potentially of an engineer's duty to protect the health and welfare of the public. The professional issues inherent in the current practices of commercial wall designers, such as the standard of care for MSE wall design and what constitutes adequate design plans, are an area deserving additional study, discussion, and clarification.

Step 1 – Identify uncertainty: Current design and construction practices (e.g., the failure to include global stability, and address utility and drainage issues) increase the likelihood of MSE wall failure.
Step 2 – Evaluate risk(s): Global stability, utility and drainage issues must be addressed in the MSE wall plans. Expected wall movements should be included in the design package, as well.
Step 3 – Communicate: The writer recommends MSE wall designers be compelled by contract to provide a complete design. This requires educated owners, design professionals, and contractors. Geotechnical engineers should help provide this education.
Step 4 – Recommend: Geotechnical design reports should contain specific language to address design and construction responsibility for MSE walls.

CONCLUDING REMARKS

A four-step framework has been provided as the basis for communicating risk and uncertainty in geotechnical engineering practice.

(1) Identify the uncertainty
(2) Evaluate the risk(s) associated with the uncertainty
(3) Communicate the risk and uncertainty
(4) Recommend a solution.

The art of geotechnical engineering lies in you, as you craft a geotechnical engineering report to fit both the project and the owner. Innovative solutions do not just appear, they arise from the mesh of known and unknown, from the communication and interactions in the course of a project. Use clear, direct language to describe issues. Do not use *weasel wording* in identifying options and making recommendations. Don't just identify problems, provide solutions.

Six vignettes have been included to highlight the application of this framework to real geotechnical engineering problems. Drilled shaft construction provides an example where engineers, architects and contractors worked together to create fair construction specifications that accurately and fairly portray site conditions and construction methods. This in contrast to the current state of the practice for MSE wall design and construction, where wall designers are encouraged by current design guidance to provide incomplete and potentially dangerous wall designs.

REFERENCES

Bhate (2010). Interview with Mr. Uday R. Bhate, PE, PG

NCMA (1997). *Design Manual for Segmental Retaining Walls*, Second Edition, National Concrete Masonry Association Publication No. TR-127-A.

NCMA (2010). *Design Manual for Segmental Retaining Walls*, Third Edition, National Concrete Masonry Association Publication No. TR-127B.

Newton, J.G. (1976). *Early Detection and Correction of Sinkhole Problems in Alabama, with a Preliminary Evaluation of Remote Sensing Applications*, Alabama Highway Department.

Scarborough, J.A.(2005). *A Tale of Two Walls: Case Histories of Failed MSE Walls; Slopes and Retaining Structures under Seismic and Static Conditions*, ASCE Geotechnical Special Publication 140.

TM 5-818-7, Department of the Army USA, Technical Manual TM 5-818-7, Foundations in Expansive Soils, (1983).

Reliability Analysis of Deep Excavation based on a Semi-Empirical Approach

J. K. Park[1], S.M.ASCE, G. Biscontin[2], M.ASCE, and P. Gardoni[3], M.ASCE

[1]Graduate Student, Zachry Department of Civil Engineering, Texas A&M University, College Station, TX, 77843-3136; PH (979) 422-9888; email: jkpark0215@tamu.edu
[2]Associate Professor, Zachry Department of Civil Engineering, Texas A&M University, College Station, TX, 77843-3136; PH (979) 845-6303; email: gbiscontin@civil.tamu.edu
[3]Associate Professor, Zachry Department of Civil Engineering, Texas A&M University, College Station, TX, 77843-3136; PH (979) 845-4340; email: pgardoni@civil.tamu.edu

ABSTRACT

The design and construction of deep excavations in urban environment is often governed by serviceability limit state related to the risk of damage to adjacent buildings. In current practice, the assessment of excavation-induced building damage has focused on a deterministic approach. This paper presents a component/system reliability analysis framework to assess the probability that specified threshold design criteria for multiple serviceability limit states are exceeded. A recently developed Bayesian probabilistic framework is used to update the predictions of ground movements in the later stages of excavation based on the recorded deformation measurements. An example is presented to show how the serviceability performance for excavation problems can be assessed based on the component/system reliability analysis.

INTRODUCTION

Excavation projects related to urban redevelopment and infrastructure improvement are often governed by serviceability-based design rather than failure prevention criteria. Deformation tolerance specifications are generally prescribed based on minimizing potential damage to adjacent structures. The damage to a building due to an excavation is influenced by many factors, including the properties of the soil and building, the type and size of structure, the relative location of building and excavation, the magnitude and distribution of load of building including self-weight, the rate and distribution of settlement, and the foundation characteristics of a building. Therefore, analytical solutions for allowable settlement for structures cannot be easily applied and most criteria for building damage potential have been developed on the basis of empirical evidence from field observations and damage in existing buildings. A comprehensive procedure for the analysis of building damage caused by an excavation involves three main components: (1) determination of the lateral and vertical ground movement profiles, (2) estimation of the angular distortion and lateral strain that develop in a building based on ground movement, building characteristics, and soil-structure interaction, and (3) assessment of the building

damage based on the serviceability criteria.

Recent applications of reliability concepts to excavation design have mainly focused on assessing the stability of the structure itself, with limited research focusing on the component reliability assessment of serviceability criterion (Son and Cording 2005; Hsiao et al. 2008; Schuster et al. 2008). Although an assessment of the probability of damage to an adjacent building could be conducted by providing certain ranges of the probability based on component reliability analysis considering the stability and/or serviceability, the system reliability analysis that considers multiple limit state functions was not addressed. This paper presents a component/system reliability analysis framework to assess the probability that specified threshold design criteria for multiple serviceability limit states are exceeded. A previously developed Bayesian probabilistic framework is used to predict excavation-induced deformations based on the updating the semi-empirical design chart using field measurement data (Park et al. 2010). A Bayesian updating methodology is used to assess the three-dimensional deformation shape including maximum horizontal displacements, surface settlements and ground movement profile at different locations and for each incremental excavation stage. An example is presented to show how the multiple serviceability performances for deep excavation problems can be assessed. By considering multiple failure modes of an excavation, the component/system reliability indices for each excavation step are assessed during the entire excavation process.

PROBABILISTIC BAYESIAN SEMI-EMPIRICAL METHOD

Analytical formulation of the semi-empirical chart. Excavation deformations are frequently assessed in geotechnical engineering practice using the Clough and O'Rourke chart (1990) as shown in Figure 1.

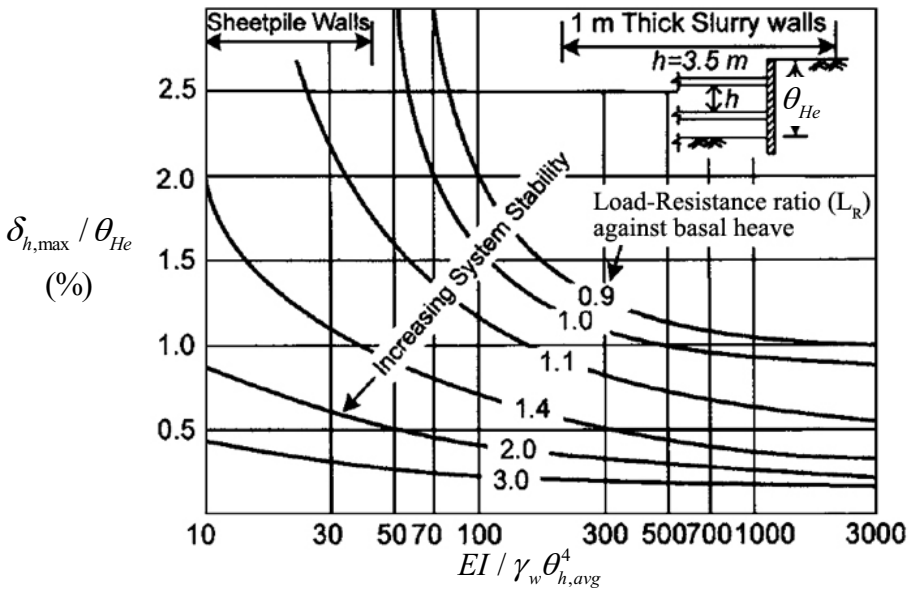

Figure 1. Design charts for maximum horizontal displacements (Modified from Clough and O'Rourke 1990)

This chart provides curves of the normalized horizontal displacement, $\delta_{h,\max} / \theta_{He}$, versus the system stiffness, $EI / \gamma_w \theta_{h,avg}^4$, where $\delta_{h,\max}$ = the maximum horizontal displacement, θ_{He} = the excavation depth, EI = the wall stiffness, γ_w = the unit weight of water, and $\theta_{h,avg}$ = the average support spacing. The curves are parametrized with respect to the load-resistance ratio, L_R, against the basal heave given by Terzaghi (1943) as

$$L_R = \frac{5.7\theta_{Sub}B}{(\gamma\theta_{He} + q)B - \theta_{Suh}\theta_{He}} \tag{1}$$

where, θ_{Sub} and θ_{Suh} = the undrained shear strength above and below the excavation, respectively, B = the width of the excavation, γ = the unit weight of the soil, and q = the surcharge load. Clough and O'Rourke (1990) also proposed dimensionless settlement profiles for estimating surface settlements for the different soil types as shown in Figure 2.

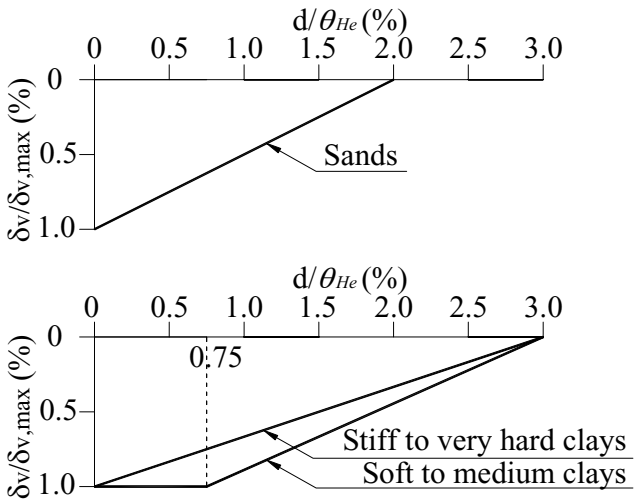

Figure 2. Design charts for estimating the profile of surface settlement for different soil types (Modified from Clough and O'Rourke 1990)

A mathematical description of these curves is needed to update the predictions of the ground movements in the later stages of excavation based on recorded deformation measurements. The Box and Cox transformation (1964) is used to formulate the following analytical expression:

$$\left[\frac{\left(\delta_{h,\max} / \theta_{He}\right)^{(\theta_1+\theta_2 L_R)} - 1}{(\theta_1 + \theta_2 L_R)}\right] = (\theta_3 + \theta_4 L_R) + (\theta_5 + \theta_6 L_R)\left[\frac{\left(EI / \gamma_w \theta_{h,avg}^4\right)^{(\theta_7+\theta_8 L_R)} - 1}{(\theta_7 + \theta_8 L_R)}\right] \tag{2}$$

where, $\boldsymbol{\theta}_{BC} = (\theta_1, \ldots, \theta_8)$ = a set of unknown model parameters first estimated by

fitting the model in Eq. (2) to the existing curves in Clough and O'Rourke chart, and later updated as deformation measurements become available.

Probabilistic model for maximum deformations. A probabilistic model that describes the deformation at the *k*th excavation stage can be written as

$$D_k = \hat{d}_k\left(\boldsymbol{\theta}_{CO}\right) + \sigma\varepsilon_k, \quad k = 1,\ldots,m \tag{3}$$

where, $D_k = \delta_{h,\max}$ or $\delta_{v,\max}$, $\hat{d}_k =$ the deformation estimate of $\delta_{h,\max}$ or $\delta_{v,\max}$ using Clough and O'Rourke chart, $\boldsymbol{\theta}_{CO} = (\theta_{Sub}, \theta_{Suh}, \theta_R) =$ a set of unknown parameters, $\sigma\varepsilon_k =$ the model error, $\sigma =$ the unknown standard deviation of the model error, $\varepsilon_k =$ a random variable with zero mean and unit variance. In assessing the probabilistic model, the following three assumptions are made: (a) the homoskedasticity assumption (the model variance σ^2 is independent of $\boldsymbol{\theta}_{CO}$), (b) the normality assumption (ε_k follows the normal distribution), and (c) the ε_k values at two different excavation stages are uncorrelated The total deformations and their estimates at the *j*th excavation stage can be described as

$$\begin{aligned} D_j &= \Delta D_1 + \cdots + \Delta D_j = \sum_{i=1}^{j} \Delta D_i \\ \hat{d}_j\left(\boldsymbol{\theta}_{CO}\right) &= \Delta\hat{d}_1\left(\boldsymbol{\theta}_{CO}\right) + \cdots + \Delta\hat{d}_j\left(\boldsymbol{\theta}_{CO}\right) = \sum_{i=1}^{j} \Delta\hat{d}_i\left(\boldsymbol{\theta}_{CO}\right) \end{aligned} \tag{4}$$

where $\Delta D_j = D_j - D_{j-1} =$ the incremental deformation at the *j*th excavation stage, $\Delta\hat{d}_j(\boldsymbol{\theta}_{CO}) = \hat{d}_j(\boldsymbol{\theta}_{CO}) - \hat{d}_{j-1}(\boldsymbol{\theta}_{CO}) =$ the incremental deformation estimate at the *j*th excavation stage, $D_0 = \hat{d}_0(\boldsymbol{\theta}_{CO}) = 0$. Using Eq. (3) we can define the deformation residual as $r_k(\boldsymbol{\theta}_{CO}) = [D_k - \hat{d}_k(\boldsymbol{\theta}_{CO})]$. If the deformation has been recorded at the *j*th stage, the deformation at the *k*th stage where $k > j$ can be obtained by adding the predicted incremental deformation $\Delta D_{j+1},\ldots,\Delta D_k$ to the measured deformation at the *j*th stage. It follows that

$$r_k\left(\boldsymbol{\theta}_{CO}\right) = D_k - \hat{d}_k\left(\boldsymbol{\theta}_{CO}\right) = \left(\Delta D_{j+1} + \cdots + \Delta D_k\right) - \left[\Delta\hat{d}_{j+1}\left(\boldsymbol{\theta}_{CO}\right) + \cdots + \Delta\hat{d}_k\left(\boldsymbol{\theta}_{CO}\right)\right] \tag{5}$$

The Clough and O'Rourke (1990) chart only provides estimates of $\delta_{h,\max}$ and $\delta_{v,\max}$. However, the locations of $\delta_{h,\max}$ and $\delta_{v,\max}$ and the deformation profile cannot be estimated from the chart. Therefore, a functional form for the shape of the deformation profile is needed to compare with the field measurement data.

The three-dimensional profile of ground movements. This study adopts the

shape of the three-dimensional deformation profiles perpendicular and parallel to an excavation as shown in Figure 3. These shape functions are established after consideration of numerous alternatives with the objective of capturing the correct shape, while maintaining a relatively simple form. The three-dimensional ground movement distribution around an excavated area is predicted using a combination of the shape functions, an assessment of the maximum ground deformation, and knowledge of the geometry of the excavation. The four shape functions, (1) $f_h(z) =$ the horizontal displacement profile, (2) $f_h(x) =$ the horizontal displacement parallel to an excavation, (3) $f_v(y) =$ the ground surface settlement profile in a direction perpendicular to the excavation, and (4) $f_v(x) =$ the surface settlement parallel to the excavation, define the three-dimensional ground movement around the excavated area. In this study, $\boldsymbol{\Theta} = (\boldsymbol{\theta}_{BC}, \boldsymbol{\theta}_{CO}, \boldsymbol{\theta}_{SF}, \sigma)$ need to be estimated/updated where $\boldsymbol{\theta}_{SF} =$ unknown parameters in shape functions. The detailed procedure to predict the three-dimensional ground movements is described in Park et al. (2010). In this paper, we assume that the building moves with the ground displacement profiles and provides no restraint to the soil.

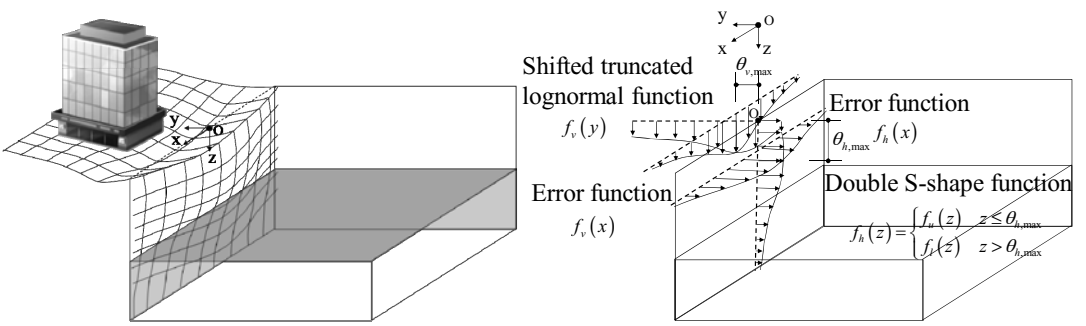

Figure 3. The three-dimensional ground movements (a) conceptual view (b) different functions to describe the deformation profiles

LIMIT STATE FOR BUILDING DAMAGE EVALUATION

Establishment of multiple serviceability limit state functions. Previous research results have concluded that damage to buildings caused by an excavation is a result of both settlement and horizontal movement of the ground (Bjerrum 1963; Boscardin and Cording 1989; Burland 1995; Son and Cording 2005). In current practice, the excavation-induced maximum surface settlement, $\delta_{v\max}$, angular distortion, ω, horizontal strain, ε_l, and deflection ratio, DR, are often used as performance indicators for estimating the damage potential of buildings adjacent to an excavation. Son and Cording (2005) developed a phased procedure to estimate the potential for building damage based on ω and lateral strain, ε_l, to express the strains induced in a building; and these two parameters can be combined into a single parameter termed as the principal tensile strain in the building. The first limit state function,

$g_1(\mathbf{x},\boldsymbol{\Theta})$, can be described as

$$g_1(\mathbf{x},\boldsymbol{\Theta}) = \varepsilon_{p,T} - \varepsilon_p(\mathbf{x},\boldsymbol{\Theta}) \tag{6}$$

where, $\mathbf{x}_i = (A_i, S_i, G_i)$ = relative location to excavation, A_i, size, S_i, and geometry of adjacent building, G_i, that in general are random, and $\mathbf{x} = (\mathbf{x}_1, \ldots, \mathbf{x}_r)$ for multiple buildings, $\varepsilon_{p,T}$ = a specified principal tensile strain and $1/600$ suggested by Schuster et al. (2008) is used, $\varepsilon_p(\mathbf{x},\boldsymbol{\Theta})$ = the principal tensile strain and can be written as

$$\begin{aligned}\varepsilon_{p,D}(\mathbf{x},\boldsymbol{\Theta}) &= \omega \sin\alpha_{\max}\cos\alpha_{\max} + \varepsilon_l(\cos\alpha_{\max})^2 \\ &= \frac{\delta_v(\mathbf{x},\boldsymbol{\Theta})}{L}\sin\alpha_{\max}\cos\alpha_{\max} + \frac{\delta_l(\mathbf{x},\boldsymbol{\Theta})}{L}\times(\cos\alpha_{\max})^2\end{aligned} \tag{7}$$

where ω = angular distortion as defined in Figure 4(a), ε_l = lateral strain as defined in Figure 4(b), $\delta_v(\mathbf{x},\boldsymbol{\Theta})$ = the vertical settlement of the adjacent building, $\delta_l(\mathbf{x},\boldsymbol{\Theta})$ = the horizontal displacement of the adjacent building, L = the length of the adjacent building, and $\alpha_{\max}$ = angle of the plane on which ε_p acts and direction of crack formation measured from the vertical plane,

$$\alpha_{\max} = 0.5\tan^{-1}(\omega/\varepsilon_l) = 0.5\tan^{-1}\left(\delta_v(\mathbf{x},\boldsymbol{\Theta})/\delta_l(\mathbf{x},\boldsymbol{\Theta})\right) \tag{8}$$

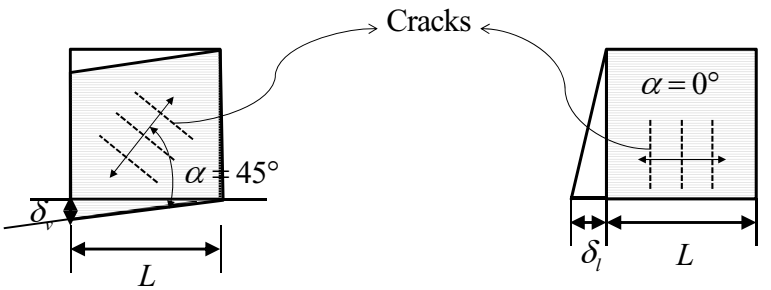

Figure 4. State of strain at the distorted portion of a building (a) angular distortion (b) lateral strain (modified from Son and Cording 2005)

The second limit state function is in terms of a deflection ratio (DR_{sag} or DR_{hog}) as proposed by Burland (1995). By assuming no rigid rotation and a single deformation mode, the deflection ratio is equal to the angular distortion of the building and is often employed to assess the potential of damage to buildings adjacent to an excavation. A ratio of 1/600 is used in this study as the threshold value for the evaluation of this limit state function.

$$g_2(\mathbf{x},\boldsymbol{\Theta}) = DR_T - \frac{\delta_v(\mathbf{x},\boldsymbol{\Theta})}{L} \tag{9}$$

where DR_T = the limiting deflection ratio.

The third limit state function can be specified with respect to the maximum surface settlement, $\delta_{v\max}$, to assess the excavation-induced building damage potential. Even though the more advanced evaluation criteria described above are available, the δ_{vm} has the advantage of being much easier to measure in the field than ω, ε_l and DR. The tolerable limit of the maximum surface settlement, $\delta_{v\max,T}$, is assumed to be 75 mm according to Hsiao et al. (2008). The limit state function can be expressed as:

$$g_3(\mathbf{x},\boldsymbol{\Theta}) = \delta_{v\max,T} - \delta_v(\mathbf{x},\boldsymbol{\Theta}) \tag{10}$$

Fragility assessment for multiple serviceability criteria. Fragility is defined as the conditional probability of failure, attaining or exceeding a prescribed limit states, of a component or system for a given set of demand variables. The failure event for the system is described in terms of unions of componential failure events. In this paper, we focused on the estimation of component and system fragility assessment. We estimate the fragility of attaining or exceeding specified limiting criteria for the assumed values of building properties. The limit state function $g_i(\mathbf{x},\boldsymbol{\Theta})$ is defined such that the event $\{g_i(\mathbf{x},\boldsymbol{\Theta}) \le 0\}$ denotes the attainment or exceedance of the limit state. Using the model for three-dimensional profile of ground movement as described above and considering specified thresholds for multiple serviceability criteria, the system fragility can then be formulated as

$$F(\mathbf{s},\boldsymbol{\Theta}) = \mathrm{P}\left[\bigcup_{i=1,\ldots,3} \left\{g_i(\mathbf{x},\boldsymbol{\Theta}) \le 0\right\} \middle| \mathbf{s}\right] \tag{11}$$

where $\mathrm{P}[A|\mathbf{s}]$ = the conditional probability of event A for the given values of variable(s) $\mathbf{s}$, $\mathbf{s} = (\varepsilon_{p,T}, DR_T, \delta_{v\max,T})$ = a specified threshold value for each limit state function. The uncertainty in the event for the given $\mathbf{s}$ arises from the inherent randomness in the variables $\mathbf{x}$, the inexact nature of the three-dimensional profile of ground movement model (or its sub-models to estimate $\varepsilon_p(\mathbf{x},\boldsymbol{\Theta})$, $\delta_v(\mathbf{x},\boldsymbol{\Theta})$, $\delta_l(\mathbf{x},\boldsymbol{\Theta})$), and the uncertainty inherent in the model parameters $\boldsymbol{\Theta}$. To incorporate the epistemic uncertainties inherent in the model parameters $\boldsymbol{\Theta}$, we consider $\boldsymbol{\Theta}$ as random variables. The predictive estimate of fragility $\tilde{F}(\mathbf{s})$ is then the expected value of $F(\mathbf{s},\boldsymbol{\Theta})$ over the posterior distribution of $\boldsymbol{\Theta}$ (Gardoni et al. 2002), i.e.,

$$\tilde{F}(\mathbf{s}) = \int F(\mathbf{s}, \boldsymbol{\Theta}) f(\boldsymbol{\Theta}) d\boldsymbol{\Theta} \tag{12}$$

where $f(\boldsymbol{\Theta})$= the posterior probability density function of $\boldsymbol{\Theta}$. The Monte Carlo simulation is used in this study to estimate the fragility, since a closed-form solution of Eq. (12) is generally not available.

APPLICATION

The proposed reliability analysis approach is applied to an actual supported excavation project for the Robert H. Lurie Medical Research Building in Evanston, Illinois with an imaginary concrete building as shown in Figure 5(a). The dimensions of building are assumed to be 20m (width), 15m (length) and 10m (height). Figure 5(b) also shows a schematic representation of the cross-section with an excavation of 80m (width) and 12.8m (depth). Detailed description and ground response of the excavation are provided in Finno and Roboski (2005) and Park et al. (2010). Measurements of both lateral and vertical ground surface settlements were obtained from inclinometers and optical survey from every side of excavation.

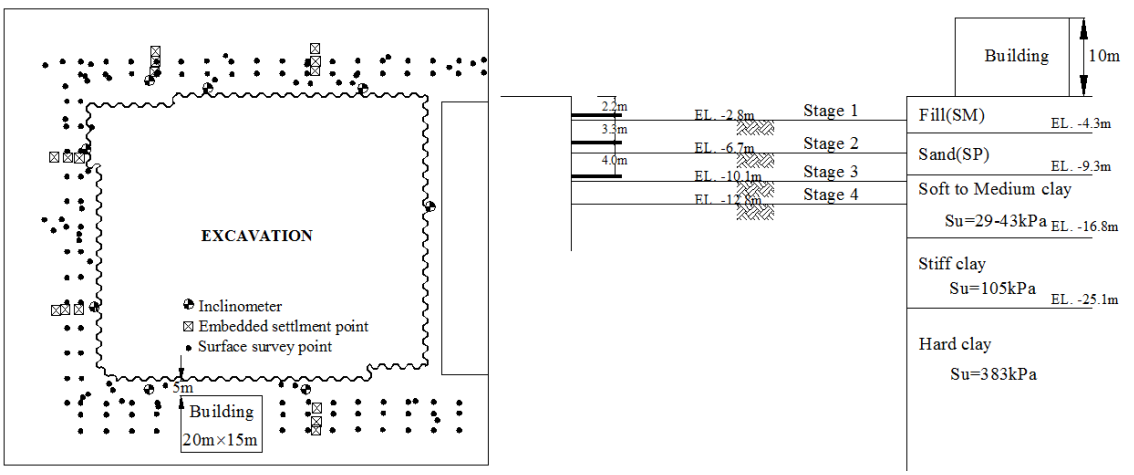

(a) (b)

Figure 5. General layout of example site (a) Building location and instrumentation (b) cross-section (modified from Finno and Roboski 2005)

For each excavation stages, the component reliability analyses are performed for each limit state function criterion. The variation of the reliability index, β, with excavation depth is roughly concave as shown in Figure 6(a), which in turn means a progressive increase of probability of failure with an increase in excavation depth.

The whole excavation is defined as a series system because system failure is defined by a failure of any individual component of different limit state function. The system reliability index, β_{sys}, is shown in Figure 6(b). A small decrease of the reliability index is calculated, which is smaller than the reliability index calculated from each component reliability analysis as shown in Figure 4(a). For example,

even if the excavation system is in the safe region of $g_1(\mathbf{x},\boldsymbol{\Theta})$ (i.e. the principal tensile strain will not exceed 1/600), the failure point can be located in failure region of $g_2(\mathbf{x},\boldsymbol{\Theta})$ (i.e. the deflection ratio of a building could exceed 1/600).

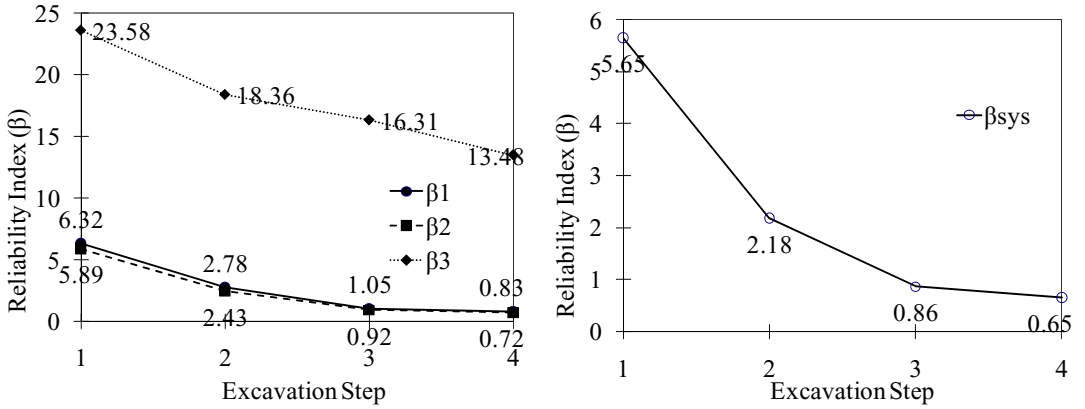

(a) Component (b) System

Figure 6. Plot of reliability index for each excavation step

In this paper, we present multiple serviceability limit state functions for damage potential of building. A threshold value for each limit state function is arbitrarily selected for simple illustrative purposes. However, the reliability index for criteria for different size and type of building can be easily calculated by just changing the threshold values. This proposed approach also can be applied to the different side of excavation side. The reliability index for other sides will be different because the three-dimensional displacement profiles are changed in the reliability analysis.

CONCLUSIONS

A reliability analysis framework is proposed to assess the fragility of excavation-induced building damage for multiple serviceability limit states. A Bayesian probabilistic framework is adopted to predict three-dimensional displacement profiles during supported excavations using a semi-empirical approach. The proposed approach can be used for an adaptive reliability-based optimal design of the excavation system in which the design is modified after each excavation stage to minimize costs and maintain a minimum reliability requirement. This method can also be expanded to a system reliability approach for excavation projects related to urban redevelopment and infrastructure improvement. For example, additional limit state functions can be added to the system reliability analysis to consider the serviceability of tunnel for a deep excavation within the influence zone of an existing tunnel.

REFERENCES

Bjerrum, L. (1963). "Allowable settlement of structures." The 3rd European

Conference on Soil Mechanics and Foundation Engineering, Weisbaden, Germany, 135-137.

Boscardin, M. D., and Cording, E. J. (1989). "Building response to excavation-induced settlement." *Journal of Geotechnical Engineering*, 115(1), 1-21.

Box, G. E. P., and Cox, D. R. (1964). "An Analysis of Transformations." *Journal of the Royal Statistical Society. Series B (Methodological)*, 26(2), 211-252.

Burland, J. B. (1995). "Settlement of Buildings and Associated Damage." Proceedings of IS-Tokyo '95 The First International Conference on Earthquake Geotechnical Engineering, Tokyo, Japan, 1189-1201.

Clough, G. W., and O'Rourke, T. D. (1990). "Construction Induced Movements of Insitu Walls." Design and Performance of Earth Retaining Structures, P. Lambe and L. A. Hansen, eds., ASCE, Ithaca, New York, 439-470.

Finno, R. J., and Roboski, J. F. (2005). "Three-dimensional responses of a tied-back excavation through clay." *Journal of Geotechnical and Geoenvironmental Engineering*, 131(3), 273-282.

Gardoni, P., Der Kiureghian, A., and Mosalam, K. M. (2002). "Probabilistic Capacity Models and Fragility Estimates for Reinforced Concrete Columns based on Experimental Observations." *Journal of Engineering Mechanics*, 128(10), 1024-1038.

Hsiao, E. L., Schuster, M., Juang, C. H., and Kung, G. C. (2008). "Reliability analysis and updating of excavation-induced ground settlement for building serviceability assessment." *Journal of Geotechnical and Geoenvironmental Engineering*, 134(10), 1448-1458.

Park, J. K., Gardoni, P., and Biscontin, G. (2010). "A Bayesian Framework to Predict Deformations during Supported Excavations Based on a Semi-Empirical Method." The 11th International Conference on Applications of Statistics and Probability in Civil Engineering, Zürich, Switzerland, submitted.

Schuster, M. J., Juang, C. H., Roth, M. J. S., and Rosowsky, D. V. (2008). "Reliability analysis of building serviceability problems caused by excavation." *Géotechnique*, 58(9), 743-749.

Son, M., and Cording, E. J. (2005). "Estimation of building damage due to excavation-induced ground movements." *Journal of Geotechnical and Geoenvironmental Engineering*, 131(2), 162-177.

Terzaghi, K. (1943). *Theoretical soil mechanics*, John Wiley & Sons, New York.

Jet-Grouting in Cohesive Soils for Ground Improvement in Hawaii

John Y.L. Chen[1], A.M. ASCE, P.E., Robin M. Lim[2], A.M. ASCE, P.E., and Kyle Furuhashi[3], P.E.

[1] Geolabs, Inc., Senior Project Engineer, 2006 Kalihi Street, Honolulu, HI 96819; PH (808) 841-5064; FAX (808) 847-1749; email: johnc@geolabs.net
[2] Geolabs, Inc., Vice President, 2006 Kalihi Street, Honolulu, HI 96819; PH (808) 841-5064; FAX (808) 847-1749; email: robin@geolabs.net
[3] Project Manager, Department of Transportation, State of Hawaii; PH (808) 392-3327; FAX (808) 487-2468; email: Kyle.Furuhashi@hawaii.gov

ABSTRACT

A new highway widening project specified jet-grouted columns for supporting the new embankment fill and stabilizing an under-consolidated soft cohesive soil layer. Jet-grouted columns were installed and extended down to depths ranging from about 30 to 70 feet below the existing ground surface. An extensive QA/QC program was implemented to evaluate the effectiveness of the ground improvement, including performing a test section, monitoring the jet-grouting operations, coring and sampling the jet-grouted columns, performing standard penetration tests (SPT) and cone penetration tests (CPT) of the jet-grouted improved areas, monitoring the pore water pressures in the soft soils between the jet-grouted columns, and measuring the ground settlement due to the embankment fill placement. Some of the lessons learned from this project are presented and shared in this paper.

INTRODUCTION

The existing highway embankment fills (about 20 to 40 feet thick) were placed over the soft, cohesive soil deposit about 35 years before the highway widening project. The soft, cohesive soil deposit was characterized as under-consolidated recent alluvium (silty clays, CH/OH). The highway embankment supports a heavily traveled 10-lane interstate highway. The highway has experienced continual settlements from consolidation of the soft soils under the surcharge pressure of the embankment fills during the last 40 years.

A soft soil stabilization program was implemented during the original highway construction in the late 1960s through the early 1970s, including the installation of sand drains and the placement of some localized surcharge fills in incrementally phased construction. The embankment fills and surcharge fills placed were on the order of up to about 40 to 50 feet in vertical height.

Following the highway embankment construction and settlement waiting period, some continual ground settlement of the embankments occurred causing distress to the Portland cement concrete pavements on the highway. Several layers of asphaltic concrete overlays were placed over the original concrete pavements to restore the grades of the highway pavements.

The project required widening of the existing highway by another 30 feet on one side of the embankment to accommodate a sixth traffic-lane and a new shoulder lane in the westbound direction. To support the new embankment fills (approximately 20 feet of new fills placed on about 20 feet of existing fills) and to reduce the potential for significant ground settlements in the future, approximately 270 jet-grouted columns (specified 5-foot diameter spaced at 10 feet on-center in a triangular grid pattern) were installed to support the embankment fill for the highway widening.

The jet-grouted columns (up to 60 feet in height) extended down to depths ranging from about 30 to 70 feet below the existing ground surface.

GEOLOGY AND SUBSURFACE CONDITIONS

The Island of Oahu was built by the extrusion of basaltic lavas from two main shield volcanoes, Waianae (older) and Koolau (younger). The project site is located along the southern flank of the Koolau Volcano, about 0.75 miles to the north of Pearl Harbor. The existing highway traverses a gulch, a branch of the numerous streams that drain from the Koolau Summit into the East Loch of Pearl Harbor, as shown on Figure 1 – Vicinity Map. The gulch was formed by stream incision and mass wasting erosion of the valley walls due to sea level changes.

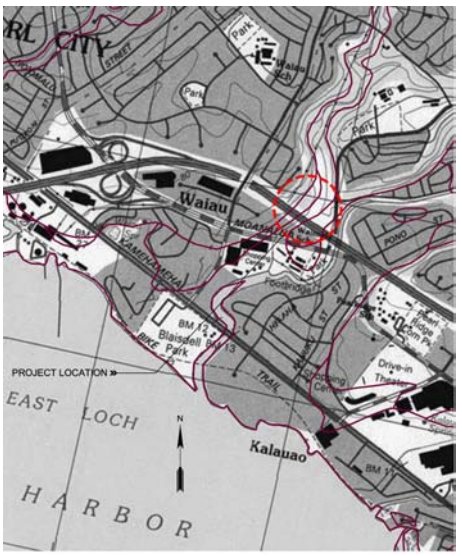

Figure 1. Vicinity Map.

Therefore, the gulch floor contains some soil deposits that are representative of both shallow marine and terrestrial origin as evidenced by the presence of some organic-rich alluvial sediments containing sea-shell fragments. In addition to the geology of the gulch, some past agricultural land uses, such as drainage ditches, also may have contributed to the soft soil conditions encountered at the existing gulch.

Based on the subsurface investigation conducted, the existing gulch floor is underlain by a substantial thickness of recent alluvium. The maximum thickness of the soft recent alluvium encountered was 44 feet. Groundwater was encountered at depths of about 15 to 44 feet below the existing ground surface in the borings drilled at the approach fill area during our field investigation. These groundwater levels generally correspond to about Elevations +10 to +20 feet MSL.

Laboratory consolidation test results indicated the soft recent alluvium to be under-consolidated. Based on consolidation evaluations, it appears that approximately 60 to 80 percent (average 70 percent) of the consolidation settlement had occurred before the widening construction. Therefore, on-going consolidation settlements of another 30 percent (estimated at about another 12 inches) could occur at the existing highway in the future. In the area of the new highway widening, we anticipate additional consolidation settlements caused by the new embankment fill loads may be on the order of about 45 inches instead of 12 inches.

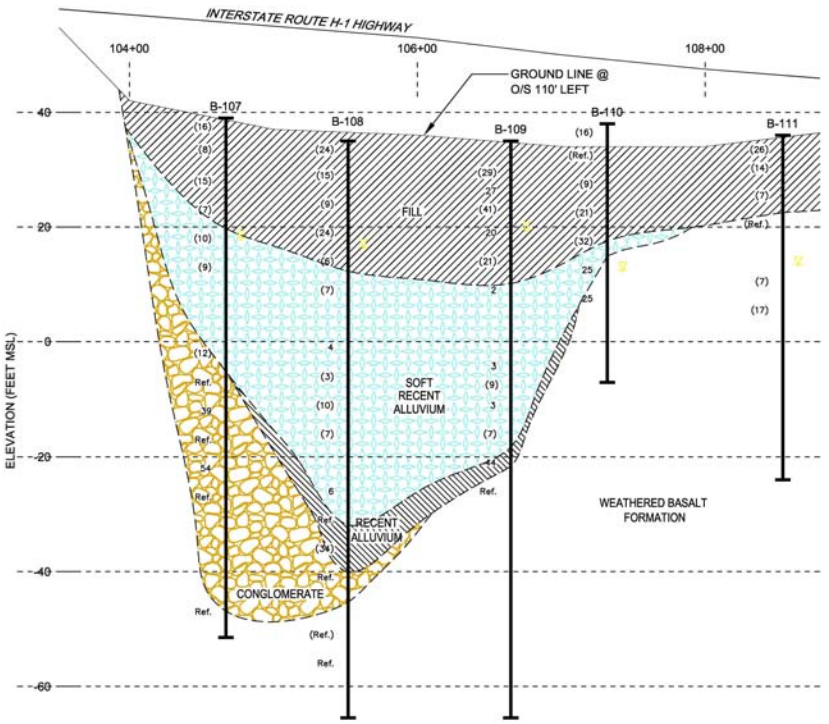

Figure 2. Generalized subsurface conditions under jet-grouting areas.

Vibrating wire piezometers were installed in the soft recent alluvium to evaluate the excess pore water pressures in the under-consolidated recent alluvium. Field measurements indicated about 11 feet of excess pore water head were present in the soft recent alluvium before the start of construction. The field measurements suggest that about 72 percent of the consolidation settlement may have occurred in the soft recent alluvium before the highway widening construction commenced.

CONSTRUCTION METHODS AND DESIGN PARAMETERS

Several deep soil stabilization methods were considered during the design, including jet-grouting, stone columns and compaction grouting. Due to the thick soft recent alluvium underlying the existing embankment fill, soil stabilization by the jet-grouting method was recommended to stabilize the under-consolidated soft recent alluvium and to support the new embankment fill.

Jet-grouting is a technique utilizing a special drill bit and injection monitor with radial horizontal nozzles to produce stabilized soil-cement columns. Neat cement grout slurry is injected through horizontal nozzles at high pressure cutting and

mixing the surrounding in-situ materials, as the drill bit is slowly rotated and withdrawn to form a soil-cement column.

To support the new embankment fill, jet-grouted columns were recommended under the existing embankment fill to underpin the existing embankment and were extended down to bear on stiff soils. The 5-foot diameter jet-grouted columns were designed at 10 feet on-center in a triangular grid pattern with an area replacement ratio of about 0.23, deriving vertical support primarily from bearing on the stiff soils and from skin friction along the sides of the jet-grouted columns.

The grout mix used in the soil stabilization had a specific gravity of at least 1.60. The jet-grouted columns (soilcrete) had to achieve 7-day and 28-day unconfined compressive strengths of at least 200 and 400 psi, respectively.

A probing program was implemented to delineate the lateral and vertical extents of the soil stabilization zones due to the highly variable subsurface conditions, to supplement the geotechnical investigation during design. Twenty-four probe holes were advanced into the stiff soils and/or weathered basalt. After the probing program, the revised length of the jet-grouted columns ranged from 25 to 60 feet.

TEST SECTION

Prior to production jet-grouted column construction, a jet-grout test section was conducted to evaluate the proposed grouting methods and the ability of the proposed grout mix to produce jet-grout columns meeting the depth, diameter, and material property requirements. The test section consisted of a minimum of three jet-grouted columns installed at the design spacing and depth. The jet-grouted test columns were extended from the underlying stiff/dense soil materials through the soft recent alluvium and up to near the existing ground surface to allow for later excavation for physical inspection.

Figure 3. Relatively consistent soilcrete.

Figure 4. Poor-quality soilcrete.

After installation of the test columns and allowing some time for curing, core samples of the test columns were obtained using PQ size core barrel for the full depth of the test columns to verify the soilcrete's consistency and 28-day compressive strength. The coring results indicated relatively consistent soilcrete was retrieved from the test columns within the soft recent alluvium with virtually no organic content (Figure 3). However, consistently poor-quality soilcrete was retrieved from the test columns within the soft recent alluvium with high organic content (Figure 4).

The tops of the three jet-grout test column cluster were exposed for physical inspection, as shown on Figure 5. Due to site constraints, only the top 20 feet of the test columns were exposed. The upper 27 feet of the soils consisted of relatively stiff silty clay soils; therefore, the exposed test columns consisted of soilcrete formed within the stiff embankment fill materials, not the recent alluvium.

Figure 5. Tops of jet-grouted test columns were exposed.

The test section suggested that the proposed jet-grout parameters were not able to produce the jet-grouted columns meeting the design diameter and the 28-day unconfined compressive strength. As a result, the jet-grouting parameters were revised in the following manner:

- Grout injection pressure – 500 bars minimum (at the pump metering device);
- Air injection pressure – 5 to 6 bars;
- Grout injection nozzles – six nozzles, 2 mm in diameter each;
- Grout Specific Gravity – 1.60 (minimum);
- Retraction rate – 6 inches every 25-second time step or 27-second time step (in thicker soft recent alluvium);
- Rotation rate – 8 rpm (3 rev/step) maximum.

The production jet-grouted columns were installed and monitored by an automatic recording device attached to the jet grouting rig. The output from the automatic recording device, which recorded the above jet grouting parameters, was used as the basis for acceptance of the jet-grouting work.

QUALITY CONTROL (QC) AND QUALITY ASSURANCE (QA) PROGRAM

A total of 270 production jet-grouted columns were installed and extended down to Elevation -40 feet with an average retraction rate of about 11.6 inches per minute, equivalent to about 4.8 inches every 25-second time step or about 5.2 inches every 27-second time step. The length of the columns ranged from about 30 to 60 feet. The average grout volume per column was computed to be about 75 gallons of grout per linear foot of jet-grouted column.

To verify the effectiveness of the jet-grouting operations, the QA/QC program consisted of performing standard penetration tests (SPT) and cone penetration tests (CPT), reading the pore water pressures from piezometers, and evaluating settlement plate movements after the jet-grouting work was completed.

SPT and CPT were performed within and between the jet-grouted columns to verify the effectiveness and lateral extent of the treatment zone, as shown in Figure 6.

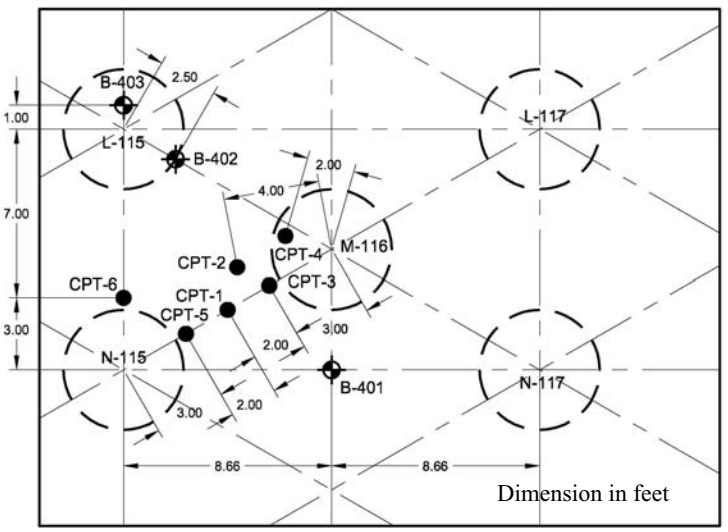

Figure 6. Typical SPT/CPT location within and between the selected columns.

Based on the SPT and CPT results, it appeared that the jet-grout stabilized zone extended beyond the specified 5-foot diameter column footprint. The stiffness of the treated area measured by SPT blow counts and CPT tip resistance showed similar consistency within the 5-foot diameter column and between the columns. The SPT blow counts and the CPT tip resistances are summarized in Table 1. In addition, the average value of the SPT blow counts taken after the jet-grouting operation was appreciably higher than the average value taken before the jet-grouting, as summarized in Table 1. The average CPT tip resistances following the jet-grouting operation were more indicative of stiff soils instead of soft soils.

Table 1. Soil stiffness comparison in jet-grout stabilized zone.

	SPT Blow Counts (bpf)		CPT Tip Resistance (tsf)	
	Before	After	Before	After
Average	4	13	N/A	18
Max.	7	59		75
Min.	2	4		8

Six multi-level vibrating wire piezometers and twelve settlement plates were installed at selected locations within the jet-grout stabilized zones. The multi-level vibrating wire piezometers were installed in between and near the center of the three adjacent jet-grout columns prior to production jet-grouting work. Each set of the multi-level vibrating wire piezometers consisted of three individual piezometers located at about 3 feet above, 3 feet below and 10 feet below the top of the jet-grouted column. Pore water pressures were measured to evaluate the load transfer from the new embankment onto the soft soils located between the jet-grouted columns.

A relatively small pore water pressure increase ranging from 0.5 to 1.5 feet of hydrostatic water head was measured at about 10 feet below the top of the jet-grouted columns. A higher pore water pressure increase ranging from 0.75 to 8.0 feet of hydrostatic water head was monitored above or near the top of the jet-grout columns. The pore water pressure measurements suggest that the embankment load was effectively transferred onto the stiffer jet-grouted stabilized zone.

Settlement plates equipped with vibrating wire pressure sensors were installed within the jet-grout stabilized zone prior to embankment construction including reinforced soil slope (RSS) and segmental retaining wall (SRW) installation after the production jet-grouting work. The settlement plates were connected via two liquid filled tubes, extending laterally, to a reservoir placed within a remote readout shelter located on stable ground beyond the toe of the embankment (RSS and/or SRW). The settlement plates were embedded below the existing ground surface by about 3 feet with sand backfill.

The settlement plate results indicated that the total ground settlement at the selected jet-grout stabilized zone was less than 3 inches in about 4 to 5 months after 20 to 30 feet (vertical height) of RSS and SRW were constructed on the jet-grout stabilized zone.

LESSONS LEARNED AND CONCLUSIONS

Organic-rich alluvial soils were anticipated within the jet-grout stabilized zones. Soft clayey soils (CH/OH) with less than 10% organic content were encountered in the borings from the geotechnical investigation. However, during construction, highly organic soft soils (OH) with organic contents ranging from about 20% to 47% were retrieved from the probe holes and the core samples in the jet-grout test columns. The high organic content has the potential for retarding the hydration of the cement to form the soilcrete meeting the specified strength.

Extensive investigations involving closely spaced borings may be necessary to fully characterize the soils (host materials) to be treated within the jet-grout stabilized zones, including SPT/CPT and pore water pressure monitoring prior to the jet-grouting operation. The detailed site characterization would allow the engineer to design an efficient soil stabilization method and to specify the contract requirements accordingly.

The test sections should include extensive SPT/CPT program before and after the jet-grouting operations to verify that the test columns meet the specified diameter and compressive strengths. These additional measures would assist to establish the jet-grouting parameters for the production work.

Post SPT/CPT program is also necessary to verify the production jet-grouting work for soil stabilization effectiveness by comparing the post SPT/CPT data to the initial SPT/CPT data taken before the construction. Coring of the test columns and testing of the resultant cores is the most effective measure to verify the soilcrete unconfined compressive strength.

Ground heave was experienced due to excessive air pressures (about 5 to 6 bars) being used during jet-grouting operations under the pavement (asphaltic concrete pavement placed on Portland cement concrete pavement). Ground heave was mitigated by reducing the air pressure to 3 bars. The jet-grouting operation is illustrated in Figure 7.

Figure 7. Construction adjacent to active highway (220,000 vehicles/day).

The jet-grouting operation in conjunction with an extensive QC/QA program conducted at the project site proved to be an effective stabilization method for the highway widening project. It improved the under-consolidated soft recent alluvium, which underlies 20 to 40 feet of embankment fill. The estimated 45 inches of consolidation settlement from the thick soft recent alluvium should be kept to a minimum. The jet-grouting construction work was completed in early 2006. No noticeable ground settlement has been observed in the past five years.

ACKNOWLEDGEMENT

The project was administered and funded through the Federal Highway Administration and State of Hawaii Department of Transportation (HDOT). The prime design consultant was R. M. Towill Corporation (RMTC). We appreciate the invaluable assistance afforded by the HDOT and RMTC staffs during the design and construction of this project.

Risk Assessment of Success Dam, California: Evaluation of Operating Restrictions as an Interim Measure to Mitigate Earthquake Risk

by

D. Bowles[1], M. Ruthford[2] and L. Anderson[1]

[1]Utah State University, 8200 Old Main Hill, Logan, UT 84322; emails: david_s_bowles@hotmail.com and loren.anderson@usu.edu
[2]US Army Corps of Engineers, Sacramento District, 1325 J Street, Sacramento, CA 95814; emails: Michael.E.Ruthford@usace.army.mil,

ABSTRACT

Seismic deficiency of Success Dam, California has been determined and the need of remediation for improving the performance of the dam under earthquake loading has been identified. Consequently, the dam is currently operated under reservoir pool elevation restriction, pending rehabilitation implementation. Justification of operation restrictions and establishing the priority of remediation activities required preparation of a baseline risk assessment. This paper describes the overall risk model and the results of the risk assessment supporting the justification of operation restrictions. Two companion papers describe the potential failure modes related to earthquake events and flood events.

PROJECT DESCRIPTION

Lake Success has been operated by the Sacramento District of the US Army Corps of Engineers (USACE) since completion of construction in 1961. The project comprises the dam, the Frazier Dike and a reservoir located on the Tule River about 10 km (6 miles) east of Porterville and 72 km (45 miles) north of Bakersfield, California. The reservoir captures runoff from a 1,013 km^2 (391 square miles) mountainous watershed. It is part of a system of reservoirs that provide flood protection to the Tulare Lakebed and adjacent areas. It also provides irrigation water storage and recreation benefits.

Success Dam is a compacted earthfill embankment dam 44.2 m (145 feet) high, 1,038 m (3,404 feet) long and with a crest elevation of 210.8 m (691.5 feet) as shown in a companion paper by Anderson et al. (2011). The dam has a central core of sandy clay and clay, and a pervious shell. The shell material is protected by a 3.7 m (12 feet) thick transition zone, which partially meets modern filter criteria between the core and the transition material and between the transition material and the pervious shell. There is a cutoff trench under the core that extends through the recent alluvium to either bedrock or in some cases to an older alluvium stratum. The recent alluvium was not excavated in the area beneath the pervious shell. Shear wave velocity measurements and standard penetration tests in the recent alluvium and the upstream and downstream embankment shoulders indicate that these materials are loose and could be subject to liquefaction during an earthquake.

There is a 3.7 m (12 feet) diameter outlet works conduit founded on bedrock under the right side of the dam. It has an upstream bulkhead gate as well as operating gates located in the control tower. A free overflow spillway is located in the right abutment with a crest at the full pool elevation of 198.9 m (652.5 feet).

Frazier Dike is a containment dike located at the north end of Lake Success. The toe of the dike is at approximately the full pool level and the crest elevation of 210.8 m (691.5 feet) is the same as the Main Dam. It is a compacted homogeneous embankment without slope protection except for a thick grass cover.

Concern about earthquake induced liquefaction in the recent alluvium foundation leading to significant crest settlement and horizontal movements for the Main Dam lead to the District's decision in 2004 to commission a risk assessment to explore the justification for an operating restriction until a permanent structural solution is completed (Bowles et al 2005). A follow up study was completed in 2009 and is summarized in this paper and two companion papers by Anderson et al (2011) and Ruthford et al (2011).

POTENTIAL OPERATING RESTRICTIONS

The authorized (No Restriction) Flood Control Diagram (FCD) for Lake Success sets a maximum target pool elevation of 198.9 m (652.5 feet) in the summer. An operating restriction would reduce that maximum target pool elevation as shown in Figure 3. This would reduce the durations of high pool elevations and hence the probability and consequences for failure modes other than those associated with major floods. Five potential operating restrictions (ORs) were considered in the risk assessment and are referred to by a code, which includes their reduced maximum target pool elevation in feet, as follows: OR.640, OR.630, OR.620, OR.600 and OR.580.

In the 2004 Study a daily reservoir simulation for the 44-year period of record was used to estimate modified stage-duration relationships for each potential operating restriction (Figure 3). The costs of the potential operating restrictions were based on their estimated economic impacts. The effects on seasonal patterns of reservoir releases and pool elevations were simulated and provided to water user's representatives to estimate the two types of economic impacts of the potential operating restrictions that are listed below:

- Agricultural losses associated with reductions in irrigation water.
- Increased flood damages in an historic terminal lake, Tulare Lake, which is a highly productive agricultural area in Kings County.

Net recreational losses, allowing for shifts to other lakes in the region, were estimated to be US$2.1 M for OR.630 and OR.640, and US$2.8 M for OR.580, OR.600 and OR.620, respectively.

RISK ASSESSMENT APPROACH

Earthquake failure modes. Three types of Earthquake liquefaction-induced failure modes were considered: a) vertical crest deformation and failure by above-core erosion (ACE) of the dam if the concomitant reservoir pool elevation is high enough;

b) seepage erosion through cracks (SEC) resulting from disrupted filters and drains and transverse cracking induced by deformation; and c) embankment and tower deformation resulting in failure by piping into a rupture in the control tower - outlet works system, referred to as a tower-induced piping (TIP) failure. The ACE failure could lead to initiation of a breach of the dam immediately after the earthquake or, like the SEC and TIP failure modes, it could be delayed for some time after the earthquake in which case warning times can be longer than for an immediate ACE failure. System response probability relationships associated with these failure modes are described in a companion paper by Ruthford et al. (2011).

Vertical embankment deformation greater than one foot could damage the control tower resulting in a loss of the capability to operate the outlet works gates, and hence, a loss of reservoir control. Vertical embankment deformation greater than 0.9 m (3 feet) would be expected to damage the control tower beyond the point where regaining outlet works gates operation is feasible. The District estimates that, if feasible, it would take about three weeks to regain operation of the outlet gates, or to implement a controlled breach of the dam, if needed, in the event that the control tower damage is too great to regain outlet works operation capability. During this period the reservoir pool could rise. Therefore, the ACE, SEC and TIP liquefaction-induced failure modes were also considered to have the potential to occur in a delayed manner during a three-week period following the earthquake.

The Earthquake event tree in Figure 1 is slightly simplified from the full form that is used in the DAMRAE software. DAMRAE is software that has been developed at Utah State University for USACE as the risk analysis engine for their dam safety risk management program (Srivastava et al 2008, 2009a and 2009b).

The Earthquake event tree was applied separately to each of three Earthquake magnitudes to represent Earthquake loading over a range of peak ground accelerations (PGAs) and their associated annual exceedance probabilities (AEPs) for each magnitude range, as follows:

a) From 0.1 g to 0.65 g for the less than M 6.5.
b) From 0.1 g to 0.3 g for the M 6.5 - M 7.0.
c) From 0.05 g to 0.25 g for the greater than M 7.0.

The Earthquake magnitude range is specified in branch Level 1 in the event tree as labeled in Figure 1. The “fan-shaped” symbol in Level 2 of the event tree represents a continuous event branch group comprising a set of 21 branches that cover each range of PGAs listed above, and their AEPs for the Earthquake magnitude specified in Level 1 based on the PGA versus AEP relationships derived from URS (2004) and shown in Figure 1a.

Level 3 in the Earthquake event tree is a continuous branch to represent the range of pool elevations at the time that an earthquake occurs and the fraction of time that each interval of pool elevations occurs. This type of loading is represented by the stage-duration relationships for each potential operating restriction that were obtained using the daily reservoir simulation. For the No Restriction alternative, the historical stage-duration relationship was used (see Figure 1b). For the risk model runs that considered potential operating restrictions, stage-duration relationships were estimated using a daily reservoir simulation model in the 2004 Study. Twenty-four,

1.2 m (4 feet) intervals of reservoir stage or pool elevation were considered between mid-point elevations of 172.8 m (567 feet) and 200.9 m (659 feet).

Level 4 is a state function branch in which vertical embankment deformation is interpolated from relationships (see Figure 1c) developed by the District using results from FLAC model runs (see Ruthford et al., 2011) for a range of Earthquake magnitudes, PGAs and reservoir pool elevations using the values of these three loading variables specified in Levels 1, 2 and 3, respectively. These are considered to be most likely (mode) estimates of the vertical deformation and uncertainty bounds were judgmentally estimated to calculate the conditional probability of Earthquake-induced above-core erosional (ACE) failure (Level 5) based on the vertical deformation being sufficient for the top of the core to fall below the pool elevation (Level 3) at the time of the earthquake as illustrated by the shaded area in the triangular probability distribution in Figure 1d and entered in the failure branch in Level 5 of the event tree.

Level 6 of the event tree is a failure branch that represents the occurrence of a SEC failure, a tower-induced piping (TIP) failure, or no failure. The system response probabilities (SRPs) for these failure modes are shown in Figure 1e and are conditioned on embankment vertical deformation (Level 4) and pool elevation (Level 3). They were estimated by expert judgment. These two failure modes are not mutually exclusive. They are classified as common-cause failure modes because they can occur simultaneously as the result of a "common cause"; that is, the earthquake-induced deformation of the embankment and the tower. To properly estimate the overall probability of failure and associated consequences, a common cause adjustment (Bowles et al 2001) was applied to the SRPs for these three failure modes in Level 6 using DeMorgan's rule (Ang and Tang, 1984) based on an assumption that their occurrence is statistically independent.

The two branches in the upper part of Level 7 of the Earthquake event tree represent the events that the outlet works remains functional after the earthquake (the upper branch) or that it becomes non-functional (the lower branch) given that the dam has not failed immediately or soon after the earthquake. The latter outcome includes the possibility that reservoir control is recoverable for vertical embankment deformations less than 0.9 m (3 feet), or that it is not recoverable for larger deformations. The SRP for the outlet works becoming non-functional is estimated to be dependent on embankment vertical deformation (Level 4) as presented in Figure 1i.

The continuous event branch in Level 8 of the event tree covers a range of 1.2 m (4 foot) reservoir pool elevation intervals that the reservoir can attain during a three-week period following the earthquake as a result of the loss of reservoir control. Twenty-three 1.2 m (4 foot) intervals of reservoir stage or pool elevation were considered between elevations 178.9 m (587 feet) and 204.5 m (671 feet), plus an open interval at elevation 178.3 m (585 feet) and below. Each interval of reservoir pool elevation has an estimated probability of occurring based on the reservoir pool elevation at the time of the earthquake (Level 3). This relationship is represented as a probability transition matrix for each potential operating restriction alternative as illustrated graphically in Figure 1g for Operation Restriction OR.620. These relationships were estimated using the daily reservoir simulation under the

assumption of loss of reservoir control resulting in the outlet gate being jammed in its current position for a three-week period starting on any day of the period of record.

Levels 9 and 10 of the Earthquake event tree represent the delayed manifestations of the same initial failure modes that are represented in Levels 5 and 6, respectively, as initial failure modes. When considered as initial failure modes, their SRPs depend on the average of the pool elevation interval specified in Level 3. For the delayed failure case, their SRPs depend on the average of the pool elevation interval specified in Level 8. For the delayed failure modes, the SRPs applied in Levels 9 and 10 are calculated as the increase in the SRPs due to any rise in pool elevation between the time of the earthquake (Level 3) and three weeks later (Level 8). In the case that the reservoir pool remains at the same elevation or decreases, a value of zero is assigned to the SRPs.

The three continuous event branches in the three lowest failure branches of Level 10 of the Earthquake event tree represent the time from occurrence of the earthquake until an ACE, SEC or TIP breach initiates, which is defined as the start of the breach process in the dam break-inundation modeling. These ranges of times were needed for calculation of warning times that are an important predictor of life loss. The estimated probability of various times to breach initiation conditioned on pool elevation (Level 3) are presented in Figure 1h for the ACE failure mode and in Figure 1f for the SEC and TIP failure modes.

No Earthquake failure modes were considered for Frazier Dike. Although the dike may be damaged in a major earthquake, little is known about its likely seismic performance, and the dike only retains water when the pool is above the current full pool level. The performance of the Frazier Dike under earthquake loading should be included in a Dam Safety Modification Study risk analysis.

Flood and flood-internal failure modes. Flood failure modes (i.e. overtopping and wave erosion for the Main Dam and overtopping for Frazier Dike) and Flood-internal failure modes (i.e. piping and slope instability for the Main Dam) were included in the event tree shown in Figure 2. The following six piping failure modes were considered: a) piping into terrace deposits in the left abutment; b) piping into rock in the right abutment; c) piping through the rock foundation; d) piping through the embankment; e) piping through the foundation in the old alluvium; and f) embankment piping along the outlet works. System response probability relationships associated with these failure modes are described in a companion paper, by Anderson et al., (2011).

Level 1 in the Flood event tree shown in Figure 2 is a continuous event branch representing 500 intervals of peak reservoir pool elevation and their corresponding annual probabilities of occurrence, obtained from the peak reservoir pool elevation - AEP relationships in Figure 2a for each potential operating restriction alternative. The high frequency part of these relationships were developed using results from the daily reservoir simulation for each potential operating restriction. Peak reservoir pool elevations considered in the event tree ranged from a failure threshold event with an AEP of about 1 in 1.2 up to events that exceed the AEP of 1 in 10,000 assigned to the PMF by two orders of magnitude of AEP consistent with new USACE guidance. The threshold event corresponds to an annual peak pool elevation of about 189 m (620

feet) for the No Restriction alternative and about 177.1 m (581 feet) for OR.580 (see Figure 2a).

Level 2 is a state function branch in which the peak overtopping depth is calculated by subtracting the dam crest elevation from the peak reservoir pool elevation (Level 1).

Level 3 is a failure mode branch that represents the ten Flood and Flood-internal failure modes. The conditional probability of occurrence of each failure mode is represented by their respective SRPs, which are conditioned on peak reservoir pool elevation (Level 1) or peak reservoir overtopping depth (Level 2). A common-cause adjustment was applied to all ten SRPs with "freezing" to fix the contributions to total probability of failure and failure consequences at the pool elevation where one SRP first becomes 1.0 (Bowles et al., 2001). The SRPs for each of the piping failure modes (see Figure 2d) were estimated using guidance from the USACE Piping and Seepage Toolbox (USACE 2009b) and for the instability failure mode (see Figure 2e) using a probabilistic slope stability analysis performed by the District using the SLOPE/W software. Overtopping and wave erosion SRPs (see Figures 6c and b, respectively) were estimated by expert judgment.

CONSEQUENCES OF FAILURE

All consequences estimates were based on the results from dam breach-inundation modeling and life loss was estimated using the Reclamation (Graham 1999) method with consideration given to the timing of the issuance of warnings, including the probability distribution of time from the occurrence of the earthquake until initiation of an ACE, SEC or TIP-induced breach as a function of pool elevation (see Figures 5h and f). No consequences were estimated for Frazier Dike failure.

The Earthquake and Flood and Flood-internal event trees, shown in Figures 1 and 2, respectively, provide the structure for the risk model that was used to estimate the probability of failure for Success Dam. Economic and life-loss consequences were incorporated into the event tree risk model using consequences subtrees that were appended to each branch of the event trees but which are not shown in this paper. They comprise exposure (day and night) and consequences branches in the DAMRAE event tree risk models.

USACE TOLERABLE RISK GUIDELINES

The proposed USACE tolerable risk guidelines (USACE 2009a, Munger et al 2009) were applied to assess the significance of estimated risks for each operating restriction alternative. These guidelines include a two-part evaluation process. The first part compares total estimated risk for all failure modes against the following tolerable risk limit values for existing dams:

1) An Annual Probability of Failure (APF) of 1 in 10,000 /year as a measure of the performance of the dam (Figure 3);
2) An Individual Risk (IR) expressed as a probability of life loss for the identifiable person(s) most at risk of 1 in 10,000 /year as a measure of life-safety risk (Figure 4);

3) A Societal Risk (SR) expressed as a limit of tolerability on a cumulative probability distribution (F-N chart) of exceeding various magnitudes of (random) life loss as a measure of life-safety risk (Figure 5); and
4) An Annualized Life Loss (ALL) of 0.001 lives/year as the average magnitude of life loss from the probability distribution of life loss in 3) as a measure of life-safety risk (Figure 3).

The second part of the risk evaluation process is a determination of whether risks have been reduced to be as low as reasonably practicable (ALARP). This evaluation is both qualitative and quantitative in nature and should take the following into account: the level of risk in relation to the tolerable risk limits; the disproportion between the sacrifice (money, time, trouble and effort) in implementing the risk reduction measures and the subsequent risk reduction achieved; the cost-effectiveness of the risk reduction measures; compliance with essential USACE guidelines; and societal concerns as revealed by consultation with the community and other stakeholders.

The consideration of the cost effectiveness or "disproportionality" associated with the cost of achieving life-safety risk reduction relative to the life-safety benefit achieved is a quantitative aspect of an ALARP evaluation. This introduces the consideration of cost, but only to justify further incremental risk reduction below the tolerable risk limits, and not to justify achieving those limits in the first place. Hence, there should be no consideration of "balancing" the economic impacts of operating restrictions and reductions in life-safety risk in meeting the tolerable risk limits.

SUMMARY OF FINDINGS – NO RESTRICTION ALTERNATIVE

Engineering Assessment against USACE dam safety requirements. An Engineering Assessment identified the following confirmed deficiencies against USACE engineering guidelines: liquefaction and stability of the embankment and foundation under Earthquake loading; control tower stability under Earthquake loading; abutment, foundation and outlet works piping; PMF flood capacity; and spillway and stilling basin system erodibility. Apparent deficiencies against USACE Guidelines, which need confirmation through further investigation, were identified for the following: outlet works – control tower under Earthquake loading; the Main Dam embankment piping; and wave action under Flood loading. Several other Earthquake and Flood factors were found to apparently meet USACE guidelines, but need further investigations to satisfy the normal level of confidence required by USACE.

Risk estimates and evaluation against USACE tolerable risk guidelines. As shown on Table 1, the existing Success Dam with No Restrictions does not meet any of the proposed USACE tolerable risk guidelines including Total Annual Probability of Failure, Total Individual Risk, Total Societal Risk and Total Annualized Life Loss. The total probability of failure is estimated to be about 1 in 3,600 /year. Flood, Flood-internal and Earthquake failure modes are estimated to contribute about 18%, 59% and 23% to the total probability of failure, respectively. A breakdown of the

contributions from each failure mode was tabulated and used to evaluate the relative importance of each failure mode to the overall risk.

SUMMARY OF FINDINGS - POTENTIAL OPERATING RESTRICTIONS

Table 1 provides a summary of risk assessment results for the potential operating restriction alternatives. Estimated residual risks associated with implementation of each potential operating restriction alternative are summarized as percentages of the No Restriction risk for the following risk measures: a) total annual probability of failure in Column 2.1; b) total annualized life loss in Column 2.2; and c) total risk cost ($M/year) in Column 2.3. Columns 3.1 – 3.4 include the outcomes of evaluating these residual risks for each potential operating restriction alternative against the four types of USACE tolerable risk limit guidelines listed above. Columns 4.1 – 4.4 contain the estimated annual economic impact costs of the operating restrictions.

THE CORPS' DECISION ON OPERATING RESTRICTIONS

Following this Update Study the District decided to slightly relax the operating restriction from OR.620 to OR.630. The following are some of the factors that were considered in that decision:

1) Under the proposed USACE tolerable risk guidelines, the least restrictive potential operating restriction alternative that is demonstrated to meet all limit guidelines should be considered as the candidate operating restriction. The next more restrictive operating restriction alternative should then be evaluated to determine if the further estimated risk reduction associated with that alternative can be justified because it does not represent a significantly disproportionate additional impact cost relative to its additional life-safety benefits.
2) Following the procedure summarized in 1), would lead to the adoption of OR.600. However, it is noted that OR.630 is estimated to meet the proposed USACE SR and IR limit guidelines, which are the most widely-used types of life-safety guidelines, but not the APF and ALL limit guidelines.
3) The proposed USACE tolerable risk guidelines interpret risks that exceed the tolerable risk limit as "unacceptable except in exceptional circumstances." The explanation of the exceptional circumstances qualifier refers to a situation in which "the probability of failure is very low" (USACE 2009a, Munger et al 2009). It is noted that for OR.630, while the total probability of failure estimated for Success Dam exceeds the APF tolerable risk limit guideline of 1 in 10,000 /year, the estimated individual risk, based on failure of the Main Dam, is estimated to meet the IR limit guideline.
4) The proposed USACE tolerable risk guidelines do not provide for a less restrictive tolerable risk target for interim risk reduction measures than for long-term risk reduction measures. Thus the use of Reclamation's 0.01 lives/year guideline, which was used as a key basis for the 2004 decision to implement OR.620 following the 2004 Study, is not consistent with proposed

USACE guidance or other tolerable risk guidelines. Instead the ALL limit value of 0.001 lives/year should be used along with the limit values for the APF, IR and SR tolerable risk limits and the requirement to satisfy ALARP considerations. This is the basis on which risk evaluations have been performed and reported in this Update Study.

CONCLUSIONS

The use of risk assessment was found to be valuable in providing a rational and defensible basis for exploring the justification for implementing potential operating restrictions at Success Lake. It provided new insights and understanding of the potential failure modes, including the relative likelihood of sudden vs. delayed failure modes, and the relationship between pool elevation and dam failure risk, including the potential for large scale life loss and major economic damages. The evaluation against the USACE tolerable risk guidelines provided a basis for decision making.

Unlike most other dam safety risk reduction measures, the cost of operating restrictions is borne by the project beneficiaries through reduced water supply, flood control and recreation benefits. It was therefore important that the agricultural water users undertook the estimation of their economic impacts from the potential operating restrictions.

While Earthquake-related failure modes were the initial reason for considering the need for operating restrictions, this Study demonstrated that piping failure modes are also a significant contributor to the risk of failure. It also illustrates a strategy of approaching interim risk reduction decisions from the conservative side in the face of uncertainty about life-safety risks.

The loss of project benefits associated with the loss of outlet works gates operation resulting from earthquake-induced damage to the control tower are not considered in this risk assessment for non-dam failure cases and for the controlled breach case. This approach is consistent with the USACE consideration of only dam failure consequences in dam safety risk assessments. However, these non-dam failure economic losses should be estimated in future risk assessments for Success Dam so that they can be considered in the overall USACE decision process for both interim and long-term risk reduction for Success Dam.

ACKNOWLEDGEMENTS

This paper is based on a project that was conducted for the Sacramento District of the U.S. Army Corps of Engineers by RAC Engineers & Economists and Utah State University. Mr. Paul V. Zianno, P.G., Dr. Vlad G. Perlea, P.E., Mr. Michael D. Ramsbotham, P.E., Mr. David Serafini, P.E., and Mr. Jack Montgomery of the Sacramento District, and Dr. Michael H. Beaty, P.E., Consultant to the Sacramento District, played a significant role in the failure modes identification and development of inputs for the risk analysis, including extensive supporting analyses. Important inputs to the 2004 Study were provided by representatives of the J.G. Boswell Company, the Lower Tule River Irrigation District/Pixley Irrigation District,

the Tule River Association, the City of Porterville, Tulare County and Kings County. The authors wish to thank Dr. Jeffrey Schaeffer, P.E., P.G. and Mr. Jason Needham, P.E., USACE Risk Management Center, for their valuable review comments on the Update Study.

REFERENCES

Anderson, L. M. Ruthford, V. Perlea, D. Serafini, J. Montgomery, and D. Bowles. 2011. Risk Assessment of Success Dam, California: Flood Related Potential Failure Modes. Proceedings of GeoRisk 2011.

Ang, A.; Tang, W.H. 1984. Probability concepts in engineering planning and design, decision, risk, and reliability. Vol. 2. John Wiley & Sons, New York, NY.

Bowles, D.S.; Anderson, L.R.; Chauhan, S.S. 2001. Approaches to the common cause adjustment in event trees used in dam safety risk analysis. An IDSRM-USU Working Paper.

Bowles, D.S.; Anderson, L.R.; Glover, T.F.; Chauhan, S.S.; Rose, R.S. 2005. Risk-based Evaluation of Operating Restrictions to Reduce the Risk of Earthquake-induced Dam Failure. Proceedings of the 2005 USSD Annual Lecture, Salt Lake City, Utah.

Graham, W. 1999. A procedure for estimating loss of life caused by dam failure. U.S. Bureau of Reclamation, Denver, Colorado. September.

Munger, D.F.; Bowles, D.S.; Boyer, D.D.; Davis, D.W.; Margo, D.A.; Moser, D.A.; Regan, P.J.; Snorteland, N. 2009. Interim Tolerable Risk Guidelines for US Army Corps of Engineers Dams. Proceedings of US Society on Dams 2009 Annual Lecture, Nashville, Tennessee. April.

Ruthford, M., V. Perlea, D. Serafini, M. Beaty, L. Anderson, and D. Bowles. 2011. Risk Assessment of Success Dam, California: Earthquake Induced Potential Failure Modes. Proceedings of GeoRisk 2011.

Srivastava, A., Bowles, D.S.; Chauhan, S.S. 2008. Generalized event tree algorithm and software for dam safety risk assessment. Proceedings of the US Society on Dams Annual Lecture, Portland, Oregon. April.

Srivastava, A.; Bowles, D.S.; Chauhan, S.S. 2009a. Improvements to DAMRAE: A Tool for Dam Safety Risk Analysis Modeling. Proceedings of the ASDSO Conference on Dams.

Srivastava, A.; Chauhan, S.S.; Bowles, D.S. 2009b. DAMRAE User Guide. Institute for Dam Safety Risk Management, Utah State University, Logan, Utah.

USACE (U.S. Army Corps of Engineers). 2009a. Dam safety regulation. Draft. EC 1110-2-1156.

USACE (U.S. Army Corps of Engineers). 2009b. Internal Erosion Toolbox.

URS. 2004. Deterministic and probabilistic seismic hazard analyses for Success Dam. Final Report by URS Corporation, Oakland, California. January.

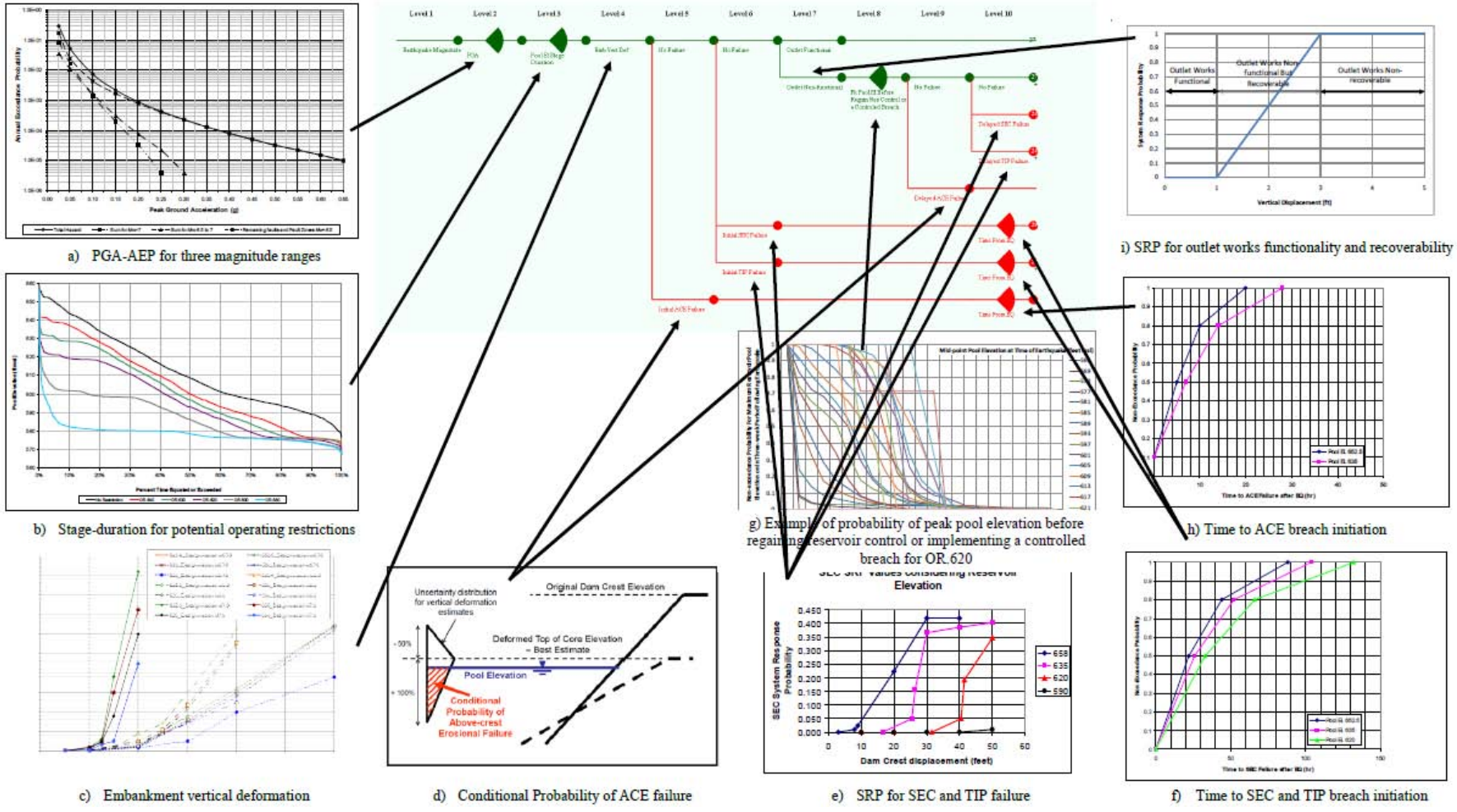

Figure 1. **Earthquake Event Tree for Success Dam with Earthquake Loading, SRP and Other Relationships**

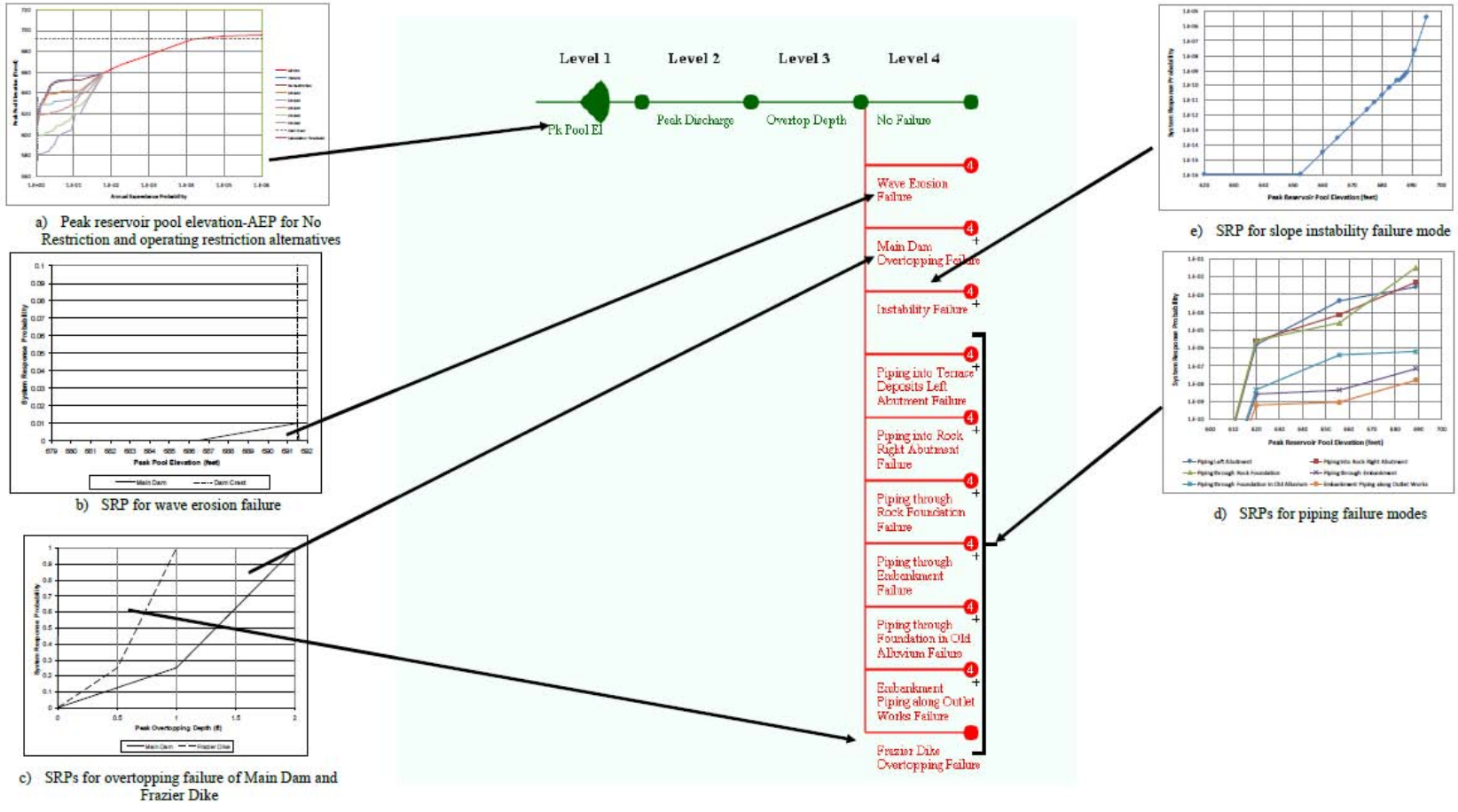

Figure 2. **Flood and Flood-internal Event Tree for Success Dam with Flood Loading and SRP**

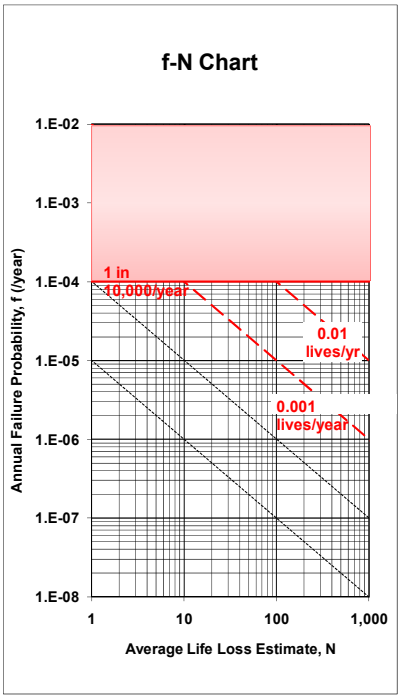

Figure 3. f-N Chart USACE APF and ALL Tolerable Risk Limit Guidelines

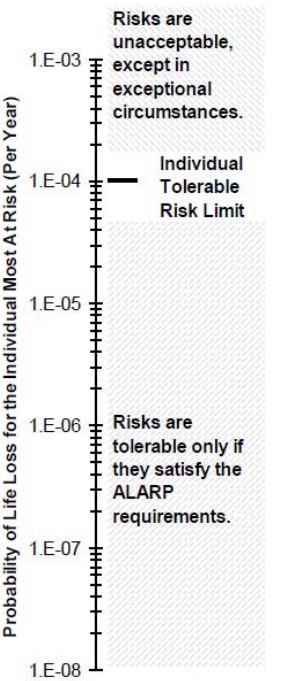

Figure 4. USACE Individual Risk Guideline for Existing Dams

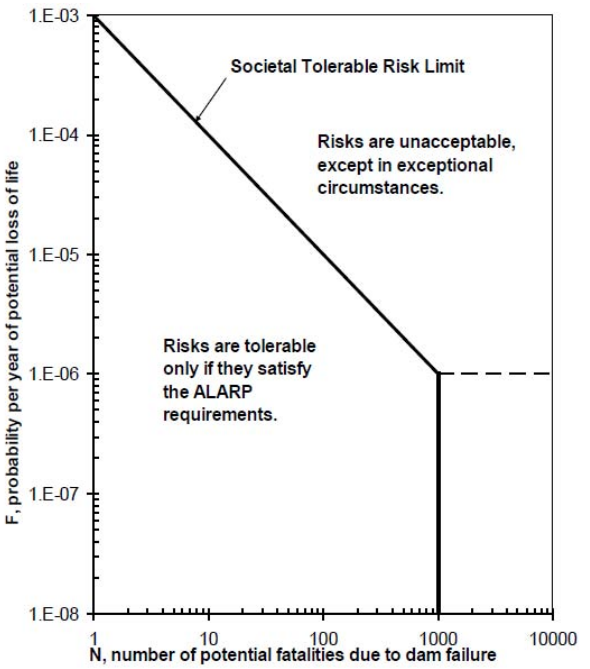

Figure 5. USACE Societal Risk Guideline for Existing Dams

(1)	(2.1)	(2.2)	(2.3)	(3.1)	(3.2)	(3.3)	(3.4)	(4.1)	(4.2)	(4.3)	(4.4)
DECISION OPTION: OPERATING RESTRICTION ALTERNATIVE	**ESTIMATED RESIDUAL DAM FAILURE RISK AS PERCENT OF NO RESTRICTION RISK**			**EVALUATION AGAINST PROPOSED USACE TOLERABLE RISK GUIDELINES**				**ANNUAL AVERAGE ESTIMATED IMPACT COSTS** (Range of Estimated Annual Impact Costs)			
	TOTAL Annual Probability of Failure (APF)	**TOTAL Annualized Life Loss (ALL)**	**TOTAL Risk Cost (RC)**	**TOTAL Annual Probability of Failure (APF)**	**TOTAL Individual Risk (IR)**	**TOTAL Societal Risk (SR)**	**TOTAL Annualized Life Loss (ALL)**	**Impact on Agricultural Water Users**	**Flood Damages in Tulare Lakebed**	**Impact on Recreation**	**Total**
	(/year)	Life Loss x Probability (lives/year)	Dam Failure Damages x Probability ($M/year)					($M/year)	($M/year)	($M/year)	($M/year)
No Restriction (100% Normal Capacity)	100% (1 in 3,600 /year)	100% (0.0046 lives/year)	100% ($0.17 M/year)	**UNACCEPTABLE**	**UNACCEPTABLE**	**UNACCEPTABLE**	**UNACCEPTABLE**				
OR.640 (68% Normal Capacity)	61% (1 in 5,900 /year)	41% (0.0019 lives/year)	52% ($0.087 M/year)	**UNACCEPTABLE**	**UNACCEPTABLE**	**UNACCEPTABLE**	**UNACCEPTABLE**	$0.4M ($0 - $3.0M)	$0.6M ($0 - $3.1M)	$2.1M	$3.1M
OR.630 (50% Normal Capacity)	48% (1 in 7,400 /year)	28% (0.0013 lives/year)	37% ($0.062 M/year)	**UNACCEPTABLE**	**TOLERABLE if ALARP**	**TOLERABLE if ALARP**	**UNACCEPTABLE**	$1.0M ($0 - $2.2M)	$0.6M ($0 - $3.1M)	$2.1M	$3.7M
OR.620 (35% Normal Capacity)	39% (1 in 9,100 /year)	21% (0.0010 lives/year)	26% ($0.044 M/year)	**UNACCEPTABLE**	**TOLERABLE if ALARP**	**TOLERABLE if ALARP**	**TOLERABLE if ALARP**	$1.4M ($0 - $3.0M)	$0.6M ($0 - $3.2M)	$2.8M	$4.9M
OR.600 (16% Normal Capacity)	34% (1 in 10,600 /year)	17% (0.0008 lives/year)	21% ($0.035 M/year)	**TOLERABLE if ALARP**	**TOLERABLE if ALARP**	**TOLERABLE if ALARP**	**TOLERABLE if ALARP**	$2.4M ($0.9M - $3.8M)	$1.5M ($0 - $7.5M)	$2.8M	$6.7M
OR.580 (5% Normal Capacity)	32% (1 in 11,000 /year)	16% (0.0008 lives/year)	19% ($0.032 M/year)	**TOLERABLE if ALARP**	**TOLERABLE if ALARP**	**TOLERABLE if ALARP**	**TOLERABLE if ALARP**	$3.1M ($1.1M - $4.8M)	$1.9M ($0 - $9.4M)	$2.8M	$7.7M

UNACCEPTABLE except in exceptional circumstances	**TOLERABLE providing all ALARP considerations are met on an on-going basis**

Table 1. Summary of Decision Options

Some Observations on Reliability-Based Design of Rock Footings

Widjojo A. Prakoso, A.M.ASCE [1] and Fred H. Kulhawy, Dist.M.ASCE [2]

[1]Lecturer, Civil Engineering Department, University of Indonesia, Depok 16424, Indonesia; email: wprakoso@eng.ui.ac.id
[2]Professor Emeritus, School of Civil and Environmental Engineering, Cornell University, Ithaca, NY, USA; email: fhk1@cornell.edu

ABSTRACT

This paper continues our development of a simplified reliability-based design method for rock footings in an LRFD format. Two issues are addressed herein: the robustness of the empirical model and the proper approach to evaluate the rock strength variability. Results of simulations using three calculation models indicate that the empirical model is reasonably conservative and that the strength variability to be used in the calculations is that of the rock mass, not the intact rock.

INTRODUCTION

The development of a reliability-based design (RBD) method for the ultimate limit state (ULS) of rock footings in compression, calibrated for transmission line or similar structures subjected to ASCE wind load provisions (Task Committee 1991), was described briefly by Prakoso and Kulhawy (2003). The proposed method was in a Load and Resistance Factor Design (LRFD) format and consisted of two components: an empirical calculation model and the intact rock strength and its variability.

This paper addresses two issues that were not discussed in detail in the 2003 paper: the robustness of the empirical model and the proper approach to evaluate the rock strength variability. After presenting the proposed LRFD model, the variability of the rock strength is discussed, and the calculation models are assessed. Recommendations then are given, particularly for evaluating the rock strength variability.

CAPACITY OF ROCK FOOTINGS

The compression capacity of rock footings (Q_c) is a function of the tip resistance (Q_{tc}), side resistance (Q_{sc}), and footing weight (W). Because of their relative magnitude, Q_{sc} and W commonly are neglected in practice, so Q_c is given by:

$$Q_c = Q_{tc} + Q_{sc} - W \approx Q_{tc} \quad (1)$$

The compression capacity involves a complex interaction among the intact structure, discontinuities, and imposed stress effects in the rock mass within the influence zone of the footing. This interaction typically is difficult to measure and estimate, and consequently the use of theoretical solutions require considerable

judgment. As a practical alternative, it is assumed commonly that Q_c can be related directly to the intact rock uniaxial compressive strength (q_u), as follows:

$$Q_c = 0.25\ \pi\ B^2\ N_c^*\ q_u \quad (2)$$

in which B = footing diameter and N_c^* = empirical bearing capacity or resistance factor. The inherent assumptions within this model are that N_c^* represents the "failure mode" and that q_u represents the material conditions. It is recognized that the uncertainties associated with the calculation model and the intact rock strength should be evaluated at every specific site. However, in the absence of site-specific data, guidelines on the probable variation resulting from the calculation models are useful as first-order approximations.

The development of N_c^* was described by Prakoso and Kulhawy (2002), using twelve field axial load tests on circular footings in four fine-grained sedimentary and igneous pyroclastic rock sites. The back-calculated N_c^* ranged from 2.40 to 14.8. Three tests yielded very high N_c^* values (N_c^* = 8.35 – 14.8) and, to retain some degree of conservatism, these values were not considered in further statistical and regression analyses. The remaining nine test data ranged from 2.40 to 5.21, and the mean of the footing resistance factor (m_{Nc*}) and its coefficient of variation (COV) or COV_{Nc*} are 3.46 and 26.8%, respectively, as shown in Figure 1.

LRFD FOR ROCK FOOTINGS

A reliability-based design equation in the following LRFD format was used in the calibration of the ULS for rock footings:

$$F_{50} = Q_{cn}\ \Psi_c^{ULS} \quad (3)$$

in which F_{50} = 50-year return period wind load (Task Committee 1991) and Ψ_c^{ULS} = resistance factor for ULS. The nominal compression capacity then is defined as:

$$Q_{cn} = 0.25\ \pi\ B^2\ m_{Nc*}\ m_{qu} \quad (4)$$

in which m_{Nc*} = nominal empirical footing resistance factor and m_{qu} = mean intact rock uniaxial compressive strength.

The calibration of Ψ_c^{ULS} was performed for three domains of COV of q_u (COV_{qu}) that represent the overall rock strength variability, and each was calibrated to achieve a target reliability index (β_T) of 3.2. The results are given in Table 1 and show that Ψ_c^{ULS} decreases with increasing COV_{qu}. A higher value of COV_{qu} gives a less reliable capacity estimate, and therefore a lower Ψ_c^{ULS} is required to achieve the design β_T. The calibration details are discussed by Prakoso and Kulhawy (2003).

In traditional allowable stress practice, rock footings are designed as follows:

$$F_{50} = Q_{cn} / FS \quad (5)$$

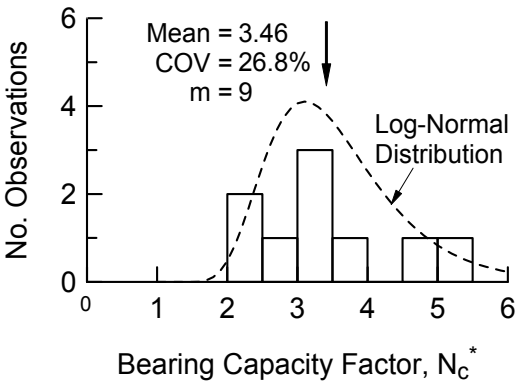

Figure 1. Footing empirical N_c^* (Prakoso & Kulhawy 2002)

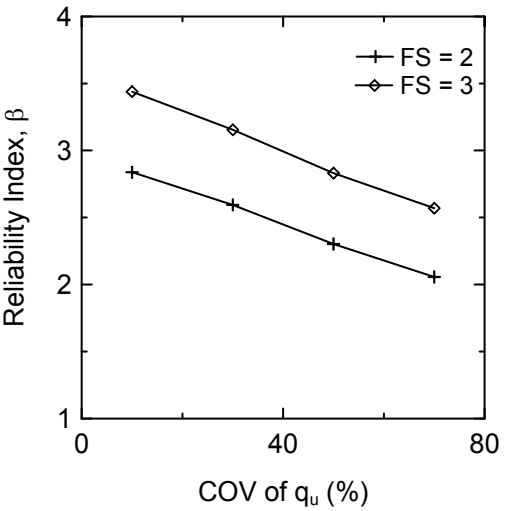

Figure 2. Effect of COV_{qu} on β

Table 1. Compression resistance factors (Prakoso & Kulhawy 2003)

COV_{qu} (%)	Ψ_c^{ULS}
10 – 30	0.36
30 – 50	0.29
50 – 70	0.23

in which FS = global factor of safety (typically between 2 and 3). However, the implicit reliability index (β) in practice is shown in Figure 2. As can be seen for a wide range of COV_{qu}, the range of β is between 2.06 (probability of failure, p_f = 1.99%) to 3.44 (p_f = 0.03%), and β is higher for a higher safety factor. Furthermore, Figure 2 shows that β is influenced significantly by COV_{qu}.

The empirical N_c^* might change with a change in the data base, and therefore the effect of N_c^* statistics on β also was evaluated. For changes of m_{Nc*} from 2.50 to 4.50, β changes from 2.752 to 2.726 (empirical m_{Nc*} = 3.46, β = 2.723). For changes of COV_{Nc*} from 20% to 35%, β changes from 2.816 to 2.637 (empirical COV_{Nc*} = 26.8%, β = 2.796). These results show that the statistics of N_c^* do not affect β significantly, specifically compared to the effect of COV_{qu}. Accordingly, the proposed RBD equations should not change significantly as more data on footing capacity become available and the statistics of N_c^* change.

VARIABILITY OF ROCK MECHANICAL PROPERTIES

The variability of rock mechanical properties can be evaluated in terms of the intact rock or the rock mass. For the intact rock, the variability has been assessed by Prakoso and Kulhawy (2011). The COV values for ranges of mean property values (strength properties q_u, $q_{t\text{-Brazilian}}$, and I_s, and deformation property $E_{t\text{-}50}$) are shown as Figure 3. Overall, the mean COV values tend to decrease with increasing mean property values, from 10 - 45% for weaker rocks to 5 - 15% for stronger rocks.

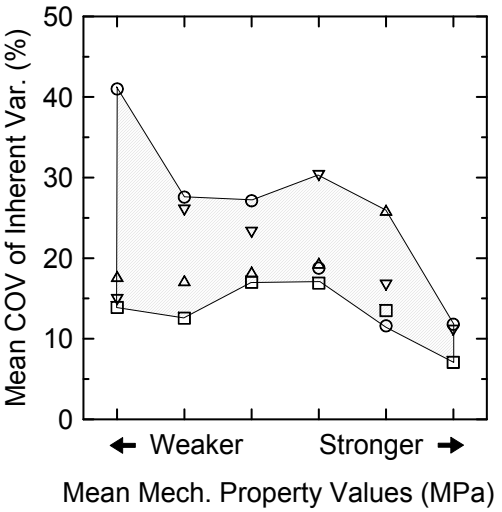

Figure 3. Mean and COV mean of intact rock mechanical properties (Prakoso & Kulhawy 2011)

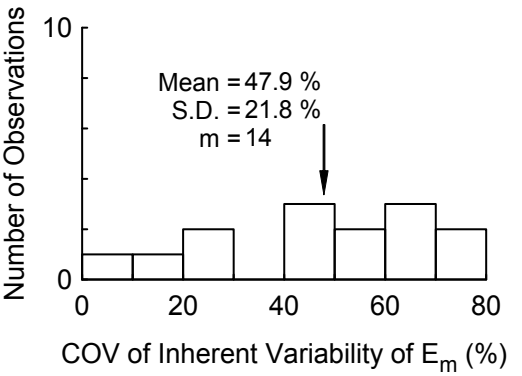

Figure 4. Variability of rock mass modulus (Prakoso & Kulhawy 2004b)

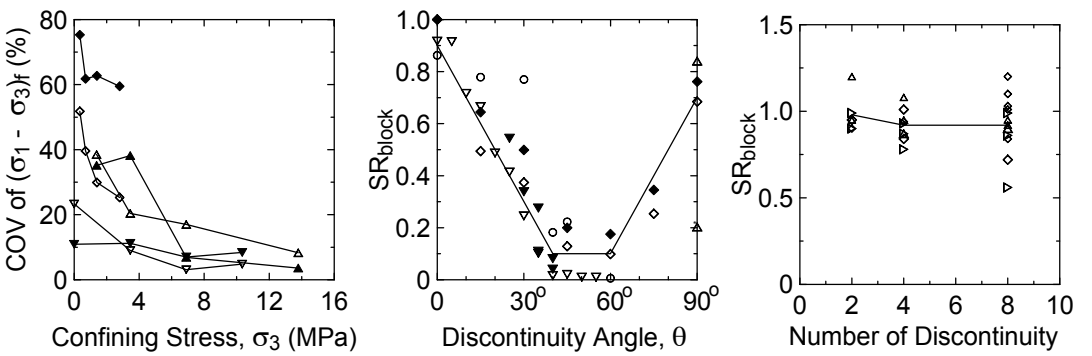

Figure 5. Artificial rock block strength variability (Prakoso & Kulhawy 2004b)

For the rock mass, the property variability has been examined by Prakoso and Kulhawy (2004b). Two data groups were evaluated: field load tests and laboratory, artificial rock block tests. For the field tests, fourteen sets of rock mass Young's modulus (E_m) were back-calculated. The COV of E_m (COV_{Em}) ranged from 10 to 80%, and the mean and S.D. of COV_{Em} are 47.9% and 21.8%, respectively, as shown in Figure 4. For the artificial rock block tests, the effect of rock mass structure on its strength could be estimated, as shown in Figure 5. These data show: (a) variability is most significant for rock masses with low confining stress, in which COV varies from 10 to 75%, (b) variability is most significant for discontinuity angles between 40° and 60°, and (c) variability tends to increase with increasing number of discontinuities.

Overall, the mechanical property variability for intact rock tends to be lower than that for the rock mass. The bearing capacity is actually controlled by the rock mass, and therefore the variability of the rock mass should be assessed, in addition to that of the intact rock, in the determination of the COV_{qu} for Ψ_c^{ULS}.

EVALUATION OF BEARING CAPACITY FACTOR

Forty sets of Monte Carlo simulations were performed on three theoretical bearing capacity models to evaluate the possible range of N_c^* and to evaluate the significance of variability of strength parameters on N_c^*. The models are shown in Figure 6 and include: (a) the general wedge (Model 1) (Prakoso & Kulhawy 2006), (b) the rock mass with two ubiquitous, closed discontinuity sets (Model 2) (Prakoso & Kulhawy 2004a), and (c) the rock mass with open vertical discontinuities that consists of three transitional failure modes from uniaxial to splitting to wedge (Model 3) (Prakoso & Kulhawy 2006). Two thousand simulations were performed for each set, using the parameters given in Table 2. For all three models, the rock

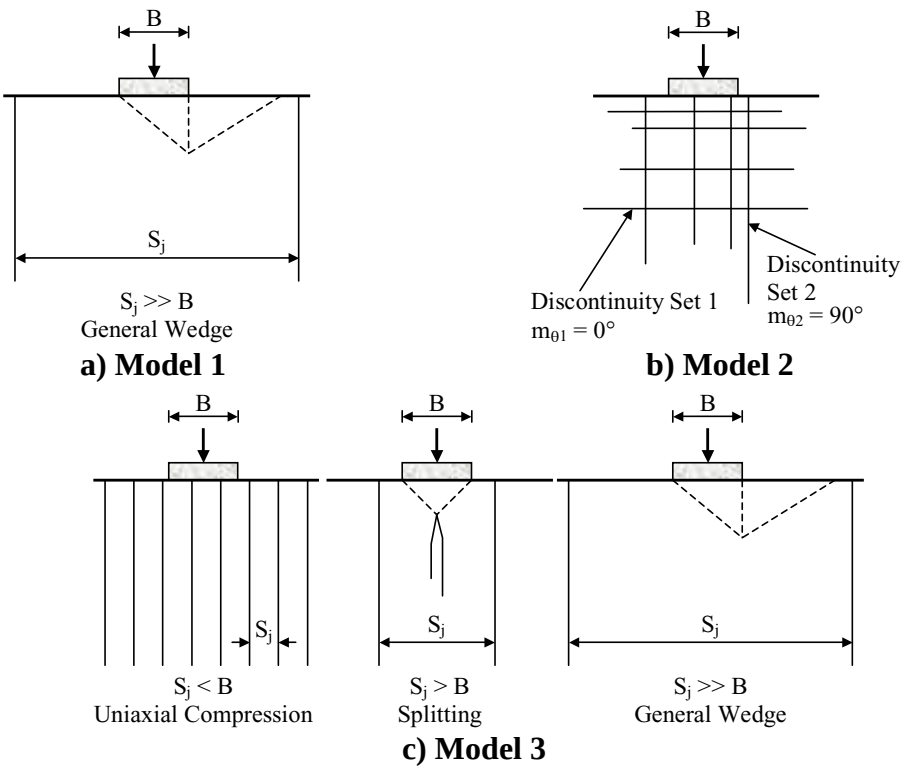

Figure 6. Theoretical models for bearing capacity of rock footings

Table 2. Discontinuity parameters for Monte Carlo simulations

Model		Discontinuities
1.	General Wedge	-
2.	Two Ubiquitous, Closed Discontinuity Sets	Orientation of discontinuities θ_1 = -10° to 10°, θ_2 = 80° to 100° Strength of discontinuities ϕ_j/ϕ_r = 0.5-0.7 to 0.8-1.0 c_j/c_r = 0.05-0.15 to 0.2-0.3
3.	Open Vertical Discontinuities	Vertical discontinuity spacing Mean S_j/B = 2 to10 COV S_j/B = 20% to 80%

friction angle is characterized by a beta distribution with mean ϕ_r = 35°-50°, COV ϕ_r = 5-15%, lower bound = 27°, and upper bound = 70°. The discontinuity properties for Model 2 follow a uniform distribution, while those for Model 3 follow a log-normal distribution; detailed descriptions of the properties are given in each respective reference. For each simulation, $N_c^*{}_{sim}$ was calculated using the following:

$$N_c^*{}_{sim} = q_{ult\text{-}sim} / q_{u\text{-}sim} \quad (6)$$

in which $q_{ult\text{-}sim}$ = simulation bearing capacity and $q_{u\text{-}sim}$ = simulation intact rock uniaxial compressive strength. Subsequently, the mean and COV of $N_c^*{}_{sim}$ (m_{Nc*sim} and COV_{Nc*sim}) of each set were evaluated. For Models 2 and 3, each m_{Nc*sim} value represents a different "failure mode" or, in terms of the proposed RBD method, each m_{Nc*sim} represents a possible m_{Nc*}. On the other hand, each COV_{Nc*sim} value represents the effect of rock strength variability or, in terms of the proposed RBD method, each COV_{Nc*sim} would represent a possible value of COV_{qu}.

Values of m_{Nc*sim} for the models are given in Figure 7, which shows that as m_ϕ increases, m_{Nc*sim} increases. However, the increase for Model 1 is much more significant than for the other models, suggesting that, once discontinuities are considered explicitly, the intact rock properties do not control the behavior too significantly. The range of m_{Nc*sim} shown in Figure 7 is similar to the empirical N_c^* values discussed previously. The results of Models 2 and 3 suggest that m_{Nc*} of 3.46 is reasonably conservative for a wide range of rock types and conditions.

The effect of discontinuity properties on m_{Nc*sim} was evaluated as well, as shown in Figure 8 for Model 2 and in Figure 9 for Model 3. These figures show that the discontinuity properties have a relatively small effect on m_{Nc*sim}, which suggests that m_{Nc*} of 3.46 is reasonably conservative for a wide range of rock structures.

The effect of rock friction angle variability (COV_ϕ) on COV_{Nc*sim} is given in

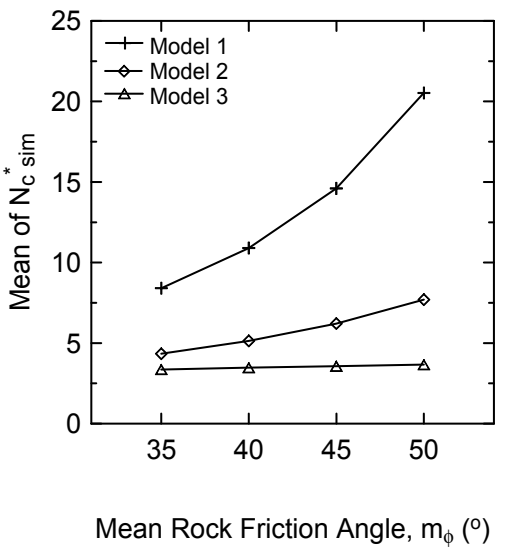

Figure 7. Effect of models on m_{Nc*sim}

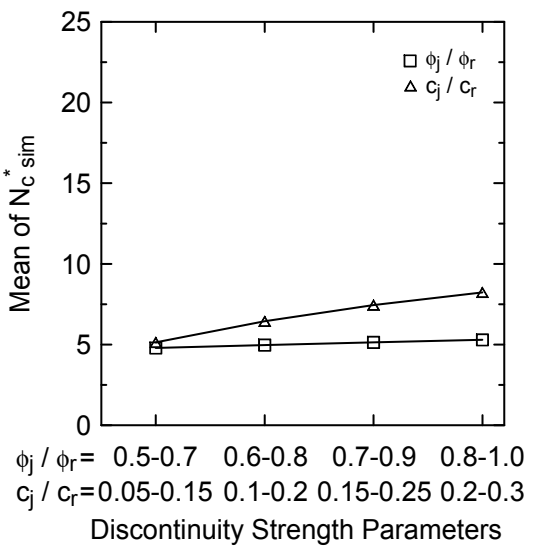

Figure 8. Effect of Model 2 discontinuity strength parameters on m_{Nc*sim}

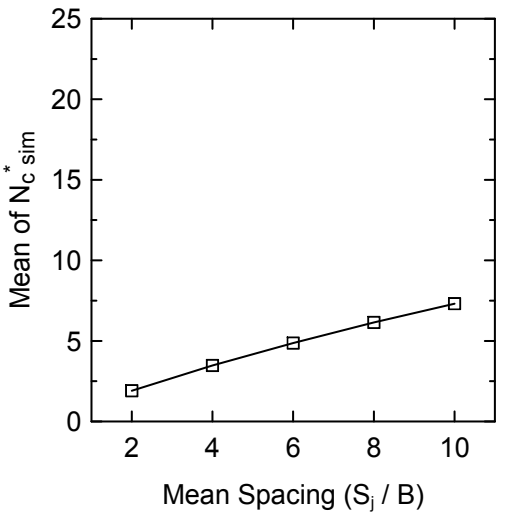

Figure 9. Effect of Model 3 discontinuity spacing on m_{Nc*sim}

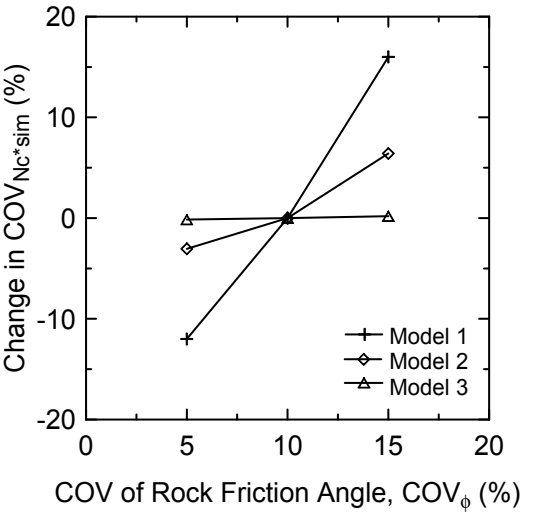

Figure 10. Effect of Model 2 discontinuity strength parameters on m_{Nc*sim}

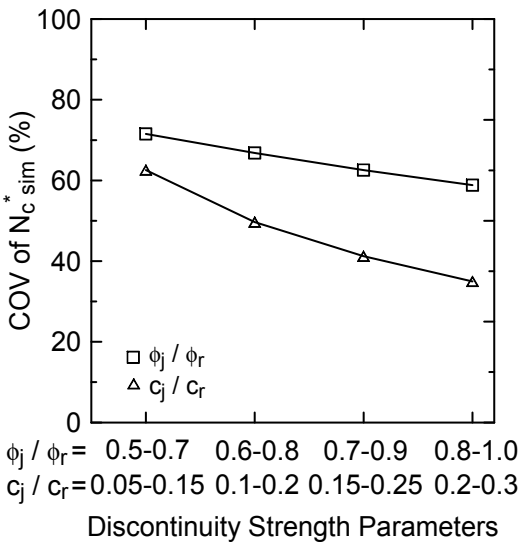

Figure 11. Effect of discontinuity strength parameters

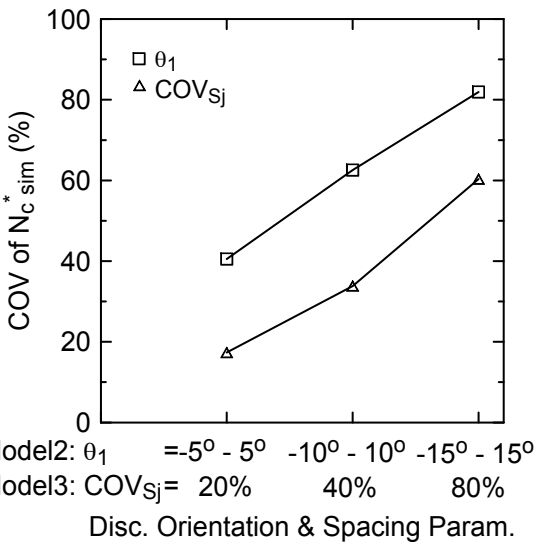

Figure 12. Effect of discontinuity orientation and spacing parameters

Figure 10 and shows a significant effect for Model 1, but not for Models 2 and 3. Furthermore, as shown as Figures 11 and 12, the discontinuity properties have significant effects on COV_{Nc*sim}. This observation suggests that, for most cases, the variability of intact rock strength would not affect significantly the variability of the bearing capacity or, in terms of the proposed RBD method, the COV_{qu} range to be used in determining Ψ_c^{ULS} should not be determined solely based on the intact rock strength variability. On the other hand, the variability of discontinuity properties would affect the variability of bearing capacity significantly and would have to be considered in the determination of the COV_{qu} for Ψ_c^{ULS}.

SUMMARY AND CONCLUSIONS

This paper continues our development of a simplified reliability-based design method for rock footings in an LRFD format. Two issues were addressed herein: the robustness of the empirical model and the proper approach to evaluate the rock strength variability. The results of simulations indicate that the empirical calculation model is reasonably conservative. In any case, the footing reliability would not be influenced significantly by the model statistics. The results of an extensive evaluation of rock properties, and the simulation results, suggest that the variability of rock mass strength should be used in evaluating the rock variability in the proposed LRFD format.

REFERENCES

Prakoso, W.A. and Kulhawy, F.H. (2002). Uncertainty in capacity models for foundations in rock. *Proc. 5th North American Rock Mech. Symp.*, Toronto, 1241-1248.

Prakoso, W.A. and Kulhawy, F.H. (2003). Reliability-based design for rock footings. *Proc. Int. Workshop on Limit State Design in Geotech. Eng. Practice*, Cambridge, 23-24 (extended abs) + 5 p (on CD).

Prakoso, W.A. and Kulhawy, F.H. (2004a). Bearing capacity of strip footings on jointed rock masses. *J. Geotech. Eng.*, ASCE, 130(12), 1347-1349.

Prakoso, W.A. and Kulhawy, F.H. (2004b). Variability of rock mass engineering properties. *Proc. 15th Southeast Asian Geotech Conf.*, Bangkok, 97-100.

Prakoso, W.A. and Kulhawy, F.H. (2006). Capacity of foundations on discontinuous rock. *Proc. 41st U.S. Symp. Rock Mech.*, Golden, Paper 06-972, 7 p. (on CD).

Prakoso, W.A. and Kulhawy, F.H. (2011). Variability of intact rock mechanical properties. (to be submitted)

Task Committee on Structural Loadings. (1991). *Guidelines for electrical transmission line structural loading*. Manual & Report on Eng. Practice 74. ASCE, Reston, 139 p.

A Practical LRFD Design Method for Deep Foundations Using Side Friction and End Bearing

H. Klammler[1,2], M. McVay[1], Jeongsoo Ko[1], P. Lai[3], R. Herrera[3].

[1]Department of Civil and Coastal Eng., University of Florida, 365 Weil Hall, Gainesville, Florida, 32611; haki@gmx.at, mmcva@ce.ufl.edu, kjs6022@ufl.edu.
[2]Department of Environmental Sciences and Sustainable Development, Federal Univesity of Bahia, Barreiras, Bahia, 47805, Brazil.
[3]Florida Department of Transportation, 605 Suwannee Street, MS 33, Tallahassee, Florida, 32399; peter.lai@dot.state.fl.us, rodrigo.herrera@dot.state.fl.us.

ABSTRACT

One of the uncertainty components in Load and Resistance Factor Design (LRFD) stems from spatial variability in design parameters, such as local soil / rock strength or modulus. A solution is presented for uncertainty propagation of effective rock mass modulus through O'Neill's (non-linear) equations for drilled shaft settlement in intermediate geomaterials. Associated tip resistance is combined with side friction resistance (fully mobilized) of one or more geological layers to form total ultimate shaft resistance with respective uncertainty. Based on this, a graphical iteration chart (existing for side friction in a single layer without end bearing) is generalized to find shaft length as a function of given reliability (probability of failure), factored design load and site conditions. Results are demonstrated by a practical example.

INTRODUCTION

Load and Resistance Factor Design (LRFD; AASHTO, 2004) aims at meeting prescribed levels of probability of failure (reliability) of engineered structures. This requires investigation of the probabilistic behavior of both loads and resistances for different limit states. An important source of uncertainty on the resistance side is spatial variability in ground properties. For shallow foundations, for example, Fenton and Griffiths (2005) use an effective modulus based on geometric averaging of spatially variable soil / rock modulus underneath a footing to relate settlement to bearing capacity. Ko et al. (2011) investigate end bearing of drilled shafts and conclude that harmonic averaging of local modulus underneath the shaft tip leads to an appropriate effective modulus of tip resistance. Also for drilled shafts, Klammler et al. (2010a) study the impact of spatially variable soil / rock strength on ultimate axial side friction resistance. Klammler et al. (2010b) extend the approach to account for limited availability of data at a site and present a practical design chart to graphically iterate towards required shaft length for given geostatistical properties of local strength, target probability of failure as well as design load.

The present work attempts to contribute to the field of reliability based design of deep foundations in two ways: (1) By adding a probabilistic (random) component

to the deterministic design equations of O'Neill et al. (1996) for drilled shaft settlement in intermediate geomaterials and (2) by generalizing the design chart of Klammler et al. (2010b) to allow for the presence of more than a single layer as well as contribution of end bearing. The following sections develop the theoretical foundation and a practical example is given thereafter.

DISTRIBUTION OF TIP RESISTANCE

O'Neill et al. (1996) determine end bearing resistance R_b for a given shaft top settlement w_t by

$$R_b = A_b \Lambda \left(\frac{w_t}{L} \right)^{2/3} \tag{1}$$

where A_b and L are the cross sectional area and length of the shaft, respectively, and

$$\Lambda = 0.21 E_{eff} \frac{L}{D} \left(1 + \frac{L}{D} \right)^{-1/3} \left[\left(\frac{L}{D} \right)^{1/2} - \Omega \right]^{2/3} \Gamma^{-2/3} \tag{2}$$

$$\Omega = 1.14 \left(\frac{L}{D} \right)^{1/2} - 0.05 \left[\left(\frac{L}{D} \right)^{1/2} - 1 \right] \log_{10} \left(\frac{E_c}{E_{eff}} \right) - 0.44 \tag{3}$$

$$\Gamma = 0.37 \left(\frac{L}{D} \right)^{1/2} - 0.15 \left[\left(\frac{L}{D} \right)^{1/2} - 1 \right] \log_{10} \left(\frac{E_c}{E_{eff}} \right) + 0.13 \tag{4}$$

D and E_c are the diameter and Young's modulus of the shaft, while E_{eff} is an effective Young's modulus of the rock mass (i.e., including fissures, voids, etc.) underneath the shaft tip. Thus, for a given shaft and top settlement, parameters L, D, A_b, E_c and w_t in the above equations are constants. In contrast, E_{eff} is a function of soil / rock heterogeneity and it is hereafter treated as a log-normal random variable of known mean μ_{Eeff} and variance σ^2_{Eeff}. Different approaches are available for determination of μ_{Eeff} and σ^2_{Eeff} (or $CV_{Eeff} = \sigma_{Eeff}/\mu_{Eeff}$) from locally measured modulus data over a site (e.g., Fenton and Griffiths, 2005; Ko et al., 2011), which also support the log-normality assumption taken.

As shown in Appendix A, Equation 1 may be accurately approximated by

$$R_b = C_1 E_{eff}^{C_2} A_b \left(\frac{w_t}{L} \right)^{2/3} \tag{5}$$

where C_1 and C_2 are constants (Equations A7 and A8). Based on Equation 5 and log-normality in E_{eff}, Appendix B further shows that R_b is also log-normal with mean and coefficient of variation

$$\mu_{Rb} = C_1 A_b \left(\frac{w_t}{L}\right)^{2/3} \left[\mu_{Eeff}\left(1+CV_{Eeff}^2\right)^{\frac{C_2-1}{2}}\right]^{C_2} \tag{6}$$

$$CV_{Rb} = \sqrt{\left(1+CV_{Eeff}^2\right)^{C_2^2} - 1} \tag{7}$$

TOTAL RESISTANCE AND LRFD DESIGN CHART

In order to meet the fundamental LRFD goal of not exceeding a desired probability of failure, AASHTO (2004) assumes log-normal load and resistance distributions. This honors positivity as well as typically observed distribution skewness and allows defining a relatively simple relationship between LRFD resistance factor Φ, reliability β as well as load and resistance uncertainties (CV_Q and CV_R). In order to achieve a prescribed level of reliability of a shaft as a whole, design needs to be based on the total load it receives in combination with the shaft's total resistance. The latter may be composed of side friction from several layers plus end bearing as illustrated by Figure 1. Under the simplifying but possibly unconservative assumption of negligible correlation between side and tip resistance components, the coefficient of variation CV_R of total resistance R results as (Klammler et al., 2010a)

$$CV_R = \frac{\sqrt{\sum_{i=1}^{n_L}\sigma_{Rsi}^2 + \sigma_{Rb}^2}}{\sum_{i=1}^{n_L}\mu_{Rsi} + \mu_{Rb}} = \frac{\sqrt{\sigma_{R0}^2 + \sigma_{RsnL}^2 + \sigma_{Rb}^2}}{\mu_{R0} + \mu_{RsnL} + \mu_{Rb}} \tag{8}$$

where σ^2_{Rsi} are the variances of side friction resistances R_{si} in each of i = 1, 2, …, n_L layers and σ^2_{Rb} is the variance of tip resistance; μ_{Rsi} and μ_{Rb} are the respective mean resistance values. While μ_{Rsi} and σ^2_{Rsi} for full mobilization of side friction may be found as discussed in Klammler et al. (2010a), μ_{Rb} and σ^2_{Rb} may be obtained from Equations 6 and 7 ($\sigma^2_{Rb} = CV_{Rb}^2\mu_{Rb}^2$). With this, AASHTO (2004) may be used as in Klammler et al. (2010a, b) to determine β for given load, shaft and site conditions.

In design practice, however, β is prescribed and respective shaft dimensions (e.g., L for a desired D) need to be defined. For a single layer (n_L = 1) and neglecting end bearing ($\mu_{Rb} = \sigma^2_{Rb} = 0$), Klammler et al. (2010b) present a graphical iteration solution to this problem in the form of a quadrant chart. Using the final expression of Equation 8 this approach may be generalized to account for the possible presence of end bearing as well as multiple layers contributing to side friction. For a given shaft diameter D, the design process under this scenario is to find the embedment length L_{nL} of the shaft in the bottom most (n_L^{th}) layer penetrated by the shaft (embedment lengths in the overlaying layers are known and equal to respective layer thicknesses). Thus, $\mu_{R0} = \sum_{i=1}^{n_L-1}\mu_{Rsi}$ and $\sigma^2_{R0} = \sum_{i=1}^{n_L-1}\sigma^2_{Rsi}$ are mean and variance of total shaft resistance

component R_0 due to side friction in all layers (of combined thickness $L_0 = \sum_{i=1}^{n_L-1} L_i$) without the bottom layer where the tip resides. As such, these parameters are independent of tip embedment length L_{nL} and are known a priori from Klammler et al. (2010a). The remaining terms in Equation 8 correspond to the mean $\mu_{RsnL} = \pi D \mu_{qnL} L_{nL}$ and variance $\sigma^2_{RsnL} = (\pi D L_{nL})^2 \alpha_{nL} \sigma^2_{qnL}$ of side friction resistance R_{snL} in the bottom most layer. α_{nL} is a function of L_{nL} as well as the vertical correlation length a_{vqnL} and represents a dimensionless variance reduction factor (Klammler et al., 2010a) applied to local strength variance σ^2_{qnL}; μ_{qnL} is the respective mean value of local strength in the bottom layer.

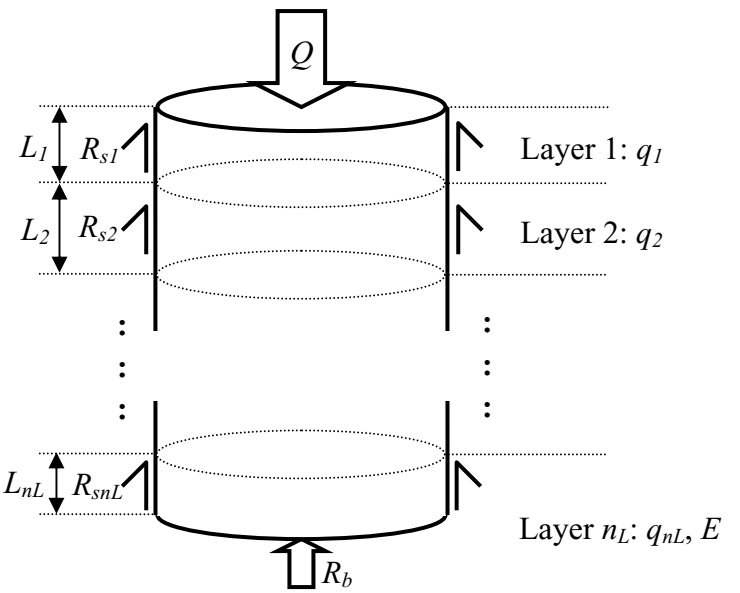

Figure 1. Schematic of shaft penetrating multiple layers with respective side and tip resistance components.

In a similar way, the fundamental LRFD design equation $Q_{des} \leq \Phi R_n$ (where Q_{des} is the factored design load equal to the mean μ_Q of random load Q and R_n is the nominal resistance equal to the mean μ_R of random total shaft resistance $R = R_0 + R_{snL} + R_b$) may be rewritten as $Q_{des} \leq \Phi(\mu_{R0} + \pi D \mu_{qnL} L_{nL} + \mu_{Rb})$ or

$$L_{nL} \geq \frac{\frac{Q_{des}}{\Phi} - \mu_{R0} - \mu_{Rb}}{D \pi \mu_{qnL}} \tag{9}$$

With Equations 8 and 9 the quadrant chart of Klammler et al. (2010b) may be generalized to account for multiple layers contributing to side friction plus end bearing as illustrated in Figure 2. Note that the approach remains general in the sense that the third quadrant may consider a limited number n_b of test borings as well as a possibly known horizontal correlation length a_{hqnL} of local strength.

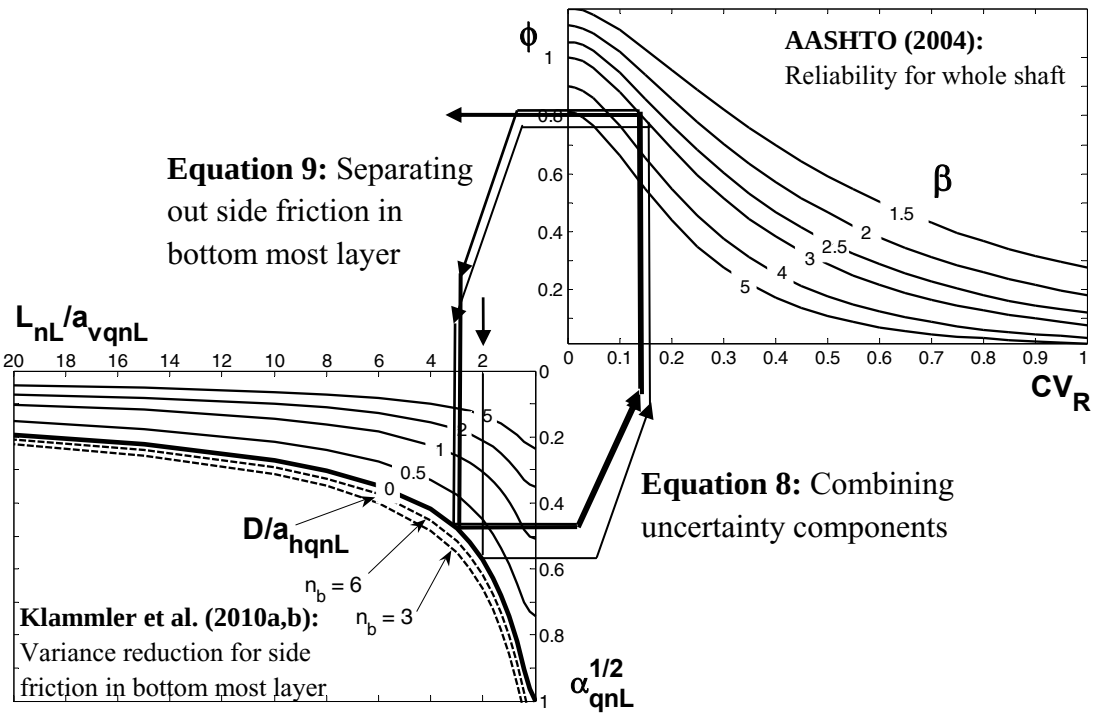

Figure 2. Quadrant chart for semi-graphical iteration towards required shaft length in the presence of one or more layers plus end bearing.

PRACTICAL EXAMPLE

Based on parameter ranges observed in existing studies for Florida limestone (Klammler et al., 2010a; Ko et al., 2011) the following parameters are used for an example problem assuming two layers of local strength parameters: L_1 **= 3 m,** μ_{q1} **= 2 MN/m²,** CV_{q1} **= 0.50,** a_{vq1} **= 1.5 m;** μ_{q2} **= 4 MN/m²,** CV_{q2} **= 0.40,** a_{vq2} **= 1 m**; for effective modulus in the bottom layer: μ_{Eeff} **= 542 MN/m²,** CV_{Eeff} **= 0.29**. Data is assumed to be reliably known (i.e., no uncertainty about given parameters) and horizontal correlation lengths are not available. For a factored design load Q_{des} **= 75 MN** and reliability β **= 3** limit state is defined by shaft top settlement of w_t **= 4 cm,** such that side friction may be assumed to be fully mobilized. Thus, for a chosen shaft of E_c **= 27500 MN/m²** and D **= 1.5 m**, nominal (mean) side friction in the top layer is $\mu_{R0} = \mu_{Rs1} = L_1 D\pi\mu_{q1}$ **= 28.3 MN** with variance $\sigma^2_{R0} = \sigma^2_{Rs1} = \alpha_{q1}(\mu_{R0}CV_{q1})^2$ = **67.4 MN²**, where $\alpha_{q1}^{1/2}$ = 0.58 is obtained from the conservative line shaft approximation (Klammler et al., 2010a; bold graph for $D/a_{hqnL} = 0$ in third quadrant of Figure 2) with $L_1/a_{vq1} = 2$.

To proceed further, an initial estimate of L_2 = 2 m is used giving $\mu_{Rs2} = L_2 D\pi\mu_{q2}$ = **37.7 MN** and to start iteration by entering the third quadrant of Figure 2 from the top at L_2/a_{vq2} = 2 (downward arrow) giving $\alpha_{q2}^{1/2}$ = 0.58 and $\sigma^2_{Rs2} = \alpha_{q2}(\mu_{Rs2}CV_{q2})^2$ = **76.5 MN²**. Equations 6 and 7 are applied with $L = L_1 + L_2$ = 5 m to find μ_{Rb} **= 9.23 MN** and CV_{Rb} **= 0.26** (C_1 = 0.48 and C_2 = 0.89 from Appendix A). Next, Equation 8 may be evaluated in the fourth quadrant of Figure 2 to reach CV_R **= 0.16** and Φ **= 0.77** after passing the first quadrant. With this, Equation 9 in the second

quadrant leads back to a value of L_2 = 3.18 m meaning that the chosen value of 2 m was too small and iteration has to be continued. The iteration lines (from thin to bold) in Figure 2 show that two more cycles are required to reach a steady result of $\boldsymbol{L_2}$ = **3 m** corresponding to a LRFD $\boldsymbol{\Phi}$ **= 0.80** (arrow pointing to left). Note, however, that in the present design context Φ is a function of site and shaft parameters and as such its role is reduced to that of an auxiliary variable expressing the ratio between design load and nominal resistance of the whole shaft. What eventually matters are the dimensions of the shaft, such that required reliability is met (i.e., target probability of failure is not exceeded).

SUMMARY

A highly accurate power approximation is used to reformulate O'Neill et al.'s (1996) equations for drilled shaft settlement in intermediate geomaterials. This allows for a relatively simple analytic uncertainty propagation of the effective rock mass modulus into tip resistance. Resulting nominal tip resistance and uncertainty are subsequently combined with nominal resistances and uncertainties from fully mobilized side friction resistances in one or more layers. Finally, a generalized quadrant chart is presented for semi-graphical iteration towards a required shaft design length for given design load, target reliability (both for the whole shaft) and site conditions.

Results show that for a log-normally distributed effective rock mass modulus and a given shaft top settlement, the distribution of shaft tip resistance is also log-normal. The iterative design process is explained and demonstrated through a practical example using generic data within typical ranges of Florida limestone. Convergence is observed to be fast and fully computational implementation is possible.

ACKNOWLEDGEMENTS

A portion of this work was supported by Florida Department of Transportation Research Contract No. BD-545, RPWO # 59 entitled "Distribution of End Bearing and Tip Shear on Drilled Shafts Founded in Florida Limestone".

APPENDIX A – POWER APPROXIMATION OF O'NEILL'S EQUATIONS

Introducing $C_3 = (L/D)^{1/2}$ and $C_4 = (L/D)^{1/2} - \Omega$ in Equations 2, 3 and 4 gives

$$\Gamma = 0.37C_3 - 0.15(C_3 - 1)\log_{10} E_c + 0.13 + 0.15(C_3 - 1)\log_{10} E_{eff} \quad \text{(A1)}$$

$$C_4 = -0.14C_3 + 0.05(C_3 - 1)\log_{10} E_c + 0.44 - 0.05(C_3 - 1)\log_{10} E_{eff} \quad \text{(A2)}$$

$$\Lambda = 0.21E_{eff}C_3^2\left(1 + C_3^2\right)^{-1/3}\left(\frac{C_4}{\Gamma}\right)^{2/3} \quad \text{(A3)}$$

By further using $C_5 = 10^{0.37C_3 - 0.15(C_3-1)\log_{10}E_c + 0.13}$ and $C_6 = 10^{-[-0.14C_3 + 0.05(C_3-1)\log_{10}E_c + 0.44]}$ Equations A1 and A2 become

$$\Gamma = 0.15(C_3 - 1)\log_{10}\left(E_{eff}C_5^{1/0.15(C_3-1)}\right) \tag{A4}$$

$$C_4 = -0.05(C_3 - 1)\log_{10}\left(E_{eff}C_6^{1/0.05(C_3-1)}\right) \tag{A5}$$

The function $y = \log_{10}(kE_{eff})$ in equations A4 and A5 may be approximated by the power function $y_p = aE_{eff}^{\ b}$. With the two degrees of freedom a and b it may be imposed that $y = y_p$ and $dy/dE_{eff} = dy_p/dE_{eff}$ for an arbitrary value of $E_{eff} = m$. For $E_{eff} \neq m$ the approximation is inexact, however, power functions such as hyperbolas and parabolas (e.g., root functions) bear a fair degree of similarity with the logarithmic function. Knowing that $\log_{10}(km) = 0.43\ln(km)$, the above equivalence conditions for y and y_p lead to the equations $am^b = 0.43\ln(km)$ and $abm^{(b-1)} = 0.43/m$, which may be solved for a and b, giving

$$\log_{10}\left(kE_{eff}\right) \approx \left(\frac{E_{eff}}{m}\right)^{0.43/\log_{10}(km)} \log_{10}(km) \tag{A6}$$

after substitution into the equation for y_p. Using this result with $k = C_7 = C_5^{1/0.15(C_3-1)}$ in Equation A4 and $k = C_8 = C_6^{1/0.05(C_3-1)}$ in Equation A5 leads to approximate expressions for Γ and C_4. The approximate ratio C_4/Γ is then used in Equation A3, which, in turn, delivers the approximate expression of the parameter Λ in Equation 1. Finally, after several simple but quite lengthy algebraic manipulations, the form of Equation 5 is obtained, where

$$C_1 = 0.10C_3^2\left(1 + C_3^2\right)^{-1/3}\left[\frac{-\log_{10}(C_8 m)}{\log_{10}(C_7 m)}\right]^{2/3} m^{1-C_2} \tag{A7}$$

$$C_2 = 1 + 0.29\left[\frac{1}{\log_{10}(C_8 m)} - \frac{1}{\log_{10}(C_7 m)}\right] \tag{A8}$$

Based on a numerical investigation, the approximation error of Equation A6 is found to be less than 5 % if E_{eff}/m lies within the range $(km)^{\pm 0.3}$. In order to best explore this logarithmic range in both directions about the approximation point, m should be adopted as the geometric average of the distribution of E_{eff} (508 MN/m^2 in the practical example). Together with C_7 = 22.9 m^2/MN and C_8 = 2.29e-8 m^{2}MN for the final shaft length of the example, this means that Equation A6 is accurate within 5 % for $30 < E_{eff} < 8500$ MN/m^2, which spans more than 50 times σ_{Eeff}. Note that C_1 and C_2 depend on shaft length L and their values change in each design iteration step.

APPENDIX B – POWERS OF LOG-NORMAL VARIABLES

The relationship between a standard normal variable N_s to a log-normal variable LN is given by $LN = \exp(\mu_N + \sigma_N N_s)$, where μ_N and σ_N are the mean and standard deviation of the log-transformed variable, i.e., $\ln(LN)$. These parameters can be expressed in terms of the mean μ_{LN} and coefficient of variation CV_{LN} of LN as (Journel and Huijbregts, 1978)

$$\mu_N = \ln \frac{\mu_{LN}}{\sqrt{1 + CV_{LN}^2}} \quad \leftrightarrow \quad \mu_{LN} = e^{\mu_N + \frac{\sigma_N^2}{2}} \tag{B1}$$

$$\sigma_N^2 = \ln\left(1 + CV_{LN}^2\right) \quad \leftrightarrow \quad CV_{LN} = \sqrt{e^{\sigma_N^2} - 1} \tag{B2}$$

with respective inverse relationships given on the right-hand-side.

Taking the natural logarithm of Equation 5 leads to $\ln R_b = \ln[C_1 A_b (w_t/L)^{2/3}] + C_2 \ln E_{eff}$. If E_{eff} is log-normal, then $\ln E_{eff}$ is normal with mean and variance $\mu_{lnEeff} = \ln[\mu_{Eeff} / (1 + CV_{Eeff}^2)^{1/2}]$ and $\sigma_{lnEeff}^2 = \ln(1 + CV_{Eeff}^2)$, respectively (left-hand-sides of Equations B1 and B2). Since normality is preserved after addition and / or multiplication by an constant, $\ln R_b$ is also normal with parameters $\mu_{lnRb} = \ln[C_1 A_b (w_t/L)^{2/3}] + C_2 \mu_{lnEeff}$ and $\sigma_{lnRb}^2 = C_2^2 \sigma_{lnEeff}^2$. Consequently, R_b is log-normal and the right-hand-sides of Equations B1 and B2 with substitution from intermediate results of this paragraph lead to Equations 6 and 7.

REFERENCES

AASHTO. (2004). "*LRFD bridge design specifications*", 3rd ed. American Association of State Highway and Transportation Officials.

Ko, J., Chung J., Klammler, H., McVay, M., and Lai, P. (2011). "A two-dimensional numerical and experimental study of tip resistance of a deep foundation in heterogeneous rock". *Computers and Structures*, in review.

Fenton, G.A., and Griffiths, D.V. (2005). "Three-dimensional probabilistic foundation settlement". *J. of Geotech. and Geoenv. Eng.*, 131(2), 232-239.

Journel, A.G., and Huijbregts, C.J. (1978). "*Mining geostatistics*". Blackburn Press, Caldwell, NJ.

Klammler, H., McVay, M., Horhota, D., and Lai, P. (2010a). "Influence of spatially variable side friction on single drilled shaft resistance and LRFD resistance factors". *J. of Geotech. and Geoenv. Eng.*, 136(8), 1114-1123.

Klammler, H., McVay, M., Lai, P., and Horhota, D. (2010b). "Incorporating geostatistical aspects in LRFD design for deep foundations". In: *GeoFlorida 2010: Advances in Analysis, Modeling and Design*. E.O. Fratta, B. Muhunthan, A.J. Puppala, eds. ASCE Geotechnical Special Publication N^o 199, ISBN 978-0-78441-095-0, CD-ROM.

O'Neill, M.W., Townsend, F.C., Hassan, K.H., Buller, A., and Chan, P.S. (1996). "*Load transfer for drilled shafts in intermediate geomaterials*". Report FHWA-RD-95-1 72, Federal Highway Administration, Washington, D.C.

Reliability-Based Design of Shallow Foundations in Cohesionless Soils Under Compression Loading: Serviceability Limit State

Sami O. Akbas[1], M.ASCE and Fred H. Kulhawy[2], Dist.M.ASCE

[1]Assistant Professor, Department of Civil Engineering, Gazi University, Celal Bayar Bulvari, Maltepe, Ankara, Turkey 06570; email: soakbas@gazi.edu.tr
[2]Professor Emeritus, School of Civil and Environmental Engineering, Hollister Hall, Cornell University, Ithaca, NY 14853-3501; email: fhk1@cornell.edu

ABSTRACT

The reliability-based design (RBD) of shallow foundations in cohesionless soils under drained compression loading is examined for the serviceability limit state (SLS). This SLS is defined when the compression capacity at the allowable settlement limit imposed by the structure is equal to the applied load. The uncertainties in both the load and the capacity sides are considered. A Monte Carlo simulation-based parametric study indicates that the most influential parameters on the reliability index are the statistics of the effective stress friction angle and the ratio of the 50-year snow load to total load, where snow is present. These results were used to select the appropriate domains for the calibration of the simplified RBD equations that can be presented for general use. The target reliability index for calibration was selected after examining the range of reliability levels implicit in existing deterministic foundation designs. The resulting resistance factors are tabulated in a form that can be applied readily in foundation engineering practice.

INTRODUCTION

Predicting the settlement of shallow foundations in cohesionless soils is a very difficult task. First, uncertainties in evaluating the compressibility parameters are substantial. Even if deposited under apparently consistent geologic conditions, the relative density and compressibility of sands vary erratically and significantly within small distances. Also, since it is hard to obtain undisturbed samples for cohesionless soils, laboratory tests to determine compressibility parameters can be misleading. Second, the compressibility of cohesionless soils depends on many factors, such as the lateral stresses, which are a function of the soil stress history and the frictional forces that develop on the base of the footing when it is loaded. In addition, construction effects on foundation performance can not be incorporated fully in most analytical models. Therefore, empirical methods that mostly rely on in-situ test results still are used widely for estimating settlements (e.g., Akbas 2007).

An evaluation of the many popular empirical settlement estimation methods indicated that high degrees of uncertainty are inherent in the calculated to measured settlement ratios (Akbas & Kulhawy 2010). Therefore, the uncertainties in foundation settlement predictions can be expected to have a large effect on the reliability of foundation designs. For shallow foundations on cohesionless soils, settlement issues

usually govern the design. However, most RBD studies have focused on capacity, even though settlement predictions usually are more important. This study focuses on developing RBD equations for SLS of shallow foundations on cohesionless soils.

PREDICTION OF SETTLEMENTS

A robust predictive model for foundation settlement is required to determine the appropriate RBD equations. A load test database for shallow foundations was presented by Akbas and Kulhawy (2009a). Using the information in this database, a normalized plot was obtained that describes the load-settlement behavior of shallow foundations on cohesionless soils. The load–settlement curve for each load test in the database was approximated using a hyperbolic fitting method. The details of this method are given in Akbas (2007). Two fitting parameters, a and b, were obtained for each load test by describing the hyperbolic equation as below:

$$Q / Q_{L2} = (\rho / B) / \left[a\left(\rho / B\right) + b \right] \tag{1}$$

in which Q/Q_{L2} = ratio of applied load to failure load interpreted from the load tests, B = footing width, and ρ = settlement. Statistical analyses then were conducted to obtain the parameters for the mean normalized curve. Summary statistics for parameters a and b are given in Table 1 for the entire database; in parentheses, average values are given for every site, with residual and cemented soils excluded. The resulting mean load-settlement curve, which is used as the predictive model in this study, is a useful representation of the load-settlement behavior of shallow foundations in cohesionless soils. Details are given in Akbas and Kulhawy (2009a).

The SLS of a shallow foundation under compression loading is defined as the state in which the compression capacity at the allowable settlement limit is equal to the applied load. The foundation is considered to be unserviceable if the capacity at the allowable settlement limit is less than the applied load. Conversely, the foundation is considered serviceable if the capacity is greater than the applied load. These three conditions can be described by the following performance function, P:

$$P = Q_{ca} - F \tag{2}$$

in which Q_{ca} = allowable compression capacity at the allowable settlement limit, and F = foundation load. The conditions described above mathematically correspond to $P = 0$, $P > 0$, and $P < 0$, respectively.

Using Eq. (1), the allowable compression capacity can be determined as follows:

$$Q_{ca} = Q_c(\rho_a / B) / \left[a\left(\rho_a / B\right) + b \right] \tag{3}$$

in which Q_c = compression capacity, and ρ_a = allowable settlement limit. The good correlation between the predicted (Q_c) and measured (Q_{L2}) values for the bearing capacity of the shallow foundations in the database (Akbas and Kulhawy 2009b) allows Eq. (1) to be expressed in the form of Eq. (3).

Table 1. Summary of Statistics for Hyperbolic Curve Fitting Parameters a and b (Averaged per Site with Residual and Cemented Soils Excluded)

Parameter	n	Minimum	Maximum	Mean	COV (%)
a	125 (25)	0.14 (0.32)	1.13 (0.90)	0.70 (0.69)	22 (21)
b	125 (25)	0.41 (090)	5.01 (3.33)	1.77 (1.68)	54 (38)

RANDOM VARIABLES

Because of the variabilities in the load and soil parameters, the performance of a shallow foundation can not be evaluated with absolute certainty. The dead load is considered as normally distributed, with a bias equal to 1.05, and a coefficient of variation (COV) equal to 10% (Ellingwood et al. 1980). From a statistical point of view, it is convenient to represent the total live load by a sustained live load component and a transient or extraordinary live load component. The magnitude of the sustained live load is modeled by a gamma distribution, and its duration is modeled by an exponential distribution. The magnitude of the transient live load also is assumed to follow a gamma distribution, but its frequency is modeled as a Poisson distribution. The required live load statistics are obtained from ASCE 7-02 (ASCE 2002) for five different occupancy types. Details are given in Akbas (2007).

In many parts of the world, the snow load is of particular importance. Its variability arises from two main sources. The first is the ground snow load, which is modeled by a lognormal random variable with a COV of 77%. The ground to roof conversion factor for the snow load also is a lognormally distributed random variable, with a mean of 1.09 and a COV of 44%. The occurrence of snow storms is modeled by a Poisson process, and therefore the elapsed time between two snow storms has an exponential distribution with a mean of $1/\lambda$, where λ is the rate of the Poisson process, i.e., the number of snow storms per year. The duration of each snow storm is assumed to be equal to the magnitude of the annual maximum ground snow load times an exponentially distributed constant, with a mean value of 25 days/kN/m^2.

The total load at any time was modeled conveniently as a sum of the individual load components. Each load effect was simulated separately, and then they were combined by superposition. The simulations for loads were performed in 50-year "subintervals", i.e., if 20,000 simulations are required, 400 simulations of these 50-year intervals were made. The dead load is considered as time independent. Sustained live load was simulated using the typical temporal constants given in Table 2, for each 50-year interval. The transient live load and snow load were simulated for every year separately in every 50-year interval, because of their specific time variation properties. For example, the transient live load for offices has a mean rate of occurrence of one load event per year, while for hotel guest rooms the mean rate is twenty events per year. The maximum load for every year is calculated subsequently to be used in the reliability analyses as the value for a single simulation run.

When Eq. (3) is examined, it can be seen that the uncertainty in the allowable compression capacity, as determined by the allowable settlement limit, is caused by: (a) random variables in Q_c and (b) uncertainties in the curve-fitted parameters a and b. In the calculation of Q_c, the main uncertain parameters are the effective stress friction angle and the shear modulus. Note that the shear modulus is used in calculating the rigidity index, which determines the mode of soil failure. The effective stress friction

Table 2. Typical Temporal Constant Values (ASCE 2002)

Occupancy or use	Mean Temporal Constants		
	τ_s [a] (years)	ν_e [b] (per year)	T [c] (years)
Offices	8	1	50
Residential / Renter occupied	2	1	50
Residential / Owner occupied	10	1	50
Hotel guest rooms	5	20	50
School classrooms	1	1	100

a - τ_s = duration of average sustained load occupancy; b - ν_e = mean rate of occurrence of transient load; c - T = reference period

angle (ϕ') can be modeled as a lognormal random variable (e.g. Spry et al. 1988). Drained conditions are more applicable to cohesionless soils, such as sands, for which a realistic range for the mean friction angle ($m_{\phi'}$) is between 30 and 45 degrees. The COV for the friction angle is assumed to take values between 5 and 20%. The probability distribution for the shear modulus (G) is assumed to be lognormal because: (a) most soil properties can be modeled adequately as lognormal random variables (Spry et al. 1988), and (b) negative values of G are not possible. The typical range of values for the drained elastic modulus is between 10 and 100 MN/m^2. For a typical Poisson's ratio of 0.25, the ratio between the elastic and shear moduli is 2.5. Therefore, an approximate range for the shear modulus is between 4 and 40 MN/m^2. Mean values for the shear modulus (m_G) can be selected accordingly using this range as a guide. The probable range of COV for soil modulus has been estimated to be on the order of 30 to 90% (Phoon et al. 1995), and this range also is adopted herein. From the case history evaluation in Akbas and Kulhawy (2009a), the mean and COV of the parameter a (m_a and COV_a) were determined to be 0.69 and 21%, respectively. The corresponding statistics for parameter b were 1.68 and 38%, respectively. Both curve-fitted parameters are modeled as lognormal random variables.

PARAMETRIC STUDY

To evaluate the variation of the reliability index (β) and the probability of failure (p_f) with respect to each significant design parameter, a parametric study was conducted. The results indicate the most influential design parameters, and therefore the domains of calibration can be determined. The performance function, as well as the random variables that are required to conduct the RBD calculations, were defined in the previous section. The parametric study was conducted primarily using Monte Carlo simulations because of the complex probabilistic modeling associated with snow and transient live loads.

To conduct a realistic parametric study, typical values of the design parameters should be used. The foundation width (B) was taken between 1 and 5 m. The typical range for depth to width ratio (D/B) is between 0 and 1, which is consistent with the general definition of shallow foundations. The foundation length to width ratio (L/B) was taken between 1 and 10. The statistics of the effective stress friction angle (ϕ') and shear modulus (G) were given above. Note that the statistics of

the shear modulus do not affect the RBD calculations for general shear failure. For local shear failure, relatively small values for the mean G and large values of mean ϕ' were considered.

The parametric study was conducted by calculating β as a function of one independent or variable parameter only [i.e., the 50-year mean recurrence interval ground snow load, foundation geometry (B, D/B, and L/B), snow load to total load ratio, dead load to live load ratio, type of occupancy or use, statistics of the effective stress friction angle and shear modulus] for a design situation in which all other remaining parameters are kept at a constant value. An illustrative allowable settlement (ρ_a) of 25 mm was selected for the parametric study. As an example, the effect of snow load to total load ratio on the SLS reliability level is shown in Table 3.

The results of the parametric study showed that the reliability level varies significantly with $m_{\phi'}$, $COV_{\phi'}$, and the ratio of 50-year mean recurrence interval snow load to total load. The influential parameters are the same ones for the ULS (Akbas 2007), although it should be noted that the foundation depth and allowable settlement limit also have small influences on the reliability level for SLS design. Since the parameters that are effective in the resulting reliability index values are the same, the same calibration domains can be used both for ULS and SLS design of shallow foundations under drained compression loading.

RANGE OF RELIABILITY LEVELS IMPLICIT IN EXISTING DESIGNS

Shallow foundations subjected to drained compression loading typically are designed by comparing the working load with the nominal allowable compression (or bearing) capacity. Although it is not possible to quantify the full range of reliability levels implicit in existing designs, Akbas (2007) showed that the reliability indices range from about 1.5 to 1.9, with an average reliability index of about 1.7. These values are significantly lower than those estimated for the ULS. This difference is to be expected, because the consequences of failure associated with the ULS and SLS differ significantly (Phoon et al. 1995). However, because of the large uncertainties in foundation settlement predictions and because of the absence of a safety factor in traditional design practice for the SLS, engineers can use other indirect means of introducing safety, which includes applying conservative design parameters or interpreting the results conservatively. Considering this point, and for consistency

Table 3. Effect of 50-Year Snow Load to Total Load Ratio on Serviceability Limit State Reliability Level of Shallow Foundations in Drained Compression

50-Year Snow Load / Total Load α	Reliability Index β	Probability of Failure p_f (%)
0.00	1.808	3.63
0.25	1.790	3.67
0.50	1.682	4.63
0.75	1.512	6.53

Note: B = 2 m, D/B = 0, L/B = 1, $m_{\phi'} = 35^o$, $COV_{\phi'} = 10\%$, $p_{g50} = 3$ kN/m^2, LL/DL = 1, $m_G = 30$ MN/m^2, $COV_G = 60\%$, $\rho_\alpha = 25$ mm; residential, renter-occupied building.

with previous studies (e.g. Phoon et al. 1995), a target reliability index of 2.6 is adopted in this study for the SLS design of shallow foundations in cohesionless soils.

CALIBRATION STUDIES

The following simplified RBD format was selected for the calibration of the SLS of shallow foundations in cohesionless soils under compression loading:

$$F_{50} = \Psi_c^{SLS} Q_{can} \quad (4)$$

in which F_{50} = 50-year return period total load on the foundation that, as discussed previously, consists of dead, live, and snow load components, Ψ_c^{SLS} = deformation factor in compression for SLS, and Q_{can} = nominal allowable bearing capacity (or compression capacity). The Ψ_c^{SLS} factor is calibrated to achieve a target reliability index of 2.6 for all the domains selected, as consistently as possible. The resulting deformation factors are given in Table 4.

Table 4. Deformation Factors for Shallow Foundations in Drained Compression Designed Using $F_{50} = \Psi_c^{SLS} Q_{can}$ for General / Local Shear Failure Mode

Mean ϕ' $m_{\phi'}$	COV ϕ' $COV_{\phi'}$ (%)	50-Year Snow Load / Total Load, α	Ψ_c^{SLS} General Shear/ Local Shear
30 - 35	5 - 10	0.00 - 0.25	0.61 / 0.60
		0.25 - 0.50	0.59 / 0.59
		0.50 - 0.75	0.56 / 0.57
	10 - 15	0.00 - 0.25	0.60 / 0.59
		0.25 - 0.50	0.59 / 0.58
		0.50 - 0.75	0.55 / 0.56
	15 - 20	0.00 - 0.25	0.58 / 0.57
		0.25 - 0.50	0.56 / 0.56
		0.50 - 0.75	0.54 / 0.55
35 - 40	5 - 10	0.00 - 0.25	0.57 / 0.58
		0.25 - 0.50	0.51 / 0.52
		0.50 - 0.75	0.49 / 0.49
	10 - 15	0.00 - 0.25	0.54 / 0.55
		0.25 - 0.50	0.49 / 0.50
		0.50 - 0.75	0.46 / 0.48
	15 - 20	0.00 - 0.25	0.51 / 0.53
		0.25 - 0.50	0.46 / 0.48
		0.50 - 0.75	0.43 / 0.45
40 - 45	5 - 10	0.00 - 0.25	0.47 / 0.48
		0.25 - 0.50	0.41 / 0.41
		0.50 - 0.75	0.38 / 0.38
	10 - 15	0.00 - 0.25	0.46 / 0.45
		0.25 - 0.50	0.40 / 0.41
		0.50 - 0.75	0.36 / 0.37
	15 - 20	0.00 - 0.25	0.44 / 0.45
		0.25 - 0.50	0.39 / 0.40
		0.50 - 0.75	0.34 / 0.35

The performance of the proposed RBD format was evaluated by investigating the range of inherent reliability index values obtained for a specific design problem by varying the COV_{ϕ}. The reliability index was calculated for two different 50-year snow load to total load ratios. It can be seen from Figure 1 that, for the allowable stress design, the reliability index decreases consistently with increasing $COV_{\phi'}$. Also, the reliability index values are consistently lower for designs with $\alpha = 0.75$ than those for designs with $\alpha = 0.5$, when allowable stress design is used. Note that, as stated previously, the range of reliability levels for existing designs is likely to be much larger than indicated in Figure 1. On the other hand, by using resistance factors from reliability analysis, comparably uniform reliability index values are obtained throughout the whole range of COV_{ϕ} and α. This result is a clear advantage over allowable stress design because the safety level of the design is fairly constant even though the variability of the geotechnical parameters or the load increases.

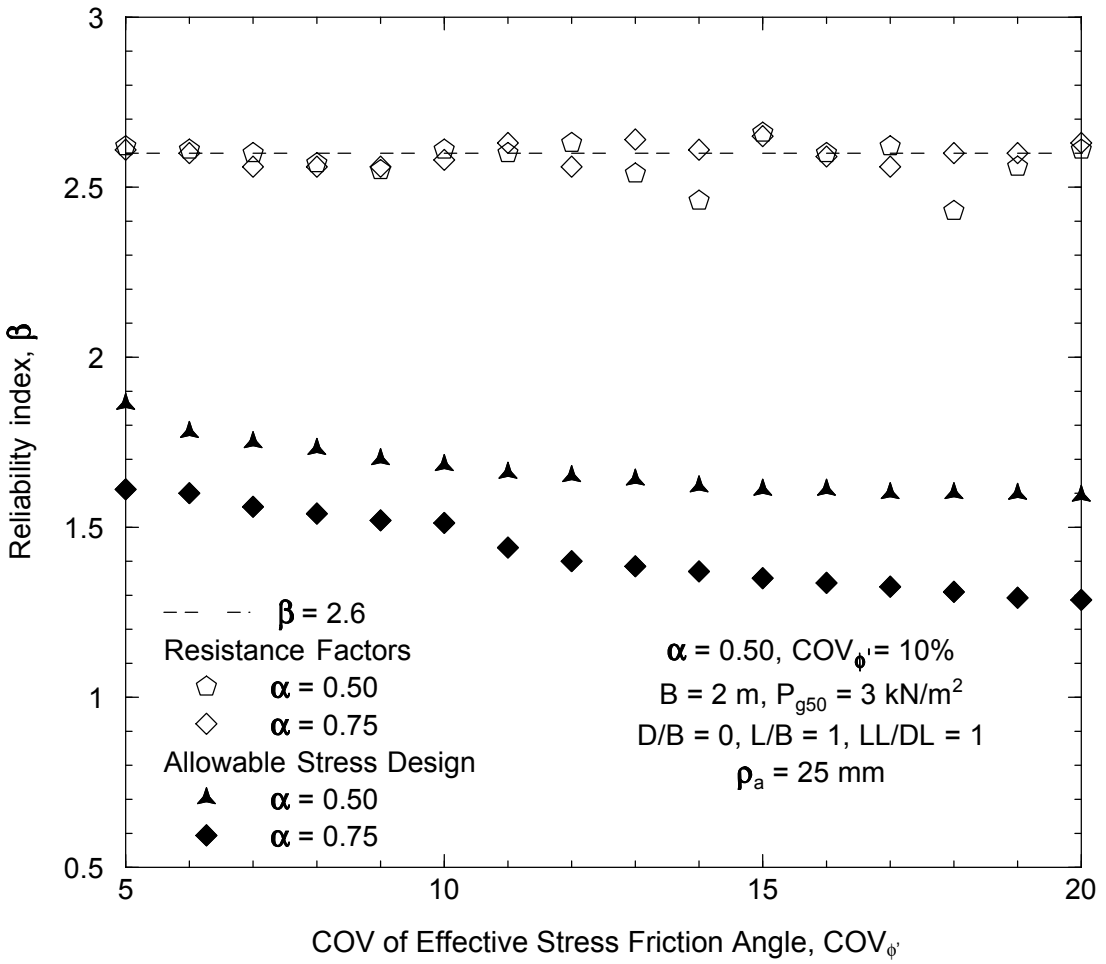

Figure 1. Comparison of Uniformity of Reliability Levels Using Deformation Factors and Allowable Stress Design

SUMMARY AND CONCLUSIONS

The reliability-based design (RBD) of shallow foundations under drained compression loading was examined. RBD equations for the SLS were developed to achieve a target reliability index of 2.6. The mean and COV of the effective stress friction angle and the ratio of the 50-year snow load to total load (where present) were determined to be the most influential parameters on the reliability index. Therefore, the same calibration domains can be used for both ULS and SLS design of shallow foundations under drained compression loading. The resulting deformation factors are significantly smaller than 1, and they vary between 0.61 and 0.34.

The insignificant difference between the deformation factors for the general and local shear failure modes suggests that a single set of resistance factors are adequate for design, without considering the failure type. The uniformity of the reliability levels obtained by using the corresponding deformation factors also was illustrated by a simple design example.

REFERENCES

Akbas, S.O. (2007). Deterministic and probabilistic assessment of settlements of shallow foundations in cohesionless soils. *PhD Thesis,* Cornell Univ, Ithaca, NY.

Akbas, S.O. & Kulhawy, F.H. (2009a). "Axial compression of footings in cohesionless soils. I: Load-settlement behavior." *J. Geotech. & Geoenvir. Eng.,* ASCE, 135(11), 1562-1574.

Akbas, S.O. & Kulhawy, F.H. (2009b). "Axial compression of footings in cohesionless soils. II: Bearing capacity." *J. Geotech. & Geoenvir. Eng.*, ASCE, 135(11), 1575-1582.

Akbas, S.O. & Kulhawy, F.H. (2010). "Model uncertainties in 'Terzaghi and Peck' methods for estimating settlement of footings on sand" *Advances in Analysis, Modeling & Design (GSP 199)*, ASCE, Reston, 2093-2102.

ASCE. (2002). *Minimum design loads for buildings and other structures*, ASCE 7-02. ASCE, Reston.

Ellingwood, B.R., Galambos, T.V., MacGregor, J.G., & Cornell, C.A. (1980). "Development of probability-based load criterion for American National Standard A58." *Special Publication 577*, National Bureau of Standards, Washington.

Phoon, K.K., Kulhawy, F.H., & Grigoriu, M.D. (1995). "Reliability-based foundation design for transmission line structures." *Report TR-105000*, Electric Power Research Institute, Palo Alto.

Spry, M.J., Kulhawy, F.H., & Grigoriu, M.D. (1988). "Reliability-based foundation design for transmission line structures: Geotechnical site characterization strategy." *Report EL-5507(1)*, Electric Power Research Institute, Palo Alto.

Quantile Framework for Simplified Geotechnical Reliability-based Design

Jianye Ching[1], M. ASCE and Kok-Kwang Phoon[2], F. ASCE

[1] Associate Professor, Dept of Civil Engineering, National Taiwan University, Taipei, Taiwan. Tel: 886-2-33664328; Email: jyching@gmail.com
[2] Professor, Dept of Civil & Environmental Engineering, National University of Singapore, Department of Civil Engineering, Singapore

ABSTRACT

This paper proposes a quantile-based framework for calibrating reliability-based design factors. The quantile framework is quite versatile: it is applicable to various design formats, such as safety factor design, partial factor design, load and resistance factor design (LRFD), and multiple resistance factor design (MRFD). The advantage of the framework is to allow a single set of design factors to maintain a more uniform reliability over a wider range of design parameters. The proposed framework does not require the capacity to be lumped as a single lognormal random variable as assumed in the LRFD format nor does it require tedious segment by segment optimization of the resistance factors in the MRFD format. The applicability and usefulness of the proposed framework are illustrated using a geotechnical design example. The results show that the proposed approach is able to maintain a uniform reliability over a wide range of design parameters with a single set of design factors.

INTRODUCTION

In structural reliability-based design (RBD), it is common to represent variables with small sensitivity coefficients at their means and variables with large sensitivity coefficients at their quantiles. It is well known empirically that doing so would allow a single set of partial factors to maintain a more uniform reliability over a broader range of coefficients of variation in the underlying random variables (e.g., Construction Industry Research & Information Association 1977). The simplest form is the baseline technique that involves the matching of a suitably chosen quantile load and quantile capacity to achieve a consistent level of reliability without any partial factors (Phoon et al. 2003). The Task Committee on Structural Loadings of ASCE (1991) adopted the baseline technique to calibrate the RBD format for transmission line structures. This paper proposes a quantile-based reliability calibration approach that shares some conceptual similarities with the above baseline technique. The proposed framework does not require the capacity to be lumped as a single lognormal random variable as implicitly assumed in the LRFD format nor does it require tedious segment by segment optimization of the resistance factors in the MRFD format. The proposed approach is quite versatile: it is applicable to various design formats, such as safety factor design, partial factor design, LRFD, and MRFD. The applicability of the proposed approach is demonstrated using a drilled shaft example.

DESIGN EXAMPLE FOR DEMONSTRATION

For concreteness, we adopt a specific geotechnical design example to demonstrate the quantile-based RBD methodology. The example involves a drilled shaft of diameter B and length L installed at a site with ground profile shown in Table **1**. There are four strata, clay 'c', sand 's', gravel 'g', and rock 'r' layers. The parameters d_x and t_x respectively denote the mid-depth and thickness of each layer ('x' may be either 'c', 's', 'g', or 'r', depending on the associated stratum type); $\sigma'_{vs,m}$, $\sigma'_{vg,m}$, $s_{u,m}$, and $q_{u,m}$ are respectively the measured in-situ effective stress in sand layer, in-situ effective stress in gravel layer, undrained shear strength of clay layer, and uniaxial compression strength of rock layer. The measurement is subjected to measurement errors:

$$\ln\left(\sigma'_{vs,m}\right)=\ln\left(\sigma'_{vs}\right)+e_{\sigma'_{vs}} \qquad \ln\left(\sigma'_{vg,m}\right)=\ln\left(\sigma'_{vg}\right)+e_{\sigma'_{vg}}$$
$$\ln\left(s_{u,m}\right)=\ln\left(s_u\right)+e_{s_u} \qquad \ln\left(q_{u,m}\right)=\ln\left(q_u\right)+e_{q_u} \tag{1}$$

where σ'_{vs} , σ'_{vg} , s_u , q_u are the actual values and $e_{\sigma'vs}$, $e_{\sigma'vg}$, e_{su} , e_{qu} are the measurement errors, modeled as zero-mean normal random variables with standard deviations chosen to be 0.1, 0.1, 0.2, and 0.5, respectively. The axial compression capacity of the drilled shaft is primarily provided by the side resistance (S): $S = S_c + S_s + S_g + S_r$, where S_c , S_s, S_g, and S_r are side resistances for the clay, sand, gravel, and rock layers, respectively. The side resistance in a given layer can be computed as $S_x = \pi B f_{sx} t_x$, where f_{sx} is the unit side resistance provided by layer 'x'. Useful correlation equations for f_s are listed in Table **2**, where ε denotes the transformation uncertainty, modeled as zero-mean normal variables with standard deviations listed in the table.

Table 1. Ground Profile for the Example Design Site

Type	Depth (m)	Middle depth d (m)	$\sigma'_{v,m}$ (kN/m^2)	Thickness t (m)	$s_{u,m}$ (kN/m^2)	$q_{u,m}$ (kN/m^2)
Clay	0.0 – 42.1			42.1 = t_c	70	
Sand	42.1 – 49.6	45.85 = d_s	350 = $\sigma'_{vs,m}$	7.5 = t_s		
Gravel	49.6 – 69.7	59.65 = d_g	480 = $\sigma'_{vg,m}$	20.1 = t_g		
Sandstone	69.7 – 74.7			5.0 = t_r		900

It is then clear that

$$S_c=\pi B e^{2.70+0.30\left[\ln s_{u,m}-e_{s_u}\right]+\varepsilon_{S_c}} t_c \qquad S_s=\pi B e^{1.08-0.66\ln(d_s)+\left[\ln(\sigma'_{vs,m})-e_{\sigma'_{vs}}\right]+\varepsilon_{S_s}} t_s$$
$$S_g=\pi B e^{2.18-0.75\ln(d_g)+\left[\ln(\sigma'_{vg,m})-e_{\sigma'_{vg}}\right]+\varepsilon_{S_g}} \min\left(L-t_c-t_s,t_g\right) \qquad S_r=\pi B e^{3.03+0.41\left[\ln q_{u,m}-e_{q_u}\right]+\varepsilon_{S_r}} \min\left(L-t_c-t_s-t_g,0\right) \tag{2}$$

where min(X,Y) is the minimum value between X and Y. The two terms min(L-t_c-t_s, t_g)

and min(L-t_c-t_s-t_g, 0) are present because the gravel and rock layers may not be fully penetrated due to insufficient length L. The drilled shaft is subjected to dead load L_D and live load L_L, modeled as lognormal random variables with mean values $\{\mu_{LD}, \mu_{LL}\}$ and coefficients of variation (c.o.v.) $\{\delta_{LD} = 0.1, \delta_{LL} = 0.25\}$.

Table 2. Correlation Models for Evaluating Unit Side Resistance

	Correlation Model for Unit Side Resistance f_s (kN/m^2)	Standard Deviation of Transformation Uncertainty ε
Clay	$f_s = \exp\left(2.70 + 0.30\ln(s_u) + \varepsilon_{S_c}\right)$	0.32
Sand	$f_s = \exp\left(1.08 - 0.66\ln(d) + \ln(\sigma'_{vs}) + \varepsilon_{S_s}\right)$	0.54
Gravel	$f_s = \exp\left(2.18 - 0.75\ln(d) + \ln(\sigma'_{vg}) + \varepsilon_{S_g}\right)$	0.67
Rock	$f_s = \exp\left(3.03 + 0.41\ln(q_u) + \varepsilon_{S_r}\right)$	0.72

The collection of random variables is denoted by Z, including measurement errors $\{e_{\sigma'vs}, e_{\sigma'vg}, e_{su}, e_{qu}\}$, transformation uncertainties $\{\varepsilon_{Sc}, \varepsilon_{Ss}, \varepsilon_{Sg}, \varepsilon_{Sr}\}$ and loads $\{L_D, L_L\}$. The collection of design parameters is denoted by θ, including diameter B and shaft length L. Let F denotes the failure event: F={SR(Z,θ)<1}, where SR(Z,θ) is called the safety ratio. For this particular example, the safety ratio SR(Z,θ) can be defined as $SR = (S_c + S_s + S_g + S_r)/(L_D + L_L)$.

QUANTILE-BASED RELIABILITY-BASED DESIGN

For RBD, the objective is to enforce the following *probabilistic* constraint during the design process: $P[SR(Z, \theta)<1|\theta] \le P_F^*$, where P_F^* is the target failure probability. According to Ching and Phoon (2010), this probabilistic design constraint can be transformed into a deterministic *algebraic* constraint of the following format: $c(\theta) \ge 1$. Intuitively, $c(\theta)$ should be taken to be a conservative version of $SR(z^*,\theta)$, i.e., $c(\theta) < SR(z^*,\theta)$, where z^* is the characteristic value of Z. As a result, requiring $c(\theta) \ge 1$ is much stronger than requiring $SR(z^*,\theta) \ge 1$, leading to a more conservative design with a small target failure probability P_F^*. Depending on how this conservatism is applied based on quantiles, there are four possible algebraic design formats:

a. Quantile-based safety factor design

For this design format, $c(\theta)$ is taken to be the η quantile (η is called the probability threshold) of SR(Z,θ), denoted by $SR^{\eta}(\theta)$. The probability threshold η is typically taken to be a small number, e.g., 0.05, to ensure a conservative design. This definition is sensible because we are applying a value less than the mean. Requiring $c(\theta) \ge 1$ is equivalent to requiring

$$c(\theta)=\frac{SR\left(z^*,\theta\right)}{SR\left(z^*,\theta\right)/c(\theta)}=\frac{SR\left(z^*,\theta\right)}{SR\left(z^*,\theta\right)/SR^{\eta}(\theta)}=\frac{SR\left(z^*,\theta\right)}{SF^{\eta}}\geq 1 \tag{3}$$

where SF is the safety factor, which clearly depends on η. Note that the required SF is simply the nominal safety ratio $SR(z^*,\theta)$ divided by the η quantile $SR^{\eta}(\theta)$.

b. Quantile-based LRFD

For the drilled shaft, $SR(z,\theta)$ has the format of $S(z,\theta)/[L_D(z,\theta)+L_L(z,\theta)]$, where S is the total resistance. A possible choice for $c(\theta)$ is $S^{\eta}(\theta)/[L_D{}^{1-\eta}(\theta)+L_L{}^{1-\eta}(\theta)]$, where $S^{\eta}(\theta)$ is the η quantile of $S(Z,\theta)$, and $L_D{}^{1-\eta}(\theta)$ and $L_L{}^{1-\eta}(\theta)$ are the 1-η quantiles of $L_D(Z,\theta)$ and $L_L(Z,\theta)$. The same probability threshold η (e.g., 0.05) is applied to all three random variables. This would not only ensure a conservative design but also ensure all random variables have the same exceedance/non-exceedance probability over the corresponding quantiles. Requiring $c(\theta)\geq 1$ is equivalent to requiring

$$c(\theta)=\frac{\frac{S^{\eta}(\theta)}{S\left(z^*,\theta\right)}S\left(z^*,\theta\right)}{\frac{L_D^{1-\eta}(\theta)}{L_D\left(z^*,\theta\right)}L_D\left(z^*,\theta\right)+\frac{L_L^{1-\eta}(\theta)}{L_L\left(z^*,\theta\right)}L_L\left(z^*,\theta\right)}=\frac{\gamma_S^{\eta}\cdot S\left(z^*,\theta\right)}{\gamma_{LD}^{\eta}\cdot L_D\left(z^*,\theta\right)+\gamma_{LL}^{\eta}\cdot L_L\left(z^*,\theta\right)}\geq 1 \tag{4}$$

where γ_S is the resistance factor, while γ_{LD} and γ_{LL} are the load factors. These factors clearly depend on η. Note that the required resistance factor is simply the η quantile $S^{\eta}(\theta)$ divided by the nominal resistance $S(z^*,\theta)$, and the required load factor is simply the 1-η quantile $L^{1-\eta}(\theta)$ divided by the nominal load $L(z^*,\theta)$.

c. Quantile-based MRFD

In this case, a possible choice for $c(\theta)$ is $[S_c{}^{\eta}(\theta)+S_s{}^{\eta}(\theta)+S_g{}^{\eta}(\theta)+S_r{}^{\eta}(\theta)]/[L_D{}^{1-\eta}(\theta)+L_L{}^{1-\eta}(\theta)]$. Again, the same probability threshold η is applied to all six random variables. Requiring $c(\theta)\geq 1$ is equivalent to requiring

$$c(\theta)=\frac{\frac{S_c^{\eta}(\theta)}{S_c\left(z^*,\theta\right)}S_c\left(z^*,\theta\right)+\ldots+\frac{S_r^{\eta}(\theta)}{S_r\left(z^*,\theta\right)}S_r\left(z^*,\theta\right)}{\frac{L_D^{1-\eta}(\theta)}{L_D\left(z^*,\theta\right)}L_D\left(z^*,\theta\right)+\frac{L_L^{1-\eta}(\theta)}{L_L\left(z^*,\theta\right)}L_L\left(z^*,\theta\right)}=\frac{\gamma_{Sc}^{\eta}\cdot S_c\left(z^*,\theta\right)+\ldots+\gamma_{Sr}^{\eta}\cdot S_r\left(z^*,\theta\right)}{\gamma_{LD}^{\eta}\cdot L_D\left(z^*,\theta\right)+\gamma_{LL}^{\eta}\cdot L_L\left(z^*,\theta\right)}\geq 1 \tag{5}$$

where γ_{Sc}, γ_{Ss}, γ_{Sg}, and γ_{Sr} are the resistance factors, while γ_{LD} and γ_{LL} are the load factors. Note that the required resistance factor is simply the η quantile $S^{\eta}(\theta)$ divided by the nominal resistance $S(z^*,\theta)$, and the required load factor is simply the 1-η quantile $L^{\eta}(\theta)$ divided by the nominal load $L(z^*,\theta)$.

d. Quantile-based partial factor design

In contrast to LRFD and MRFD where the factors are applied to load and re-

sistance terms, the partial-factor design format applies the (partial) factors to Z directly, i.e.,

$$c(\theta) = SR\left(z_1^{\eta}, z_2^{\eta}, ..., z_p^{1-\eta}, \theta\right) \geq 1 \tag{6}$$

where either the η or 1-η quantile of Z_i is taken depending on its stabilizing or destabilizing role. For Z_i that is clearly stabilizing, η quantile of Z_i should be taken, while 1-η quantile should be adopted for destabilizing Z_i. For Z_i that is not influential or whose effect cannot be clearly discerned as stabilizing or destabilizing, the mean or median value may be taken. Requiring $c(\theta) \geq 1$ is equivalent to requiring

$$c(\theta) = SR\left(\frac{z_1^{\eta}}{z_1^*} z_1^*, \frac{z_2^{\eta}}{z_2^*} z_2^*, ..., \frac{z_p^{1-\eta}}{z_p^*} z_p^*, \theta\right) = SR\left(\gamma_1^{\eta} z_1^*, \gamma_2^{\eta} z_2^*, ..., \gamma_p^{\eta} z_p^*, \theta\right) \geq 1 \tag{7}$$

where γ's are the partial factors. Note that the required partial factor is simply the η quantile z_i^{η} divided by its characteristic value z_i^* if z_i is stabilizing and is the 1-η quantile $z_i^{1-\eta}$ divided by its characteristic value z_i^* if z_i is destabilizing.

Note that algebraic design constraints based on the above four formats are convenient, because to make sure $c(\theta) \geq 1$ holds, it only requires a *single* algebraic evaluation of $SR(Z,\theta)$ using deterministic factors γ's and characteristic values z^*. In Ching and Phoon (2010), it is postulated that the four algebraic design formats associated with a proper probability threshold η can be made equivalent to rigorous RBD by the following steps:

Step 1 – find the relation between η and design factors by Monte Carlo simulation:

a. For the safety-factor design format, the safety factor SF^{η} is $SR(z^*,\theta)/SR^{\eta}(\theta)$, which can be easily estimated by MCS.

b. For the safety-factor design format, the safety factor SF^{η} is $SR(z^*,\theta)/SR^{\eta}(\theta)$, which can be easily estimated by MCS.

c. For LRFD, the resistance factor γ_S^{η} is $S^{\eta}(\theta)/S(z^*,\theta)$, while the load factor γ_{Lx}^{η} is $L_x^{1-\eta}(\theta)/L_x(z^*,\theta)$.

d. For MRFD, the resistance factor γ_{Sx}^{η} is $S_x^{\eta}(\theta)/S_x(z^*,\theta)$, while the load factor γ_{Lx}^{η} is $L_x^{1-\eta}(\theta)/L_x(z^*,\theta)$.

e. For the partial-factor design format, the partial factor γ_i^{η} for Z_i is z_i^{η}/z_i^* if Z_i is stabilizing and is $z_i^{1-\eta}/z_i^*$ if Z_i is destabilizing.

Step 2 – find the relation between the pair (η, P_F^*). The algorithm for obtaining this relation was developed in Ching and Phoon (2010) – it is based on the fact that P_F^* is simply the probability that $c(\theta)/SR(Z,\theta)$ exceeds 1.

Step 3 – given the prescribed target failure probability, P_F^*, find the corresponding probability threshold η from the result in Step 2.

Step 4 – once the corresponding probability threshold η is found, the required design factor can be determined accordingly according to the relations presented in Step 1.

a. For safety-factor design format, the resulting algebraic design constraint is $c(\theta)$

$= SR(z^*,\theta)/SF^\eta \geq 1$.

b. For LRFD, the resulting algebraic design constraint is $c(\theta) = \gamma_S{}^\eta S(z^*,\theta)/[\gamma_{LD}{}^\eta L_D(z^*,\theta)+\gamma_{LL}{}^\eta L_L(z^*,\theta)] \geq 1$.

c. For MRFD, the resulting algebraic design constraint is $c(\theta) = \Sigma_x[\gamma_{Sx}{}^\eta S_x(z^*,\theta)]/[\gamma_{LD}{}^\eta L_D(z^*,\theta)+\gamma_{LL}{}^\eta L_L(z^*,\theta)] \geq 1$.

d. For partial-factor design format, the resulting algebraic design constraint is $c(\theta) = SR(\gamma_1{}^\eta z_1{}^*,\gamma_2{}^\eta z_2{}^*,\ldots,\gamma_p{}^\eta z_p{}^*,\theta) \geq 1$.

Let the diameter B and length L be the two design parameters that can be optimized. Let us further assume there are constraints associated with constructability: 0.8 m ≤ B ≤ 1.5 m and 49.6 m ≤ L ≤ 74.7 m. The target failure probability $P_F{}^*$ is taken to be 0.001, i.e., the design goal is to adopt a certain combination of B and L so that $P(SR(Z,\theta)<1|\theta) \leq 0.001$. Only the detailed steps for MRFD will be demonstrated, but the results for the safety-factor design, LRFD, and partial-factor design will be still presented.

Step 1 – determine the relations between η and the MRFD design factors. Recall that the resistance factor corresponding to η is $S_x{}^\eta(\theta)/S_x(z^*,\theta)$, while the load factor corresponding to η is $L_x{}^{1-\eta}(\theta)/L_x(z^*,\theta)$. The nominal values $S_x{}^*$ and those for the dead and live loads are taken to be

$$\begin{aligned}
&S_c^* = S_c\left(z^*,\theta\right) = \pi B e^{2.70+0.30\ln s_{u,m}} t_c \qquad S_s^* = S_s\left(z^*,\theta\right) = \pi B e^{1.08-0.66\ln(d_s)+\ln(\sigma'_{vs,m})} t_s \\
&S_g^* = S_g\left(z^*,\theta\right) = \pi B e^{2.18-0.75\ln(d_g)+\ln(\sigma'_{vg,m})} \min\left(L-t_c-t_s,t_g\right) \qquad S_r^* = S_r\left(z^*,\theta\right) = \pi B e^{3.03+0.41\ln q_{u,m}} \min\left(L-t_c-t_s-t_g,0\right) \\
&L_D^* = \mu_{LD} = 8000kN \qquad L_L^* = \mu_{LL} = 4000kN
\end{aligned} \tag{8}$$

As a result,

$$\begin{aligned}
&\gamma_{Sc}^\eta = \left[\eta \text{ quantile of } S_c\left(Z,\theta\right)\right]\Big/ S_c\left(z^*,\theta\right) = \eta \text{ quantile of } \left[S_c\left(Z,\theta\right)\Big/ S_c\left(z^*,\theta\right)\right] = \eta \text{ quantile of } e^{\varepsilon_{S_c}-0.30e_{s_u}} \\
&\gamma_{Ss}^\eta = \eta \text{ quantile of } e^{\varepsilon_{S_s}-e_{\sigma'_{vs}}} \qquad \gamma_{Sg}^\eta = \eta \text{ quantile of } e^{\varepsilon_{S_g}-e_{\sigma'_{vg}}} \qquad \gamma_{Sr}^\eta = \eta \text{ quantile of } e^{\varepsilon_{S_r}-0.41e_{q_u}} \\
&\gamma_{LD}^\eta = \left[(1-\eta) \text{ quantile of } L_D\left(Z,\theta\right)\right]\Big/ L_D^* = (1-\eta) \text{ quantile of } \left[L_D\left(Z,\theta\right)/8000\right] \\
&\gamma_{LL}^\eta = (1-\eta) \text{ quantile of } \left[L_L\left(Z,\theta\right)/4000\right]
\end{aligned} \tag{9}$$

Figure 1 shows the relations between η and the MRFD design factors.

Step 2 – find the relation between $(\eta, P_F{}^*)$. For instance, when $\eta = 0.1$, the corresponding design factors can be readily from Figure 1 to be $\gamma_{Sc} = 0.658$, $\gamma_{Ss} = 0.495$, $\gamma_{Sg} = 0.422$, $\gamma_{Sr} = 0.387$, $\gamma_{LD} = 1.136$, and $\gamma_{LL} = 1.370$. Therefore,

$$\begin{aligned}
\frac{c(\theta)}{SR(Z,\theta)} &= \frac{\left[\gamma_{Sc}^\eta S_c^* + \gamma_{Ss}^\eta S_s^* + \gamma_{Sg}^\eta S_g^* + \gamma_{Sr}^\eta S_r^*\right]\times\left[L_D\left(Z,\theta\right)+L_L\left(Z,\theta\right)\right]}{\left[S_c\left(Z,\theta\right)+S_s\left(Z,\theta\right)+S_g\left(Z,\theta\right)+S_r\left(Z,\theta\right)\right]\times\left[\gamma_{LD}^\eta L_D^* + \gamma_{LL}^\eta L_L^*\right]} \\
&= \frac{\begin{bmatrix} 0.658e^{2.70+0.30\ln s_{u,m}} t_c + 0.495e^{1.08-0.66\ln(d_s)+\ln(\sigma'_{vs,m})} t_s + 0.422e^{2.18-0.75\ln(d_g)+\ln(\sigma'_{vg,m})} \min\left(L-t_c-t_s,t_g\right) \\ +0.387e^{3.03+0.41\ln q_{u,m}} \min\left(L-t_c-t_s-t_g,0\right) \end{bmatrix}\cdot\left[L_D\left(Z,\theta\right)+L_L\left(Z,\theta\right)\right]}{\begin{bmatrix} e^{2.70+0.30\left[\ln s_{u,m}-e_{s_u}\right]+\varepsilon_{S_c}} t_c + e^{1.08-0.66\ln(d_s)+\left[\ln(\sigma'_{vs,m})-e_{\sigma'_{vs}}\right]+\varepsilon_{S_s}} t_s + e^{2.18-0.75\ln(d_g)+\left[\ln(\sigma'_{vg,m})-e_{\sigma'_{vg}}\right]+\varepsilon_{S_g}} \min\left(L-t_c-t_s,t_g\right) \\ +e^{3.03+0.41\left[\ln q_{u,m}-e_{q_u}\right]+\varepsilon_{S_r}} \min\left(L-t_c-t_s-t_g,0\right) \end{bmatrix}\cdot\left[1.136\times 8000 + 1.370\times 4000\right]}
\end{aligned} \tag{10}$$

According to Ching and Phoon (2010), the corresponding $P_F{}^*$ is exactly $P(c(\theta)/SR(Z,\theta)>1)$. Monte Carlo simulation can be taken to simulate many

c(θ)/SR(Z,θ) samples, and the estimate of the probability of exceeding 1 is exactly the P_F^* value corresponding to η = 0.1. The entire (η, P_F^*) relation can be obtained by changing the probability threshold η and conducting the same MCS. Figure 1 shows the resulting relation between (η, P_F^*). Since the target failure probability P_F^* is 0.001, the required probability threshold should be 0.071 (see Figure 1).

Step 3 – by inverting Figure 1 with η = 0.071, it can be found that γ_{Sc} = 0.618, γ_{Ss} = 0.446, γ_{Sg} = 0.372, γ_{Sr} = 0.336, γ_{LD} = 1.158, and γ_{LL} = 1.436. These are the MRFD factors that should be taken for a RBD with P_F^* = 0.001.

Step 4 – the resulting algebraic design constraint is

$$c(\theta)=\frac{0.618\times S_c^*+0.446\times S_s^*+0.372\times S_g^*+0.336\times S_r^*}{1.158\times 8000+1.436\times 4000}\geq 1 \tag{11}$$

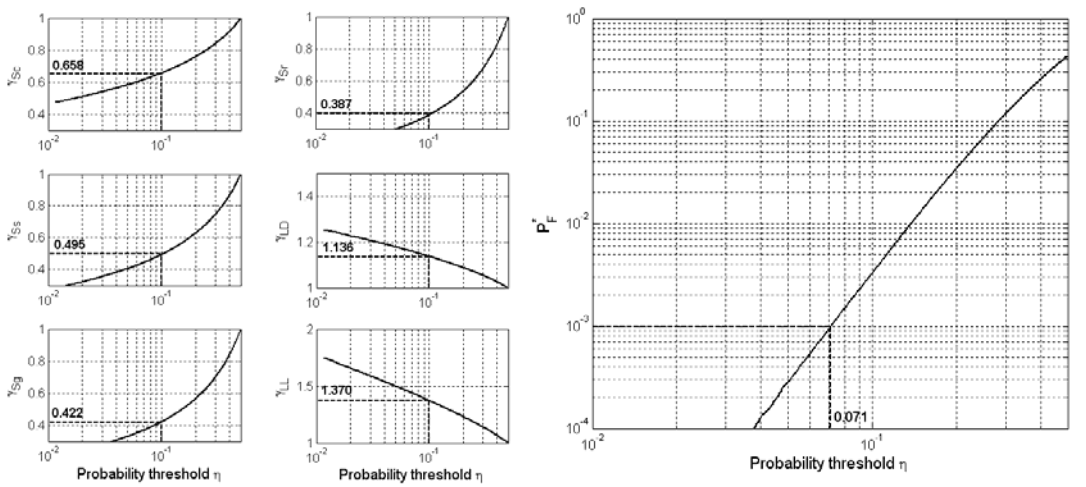

Figure 1 Left: relations between η and the MRFD Design Factors; right: relation between (η,P_F^*)

To examine the robustness of the resulting MRFD design factors for P_F^* = 0.001, the following approach is taken. In the allowable design region 0.8 m ≤ B ≤ 1.5 m and 49.6 m ≤ L ≤ 74.7 m, each of the coordinate axes is discretized into discrete points, creating grid points. MCS with a very large sample size is then conducted at each grid point, giving each point an estimate of the failure probability P(SR(Z,θ)<1|θ). The dividing boundary for P(SR(Z,θ)<1|θ) less and greater than 0.001 is plotted shown in Figure 2. Therefore, the region above the boundary is exactly the allowable reliability design set $\Sigma_R = \{\theta: P(SR(Z,\theta)<1|\theta) \leq P_F^*\}$. On the other hand, the allowable design region for the algebraic constraint, i.e., $\Sigma_S = \{\theta: c(\theta) \geq 1\}$, can be also found and is marked with label 'o'. For the unsatisfactory region with c(θ) < 1, it is marked with label 'x'. Such comparisons are made in Figure 2, not only for the MRFD design format but also for the other three aforementioned design formats, although the detailed steps of those three design formats are not presented. It can be seen from Figure 2 that the two sets match one another reasonably well for all four design methods.

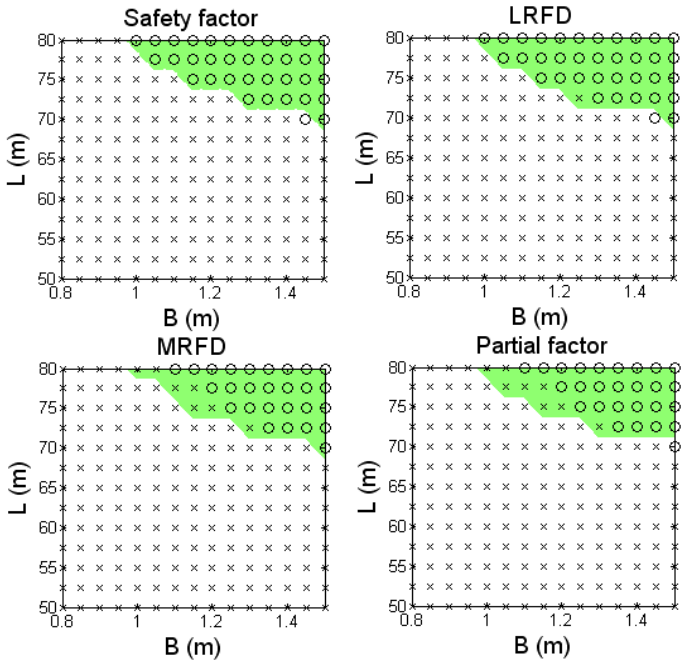

Figure 2 Comparison between Algebraic Design Constraints and Rigorous RBD

CONCLUSION

This paper proposes a reliability-based design framework that can be applied to calibrate common design formats, such as safety factor design, partial factor design, load and resistance factor design, and multiple resistance factor design. The basic idea involves tuning a single quantile in all the underlying random variables to achieve a prescribed target failure probability. The usefulness of this framework is demonstrated using a drilled shaft in a layered soil consisting of clay, sand, gravel, and rock.

REFERENCES

Ching, J. and Phoon, K.K. (2010). "A quantile-based approach for calibrating reliability-based partial factors". Submitted to *Structural Safety*.

Construction Industry Research & Information Association (1977). Rationalization of safety and serviceability factors in structural codes. Report 63, CIRIA, London.

Phoon, K. K., Kulhawy, F. H. & Grigoriu, M. D. (2003). "Multiple Resistance Factor Design (MRFD) for Spread Foundations", *Journal of Geotechnical and Geoenvironmental Engineering*, ASCE, 129(9), 807 – 818.

Task Committee on Structural Loadings (1991). "Guidelines for Electrical Transmission Line Structural Loading", Manual and Report on Engineering Practice 74, ASCE, New York.

Reliability Assessment of Eurocode 7 Spread Foundations Design Methodology

Sónia H. Marques[1], A. Topa Gomes[2], and A. Abel Henriques[3]

[1]PhD Researcher, University of Porto, Faculty of Engineering, Department of Civil Engineering, Rua Dr. Roberto Frias, 4200-465 Porto, Portugal, Phone (+351)225081400, Fax (+351)225081440, Email sonia.h@fe.up.pt
[2]Assistant Professor, University of Porto, Faculty of Engineering, Department of Civil Engineering, Rua Dr. Roberto Frias, 4200-465 Porto, Portugal, Phone (+351)225081400, Fax (+351)225081440, Email atgomes@fe.up.pt
[3]Associate Professor, University of Porto, Faculty of Engineering, Department of Civil Engineering, Rua Dr. Roberto Frias, 4200-465 Porto, Portugal, Phone (+351)225081400, Fax (+351)225081440, Email abel.henriques@fe.up.pt

ABSTRACT

This paper is a contribution for the application of Eurocode 7 design methodology and analysis of related features in geotechnical engineering, such as uncertainty, risk and reliability. The design methodology of Eurocode 7 is applied to a strip foundation resting on a relatively homogeneous c-φ soil, and the different design approaches are compared to deterministic and semi-probabilistic solutions. A reliability assessment is performed for different conditions, particularly selecting different characteristic values and coefficients of variation of soil properties. Several uncorrelated and correlated random variables are considered, and probabilistic solutions are achieved and compared with a target reliability index. For this purpose, reliability techniques such as the first-order reliability method (FORM) and the Monte Carlo simulation (MCS) are applied and compared to other methodologies. Based on the obtained results, the Eurocode 7 design methodology is discussed, and the indispensable engineering judgment is outlined.

INTRODUCTION

The Eurocodes are a set of European Standards for the design of buildings and other civil engineering works, which replace the different rules in the various Member States. A system of nationally determined parameters provides flexibility in national implementation and allows the Member States to decide the level of safety. Therefore, in this context the Eurocodes may be used worldwide, also outside European Union.

Eurocode 7 is a geotechnical design code that shares common bases with the design methodology for structures. An European Technical Committee was established to evaluate the geotechnical design process covered by Eurocode 7, carrying out a number of design examples and inviting geotechnical engineers worldwide to submit Eurocode 7 exercises. This paper presents design concepts of Eurocode 7 with regard to spread foundations on a relatively homogeneous c-φ soil,

and a reliability-based design (RBD), level I and level II, is performed by selecting different characteristic values and coefficients of variation of soil properties, and considering several uncorrelated and correlated random variables.

UNCERTAINTY, RISK AND RELIABILITY

In the small number of things which we are able to know with certainty, the principal means of ascertaining truth are based on probabilities. Satisfactory performance cannot be absolutely ensured, and assurance can only be given in terms of the probability of success in satisfying some performance criterion. In engineering terminology, this probabilistic assurance of performance is referred to as reliability. An alternative way to look at the problem is to consider unsatisfactory performance of the system, and in this case, one might measure the probability of failure to satisfy some performance criterion and the corresponding term is risk. Thus, risk and reliability are complementary (Haldar *et al*., 2000).

The first step in evaluating the reliability or probability of failure of a structure is to decide on specific performance criteria and the relevant parameters called the basic random variables X_i, as well as the functional relationships among them. Mathematically, this relationship or performance function can be described by equation (1):

$$M=f(X_1,X_2,...,X_n) \qquad (1)$$

The failure surface or the limit state of interest can be defined as M=0. This is the boundary between the safe and unsafe regions in the design parameter space, and it also represents a state beyond which a structure can no longer fulfill the function for which it was designed.

DESIGN METHODOLOGIES AND JUDGMENT

Engineering design is usually a trade-off between maximizing safety levels and minimizing cost, and a design methodology that accomplishes both of these goals is highly desirable (Haldar *et al*., 2000).

For several years, working or allowable stress design (WSD/ASD) has been the traditional basis for geotechnical design relating to failure conditions. Essentially, working or allowable stress design (WSD/ASD) ensures that the characteristic load does not exceed some allowable limit. The nominal factor of safety Fs_k can be defined as the ratio of the characteristic resistance to the characteristic load:

$$Fs_k = \frac{\text{characteristic resistance}}{\text{characteristic load}} \qquad (2)$$

In general, the characteristic resistance is computed by geotechnical formulas using conservative estimates of the soil properties, while the characteristic load is the sum of conservative unfactored estimates of characteristic load actions acting on the system. The choice of a safety factor, although guided to some extent by geotechnical codes, is left largely up to the engineer doing the design. Engineering

judgment is an essential component of design, but just stating that the safety factor should lie between 2 and 3 does not provide any guidance which considers spatial variability or the understanding on the probability of failure. All uncertainty is lumped under a single factor of safety, commonly defined in terms of the mean values:

$$\mathrm{Fs_m} = \frac{\text{mean resistance}}{\text{mean load}} \qquad (3)$$

Different geotechnical systems, having the same mean factor of safety $\mathrm{Fs_m}$, can have different probabilities of failure, and the mean factor of safety does not adequately reflect the actual design safety (Fenton *et al*., 2008).

The literature on probabilistic analysis and design and the number of engineering applications have greatly increased in recent years, expanding the acceptance of this methodology. While probabilistic analysis brings rationality to the consideration of uncertainty in design, it does not discount the expertise gathered from a particular system. The use of probabilistic analysis provides more information about system behavior, the influence of different uncertain variables on system performance, and the interaction between different system components. Probabilistic design addresses the necessary design conservatism explicitly and comprehensively, through treatment of the uncertainty of the random variables, and selection of the design values and desired underlying reliability. Engineers are empowered to use judgment in selecting these factors on a case-by-case basis. This concept is in the essence of all the reliability-based design (RBD) codes developed in different areas of engineering worldwide (Haldar *et al*., 2000).

Current practices of geotechnical reliability-based design (RBD) are differently adopted all over the world. Limit state design (LSD) codes as Eurocode 7 are increasingly used in geotechnical engineering. They are philosophically akin to the load and resistance factor design (LRFD) approach, which account for the variability in load, material properties and construction, model error and failure consequences, with the purpose of improving design.

CHARACTERISTIC VALUES

For each geotechnical design situation it shall be verified that no relevant limit state is exceeded. In geotechnical practice, the choice of a characteristic value depends on the experience and risk tolerance of the engineer performing the design, and shall be based on the results of field and laboratory tests. It is not logical to apply resistance factors to poorly defined characteristic resistance values, thus a clear definition of characteristic values is essential. Geotechnical design codes as Eurocode 7 recommend that the characteristic value of a geotechnical parameter shall be selected as a cautious estimate of the value affecting the occurrence of the limit state (clause 2.4.5.2(2)P), the mean value or the lowest/highest value occurring in the zone governing the behavior, when a local failure is concerned.

This paper presents results based on the definition of eight sets of characteristic values of soil properties X_k - pure mean values (considered as a superior reference) (4), Schneider's equation values (5), Ovesen's equation values

(6), 95% reliable mean values (according to the number of test results and for unknown or known Cv_x, referenced as mean) (7), 5% fractile values (from a normal probability distribution) (8), and 5% fractile values (according to the number of test results and for unknown or known Cv_x, referenced as low) (9):

$$X_k=X_m \text{ (4)}; \quad X_k=X_m-0.5\sigma_x \text{ (5)}; \quad X_k=X_m-1.645\sigma_x/\sqrt{N} \text{ (6)};$$

$$X_k=X_m(1-k_{n,mean}Cv_x) \text{ (7)}; \quad X_k=X_m-1.645\sigma_x \text{ (8)}; \quad X_k=X_m(1-k_{n,low}Cv_x) \text{ (9)}$$

in which X_m is the mean value, σ_x is the standard deviation, Cv_x is the coefficient of variation, N is the number of test results, and $k_{n,mean}$ and $k_{n,low}$ are statistical coefficients taking into account the sampling (only local, when Cv_x is considered unknown, or local in conjunction with relevant experience, when Cv_x is considered known), the number of test results, the value affecting the occurrence of the limit state (the mean value, or the lowest value, respectively), and the statistical level of confidence required for the assessed characteristic value, expressed by a considered t factor of Student's distribution (Frank *et al*., 2004; Lo, 2005; Schneider, 1999). Therefore, equations (7) and (9) are related, respectively, to the cautious estimate of the mean value and the lowest value occurring in the zone governing the behavior, considering a relatively homogeneous soil and normal probability distributions for the values of soil properties, although this assumption is not always valid (for the considered example, all characteristic values of soil properties yield positive results). Moreover, when the Cv_x is considered unknown, all the statistical parameters are estimated from the results of the tests, but when the Cv_x is considered known, the mean value and the standard deviation are estimated from the results of the tests and from the known Cv_x derived from published data, respectively. For the following example, and considering five test results: $k_{n,mean}$ was considered 0.95 or 0.74 for Cv_x unknown or known, respectively; and $k_{n,low}$ was considered 2.33 or 1.80 for Cv_x unknown or known, respectively (Frank *et al*., 2004). Characteristic load values were considered as 95% fractile values (from a normal probability distribution).

EXAMPLE

A strip foundation is shown in Figure 1. For bearing capacity predictions the considered performance function is:

$$M(B, D, c, \varphi, \gamma_1, \gamma_2, P, Q) = cN_c(\varphi) + \gamma_1 DN_q(\varphi) + 0.5\gamma_2 BN_\gamma(\varphi) - \frac{P+Q}{B} \qquad (10)$$

where c is the cohesion, $\gamma_1 D$ is the overburden stress, γ_2 is the unit soil weight, B is the foundation width, $N_c(\varphi)$, $N_q(\varphi)$, and $N_\gamma(\varphi)$ are the bearing capacity factors which are functions of the friction angle φ , P is the dead load, and Q is the live load.

Table 1 summarizes the data based on the results of some tests on a c-φ soil or published values, where the coefficient of variation is both considered unknown or known.

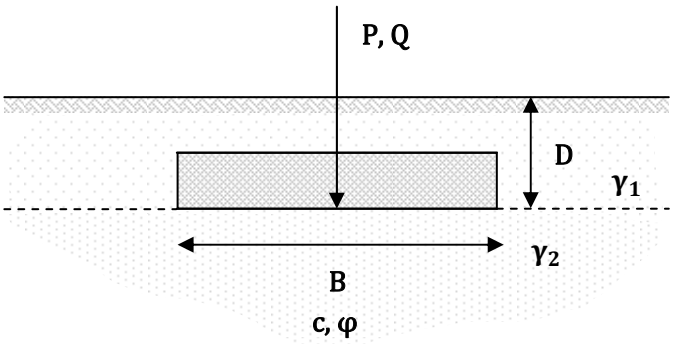

Figure 1.Strip foundation.

Table 1.Data based on the results of some tests on a c-φ soil or published values.

Basic random variables	Probability distribution	Number of test results	Mean value μ	Standard deviation σ	Coefficient of variation Cv
B (m)	Normal	-	-	-	0.04
D (m)	Normal	-	1.00	0.10	0.10
c (kN/m²)	Normal	5	14.00	4.3012[a] μ*Cv[b]	0.3072[a] 0.20;0.40;0.60[b]
φ (°)	Normal	5	32.00	2.3452[a] μ*Cv[b]	0.0733[a] 0.05;0.10;0.15[b]
γ_1(kN/m³)	Normal	5	16.80	0.8367[a] μ*Cv[b]	0.0498[a] 0.05[b]
γ_2(kN/m³)	Normal	5	17.80	0.8367[a] μ*Cv[b]	0.0470[a] 0.05[b]
P (kN/m)	Normal	-	370.00	37.00	0.10
Q (kN/m)	Normal	-	70.00	17.50	0.25

[a]Coefficient of variation unknown, obtained from the results of some tests on a c-φ soil.
[b]Coefficient of variation known, obtained from published values; central values of Cv are recommended values and were generally used (exception for Figure 5).

RESULTS

Based on the definition of eight sets of characteristic values of soil properties X_k, the minimum foundation width B was determined for the different Design Approaches of Eurocode 7: DA.1.1 (Design Approach 1 Combination 1, essentially a STR limit state approach), DA.1.2 (Design Approach 1 Combination 2, essentially a GEO limit state approach), DA.2 (Design Approach 2, an action and resistance factor approach), and DA.3 (Design Approach 3, an action and material factor approach); the design for DA.1 is governed by DA.1.2; partial factors from Annex A of EC 7-1. Figure 2 shows the characteristic values of soil properties X_k and the corresponding foundation width B for the critical Design Approach DA.3, where different trends for the estimated X_k are possible and dependent on the considered coefficients of variation (for example, between sets 4 to 5 and 7 to 8, c_k and φ_k are decreasing and γ_{1k} and γ_{2k} are increasing). The factors of safety Fs_m, Fs_k, and also the reliability index β are shown in Figures 3 and 4, for DA.1.1, DA.1.2, DA.2, and DA.3.

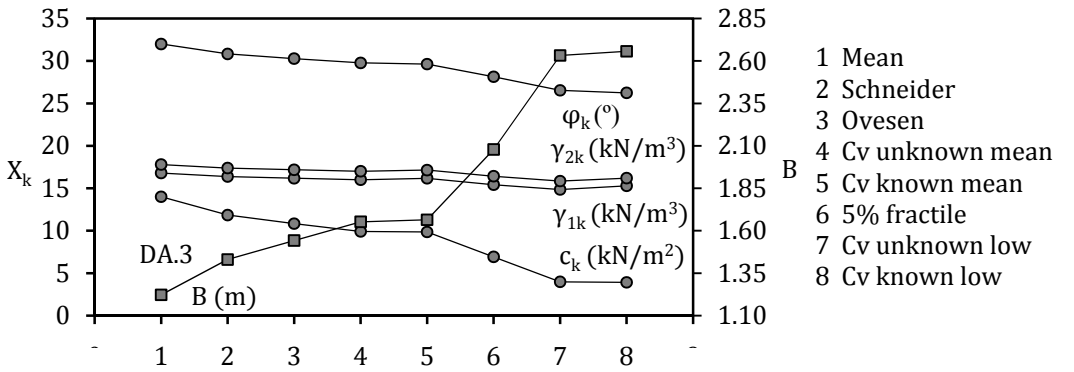

Figure 2.Characteristic values of soil properties X_k and the corresponding foundation width B for DA.3.

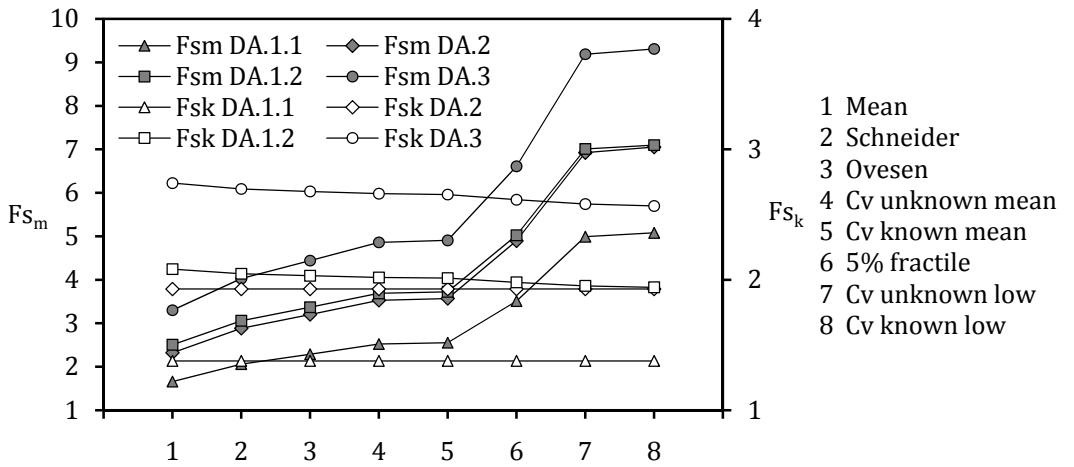

Figure 3.Factors of safety Fs_m and Fs_k for the Design Approaches DA.1.1, DA.1.2, DA.2, and DA.3.

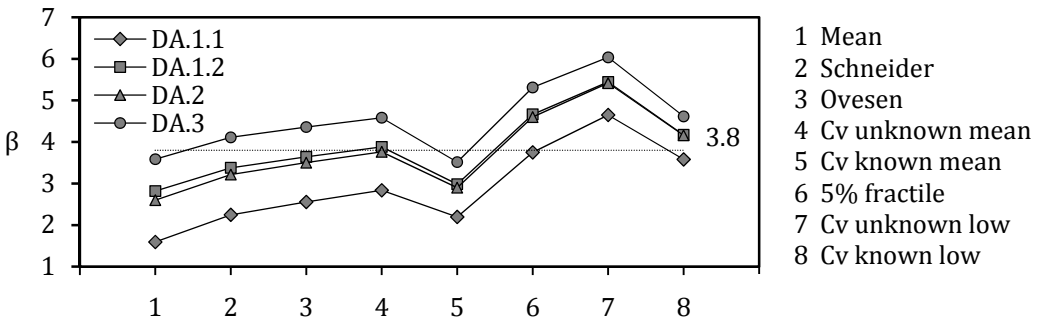

Figure 4.Reliability index β obtained by FORM (uncorrelated random variables) for the Design Approaches DA.1.1, DA.1.2, DA.2, and DA.3.

The reliability index β for different coefficients of variation of c and φ, considered the case Cv known mean, is shown in Figure 5, and the influence of correlation between c and φ is illustrated in Figure 6, considered the cases Schneider, Ovesen and Cv unknown mean. Finally, the reliability index β obtained by different methodologies, considered the case Schneider, is shown in Figure 7.

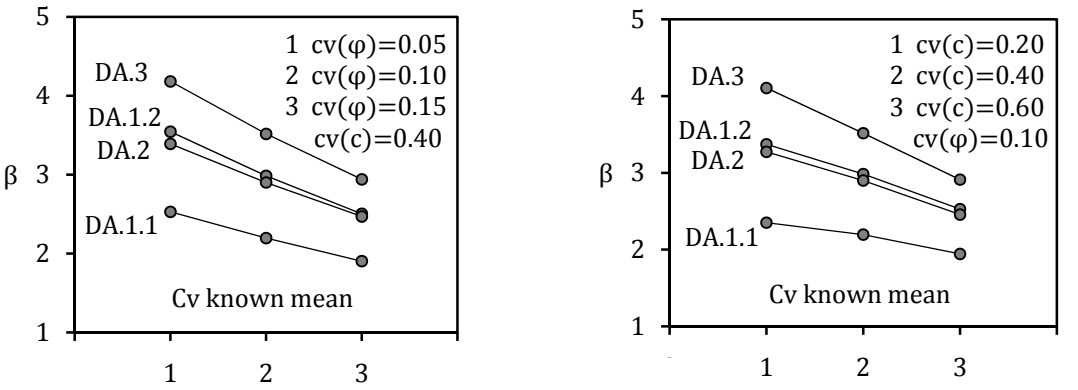

Figure 5.Reliability index β obtained by FORM (uncorrelated random variables) for different coefficients of variation of c and φ and for the Design Approaches DA.1.1, DA.1.2, DA.2, and DA.3.

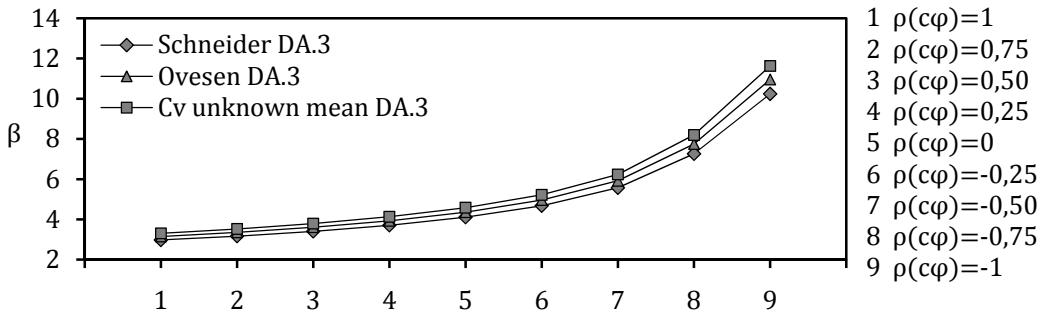

Figure 6.Reliability index β obtained by FORM for different coefficients of correlation between c and φ and for DA.3.

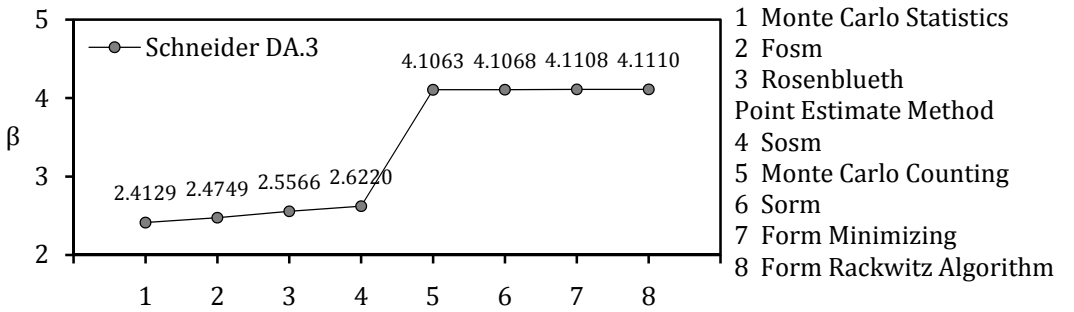

Figure 7.Reliability index β obtained by different methodologies (uncorrelated random variables) for DA.3 (MCS results from 50 simulation runs, each one with 1000000 simulation steps; MCS failure probability percentage error 6.3%).

CONCLUSIONS

Characteristic values are determined by experience and risk tolerance, and inadequate site investigation, one of the major causes of structural failure, leads to an ambiguous assessment. Depending on the considered case, the minimum foundation width B is variable from: 1.43 m to 2.66 m for the critical Design Approach DA.3;

1.15 m to 2.19 m for the Design Approach DA.1; and 1.10 m to 2.18 m for the Design Approach DA.2 (case Mean excluded). Therefore, significantly different characteristic values leads to considerable differences in geotechnical design, and beyond this condition, the selected design approaches and values of the partial factors specified by each Member State are variable. Direct comparison with traditional practice is only possible when the serviceability limit state has been checked, however it is verified that an acceptable overall factor of safety between 2 and 3, Fs_m or Fs_k, cannot ensure that Eurocodes' target ultimate limit state reliability index β, defined as 3.8 for a medium risk structure and fifty years reference period, is achieved: β is variable, sometimes lower or even much higher than 3.8, and influenced by the considered characteristic values and coefficients of variation of soil properties. Correlation between c and φ depends particularly on the material, and the influence of negative correlation is favorable and considerable when compared with the effects of positive correlation. MCS Statistics, FOSM, Rosenblueth Point Estimate Method and SOSM consider the reliability index β as a ratio of the mean and standard deviation of the performance function M, and FORM consider β as a distance between the point defined by the expected values of the random variables and the most probable failure point. These concepts may differ significantly when the performance function M is nonlinear and nonnormal, which is the case, explaining the important differences shown in Figure 7 between methodologies 1 to 4 and 7 to 8. Nonlinearity is more evident when comparing FOSM/SOSM than FORM/SORM. MCS Counting and FORM/SORM results are concordant.

Summarizing: it is demonstrated that risk and reliability are dependent on the considered analysis model, and that engineering judgment is required for the selection of reliable characteristic values. It may be worthwhile to discuss if one should insist on simplicity in the perspective that there are no simple methods of replacing reliability analysis for complex problems: in view of the complexities of describing geotechnical conditions characterized by an intrinsic fuzziness, it may be preferable to perform a complementary direct reliability-based design (RBD). In other words, reliability-based design (RBD) codes are increasingly becoming attractive in geotechnical practice, but judgment is still important.

REFERENCES

Fenton, G.A.; Griffiths, D.V. (2008). *Risk Assessment in Geotechnical Engineering.* John Wiley & Sons.

Frank, R.; Bauduin, C.; Driscoll, R.; Kavvadas, M.; Ovesen, N.K.; Orr, T.; Schuppener, B. (2004). *Designers' Guide to EN 1997-1 Eurocode 7: Geotechnical design-General rules.* Thomas Telford.

Haldar, A.; Mahadevan, S. (2000). *Probability, Reliability and Statistical Methods in Engineering Design.* John Wiley & Sons.

Lo, S.R. (2005). "Design with considerations of reliability and risk". 'Geotechnical Engineering for Disaster, Mitigation and Rehabilitation': *Proc. of the 1st International Conference*, Singapore, 115-130.

Schneider, H.R. (1999). "Definition and determination of characteristic soil properties". *Proc. of the 12th International Conference on Soil Mechanics and Geotechnical Engineering*, Hamburg, 4, 2271-2274.

Deterministic and probabilistic seismic analyses of a slope-footing system

Nancy Salloum[1], Dalia Youssef Abdel Massih[2], Abdul-Hamid Soubra[3], Jacques Harb[4]

[1]PhD student, Lebanese University, Hadath, Lebanon.
[2]Assistant professor, Department of Civil and Environmental Engineering, NotreDame University, Zouk Mosbeh Lebanon; email: dabdelmassih@ndu.edu.lb
[3]Professor, University of Nantes – France.
[4]Associate Professor, Department of Civil and Environmental Engineering, Notre Dame University, Zouk Mosbeh Lebanon.

ABSTRACT

This paper details deterministic and reliability-based analyses at the ultimate limit state of a slope-footing system. The seismic effect is simulated by a pseudo-static approach. The deterministic analysis aims at determining the safety factor Fs of the soil-footing system while the probabilistic one is devoted to the computation of the Hasofer-Lind reliability. The deterministic models used for both deterministic and probabilistic analyses are based on the upper-bound approach in limit analysis using three failure mechanisms. The deterministic results obtained from the limit analysis are validated by comparison with those obtained from numerical simulations based on the finite element software PLAXIS. Also, a parametric study is performed to analyze the effect of the different geometrical and mechanical parameters on both the safety factor and the reliability index.

INTRODUCTION

The geologic structure of slopes in the Lebanese environment is very heterogeneous. The fast urban expansion with the presence of hilly topography pushed the population to build on slopes, therefore enhancing the risk of human induced slope instability. On the other hand, Lebanon is known for being located on a seismic zone. These factors have initiated this research about the seismic deterministic and probabilistic analyses of foundations situated on slopes.

The bearing capacity of a shallow strip foundation located on a horizontal surface has been widely investigated using the limit analysis approach [Michalowski and Dawson (2002), Soubra (1999)]. On the other hand, the literature is scarce when the foundation is on slope and subjected to seismic or different loading conditions.The primary studies available related to the analysis of foundation on slope go back to Giroud and Tran-Vo-Nhiem (1971). Since then, a series of real scale experiments were conducted [e.g. Marechal et al. (1998)]. Recently, the work of Soubra et al. 2004

consisted of developing a model based on the upper boundary of the limit analysis of bearing capacity. Nevertheless, the work remained limited, since it only considered a very high slope where the failure surface can only pass above the toe. Besides, the seismic effect was not considered. On the other hand, the traditional analysis and sizing of geotechnical work are based on the deterministic approach. In this approach, the risks and uncertainties of the different parameters (soil properties, loading, etc.) are considered in a simplistic manner under the global safety factor. In order to account for the risks and uncertainties associated with the parameters used, the reliability theory is getting more and more momentum in geotechnical engineering. These approaches are getting to be very popular among researchers for the analysis of slope stability [i.e. Bhattacharaya et al. (2003), Griffiths and Fenton (2000),] for the slope stability analysis with seismic loading [Youssef Abdel Massih et al. (2010), Al-Homoud and Tahtamoni (2002)], for the behavior of shallow foundations (Soubra and Youssef Abdel Massih (2010), ,…. Nevertheless, almost none of the authors have applied these approaches on the seismic analysis of foundations located on slopes.

This paper aims at highlighting the seismic reliability of the behavior of foundations located on the near slopes, taking into account the uncertainties associated with the different parameters used. The seismic effect is modelled by a pseudo-static approach through the use of the horizontal seismic coefficient K_h given as a percentage of the gravity acceleration. Two deterministic models are proposed. The first one is based on the upper bound method of limit analysis. The second one used to validate the first model, is based on numerical simulations using the finite element software PLAXIS. The computation of the reliability will concern only the limit analysis model.

DETERMINISTIC MODELS

Limit analysis models – Failure mechanisms. The deterministic models used for the reliability analysis are based on the upper bound method of limit analysis using three failure mechanisms.

The first one (M1 Mechanism) is a translational mechanism that may pass by, below or above the toe of the slope (Figures 1a and b). This type of failure may occur when the footing is situated near the slope and thus, it has an influence on the slope instability. Soubra et al. (2004) proposed the translational mechanism (M1 Figure 1a) that may pass above the toe of the slope when the footing is situated near the slope. However, this mechanism didn't take into account the influence of the slope height when elaborated in 2004. Thus, the failure was not allowed to pass by or below the toe. In this paper, this mechanism is developed in order to account for the slope height, and is allowed to pass by or below the slope toe by adding the new failure block $A_1A_2A_3$ as shown in figure 1b.

The second failure mechanism is also a translational one developed by Soubra (1999) for the case of a foundation situated on a horizontal soil. The type of failure for this mechanism is symetrical for the case of a vertical central load (Figure 2a, M2 mechanism) and non-symetrical for the case of an inclined or seismic load (Figure 2b, M3 Mechanism). This failure may occur when the footing is far from the slope and the soil punching under the footing is more critical than the slope instability.

The third failure mechanism involves a rotational failure bounded by a log-spiral slip surface passing by or below the toe (Figure 3, M4 mechanism). This mechanism may occur when both conditions are satisfied: (i) the footing is placed far from the slope, and (ii) the slope instability is the predominant mode of failure compared to the footing punching.

In this paper, the minimal safety factor Fs and the minimal reliability index deduced from all these types of failure is considered. The safety factors of each mechanism are obtained using the shear strength reduction method by dividing c and tanφ by F_s in the energy equation of the upper bound limit analysis method. For given slope and foundation geometries, soil characteristics and a presccribed applied seismic or non seismic load, the safety factors obtained from all these mechanisms are compared together and the smallest (i.e. most critical one) is adopted.

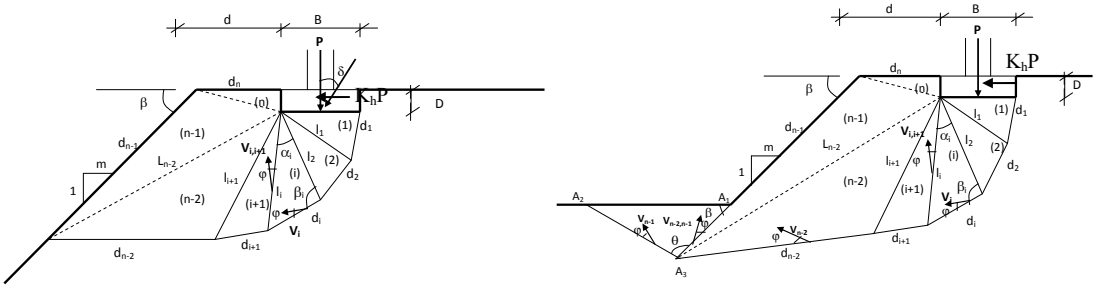

Figure 1. M1 Mechanism passing a) above the toe b) below the toe of the slope

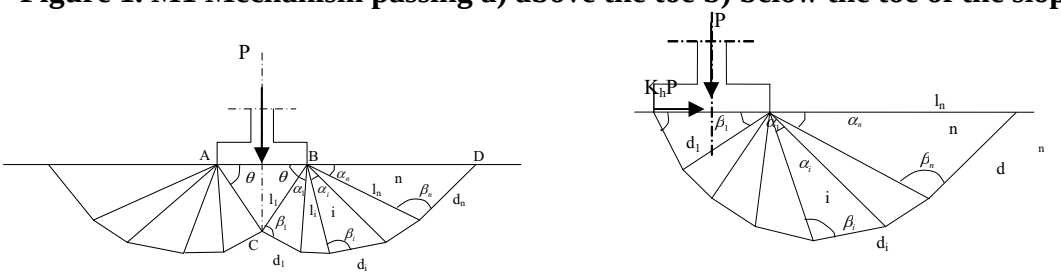

Figure 2. a) Translational symetrical failure mechanism (M2); b)Translational non-symetrical failure mechanism (M3)

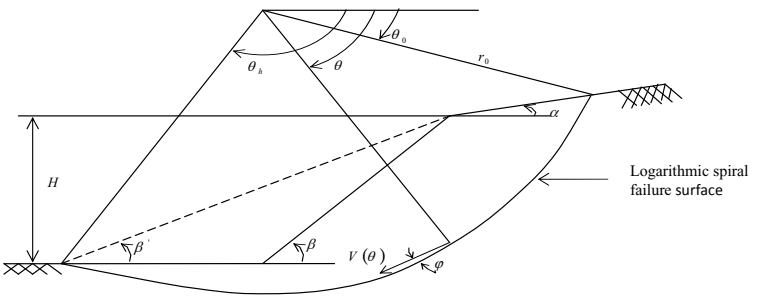

Figure 3. Logarithmic spiral failure mechanism (M4) for the case of a simple slope

Finite element model. In order to validate the limit analysis models (LA), the deterministic results obtained using the failure mechanisms presented above are compared to finite element numerical simulations performed using Plaxis software. The mesh used in the finite element model is optimized. The footing is modeled by an elastic rigid plate element and the soil by a Mohr Coulomb model for which the

dilation angle is chosen equal to the soil friction angle in order to allow a reasonable comparison between the two models (LA and Plaxis). The shear strength reduction technique is used for the calculation of the safety factor.

PROBABILISTIC MODELS

Reliability index, performance function and random variables. The widely used reliability index is the one defined by Hasofer and Lind (1974). Its matrix formulation is given by:

$$\beta_{HL} = \min_{x \in F} \sqrt{(x-\mu)^T C^{-1} (x-\mu)} \quad (1)$$

in which x is the vector representing the n random variables, μ is the vector of their mean values, C is their covariance matrix and F is the failure region. The minimization of equation (1) is subjected to the constraint $G(x) \leq 0$ where the limit state surface $G(x) = 0$ separates the n-dimensional domain of random variables into two regions: A failure region F represented by $G(x) \leq 0$ and a safe region given by $G(x) > 0$ wher $G(x)$ denotes the performance function.

The performance function G of the reliability-based approach makes use of the safety factor Fs defined with respect to the soil shear strength parameters c and tan(φ) as follows:

$$G = F_s - 1 \quad (2)$$

F_s is equal to the ratio between the maximal shear stress and the mobilized one.

The random variables used in the analysis are: the cohesion c, the angle of internal friction φ, the vertical applied load P_s and the seismic coeffcient K_h. The cohesion, the friction angle, and the vertical applied load are modeled by the the use of a Lognormal distribution where the seismic coefficient is considered to follow an Extreme Value Distribution (Youssef Abdel Massih et al. 2008).

RESULTS

Deterministic results. *Without seismic loading K_h=0*. In order to validate the results of the limit analysis failure mechanism models, the static safety factors obtained by these models and those determined by Plaxis simulations are plotted as a function of d/B for different values of H/B in figure 4, where d is the distance from the footing edge to the slope, H is the height of the slope and B is the width of the footing. The soil properties considered in the analysis are as follows: cohesion c=20kPa, friction angle $\varphi=30^o$, B=2m and the unit weight $\gamma=18kN/m^3$. From figure 4, one can notice a good agreement between the two results. It is found that the safety factor tends to a constant value when d/B>4. For H/B=2, 3 and 4, this value is equal to the safety factor obtained by the M4 logspiral failure mechanism of the simple slope. This case corresponds to the situation where the footing is far enough from the slope and when the safety factor of the slope is more critical than that obtained from the M2 mechanism (case of a foundation resting on a horizontal soil). However, for a small value of the slope height when H/B=1, the asymptotic value of the safety factor is

obtained using the M2 mechanism. For this case, since the slope height is small and d/B is high, the mechanism M2 is more critical than M4. For d/B<4, the M1 mechanism is found to be the most critical one and is used for the safety factor calculation.

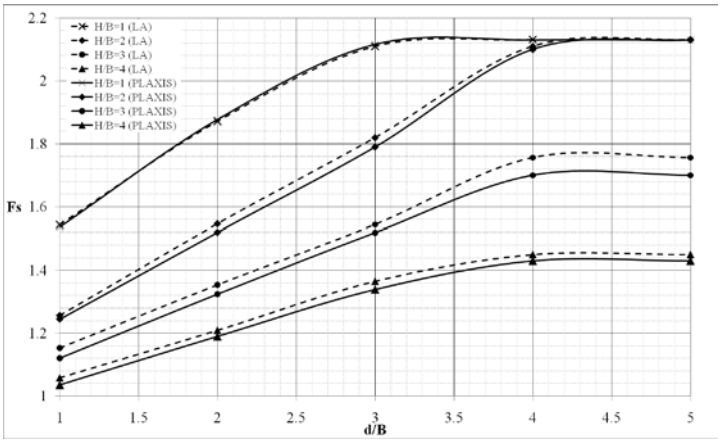

Figure 4. Variation of Fs with d/B and H/B for the limit analysis models and Plaxis simulations for K_h=0

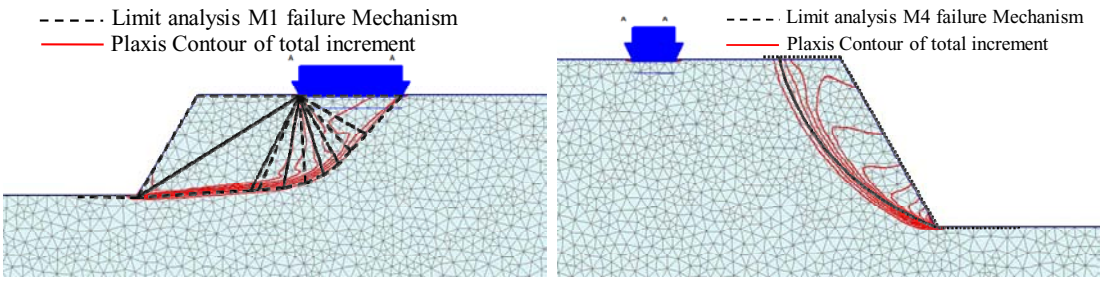

Figure 5. Failure surfaces obtained from the limit analysis and PLAXIS models

A comparison between the failure surface obtained from the limit analysis mechanisms and Plaxis contour of total incremental displacement is presented in figure 5a and b for two cases: (i) when the M1 mechanism is found to be the critical one for H/B=1 and d/B=1, (ii) when the M4 mechanism is critical for H/B=4 and d/B=4. Good agreement between the two models is obtained.

With seismic loading. Figure 6 presents a comparison between the pseudostatic safety factors K_h obtained from the Limit analysis models and Plaxis numerical simulations. It is noticed that the LA safety factors are slightly higher than those obtained by Plaxis model. The maximum percent difference is equal to 3%.

Probabilistic results. For the probabilistic results, concerning the statistical parameters of the random variables, a reference case was chosen as follows: for the mean values $\mu_c = 20$ kPa, $\mu_\varphi = 30^\circ$, $\mu_{K_h} = 0.15$, $\mu_{P_S} = 300$ kN, and for the coefficients of variation $COV_c = 40\%$, $COV_\varphi = 10\%$, $COV_{K_h} = 40\%$, $COV_{P_S} = 40\%$ (Youssef Abdel Massih et al. 20008). The critical reliability (i.e. the

smallest one) obtained among the 3 cases of failures described above is considered as the reliability index of the slope-footing system.

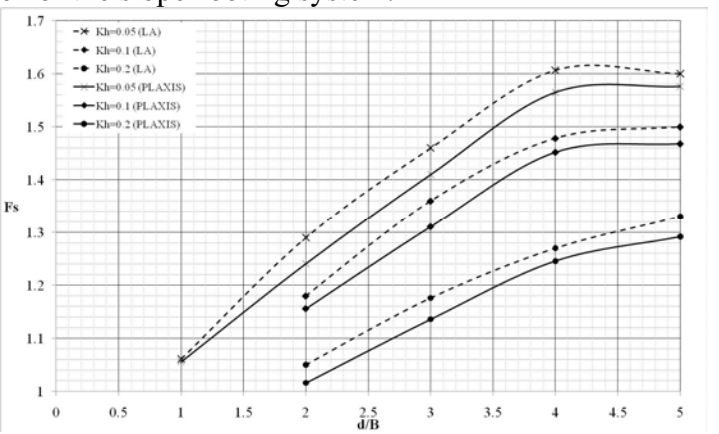

Figure 6. Variation of Fs with d/B and H/B for the limit analysis models and Plaxis simulations with seismic loading

Effect of d/B and H/B on the reliability index. Figure 7 presents the reliability index as a function of d/B and H/B when no seismic loading exists. It is found that when d/B increases for a small H/B (H/B=1), the critical reliability index is obtained using the M2 mechanism for the case of a foundation resting on a horizontal soil. However, for higher values of H/B, when d/B increases (higher than 4 for the case of H/B=3), β_{HL} tends to the value obtained from the M4 mechanism of a simple slope. This limit value of d/B=4 is the same value obtained from the deterministic results.

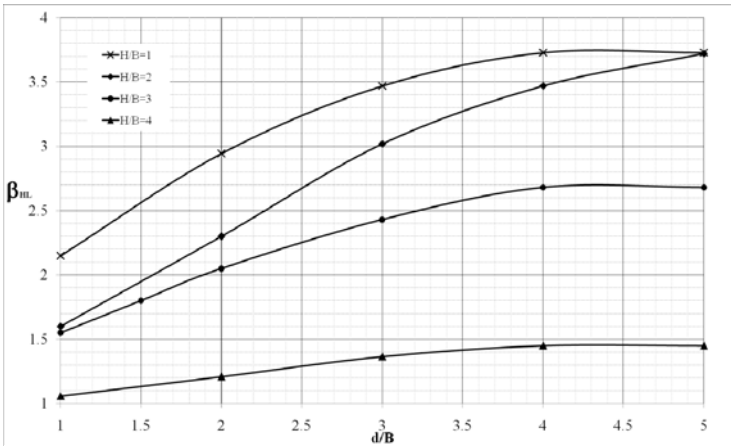

Figure 7. Variation of β_{HL} with d/B and H/B without seismic loading

Effect of K_h and Ps on the reliability index. Figure 8 presents the reliability index as a function of K_h for different values of Ps when d/B=1 and H/B=3. When K_h increases and Ps decreases, the critical failure tends to be produced in the slope only (i.e. M4 mechanism). This is presented by the 2 upper curves in the figure where we can notice that the reliability index calculated using M4 mechanism is smaller i.e. more critical than the one obtained by the M1 mechanism. The results of the two mechanisms are close to each others when K_h is small. For higher Ps values, the M1 mechanism was found the most critical one.

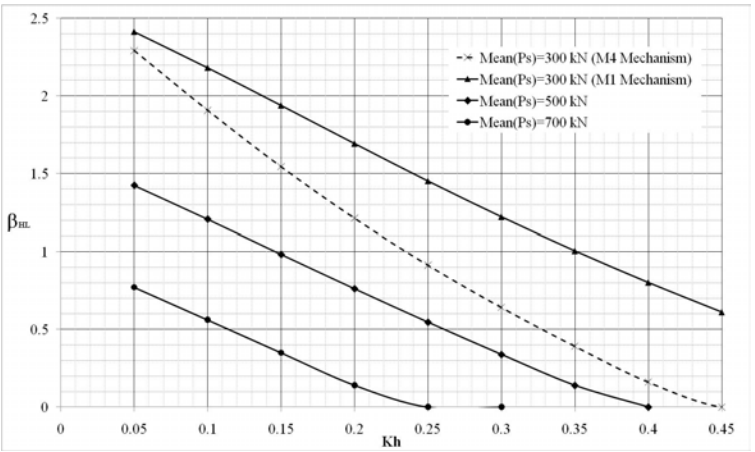

FIG. 8. Variation of β_{HL} with K_h and P_s

Effect of the random variable uncertainties on the reliability index. Figure 9 shows the effect of the coefficient of variation of each random variable on the reliability of the slope-footing system for d/B=1 and H/B=3. Each curve corresponds to a variation of COV from 5% till 60% for a given random variable. The results of the M1 and M4 mechanism are presented. The results of the M2 mechanism are found too high compared the M1 and M4 (i.e. less critical) and are not presented in this figure. From figure 9, one can notice that for the given soil and load variability, the reliability index obtained from the M1 mechanism is more critical than the one obtained from the M4 mechanism. However, the results of the M1 mechanism are kept on the graph in order to understand the effect of the variability of each parameter on the reliability index obtained by mechanism M1.

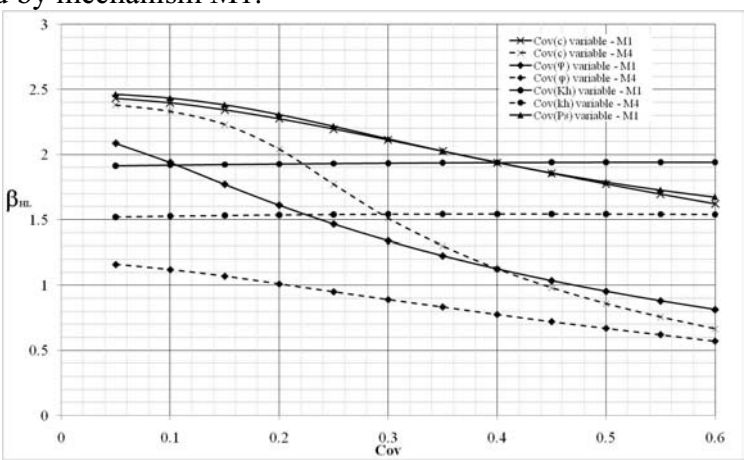

Figure 9. Variation of β_{HL} with the coeffcient of variation

For mechanism M1, the variation of c, φ, and P_s affect highly the reliability index and have approximately the same degree of influence on the slope-footing system reliability. However, the variation of K_h slightly affect the reliability of the system obtained either using the M1 or the M4 mechanism. For mechanism M4, the effect of the variation of c is very important in the determination of the reliability index (Youssef Abdel Massih et al. 2007). The effect of φ is smaller but also not negligible.

CONCLUSION

A seismic deterministic and probabilistic analysis of a footing resting at the top of a sloep is analyzed using limit analysis models and finite element numerical simulations. The major conclusion of the paper can be summarized as follows: In the deterministic analysis, good agreement is found between the limit analysis and Plaxis results with or without seismic loading. Also, for a given case, when the slope height H is small and d/B increases to reach a limit value, the failure tends to be developped under the footing only without passing by the slope. However, when H is high and d/B increases, the most critical failure was found to be the one passing by the slope only. In the reliability analysis, the same limit for d/B obtained using the deterministic analysis is obtained. The variation of c, φ, and P_s affect highly the reliability index and have approximately the same degree of influence on the slope-footing system reliability obtained by the M1 mechanism.

REFERENCES

Bhattacharya, G., Jana, D., Ojha, S., and Chakraborty, S. (2003). "Direct search for minimum reliability index of earth slopes." *Comp. and Geotech.*, 30, 455-462.

Giroud, J.-P. and Tran-Vo-Nhiem (1971). "Force portante d'une fondation sur une pente", Annales de l'ITBTP, Théorie et Méthodes de calcul, Vol. 142, 132-179.

Griffiths, D.V., and Fenton, G.A. (2000). "Influence of soil strength spatial variability on the stability of an undrained clay slope by finite elements." *In D. V. Griffiths et al*, *editor*, *Slope Stability 2000*, ASCE Geotechnical Special Publications, N° 101, pp. 194-208.

Maréchal, O., Garnier, J., Canepa, Y., and Morbois, A. (1998) « Bearing capacity of shallow foundations near slopes under complex loads». *Centrifuge 98*, Tokyo, vol.1, 459-464.

Mikalowski, R.L. and Dawson, E.M. (2002). "Three-dimensional analysis of limit loads on Mohr-Coulomb soil", *Foundations of Civil and Environemental Engineering*, 1(1), 137-147.

Soubra, A.-H. (1999). "Upper-bound solutions for bearing capacity of foundations." *J. of Geotech. and Geoenv. Eng., ASCE*, 125(1), 59-68.

Soubra, A.-H., and Youssef Abdel Massih, D. (2010). "Probabilistic analysis and design at the ultimate limit state of obliquely loaded strip footings." *Geotechnique, ICE*, 60(4), pp. 275–285.

Soubra, A.-H., Garnier, J., Thorel, L., Chambon, P., El Hachem, E., Cortas, J., Oueidat, H., and Chehade, R. (2004). "Portance des fondations superficielles établies à proximité d'une pente: Etude théorique et expérimentale". *Congrès Int. de Géotechnique*, Beyrouth, 19-22 May 2004.

Youssef Abdel Massih, D., Soubra A.-H. and Low, B.K. (2008). "Reliability-based analysis and design of strip foundations against bearing capacity failure." *Journal of Geotechnical and Geoenvironmental engineering, ASCE*, 134(7), 917-928.

Youssef Abdel Massih, D., Soubra, A.H., Harb J. and Rouainia, M. (2010). "Dynamic slope stability analysis by a reliability-based approach." Fifth *International Conference on Recent Advances on Geotechnical Earthquake Engineering and Soil Dynamics*, San Diego, California, May 24-29 2010,10p.

A Comparative Study of Drilled Shaft Design Using LRFD and Expanded RBD

Yu Wang[1], M.ASCE, Zijun Cao[2], and Fred H. Kulhawy[3], Dist.M.ASCE

[1]Department of Building and Construction, City University of Hong Kong, Hong Kong; PH (852) 3442-7605; FAX (852) 3442-0427; email: yuwang@cityu.edu.hk
[2]Department of Building and Construction, City University of Hong Kong, Hong Kong; PH (852) 3442-6492; email: zijuncao3@student.cityu.edu.hk
[3]School of Civil and Environmental Engineering, Cornell University, Hollister Hall, Ithaca, NY 14853-3501; PH (607) 255-4820; email: fhk1@cornell.edu

ABSTRACT

A comparative study of drilled shaft design is presented using a Load and Resistance Factor Design (LRFD) method and an expanded reliability-based design (RBD^E) method recently developed by the authors. A design example that has been used in the literature to illustrate LRFD is re-analyzed using Monte Carlo Simulation (MCS) and is re-designed using RBD^E. The MCS results show that the feasible design obtained from LRFD might have a failure probability different from the target failure probability (p_T) adopted in the LRFD calibration. The RBD^E method gives a design that corresponds to the p_T or a design that is consistent with the LRFD feasible design at its real level of failure probability. RBD^E allows design engineers to adjust p_T without additional calculations, and they have the flexibility to make assumptions and/or simplifications deemed appropriate. Such flexibility is illustrated by exploring the effect of the dead to live load ratio on design.

INTRODUCTION

Reliability-based design (RBD) of foundations has attracted increasing interest over the last two decades, and several RBD methodologies have emerged, such as the LRFD for highway structure foundations (Barker et al. 1991, Paikowsky et al. 2004) and the LRFD and Multiple Resistance Factor Design (MRFD) for transmission line structure foundations (Phoon et al. 1995). The LRFD uses reliability theory to deal rationally with uncertainties that arise in loads, geologic site interpretations, geotechnical properties, calculation models, construction effects, etc. Through some reliability calibration process, LRFD codes provide tabulated load and/or resistance factors that have been calibrated to some target failure probability (p_T) or target reliability index (β_T). Design engineers select appropriate load and/or resistance factors from the table and carry out design calculations using a trial-and-error approach. Because the load and/or resistance factors in LRFD codes often are calibrated for some pre-defined value of p_T only, load and/or resistance factors for other p_T values commonly are not available. This fact limits a designer's flexibility to adjust the p_T to accommodate specific needs of a particular project. In addition, many assumptions and/or simplifications (e.g., probability distributions of loads and

geotechnical properties) adopted in the calibration processes usually are "invisible" to the designer, which leads to potential misuse of the load and/or resistance factors.

To address these limitations, Wang et al. (2011) recently proposed an expanded reliability-based design (RBD^E) method that formulates the foundation design as an expanded reliability problem. In this paper, a comparative study of drilled shaft design using LRFD and RBD^E is described. Following a brief introduction of LRFD and RBD^E, a drilled shaft design example is described that has been used to illustrate LRFD for highway structure foundations (Paikowsky et al. 2004). The failure probability of the feasible design obtained from LRFD then is re-evaluated by MCS and is re-designed using RBD^E to illustrate its flexibility. The effect of the dead to live load ratio on designs also is explored using RBD^E.

LOAD AND RESISTANCE FACTOR DESIGN (LRFD)

Conceptually, the general process of LRFD contains five basic steps: (1) establish the probabilistic distribution of the load (Q), including both dead and live load, (2) establish the probabilistic distribution of capacity (R), (3) select the nominal values of R and Q (i.e., R_n, Q_D, and Q_L for capacity, dead load, and live load, respectively) and establish the LRFD design equation below:

$$\eta_D Q_D + \eta_L Q_L = \psi R_n \tag{1}$$

in which η_D and η_L = dead and live load factors that are both larger than one, and ψ = resistance factor that is smaller than one, (4) select a target reliability index (β_T) or target probability of failure (p_T) that would establish the design risk, and (5) perform calibration analyses that incorporate steps 1-4 to determine values of η_D, η_L, and ψ that achieve a consistent design risk (i.e., β_T or p_T) across the range of the input parameters and their variability.

EXPANDED RELIABILITY-BASED DESIGN (RBD^E) APPROACH

An expanded reliability problem herein refers to a reliability analysis of a system in which a set of system design parameters are artificially considered as uncertain with probability distributions specified by the user for design exploration purposes (Wang et al. 2011, Wang 2011). In the context of RBD^E, the diameter (B) and depth (D) of the drilled shaft are considered as independent discrete random variables with uniformly distributed probability mass function p(B,D). The drilled shaft design process is re-formulated as a process of finding failure probabilities corresponding to designs with various combinations of B and D [i.e., conditional probability p(F|B,D)] and comparing them with p_T. Failure refers to events in which the load exceeds capacity (i.e., Q > R). Feasible designs are those with $p(F|B,D) \leq p_T$. Using Bayes' Theorem (e.g., Ang and Tang 2007), the conditional probability p(F|B,D) is given by:

$$p(F|B,D) = \frac{p(B,D|F)}{p(B,D)} p(F) \tag{2}$$

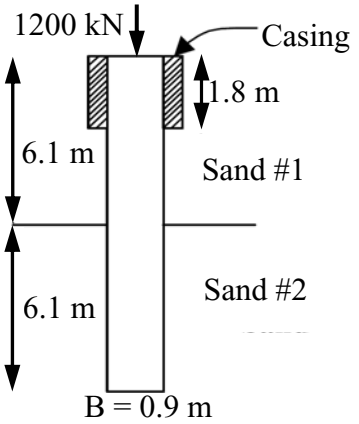

Figure 1. Drilled shaft design example (After Paikowsky et al. 2004).

Table 1. Summary of soil properties at different depths (After Paikowsky et al. 2004).

Depth (m)	Uncorrected SPT N Values	Unit Weight (kN/m^3)
0	0	16.0
3.0	10	16.0
6.1	10	16.0
7.6	15	16.0
≥18.3	15	16.0

in which p(B,D|F) = conditional joint probability of B and D given failure. Using a single run of MCS, p(F) and p(B,D|F) can be estimated. Details of the RBD^E and MCS are given by Wang et al. (2011).

RBD^E can result in a large number of feasible designs. The requirement of the economic optimization limit state (EOLS) then is adopted to finalize the design as the one with the minimum construction cost (Wang and Kulhawy 2008, Wang 2009). The construction cost of drilled shafts is estimated using published, annually-updated, unit cost data, such as Means Building Construction Cost Data (Means 2007). The construction costs for all feasible designs are calculated as the product of their unit costs and shaft depths, and the final design is determined accordingly by comparing their construction costs.

DRILLED SHAFT DESIGN EXAMPLE

Paikowsky et al. (2004) illustrated LRFD for highway structure foundations using the drilled shaft design example shown in Figure 1. The shaft is installed in sand with a total unit weight of 16.0 kN/m^3. The uncorrected SPT N values at different depths vary from 0 to 15, as shown in Table 1. Using LRFD, Paikowsky et al. (2004) showed that, under non-redundant conditions (i.e., four or less piles under one pile cap) with $p_T = 0.001$ or $\beta_T = 3.0$, a trial design with B = 0.9 m and D = 12.2 m has a factored capacity of 1270 kN. This trial design is feasible to support a factored axial compression load of 1200 kN (including factored dead load and factored live load). Using Eq.(1), the factored load (i.e., 1200 kN) is equivalent to a nominal dead load (i.e., Q_D) of 564 kN plus a nominal live load (i.e., Q_L) of 282 kN given η_D=1.25, η_L=1.75, and a ratio of dead to live load (i.e., $r = Q_D/ Q_L$) = 2 (Paikowsky et al. 2004).

RE-EVALUATION OF THE LRFD FEASIBLE DESIGN USING MCS

The failure probability of the feasible design obtained from LRFD described above now is re-evaluated using MCS. In MCS, the deterministic axial capacity of

the drilled shaft is calculated using the FHWA method (Reese and O'Neill 1988), as done by Paikowsky et al. (2004). The uncertainty modeling and the MCS results are described below.

Uncertainty Modeling. To enable a consistent comparison with the design by Paikowsky et al. (2004), the uncertainty modeling follows that adopted in their study. The uncertain variables include the dead load, live load, and resistance bias factor (λ_R). The dead and live loads are considered as lognormal random variables with coefficients of variation (i.e., COV_D and COV_L) = 0.1 and 0.2, respectively. The mean values (i.e., $\overline{Q}_D$ and $\overline{Q}_L$) of dead load and live load are calculated as

$$\overline{Q}_D = \lambda_D Q_D \quad \text{and} \quad \overline{Q}_L = \lambda_L Q_L \tag{3}$$

in which λ_D and λ_L = bias factors for dead load and live load, respectively. Using Q_D = 564 kN, Q_L = 282 kN, λ_D = 1.05, and λ_L = 1.15 (Paikowsky et al. 2004), $\overline{Q}_D$ and $\overline{Q}_L$ are estimated as 592 kN and 324 kN, respectively. In addition, λ_R is modeled as a lognormal random variable with a log-mean of 0.326 and a log-standard-deviation of 0.738 (Paikowsky et al. 2004).

Monte Carlo Simulation (MCS) and Results. MCS is performed using the software package Matlab (Mathworks 2007), which is equipped with random number generators for various probability distributions, such as "lognrnd" for lognormal variables and "rand" for uniform variables. Random samples of lognormally distributed dead load, live load, and resistance bias factor are generated by "lognrnd" with their respective means and standard deviations. Given B = 0.9 m and D = 12.2 m, the deterministic capacity of the drilled shaft is calculated using the FHWA method. Then, the deterministic capacity is corrected by the resistance bias factor (λ_R) that is generated from the random number generator. For each set of random samples, the drilled shaft is considered as "failed" when the sum of the dead and live loads exceeds the corrected capacity. A run of MCS with a sample size of 1,000,000 is performed, and the failure probability p(F) of the LRFD feasible design is estimated as 0.017.

Although the target failure probability is 0.001 (i.e., p_T = 0.001) in the LRFD example, the MCS results show that the feasible design from this LRFD method, in fact, has a failure probability = 0.017. Therefore, the real failure probability of the design drilled shaft is different from its intended p_T, which implies that using LRFD does not necessarily guarantee that the p_T actually is achieved in the design. It is also interesting to note that, although the failure probability from MCS seems quite different from the target failure probability (i.e., 0.017 versus 0.001), it does fall between the typical range (i.e., 0.001 to 0.08) of failure probability for a single pile reported in the literature (Tang et al. 1990, Barker et al. 1991, Zhang et al. 2001).

RBD^E DESIGN

This drilled shaft design example now can be re-designed using the RBD^E

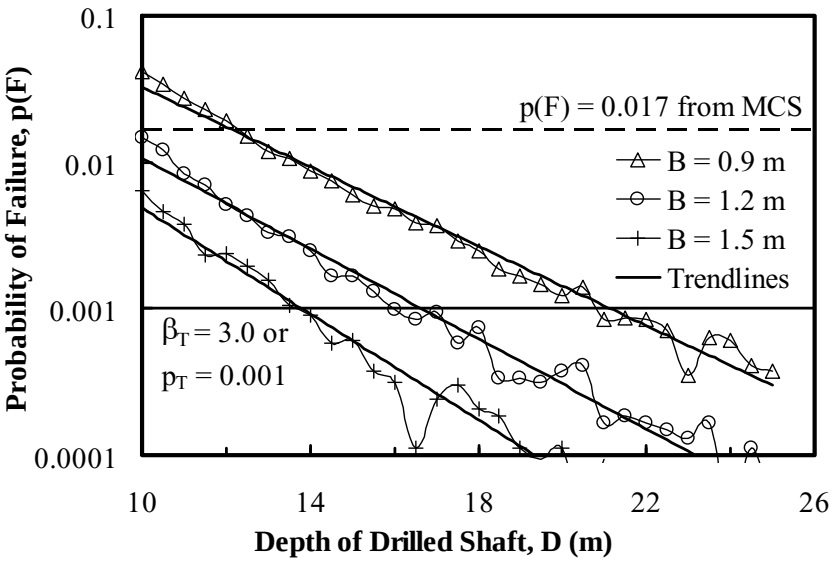

Figure 2. Conditional probability of failure from Monte Carlo Simulation.

approach (Wang et al. 2011). In addition to the uncertainties in dead load, live load, and resistance bias factor described above, the shaft design parameters B and D are treated as independent discrete uniform random variables. Three possible B values of 0.9 m, 1.2 m, and 1.5 m are considered in the design, and the possible D values vary from 10 m to 25 m with an increment of 0.5 m. Random samples of uniformly distributed B and D are generated by the Matlab functions "rand". A single run of MCS with a sample size of 5,000,000 is performed for RBD^E, and the p(B,D|F), p(F), and conditional failure probability p(F|B,D) are estimated from MCS using Eq (2) accordingly.

Figure 2 shows the conditional failure probability p(F|B,D) obtained from a single run of MCS. Note that p(F|B,D) is a variation of failure probability as a function of (B,D). For a given value of B, p(F) decreases as D increases. Similarly, for a given value of D, p(F) decreases as B increases. Figure 2 also includes the p_T = 0.001 adopted in the LRFD calibration, and feasible designs are those that fall below the p_T, as shown in the figure. In this example, the feasible designs include the drilled shafts with B = 0.9 m and D ≥ 21.0 m, B = 1.2 m and D ≥ 16.0 m, or B = 1.5 m and D ≥ 14.0 m.

The economic requirement then is adopted to determine the final design (Wang and Kulhawy 2008, Wang 2009). Since the construction cost is the product of shaft depths and unit costs, the economic design for a given value of B is the one with minimum D value. Therefore, among the pool of feasible designs obtained from RBD^E, calculations of construction costs are required only for three cases (i.e., drilled shafts with B = 0.9 m and D = 21.0 m, B = 1.2 m and D = 16.0 m, or B = 1.5 m and D = 14.0 m). The U. S. national average unit costs for constructing a unit depth (i.e., 0.3 m) of drilled shafts with diameters of 0.9 m, 1.2 m, and 1.5 m are USD 77.5, 116, and 157 (Means 2007), respectively (USD = U. S. Dollars). Using these unit costs, construction costs of the three cases are estimated as USD 5425, 6187, and 7327, respectively. Therefore, the final design is a drilled shaft with B = 0.9 m and D = 21.0

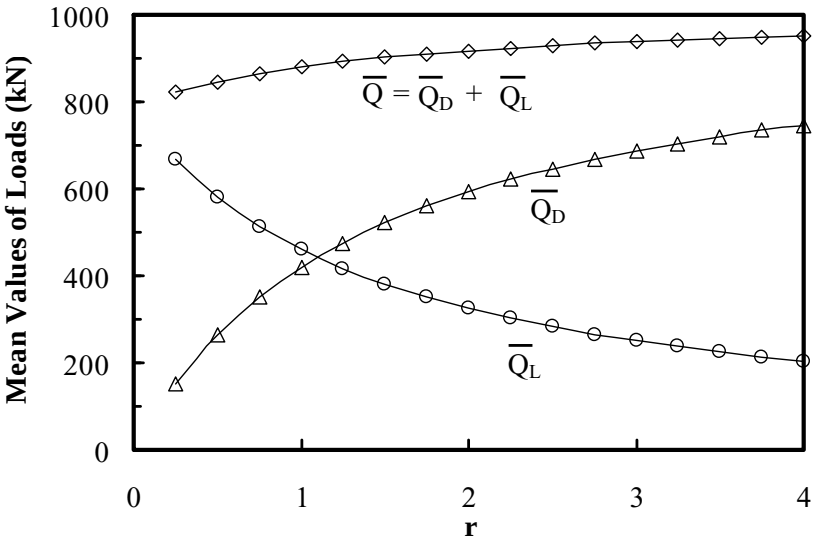

Figure 3. Mean values of loads for different values of r.

m, which has a construction cost of USD5425.

RESULT COMPARISONS

For $p_T = 0.001$ (i.e., $\beta_T = 3.0$), the final design (B = 0.9 m and D = 21.0 m) obtained from RBD^E is different from the LRFD feasible design (B = 0.9 m and D = 12.2 m). The difference can be attributed to the different values of failure probability for these two designs. Note that the MCS in the previous section showed that the feasible design from LRFD has a real p(F) value = 0.017, as opposed to $p_T = 0.001$ for the design from RBD^E. As the failure probability decreases from 0.017 to 0.001, it is not surprising to see that D increases from 12.2 m to 21.0 m. A target failure probability of 0.017 also is included in Figure 2 for reference, and the feasible design obtained from RBD^E is the drilled shaft with B = 0.9 m and D ≥ 12.5 m. The final design for $p_T = 0.017$ is, therefore, the drilled shaft with B = 0.9 m and D = 12.5 m, which agrees well with the feasible design from LRFD. In addition, it is worth noting that, in RBD^E, feasible designs for different p_T values (e.g., 0.017 and 0.001) are inferred directly from Figure 2 without additional calculations, which allows designers to adjust the design p_T to accommodate the needs of a particular project.

EFFECT OF DEAD TO LIVE LOAD RATIO

The RBD^E approach allows designers to make assumptions and/or simplifications deemed appropriate in designs. This section illustrates this flexibility by using different values of dead to live load ratio (r) in the design and exploring its effect. Given the same factored load of 1200 kN and different r values, using Eqs.(1) and (3) results in different mean values of dead load and live load, as shown in Figure 3. As r increases from 0.25 to 4, the mean value of dead load ($\overline{Q}_D$) increases from about 150 kN to about 750 kN, while the mean value of live load ($\overline{Q}_L$) decreases from about 670 kN to about 200 kN.

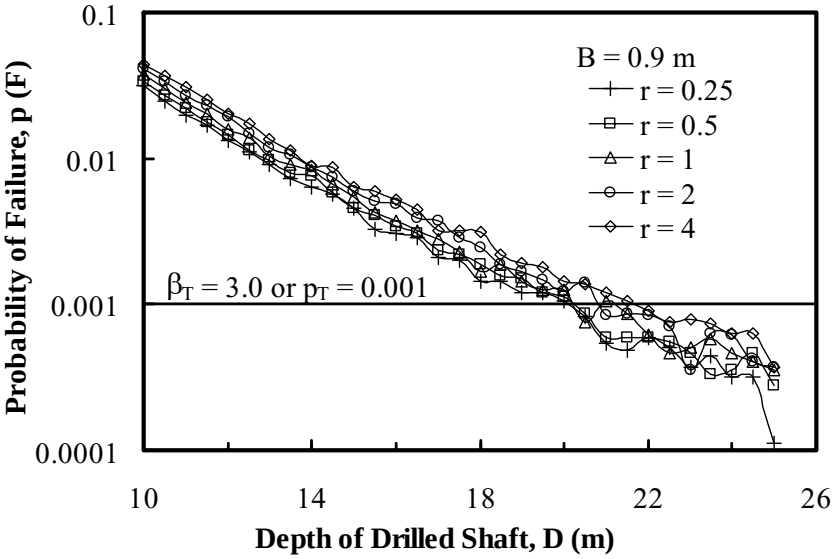

Figure 4. Effect of dead to live load ratio r.

RBD^E designs were carried out for r = 0.25, 0.5, 1, 2, and 4, respectively, and the results are shown in Figure 4. The feasible designs change from D ≥ 20.5 m to D ≥ 22.0 m as r increases from 0.25 to 4. The p(F) versus D relationships in the figure are five approximately parallel lines. As r increases from 0.25 to 4, the p(F) versus D relationship gradually moves upward, indicating an increase of p(F). In other words, as r increases, p(F) increases. This result might be attributed to the increase of equivalent load as r increases. As shown in Figure 3, the mean value of the total load $\overline{Q}$ that approximates the sum of $\overline{Q}_D$ and $\overline{Q}_L$ increases from 820 kN to 950 kN as r increases from 0.25 to 4. On the other hand, the COV of total load remains more or less unchanged because it approximates $\sqrt{COV_D^2 + COV_L^2}$ (Phoon 2008) and has a constant value of $\sqrt{0.1^2 + 0.2^2}$ for different r values. This result leads to an increase of equivalent load, and therefore an increase of design shaft depth as r increases (see Figure 4).

SUMMARY AND CONCLUSIONS

A comparative study was presented for drilled shaft design using LRFD and RBD^E. An example that was used to illustrate LRFD in the literature was re-analyzed using MCS and was re-designed using RBD^E. The MCS results show that the feasible design obtained from LRFD might have a failure probability very different from the target failure probability (p_T) adopted in the LRFD calibration. On the other hand, the RBD^E method gives a design that corresponds to the p_T or design that is consistent with the LRFD feasible design at its real level of failure probability. In RBD^E, feasible designs for different p_T values are inferred directly without additional calculations. This process allows designers to adjust the design p_T easily to accommodate the needs of a particular project. In addition, the RBD^E approach gives designers the flexibility to make assumptions and/or simplifications deemed

appropriate in designs. This flexibility was illustrated further by using different values of dead to live load ratio (r) in the design and exploring its effect. It was found that, as r increases, the failure probability increases, and therefore the design shaft depth increases.

ACKNOWLEDGMENTS

The work described herein was supported by a grant from the Research Grants Council of the Hong Kong Special Administrative Region, China [Project No. 9041260 (CityU 121307)] and a grant from City University of Hong Kong (Project No. 7002568). The financial supports are gratefully acknowledged.

REFERENCES

Barker, R. M., Duncan, J. M., Rojiani, K. B., Ooi, P. S. K., Tan, C. K., and Kim, S. G. (1991). "Manuals for the design of bridge foundations." *NCHRP Report 343,* Transportation Research Board, Washington, DC.

Mathworks, Inc. (2007). MATLAB – the language of technical computing, <*http://www.mathworks.com/products/matlab/*> (March 9, 2007).

Means (2007). 2008 *RS Means Building Construction Cost Data*. R.S. Means Co., Kingston, MA.

Paikowsky, S. G., Birgisson, B., McVay, M., Nguyen, T., Kuo, C., Baecher, G., Ayyub, B., Stenersen, K., O'Malley, K., Chernauskas, L., and O'Neill, M. (2004). "Load and resistance factor design (LRFD) for deep foundations." *NCHRP Report 507,* Transportation Research Board, Washington, DC.

Phoon, K. K., Kulhawy, F. H. and Grigoriu, M. D. (1995). "Reliability-based design of foundations for transmission line structures." *TR-105000*, Electric Power Research Institute, Palo Alto, CA.

Phoon, K. K., Ed. (2008). *Reliability-based design in geotechnical engineering: computations and applications*, Taylor & Francis, London.

Reese, L. C. and O'Neill M. W. (1988). "Drilled shafts: construction procedures and design methods." *FHWA-HI-88-042*. Federal Highway Admin., McLean, VA.

Tang, W. H., Woodford, D. L., and Pelletier, J. H. (1990). " Performance reliability of offshore piles." *Proc. 22nd Offshore Technology Conf.*, Houston, TX, 299-307.

Wang, Y. (2009). "Reliability-based economic design optimization of spread foundations." *J. Geotech. and Geoenvir. Eng.*, 135(7), 954-959.

Wang, Y. (2011). "Reliability-based design of spread foundations by Monte Carlo simulations." *Geotechnique*, doi: 10.1680/geot.10.P.016.

Wang, Y. and Kulhawy, F. H. (2008). "Economic design optimization of foundations." *J. Geotech. and Geoenvir. Eng.*, 134(8), 1097-1105.

Wang, Y., Au, S. K., and Kulhawy, F. H. (2011). "Expanded reliability-based design approach for drilled shafts." *J. Geotech. and Geoenvir. Eng.*, 137(2), 140-149.

Zhang, L., Tang, W. H., and Ng, C. W. W. (2001). "Reliability of axially loaded driven pile groups." *J. Geotech. and Geoenvir. Eng.*, 127(12), 1051-1060.

Limit States Design of Pile Foundations in Clay Under Combined Action of Transient Uplift Loads and Frost Jacking

Konstantin Ashkinadze, PhD, P.Eng.[1]

[1]Eco-Technica Inc., 3821−78 Avenue, Edmonton, Alberta T6B 3N8, Canada; mailing address: 1228 Wershof Road, Edmonton, Alberta T6M 2M2, Canada; PH (780) 945-9746; email: konstant@planspls.com

ABSTRACT

The paper addresses design of friction and end-bearing piles in clayey soil under combined action of transient uplift loads and frost adfreeze. This practically important subject has been insufficiently studied by researchers. Conventional design practice is based largely on common sense and engineering intuition. The paper introduces a new type of analytical model called "three-column model" for rigorous nonlinear finite element analysis of the soil-pile-soil system. By numerical experiment, the nature of interaction of the transient and frost load was found to be complex; they are neither directly additive nor mutually exclusive. The conventional design practice for structural analysis of friction piles, which discounts this interaction, is therefore non-conservative. Limit states pertinent to the problem are identified and geotechnical and structural design of the piles in terms of Limit States Design paradigm is discussed.

INTRODUCTION

Design of pile foundations for the combined action of transient (i.e. produced by forces acting on the supported structure) and soil-induced loads is one of the most practically important, yet largely overlooked by researchers, aspects of their design. Among the soil-induced actions, specifically frost adfreeze is considered in this paper.

It is widely believed in the geotechnical engineering community that for purely friction-type piles, transient uplift forces are not additive to the adfreeze forces (El-Naggar 2000). The reason is, the relative movement of the pile and the surrounding soil in these two cases occurs in two opposite directions. Under the action of an uplift transient force, the pile moves upwards past the soil, whereas the frost jacking causes the soil to move upwards past the pile, one relieving the other. Contrary to it, in end-bearing piles both the transient force and the adfreeze force are counteracted by the reaction of the base, so these two loads can be compounded.

Such conclusions are based almost exclusively on common sense and engineering intuition. In reality, the sign of the contact stresses depends on the direction of relative movement of the corresponding segments of the pile and the soil, which can only be found by accurate structural analysis, not established a priori.

Similarly, considering end-bearing piles, distinction must be made between rigid end bearing, as in piles socketed into sound rock, and flexible anchorages produced by forming expanded bases or bells in clay. These end-bearing devices show large deformability, especially in the upward direction where the soil is already disturbed by the bell installation; hence the relative movement of such a pile and the freezing soil is also a non-trivial problem.

The present work pursued three main research goals:

− To develop a rigorous approach to the problem;
− To establish the principal facts about the transient load − frost interaction;
− To develop pile design procedures in terms of Limit States Design (LSD).

All three tasks are important for the risk assessment in the problem considered. Although the larger part of the paper is devoted to a deterministic problem of static response of a pile to transient and frost action, it is essential to establish the nature of failure (i.e. abrupt or gradual) and formulate the pertinent limit states (safety or serviceability) before the load and resistance factors can be assigned.

THE NUMERICAL EXPERIMENT

The *t-z* curves method and the three-column model. To develop a rational approach to the problem, a numerical experiment was conducted on a structural model consisting of three vertical columns, the middle one representing the pile and the two outer ones simulating the surrounding soil (Figure 1).

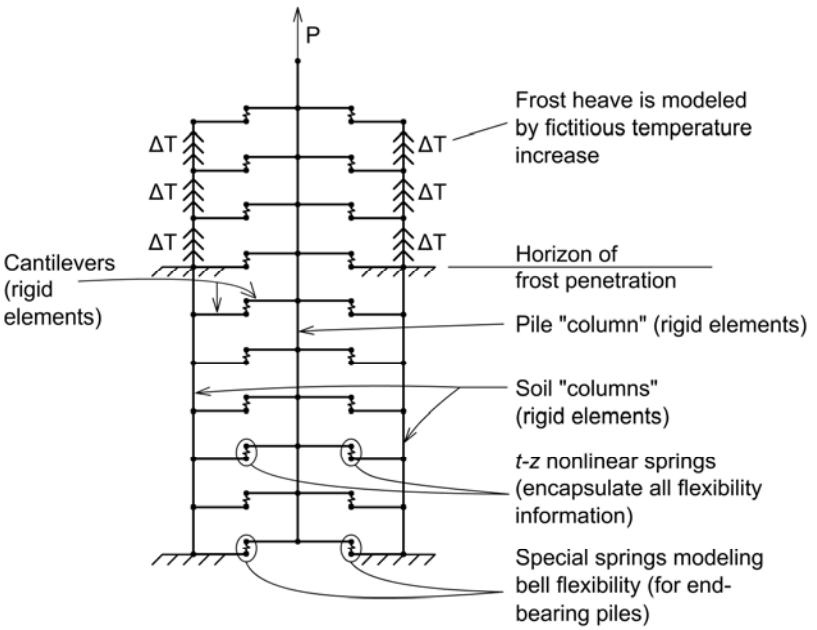

Figure 1. The three-column model.

The three-column model is an extension of the well-known method of *t-z* curves for analysis of vertical interaction between the pile and the soil (USDOT 2006). In the *t-z* curves method, only the pile vertical stiffness is modeled directly, while all relative movements of the pile and the soil are encapsulated in the (usually

nonlinear) deformation curves assigned to fictitious connection springs. These curves are back-calculated from test results and represent both the flexibility of the soil and the boundary phenomena. As a result, no model for the soil itself is needed.

In the three-column model, the soil elastic properties are also not directly modeled. However, the actual members representing the soil are introduced, which allows modeling forced displacements of the soil. The back influence of the pile on the soil displacements is considered through the nonlinear contact springs but the applied frost heave is not dissipated through shear deformation of the soil near the pile, and is applied to the pile more harshly than in reality. The proposed model of frost action is therefore conservative.

The pile-soil interaction was modeled by connecting the corresponding nodes of the columns with nonlinear springs with Prandtl-type (elastic-perfectly plastic) *t-z* curves, whose stiffness and shear-off forces were set to model the displacements, skin friction and maximum adfreeze forces of a real sample pile. The sample pile[1] was a concrete pile 18″ diameter × 22′-0″ deep. The "allowable" skin friction in the Working Stress Design format was taken as 400 psf and reached at the displacement 0.25″. Beyond this limit, the reaction of the nonlinear spring remained constant with an infinite growth of displacements (Figure 2, a).

Prandtl-type *t-z* curves were also used for the adfreeze stresses and stiffness representation. The simplified Berggren equation was used to establish the depth of frost penetration (DOFP) based on the mean freezing index at the locality (CGS 2006). The average adfreeze stress acting within these areas was assumed to be 65 kPa (1350 psf) for concrete piles (Penner 1974). This served to establish the shear-off strength of the nonlinear springs representing adfreeze ties (Figure 2, b). The stiffness constant of the frozen soil "tie" was assumed to be 100 times greater than the stiffness of the unfrozen soil.

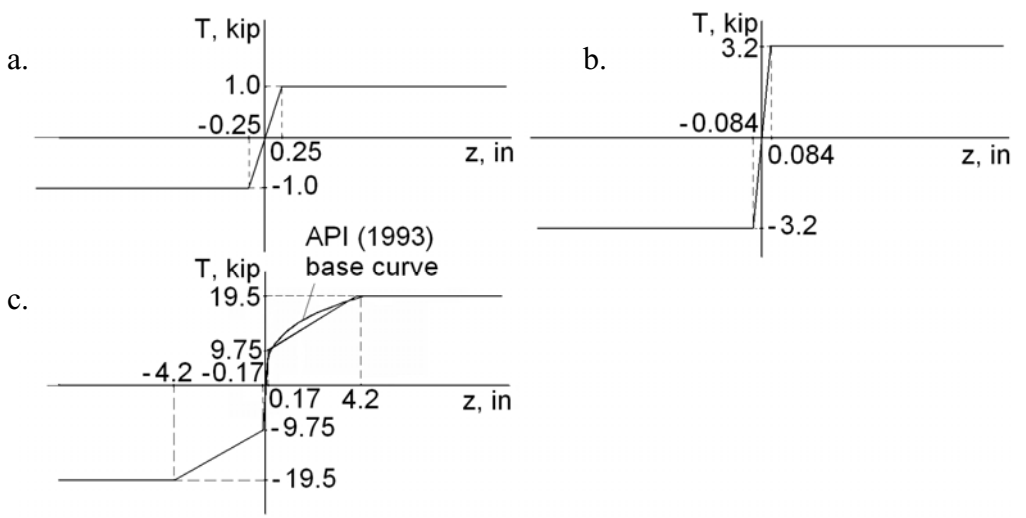

Figure 2. *t-z* curves of elementary nonlinear springs in the three-column model: a. – skin friction; b. – adfreeze forces; c. – end-bearing in clay.

[1] The pile and soil data were assumed for existing piles in Petro Canada RCP project (Edmonton, Alberta, Canada, 2006-2009), which used Imperial units. For SI conversion see Appendix I below.

For *end-bearing piles*, their stiffness was modeled with trilinear *t-z* curves as defined in API (1993) (Figure 2, c). The bell in the analysis was assumed to be 42″ in diameter and the soil had 5,000 psf allowable bearing stress. For the purposes of this study, the end-bearing pile was assumed to have no shaft skin friction, and vice versa. Under the assumed conditions, the "allowable" transient design force on the friction pile in the upward direction was 32 kips and the allowable capacity of the end-bearing pile was 39 kips.

The frost heave was simulated by a fictitious temperature increase of the upper soil elements. The DOFP was taken as 5′, which produced a frost jacking force of 32 kips. The resulting soil heave at the ground surface was 2″.

Using the general purpose S-Frame® finite element program (Softek 2009), the system was subjected to the upward transient force and the frost jacking force of 0, 0.2, 0.4, 0.6, 0.8 and 1.0 of the maximum allowable force for this pile. As a result of nonlinear incremental static analysis, the maximum pile force and the maximum pile top displacement were recorded on 3-dimensional interaction diagrams.

Results of the analyses. The study showed that the forces due to frost action and the transient forces are not directly additive, nor are they mutually exclusive. This is illustrated by the "pile force vs. transient load vs. frost load" diagrams for friction piles (Figure 3) and for end-bearing (belled) piles in clay (Figure 4). With an amount of frost 0.15 – 0.2 of the maximum, the force in the pile ascends to a plateau that gradually rises as the transient force increases. In the analysis, the maximum force attainable in the pile was 30-60% greater than its nominal uplift capacity, with the corresponding increase of the displacement. Despite the apparent "overload", the pile remains stable and no abrupt increase of the displacement occurs. As seen from Figures 3 and 4, there is no significant difference between the behavior of friction piles and end-bearing piles.

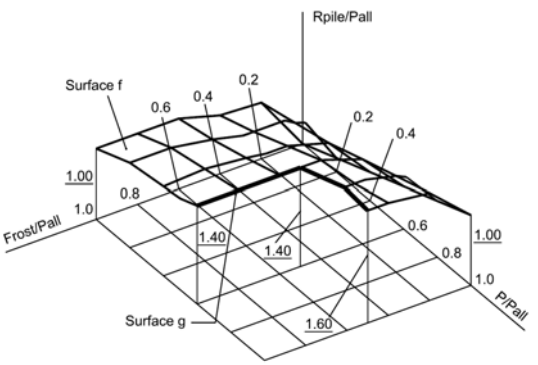

Figure 3. Pile force vs. transient load vs. frost jacking force diagram for friction piles.

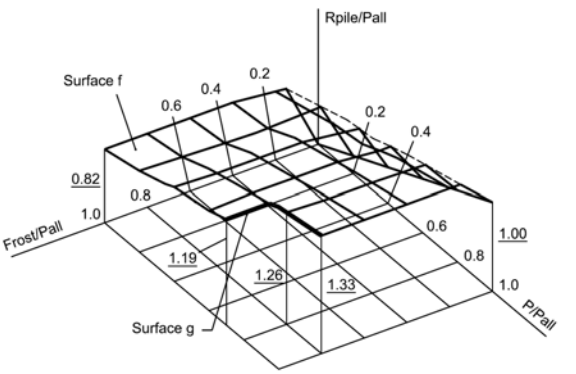

Figure 4. Pile force vs. transient load vs. frost jacking force diagram for end-bearing piles in clay.

On Figure 5, the "pile top displacement vs. transient load vs. frost jacking load" diagram for friction piles is presented. It is similar in nature to the "pile force" diagram on Figure 3, except it shows more variation within the plateau. At small

magnitudes of the frost uplift, the displacement was smaller than if no frost were considered at all; the reasons of such behavior are discussed below. This situation is illustrated on Figure 5 by "squaring off" the displacements near the "zero frost" axis. For end-bearing piles without skin friction, the displacements were always significantly larger in the absence of the frost than in its presence. For this reason, the pile top displacements interaction diagram for end-bearing piles is not presented.

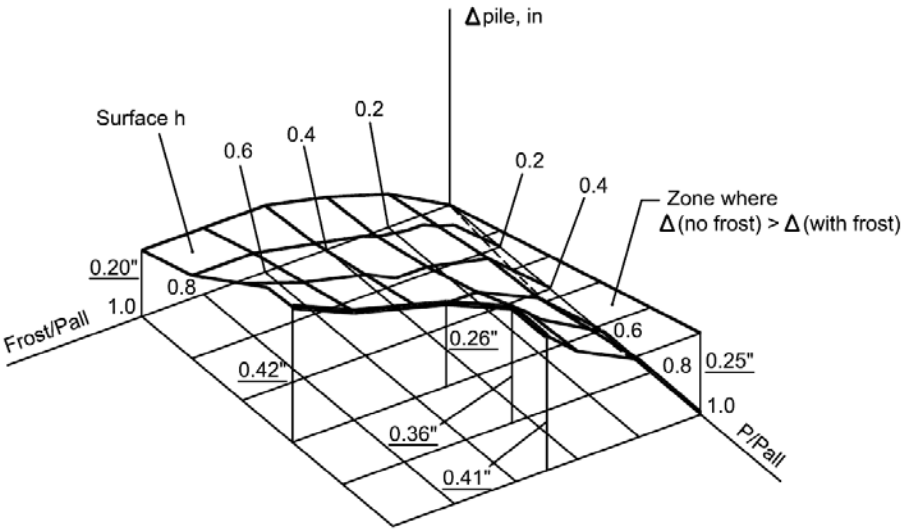

Figure 5. Pile top displacement vs. transient load vs. frost jacking force diagram for friction piles.

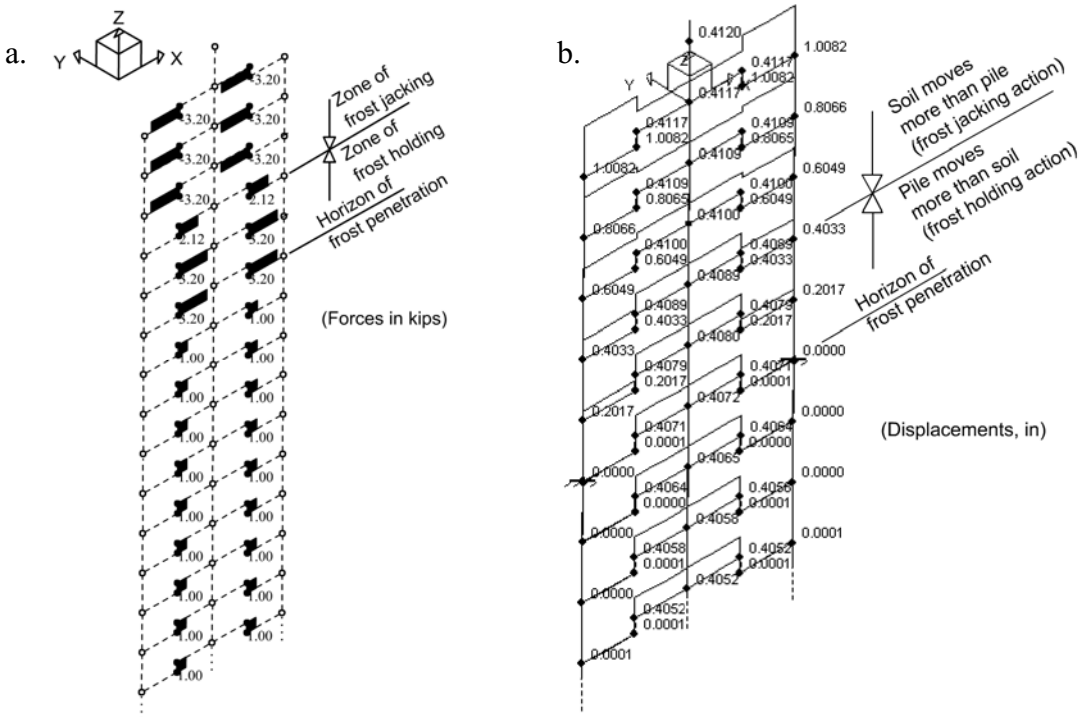

Figure 6. Soil-pile interaction at 1.0 Transient force + 0.5 Frost (friction piles): a. – contact forces in nonlinear springs; b. – relative displacements.

The physical nature of the interaction between the frost and the transient force is illustrated by Figure 6. First of all, *the claim that the transient force" relieves" the stresses in the pile caused by the frost is not true.* The mismatch of the displacement between the pile and the frost-swollen soil is so large that the corresponding nonlinear springs behave in a distant plastic region of their respective *t-z* curves. The moderate transient load counterimposed is unable to return them on the elastic branch where the contact stresses could be reduced.

Secondly, Figure 6 suggests that the relative movement of the pile and the soil within the freezing zone occurs in two opposite directions. At the surface, the frozen soil swells more than the pile can move. However, near the bottom of the frost penetration horizon, the soil movement reduces to zero, whereas the pile continues to move upwards due to its integrity. Therefore, at the bottom of the frozen zone, *the frost actually helps resist the action of both the adfreeze and the transient load*. This explains the excess force developing in the pile past its theoretical allowable capacity. This effect is unexpected and emphasizes the importance of rigorous analysis rather than relying on intuition in dealing with this problem.

If a transient load is also applied, it increases the zone in which the pile moves more than the soil, triggering additional resistance of the frozen soil to pile jacking near its upper boundary. This additional resistance explains why R_{pile} is significantly larger than the maximum frost adfreeze force or the maximum transient force alone.

THE PROCEDURES FOR LIMIT STATES DESIGN

Definition of limit states in the considered problem. For the design of pile foundations, 3 analyses need to be carried out:

− ULS (Ultimate Limit States) analysis for geotechnical failure of pile embedment, i.e. the onset of large or theoretically unlimited displacements;

− SLS (Serviceability Limit States) analysis for the allowable pile displacement;

− ULS analysis for the structural strength of the pile.

The "plateau" function on Figures 3 and 4 can be expressed symbolically as

$$\frac{R_{pile}}{P_{all}} = f\left(\frac{Frost}{P_{all}}, \frac{P}{P_{all}}\right) \tag{1}$$

It was not attempted to derive a closed-form equation for this function; this would require more extensive parametric studies. Eq. 1 defines the *geotechnical resistance* of the pile. Anywhere on the plateau, the pile geotechnical failure in terms of the ULS does not occur and the rate of increase of the pile displacements under the increasing loads is moderate.

In our analyses, the ULS failure was never reached. However, in the upper corner of the *P–Frost* plane on Figures 3 and 4 where the applied loads were the largest, the nonlinear analysis procedure did not converge. Pending additional research, we propose to admit that this zone "may be" characterized by rapid increase of the displacements, and express the resulting geotechnical ULS failure criterion as

$$g\left(\frac{Frost}{P_{all}},\frac{P}{P_{all}}\right)\le 1 \tag{2}$$

The function g was also kept generic because its universality cannot be assured at this stage of the research. If $g > 1$, the pile is physically pulling out of the ground. If $g \le 1$, the pile remains geotechnically stable but it must satisfy the following condition of the SLS for displacements:

$$\Delta = h\left(\frac{Frost}{P_{all}},\frac{P}{P_{all}}\right)\le \Delta_{\max} \tag{3}$$

where h is the plateau function defined by Figure 5. Δ_{max} here is the maximum allowable displacement dictated by the intended use of the pile foundation. Δ must be calculated with consideration of accumulation of displacements over the service life of the foundation (this aspect will be dealt with in a subsequent study).

Finally, the pile must be designed to withstand the load R_{pile} structurally. As shown above, this load may be significantly larger than the maximum frost adfreeze force or the maximum transient force alone. In this regard, ***the current practice of pile design for the maximum effect of transient forces or frost action alone, disregarding their interaction, is non-conservative.*** This is the most important practical implication of the present study.

Design formulations in LSD format. Transitioning from WSD to LSD is performed by substitution $F.S. = \alpha/\phi$ where α = the load factor and ϕ = the resistance factor. However, since the frost load has no assigned load factor in the Canadian code (NRC 2005), usually the force corresponding to the "factored" DOFP is used ($h_f = h_1$ – the 1/50-year maximum DOFP). $R_{pile,f} = \alpha R_{pile}$ is given by modified Eq. 1 ($P_r = \phi P_{ult}$ is the factored resistance of the pile, $P_f = \alpha P$ is the factored transient load):

$$\frac{R_{pile,f}}{P_r} = f\left(\frac{Frost\left(h_f\right)}{P_r},\frac{P_f}{P_r}\right) \tag{4}$$

The geotechnical failure criterion (Eq. 2) in terms of factored parameters is:

$$g\left(\frac{Frost\left(h_f\right)}{P_r},\frac{P_f}{P_r}\right)\le 1 \tag{5}$$

Regarding the SLS criterion of limitation of pile displacements, Eq. 3 can be rewritten in LSD format in terms of "service" loads as opposed to "ultimate" loads (Re: "conservative mean" vs. "upper bound" loads):

$$\Delta = h\left(\frac{Frost\left(h_s^{SLS}\right)}{P_r},\frac{\alpha^{SLS}P}{P_r}\right)\le \Delta_{\max} \tag{6}$$

Note that typically $\alpha^{SLS} < \alpha^{ULS}$ but not necessarily $\alpha^{SLS} = 1.0$, as "conservative mean" may be different from "simple mean". Distinct values of α^{SLS} and α^{ULS} are provided for some types of loads (wind) in the current Canadian code (NRC 2005).

CONCLUSIONS

The simultaneous action of frost adfreeze and transient loads on pile foundations is a practically important, yet insufficiently researched, aspect of pile design. The prevailing concepts of pile behavior are based on intuition rather than analysis.

In the paper, the pile behavior under combined frost and transient loading is examined by numerical experiment using nonlinear analytical "three-column" model. It is an extension of the *t-z* curves method for vertical loading of piles.

The correlation between the frost and the transient load on piles is complex; they are not directly additive, nor are they mutually exclusive. The currently adopted practice, which considers that the frost load is not additive to transient tension load, is ***non-conservative*** for the structural design of the pile.

The three limit states to be considered are (i) ULS for geotechnical resistance, (ii) SLS for geotechnical resistance (limitation of displacements), and (iii) ULS for structural resistance of the pile. The design procedure is formulated in LSD terms.

REFERENCES

American Petroleum Institute (API). (1993). *Recommended practice for planning, designing and constructing fixed offshore platforms − Working stress design*, 20th ed., Washington, DC.

Canadian Geotechnical Society (CGS). (2006). *Canadian Foundation Engineering Manual*, 4th ed., , Richmond, BC.

El-Naggar, M. H. (2000). *Deep Foundation Design*, Geotechnical Research Centre, The University of Western Ontario, London, ON.

National Research Council of Canada (NRC). (2005) *National Building Code of Canada*, Ottawa, ON.

Penner, E. (1974). "Uplift Forces on Foundations in Frost Heaving Soils", *Can. Geotech. J.,* 11(3), 323-338.

SOFTEK Services Ltd. (2009) "S-FRAME® (2D/3D/4D Structural Analysis)", <http://www.s-frame.com/index_files/SFRAME.htm> (Sept 18, 2010).

U.S. Department of Transportation, Federal Highway Administration (USDOT). (2006). "Analyses of the Axial Load Tests at the Route 351 Bridge", *Laboratory and Field Study of Composite Piles for Bridge Substructures* (Rept. No. FHWA-HRT-04-043), Chapter 7. <http://www.tfhrc.gov/structur/pubs/04043/index.htm> (Sept 18, 2010).

APPENDIX I. CONVERSION TO SI UNITS

Inch (in or ″) × 25.4 = millimeters (mm); feet (ft or ′) × 0.3048 = meter (m)
Pounds per square foot (psf) × 0.048 = kilopascal (kPa)
Kip (= 1000 pounds) × 4.448 = kilonewtons (kN)

Safety Margin in Design of Pile-Supported Structural Slabs for Frost Action

Konstantin Ashkinadze, PhD, P.Eng.[1]

[1]Eco-Technica Inc., 3821−78 Avenue, Edmonton, Alberta T6B 3N8, Canada; mailing address: 1228 Wershof Road, Edmonton, Alberta T6M 2M2, Canada; PH (780) 945-9746; email: konstant@planspls.com

ABSTRACT

The paper addresses design of structural slabs supported by piles founded in clay. The conventional practice of pile design for such slabs is to add together the forces produced by upward heaving pressure on the bottom of the slab and adfreeze jacking force on the piles. This leads to overly conservative designs. It is argued that the heaving force on the slab is akin to a transient uplift load for the piles, which is not directly additive to the pile adfreeze forces. A numerical experiment was conducted on free-standing piles loaded beyond their theoretical frost-resisting capacity, and on piles supporting the structural slab using a special type of nonlinear analytical model named "three-column model". The analysis showed that the design requirements can be substantially relaxed. The limiting design factor is the allowable displacement of the slab, not the ultimate pile force. A probabilistic model has been proposed to account for displacement accumulation over the service life of the structure.

INTRODUCTION

Pile-supported structural slabs founded on clayey soils experience two-fold action of frost: the upward heaving pressure on the bottom of the slab and the adfreeze jacking force on the piles. Commonly in design practice, these two forces are added, resulting in very conservative design of the piles.

It can be argued that the frost heaving force on the slab is akin to a transient uplift load for the piles. It is widely accepted in the geotechnical engineering community that at least for purely friction-type piles, transient uplift forces are not additive to adfreeze forces (El-Naggar 2000). The reason is, the relative movement of the pile and the surrounding soil in these two cases occurs in two opposite directions. Under an uplift transient force, the pile moves upwards past the soil, whereas the adfreeze causes the soil to move upwards past the pile, one relieving the other.

Following this logic, the upward pressure on the slab due to frost heave also pulls the piles out of the ground. Then, the forces in the piles due to heaving pressures on the slab should not be added to the pile adfreeze forces. This was first pointed out by Ashkinadze (2007), although it was not rigorously proven at that time. The noted fact, in turn, spurred the current research, which aimed at establishing the actual safety margin of pile foundations subjected to frost loading.

METHODOLOGY OF THE RESEARCH

The problem of risk assessment of a structural slab has the following subproblems:
− To examine the behavior of the piles subjected to frost loads in excess of their theoretical jacking resistance (Ultimate Limit State vs. Serviceability Limit State);
− To explore the interaction between the frost adfreeze to the piles and the transient load caused by the heaving of the slab;
− For Serviceability Limit State, to account for accumulation of displacements over the service life of the structure.

The first two subproblems are deterministic, striving to establish the nature of failure (abrupt vs. gradual) and formulate the pertinent limit states (ULS or SLS). This is an important step in the risk assessment. The third subproblem was treated probabilistically, assessing not only the mean value of the accumulated displacement but also its scatter.

The behavior of the piles under frost actions was studied by numerical experimentation on a structural model consisting of three vertical columns, the two outer ones simulating the surrounding soil and the middle one representing the pile. This "three-column" model extends the well-known method of *t-z* curves for vertical deformations of the pile. It can capture the real "play" of contact forces, linked to the relative displacements at each segment of the pile and the soil.

The pile-soil interaction was modeled by connecting the corresponding nodes of the "columns" with nonlinear springs with Prandtl-type *t-z* curves calibrated for a real sample pile. Two types of *t-z* curves were introduced: one for ordinary soil and one for frozen soil. The frost heave was simulated by fictitious temperature increase of the upper soil elements. More detailed descriptions of the three-column model have been provided in our earlier research[1]. The analysis was carried out by S-Frame® finite element program (Softek 2009) using nonlinear incremental loading.

BEHAVIOR AND FAILURE OF SINGLE FROST-UNSTABLE PILES

Analytical model of non-frost-stable piles. The behavior of non-frost-stable piles was first examined by Ashkinadze (2007). The practical significance of this problem stems from the fact that in modernization of mature industrial facilities, existing non-frost-stable piles are often used as supports for newly installed piping and equipment. Prediction of movement of these piles is important for pipe stress analysis.

There are currently no rational methods for engineering analysis of a frost-unstable pile. Under the action of an unbalanced heaving force, the pile is not in equilibrium, hence the resulting pile displacement cannot be found from static and elasticity conditions. Likewise, it cannot be found by deformation compatibility conditions because the contact between the pile and the soil both above and below the horizon of frost penetration is broken, first when the skin friction is exceeded and then when the adfreeze bond shears off. After this, the upper soil, the pile and the lower soil will all move separately, each by its own amount. However, the pile heave is still not equal to the heave of the surrounding soil s_{soil} because the pile, remaining

[1] Ashkinadze, K. Limit States Design of Pile Foundations in Clay Under Combined Action of Transient Uplift Loads and Frost Jacking (being published in the same volume).

an integral body, cannot match the tremendous relative deformation of the frozen soil. The pile will act like a reinforcing pin in an expanding media, with $s_{pile} < s_{soil}$.

Ashkinadze (2007) proposed a formula that considered movement of the pile as a rigid body under the action of the uncompensated net adfreeze force. The resulting pile top displacement s_{pile} is:

$$s_{pile} = s_{soil} \frac{\gamma_{soil}}{\gamma_{pile}} \frac{P_{\max} - P_{res}}{q_{soil}} \frac{h}{LA_{pile}} + s_{res} \quad (1)$$

where q_{soil} – the pressure that needs to be applied to the soil to prevent its frost swelling, taken as 2000 kPa (40,000 psf) based on CGS (2006);
γ_{soil} and γ_{pile} – unit weight of the soil and the pile material, respectively;
P_{max} – the maximum adfreeze force, equal to $f_{adf} \times \pi D \times h$;
P_{res} – the maximum resistance force, equal to $f_{sk} \times \pi D \times (L - h)$;
h – the depth of frost penetration (DOFP);
D and L – diameter and length of the pile, respectively;
A_{pile} – the section area of the pile;
s_{res} – the amount of movement undergone by the pile before its jacking resistance was exceeded. Typically is taken as 6 mm (0.25″).

Eq. 1 predicted that, as the frost penetration deepens, the movement of the pile will progressively increase but that there will be no abrupt failure. The corroborating evidence for this fact, obtained by numerical experiment, is provided in this paper.

The numerical experiment. A single concrete pile 460 mm (18″) diameter × 6.7 m (22′-0″) long was considered. The soil is clay with an allowable skin friction of 19 kPa (400 psf). The pile is frost-stable for DOFP not exceeding 1.5 m (5′).

In the analysis, the DOFP was eventually increased to 3.35 m (11′). The analysis shows that after the pile jacking resistance is overcome, it moves together with the soil, experiencing increasing force. The additional resistance is caused by the bottom part of the frozen soil, which moves less than the pile and actually helps to hold the pile in place (Figure 1). The displacement of the pile increases faster than the soil heave but there is no pronounced failure; the force the pile was able to sustain in the analysis was 50% greater than P_{res} (see Eq. 1). However, the pile heave at 3.35 m frost depth reached 33.5% of the soil heave, whereas at 1.5 m it was only 12.5%.

On Figure 2, the pile top movement relative to the soil heave is plotted as a function of the DOFP. The apparent bumps on the graph are due to the discrete nature of the numerical simulation (discrete nodes and sharp breaks on the *t-z* curves). On the same graph, the theoretical curve resulting from Eq. 1 is depicted, and it agrees well with the results of a detailed nonlinear analysis.

Of course, this only corroborates Eq. 1 for this one example. A general validation of the analytical model vs. the more accurate numerical model, and of both models vs. the experimental data, is the topic of a separate study. For the same reason, the discussion does not touch upon the subject of "transformation uncertainty" pertinent to Eq. 1, since it was obtained not by a "transformation" (such as curve fitting or regression) from the numerical model but was derived separately.

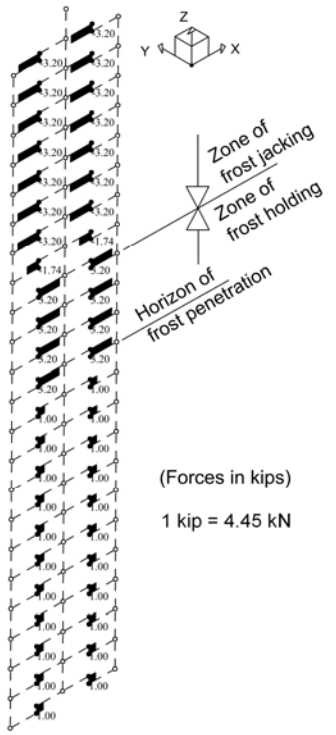

Figure 1. Frost unstable pile, frost depth 3.35 m (11′) – forces in the springs.

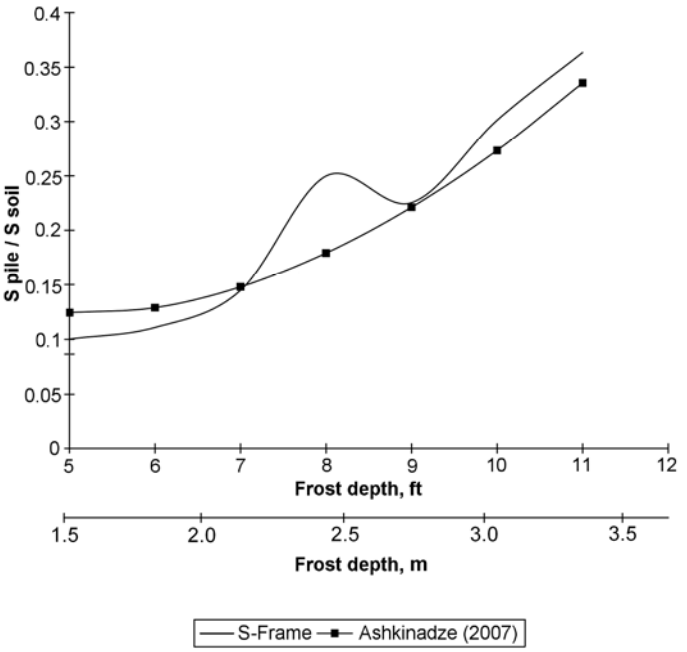

Figure 2. Frost unstable pile: relative pile top movement vs. frost depth.

FROST ACTION ON THE STRUCTURAL SLAB

Another factor that may help reduce the capacity demand of the piles is the counteracting nature of the pullout forces produced by the upward heave of the soil under the slab to the adfreeze forces on the piles − a paradoxical effect when frost relieves frost!

Model for analysis. The behavior of the piles attached to a structural slab was investigated by the same 3-column model, with the following modifications:

− A horizontal member was attached to the top of the pile "column" to represent the structural slab (Figure 3, a);

− Special nonlinear springs were introduced between the top of the soil "columns" and the slab element, simulating the load-displacement curve of Geospan® void form material (PlastiFab 2004) (Figure 3, b). The void form thickness was 150 mm (6″). The piles were spaced at 6′4″ on centre (approximately 2 m) each way.

Results of analysis. Varying the amount of frost heave s_{soil} at the surface, it was found that the system did not exhibit a pronounced failure. While the nominal uplift capacity of the pile P_{res} was only 142 kN (32 kips), it was possible to attain the force in the pile 240 kN (54 kips), or 70% more, with the progressive increase of the displacement but no abrupt failure.

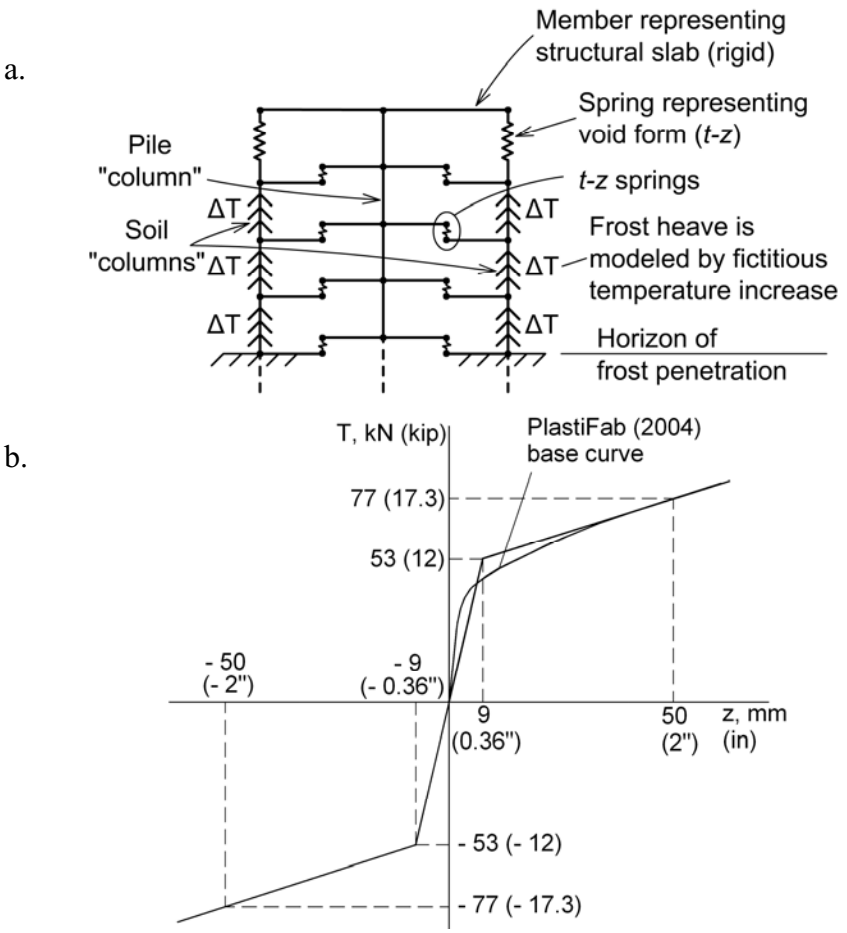

Figure 3. Modeling of frost action on a structural slab: a. – structural model (fragment); b. – deformation diagram for void form elements.

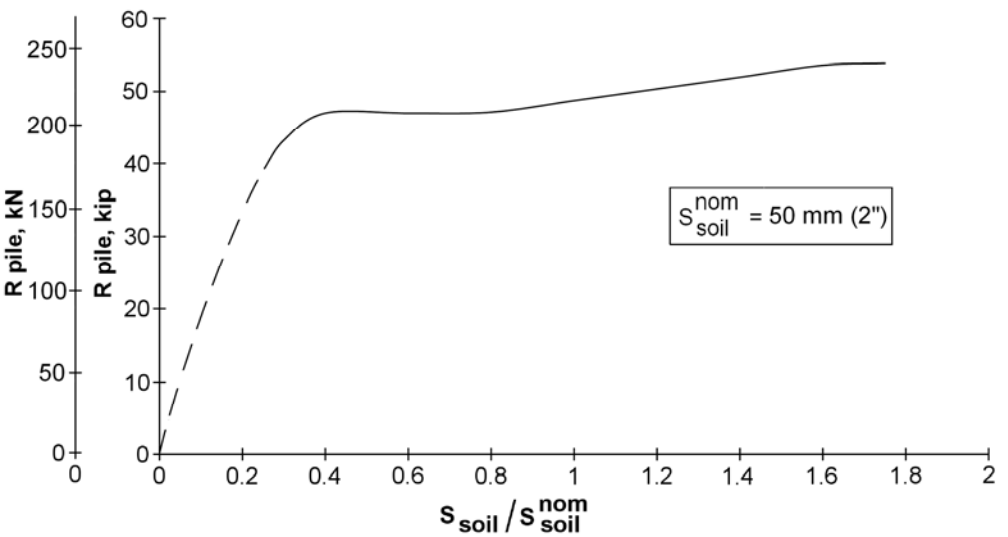

Figure 4. Axial force in the pile vs. relative frost heave displacement.

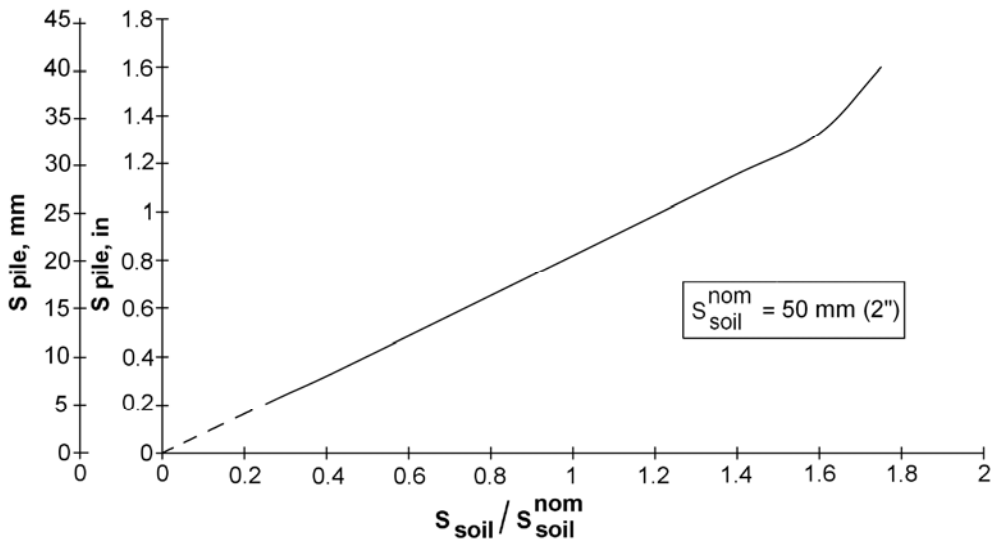

Figure 5. Pile top displacement vs. relative frost heave displacement.

At the same time, the force in the pile was smaller than the direct sum of the adfreeze + heave pull force, which amounted to 296 kN (66.5 kips). The graphs of the attained pile force and pile top displacement vs. the frost heave displacement are shown on Figures 4 and 5, and they suggest that the relieving action of the upheaval pull on the adfreeze jacking forces in the pile indeed exists.

The study shows that the conventional practice of design of piles for the total effect of the vertical heaving force and the adfreeze force is overly conservative. The limiting factor in the design is the allowable slab displacement, not the ultimate pile force. Therefore, their design should be driven by the SLS, not by the ULS.

At the same time, knowledge of the force developing in the pile, as given by the three-column model, is necessary for its proper structural design. For the pile as a structural element, the governing limit state is the ULS.

ACCUMULATION OF DISPLACEMENTS

The displacement tolerance of the structural slab depends on the application, whether the excessive jacking movement causes just a nuisance (SLS) or it may damage sensitive equipment or materials (ULS for these components). To distinguish between these conditions, it is important to know not only the mean value of the attained displacement but also its variance, hence the assessment must be done statistically.

Moreover, the displacements occur not in a single year but accumulate over the years of service life of a structure. Although melting of the ice in spring may lead to recovery of some of the displacements, many factors beyond the engineer's control may prevent the pile from retaking its former position. In the design, it is prudent to consider that the pile under the action of frost moves only "up" but never "down".

Here in, a probabilistic model is proposed for the displacement accumulation. This model assumes a log-normal distribution for the DOFP. This type of distribution is often used in climatology, such as in prediction of annual maximum accumulated rainfall (http://en.wikipedia.org/wiki/Log-normal_distribution#Occurrence). In this

instance, it was chosen because it conforms to the general physical sense of the problem (is defined for any positive values of the argument; has a pronounced mean; larger values are possible with decreasing probability). Within this framework, there is sufficient freedom to model the available field data. The corresponding probability density function for maximum annual DOFPs will be

$$p(h) = \frac{1}{\sigma\sqrt{2\pi}h} e^{-(\ln h - M)^2/2\sigma^2} \tag{2}$$

The distribution depends on two parameters: mean M and standard deviation σ. To assign these parameters, two conditions are used:

$$E(h) \text{ [expectancy]} = e^{M+\sigma^2/2} = h_0 \text{ [the mean annual DOFP]} \tag{3a}$$

$$D(h) \text{ [cumulative probability]} = \frac{1}{2}\left[1 + \operatorname{erf}\left(\frac{\ln h - M}{\sigma\sqrt{2}}\right)\right] = 0.98 \text{ when } h = h_1$$

[maximum DOFP, reached once in 50 years] (3b)

The quantities h_0 and h_1 are readily accessible for a given soil, knowing the mapped mean-annual freezing index and the maximum freezing index for the locality (CGS 2006). These two quantities constitute the only input data used; their variation with time under the alleged "climate change" need not be considered herein, as it is overshadowed by much more pronounced uncertainties in soil properties and ice segregation mechanisms responsible for the frost heave.

Solving Eqs. 3 leads to the expressions $\sigma = 2.054 - \sqrt{2.054^2 - 2\times\ln(h_1/h_0)}$ and $M = \ln h_1 - 2.054\sigma$ for the parameters of the distribution.

The theory presented herein does not consider variations of the magnitude of average adfreeze stress, or of the soil heave ratio to the DOFP. Thus, the resulting s_{pile} is a function of h alone. Then, the total displacement over N years can be obtained from Eq. 2 using Monte Carlo method. Namely, generate N values of h and calculate N values of yearly s_{pile} using either Eq. 1 or the actual nonlinear analysis. Adding them together, obtain one "accumulated" value of s_{tot}. Repeating this procedure, obtain as many realizations of s_{tot} as necessary and place them on a histogram.

An example of this procedure for the 460 mm (18″) diameter × 6.7 m (22′-0″) deep pile as above, subject to frost load with mean annual penetration h_0 = 1.5 m (5′) and maximum (1/50 year) penetration h_1 = 2.3 m (7.5′) over the period of 10 years, is shown on Figure 6. In this example, there was only one stochastic parameter, and after approximately 150 realizations the final histogram showed little variation. The model has many other parameters that in the future research, can be treated as stochastic too, then the number of tests will need to be increased.

The modal (most often encountered) value of s_{tot} can be closely approximated as $s_{pile}(h_0) \times N$ (years) = 64 mm (2.5″). However, the histogram allows evaluating the variance and choosing the appropriate value of the "conservative mean", depending on whether this is an SLS or a ULS requirement in terms of Limit States Design.

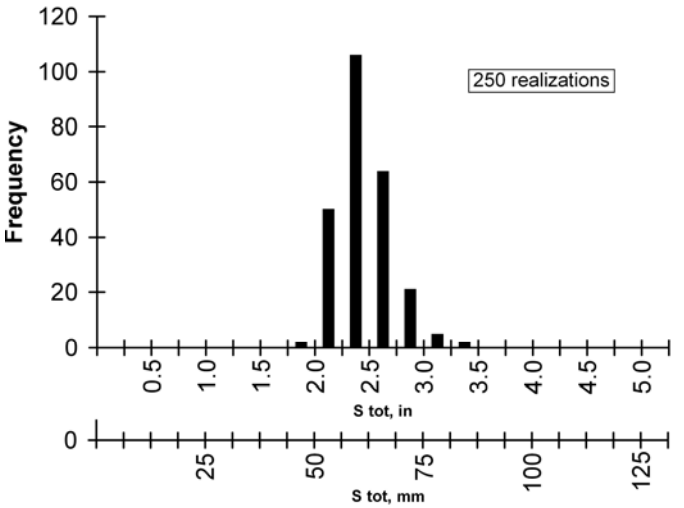

Figure 6. Histogram of accumulated pile top displacements over N = 10 years.

CONCLUSIONS

The proposed "three-column model" for nonlinear analysis of piles for frost actions accurately represents their behavior, even for "non-frost-stable" piles.

The existing practice of design of pile-supported structural slabs by adding forces in the piles due to frost heave pressure on the slab and adfreeze to the sides of the piles is ***overly conservative***. These two load factors partially relieve one another.

Assessing risk in the design of pile-supported structural slabs for frost action, it is notable that these piles can sustain more load than their nominal design force, only with a greater displacement. The most dangerous Ultimate Limit State is not typical for these problems. The design is governed by the Serviceability Limit State.

The displacements of piles and pile foundations accumulate over years. A probabilistic model has been proposed for this factor, involving a statistical distribution for the depths of frost penetration; a methodology to calculate the heave displacement of the pile from the known DOFP, and Monte Carlo method to produce a final histogram of the accumulated displacements. The information about the mean and variance of the displacement can serve to properly assign the resistance factors.

REFERENCES

Ashkinadze, K. (2007). "Simplified Assessment of Frost Penetration and Heave of Shallow and Deep Foundations", *Proc. Int. Cold Regions Engineering & Construction Conf. & Expo (IWCSE 2006)*, Edmonton, Canada.

Canadian Geotechnical Society (CGS). (2006). *Canadian Foundation Engineering Manual*, 4th ed., , Richmond, BC.

El-Naggar, M. H. (2000). *Deep Foundation Design*, Geotechnical Research Centre, The University of Western Ontario, London, ON.

PlastiFab (2004). "GeoSpan® − Compressible Fill Material", <http://www.plastifab.com/dealers/downloads/products/04042_GeoSpan.pdf> (Sept 19, 2010).

SOFTEK Services Ltd. (2009) "S-FRAME® (2D/3D/4D Structural Analysis)", <http://www.s-frame.com/index_files/SFRAME.htm> (Sept 18, 2010).

Statistical Characterization And Stochastic Simulation Of Load-Displacement Behavior Of Shallow Footings

Marco Uzielli[1], A.M. ASCE and Paul W. Mayne[2], M. ASCE

[1] Chairman, Georisk Engineering S.r.l., via Giuseppe Giusti 16/5, 50121 Firenze (Italy), muz@georisk.eu
[2] Professor, GeoSystems Group, Civil & Environmental Engineering, Georgia Inst. of Technology, Atlanta, Georgia 30332-0355 USA, paul.mayne@ce.gatech.edu

ABSTRACT: This paper focuses on the statistical characterization and stochastic modeling of the load-displacement behavior of full-scale quasi-square footings. The study relies on a large and comprehensive field database of 66 full-scale footings subjected to vertical loading on 4 different soil types (sands, silts, intact clays, fissured clays) with CPT cone resistances available for each site. The performance of 2 analytical load-displacement models in replicating empirical field data is assessed comparatively through statistical modeling of load-displacement data. Correlation between model parameters is investigated and replicated using copula theory. Following the identification of best-performance models for each soil type, load-displacement curves are simulated stochastically. The influence of soil type on statistical properties and modelling details are discussed. Best-performing configurations of modelling options are provided for practical implementation in geotechnical limit state design.

INTRODUCTION

In Limit State Design (LSD) of shallow footings, it is paramount to adequately characterize a load-displacement model which suitably approximates load-displacement data at all loading levels. At the ultimate limit state (ULS), each measured load-displacement curve will produce a single capacity. At the serviceability limit state (SLS), the capacity is replaced by an 'allowable capacity' which is related to an allowable displacement. At SLS, the load-displacement curve is considered in its entirety as different allowable settlements may be selected as reference parameters. LSD entails the acknowledgment and assessment of uncertainty. Load-displacement behavior is affected by multiple sources of uncertainty. When several tests are considered together in developing a general load-displacement model, the uniqueness of each test, site and soil-foundation interaction will result in an aleatory data scatter; second, an epistemic uncertainty related to imperfect measurement of the soil-foundation system is always present; third, when parameterizing the load-displacement relation through suitable techniques such as statistics, a transformation uncertainty, which parameterizes the imperfect representation of the physical world, will result. This paper addresses the statistical characterization and stochastic modeling of load-displacement behavior of vertically loaded footings in a wide variety of foundation soil types.

DATABASE

The reference database comprises 66 footings on 4 different soil types that were subjected to vertical loading, namely: 31 footings on sand (hereinafter ST1); 10 on silts (ST2); 13 on intact clays (ST3); and 12 on fissured clays (ST4). The origins of ST1 included natural marine deposits, alluvial sediments, aeolian dune sands, and compacted sand fills. The ST2 set were on silt deposits and ST3 series located on clays of marine, glacio-marine, and estuarine deposits, as well as a residual clay formation. The fissured geomaterials of ST4 were comprised of overconsolidated clays of marine or deltaic deposits that had been subjected to erosion and/or desiccation. The footings included 44 square, 8 rectangular, and 14 circular shallow foundations, with the equivalent square footing width B_{eq} (equal to the square root of the surface area) varying from 0.40 m to 8.37 m. Only full-scale foundations were considered in order to avert difficulties associated with 1-g model tests and scaling problems (e.g. Cerato and Lutenegger 2007).

Table 1. Main Features Of Load Test Database

	sites	tests	B_{eq}[m]	z_e[m]	$q_{t,net}$[MPa]
ST1	10	31	0.46-6.09	0.00-2.35	0.88-10.72
ST2	4	10	0.50-2.00	0.00	1.01-3.67
ST3	6	13	0.40-8.37	0.00-2.20	0.20-0.77
ST4	2	12	0.55-2.74	0.00-1.50	0.60-1.60

The load-displacement behavior of footings has been shown to be unique for a given soil when the results are presented in terms of a characteristic stress vs. normalized displacement curve (e.g. Briaud 2007). For the CPT, the stress axis can be normalized by a representative value of in-situ net cone tip resistance $q_{t,net}=q_c+(1-a_c)u_2-\sigma_{v0}$ where q_c is the measured cone tip resistance, a_c is the cone factor, u_2 is the pore pressure measured behind the cone tip and σ_{v0} is the total in-situ vertical stress. The representative value of $q_{t,net}$ is taken, for each load test, as the mean value over $1.5B_{eq}$ depth below the bearing elevation. The number of tests for each soil type, as well as the maximum and minimum values of B_{eq}, embedment depth z_e and $q_{t,net}$ are given in Table 1.

STATISTICAL CHARACTERIZATION

In this study, statistical characterization of load-displacement uncertainty is performed by soil type prior to stochastic modeling for LSD purposes. Aleatory scatter and transformation uncertainty are addressed jointly, while measurement uncertainty is not considered. To characterize load-displacement behavior statistically, two load-displacement model types were considered:

Model type HYP (hyperbolic model):

$$\theta_q = \frac{\eta}{k_2 + k_3 \cdot \eta} \tag{1}$$

Model type PWR (power law model):

$$\theta_q = k_4 \cdot \eta^{k_5} \tag{2}$$

in which $\theta_q = q_{app}/q_{t,net}$ is the dimensionless capacity-normalized applied stress and $\eta = s/B_{eq}$ is the dimensionless pseudo-strain. The HYP and PWR models have been implemented for load-displacement curves of shallow and deep foundations (see Uzielli and Mayne 2011a for a list of references). The two models were fitted to the data from each of the 66 tests in the source database using generalized least-squares regression. An example regression is shown in Figure 1.

Figure 2a and Figure 2b show the bivariate scatterplots of model parameters for HYP (in log-log scale) and PWR (in semi-log scale), respectively, for all soil types. Points referring to ST1 and ST3 cluster quite distinctly from the other soil types for both HYP and PWR. ST2 and ST4 are superimposed to some degree, though the ranges of HYP parameters are greater for ST2 points than for ST4 points, and, conversely, ranges of PWR parameters are larger for ST4 than for ST2, with the exception of one ST2 point. It is interesting to note the disjunction between ST1 and ST3 points as these refer to more geotechnically definite soil behavior, while ST2 and ST4 could be associated with a more intermediate/hybrid behavior.

The performance of HYP and PWR was assessed comparatively in terms of: (a) goodness-of-fit of the load-displacement to empirical data; (b) second-moment statistics; and (c) goodness-of-fit of marginal lognormal distributions. The regression goodness-of-fit was parameterized by the root mean square error (RMSE). For ST1, PWR outperformed HYP in 24 cases out of 31; for ST2, each of the two models showed a lower RMSE in 5 of the 10 cases; for ST3 and ST4, HYP outperformed PWR in 8 and 7 cases, respectively. On the basis of the available data, it appears that the PWR model is significantly more suitable than HYP for cohesionless-behavior soils, while the performance of the latter increases with the degree of cohesive behavior.

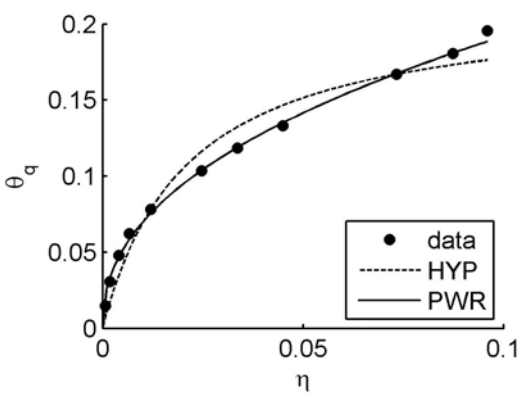

Fig. 1. Example of nonlinear least squares fitting

In order to assess the magnitude of load-displacement uncertainty, regressed model parameters were investigated in terms of second-moment sample statistics, namely the sample mean, and the sample coefficient of variation (COV). The COV can be conceptually associated with the level of aleatory uncertainty in the sampled random variate. As can be seen in Table 2, the COVs of the PWR model parameters (k_4 and k_5) are univocally smaller than those of the HYP model (k_2 and k_3) for ST1 and ST2. For ST3, the COVs of k_2 and k_4

Table 2. Second-Moment Sample Statistics

	ST1		ST2		ST3		ST4	
	mean	COV	mean	COV	mean	COV	mean	COV
k_2	0.11	0.56	0.05	0.81	0.01	0.33	0.05	0.30
k_3	7.34	0.62	3.22	0.54	1.73	0.29	1.92	0.27
k_4	0.62	0.46	1.34	0.70	2.18	0.34	1.53	0.39
k_5	0.49	0.19	0.45	0.16	0.41	0.17	0.48	0.24

are comparable, while that of k_3 largely exceeds that of k_5. For ST4, the COV of k_2 is smaller than that of k_4, while those of k_3 and k_5 are comparable. Hence, the PWR model ensures lower transformation uncertainty for ST1 (especially), ST2 and ST3, while HYP displays less dispersion for ST4. With the exception of COV(k_5) for ST2 and ST3, the magnitude of sample COVs appears to be high, thus attesting for the relevance of transformation uncertainty in load-displacement models.

STOCHASTIC SIMULATION

For LSD purposes, it is important to reach beyond the descriptive statistical characterization of transformation uncertainty, and to model the uncertainty in load-displacement behavior probabilistically (e.g. for simulation purposes). For two-parameter models such as PWR and HYP, load-behavior uncertainty can be conveniently modeled using a bivariate probability distribution with suitable marginals. Lognormal marginal distributions ensure the condition of non-negativity of model parameters. The probability density function of a lognormal distribution of a generic non-negative random variable x is given by

$$f\left(x,\xi,\lambda\right)=\frac{1}{x\cdot\xi\cdot\sqrt{2\pi}}\exp\left[-\frac{\left(\ln x-\lambda\right)^2}{2\cdot\xi^2}\right] \tag{3}$$

where λ and ξ are the log-mean and log-standard deviation of the distribution, respectively. Best-fit parameters were obtained for the empirical samples HYP and PWR model parameters by maximum likelihood estimation. As an example, Figure 3 shows the relative frequency histogram of k_2 for ST2 from regression on the database load tests, along with the superimposed best-fit lognormal distribution. In order to assess the goodness of fit of lognormal distributions to sample data, it was checked that the natural logarithms of the latter were Gaussian (at the 0.10 significance level). using the Anderson-Darling test. Samples of regressed values of k_2, k_3, k_4 and k_5 were found to be lognormal at the 0.10 significance level for all soil types, with the sole exception of k_4 for ST2. On the basis of the above, it is deemed advisable to employ the PWR model for ST1 and HYP for ST2, ST3 and ST4.

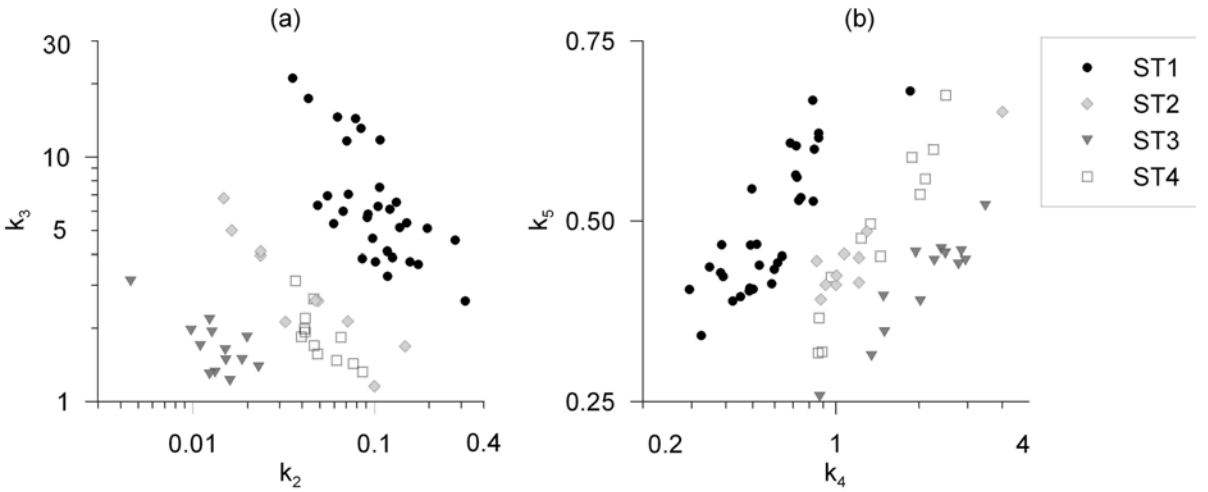

FIG. 2. Scatterplots of regressed model parameters for: (a) HYP and (b) PWR

To correctly simulate a two-parameter load-settlement model for applicative purposes, it is important to adequately account for the correlation between model parameters, i.e. to investigate the existence and magnitude of statistical dependence between the empirical samples load-displacement model parameters. For instance, with reference to Figure 2b, it would be inappropriate to simulate the PWR model for a sand using k_4=0.8 and k_5=0.3 since there is descriptive statistical evidence that the two values are unlikely to occur jointly in a load-displacement curve. Neglecting dependence would result in unrealistic simulation instances. Copulas provide an efficient tool for generating multivariate distributions of random variables with a given degree of dependence while preserving the marginal distributions of the random variables themselves. A copula is a multivariate joint distribution such that every marginal distribution is uniform on the interval [0, 1]. As the PWR and HYP load-displacement models are two-parameter models (n=2), bivariate copulas were employed. Four copula types were considered, namely: one elliptical copula type (Gaussian) and three Archimedean copulas (Frank, Clayton, Gumbel). Theoretical details of elliptical and Archimedean copulas can be found in Nelsen (1999), while applications to geotechnical engineering are given in Uzielli and Mayne (2011a, 2011b). Operationally, the generation of a bivariate copula requires the definition of the marginal distributions (achieved in the previous section through MLE estimation of lognormal distribution parameters) and the parameterization of correlation. Kendall's tau statistic, ranging from -1 (perfect negative

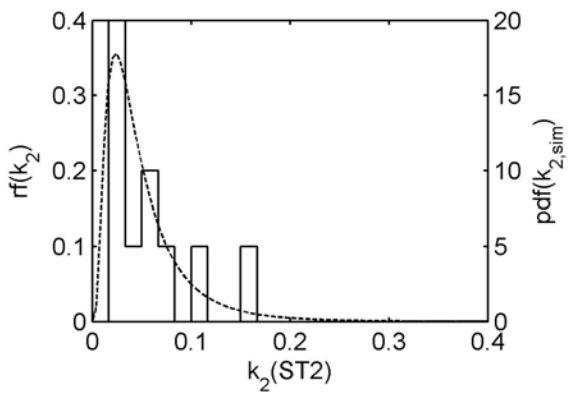

FIG. 3. Relative frequency histogram of regression sample and fitted lognormal distribution for k_2(ST2)

Table 3. Kendall' Tau Statistic

	ST1	ST2	ST3	ST4
HYP	-0.48	-0.82	-0.41	-0.64
PWR	0.63	0.64	0.62	0.85

correlation) to +1 (perfect positive correlation), was calculated for both models and for each soil type (see Table 3).

Kendall's tau provides a very useful statistic, as it can be used to calculate copula parameters directly for the 4 copula types using appropriate relations. The most suitable copula type was selected by identifying the copula type which yields the minimum Euclidean distance between the cumulative distribution of the empirical bivariate copula and the cumulative distribution of the user-defined copula. For ST1, the best-performing copula for the simulation of bivariate distributions (k_4, k_5) was the Frank copula. For ST2-ST4, the Frank and Gaussian copulas performed almost equally; hence, the latter was adopted for all 3 soil types as its copula parameter is more easily calculated from Kendall's tau. Bivariate lognormal distributions of model parameters with the appropriate degree of dependence can then be generated using the inverse transformation method.

Table 4 reports the best-performing configurations (load-displacement model, lognormal parameters, copula type and copula parameter) by soil type. Figure 4 shows the bivariate lognormally distributed simulated samples of model parameters (black dots) of size 1,000 with superimposed the regressed sample values (grey circles) for the best-performing configurations listed in Table 4. Figure 5 shows corresponding simulations of normalized load-displacement curves (100 simulations for each soil type) for pseudo-displacements ranging from 0 to 0.1. Once again, it is possible to appreciate the difference in load-displacement behavior between sandy, silty and clayey soils. Fissured clays display a simulated behavior which is similar to that of silts, though there is less scatter in normalized stress for any given pseudo-displacement. The scatter in the curves reflects the aleatory uncertainty in load-displacement (stemming from the real variability in behavior inside each soil type) as well as the transformation uncertainty in the selected load-displacement models. Table 5 illustrates the sample mean, COV, minimum and maximum of simulated normalized stress for low (0.001), medium (0.01) and high (0.1) pseudo-strain η and by soil type. The selected statistics are useful for assessing the similarities and differences in the simulated load-displacement behavior in terms of magnitudes and scatter.

Table 4. Best-Performing Configurations For Stochastic Simulation

		$\lambda(p_1)$	$\xi(p_1)$	$\lambda(p_2)$	$\xi(p_2)$	Copula type	Copula param.
ST1	PWR[a]	-0.547	0.369	-0.724	0.180	Frank	8.662
ST2	HYP[b]	-3.219	0.731	1.041	0.509	Gaussian	-0.961
ST3	HYP	-4.324	0.387	0.514	0.248	Gaussian	-0.601
ST4	HYP	-2.983	0.267	0.622	0.242	Gaussian	-0.841

[a] for PWR, $p_1=k_4$ and $p_2=k_5$

[b] for HYP, $p_1=k_2$ and $p_2=k_3$

Table 5. Statistics of simulated normalized stress θ_q

	η=0.001				η=0.01				η=0.1			
	ST1	ST2	ST3	ST4	ST1	ST2	ST3	ST4	ST1	ST2	ST3	ST4
mean	0.02	0.03	0.07	0.02	0.06	0.13	0.33	0.14	0.20	0.30	0.57	0.42
COV	0.38	0.53	0.33	0.24	0.29	0.22	0.16	0.13	0.29	0.26	0.19	0.15
min	0.00	0.00	0.02	0.01	0.02	0.04	0.20	0.10	0.11	0.10	0.33	0.26
max	0.05	0.07	0.14	0.03	0.14	0.17	0.45	0.18	0.46	0.44	0.87	0.53

CONCLUDING REMARKS

This paper has addressed the statistical modeling and stochastic simulation of uncertainty in load-displacement behavior for shallow footings. The study relied on a large and comprehensive field database. It was assessed that load-displacement uncertainty is relevant for all foundation soil types. Moreover, the study revealed significant differences in the magnitude and character of uncertainty in load-displacement behavior of footings for different foundation soil types. The final product of the study is a table of best-performing configurations in terms of statistical characterization and stochastic modeling of uncertainty by soil type. It should be emphasized that the results obtained are not definitive, as new data would certainly result in variations in the sample statistics and in the stochastic modeling parameters.

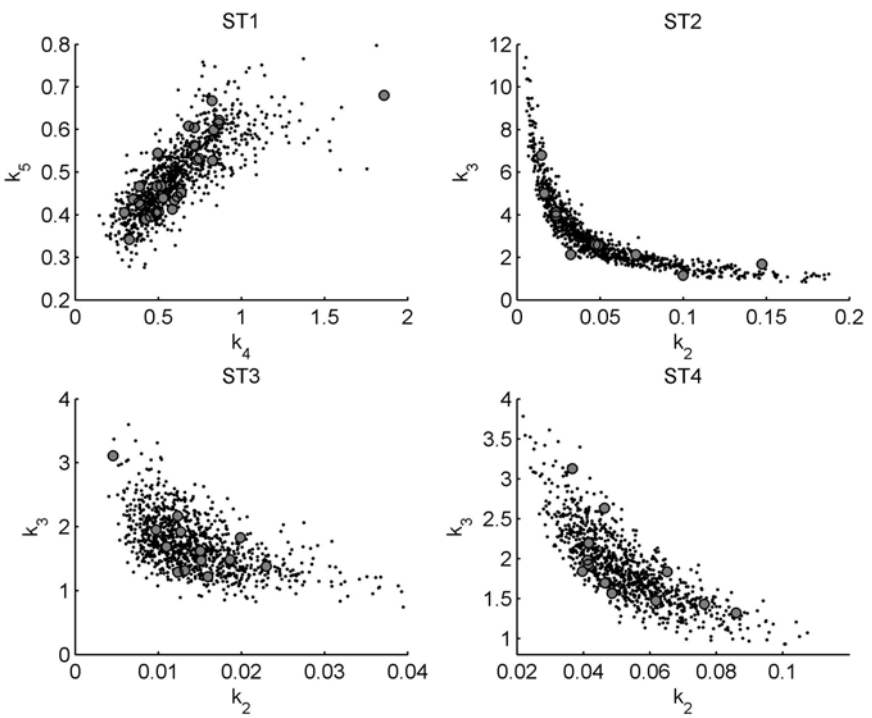

FIG. 4. Best-performing simulations and regressed values of model parameters

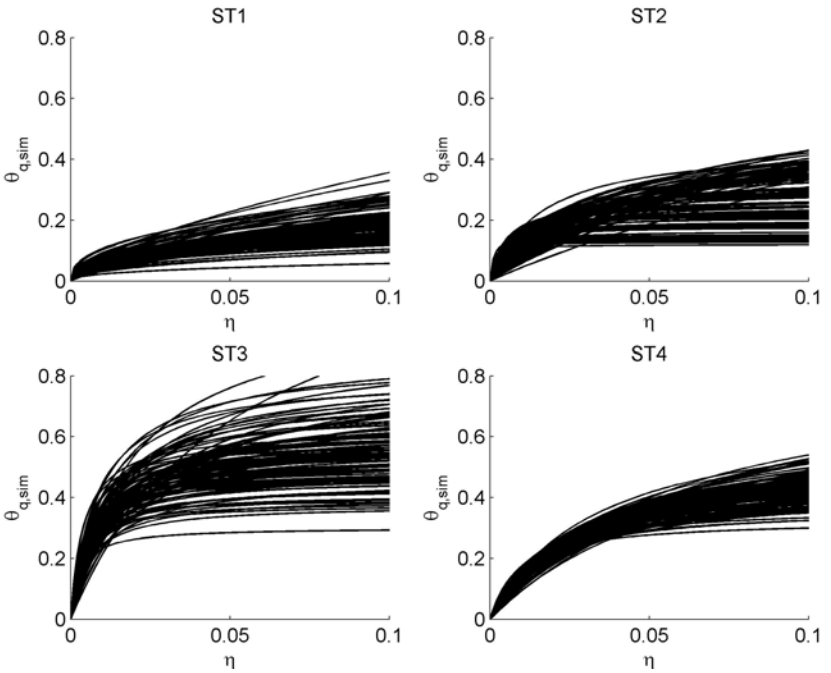

FIG. 5. Simulated normalized load-displacement curves

REFERENCES

Akbas, S.O., and Kulhawy, F.H. (2009). "Axial compression of footings in cohesionless soils. I: load-settlement behaviour." *Journal of Geotechnical and Geoenvironmental Engineering*, ASCE, 135(11): 1562-1574.

Briaud, J.L. (2007). "Spread footings in sand: load settlement curve approach." *Journal of Geotechnical and Geoenvironmental Engineering*, ASCE, 133(8): 905-920.

Cerato, A.B., and Lutenegger J. (2007). "Scale effects of shallow foundation bearing capacity on granular material." *Journal of Geotechnical & Geoenvironmental Engrg*, ASCE, 133 (10): 1192-1201.

Nelsen, R. (1999). "An introduction to copulas". Springer, Berlin.

Phoon, K.K., and Kulhawy, F.H. (2008). "Serviceability limit state reliability-based design." *Reliability-based design in geotechnical engineering – computations and applications*, K.K. Phoon, ed., Taylor & Francis, London, 344-384.

Thode, H.C., Jr. (2002). "Testing for normality." Marcel Dekker, New York.

Uzielli, M. and Mayne, P.W. (2011). "Serviceability limit state CPT-based design for vertically loaded shallow footings on sand". *Accepted for publication in Geomechanics and Geoengineering*, Taylor & Francis Group, London.

Uzielli, M. and Mayne, P.W. (2011). "Load-displacement uncertainty of vertically loaded shallow footings on sands and effects on probabilistic settlement estimation". *Submitted for possible publication in Georisk - Assessment and Management of Risk for Engineered Systems and Geohazards*, Taylor & Francis Group, London.

Reliability Based Design of Base Heave Stability in Wide Excavations

Shih-Hsuan Wu[1], Chang-Yu Ou[2] and Jianye Ching[3]

[1]Ph.D. Student, Dept of Construction Engineering, National Taiwan University of Science and Technology, # 43, Sec. 4, Keelung Rd., Taipei, 106, Taiwan, R.O.C; PH +886-2-27333141(ext. 7519); email: D9505001@mail.ntust.edu.tw.
[2]Professor, Dept of Construction Engineering, National Taiwan University of Science and Technology, # 43, Sec. 4, Keelung Rd., Taipei, 106, Taiwan, R.O.C; PH +886-2-27376578; email: ou@mail.ntust.edu.tw.
[3]Associate Professor, Dept of Civil Engineering, National Taiwan University, #1, Sec. 4, Roosevelt Rd., Taipei, 10617, Taiwan, R.O.C; PH +886-2-33664328 Fax: 886-2-23631558; email: jyching@gmail.com.

ABSTRACT

Base heave stability is an important issue for excavations in clay. Many design equations for base heave stability are simplified for ease of use and typically have a conservative bias for design safety. In this study, three popular base heave design equations are calibrated based upon real case histories with wide excavation. It is found that modified Terzaghi's method is nearly unbiased, while Bjerrum and Eide's and slip circle methods are obviously biased to the conservative side. The model uncertainty associated with Bjerrum and Eide's method is the lowest, while that associated with the slip circle method is the highest. The reliability levels for the design code regulations are verified, and reliability-based design charts are provided. The conclusions can be applied for reliability-based design of base heave stability for wide excavations in clay.

INTRODUCTION

For the base heave stability of deep excavations, the most popular design equations, such as the ones proposed by Terzaghi (1943) and Bjerrum and Eide (1956) as well as the slip circle method (JSA 1988, TGS 2001), usually employ reasonable assumptions to facilitate the calculation of closed-form factors of safety (FS). However, these assumptions may introduce systematic bias into the calculated FS. Hashash and Whittle (1996) reported that Terzaghi's and Bjerrum and Eide's methods are less conservative than the MIT-E3 model in deep clay deposits. Ukritchon et al. (2003) and Faheem et al. (2003) reported that base stability can be enhanced by incorporating the stiffness of wall embedment, which is not modeled by Terzaghi's and Bjerrum and Eide's methods. Furthermore, the staged construction

sequence, dewatering, wall stiffness and soil-wall interaction are typically not modeled in the simplified design equations. Up to date, the biases brought by these simplifications are still not well understood.

With the biases unknown, reliability-based design (RBD) may lead to recommendations inconsistent to engineering practices. For instance, Goh et al. (2008) considered Terzaghi's and Bjerrum and Eide's design equations for RBD. Without considering the possible biases, it was concluded that the required FS to achieve failure probability of 0.01 is about 2.0. This value is quite high compared to 1.5 required in codes (JSA 1988). Wu et al. (2010) further considered the impact of spatial variability in soil shear strengths, without considering the possible biases. The required FS is reduced to the range of 1.4-1.9, yet in overall still higher than the recommended 1.5. Wu et al. (2010) also studied the slip circle equation, and the required FS to achieve 0.01 failure probability is also higher than the recommended 1.2 in codes (JSA 1988; TGS 2001). A possible explanation for the aforementioned inconsistency between analytical studies and engineering practices is that these design equations are more or less biased to the conservative side.

In this paper, the bias and uncertainty associated with each of the three design equations are calibrated by using real case histories with wide excavation where the excavation depths are less than the excavation widths. The calibration results could provide a basis for RBD of the base heave stability for wide excavations in clay.

DESIGN EQUATIONS FOR BASE HEAVE STABILITY

Before studying the model bias and uncertainties, three design equations are briefly reviewed in this section. The most commonly used design equations for base heave stability are Terzaghi's, Bjerrum and Eide's and slip circle methods, and the calculated FS, denoted by FS_C and the schematic diagrams of those methods are summarized in Table 1. Terzaghi's and Bjerrum and Eide's equations are based on bearing capacity theory, while the slip circle equation is empirical and is widely employed in Asia countries as design codes (JSA 1988, TGS 2001) for a long period of time. Most symbols used in the equations are explained in the schematics. The arc segment (e.g. $\overline{bde}$) in the superscript denotes the arc along which the soil parameter is taken averaging. The average soil parameters along arcs will be mentioned as "arc-average", e.g., $s_u^{\overline{bde}}$ is the arc-average undrained shear strength s_u along *bde*.

RESULTING MEAN VALUES AND C.O.V.S OF FS_C FOR ALL CASES

In this study, fifteen case histories are collected to calibrate the model bias and uncertainties of the design equations. Besides the fifteen real cases, there are four numerical cases done by Hashash and Whittle (1996) with the MIT-E3 soil model. Except 2 cases, all cases are wide excavation cases where excavation depths less than the excavation widths. The estimates of s_u are according to the mobilized s_u (s_u(mob)) as suggested by Bjerrum (1972) for undrained shear strength for field vane shear s_u(FV) and Mesri and Huvaj (2007) for triaxial laboratory tests with the strain rate correction in accordance with Kulhawy and Mayne (1990) in this study.

Table 1. Summary of the Most Commonly Used Design Equations for Base Heave Stability.

Methods	Design equation	Schematic diagram
Modified Terzaghi	For $H_d \le d_T$ $FS_C = \dfrac{5.7 s_u^{\overline{bde}} d_T + s_u^{\overline{ab}} H_e}{(\gamma^{\overline{ab}} H_e + q_s) d_T}$ (1) For $H_d > d_T$ $FS_C = \dfrac{5.7 s_u^{\overline{bde}} d_T + s_u^{\overline{af}} H_e + s_u^{\overline{fb}} (H_d - d_T)}{(\gamma^{\overline{af}} H_e + q_s) d_T}$ (2)	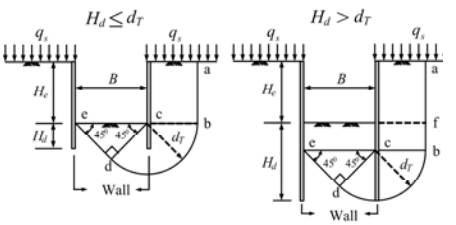
Bjerrum and Eide's	$FS_C = \dfrac{N_c \cdot s_u^{\overline{cdef}}}{\gamma^{\overline{ab}} H_e + q_s}$ (3) $N_c = 5(1+0.2\dfrac{H_e}{B})(1+0.2\dfrac{B}{L}) \le 7.5 \cdot (1+0.2\dfrac{B}{L})$ (4)	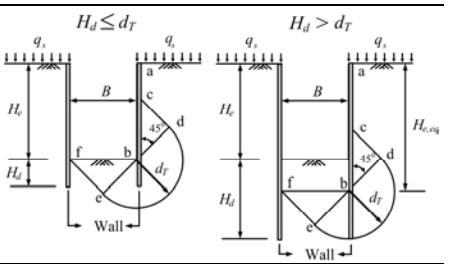
Slip circle	$FS_C = \dfrac{M_r}{M_d} = \dfrac{s_u^{\overline{cbde}} r^2 \cdot \left[\dfrac{\pi}{2} + \cos^{-1}\left(\dfrac{H_s}{r}\right)\right]}{\gamma^{\overline{ab}} \cdot H_e \cdot \dfrac{r^2}{2} + q_s \cdot \dfrac{r^2}{2}}$ (5)	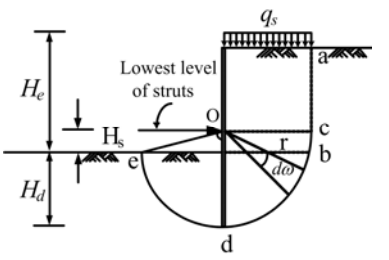

As seen in the preceding section, the calculated factors of safety FS_C for various design equations are functions of arc-average soil parameters and surcharge. Therefore, FS_C is in principle uncertain because arc-average soil parameters and surcharge are always uncertain. The quantification of the model bias and uncertainties requires the estimation of the mean value and coefficient of variation (c.o.v.) of the FS_C for each case history. The mean value of FS_C, denoted by μ_{FSc}, can be readily evaluated by replacing the arc-average s_u and unit weights in Eqs. (1), (3) and (5) with their mean values and by replacing q_s by its nominal value. Accurate estimates for the surcharge pressures are not possible. From sensitivity analysis, the nominal surcharge pressure in the range of 5-20 kPa is found to have insignificant effect on the analysis results, so a typical value of 10 kPa for design surcharge pressure is adopted in this study. FS_C depends on the arc-average s_u, arc-average unit weight and surcharge. Therefore, the c.o.v. of FS_C, denoted by δ_{FSc}, should depend on the c.o.v.s of these parameters. In this study, the δ_{FSc} is calculated by assuming the parameters in design equations are independent, and the denominator and numerator

of the design equations are assumed be lognormally distributed and are independent.

Based on the mean values and c.o.v.s of all input parameters, the resulting mean values and c.o.v.s of FS_C for all cases and for all design equations are plotted in Fig. **1**. By comparing μ_{FSc} for the failure cases (open circles in the figure) with the limit state FS = 1, it is obvious that modified Terzaghi's equation is nearly unbiased, while the other two design equations are more or less biased to the conservative side. Modified Terzaghi's and the slip circle equations perform well with respect to the non-failure cases (solid circles), judging from the fact that none of the non-failure cases has μ_{FSc} less one. For Bjerrum and Eide's equation, three non-failure cases have μ_{FSc} less than one. This may be either due to the bias in the equation or due to the higher variability in FS_C.

It is of interest to compare the results shown in Fig. **1** with well documented numerical failure cases. One set of such examples are the numerical failure cases investigated by Hashash and Whittle (1996) by using the MIT-E3 model. For all the failure cases, the Direct Simple Shear (DSS) undrained shear strength and unit weights profiles are known. The excavation stages are simulated by incrementally removing soil layers with thickness of 2.5 m, up to the stage of numerical divergence. As a result, the FS for the excavation geometries at the point of divergence should be close to and slightly less than one.

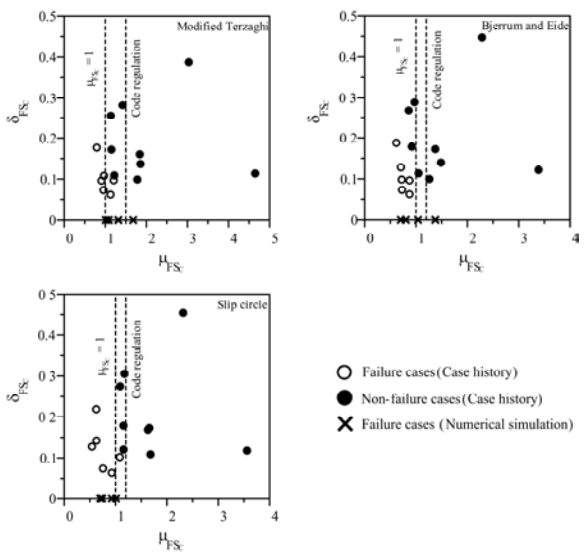

Figure 1. Relation between mean values and c.o.v.s of FS_C for all cases and for all design equations.

With the excavation geometries at the point of divergence, the given DSS s_u profiles and soil unit weights are therefore taken to obtain the depth-dependent trends for s_u(mob) and unit weight, and FS_C for the three design equations can then be calculated based on these trends. The resulting FS_C are plotted on the horizontal axes in Fig. **1**. There is no uncertainty in the soil properties for numerical cases. The FS_C for these numerical failure cases should be directly compared to the open circles (real failure cases) in Fig. 1. However, as a first glance, the FS_C for these cases seem to have different patterns compared to the open circles. Moreover, the FS_C for the four

numerical cases can be either all less than one (slip circle), all greater than one (modified Terzaghi) or the mixture of the above two (Bjerrum and Eide), depending on which design equation is used. In other words, the FS predicted by the numerical MIT-E3 model is on average more conservative than modified Terzaghi's equation, on average less conservative than the slip circle equation and on average similar to Bjerrum and Eide's equation. The above conclusion for the comparisons over modified Terzaghi's and Bjerrum and Eide's equation is largely consistent to the findings by Hashash and Whittle (1996).

CALIBRATION OF MODEL FACTOR

As discussed in the preceding section, the actual FS (FS_A) for the failure cases (they should be exactly unity) may be different from μ_{FS_C} for the three design equations. It is quite possible that FS_C from the design equations should be corrected by a model factor:

$$FS_A = \alpha \cdot FS_C \tag{6}$$

where FS_A is the actual FS; α is the model factor; FS_C is the FS calculated from the design equations. Moreover, α should not be a fixed number among all cases because the deviations between FS_A and FS_C vary throughout all cases. In this study, α is modeled as a lognormal random variable with mean value μ_α and c.o.v. δ_α. Note that these mean value and c.o.v. should depend on the adopted design equation. Since FS_C is lognormal, FS_A is also lognormal. Moreover, the mean value and c.o.v. of FS_A are

$$\mu_{FS_A} = \mu_\alpha \mu_{FS_C} \qquad \delta_{FS_A} = \sqrt{\left(1+\delta_\alpha{}^2\right)\cdot\left(1+\delta_{FS_C}^2\right)-1} \tag{7}$$

by assuming independence between α and FS_C.
Based on the principle of maximum likelihood, the resulting optimal estimates for $(\mu_\alpha, \delta_\alpha)$ are listed in Table 2 for all three design equations.

Table 2. Summary of Mean Values and c.o.v.s of the Model Factor for All Design Equations.

	Modified Terzaghi	Bjerrum-Eide	Slip circle
μ_α	1.01	1.31	1.39
δ_α	0.072	0.064	0.21
Recommended FS in codes	1.5	1.2	1.2
Recommended FS after bias correction	1.52	1.57	1.67

RELIABILITY-BASED DESIGN FOR BASE HEAVE STABILITY

With the model factors calibrated, the base heave failure probability can then be expressed as a function of μ_{FS_A} and δ_{FS_A} as follows:

$$P\left(FS_A<1\right)=\Phi\left(-\frac{\log\left(\mu_{FS_A}\Big/\sqrt{1+\delta_{FS_A}^2}\right)}{\sqrt{\log\left(1+\delta_{FS_A}^2\right)}}\right)=\Phi\left(-\beta\right) \tag{8}$$

where β is the reliability index, and μ_{FS_A} and δ_{FS_A} are related to μ_α, μ_{FS_C}, δ_α and δ_{FS_C} through Eq. (7). The values of μ_α and δ_α can be found in Table 2. For reliability-based design, a design engineer is given the target reliability index β^T, and he/she must determine the required μ_{FS_C} to achieve this target level of safety. If an estimate of δ_{FS_C} is available, the design engineer can easily find the required μ_{FS_C} by inverting Eq. (8):

$$\mu_{FS_C}=\frac{\sqrt{\left(1+\delta_\alpha{}^2\right)\cdot\left(1+\delta_{FS_c}^2\right)}\cdot\exp\left[\beta^T\sqrt{\log\left(1+\delta_\alpha{}^2\right)+\log\left(1+\delta_{FS_c}^2\right)}\right]}{\mu_\alpha} \tag{9}$$

Fig. 2 show the relation between required μ_{FS_C} and β^T for various levels of δ_{FS_C} for modified Terzaghi's, Bjerrum and Eide's and the slip circle design equations, respectively. Note that the required design FS μ_{FS_C} is the FS based on s_u(mob), so the design engineer needs to make sure all s_u measurement to be converted into s_u(mob) when calculating the FS.

Note that the aforementioned design requires an estimate for δ_{FS_C}. From Fig. 2, it is clear that the resulting design FS (i.e. μ_{FS_C}) is very sensitive to the δ_{FS_C} estimate, hence the estimation for δ_{FS_C} must be done cautiously. One will first need to estimate the c.o.v.s for all input parameters for the chosen design equation. They can be roughly estimated based on the statistics compiled by Phoon (1995) when site investigation is not already done.

As mentioned, the recommended FS in current codes for modified Terzaghi's, Bjerrum and Eide's and slip circle methods are 1.5, 1.2 and 1.2, respectively. For the fifteen real case histories, most δ_{FS_C} ranges from 0.05 to 0.2. Under this range, the required FS for modified Terzaghi's equation corresponds to β^T of 1.8-4.6, for Bjerrum and Eide's equation corresponds to β^T of 2-5, and for the slip circle equation corresponds to β^T of 1.6-2.4. Note that the narrow range of 1.6-2.4 for the slip circle method is because the c.o.v. of its model factor is relatively large, so the change of δ_{FS_C} does not affect the β^T range as much as the other two equations. Further

investigation for Fig. 2 reveals that when δ_{FS_C} is in the range of [0.2, 0.3], the target reliability indices for the three design equations corresponding to the code regulations do not differ much.

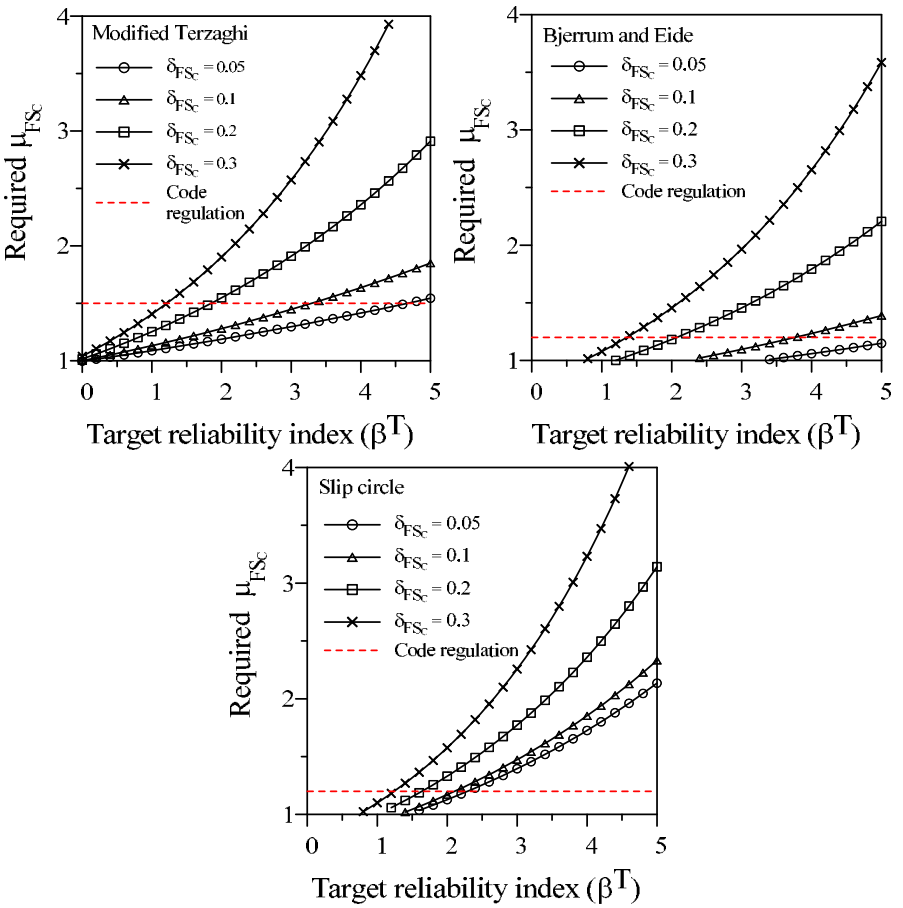

Figure 2. Relation of β^T and required μ_{FS_C} under various δ_{FS_C} for different design equations.

CONCLUSIONS

In this study, the three popular design equations of base heave are calibrated based on real case histories with wide excavation. The actual FS is expressed as the FS calculated from design equations corrected by a model factor α due to model uncertainty, and the probabilistic characterization of model factor for three design equations are calibrated from real case histories. From the calibration results, modified Terzaghi's equation is the least biased with a reasonably small model c.o.v., while Bjerrum and Eide's equation is somewhat more conservative with the smallest model c.o.v. The slip circle equation is the most conservative with the largest model c.o.v. It is interesting to see that modified Terzaghi's and Bjerrum and Eide's equations, which are derived from bearing capacity theories, seems to have less model uncertainties than the slip circle, which is fundamentally more empirical.

Before the bias correction, the recommended FS in current codes for the three

design equations are rather non-uniform: 1.5 for modified Terzaghi's equation and 1.2 for Bjerrum-Eide's and slip circle equations. Nonetheless, after the bias correction, the resulting recommended FS are quite uniform: 1.52, 1.57 and 1.67 for modified Terzaghi's, Bjerrum-Eide's and slip circle equations, respectively. Note that for the slip circle equation, the recommended FS after correction is the largest: this is because the model uncertainty for the slip circle equation is the largest.

For the purpose of reliability-based design, design charts that relate required FS and target reliability index are provided for the three design equations and for various levels of FS c.o.v. With the target reliability index prescribed, the required design FS can be obtained from these charts to facilitate reliability-based design for base heave stability for wide excavation.

REFERENCES

Bjerrum, L. and Eide, O. (1956). "Stability of strutted excavations in clay." *Geotechnique*, 6(1), 32-47.

Bjerrum, L. (1972). "Embankments on soft ground." *Proceedings of Specialty Conference on Performance of Earth and Earth supported Structures*, 2, 1-54.

Faheem, H., Cai. F., Ugai, K. and Hagiwara, T. (2003). "Two dimensional base stability of excavations in soft soils using FEM." *Computers and Geotechnics*, 30(2), 141-163.

Goh, A.T.C., Kulhawy, F.H. and Wong, K.S. (2008). "Reliability assessment of basal-heave stability for braced excavations in clay." *Journal of Geotechnical and Geoenvironmental Engineering*, ASCE, 134(2), 145-153.

Hashash, Y.M.A. and Whittle, A.J. (1996). "Ground movement prediction for deep excavations in soft clay." *Journal of Geotechnical Engineering*, ASCE, 122(6), 474-486.

Japanese Society of Architecture (JSA). (1988). *Guidelines of Design and Construction of Deep Excavation*, Tokyo, Japan.

Kulhawy, F.H. and Mayne, P.W. (1990). *Manual on Estimating Soil Properties for Foundation Design*, Report EL-6800, Electric Power Research Institute, Palo Alto.

Mesri, G. and Huvaj, N. (2007). "Shear strength mobilized in undrained failure of soft clay and silt deposits." *Geotechnical Special Publication 173*, ASCE Geo-Denver.

Phoon, K.K. (1995). *Reliability-Based Design of Foundations for Transmission Line Structures*. Ph.D. Dissertation, Cornell University.

Terzaghi, K. (1943). *Theoretical Soil Mechanics*, Wiley, New York.

Taiwan Geotechnical Society (TGS). (2001). *Design Specifications for the Foundation of Buildings*, Taipei, Taiwan.

Ukritchon, B., Whittle, A.J. and Sloan, S.W. (2003). "Undrained stability of braced excavations in clay." *Journal of Geotechnical and Geoenvironmental Engineering*, ASCE, 129(8), 738-755.

Wu, S.H., Ou, C.Y., Ching, J. and Juang, C.H. (2010). "Reliability-based design for basal heave stability of deep excavations in spatially varying soils." submitted to *Journal of Geotechnical and Geoenvironmental Engineering*, ASCE. (in review)

Probabilistic Analysis of Shallow Foundations on Rocks Obeying Hoek-Brown Failure Criterion

Nut Mao[1], Tamara Al-Bittar[2] and Abdul-Hamid Soubra[3], M.ASCE

[1]PhD student, University of Nantes, GeM, UMR CNRS 6183, Bd. de l'université, BP 152, 44603 Saint-Nazaire, France; PH (33) 240 905 106; FAX (33) 240 905 109; email: nut.mao@univ-nantes.fr
[2]PhD student, University of Nantes, GeM, UMR CNRS 6183, Bd. de l'université, BP 152, 44603 Saint-Nazaire, France; PH (33) 240 905 106; FAX (33) 240 905 109; email: tamara.al-bittar@univ-nantes.fr
[3]Professor, University of Nantes, GeM, UMR CNRS 6183, Bd. de l'université, BP 152, 44603 Saint-Nazaire, France; PH (33) 240 905 108; FAX (33) 240 905 109; email: abed.soubra@univ-nantes.fr

ABSTRACT

A probabilistic analysis using Polynomial Chaos Expansion method is presented to compute the probability density function (PDF) of the ultimate bearing capacity of a strip footing resting on a rock mass and subjected to a vertical/inclined load. The rock is assumed to follow Hoek-Brown failure criterion. The kinematic approach of the limit analysis theory is used. The results of the vertical load case have shown that: (i) the Geological Strength Index GSI and the uniaxial compressive strength of the intact rock σ_c have the most significant weight in the variability of the ultimate bearing capacity, (ii) the non-normality of the input variables has a significant effect on the shape of the PDF of the ultimate bearing capacity and, (iii) a negative correlation between GSI and σ_c leads to less spread out PDF. Finally, it was shown in the inclined load case that the variability of the ultimate bearing capacity decreases with the increase of the footing load inclination.

INTRODUCTION

Traditionally, the stability analysis of shallow foundations resting on rocks is based on deterministic approaches. The present paper aims at determining the ultimate bearing capacity of a centrally loaded shallow strip footing (i.e. a footing subjected to a vertical or an inclined load) using a probabilistic analysis. The footing rests on a rock mass that follows the modified Hoek-Brown failure criterion. The deterministic models are based on the kinematic approach of limit analysis theory using translational multiblock failure mechanisms. The Polynomial Chaos Expansion (PCE) method (Huang et al. 2009) is used for the probabilistic analysis. Four uncertain parameters related to the modified Hoek-Brown failure criterion are modeled as random variables. These are the Geological Strength Index (*GSI*), the uniaxial compressive strength of the intact rock (σ_c), the intact rock material constant (m_i) and the disturbance coefficient (D). The paper is organized as follows: The first section aims at presenting the basic idea of the PCE methodology. It is followed by a presentation of the deterministic model used for the computation of the ultimate

bearing capacity. Finally, the probabilistic results are presented and discussed. The paper ends with a conclusion.

POLYNOMIAL CHAOS EXPANSION (PCE) METHODOLOGY

In the PCE methodology, the response of the mechanical model Γ with M input random variables is expressed by a PCE of order p pre-defined by the user as follows:

$$\Gamma_{PCE}(\xi) = \sum_{\beta=0}^{\infty} a_\beta \Psi_\beta(\xi) \cong \sum_{\beta=0}^{P-1} a_\beta \Psi_\beta(\xi) \quad (1)$$

where ξ are independent standard normal random variables representing the input random variables, a_β are unknown coefficients to be determined, Ψ_β are chosen as multidimensional Hermite polynomials and $P = (M+p)!/(M!\,p!)$ is the number of terms retained in the truncation scheme (which is equal to the number of unknown coefficients). To compute the coefficients a_β in Equation 1, two non intrusive methods have been proposed in literature: the projection and the regression approach. In this paper, the regression approach (Huang et al. 2009) is used. In this approach, each input random variable is assumed to take the roots of the one-dimensional Hermite polynomial (of one degree higher than the PCE order p). For M input random variables and a PCE of order p, the available collocation points (sample points) are the result of all possible combinations of these roots. Their number $\left\lfloor N = (p+1)^M \right\rfloor$ dramatically increases as p and M increase and it is always higher than the number P of the unknown coefficients (for $M \geq 2$). This leads to a linear system of equations whose number of equations is greater than the number of unknowns. Several attempts have been made in literature to select the most efficient collocation points among the N available ones in order to reduce the number of calls to the deterministic model. The approach proposed by Sudret (2008) is used herein. In order to check the goodness of fit of the PCE, the coefficient of determination R^2 is computed. The value $R^2 = 1$ indicates a perfect fit of the true model response Γ, whereas $R^2 = 0$ indicates a nonlinear relationship between the true model Γ and the PCE model Γ_{PCE}. Once the output approximation *via* a PCE is obtained, this PCE will be called meta-model and will be employed for the probabilistic analyses. The PDF and the statistical moments of the system response can be estimated. This can be done by simulating a large number of realizations of the standard normal variables on the meta-model using Monte Carlo technique. Another important advantage of the meta-model is that a global sensitivity analysis (GSA) based on Sobol indices can be performed analytically using the coefficients of the PCE (Sudret 2008). These indices indicate the contribution of each random variable or combination of random variables to the variability of the system response. This is important because it helps engineers in detecting the input uncertain parameters which have a significant influence in the variability of the system response.

DETERMINISTIC BEARING CAPACITY OF A CENTRALLY LOADED STRIP FOOTING

The modified Hoek-Brown failure criterion is used in this paper. This failure criterion only deals with intact rocks or heavily jointed rock masses. A heavily jointed rock mass involves sufficiently dense and randomly distributed joints so that in the scale of the problem, it can be regarded as an isotropic assembly of interlocking particles. Consequently, rocks with few discontinuities cannot be considered in this framework. This failure criterion can be described by the following equation (Hoek et al. 2002):

$$\sigma_1 - \sigma_3 = \sigma_c \left[m\left(\sigma_3 / \sigma_c\right) + s \right]^n \tag{2}$$

where σ_1 and σ_3 are respectively the major and minor principal stresses at failure and σ_c is the uniaxial compressive stress of the rock at failure. The parameters m, s and n are given by the following equations:

$$m = m_i . e^{\left(\frac{GSI-100}{28-14D}\right)}; \qquad s = e^{\left(\frac{GSI-100}{9-3D}\right)}; \qquad n = \left(1/2\right) + \left(1/6\right)\left[e^{-GSI/15} - e^{-20/3} \right] \tag{3}$$

In these equations, the geological strength index (*GSI*) characterizes the quality of rock masses, and it depends on the rock mass structure as well as the surface condition of joints (Hoek et al. 2002). On the other hand, the parameter m_i is the value of parameter m for intact rock and can be obtained from experimental tests. It varies from 4 for very fine weak rock like claystone to 33 for coarse igneous light-colored rock like granite. Finally, D is the disturbance coefficient. It varies from 0.0 for undisturbed in situ rock masses to 1.0 for very disturbed rock masses.

Two kinematically admissible failure mechanisms M1 and M2 based on the upper-bound theorem of limit analysis are used herein. They are described in Soubra (1999) in the case of a Mohr-Coulomb material whose failure criterion is linear. M1 is a translational symmetrical multiblock failure mechanism (Figure 1a) and is used for the computation of the ultimate bearing capacity of a vertically loaded strip footing. It is composed of $2k+1$ triangular rigid blocks (a central symmetrical block under the footing and $2k$ symmetrical rigid blocks at both sides of the footing). This mechanism can be completely described by $2k$ angular parameters which are α_i (i=1, …, k-1), β_i (i=1, …, k) and θ. On the other hand, M2 is a translational non-symmetrical multiblock failure mechanism (Figure 1b) and is suitable for the calculation of the ultimate bearing capacity of obliquely loaded strip foundations. This mechanism is composed of k triangular rigid blocks. It can be completely described by $2k-1$ angular parameters which are α_i (i=1, …, k-1) and β_i (i=1, …, k).
For the case of rock masses obeying the modified Hoek-Brown non linear failure criterion, Yang and Yin (2005) have replaced this criterion by an equivalent linear Mohr-Coulomb failure criterion (Figure 2). Recently, a more rigorous and efficient approach which preserves the original non linear form of the modified Hoek-Brown failure criterion, was proposed by Saada et al. (2008). A similar approach is used herein for both M1 and M2 mechanisms. Notice that the energy dissipation takes

place at the discontinuity surfaces d_i between the material at rest and the material in motion, and at the discontinuity surfaces l_i within the radial shear zone (Figure 1). In this paper, the inter-block velocities $v_{i,i+1}$ will be assumed as being inclined at angles $\varphi_{i,i+1}$ to lines l_{i+1} (Figure 3) where $\varphi_{i,i+1}$ will be different along the different lines l_{i+1}. Also, the block velocities v_{i+1} will be assumed as being inclined at angles φ_{i+1} to lines d_{i+1} (Figure 3) where φ_{i+1} will be also different along the different lines d_{i+1}.

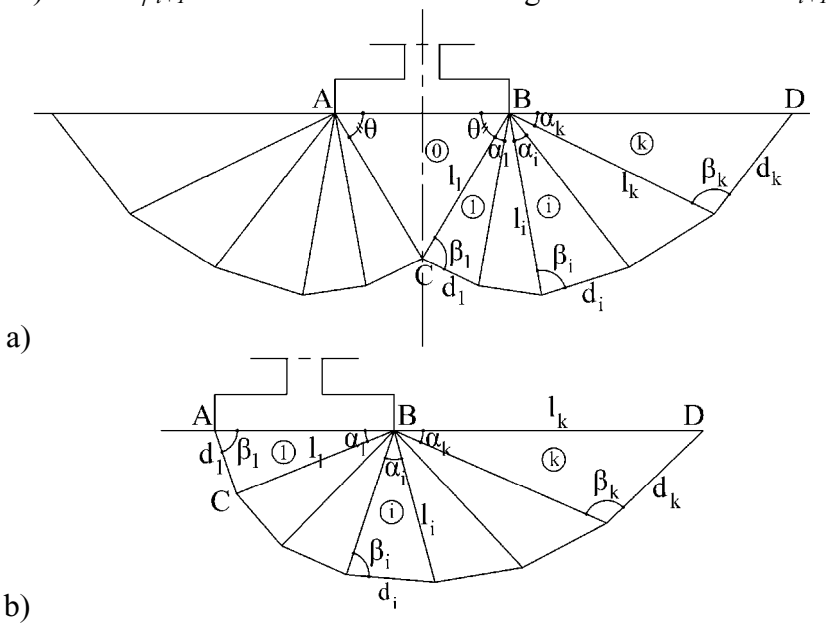

Figure 1. Failure mechanisms for the computation of the bearing capacity in the case of a) vertical load and b) inclined load.

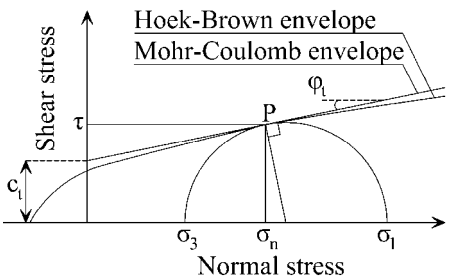

Figure 2. Failure envelope the Hoek-Brown and the equivalent mechanism Morh-Coulomb failure criteria.

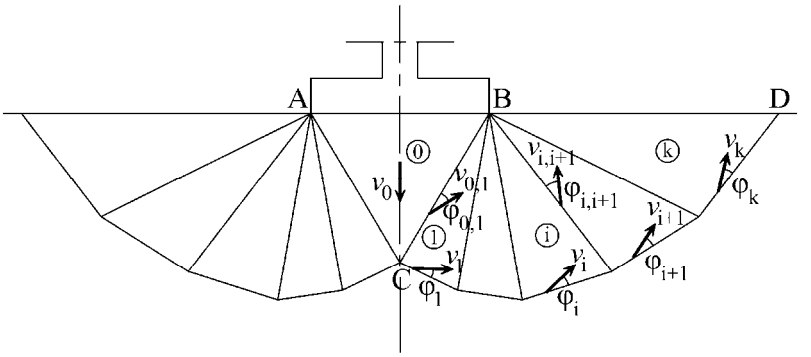

Figure 3. Velocity field of M1 mechanism.

For both M1 and M2 mechanisms, it was found that an upper-bound of the ultimate bearing capacity can be defined as:

$$q_u = \frac{1}{2}\gamma B_0^2 N_\gamma + qB_0 N_q + \sigma_c B_0 N_{\sigma_c} \quad (4)$$

where N_γ, N_q *and* N_{σ_c} are non-dimensional functions which can be expressed in terms of the mechanism geometrical parameters and in terms of the tangential frictional angle φ_{i+1} and $\varphi_{i,i+1}$ where i=0, …, k-1. For each failure mechanism, the ultimate bearing capacity is obtained by minimization with respect to the angular parameters of the failure mechanism and with respect to φ_{i+1} and $\varphi_{i,i+1}$.

PROBABILISTIC NUMERICAL RESULTS

The aim of this section is to present the probabilistic results of the ultimate bearing capacity. The footing of width B_0=1m is placed on a weightless (γ=0) rock mass, with no surcharge loading on the ground surface (q=0). The illustrative values of the statistical moments of the random variables as well as the correlation coefficient are presented in Table 1 [Hoek 1998 and Hoek et al. 2002].

Table 1. Input random variables and their statistical characteristics.

Variables	Mean	COV	Probability distribution	Coefficient of correlation ρ
GSI [-]	25	10%	Log-normal	$-0.75 \leq \rho(GSI, \sigma_c) \leq +0.75$
m_i [-]	8	12.5%	Log-normal	
σ_c [MPa]	10	25%	Log-normal	
D [-]	0.3	10%	Log-normal	

CASE OF A VERTICAL LOAD

Optimal PCE order and Sobol indices

The coefficient of determination R^2 of the PCEs of orders 2, 3, 4 and 5 were computed. It was found that R^2 of order 4 and order 5 are close to 1 (i.e. higher than 0.999999). Consequently a PCE of order p=4 provides a good fit between the meta-model and the true model, and will be adopted in the rest of the probabilistic studies performed in this paper. For the prescribed values of the statistical moments of the input random variables presented in Table 1, the Sobol indices have been computed. The Sobol indices of parameter σ_c (0.5378) and *GSI* (0.3141) are much higher than those of parameters m_i (0.0866) and D (0.0308). A thorough experimental investigation will thus be required by the engineer for only the influential parameters (i.e. *GSI* and σ_c) to obtain reliable results of the system response.

Effect of the coefficient of variation (COV) of the random variables

The effect of COV of the random variables is presented in Table 2. This table shows that the COV has practically no effect on the mean value of the ultimate bearing capacity and that the increase in the COV of parameters *GSI* or σ_c has a significant effect on the variability of the ultimate bearing capacity. Table 2 also

shows the effect of COV on Sobol indices. One can note that the increase in COV of a certain variable increases its Sobol index and decreases the Sobol indices of the other variables.

Table 2. Effect of the coefficients of variation of the input random variables on the statistical moments (μ, σ) of the bearing capacity and on Sobol indices.

Coefficient of variation		μ	σ	SU(GSI)	SU(m_i)	SU(σ_c)	SU(D)
COV(GSI)	5%	1.4937	0.4396	0.1031	0.1165	0.7207	0.0417
	10%	1.5056	0.5129	0.3141	0.0866	0.5378	0.0308
	15%	1.5254	0.6258	0.5063	0.0594	0.3712	0.0209
COV(m_i)	6.25%	1.5059	0.4948	0.3384	0.0233	0.5789	0.0332
	12.5%	1.5056	0.5129	0.3141	0.0866	0.5378	0.0308
	18.75%	1.5050	0.5426	0.2805	0.1743	0.4807	0.0275
COV(σ_c)	12.5%	1.5052	0.3895	0.5451	0.1502	0.2333	0.0534
	25%	1.5056	0.5129	0.3141	0.0866	0.5378	0.0308
	37.5%	1.5051	0.6700	0.1840	0.0507	0.7093	0.0181
COV(D)	5%	1.4937	0.5062	0.3225	0.0888	0.5515	0.0080
	10%	1.5056	0.5129	0.3141	0.0866	0.5378	0.0308
	15%	1.5254	0.5239	0.3013	0.0832	0.5168	0.0657

Effect of the correlation coefficient and the distribution type of the random variables

The PDFs presented in Figure 3 show that the increase in the coefficient of correlation between *GSI* and σ_c significantly increases the variability of the ultimate bearing capacity. The smallest response variability is thus obtained for negatively correlated variables.

Concerning the distribution type of the input random variables, two cases of normal and nonnormal (i.e. log-normal) random variables combined with two configurations of COVs were considered (Figure 4).

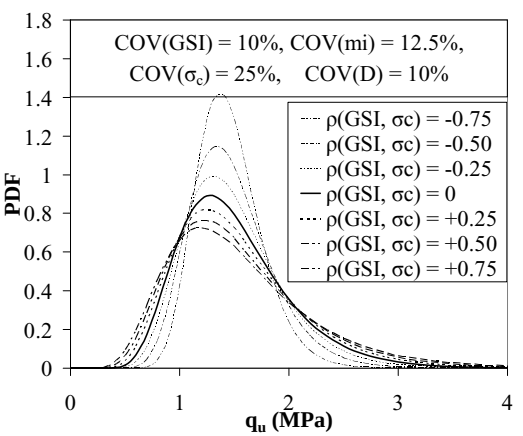

Figure 3. Influence of ρ(GSI, σ_c) on the PDF of the bearing capacity.

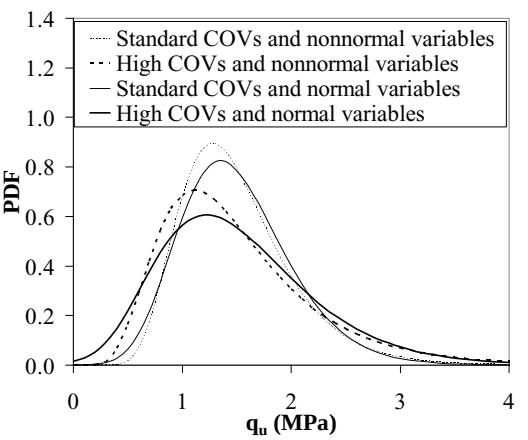

Figure 4. Influence of the distribution type of the input random variables on the PDF of the bearing capacity for two different sets of COVs.

The "standard COVs" corresponds to the reference case presented in Table 1 while the "high COVs" corresponds to these values increased by 50%. For these two sets of COVs, the non-normality of the distribution type of the input random variables has significant influence on the shape of the PDF of the ultimate bearing capacity as can be seen from Figure 4; the influence being more important for the case of "high COVs" than the case of "standard COVs". Notice however that the probability distribution of the random variables has practically no influence on the mean and the standard deviation of the system response and consequently, no effect on the coefficient of variation of this response (results not shown here).

CASE OF AN INCLINED LOAD

Figure 5 shows the PDFs of the ultimate bearing capacity for different values of the load inclination α. One can see that the variability of the ultimate bearing capacity is significant in the case of small load inclination α and it decreases when α increases. This may be explained by the fact that the response involved in the analysis is the ultimate bearing capacity. Thus, it would be logical to have the most significant variability when the punching is most predominant (i.e. for small load inclination).

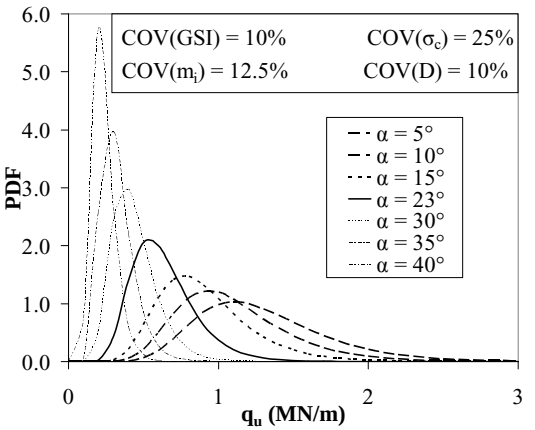

Figure 5. PDF of the bearing capacity for different cases of load inclination.

Table 3. Statistical moments of the ultimate bearing capacity for different cases of load inclination α.

α (°)	5	10	15	23	30	35	40
μ	1.3032	1.1004	0.9090	0.6367	0.4405	0.3260	0.2325
σ	0.4443	0.3758	0.3104	0.2178	0.1509	0.1119	0.0800
COV	0.3410	0.3415	0.3415	0.3421	0.3426	0.3432	0.3439
δ	1.0627	1.0672	1.0693	1.0698	1.0709	1.0712	1.0742
κ	2.0710	2.0928	2.1113	2.0969	2.1051	2.095	2.1153

Table 3 shows that the mean and standard deviation of the ultimate bearing capacity vary with the load inclination. However, the coefficient of variation, the skewness δ and the kurtosis κ do not vary with this inclination; this observation may be explained by the fact that the variability of the input random variables is similar for the different load inclinations.

CONCLUSION

A probabilistic analysis of a centrally loaded strip foundation resting on a rock mass obeying Hoek-Brown failure criterion has been performed. The deterministic model was based on the kinematical approach of the limit analysis theory. The polynomial chaos expansion methodology was used for the probabilistic analysis. The uncertain parameters involved in the analysis were the Geological Strength Index (*GSI*), the uniaxial compressive strength of the intact rock (σ_c), the intact rock material constant (m_i) and the disturbance coefficient (D). For the vertically loaded footing, it was shown that (i) a fourth order PCE is sufficient to accurately represent the system response; (ii) the parameters m_i and D have smaller effect on the variability of the ultimate bearing capacity compared to the other two parameters *GSI* and σ_c; (iii) the assumption of negatively correlated variables leads to less spread out PDF of the ultimate bearing capacity; (iv) the non-normality of the input random variables has a significant impact on the shape of the PDF of the ultimate bearing capacity, there is an almost no effect on its mean and standard deviation; (v) the COV of the random variables has practically no effect on the mean value of the ultimate bearing capacity, the increase in the COV of the parameters *GSI* or σ_c has a significant effect on the variability of the ultimate bearing capacity; (vi) the increase in the COV of a certain variable increases its Sobol index (i.e. it increases its weight in the variability of the system response) and decreases the Sobol indices of the other variables. For the inclined load case, it was found that the variability of the ultimate bearing capacity decreases with the increase of the footing load inclination; however the coefficient of variation of this bearing capacity is constant regardless of the load inclination.

REFERENCES

Hoek, E. (1998). "Reliability of Hoek-Brown estimates of rock mass properties and their impact on design." Technical note. *Int. J. Rock. Mech. Mining Sci*., 35, 63-68.

Hoek, E., Carranze-Torres, C., Corkum, B. (2002). "Hoek-Brown failure criterion-2002 edition." *In: Proceeding of the North American rock mechanics society meeting*, Toronto, 267-73.

Huang, S. P., Liang, B., Phoon, K. K. (2009). "Geotechnical Probabilistic Analysis by Collocation-based Stochastic Response Surface Method: An EXCEL Add-in Implementation." *Georisk 2009*, 3(2), 75-86.

Saada, Z., Maghous, S., Garnier, D. (2008). "Bearing capacity of shallow foundations on rocks obeying a modified Hoek–Brown failure criterion. Comput." *Comp. and Geotech*., 35, 144–54.

Soubra, A. H. (1999). "Upper-bound solutions for bearing capacity of foundations." *J. Geotech. Geoenviron. Eng.*, ASCE , 125(1), 59-68.

Sudret, B. (2008). "Global sensitivity analysis using polynomial chaos expansion." *Reliab. Eng. And System Safety*, 93, 964-979.

Yang, X. L., and Yin, J. H. (2005). "Upper bound solution for ultimate bearing capacity with a modified Hoek-Brown failure criterion." *Int. J. Rock. Mech. Mining Sci.*, 42, 550-60.

Influence of aging on the mechanical behavior of Municipal Solid Waste

A. Nayebi[1], N. Shariatmadari[2], M. H. Hamzeie Tehrani[3], and P. Oskouie[4],

[1]M. Sc. School of Civil Engineering, Iran University of Science and Technology, P. O. Box 16765-163, Narmak, Tehran, IRAN, email: ahmadnayebi@civileng.iust.ac.ir
[2]Associated Professor, School of Civil Engineering, Iran University of Science and Technology, P. O. Box 16765-163, Narmak, Tehran, IRAN. PH (98) 21-77240093, FAX (98) 21-77240398; email: shariatmadari@iust.ac.ir
[3]M. Sc. School of Civil Engineering, Iran University of Science and Technology, P. O. Box 16765-163, Narmak, Tehran, IRAN, email: mhh_tehrani@civileng.iust.ac.ir
[4]B. Sc. School of Civil Engineering, Iran University of Science and Technology, P.O. Box 16765-163, Narmak, Tehran, IRAN, email: pedramoskouie@civileng.iust.ac.ir

ABSTRACT

Study of the mechanical behavior of Municipal Solid Waste (MSW) is accompanied by many complications. Great interest in considering the most parameters involved in this behavior caused the achievement of useful properties of Municipal Solid Waste in recent years. These parameters are waste composition, leachate recirculation, unit weight, moisture, weather condition and aging. However, in the literature, researchers take into account all these parameters but the effect of age is not clearly obtained and its influence is not systematically measured. Impact of this factor on the mechanical behavior of the solid waste is quite complex. Some researchers have made conclusion that, when the waste's age increases, the strength would be diminished, but there are also some indications that the strength of the solid waste is increased by the growth of age (Machado et al. 2008).

In this paper, Large Scale direct Shear tests are applied on samples obtained from Iranian MSW landfills. The results show that mechanical behavior of MSW is significantly relative to the changes of composition with time (aging). As the composition becomes more monotonous the strength increases.

INTRODUCTION

By considering daily increase in population on earth and growth of production and consumption all over the world, waste production and its issues have become one of the serious subjects that governments are facing today. As the result, waste management or upper, materials cycle management has become one of the most main and important elements of sustainable development. Although, there have been lots of efforts made such as reducing waste production (Revising the consumption pattern), reusing some materials (Reusing the glass) or utilization by recycling (departing and reusing paper as cartoon) in order to reduce buried waste or even after this process, reducing the volume of waste to a very tiny amount by burning or composting, there

will be need to bury the burned waste or the compost leftover. According to above statements, necessity of secure and hygienic burying of waste is and going to be one of the priorities for human communities. As the result, we should extend available sanitary or provide new landfills.

Due to the fact that finding suitable location of landfill site is extremely subtle issue, there are some important points that have to be considered, for instance, some necessities such as living environment, mental impacts on the people living in the vicinity of landfills (if it be close to city) and financial effects in the intervals of transportation and transfer of waste with increase of distance must be considered for choosing the location of new landfill center. All these points have persuaded the city authorities and governments to develop the existing landfills.

This type of development may take place in two forms: 1) horizontal and 2) vertical development.

Since, vertical development of landfills will be feasible to the highest border allowed by site and design, the investors and policy makers of the waste burial mostly insist on the vertical development. It has resulted in the fact that some of these landfills built with approximately 100 meters height.

Although, the development of vertical landfills which hygienic burial has been performed there previously looks appropriate in the first view to environment, but immediate implementation of this task while neglecting complicated properties of waste, can danger the stability (slopes) of landfills.

Thanks to mentioned reasons, a secure design contains inevitable needs for prevention of financial, life and environmental losses which are going to occur if rupture takes place.

What is presently defined as Waste Mechanics requires extensive completion. Assessment of geometric specifications and thereafter waste behavior is a disputable issue due to changes in the materials present therein. The best method is testing on the real and intact sample. The intact sample cannot be provided; therefore the remolded materials must be placed in the test apparatus by reconsolidation. One of the existing problems is that waste structure will be destroyed by this method and meanwhile the obvious difference in the waste compositions may cause the fact that the sample cannot represent the behavior of the whole waste and also systematic change in ingredients will be problematic to clarify the impact of each of them.

Further to all above mentioned, the future changes (age) and their impact on the waste compositions as well as choosing a device with suitable size for sampling and testing are among the important points which should be considered in this research.

Although, the effect of biodegradation on the shear strength of the Municipal Solid Waste has been examined by various researchers, but there is no consensus in this regard, in the way that some of them such as Landva and Clark (1986), Turczynski (1988), Md. Sahadat Hossain (2002), Kolsch & Ziehmann (2004) demonstrated the decrease and some others such as Owesis (1993), Van Impe (1998), Machado et al (2008) and Nascimento (2007) demonstrated the increase of shear strength level with age increasing and biodegradation. The amounts of shear strength parameters provided by these researchers are also very different. Considering the fact that there is no specific definition of the waste deterioration level, the problem even becomes worse. The age parameter is quite important but other factors such as waste

compositions, climatic conditions of the area, percentage of humidity, method of landfill operation, waste permeability and daily cover may also have remarkable impacts on the waste deterioration.

Shear Strength. A few methods have been adopted by various investigators in their quest to establish reliable geotechnical strength parameters for municipal solid wastes. Shear strength is perhaps the most important mechanical property of solid waste in landfill engineering. Direct shear test was applied to majority of reported studies because of its simplicity, reliability and adaptability. The waste is typically screened to remove the large particles that would not fit into the standard direct shear equipment. For this purpose the Large Scale Direct Shear apparatus (with dimensions of 300 mm x 300 mm x 150 mm) is used in this research. A total of 36 large-scale direct shear tests were performed in this study.

Bio-Degradation. Available information indicates that drained shear strength of degraded MSW is similar to undegraded waste. For long-term behavior and due to the complexity of the waste degradation process, it is difficult to incorporate the time dependent degradation behaviour in the constitutive model. There is not adequate information regarding older waste behaviour.

Moreover, there is lack of information about the effect of degradation on mechanical behaviour of MSW in the literature.

Fiber. Fiber materials are usually composed of plastic, paper, textile etc. The influence of reinforcement on MSW shear behaviour is currently poorly understood. It was assumed that total shear strength is consisted of friction in shear plane and tensile force in fibers.

Testing Procedure. The waste samples used in laboratory tests were fresh, one year and three years old and presented the following average physical composition: wood (0.8%), paper (3.4%), plastic (6.7%), Fabric (0.19%), metal (1.61%), glass (2.1%), rubber (0.80%), PET (0.85%), wet waste (72%), Cardboard (4.75%) and Soil & Trash (6.8%).

The water content was determined by drying the specimens at 70º C, over a period of 24 hours, and was expressed as a percentage of wet weight of the material. The average water content for these samples was 74.24%, 149.85% and 86.55% respectively. The initial normal stress (20, 50, 100 and 200 kPa were applied) was then applied and the samples were allowed to consolidate under new load for approximately 24 hours. At this point, shear test was started. The tests were run at a very slow rate to create drained conditions. The strain rate used for direct shear test was 0.8 mm/ min. Tests were performed in accordance with ASTM Method for Direct Shear Tests of Soil under Consolidated Drained conditions. The tests were strain controlled and readings were taken at particular strain interval. However, the samples in many of studies did not undergo shear failure even at large strains. In our tests, we limited the relative displacement to 6 cm, or about 20% strain, in an attempt to remain within the relative operating range of the apparatus.

RESULTS AND DISCUSSION

Shear stresses were plotted against the corresponding applied horizontal displacement (Figure 1).

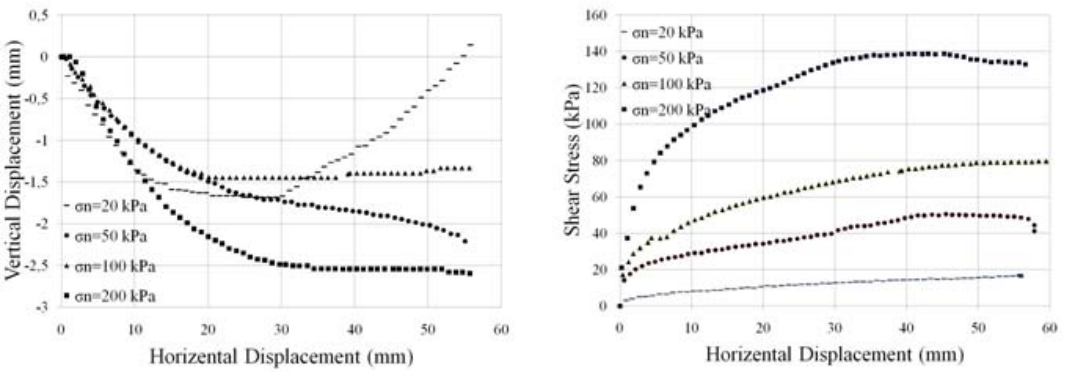

Figure1. Example results of Large Scale Direct Shear tests on one year old MSW (effect of normal stress).

The results indicated increase in shear strength with displacement which is compatible with findings of Gabr and Valero (1995), Thomas et al. (2000), Pelky et al. (2001), Md. Sahadat Hossain (2002) and Karimpour-Fard (2009).

As it is observed, with increasing the normal stress, the level of shear strength increases which indicates the frictional nature of these geo-materials. This result is compatible with findings of Mahler & De Lamare Netto (2003), zekkos (2005), Langer (2005) and Karimpour-Fard (2009). As the result of method for sample preparation that material are compacted in horizontal layers, fibers and plastic parts may locate parallel to forced shear plane. As another considerable factor, waste response is probably more dilative at lower normal stresses rather the case for reinforced earth materials (Figure 1). This dilative response is more effective in mobilizing fibrous materials during shear response. However, results show that in higher normal stresses the results tend to be more ductile and compressible which Aburatani et al. (1998) results also support this outcome.

Thanks to Figure 2, it can be stated that the old waste have more strength than fresh one. This increasing in strength is completely obvious in normal stresses more than 50 kPa.

This can be clarified by some following points:

A) With time passing, the bio-degradation rate (related to environmental circumstances) increases. On the other hand, in a long period mass loss due to biodegradation is high; but fiber content during time almost remains constant. It means an increase in fibers content in this period. Since strength of plastic fibers do not change in time so much, shear strength of MSW materials increases (Machado et al., 2008).

B) As we observed in Figure 2, the fresh sample has more tendency to be compressed rather than samples with one year and three years old. It should be noticed that this material after aging has less free void than fresh state.
By this way after a period, we have more monotonous waste (than fresh waste) so friction angle due these wastes were higher than fresh wastes (table 1).

Table 1. Effect of the age on the shear strength parameters (in normal stress =100 kPa)

Age (year)	Internal Friction Angle (ϕ) [Degrees]	Cohesion (C) [kPa]
Fresh	32.90	5.73
1	35.83	7.60
3	39.91	15.38

Strength increase with bio-degradation is compatible with findings of Owe is (1993), Van Impe (1998), Nascimento (2007), Zhan, T., Y. Chen, et al. (2008) and Machado et al (2008).

The reason for part B may be described by conversion of waste materials to soil like materials after a period. But the authors still work to know how metastasis can influence on mechanical behavior of waste materials.

CONCLUSION

Shear strength parameter is one of the most important subjects in landfill design. Because of this usage, all parameters that can affect shear strength must be considered. Considering that age has most potential to affect shear strength, in this research, we tried to represent this significance by utilizing a large scale direct shear apparatus and testing on samples aged fresh, one year and three years old which were obtained from Iranian landfills. The results indicated that shear strength of MSW is considerably relative to changes of composition with time (aging). This factor (age), also affects compressibility as the result of this fact that components become more monotonous (similar to soil).

Waste vertical displacement was decreased because of changing in composition which was resulted by increasing in time. This can be illustrated with bio-degradation causing change in natural shape of waste.

Changing in shape can be responsible for increasing in friction angle; this finding is compatible with Zhan, T., Y. Chen, et al. (2008).

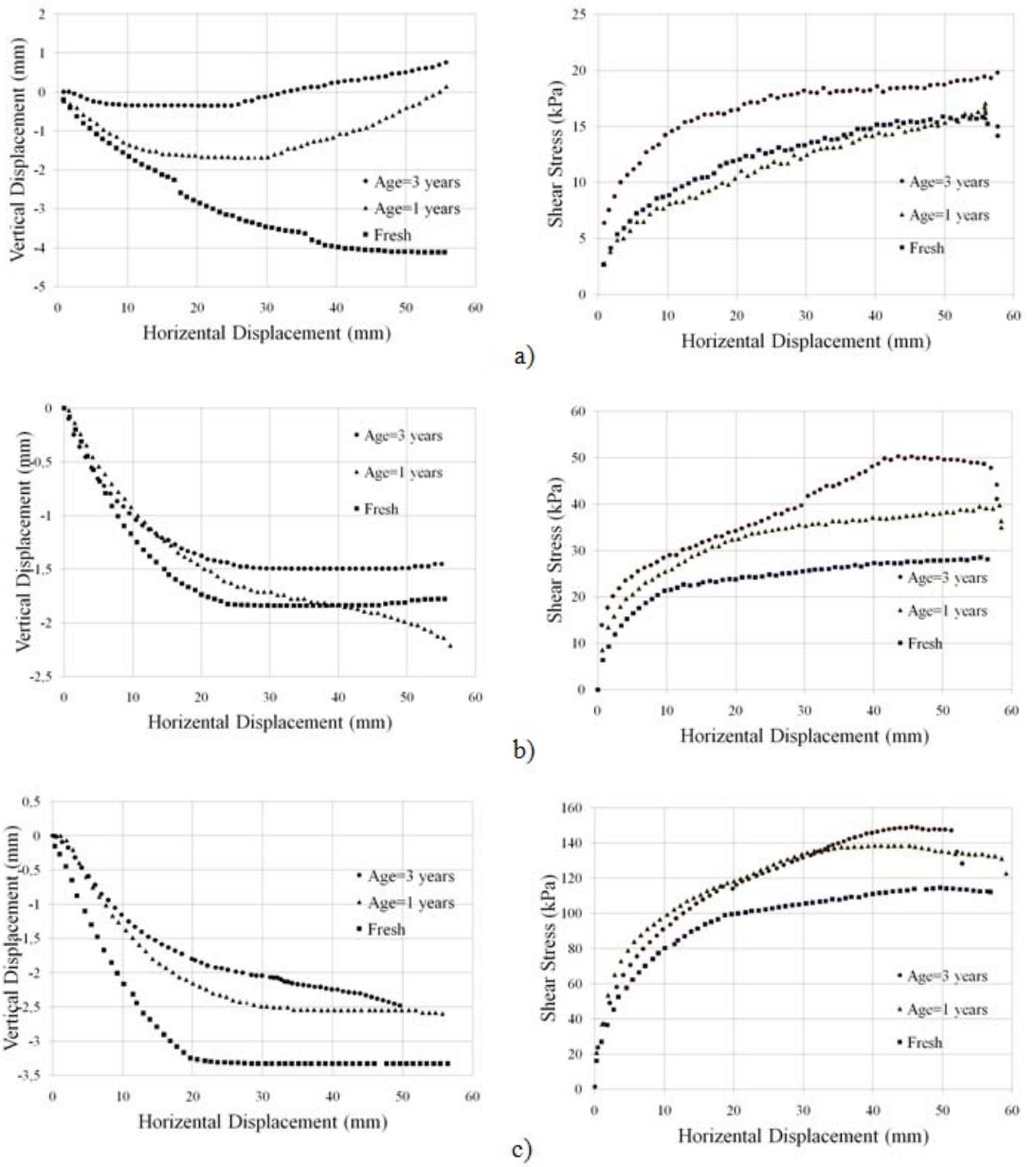

Figure 2. Effect of the age on the shear strength and waste behaviour with different normal stresses (a = 20 kPa, b = 50 kPa and c = 200 kPa).

REFERENCES

Aburatani, S., Matsui, T., Kamon, M., Wada, M. (1998), "Geotechnical Project."Environmental Geotechnics, Seco e Pinto (editor), 1998, pp. 95-100.

Gabr, M.A., and Valero, S.N. (1995), "Geotechnical properties of municipal solid waste." Geotechnical Testing Journal, Vol. 18:241-254.

Jessberger, H.L. and Kockel, R. (1993). "Determination and Assessment of the Mechanical Properties of Waste." Waste disposal by landfill - Green '93. R.W. Sarsby (edit).pp 313-322.

Karimpour Fard, M. (2009). " Mechanical Behavior of MSW materials with Different Initial Condition Under Static Loading." A dissertation submitted in partial satisfaction of the requirements for the degree of Doctor of Philosophy in Geotechnical Engineering – Iran University of Science and Technology (In Persian).

Kavazanjian, E., Jr. (2001a) "Mechanical Properties of Municipal Solid Waste," Proc. Sardinia '01 - 8th International Waste Management and Landfill Symposium, Environmental Sanitary Engineering Centre, Vol. III, pp. 415-424.

Kavazanjian, E., Jr. (2008) "The Impact of Degradation on MSW Shear Strength." Proc. '08, the Annual Meeting of the ASCE Geo-Institute, American Society of Civil Engineers Geotechnical Special Publication 177, pp. 224-231

Kölsch, F., Ziehmann, G. (2004), "landfill stability - risks and challenges." Waste Management World, May-June 2004, pp. 55-60.

Landva. A. O, and Clark. J. I. (1986), "Geotechnical testing of wastefill, Proceeding." 39th Canadian Geotechnical Conference Ottawa, 371-385.

Machado, Vilar, O.M., S.L and Carvalho, M.F. (2008). "Constitutive Model for Long Term Municipal Solid Waste Mechanical Behavior." Computers and Geotechnics, Vol 35, issue 5,pp. 775-790.

Machado, S.L , Carvalho, M.F. and Vilar, O.M. (2002). "Constitutive Model for Municipal Solid Waste." Journal of Geotechnical and Geoenvironmental Engineering, Vol. 128, No. 11, pp. 940-951.

Mahler. C. F, and De Lamare Netto. A. (2003), "shear resistance of mechanical biological pretreated demistic urban waste." Proceedings Sardinia 2003, 9th International Waste Management and Landfill Symposium, 6-10 October 2003.

Md. Sahadat Hossain (2002), "Mechanics of compressibility and strength of solid waste in bioreactor landfills." A thesis submitted to the Graduated Faculty of North Carolina State University at Raleigh in partial fulfillment of the requirements for the Degree of Doctor pf Philosophy.

Nascimento, J. (2007). "Mechanical Behavior of Municipal Solid Waste." MSc. Thesis: University of Sao Paulo;(in Portuguese).

Oweiss. I. S. (1993), "Stability of landfills", Chapter 11 of Geotechnical Practice Waste Disposal." edited by D. E. Daniel, Chapman & Hall.

Pelkey. S. A, Valsangkar. A. J, and Landva. A. (2001), "Shear displacement dependent strength of municipal solid waste and its major constituents." Geotechnical Testing Journal, Dec 2001, 381-390.

Shariatmadari, N, Machado, S, L, Noorzad, A and Karimpour Fard, M. (2009). "Municipal Solid Waste Effective Stress Analysis." Waste Management, doi:10.1016/j.wasman.2009.07.009.

Towhata, I., Kawano, Y., Yonai, Y. and Koelsh, F. (2004). "Laboratory Tests on Dynamic Properties of Municipal Wastes." 11th Conference in Soil Dynamics and Earthquake Engineering and 3rd International Conference on Earthquake Geotechnical Engineering, (1): 688-693.

Turczynski, U. (1988), Geotechnische aspekte beim aufbau von Mehrkimponentendeponien, Dissertation an der Bergakademie Freiberg (in German).

Van Impe, W. F.(1998), "Environmental Geotechnics: ITC5 activities – State of the art." Proceedings of the Third International Congress on Environmental Geotechnics, ISBN 90 5809 006x, pp. 1163–1187.

Vilar, O. M. M., A.C.M.; Carvalho, M.F. and Machado, S.L. (2006). "Some remarks on the mechanical properties and modeling of municipal solid waste." Simpósio Internacional de Tecnologias e Tratamento de Resíduos Sólidos: 12.

Zekkos, D. P. (2005). "Evaluation of Static and Dynamic Properties of Municipal Solid-Waste." A dissertation submitted in partial satisfaction of the requirements for the degree of Doctor of Philosophy in Geotechnical Engineering – University of California, Berkeley.

Zekkos, D., Bray, J. D., Stokoe, K., Kavazanjian, E., Rathje, E., Athanasopoulos, G.A.,Riemer, M., Matasovic, N., Lee, J.J., Seos, B. (2008). "Recent Findings on the Static and Dynamic Properties of Municipal Solid Waste." Proceedings of GeoCongress 2008: Geotechnics of Waste Management and Remediation(GSP 177): 176-183.

Zhan, T., Y. Chen, and Ling, W. A. (2008). "Shear strength characterization of municipal solid waste at the Suzhou landfill, China." Engineering Geology 97(3-4): 97-111.

Effect of 1D Infiltration Assumption on Stability of Spatially Variable Slope

Anastasia M. Santoso[1], Kok-Kwang Phoon[2], F. ASCE, and Ser-Tong Quek[2]

[1]Ph.D student, Department of Civil & Environmental Engineering, National University of Singapore, Blk E1A, #07-03, 1 Engineering Drive 2, Singapore 117576; g0600999@nus.edu.sg.
[2]Professor, Department of Civil & Environmental Engineering, National University of Singapore.

ABSTRACT

Rainfall-induced landslides are often analyzed using the infinite slope model, in which each slice of the slope is treated as a soil column subjected to one-dimensional, vertical infiltration. This one-dimensional (1D) assumption means that slope inclination and lateral downslope flow of water are ignored. Some studies have shown that the impact of lateral flow on slope stability is not significant. Hence, 1D infiltration analysis is sufficient to analyze rainfall-induced landslides. However, those studies are based on homogeneous soils, i.e. soil spatial variability is not considered in the analysis. This paper investigates the significance of slope inclination and lateral flow on the stability of an infinite slope with spatially varying soil in the depth direction. Only the saturated hydraulic conductivity of the soil is assumed to be spatially varying in the form of a stationary lognormal random field. It was found that the impact of the inclination on the pressure head and the factor of safety is not significant. However, the impact on the probability of slope failure is significant for some examples studied in this paper.

INTRODUCTION

Infiltration of rainwater into a soil slope often leads to shallow slope failures, particularly for slopes that rely on negative pore-water pressure in the unsaturated zone above the water table for stability (Gasmo et al. 2000, Rahardjo et al. 2007, Phoon et al. 2009). The negative pore-water pressure, commonly equated to matric suction, contributes to both effective stress and soil shear strength (e.g. Fredlund and Rahardjo 1993). As rainwater infiltrates the soil, the soil matric suction decreases and after some time positive pore-water pressure may develop. As a result, the stability of the slope may decrease to the extent of producing shallow slides.

In rainfall-induced landslides, failure often occurs at shallow depth and the failure surface is approximately parallel to the slope surface. Hence, it is reasonable to apply the infinite slope assumption for such stability analyses (Cho and Lee 2002, Collins and Znidarcic 2004, Phoon et al. 2009). Each slice of the infinite slope is subjected to the same amount and intensity of rainfall. An individual slice can thus be treated as a soil column subjected to one-dimensional, vertical infiltration. This one-dimensional (1D) assumption usually involves ignoring the inclination of the slope and the associated lateral downslope flow of water along the inclined surface.

Collins and Znidarcic (2004) compared the infinite slope results to 2D analysis results, in which the lateral flow is considered and the failure surface is not constrained to be parallel to the sloping surface. They showed that the infinite slope model is reasonable for rainfall-induced failure. Phoon et al (2009) adopted the infinite slope model to predict the failure depth for some case studies. They showed that their predictions generally agree with field observations. The above studies suggested that the infinite slope assumption and the 1D infiltration assumption are sufficiently accurate for analysis of rainfall-induced landslides. However, these studies are deterministic in nature. Soil is assumed to be homogeneous or at most a simple layered medium. Spatial variability is not considered in a typical "deterministic" analysis. It is usually associated with random field analysis, where each realization is spatially heterogeneous by definition.

In reality, soil is inherently variable (e.g. Christian et al. 1994, Phoon and Kulhawy 1999). Soil properties vary from point to point even if the soil deposit is nominally homogeneous. Hence, it is of interest to study the ramification of the 1D infiltration simplification when spatial variability in the depth direction is considered. The saturated hydraulic conductivity of the soil (k_s) is the only spatially variable parameter considered in this study. When k_s varies in the depth direction, the soil can be roughly viewed as a multi-layered system with more permeable layer interbedding less permeable layer in a fairly complex way. The lateral flow may be more significant in such a scenario than in the case of homogeneous soil.

This paper investigates the effect of slope inclination and lateral flow on the stability of an infinite slope with spatially varying soil in the depth direction. The spatial variability of the soil is introduced in the analysis by modeling k_s as a stationary lognormal random field. The pressure head distributions obtained from 1D and 2D seepage analyses are compared. Based on these pressure head distributions, the slope factor of safety and the probability of slope failure are estimated.

SEEPAGE THROUGH UNSATURATED SOILS

The governing equation for the one-dimensional flow of water through an unsaturated soil element is given as follows (Fredlund and Rahardjo 1993, Cheng et al. 2008),

$$\frac{\partial}{\partial z}\left(k\frac{\partial H}{\partial z}\right)+q=\lambda\frac{\partial H}{\partial t} \tag{1}$$

in which k is the hydraulic conductivity in the direction of the flow; H is the total head, summation of pressure head h and elevation z; q is the applied boundary flux (negative q denotes infiltration); λ is the specific storage capacity which is related to the slope of the soil water characteristic curve (SWCC); and t is the elapsed time.

In the unsaturated zone, the water content and the hydraulic conductivity of the soil depend on the pore-water pressure. The relation between soil-water content θ and matric suction $(u_a - u_w)$ is modeled using the van Genuchten (1980) SWCC equation. Gardner's model (1958) describes the unsaturated hydraulic conductivity k as an exponential function of the matric suction,

$$k=k_s\exp\left[-a\left(u_a-u_w\right)\right] \tag{2}$$

in which k_s is the saturated hydraulic conductivity; and a is the curve-fitting parameter inversely related to the air-entry value. Matric suction is related to the pressure head as $(u_a - u_w) = -\gamma_w h$, in which γ_w is the unit weight of water.

Using the SWCC and the conductivity function, Eq. (1) can be solved to obtain the pressure head h at elapsed time t. In this study, a finite element program THFELA (Cheng et al. 2008) is used to solve Eq. (1). THFELA is applicable to both 1D and 2D seepage analysis.

STABILITY OF UNSATURATED INFINITE SLOPE

The slope factor of safety incorporating the suction stress is given by (Phoon et al. 2009):

$$FS(z) = \frac{2c'}{\gamma(L-z)\sin 2\beta} + \frac{\tan\phi'}{\tan\beta} + \frac{\chi(-\gamma_w h)\tan\phi'(\tan\beta + \cos\beta)}{\gamma(L-z)} \quad (3)$$

in which c' is the effective cohesion of the soil; γ is the total soil unit weight; ϕ' is the effective friction angle; and χ is the coefficient of effective stress, which can be approximated by the normalized water content (Lu and Griffiths 2004). The effective stress friction angle is modeled as a function of depth of the weathering zone (Lu and Godt 2008, Phoon et al. 2009).

The infinite slope is considered to have failed when the minimum value of $FS(z)$ is less than unity and the layer at elevation z which has this minimum FS forms the failure surface. In rainfall-induced slope failure, the failure surface is commonly found around the wetting front. The soil above the wetting front has become saturated. Hence it is reasonable that failure occurs within this saturated zone.

In this study, two different seepage analyses are performed. The first case is a 1D analysis for an individual slice of the slope. The second is a 2D analysis for the entire slope. The infinite slope model is used in this study for both cases. For the 2D model, the pressure head at the vertical section mid-way between the crown and toe of the slope is substituted into Eq. (3).

SOIL SPATIAL VARIABILITY

When the 1D simplification is adopted, only the saturated hydraulic conductivity in the depth direction ($k_{s,z}$) governs the flow. For fair comparison, it is assumed that $k_{s,z}$ varies only along the depth direction for both 1D and 2D analyses. In other words, $k_{s,z}$ is uniform along the lateral direction for 2D analyses. To be more specific, this means that $k_{s,z}$ of each slice in the 2D slope is represented by the same realization of the 1D random field, regardless of its lateral position. In reality, soil exhibits spatial variability in the vertical and lateral direction. The significance of the spatial variability in the lateral direction is beyond the scope of this present study. Other sources of uncertainties, such as model uncertainties, are not considered.

Following previous studies (Sudicky 1986, KSTAT 2008), $k_{s,z}$ is modeled here by a 1D lognormal stationary random field. For brevity, $k_{s,z}$ is denoted as k_s from hereon. A translation field is assumed. Hence, $\ln k_s$ is a normal random field. The spatial correlation of $\ln k_s$ is described by an exponential correlation function $R(\tau) = \exp(-2\tau^2 / \delta)$, in which $R(\tau)$ is the correlation between the values of $\ln k_s$ at two points separated by a vertical distance τ, and δ is the correlation

length of ln k_s in the vertical direction. A large correlation length ($\delta/L \rightarrow \infty$) implies a uniform profile with constant k_s for $0 \leq z \leq L$. In this case, k_s is simply a single random variable. Another extreme case is $\delta/L \rightarrow 0$ which implies that the conductivity at all points become independent of each other.

In this study, realizations of ln k_s are simulated using the spectral representation method (Shinozuka and Deodatis 1991) with a depth discretization of dz = 0.05 m. In seepage analysis, particularly when finite element method is employed to solve the flow equation, the soil profile is discretized into layers or elements each having a uniform k_s. The value of ln k_s for each element is obtained by averaging (arithmetically) the values of the normal random field at the points within the element. The conductivity of each element is obtained as k_s = exp (ln k_s). Figure 1 shows schematically the spatial variability of k_s within the finite element models.

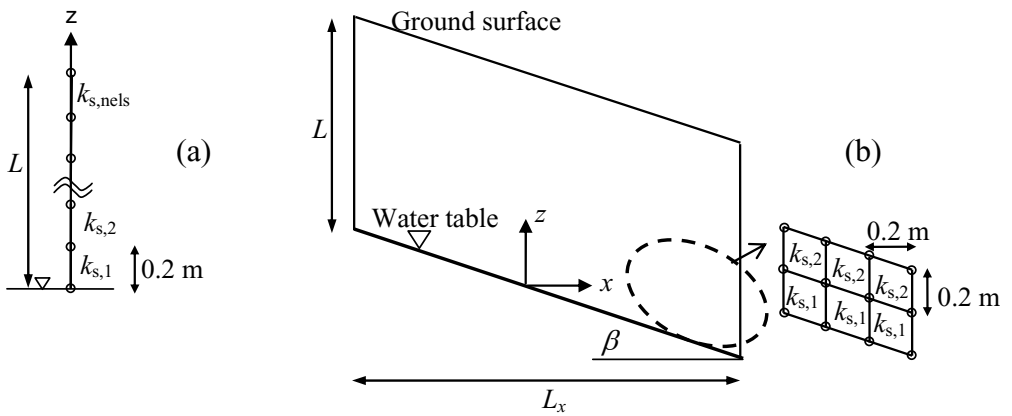

Figure 1. Geometry and finite element mesh of the slope: (a) 1D soil column (b) 2D inclined soil mass.

NUMERICAL STUDY

A slope of 6 m depth subjected to rainfall infiltration is adopted as a numerical example. The initial pore water pressure is assumed to be hydrostatic, with the ground water table located at the base of the slope. To simulate the infiltration problem, a constant flux of $q = -5\times10^{-7}$ m/s is applied at the ground surface and the pressure head at the base of the slope is maintained at zero. In other words, it is assumed that the ground water table is not affected by rainfall and does not rise. Soil properties and the geometry of the slope are summarized in Table 1 (adapted from Phoon et al. 2009).

For the 1D analysis, an individual slice of the slope is discretized into 30 two-noded 1D elements with element length of 0.2 m, as shown schematically in Figure 1(a). For the 2D analysis, the inclined soil mass is discretized into 1800 four-noded quadrilateral elements with element size of 0.2 × 0.2 m, as shown in Figure 1(b). It has been verified that the 1D model gives the same results as a 2D model with zero inclination.

Homogeneous profile. In this case, no spatial variability is considered and k_s = 10^{-6} m/s at every point in the slope. For the 2D inclined soil mass, it has been verified that the contours of the pressure head around the mid-sections of the slope ($-2 < x < 2$ m) are parallel to the slope. This indicates that the slope is sufficiently long to be analyzed as an infinite slope.

Table 1. Input Parameters.

Parameters	Numerical value
$k_{s,z}$	Mean of $k_s = 10^{-6}$ m/s, coefficient of variation of k_s = 1, $\delta / L = 1$, $dz = 0.05$ m
$k_{s,x}$	10^{-6} m/s
SWCC parameters	$\theta_s = 0.395$, $\theta_r = 0$, $a = 0.2$ kPa^{-1}, $n = 1.35$
Infiltration flux q	-5×10^{-7} m/s
Soil unit weight γ	20 kN/m^3
Shear strength parameters	$c' = 0$, $\phi'_0 = 29°$, $d\phi' = 4°$, $z_w = 0.5$ m
Slope geometry	$\beta = 30°$, $L = 6$ m, $L_x = 12$ m

The pressure head profiles at the mid-section of the slope (x = 0) for different values of inclination were compared. Figure 2 illustrates the pressure head profile for $\beta = 30°$. It was found that a steeper slope (higher β) leads to a deeper wetting front. As failure surface develops at the saturated zone, our interest is on the layers above the wetting front. At layers above the wetting front, the slope with higher β has higher matric suction, i.e. more dry. However, the difference in the pressure head due to inclination is not significant.

As the difference in the pressure head is not significant, the difference in factor of safety (FS) is also not significant (see Figure 2). In this example, at elapsed time of 4, 8 and 12 days, the 1D analysis gives the minimum factor of safety within the saturated zone of 1.58, 1.31 and 1.23, respectively (as indicated by arrows). The 2D analysis gives 1.6, 1.32 and 1.24, respectively. As these values are higher than FS at the base, FS_{min} is found at the base of the slope both for 1D and 2D analyses (see Figure 2). In this example, it appears that the infiltration flux ($|q|/k_s$ = 0.5) does not induce a shallow failure although matric suction is reduced. This result is in agreement with analyses of real case studies carried out by Phoon et al (2009). They found that shallow failures do not take place in homogeneous profiles, unless the infiltration flux is very close to the saturated hydraulic conductivity. Hence, the nominal homogeneous profile routinely assumed in deterministic analysis is potentially unable to reproduce observed shallow failures even qualitatively in terms of failure depths.

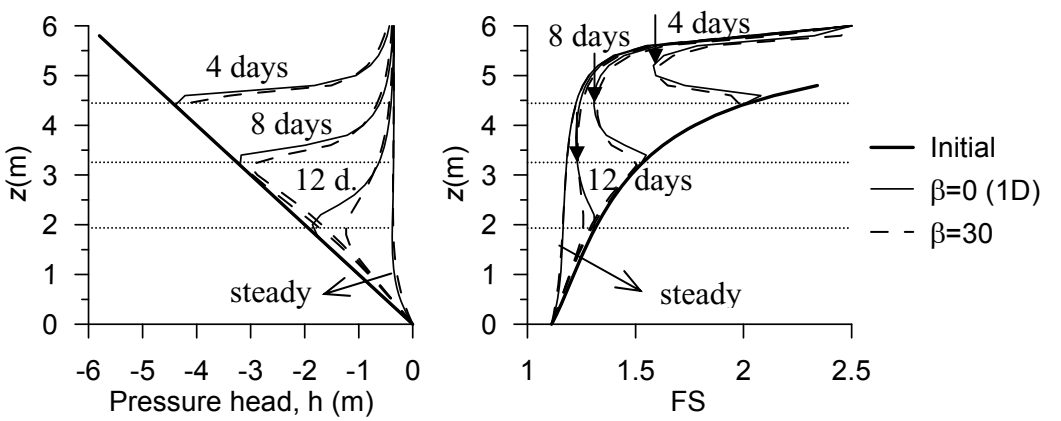

Figure 2. Pressure head and factor of safety for slope with homogeneous profile.

Spatially variable profile. In this case, the saturated hydraulic conductivity is modeled by the 1D random field described in the preceding section. Figure 3 shows a single realization of this random field (for normalized correlation length

of δ/L = 1) and the resulting pressure head profile. There is only a slight difference between the pressure head obtained with and without considering slope inclination.

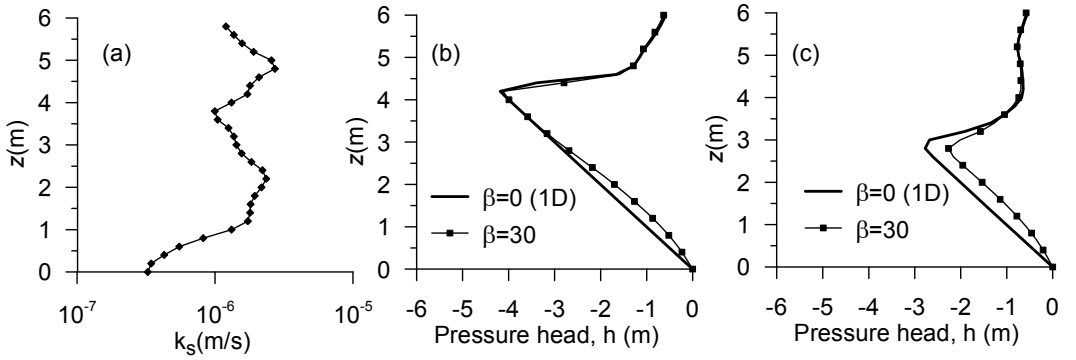

Figure 3. A single realization of the random field and the resulting pressure head: (a) k_s(z) (b) pressure head at t = 4 days (c) at t = 8 days.

For a more thorough statistical comparison, many realizations of the random field are simulated and the resulting pressure head profiles are compared. To obtain sufficient failure samples for failure probability estimation, the realizations are generated by subset simulation (Au and Beck 2003, Santoso et al. 2010) with sample size of 1000 in each subset. Figure 4 shows a typical failure sample arising from a spatially variable profile. Note that the failure surface is about 1 m below the ground surface. In contrast, a homogeneous profile is unable to produce this realistic shallow failure. When k_s varies with depth, positive pore-water pressures may develop at some layers above the wetting front (the saturated zone) and these positive pore-water pressures can decrease the shear strength along a shallow layer sufficiently to cause failure. This ability to reproduce a shallow failure mechanism widely observed in real rainfall-induced landslides is critical and may imply that it is not possible to simplify naturally varying soil profiles into some equivalent homogeneous profiles.

With regard to the effect of inclination, a trend similar to that found for the homogeneous profile can be observed in Figure 4. The 2D inclined slope produces slightly deeper wetting front compared to the 1D soil column. A positive pore-water pressure develops at the saturated zone. The 2D analysis produces lower positive pressure. As a result, the 2D analysis produces slightly higher FS_{min} than the 1D analysis.

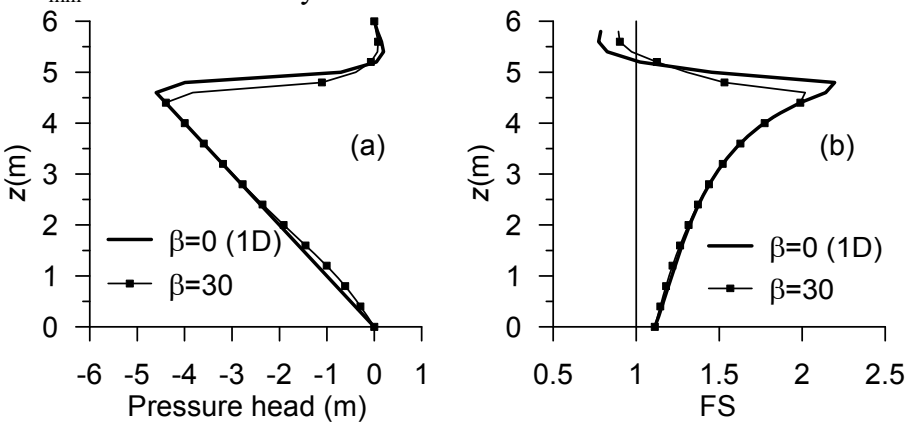

Figure 4. A failure sample at t = 4 days obtained from subset simulation: (a) pressure head profile (b) factor of safety profile.

The impact of the slope inclination on the probability of slope failure is more significant. When the 1D soil column is adopted in the seepage analysis, the failure probability for elapsed time of 4 days is $P_F = 1.5\times10^{-3}$. For the 2D inclined slope, $P_F = 2\times10^{-4}$. This lower failure probability is reasonable as the 2D inclined slope produces higher FS at the saturated zone (above the wetting front).

Effect of inclination angle β. To study whether the effect of the 1D assumption is more significant for a steeper slope, the example is re-analyzed with $\beta = 40^o$. The correlation length of the random field is fixed at $\delta/L = 1$. For natural slopes, a steeper slope indicates that the soil has a higher friction angle. To account for this, the friction angle is adjusted, $\phi'_0 = 39^o$, while the weathered zone parameter are kept as in Table 1. These numerical values are selected so that the mean FS at initial condition obtained with $\beta = 40^o$ and $\phi'_0 = 39^o$ is comparable to the mean FS obtained previously with $\beta = 30^o$ and $\phi'_0 = 29^o$.

For a given rainfall intensity, some amount of the water will infiltrate the soil vertically and the rest will be carried away as surficial runoff. For a steeper slope, the amount of runoff is larger. Thus the vertical infiltration flux is smaller in a steeper slope. A possible approach to incorporate runoff in the numerical simulation is by introducing a surface layer with high permeability. This current study does not pursue this aspect in detail. The same value of vertical infiltration flux $q = 5 \times 10^{-7}$ m/s is used for analyses with different inclination angle.

The failure probability estimated using the 1D analysis is approximately the same as the previous result for $\beta = 30^o$ (see the first row of Table 2). This is because the friction angle is adjusted. The 2D results show that the steeper slope is actually more stable (it has lower P_F). This is reasonable because the lateral flow inside the slope becomes more significant in a steeper slope. Thus for the same infiltration flux, the vertical flow inside the slope becomes less and matric suction dissipates more slowly. The practical outcome is that the effect of 1D assumption can be very conservative for a steeper slope.

Table 2. Failure probability estimated using 1D and 2D analyses.

β	30	40
P_F (1D)	1.5×10^{-3}	2×10^{-3}
P_F (2D)	2×10^{-4}	5×10^{-6}

CONCLUSION

This paper investigates the significance of slope inclination and lateral flow on the stability of an infinite slope with spatially varying soil in the depth direction. Only the saturated hydraulic conductivity of the soil is assumed to be spatially varying in the form of a stationary lognormal random field. Results of 1D seepage analysis through a soil column and 2D seepage analysis through an inclined soil mass are compared. For both 1D and 2D analyses, the slope stability is analyzed using the infinite slope assumption. It was found that the 2D seepage analysis produces slightly higher negative pressure heads (drier soil) and a slightly higher factor of safety at layers above the wetting front. The difference is more significant for the probability of slope failure P_F. The 1D seepage analysis produces a higher estimate of P_F, thus the 1D simplification commonly adopted in analyses of rainfall-induced landslides is a conservative approximation. The

difference in P_F between the 1D and 2D analysis is most significant in the case of steep slope.

REFERENCES

Au, S.K. and Beck, J.L. (2003). "Subset simulation and its application to seismic risk based on dynamic analysis." *J. Eng. Mech.*, ASCE, 129(8), 901-917.

Cheng, Y.G., Phoon, K.K., and Tan, T.S. (2008). "Unsaturated soil seepage analysis using a rational transformation method with under-relaxation." *International Journal of Geomechanics*, ASCE, 8(3), 207-212.

Cho, S.E. and Lee, S.R. (2002). "Evaluation of surficial stability for homogeneous slopes considering rainfall characteristics." *J. Geotech. Geoenviron.*, ASCE, 128, 756-763.

Christian, J.T., Ladd, C.C., and Baecher, G.B. (1994). "Reliability applied to slope stability analysis", *J. Geotech. Eng.*, ASCE, 120(12), 2180-2207.

Collins, B.D., and Znidarcic, D. (2004). "Stability analyses of rainfall induced landslides", *J. Geotech. Geoenviron.*, ASCE, 130(4), 362-372.

Fredlund, D.G. and Rahardjo, H. (1993). *Soil Mechanics for Unsaturated Soils*. John Wiley & Sons, New York.

Gardner, W.R. (1958). "Some steady state solutions of the unsaturated moisture flow equation with application to evaporation from a water table." *Soil Sci.*, 85(4), 228-232.

Gasmo, J.M., Rahardjo, H. and Leong, E.C. (2000). "Infiltration effects on stability of a residual soil slope." *Comput. Geotech.*, 26, 145-165.

KSTAT Standards Committee [H.A. Loaiciga (chair)]. (2008). *Standard Guideline for Fitting Saturated Hydraulic Conductivity using Probability Density Functions*, ASCE / EWRI Standard 50-2008, ASCE, Reston.

Lu, N. and Griffiths, D.V. (2004). "Profiles of steady-state suction stress in unsaturated soils." *J. Geotech. Geoenviron.*, ASCE, 130(10), 1063-1076.

Lu, N. and Godt, J. (2008). "Infinite-slope stability under steady unsaturated seepage conditions." *Water Resour. Res.*, 44, W11404.

Phoon, K.K. and Kulhawy, F.H. (1999). "Characterization of geotechnical variability." *Can. Geotech. J.*, 36(4), 612-624.

Phoon, K.K., Toll, D.G., and Karthikeyan, M. (2009). *Study on the Effects and Impacts of Climate Change on Singapore, Volume V: Slope Stability.* Tropical Marine Science Instistute, National University of Singapore.

Rahardjo, H., Ong, T.H., Rezaur, R.B., and Leong, E.C. (2007). "Factors controlling instability of homogeneous soil slopes under rainfall." *J. Geotech. Geoenviron.*, ASCE, 133(12), 1532-1543.

Santoso, A.M., Phoon, K.K. and Quek, S.T. (2010). "Modified Metropolis-Hastings algorithm with reduced chain-correlation for efficient subset simulation." *Probab. Eng. Mech.*, doi:10.1016/j.probengmech.2010.08.007.

Shinozuka, M. and Deodatis, G. (1991). "Simulation of stochastic processes by spectral representation." *Appl. Mech. Rev.*, 44(4), 191-203.

Sudicky, E.A. (1986). "A natural gradient experiment on solute transport in a sand aquifer: spatial variability of hydraulic conductivity and its role in the dispersion process." *Water Resour. Res.*, 22(13), 2069-2083.

Van Genuchten, M.T. (1980). "A close-form equation for predicting the hydraulic conductivity of unsaturated soils." *Soil Sci. Soc. Am. J.*, 44(5), 892-898.

Old Sewer, Big Risks: Managing Risks during the Design and Construction of a 21-Story Building Adjacent to a Critical 100-year Old Sewer Structure

Damian R. Siebert, PE[1], Joel S. Mooney, PE, LSP[2], Richard Marks[3], Daniel Ocasio, AIA[4], and Kevin McKenna[5]

[1]Senior Engineer, Haley & Aldrich, Inc., 465 Medford Street Suite 2200, Boston, MA 02129; 617-886-7399; dsiebert@haleyaldrich.com
[2]Senior Vice President, Haley & Aldrich, Inc., 465 Medford Street Suite 2200, Boston, MA 02129; 617-886-7435; jmooney@haleyaldrich.com
[3]Daedalus Projects, Inc. 112 South Street, 5th Floor, Boston, MA 02111; 617-451-2717; rmarks@dpi-boston.com
[4]Senior Project Manager, Massachusetts State College Building Authority, 253 Summer Street, Boston, MA 02210; 617-933-8343; docasio@MSCBA.org
[5]Massachusetts Water Resources Authority; Charlestown Navy Yard, 100 First Ave., Building 39, Boston, MA 02129; 617-305-5956; Kevin.McKenna@mwra.state.ma.us

ABSTRACT

Communication and risk-reduction measures implemented during the design and construction of a 21-story pile-supported building adjacent to a below-grade 100-year old sewer structure were keys to successful foundation construction. Damage to the existing sewer structure during construction activities and the future ability to access the structure post-construction were the main concerns for the utility owner.

Clear communication and a deliberate design process between all parties – utility owner, building owner, structural engineer, geotechnical engineer, architect, and the contractor – were integral to the project's success. This process helped all parties to understand the risks, both real and perceived, and to develop mitigation measures to reduce the risks.

Bringing together all parties to engage in dialogue and encouraging open communication throughout the project were paramount to its success. By implementing the joint design plan, using mutually acceptable construction techniques, and careful monitoring, the building foundation was successfully installed and all parties' risks were averted.

INTRODUCTION

The Massachusetts State College Building Authority (owner) along with the Massachusetts College of Art and Design (MassArt) is currently constructing a 21-story residence hall on Huntington Avenue in Boston, Massachusetts, scheduled to be completed March 2012. The new residence hall is a key addition to the College since it will provide 493 new beds, guaranteeing housing to all first and second-year students. In Boston, a dense urban environment, available land is in short supply and often comes at a premium. The desired available land presented several challenges. The parcel for the building, which is contiguous to the MassArt campus, included land under lease to MassArt for parking from an adjacent college. In addition, the Massachusetts Water Resources Authority (MWRA) had an easement running

through the parcel containing a critical 100-year old sewer. An existing partnership between the colleges allowed for the acquisition of the leased parcel and for construction to proceed; portions of the new space will be used by students from both schools. However, the presence of the MWRA easement, and more specifically the critical sewer structure, posed difficult design and construction challenges.

CHALLENGES, RISKS, AND CONCERNS

During the schematic design phase, it was clear that the program space requirements would require the proposed building footprint and foundation to be installed as close as possible to the existing below-grade sewer structure in order to optimize the square footage available on the site. The sewer structure consists of a reinforced concrete culvert 11.5-ft wide and 10.25-ft high, with the top located approximately 25-ft below existing ground surface. MassArt correctly realized that the MWRA needed to be engaged collaboratively to discuss concerns and develop a foundation system for the building that would not negatively impact the sewer.

A meeting between all parties – MWRA, owner, structural engineer, geotechnical engineer, architect, and the contractor – was initiated to discuss the risks associated with the construction and to collaboratively develop a design and construction approach that would adequately address all parties' concerns and reduce the risks associated with them. The items discussed were categorized into design or construction risks/concerns as indicated below:

Design Risk/Concern

- Develop a cost-effective building foundation system
- Future access to the sewer structure in case of an emergency
- Protection of the completed building if the sewer structure was accessed
- Uncertainty of the existing sewer structure location with respect to the proposed building location

Construction Risk/Concern

- Current condition of the sewer structure given its age
- Damage to the sewer structure during construction

The above items were discussed in detail and a plan was developed to effectively manage the concern or risk.

DESIGN RISK MANAGEMENT

Several concerns were raised during the design process that weighed risk and cost, and required creative solutions.

Cost-effective building foundation. Funded entirely by tax-exempt revenue bonds, the project was under significant budget constraints to make the proposed building economically feasible. Challenging soil conditions at the site, in combination with the magnitude and distribution of the building loads, required a deep foundation system to support the proposed building. In general, the depth to a suitable bearing stratum (bedrock) varies between approximately 120 ft to 170 ft below existing ground surface. Several deep foundation options were evaluated for overall cost to the project and risk to the sewer structure and included drilled shafts and driven piles, such as: steel H-piles, steel pipe piles, and prestressed-precast concrete piles (PPC).

Drilled shafts would provide the lowest installation risk to the adjacent sewer structure due to non-displacement installation techniques, where soil is removed from the shaft as it is advanced to a competent bearing strata and then filled with concrete. However, the drilled shaft foundation system was the most expensive option and would take the longest time to construct. The review of the cost and time considerations made this foundation option not economically viable.

Driven piles, which are advanced into the ground via impact or vibration techniques, were separated in two types for evaluation based on cost and installation risk: type one, displacement piles (steel pipe piles and PPC) and type two, low-displacement piles (H-piles). The physical difference between the pile types is that displacement piles have a larger cross-sectional area which tends to densify or compress the soil as the pile is installed in the ground, and this condition also propagates larger vibrations during the pile installation. Due to this densification, the displacement piles typically "take-up" or stop sooner in the bearing stratum resulting in a shorter overall pile than the non-displacement piles. In order to evaluate the installation risk associated with vibrations for the two pile types, Haley & Aldrich compiled vibration levels (referred to as Peak Particle Velocity – PPV) and plotted them in relationship to distance from the vibration source (pile locations). Figure 1 illustrates that vibration levels with displacement piles are typically greater than those from low-displacement piles. The project team weighed the reduced cost, based on the material type and anticipated total length of the displacement piles, with the potential risk associated with vibration. The team determined that even though the low-displacement H-piles were more expensive, they were best choice to manage risk since installing them produced lower vibration levels.

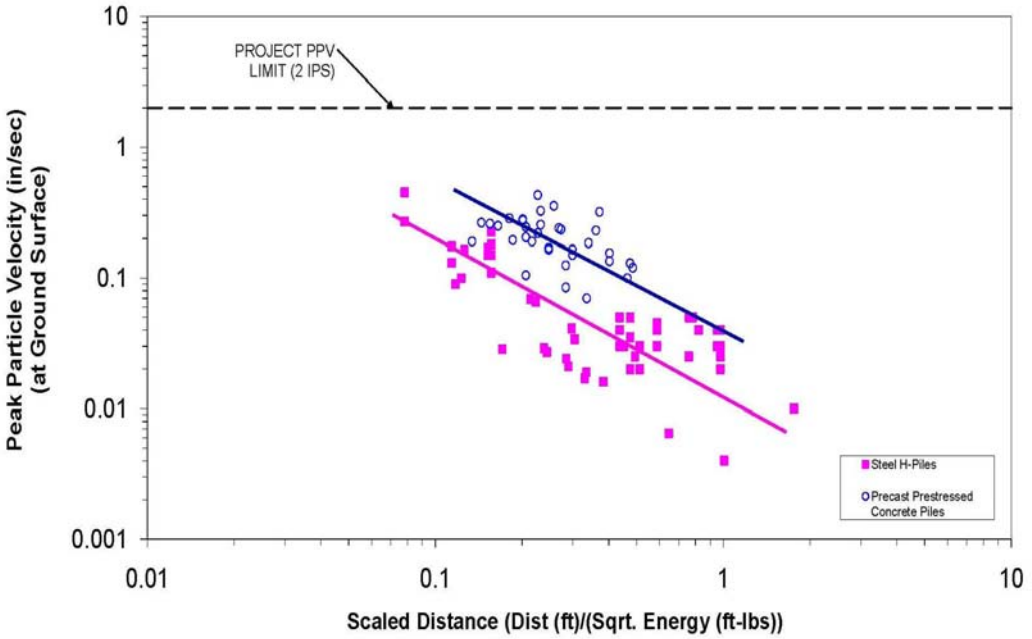

Figure 1 – Building Response to Typical Pile Driving Vibrations

To further reduce the vibration levels and risk of damage to the sewer structure, several unique pile installation procedures were required during construction. Pre-auguring, drilling a hole slightly smaller than the proposed pile, through the fill, organic soils, and stiff upper clay to a depth of approximately 50 ft below ground surface and bottom of the sewer structure, was specified prior to pile installation. By locally removing the soil from the pile area above the bottom of the sewer structure elevation, the proposed piles could essentially be installed the first 50 ft by their own weight, requiring little to no forces that could produce vibrations in the ground zone at the same level as the critical structure. In addition, the use of a variable moment vibratory hammer[1] was required below the pre-auger depth. The intent was to minimize vibration by advancing the pile as far as a possible before using the standard impact hammer techniques required to reach the final pile capacity.

By selecting low-displacement steel H-piles, along with unique installation techniques, the project was able to stay within budget, on schedule and mitigate the risk of damage to the adjacent sewer structure.

Future access to sewer structure and protection of the MassArt building. Both parties had concerns about the ability of the MWRA to access the sewer structure quickly in a case of an emergency. Maintaining the integrity of the new MassArt building needed to be evaluated since the structure would be supported on deep piles, some as close as 5 ft to the sewer structure. To alleviate the potential risks of damage

[1] A vibratory hammer uses two sets of eccentric weights that oppose each other and are oscillated in phases to minimize the radial vibration into surround soils. More information is located at Http://www.apevibro.com/asp/products/vibro/variable.asp.

to the MassArt building and provide the ability to quickly access the sewer structure, it was agreed that the MassArt project team would design and install a portion of a temporary support of excavation (SOE) system as part of the project. In the event of an emergency repair, the SOE system would then be in place and allow for future access to the sewer structure without damaging the building.

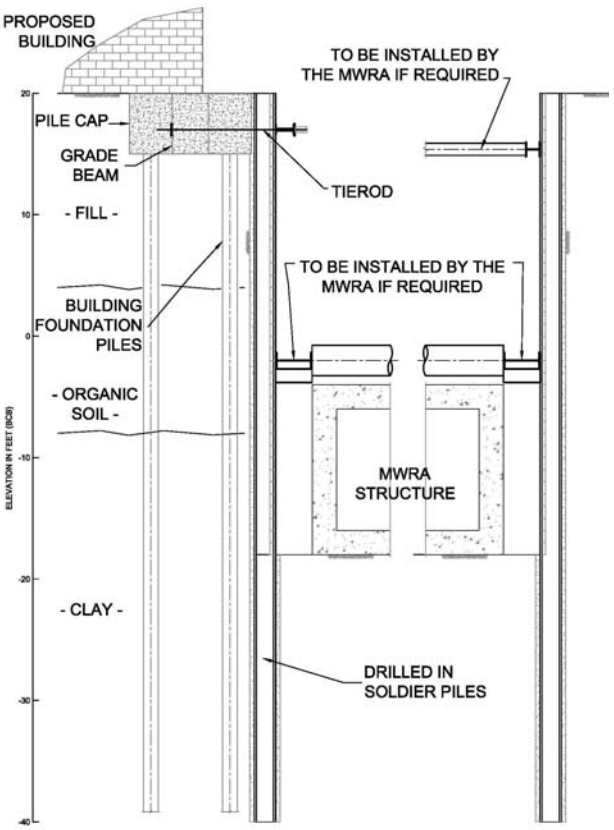

Figure 2 – Support of Excavation Cross Section

The specific SOE system consisted of a series of drilled-in soldier beams on either side of the sewer with a waler beam and tierods connecting the soldier beams to the building. As a result, the MWRA could safely excavate to the top of the sewer structure without undermining the MassArt building or exposing the foundation piles. The building foundations were designed to resist the lateral force of the SOE system in the event the sewer structure was accessed. Additionally, to reduce the risk associated with the long-term corrosion of the SOE members, the soldier beams, wales and tierods were encased in concrete. The soldier beams were designed and sized to allow excavation to the bottom of the structure with the installation of an additional lower level of bracing (Figure 2). A complete PE stamped design of the system was provided to the MWRA for their future use.

This approach successfully managed the concerns of both parties by providing safe future access to the sewer structure while also protecting the MassArt building.

Uncertainty of the sewer structure location. The MWRA was able to locate and provide historic design drawings of the sewer structure including cross-sections and plan location. To confirm the location of the sewer structure the design team first employed a non-intrusive technique called Ground Penetrating Radar (GPR), a geophysical method that uses radar pulses to image the subsurface. The results from the GPR survey were overlaid on the historic design drawings. Based on the overlay it was determined the sewer structure may be located several feet closer to the proposed building's location than the historic design plans had shown, potentially further complicating the structural design. Due to the depth of the structure below the ground, water table, and soil conditions, the accuracy of the GPR was questioned and

deemed not accurate enough to assess the potential risk of foundation installation adjacent to the structure.

It was critical to the feasibility of the design to install the foundation system as close as possible to the sewer structure. Because the GPR survey was not exact, additional measures were required to more accurately locate the sewer structure. Due to the depth and water conditions, test pits to expose the top of the structure would be very disruptive, expensive, and time prohibitive. Haley & Aldrich developed a method of using a Geoprobe drill rig to carefully probe and accurately locate the top and profile the horizontal limits of the sewer structure. A series of probes were advanced at 15 ft intervals and later surveyed to produce the actual location of the sewer structure.

The use of the Geoprobe system provided the identification of the plan location of the sewer structure in a cost effective manner and allowed the design team to confidently locate the building and SOE piles for the MassArt building. The SOE system was installed in its design location on schedule.

CONSTRUCTION RISK MANAGEMENT

Just prior to and during construction, the project team performed several critical tasks to ensure the protection of the sewer. In addition, through careful observation and instrumentation monitoring the team was able to adjust construction techniques to save the project time and money.

Condition of sewer structure. The sewer structure had not been inspected in over 10 years and the current condition/integrity of the structure was unknown. The MassArt team proposed to perform a pre-construction video survey before construction activities and a post-construction video survey after the project was completed. The pre-construction survey was intended to evaluate the current condition of the sewer and set a baseline against which the post-construction survey could be compared. The flow conditions in the sewer required a dive crew to enter into the structure for the video survey early in the morning when the weather forecast was clear from rain and flows were at the lowest.

Taking this extra step provided a better understanding of the current condition of the sewer structure and information to evaluate the impact of the construction on the sewer structure.

Full time and careful monitoring of construction activities. The success of the project depended on the successful implementation of the foundation installation procedures agreed upon during the design phase. During design Haley & Aldrich analyzed other similar pile driving projects to determine the potential vibration levels with the anticipated pile hammer energy at the MassArt site. The analysis of comparable projects estimated that the vibration levels due to pile driving would be at or below 2 in./sec. Based on the structure type, depth below grade, and sewer condition it was determined that the risk of damage to the structure was acceptable if vibration levels were kept below 2 in./sec. Haley & Aldrich provided full-time, on-site observation during the installation of the foundation piles and also monitored vibrations. Seismographs[2] were placed at strategic locations on the site to monitor the vibration levels. One seismograph was located on the ground over the sewer structure. The second seismograph was placed on a manhole that directly connected to the sewer structure. Vibration levels were continuously monitored to ensure the 2 in./sec limit set to minimize the risk to the sewer structure was not exceeded. Figure 3 presents the vibration data (PPV vs. frequency) for a typical week of pile driving.

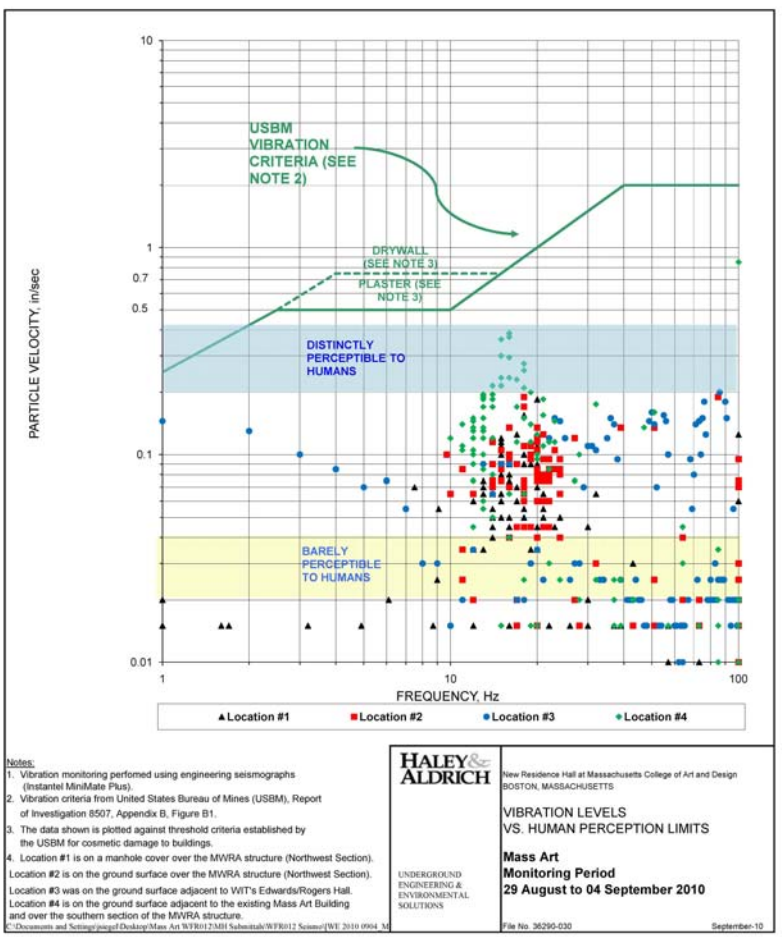

Figure 3 – Peak Particle Velocity for a Typical Week of Pile Driving

The unique foundation installation procedure thoughtfully devised during the design phase proved successful and the vibration levels were kept below criteria established to minimize the risk of damage to the sewer structure.

[2] A seismograph is an instrument that detects and records the intensity, direction, and duration of ground movements.

Adjustment of construction techniques. During construction, the effectiveness of the variable moment vibratory hammer was evaluated with respect to the ability to advance the pile below the pre-augered depth and reduce vibration. The hammer was less effective and had reduced production in penetrating the stiff clay soil at the bottom of the pre-augured pile locations. In the midst of installation, it was decided to stop use of the variable moment vibratory hammer. Seismographs were installed near several "test" piles located as far as possible from the sewer structure, in order to record vibrations using a standard impact hammer. As a result of using this observational approach and flexible decision-making, the standard impact hammer was used in place of the variable moment hammer.

By using the real-time vibration results, we were able to cease the use of the variable moment hammer, maintain vibration levels below permissible limits, keep pile production at desired levels, and hold schedule.

CONCLUSIONS

Through this process of dealing with multiple parties, we have learned that it is important to:

- *Listen*—it is amazing how much can be learned about each party's concerns and how they view success simply by having everyone discuss and listen to each other.
- *Understand complex systems*—not until the project risks, concerns, constraints, etc. are completely understood can a successful project be completed.
- *Compromise*—everyone must be willing to negotiate and compromise together to reach a mutually acceptable outcome.
- *Be flexible*—it is critical to be able to adjust quickly (in construction and design) to solve problems and improve on procedures.

By bringing together all parties early in the design process and engaging, understanding, and appreciating the needs of all the project stakeholders, the project was a success. By adding open and honest communication to a creative and thoughtful design process, construction procedures and monitoring techniques were developed so that the building foundations were successfully installed and all parties' risks were successfully managed.

ACKNOWLEDGMENTS

The authors appreciate the support ADD Inc. the project architect and Odeh Engineering, Inc. the projects structural engineer.

Effect of leachate recirculation and extent of degradation on the Stability of bioreactor landfill slopes

Amit Srivastava[1], G. L. Sivakumar Babu[2], Krishna R. Reddy[3], Hanumanth S. Kulkarni[4]

[1]Assistant Professor, Department of Civil Engineering, Jaypee University of Engineering & Technology, Guna, MP-473226, India.
Email: amit.srivastava@jiet.ac.in, 2002.lala@gmail.com
[2]Professor, Department of Civil Engineering, Indian Institute of Science, Bangalore, Karnataka, 560012, India Email: gls@civil.iisc.ernet.in
[3]Professor, Department of Civil and Materials Engineering, University of Illinois at Chicago, 842, West Taylor Street, Chicago, Illinois – 60607, USA. Email: kreddy@uic.edu
[4]Graduate Research Assistant, Department of Civil and Materials Engineering, University of Illinois at Chicago, 842, West Taylor Street, Chicago, Illinois – 60607, USA. Email: hkulka2@uic.edu

ABSTRACT

The stability of a bioreactor landfill slope is influenced by the quantity and method of leachate recirculation as well as on the degree of decomposition. Other factors include properties variation of waste material and geometrical configurations, i.e., height and slope of landfills. Conventionally, the stability of slopes is evaluated using factor of safety approach, in which the variability in the engineering properties of MSW is not considered directly and stability issues are resolved from past experiences and good engineering judgments. On the other hand, probabilistic approach considers variability in mathematical framework and provides stability in a rational manner that helps in decision making. The objective of the present study is to perform a parametric study on the stability of a bioreactor landfill slope in probabilistic framework considering important influencing factors, such as, variation in MSW properties, amount of leachate recirculation, and age of degradation, in a systematic manner. The results are discussed in the light of existing relevant regulations, design and operation issues.

INTRODUCTION

A bioreactor landfill is a municipal solid waste (*MSW*) landfill that uses enhanced biochemical processes to transform and stabilize the decomposable organic waste within short time (typically 5 to 10 years) as compared to long time (typically 30 to 100 years) for conventional landfills (Sharma and Reddy, 2004). In recent years, the operations of *MSW* landfills as bioreactor are under intensive study to optimize design and operation methods (Reinhart et al., 2002). These facilities are designed to perform leachate recirculation and instrumented to monitor leachate distribution and leachate head on the liner.

Injection of leachate and other liquids in a bioreactor landfill can endanger the stability of slopes due to the following reasons (Kavazanjian, 2001) : (i) increased driving force due to the increase in unit weight of the waste mass following liquid injection, (ii) decrease strength due to decrease in effective stress corresponding to the increase in pore pressure that result from liquid injection, and (iii) decreased strength due to transformation of waste mass by the biological and chemical processes that enhance degradation, turning the waste into an inherently weaker material.

Overly aggressive leachate recirculation (compounded by the use of an impermeable cover layer) has been cited as contributing factor to the catastrophic slope failure of landfill. Therefore, to minimize such risk, one needs to better define the shear strength of stabilized waste and to provide appropriate input to accurately assess the bioreactor landfill stability. The important geotechnical properties needed for stability analysis is the shear strength of waste, its unit weight and hydraulic conductivity. For stability analysis, both drained (for fresh MSW landfills) and undrained (for old waste with leachate recirculation) shear strength of degraded waste are required. Unfortunately, the available shear strength data are limited.

The purpose of slope stability analysis is to provide a quantitative measure of the stability of a slope or part of a slope. Traditionally, it is expressed in terms of *factor of safety* with respect to failure, which is defined as the ratio of the summation of restoring forces to the summation of disturbing forces. To ensure long term stability, with due consideration of various sources of uncertainties involved in the estimation of MSW properties, it is suggested that the calculated *factor of safety* should be in the range of 1.5 – 3.0.

A question that often arises, in practice, is to know “how safe is safe?” or to what extent the factors of safety that are routinely used to address the question of safety and economy are adequate. These factors of safety represent the combined influence of total variability and deviations of analytical formulations based on simplified assumptions and a selection of appropriate value of *factor of safety* comes from past experiences and good engineering judgment. It is well understood that the approach is simple and straightforward but does take into account the variability in an appropriate manner.

On the other hand, in a probabilistic approach, the performance of the structure is expressed in a probabilistic framework, i.e., either probability of failure (p_f) or in terms of safety index known as reliability index (β). The development of reliability based design procedures is receiving considerable attention and guidelines on the targeted reliability indices have been suggested in literature. USACE (1997)

made specific recommendations on target probability of failure (p_f) and reliability indices (β) in geotechnical and infrastructure projects and suggests that a reliability index (β) value of at least 4.0 is required for good performance of a system while a value of at least 3.0 is needed for an above-average performance. Methods of reliability analysis such as first order reliability method (*FORM*), second-order reliability method (*SORM*), Point Estimate Method (*PEM*), and Monte Carlo simulation (*MCS*) are available in literature (Baecher and Christian 2003).

Quantitative assessment of uncertainty modeling requires the use of statistics as well as probabilistic modeling, which relies on sets of measured data. The uncertainty in the measured data (say *m* number of measured data sets) is expressed in terms of sample mean (μ) and variance (σ^2). The coefficient of variation (CoV%), which is obtained by dividing the sample standard deviation (σ) by the sample mean (μ), is commonly used in quantifying the geotechnical uncertainty analysis. Several studies in the past (Duncan, 2000) provided the generic range of coefficient of variation (CoV %) in the geotechnical (soil) parameters, but variation in *MSW* properties is not yet reported in the literature.

OBJECTIVES OF THE PRESENT STUDY

To perform a parametric study on the stability of typical bioreactor landfill slope in a probabilistic framework with due consideration of variation in the engineering properties of MSW in bioreactor landfills and other influencing factors such as effect of waste degradation, extent of leachate recirculation. The bioreactor landfill configuration used in the present study consists of the following: (i) composite bottom liner (e.g., smooth geomembrane over compacted clay soil) sloping at 2.5% toward a perimeter leachate collection pipe (ii) maximum waste height 50 m (iii) 1V:3H final side slopes with benches at 10 m vertical interval. (iv) 5% minimum final cover slope.

Four different types of bioreactors were assumed as designated as **Type O**: Baseline condition; no liquid recirculation practiced (conventional subtitle D landfill; **Type I**: Limited and/or intermittent liquid recirculation and application practiced; **Type II**: Moderate and well controlled liquid recirculation practiced; below field capacity; **Type III**: Heavy liquids recirculation and application; maximum lateral and vertical extent; approaches field capacity or beyond

OVERVIEW OF IMPORTANT ASPECTS OF BIOREACTOR LANDFILLS

Leachate/ moisture distribution. The generation and distribution of leachate in bioreactor landfills is being investigated through laboratory studies and through field monitoring at bioreactor landfill sites under different operating condition. Based on field observations, the moisture content in waste could be in excess of the ambient levels of 10 to 20 % to promote full bioreactor (aerobic or anaerobic) activity (Yuen, 1999). Previous data suggests that the ideal moisture content should be 45%.

Waste degradation and gas generation. When solid waste is buried in a landfill, the biodegradable fractions decompose via a complex series of microbial reactions under anaerobic conditions. These fractions include readily degradable food waste, more

slowly degradable paper (cellulosic) wastes, and garden or commercial wastes containing slow to rapidly degradable components. Major intermediate products during decomposition include acetic acid (CH_3COOH), other carboxyl acids, carbon dioxide (CO_2) and hydrogen (H_2). The terminal reaction is the production of methane (CH_4) by methanogenic microorganisms.

Classical modeling of gas generation in landfills involves 4-5 phases wherein Phase 1 (aerobic) involves initial aerobic degradation until available oxygen is depleted; Phase II (initial anaerobic/acidogenic) involves the activity of hydrolytic and fermentative microorganism with the generation of CO_2, H_2, and carboxylic acids; Phase III (acetogenic) involves acetate generation (CH_3COOH) from precursor carboxylic acids; and Phase IV (methanogenic) involves steady methane generation from acetate cleavage or the reduction of CO_2 with H_2. As a result of these two pathways landfill gas typically consist of 50-60% CH_4 (v/v) with the remainder primarily CO_2 (Bogner et al., 1996). An optional Phase V involves the slow onset of secondary aerobic conditions after 2-3 decades. Some recent literatures have proposed CH_4 yields ranging from 0.07 – 0.13 kg CH_4/kg of (dry) solid waste (Kura and Lee, 1995; Li et al., 1999).

Engineering properties of waste. For the stability analysis of bioreactor landfill slopes, the important engineering properties of waste are moisture content, unit weight, and shear strength. These properties affect the waste degradation, leachate generation and distribution, and the overall geotechnical stability of bioreactor landfills. Gabr *et al* (2007) characterized relative changes in waste shear strength parameters during waste decomposition. The findings were based on direct shear tests results performed on waste specimens ranging from fresh to well-decomposed residential refuse. Results indicate that the friction angle of refuse decreased with decomposition. As refuse decomposed, the plastic content increased, which contributed to a decrease in friction angle as the friction angle of plastics is 18–19° as compared to 33° for fresh shredded waste. The mechanical response of MSW materials under shearing has been reported by researchers such as Machado *et al*. (2008).

Previous experience and research indicates that the control of waste **moisture content** is the single most important factor in enhancing waste decomposition in landfills. The type of leachate recirculation system utilized and the method of operation are selected after appropriate consideration of project goal related to moisture distribution.

The **unit weight** of waste is dependent of waste type, water content, and time since placement. Hater (2000) measured unit weight of the wastes at four landfills where leachate recirculation was used and the average unit weight was found to be 112 lb/ft^3 (17.94 kN/m^3), i.e., about 66% more dense than for conditions without leachate recirculation which had the average unit weight of 67 lb/ft^3 (10.73 kN/m^3).

For **shear strength** properties, Reddy et al. (2009) performed comprehensive laboratory study on 1.5-year-old municipal solid waste (MSW) exhumed from a landfill cell where low amounts of leachate were recirculated. Based on direct shear tests, drained cohesion and friction angle were found to be in the range of 12–64 kPa and 31–35° for landfilled MSW and 31–64 kPa and 26–30° for fresh MSW,

respectively. Neither cohesion nor friction angle demonstrated any correlation with the moisture content. Gabr and Valero (1995) conducted direct shear tests on 15–30-year-old MSW and the resulting shear strength properties ranged from 0–28 kPa and 20–39°.

RESULTS OF THE ANALYSIS AND DISCUSSION

As suggested by Bogner *et al*. (2001), the unit weights were assumed to increase with depth and the values applied to the base line case (Type O) were 8.8 kN/m^3 to 10.4 kN/m^3 from top to bottom the landfill. To model the combined influence of higher moisture content and waste settlement, unit weight values for Type I, II, and III bioreactors were represented by increase of 25%, 50%, and 75%, respectively, over the baseline case. The friction angle and cohesion values were assumed to vary linearly from 26° to 34° and from 9.5 kPa to 14.5 kPa from top to bottom, respectively, for the baseline case.

As mentioned, the cohesion and friction angle parameters do not show any correlation with moisture content, characterization of shear strength parameters, i.e., its amount and variation, were assumed to be same for all types of landfills. It is also assumed that waste will not be saturated under controlled recirculation and no pore pressure build up would occur. To see the effect of age of degradation of MSW on the stability of bioreactor landfill slope, linear variation (from top to bottom) of shear strength parameters, i.e., cohesion (c) and friction angle (ϕ), were taken from Table 1.

Table 1: Range of variation of shear strength parameters for MSW with age of degradation

Sr. no.	Age of MSW	Cohesion (kPa)	Friction angle (°)
Case 1	Fresh MSW	31 – 64 (avg = 47.5 kPa)	26 – 30 (avg = 28°)
Case 2	1.5 to 2.0 years old	12 – 64 (avg = 38 kPa)	31 – 35 (avg =33°)
Case 3	10 – 15 years old	0 – 28 (avg = 14 kPa)	20 – 39 (avg = 29°)

For the probabilistic slope stability analysis of MSW in bioreactor landfill, the mean values are taken from Table 1. It is assumed that properties are log-normally distributed and coefficient of variations (*CoVs*) in the MSW properties are taken in the range of 50 – 100% and Monte Carlo simulations are performed for the estimation of probability of failure (p_f) or reliability index (β) of landfill slope.

It should be noted that an increase in the number of simulations increases the accuracy of the results but at the same time it also increases computational efforts. Therefore, a compromise between accuracy and computational time is achieved by accepting some amount of error and in terms of confidence level in the estimation of mean and variance. From the literature (Baecher and Christian, 2003), a minimum sample size of 1536 is suggested for an acceptable error of 5.0 % and $\alpha = 0.05$, i.e., 95% confidence level in the estimated mean and variance of the output response. Therefore, in the present analysis, 2000 Monte Carlo simulations are performed.

The study incorporates use of finite element software PLAXIS 2D for the stability analysis of MSW bioreactor landfill slope. The software involves strength reduction technique for the evaluation of factor of safety for each realization of MSW

properties. The statistical information about the mean and variance of the calculated *factor of safety* is obtained from a number of Monte Carlo Simulation (*MCS*) runs.

Assuming lognormal distribution of calculated factor of safety values from 2000 number of simulations, the reliability index (β) is calculated using the following equation (3).

$$\beta = \frac{\ln\left[FS\sqrt{\frac{1}{1+CoV^2}}\right]}{\sqrt{\ln\left[\left(1+CoV^2\right)\right]}} \quad (1)$$

Where, FS is the mean factor of safety evaluated from 2000 simulations and CoV is its coefficient of variation.

Effect of variation in MSW properties and method of leachate recirculation. Figure 1 shows influence of variation in MSW properties as well as method of addition of leachate recirculation on the stability of bioreactor landfill slope comprised of fresh MSW. It can be noted that with increase in variation in the MSW properties, the stability of the slope assessed in terms of reliability index (β) gets reduced. It can also be noted that reliability index values for fresh MSW TYPE-O (baseline case) landfill is more than the corresponding values obtained for Type I, II, and II bioreactor landfills and the values are lowest for Type III bioreactor landfills where heavy liquids recirculation and application of leachate is observed.

Effect of age of degradation. Figure 2 shows the influence of variation in MSW properties and age of degradation on the stability of Type II bioreactor landfill slope. It is noted that with the assumed shear strength properties variation, the stability of the landfill slope increases with age as the values of reliability index for 10-15 years landfill slopes are slightly more than the corresponding values obtained for fresh MSW landfills.

It should be noted that slope stability analysis for bioreactor landfills need to consider site-specific conditions and bioreactor management strategies in order to make reasonable judgments for slope stability. Probabilistic analysis is a useful tool in order to achieve the goal.

CONCLUSION

The study highlights the importance of consideration of variation of geotechnical parameters, method of leachate recirculation and degree of decomposition in the probabilistic slope stability assessment of *MSW* bioreactor landfills. Monte Carlo simulation technique, combined with numerical analysis, is a very useful approach in this regard and provides realistic treatment to the reliability analysis of landfill slopes.

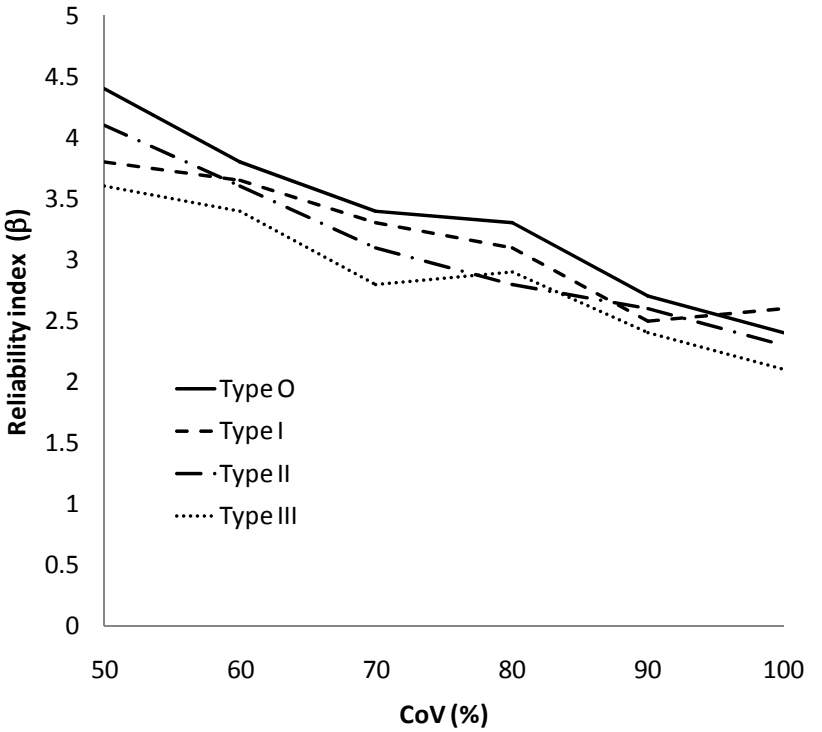

Figure 1: Effect of variation in MSW properties (*CoV%*) and method of moisture addition on Fresh MSW bioreactor landfill slopes

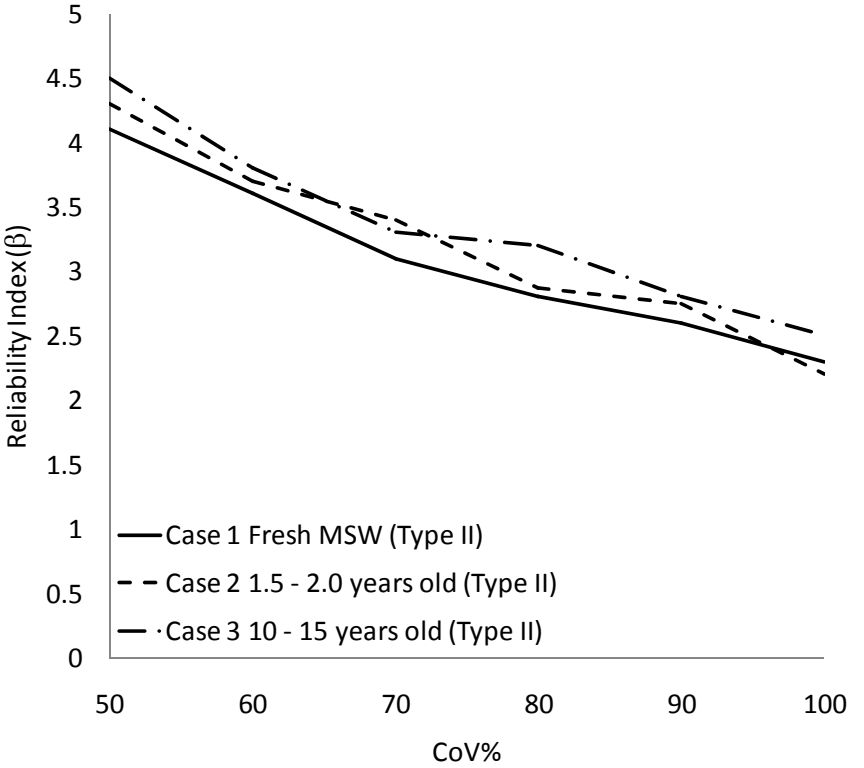

Figure 2: Effect of age of degradation and variation in MSW properties on the bioreactor landfill slope

REFERENCES

Baecher, G. B., and Christian, J. T. (2003). *Reliability and statistics in geotechnical Engineering*. Chi Chester, John Wiley Publications.

Bogner, J. E., Sweeney, R. E., Coleman, D., Huitric, R., and Ririe, G. T. (1996). "Using Isotopic and Molecular Data To Model Landfill Gas Processes." *Waste Management and Research*, 14, 367-376.

Duncan, J. M. (2000). "Factors of safety and reliability in geotechnical engineering", *J of Geotechnical and Geoenvironmental Engineering*, ASCE, 126(4), 307-316.

Gabr, M. A., and Valero, S. N. (1995). "Geotechnical properties of municipal solid waste." *Geotechnical Testing Journal*, ASTM, 18(2), 241–251

Gabr, M. A., Hossain, M. S., and Barlaz, M. A. (2007). "Shear strength parameters of municipal solid waste with Leachate recirculation", *J Geotech Geoenviron Eng*, ASCE, 133(4), 478 – 484.

Hater, G. R. (2000). "Leachate recirculation, landfill bioreactor development and data acquisition at waste management. *Presented at: landfill methane outreach program, third annual LMOP Conference*, Washington, D.C.

Kavazanjian, E. Jr. (2001). "Mechanical properties of municipal solid waste", Eight International Landfill Symposium, Proc. Sardinia '01 – 8th International Waste Management and Landfill Symposium, Environmental Sanitary Engineering Centre (CISA), University of Padua, Italy Vol. III, 415-424.

Kura, B., and Lea, W. R. (1995). "Prediction of Worst Case Methane Concentrations Due To Landfill Emissions in Absence of Historical Meteorological Data." *Proceedings of 18th Annual Landfill Gas Symposium*, New Orleans, LA, March 28 30, 1995, 116-131.

Li, Q., Guo, X., and Liang, S. (1999). "Study on formation of waste gases from municipal refuse landfill sites." *Shanghai Huanjing Kexue*, 18(6), 270-272.

Reddy, K. R., Kosgi, S., and Motan, E. S. (1996). "Interface shear behavior of landfill composite liner systems: A finite element analysis." *Geosynthetics International*, 3(2), 247-275.

Machado, Vilar, O.M., S.L and Carvalho, M.F. (2008), Constitutive model for long term municipal solid waste mechanical behavior, Computers and Geotechnics, Vol 35, issue 5, 775-790

Reinhart, D. R., McCreanor, P. T., and Townsend, T. (2002). "The bioreactor landfill – its status and future." *Waste Management and Research*, ISWA, 30, 172-186.

Sharma, H. D., and Reddy, K. R. (2004). *Geoenvironmental Engineering: Site Remediation, Waste Containment and Emerging Waste Management Technologies.* John Wiley, NY.

USACE (1997). *Engineering and design: introduction to probability and reliability methods for use in geotechnical engineering*. Department of the Army, Washington, D.C. Engineering Circular No. 1110-2-547.

Sustainable Flood Risk Management: Lesson from Recent Cases

Xiong (Bill) Yu[1] and Yuewen Huang[2]

[1]Assistant Professor, Department of Civil Engineering, Case Western Reserve University, Cleveland, OH 44106-7201, xiong.yu@case.edu
[2]Senior Engineer, Guangzhou Investigation Design and Research Institute of Water Conservancy & Hydropower, Guangzhou, Guangdong, China, 510640,

ABSTRACT

Mitigation of flood damage has accompanied the development of human cultures. Flood remains one of the biggest natural hazards threatening the prosperity of modern society. Flood related fatalities and damages continue to increase over the world. Flood research and flood protection policy is currently dominated by a technical world view. The recent decades however foresee the importance of social and socio-economic aspects due to expansive and intensified land use and the rising damage potentials in floodplain areas (Schanze 2002, Messner and Meyer 2005). The lesson from hurricane Katrina presses embracing a sustainable flood risk management strategy, which requires integration of both structural and non-structural measures. An optimal flood risk management can be achieved only by concerted implementing both non-structural and structural measures. Such strategies will contribute to a sustainable flood risk management practice. The core of flood risk management lies in the proper planning and policy design to form an appropriate feedback loops in the engineering and social-economic system. This paper gives an overview about the existing and emerging practice over the world to implement sustainable flood risk management.

INTRODUCTION

Reducing the impacts of natural disaster is a long term task facing the human society (Dilley et al. 2005). To accommodate diversified public needs, the modern infrastructure systems (such as communications, transportation, water supply, power supply etc) are becoming increasingly technology enhanced and complex, which are also becoming increasingly vulnerable to various natural and man-made hazards (Newman et al. 2005). How to effective prevent and respond to these threats is a new challenge facing decision-makers.

Among the various natural hazards, flood is one of the biggest treat to the human culture. Globally flood risk, defined as a function of both flood probability and potential damage, concentrates in the middle and eastern part of U.S., eastern Asia and Most part of Europe. For the United States, despite of extensive investment in flood protection infrastructures, flood damage continues to increase. Flooding was estimated to have caused approximately $50 billion damage in the U.S. in the 1990s (NWS-HIC 2001). Although flood damage fluctuates greatly from year to year, estimates indicate that there has been an increasing trend of flood damages over the

past century (Pielke and Downton 2000, Fig. 1). This is attributed to factors such as a change in climate (Hamburger 1997), population growth and development (Kerwin and Verrengia, 1997). Another important factor is the flood policies, which are successful to certain degree yet are insufficient (Coyle 1993, Labaton 1993).

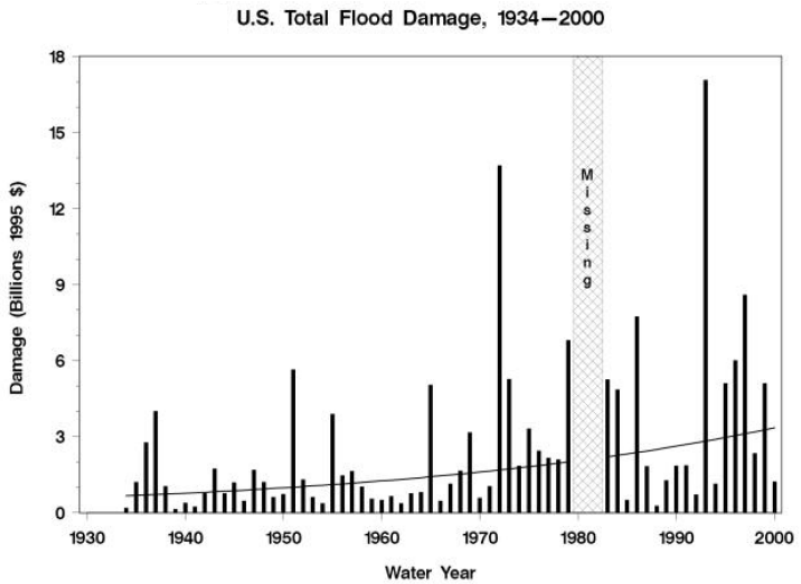

Fig. 1 Total U.S. Flood Damage between 1934 and 2000 (NWS, 2001)

Exploring scientific guidelines for flood risk mitigation and management are crucial to ensure the sustainable development of human society. To understand its increasing damage and to assess its implications for policy, decision makers need to resolve the independent and interdependent influences of climate, population growth and development (Pielke et al. 2002). This paper discusses the factors that contribute to flood vulnerability and will present recent development of system level vision to optimize flood risk reduction activities.

BACKGROUND

The catastrophic failure of New Orleans levee system during hurricane Katrina, which caused over 1,500 causalities and over $150 billion in economic damage (the most costly peace-time failure of an engineered system in North American history) (IPET 2006), calls for radically improvement of the current management practice for flood risks. According to the reconnaissance of New Orleans levee failure by U.S. Army Corps' Integral Performance Evaluation Team (IPET, 2006), not a single factor has contributed to the failure. The failure roots from incompetence decisions at different system levels. Among these, a general misconception occurs at all levels among administrators, engineers and local residents in terms of insufficient appreciation of the potential flood risks. As the results, the levee system was not properly designed, constructed and maintained to withstand hurricane Katrina. The potential of risks are also not effectively communicated to residents both prior to the events and at the on-set of Katrina. A general misconcept in local developers and residents causes unsound selection of residential zones which is

subject to high risk potential under large scale hurricane event (Seed et al. 2007, Sills et al. 2007).

The lesson by Katrina not only presses a comprehensive review of the design, construction and maintenance of critical levee and dam structures, but also requires a systematic vision to be established as the efforts to prevent similar tragedies.

Placing Flood Risk Management under Socio-economic scenaries: Flood research and flood protection policy is currently dominated by a technical world view. The recent decades however foresee the importance of social and socio-economic aspects due to expansive and intensified land use and the rising damage potentials in floodplain areas global-wise. All these bring about increasingly conflicts between socio-economic land use and flood protection policy (Granger 2000, Schanze 2002, Messner and Mayer 2005). A shift in paradigms is necessary from a pure technical oriented flood protection towards flood risk management, which places the flood protection system design and maintenance into the societal sceneries. A system vision is necessary to develop a sustainable and resilient flood protection system. A new interdisciplinary view on flood management policy is needed to overcome the existing technical alignment of flood research area. The interactions and social dynamics of flood risk perception, preparedness, and vulnerability need to be properly accounted for to develop sound strategy for flood risk management.

Risk Perception and Preparedness and Its Relationship to Flood Vulnerability: Flood damage analysis aims at quantifying flood damages for specific future scenarios with different flood events and flood policies in order to quantify the benefits of flood protection measures and support policy decisions (Plate 2002, Plattener 2005, Delitala 2005). Flood induced damages are decided by the level of flood and the vulnerability of a given region. The inundation depth is commonly used as vulnerability indicator in current flood damage analysis. When placed under the social-economic sceneries, risk perception and the resultant preparedness are also crucial for flood induced damages. Regions with low flood risk perception lead to low degree of preparedness for flood events. The vulnerability to flood events is usually high. Therefore there exist vulnerability factor which is also related to risk perception and preparedness of communities and individuals (Messner and Meyer 2005, Olczyk 2004, Motoyoshi 2006).

The issue with flood risk perception caused paradox in flood plain development and structural flood protections in New Orleans. While the flood plain of this city has been cited as to be more appropriate for a lake, the construction of flood protection structures caused the wrong perception among local residents on the level of flood protection they are provided. As the results, unregulated flood plain development plan was not actively discouraged. This not only increased the vulnerability but also compromised the ability of flood protection structures (Figure 2).

Fig. 2View looking up the east side of the London Avenue Canal near Robert E. Le Boulevard crossing showing the encroachment of homes against the slope of the levee. (photo by Watkins).

This then naturally brings about the question, why this happens? Engineering structure has been perceived as the major methods for flood risk mitigation. This example elucidates that exclusively reliance on engineering structures, however, brings about unsound flood management practice. From psychological perspective, low flood risk perception causes incompetent decisions in both administrative authorities and local residents. As the consequence, the developed zone is under high vulnerability.

As described by Kron and Thumerer (2002), two major flood events of comparable size occurred in 1993 and 1995 in the Rhine River basin. While people were less aware of the flood risk in 1993, their experience of the 1993 increased their awareness and preparedness. As a consequence, the amount of damage was only half in 1995 compared to 1993. Another case occurred in China in 2005. On June 22, 2005, historical level of flood hit Wuzhou City in the Southern province of Guangxi. The flood level is over 1 m higher than the designed flood level by this levee. Thus excessive overtopping occurs (Huang and Yu 2007). This however caused no fatalities. Investigation shows as this city is subjected to flood throughout the history, the local residents have extensive experience that enables them to adopt proper survival strategies. This example illustrates that increased preparedness helps to reduce flood risks.

These cases indicate that risk perception and preparedness are important for flood risk mitigations. Considering solely the technical issues will be insufficient. A sustainable management strategy needs to embrace both structural and socio-economic methods to optimize the investment/benefits of flood risk mitigation.

SUSTAINABLE FLOOD RISK MANAGEMENT

For over two centuries, structural measures are the dominant methods over the responses over the world. In the United States, the principal approach to flood damage reduction was the construction of levees. In the early 20th century, levees

were augmented by channel work to speed floodwaters to their ultimate destinations. In the mid-1950s initial proposals were made for the use of non-structural measures for flood damage reductions. In 1969, the federal government instituted the National Flood Insurance Programme (NFIP), which combines subsidized flood insurance with requirements for participating communities to regulate land use in the floodplain. Although flood insurance has been available to floodplain residents since 1969, only 20-30% of those eligible participate in the insurance program (Gallova 2004).

The concept of sustainable flood risk management is emerging to achieve the optimal flood risk reduction. This is especially important considering the funding restraints. The key idea of sustainable flood risk management is to engage people and local communities into flood risk reduction process. "Sustainable flood management provides the maximum possible social and economic resilience against flooding by protecting and working with the environment, in a way which is fair and affordable both now and in the future" The inclusion of social resilience designed to "enhance community benefit with fair outcomes for everyone" is noteworthy (Werritty et al. 2007). Implementing sustainable flood risk management provides new horizon to deal with a traditional problem facing the modern society. Further study in this area is needed to uncover the most efficient approaches to achieve the sustainability in flood risk management and to provide decision support to different levels of administrations.

Benefits of Sustainable Flood Management and Its Implementation: Sustainable flood management requires to treat the flood protection system as a system that integrate the structural components (i.e., dams, levees, flood gates, etc) with the non-structural socio-economic factors (population, economy). A paradox situation can occur between structural and non-structural measures for flood risk control. For example, the construction of structural measures tends to prompt the perceived reduction in flood vulnerability. As the consequence, there are increased floodplain development activities. This subsequently leads to increased flood risk. A positive feedback process can be developed which encourages unregulated flood plain developments. This process continues like rolling snowball, which increases the vulnerable of system under unexpected flood events.

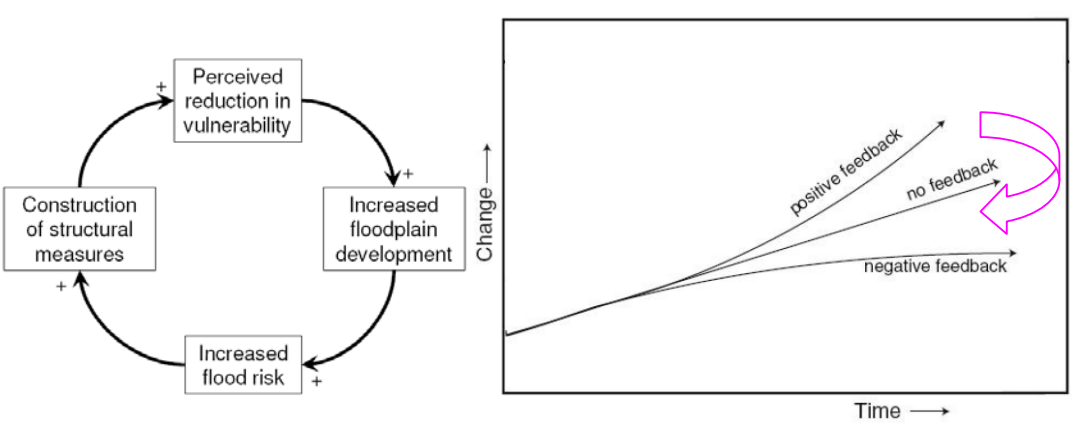

Fig. 3 Feedback cycle related to flood vulnerability (pink arrow indicates desirable trend)

The situations illustrated in Fig. 3 can be mathematically described by employing control system theory. A feedback process through effective risk communications changes the risk perception. This subsequently leads to regulated floodplain development, preparedness, and compliance with flood risk regulations. The subsequence increase in the resilience of local communities will bring about reduced vulnerability that can't be achieved by structural measures along.

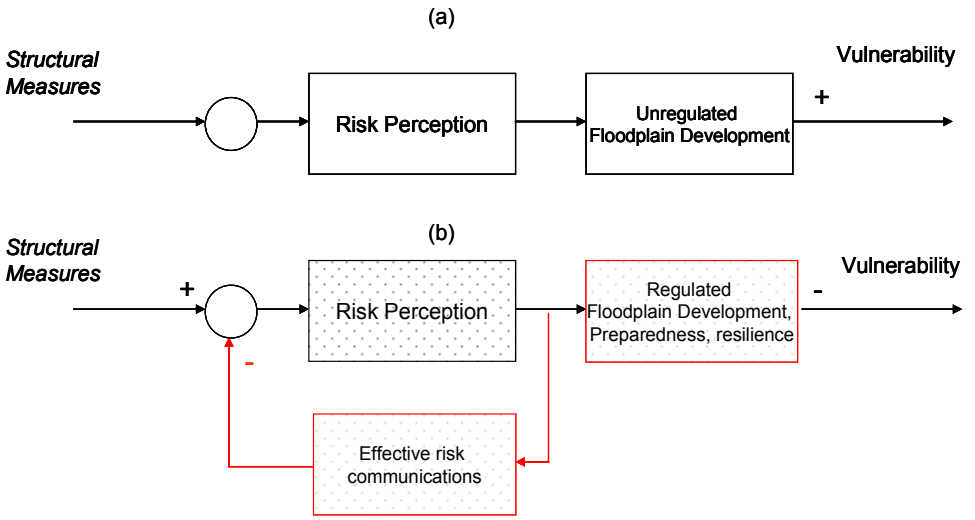

Fig. 4 Conceptual models for flood management strategies a) solely reliance on structural measures lead to increased vulnerability; b) concerted structural and non-structural measures (red boxes) leads to reduced vulnerability (or increased resilience)

A sustainable flood management strategy encourages residents and local communities to be involved into flood management practice. This helps to increase the local resilience and preparedness. By incorporating people dimension into flood risk management, the vulnerability of flood damage reduces under the similar level of structural protections, which helps achieve the maximal flood risk reductions under

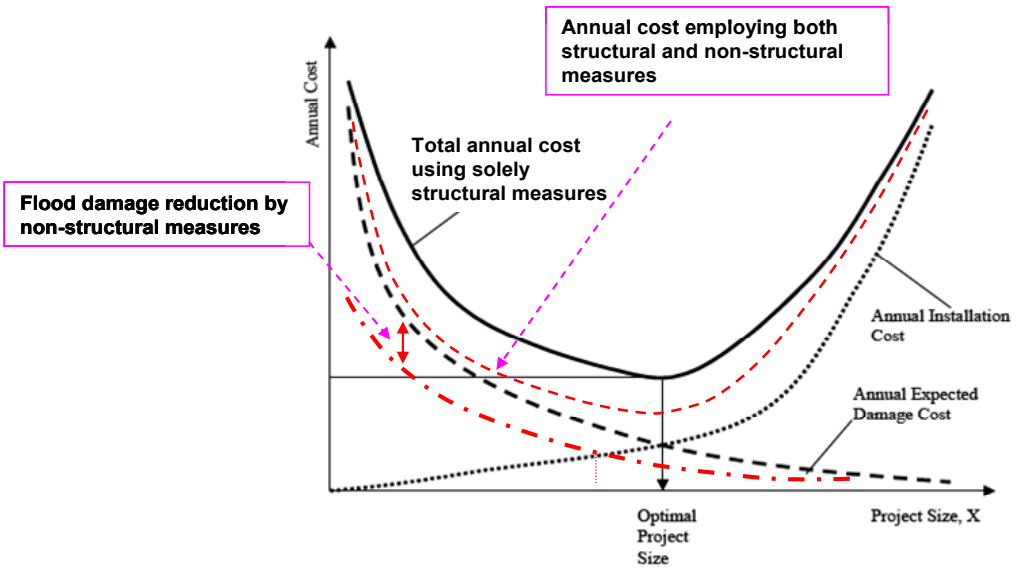

Fig. 5 Economic analyses of sustainable flood risk management practice by incorporating non-structural measures (modified from Tung 2002)

constraints of practical economic conditions (Fig. 4). The additional benefits include the reduced annual cost for maintaining and upgrading flood protection structures. This is especially important under the current societal sceneries where funding resources have diversified usages.

To implement sustainable flood management, guidelines need to be developed in the all phases of flood protection (Fig. 5). These guidelines will include recommendations to implement a variety of pre-flood activities, operational flood management and post-flood activities. As seen from Fig. 5, these guidelines, which combines the structural and non-structural measures, will result in effective flood damage mitigation in the most efficient and economic fashion. The decision will be optimized over solely considering structural or non-structural measures.

CONCLUSIONS

This paper provides an overview about the emerging practice over the world of integration of both structural and non-structural methods for flood risk mitigation. Flood research and flood protection policy is currently dominated by a technical world view. The recent decades however foresee the importance of social and socio-economic aspects due to expansive and intensified land use and the rising damage potentials in floodplain areas. The sustainable flood risk management concept aims to achieve flood risk reduction by establishing resiliency into every component of flood protection system and floodplain. An optimal flood risk management can be achieved only by concerted implementing both these non-structural and structural measures. The core of flood risk management lies in the proper planning and policy design to form an appropriate feedback loops in the engineering and social-economic system. This will result in flood damage mitigation practice that is the most efficient and economic in the long term.

REFERENCES

Coyle, K. (1993). River tinkering worsened flooding. *USA Today* (July 14).

Delitala, A. M. S. (2005). Perception of intense precipitation events by public opinion, *Nat. Hazards Earth Syst. Sci.,* 5, 499–503.

Dilley, Maxx, Chen, Robert S., Deichmann Uwe, Lerner-Lam, Arthur L., and Arnold, Margaret (2005). Natural Disaster Hotspots: A Global Risk Analysis, *Report by World Bank*, April 2005.

Gallowa, G.G. (2004). Integrated Flood Management Case Study USA: Flood Management – Mississippi River, *The Associated Programme on Flood Management*.

Granger, K. (2000). Hazards and risk concepts, in: Natural hazards and the risks they pose to South-East Queensland, edited by: Granger, K. and Hayne, M., in conjuction with the Bureau of Meteorology, pp. 1.1–1.13, *Australian Geological Survey Organisation*.

Hamburger, T. (1997). Floods renew interest in climate changes: Is global warming causing more precipitation? Minneapolis Star-Tribune (April 29).

Huang Y.W. and Yu, X., 2007, "Risk-Based Design of Levee System", *ASCE Geo-Congress Conference*, New Orleans.

IPET (2006). "Performance evaluation of New Orleans and Southeast Louisiana

hurricane protection system, *Draft final report of the Interagency Performance Evaluation Task Force*, Volume VI- the performance-Interior drainage and pumping". June 2005 (http://ipet.wes.army.mil).

Kerwin, K. and Verrengia, J.B. (1997). Rare storm loosed Fort Collins flood: Hazard experts say deluge should serve as 'wake-up call' for growing population. *Rocky Mountain News* (August 3).

Lastoria, B., M. R. Simonetti, M. Casaioli, S. Mariani, and G. Monacelli. (2006). Socio-economic impacts of major floods in Italy from 1951 to 2003, *Advances in Geosciences*, 7, 223–229, 2006.

Labaton, S. (1993). US weighs scrapping levees for flood control. *New York Times*

Linstone, H.A. and Turoff, M. (1975). *Introduction. In: The Delphi Method: Techniques and Applications* (Linstone, H.A. and Turoff, M. eds.) Addision Wesley Publishing Co., pp.3-12.

Messner F. and Meyer, V. (2005). Flood damage, vulnerability and risk perception – challenges for flood damage research, *UFZ discussion papers*, April 2005, 26p.

Motoyoshi, T. (2006). Public Perception of Flood Risk and Community-based Disaster Preparedness, *A better integrated management of disaster risks: Toward resilient society to emerging disaster risks in mega-cities*, Eds., S. Ikeda, T. Fukuzono, and T. Sato, pp. 121–134.

Newman, D. E., B. Nkei, B. A. Carreras, I. Dobson, V. E. Lynch, P. Gradney (2005). "Risk assessment in complex interacting infrastructure systems", *Thirty-eighth Hawaii International Conference on System Sciences*, Hawaii, January 2005.

NWS-HIC (National Weather Service-Hydrologic Information Center) (2001). Flood Losses. http://www.nws.noaa.gov/oh/hic/flood_stats/Flood_loss_time_series.htm [accessed August 1, 2007].

Olczyk, M. (2004). Flood Risk Perception in Red River Basin: Impllications for Hazard and Disaster Management, *Thesis*, University of Manitoba

Pielke, R.A. Jr. and Downton, M.W. (2000). Precipitation and Damaging Floods: Trends in the United States, 1932–1997. *J. Climate*, 13(20), 3625–3637.

Pielke, R.A., Downton, M.W. and Miller, J.Z.B. (2002). Flood Damage in the United States, 1926–2000, A Reanalysis of National Weather Service Estimates.

Plate, E. J. (2002). Flood risk and flood management, *J. Hydrol.,* 267, 2– 11.

Plattner, T. (2005). Modelling public risk evaluation of natural hazards: a conceptual approach, *Nat. Hazards Earth Syst. Sci.*, 5, 357–366.

Schanze, J. (2002), Nach der Elbeflut 2002: Die gesellschaftliche riskovorsorge bedarf einer transdisziplinären Hochwasserforschung. *GAIA* 11(4), pp. 247-254.

Seed R.B. et al. (2007). "Investigation of the performance of the New Orleans regional flood protection systems during hurricane Katrina: lessons learned", *Geotechnical Special Publication 161 Embankments, Dams and Slopes*.

Sills G.L., Vroman, N.D., Wahl, R.E. and Schwanz N.T. (2007). "Lessons learned from the levee failures in the New Orleans area and their impact on levee design and assessment across the nation*", Geotechnical Special Publication 161, Embankments, Dams and Slopes*.

Werritty, A., Donald Houston, Tom Ball, Amy Tavendale and Andrew Black (2007). "Exploring the Social Impacts of Flood Risk and Flooding in Scotland". *Scottish Executive Social Research*.

Life Cycle Approaches for Brownfields Redevelopment

Patricia M. Gallagher[1] and Sabrina Spatari[2]

[1]Associate Professor, Civil, Architectural and Environmental Engineering (CAEE), Drexel University, 3141 Chestnut St, Philadelphia, PA 19104; PH (215) 895-6426, FAX (215) 895-1363; email: pmg24@drexel.edu
[2]Assistant Professor, CAEE, Drexel University, 3141 Chestnut St, Philadelphia, PA 19104; PH (215) 571-3557; email: ss3226@drexel.edu

ABSTRACT

Life cycle assessment (LCA) has emerged as a comprehensive analytical method to evaluate products, processes and activities and is increasingly being used within engineering decision making. The LCA framework offers a unique analytical perspective for integrating global as well as regional and local-scale sustainability goals into engineering decisions. The purpose of this paper is to compare life cycle cost and select life cycle environmental impact criteria for different soil remediation technologies through solidification or stabilization for comparably-sized projects. The main hypothesis posed here is that economies of scale effects influence cost and environmental decision metrics for contaminated soils and sites; and moreover that economies of scale identified for Superfund remediation activities can be applied to brownfields sites. LCA methods are used in conjunction with case histories to investigate these hypotheses.

Data from the Annual Status Report (ASR) Remediation Database for Superfund sites were mined to produce cost curves related to solidification/ stabilization techniques used for remedial action on past projects. These data were analyzed to estimate returns to scale for different remediation techniques. Data analysis shows a decrease in unit cost as the scale of the project increases. The methods used for Superfund projects will subsequently be applied to brownfields remediation projects. Given that the majority of brownfields remediation rests with the private sector, comprehensive cost data from specific brownfields projects is not readily available for analysis.

A major impediment to many brownfields redevelopment projects is cost of remediation. Determining economies of scale for different remedial alternatives may provide insight into the most cost effective approach for brownfields redevelopment projects of different sizes. Different remediation approaches can often be used to meet the multiple challenges and objectives of brownfields redevelopment. The results of this study will provide a basis for decision makers to determine the most economical remedial alternatives based on the scale of the project and remedial technology.

INTRODUCTION

Life cycle assessment (LCA) has emerged as a comprehensive analytical method to evaluate products, processes and activities and is increasingly being used within engineering decision making. The LCA framework offers a unique analytical perspective for integrating global as well as regional and local-scale sustainability goals into engineering decisions. The purpose of this paper is to compare life cycle cost and select life cycle environmental impact criteria for different soil remediation technologies through solidification or stabilization for comparably-sized projects. It is hypothesized that economy of scale effects influence cost and environmental decision metrics for contaminated soils and sites. It is further hypothesized that economies of scale identified for Superfund remediation activities can be applied to brownfields sites.

Economies of scale have been addressed in literature pertaining to manufacturing (Argote and Epple 1990), construction (Farghal and Everett 1997), transportation (Wang et al. 2007), infrastructure (Levinson 2010), and electric and water utilities (Kumar et al. 2008, Ghafoori and Flynn 2007, Nafi and Kleiner 2010). Argote and Epple (1990) discuss organizational "learning curves" whereby large increases in productivity are realized as the organization gains experience in production. Farghal and Everett (1997) apply the concept of learning curves to construction, suggesting that the greatest potential value of learning curves lies in their ability to predict future performance instead of fitting historical data. They present a method for using learning curves to predict the time or cost to complete the remaining cycles of an activity in progress that is more accurate than the standard method using the cumulative average. Nafi and Kleiner (2010) present a multi-objective genetic algorithm scheme to optimize strategies for rehabilitation and/or replacement of individual water mains. The authors propose an approach for the efficient scheduling of individual water mains for replacement in a short to medium predefined planning period and subject to various budgetary constraints. Their approach accounts for economies of scale considerations as well as harmonization with other known infrastructure works.

Certain technologies that are in development may not be as well characterized in literature in terms of returns to scale due to limited experience at commercial scale production. An example of such technologies is biomass-to-energy, including power and liquid fuels, where only a few commercial scale systems exist in North America. For example, Kumar et al. (2008) conducted a preliminary techno-economic analysis of power generation in forest regions of Western Canada. They emphasize that the cost of power generation decreases dramatically as the size of the plant increases. For two plant sizes in each of two locations in British Columbia, they estimated that the cost of power generation would be comparable with other "green power" options in British Columbia. Similarly, Ghafoori and Flynn (2007) consider the use of anaerobic digestion of manure to produce biogas and in turn electric power. They compare farm or feedlot based units with centralized plants in two different settings in Alberta, Canada. The results of the analysis show that a centralized plant drawing manure from different sources in the mixed farming area would be more economical. In contrast, where beef feedlots are concentrated, an individual feedlot could produce

power at a lower cost than the centralized plant. An important observation from each of these studies is that transportation distances, when moving raw materials to and from facility sites, can be an important variable affecting total cost of an operation. When production operation scales, there is a point at which additional transport costs can be overcome by economies of scale effects. We explore this dynamic with respect to treatment technologies used in the remediation of contaminated soil by solidification or stabilization, and specifically how the cost of treatment technology scales with job size. An objective of this work is to explore cost reduction for risk mitigation of contaminated sites through economies of scale and treatment technology.

For contaminated site remediation, solidification is a process in which soil, sludge or sediment is mixed with a binder or reagent to change its physical properties and make it a solid. Stabilization involves a chemical reaction that reduces the ability for the contaminant to leach out of the waste. These techniques are widely used at hazardous waste sites to prevent migration of contaminants from the site. Mixing the binder can be done either in situ or ex situ. In situ treatment involves mixing the binder or chemical agent into the soil in place, typically using augers. Ex situ treatment involves excavating the soil, sludge or sediment and mechanically mixing it with the binder or chemical agent. The treated material may then be placed at the site or disposed in a landfill. Common types of binders include organic materials such as asphalt, organophilic clay, or activated carbon. Inorganic binders include cement, fly ash, lime, phosphate, soluble silicates, and sulfur. The amount of reagent for solidification or stabilization typically ranges from 5 to 30% by volume. In general, solidification or stabilization (S/S) costs vary according to site, contaminants, and ex situ or in situ treatment.

METHODS

Data mining techniques were applied to the United States Environmental Protection Agency Annual Status Report (ASR) Remediation Database (EPA 2007) to extract data-profiles on S/S techniques used for remedial action on past projects. The database contains information about the status and achievements of treatment technology applications for soil, solid wastes and groundwater at National Priorities List (NPL, or Superfund) sites for remedy decisions between 1982 and 2005. The current version of the ASR Remediation Database includes a total of 1,915 treatment technology applications. Its release coincided with the Annual Status Report 12th Edition (EPA 2007), which includes information on projects through October 2006.

In the Superfund Amendments and Reauthorization Act of 1986 (SARA), preference was given to treatment rather than containment or removal and disposal for remediating Superfund sites. By September 2005, the NPL had 1,229 sites with 54 additional sites proposed for listing. At that time, 307 sites had been deleted from the NPL. About 65% of Superfund sites have instituted or will institute source treatment, groundwater treatment, or both, as part of the remediation. Almost 30% of the sites have used both source treatment and groundwater treatment.

In the ASR Remediation Database, the status of 1,915 projects is tracked for application of treatment technologies for both source control and groundwater

treatment. Treatment technologies include both in situ and ex situ treatment projects. The database includes information collected from the Comprehensive Environmental Response, Compensation, and Liability Act Information System (CERCLIS) for FY 1982 to 2005 that had been documented as of October 2006. Information was also gathered from site-specific decision documents such as Records of Decision and Closeout Reports as well as other online EPA sources. The Record of Decision establishes the remedial action selected for the site. If a significant change occurs between the Record of Decision (ROD) and implementation of the remedial action, an Explanation of Significant Differences (ESD) is filed. For each Superfund site, the EPA maintains electronic copies of the ROD and any ESD that are filed. However, Closeout Reports are not readily available through the EPA Superfund website.

For this particular study, case histories which used S/S technologies were selected for analysis. This broad category includes case histories in which the mobility of hazardous substances and contaminants in the environment is reduced through physical and chemical means. This includes cases in which the contaminants are physically bound or enclosed within a stabilized mass either ex situ or in situ. In ex situ S/S, the material to be treated is excavated and the resultant material is disposed. With in situ S/S, the binder is added to the contaminated soil or waste in place and the stabilized material is left in place.

Of the 2010 records in the database, 207 were returned as using S/S. For each record, a "Detailed Information" form was provided, which included space to provide details on the site, the operable unit, the technology used, the media and quantity treated, contaminants present at the site, site status, completed project information, and additional information about the dates of treatment and cost. Many of the records were only partially complete. In cases where records were incomplete, the RODs and ESDs were downloaded from the EPA website and consulted to determine if the additional information could be readily obtained. Closeout Reports were not obtained. Therefore, while unlikely, it is possible that information obtained from an ROD could have been superseded by a Closeout Report. The data were analyzed to estimate returns to scale for different remediation techniques. Cost data were adjusted to 2010 dollars assuming a constant inflation rate of 3%.

RESULTS

Of the 207 records in which S/S technologies were used, 37 contained cost data in conjunction with estimated quantities of treated material. Of these 37 case histories, the following general comments can be reported:

- The sites were located in 22 states.
- Solidification was used in 29 cases, stabilization was used in 7 cases and both solidification and stabilization were used in 1 case.
- Treatment was ex situ in 29 cases and in situ in 8 cases
- A wide variety of reagents or binders were used, including cement, lime, phosphate, sulfur, cement kiln dust, acrylamide, calcium carbonate, calcium chloride, and flyash. In 3 cases, the stabilizer was listed as "pH controlled." In 2 cases, "proprietary additives" were reported, once as a stand-alone treatment and once in conjunction with cement.

- Treatment quantities ranged from 125 cubic yards (cy) to 1,033,000 cy.
- Unit costs ranged from a low of $3.30 for the largest quantity treated (1,033,030 cy) to a high of $9,971 for the smallest quantity treated (125 cy).
- Treatment dates ranged from 1987 to 2002.

Figure 1 shows the data from the 37 sites that provided both quantity and cost information in the ASR Remediation Database. The trend line was fit using a power regression. The curves have the hypothesized shape, indicating that returns to scale generally exist for remediation by stabilization or solidification. However, there is a large amount of scatter in the data, as demonstrated by the low R^2 value.

The scatter is attributed to several factors. First, there is much uncertainty in the data set alone, as well as expected variability in cost adjustment parameters (e.g., inflation), and that specific commodity markets such as those that supply remediation materials (e.g., cement, binders, etc.) are subject to changes in market price dynamics. Next, records often contained approximate costs and estimated quantities. In addition, there was a wide variety of stabilizers used both in situ and ex situ. For the in situ treatment, the depth of treatment was not always provided. Another complicating factor is that many of the records had incomplete data on the stabilizers used and the contaminants treated. Finally, the sites were geographically dispersed across the U.S.

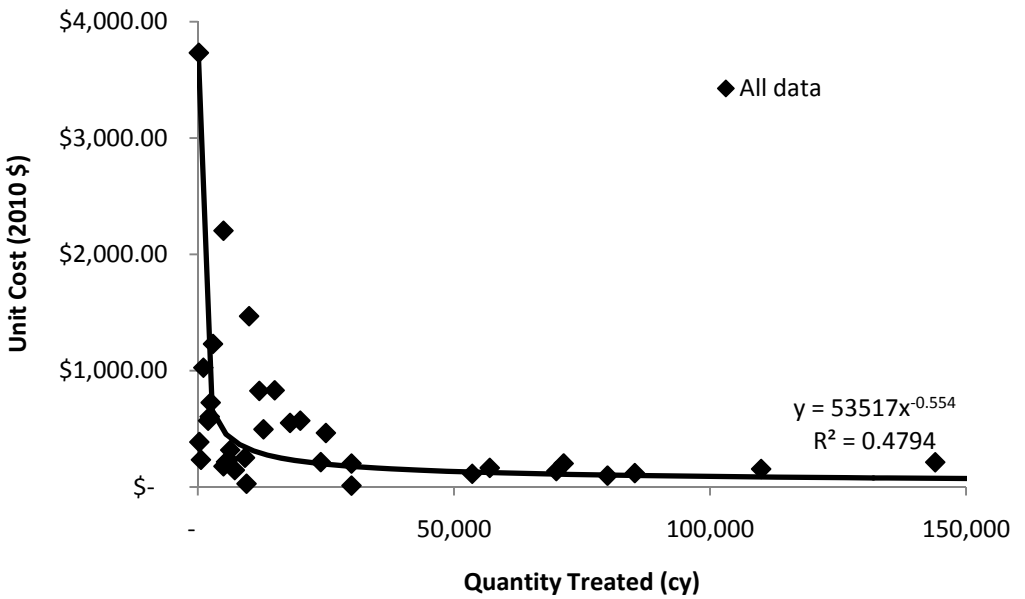

Figure 1. Variation in unit cost with treatment quantity for all data. Data points at the extreme ends of the axes are not displayed, but were used in the analysis. Points omitted from the graph include ([125, $9,971], [1,200, $9,227], and [1,033,030, $3.30]).

In order to consider the effects of treatment method (in situ vs. ex situ), treatment type (stabilization vs, solidification) and type of stabilizer used, subsets of the data were extracted and plotted as shown in Figures 2 through 4. Figure 2 shows ex situ and in situ data, respectively. The ex situ data consists of 29 sites (26 are shown on the graph). The stabilizers used were reported in all but 5 of these cases and

included cement, lime, phosphate, cement kiln dust, flyash, proprietary admixtures, pH control admixtures, sulfur, and/or organophilic clay (some sites used more than one admixture). Quantities ranged from 125 cy to 1,033,000 cy, with unit costs ranging from $13,300 to $4.66 (2010 $), respectively. As shown in Figure 2, the power regression yields an R^2 coefficient close to that computed for the full data set (Figure 1). In situ treatment includes 8 cases histories, in which cement, acrylamide, phosphate, sulfur, flyash, calcium carbonate, calcium chloride, and/or pH control admixtures were used. Quantities ranged from 180 cy to 71,000 cy, with unit costs ranging from $3700 to $200 (2010 $), respectively. These data show a higher R^2 value than either the full data set or the ex situ data.

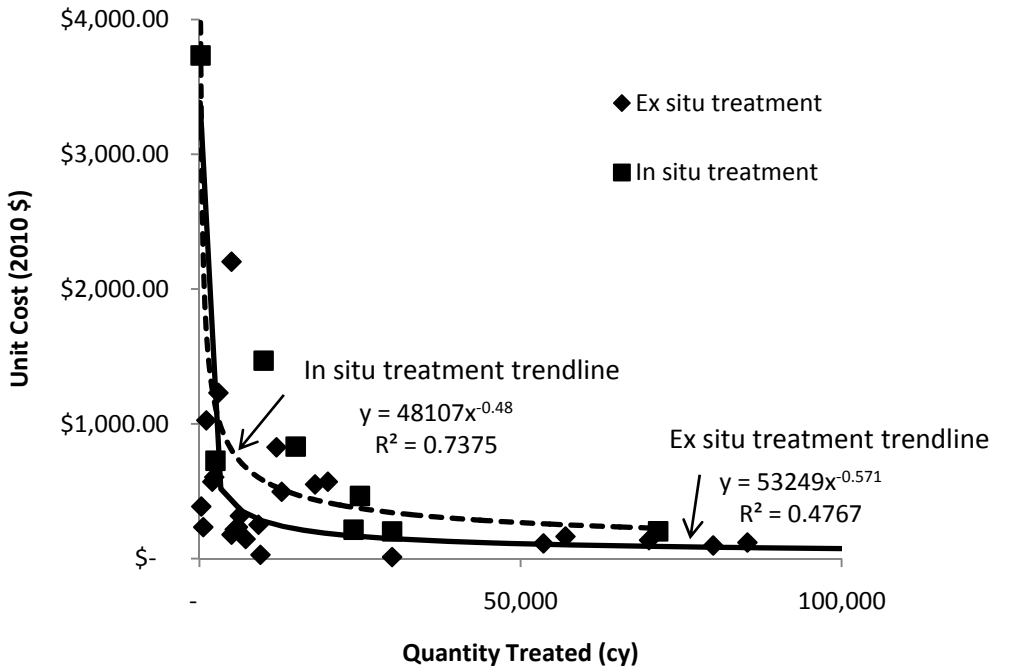

Figure 2. Variation in unit cost with treatment quantity comparing ex situ and in situ treatment. Data points at the extreme ends of the axes are not displayed, but were used in the analysis. Points omitted from the graph include ([125, $9,971], [1,200, $9,227], and [1,033,030, $3.30]).

As discussed earlier, solidification is a process in which soil, sludge or sediment is mixed with a binder or reagent to change its physical properties and make it a solid, whereas stabilization involves a chemical reaction that reduces the ability for the contaminant to leach out of the waste. In Figure 3, sites at which solidification was used were compared with sites at which stabilization was used. R^2 values were higher for sites at which stabilization was done than for sites at which solidification was done.

Figure 4 shows data from case histories in which cement was used either separately or with other admixtures. These data include both in situ (6 sites) and ex situ (19) treatment. At some of the sites, admixtures besides cement were used and included sulfur, acrylamide, flyash, organophilic clay and/or proprietary additives.

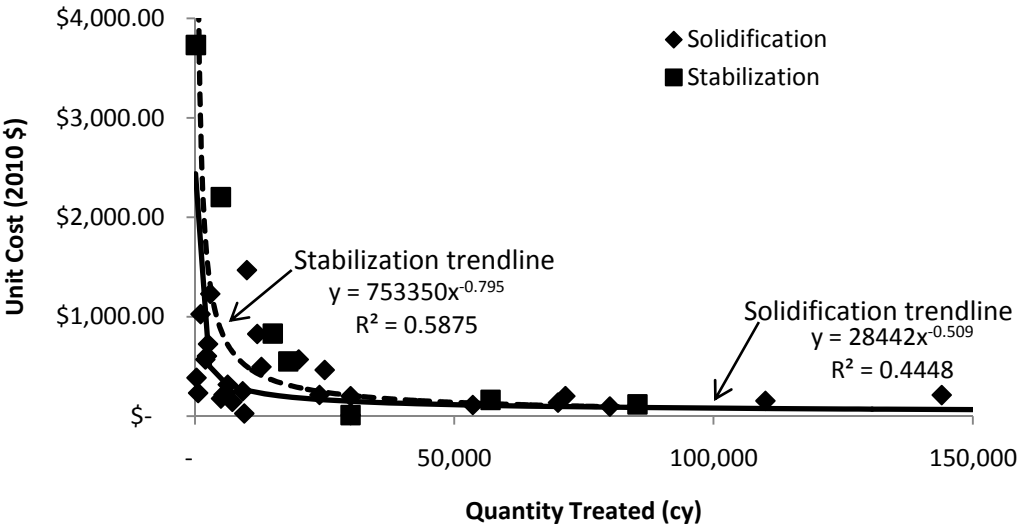

Figure 3. Variation in unit cost with treatment quantity comparing solidification and stabilization. Data points at the extreme ends of the axes are not displayed, but were used in the analysis. Points omitted from the graph include ([125, $9,971], [1,200, $9,227], and [1,033,030, $3.30]).

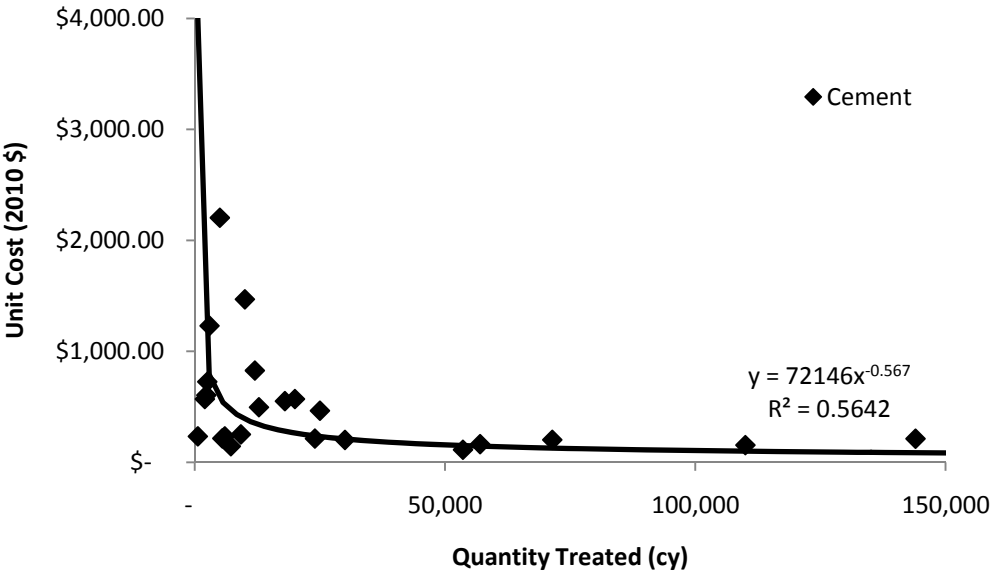

Figure 4. Variation in unit cost with treatment quantity for treatment with cement. Data points at the extreme ends of the axes are not displayed, but were used in the analysis. Points omitted from the graph include ([125, $9,971], [1,200, $9,227], and [1,033,030, $3.30]).

CONCLUSIONS

There is a clear trend showing returns to scale for the case histories analyzed in this study. We expect that as additional data are collected for each case history,

scatter and uncertainty may both decline. At this time, results show the best correlation for returns to scale for in situ stabilization or solidification. While it appears that the in situ treatment is marginally better at small scales, ex situ treatment converges to a similar unit cost at larger scales. A similar trend is noted for solidification and stabilization. While solidification appears to be marginally better at small scales, stabilization converges to a lower unit cost at larger scales.

The results of this study will be refined by collecting additional data to reduce scatter and uncertainty. Ultimately, we expect this analysis to provide a basis for decision makers to determine the most economical remedial alternatives based on the scale of the project and remedial technology. The work will subsequently be extended to explore environmental criteria such as life cycle energy and other global environmental metrics to ascertain if it tracks with cost.

ACKNOWLEDGEMENTS

The authors thank Patrick Gurian for valuable suggestions regarding the manuscript.

REFERENCES

Argote, L. and Epple, D. (1990). "Learning curves in manufacturing." *Science 247*, 920-924.

Farghal, S. H. and Everett, J. G. (1997). "Learning curves: accuracy in predicting future performance." *Journal of Construction Engineering and Management*, ASCE, 123, (1), 41-45.

Kumar, A., Flynn, P. and Sokhansanj, S. (2008). "Biopower generation from mountain pine infested wood in Canada: An economical opportunity for greenhouse gas mitigation." *Renewable Energy* 33:1354-1363.

Levinson, D. M. (2001). "Financing infrastructure over time." *Journal of Urban Planning and Development,* ASCE, 127, (4), 146-157.

Nafi, A. and Kleiner, Y. (2010). "Scheduling renewal of water pipes while considering adjacency of infrastructure works and economies of scale". *Journal of Water Resources Planning and Management*, ASCE, 136, (5), 519-530.

U.S. EPA (2007). *Treatment Technologies for Site Cleanup: Annual Status Report (Twelfth Edition)*, EPA-542-R-07-012, September 2007, available online at http://clu-in.org/asr/.

Wang, X.; Duan, Z.; Zhang, R.; Yin, M.; and Xu, B (2007). "Economy of scale and routes optimization of large containerships." *International Conference on Transportation Engineering*, Chengdu, China, 2007; ASCE, pp. 328-328.

Strain Localization Effect on System Reliability Based Design of Bridge Abutments under Earthquake Loading

B Munwar Basha[1] and G L Sivakumar Babu[2]

[1]Assistant Professor, Department of Civil Engineering, Indian Institute of Technology Delhi, Hauz Khas, New Delhi, 110016, India, Tel.: +91-9968668416, fax:+ 91-11-2658 1117, basha@civil.iitd.ac.in.
[2]Professor, Department of Civil Engineering, Indian Institute of Science, Bangalore-560012, India, Tel.: + 91-80-22933124, fax:+ 91-80-23600404, gls@civil.iisc.ernet.in.

ABSTRACT: The component and system reliability based design of bridge abutments under earthquake loading is presented in the paper. Planar failure surface has been used in conjunction with pseudo-dynamic approach to compute seismic active earth pressures on an abutment. The pseudo-dynamic method, considers the effect of phase difference in shear waves, soil amplification along with the horizontal seismic accelerations, strain localization in backfill soil and associated post-peak reduction in the shear resistance from peak to residual values along a previously formed failure plane. Four modes of stability viz. sliding, overturning, eccentricity and bearing capacity of the foundation soil are considered in the analysis. The series system reliability is computed with an assumption of independent failure modes. The lower and upper bounds of system reliability are also computed by taking into account the correlations between four failure modes, which is evaluated using the direction cosines of the tangent planes at the most probable points of failure.

INTRODUCTION

Design of bridge abutments considers a variety of failure modes that influence external stability considerably. External stability issues need to be addressed in the design for earthquake loading. In this study, a reliability based design for external stability is focused. The external stability design of a bridge abutment must ensure safety against overturning, sliding, eccentricity and bearing failure modes and these are the most important consideration in the design. Sufficient base width of the abutment must be used to ensure that they neither fail in any of the external failure modes. If a bridge abutment is subjected to an earthquake loading, the backfill may be subjected to earthquake acceleration. Horizontal earthquake accelerations directed towards the open side of the retaining wall destabilize the system considerably.

The vulnerability of bridge abutments to earthquake ground motion was clearly apparent in the literature. Richard and Elms (1979) documented the damages to bridge abutments in the past major earthquakes. The design earthquake imposes several types

of dynamic loads on the structure. The greatest dynamic load is the inertia load caused by the response of the backfill soil to ground motion accelerations. U.S Department of the Army (2002), Japan Road Association JRA (2002) and Caltrans (2004) reported that the bridge abutments must be designed to avoid external modes of failure, viz. sliding failure on its base, overturning failure (evaluated by determining the eccentricity of the resultant force acting on the footing base) and bearing failure of the foundation soil below the wall base. The above codes provide broad guidelines on the dimensions of abutments in static condition and use a factor of safety approach for evaluating the overall stability of abutments. In addition, the optimization of abutments is interesting for the design engineers, as it leads to effective cost reduction. In this sense, the optimization process has a large effect on the safety of a bridge abutment system. To construct more reliable and affordable retaining structures, there is a great need for designs that balance performance, reliability and cost.

U.S Department of the Army (2002) and Caltrans (2004) provided the recommendations for static and seismic design of abutments. It states that during seismic conditions, a minimum factor of safety of 1.0 shall be used for the design of walls for seismic loads. It is also reported that the abutment width should be 0.5 to 0.7 times of the abutment height and minimum width of abutment stem should be 0.15 times of abutment height. The present design manuals rely primarily on the traditional allowable stress design format in which the safety factors are prescribed deterministically. The drawbacks of deterministic safety factors are based on several years of experience and supporting observations from the test data. It may often leads to conservative designs, which are inefficient from the optimization point of view. Probabilistic methods received a considerable attention in other branches of engineering and are useful in this context. Recently, Basha and Babu (2010a,b) reported a reliability based optimum design methodology for the external and internal seismic stability of geosynthetic reinforced soil walls respectively, by taking into account the uncertainties using pseudo-dynamic approach.

Effect of phase change

In the pseudo-static method for seismic stability proposed by Mononobe-Okable (M-O) (Kramer, 2003), the effect of earthquakes is represented by a constant, time-independent horizontal and/or vertical force. Also, the effect of shear and primary waves generated due to earthquakes and amplification of base acceleration on geotechnical structures is not considered. This drawback was first overcome by Steedman and Zeng (1990) in more realistic way by considering the time and phase difference due to finite shear wave propagation behind a retaining wall in the pseudo-dynamic method. Choudhury and Nimbalkar (2006) computed the active earth pressures considering both shear and primary waves propagating through the backfill with variation in time by considering sinusoidal horizontal and vertical seismic accelerations for rigid retaining walls. Basha and Babu (2010b) presented a formulation for the seismic reliability assessment of reinforced soil structures using pseudo-dynamic method considering the amplification of vibrations. However the above studies did not take into account the effect of strain localization in the shear zone and the effect of the resultant strain softening as discussed in the following

section.

Effects of strain localization

The Mononobe-Okabe (M-O) method further assumes that the shear strength of backfill is isotropic and constant. In reality, the friction angle of backfill along a failure surface decreases from the peak strength to residual strength. For example, Bolton and Steedman (1985) conducted shake table tests on cantilever retaining wall and observed that the shear resistance angle mobilized along a failure plane reduces from 50^o to 33^o. Koseki et al. (1998) proposed a modified M-O procedure that takes into account the effect of strain localization in the shear zone and the effect of the resultant strain softening as illustrated below:

1). For the calculation of the angle of failure plane, the peak internal friction angle of backfill (ϕ_{peak}) should be employed. In addition, it assumes that the first failure plane forms at k_h = 0.0 and the same failure plane continues to be activated up to certain level of k_h value. However, as the seismic coefficient, k_h is increased to a certain level (i.e. 0.6 – 0.8), another failure plane will be activated.

2). For the computation of active earth pressure, the residual internal friction angle (ϕ_{res}) should be used, since the post peak reduction of internal friction angle evolves after the shear band formation.

As stated by Koseki et al. (1998), the proposed hypothesis has a few advantages: 1). It computes active earth pressure coefficients even at high seismic loads (0.6 to 0.8g are considered in the seismic design against the level 2 earthquakes), and 2). It provides more realistic values of seismic active earth pressure coefficients and size of active failure zone than the conventional methods. For the practical considerations, Shirato et al. (2006) further modified the above stated procedure which was introduced in Japanese Specifications for Highway Bridges (JRA, 2002) as follows. It is suggested to evaluate the angles of the initial failure plane at k_h = 0.0 and second failure plane at k_h = 0.42, but consider only the second failure plane for the computation of seismic active earth pressure coefficients for all values of k_h. Accordingly, JRA (2002) has adopted the following two equations to evaluate the seismic active earth pressure coefficients (K_{ae}) in the revised seismic design specifications of highway bridges:

$K_{ae} = 0.22 + 0.81k_h$ for dense sand and gravel (1)

OBJECTIVE OF THE PRESENT STUDY

The above discussion clearly brought out the need to consider the revisions suggested by Steedman and Zeng (1990) in M-O method, like the influence of phase change in the horizontal acceleration in the backfill behind an abutment as shear waves propagate from the base of wall towards ground surface, and amplification of soil vibration. It should also consider the revised seismic design specifications suggested in JRA (2002) like strain localization in the backfill soil and associated

post-peak reduction in the internal friction angle from peak to residual values along a previously formed failure plane. Therefore, a proper design procedure is presented in this paper to address these issues. Recently, Basha and Babu (2010c) reported a study on optimum design of bridge abutments under high seismic loading using pseudo-dynamic method. The similar methodology has been extended for the reliability based seismic design of bridge abutments by considering variability associated with static and earthquake loading, the influence of strain localization and phase change. A target reliability based design optimization methodology developed by Basha and Babu (2010a,b) is used to compute the reliability indices in relation to external stability modes in the study.

SYSTEM RELIABILITY ASSESSMENT

To evaluate the probability of fulfilling several criteria at the same time, system reliability assessment methods are required. Failure of a bridge abutment is governed by four external failure criteria. The abutment system can be approximated by a series system because it fails if any of the components (criteria for overturning, sliding, eccentricity and bearing capacity) fails. A practice in system reliability studies is to assume that the components making up these systems fail independently, i.e., correlation effects are ignored. But, the assumption of independence between failure modes over predicts the probability of system failure with reference to lower bound and upper bounds of system probability of failure. Hence, the reliability assessment of series system with correlated failure modes is considered. The correlations between three failure modes are evaluated using the direction cosines of the tangent planes at the most probable points of failure. Further, the Ditlevsen's bounds of system probability of failure ($P\left(\bigcup_{i=1}^{mf} E_i\right)$) (Ditlevsen 1979; Song and Kiureghian 2003) are computed using the following expressions:

$$P_1 + \sum_{i=2}^{mf} \max\left(P_i - \sum_{j=1}^{i-1} Pf_{ij},\quad 0\right) \le P\left(\bigcup_{i=1}^{mf} E_i\right) \le \sum_{i=1}^{mf} P_i - \sum_{i=2}^{mf} \max_{j<i}\left(Pf_{ij}\right) \qquad (2)$$

where mf = number of modes of failure, $P_i = P\left(E_i\right)$ is component probability, $P_{ij} = P\left(E_i E_j\right)$ is the joint probability of component events E_i and E_j.

SEISMIC ACTIVE EARTH PRESSURE

During earthquakes, the peak values of horizontal inertial force, vertical inertial force and active earth pressure may not be activated simultaneously and the phase differences among these three components should be largely different among different earthquakes. Seed and Whitman (1970) reported that for most earthquakes the horizontal acceleration components are considerably greater than the vertical components and concluded that vertical acceleration can be neglected for practical purposes. Accordingly, following the suggestions of Seed and Whitman (1970), Koseki et al. (1998), Shirato et al. (2006) and Japan Road Association JRA (2002), the vertical ground acceleration is neglected in the present study.

Phase angle and amplification effect on sinusoidal accelerations

The present method considers finite shear wave velocity within the backfill behind the abutment. It is assumed that the horizontal seismic acceleration in soil vary linearly from the input seismic acceleration at the base to the higher value at the top of the wall as shown in **Fig. 1**. The horizontal sinusoidal acceleration at any depth, z below the top of the wall and time (t) with soil amplification factor (f) can be expressed as follows:

$$a_h(z,t) = \left(1 + \frac{H-z}{H}(f-1)\right) k_h g \sin\omega\left(t - \frac{H-z}{v_s}\right) \tag{3}$$

where H = height of the wall, $\omega = 2\pi/T$ is the angular frequency of the base shaking, T = period of lateral shaking, v_s = shear wave velocity propagating through the backfill. It is assumed in the present study that the base of the wall is subjected to horizontal sinusoidal acceleration with amplitude of accelerations, $k_h g$, where 'g' is the acceleration due to gravity. After computing seismic active earth pressure (Basha and Babu 2010c), the expressions of limit state functions for overturning, sliding, eccentricity and bearing modes of failure are presented below.

LIMIT STATE FUNCTIONS

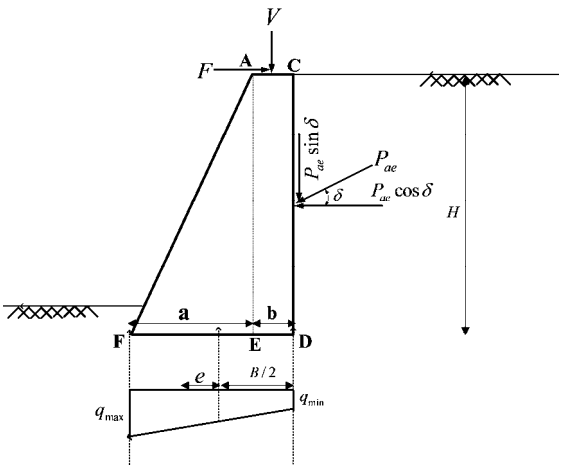

Figure 1. Forces acting on the bridge abutment under active condition.

For the stability against sliding failure along the base of abutment, sum of the horizontal resisting forces ($\sum F_r$) should be more than sum of the horizontal driving forces ($\sum F_d$). The factor of safety against sliding failure is given by,

$$FS_{sli} = \frac{\sum F_r}{\sum F_d} \tag{9}$$

In Fig. 1, V refers to the vertical load and F_D refers to the horizontal load. For the stability against overturning failure about the toe of wall, sum of resisting moments ($\sum M_r$) should be more than sum of the overturning moments ($\sum M_o$).

The factor of safety against overturning failure is given by,

$$FS_{ot} = \frac{\sum M_{\mathrm{r}}}{\sum M_{\mathrm{o}}} \tag{10}$$

Caltrans (2004) further reported that for the stability in terms of eccentricity of resultant force, the eccentricity should be lesser than one sixth of the base width of the wall ($L/6$) (Refer **Fig. 1**). Eccentricity of the resulting force (e) on the base can be calculated by summing the moments of resisting forces and disturbing forces about the toe of the wall base. The factor of safety against eccentricity failure is

$$FS_e = \frac{L/6}{e}$$

The factor of safety against bearing failure can be estimated as the ratio of ultimate bearing capacity (q_u) of a shallow foundation below the base slab of retaining wall and vertical stress at the base ($q_{\max}$) calculated as shown in **Fig. 1**, which is written as

$$FS_b = \frac{q_u}{q_{\max}} \tag{12}$$

The probabilistic constraints in the form of performance functions are:

$$g_{ot}(x) = FS_{ot} - 1;\quad g_{sli}(x) = FS_{sli} - 1;\quad g_e(x) = FS_e - 1;\ g_b(x) = FS_b - 1 \tag{13}$$

RESULTS AND DISCUSSION

A 6m high reinforced earth wall founded on $c-\phi$ soil is considered for the stability analysis. This study includes the influence of the strength parameters of backfill and characteristics of earthquake ground motions. The parameter values involved in the study are the unit weight (γ) = 18 kN/m^3, ϕ_{peak} = 50$^{\mathrm{o}}$, ϕ_{res} = 35$^{\mathrm{o}}$, δ/ϕ = 0.5, k_h = 0.0 - 1.0, f = 1.0, v_s = 65 m/s, T = 0.3 and $H/\lambda = H/(Tv_s)$ = 0.3. Basha and Babu (2010c) reported that the values of seismic active earth pressure coefficient (K_{ae}**)** predicted by the pseudo-dynamic method are lower than the modified M-O method by Shirato et al. (2006) approach. This difference occurs due to the limitations of pseudo-static analysis such as non-consideration of the effect of time and phase difference due to finite shear wave velocity.

Comparison of Reliability Indices, β_{ot}, β_{sli}, β_e and β_b

Results presented in **Table 1** shows the effect of strain localization and phase change (H/λ) on magnitudes of reliability indices, β_{ot}, β_{sli}, β_e and β_b for f = 1.0, γ = 18 kN/m^3, γ_b = 19 kN/m^3, a/H = 0.45, b/H = 0.15, V = 250 kN, F = 25, v_s = 67 m/s, ϕ_{peak} = 50$^{\mathrm{o}}$, ϕ_{res} = 35$^{\mathrm{o}}$ ϕ_b = 30$^{\mathrm{o}}$, c = 10 kN/m^2, δ/ϕ_{res} = 0.5, δ_b/ϕ_b = 2/3, and COV s of ϕ_{peak}, ϕ_{res}, ϕ_b, k_h, c, V and F = 5, 5, 5, 5, 10, 5 and 5 respectively. It is also assumed that ϕ_{peak}, ϕ_{res}, ϕ_b and c are log normally distributed and the remaining parameters are normally distributed (Basha and Babu, 2010a).

Table 1. The comparison of reliability indices computed using three approaches.

k_h	β_{ot}			β_{sli}			β_e			β_b		
	M-O method	Shirato et al. (2006)	Present	M-O method	Shirato et al. (2005)	present	M-O method	Shirato et al. (2005)	present	M-O method	Shirato et al. (2005)	present
0.00	24.05	24.05	24.05	21.31	21.31	21.31	20.81	20.81	20.81	12.59	12.59	12.59
0.02	23.67	23.86	23.80	19.99	20.82	20.47	20.06	19.79	19.58	11.17	12.23	11.84
0.04	23.39	23.57	23.51	19.35	19.92	19.74	19.01	18.77	18.62	10.49	11.31	11.05
0.06	23.10	23.25	23.21	18.67	19.13	19.02	17.95	17.75	17.67	9.83	10.44	10.29
0.08	22.80	22.92	22.90	17.92	18.30	18.12	16.90	16.73	16.71	9.18	9.62	9.57
0.10	22.48	22.57	22.58	17.07	17.37	17.41	15.84	15.72	15.76	8.82	8.85	8.89
0.12	22.14	22.21	22.25	16.13	16.34	16.47	14.79	14.70	14.81	8.08	8.14	8.15
0.14	21.78	21.82	21.90	15.17	15.29	15.50	13.58	13.67	13.85	7.32	7.43	7.62
0.16	21.40	21.42	21.54	14.21	14.26	14.54	12.64	12.68	12.91	6.72	6.77	7.03
0.18	21.00	21.01	21.15	13.26	13.28	13.62	11.66	11.67	11.97	6.14	6.15	6.47
0.20	20.57	20.57	20.76	12.35	12.35	12.73	10.64	10.64	11.01	5.57	5.57	5.94
0.22	20.12	20.12	20.36	11.46	11.47	11.89	9.60	9.61	10.04	5.00	5.00	5.42
0.24	19.64	19.66	19.94	10.60	10.63	11.09	8.54	8.57	9.07	4.44	4.47	4.93
0.26	19.13	19.18	19.50	9.77	9.84	10.33	7.46	7.53	8.09	3.90	3.97	4.46
0.28	18.59	18.68	19.05	8.97	9.09	9.61	6.37	6.51	7.13	3.36	3.48	4.01
0.30	18.01	18.16	18.58	8.19	8.37	8.91	5.28	5.51	6.17	2.82	3.01	3.58
0.32	17.40	17.63	18.10	7.43	7.69	8.25	4.19	4.53	5.24	2.29	2.56	3.16
0.34	16.74	17.08	17.61	6.69	7.04	7.62	3.11	3.57	4.32	1.76	2.14	2.76
0.36	16.05	16.51	17.09	5.97	6.42	7.02	2.04	2.64	3.43	1.24	1.72	2.37
0.38	15.33	15.94	16.57	5.26	5.83	6.44	0.98	1.75	2.57	0.72	1.31	1.99
0.40	14.56	15.35	16.03	4.57	5.27	5.89	-0.07	0.88	1.73	0.20	0.94	1.63
0.42	13.76	14.75	15.48	3.89	4.72	5.36	-1.61	0.05	0.92	-0.34	0.56	1.27
0.44	12.91	14.14	14.92	3.22	4.20	4.85	-2.68	-1.30	0.14	-0.85	0.20	0.93
0.46	12.03	13.53	14.35	2.56	3.70	4.36	-3.77	-2.10	-1.17	-1.38	-0.15	0.59
0.48	11.12	12.90	13.77	1.90	3.22	3.89	-4.89	-2.90	-1.92	-1.91	-0.49	0.26
0.50	10.17	12.28	13.18	1.24	2.76	3.43	-6.08	-3.69	-2.67	-2.46	-0.82	-0.05

It can be noted from **Table 1** that the magnitudes of β_{ot}, β_{sli}, β_e and β_b obtained using pseudo dynamic method are higher than the values predicted by M-O method and modified earth pressure theory by Shirato et al. (2006) approach. It can be attributed to the fact that the pseudo dynamic approach predicts lower seismic active earth pressure due to consideration of the influence of phase change in the shear wave.

System Reliability Analysis of Bridge Abutment

Based on the results of system reliability presented in **Table 2**, the following observations can be made. The lowest value of reliability index among the components influences the series system reliability. It can also be noted that for a typical set of values mentioned in **Table 2**, limit states corresponding to eccentricity and bearing capacity failure influence the system reliability considerably whereas the influence of overturning and sliding limit states is less. This trend may be different for

Table 2. The magnitudes of component reliability indices (β_{ot}, β_{sli}, β_e and β_b), series system reliability index (β_{sys}), correlation coefficients (ρ_{12}, ρ_{13}, ρ_{14}, ρ_{23}, ρ_{24} and ρ_{34}), lower and upper bounds of system reliability indices (β_{lb} and β_{ub}), and lower and upper bounds of system probability of failure (Pf_{lb} and Pf_{ub}) for a/H = 0.45, b/H = 0.15, V = 250 kN, F = 25, v_s = 67 m/s, ϕ_{peak} = 50°, ϕ_{res} = 35° ϕ_b = 30°, c = 10 kN/m^2, δ/ϕ_{res} = 0.5, δ_b/ϕ_b = 2/3, and COV s of ϕ_{peak}, ϕ_{res}, ϕ_b, k_h, c, V and F = 5, 5, 5, 5, 10, 5 and 5 respectively.

k_h	β_{ot}	β_{sli}	β_e	β_b	β_{sys}	Pf_{sys}	ρ_{12}	ρ_{13}	ρ_{14}	ρ_{23}	ρ_{24}	ρ_{34}	β_{lb}	β_{ub}	Pf_{lb}	Pf_{ub}	ε (in %)
0.20	20.76	12.73	11.01	5.94	5.94	0.00000	0.30	0.94	0.42	0.41	0.73	0.46	5.94	5.94	0.00000	0.00000	0.00
0.22	20.36	11.89	10.04	5.42	5.42	0.00000	0.29	0.93	0.41	0.41	0.73	0.45	5.42	5.42	0.00000	0.00000	0.00
0.24	19.94	11.09	9.07	4.93	4.93	0.00000	0.29	0.92	0.41	0.41	0.72	0.45	4.93	4.93	0.00000	0.00000	0.00
0.26	19.50	10.33	8.09	4.46	4.46	0.00000	0.29	0.91	0.41	0.42	0.71	0.44	4.46	4.46	0.00000	0.00000	0.00
0.28	19.05	9.61	7.13	4.01	4.01	0.00003	0.29	0.91	0.41	0.42	0.70	0.44	4.01	4.01	0.00003	0.00003	0.00
0.30	18.58	8.91	6.17	3.58	3.58	0.00017	0.29	0.91	0.40	0.42	0.70	0.43	3.58	3.58	0.00017	0.00017	0.00
0.32	18.10	8.25	5.24	3.16	3.16	0.00078	0.29	0.90	0.40	0.43	0.70	0.43	3.16	3.16	0.00078	0.00078	0.00
0.34	17.61	7.62	4.32	2.76	2.76	0.00293	0.29	0.90	0.40	0.43	0.69	0.42	2.76	2.76	0.00293	0.00293	0.02
0.36	17.09	7.02	3.43	2.37	2.36	0.00923	0.29	0.90	0.40	0.44	0.69	0.42	2.36	2.36	0.00915	0.00918	0.35
0.38	16.57	6.44	2.57	1.99	1.91	0.02813	0.29	0.90	0.40	0.44	0.68	0.41	1.92	1.93	0.02682	0.02746	2.33
0.40	16.03	5.89	1.73	1.63	1.33	0.09120	0.29	0.90	0.40	0.45	0.68	0.41	1.36	1.40	0.08051	0.08681	7.26

Note: $\varepsilon = \left(\frac{Pf_{ub} - Pf_{lb}}{Pf_{ub}} \right) \times 100$

other set of design values. It may be observed from **Table 2** that the correlation coefficients are range from 0.29 to 0.94. It indicates that all modes are correlated and hence the magnitudes are different. It may be noted from **Table 2** that the assumption of independence between failure modes over predicts the series system probability of failure (Pf_{sys}) with reference to lower bound (Pf_{lb}) and upper bound (Pf_{ub}) of system probability of failure for $k_h > 0.34$.

The difference between the lower and upper bounds in **Table 2** obviously depends on the number of potential failure modes and on the relative magnitudes of individual component probabilities. For example, in the present case, the system probability of failure is dominated by eccentricity and bearing capacity modes. It can be noted that the percentage difference between Pf_{lb} and Pf_{ub} increases with increase in k_h value (i.e. the bounds are narrow for $k_h > 0.34$) as can be observed from **Table 2**. Therefore the influence of correlation on the system probability of failure is significant for higher magnitudes of k_h and it has a practical significance for the case considered in the study. However, the degree of over estimation and the difference between the bounds will depend on a case by case basis and on the statistical input given for the performance functions.

CONCLUSIONS

A system reliability analysis for the external stability of bridge abutments is outlined in this paper. The influence of strain localization in the shear zone and the effect of the resultant strain softening in the framework of pseudo-dynamic method is considered. The effect of oscillatory nature of earthquake loading like time, soil amplification and phase difference in the shear wave propagating through the backfill behind the abutment is also considered. It is shown that the reliability indices predicted by the present method are higher than the modified Mononobe-Okabe earth pressure theory by Shirato et al. (2006) which does not take into account the effect of phase difference in body wave propagating through the backfill soil. The series system probability of failure is computed with the assumption of independent failure modes, and the lower and upper bounds of system probability of failure are evaluated by taking into account correlations between failure modes. The results of the system reliability analysis indicate that the influence of correlation on the system probability of failure.

REFERENCES

Basha, B.M., and Babu, G.L.S. (2010a). "Optimum design for external seismic stability of geosynthetic reinforced soil walls: A Reliability Based Approach." *J Geotech. Geoenviron. Engg., ASCE*, 136(6), 797-812.

Basha, B.M., and Babu, G.L.S. (2010b). "Reliability assessment of internal stability of reinforced soil structures: a pseudo-dynamic approach." *Soil Dyn. Earthquake Engg.,* 30(5), 336 - 353.

Basha, B.M., and Babu, G.L.S. (2010c). Optimum design of bridge abutments under

high seismic loading using modified pseudo-static method. *J Earthquake Engg.*, 14(6): 874 – 897.

Bolton, M.D., and Steedman, R.S. (1985). *Modeling the seismic resistance of retaining structures*, In Proc. of 11th International conference on soil mechanics and foundation engineering, 4, 1845-1848.

Caltrans (2004). *Bridge design specifications, Section 5: Retaining Walls*. California Department of Transportation, Sacramento, CA.

Choudhury, D., and Nimbalkar, S.S. (2006). "Pseudo-dynamic approach of seismic active earth pressure behind retaining wall." *Geotech. Geolog. Engg.,* 24(5), 1103 - 1113.

Ditlevsen, O. (1979). Narrow reliability bounds for structural systems. *J. Struct. Div. ASCE* 7(4), 453-472.

JRA (2002). *Specification for Highway Bridges*. Part V, Seismic Design. Japanese Road Association.

Koseki, J., Tatsuoka, F., Munaf, Y., Tateyama, M., and Kojima, K. (1998) "A modified procedure to evaluate active earth pressure at high seismic loads," (Special Issue) *Soils and Foundations,* 209-216.

Kramer, S.L. (2003). *Geotechnical earthquake engineering*, Englewood Cliffs, NJ: Prentice-Hall.

Richards, R., and Elms, D.G. (1979). ''Seismic behavior of gravity retaining walls,'' *J Geotech. Geoenviron. Engg., ASCE*, 105(4), 449 – 464.

Seed, H.B., and Whitman, R.V. (1970). *Design of earth retaining structures for dynamic loads, State-of-the-art paper*. In Proceedings of the 1970 ASCE Specialty Conference on Lateral Stresses in the Ground and Design of Earth Retaining Structures, Ithaca, N.Y. American Society of Civil Engineers, New York, 103–147.

Shirato, M., Fukui, J., and Koseki, J. (2006). "Current status of ductility design of abutment foundations against large earthquakes", *Soils and Foundations,* 46(3), 377-396.

Song, J., and Kiureghian, A. R. (2003). Bounds on system reliability by linear programming. *J Engg. Mech. ASCE*, 129(6), 627-636.

Steedman, R.S., and Zeng, X. (1990). "The influence of phase on the calculation of pseudo-static earth pressure on a retaining wall," *Geotechnique,* 40(1), 103 – 112.

US Department of the Army (2002). *Field Manual: Military Nonstandard Fixed Bridging*, FM 3-34.343 (FM 5-446), Washington, D.C.

Serviceability Considerations in the Design of Sheet Pile Walls for Risk Management

Ömer Bilgin, P.E., M.ASCE[1], Eman Mansour[2], and Mohamad Gabar[2]

[1] Assistant Professor, University of Dayton, Department of Civil and Environmental Engineering, Dayton, OH 45469-0243; PH (937) 229-2985; FAX (937) 229-3491; email: bilgin@udayton.edu

[2] Graduate Student, University of Dayton, Department of Civil and Environmental Engineering, Dayton, OH 45469-0243

ABSTRACT

The common design practice of sheet pile walls, cantilever or anchored, is based on limit equilibrium approach. A wall design using the limit equilibrium approach utilizes force and moment equilibriums and considers only the soils in contact with the wall to determine lateral earth pressures. The method does not consider several factors during the design which affect the overall wall performance and deformations. Some of the factors not considered in the structural design of the wall are the soils types below the wall tip, the extent of loading behind the wall, and the methods involved during construction, such as cut in the front or fill behind the wall. These factors can adversely affect the wall behavior and cause problems for the wall as well as the structures nearby. The variability and uncertainty involved in the geotechnical engineering field compared to the other fields of civil engineering also magnify the importance of wall deformations, as they are affected by the changes in soil properties. This paper studies the effect of soil variability on wall deformations and provides an overview and analysis on factors affecting the deformations.

INTRODUCTION

Sheet pile walls are used for various purposes; such as excavation support system, cofferdams, cut-off walls under dams, slope stabilization, waterfront structures, and floodwalls. The sheet pile walls can be either cantilever or anchored depending on the wall height. While relatively shorter sheet pile walls can be cantilever, higher walls require anchors. The selection of wall type, either cantilever or anchored, is based on the function of wall, the characteristics of foundation soils, and the proximity of wall to existing structures (ASCE 1996).

The movement of in-situ walls is an important issue because of the development of recent technologies in this field and increase in litigation associated with damages caused by the movements of these walls to adjacent structures (Clough and O'Rourke 1990). The sheet pile walls, being considered as flexible walls due to their relatively lower system stiffness, experience more movements compared to diaphragm walls, such as slurry walls. The conventional methods used in the design

of anchored sheet pile walls are based on active and passive earth pressures that are concerned with the failure condition based on the Mohr-Coulomb failure criterion. These design methods do not specifically consider wall displacements.

Earlier studies showed that several conditions which have not been considered during design using conventional methods can adversely affect the wall behavior and deformations. Large area loading behind floodwalls during flooding event causes more wall displacements compared to limited area loading (Bilgin 2006). The presence of a soft soil layer below the tip of wall causes an increase in the floodwall deformations (Bilgin 2009).

Geotechnical engineering field has more variability and uncertainty involved compared to the other fields of civil engineering. The pressures acting on a sheet pile wall, and therefore the wall deformations, are also affected by the variations in soil properties around the wall. The variability in geotechnical engineering comes from three primary sources of uncertainties (Phoon and Kulhawy 1999): (1) inherent variability, (2) measurement error, and (3) transformation uncertainty. The inherent variability comes from the complex nature of soil which has been produced by combination of geologic, environmental, and chemical processes. The measurement error is caused by equipment, procedural, operator, and random testing effects. The transformation uncertainty is due to the use of empirical or other correlation models. The levee failures during the flooding after Hurricane Katrina in New Orleans due to the presence of soft soils at the tip of the walls (Seed et al. 2008) emphasize the importance of consideration of several factors, such as soft soils at and below the wall tip, in the wall design not only for the serviceability criteria but also for safe and sustainable structures.

The objective of this paper is to study the effect of soil variability on wall deformations and to provide an overview and analysis of sheet pile wall deformations, and some of the factors affecting the deformations, to raise the awareness for risk management of retaining walls and adjacent structures.

CONVENTIONAL VERSUS NUMERICAL METHODS

The conventional methods used in the design of sheet pile walls are based on limit equilibrium approach and they do not consider the construction method, such as excavation in front of the wall or backfilling behind the wall. In addition, they only take into account the soils in contact with the wall to determine the lateral earth pressures for structural design of the wall and do not consider the effect of soils below the tip of the pile. The conventional design methods also do not take into account the wall deformations which are important for serviceability considerations. The continuum mechanics numerical models, such as the finite element method, on the other hand, allow the exploration of stresses and displacements based on a range of anticipated loading history for the entire stress and deformation field for a soil-structure interaction problem. Because of these capabilities of the finite element method, it is possible to model and investigate the effect of several factors mentioned above on the behavior and deformations of wall and surrounding soil for various conditions. Although finite difference method also used as a numerical tool in the analyses and design of retaining walls, the finite element method has been used

extensively for modeling the soil-structure interaction for different types of retaining walls for varying loading conditions (Briaud and Lim 1999, Tan and Paikowsky 2008, Bilgin 2010).

NUMERICAL MODELING AND ANALYSIS

A typical wall schematic and the notations used for numerical analysis are shown in Figure 1. Three different wall heights (6, 9, and 12 m) were considered for the parametric study. The mean soil property values and their ranges considered in the study are given in Table 1. By using the free earth support method, the anchored sheet pile walls were designed for the three wall heights. The conventional wall design required PZ22 pile profile for the walls with mean soil property values. The cross-sectional area and moment of inertia were 136.9 cm^2/m and 11,500 cm^4/m, respectively, for PZ22, with the elastic modulus of 200 GPa. The depth of wall penetration calculated and pile section selected using conventional design method were used in numerical modeling for the parametric study.

The finite element analyses were performed as two-dimensional plane strain analysis. The soil and sheet pile wall were modeled using 6-node triangular elements and 3-node plate elements, respectively. The Mohr-Coulomb constitutive model was used to model soil behavior. Maximum wall horizontal deformations obtained from the analysis of three wall heights using the mean soil property values are presented in Figure 2. The figure shows that as the wall height increases the rate of change of wall deformations increases, as expected.

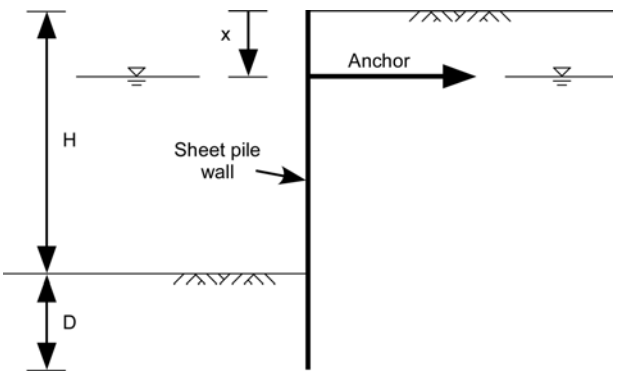

Figure 1. Typical schematic of an anchored sheet pile wall

Table 1. Soil Properties

Property	Mean value	Range
Friction angle (°)	36	30 – 42
Saturated unit weight (kN/m^3)	18	16 – 20
Unsaturated unit weight (kN/m^3)	17	16 – 18
Dilatancy angle (°)	6	0 – 12
Modulus of elasticity (MPa)	35	15 – 75
Interface friction ratio, δ/ϕ	0.7	constant

Note: δ=interface friction angle; ϕ=soil friction angle

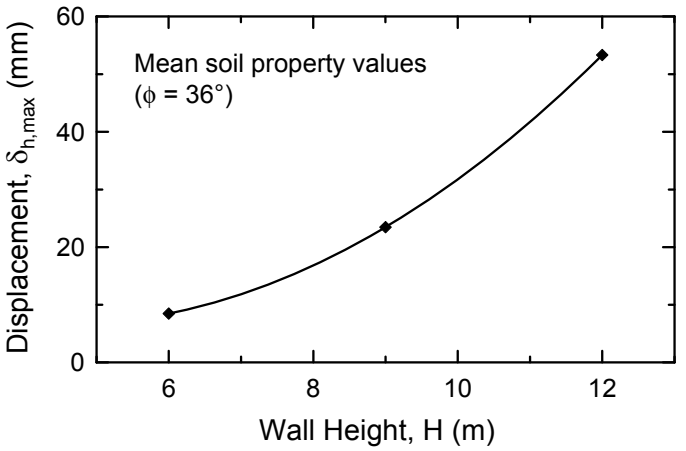

Figure 2. Maximum horizontal wall deformations

GEOTECHNICAL VARIABILTY ON WALL DEFORMATIONS

The effect of inherent variability in soil properties on the wall deformations was studied for coefficient of variation (COV) values of 5%, 10%, and 15% of soil friction angle. The coefficient of variation for soil friction angle, COV_ϕ, of 5% to 11% has been reported by Phoon and Kulhawy (1999). The range of soil friction angle considered for each COV_ϕ value was within the standard deviation, from $-\sigma$ to $+\sigma$. The other soil properties needed for the numerical analysis, such as the ones given in Table 1, were also adjusted within their own range based on the amount of change of friction angle from the mean value. For example, when the soil friction angle decreased from the mean value for an analysis, the unit weight and other soil properties were also reduced at a similar ratio within their own range considered.

The effect of friction angle on wall displacements within the range of standard deviation for varying COV values for the 12-m-high wall is shown in Figure 3. For the mean soil friction angle of μ_ϕ=36°, as the soil coefficient of variation, COV_ϕ, increases the variability in wall displacements also increases since the range of soil friction angle is wider due to an increased standard deviation, σ_ϕ. Figure 3 shows that within the range of standard deviation of friction angle, $\pm\sigma_\phi$, the horizontal wall displacements can change as much as 14% and 50% for COV_ϕ of 5% (Figure 3a) and 15% (Figure 3c), respectively. Relative comparison of the effect of soil friction angle on the normalized wall deformations for varying COV_ϕ values is shown in Figure 4. The maximum wall deformation from each analysis was normalized by the maximum wall deformation obtained from the analysis performed by mean soil property values. Figure 4 shows that as the soil friction angle increases the wall deformations decreases, while the friction angle decreases the wall deformations increases. The effect is more significant for higher COV_ϕ values as the range of friction angles considered, within $\pm\sigma_\phi$, increases. The analyses results showed that all three wall heights (6, 9, and 12 m) considered in the parametric study yielded almost the same results given in Figure 4 for each COV_ϕ value, i.e. the results shown in Figure 4 is independent of the wall height.

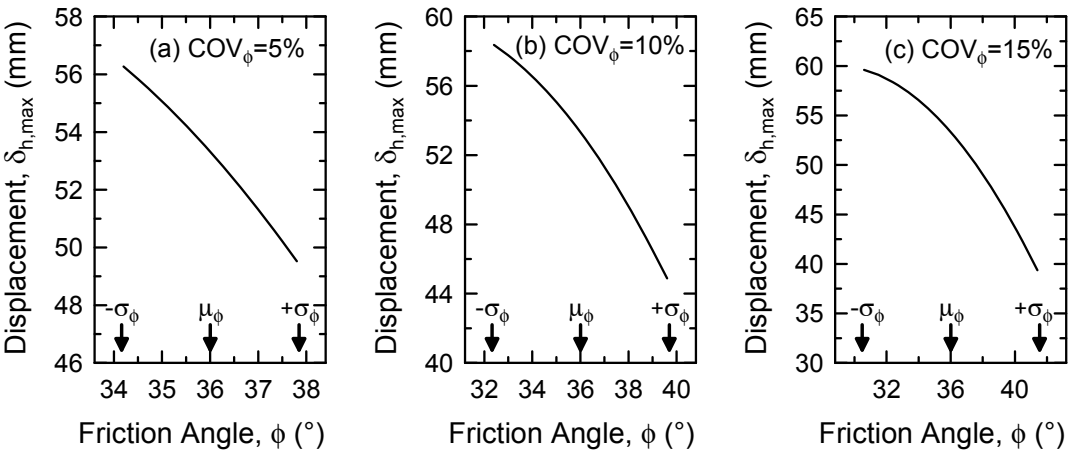

Figure 3. Effect of COV$_\phi$ on wall deformations (12-m-high wall)

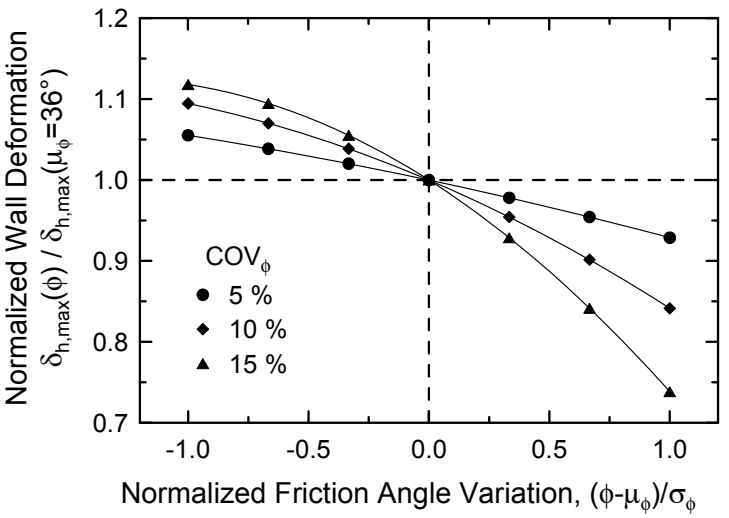

Figure 4. Effect of ϕ and COV$_\phi$ on normalized wall deformations

ANCHOR AND PILE PROFILE ON WALL DEFORMATIONS

The deformations of anchored sheet pile walls designed using conventional methods and the effect of several factors on wall deformations have been investigated by using the finite element method (Bilgin and Erten 2009). The study included a parametric numerical experiment for varying anchor depth, wall bending stiffness, and number of anchor levels. The results of the numerical analyses performed using the finite element method as summarized below show that the walls experience the minimum horizontal deformations when the anchor is installed at a depth equal to 25 percent of the wall height, *H*, from the top of wall.

Figure 5 shows the effect of anchor location on maximum horizontal wall deformation and soil settlement behind the wall. The deformations and settlements

were normalized by the results obtained when the anchor location is at 0.25*H* from the top of wall. The figure shows that as the wall height increases a relatively small change in the location of anchor along the wall height results in significant increase in wall and soil deformations. Since the purpose of the study was to determine the optimal location for the anchor considering the wall deformations, the same wall penetration and the pile profile properties were used for all the cases.

The effect of pile profiles used on maximum horizontal wall deformation is shown in Figure 6(a). The results are presented as normalized maximum horizontal wall displacements with respect to the deformations obtained using larger pile profile. The results show that as the pile size decreases both wall and soil deformations increase, as expected. Using larger pile sections has more effect on reducing the deformations when the walls are relatively higher. Bilgin and Erten (2009) concluded that using larger sections can reduce the wall deformations by 50% while the decrease in soil settlements behind the wall can be as much as 80%. Figure 6(b) shows that the wall deformations can be reduced more than 50% if additional level of anchor is used.

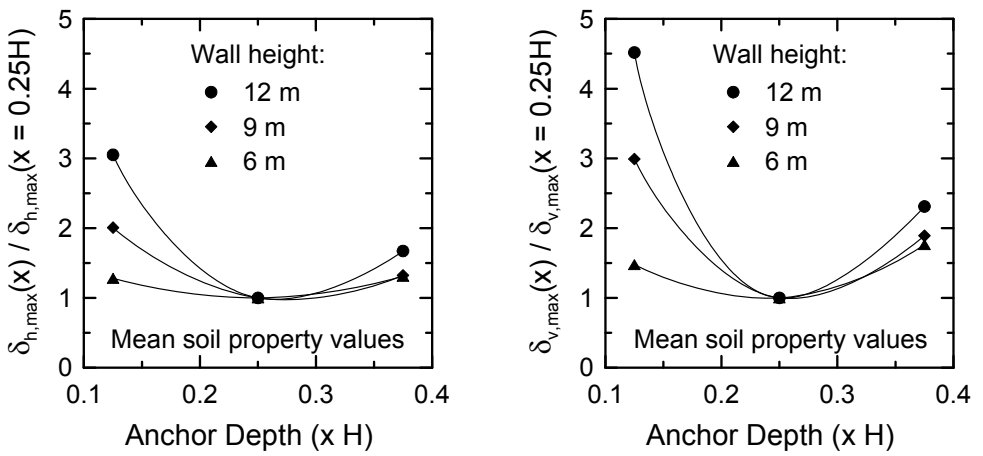

(a) Horizontal wall displacement (b) Soil settlement behind the wall

Figure 5. Effect of anchor location on wall and soil movements

SOFT SOIL LAYER BELOW WALL TIP ON WALL DEFORMATIONS

The traditional design approach, only considers soils above the bottom of pile, i.e. the soils in direct contact with the wall, and does not take into account the effect of soils below the bottom of pile. The effect of varying soil conditions below the bottom of piles on the behavior of cantilever walls during flooding and the extent of loading behind the wall were analyzed by Bilgin (2006 & 2009). The wall deformations were analyzed using the finite element method for varying soil conditions. The study showed that although the pile top deformations are affected only slightly (less than 10%) by the presence of the soft layer, the pile tip deformations increased as much as 70% for the cases studied.

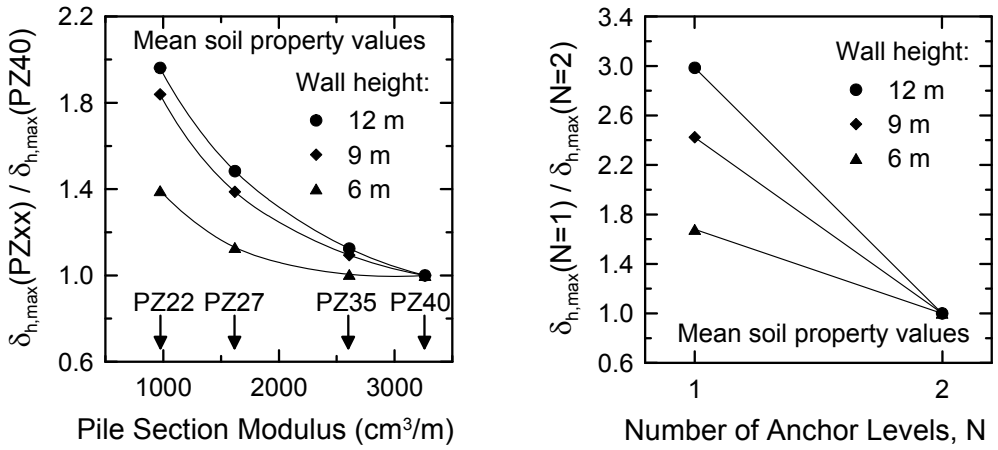

(a) Pile section (b) Number of anchor levels

Figure 6. Effect of sheet pile section and number of anchor levels on wall displacements

DISCUSSION OF RESULTS

The cases presented above show that the wall deformations can vary significantly based on the condition of each wall and the soils around and below the wall. The wall design using the current traditional methods may be perfectly fine for the structural design and performance of the wall. However, excessive wall movements may be considered as failure from the serviceability point of view because they may bring several risks associated with them. Risk assessment can be specified based on the consequences that these deformations may cause. Failure of a floodwall due to an excessive displacement at the tip can allow water to seep through the joints and cause flooding. Depending on the magnitude of the flooding the damages can be only monetary. However, if the wall completely fails, due to the excessive movements, then the associated risks can even include a loss of life. Therefore, it is very important to understand and consider the wall deformations during the design along with the risk assessment associated with wall deformations. Once the risks associated are established, the effect of inherent variability of soil properties or the subsurface conditions on wall deformations can be compensated by altering the structural design of the wall, such as using larger pile profiles or additional level of anchors (Figure 6).

CONCLUSIONS

The wall design using conventional methods, such as the free earth method used for anchored sheet pile walls, does not consider wall deformations for serviceability conditions. The design concentrates on the structural design of the wall and the effect of soil deformations around the wall due to various soil and loading conditions are not taken into account. These factors, such as inherent variability of soil properties or subsurface soil conditions, can cause significant increase in wall

deformations. These deformations not only can cause damage to the wall system but also can damage the structures around the wall. The structures affected can be adjacent buildings, pavements, and/or pipes buried in the front or behind the wall. The design of walls, especially when other structures in close vicinity are present, should consider the wall deformations and include a risk analysis, e.g., in the event of a gas pipeline break due to large wall deformations. Depending on the risks associated for a specific project, the design engineers can make informed decisions to reduce wall deformations, such as by using larger pile sections, increasing the number of anchor levels, and/or improve ground conditions using ground modification methods.

REFERENCES

ASCE (1996). *Design of sheet pile walls*. Technical engineering and design guides as adapted from the US Army Corps of Engineers, No. 15.

Bilgin, Ö. (2006). "Size effect analysis of full-scale floodwall tests using numerical methods." *Proceedings, International Conference on Physical Modeling in Geotechnics*, Kowloon, Hong Kong, August, 1389-1393.

Bilgin, Ö. (2009). "Effect of subsurface soil conditions on floodwall behavior." *Contemporary topics in in-situ testing, analysis, and reliability of foundations (GSP 186). Proceedings, International Foundation Congress & Equipment Expo 2009*, Florida, 538-545.

Bilgin, Ö. (2010). "Numerical studies of anchored sheet pile wall behavior constructed in cut and fill conditions." *Journal of Computers and Geotechnics*, Elsevier. Vol. 37, No. 3, 399-407.

Bilgin, Ö. and Erten, M. B. (2009). "Analysis of anchored sheet pile wall deformations." *Contemporary topics in ground modification, problem soils, and geo-support (GSP 187). Proceedings, International Foundation Congress & Equipment Expo 2009*, Florida, 137-144.

Briaud, J. L. and Lim, Y. (1999). "Tieback walls in sand: numerical simulation and design implications." *Journal of Geotechnical and Geoenvironmental Engineering*, ASCE, 125(2), 101-109.

Clough, G. W. and O'Rourke. T. D. (1990). "Construction induced movements of insitu walls." *Proceedings, ASCE Specialty Conference on Design and Performance of Earth Retaining Structures*, Ithaca, New York, 439-470.

Phoon, K. K. and Kulhawy, F. H. (1999). "Characterization of geotechnical variability." *Canadian Geotechnical Journal*, 36(4): 612-624.

Seed, R. B., Bea, R. G., Athanasopoulos-Zekkos, A., Boutwell, G. P., Bray, J. D., Cheung, C., Cobos-Roa, D., Harder, L. F. Jr., Moss, R. E. S., Pestana, J. M., Riemer, M. F., Rogers, J. D., Storesund, R., Vera-Grunauer, X., and Wartman, J. (2008). "New Orleans and Hurricane Katrina III: The 17th Street Drainage Canal." *Journal of Geotechnical and Geoenvironmental Engineering*, ASCE, 134(5), 740-761.

Tan, Y. and Paikowsky, S. G. (2008). "Performance of sheet pile wall in peat." *Journal of Geotechnical and Geoenvironmental Engineering*, ASCE, 134(4), 445-458.

Reliability based performance evaluation of earth retaining structures

Manojit Chakraborty[1], A. Murali Krishna[2] and Arunasis Chakraborty[3]

[1] Postgraduate student, Department of Civil Engineering, Indian Institute of Technology Guwahati, Guwahati, India, 781039. email: manojit@iitg.ernet.in.
[2] Assistant professor, Department of Civil Engineering, Indian Institute of Technology Guwahati, Guwahati, India, 781039. email: amurali@iitg.ernet.in.
[3] Assistant professor, Department of Civil Engineering, Indian Institute of Technology Guwahati, Guwahati, India, 781039. email: arunasis@iitg.ernet.in.

ABSTRACT

In this paper, attention is focused on the reliability based performance evaluation of a cantilever retaining structure with cohesionless dry backfill subjected to random surcharge loading. Keeping this in view, a limit surface has been defined as the difference between the resisting moment and overturning moment acting on the structure while considering the randomness of different parameters contributing to the stability of the retaining structure e.g. random surcharge loading, unit weight of soil and concrete, friction angle of soil and wall friction angle etc. Probability of failure due to overturning of wall with random surcharge loading has been evaluated using Cornel's reliability index. Sensitivity analysis of probability of failure is carried for different wall heights, base slab length and thickness of the wall.

INTRODUCTION

In the practical engineering problems deterministic approach is generally practiced for the design of the structures. But it has been observed that the performance of the structures depends on many uncertainties associated with material properties and loading conditions. To overcome this problem some methodologies has been developed on the basis of conventional probability principles (Phoon, 2008). From past few decades these techniques has gained considerable amount of attention and popularity as the prime objective of these methodologies are to take the randomness of the input parameters into account and calculate the reliability of the structures. One of these techniques popularly known as variance algebra has been used in this paper to find out the reliability index of a vertical cantilever retaining wall with horizontal backfill and random surcharge loading. Randomness of the surcharge along with the randomness of the soil and concrete properties has been taken into account.

The main objective of any reliability based design is to find out reliability index (β) which is the shortest measured distance from the safe mean value point to the most probable failure combination of parameters on the limit state surface. Probability of failure (PF) can be derived from reliability index (β) by using the established relationship between them (Ranganathan, 1999).

$$PF = 1 - \emptyset(\beta)$$

where $\emptyset$ is the cumulative probability of any normal variable.

In past decades, different approaches have been proposed by different researchers for reliability based design of earth retaining structures. Basha and Babu (2008) have used inverse reliability method for obtaining depth and section modulus of the cantilever sheet pile wall and also performed sensitivity analysis to assess the impact of the random parameters on the overall reliability of the wall. Low (2005) has suggested First Order Reliability Method and Hasofer-Lind index to address the reliability in the design of retaining walls. A performance function has been developed considering random soil properties as normal and non normal variable and reliability index as well as probability of failure has been calculated from that, which was further verified using Monte Carlo simulation. Phoon et al. (2000) have used first order reliability method for design of a transmission line structure foundation. Duncan (2000) used Taylor series expansion for evaluating reliability of a cantilever retaining wall wherein the random variables are considered uncorrelated. Furthermore Cherubini (2000) discussed both deterministic and probabilistic design of an anchored sheet pile wall, he found reliability based design is more practical as compared to deterministic design as the inherent variability is considered in analysis Biernatowski and Puła (1988) developed a probabilistic method based on simulation techniques to evaluate the stability of massive bridge abutments. Zevgolis and Bourdeau (2010) adopted the method developed by Biernatowski and Puła (1988) and suggested a modified methodology for the probabilistic analysis of reinforced concrete cantilever walls. The wall's external stability has been computed for static case and modeling has been done as a series system with correlated failure modes. Monte Carlo simulation was used to address the reliability based design.

Variance algebra is another method to evaluate reliability index and is used in this paper. This method is popularly known as mean value first order second moment method (MVFOSM). This method is comparatively simple method as compared to the other methods and gives satisfactory results. The basic principle of this method is to evaluate mean and standard deviation value of the resistance function and overturning function and compute reliability index from them. For preliminary design cases this method can be used and proved to be very useful as the tedious calculation can be avoided.

RELIABILITY ANALYSIS OF A CANTILEVER RETAINING WALL

A typical configuration of a vertical cantilever retaining wall with horizontal backfill shown Figure 1 is adopted in the analysis. The wall is subjected to random surcharge loading of intensity q per unit area. In the Figure 1, H and d are the height and thickness of the wall and b, t are the width and thickness of the base slab respectively, l is the distance between the centre line of the stem and heel (all units are in meter). Ground water table is assumed to be much below the base of the retaining wall.

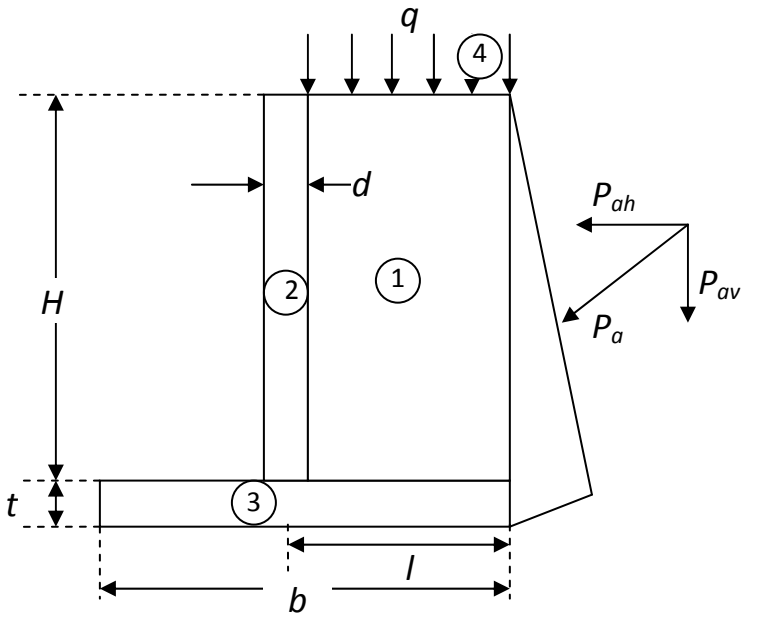

Figure 1. Schematic diagram of a cantilever retaining wall

Surcharge, unit weight of soil, unit weight of concrete, friction angle of soil and wall friction angle are five random variables and they have been represented by $\boldsymbol{q}$, $\boldsymbol{w_s}$, $\boldsymbol{w_c}$, $\emptyset$ and $\boldsymbol{\delta}$ respectively. All parameters are assumed to be normally distributed with realistic mean and standard deviation value. For simplification random parameters are assumed to be non-correlated.

Retaining walls are generally subjected to three types of failures: overturning failure, bearing capacity failure and sliding failure. The objective of this paper is to evaluate the probability of failure of the wall due to overturning mode while assuming the wall is safe for sliding and bearing capacity failure.

All mathematical formulation has been carried out by categorize the whole system into four separate components: 1. backfill soil; 2. stem of the retaining wall; 3.base slab; and 4. surcharge loading as shown in the Figure 1. The force impart by each of these components (W_1, W_2, W_3, W_4) and the moments of these forces with respect to the heel of the wall (M1, M2, M3, M4) has been calculated.

$$M_1 = W_1 l_1 = w_s \frac{\left(l - \frac{d}{2}\right)^2}{2}(H - t)$$

$$M_2 = W_2 l_2 = w_c d(H - t)l$$

$$M_3 = W_3 l_3 = w_c t \frac{b^2}{2}$$

$$M_4 = W_4 l_4 = \frac{q}{2}\left(l - \frac{d}{2}\right)^2$$

l_1, l_2, l_3, l_4 are the lever arm distances of the corresponding forces imparted by components 1, 2, 3 and 4, respectively, from the heal.

Active earth pressure acting on the wall calculated using Coulomb's earth pressure expression (Verruijt, 2010) Coulomb's earth pressure expression is based on planner failure surface of the backfill soil. As the wall is vertical so that the force acting on

the wall is inclined from vertical at an angle equal to the wall friction angle of the soil and wall. The earth pressure is assumed to act at one third height from the bottom surface of the soil.

$$P_a = \frac{1}{2} K_a w_s (H - t)^2$$

Where, K_a is the active earth pressure co-efficient.

$$K_a = \frac{\cos^2(\emptyset - \alpha)}{\cos^2(\alpha) \cdot \cos(\alpha + \delta) \cdot \left[1 + \sqrt{\frac{\sin(\emptyset + \delta) \cdot \sin(\emptyset - \beta)}{\cos(\alpha + \delta) \cdot \cos(\beta - \alpha)}}\right]^2}$$

Where, α and β are the inclination of wall with respect to vertical and inclination of backfill with respect to horizontal respectively. For the present case α and β are assumed as 0.

For ease of calculation the active earth pressure acting on retaining wall can be divided into two components: horizontal and vertical.

$$P_{av} = P_a \sin(\delta)$$

$$P_{ah} = P_a \cos(\delta)$$

Hence total vertical force $W = W_1 + W_2 + W_3 + W_4 + P_{av}$ and total moment due to vertical loads with respect to heel is $M_w = M_1 + M_2 + M_3 + M_4$.

Let x_w is the distance of point of action of all the vertical loads from the heel

$$x_w = \frac{M_w}{W}$$

So the stabilizing moment and the overturning moment acting on the wall can be written as

$$M_r = W(b - x_w)$$

$$M_o = (P_a \cos\delta)\frac{H}{3}$$

The performance function is the difference between the resisting moment and the overturning moment, where resisting moment is the product of total vertical moment and the distance between the point of action of the vertical load and toe of the wall. The performance function (G) can be written as the difference between resisting moment and overturning moment.

$$G = M_r - M_o$$

To imply reliability principle in the performance function the principle of variance algebra has been used. To calculate the reliability index which is knows as Cornel's reliability index in variance algebra is actually the ratio of the mean of the performance function to the standard deviation of the performance function.

Let $G(x)$ is a performance function and it can be defined as

$$G(x) = G(x_1, x_2, x_3, x_4, \ldots\ldots)$$

Where, $x_1, x_2, x_3, x_4, \ldots$ are the random variable then the mean value of the performance function can be obtained as (Ranganathan, 1999)

$$G(x)_\mu = G(\mu_1, \mu_2, \mu_3, \mu_4, \ldots\ldots)$$

Where, $G(x)_\mu$the mean value of the performance function and $\mu_1, \mu_2, \mu_3, \mu_4, \ldots$ are the mean values of the random variable $x_1, x_2, x_3, x_4, \ldots$ correspondingly.
Unlike the mean of the performance function to calculate the variance of the performance function partial differentiation of the performance function with respect to each random variable need to be performed. The general algorithm for calculation of the variance of the performance function can be written as (Ranganathan, 1999).

$$VAR(G) \cong \sum_{i=1}^{n}\sum_{j=1}^{n}\left[\frac{\partial G}{\partial X_i}\right]_\mu COV(X_i, X_j)$$

Where G, X_i, COV, are the performance function, i^{th} random variable of the performance function and covariance of the parameters, respectively. The calculation has been performed in Matlab.
Cornel's Reliability index (β) has been obtained from the ratio of the mean of the performance function to the standard deviation of the performance function ($\sqrt{VAR(G)}$).

$$\beta = \frac{G(x)_\mu}{\sqrt{VAR(G)}}$$

Alternatively reliability index can be evaluated directly from the resisting moment and overturning moment by the following formulation.

$$\beta = \frac{\mu_R - \mu_o}{\sqrt{({\sigma_R}^2 + {\sigma_o}^2)}}$$

Furthermore probability of the failure can be obtained from the reliability index by the following relationship

$$Pf = 1 - \emptyset(\beta)$$

A sensitivity analysis has been performed by plotting the value of beta against different parameters.

RESULTS & DISCUSSION

A sensitivity analysis has been performed to evaluate the Cornel's reliability index and probability of failure of the retaining wall for different wall heights, stem thickness and base slab thickness. The random parameters considered here are surcharge load, unit weight of soil, unit weight of concrete, friction angle of the soil and the wall friction angle and the mean values of these parameters considered in calculation are 40 kN/m^2, 18 kN/m^3, 24 kN/m^3, 35^o, 20^o respectively. To evaluate the standard deviation a coefficient of variation assumed for each of these parameters such as 0.10, 0.05, 0.09, 0.10 and 0.10 respectively (coefficient of variation can be

defined as the ratio of mean and standard deviation of any variable). The mean and COV values of ϕ and δ are taken from the paper of Low et al. (2005) and the mean and COV value of unit weight of soil are taken from Zevgolis et al. (2010) other random parameter mean and COV values are assumed.

For the first case sensitivity analysis with respect to the height of the wall has been considered. The other constant parameters considered there was base slab thickness and length of 3 m and 0.35 m respectively and thickness of stem of the retaining wall as 0.45 m. The calculations have been performed in Matlab and the obtained results are shown in Figure 2.

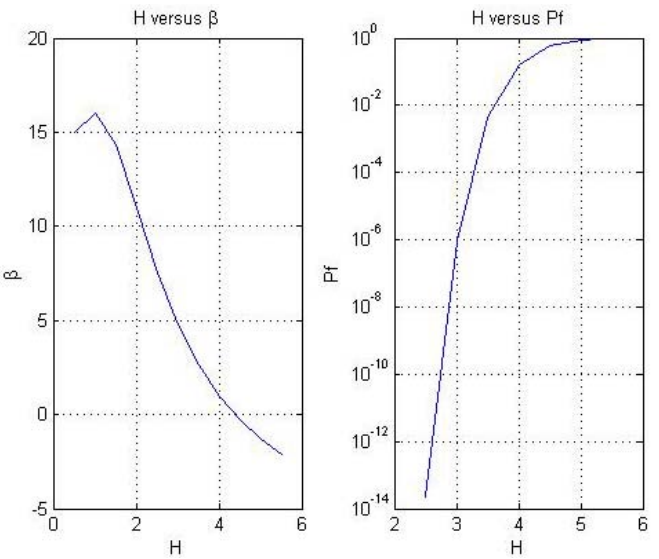

Figure 2.Variation of β and probability of failure with respect to height of the wall

Figure 2 evokes that as height of the wall increases the probability of failure also increases that is because the horizontal component of the earth pressure increases with increase of height. Conversely if the length of the base slab increased, the probability of failure decreases (Figure 3). Probability of failure is near to the 1 if the base slab length is less than 1m, (calculation has been performed keeping height of the wall as 4m).

Finally a sensitivity analysis has been performed keeping the thickness of the stem in consideration. It can be observed from Figure 4 that, for practically possible values of stem thickness there is no chance of failure of the wall hence stem thickness is not a very important parameter from overturning point of view. However, it should satisfy minimum thickness criterion to provide proper support to the backfill soil.

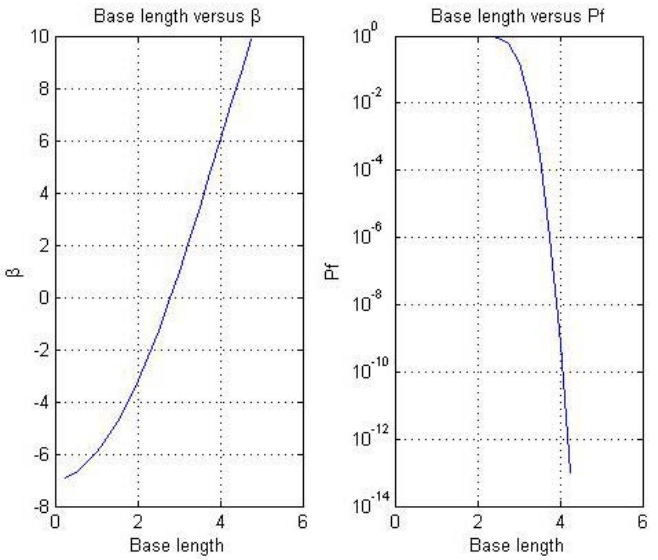

Figure 3. Variation of β and Pf with respect to the base slab length of the wall

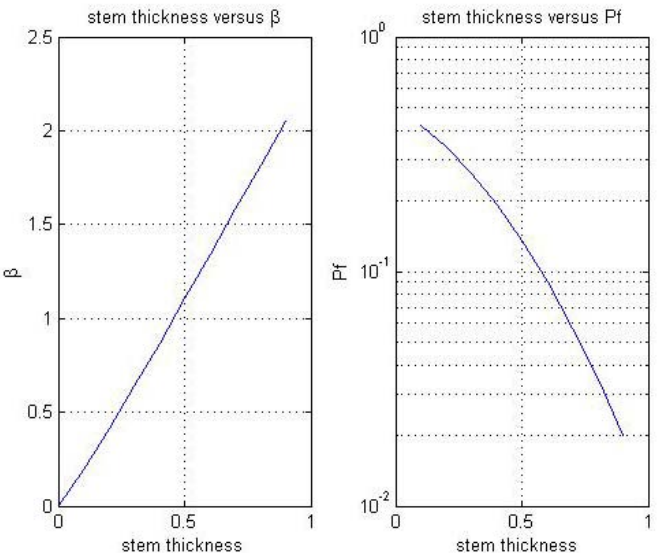

Figure 4. Variation of β and Pf with respect to the stem thickness of the wall

CONCLUSIONS

A reliability analysis of a cantilever retaining wall has been performed. Random material properties and random surcharge loading were considered in the analysis. It was observed that, for retaining walls reliability analysis can be used to restrict its maximum height, minimum base slab length and minimum thickness of stem. It can also be seen that the variance algebra method used can calculate reliability of the

retaining wall quite simply and without much tedious calculations. So this method can be used in preliminary design problems to check the design parameters.

REFERENCES

Babu, G. L. S. and Basha, B. M. (2008). "Optimum design of cantilever sheet pile walls in sandy soils using inverse reliability approach." *Computers and Geotechnics*. 35(2), 134-143.

Biernatowski, K. and Puła, W. (1988). "Probabilistic analysis of the stability of massive bridge abutments using simulation methods." *Structural Safety* 5(1):1–15.

Cherubini, C. (2000). "Probabilistic approach to the design of anchored sheet pile walls." *Computers and Geotechnics*, 26(4), 309-330.

Duncan, J. M. (2000). "Factors of safety and reliability in geotechnical engineering." *Journal of Geotechnical and Geoenvironmental Engineering*, ASCE, 126(4), 307-316.

Low, B. K. (2005). "Reliability-based design applied to retaining walls." *Geotechnique* 55(1), 63–75.

Phoon, K. (2008). *Reliability-based design in geotechnical engineering: computations and applications*, Taylor & Francis, USA.

Phoon,K., Kulhawy, F. H., Grigoriu, M.D. (2000). "Reliability-based design for transmission line structure foundations." *Computers and Geotechnics*, 26, 169-185.

Ranganathan, R. (1999). *Structural Reliability analysis and design*, Jaico Publishing House, India,

Verruijt, A. (2010). *Soil mechanics*, Delft University of Technology.

Zevgolis, I. E. and Bourdeau, P. L. (2010). "Probabilistic analysis of retaining walls." *Computers and Geotechnics*, 37, 359–373.

Wall and ground responses in a braced excavation considering spatial variability

Zhe Luo[1], C. Hsein Juang[2], F.ASCE, and Fu-Kuo Huang[3]

[1] Research Assistant, Department of Civil Engineering, Clemson University, Clemson, SC 29634. Email: zluo@clemson.edu.
[2] Professor, Department of Civil Engineering, Clemson University, Clemson, SC 29634. Email: hsein@clemson.edu. Telephone: 864-656-3322. Fax: 864-656-2670; also affiliated with National Central University, Jhongli, Taoyuan, 32001, Taiwan.
[3] Associate Professor, Department of Water Resources and Environmental Engineering, Tamkang University, Tamsui, Taiwan 25137, R.O.C. Email: fkhuang@mail.tku.edu.tw.

ABSTRACT

A framework for evaluating the probability of exceeding the specified limiting wall and ground responses in a braced excavation is presented in this paper. In this framework, the wall and ground responses in a braced excavation are computed with finite element method (FEM). To model uncertainty with limited data, fuzzy numbers are used to characterize the uncertainty, and the spatial variability of soil properties are incorporated into fuzzy parameters using spatial averaging technique. The FEM analysis of braced excavations with fuzzy parameters is carried out using the vertex method, in which "sampling" of uncertain soil parameters is by means of α-cut intervals, rather than the Monte Carlo technique. The output (the maximum wall deflection and ground settlement) of the FEM analysis in this case are fuzzy numbers, and a technique called fuzzy point estimate method (FPEM) is used to interpret the resulting fuzzy numbers. A well-documented excavation case history is analyzed to demonstrate the proposed framework. The results show that the proposed framework is effective for assessing the probability of exceeding the specified limiting wall and ground response in a braced excavation.

INTRODUCTION

One main concern in a braced excavation in urban area is the damage to the adjacent infrastructures caused by the excessive wall deflection and ground settlement. Due to the uncertainty in the soil parameters, it would be a sensible approach to derive the probabilities of exceeding the *limiting* wall and ground responses, and then to make the design decisions based on these exceedance probabilities. It is noted that the inherent spatial variation of soil properties has been

demonstrated in many geotechnical problems and modeling of this variation with random field theory has been reported (e.g., Vanmarcke, 1977; Griffiths and Fenton, 2004). This paper focuses on a simplified approach for estimating the probability of exceeding the limiting wall and ground responses in a braced excavation in clay. The proposed framework consists of the following elements: 1) finite element method (FEM) for analyzing the wall and ground responses, 2) fuzzy set representation of parameter uncertainty, 3) spatial averaging technique for handling spatial variability, 4) vertex method for propagating fuzzy input through FEM model, and 5) fuzzy point estimate method (FPEM) for interpreting fuzzy output.

FINITE ELEMENT MODELING WITH SMALL-STRAIN NONLINEARITY

In this paper, the wall and ground responses in a braced excavation in clays are analyzed using a commercially available finite element code, PLAXIS (Brinkgreve and Vermeer, 1998). It should be noted that use of this software in this paper does not represent an endorsement of the software; other FEM codes can be employed. In the work by Kung et al. (2007), a small-strain nonlinear soil model, known as the Modified Pseudo Plasticity (MPP) model for clays with consideration of anisotropic, high stiffness at small-strain, and degradation behavior, was implemented in a computer code AFENA for the analysis of braced excavations. To follow up on this previous work (Kung et al., 2007), it is desirable to implement the MPP model as a user-defined model in PLAXIS. To this end, it is noted that such an implementation has been carried out by Dang (2009). Thus, PLAXIS code with the MPP soil model (implemented by Dang) is used as an FEM tool in the present study.

MODELLING SPATIAL VARIABILITY IN BRACED EEXCAVATIONS

Among the methods dealing with the spatial variability of soil (e.g., Griffiths and Fenton 2004), the spatial averaging of the variation of the soil properties has shown to be an effective tool (e.g., Phoon and Kulhawy, 1999). The spatial variability of the soil parameters can be averaged in order to approximate a random variable that represents a soil parameter. The concept of the spatial averaging was described by Vanmarcke (1977) as follows: the variability of the averaged soil properties over a large domain is less than that over a small domain. For the commonly used single exponential model, the variance reduction factor (Γ^2) is given as:

$$\Gamma^2 = \frac{1}{2}\left(\frac{\theta}{L}\right)^2\left[\frac{2L}{\theta} - 1 + \exp\left(-\frac{2L}{\theta}\right)\right] \tag{1}$$

where L is the characteristic length with respect to a potential failure surface. In this paper, the characteristic length is assumed to be the length of the sliding surface in a stability analysis of a braced excavation (Schweiger and Peschl, 2005). The implication here is that the shear resistance along the sliding surface is roughly stationary, which is considered reasonable for the case study presented later in this paper. With the known characteristic length (L) and the scale of fluctuation (θ), the reduced variance can then be obtained with the following equation:

$$\sigma_{\Gamma}^2 = \Gamma^2 \cdot \sigma^2 \tag{2}$$

where σ^2 is the variance of the soil parameter of concern (such as normalized undrained shear strength), and Γ^2 is the variance reduction factor.

FUZZY SETS METHODOLOGY

Fuzzy set theory

The fuzzy set theory was first developed by Zadeh (1965) and has been widely used in many engineering and non-engineering fields. When the data is scarce, as in many geotechnical projects, use of a fuzzy number to represent an uncertain soil parameter is a reasonable alternative to modeling with a probability distribution. A fuzzy set is a set of paired values [x, $\mu_A(x)$], where an element x belongs to the set A to a degree, defined by its membership function $\mu_A(x)$. The membership grade, ranging from 0 to 1, is used to characterize the degree of belief that x belongs to A. A fuzzy number is a fuzzy set that is normal and convex—the shape of the membership function is single humped and has at least one value whose the membership grade (or degree of belief) is 1.

Constructing membership function that represents a fuzzy number

A triangular fuzzy number representing an uncertain soil parameter can be readily established with the estimates of lower bound (a), upper bound (b), and mode (m). As shown in Fig. 1(a), the two bounds are assigned with a membership grade of 0 and the mode is assigned a membership grade of 1. Following Duncan's approach (Duncan, 2000), given the mean μ_X and standard deviation σ_X of the soil parameter of concern, the upper bound and the lower bound of the intended fuzzy number can be taken as $\mu_X \pm 2\sigma_X$, respectively. In this paper, we adopt the procedure suggested by Peschl and Schweiger (2003) to compute the mode of the fuzzy number. Then the fuzzy numbers can be constructed with the knowledge of a lower bound, an upper bound, and a mode (which is the most probable value).

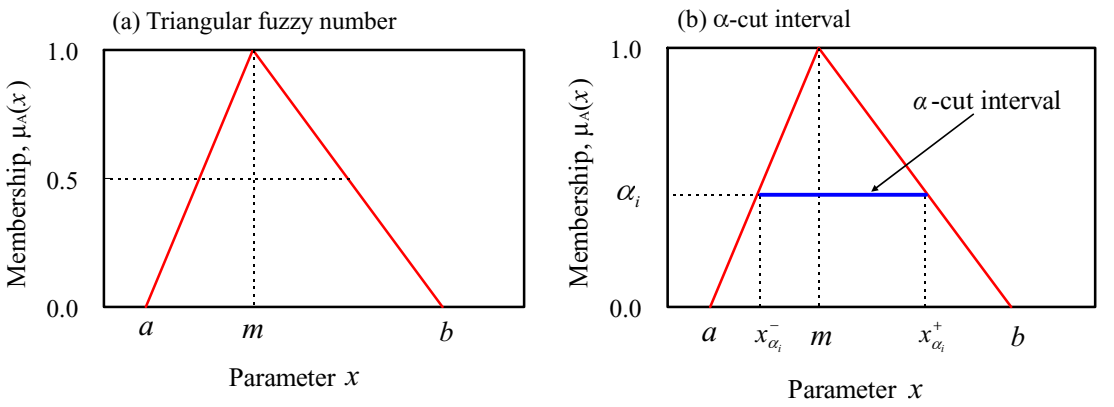

Figure 1. Example of triangular fuzzy number and α-cut interval.

Fuzzy data processing by means of vertex method

To propagate fuzzy input through PLAXIS, the vertex method proposed by Dong and Wong (1987) is adopted. This method is based on the α-cut concept. As shown in Fig. 1(b), at a membership grade of α_i, an interval with a lower bound of $x_{\alpha_i}^-$ and an upper bound of $x_{\alpha_i}^+$ can be formed. Mathematically, it can be shown that any fuzzy number can be represented by a set of α-cut (or α-level) intervals with α ranging from 0 to 1. Thus, to propagate fuzzy input through PLAXIS, fuzzy numbers are first discretized into a set of α-cut intervals (for example, taking α = 0, 0.2, 0.4, 0.6, 0.8, and 1.0). At each α-level, the intervals of the fuzzy input variables are obtained and the combinations of vertexes (i.e., the lower bounds and the upper bounds of the α-cut intervals of all fuzzy input) are determined. Given n fuzzy input variables, the number of combinations of vertexes is 2^n. Each vertex represents a set of fixed values of input variables that can readily be put into PLAXIS for a deterministic analysis. Each of the 2^n combinations of vertexes is used one-by-one in the FEM analysis, which yields a set of 2^n solutions. Taking the minimum and the maximum of these solutions, an interval is obtained at the specified α-level. Repeating the above process for a set of α values, a set of interval solutions are obtained. Recalling that a fuzzy set is defined by a set of paired values $[x, \mu_A(x)]$, thus the lower bounds and the upper bounds of these intervals along with the corresponding α values define a fuzzy number that represents the outcome of the fuzzy PLAXIS analysis.

Interpretation of the resulting fuzzy number

The fuzzy point estimate method (FPEM), proposed by Dodagoudar and Venkatachalam (2000), is employed to interpret the resulting fuzzy number. First, assume that at a given α-level, the lower bound and the upper bound of the resulting fuzzy number (either for wall deflection or ground settlement) are $\delta_{\alpha_k^-}$ and $\delta_{\alpha_k^+}$, respectively [note: the subscript "–" denotes the lower bound and the subscript "+" denotes the upper bound of the α-cut interval; the index k = 1,⋯,N, where N is the number of α-cut levels]. To apply the FPEM, a point estimate $\delta_{\alpha_k}^r$ is created to represent this α-cut interval (modified from Dodagoudar and Venkatachalam (2000)):

$$p_{\pm} = 1 \pm \sum_{i=1}^{M-1} \left(\sum_{j=i+1}^{M} \frac{\rho_{ij}}{\sqrt{\prod_{i=1}^{M} \left[1 + \left(\frac{\theta_i}{2} \right)^2 \right]}} \right) \tag{3}$$

where, M = number of fuzzy input variables [in this paper, M = 2]; θ_i = the coefficient of skewness of a triangular fuzzy input variable I; ρ_{ij} = the coefficient of correlation between fuzzy input variables i and j. Finally, the r^{th} moment of the response (output) δ_α^r can be obtained by taking a weighted average of a set of $\delta_{\alpha_k}^r$ values:

$$E\left[\delta^r\right] = \frac{\sum_{k=1}^{N} \alpha_k \cdot \delta_{\alpha_k}^r}{N} \tag{4}$$

The mean and the standard deviation of the output fuzzy number can be computed with the first and second moments (r = 1 and 2).

CASE STUDY - TNEC EXCAVATION CASE

The TNEC excavation case in Taiwan (Ou et al., 1998) is used herein as an example to illustrate the *fuzzy finite element approach* (FFEA). To verify the accuracy of PLAXIS code with the MPP soil model, we re-analyze the case of the Taipei National Enterprise Center (TNEC). The results are compared with those reported previously by Kung et al. (2007). Fig. 2 compares the results of FEM predictions of the maximum wall deflections and the maximum ground settlements, respectively. The results show that the PLAXIS solutions in this paper are as accurate as those obtained by Kung et al. (2007) using AFENA and both agree well with field observations.

It is noted that the second layer (8 m – 33m) in the soil profile is a clay layer that dominates the maximum wall and ground responses in this excavation. For this case study of the TNEC excavation, the normalized undrained strength and the normalized initial tangent modulus of the clay are s_u/σ'_v = 0.32 and E_i/σ'_v = 672, respectively (Kung et al., 2007). Thus, the standard deviations of the two parameters are estimated to be 0.05 and 108, respectively, based on a reported coefficient of variation (COV) of 0.16 (Hsiao et al., 2008). The two soil parameters are treated here as triangular fuzzy numbers, since the available data is not sufficient to characterize them in term of probability distributions.

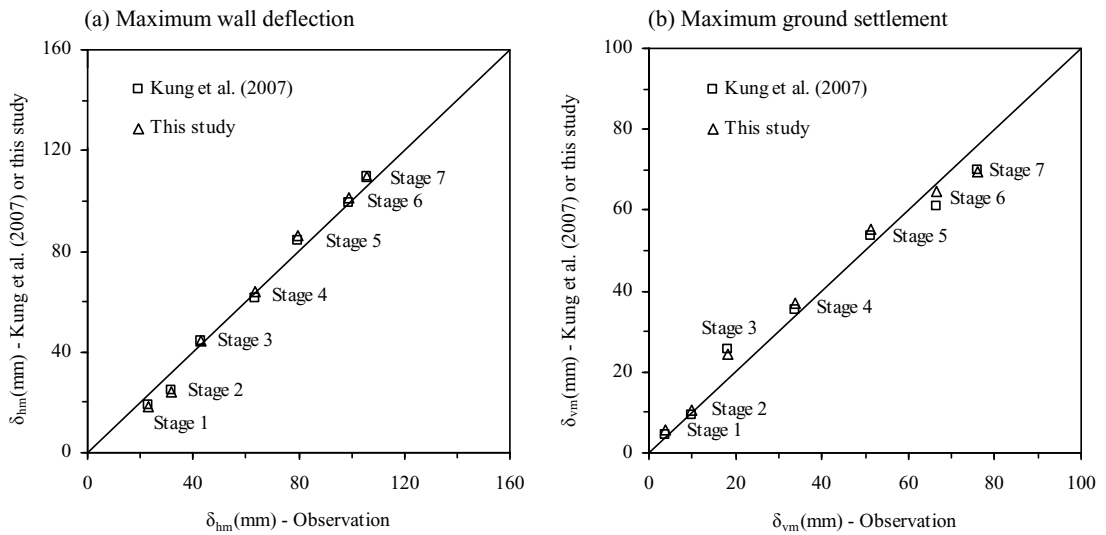

Figure 2. Maximum wall deflections and maximum ground settlements at various stages of excavation of the TNEC case.

To consider the effect of the spatial variability, let's *first* assume that the field has an infinite scale of fluctuation. The variance reduction factor (Γ^2) in this case is 1 (no reduction) and the fuzzy numbers for s_u/σ'_v and E_i/σ'_v can be constructed using the procedure described previously. Fig. 3 shows the constructed fuzzy numbers for s_u/σ'_v and E_i/σ'_v (note: the triangular membership function labeled *a-m-b* in this figure). All other input variables in the PLAXIS analysis are assumed to have non-random, non-fuzzy values. Analysis of the braced excavation in the TNEC case is carried out using PLAXIS with the MPP soil model. The resulting fuzzy numbers that represent the maximum wall deflection (δ_{hm}) and the ground-surface settlement (δ_{vm}) for the last excavation stage obtained from PLAXIS are shown in Fig. 4.

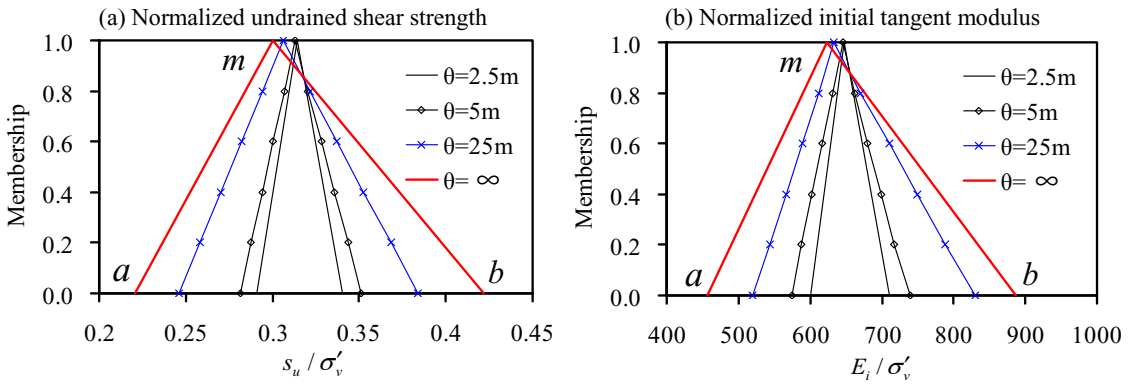

Figure 3. Fuzzy input parameters at different scales of fluctuation

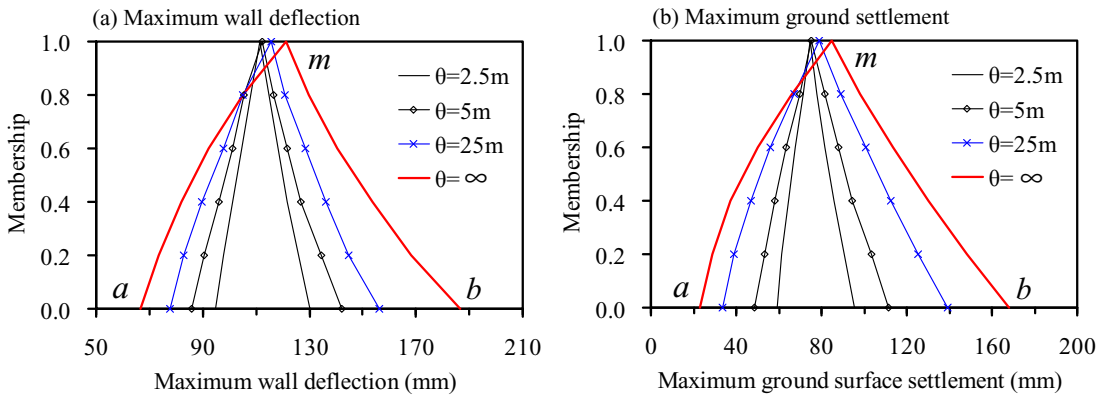

Figure 4. Resulting fuzzy numbers for maximum wall deflection and ground surface settlement

The entire processes of the above FFEA analysis can be repeated for any assumed scale of fluctuation. For simplicity and as an example here, the scales of fluctuation of the two soil parameters in this TNEC case are assumed to be the same; that is, $\theta = \theta_{s_u/\sigma'_v} = \theta_{E_i/\sigma'_v}$. For demonstration purposes and as a way to investigate the effect of spatial variability, the FFEA analysis is repeated for three additional scales of fluctuation (2.5m, 5m, and 25m). For each scenario involving a different scale of fluctuation, the variance reduction factor (Γ^2) is computed with Eq. (1) and the characteristic length L which is estimated to be 71 m in this case (the length of the

sliding surface in this case). The constructed fuzzy numbers for these three scenarios are shown in Fig. 3. The resulting fuzzy numbers are also shown in Fig. 4.

For illustration purposes, the probabilities of exceedance are computed under a few assumed limiting wall and ground responses. The results are plotted in Fig. 5 for the probabilities of exceeding the chosen limiting wall deflection ($\delta_{\lim,hm}$) and ground settlement ($\delta_{\lim,vm}$). The probability of exceedance is seen to decrease with the chosen limiting deformation (either wall deflection or ground settlement) which is consistent with the study by Hsiao et al. (2008). The effect of the scale of fluctuation on the probability of exceedance is clearly observed. When relatively smaller limiting $\delta_{\lim,hm}$ and $\delta_{\lim,vm}$ are adopted, the scenario with a smaller scale of fluctuation yields a higher probability of exceedance. The trend reverses when relatively larger limiting $\delta_{\lim,hm}$ and $\delta_{\lim,vm}$ are adopted. For the probability of exceeding the limiting wall deflection, the reversal of the trend occurs when $\delta_{\lim,hm} \approx 108$ mm is adopted. Similarly, for the probability of exceeding the limiting ground settlement, the reversal of the trend occurs when $\delta_{\lim,vm} \approx 72$ mm is adopted. Of course, this observation may not be generalized as it may be specific to the TNEC case. Further studies are needed to confirm this observation. Nevertheless, the results show that neglecting the spatial soil variability in the analysis can lead to either overestimation or underestimation of the probability of exceedance, depending on the chosen limiting wall and ground responses. Thus, it is important to assess the spatial variability in site investigation and to incorporate this variability in the probability analysis. A similar conclusion of the effect of scale of fluctuation on the probability of failure for slope stability problems was reported by Griffiths and Fenton (2004) using the rigorous random FEM approach, which shows the validity of the proposed approach.

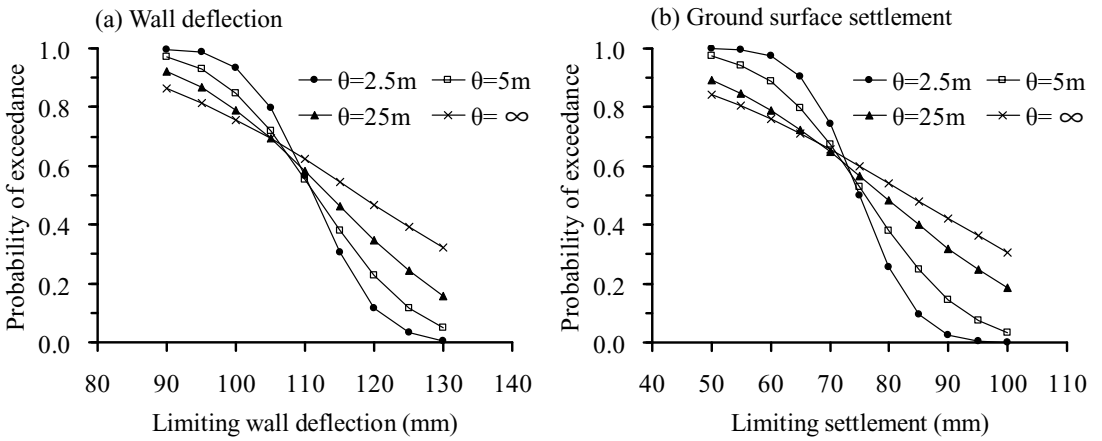

Figure 5. Computed probability of exceedance at various levels of limiting wall deflection and ground surface settlement

CONCLUSIONS

The fuzzy finite element approach (FFEA) is shown to be effective in the analysis of the wall and ground responses in a braced excavation through the study of

a well-documented excavation case history. PLAXIS with the modified pseudo plasticity (MPP) soil model is found satisfactory for predicting the wall and ground responses in a braced excavation. The spatial averaging technique in the finite element analysis of the braced excavation in clays demonstrates the effect of spatial correlation of soil properties on the responses in a braced excavation. Neglecting the spatial variability in the finite element analysis can lead to either overestimation or underestimation of the probability of exceedance, depending on the specified limiting wall and ground responses.

REFERENCES

Brinkgreve, R. B. J., and Vermeer, P.A. (1998). *PLAXIS-Finite Element Code for Soil and Rocks Analysis*, Version 8, Balkema, Rotterdam.

Dang, H.P. (2009). "Excavation behavior and adjacent building response analyses using user defined soil models in PLAXIS." MS Thesis, National Taiwan University of Science and Technology, Taipei, Taiwan.

Dodagoudar, G.R., and Venkatachalam, G. (2000). "Reliability analysis of slopes using fuzzy sets theory." *Computers and Geotechnics*, 27(2), 101-115.

Dong, W.M., and Wong, F.S. (1987). "Fuzzy weighted averages and implementation of the extension principle." *Fuzzy Set and Systems*, 21(2), 183-199.

Duncan, J.M. (2000). "Factors of safety and reliability in geotechnical engineering." *Journal of Geotechnical Geoenvironmental Engineering*, 126(4), 307-316.

Griffiths, D.V., and Fenton, G.A. (2004). "Probabilistic slope stability analysis by finite elements." *Journal of Geotechnical and Geoenvironmental Engineering*, 130(5), 507-518.

Hsiao, E.C.L., Schuster, M., Juang, C.H., and Kung, T.C. (2008). "Reliability analysis of excavation-induced ground settlement for building serviceability evaluation." *Journal of Geotechnical and Geoenvironmental Engineering*, 134(10), 1448-1458.

Kung, T.C., Hsiao, C.L., and Juang, C.H. (2007). "Evaluation of a simplified small-strain soil model for finite element analysis of excavation-induced movements." *Canadian Geotechnical Journal*, 44(6), 726-736.

Ou, C.Y., Liao, J.T., and Lin, H.D. (1998). "Performance of diaphragm wall constructed using top-down method." *Journal of Geotechnical and Geoenvironmental Engineering*, 124(9), 798-808.

Peschl, G.M., and Schweiger, H.F. (2003). "Reliability analysis in geotechnics with finite elements - comparison of probabilistic, stochastic and fuzzy set methods." *In: Proceedings of the 3rd international symposium on imprecise probabilities and their applications* (ISIPTA'03), Carleton Scientific, Canada, 437-451.

Phoon, K.K., and Kulhawy, F.H. (1999). "Evaluation of geotechnical property variability." *Canadian Geotechnical Journal*, 129(4), 625-639.

Schweiger, H.F., and Peschl, G.M. (2005). "Reliability analysis in geotechnics with the random set finite method." *Computers and Geotechnics*, 32(6), 422-435.

Vanmarcke, E.H. (1977). "Probabilistic modeling of soil profiles." *Journal of the geotechnical engineering division*, 103(11), 1227-1246.

Zadeh, L.A. (1965). "Fuzzy sets." *Information and Control*, 8(3), 338-353.

Evaluation of LRFD Resistance Factors and Risk for Mechanically Stabilized Earth Walls

S. Wasman[1*], M. McVay[2], D. Bloomquist[3], M. Harrison[4], and P. Lai[5]

[1*] PhD Student, Department of Civil and Coastal Engineering, University of Florida, 365 Weil Hall, Gainesville, Fl, 32611, ph (352) 392-9537, fx (352) 392-3394, e-mail: swasman@ufl.edu
[2] Professor, Department of Civil and Coastal Engineering, University of Florida, Gainesville, Fl, e-mail: mcm@ce.ufl.edu
[3] Associate Professor, Department of Civil and Coastal Engineering, University of Florida, Gainesville, Fl, e-mail: dave@ce.ufl.edu
[4] Assistant Professor, Department of Nuclear and Radiological Engineering, University of Florida, Gainesville, Fl, e-mail: marc.harrison@ufl.edu
[5]Florida Department of Transportation, Tallahassee, Fl, e-mail: peter.lai@dot.state.fl.us

ABSTRACT

The use of Mechanically Stabilized Earth (MSE) walls is very common in congested urban areas. AASHTO's current LRFD resistance values were established from Allowable Stress Design Factors of Safety. Variability of soil friction angle, unit weight, cohesion, etc. is not considered. This study investigates the influence of soil property variability on MSE wall sliding and bearing stability and compares Capacity Demand Ratio (CDR) distributions from conventional analytical approaches with laboratory centrifuge model results. Next, the probability of failures (CDR < 1.0) and associated variability is applied in risk assessment of two MSE walls used in existing transportation infrastructure subsystems. The risk assessment was used to develop recommended probability of failures in design to meet the associated cost of repair if catastrophic failures of the walls are to occur.

INTRODUCTION

Geotechnical design codes have moved towards a reliability-based approach such as the Load and Resistance Factor Design (AASHTO, 2009) and away from Allowable Stress Design (ASD) with factors of safety. Resistance factors for all modes of failure in the code for retaining walls were developed through calibration with ASD Factors of Safety (FS). Unfortunately, the latter approach does not account for the influence of the soil properties variability on the resistance factors. Moreover, the resistance and loads calculated in a retaining wall external stability analysis are directly influenced by the soil properties. Soil variability and its influence on the stability of retaining walls has been investigated through a number of probabilistic analyses (Chalermyanont and Benson, 2005; Fenton and Griffiths, 2005; Zevgolis and Bourdeau, 2008; Babu and Basha, 2008).

This work also characterizes the variability through Monte Carlo simulations of reinforced backfill and foundation soils with rigid body mechanics using Rankine earth pressure assumptions (Chalermyanont and Benson, 2005) to establish a probability distribution of CDR (capacity demand ratio = resistance force/driving force) as a function of soil properties. Next, to identify the bias in the external stability methods, small scale centrifuge tests were performed to establish experimental CDR histograms based on soil properties (e.g. angle of internal friction angle and unit weight of backfill). Next, using a Monte Carlo bias correction similar to Goh (2008), for cantilever retaining walls, LRFD resistance values are suggested for specific probabilities of failure. Note, the fitting of the measured CDR histogram with the analytical probability distribution should provide more realistic resistance values than those proposed in AASHTO for external stability of MSE walls.

Since 90% of the retaining walls in the State of Florida are MSE with a significant portion in urban areas, a failure is potentially hazardous, depending on the mode. Therefore, a risk assessment which quantifies the probability of failure, P_f, in terms of consequence values (i.e., risk = P_f X consequence) was undertaken. Such an assessment allows for owners, engineers, contractors, etc. to identify where the risk lies and where to focus in the design to decrease the P_f and thereby the risk. The paper presents a probability risk assessment for two failure modes (sliding and bearing) with varied consequences in different settings (urban city, arterial overpass abutments, suburban areas, etc.).

PROBABILISTIC ANALYSIS

For this work, a prototype wall height of 9.1m with L/H ratio of 1.0 and surcharge load of 12 kN/m^2 was considered (Figure 1). The unit weight and friction angle were modeled as lognormal (non-negative values and accounts for possible outliers) and, conservatively, as having no correlation (Goh, 2009; Fenton and Griffiths, 2005). Mean and coefficient of variation, CV, values consistent with those

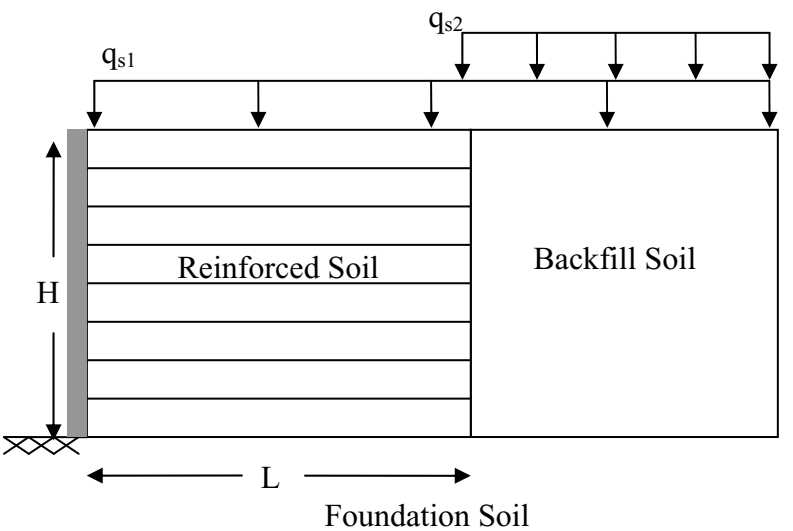

Figure 1. MSE wall with acting surcharge.

reported in research literature (Duncan, 2000; Zevgolis and Bourdeau, 2006; Fenton and Griffiths, 2008) were considered and are presented as the base model values in Table1.

The probability of failure for each mode (sliding and bearing capacity) was defined with the limit state, in terms of a Capacity Demand Ratio (CDR<1). Equations 1 and 2 show each CDR as a function of the factored driving and resisting forces and stresses. The modes of failure were considered to be independent in this study, i.e., the probabilities presented are not inducing failure in another mode. The loads and resistances were factored with values suggested in the AASHTO LRFD Bridge Design Specifications (AASHTO, 2009).

Table 1. Range of statistical parameters of soil properties and surcharge for analysis. Base model parameters shown in parenthesis.

Soil	Mean (μ)	Coefficient of Variation (CV)	Distribution
Reinforced Soil ϕ	20° - 40° (30°)	5% - 20% (10%)	Lognormal
Reinforced Soil γ	15kN/m^3 - 19kN/m^3 (16.5 kN/m^3)	5% - 20% (5%)	Lognormal
Backfill Soil ϕ	20° - 40° (30°)	5% - 20% (10%)	Lognormal
Backfill Soil γ	15 kN/m^3 - 19 kN/m^3 (16.5 kN/m^3)	5% - 20% (5%)	Lognormal
Foundation Soil ϕ	20° - 40° (35°)	5% - 20% (10%)	Lognormal
Foundation Soil γ	15 kN/m^3 - 19 kN/m^3 (16.5 kN/m^3)	5% - 20% (5%)	Lognormal
Surcharge q_s	12 kN/m^2	5% - 20% (25%)	Lognormal

The equations of CDR for sliding and bearing stability of an MSE wall are shown below:

$$CDR_{sliding} = \frac{F_{\text{Re sisting}}}{F_{Driving}} = \frac{\gamma HTan(\phi)\cdot\phi_g}{\frac{1}{2}\gamma H^2 K_a EH + q_s HK_a LS} \quad \text{Eq. 1}$$

$$CDR_{bearing} = \frac{q_{ultimate}}{q_{vertical}} = \frac{(\gamma D_f N_q + \frac{1}{2}\gamma LN_\gamma)\phi_g}{\gamma HEV + q_s LS} \quad \text{Eq. 2}$$

where $F_{Resisting}$ is the factored shear resistance at the reinforced-foundation soil interface, $F_{Driving}$ is the factored active driving force, $q_{ultimate}$ is the factored bearing

capacity, and $q_{vertical}$ is the factored vertical stress at the reinforced-foundation soil interface due to the weight of the soil and the surcharge (q_{s2}).

SCALE MODEL TESTS

As part of an the ongoing study, centrifuge tests to model sliding of a 15 cm high MSE wall with length equal to height (L/H =1) were done in the 12-G Ton facility at the University of Florida. The wall modeled full scale MSE walls, i.e., to allow flexibility of the reinforced zone (Fig. 1) and with non-extensible reinforcement according to the Florida structures guidelines. Model soils used in the tests were selected to obtain internal friction angles within the ranges considered (Table 1). The model wall was 15 cm in height and had a reinforcement length equal to the height (L/H = 1). The reinforced, backfill and foundation soils were varied to obtain μ_ϕ, μ_γ, CV_ϕ and CV_γ values in the range of those in Table 1. Surcharge loading (12 kN/m^2) was modeled using a Bimba piston applied to a flexible surface for uniform contact stresses. During testing, wall displacements were monitored for vertical movement and horizontal movement near the top and bottom of the wall face. To determine the CDR of sliding, horizontal and vertical force sensors measured soil forces that contributed to the total driving (P_a) and resisting forces (τ) in the model.

Multiple tests were performed and from each test a CDR value was obtained so that a frequency distribution could be established along with distribution type and summary statistics (i.e., μ_{CDR}, CV_{CDR}). Figure 2 is a distribution of 16 centrifuge test results for sliding where the variability of the reinforced and backfill soil was held at

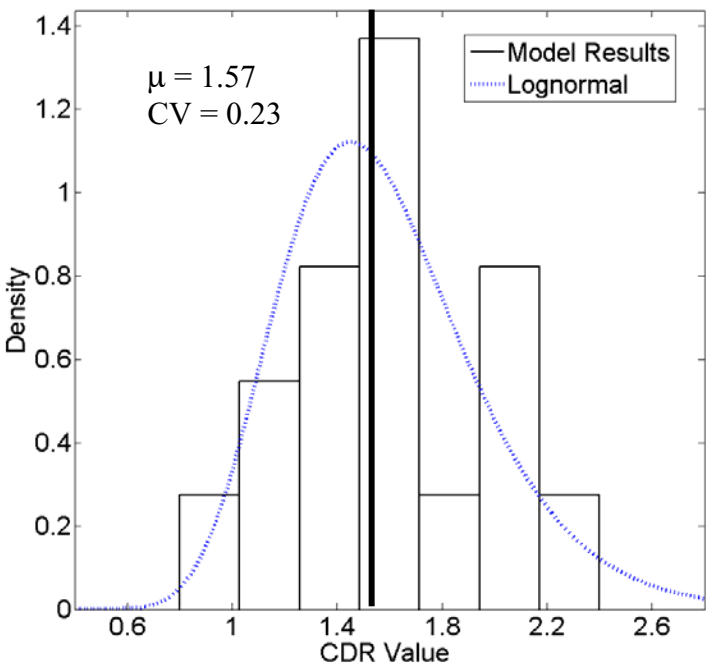

Figure 2. Distribution of centrifuge sliding model tests: μ_ϕ = 35° and CV_ϕ = 4% of reinforced and backfill soil.

$\mu_\phi = 35°$ and $CV_\phi = 4\%$. Based on a fit test presented by Klammler et al. (2011) a ratio of skewness, *sk*, to CV of the model data suggests a gamma distribution. However, since the analytical expression (Eq. 1) of the CDR is lognormal, the latter was selected here, with the area under the tail i.e. CDR<1 defined as the probability of failure of interest. As suggested by Paikowksy et al. (2010), a new LRFD Φ factor for a target P_f may be found by equating the areas underneath the tails where CDR <1 between the experimental and analytical values. Also, the ratio of the P_f's for the measured (centrifuge) to predicted (analytical) should be determined for each external case considered as well as the soil variability investigated.

RISK ASSESSMENT

Risk is the probability of failure times the consequence of the failure. Geotechnical structures such as MSE walls (soil-soil interaction) have been shown to have P_f values associated with independent modes of stability. Consequences of structural failures include loss of life, economic impact, social impact, and environmental impacts with attempts at quantifying values associated with each have been made for Civil Infrastructure systems, e.g. the levee system failures in New Orleans during Hurricane Katrina (USACOE, 2007). Methods of modeling complex systems with P_f analysis consists of fault trees, event trees and master logic diagrams. They allow a logical representation of the system (e.g., MSE) in terms of the P_f and associated components. For example, a fault tree diagram for the MSE wall would have the top event as the global stability of the wall. Underneath the top event, events, or all stability modes (i.e., sliding, bearing, overturning and overall), are listed which contribute to the top events occurrence. Each mode of stability and its P_f is a component of the system and each mode also has components which are function of the soil properties (characterized by μ and CV). The result is a total P_f for the system (i.e., MSE) which can be calculated by a consequence term to obtain an associated risk value.

Risk assessments and methods for geotechnical engineering have been presented for landslides (Fell, 1994), flooding (Fenton and Griffiths, 2008), and talus slopes (Liu et al., 2009). In these studies, specific risks were assessed based on different consequences. For example, the landslide risk assessment considered the vulnerability of houses and persons, the houses having a more easily quantifiable $ value associated with damage incurred. The example of different flooding cases considered cost ($) due to repair, cost ($) to flood proof the houses and cost ($) to prevent flooding by constructing a levee. The risk assessment presented in this paper considers specific risk for the MSE wall's components P_f.

The simplest and most common value quantified is economic consequence (dollars-$), whether its cost to a region or cost of structural repair. In cases where MSE walls are part of the transportation infrastructure, a risk assessment can be made where the economic consequence is determined from the negative impact on value travel time (VTT). For instance, in transportation engineering, the incremental consumer surplus is a measure by which designers assess benefit of increased traffic

lanes (Lee, 2000). Incremental consumer surplus is the area under a demand curve between the initial and improved cost to the user. In the case of MSE wall failure, the resulting economic loss of traffic lanes, may be taken as the negative of the incremental consumer surplus, or that the user will incur costs which will be reflected as a loss in the consumer surplus.

In addition to the costs incurred by the roadway users, other economic consequences can include the repair cost for the MSE wall and roadway. Repair costs are commonly the only consequence considered, as assessing other consequences are quite difficult or beyond the responsibility of the engineer.

RISK ASSESSMENT EXAMPLES

Two examples where MSE walls serve as part of the transportation infrastructure were considered for risk assessment. Site A is a two lane overpass and is a commuter artery for east and west bound traffic with the major employer in the area located 16.9 km southeast of an urban area. Site B is a US Interstate overpass with six lanes separated by a median. Each site is located in north Florida and FDOT publishes traffic data for each (FDOT, 2009). The economic consequence value used in the examples is the negative incremental consumer surplus (NICS) for an inelastic demand along with repair costs. NICS is a function of the cars per day which pass the specific location, a value travel time (VTT) based on typical values for local and interstate roads (US DOT, 1997), and the occupancy rate for the region. The estimated repair costs are per square meter of MSE wall and per kilometer of roadway (FDOT, 2010) as shown in Table 2, along with the other parameters described. The total cost value (NICS + Repairs) for each site is based on the number of traffic lanes out of service for 15 days following MSE wall failure.

Table 2. Economic consequence values for example sites (US$).

Site	Cars/day	VTT $/per./hr.	Occ. Rate Pers./car	Days	NICS ($mil)	$/m^2	$mil/km	Repairs ($mil)	Total Cost ($mil)
A	22,000	12.13	1.14	15	4.6	484	2.4	0.4	5
B	59,000	16.89	1.14	15	17	484	5.9	0.5	17.5

Maximum P_f values for sliding and bearing modes (equations 1 and 2) obtained in the Monte Carlo simulations are shown in Table 3. In a simulation, the property in each column was varied over a range while the other properties were held constant at the base model (values in parenthesis in Table 1). Each P_f was obtained from 4,000,000 realizations of CDR, the number required to ensure $CV_{Pf} < 10\%$. With the consequence values (total cost) given in Table 2, the risk specific to each parameter in Table 3 is calculated (P_f x consequence) and presented in Tables 4 and 5 in units of millions of US$.

Table 3. Results from probabilistic analysis on sliding and bearing stability.

	$\mu_{\phi fs}$	$CV_{\phi fs}$	$\mu_{\gamma fs}$	$CV_{\gamma fs}$	$\mu_{\phi rs/bf}$	$CV_{\phi rs/bf}$	$\mu_{\gamma rs/bf}$	$\mu_{\gamma rs/bf}$	$CV_{\gamma rs/bf}$
	20°	25%	15 kN/m^3	25%	20°	25%	15 kN/m^3	19 kN/m^3	25%
Sliding P_f	0.298	0.0121			0.134	0.0221	$3(10^{-5})$	$8(10^{-6})$	0.056
Bearing P_f	0.987	0.108	0.0014	0.0035	0.0026	0.001	$8(10^{-6})$	0.002	0.0018

Table 4. Specific risk values for Site A.

Site	Specific Risk ($mil)								
	$\mu_{\phi fs}$	$CV_{\phi fs}$	$\mu_{\gamma fs}$	$CV_{\gamma fs}$	$\mu_{\phi rs/bf}$	$CV_{\phi rs/bf}$	$\mu_{\gamma rs/bf}$	$\mu_{\gamma rs/bf}$	$CV_{\gamma rs/bf}$
Sliding	1.49	0.061			0.67	0.11	$1.5(10^{-4})$	$4(10^{-5})$	0.28
Bearing	4.94	0.54	0.007	0.018	0.013	0.005	$4(10^{-5})$	0.01	0.009

Based on the results of the risk assessment at the two sites, it is clear that bearing failure has the greatest risk (e.g., Total Risk at Site A: Sliding-Σ Specific Risk = $2.6 mil, Bearing-Σ Specific Risk = $5.5 mil; Total Risk at Site B: Sliding-Σ Specific Risk = $9.2 mil, Bearing-Σ Specific Risk = $19.4 mil). The risk is mostly associated with the low friction angle, ϕ, (20°) of the foundation soil. Its specific risk alone is greater than the total risk associated with sliding for each site. In the bearing

Table 5. Specific risk values for Site B.

Site	Specific Risk ($mil)								
	$\mu_{\phi fs}$	$CV_{\phi fs}$	$\mu_{\gamma fs}$	$CV_{\gamma fs}$	$\mu_{\phi rs/bf}$	$CV_{\phi rs/bf}$	$\mu_{\gamma rs/bf}$	$\mu_{\gamma rs/bf}$	$CV_{\gamma rs/bf}$
Sliding	5.22	0.212			2.35	0.39	$5.2(10^{-4})$	$1.4(10^{-4})$	0.98
Bearing	17.3	1.89	0.025	0.061	0.046	0.018	$1.4(10^{-4})$	0.035	0.032

capacity equation, the N_γ term is greatly influenced by small changes in ϕrather than by changes in the other terms. Therefore, based on this assessment, the designer should focus on modifying the foundation soil to ensure higher ϕ values. Additionally, the designer can identify where the cost lies and relay the results to persons in policy positions for decisions on what is acceptable in terms of cost.

CONCLUSION

This paper presented part of a larger study into the influence of variability in soil properties on the probability of failure of an MSE wall subject to sliding and bearing capacity. Comparison of experimental (centrifuge) and analytical capacity demand ratio (CDR) distributions, and probability of failures were presented for wall sliding.

To assist with assessment of acceptable probabilities of failure, two risk assessments of sliding and bearing at two typical overpass sections. It was discovered that the highest risk for both sites occurred for bearing capacity when the foundation soil was characterized with low friction angles. Both sites considered are

in urban settings and are arterial roadways for the region, one being an interstate overpass.

As geotechnical design moves towards estimating the probability of failure, through simulations techniques or analytical methods, the resistance factors suggested in codes like AASHTO LRFD can be evaluated for site to site variability characteristics. With a better understanding of the factored resistance in such a design, a more extensive risk assessment as presented in this paper can be performed. The justification for doing so lies in the cost comparison between construction of an MSE wall and the consequence of a catastrophic failure. Based on this work, designers can select an acceptable risk (in terms of dollars or lives) and address and adjust the P_f associated with a specific component of a system. Future work includes developing this design approach into nomographs that designers can use in risk assessments of common cases (i.e., traffic overpass) with similar consequence factors.

REFERENCES

AASHTO (2009). *AASHTO LRFDBridge Design Specifications(US Customary Units), Fourth Edition*, AASHTO, Washington, D.C.

Babu, G.L.S. and Basha, B.M. (2008). "Optimum design of cantilever retaining walls using target reliability approach." *International Journal of Geomechanics*, ASCE, 8(4), 240-252.

Chalermyanont, T. and Benson, C.H. (2005). "Reliability-based design for external stability of mechanically stabilized earth walls." *International Journal of Geomechanics*, ASCE, 5(3), 196-205.

Duncan, J.M. (2000). "Factors of safety and reliability in geotechnical engineering." *Journal of Geotechnical and Geoenvironmental Engineering*, ASCE, 126(4), 307-316.

FDOT (2009). *FDOT Florida Traffic Online*, http://www2.dot.state.fl.us/FloridaTrafficOnline/viewer.html

FDOT (2010). "Generic cost per mile models." http://www2.dot.state.fl.us/SpecificationsEstimates/costpermile.aspx

Fell, R. (1994). "Landslide risk assessment and acceptable risk." *Canadian Geotechnical Journal*, 31, 261-272.

Fenton, G.A. and Griffiths, D.V. (2008). *Risk Assessment in Geotechnical Engineering*, John Wiley and Sons, Hoboken, 461 pp.

Fenton, G.A., Griffiths, D.V. and Williams, M.B. (2005). "Reliability of traditional retaining wall design." *Geotechnique*, 55(1), 55-62.

Goh, A.T.C., Phoon, K.K. and Kulhawy, F.H. (2008). "Reliability analysis of partial safety factor method for cantilever retaining walls in granular soils." *Journal of Geotechnical and Geoenvironmental Engineering*, ASCE, 135(5), 616-622.

Klammler, H., Hatfield, K., McVay, M. and Guimarães de Luz, J.A. (2011). "Approximate up-scaling of geo-spatial variables applied to deep foundation design." *Georisk*, iFirst article, 1-10.

Lee, D.B. (2000). "Methods for evaluation of transportation projects in the USA." *Transport Policy*, 7(1), 41-50.

Liu, Z.Q., Huang, H.W. and Xue, Y.D. (2009). "The application of quantitative risk assessment in talus slope risk analysis." *Georisk*, 3(3), 155-163.

Paikowsky, S.G., Canniff, M.C., Lesny, K., Kisse, A., Amatya, S. and Muganga, R. (2010). *NCHRP Report 651-LRFD Design and Construction of Shallow Foundations for HighwayBridge Structures*, Transportation Research Board, Washington, D.C.

USACOE (2007). *Final Report of the Interagency Performance Evaluation Rask Force, Vol. VII-The Consequences*, USACE, Washington, D.C.

USDOT (1997). *The Value of Saving Travel Time: Departmental Guidance for Conducting Economic Evaluations*, Washington, D.C.

Zevgolis, I.E. and Bourdeau, P.L. (2006). "System reliability of cantilever retaining walls with correlated failure modes." *Proceedings*, Geocongress: geotechnical Engineering in the Information Technology Age, Atlanta, February 26 – March 1.

Zevgolis, I.E. and Bourdeau, P.L. (2008). "Probabilistic analysis of the external stability of MSE structures using MonteCarlo simulations." *Proceedings*, International Association for Computer Methods and Advances in Geomechanics, India, October 1-6.

(Sub)Global Rock Slope Stability: Using Rock Mass Indices to Characterize and Manage Rockfall Risk

Brian Bruckno, Ph.D. [1]

[1] Virginia Department of Transportation, Materials Section, 811 Commerce Rd., Staunton, VA 24401, (540) 480-5896, brian.bruckno@vdot.virginia.gov

ABSTRACT

Current approaches to rockfall risk mitigation are dominated by a model in which rockfall is treated as an event-triggered phenomenon. Methods emerging from this conceptualization are best applied to ideal slopes, where global slope stability is the only hazard being addressed. Such globally-stable slopes still present rockfall hazard due to complex structure, varying lithologies, or tectonic deformation. New data on rockfall patterns in the Virginia Valley and Ridge show that a significant component of rockfall is not triggered by discrete events, but depends heavily on the characteristics of the rock mass; each slope therefore exhibits a characteristic rockfall signal independent of the slope's global stability. Integrating both global and sub-global slope stability allows a more comprehensive, safer design philosophy for all types of rock slopes, lowering both hazard and risk. Common rock mass indices correlate well with rockfall hazard and allow the risk of unexpected rockfall to be minimized and protection methods to be optimized.

INTRODUCTION

The approach to mitigation of any hazard or risk necessarily follows from the conceptualization of the phenomenon; if the conceptualization is wrong, over-broad, or incomplete, it suggests that mitigation may have resulted in wasted resources, increased liability, or unnecessary risk. The model of rockfall illustrated in Figure 1, or a version of it, is pervasive within the geotechnical literature, and has become so well-known that it is often reproduced without attribution. This is a broad and simplified model which forces focus on global rock slope stability.

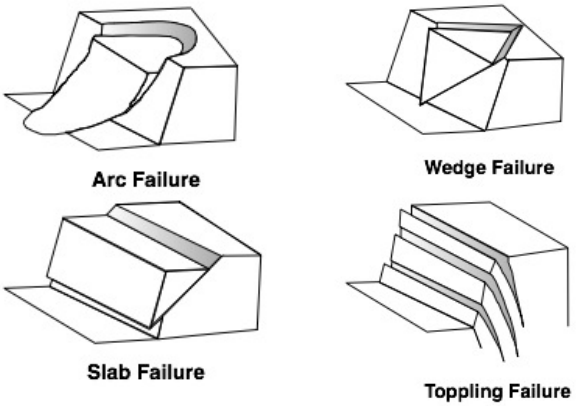

After Department of the Army, 1994

Figure 1. Conceptual model related to geomechanical conceptualization of rock slope stability

This model (after Department of Army, 1994), when combined with stereonet analysis, can be a very powerful tool in assessment of global slope stability and selection of remediation methods. Even in areas where the rock slopes are globally stable, however, significant risk of rockfall will still exist. These events, which consist of a small number of blocks detaching from a rock face, although generally smaller in magnitude than globally-controlled events, still present a clear risk to the traveling public and infrastructure. Even remarkably small rocks have considerable impact force. The rock which caused the damage in Figure 2 was approximately the size of a bowling ball. This small event was not associated with recent precipitation, occurred along a route considered globally stable, and can not be clearly associated with any of the styles of rock slope instabilities illustrated in Figure 1. It had the potential to cause great harm to the vehicle's occupants, who were fortunately not seriously injured.

Figure 2: Rockfall Hazard

To minimize the occurrence of such events, the significance of non-structurally controlled (non-global) rockfall must be understood. Recent work in rockfall hazard and risk mitigation has re-focused attention on the contribution of structural geology and lithology of the rock mass to these small but still dangerous rockfall patterns (Nicolson, D.T 2004, Vandewater et al. 2005). Recent observations in the Valley and Ridge of Virginia suggest that a structural approach to rockfall hazard may provide a better tool than older, mechanistic and hazard-rating approaches, which fail to take into account all levels of rockfall.

BLUE SKY ROCKFALL: ROCKFALL VERSUS RAINFALL

The association of rockfall with rainfall events has been exaggerated in the case of smaller, more frequent rockfall events. Any increase in pore fluid pressure or lowering of the friction angle along a sliding plane can trigger events; however, a large proportion of the volume shed from rock slopes occurs in discrete events not associated with rainfall or snowmelt. Figures 3 and 4 represent rainfall versus rockfall events for rock slopes at the Interstate 64 Afton Mountain pass and the US 259 Chimney Rock pass in Nelson and Rockingham Counties, Virginia, respectively. Neither figure shows a clear rockfall response to rainfall. While some rockfall events appear to coincide with the onset or peak intensity of rainfall, most events show no clear correlation with rainfall, either in the sense of immediate response or response after a time lag. Nor is there any clear variability with annual climatic cycles, either with the onset of freezing weather or during the spring snowmelt.

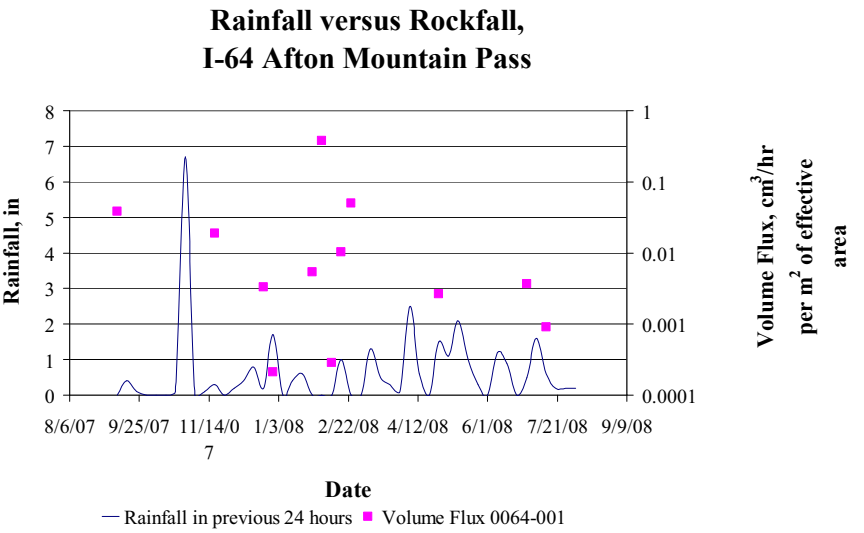

Figure 3. Rainfall versus Rockfall, I-64

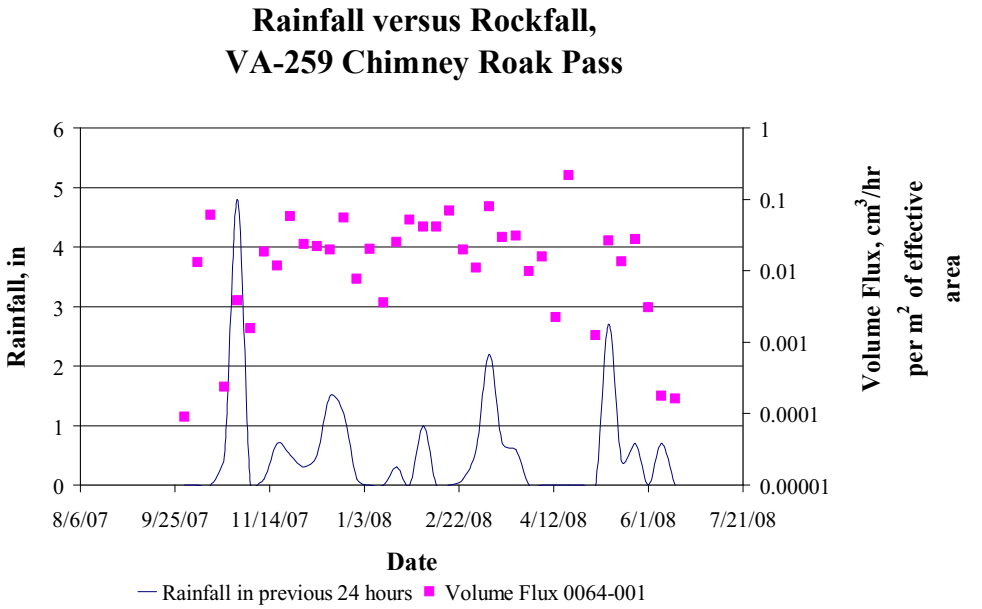

Figure 4. Rainfall versus Rockfall, VA-259

Nor does thermal expansion/contraction appear to have a great affect on rockfall. Figure 5 illustrates the relationship between the temperature swing during the 24-hour period immediately before recorded rockfall events, and the volume flux of those events.

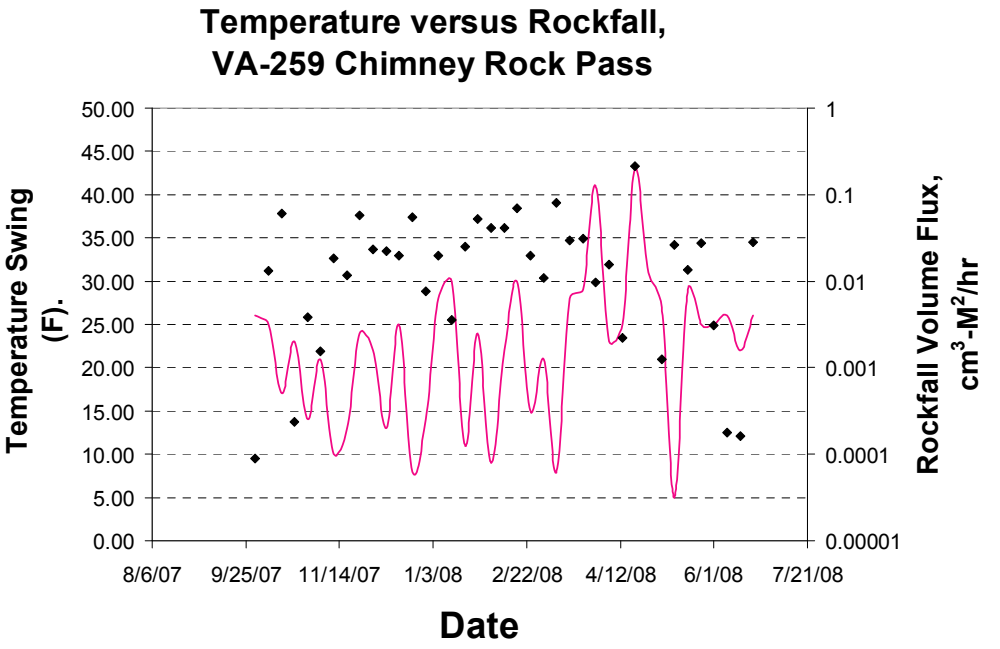

Figure 5. Rainfall versus temperature swing, VA-259

Nor does seismic energy correlate with rockfall events. The Valley and Ridge of Virginia is a tectonically quiescent region, far removed from the Central Virginia Seismic Zone. The United States Geological Survey National Earthquake Information Center records no earthquakes for the data-recording period reflected in Figures 3 and 4 (NEIC, 2010). The lack of triggering mechanisms gives these smaller rockfalls the appearance of coming "out of the clear, blue sky."

STRUCTURAL AND LITHOLOGICAL CORRELATIONS WITH OBSERVED ROCKFALL BEHAVIOR

Rockfall events below a certain energy threshold occurring in the absence of triggering mechanisms occurred in slopes of varying lithology, size, and slope aspect; the volume and energy-flux distributions of rockfall in all observed slopes appear to follow a self-organized distribution, which is also suggested by long-term studies of rockfall talus (Van Steijn, 2002). While every slope showed such a distribution, each showed a distinct rockfall signal within that distribution, as seen in Figures 3 and 4. Smaller, more frequent rockfall dominates the Chimney Rock slope, while the Afton slope is dominated by less frequent but much larger events. The rockfall pattern for Chimney Rock also shows a narrower range in the volume of the individual rockfalls. This behavior is characterized by the V_{90}: The cumulative volume of the 90^{th}-percentile block size related to the cumulative volume of all rockfall measured over the entire collection period. The V_{90} of Afton is 30%, while the V_{90} of Chimney rock is 19%. The contribution of the impact energy of the single largest block to the total energy released from the slope during the analysis period is even more pronounced. In the case of Chimney Rock, the single largest block represented an impact energy at the toe of the slope of 14% of the total impact energy during the analysis period; the corresponding value for Afton is 73%. Because the risk of a slope is controlled by the peak impact energy (i.e., the largest single clast represents the greatest impact force and the greatest rollout distance), lithology and structure assume a disproportionate importance with regard to risk. The V_{90} therefore characterizes the risk – i.e., likelihood of high-energy impacts – of any slope.

The V_{90} correlates to the lithology and structure of the slopes: Chimney Rock consists of a moderately hard, moderately widely-jointed sandstone, while Afton consists to a tenacious, widely-jointly greenschist. Because weaker slopes tend to shed more volume in the form of frequent, smaller-sized rockfalls, while stronger lithologies will shed less volume in the form of larger blocks (which resist further breakup during the fall or impact), understanding the correlation of the rock mass quality to rockfall patterns suggests a useful tool in rockfall management. Unfortunately, while the V_{90} is a useful tool in characterizing the risk posed by a rock slope, it is difficult to measure directly. Although is can be estimated from the size-distribution of clasts in undisturbed talus piles, it is easier to use commonly accepted rock mass qualities as proxies for the V_{90}, and therefore as proxies for sub-global rockfall risk.

Numerous methods of measuring overall rock mass quality have been proposed. Three of the most widely-accepted are the Rock Mass Rating System (RMR), the Norwegian Geotechnical Institute's Q-System (Q), and the Geological

Strength Index (GSI). All three systems take into account the structural characteristics of the rock mass, particularly block size, degree of tectonic deformation, and the quality, number, and orientation of the joint sets, with higher values reflecting better rock mass quality (Barton 1974; Bieniawski 1974, 1989; Hoek et al., 1998, Marinos et al. 2005).

Figures 6 relates the V_{90} to the RMR, Q, and GSI of 5 slopes in the Valley and Ridge of Virginia varying in lithology and structural characteristics.

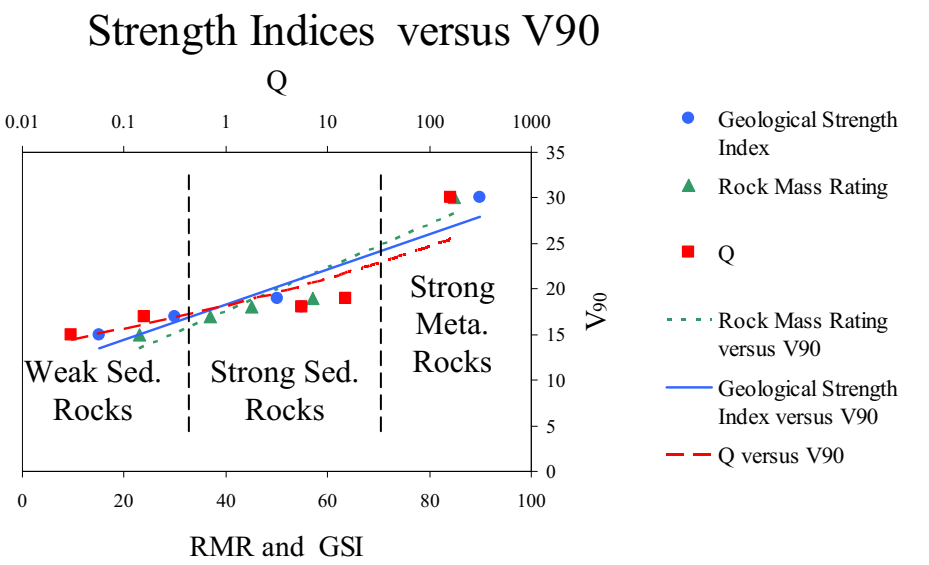

Figure 6. V_{90} and strength indices versus structural and lithological characteristics

The strength indices correlate well with lithology and observed rockfall behavior. Measurements of rockfall volume and energy during 2007-2009 in the Valley and Ridge of Virginia fell into three broad areas: weak sedimentary rock masses, strong sedimentary rock masses, and strong metamorphic rock masses (igneous cliff-forming formations are rare in the Valley). Weak rock masses tend to exhibit frequent rockfalls, but the weakness of the rock ensures that the falls are small in both volume and energy. Strong metamorphic rock tends to exhibit very infrequent rockfall, but the fact that more of the fall occurs in the form of a small number of large blocks makes the fall more energetic and dramatically raises risk. The "Hockey Stick" shape of the relationship at higher index values suggests that all of the indices under-estimate the risk of the strongest slopes and have the potential for infrequent but very high-energy events. The magnitude of these so-called "Heavy-Tail events" is a characteristic of phenomena that display a self-organized pattern, such as earthquakes and forest fires (Turcotte et al., 2002). Phenomena which have strong heavy-tail behavior are among the most damaging. Strong sedimentary rock masses appear to offer the most troublesome combination of hazard and risk, because they combine the characteristics of weak sedimentary and strong metamorphic rocks: the falls are more frequent than those occurring in stronger masses, but the strength of the rock allows falls to consist of relatively large rocks, raising both hazard and risk.

CONCLUSION

Over a large enough sample area, most rock slopes will fail in a variety of manners. In areas of differing structure (i.e., along fold limbs), across contacts or terrain boundaries, or within fault zones, the same formation or lithology may exhibit markedly different structural characteristics, and therefore may fail in a number of different manners and exhibit greatly different risk. Some areas of a rock slope may be susceptible to triggering events, while others may fail at a rate controlled by the structure and be relatively insensitive to weather. Focusing solely on the role of triggering events and focusing analysis and remediation efforts on those areas susceptible to them may therefore cause neglect of areas that fail lacking triggers: observations in the Valley and Ridge of Virginia illustrate that even globally-safe (Factor of Safety greater than 1.5), remediated slopes still shed rock at a characteristic rate, and that these events can be pose significant risk. In practice, this leads to the inability to predict rockfall unless practitioners pay more attention to the structural geology and lithology of the rock mass. Strength indices such as RMR, Q, and GSI are easy to apply with field observations or minor laboratory data and characterize the rock mass well. Designers can not ignore the need to assess all slopes for global stability and perform remediation by standard methods; but further characterizing the remaining rock slope by use of a rock mass strength index allows protection methods to be tailored to the level of risk tolerable, particularly as that risk develops due to the slope's characteristic response to unloading and weathering. Slopes exhibiting low-frequency, high-risk behavior, such as high strength slopes, will require high-energy absorbing devices (such as rockfall or debris-flow fences), while slopes exhibiting higher-frequency, lower-risk behavior will require remediation methods tailored to greater volume but lower energy events (such as rock mesh drape). We return to the conceptualization of the phenomenon: rather than seeing rockfall as a series of events triggered by rainfall, freeze-thaw, root wedging, or seismic energy, and which can be avoided by managing the response to these events, rockfall should be seen as a characteristic, continuous signal unique to each slope. Rock mass strength properties can place that signal into one of a small number of broad families of behavior, which allows rockfall management that maximizes safety and minimizes risk. Particularly when implemented early in the design process, this can function as a screening tool to narrow the range of possible protection measures and include their construction in budgeting and right-or-way acquisition.

REFERENCES

Barton, N.R., Lien, R. and Lunde, J. (1974) "Engineering classification of rock masses for the design of tunnel support." *Rock Mechanics*, 6(4), 189-239.

Bieniawski, Z.T. (1974) "Engineering classification of jointed rock masses." *Transactions of the South African Institute of Civil Engineers*, 335-344.Bieniawski, Z.T. (1989) "Engineering rock mass classifications." Wiley, New York, 251 p.

Department of the Army (1994) Rock Foundations, U.S. Army Corps of Engineers Field Manual 5-410, 337 p.

Hoek E., Marinos, P. and Benissi, B. (1998) "Applicability of the geological strength index (GSI) classification for very weak and sheared rockmasses. The case of the Athens Schist Formation." *Bulletin of Engineering Geology and the Environment*, 57, 151–160

Marinos, V., Marinos, P., and Hoek, E. (2005) "The geological strength index: applications and limitations." *Bulletin of Engineering Geology and the Environment*, 64, 55–65

National Earthquake Information Center (NEIC) Downloaded October 2010, http://geohazards.usgs.gov/eqprob/2009/index.php

Nicolson, D.T. (2004) "Hazard assessment for progressive, weathering-related breakdown of excavated rockslopes." *Quarterly Journal of Engineering Geology and Hydrogeology*, 37, 327-346

Turcotte, D.L., Malamud, B.D., Guzetti, F., and Reichenback, P.C. (2002) "Self-organization, the cascade model, and natural hazards." *Proceedings of the Natural Academy of Sciences*, 99, (1), 2530-2637

Vandewater, C.J., Dunne, W.M., Maulton, M., Drumm, E.C., and Bateman, V. (2005) "Classifying and Assessing the Geologic Contribution to Rockfall Hazard." *Environmental & Engineering Geoscience*, 11(2), 141-154

Van Steijn, H. (2002) "Long-term landform evolution: evidence from talus studies." *Earth Surfaces Processes and Landforms*, 27, 1189-1199

Evaluation of the susceptibility of landslides and debris flows on Costa Rica's national road network: Analysis of a segment of the National Route 32

Diego A. Cordero Carballo[1]

[1]Laboratorio Nacional de Materiales y Modelos Estructurales (LanammeUCR), Universidad de Costa Rica, P.O. Box 11501-2060, San José, Costa Rica; PH (506) 2511-4011; FAX (506) 2511-4442; email: diego.cordero@ucr.ac.cr

ABSTRACT

Costa Rica's National Route 32 has historically been exposed to landslides and other geohazards since the day it opened in 1987, being one of the country's most vulnerable roads and with a very high socio economic impact when closed to traffic.

The susceptibility of landslides in cut slopes and debris flows in a critical segment of 30 kilometers of the National Route 32 was evaluated by LanammeUCR through methodologies that allowed determining that this segment presents a median to very high susceptibility to landslides and that almost 50% of the watersheds crossed by this critical segment present a high susceptibility to debris flows, with the associated impact on drainage structures such as culverts. LanammeUCR applied the critical angle method along the analyzed section in order to identify other locations susceptible to landslides. The model used to analyze the susceptibility to landslides was calibrated with historical data, confirming that landslides have occurred in recurrent sites, an aspect that will require special attention for the planning and execution of the possible solutions.

INTRODUCTION

Costa Rica's National Route 32, with a length of 160 kilometers, has historically been exposed to landslides and other geohazards since the day it opened in 1987, being one of the country's most vulnerable roads and with a very high socio economic impact when closed to traffic.

The route, also known as the Braulio Carrillo highway since it crosses the homonym National Park, links Costa Rica's central valley with the Atlantic coast. It starts in the capital city, San José, crosses the country central volcanic range, with a maximum altitude of 1530 meters above sea level, and ends in the Atlantic plains of Costa Rica, at sea level.

Since the route crosses a national park, the solutions to manage the geohazards, such as landslides and debris flows, must be very well conceptualized, designed and executed, and must have a minimal ecological impact on the environment during the construction and maintenance phases. So far, few actions have been taken and landslides and rock falls have occurred frequently affecting the communications between San José and the Atlantic coast.

The route possesses very high economical importance for Costa Rica, since it conveys almost 75% of the total volume of transport of goods through the country's ports: Limón and Moín. In addition, the route is the road to many tourist sites on the Atlantic coast of Costa Rica.

The susceptibility of landslides in cut slopes and debris flows in a critical segment of 30 kilometers of the National Route 32 (See Figure 1) was evaluated by the Unidad de Evaluación de la Red Vial Nacional (National Road Network Evaluation Unit) of the Laboratorio Nacional de Materiales y Modelos Estructurales (LanammeUCR, National Laboratory of Materials and Structural Models) of the Universidad de Costa Rica (UCR, University of Costa Rica) through methodologies that allowed determining that this segment presents a median to very high susceptibility to landslides and that almost 50% of the watersheds crossed by this critical segment present a high susceptibility to debris flows, with the associated impact on drainage structures such as culverts. LanammeUCR applied the critical angle method, developed by Vargas and Garro (2006) along the analyzed section in order to identify other locations susceptible to landslides. The model used to analyze the susceptibility to landslides was calibrated with historical data, confirming that landslides have occurred in recurrent sites, an aspect that will require special attention for the planning and execution of the possible solutions.

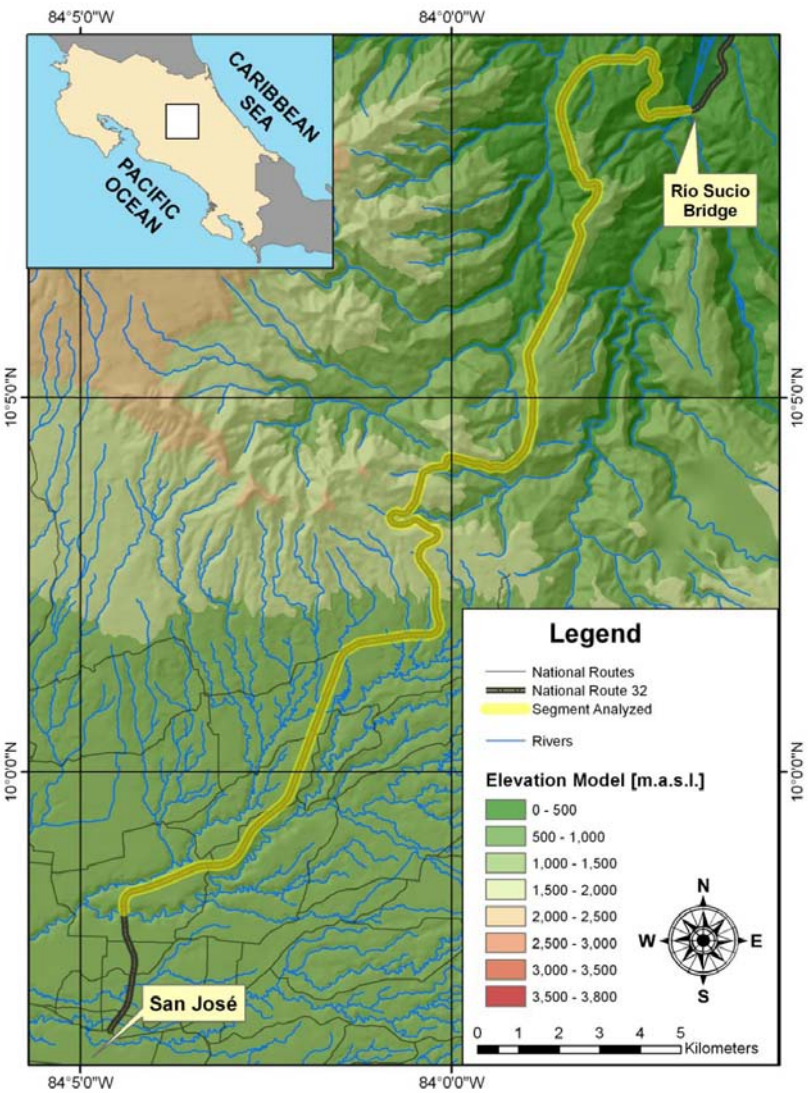

Figure 1. Digital elevation model of the zone considered in the study.

The decision making process towards the most feasible solution for reducing the vulnerability of the route infrastructure and mitigating the potential risk to users is currently under discussion in Costa Rica.

CLIMATOLOGICAL SETTINGS

From a climatologically point of view, the route is under the influence of a very humid regime, with maximum average temperatures of 30°C on the low altitude segments, and minimum average temperatures of 15°C on its highest points. On the mountain section minimum, temperatures of 8°C have been registered.

Annual precipitation varies from 2000 mm to 4500 mm. The average climate of the zone combined with this high precipitation results in a very high humidity, which together with the topographic and lithological conditions makes this route prone to landslides and debris flows.

TOPOGRAPHICAL, GEOLOGICAL AND GEOTECHNICAL SETTINGS

The segment of the National Road under analysis begins at the Pk. 0+000 in the north side of Costa Rica's capital city, San José, and ends at the Pk. 37+500, in the intersection between the National Route 32 with the Sucio River.

The topographic conditions of the segment are typical of a mountain road, with an elevation of 1136 m a.s.l. at Pk. 0+000, 1530 m a.s.l. at Pk. 20+000 and 500 m a.s.l. at Pk. 40+000.

The mountain area is geologically young and in active process of dissection by natural erosion. It is composed entirely of volcanic deposits, lavas, lahars and small pyroclastic rocks, mainly andesites, and to a lesser degree, basalt. Locally, rhyodacitic pumice deposits can be found. All the material is of Quaternary origin and subject to new ash deposits from the active volcanoes Irazu and Turrialba. These rocks vary in strength and degree of weathering, from very strong old lavas to weak recent pyroclastic deposits. On deposition surfaces on steep slopes, especially at high and medium elevations, materials tend to be lightly weathered lavas and intrusive rocks, exposed due to the erosion of ash and pyroclastic deposits. In such places, soils are shallow but resistant to sheet erosion when they are protected by the original forest vegetation.

These peculiarities of geological origin exert a marked control on the pattern of dissection and natural erosion that give this region its special slope and geomorphology characteristics. Given the intense runoff from heavy rains in this area, and the short distance between the upper headwaters of the basin and the Atlantic plain, a very dense drainage network with steep slopes has developed.

From a geotechnical perspective, the analyzed segment spans a wide range of lithological conditions. Table 1 summarizes these conditions classified by homogeneous sections.

Table 1. Basic lithological description of the analyzed segment.

Pk.	Lithological description
0+000 to 2+950	Volcanic ashes. Slope heights of less than 10 meters and inclinations of 45 to 60° with herbaceous vegetation. No instability problems have been detected, and due to the vegetation cover the susceptibility to erosion is very low.
2+950 to 3+200	Bridge structure. The conditions of the bridge foundation are not covered in this paper.
3+200 to 9+500	Pumice tuff and weakly welded ignimbrite with tephras consisting of ashes, lapilli and blocks of fine slag that locally form tuffaceous agglomerates.
9+500 to 10+900	Ashes, unconsolidated lahars and tuff. Slope height varies from 5 to 6 meters and inclinations from 40° to 45° with herbaceous vegetation. This section presents signs of instability with landslides affecting the total height of the slopes, creeps and erosion processes.
10+900 to 12+000	Colluvial materials with cuts heights lower than 2 meters.
12+000 to 16+750	Ashes, unconsolidated lahars and tuff. Slope heights lower than 15 meters and inclinations between 65° and 90°. Numerous evidences of shallow instabilities, with rock falls and loss of vegetation, increasing the susceptibility to erosion. The soil presents a very low shear strength and high plasticity. Creep processes observed on natural slopes.
16+750 to 37+500	National Park Braulio Carrillo. This section runs next to slopes on a very rugged terrain with natural and man-induced instability processes.

SUSCEPTIBILITY TO LANDSLIDES

Landslides have occurred on the National Route 32 since the day it was open to public. Madrigal (1997) collected historical information on landslides along this route from 1987 to 1997. He identified about 40 landslide locations, some of them with more than one occurrence where ground movements are still registered at present. These landslides are concentrated on the section from Pk. 10+000 to Pk. 38+000. Since the day the route was opened, landslides and debris flows have been reported (the route was open on March 28th, 1987 and the first landslide was reported four days later, on April 1st).

The critical angle approach (Vargas and Garro, 2006) permits zoning an area with influence over a road, by linking the type of geology of a zone, the slope of the terrain and a database of landslides occurred in the past. Although there are other factors that control susceptibility and triggering, their influence is considered minor on areas of limited size by the critical angle approach. One of these factors is precipitation, which is strongly connected to soil moisture. Even when short term maxima of extreme precipitation controls triggering conditions, the precipitation factor is considered in the landslide database, since it records events happened under different conditions of soil moisture.

The methodology to analyze the susceptibility of cut and fill slopes on mountain roads consists on determining a regional average angle of unstable slopes per geologic unit in areas that directly affect the road, and then classify each geology unit by ranges to assign levels of susceptibility, as shown in Figure 2.

The model used to analyze the susceptibility to landslides was calibrated with historical data, confirming that landslides have occurred in recurrent sites, an aspect that will require special attention for the planning and execution of the possible solutions.

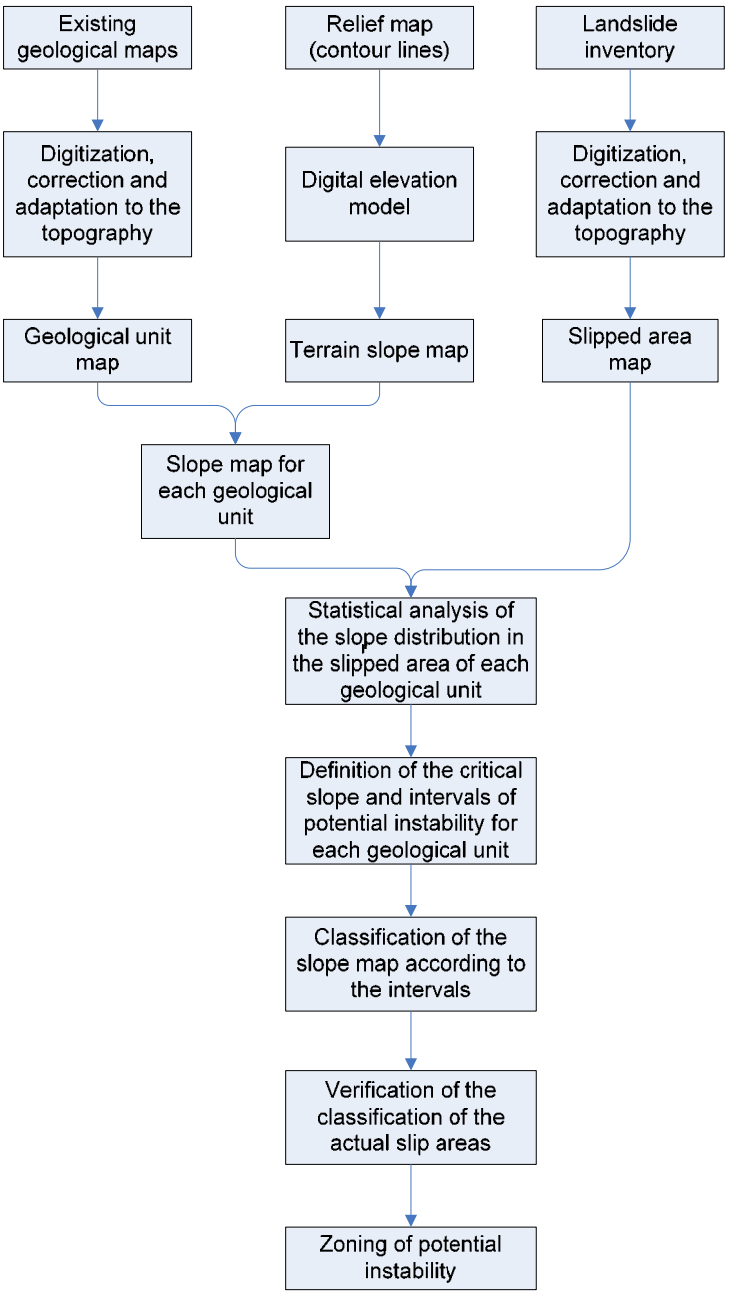

Figure 2. Critical angle methodology for zoning areas with potential instability. (Navarro, 2004).

SUSCEPTIBILITY TO DEBRIS FLOWS

For the evaluation of the susceptibility to debris flows the methodology proposed by Kanji (2001) was used. This method considers the combination of several factors that contribute to the occurrence of such phenomenon.

The factors that intervene are: rainfall intensity (R) as the main triggering factor, therefore is assigned with the largest weight; slope inclination (S) at the source area; the inclination of the drainage channels or river beds where sediments can be eroded; the catchment area (A);height of hillsides (H), which there is associated to the potential energy; geoindicators (G) that represent the geology conditions of the area, indicating the erodibility for the generation of debris flows; and the vegetation and soil use (V), which corresponds to the percentage of the area occupied and deforested, exposing the soil to the external dynamics.

Each of the factors previously mentioned are divided in classes (C) and attribute intervals (R1…R4, S1…S4, etc.), each one corresponding to a partial grade (GP) being the maximum a value of 10 for the most critical class for debris flow generation, and 0 for the least critical.

The final grade (FG) can vary from 0 to 100 and it is obtained by adding the product of multiplying the partial grades for their respective weights, P, which vary from 0.5 to 3.

$$FG = \sum(GP * P) \qquad (1)$$

The final grades can be assigned to a level of susceptibility as shown in Table 2. Figure 3 shows the methodology followed to analyze the susceptibility to debris flows.

Table 2. Relationship between final grade and susceptibility level.

Final grade	Susceptibility
80-100	Very high
60-80	High
40-60	Medium
20-40	Low
0-20	Very low

The analyzed segment of the national route 32 is affected by 7 major catchments, with areas that vary from 0.24 km^2 to 2.75 km^2. The main factors, as per Kanji's methodology, that affect this segment are the rainfall intensity and the geological conditions. By applying Kanji's methodology, it was identified that the catchment areas with affectation on the road present a medium to high susceptibility to debris flow. A parallel analysis using the methodology proposed by Rodríguez (1989) identified that the drainage structures linked to these catchment areas present a high to very high vulnerability from a hydraulical point of view.

The combination of these conditions makes the drainage structures, such as culverts and storm water drainage systems, very vulnerable. If failure occurs, they will have a direct impact on the road embankments and consequently on traffic.

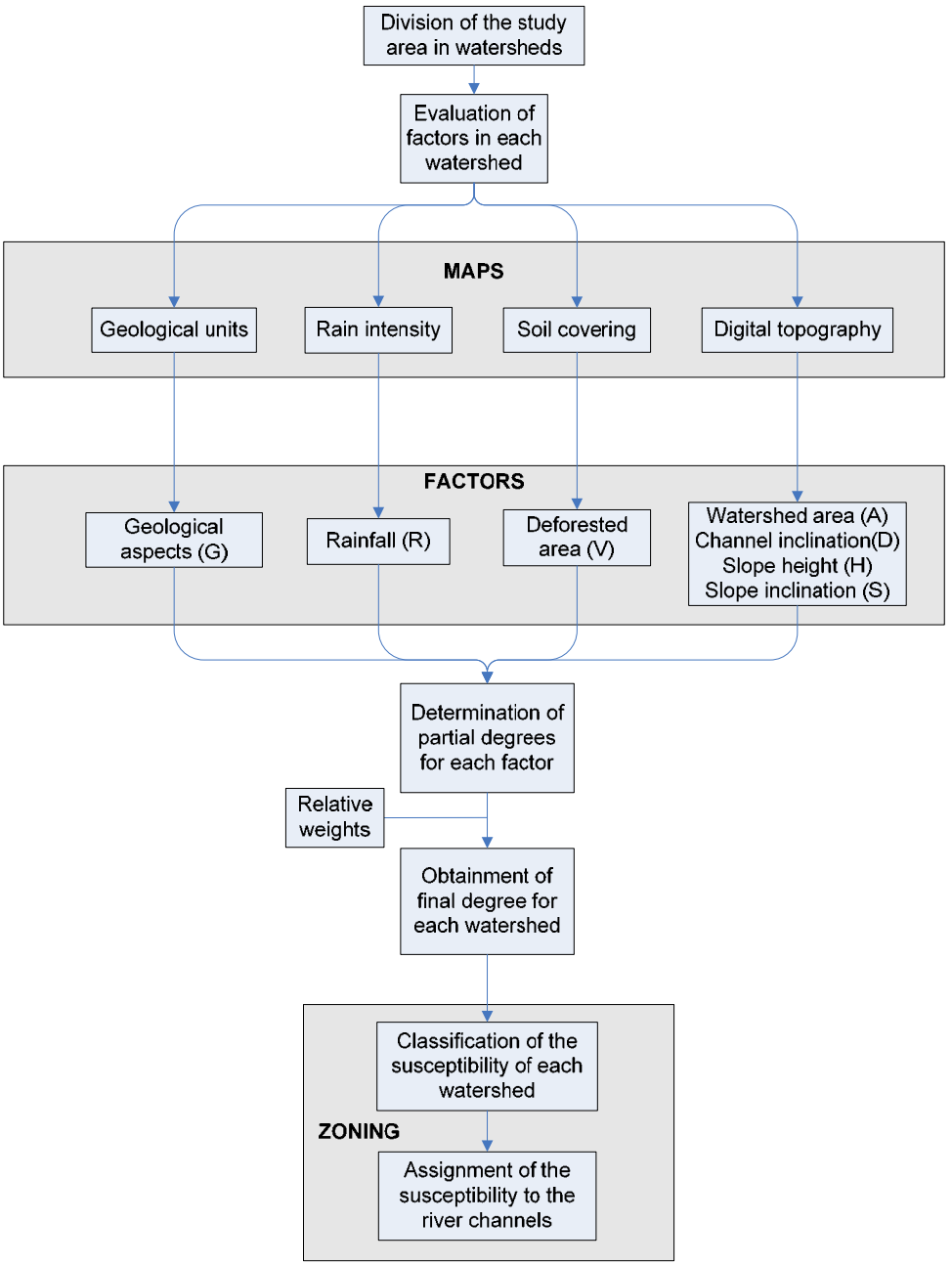

Figure 3. Kanji's methodology for zoning potential debris flows. (Castro, 2005; after Kanji, 2001)

POSSIBLE SOLUTIONS

As mentioned above the segment under analysis crosses a national park, which imposes that the type of interventions must have the least impact on the

environment. The solution so far has been to let nature do its work and let the slopes stabilize themselves.

This conception of solution is wrong and lacks of any engineering basis. In the past two rainy seasons, the problem has worsened since rainfall intensity has increased due to climate anomalies caused mainly by La Niña (Instituto Meteorológico Nacional, 2010) and there is a social, political and economical pressure to keep the road open during all year.

Cut-and-cover tunnels emerge as an alternative to solve the affectation of the route, with a minimum impact on the environment, since they would be built over the footprint of the existing road. Nonetheless, they do not solve the problems of potential landslides that can be produced, especially on the cut slopes on the original location of the route.

In addition, the high susceptibility to debris flow on the watersheds affecting the road requires revising the hydraulic structures that in a parallel evaluation (Cordero, Sanabria, Garro, Vargas & Barrantes, 2009) showed evidence of very high vulnerability regarding their hydraulic capacity.

CONCLUSIONS

The National Route 32 has presented landslide problems almost since the day it was open to the public, with the associated risk to the users and the economical impact this has had on Costa Rica economy.

The solution to this problem goes far beyond the best technical solution geotechnical engineering can provide, since as the critical segment crosses a national park, the solution must have the least environmental impact during the construction and service stages.

Considering the strict environmental protection policies of the Costa Rican government, these problems should be addressed making a balance between the environmental impact of the solutions and acceptable levels of risk for users of this route, which in the recent past has claimed human lives.

Cut-and-cover tunnels emerge as one of the most viable alternatives to solve the affectation landslides have on the route, since they would be built over the location of the existing road and will not require any earthworks or construction on the forest adjacent to the road.

To control potential debris flows, construction such as channels and levees should be undertaken on the channels of rivers and streams upstream the intersections with the route; nonetheless, since this would have a direct impact on the environment, this solution does not seem to be considered for the near future.

The decision making process towards the most viable and feasible solution to reduce the vulnerability of the route infrastructure and mitigate the potential risk to users is under discussion in Costa Rica.

REFERENCES

Castro, K. (2005). *Vulnerabilidad física de la infraestructura vial en las rutas 130, 712, 146, 120 y 126 tramo Alajuela-Fraijanes-Vara Blanca-San Miguel de Sarapiquí.* Informe de proyecto de graduación para obtener el grado de

Licenciado en Ingeniería Civil. San José, Costa Rica: Escuela de Ingeniería Civil, Universidad de Costa Rica.

Cordero, D., Sanabria, J., Garro, J., Vargas, W. & Barrantes, R. (2009). *Evaluación de la vulnerabilidad ante amenazas naturales, Ruta Nacional 32, tramo San José-Río Sucio.* Laboratorio Nacional de Materiales y Modelos Estructurales, Universidad de Costa Rica, San José, Costa Rica.

Denyer, P., Arias, O., Soto, G., Obando, L. and Salazar, G. (1993). *Mapa geológico de la Gran Área Metropolitana.* Escuela de Geología, Universidad de Costa Rica, San José, Costa Rica.

Denyer, P. and Kussmaul, S. (1994). *Atlas Geológico Gran Área Metropolitana.* Editorial Tecnológica de Costa Rica, Cartago, Costa Rica.

Instituto Meteorológico Nacional. (2010). *Boletín meteorológico mensual diciembre 2010.* San José, Costa Rica: the author.

Kanji, M. (2001). *Metodología para estimar la vulnerabilidad del terreno con relación a flujo de detritos.* 1er Simposio Internacional de Movimientos en Masa. Ecuador.

Navarro, E. (2004). *Susceptibilidad ante amenazas naturales de la subcuenca del río General, Pérez Zeledón, Costa Rica.* Informe de proyecto de graduación para obtener el grado de Licenciado en Ingeniería Civil. San José, Costa Rica: Escuela de Ingeniería Civil, Universidad de Costa Rica.

Orozco, E. (2007). *Zonificación climática de Costa Rica para la Gestión de Infraestructura Vial.* Informe de proyecto de graduación para obtener el grado de Licenciado en Ingeniería Civil. San José, Costa Rica: Escuela de Ingeniería Civil, Universidad de Costa Rica.

Rodríguez, E. (1989). *Revisión de métodos de diseño hidrológico e hidráulico de alcantarillas para carreteras.* Informe final de proyecto de graduación para optar por el grado de Licenciado en Ingeniería Civil. San José, Costa Rica. Escuela de Ingeniería Civil, Universidad de Costa Rica.

Vargas, L. (2002). *Sistemas de alerta para la prevención de deslizamientos por lluvia.* Tesis sometida a la consideración del Programa de Estudios de Posgrado en Ingeniería Civil para optar al grado de Magister Scientiae. Costa Rica: Programa de Estudios de Posgrado, Universidad de Costa Rica.

Vargas, W. & Garro, J. (2006). *El ángulo critico de la pendiente y la susceptibilidad a deslizamientos de laderas naturales.* IX Seminario Nacional de Geotecnia. Costa Rica: Asociación Costarricense de Geotecnia.

Spatial Prediction of Groundwater Depth to Trigger Liquefaction in St. Louis

Jae-Won Chung[1] and J. David Rogers, P.E., M.ASCE[2]

[1] Postdoctoral Fellow, Dept. of Geological Sciences and Engineering, Missouri Univ. of Science and Technology, Rolla, MO 65409, jc8r4@mst.edu
[2] K.F. Hasselmann Chair in Geological Engineering, Dept. of Geological Sciences and Engineering, Missouri Univ. of Science and Technology, Rolla, MO 65409 (corresponding author), rogersda@mst.edu

ABSTRACT

When the liquefaction potential of a mapped stratigraphic unit is statistically averaged and assessed spatially, uncertainties associated with groundwater levels are pervasive, due to natural variability in the landscape models, the variations in groundwater depth over time and space, measurement errors, and term vagueness in boring logs. Instead of assessing liquefaction potential assuming an unchanging groundwater level, this study sought to predict and contour the threshold depth-to-groundwater to trigger severe liquefaction in the St. Louis for an assumed M7.5 earthquake emanating from the New Madrid Seismic Zone. The simplified SPT-based procedure and scenario PGA of 0.20g were applied to evaluate the groundwater depth that would exceed a Liquefaction Potential Index of 15. This study revealed that alluvium lying with deeper bedrock surfaces and deeper threshold water depths were both more prone to liquefaction than loess/till deposits, because of their greater thickness and tendency to remain saturated, year-round.

INTRODUCTION

Liquefaction is a soil failure mechanism that occurs when the pore water pressure in cohesionless soils rises to a level that equals or exceeds the effective confining stress acting upon them, causing them to lose shear strength and temporarily behave as a fluid. Liquefaction hazards are traditionally assessed using geodata, such as historic liquefaction features, knowledge of surficial geologic units of late Quaternary or Holocene age, physical properties of the sediments, depth to groundwater, and/or regional scenario earthquakes. Regional liquefaction hazard maps provide geotechnical engineers and developers with an indication of the severity or probability of liquefaction hazard that can be useful for hazard mapping by delineating those zones where site-specific liquefaction hazard assessments may be prudent, or even required (as is the practice in California). These hazard maps present the relative liquefaction susceptibility of the geologic units or liquefaction potential associated with estimated earthquake shaking hazards.

Recently, the liquefaction potential index (LPI; Iwasaki et al., 1978 and 1982) of the soil column in discrete boreholes have been increasingly applied to evaluate liquefaction risk for earthquake scenario maps, and to characterize the spatial

variability of the liquefaction potential of youthful geologic units, such as terrace deposits, alluvium, and artificial fills; the lower the index, the less the potential for liquefaction-induced ground failure. LPI allows the prediction of the severity of liquefaction-induced ground failure by considering the entire soil column, not just the surficial cover, which is what is portrayed on most soil survey and geologic maps.

Statement of Problem. The depth to the groundwater table is a significant factor for LPI-based hazard mapping because liquefaction occurs in saturated soils, and the thickness of liquefiable layer only affects the value of LPI; the LPI is inversely proportional to the factor of safety (FS), and the depth of the groundwater (Holzer, 2008; Chung and Rogers, 2011).

The absence of confidence in depth-to-groundwater is pervasive, due to term vagueness, natural variability over time and space, and/or measurement errors (Aldrich and Lambrechts, 1986; Elith et al., 2002; Snyder, 2008). The groundwater table is defined as the upper surface of a saturated zone in an unconfined aquifer. This definition excludes partially or isolated saturated zones such as capillary fringe water, confined water, or perched water (Bates and Jackson, 1987; Snyder, 2008), but they may often be included, loosely (Aldrich and Lambrechts, 1986). Absent groundwater instrumentation, most geotechnical practitioners also ignore semi-confined aquifers, which are actually quite common in geologically youthful flood plains (e.g. a pervious sandy gravel channel covered by low permeability silts and clays). Water level fluctuations depend on the quantity and timing of precipitation, which can occur on time scales ranging from hours to years, depending in changes in climate or land use (Snyder, 2008). Spatial sampling bias is probably the greatest single problem, creating a paucity of converging population sizes (e.g., borings are preferentially situated along highways or major construction sites, not spatially dispersed across large areas). Measurement errors include not only imperfections in measuring techniques and equipment, but also multiple observations with different depths to groundwater (Chung and Rogers, 2010).

Objectives. The main goal of this study was to predict the threshold depth-to-groundwater that would trigger severe liquefaction (LPI>15) in an attempt to overcome the data uncertainty associated with ground level, which leads to erroneous LPI estimates. This study employed the standard penetration test (SPT)-based LPI method using a M7.5 scenario earthquake with peak ground accelerations (PGA) values of 0.20g in St. Louis, where historic liquefaction features have been documented (Tuttle et al., 1999; Tuttle, 2005) in Quaternary and Holocene age alluvial deposits.

METHODOLOGY

Data. Liquefaction analyses were performed using 1080 SPT profiles obtained from the Missouri and Illinois State Geological Surveys (MoDGLS and ISGS), U.S. Geological Survey (USGS), and private sector consultants. This study included all of the available SPT profiles, whether they reported groundwater levels or did not (e.g. some boring logs only note the depth of water “at time of drilling”). The surficial

geologic map in this study was compiled from ISGS and USGS. Figure 1 shows the SPT data locations and the surficial geology in the St. Louis area, in Missouri and Illinois.

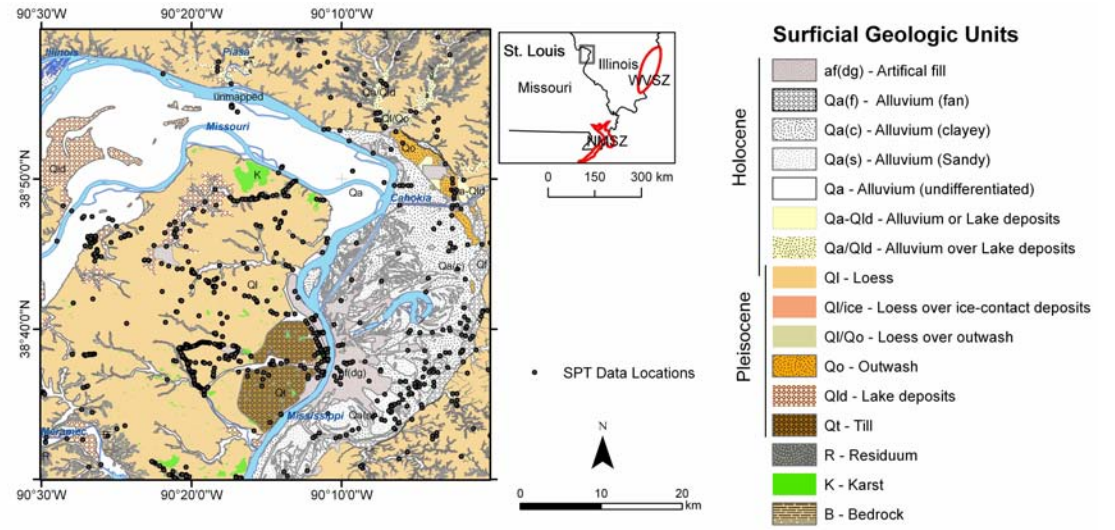

Figure 1. Locations of SPT Data on Surficial Geologic Map of the St. Louis

Scenario Earthquake. The possible seismic sources for St. Louis are the New Madrid Seismic Zone (NMSZ), which generated > M7 events in 1811-1812, and the Wabash Valley Seismic Zone (WVSZ), not recognized until 1999. A scenario earthquake with a PGA was employed to evaluate the LPI exceeding value of 15. Based on the 2008 National Seismic Hazard Map (Petersen et. al., 2008) and St. Louis scenario earthquake (Toro and Silva, 2001), a M7.5 earthquake emanating from these seismic zones with a PGA of 0.20 g was selected as the moderate possible condition for ground shaking.

Liquefaction Potential Index (LPI). The LPI was originally proposed by Iwasaki et al. (1978 and 1982). Iwasaki et al. (1982) validated their SPT-based LPI values by comparing them to historic features at liquefied sites and non-liquefied sites. Its risk criteria correlate well with liquefaction case histories (Iwasaki et al., 1982; Toprak and Holzer, 2003). The LPI defined by Iwasaki et al. (1978 and 1982) can be expressed as follows;

$$LPI = \int_o^{20} F(z) \cdot w(z)\, dz$$

where z = depth (0~20m), dz = the differential increment of depth, $F(z)$ = severity; and $w(z)$ = weight function (= 10-0.5z). Severity is defined as

$$F = 1 - FS \quad for\ FS \le 1.0$$
$$F = 0 \quad for\ FS > 1.0$$

where FS = factor of safety. A weighting function gives more value to the layers closest to the ground surface, and decreases linearly to zero, at a depth of 20m. Iwasaki et al. (1982) suggested that none to minor or severe liquefaction effects are likely to occur whenever the LPI less than 5 or the LPI greater than 15, respectively.

Correction of SPT-N Values. A FS for the liquefaction potential was calculated using SPT-based simplified procedure of Seed and Idriss (1971) and liquefaction resistance curve of Seed et al. (1985). The SPT *N*-values were corrected to account for rod length, energy losses, and effective overburden pressure (Liao and Whitman, 1986; Rogers 2006). The corrected SPT blow count, $(N_1)_{60}$, for soils with fines contents >5 % were adjusted to an equivalent clean-sand value [$(N_1)_{60CS}$; Youd et al., 2001]. This study disregarded the effect of groundwater on SPT raw values, because it is debatable whether the recorded blowcounts already include the effect of groundwater in the measurement (Budhu, 2007).

RESULTS

Threshold Groundwater Depth. Instead of assessing LPI values and its liquefaction potential with unchanging groundwater level, this study computed LPI values while varying the depth-to-groundwater for each SPT profile, in order to predict its threshold depth-to-groundwater for LPI>15, which Iwasaki et al. (1982) proposed as the lower bound of severe liquefaction effects. Figure 2 shows the variations of LPI with changing depth-to-groundwater and how to predict the threshold value for LPI exceeding a specific value.

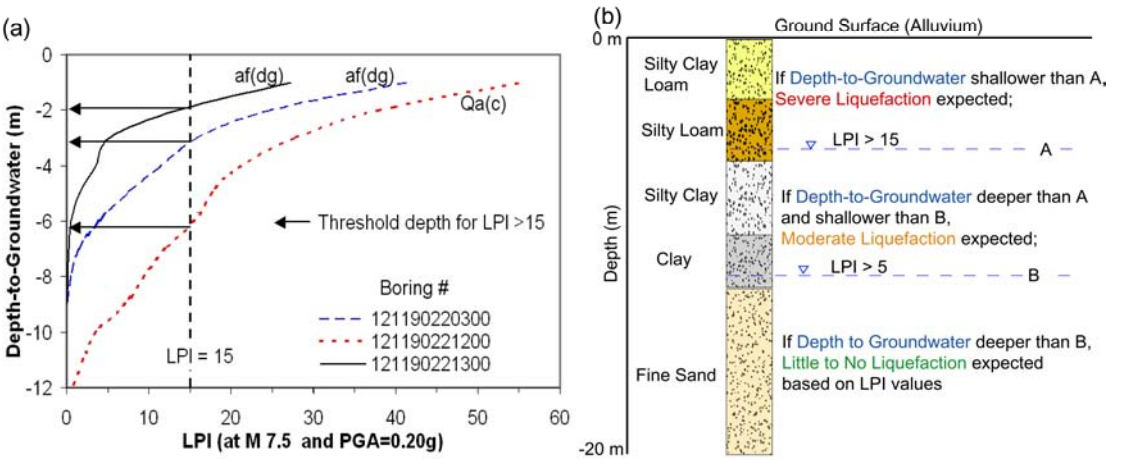

Figure 2. (a) Effect of groundwater depth on LPI and prediction of threshold depth-to groundwater for LPI>15. (b) Schematic illustration for determining minor (LPI< 5) and severe (LPI >15) liquefaction effects.

Spatial Prediction. To spatially assess the liquefaction hazard with insufficient number of boreholes, most LPI-based liquefaction potential maps are generated geostatistically by: (1) interpolating the LPI values between sampled sites (Sonmez,

2003; Lenz and Baise, 2007), or (2) predicting the probabilities of LPI>5 or LPI>15 within a given geologic unit (Holzer et al., 2006; Cramer et al., 2008). These methods assume that the surficial geologic unit spatially exhibits similar soil properties for a liquefaction hazard, but exhibits variability of the predicted liquefaction potential, usually ascribable to vulnerable layers thinning out, pinching off, or diving downward (increasing confinement).

In order to contour the threshold groundwater depth between data locations, the geostatistical technique of ordinary kriging was employed in this study. This geostatistical technique has been widely used to interpolate groundwater levels, because it honors the actual values at sampled points, as well as providing estimates across unsampled areas (Alley, 1993; and Snyder, 2008). This method assumes that close data pairs exhibit similar values and those separated by greater distance exhibit increasing uncertainty. Using ArcGIS software, spherical semivariograms were calculated for (1) Holocene alluvial units, and (2) Pleistocene units and artificial fills (Figure 3a). The kriged predictions of threshold depths-to-groundwater were estimated and compiled into a single map, shown in Figure 3b.

DISCUSSION AND CONCLUSIONS

Application of Proposed Method. The usefulness of the proposed method can be appreciated by comparing the map of predicted threshold groundwater depth (severe liquefaction when LPI >15) with the detailed depth-to-groundwater map. If the actual groundwater level lies below the threshold depth, severe liquefaction would not be expected; and, if the actual groundwater level lies above the threshold depth, we would assume the area is particularly susceptible to severe liquefaction (Figure 2b). The latter case might then require that a more rigorous assessment of liquefaction potential be required in these areas.

.

Comparison of the Threshold Depths for Stratigraphic Units. Surficial geologic maps group stratigraphic units that exhibit similar depositional origins, lithlogy, and age. Each unit is approximately spatially homogeneous from a liquefaction hazard perspective (Holzer, 2008). Figure 4 shows (1) the threshold groundwater depth for LPI>15 grouped by geologic unit and (2) the corresponding depths-to-bedrock, based on borehole data. Comparisons of surficial geologic units indicate that Holocene alluvial deposits exhibit deeper median values of threshold water depth [map unit Qa(f)-3.5 m, Qa(c)-4 m, and Qa(s)-3 m] than Pleistocene loess or till (Ql-0.5 m and Qt-1.5 m). This is an expected outcome.

Loess and till units tend to overlie shallower bedrock surfaces (median values of Ql and Qt are approximately ~9 m) than their alluvial counterparts [thickness of Qa(f), Qa(c), and Qa(s) are 21 m, 30 m, and 33 m, respectively]. These attributes explain why thicker (~20 m) unconsolidated sediments of Holocene age alluvium typically exhibit low SPT values, and consequently, deeper threshold water depths for triggering liquefaction.

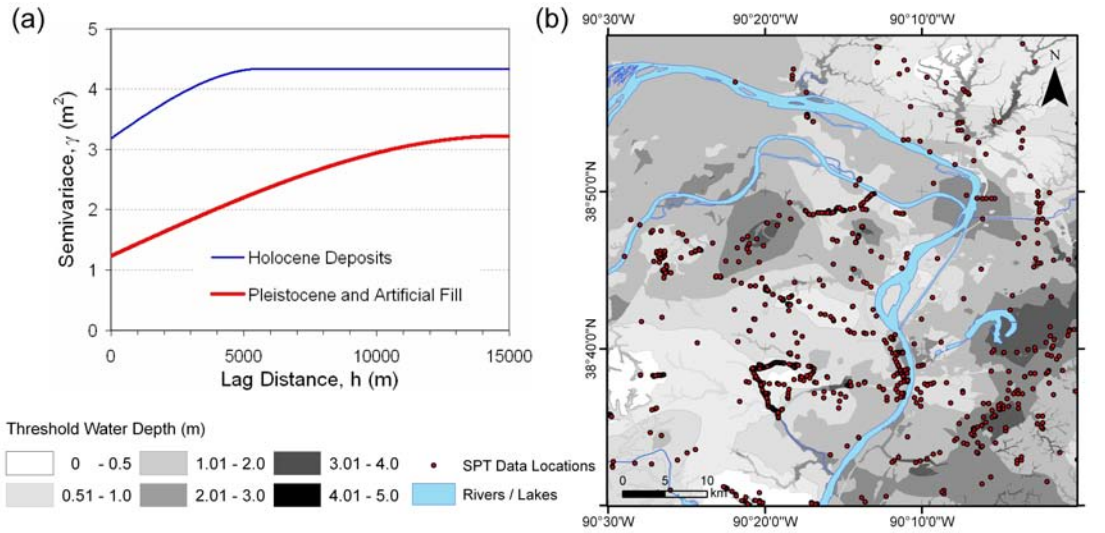

Figure 3. (a) Spherical semivariograms for threshold depth-to-groundwater. (b) Ordinary kriging map illustrating the threshold groundwater depth when LPI > 15 (severe liquefaction) for earthquake of M7.5 and PGA of 0.20 g.

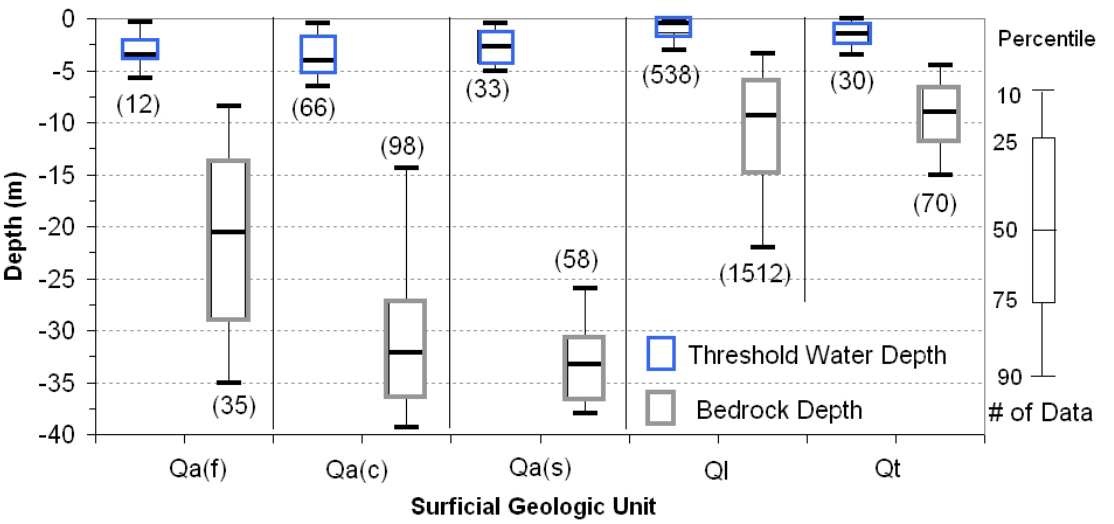

Figure 4. Comparison of threshold depths for distinct surficial geologic units and the corresponding depths to bedrock. The map units are shown in Figure 1.

Limitations. It is important to recognize there are a few limitations to this study. ***Seismic Hazard Map*:** The threshold map shown in Figure 3b is based on an assumed scenario earthquake and a spatially uniform PGA of 0.20 g, which is unlikely to occur in the Midwest, because of the severe impedance contrasts. This assumption can over or underestimate realistic peak ground motions and lead to calculate erroneous LPI values. A more reliable hazard map could be constructed by estimating the variability of PGA, and therefore, LPI values, considering site amplification ascribable to the effects of local geology, such as impedance and incoherence.

***Uncertainty of LPI Values*:** Although LPI values > 15 were interpreted as exhibiting severe liquefaction potential, that threshold represents the median value extracted from liquefied sites over the past half century, which is a statistically small pool of data (Iwasaki et al., 1978 and 1982). These ranges can, therefore, be a source of uncertainty in the prediction of severe liquefaction effects (there are statistically many more light and moderate liquefaction sites than severe sites). Toprak and Holzer (2003) attempted to relate LPIs with ground damage for the 1989 Loma Prieta Earthquake. They found that LPI>12 were associated with more than 50% of all lateral spreads, and that the criteria for "sever liquefaction" should probably be lowered from LPI>15 to LPI>12.

ACKNOWLEDGEMENTS

The authors would like to express our appreciation to James Palmer (MoDGLS), Robert Bauer (ISGS), and Conor Watkins (USGS) for providing subsurface data and the other members of the St. Louis Area Hazard Mapping Project-Technical Working Group for their advice, overview, and comments. This work was supported by the Missouri S&T Hasselmann Endowment.

REFERENCES

Aldrich, Jr., H.P., and Lambrechts, J.R.(1986). "Back bay Boston, Part II: groundwater levels", *J. of the Boston Society of Civil Engineers Section*, 1(2), 31-64.

Alley, W.M. (1993). "Geostatistical models." Regional ground-water quality, W. M. Alley, ed., New York, Van Nostrand Reinhold, 87-108.

Bates, R.L., and Jackson, J.A. (1987). *Glossary of geology*, American Geological Institute, Alexandria, VA.

Budhu, M. (2007). *Foundations and earth retaining structures*, John Wiley & Sons, Hoboken, NJ.

Chung, J.-W., and Rogers, J.D. (2010). "GIS-based virtual geotechnical database for the St. Louis metro area." *Environ. Eng. Geosci.*, 16(2), 143-162,.

Chung, J.-W., and Rogers, J.D. (2011). "Method for mapping liquefaction potential based on liquefaction potential index and depth to groundwater." *J. Geotech. Engrg.* in press.

Cramer, C.H., Rix, G.J., and Tucker, K. (2008). "Probabilistic liquefaction hazard maps for Memphis, Tennessee." *Seismological Research Letters*, 79(3), 416-423.

Elith, J., Burgman, M. A., and Regan, H. M. (2002). "Mapping epistemic uncertainty and vague concepts in predictions of species distribution." *Ecological Modelling*, 157, 313-329.

Holzer, T.L., Bennett, M.J., Noce, T.E., Padovani, A.C., and Tinsley, J.C. (2006). "Liquefaction hazard mapping with LPI in the Greater Oakland, California, area." *Earthquake Spectra*, 22(3), 693-708.

Holzer, T.L. (2008). "Probabilistic liquefaction hazard mapping." *Proc., 4th Conf. on Geotechnical Earthquake Engineering and Soil Dynamics*, D. Zeng, M.T. Manzari, and D. Hiltunen eds., ASCE Geotechnical Special Publication No. 181, Sacramento, 1-32.

Iwasaki, T., Tokida, K., Tatsuko, F., and Yasuda, S. (1978). "A practical method for assessing soil liquefaction potential based on case studies at various site in Japan." *2nd Int. Conf. on Microzonation*, San Francisco, 885-896.

Iwasaki, T., Tokida, K., Tatsuoka, F., Watanabe, S., Yasuda, S., and Sato, H. (1982). "Microzonation for Soil Liquefaction Potential Using Simplified Methods." *Proc., 3rd Int. Conf. on Microzonation*, Seattle, USA, 1319-1330.

Kramer, S.L. (1996). *Geotechnical earthquake engineering*, Prentice Hall, Upper Saddle River, New Jersey.

Lenz, J.A. and Baise, L.G.. (2007). "Spatial variability of liquefaction potential in regional mapping using CPT and SPT data." *Soil Dynamics and Earthquake Eng.,* 27(7), 690-702.

Liao, S.C., and Whitman, R.V, (1986). "Overburden correction factors for SPT in sand." *J. Geotech. Eng.*, 112(3), 373-377.

Petersen, M.D., Frankel, A.D., Harmsen, S.C., Mueller, C.S., Haller, K.M., Wheeler, R.L., Wesson, R.L., Zeng, Y., Boyd, O.S., Perkins, D.M., Luco, N., Field, E.H., Wills, C.J., and Rukstales, K.S. (2008). "Documentation for the 2008 Update of the United States National Seismic Hazard Maps." *U.S. Geological Survey Open-File Report 2008-1128*.

Rogers, J.D. (2006). "Subsurface exploration using the standard penetration test and the cone penetrometer test." *Environ. Eng. Geosci.*, 12(2), 161-179.

Seed, H.B., and ldriss, I.M. (1971). "Simplified procedure for evaluating soil liquefaction potential." *J. Soil Mech. Found. Div.*, 97, 1249-1273.

Seed, H.B., Tokimatsu L.F., Harder, L.F., and Chung, R.M. (1985). "Influence of SPT procedures in soil liquefaction resistance evaluations. " *J. Geotech. Engrg.*, 111(12), 1425-1445.

Snyder, D.T. (2008). "Estimated depth to ground water and configuration of the water table in the Potland, Oregon area." *U.S. Geological Survey Scientific Investigations Report 2008-5059*.

Sonmez, H. (2003). "Modification of the liquefaction potential index and liquefaction susceptibility mapping for a liquefaction-prone area (Inegol,Turkey)." *Environ. Geol*., 44(7), 862-871

Toprak, S., and Holzer, T.L. (2003). "Liquefaction potential index: Field assessment." *J. Geotech. Geoenv. Eng.*, 129(4), 315-322.

Toro, G.R., and Silva, W.J. (2001). "Scenario earthquakes for Saint Louis, MO, and Memphis, TN, and seismic hazard maps for the central United States region including the effect of site conditions." *U.S. Geological Survey Final Technical Report.*

Tuttle, M.P. (2005). "Paleoseismological Study in the St. Louis region." *U.S. Geological Survey Final Technical Report.*

Tuttle, M.P. Chester, J., Lafferty, R., Dyer-Williams, K., and Cande, B. (1999). "Paleoseismology study northwest of the New Madrid Seismic Zone." *U.S. Nuclear Regulatory Commission, NUREG/CR-5730*, Washington, D.C.

Youd, T.L., Idriss, I.M., Andrus, R.D., Arango, I., Castro, G., Christian, J.T., Dobry, R., Finn, W.D. L., Harder, L.F., Hynes, M.E., Ishihara, K., Koester, J.P., Liao, S. S. C., Marcuson, W.F., Martin, G.R., Mitchell, J. K., Moriwaki, Y., Power, M.S., Robertson, P.K., Seed, R.B., and Stokoe, K.H. (2001). "Liquefaction resistance of soils: Summary report from the 1996 NCEER and 1998 NCEER/NSF workshops on evaluation of liquefaction resistance of soils." *J. Geotech. Geoenv. Eng.*, 127(10), 817-833.

Study on Risk Assessment for Individual Landslide

Juan Du[1] and Kun-Long Yin[2]

[1] Faculty of Engineering, China University of Geosciences（WuHan）, LuMo Road 388, WuHan, China. PH(086)-027-67883900; FAX(086)-027-67883900; email: dujuan0709@gmail.com
[2] Faculty of Engineering, China University of Geosciences（WuHan）, LuMo Road 388, WuHan, China. PH(086)-027-67883900; FAX(086)-027-67883900; email: yinkl@cug.edu.cn

ABSTRACT

Risk assessment for individual landslide is investigated in this study with the example application of Xiatudiling Landslide in the Three Gorges Reservoir. Transfer coefficient method and Monte-Carlo is used to obtain the failure probability. Meanwhile, the vulnerability is defined quantitatively as the combination of susceptibility and the landslide intensity. The vulnerable elements are divided into persons and economic elements, and influence factors of the susceptibility for each category are considered respectively. For the intensity, slipping velocity and volume of the moving mass are selected to describe the damage potential of landslide. Finally, the risk of persons and economic elements are assessed quantitatively in Xiatudiling Landslide, which may be used not only as the reference for landslide prevention but also as technical support for the early warning decision to the management department.

INTRODUCTION

According to loss statistics, the frequency of landslides increases due to extreme weather and human engineering activities (Lacasse *et al*. (2009)). In the Three Gorges Reservoir, because of human engineering activities and water level change, landslide is a serious risk for the population and economic development. Since the water level rose to 172 meters, cutoff November 2008, accelerated deformation occurs in more than sixty landslides at HuBei and ChongQing. Therefore, landslide is the main risk source in the Three Gorges Reservoir and risk assessment is the foundation of risk mitigation (Wang. (2007)). Landslide risk is a measure of the chance of slope failure causing a certain amount of harm, e.g. fatalities and economic losses (Wong et al. (2009)). Now, regional landslide risk zoning has experienced extensive development (Fell et al. (2008)). Meanwhile, for individual landslide, the risk assessment is inherently complex. Such difficulties are due to the complexity in modeling landslide hazard, intensity and the vulnerability of the environment to landslides (Uzielli et al. (2008)). Glade et al. (2003) identified several prominent hindering factors: lack of accurate data for reliable hazard analysis, strongly site-specific nature of landslide phenomena, quantitative heterogeneity of vulnerability of different elements at risk and variability in temporal vulnerability.

ENGINEERING GEOLOGICAL CONDITION

Xitudiling Landslide is an active landslide, located beside the tributary of Yangtze River in ZiGui County. Significantly deformation appears in the residential house and dormitory buildings in the landslide. Material compositions of the landslide are Upper Jurassic aubergine mudstone, argillaceous siltstone and feldspar quartz sandstone (Fig. 1). The total volume of the landslide is 25×10^4 m^3.

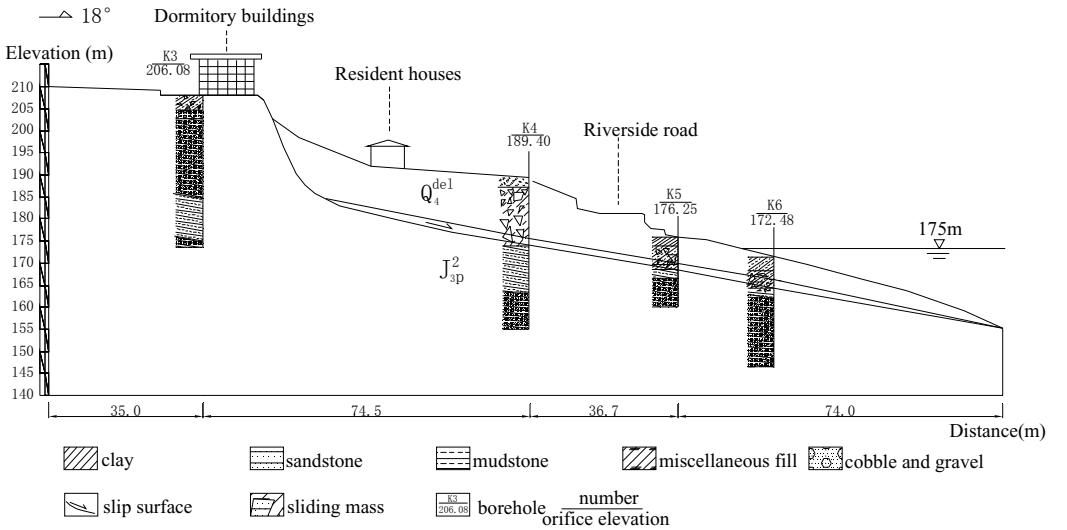

Figure 1. Engineering geological profile of Xiatudiling Landslide

HAZARD ASSESSMENT OF LANDSLIDE

Hazard assessment for individual slope usually means probabilistic analysis of the slope. The required data include slope geometry, strength parameters and possible trigger such as rainfall intensity, severity of loads and so on. Groundwater level is an important factor for the stability of landslide. Especially, in the Three Gorges Reservoir, the change of river water level is the main trigger factor for the landslides. The calculation condition is selected as water level fall from 175 meters to 156 meters and Geo-studio is used to simulate the groundwater level. The Monte-Carlo simulation method is used to obtain the failure probability. Random distribution of shear strength parameters of slip soil is considered (Table 1). Failure probability at this condition is 53.92%.

VULNERABILITY ANALYSIS

Vulnerability is the degree of loss to a set of elements within the area affected by the landslide hazard. The quantitative model (Eq. (1)) for vulnerability contents the severity of landslide action and the capacity of vulnerable elements to withstand an action of a given degree of severity (Kaynia et al. (2008)).

$$V = I \cdot S \tag{1}$$

V indicates vulnerability, I indicates landslide intensity and S indicates the susceptibility of elements at risk. The elements at risk can be divided into two

categories, namely, person and economy.

Survey data. There are 16 households, 65 persons in Xiatudiling Landslide and 1800 students in three dormitory buildings in traction zone. The distribution of vulnerable elements is shown in Fig. 2.

Susceptibility of economic elements. The economic elements include buildings, transportation lifelines and natural environment. Their resistant ability to a degree of hazard is related to structural type or characteristics and state of maintenance Eq. (2),

$$S_{eco} = 1 - \prod_{i=1}^{2} (1 - S_i) \tag{2}$$

S_{eco} is the susceptibility of economic elements. S_i is the susceptibility factor contributing to the susceptibility of economic elements, including S_{type}, S_{main}.

For buildings, structural typology decides the inherent capacity of the buildings to withstand the deformation and impact force of landslide. Six categories of structures and the values of the susceptibility factor are showed in Table 2. For roads, according to the materials of road surface, it can be divided into four categories. The corresponding values of susceptibility factor are showed in Table 3. The susceptibility factor for state of maintenance S_{main} can be assigned in a subjective manner upon qualitative assessment of the average state of maintenance of structures in the area of interest as shown in Table 4. In Xiatudiling Landslide, the typology and state of maintenance of each economic element is listed in Table 5.

Susceptibility of persons. For the slow movement of landslide, risk for persons comes from the deformation of buildings, which can be avoided because of self-protection ability. Therefore, the impact and bury effect during the rapid movement is the main risk for persons. Four susceptibility factors are considered in the paper, structural typology of buildings, average age, health condition and education level (Zhang et al. (2007)). The susceptibility model is listed as Eq. (3):

Table 1. Random distribution of shear strength parameters

State	Parameter	Average value	Standard deviation
Natural	c(Kpa)	10.0	2.1
state	φ(°)	14.7	3.4
Saturation	c(Kpa)	9.2	2.0
state	φ(°)	10.5	3.3

Table 2. Proposed values of susceptibility factor for structural typology of buildings

Structural typology	Resistance	S_{type}
Lightest, simple structures	None	1.00
Light structures	Very low	0.90
Rock masonry, concrete and timber	Low	0.70
Brick masonry, concrete structures	Medium	0.50
Reinforced concrete structures	High	0.30
Reinforced structures	Very high	0.10

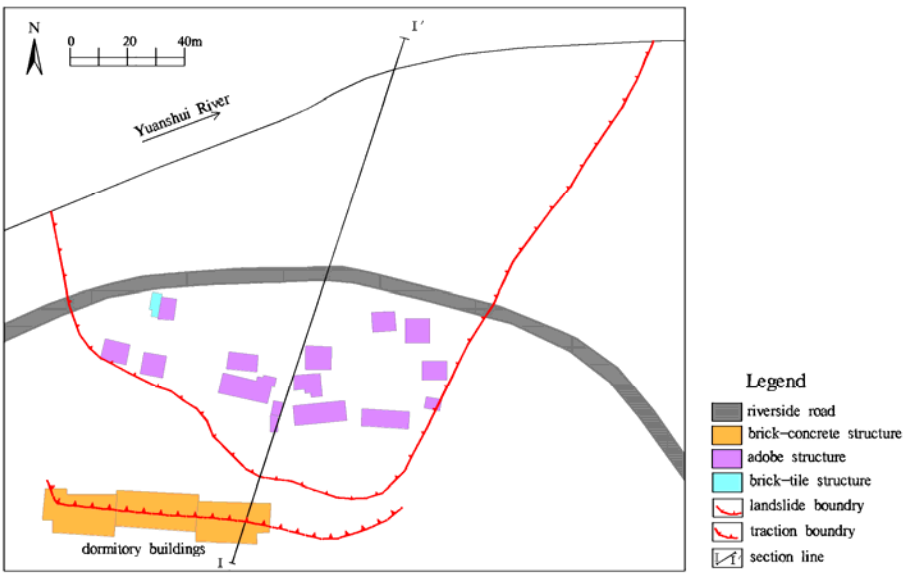

Figure 2. Distribution of vulnerable elements in Xiatudiling Landslide

Table 3. Proposed values of susceptibility factor for materials typology of roads

Materials typology	Resistance	S_{type}
Cement concrete pavement	High	0.3
Asphalt concrete pavement	Medium	0.5
Asphalt crushed stone (gravel) pavement	Low	0.7
Crushed stone (gravel) pavement	Very low	0.9

Table 4. Proposed values of susceptibility factor for state of maintenance

State of maintenance	S_{main}
Very poor	0.50
Poor	0.40
Medium	0.25
Good	0.10
Very good	0.00

Table 5. Susceptibility factors of economic elements in Xiatudiling Landslide

Elements at risk		Typology		State of maintenance	
		Typology	Resistance	State	Number /Length
Buildings	Resident houses	Adobe	Very low	good	9
				poor	6
		Brick-tile	Low	good	1
	Dormitory buildings	Brick-concrete	Medium	good	3
Transportation lifelines	Riverside road	Asphalt concrete pavement	Medium	good	300 meters

$$S_{per} = 1 - \prod_{i=1}^{4} (1 - S_i) \quad (3)$$

S_{per} is the susceptibility of persons, S_i includ S_{type}, S_{age}, S_{hel}, S_{edu}. S_{type} reflects the effect of buildings to susceptibility of persons, which can be determined referring to S_{type} in susceptibility of buildings. Moreover, the susceptibility of persons mainly depends on the cognitive and reaction ability for the occurrence of hazard, which are determined by age, health condition and education level (Table 6, Table 7). There are 1865 persons in all in Xiatudiling Landslide. The structural typology of buildings, average age, health condition and education level of them are listed in the Table 8.

Intensity. In practical risk assessment, a composite landslide intensity parameter is adopted, accounting for kinetic and kinematic characteristics of the landslide. The kinetic intensity parameter is related to the kinetic energy of landslide. The kinematic intensity parameter is related to the scale of the hazard. The proposed general model for the intensity of landslide acting on any vulnerable category is Eq. (4)

$$I = K_s \cdot [r_K \cdot I_K + r_M \cdot I_M] \quad (4)$$

K_s reflects position relationship between vulnerable elements and hazard. K_s of each vulnerable element at different position is listed in the Table 9. So, the K_s of

Table 6. Proposed values of susceptibility factor for average age of population

Average population age	S_{age}	Average population age	S_{age}
0–5	1.00	55–60	0.30
5–10	0.90	60–65	0.50
10–15	0.70	65–70	0.70
15–20	0.30	70–75	0.90
20–50	0.00	≥75	0.95
50–55	0.10		

Table 7. Susceptibility factor for health condition and education level

Susceptibility factors	Description	Range	Average value
S_{hel}	health	0.1~0.2	0.15
	disability	0.8~1	0.9
S_{edu}	university	0-0.2	0.1
	middle school	0.2-0.3	0.25
	primary school and under it	0.3-0.4	0.35

Table 8. Susceptibility factors of persons in Xiatudiling Landslide

Structural typology		Average age		Health	Education
Structure	Number	Average age	Number	condition	level
Adobe	15	20-50	39	Health	Middle school
		15-20	14	Health	Middle school
		10-15	9	Health	Primary school
Brick-tile	1	20-50	3	Health	Middle school
Brick-concrete	3	15-20	1800	Health	Middle school

persons is approximately determined according to the buildings, in which the person lives. r_K is the kinetic relevance factor; r_M is the kinematic relevance facto; I_K and I_M are the kinetic and kinematic intensity paramete (Table 10). For Xiatudiling Landslide, the velocity and volume of the moving mass are selected as kinetic intensity parameter to describe the damage potential of landslide.

The velocity of landslide. For risk assessment, the maximum velocity attracts the most attention. The slice method is used to establish equilibrium and obtains the acceleration of each movement phase and the velocity of each slice (Dai. (2008)). For persons, the degree of the threat is determined by the possibility of escaping. Considering sliding velocity and reaction rate of persons comprehensively, the sliding velocity is divided to seven grades (Table 11). The maximum velocity of Xiatudiling landslide is 4.34 m/s and I_K =0.85. The landslide belongs to rapid movement, so, for structures, r_K=0.9, r_M=0.1, for persons, r_K=0.75, r_M= 0.25.

The volume of landslide. The volume reflects movement character and strength of landslide at a certain extent. Five categories are divided as Table 12 showed. The volume of Xiatudiling landslide is $25\times10^4 m^3$ and the I_M = 0.3.

RISK ASSESSMENT OF XIATUDILING LANDSLIDE

Risk assessment of persons. The formula of risk assessment for persons (Eq. (6)**),**

$$R_p = P_h \times V_p \times N_p = P_h \times (I_p \times S_p) \times N_p \quad (6)$$

P_h is the failure probability of landslide. V_p is the vulnerability of persons. N_p is the number of persons at risk. I_P and S_p are intensity of landslide and susceptibility of

Table 9**.** Proposed values of *Ks* for each vulnerable element at different position

Categories of vulnerable elements	K_s				
	Anterior part	Middle part	Posterior part	Lateral boundary	Traction zone
Persons	0.90	0.60	0.45	0.25	0.05
Brick-concrete building	0.90	0.70	0.50	0.30	0.10
Brick-tile structure building	0.95	0.80	0.65	0.40	0.15
Adobe structure building	0.95	0.85	0.75	0.45	0.20
Railway	0.70	0.55	0.60	0.30	0.10
Highway	0.90	0.60	0.70	0.30	0.10
Bridge	0.97	0.75	0.75	0.20	0.10
Crops	0.90	0.50	0.70	0.10	0.05

Table 10**.** Examples of values for kinetic and kinematic relevance factors

Category	Landslide type	r_K	r_M
Structures	Rapid	0.90	0.10
Structures	Slow	0.15	0.85
Persons	Rapid	0.75	0.25
Persons	Slow	1.00	0.00

Table 11. Proposed values of I_K for each grade of sliding velocity

Grade	Velocity	Reaction of persons	I_K
Extremely fast	>5m/s	None	0.9
Very fast	>3m/min	Vary with each individual	0.6
Fast	>1.8m/hr	Retreat	0.5
Medium	>13m/mon	Retreat	0.4
Slow	>1.6m/a	Safeguard	0.3
Very slow	>0.016m/a	Safeguard	0.2
Extremely slow	<0.016m/a	None	0.1

Table 12. Proposed values of I_M for each category of volume ($10^4 m^3$)

Category	Small-scale	Medium-scale	Large-scale	Oversize	Huge-scale
Volume	<10	10~100	100~1000	1000~10000	>10000
I_M	0.1	0.3	0.5	0.7	0.9

persons at risk. The failure probability of Xiatudiling Landslide is 53.92%. The related parameters and result of vulnerability are listed at Table 13. Finally, at this condition, 29 persons will lose their lives taking into account of the landslide hazard.

Risk assessment of economic elements. The formula of risk assessment for economic elements (Eq. (8)),

$$R_e = P_h \times V_e \times N_e = P_h \times (I_e \times S_e) \times N_e \quad (8)$$

V_e is the vulnerability of economic elements. E_e is the value of economic elements at risk. I_e and S_e are intensity of landslide and susceptibility of economic elements at risk. The value of economic elements and related parameters of vulnerability are listed at Table 14. The economic losses are 47.21×10^4 Yuan caused by the landslide hazard at this condition.

CONCLUSIONS

For Xiatudiling Landslide, Monte-Carlo is used to obtain the failure probability. The vulnerable elements are divided into persons and economic elements; meanwhile, vulnerability was defined as the product between intensity and the susceptibility. For economic elements, the susceptibility factors include structural (or materials)

Table 13. Related parameters and result of vulnerability for persons

Category (number)	Structural typology	Average age	Health condition	Education level	S_p	K_s	V_p
33	0.9	0	0.15	0.25	0.94	0.45	0.24
6	0.9	0	0.15	0.25	0.94	0.60	0.31
14	0.9	0.3	0.15	0.25	0.96	0.45	0.24
6	0.9	0.7	0.15	0.35	0.98	0.45	0.25
3	0.9	0.7	0.15	0.35	0.98	0.60	0.33
3	0.5	0	0.15	0.25	0.68	0.60	0.23
1800	0.3	0.3	0.15	0.25	0.69	0.05	0.02

Table 14. Related parameters and result of vulnerability for economic elements

Elements at risk	Number	Value (10^4Yuan)	Structural typology	State of maintenance	S_p	K_s	V_p
Resident houses	6	42	0.9	0.1	0.91	0.75	0.42
	3	21	0.9	0.1	0.91	0.85	0.48
	6	72	0.9	0.4	0.94	0.75	0.43
	1	15	0.7	0.1	0.73	0.8	0.36
Dormitory buildings	3	450	0.5	0.1	0.55	0.1	0.03
Road	300(m)	40	0.5	0.1	0.55	0.6	0.20

typology and maintenance state. For persons, structural typology of buildings, average age, health and education level are considered. The relative position of vulnerable elements, slipping velocity and volume of the moving mass are considered to determine the intensity. Finally, the risk of persons and economic elements are assessed quantitatively in Xiatudiling Landslide.

REFERENCES

Dai, Y. X., Yin, K. L., Wang, Y. (2008) "Discussion on method of landslide velocity calculation and surge prediction," *Rock and Soil Mechanics*, 29, 407-411.

Fell, R., Corominas, J., Bonnard, C., Cascini, L. (2008). "Guidelines for landslide susceptibility, hazard and risk zoning for land use planning," *Engineering Geology*, 102, 85-98.

Glade, T., (2003). "Vulnerability assessment in landslide risk analysis," *Die Erde*, 134, 121–138.

Kaynia, A. M., Papathoma-Köhle, M., Neuhäuser, B., Ratzinger, K., Wenzel, H., Medina-Cetina, Z. (2008). "Probabilistic assessment of vulnerability to landslide: Application to the village of Lichtenstein, Baden-Württemberg, Germany," *Engineering Geology*, 101, 33-48.

Lacasse, S., Nadim, F. (2009). "Landslide risk assessment and mitigation strategy," *Geological Engineering Problems in Major Construction Projects*, ChengDu, 10-27.

Uzielli, M., Nadim, F., Lacasse, S., Kaynia, A. M. (2008) "A conceptual framework for quantitative estimation of physical vulnerability to landslides," *Engineering Geology*, 102, 251-256.

Wang, Z. H. (2007). "Landslide distribution and development in the towns of the Three Gorges Reservior area," *ZHONGGUO DIZHIZAIHAI YU FANGZHI XU*EBAO, 18(1), 33-38.

Wong, H. N. (2009). "Holistic urban landslide risk management – challenges and practice," *Geological Engineering Problems in Major Construction Projects*, ChengDu, 28-43.

Zhang, G. R., Yin, K. L., Chen, L. X. (2007) "Population Vulnerability Assessment on Regional Landslide Hazards and Casualty Risk Forecasting in Yongjia County , Zhejiang Province," *Geological Science and Technology Infor*mation, 26(4), 70-75.

Geohazard Interpretation of the Cagliari Slope (Southern Sardinia, Italy)

William J. Johnson[1], Francesca Zolezzi[2], James Nicholls[3], Eric J. Parker[2] and Ennio Morgante[4]

[1] D'Appolonia 275 Center Road, Monroeville, PA 15146 U.S.A., PH: (412) 856-9440, FAX: (412) 856-9535, email: wjjohnson@dappolonia.com
[2] D'Appolonia S.p.A. Via San Nazaro 19, 16145 Genoa, Italy, PH:00390103628148, FAX: 00390103621078, email: francesca.zolezzi@dappolonia.it; eric.parker@dappolonia.it
[3] Flintshire Geoscience Ltd., Port Erin, IM9 6BG, Isle of Man, British Isles, PH: 00447768081006, email: james.nicholls@flintgeo.com
[4] EMPD Ltd., Kingston Upon Thames, Surrey, UK, PH: 00447850372014, email: enniomorgante@msn.com

ABSTRACT

Geohazard assessment for offshore installations is a crucial engineering activity. The evaluation of Cagliari slope recognized significant geohazard features in the form of large slope failure scarps, as result of combined sea level fluctuation and salt movement. Fundamental to understanding the geohazard risk potential of these features is determining if scarp failure planes extend to the contemporary seabed or are buried by undisturbed sediment. Abnormally low sedimentation rates for the project area make this sedimentary geometry difficult to determine, with surficial units beyond the resolution of acoustic profiling systems. The solution applied was to evaluate the age of last movement and recurrence of slope failures by sampling deposits formed by multiple failure units and not the geometry of originating scarps themselves. On this basis, all studied slope failures are confirmed older than 10,000 years with return periods of the order 15,000 – 30,000 years.

INTRODUCTION

Continental slopes are geologically complex areas characterized by steeply sloping seabed, irregular bathymetry and the movement of sediment. This movement of sediment can be rapid or as a slow creep associated with the amount and rate of deposition or erosion, overpressure of internal fluids, or any other local mechanism able to cause an increase in shear stress increase or a decrease in sediment strength.

Slope failure along continental slopes represents what is probably the most significant geohazard associated with deepwater offshore development projects including fixed seabed structures and pipelines. In particular, mass gravity flow from slope failure can present critical risk to pipelines and flowlines, as predicted occurrence and frequency are often difficult or impossible to confirm with high

confidence, and resultant forces easily demonstrated to potentially exceed pipeline yield strength. Mitigation measures can be designed only if the geohazard is correctly identified, appropriately sampled and accurately modeled.

The Cagliari slope (Figure 1) represents an example of where complex slope failures are easily observed from multibeam bathymetry. They represent a potential hazard risk to the intended pipeline development, but are difficult to evaluate because of the complexity in distinguishing ancient from modern slope movements due the observed very low sedimentation rate. This paper focuses innovative interpretive techniques to be able to evaluate the risk from slope failures in this area.

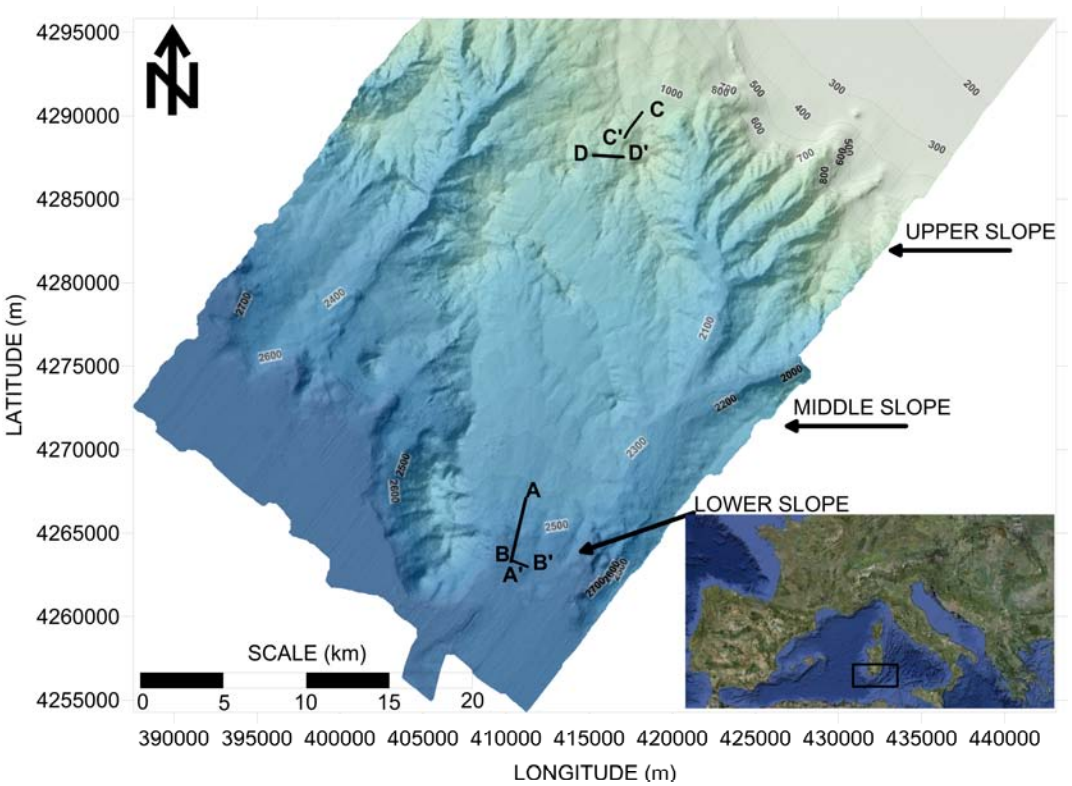

Figure 1. Shaded relief of Cagliari continental slope. Solid black lines show the location of sub-bottom profiles shown on Figures 3 through 6.

GENERAL SETTING

Sardinia is a block of continental crust that rotated away from the coast of France about 22–21 million years ago (Ma) and it reached its current position about 16–15 Ma (Rosenbaum et al., 2005). As such, Sardinia is a topographic high in what would otherwise be the middle of the Mediterranean Sea. This is significant, as a result there are no major sources of sediment to accumulate along the continental slope as seen characterising other parts of the Mediterranean, such as the Nile or Rhone deltas. Another geological episode affecting the continental slope configuration of southern Sardinia took place during the Messinian (late Miocene) – between 5.96 and 5.33 million years ago when the closure of the marine passages

between the Atlantic and the Mediterranean caused the subsequent (and repeated) complete (or near-complete) drying up of the Mediterranean Sea (Carminati et al., 2009). This left behind thick sequences of evaporites, mainly salt, buried by a thick sediment layer. Salt is mobile under pressure and it subsequently formed domes or other diapiric piercings that have also modified the shape of the Cagliari continental slope. The lowering and subsequent rising of sea level during the late Pleistocene caused extensive slope failures along the Cagliari slope, as occurred along continental slopes in most of the world. The combination of geomorphic processes and diapiric salt movements makes deciphering the development of Cagliari slope a challenging task for an interpreter.

CHARACTERIZATION OF THE CAGLIARI SLOPE

The portion of the Cagliari slope presented in this paper (Figure 1) extends for a distance of about 55 km and ranges between ~300 m to 2700 m water depth. The sea floor is characterized by a small number of major landslide scarps, but most of the slope failure morphology is associated with shallow landslides and planar slides which develop into fluid runout. The overall slope gradient is highly variable, having different morphological characteristics dependent primarily the position and degree of deformation from upwelling salt. The steepest slopes exhibiting obvious slope failure are concentrated in the upper part of the slope adjacent to the primary salt uplift. The slope passes through a middle zone with a relatively gentle slope reflecting the lower gradient flanks of the salt uplift. The lowest part of the slope also includes a zone with a steep gradient coincident with a major scarp in the underlying salt and the

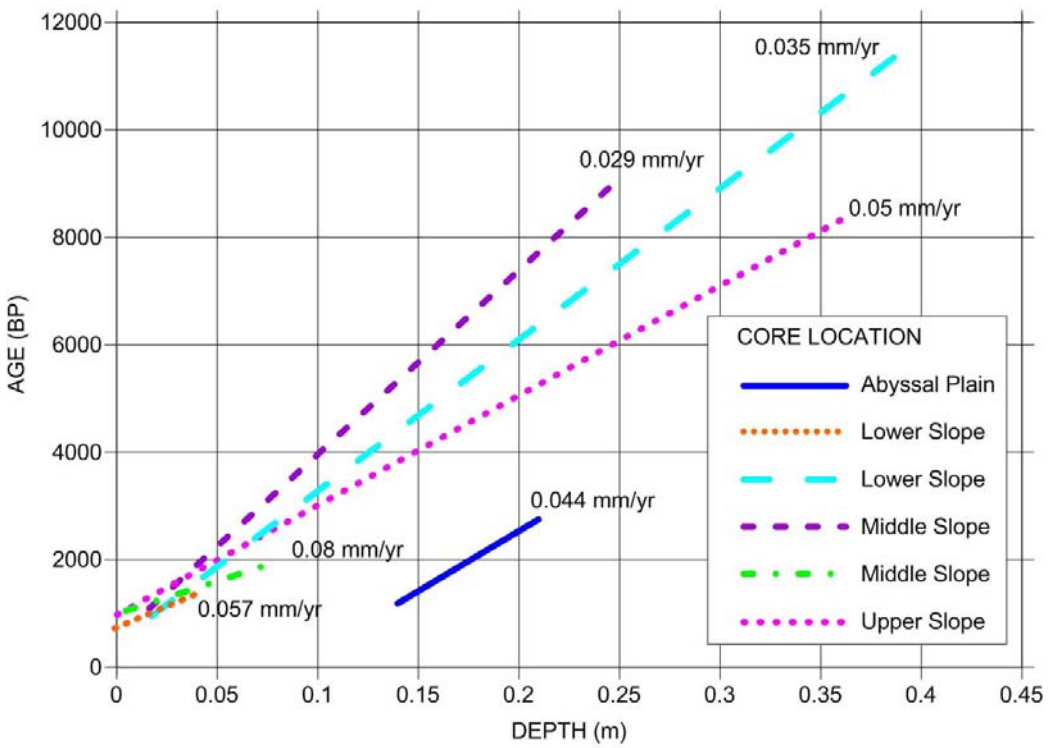

Figure 2. C14 age dating results from corehole samples (average sedimentation rate is 0.04 mm/yr)

eroded margin of an adjacent canyon system, with ample evidence that runout from failures occurring in the middle and upper zones also affect this area.

The key to understanding the activity of past slope movement is in the derivation of a reliable estimate of local sedimentation rate. Multiple samples were age-dated with the C^{14} technique from five shallow core samples along the Cagliari slope, with an additional sample taken from the abyssal plain at the toe of the slope. The sedimentation rates calculated from these coreholes are all similar and the average sedimentation rate in the area is close to 0.04 mm/year. The results were interesting in that surface samples along the slope depict ages that are from about 900 to 1200 years BP. This implies that sediments either have not accumulated over this time or that the overall surface has experienced a small amount of erosion. If we assume that the slope has been subject to erosion which has removed the upper ~1000 years of sediment accumulation, and considering the average sedimentation rate for the area of 0.04 mm/year, the missing material is on the order of 4 cm thick. This is an amount that could be associated with removal by mild low energy turbidity currents or hyperpycnal flows crossing the slope system.

The consequence of determining that the Cagliari slope has experienced an abnormally low average sedimentation rate of 0.04 mm/yr is that ancient features appear fresh and can be misinterpreted as having recently formed or even currently forming as a result of contemporary seabed processes. With a sedimentation rate this low, the past ~10,000 years is contained within the top 40 cm of sediment, which is close to the limit that could be resolved with the available CHIRP profiles. This situation required that innovative interpretive techniques be applied, as described for the Lower and Upper Slope areas.

Lower Slope The deepest part of the slope contains several erosion channels and slope deposits that appear to have originated to a large degree from the movement of underlying salt. Figure 3 provides an Airgun profile over the toe of the lower Cagliari

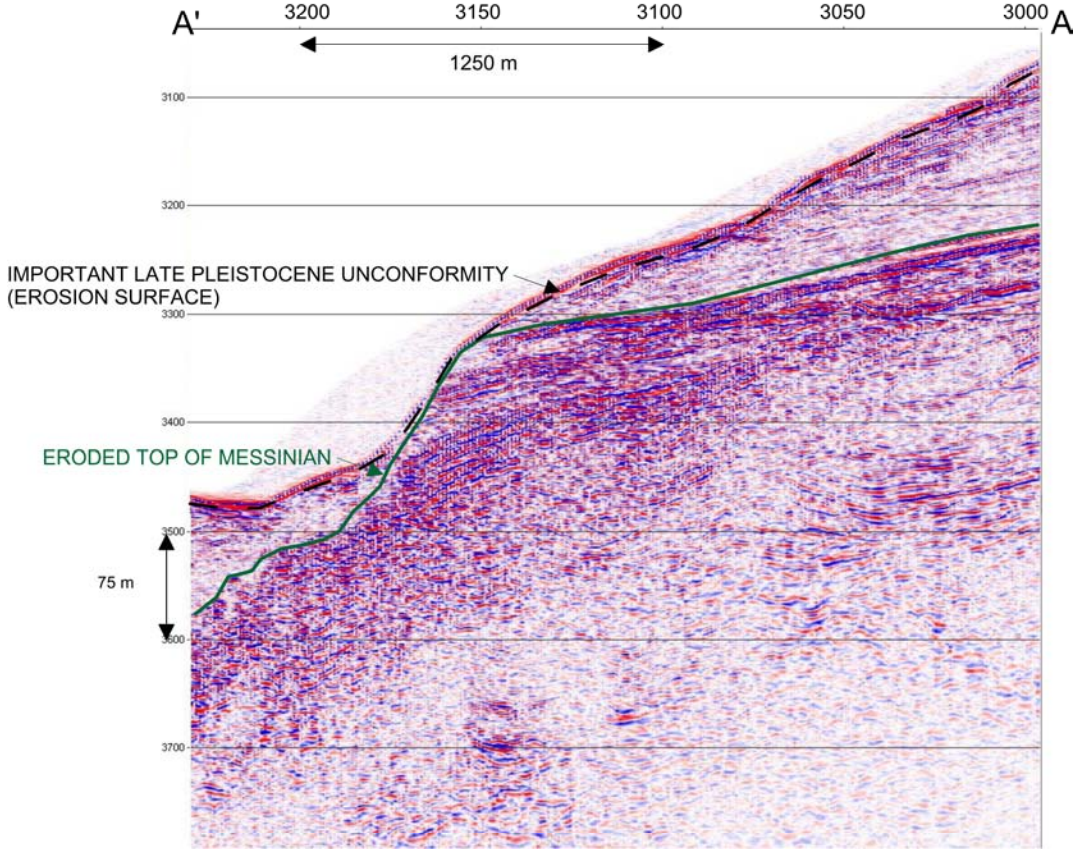

Figure 3. Airgun profile through the lower Cagliari slope

slope developed as an erosion surface over Messinian age deposits probably caused by Messinian salt movement. In general, Messinian sediments appear to be very close to the seafloor where the slope is steepest along the profile. Pliocene and Pleistocene sediments are also highly eroded and a significant Late Pleistocene unconformity appears to be covered by a thin sedimentary drape.

Characterization of the first 10-20 m of sediments was achieved through the interpretation of high-resolution CHIRP profiles, where several ancient slope failures interspersed by periods of relatively long quiescence with stratified sedimentation can be observed.

Figure 4 shows a profile crossing a channel presents in the middle of the lower slope where four paleo-slope failure deposits are distinguished. Assuming normal sedimentation for the portion of stratified sediment associated with the slide deposits (assumed to be instantaneous), the four slides and the event that formed the channel can be estimated to have occurred over a period of about 150,000 years, suggesting that the return period for failures is about 30,000 years in this area. The youngest of the slide deposits appears not to be thicker than about two meters.

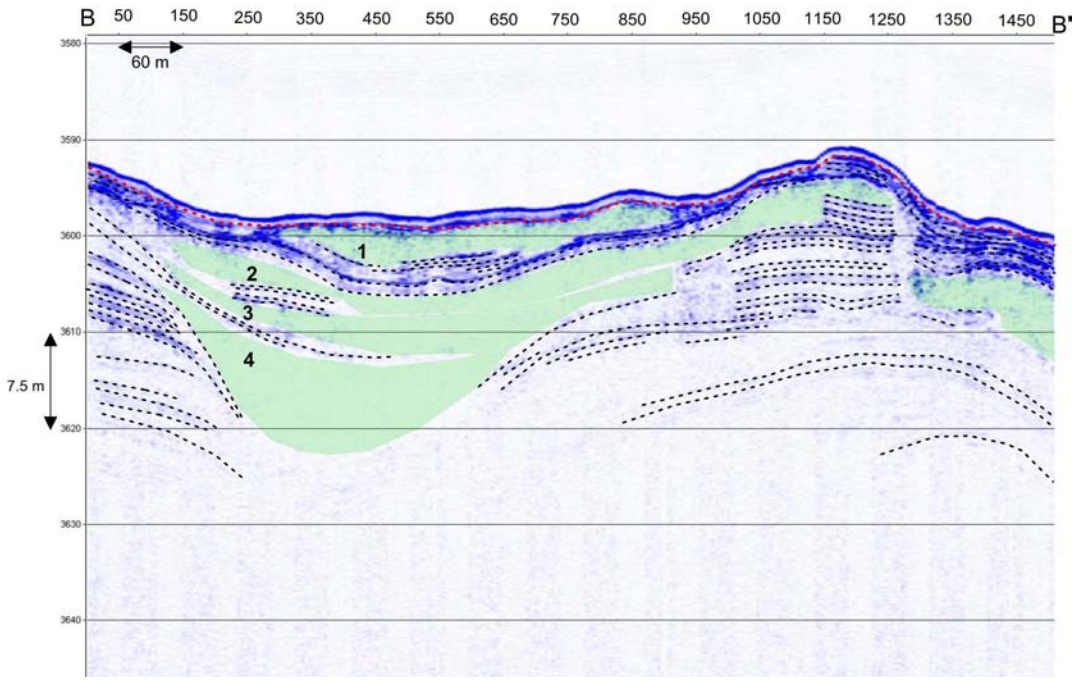

Figure 4. CHIRP profile passing through a small channel cutting the lower Cagliari slope

Buried slopes are more common at the toe of the slope while the upper (northern) part is primarily represented by channels and scarps. These characteristics are not to be interpreted as a major change in mechanism, as both channel/scarp and buried deposits are part of the same dynamic system. The channels and scarps have a corresponding area where the failure deposits have accumulated. The channels are manifestations of where the movements have been relatively recent, whereas failure scarps are not be so obviously associated with the deposits that are more deeply buried.

What is significant to the interpretation is that where the sedimentary drape may be too thin to fully resolve at the edges of scarps or where the slope is steep, the study of the zones where the slope is less steep and where slide deposits have accumulated can be a means to understand the chronology of slope failures.

Upper Slope The area of the upper slope is also strongly affected by salt-related fault movements and this affects the shape of the slope and controls slope movements (Figure 5). In general slides related to salt tectonics along the Cagliari slope do not appear to have taken place as a large, individual mass movement event, but have occurred over a long period of time in association with the slow movement of the salt.

The numerous slope failures visible at the top of the upper slope have been scoured by numerous shallow runout channels, some of which appear to be relatively fresh on the sea floor. At the toe of the scarp a sedimentary drape is observed to be present across much of the slope, but it is no thicker than about 0.5 meters and is not always visible (Figure 5). This is also an area where interpretation benefited from evaluating slope movements at the toe of the slope where several slide deposits could be identified in sequence.

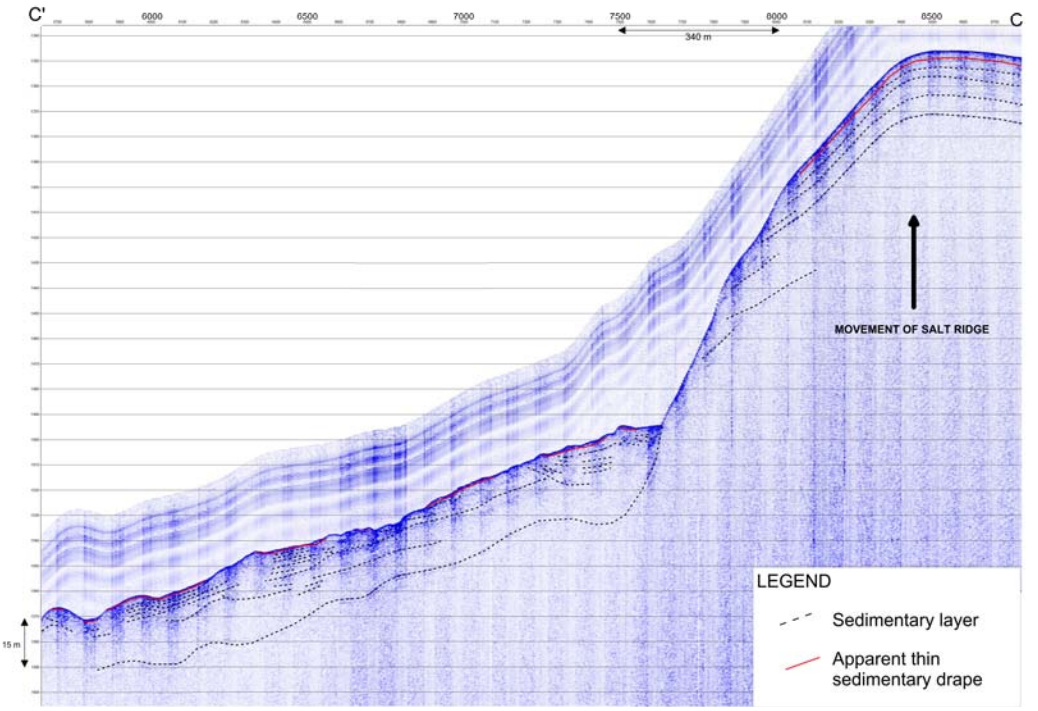

Figure 5. CHIRP profile through the upper slope

A CHIRP profile perpendicular to the line of slope is shown on Figure 6. In this example channels are incised into older slope failure deposits. Six of these deposits identified on Figure 6 are sandwiched within about 5.5 meters of stratified deposits. Assuming a sedimentation rate of 0.04 mm/year for the stratified deposits, the total age of the sedimentary column is approximately 130,000 years old and the return period of significant slope failures is about 21,000 years. In this area, the slope failure deposits have a typical (average) thickness of about 1.8 meters. There appears to be a thin drape across the surface of the profile that is no thicker than about 0.5 meters. Resolution does not permit evaluating this drape across the entire bottom of the deepest channel, but the drape can be traced far enough into the channel that it is interpreted to likely be present across the channel.

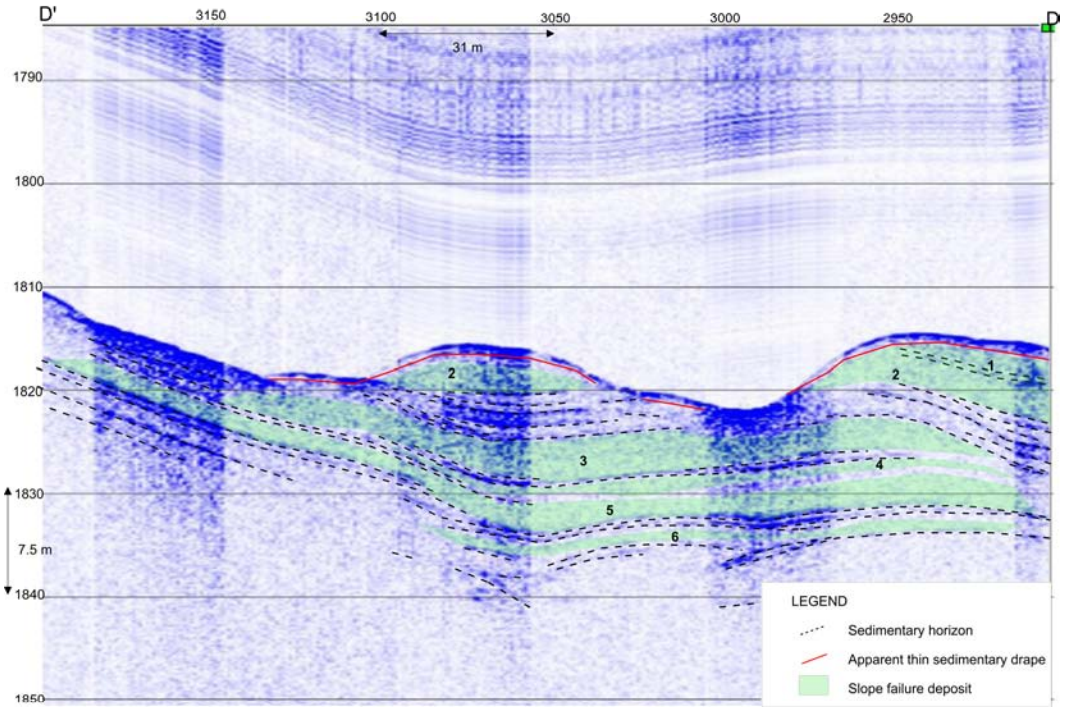

Figure 6. Transverse CHIRP profile through the upper slope

CONCLUSIONS

This paper presents the results of an interpretation of the slope failures present along the Cagliari continental slope in terms of size, age and recurrence interval. The results in terms of minimum age of last movement are considered to be reasonably accurate, but it should be noted that return periods were calculated on the basis of the estimated observation period divided by number of events. The observation period assumes that the sedimentation rate over the past ~10,000 years is applicable for older sediments, which is most likely not the case given past variations in climate, sea level and sediment input. Nevertheless, these assumptions are considered to be reasonable for an engineering risk assessment in the sense that there is uncertainty in our estimates of return period, but we can be sure that the return periods are greater than 10,000 years.

The lower slope presents several erosion channels and slope deposits covered by a minimum of 0.5 m of sedimentary drape, indicating that the failures are older than 10,000 years. The nominal return period of slides in this area appears to be of the order of 15,000 to 30,000 years.

The upper slope is the most active section of the Cagliari slope even if a thin sedimentary drape is interpreted to be present across the entire upper slope. The worst case in terms of the size of the flows is shown in Figure 6 where slope failure deposits have a thickness ~ 2 meters and a return period of about 20,000 years was estimated.

C^{14} age dating indicates that the seafloor surface along the Cagliari slope is about 1000 years old, whereas surface samples collected farther offshore from the abyssal plain show a contemporary surface. The most conservative assumption of

this phenomenon is that erosive processes, such as low intensity turbidity or hyperpycnal flows, have removed approximately 4 cm of sediments. Given the limited thickness of missing sediment, there is no indication of removal by more energetic events such as large turbidity scour or slope failures.

Several observations were made during the interpretation of the Cagliari slope that has potential application for other studies in similar areas. Firstly, it is critical that the subsurface investigation includes a program to obtain the age of sediment at varying depths to be able to calculate site-specific sedimentation rates. For this investigation a sedimentation rate of 0.04 mm/yr was calculated, which is equivalent to saying that the past 10,000 years of slope history is documented in the top 40 cm of sediment. This explains why ancient seafloor scarps might appear modern, but stretches the resolution of the CHIRP profiles.

Another observation from this study is that to interpret the age of last movement and recurrence intervals of the slope failures along a sediment starved slope, it is best to study the toes of the steep slopes where slope failure deposits can be identified within stratified sediments. In this case, layer thickness resolution was not adequate to characterize the upper scarps, so it was necessary to develop an alternate method of interpretation.

Finally, for this study multibeam bathymetric data of varying sounding density were utilized to define the seafloor morphology of slope failures, and sub-bottom profiles with different resolutions were necessary to interpret the dynamic processes that have shaped the slope. For the mutibeam bathymetry, initial surface vessel reconnaissance data acquired at 10 x 10 meter bin sounding density, enabled an essential wide area assessment of dominant seabed morphology and features of geohazard interest. Subsequent near seabed AUV data at 1 x 1 meter bin density permitted identification of detail seabed texture, highly characteristic of seabed sediment movement and shallow buried flow deposits. High-resolution AUV based CHIRP profiles were necessary to be able to interpret the characteristics of the slope failures predicted from the bathymetry data, but the deeper Airgun profiles were necessary to be able to understand that much of the morphology of the slope is due to salt tectonics.

ACKNOWLEDGMENTS

The authors would like to express their gratitude to GALSI SpA of Milan (Sara.Milanesi@galsi.it), for granting the use of the data for publication.

REFERENCES

Carminati, A., C. Doglioni, B. Gelabert, G. F. Panza, R. B. Raykova, E. Roca, F. Sabat and D. Scrocca (2009). “Evolution of the Western Mediterranean”, *in Bally A.W. and Roberts D. (eds), Principles of Phanerozoic Regional Geology, 18.4.1 (in press).*

Rosenbaum, G., K. Regenauer-Lieb and R. Weinberg (2005). “Continental Extension: from Core Complexes to Rigid Block Faulting”, *Geology*, 33(7), 609–612, doi: 10.1130/G21477.1

Delineation of slope profiles from Digital Elevation Models for landslide hazard analysis

Mesut Turel[1] and J. David Frost[2]

[1]Graduate Research Assistant, School of Civil & Environmental Engineering, Georgia Institute of Technology, 210 Technology Circle, Savannah, GA 31407, USA PH (912) 966-6872; email: mesut@gatech.edu
[2]Professor, School of Civil & Environmental Engineering, Georgia Institute of Technology, 210 Technology Circle, Savannah, GA 31407, USA. email: david.frost@ce.gatech.edu

ABSTRACT

Landslides can be one of the most damaging geohazards related to earthquakes. Production of a landslide susceptibility map for a regional hazard analysis requires selection of appropriate slope mapping units. Traditionally, a one dimensional grid based approach has been used in conjunction with the infinite slope model and Newmark's method to assess the regional slope performance under earthquake loading. However, with the advent of soft computing and metamodeling techniques, relatively accurate predictions of two dimensional slope responses can be calculated for a vast number of different slope profiles with different material properties and earthquake motions. Therefore, there is a need for a customized GIS application for delineation of slope profiles from a Digital Elevation Model (DEM) to be used in landslide hazard mapping. In this paper, a hydrologic model tool that uses the principles of delineating watersheds from DEM is adopted to allow for the extraction of slope profiles. Two alternative implementation approaches are presented.

INTRODUCTION

Assessment of regional landslide hazards involves the preliminary selection of a suitable mapping unit. A mapping unit can be defined as a segment of the land surface which encloses a similar set of ground conditions which differ from the neighboring units across definable boundaries (Hansen, 1984). Different methods have been proposed for creating mapping units for landslide hazard analysis. All methods fall into one of the five groups; grid-cells, terrain units, unique-condition grids, slope units and topographic units (Carrara and Guzzetti, 1995).

For GIS-based deterministic slope stability and earthquake-induced landslide analysis, the grid-cell approach has been commonly used in conjunction with the relatively simple infinite slope model. The grid-cell approach implies the division of the study region into cells of given size and assigning values for each factor taken into consideration such as slope angle, material properties and earthquake loads. The

infinite slope model is a one-dimensional model which assumes an infinitely long planar slip surface on which a rigid slab of soil mass slides parallel to the ground surface. This method is suitable for analysis of a soil mass that overlies a sloping drainage barrier that may be bedrock or a less permeable and well compacted soil layer (Hammond et al., 1992). The infinite slope model together with Newmark's displacement analysis has been widely used to create seismic landslide susceptibility maps.

Landslide hazard analyses using the infinite slope model are applicable to shallow landslides. The infinite slope model gives reliable results in the case of surficial landslides with depth-length ratios smaller than 0.1 (Xie et al., 2003). On the other hand, the infinite slope model cannot satisfactorily analyze deep-seated, rotational failure (Luo, 2006). In reality, deep seated landslides are common and these types of landslides are a major cause of property damage and fatalities. Therefore, more accurate analyses are needed for landslide hazard mapping. In the case of deep-seated landslides, two- or three-dimensional models are required to accurately analyze both static and dynamic performance of slopes. Two-dimensional analyses are performed along the representative soil profile sections while three-dimensional analyses are performed on the entire landslide body.

Numerous analytical methods for the evaluation of 2D or 3D seismic response of slopes have been proposed and they can be divided into three main categories; stress-deformation analysis, permanent deformation analysis and pseudostatic analysis (Ambraseys and Menu, 1988;Griffiths and Prevost, 1988;Newmark, 1965). These 2D and 3D methods are rarely used in GIS-based landslide hazard zonation because they are numerically expensive compared to 1D infinite slope models. However, with the advent of soft computing methods, relatively accurate predictions of 2D or 3D slope responses can be calculated for a regional hazard zonation. Over the last few years an increasing number of researchers have been employing various soft computing methods, such as Artificial Neural Networks (Lagaros et al., 2009;Tsompanakis et al., 2009), Self-Organizing Maps (Ferentinou and Sakellariou, 2007), Support Vector Machines (Samui, 2008) for analyzing both static and seismic response of slopes. These methods can be used to predict the responses of a vast number of different slope profiles with different material properties and earthquake motions in a more computationally efficient way.

In order to integrate the soft computing methods with geographical information systems (GIS) for landslide hazard analysis, there is a need for an automatic slope profile delineation method for 2D slope analysis and an automatic slope unit delineation method for 3D slope analysis. The methods for the extraction of primary topographic attributes such as slope, aspect, curvature, flow direction are offered by standard GIS platforms. However, the methods for integrated mapping of slope units and delineation of slope profiles are yet to be developed. Typical drawbacks of GIS approaches for landslide hazard analysis such as the lack of data to characterize soil/rock properties also exist for these proposed methods.

In recent years, some researchers have used 2D and 3D slope stability methods for regional landslide hazard analysis. Xie et al. (2003) used a column-based three-dimensional limit equilibrium method to calculate static safety factors for GIS based landslide hazard assessment. Slope unit was used as the mapping unit and the

entire study area was divided into slope units using GIS-based hydrology tools. Luo (2006) used 2D slope profiles with different limit equilibrium models and Newmark's method to analyze landslides triggered by the 2001 El Salvador earthquake. Luo (2006) selected a number of slope profiles from the profiles manually created using terrain and hydrology analysis tools.

The objective of this paper is to explore alternative methodologies to delineate 2D slope profiles from a given high resolution Digital Elevation Model (DEM). Two different approaches are presented for delineation of 2D slope profiles. Both approaches use GIS-based hydrology tools.

SLOPE PROFILE DELINEATION USING HYDROLOGY TOOLS

Slope units can be obtained by dividing the terrain into hydrological regions between drainage and ridge lines (Carrara and Guzzetti, 1995). There are many techniques for automatically generating drainage and ridge line networks (Band, 1986;Jenson and Domingue, 1988). There are also several GIS-based hydrological analysis and modeling tools available on the market. In this study, Arc Hydro tool (Maidment, 2002) is employed for generating drainage and ridge lines. Arc Hydro is an ArcGIS tool to support water resources applications. It offers a consistent method for delineating watersheds from DEM. Watershed is a polygon that is used for separating neighboring drainage basins or catchments. In the hydrologic model, the watershed polygon represents the local maximum elevations or ridge lines.

In order to delineate watersheds from DEM, there are several steps that should be performed in sequential order. Operation of individual steps is not discussed here in detail. The first step is the development of a hydrologically-correct DEM, namely filling the artificial sinks which are artifacts of DEM construction. There are two key steps after the initial step. The first one is the creation of the flow direction grid. Flow direction defines the movement of water between the terrain cells. The flow direction in Arc Hydro is based entirely on topography. It uses the most basic flow algorithm called D8. From each cell, all flow is passed to one of the eight neighboring cells with the steepest downslope gradient. The second key step is to create a drainage system. Creating a drainage system is a subjective step; there can be a number of different drainage systems created using the same flow direction grid. Subsequent to the flow direction grid, a flow accumulation grid is created. A flow accumulation grid consists of grids that contain the number of upstream cells that drain thorough each cell. There are different thresholds that can be used to create drainage networks and subsequently watersheds. The threshold used in this study is the accumulation threshold. The drainage lines are defined as the connection of the cells that have higher values than a user specified threshold. The accumulation threshold has a major influence on the total number of watersheds for a particular region. The increase in the threshold number removes the lowest-order drainage segments and eliminates the small watersheds and merges them into larger watersheds. Therefore the definition of watershed requires a user involvement, where the user selects a threshold value to obtain the desired number and size of watersheds. At the end of the above mentioned steps, watershed polygons are created for a given DEM where the outline of each watershed is the ridge line.

A slope profile is a line across the ground surface largely or entirely following the direction of the true slope. In most cases, the slope profiles should be drawn between a ridge line and a drainage line in the flow direction or the steepest path of the slope surface (Luo, 2006). Ridge lines can be created using the standard watershed delineation procedure. After the initial watershed delineation procedure, two different approaches can be followed to delineate slope profiles.

The first approach involves the delineation of slope units. A flowchart of the slope unit approach is shown in Figure 1a. A slope unit can be defined as one slope part (right/left part) of a watershed. In addition to the normal watershed polygons delineated from normal DEM, inverse watershed polygons are delineated from an inverse DEM. Inverse DEM can be created using the raster calculator in ArcGIS, wherein the high elevation values in normal DEM can be transformed to low values and low values can be transformed to high values. Inverse DEM is then fed to ArcHydro and inverse watersheds are delineated. Afterwards slope units are generated by dissolving and merging watersheds from both normal and inverse DEMs (see Figure 1b). Flat areas which have slope values smaller than 10^{o} are deleted from slope unit polygons. For the next step, using the flow direction grid created from normal DEM and ArcGIS spatial analyst zonal statistics tool, each slope unit is assigned an average flow direction angle (see Figure 1c). A buffer analysis is performed with a negative buffer distance (1 meter) on normal watershed polygons in order to avoid problems at the boundary of two neighboring normal watersheds. A code is written in Visual Basic, to create points in user defined intervals along the ridge lines (buffered normal watershed polygon) (see Figure 1d). Each ridge point is then assigned the average flow direction angle of the slope unit which they are in. Again using a Visual Basic code, a routine is executed in which a polyline is drawn from each ridge point in the direction of the flow direction angle and the polyline is extended to the border of the slope unit (see Figure 1e). Finally, slope profile polylines are converted to three dimensional polylines by interpolating elevations from normal DEM. These 3D polylines are used to calculate the geometric properties of the slope profiles, such as slope angle, height and shape. Using the slope unit approach, most of the areas inside the slope units are uniformly covered by slope profile polylines. However, the slope profile polylines are drawn using the average flow direction angle for the whole slope unit therefore they don't necessarily represent true slope.

The second approach does not involve slope units therefore there is no need for using an inverse DEM. A flowchart of the steepest descent method is shown in Figure 2a. In the process of delineating watersheds from normal DEM, a drainage network is also created (see Figure 2b). This drainage network can be used as drainage lines when drawing slope profile polylines from ridge lines to drainage lines. Watershed polygon buffers are created in a similar fashion with the first approach. The flat areas are deleted from the watershed polygons. Ridge points are created along the watershed polygons. A Visual Basic code is written which draws steepest descent polylines from each point until they intersect a drainage line or a flat area (see Figure 2c). These polylines may or may not be straight lines depending on the topography. However, slope profile is defined as a straight line. Therefore, a straight polyline is drawn from each ridge point to the point where the steepest

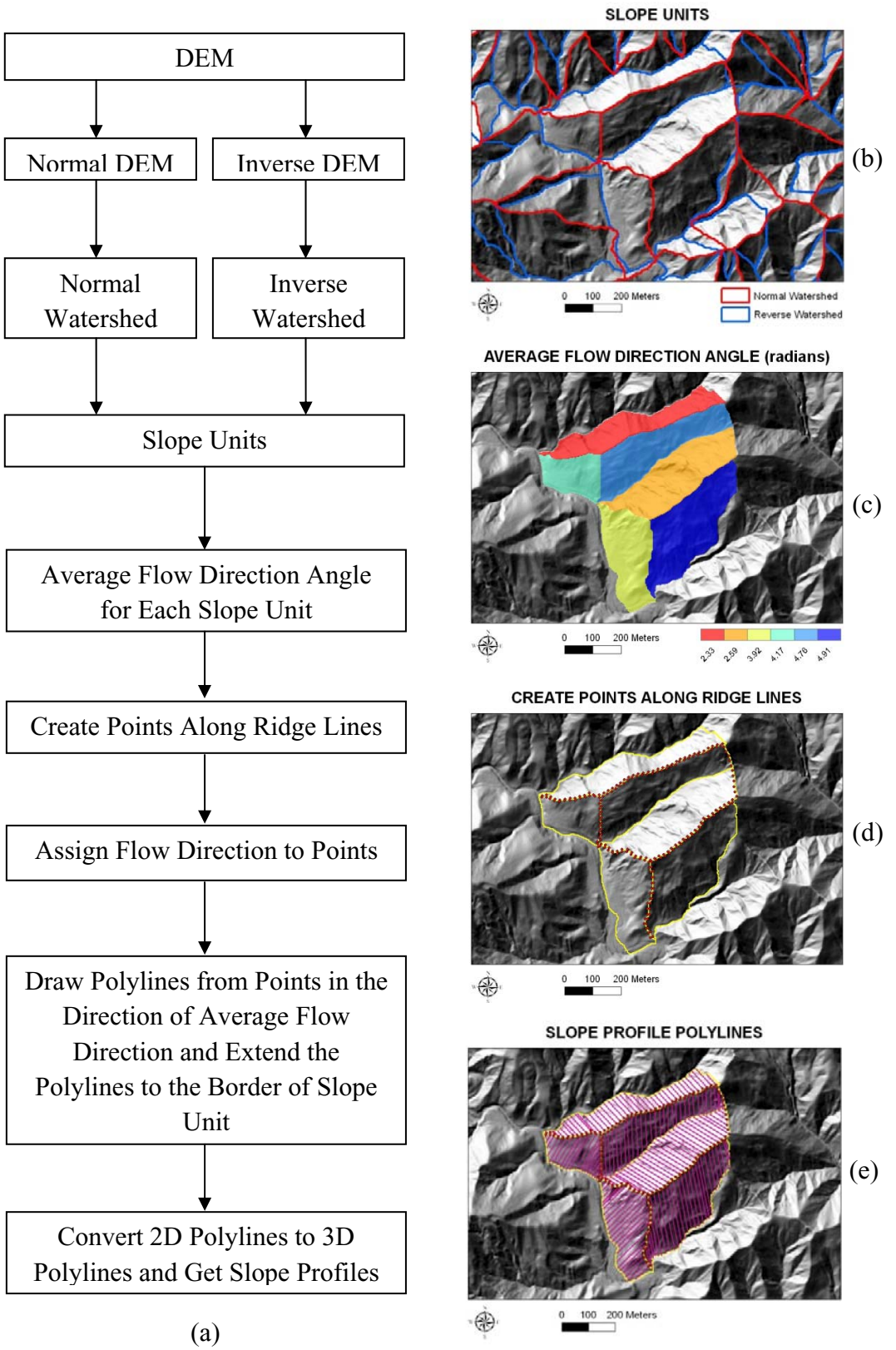

Figure 1. Slope Profile Delineation – Slope Unit Approach

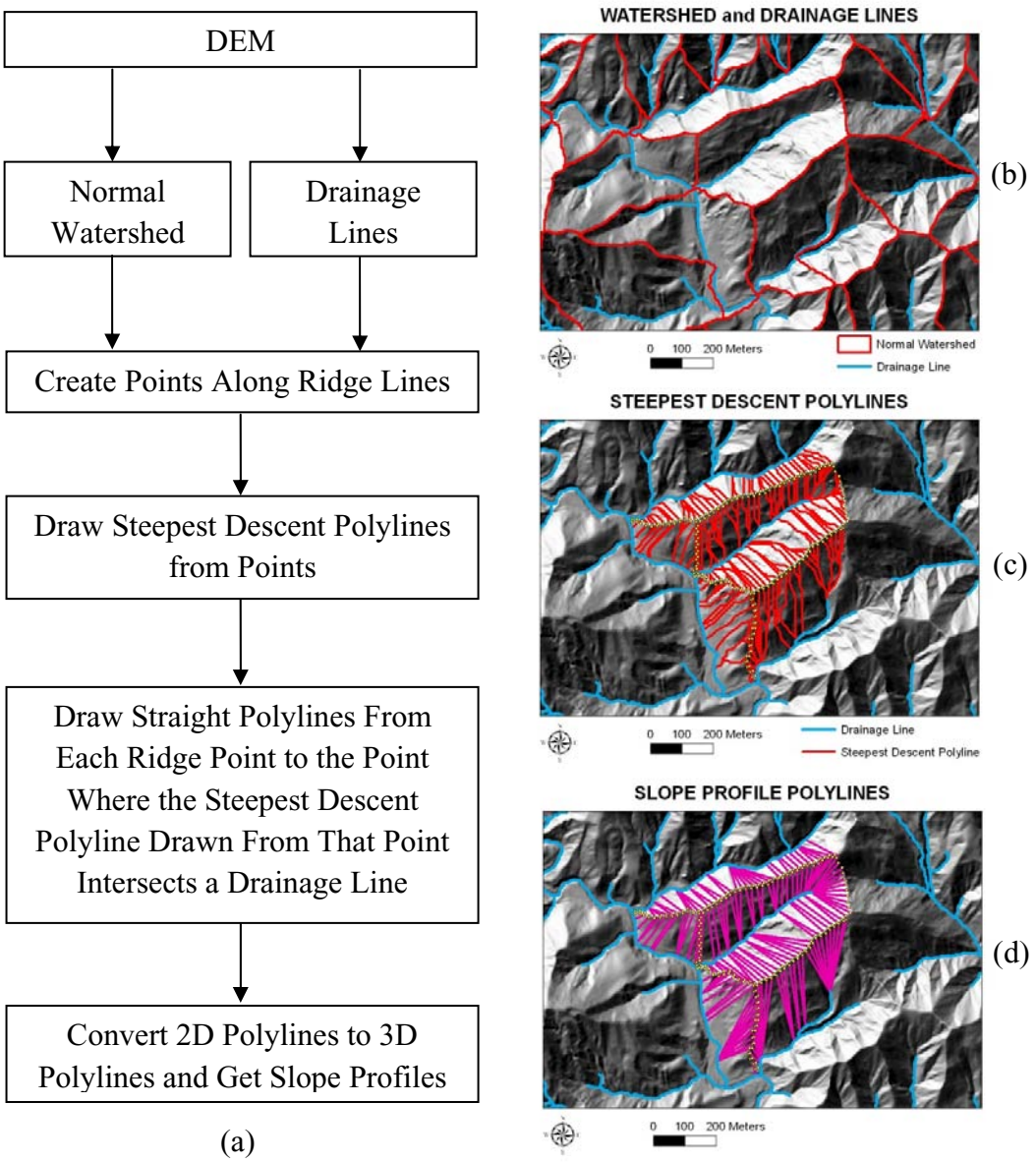

Figure 2. Slope Profile Delineation – Steepest Descent Approach

polyline drawn from that point intersects a drainage line or a flat area (see Figure 2d). Finally, slope profile polylines are converted to three dimensional polylines so that the geometric properties of the profiles can be determined. Using the second approach, some of the areas aren't covered because the slope profile polylines follow the true slope from each point.

CONCLUSION

There is a need for a method to delineate two dimensional slope profiles from a given Digital Elevation Model. These slope profiles can be used for regional landslide hazard analysis. Two alternative approaches are presented herein for delineation of slope profiles from DEMs. Both approaches use GIS-based hydrology tools to extract ridge and drainage lines. Each approach has its advantages and drawbacks. For landscapes where significant topographic irregularities exist in a given slope unit, the slope unit approach would yield a better area coverage of slope profile polylines. On the other hand, steepest descent approach may yield less area coverage because the polylines follow the direction of the true slope instead of an assigned constant direction angle. Computationally, the steepest descent method is more advantageous than the slope unit method because in the steepest descent method there is no need to delineate inverse watersheds. However, the two approaches can also be used together. The slope profiles obtained from each approach can be combined together to take into account different possible slope profiles.

REFERENCES

Ambraseys, N. N., and Menu, J. M. (1988). "Earthquake-Induced Ground Displacements." *Earthquake Eng Struc*, 16(7), 985-1006.

Band, L. E. (1986). "Topographic Partition of Watersheds with Digital Elevation Models." *Water Resour Res*, 22(1), 15-24.

Carrara, A., and Guzzetti, F. (1995). "Geographical information systems in assessing natural hazards."

Ferentinou, M. D., and Sakellariou, M. G. (2007). "Computational intelligence tools for the prediction of slope performance." *Comput Geotech*, 34(5), 362-384.

Griffiths, D. V., and Prevost, J. H. (1988). "Two-Dimensional and 3-Dimensional Dynamic Finite-Element Analyses of the Long-Valley Dam." *Geotechnique*, 38(3), 367-388.

Hammond, C. J., Prellwitz, R. W., and Miller, S. M. (1992). "Landslide Hazard Assessment Using Monte-Carlo Simulation." *Proceedings of the Sixth International Symposium On Landslides*, D. H. Bell, ed., Balkema, Chrischurch, New Zealand, 959-964.

Hansen, A. (1984). "Lanslide Hazard Analysis." *Slope instability*, D. Brunsden, and D. B. Prior, eds., Wiley, New York, 523-602.

Jenson, S. K., and Domingue, J. O. (1988). "Extracting Topographic Structure from Digital Elevation Data for Geographic Information-System Analysis." *Photogramm Eng Rem S*, 54(11), 1593-1600.

Lagaros, N. D., Tsompanakis, Y., Psarropoulos, P. N., and Georgopoulos, E. C. (2009). "Computationally efficient seismic fragility analysis of geostructures." *Comput Struct*, 87(19-20), 1195-1203.

Luo, H. (2006). "GIS-Based Approaches to Slope Stability Analysis and Earthquake-Induced Landslide Hazard Zonation." Doctor of Philosophy, University of Alaska Fairbanks, Fairbanks, Alaska.

Maidment, D. R. (2002). *Arc Hydro : GIS for water resources*, ESRI Press, Redlands, Calif.

Newmark, N. M. (1965). "Effects of Earthquakes on Dams and Embankments." *Geotechnique*, 15(2), 139.

Samui, P. (2008). "Slope stability analysis: a support vector machine approach." *Environ Geol*, 56(2), 255-267.

Tsompanakis, Y., Lagaros, N. D., Psarropoulos, P. N., and Georgopoulos, E. C. (2009). "Simulating the seismic response of embankments via artificial neural networks." *Adv Eng Softw*, 40(8), 640-651.

Xie, M. W., Esaki, T., Zhou, G. Y., and Mitani, Y. (2003). "Geographic information systems-based three-dimensional critical slope stability analysis and landslide hazard assessment." *J Geotech Geoenviron*, 129(12), 1109-1118.

Establishing Confidence in Surface Wave Determined Soil Profiles

P. Michaels[1], Member ASCE

[1]Center for Geophysical Investigation of the Shallow Subsurface, Boise State University, 1910 University Drive, Boise, Idaho 83725-1535 , PH (208) 426-1929; FAX (208) 426-1631; email: pm@cgiss.boisestate.edu

ABSTRACT

Surface waves can be used to determine the shear velocity profile from the ground surface to some depth limited by the spectral band of the seismic source. A number of factors influence the uncertainties of the determined profile. The field acquisition factors include the deployment geometry of geophones, the spectral characteristics of the geophones, recording instruments, and seismic source. A key data processing factor is the determination of a dispersion curve from the field recordings. Finally, there are important choices in conducting the inversion of the dispersion curve which leads to the final soil profile. Even if the field factors and acquired data are fixed, determination of the dispersion and the inversion decisions will have a strong influence on the final result. Different engineers will make different decisions, and a range of soil profiles can be expected. Assessment of this variability was the goal of the Surface Wave Benchmark Study sponsored by the Geophysical Engineering Committee of ASCE. Participants were invited to analyze as little or as much of the data as they wished. This paper documents one participant's analysis of a selected set of the data taken at a single location. A key finding documents how a lack of low frequency content limits the maximum depth for which one can have confidence in the soil profile.

INTRODUCTION

The near surface shear-wave velocity profile is of interest in a number of applications. These include earthquake soil dynamics, the response of foundations and structures to both earthquakes and vibrations due to construction, pile driving, and blasting. The method has also been applied to the evaluation of pavements. Frequently employed non-invasive surface wave methods used to determine the shear-wave soil profile include Spectral Analysis of Surface Waves (SASW) and Multichannel Analysis of Surface Waves (MASW) (Penumadu & Park, 2005). There has been interest in evaluating these non-invasive techniques (Tran & Hiltunen, 2008). Additionally, the uncertainty in the analysis and the impact on application risks has begun to be considered (Hiltunen *et al.* , 2006; Marosi & Hiltunen, 2004). Typical practice involves the acquisition of Rayleigh wave data using a surface seismic source and geophone receiver deployment. Recordings are digitally processed to yield phase velocity dispersion, and the dispersion curves are inverted to a 1-D shear-velocity profile (Yuan &

Nazarian, 1993). The depths penetrated depend on the recorded signal spectrum. Recent advances include an effort to extend the low frequency content of data to increase the maximum depth for which reliable results can be obtained (Rosenblad *et al.* , 2008; Rosenblad & Li, 2009).

In an attempt to further understand the variable factors leading to risk assessment and uncertainty with surface wave methods, the Geophysical Engineering Committee (GEC) of the ASCE Geo-Institute sponsored a benchmark study. Practitioners were invited analyze sets of surface wave data collected at the National Geotechnical Experimentation Site (NGES) at Texas A&M University (TAMU). This paper is one of those investigations into the risk assessment of surface wave analysis.

SELECTED DATA

This paper focuses on one of the data sets, test site 98-220. These data were collected for Multi-channel Analysis of Surface Waves (MASW). The active source was a sledge hammer located at station 78, 6.10 meters (20 ft) from the nearest geophone. Geophones were placed 0.6096 meters (2 ft) apart extending away from the source to a maximum offset of 43.28 meters (142 ft). The 62 geophones had a natural frequency of 4.5 Hz and were oriented vertically. The data were digitized at a .00078125 second sample interval, anti-alias filter of 500 Hz. The pre-trigger delay was about 10% of the 12.8 second record length. A selected portion of the data are shown in Figure 1. Figure 2 shows an all-pole estimate of the available signal spectrum.

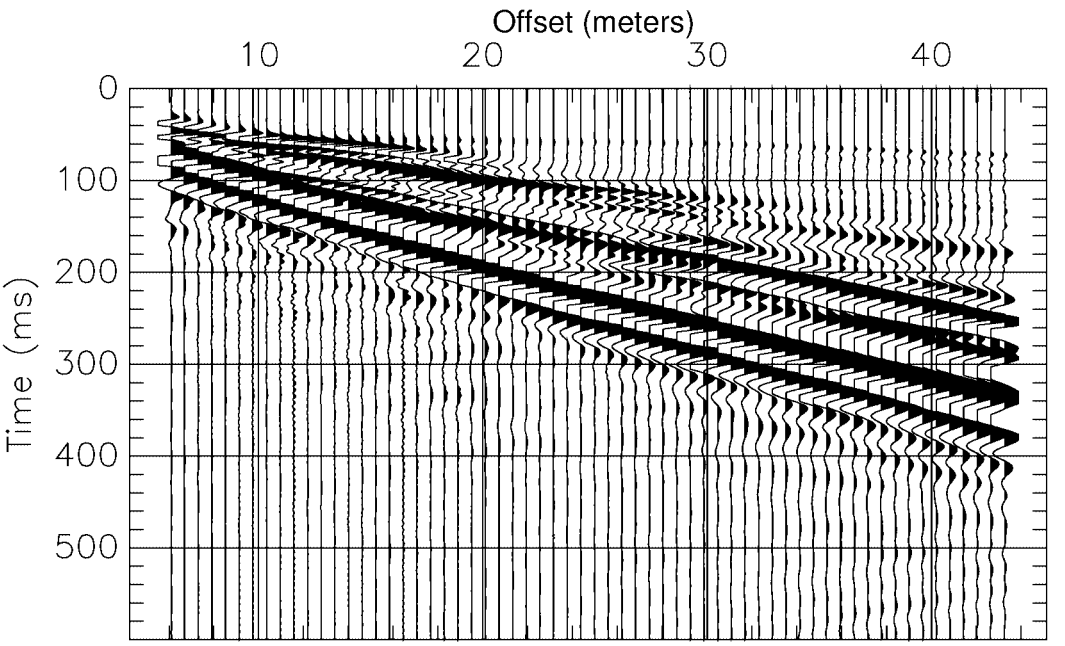

Figure 1. Selected portion of data. Each geophone channel has been rescaled by its norm to remove amplitude decay with offset and improve visibility of the waveforms.

To determine the available signal spectrum, a Yule-Walker all pole spectrum (Karl, 1989) was computed from the average of the auto-correlations (all 62 channels).

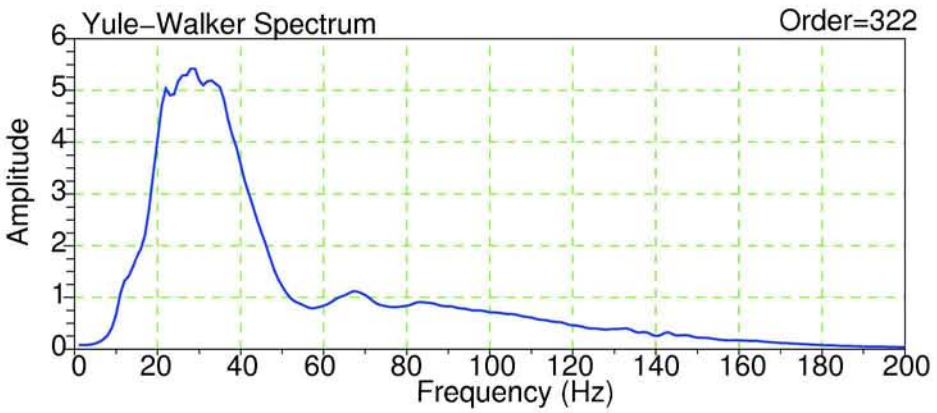

Figure 2. All pole Yule-Walker spectrum from averaged autocorrelations of the test data. Small DC shifts were removed if present prior to computation of the spectrum. The signal band from 5 Hz to 47 Hz was chosen for analysis.

Initial signal analysis showed that the fundamental mode dominated the dispersion at frequencies below about 50 Hz. The signal band from 5 to 47 Hz was chosen for analysis. This choice was limited by the decision to analyze only the fundamental mode, and use as low a frequency as could be justified by the spectral estimate. The lowest available frequency sets the maximum effective depth of exploration.

DISPERSION AND MASW ANALYSIS

The dispersion was computed in the time domain by beam steering data filtered at 1 Hz intervals (Michaels, 1998). Error bars were computed from the measured signal shifts about the best fit velocity trend and are shown for 95% confidence in Figure 3-(a) (assumes normal distribution). The measured phase velocity dispersion is plotted as distinct symbols with error bars that often fall within the plot symbol except at the low frequencies where signal strength is vanishing. The solution model is shown in Figure 3-(b). The parameterization of the soil profile is described in the next section. There are 5 control points. The depth of exploration varies with frequency as can be seen in Figure 3-(c). Only the lowest frequencies probe to a depth of 30 meters, and those results are the most uncertain due to the lack of low-frequency signal strength.

Parameterization of Soil Profile Many investigators parameterize the soil profile as a number of layers, each layer having a shear velocity as an unknown parameter. In such a choice, it has been shown that the uncertainty in shear wave velocity increases with the number of layers (Hiltunen *et al.* , 2006). That is not the case with the parameterization here. Parameters are control point pairs of depth and shear velocity. Linear interpolation of elastic moduli is performed in constant layer steps. In Figure 3, the step size is 0.2 meters. The mass density, ρ, of the soil has been held constant. At each control point, shear modulus is determined by

$$G = {V_s}^2 \cdot \rho \quad ,$$

where G is shear modulus and V_s is the control shear velocity. Poisson's ratio, $\sigma = 1/3$, is also held constant to determine P-wave velocity and Lame's constant, λ. Thus,

$$V_p = V_s \cdot \sqrt{\frac{2(1-\sigma)}{(1-2\sigma)}} \quad ,$$

and

$$\lambda = \left({V_p}^2 - 2{V_s}^2\right)\rho \quad .$$

Linear interpolation between control points of G, λ, and ρ assigns values of V_s, V_p, and ρ for each layer step. Thus, the number of parameters is greatly reduced to about twice the number of control points. Fixing parameters at the top and bottom reduces the number of unknowns further.

The inversion algorithm iteratively solves for depth and shear velocity of each control point so as to minimize the difference between the observed and computed dispersion curve. The inversion method chosen was truncated singular value decomposition (Menke, 1989). Only the 5 largest singular values were employed in this paper. The surface control point was fixed at zero depth, velocity free to vary. The bottom depth control point was fixed at 16 meters, but velocity was free to vary at that point. Properties remain constant below the bottom control point.

The results of the inversion shown in Figure 3 are tabulated in Table 1. The confidence limits determined in measuring the dispersion curve were used to compute the confidence limits of the solution parameters (non-fixed control depths and shear velocity, V_s, at all depth points). The mapping of uncertainties from measured to computed quantities is done by the formula (Menke, 1989)

$$C_m = H \cdot C_d \cdot H^T \quad ,$$

where C_m is the covariance matrix for solved parameters, H is the generalized inverse, and C_d is the covariance matrix of the data. Variance estimates were then scaled for 95% confidence assuming normally distributed errors. The covariance matrix for the dispersion measurements, C_d, was diagonal with the variance for each measured phase velocity on the diagonal. These diagonal elements correspond to the error bars of Figure 3-(a).

Table 1. Inversion Results with 95% Confidence Limits. Note that there are two degrees of freedom (depth, velocity) of uncertainty for each control point in the solution.

Depth (m)	V_s (m/s)	V_p (m/s)	ρ (kg/m^3)
0 $\pm$0.000	128.344 $\pm$0.656	256.689	2169.
1.664 $\pm$0.189	153.404 $\pm$0.085	306.808	2169.
3.184 $\pm$0.980	217.274 $\pm$0.326	434.548	2169.
6.596 $\pm$1.350	165.638 $\pm$0.326	331.276	2169.
16.000 $\pm$0.000	387.437 $\pm$1.969	774.873	2169.

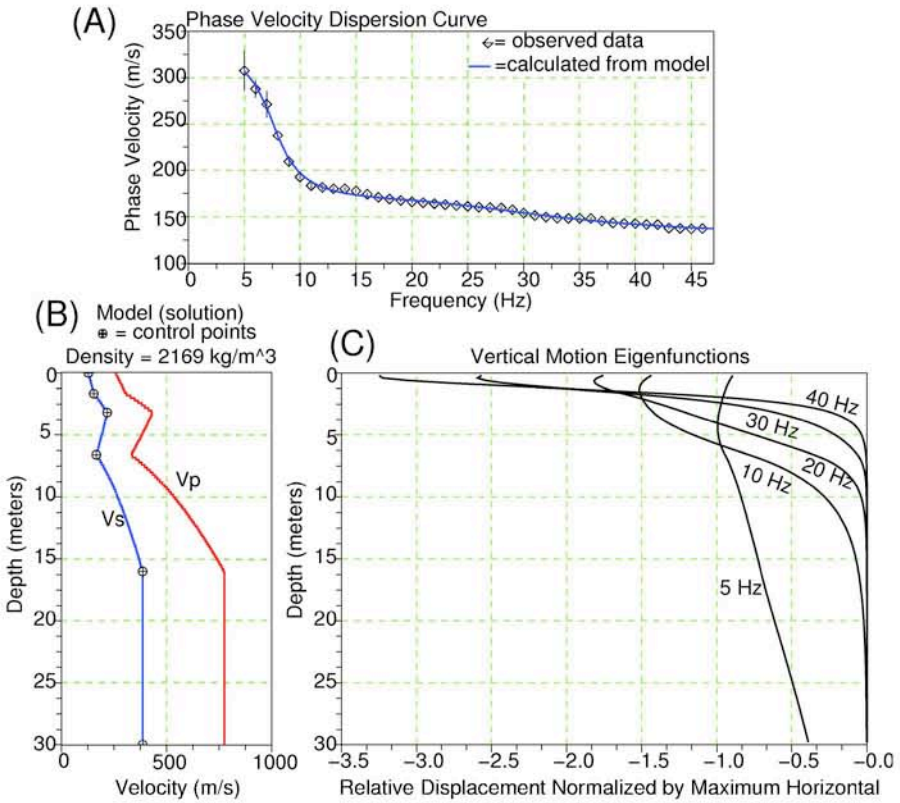

Figure 3. (A) Dispersion curve showing observed data and calculated curve from the solution. (B) The solution shear wave velocity showing the 5 control points. Linear interpolation of elastic moduli between control step wise by 0.2 meter layers. Poisson's ratio set at $\sigma = 1/3$, density held constant at $\rho = 2169kg/m^3$. (C) Vertical-motion eigenfunctions for frequencies shown, normalized by horizontal motion at each frequency. High frequencies sense shallow soil, low frequencies probe deeper. The majority of the motion is above 16 meters depth.

ALTERNATIVE FAST AND SLOW SOLUTIONS

To better estimate the risk of soil characterization by surface waves, the 95% confidence limits of Table 1 were applied to determine a maximally fast and slow alternative to the best solution. The fast alternative was formed by shifting the control depths toward the surface by the 95% error limits, and increasing the shear-wave velocity by the corresponding error limits. The slow alternative was formed by increasing the depth control points and decreasing the shear-wave velocities. The results are shown in Figure 4. Note that there are two degrees of freedom (velocity and depth) for each error estimate.

RISK ANALYSIS

The context for this paper is the problem of estimating the shear-wave velocity profile in the first 30 meters. Research on characteristics important to earthquake engineering have resulted in changes to building codes (Dobry *et al.* , 2000). Current

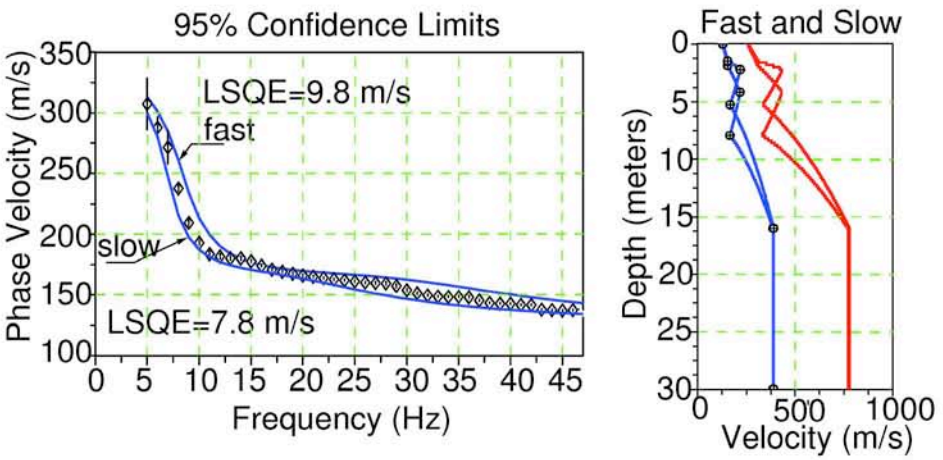

Figure 4. The computed dispersion from the two alternative fast and slow limiting cases. Since there are two degrees of freedom (depth and velocity) at each control point, the Table 1 uncertainties are larger than might be perceived by a casual observer.

building codes refer to this as Vs_{30}. It is computed for a layered profile by formula 36-1 of UBC-97, for example.

$$Vs_{30} = \frac{\sum Z_i}{\sum (Z_i / Vs_i)}$$

Uncertainties in measured dispersion do not affect Vs_{30} enough to change the soil profile type which is *SD*, *stiff soil*. The definition of *stiff soil* is $[180 < Vs_{30} < 360]\, m/s$. Table 2 summarizes the results of the computation for the solution and the two limiting cases.

Table 2. Shear velocity, Vs_{30}, from alternative soil profiles.

Case	Vs_{30}
slow	270 m/s
solution	277 m/s
fast	286 m/s

SITE AMPLIFICATION

To evaluate the possible risks associated with Vs_{30} in the context of site amplification, we can consider the amplification which would result from bedrock shear velocities that might underlie the soil profile. Figure 5 shows two cases for bedrock, $Vs_{br} = 387.5 m/s$ and $Vs_{br} = 1000 m/s$. The slower case corresponds to the fastest velocity determined from the surface wave data.

As can be seen from Figure 5, the faster bedrock assumption produces over twice as much amplification. This then begs the following question. Could the surface wave data sense such a faster bedrock at 30 meters depth, were it to be present? To evaluate this question, we can recompute the dispersion with the faster bedrock below the

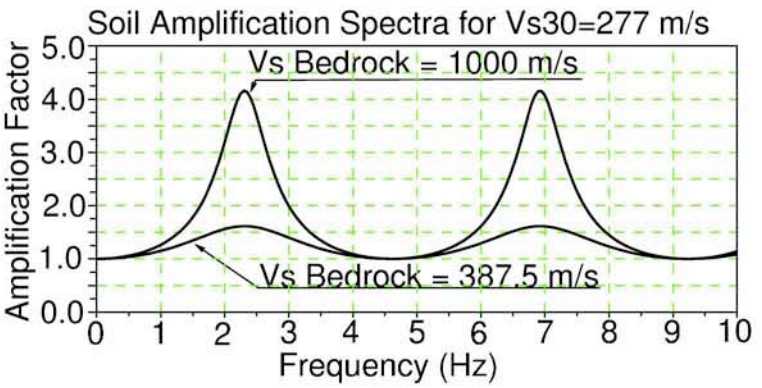

Figure 5. The site amplification factors for two possible bedrock velocities below a 30 meter soil equivalent to the Vs_{30} determined from the surface wave data. No damping other than radiation damping is assumed.

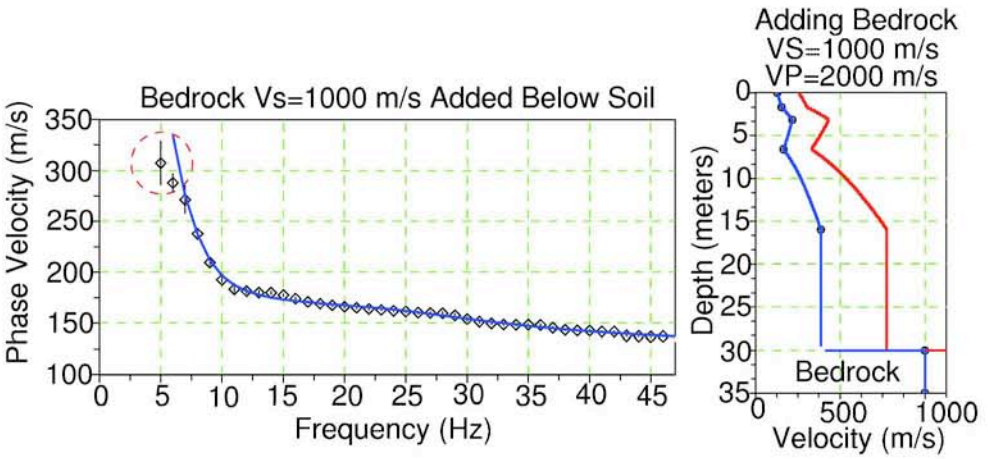

Figure 6. The addition of the faster bedrock only changes the computed dispersion at frequencies below 7 Hz (see dashed circle). This illustrates the value of low frequencies in sensing the soil profile at a depth of 30 meters.

soil model of Figure 3. The result is shown in Figure 6. Without the two measurements at 5 and 6 Hz, the surface wave data would not be able to detect the faster bedrock at a 30 meter depth, were it present.

CONCLUSIONS

The shear-velocity soil profile may be parameterized in different ways. Here, this was done by step wise linear interpolation of the elastic moduli between sparse control points. Confidence limits were computed for both depth and velocity. The sledge hammer source just barely investigates depths down to 30 meters as is evident from the motion-stress eigenfunctions (see Figure 3-(c)) and the circled points in Figure 6. Low frequencies (below 7 Hz) are needed to reduce the risk in estimating soil amplification.

ACKNOWLEDGMENTS

The author expresses his thanks to the Geophysical Engineering Committee of the ASCE GeoInstitute for conducting this benchmark testing, and to National Science Foundation and Texas A&M University for their respective roles in supporting the data acquisition.

REFERENCES

Dobry, R., Borcherdt, R. D., Crouse, C. B., Idriss, I. M., Joyner, W. B., Martin, G. R., Power, M. S., Rinne, E. E., & Seed, R. B. (2000). New Site Coefficients and Site Classification System Used in Recent Building Seismic Code Provisions. *Earthquake Spectra*, 16(1), 41–67.

Hiltunen, Dennis R., Marosi, Karen T., & Gardner, Jason M. (2006). Methodologies to Assess SASW Shear Wave Velocity Uncertainty. *Pages 94–94 of:* DeGroot, Don J., DeJong, Jason T., Frost, J. David, & Baise, Laurie G. (eds), *GeoCongress 2006: Geotechnical Engineering in the Information Technology Age*, vol. 187. ASCE.

Karl, J. H. (1989). *An Introduction to Digital Signal Processing*. Academic Press.

Marosi, Karen T., & Hiltunen, Dennis R. (2004). Characterization of Spectral Analysis of Surface Waves Shear Wave Velocity Measurement Uncertainty. *Journal of Geotechnical and Geoenvironmental Engineering*, 130(10), 1034–1041.

Menke, W. (1989). *Geophysical data analysis, discrete inverse theory*. Academic Press. San Diego 289pgs.

Michaels, P. (1998). In situ determination of soil stiffness and damping. *Journal of Geotechnical and Geoenvironmental Engineering*, 124(8), 709–719.

Penumadu, Dayakar, & Park, Choon B. (2005). Multichannel Analysis of Surface Wave (MASW) Method for Geotechnical Site Characterization. vol. 158. ASCE.

Rosenblad, Brent L., & Li, Jianhua. (2009). Performance of Active and Passive Methods for Measuring Low-Frequency Surface Wave Dispersion Curves. *Journal of Geotechnical and Geoenvironmental Engineering*, 135(10), 1419–1428.

Rosenblad, Brent L., Stokoe, Kenneth H., II, Li, Jianhua, Wilder, Brad, & Menq, Farn-Yuh. (2008). Deep Shear Wave Velocity Profiling of Poorly Characterized Soils Using the NEES Low-Frequency Vibrator. vol. 318. ASCE.

Tran, Khiem T., & Hiltunen, Dennis R. (2008). A Comparison of Shear Wave Velocity Profiles from SASW, MASW, and ReMi Techniques. vol. 318. ASCE.

Yuan, Deren, & Nazarian, Soheil. (1993). Automated Surface Wave Method: Inversion Technique. *Journal of Geotechnical Engineering*, 119(7), 1112–1126.

Surface Wave Benchmarking Exercise: Methodologies, Results and Uncertainties

B.R. Cox[1], A.M. ASCE and C.M. Wood[2], S.M. ASCE

[1]University of Arkansas, Assistant Professor, Dept of Civil Engineering, 4190 Bell Engineering Center Fayetteville, AR 72701, USA, tel: 479-575-6027, brcox@uark.edu

[2] University of Arkansas, Graduate Student, Dept of Civil Engineering, 4190 Bell Engineering Center Fayetteville, AR 72701, USA, tel: 479-879-5297, cmwood@uark.edu

ABSTRACT

This paper details the methodologies, results, and uncertainties involved in analyzing three sets of data for the Surface Wave Benchmarking Symposium. Each set of surface wave data was analyzed independently (blindly) and without prior knowledge of subsurface conditions. Both intra-method uncertainty and inter-method variability (bias) are discussed. SASW dispersion data were obtained using the phase unwrapping method, and then a full wave-field (effective mode) forward modeling algorithm available in the software WinSASW was used to determine the shear wave velocity (Vs) profile. MASW dispersion data were obtained using the frequency domain beamformer method (FDBM), wherein data from each available source offset distance were combined to form a composite dispersion curve with estimated uncertainty. A fundamental mode, least squares inversion was then used to determine the MASW Vs profiles. ReMi dispersion data were obtained using a slowness-frequency (p-f) transform. A fundamental mode forward modeling algorithm in the SeisOpt ReMi software was used to determine the Vs profiles. In general, the Vs profiles from all methods were most similar near the surface and varied by as much as 30% at depth, yielding Vs30 values that were within 25%.

INTRODUCTION

Surface wave methods have exponentially increased in use over the past decade. Generally speaking, the three most popular methods are Spectral Analysis of Surface Waves (SASW), Multi-channel Analysis of Surface Waves (MASW), and Refraction Microtremor (ReMi). However, there are many different data collection procedures, dispersion analysis schemes (e.g. phase unwrapping, linear regression of phase angles, f-k transform, p-f transforms, Park transform, beamformers, weighted linear regression of phase offsets, etc.), and inversion/forward modeling methods (e.g. stiffness matrix, propagator matrix, full wavefield, least squares, simulated annealing, neural networks, etc.) that can be used to obtain a shear wave velocity (Vs) profile for a site (Nazarian 2010). At simple, normally dispersive sites, these varied methodologies often yield similar dispersion curves and Vs profiles. However, occasionally these methods can have significant inter-method variability, typically depending on the complexity of the site.

This paper details the methodologies, results, and uncertainties involved in analyzing three sets of data (SASW, MASW, and ReMi) for the Surface Wave Benchmarking Symposium. For this exercise, a common researcher (Hiltunen) collected surface wave data with variable receiver locations from 0 to 400 ft (122 m) along a linear array at the National Geotechnical Experimental site at Texas A & M University. The data was then distributed to interested parties in the surface wave community to analyze using any desired methodology.

The SASW data was collected from two separate arrays called SASW61 and SASW128 using the common receiver midpoint geometry. Six receiver spacings from 1.22 m (4 ft) to 37.2 m (122 ft) were used with both forward and reverse source locations. Both a sledgehammer and a vibroseis were used as sources during SASW testing. The MASW data was collected from two separate arrays called MASW0-122 and MASW98-220 using 62 receivers equally spaced at 0.61 m (2 ft). A sledgehammer was used to generate surface waves at source-to-first receiver offsets of 3.05, 6.10, 9.15, 12.2, 15.25 m (10, 20, 30, 40, and 50 ft). The ReMi data was collected from one array called ReMi0-310 using 32 receivers equally spaced at 3.05 m (10 ft). Twenty six (26) separate time windows were recorded for ReMi analysis: the first 20 were passive noise records, and the last 6 were records with a person jogging next to the array providing active energy.

DATA ANALYSIS

The surface wave data from all five array locations (2 for SASW, 2 for MASW, and 1 for ReMi) were analyzed to obtain dispersion curves and Vs profiles for the site. Each set of surface wave data was analyzed independently (blindly) and without prior knowledge of the subsurface conditions. When fitting the experimental dispersion curves, Poisson's ratio was assumed to be 0.3 for the entire soil profile, expect for the active MASW results, where the depth to the water table was identified through P-wave refraction analysis of the data. The density of individual soil layers was assumed to increase as subsurface stiffness increased. The maximum depth of the Vs profiles was always set equal to ½ the maximum resolvable experimental wavelength, and the thickness of the first layer in each Vs profile was always greater than or equal to ½ the minimum experimental wavelength resolved for each method.

SASW Results. The SASW data from each array was analyzed using the phase unwrapping method. Individual experimental dispersion curves for each receiver spacing were generated using both the forward and reverse phase data. Portions of the phase data with low coherence, irregular phase (i.e. reverse phase, false cycles), or near-field waves that had propagated less than ½ a wavelength were "masked" (removed). Composite dispersion curves (Figures 1a and 2a) were then generated from the phase information from all receiver spacings for a given array. The experimental dispersion curves from both SASW arrays have a minimum wavelength of approximately 1 m and a maximum wavelength of approximately 75 m, with SASW61 having a slightly shorter maximum wavelength. Overall, each dispersion curve shows normal scatter and good agreement between individual receiver spacings.

Phase velocities calculated using the phase unwrapping method represent apparent velocities, which are the superposition of both fundamental and higher mode surface waves along with body waves (Gucunski and Woods 1992). Consequently, a fundamental mode solution is not ideal to develop the forward model for SASW data. A more appropriate solution is the "3-D" forward model in the software WinSASW, which uses the superposed-mode dynamic stiffness matrix method (Joh 1996). It considers the location of each receiver relative to the source and uses an "effective mode" solution that is a superposition of multiple surface wave modes and body waves (Roesset et al. 1991) to solve for the Vs profile. The Vs profiles for both array locations are very similar (Figures 1b and 2b), and yield identical V_{s30} values of 245 m/s.

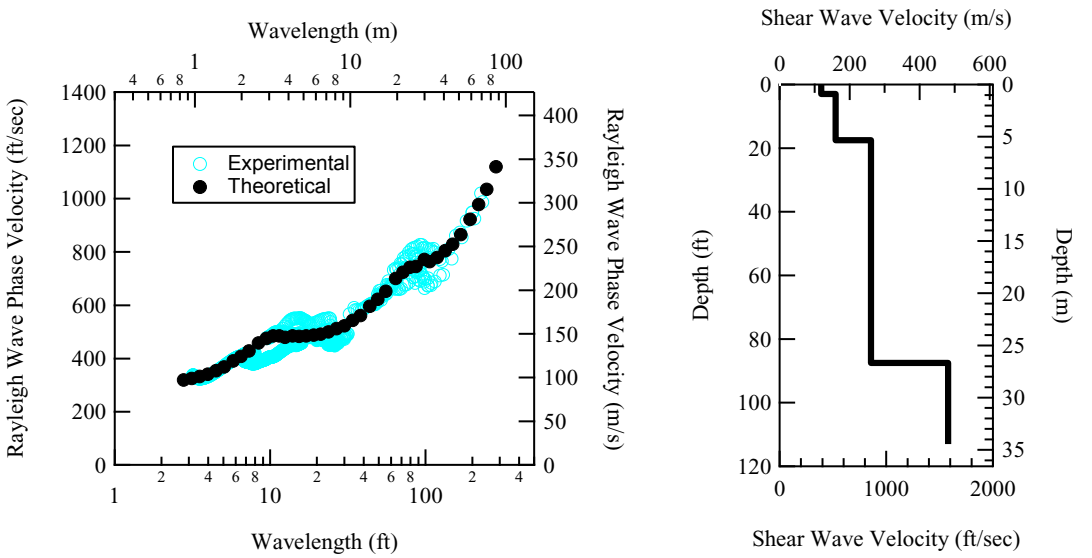

Figure 1. Dispersion curve and shear wave velocity profile for SASW61.

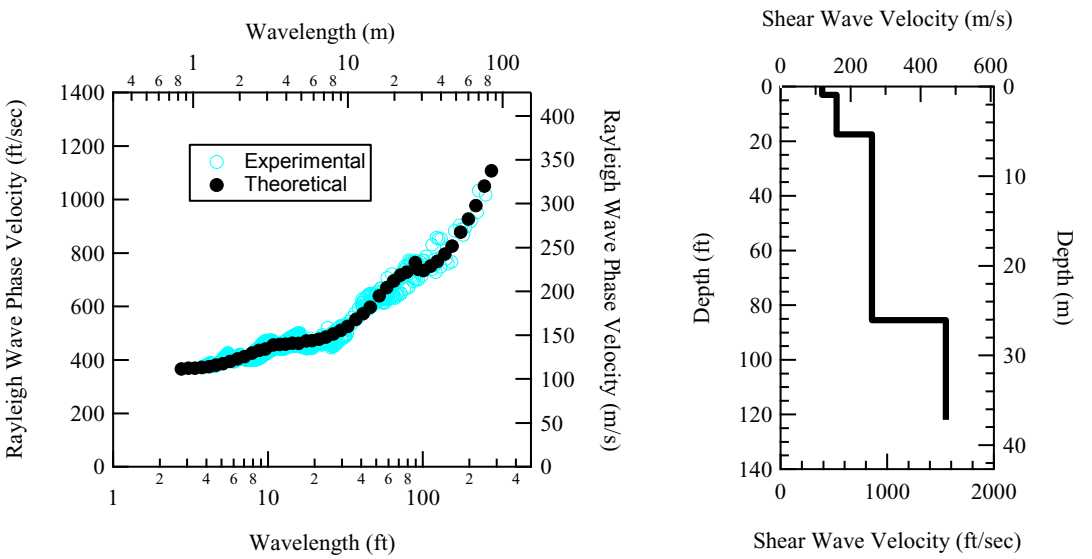

Figure 2. Dispersion curve and shear wave velocity profile for SASW128.

MASW Results. The active source MASW data from each array was analyzed using the frequency domain beamformer method (Zywicki 1999). A 3-D dispersion curve was generated for each source offset location (see Figure 3a) and the maximum spectral peak for each frequency/wavelength was picked automatically to reduce user bias. The individual dispersion curves from each source offset were then combined to form a composite dispersion curve (see Figure 3b) as a means to: (1) identify potential near-field effects, (2) aid in selecting the fundamental mode of surface wave propagation, and (3) provide a robust means for estimating dispersion uncertainty. Dispersion points clearly displaying near field effects, higher modes, or obvious inconsistencies were removed from the data. However, much of the "normal" dispersion scatter was left intact to provide a better estimate of the uncertainty in the dispersion data with increasing

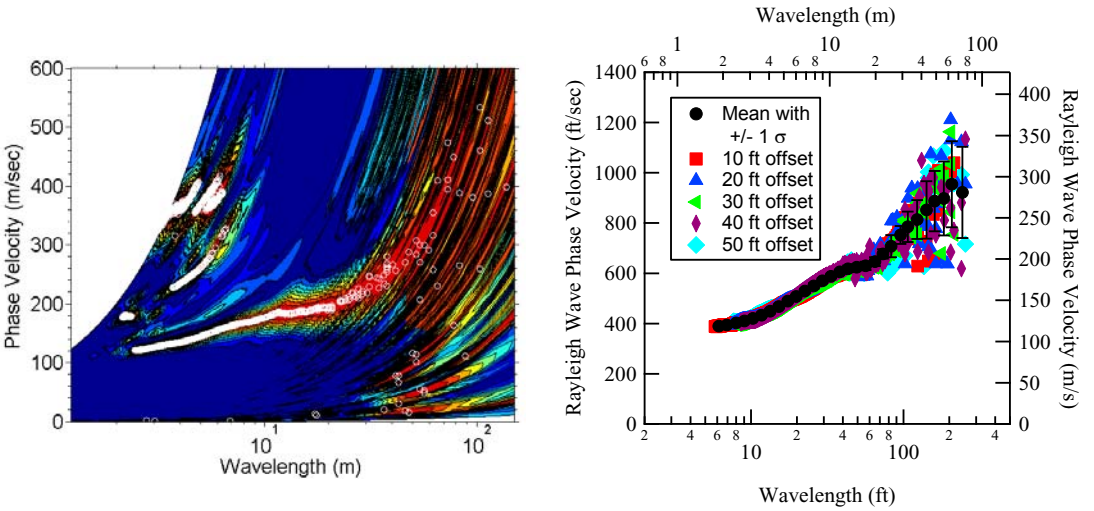

Figure 3. Example MASW 3-D experimental dispersion curve with peak values (left) and composite dispersion curve showing mean dispersion points with uncertainty (right).

wavelength. The composite experimental dispersion curve was then divided into 30 wavelength bins using a log distribution. The mean phase velocity and associated standard deviation was then calculated for each bin, resulting in an experimental dispersion curve with associated uncertainty for each array (Figures 4a and 5a). Both curves have a minimum wavelength of just less than 2 m. The standard deviation for the dispersion data starts to increase significantly for both curves at a wavelength of 30 m. One may choose to limit the maximum useable experimental wavelength based on uncertainty, or conversely, choose to accept the increasing uncertainty and account for it in the forward analysis with a range of Vs profiles.

A fundamental mode, least squares inversion was used to fit the MASW experimental dispersion curves. In addition to the mean Vs profile, an upper and lower bound Vs profile were generated (Figures 4b and 5b) by fitting the +/- 1 σ dispersion curves as a way to account for uncertainty in the Vs profile. The MASW Vs profiles for both arrays are very similar to a depth of 15 m, and indicate little variability between the mean and +/- 1 σ profiles. At depths greater than 15 meters, the +/- 1 σ profiles for MASW0-122 are within 70 m/s (19%) of the mean profile, and indicate the depth to the half space within 1 m of the mean profile. However, the depth to the half space layer for MASW98-220 occurs at a greater depth, and varies by approximately +/- 6 m from the mean profile. Below a depth of 15 m, the velocities of the +/- 1 σ profiles for MASW98-220 generally fall within 24% of the mean. The V_{s30} values for the mean and +/- 1 σ Vs profiles for MASW0-122 are 258 m/s, 282m/s, and 232 m/s, respectively. The V_{s30} values for the mean and +/- 1 σ Vs profiles for MASW98-220 are 241 m/s, 275 m/s, and 201 m/s, respectively.

ReMi Results. The ReMi (termed passive source MASW in the benchmarking study) data was analyzed using a two dimensional slowness-frequency (p-f) transform in the software SeisOpt ReMi (Optim 2006). Individual p-f images from each time window were examined and combined to form an average p-f image. The peak spectral ratio and

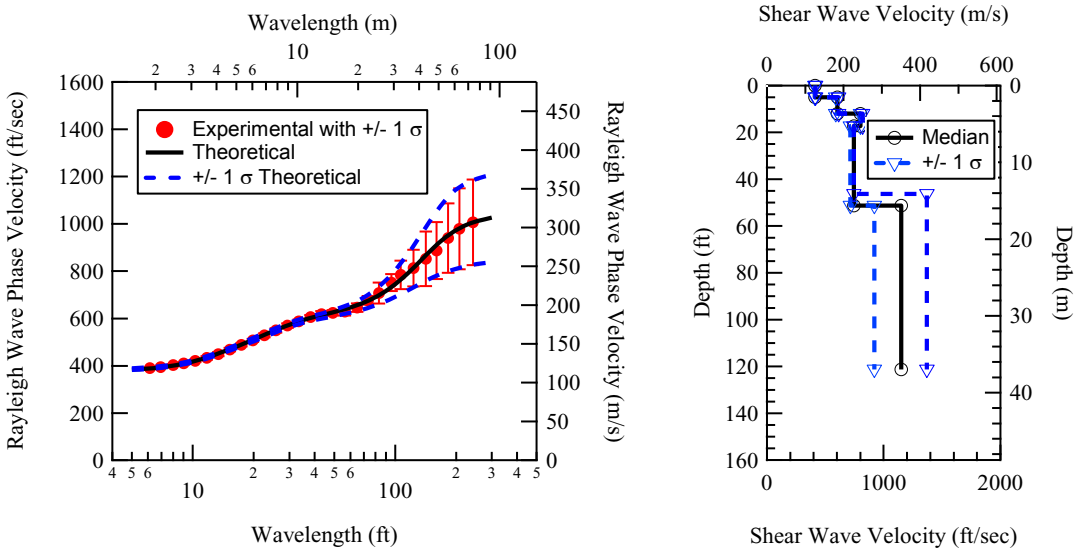

Figure 4. Dispersion curve and shear wave velocity profile for MASW0-122.

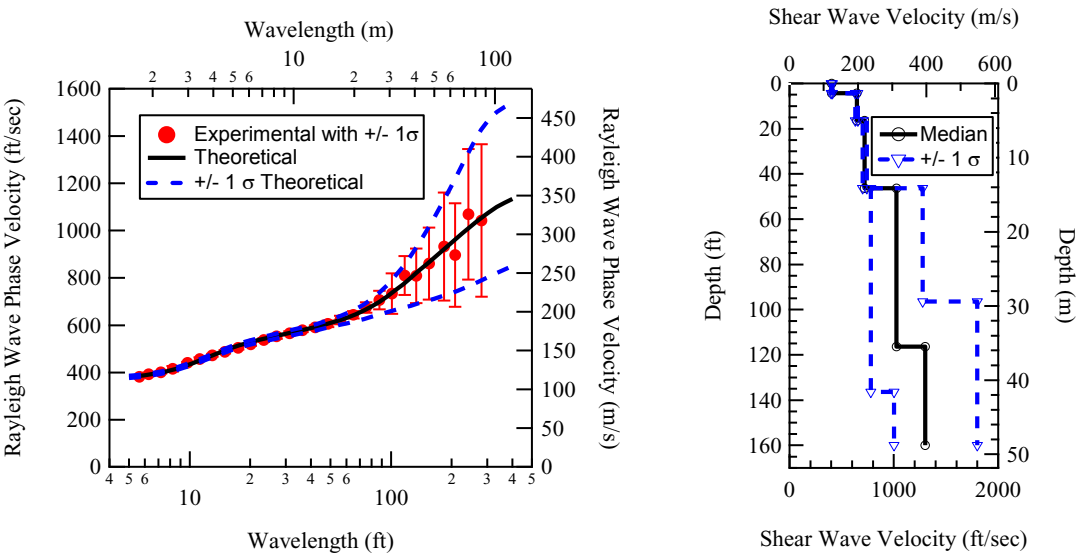

Figure 5. Dispersion curve and shear wave velocity profile for MASW98-220.

lower-bound spectral ratio were chosen by eye from two separate, average p-f images. The first p-f image was the average of time windows 2, 11, and 12, which provided good low frequency energy. The second was an average of time windows 2,11,12,22,23,24,25, and 26, which provided good high frequency energy. The dispersion picks from the high frequency and low frequency images were combined to form composite dispersion curves for the peak and lower-bound spectral ratios (see Figure 6a). Wavelengths from approximately 6 - 400 m were resolved for both the peak and lower-bound spectral ratios. The dispersion data for the peak and lower-bound spectral ratios are very similar at short wavelengths, but begin to diverge at a wavelength of approximately 40 m.

Each spectral ratio curve was fit using the fundamental mode forward modeling algorithm in the software SeisOpt ReMi (Figure 6b). The two profiles are similar to a

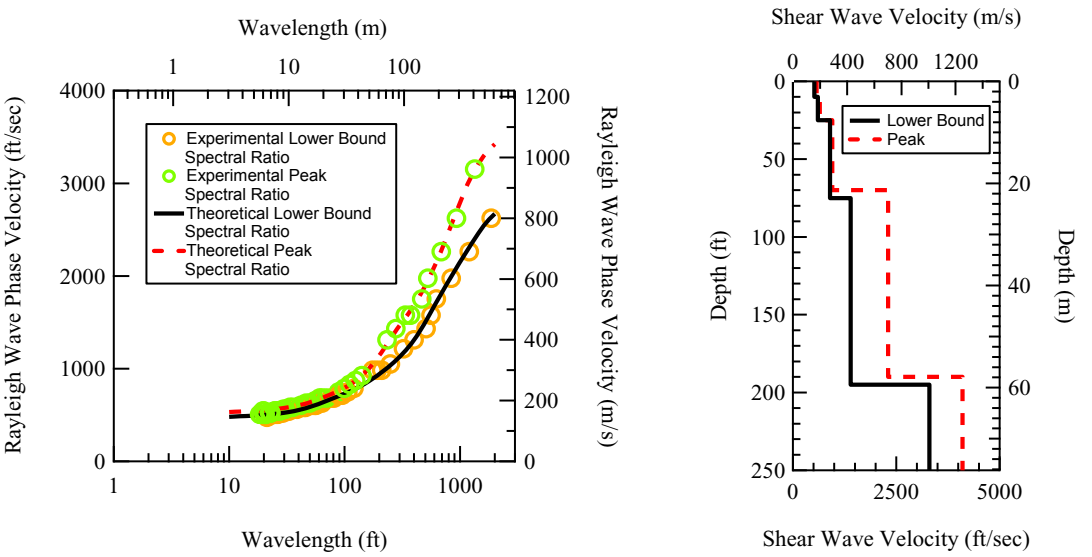

Figure 6. Dispersion curve and shear wave velocity profile for ReMi0-310.

depth of 22 m (approximately ½ the wavelength where the dispersion curves begin to deviate). Both profiles identify a stiffer layer at approximately 22 m, however, the velocities of this layer vary from 430 m/s to 700 m/s (a difference of 63%) for the lower-bound and peak spectral ratios, respectively. Additionally, a final "rock" layer was identified at approximately 60 m deep on both profiles, with velocities ranging from 1006 m/s to 1250 m/s for the lower-bound and peak spectral ratios, respectively. Theoretically, the Vs profiles could have been extended deeper based on the maximum wavelength divided by two rule-of-thumb. However, this did not seem prudent for comparison with active source methods, and furthermore the final layer shown in Figure 6b is the half-space velocity. The lower-bound and peak spectral ratio Vs profiles have V_{s30} values of 259 m/s and 302 m/s, respectively.

INTER-METHOD COMPARISONS

Comparisons between the dispersion curves and shear wave velocity profiles for each array/method are shown in Figures 7a and 7b, respectively (only the mean MASW data is presented). In general, all six dispersion curves are very similar in the region of mutual overlap, with differences in phase velocity and increased uncertainty at wavelengths greater than 40 m.

The shear wave velocity profiles for each array/method are within 12% of each other for the top 5 m of the subsurface, expect for the ReMi profile, which lacked short wavelength data and failed to resolve the 1-m thick surface layer identified on the SASW and MASW profiles. At depths greater than 5 m, the Vs profiles are generally within 20-30% of each other (neglecting the peak spectral ratio ReMi profile, which is likely the result of high apparent phase velocities from oblique wave arrivals). The SASW and lower-bound ReMi results are most similar, while the greatest differences are between the SASW and MASW profiles.

In Figure 8a, the +/- 1 σ Vs profiles for MASW98-220 are plotted with the profiles for all other arrays/methods. For depths greater than 15 m, the MASW standard

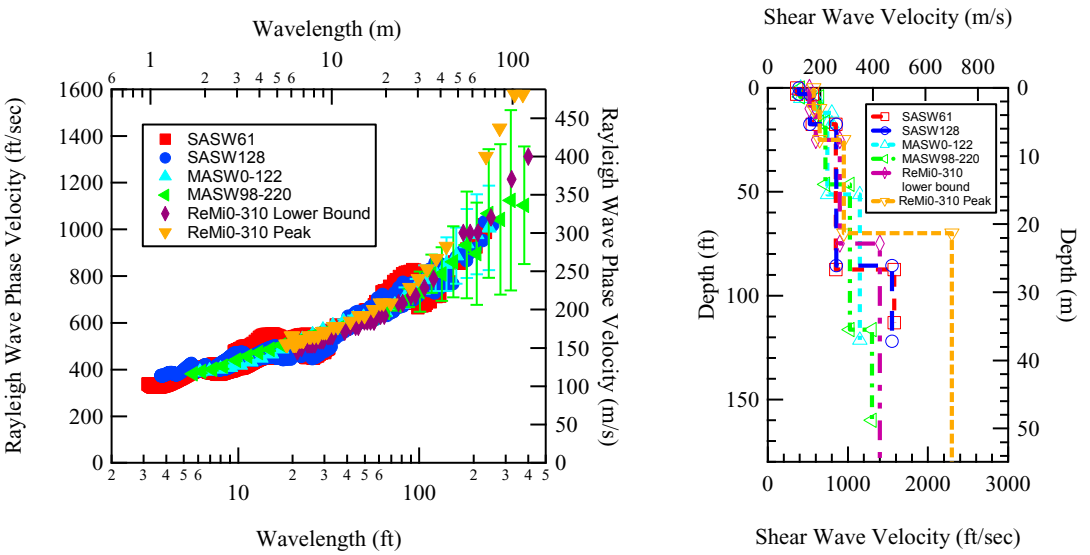

Figure 7. Dispersion curve and shear wave velocity profile comparison between methods.

error profiles virtually bracket the other shear wave velocity profiles. For this site, the MASW +/- 1 σ Vs profiles (intra-method uncertainty) seem to be a good estimate of the inter-method variability. Modified SASW and ReMi Vs profiles, which were obtained from forward analyses using the water table determined from P-wave refraction analysis of the MASW data, are presented in Figure 8b. By using a common (and presumably correct) water table at the site, the inter-method variability between all mean Vs profiles is reduced from a maximum of 30% to approximately 10%. These findings reassert the point that knowledge of the water table can be important to the accuracy of surface wave methods.

CONCLUSIONS

- Without a-priori information about the site, the Vs profiles from each of the three methods generally agreed within approximately 20-30% (inter-method variability).
- The inter-method variability was reduced to less than 10% when a common water table, obtained from P-wave refraction analysis of the MASW data, was used in the SASW and ReMi forward analyses.
- The subsurface profile of this benchmarking site is one of the simplest types of profiles (i.e. normally dispersive) to resolve with surface wave methods. Therefore, the inter-method variability noted herein is more than likely the minimum value one might expect to obtain. More complex sites with sharp velocity contrasts (i.e. soft-over-stiff profiles) or inversions will likely yield greater intra-method uncertainty and hence larger inter-method variability.
- The wavelength/depth range where the MASW data begins to exhibit significant intra-method uncertainty seems to be a good indicator of the wavelength/depth range where the results from all methods begin to deviate from one another.
- It is important for surface wave researchers to develop meaningful methods to quantify intra-method uncertainty in phase velocity estimates. Then, one may choose

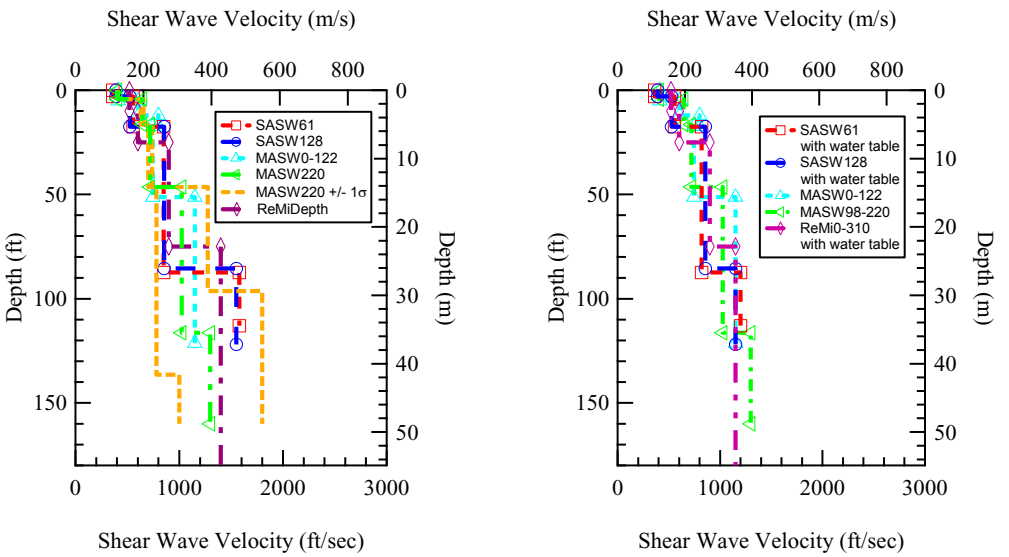

Figure 8. a) Shear wave velocity profile with +/- 1 σ profiles for MASW220 b) Shear wave velocity profiles with water table included in SASW and ReMi forward modeling analysis.

to limit the maximum useable experimental wavelength based on a predetermined uncertainty; or conversely, choose to accept the increasing uncertainty and account for it in the forward analysis with a range of Vs profiles.

REFERENCES

Gucunski N., and Woods R.D. (1992). "Numerical simulation of SASW test." *Soil Dynamics and Earthquake Eng.*, 11 (4), 213-227.

Joh, S. H., (*1996*). Advances in interpretation and analysis techniques for spectral-analysis-of-surface-waves (SASW) measurements. *Ph.D. Dissertation*, Dept. of Civil, Architectural, and Environmental Engineering, University of Texas, Austin, TX, 240 p.

Louie, J. N. (2001). "Faster, better shear wave velocity to 100 meters depth from refraction microtremor arrays." *Bulletin of Seismological Society of America,* 91 (2), 347-364.

Nazarian, S, Hiltunen, D.R., and Rix, G. L. (2010). "Surface Wave Benchmarking Symposium," *Geo-Institute ASCE.* http://saswbench.ce.ufl.edu>(Sep. 29, 2009).

Optim (2006). "User's Manual: SeisOpt® ReMi™ Version 4.0." Optim, Inc., Reno, NV. 85p.

Roesset *J.M.,* Chang D.W., Stokoe K.H. (1991). "Comparison of 2-D and 3-D models for analysis of surface wave tests." *Proc. 5th Int. Conf. on Soil Dynamic and Earthquake Engineering,* 1, Kalsruhe, 111-126.

Zywicki, D.J. (1999). Advanced signal processing methods applied to engineering analysis of seismic surface waves. *Ph.D. Dissertation*, School of Civil and Environmental Engineering, Georgia Institute of Technology, Atlanta, GA, 357 p.

Analysis of Surface Wave Benchmarking Data

Don Zhao[1]

[1]Geogiga Technology Corp, 1600, 144-4Ave SW, Calgary, Alberta, Canada T3A 5P2
PH (403)398-8098; FAX (403)269-3537; Email: don@geogiga.com

ABSTRACT

Two active and two passive MASW field datasets from the Surface Wave Benchmarking exercise are analyzed. The FK method and the SPAC method are employed to separately generate the dispersion images from active and passive surface waves. Reliable shear wave velocity profiles are obtained from the inversion of dispersion curves using the GA method. The results show the dominant energy of fundamental modes of surface waves in the dispersion images, especially at the high frequency range and the derived profiles from all dispersion curves are quite comparable. The analysis also indicates that the passive surface waves have higher resolution at the low frequency range, while active surface waves work better at the high frequency range.

INTRODUCTION

In recent years, the analysis of active and passive multi-channel array surface waves (MASW) has gained considerable attention for retrieving the subsurface shear wave velocity profiles. The active surface waves are generated by dynamic sources such as sledgehammers and vibroseis, while the passive surface waves are typically collected from cultural and natural sources. Both active and passive MASW methods involve getting the surface wave dispersion curves and then modeling the curves to obtain the corresponding shear wave velocity profiles.

In this article, the frequency-wavenumber (FK) method and the spatial auto-correlation (SPAC) method are employed to separately generate the dispersion curves from active and passive MASW field data collected at the National Geotechnical Experimental Site (NGES) at Texas A&M University (TAMU). The dispersion curves are then inverted with the genetic algorithm (GA) technique to obtain the shear wave velocity profiles. The analysis shows that the dispersion curves and the shear wave velocity profiles at the TAMU site are quite comparable.

METHODS IN DETERMINING DISPERSION CURVES

The FK method (Capon, 1969; Park, 2005) and the SPAC method (Aki, 1957; Ling, 1993; Bettig, 2001; Zhao, 2010) are commonly used in determining dispersion curves from surface wave measurements. The following sections briefly describe these two methods.

FK Method. The FK method assumes horizontal plane waves travel across the array of geophones laid out at the surface. Considering a wave with a given frequency ω, a direction of propagation θ and a velocity v, the relative arrival times are calculated at all geophone locations and the phases are shifted according to the time delays. The array output is calculated by the summation of the shifted signals in the frequency domain.

$$E(\omega, v, \theta) = \left| \sum_{ix=1}^{NX} e^{-j\phi_{ix}} R_{ix}(\omega) \right| + \left| \sum_{iy=1}^{NY} e^{-j\phi_{iy}} R_{iy}(\omega) \right| \qquad (1)$$

Where, E (ω,v,θ) is the semblance, Rix(ω)and Riy(ω) are the Fourier transformation of ith trace at the offset of xix and yiy, Φix and Φiy are the relevant phase shifts.

If the waves effectively travel with the given direction and velocity, all contributions will stack constructively, resulting in the semblance peaks. A dispersion curve is picked by analyzing the semblance spectra.

SPAC Method. The SPAC method assumes that a stochastic wavefield is stationary both in time and space. Given this assumption, the correlation of the signals recorded at a pair of geophones separated by distance r can be written:

$$\overline{\rho(\omega, r)} = J_0\left(\frac{\omega r}{c(\omega)}\right) \qquad (2)$$

Where, $\overline{\rho(\omega, r)}$ is the spatially averaged coherency, *J*o is the first order Bessel function, and c(ω) is the phase velocity at a given frequency ω. The formula shows that a dispersion curve can be generated from the observed coherencies.

ANALYSIS OF FIELD DATA

Four surface wave dispersion curves and the corresponding shear wave velocity profiles are obtained separately from two active and two passive MASW field datasets collected by Geophysical Engineering Committee for the Surface Wave Benchmarking exercise at the TAMU site.

Active MASW Data. Two active MASW field datasets are acquired from stations 122 to 0 and 98 to 220, respectively, using 62 4.5-Hz geophones at a spacing of 2 ft with a total spread of 122 ft. For each dataset, five records are collected according to five locations of the sledgehammer source at 10, 20, 30, 40, and 50 ft away from the first receiver.

For each dataset, five dispersion images are calculated from the five records with the FK method, and then the images are summed up to generate the dispersion images as shown in figures 1(a) and 1(b). The dispersion curves overlaid on the top of the dispersion images are manually picked along the peak of energy.

In figure 1(a), the valid frequency range is 5.85 ~ 43.8 Hz, while the range is 6.36~52 Hz in figure 1(b), but both dispersion images and dispersion curves are quite similar which indicates that there is no significant lateral variation between stations 122~0 and stations 98~220.

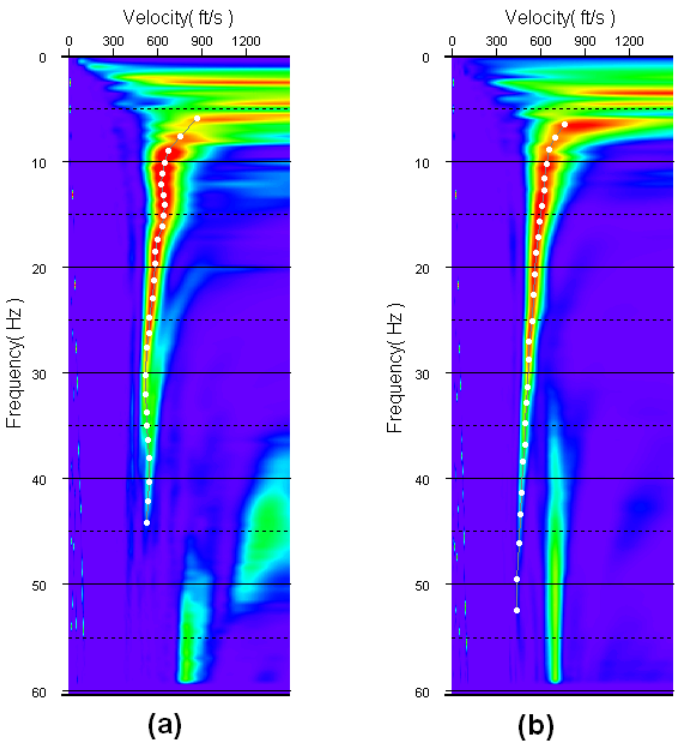

Figure 1: The dispersion images and dispersion curves derived from active MASW field datasets: stations 122 to 0 (a), and stations 98 to 220 (b).

Passive MASW Data. Two passive MASW field datasets are acquired from stations 0 to 310, using 32 4.5-Hz geophones at a spacing of 10 ft with a total spread of 310 ft. For the first passive dataset, twenty records are collected from ambient sources only; for the second passive dataset, six records are collected from ambient sources plus a

person jogging along the length of the array.

Figures 2(a) and 2(b) shows the dispersion images generated from these two passive datasets. For the first dataset, twenty dispersion images are calculated from the twenty records with the SPAC method, and then the images are summed up to generate the dispersion image; for the second dataset, the relevant six records are used to get the dispersion image with the FK method.

In figure 2(a), the dispersion curve is manually picked along the energy with low velocity. The energy with high velocity may illustrate the off line surface waves from a direction. The valid frequency range is 1.8~24 Hz.

In figure 2(b), the dispersion image shows the dominant energy of the fundamental mode of surface waves, especially at the high frequency end. The valid frequency range is 2.81~38.4 Hz and the dispersion curve is manually picked along the peak of energy.

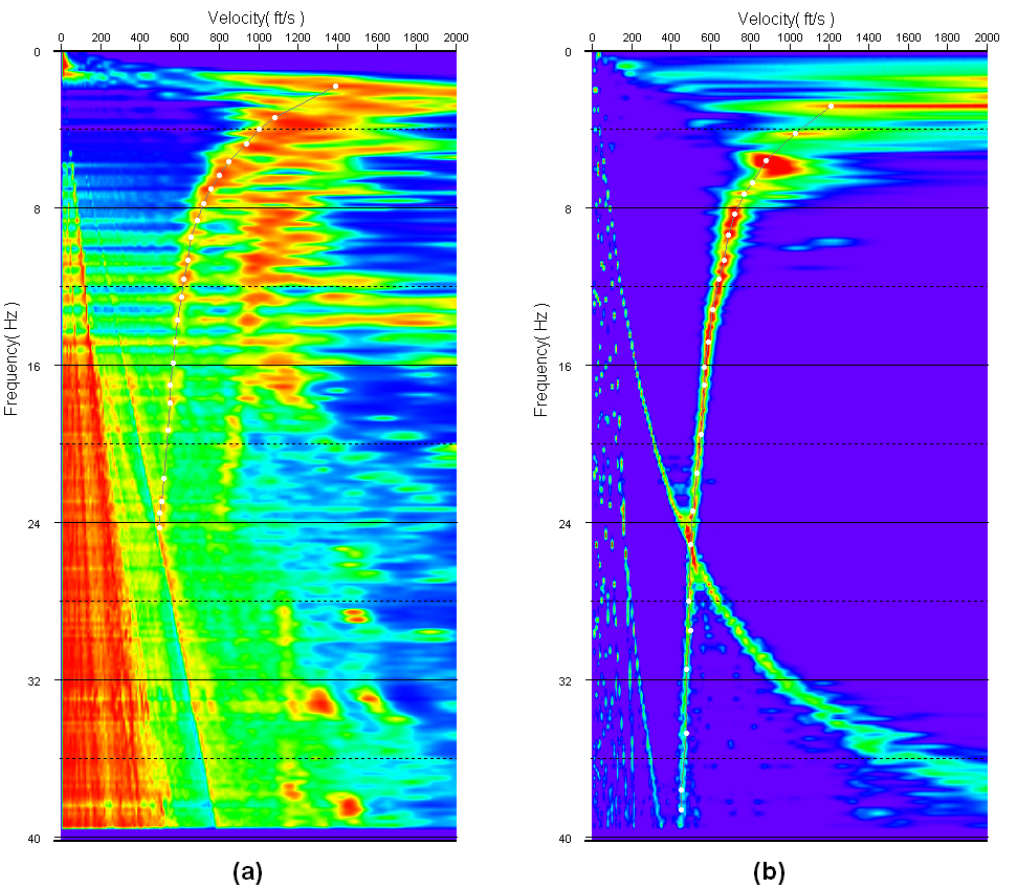

Figure 2: The dispersion images and dispersion curves derived from passive MASW field data sets from stations 0 to 310: (a) ambient sources only and (b) ambient sources plus a person jogging along the length of the array.

Shear Wave Velocity Profiles. To get the shear wave velocity profiles, the GA method is used to invert the dispersion curves. As a global nonlinear optimization method, GA can quickly obtain the reliable subsurface model. Figures 3(a) and 3(b) show the dispersion curves (velocity against wavelength) and the derived shear wave velocity profiles using the GA method. The results are quite comparable.

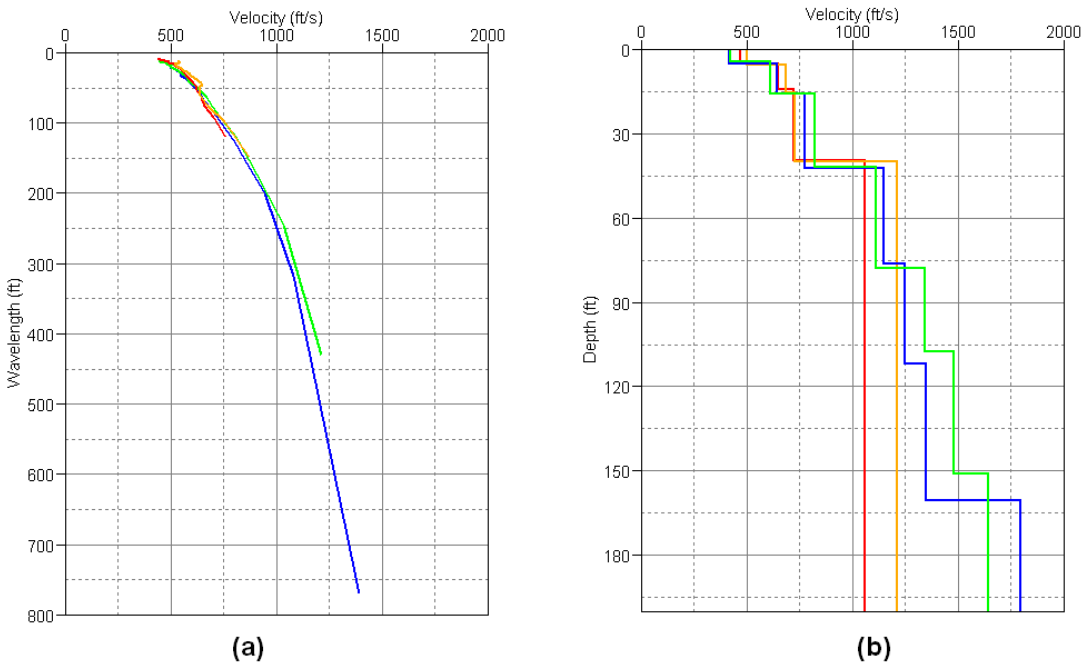

Figure 3: The dispersion curves and the derived shear wave velocity profiles: (a) disspersion curves, and (b) shear wave velocity profiles, Where, — active sources from stations 122 to 0, — active sources from stations 98 to 220, — ambient sources from stations 0 to 310, — ambient sources plus a person jogging from stations 0 to 310.

CONCLUSION

Two active and two passive MASW field datasets from the Surface Wave Benchmarking exercise are analyzed. The FK method and the SPAC method are separately used to generate the dispersion images and dispersion curves from active and passive surface waves, and the GA method is adopted to obtain the shear wave velocity profiles by modeling the dispersion curves.

The analysis shows that the passive surface waves have higher resolution at the low frequency range and the active surface waves have better resolution at the high frequency range. The derived shear wave velocity profiles from all dispersion

curves are quite comparable. The detected depth from passive surface waves is much larger than that from active surface waves.

REFERENCES

Aki, K. (1957). "Space and time spectra of stationary stochastic waves, with special reference to microtremors." *Bulletin of Earthquake Research Institute*, 35, 415-456.

Bettig B.(2001). "Analysis of dense array noise measurements using the modified spatial auto-correlation method (SPAC) – Application to the Grenoble area." *Bollettino di Geofisica Teorica ed Applicata*, 42, 281-304.

Capon, J. (1969). "High resolution frequency - wavenumber analysis." *Proceedings of the IEEE*, 57, 1408-1418.

Ling, S. (1993). "An extended use of the spatial autocorrelation method for the estimation of geological structure using microtremors." *Proc. Conf. SEGJ*, 89, 44-48.

Park, C.B. (2005). "Combined use of active and passive surface waves." *Journal of Environmental and Engineering Geophysics*, 10, 323-334.

Zhao, D. (2010). "Comparison of FK and SPAC methods in determining dispersion curves from passive surface waves." *SAGEEP*, 23, 536-542.

An Assessment of Surface Wave Techniques at the Texas A&M National Geotechnical Experimentation Site

Khiem T. Tran[1] and Dennis R. Hiltunen, M. ASCE, P.E.[2]

[1]Post-Doctoral Associate, University of Florida, Department of Civil and Coastal Engineering, 365 Weil Hall, P. O. Box 116580, Gainesville, FL 32611; ttk@ufl.edu
[2]Associate Professor, University of Florida, Department of Civil and Coastal Engineering, 365 Weil Hall, P. O. Box 116580, Gainesville, FL 32611; T: (352) 392-9537 x1468; dhilt@ce.ufl.edu

ABSTRACT

Three surface wave techniques, SASW, active MASW, and passive MASW, were conducted at the National Geotechnical Experimentation Site on the campus of Texas A&M University, and the data were made available to the professional community. Ten participants submitted results from their analyses of the collected data. The authors' analysis indicated that both the dispersion data and inverted shear wave velocity profiles were similar for the three methods, although the active MASW results typically display higher phase and shear wave velocities. For all participants, the results are generally in good agreement in an upper zone of the site profile, while the variability is typically much higher below this upper zone.

INTRODUCTION

Surface wave methods are commonly utilized for characterizing shear wave velocity profiles of geotechnical engineering sites. However, a multitude of techniques have arisen for measuring, analyzing, and interpreting surface wave test data. To date, a systematic cross comparison of these many techniques has not been accomplished on a common data set, and would be very useful to both the professional and research communities in assessing a number of issues, including the differences between various data collection and analysis techniques, differences produced by subjective judgments of individual analyzing a data set, and others.

Funded by a Geo-Institute Special Project, the Geophysical Engineering Committee organized and collected a surface wave data set via multiple field techniques, and made the data available to the community for interpretation. The data consists of raw data file records collected from two- and multi-sensor arrays using a variety of active and passive vibration sources. The data was collected at the National Geotechnical Experimentation Site (NGES) at Texas A&M University (TAMU).

The collected data was posted to a website developed specifically for the comparison study, and a public invitation was broadcasted to seek participants. Invitations requested that participants analyze the available data set using their "favorite" techniques, and post results back to the website by March 31, 2010. Ten participants analyzed the data and submitted information for the comparison. These

participants were then requested to develop and submit individual papers describing the details of their analyses.

The objective of this paper is to document the site work and data set made available to participants, and summarizes the results submitted by the ten participants. The paper will not identify the individual participants.

SURFACE WAVE TESTING

The motivation for using surface waves for soil characterization originates from the inherent nature of this kind of wave. Surface waves propagate along a free surface, so it is relatively easy to measure the associated motions, and carry the important information about the mechanical properties of the medium.

The TAMU NGES consists of an upper layer of approximately 10 m (33 ft) of medium dense, silty, fine sand followed by hard clay. The water table is approximately 5 m (16 ft) below the ground surface. Due to space limitations at the site, all the testing was conducted with 1-D receiver layouts along a straight line of nearly 400 ft. The positions were marked in one-foot increments from 0 to 400 as TestSite0_400. On the mentioned line, three kinds of tests, SASW, active MASW, and passive MASW, were conducted for comparison.

The spectral-analysis-of-surface-waves (SASW) technique was introduced by Nazarian (1984) to the engineering community. Advantages of SASW are a simple field test operation and a straightforward theory of signal analysis, but it also has some disadvantages. This method assumes that the most energetic arrivals are Rayleigh waves. When noise overwhelms the power of active sources, such as in urban areas, or where body waves are more energetic than Rayleigh waves, SASW may not yield reliable results. Also during the processing of data, this method requires some subjective judgments that can sometimes influence the final results.

SASW tests were conducted following standard common receivers midpoint (CRMP) geometry at two positions along the 1-D test line, TestSite61 and TestSite128, where the station number refers to the location of the receiver centerline. At each position, tests were conducted at several receiver spacings from 4 ft to 122 ft, and for shot positions on each side of the centerline to generate forward and reverse wave propagation. The active sources were sledgehammers for receiver spacings up to 16 ft, and a vibroseis-type vibration shaker for larger receiver spacings. The receivers were 1-Hz natural frequency velocity transducers oriented vertically.

The multi-channel analysis of active source surface waves (active MASW) technique (Park, et al. [1999]) was developed to overcome the shortcomings of SASW in the presence of noise. The most vital advantage of active MASW is that the transformed data allow identification and elimination of non-fundamental mode Rayleigh waves such as body waves, higher-mode surface waves, and other coherent noise from the analysis. As a consequence, the dispersion curve of fundamental Rayleigh waves can be picked directly from the mode-separated signal image. An additional advantage of active MASW is the speed and redundancy of the measurement process due to multi-channel recording.

The active MASW tests were conducted using 62 receivers at a spacing of 2 ft, giving a total receiver spread of 122 ft. Two receiver layouts were established at

positions TestSite122_0 and TestSite98_220. For each receiver layout, five sets of data were recorded according to five positions of the sledgehammer active source at 10, 20, 30, 40, and 50 ft away from the first receiver, and the results from five vertical blows were averaged to produce the saved record. The receivers were 4.5-Hz natural frequency velocity transducers oriented vertically.

The multi-channel analysis of passive source surface waves (passive MASW) technique uses Rayleigh surface wave energy created by ambient and cultural energy sources such as highway and railroad traffic, ocean waves, and industrial and construction activity. The most important advantage of using passive techniques is the ability to obtain low frequency surface wave energy and thus large depths of characterization with very little field effort. However, because the passive energy can arrive from any direction, this method requires more complicated treatment in data analysis than the active wave methods. Louie (2001) describes a 1-D receiver array method (commonly referred to as the ReMi method) that uses a frequency-slowness (f-p) transform to separate Rayleigh waves from other seismic arrivals, and to recognize true phase velocity against apparent velocities. Any wave that arrives obliquely to the receiver line has an apparent velocity higher than the true velocity of inline waves, and the dispersion curve is extracted by manually picking the relatively strong signals at the lowest velocities. Another more rigorous method uses 2-D receiver arrays (Park, et al. [2004]), and checks energy for different azimuths of arriving surface waves. For a given frequency and phase velocity, the energy is obtained by summing up that of all azimuths, and the energy is used to map the signal spectra for extracting dispersion curves.

The passive MASW tests recorded ambient signals from 32 receivers (4.5-Hz natural frequency velocity transducers oriented vertically) deployed at a spacing of 10 ft at station 0 to station 310. In total, 26 independent records were collected, of which 20 records contained data from ambient sources only, while 6 records contained data from ambient sources plus a person jogging along the length of the array.

UNIVERSITY OF FLORIDA ANALYSIS: PREDICTOR 1

The authors have analyzed the three data sets described above following procedures summarized in the following paragraphs. The results are identified in the summary section to follow as Predictor 1.

Dispersion Analysis. For SASW, 12 sets of data from six receiver spacings and for both forward and reverse records were used for dispersion analysis. Each set provides the dispersion relationship in a certain range of frequencies. Assembling the information from the 12 sets of data, the combined dispersion curve was derived following standard procedures (Tran [2007]), and the "supsmooth" smoothing algorithm in Mathcad was used to obtain the final dispersion curve shown in figure 1.

For the active MASW technique, many signal-processing methods have been developed to separate Rayleigh waves from other wave types and background noise, including the frequency-wavenumber (f-k), frequency-slowness (f-p), and Park, et al. transforms, and cylindrical beamformer. The traditional f-k and f-p transforms, well described by Foti (2000) and O'Neill (2003), and the Park, et al. (1998) transform, all

treat the multi-channel record as a plane wavefield, while a cylindrical beamformer (Zywicki [1999]) uses the cylindrical wave equations to transform and identify Rayleigh waves. Tran (2007) provides a detailed description of the four methods.

For active MASW, the recorded data were used to check and compare the signal processing methods, f-k, f-p, Park, et al. transform, and cylindrical beamformer. From these data it was apparent that the Park, et al. transform and the cylindrical beamformer have better imaged dispersion curves at low frequencies (<15Hz) than that of the f-k and f-p transforms (Tran [2007]). Overall, the spectrum obtained from the cylindrical beamformer was judged to provide the highest resolution, having high amplitudes and reduced side ripples over the widest range in frequencies. This can be understood that the cylindrical wavefield equations present the motions of waves created by an active point source more properly than do plane wavefield equations. The plane wavefield assumption introduces a near-field model incompatibility that can result in phase velocity estimation errors at low frequency (Zywicki [1999]). Based on these comparisons, the spectrum obtained by the cylindrical beamformer was selected for extracting the final dispersion curve for active MASW. For each receiver layout, the data recorded from the five active source locations provided similar spectra, thus the data recorded at the closest source location (10 ft) were used for the analysis herein. In addition, because they were also very similar, the two dispersion curves from TestSite122_0 and TestSite98_220 were combined, averaged, and smoothened to derive the active MASW result shown in figure 1.

For passive MASW, the data from the 1-D receiver array were analyzed using the commercial software SeisOpt ReMi that uses the Louie (2001) method of data analysis. The combined spectrum from several passive records allows obtaining the dispersion curve over a larger range of frequencies (figure 1). In fact, dispersion data was obtained for frequencies from about 5 to nearly 40 Hz.

It is observed from figure 1 that the dispersion data from all three techniques is generally in good agreement, particularly at high frequencies. However, active MASW dispersion data appear to be higher for frequencies below about 45 Hz. This is possibly caused by the model incompatibility effects noted earlier. The cylindrical beamformer more appropriately assesses the wavefield generated from a point source located a finite distance from a receiver array. However, the two-channel cross power spectrum analysis conducted in SASW, and the f-p transform used to analyze the passive MASW data, both assume plane wavefields, i.e., a source located an infinite distance from a receiver array. Zywicki (1999) has clearly demonstrated that the plane-wavefield assumption will result in underestimation of phase velocity, and the error increases as frequency decreases.

It is also observed that the active and passive MASW data are smoother than the SASW data. The ripples in the SASW data are mostly produced by slight mismatches in the combined dispersion data from multiple receiver spacings. Each spacing samples a slightly different zone of soil, and lateral variability of soil properties will produce a mismatch in dispersion data. Also, mismatches can result from improper identification of multiple Rayleigh vibration modes present in the signal. The separation of fundamental from higher modes is not possible via traditional SASW signal processing techniques.

Inversion. An inversion routine available in the SeisOpt ReMi commercial software was used to produce shear wave velocity profiles from the dispersion curves presented in figure 1. As observed from the figure, in all three cases, the inversion routine was able to match the experimental data very well, and the resulting profiles are shown in figure 2. Please note that the active and passive MASW data were analyzed separately in this case since passive signals were resolvable over a relatively wide frequency range. It is observed that the shear wave velocity profiles from the three surface wave techniques are generally in good agreement. Consistent with the dispersion curves, the SASW and passive MASW are in particularly good agreement. However, the active MASW is slightly stiffer (higher velocity) at some depths which is also consistent with the dispersion data.

SHEAR WAVE VELOCITY PROFILES: ALL PREDICTORS

As indicated above, 10 participants have chosen to submit an analysis of all or a portion of the data described herein; these participants are identified as Predictor 1 through Predictor 10. The authors have acknowledged that they are Predictor 1; the remaining nine participants have been invited to prepare a paper to discuss the details of their analyses. Each participant submitted a shear wave velocity profile resulting from their analysis for this overview, and these results are presented in figures 3 through 5 and discussed as follows.

First, four participants submitted an analysis of the SASW data and these results are shown in figure 3. As observed, the four predictions are in close agreement for depths above 10 m. Below about 10 m, there are two groups of two predictions each that present similar results.

Second, all ten participants submitted an analysis of the active MASW data, and these results are shown in figure 4. In most cases, a separate analysis was conducted of the two active MASW arrays, and these results are shown in parts 4a and 4b. As discussed above, the authors (Predictor 1) combined the data from the two arrays, and this result is shown repeated in figures 4a and 4b. As observed, the majority of the results for both arrays are in good agreement for depths up to about 15 m. However, in this upper zone, three or four of the results appear to fluctuate more erratically. Below 15 m, there is significant variability between results from the 10 participants.

Third, six participants submitted an analysis of the passive MASW data, and these results are shown in figure 5. It should be noted that figure 5 is divided into two parts, with 5b presenting a portion of the full data in 5a with an expanded scale. As with the results from SASW and active MASW, the predictions in an upper zone of the profile (approximately 20 m in this case) are generally in good agreement, while the results display considerably more variability below this upper zone. In fact, the results below 20 m are both variable and display more erratic trends with depth.

CONCLUSIONS

Based upon the results presented, the following conclusions appear to be appropriate:

- There is generally good agreement between dispersion results from SASW, active MASW, and passive MASW surface wave tests. However, the SASW and passive MASW results tend to underestimate phase velocity as compared with the active MASW results produced herein via the cylindrical beamformer.
- For all three methods, SASW, active MASW, and passive MASW, there is generally good agreement between the results submitted in an upper zone of the site profile, while the results below this upper zone are considerably more variable, and in some cases display more erratic variations with depth.

REFERENCES

Foti, S. (2000), "Multistation Methods for Geotechnical Characterization Using Surface Waves," Ph.D. Thesis, Politecnico di Torino, 229 pp.

Louie, J. N. (2001), "Faster, Better, Shear-Wave Velocity to 100 Meters Depth from Refraction Microtremor Arrays," *Bulletin of Seismological Society of America*, 91, 2, 347-364.

Nazarian, S. (1984), "In Situ Determination of Elastic Moduli of Soil Deposits and Pavement Systems by Spectral-Analysis-Of-Surface-Waves Method," Ph.D. Dissertation, The University of Texas at Austin, 453 pp.

O'Neill, A. (2003), "Full-Waveform Reflectivity for Modelling, Inversion and Appraisal of Seismic Surface Wave Dispersion in Shallow Site Investigations," Ph.D. Thesis, University of Western Australia, 420 pp.

Park, C. B., Miller, R. D., and Xia, J. (1999), "Multi-Channel Analysis of Surface Wave (MASW)," *Geophysics*, Vol. 64, No. 3, pp. 800-808.

Park, C. B., Xia, J., and Miller, R. D. (1998), "Imaging Dispersion Curves of Surface Waves on Multi-Channel Record," *Expanded Abstracts, 68th Annual Meeting of Society of Exploration Geophysicists*, pp. 1377-1380.

Park, C. B., Miller, R. D., Xia, J., and Ivanov J. (2004), "Imaging Dispersion Curves of Passive Surface Waves," *Expanded Abstracts, 74th Annual Meeting of Society of Exploration Geophysicists*, Proceedings on CD ROM.

Tran, K. T. (2007), "An Appraisal of Surface Wave Methods for Soil Characterization," M.Eng. Thesis, University of Florida, 77 pp.

Zywicki, D. J. (1999), "Advanced Signal Processing Methods Applied to Engineering Analysis of Seismic Surface Waves," Ph.D. Thesis, Georgia Institute of Technology, 357 pp.

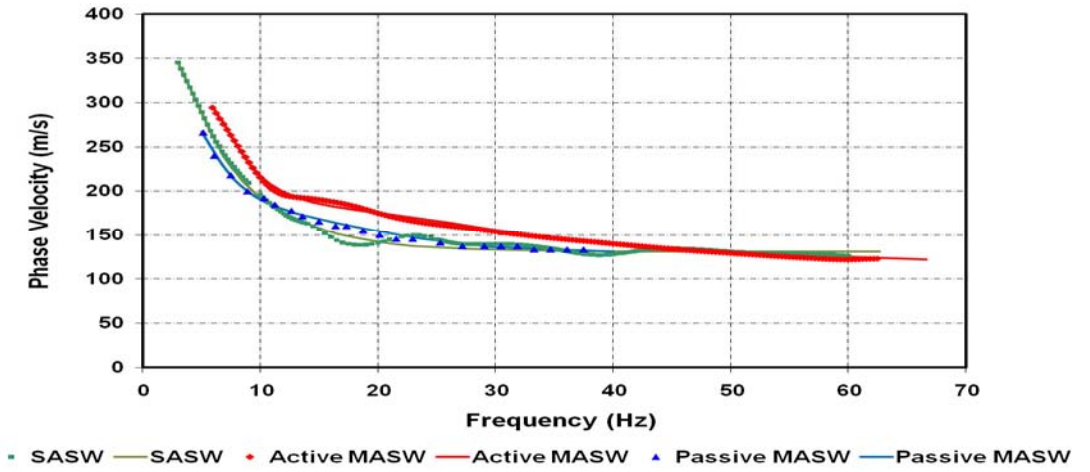

Figure 1. Dispersion curves for three techniques (data points from experiment and smooth curves from inversion model).

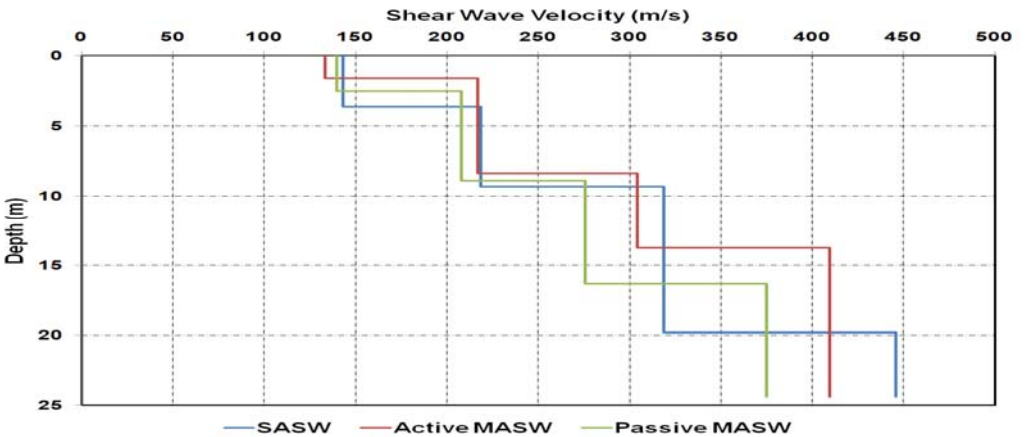

Figure 2. Shear wave velocity profiles for three techniques.

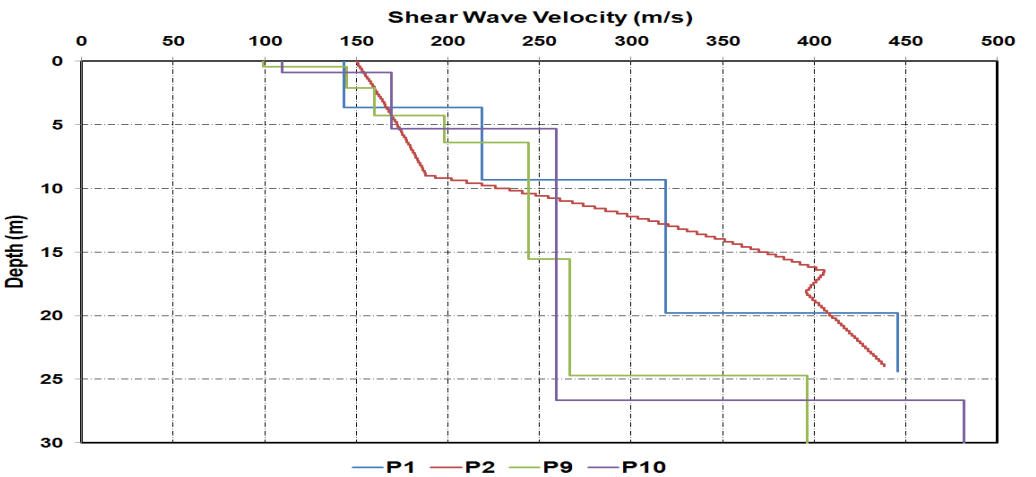

Figure 3. Shear wave velocity profiles for SASW, four predictors.

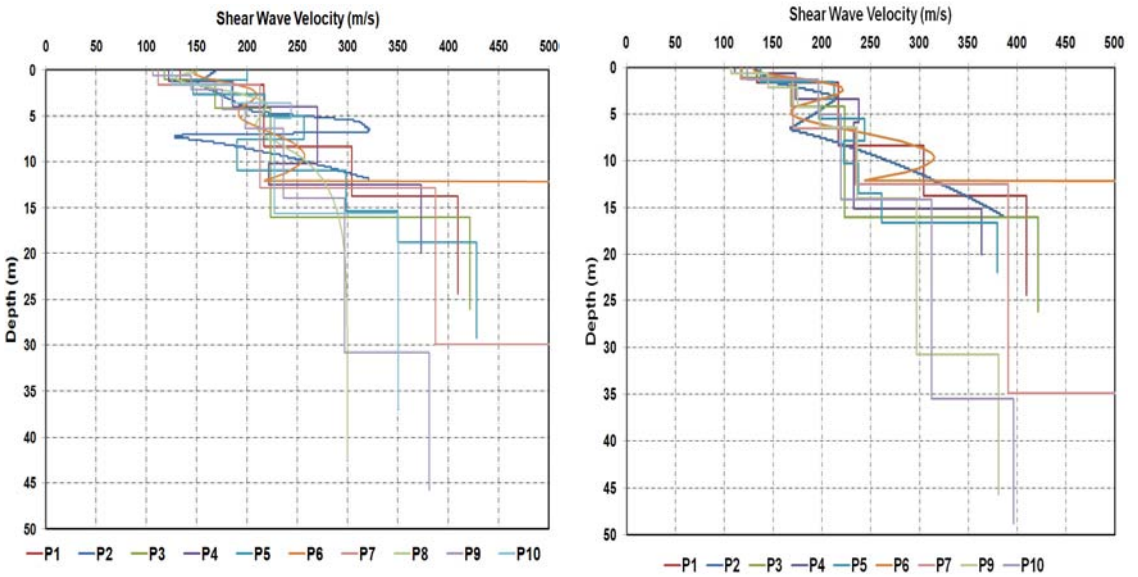

(a) TestSite122_0 **(b) TestSite98_220**

Figure 4. Shear wave velocity profiles for active MASW, 10 predictors.

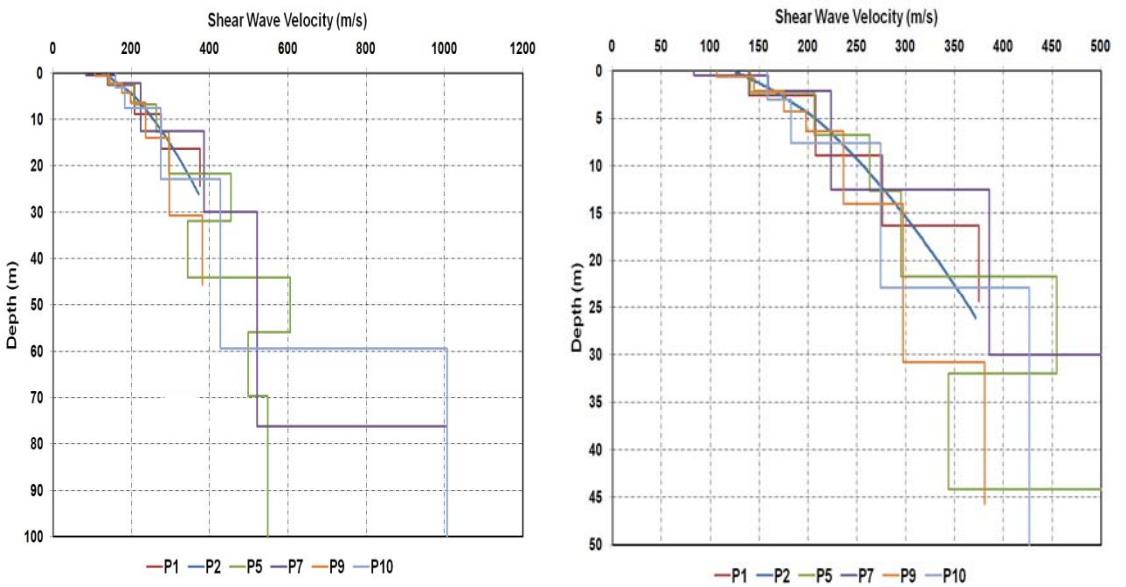

(a) Full **(b) Expanded**

Figure 5. Shear wave velocity profiles for passive MASW, six predictors.

Analysis and Interpretation of the Texas A&M University benchmark data using the Refraction Microtremor Technique

A. Pancha[1] and S. Pullammanappallil[1]

[1] Optim SDS, 200 South Virginia Street, Suite 560, Reno, NV, 89501; PH(775) 236-5891; FAX (775) 324-5662; email: aashap@optimsds.com; satish@optimsoftware.com

ABSTRACT

We applied the refraction microtremor (ReMi) technique (Louie, 2001) to determine the shear-wave velocity structure from benchmark data collected at the National Geotechnical Experimentation Site (NGSE) at Texas A&M University. Three data sets were evaluated: the active Multichannel Analysis of Surface Waves (MASW) data at Site 98 and Site 122, which were recorded by 62 receivers at 2 ft spacing and the passive MASW data, which were recorded by 32 receivers at 10 ft spacing. The essence of the ReMi technique is the separation of Rayleigh waves from other wave arrivals using a two-dimensional slowness-frequency transform of the seismic records. We use a new method introduced by Pancha *et al*. (2008) to image and evaluate the dispersion curve envelope via power-slowness profiles through the slowness-frequency plots. These images demonstrate the appropriateness of our phase picks used to invert for velocity structure beneath the test site locations.

INTRODUCTION

Many techniques exist for the determination of shallow shear wave velocity profiles for geotechnical application. A common seismic data set was collected at the National Geotechnical Experimentation Site (NGSE) at Texas A&M University. Data was collected using multiple field techniques to allow comparison between different analysis techniques. This site has been well documented, and therefore provides "excellent ground truth information" for comparison and validation of the results. We applied the refraction microtremor (ReMi) technique (Louie, 2001) to determine the shear-wave velocity structure from this benchmark data.

DESCRIPTION OF THE REFRACTION MICROTREMOR (ReMi) METHOD

The refraction microtremor (ReMi) process, developed by Louie (2001), is widely being used to determine shear wave velocity profiles using ambient noise recordings. These profiles are useful to characterize sites for both engineering investigations and site response evaluations. This array analysis technique finds average surface-wave velocity over the length of a refraction array, so it averages velocities where geology is laterally variable, thus differing from single point data obtained from downhole logs.

The essence of the technique is that ambient noise contains a usable signal that is predictable from the velocity structure that is presumably caused mainly by

human activities (e.g. trucks, trains, airplanes, etc.). The vertical component of ambient noise, dominated by Rayleigh waves, is recorded by standard refraction arrays. These Rayleigh waves are separated from other wave arrivals using a two-dimensional slowness–frequency (p–f) transform of the noise records. Energy propagating in the forward and reverse directions is analyzed. The fundamental-mode phase-velocity Rayleigh wave dispersion curve is picked along the minimum-velocity of the envelope of the energy within the slowness–frequency spectral image. The spectrum is normalized as the ratio of the power spectrum at a particular frequency and slowness (inverse velocity) over the average value for all slowness values at that frequency. Spectral ratio images from multiple noise records can be combined by arithmetic averaging. It is not generally necessary to set out two-dimensional arrays to measure the dispersion curve of Rayleigh waves because the minimum phase velocity is correlated with waves traveling parallel to the array. Louie (2001) demonstrated that picking along the minimum edge of contours on slowness-frequency plots, where the slope is steepest, is the best procedure for picking the dispersion curve to obtain the best estimate of the true phase velocity. These Rayleigh wave dispersion curve picks can be interactively modeled using trial-and-error adjustments or automatically inverted for the velocity–depth model (Pei *et al*., 2007), to obtain a shear-wave velocity versus depth profile. Modeling was done using the forward interactive modeling module of SeisOpt® ReMi™ (© Optim, 2010).

ANALYSIS OF BENCHMARK DATA

Three data sets were evaluated: the active Multichannel Analysis of Surface Waves (MASW) data at Site 98 and Site 122, which were recorded by 62 receivers at 2 ft spacing, and the passive MASW data, which were recorded by 32 receivers at 10 ft spacing. The array length of the passive data set was 310 ft while that of the active data sets was 122 ft. Data for all three data sets were analyzed in the forward and reverse directions. It was observed that for the active MASW data the active source was applied only at one end of the array. Thus dispersive energy was only observed in the forward direction.

The dispersion curve images for each of the three data sets are shown in Figure 1 along with the resultant velocity depth profiles. For the active MASW Site 122 data shown Figure 1(a), data for only four of the records were combined in the forward direction as only higher mode energy was present on the third record, as illustrated in Figure 2. For the active MASW Site 98 data shown Figure 1(b) all five records were combined in the forward direction. For the passive data set dispersive energy was present in records analyzed in both the forward and reverse directions. Energy at different frequencies is visible in varying clarity from record to record. Rayleigh wave dispersion was less distinguishable at some frequencies than others. The best resolution over all frequencies was observed from the eleventh record analyzed in the forward direction. This data is presented in Figure 1(c). Dispersive energy is observed from 5 to 50 Hz for the active source data compared to 2 to 35 Hz for the passive data set. Given the longer array length, the passive data set was able to capture longer wavelength energy, reflected by the lower frequency energy visible

in the slowness-frequency plot. This low frequency data allows determination of model velocities to greater depths (Figure 1(c), right panel).

APPROPRIATENESS OF PHASE PICKS

Phase velocity picks shown in Figure 1(a), 1(b), and 1(c) occur where the gradient of the power–slowness profile is steepest, as recommended as the ideal estimate of the minimum phase by Louie (2001). To better evaluate the appropriateness of these dispersion curve picks, profiles of the power spectral-ratio versus slowness are plotted for selected frequencies in Figures 3 and 4 for each of the three data sets. The fundamental modes of the dispersion curve, as well as higher modes are observed, as indicated by arrows. This method of evaluation was first introduced by Pancha *et al*. (2008). The phase picks shown in Figures 3 and 4 based on the lower bound dispersion curve envelope occur where the power-slowness curve is steepest. The picks shown in Figure 1 are considered best estimates for the slowness-frequency dispersion curve based on both the images in Figure 1 and the profiles shown in Figures 3 and 4. Uncertainty in the slowness estimate shown in Figures 3 and 4 could be characterized by the broadness of the low-velocity tail, but result in a range of velocity-depth models far beyond the actual profile beneath the site.

As discussed by Louie (2001), in the presence of energy arriving equally from all directions along the liner array, the shape of the power–slowness profiles shown in Figures 3 and 4 would be that of a half cosine curve, with an abrupt vertical cutoff occurring at the true slowness at a ratio maxima, and the remaining energy dispersed over smaller slowness above this. This idealized profile, shown in Figure 3(c) and 4(b) by the heavy black line, would be obtained if ambient noise records over long time periods were summed to ensure that energy from all azimuths were obtained, with a shaper cutoff for longer recording intervals. According to Heisenberg's uncertainty principle, frequency is only infinitely precise for recordings of infinite duration (Claerbout, 1992).

Profiles illustrated in Figures 3 and 4 do not exhibit this form, but instead have a tail occurring at slowness below the steep gradient of the minimum velocity envelope. This is due to four factors. The first, which is discussed by Louie (2001), is due to dominance of energy arriving obliquely to the array. This causes the peak ratio along the dispersion curve to occur at higher apparent velocity, with energy arriving more parallel to the array contributing to the commonly observed tail. The second is due to discretization of slowness (Louie, 2001). The third factor contributing to this low-velocity tail is the presence of lateral three-dimensional heterogeneity along the array. The sharp/idealized lower boundary of the dispersion curve could only occur if we were dealing with a one-dimensional case with infinite frequencies. The fourth and perhaps the most pronounced factor contributing to the absence of the sharp defining boundary is the finite bandwidth of the measurable frequencies. The resolution of the Fresnel zone is frequency dependent and therefore limited due to Heisenberg's uncertainty principle (Claerbout, 1992), resulting in the smoothing of

the minimum boundary of the power–slowness curve. Absence of a sharp cut off in the power–slowness curve, as observed in Figures 3 and 4, is also observed in the ReMi analysis of synthetically generated ground motions. Due to the combined effects of these four factors on smoothing the theoretically sharp minimum bound of the dispersion curve, the suggestion by Louie (2001) that the ideal pick is that located where the spectral ratio is high and the gradient is steepest, seems plausible.

MODELING UNCERTAINTIES

To characterize modeling uncertainties, we developed alternate velocity-depth models using the dispersion curve picks shown in Figure 1 for the three sites that fit the data with similar RMS error of fit between the calculated and observed picks. The results which are plotted in Figure 5 allow uncertainties in the variation of velocity with depth to be assessed. Models obtained using a simulated annealing algorithm (Pei *et al.*, 2007) are shown in gray with associated error bars. Velocities at shallow depths below 10 m are well constrained. Below 10 m, the velocity-depth structure is stable for the passive and active Site 122 data sets, where variations are within 10% to 11% difference. For active Site 98 data set greater variation is observed, with 8% variation in velocity and 23% (8 m) variation in the depth of the deepest interface at 36 m depth.

CONCLUSIONS

1. The refraction mictrotremor technique is able to identify the first higher mode of the Rayleigh-wave dispersion curve. Higher modes are also able to be identified.
2. The method is able to image the dispersion curve to higher frequencies than may be possible with MASW techniques. These high frequencies (30-50 Hz) control the shallow structure and add additional constraints to the velocity-depth inversion.
3. Above 10 m, the velocity-depth models for the three sites show stability.
4. Below 10 m, the passive and active Site 122 data sets exhibit the most uncertainty in the velocity-depth structure.
5. Greatest uncertainty in interface depth and velocity is observed for the active Site 98 data set.

REFERENCES

Claerbout, J. F. (1992). *Earth soundings analysis: processing versus inversion*. Cambridge, Blackwell scientific publication.

Louie J. N. (2001). “Faster, better: shear-wave velocity to 100 meters depth from refraction microtremor arrays”, *Bull. Seism. Soc. Am.,* 91, 347-364.

Pancha, A., J. G. Anderson, J. N. Louie, and Pullammanappallil S. (2008), ”Measurement of shallow shear wave velocities at a rock site using the ReMi technique”, *Soil Dynamics and Earthquake Engineering,* 28, 522-535.

Pei, D., Louie, J. N. and Pullammanappallil S. K. (2007), "Application of simulated annealing inversion on high-frequency fundamental-mode Rayleigh wave dispersion curves", *Geophysics*, 72(5), R77-R85.

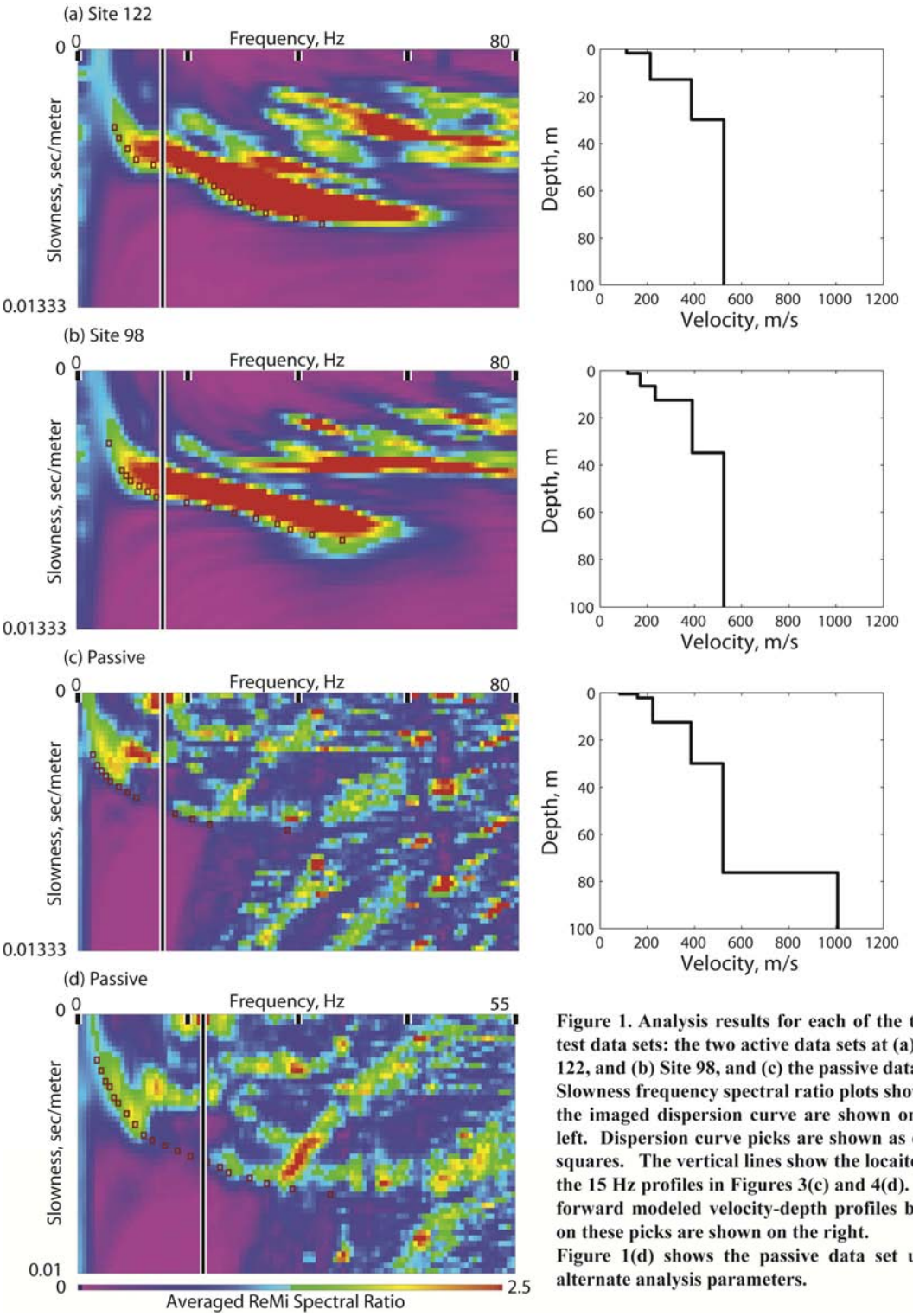

Figure 1. Analysis results for each of the three test data sets: the two active data sets at (a) Site 122, and (b) Site 98, and (c) the passive data set. Slowness frequency spectral ratio plots showing the imaged dispersion curve are shown on the left. Dispersion curve picks are shown as open squares. The vertical lines show the locaiton of the 15 Hz profiles in Figures 3(c) and 4(d). The forward modeled velocity-depth profiles based on these picks are shown on the right. Figure 1(d) shows the passive data set using alternate analysis parameters.

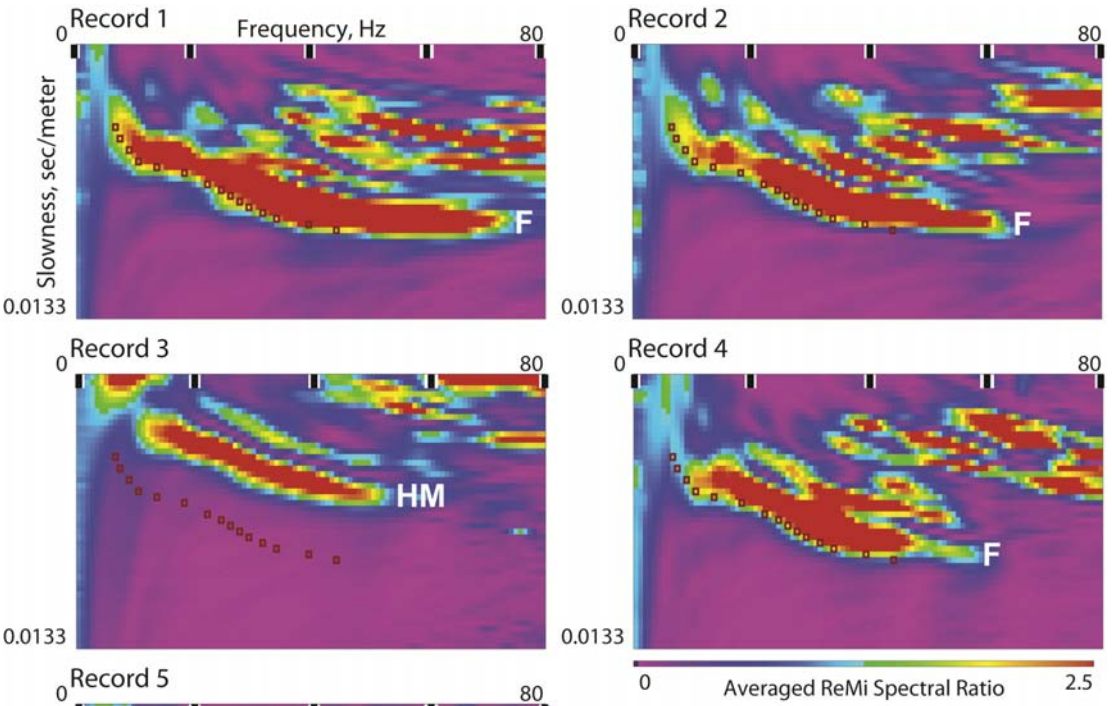

Figure 2. Dispersion curves for the five data records for Site 122 analyzed in the forward direction. Dispersion curve picks are shown as open squares along the fundamental mode (F). Only higher mode (HM) energy is visible for Record 3.

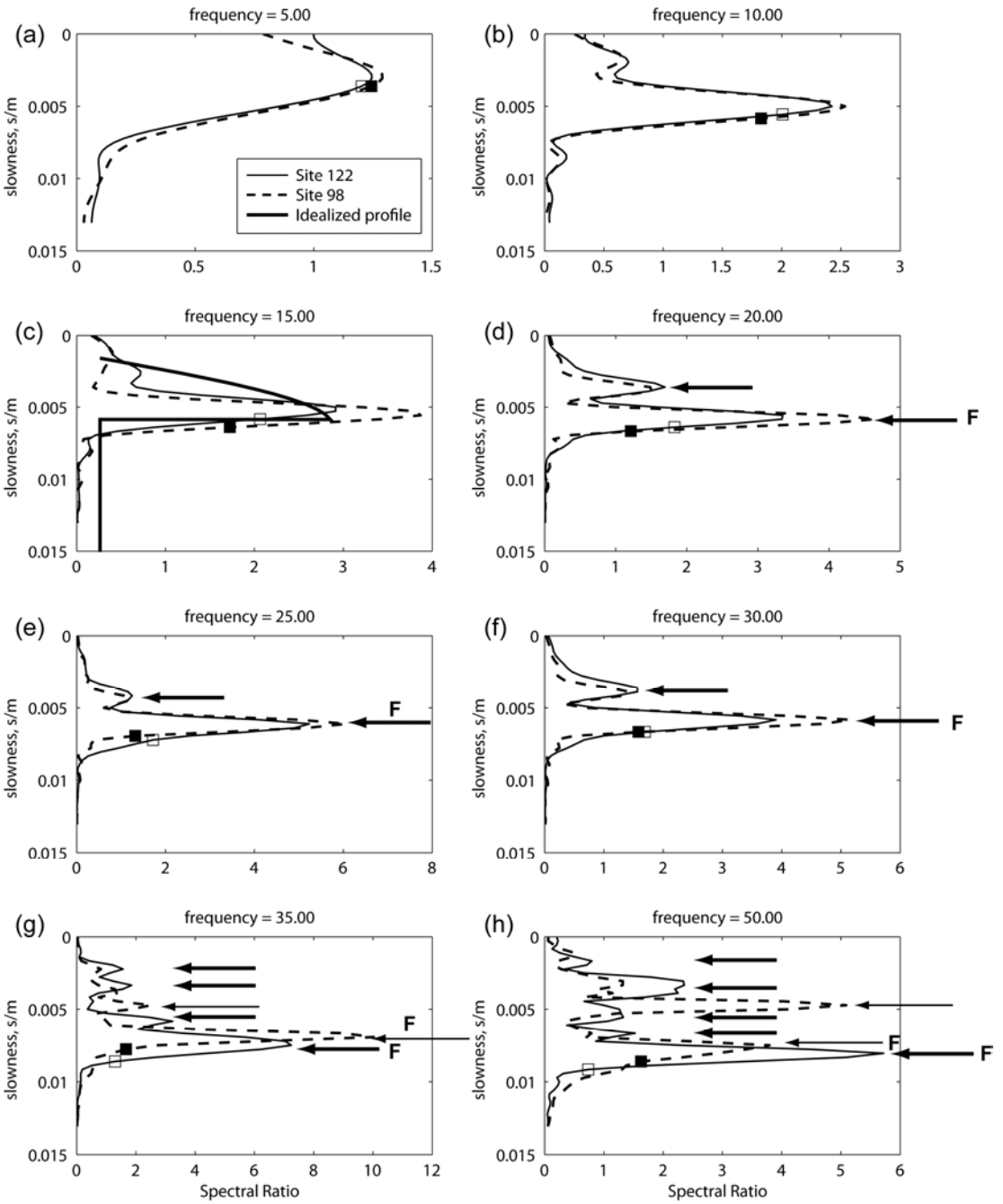

Figure 3. Profiles through slowness-frequency images at various frequencies for the two active data sets: Site 98 and Site 122. Arrows indicate the fundamental (denoted by "F") and higher modes. The idealized profile is shown in Figure 3(c) by the heavy black line. The black line shown in the left panel of Figures 1(a) and 1(b) shows the location of the 15 Hz profile line shown here in Figure 3(c). Picks below 5 Hz are less certain than those at higher frequencies.

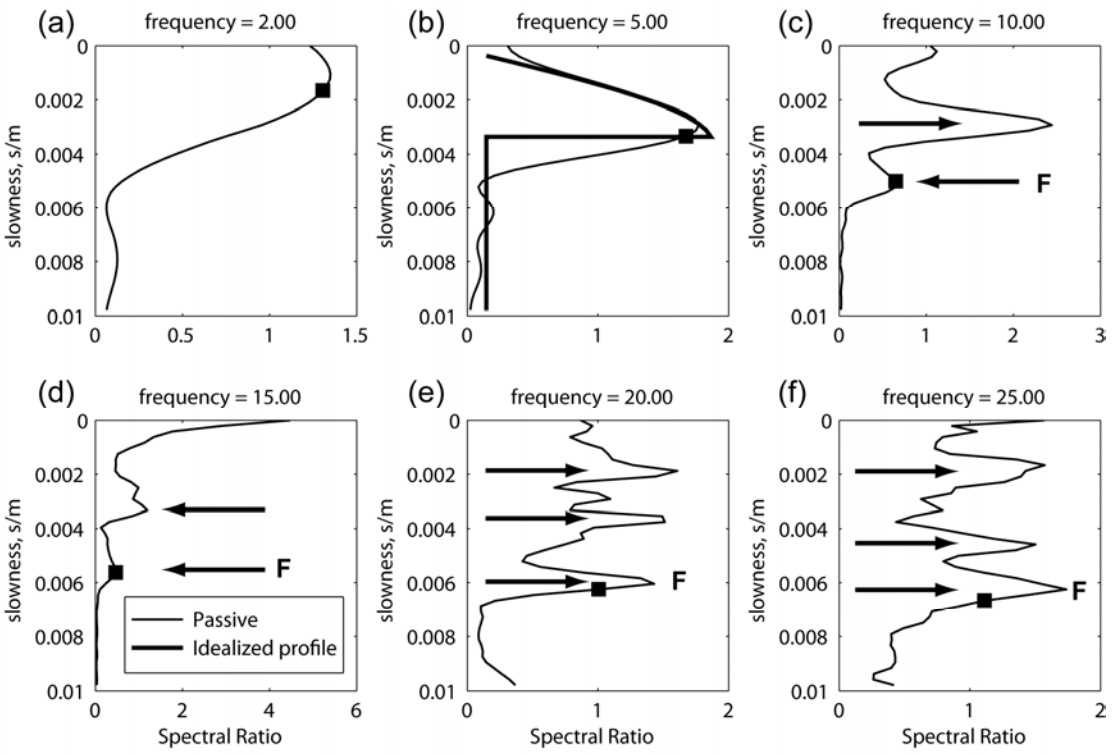

Figure 4. Profiles through slowness-frequency images at various frequencies for the passive data set. Arrows indicate the fundamental (denoted by "F") and higher modes. The idealized profile is shown in Figure 4(b) by the heavy black line. The black line shown in the left panel of Figures 1(c) shows the location of the 15 Hz profile line shown here in Figure 4(d). Picks below 3.5 Hz and from 10 to 20 Hz are less certain than those at other frequencies.

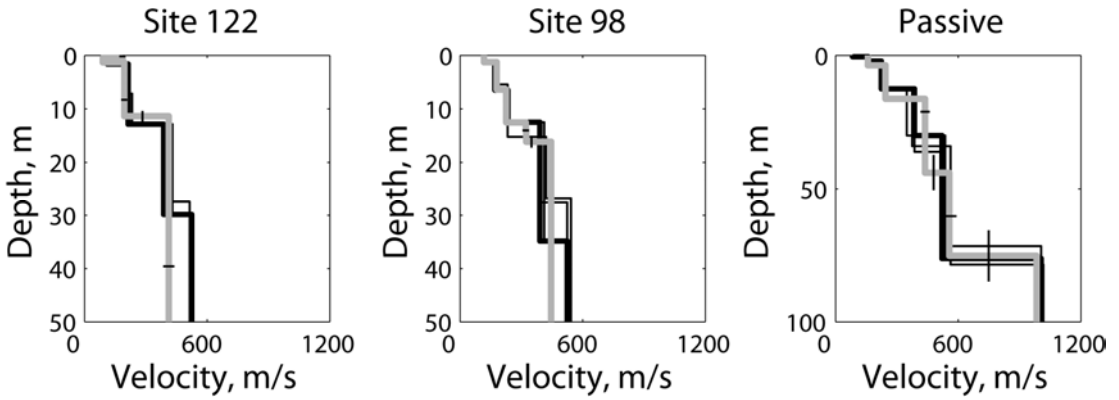

Figure 5. Alternate velocity-depth models for the dispersion curve picks shown in Figure 1 for each site. Preferred models (Figure 1) are denoted by the thick bold lines. Models obtained using a simulated annealing algorithm are shown in gray with associated error bars. Standard deviation of the interface depths range from 0.3 to 9 m for the passive data, and was at most 0.7 m for Site 98 and Site 122. Standard deviation of the velocity interfaces range from 0.5 to 26 m/s.

Determination of the Dynamic Soil Characteristics at the NGES

S.A. Badsar, M. Schevenels, G. Degrande

Department of Civil Engineering, K.U.Leuven, Kasteelpark Arenberg 40, B-3001 Leuven, Belgium

ABSTRACT: Analysis of the field data collected at the National Geotechnical Experimentation Site (NGES) at Texas A&M University (TAMU) is outlined. Data have been collected along two measurement lines from two and multi-sensor arrays using a variety of sources. The data from each measurement line are processed separately. The STA/LTA procedure is applied in order to determine the P-waves arrival time. The P-wave velocity profile is determined by solving an inverse problem, where the difference between the theoretical arrival time, corresponding to a horizontally layered halfspace, with the experimental arrival time is minimized. The classical SASW method as well as the frequency-wavenumber analysis are used to determine the experimental dispersion curve. The dispersion curve is subsequently inverted to determine the S-wave velocity profile, using the a priori determined P-wave velocity profile. The width of peaks of the response in the frequency-wavenumber domain is used to determine the experimental attenuation curve. The attenuation curve is finally inverted to give the material damping ratio profile, while the already determined P- and S-wave velocity profiles are fixed in the inversion procedure. The determined soil profile is finally used to make a comparison between the theoretical and experimental frequency-wavenumber spectrum. The correspondence with experimental results is good.

INTRODUCTION

A data set collected at the National Geotechnical Experimentation Site (NGES) at Texas A&M University (TAMU) is made available to the community for interpretation. In this paper, the Seismic Refraction (SR) method, the classical Spectral Analysis of Surface Waves (SASW) method, and the Multi-channel Analysis of Surface Waves (MASW) method are used to determine dynamic soil properties. The SR method gives the P-wave arrival time from which the P-wave velocity profile of the soil is determined. The classical SASW method results in a composite dispersion curve and subsequently the S-wave velocity profile. The MASW method gives both the dispersion and attenuation curve. The material damping ratio profile is determined from the attenuation curve. Finally, the identified soil profiles are used to simulate the wave field recorded in the SASW test to verify the accuracy of the results.

DETERMINATION OF THE P-WAVE VELOCITY

Measurements were performed using two measurement lines A and B at the NGES. For each setup, waves were generated by means of sledgehammer impacts at the soil's surface. The response was recorded by means of a set of 62 receivers spaced at 0.61 m along a straight measurement line. The position of the source was

moved from its initial point at 3 m from the first receiver to 6.1, 9.1, 12.2, and 15.2 m, giving a total length of 52.4 m for each measurement line. Five test repetitions were recorded at each position of the source, and were averaged in the time domain to increase the signal quality. The receivers were 4.5 Hz vertical velocity transducers. A sampling frequency f_S = 1280 Hz has been used in both measurement lines A and B. The corresponding Nyquist frequency is 640 Hz. For each impact, a time signal of 16384 samples (or 12.8 s) was stored. A pretrigger of 1638 samples (or 1.28 s) and a posttrigger of 14746 samples (or 11.52 s) was used.

In the present section, the SR method is applied to the measurement data to determine the P-wave arrival time and to infer the P-wave velocity profile. In the following sections, this test will also be interpreted as MASW test and the data will be used to determine dispersion and attenuation curves and to infer the S-wave velocity profile and the material damping ratio profile, respectively.

The five measurements corresponding to five source positions for both measurement lines A and B have to be combined before further processing. Since the force is not measured and only voltage data $V(r,t)$ are provided, a reference receiver is used to calculate a receiver-receiver transfer function in the frequency domain. The spectrum $\hat{V}(r,\omega)$ is calculated using the Fourier transformation from the time t to the circular frequency ω:

$$\hat{V}(r,\omega) = \int_{-\infty}^{+\infty} V(r,t)\, e^{-i\omega t}\, dt \tag{1}$$

The transfer function $\hat{H}_{ij}(\omega)$ from the reference receiver at channel i to the receiver at channel j is computed as follows:

$$\hat{H}_{ij}(\omega) = \frac{\hat{S}_{ji}(\omega)}{\hat{S}_{ii}(\omega)} \tag{2}$$

where the auto power spectra $\hat{S}_{ii}(\omega)$ and the cross power spectra $\hat{S}_{ji}(\omega)$ are defined as:

$$\hat{S}_{ij}(\omega) = \hat{V}_i(\omega)\hat{V}_j^*(\omega) \tag{3}$$

Herein, $\hat{V}_i(\omega)$ is the frequency content of the signal $V_i(t)$ recorded in channel i, and $\hat{V}_j^*(\omega)$ is the complex conjugate of $\hat{V}_j(\omega)$. The receiver located at 15.2 m from the source is considered as the reference in order to be usable for all 5 setups that result from the 5 different positions of the source.

It is noted that the transfer function $\hat{H}_{ij}(\omega)$ as defined in equation (2) is dimensionless, and equals 1 at the offset 15.2 m from the source. For visualization of the data in the time domain, the transfer function $\hat{H}_{ij}(\omega)$ is multiplied by the frequency spectrum of a Ricker pulse with a time shift 0.1 s and a characteristic period 0.03 s, to give signals $\hat{x}(r,\omega)$. An inverse Fourier transformation is next performed to produce the time signals $x(r,t)$ for measurement line A (figure 1(a)) and B (figure 1(b)). Both data sets are similar, with minor differences.

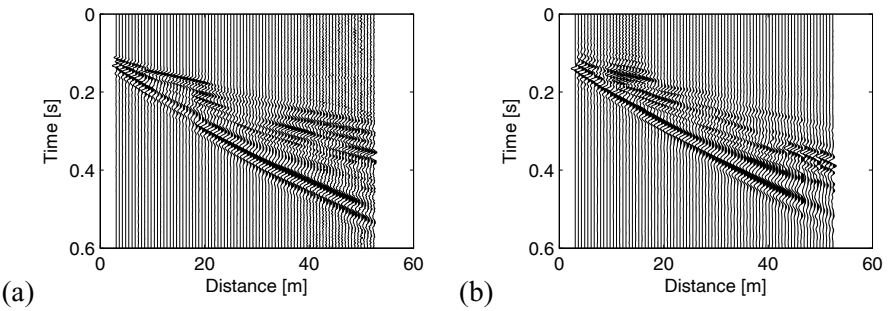

Figure 1. Time history $x(r,t)$ as calculated for the measurement lines (a) A and (b) B at the NGES.

The P-wave arrival time $t^E(r)$ at a distance r from the source is determined from the time history of the signal shown in figure 1, following the Short Term Averaging/Long Term Averaging (STA/LTA) procedure (Withers et al.; 1998). The STA/LTA ratio $\bar{x}(r,t_i)$ at time t_i is computed as:

$$\bar{x}(r,t_i)=\frac{\frac{1}{N_{STA}}\sum_{j=i-N_{STA}+1}^{i}x^2(r,t_i)}{\frac{1}{N_{LTA}}\sum_{j=i-N_{STA}-N_{LTA}+1}^{i-N_{STA}}x^2(r,t_i)} \tag{4}$$

where N_{STA} and N_{LTA} are the short and long term averaging periods. In the present analysis, the values N_{STA} = 10 (or 0.0078s) and N_{LTA} = 100 (or 0.078s) are used. These values have been tuned to yield an STA/LTA ratio $\bar{x}(r,t_i)$ with a clear peak at the arrival of the P-wave. The resulting STA/LTA ratio for measurement lines A and B are shown in figure 2.

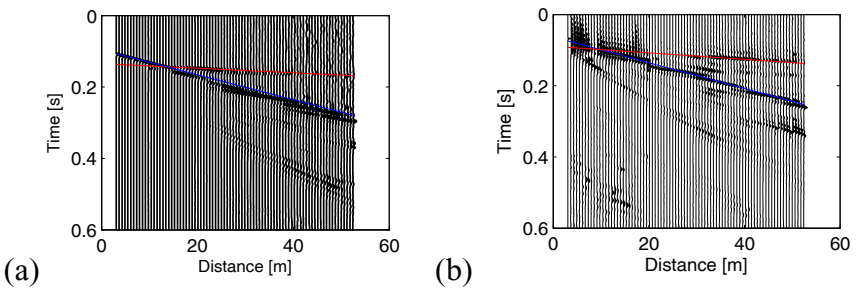

Figure 2. The STA/LTA ratio with the trace of the direct arrival (blue line) and refracted (red line) P-waves for the measurement lines (a) A and (b) B at the NGES.

Figure 2 allows for the determination of the P-wave arrival time by selecting the first peak in the STA/LTA ratio. A bilinear curve is obtained for both cases A and B: in the near field, which is up to 12.3 m from the source for the case A (figure 2(a)) and up to 11.1 m for the case B (figure 2(b)), the direct P-wave arrives first, while at

larger distances, the refracted P-wave arrives first. The P-wave velocity C_p of the soil is identified from the slopes and the intersection of the lines that constitute the arrival time curve. The resulting P-wave velocity profile is summarized in table 1.

Table 1. Identified P-wave velocity profile for the measurement lines (a) A and (b) B at the site NGES.

Layer	Thickness [m]	C_p [m/s]
1	5.18	301
2	∞	1679

(a)

Layer	Thickness [m]	C_p [m/s]
1	4.49	291
2	∞	1495

(b)

DETERMINATION OF THE S-WAVE VELOCITY

The $f-k$ analysis and the classical SASW method are used to determine the experimental dispersion curve and subsequently the S-wave velocity profile. The test setup for the $f-k$ analysis is explained in the previous section. The $f-k$ analysis is based on the response of the soil in the frequency-wavenumber domain. The frequency-wavenumber spectrum $\tilde{H}(k_r,\omega)$ of the response is computed as (Forbriger; 2003):

$$\tilde{H}(k_r,\omega)=\int_0^{\infty}\hat{H}(r,\omega)\,J_0(k_r r)\,r\,dr \tag{5}$$

where k_r is the radial wavenumber and $J_0(k_r r)$ is the zeroth order Bessel function of the first kind. Equation (5) is approximated by truncation of the integral at $r=r_{\max}$ (the array length, i.e. the position of the farthest receiver). Following Forbriger (2003), the Bessel function $J_0(k_r r)$ in equation (5) is replaced by the zeroth order Hankel function $H_0^{(1)}(k_r r)/2$ of the first kind to account for the fact that the wave field only consists of outgoing waves. The following approximation is thus obtained:

$$\tilde{H}(k_r,\omega)=\frac{1}{2}\int_0^{r_{\max}}\hat{H}(r,\omega)\,H_0^{(1)}(k_r r)\,r\,dr \tag{6}$$

The above integral is computed using trapezoidal method.

Figure 3 shows the $f-k$ spectrum $\tilde{H}(k_r,\omega)$ as determined from the data measured at the test site NGES. The spectrum is shown in terms of the phase velocity ω/k_r instead of the wavenumber k_r. The maxima in the $f-k$ spectrum $\tilde{H}(k_r,\omega)$ are due to the Rayleigh waves. In order to reveal the influence of the Rayleigh waves over the entire frequency range, the spectrum is normalized for each individual frequency. Figures 3(a) and 3(b) are used to determine the corresponding dispersion curves for the measurement lines A and B, respectively. In the following, the classical SASW test is used as well to determine the dispersion curves of the measurement lines. The resulting curves are compared with the results of the $f-k$ analysis.

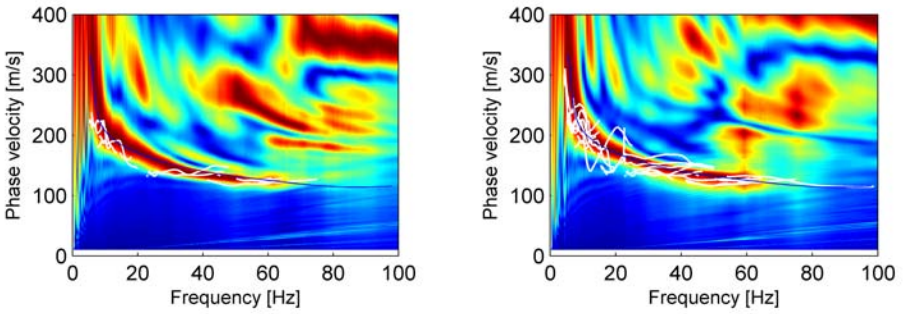

Figure 3. The $f-k$ spectrum $\tilde{H}(k_r,\omega)$ for the measurement lines (a) A and (b) B at the NGES. Superimposed are the dispersion curves determined using the classical SASW test (white dots) and the curves fitted to these results (blue line).

The classical, or the two station, SASW test is based on using receiver pairs. The phase difference between two receivers is used to calculate a frequency dependent time lag. Given the distance between the receivers, the time lag is next used to determine the frequency dependent phase velocity. The receiver pairs are chosen such that the distance between the source and the near receiver is equal to the receiver spacing (Nazarian et al.; 1983). Different spacings are used in order to record both small and large wavelengths.

The phase $\hat{\phi}_{ij}(\omega)$ of the cross power spectrum $\hat{S}_{ij}(\omega)$ is equal to the phase difference between the two receivers:

$$\hat{\phi}_{ij}(\omega) = tg^{-1}\frac{\mathrm{Im}[\hat{S}_{ij}(\omega)]}{\mathrm{Re}[\hat{S}_{ij}(\omega)]} \tag{7}$$

The phase difference $\hat{\phi}_{ij}(\omega)$ has to be unwrapped $\phi_{ij}^{unwrap}(\omega)$ for further processing by adding integer multiples n of 2π. Knowing the distance r_{ij} between two receivers, the phase velocity at different frequencies can be calculated as follows:

$$C_{ij}(\omega) = \frac{r_{ij}\omega}{\phi_{ij}^{unwrap}(\omega)} \tag{8}$$

Two classical SASW tests were performed at the test site NGES. The same measurement lines A and B were used in this experiment. The test was performed using the common receiver midpoint for several spacings and for source positions on each side of the centerline to generate forward and reverse wave propagation. Impacts of a sledgehammer were used as a source for receiver spacings up to 4.9 m, and a vibration shaker is used for larger receiver spacings. For this test, 1 Hz vertical velocity transducers were used.

The distance between the receiver pairs considered for both classical SASW tests A and B are 1.2 m, 2.4 m, 4.9 m, 9.7 m, 19.5 m, and 37.2 m. The classical SASW data from the NGES that has been made available for the authors are pre-assessed and summarized in an Excel sheet, where for each receiver spacing, the cross power spectrum, phase, and coherence value for frequencies ranging from 0 Hz to 200 Hz are given. Using these data and following the above procedure for the classical SASW, two composed dispersion curves corresponding to tests A and B are

determined as shown in figure 4.

The dispersion curves determined from the classical SASW method are superimposed to the corresponding $f-k$ spectrum in figure 3. The correspondence between the two techniques for both measurement lines is very good. At low frequencies, the $f-k$ spectrum shows a better resolution compared to the composed curve from the classical SASW. This can be explained by the longer measurement line in the MASW test. While the $f-k$ spectrum exhibits contribution of the higher modes in the response, the classical SASW does not follow the traces of the higher modes. In fact, these long wavelength data may be eliminated by the wavelength filtering in the classical SASW method. A polynomial is finally fitted to the combined results from both the $f-k$ analysis and the classical SASW method as shown in figure 3. This polynomial is subsequently inverted to determine the S-wave velocity profile C_s for the both measurement lines A and B. In the inverse problem, the C_s profile is iteratively adjusted in order to minimize the following misfit function that measures the distance between the theoretical and the experimental dispersion curve:

$$\min_x \sum_{i=}^{N} \left| C_R^T(x, f_i) - C_R^E(f_i) \right|^2$$

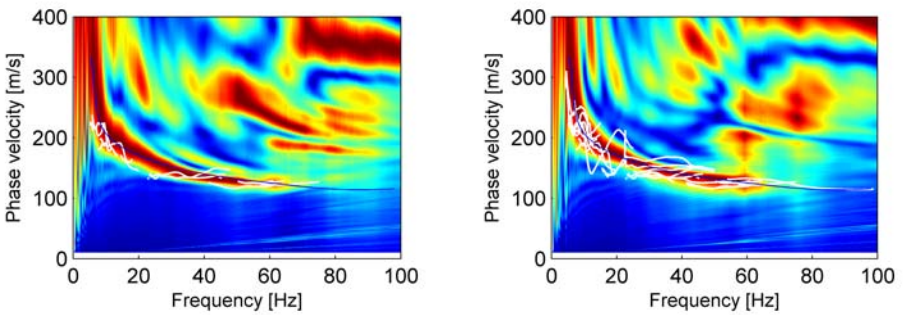

Figure 4. Experimental dispersion curves determined for the measurement lines (a) A and (b) B at the NGES using the two station method. Superimposed are the curves fitted to the combined results (blue line).

For the case A, a number of $N = 61$ frequencies f_i from 5.5 Hz to 65.8 Hz with finer steps at the lower frequencies and larger steps at higher frequencies are used. In a similar way for the case B, a number of $N = 51$ frequencies f_i from 5.6 Hz to 65.9 Hz are used. Using three layers on a halfspace is sufficient to find a theoretical fit to the experimental dispersion curve $C_R^E(\omega)$, for both cases A and B. The vector of design variables x includes the thicknesses of the layers and the S-wave velocity in the layers and the halfspace. The other soil properties (P-wave velocity as determined in the previous section, density $\rho = 1900$ Kg/m^3, and material damping ratio $D_s = D_p = 0.04$) are kept constant in the inversion procedure. The resulting C_s profile corresponding to the both tests A and B are

summarized in table 2.

Table 2. Identified S-wave velocity profile for the measurement line (a) A and (b) B at the site NGES.

Layer	Thickness [m]	C_s [m/s]	Layer	Thickness [m]	C_s [m/s]
1	1.71	129	1	1.60	132
2	3.30	192	2	3.38	191
3	12.69	250	3	12.61	243
4	∞	437	4	∞	435
(a)			(b)		

The C_s profiles determined from both measurement lines are almost the same, revealing that the average velocity of the soil under the measurement lines A and B are the same. The C_s profile along with the C_p profile obtained in the previous section are used in the following to determine the material damping ratio at the site NGES.

DETERMINATION OF THE MATERIAL DAMPING RATIO

Material damping is accounted for by means of the correspondence principle:

$$\mu^{\dagger} = \mu(1 + 2D_s i) \tag{10}$$

$$(\lambda + 2\mu)^{\dagger} = (\lambda + 2\mu)(1 + 2D_p i) \tag{11}$$

with $\mu^{\dagger}$ the complex shear modulus, λ and μ Lamé's constants, D_s the shear material damping ratio, and D_p the compressional material damping ratio. The shear D_s and compressional D_p material damping ratio are assumed to be equal (i.e. $D = D_s = D_p$) in the following. A complex wave number $k^{\dagger} = \omega / C^{\dagger}$ can be subsequently defined, with $C^{\dagger} = C(1 + Di)$ the complex S-wave velocity, and can be more simplified for small values of the material damping ratio D as follows:

$$k^{\dagger} = k(1 + A(\omega)i) \tag{12}$$

where $k = \omega / C$ is the wavenumber and $A(\omega)$ is the frequency dependent attenuation coefficient. The curve $A_R^E(\omega)$ is determined in the following from the data collected at the NGES. The method to determine the material damping ratio is based on the width of the peaks in the frequency-wavenumber spectrum $\tilde{H}(k_r, \omega)$. First, the peak corresponding to the fundamental surface wave (the first peak) is identified. The dispersion curve is derived from the peak's position in the same way as in the $f-k$ analysis discussed in the previous subsection. The experimental attenuation coefficient $A_R^E(\omega)$ is derived from the peak's width: if the attenuation is weak, the peak is high and narrow; if the attenuation is strong, the peak is low and wide. To this end, the half-power bandwidth method is used (Badsar et al.; 2010):

$$A_R^E(\omega) = \frac{\Delta k_r(\omega)}{2\sqrt{\gamma^{-2} - 1}} \tag{13}$$

where $\Delta k_r(\omega)$ is the width of the peak where the magnitude of the $f-k$ spectrum is γ times the peak value, with γ smaller than but close to 1.

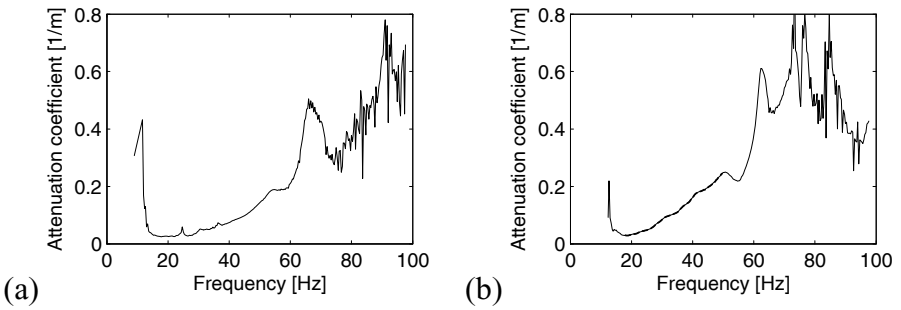

Figure 5. The experimental attenuation curve $A_R^E(\omega)$ determined for measurement lines (a) A and (b) B at the site NGES.

Table 3. Identified material damping ratio profile for the measurement lines (a) A and (b) B at the site NGES.

Layer	Thickness [m]	D [-]
1	0.95	0.070
2	3.05	0.023
3	∞	0.020

(a)

Layer	Thickness [m]	D [-]
1	1.45	0.070
2	2.85	0.029
3	∞	0.020

(b)

Table 4. Identified soil profile for the measurement lines (a) A and (b) B at the site NGES.

Layer	Thickness [m]	C_s [m/s]	C_p [m/s]	D [-]
1	0.95	129	301	0.070
2	0.76	129	301	0.023
3	2.28	192	301	0.023
4	1.02	192	301	0.020
5	0.16	250	301	0.020
6	12.5	250	1679	0.020
7	∞	437	1679	0.020

(a)

Layer	Thickness [m]	C_s [m/s]	C_p [m/s]	D [-]
1	1.45	132	291	0.070
2	0.15	132	291	0.029
3	2.71	191	291	0.029
4	0.19	191	291	0.020
5	0.48	191	1495	0.020
6	12.6	243	1495	0.020
7	∞	435	1495	0.020

(b)

The experimental attenuation curves $A_R^E(\omega)$, shown in figures 5(a) and 5(b), are subsequently inverted to determine the material damping ratio D. In the inverse problem, the material damping ratio profile D is iteratively adjusted in order to minimize the following misfit function that measures the distance between the theoretical and the experimental attenuation curve:

$$\min_{x} \sum_{i=1}^{N} \left| A_R^T(x, f_i) - A_R^E(f_i) \right|^2 \tag{14}$$

where $N = 60$ frequencies f_i from 18 Hz to 48 Hz with a step of 0.5 Hz are used for case A, and $N = 50$ frequencies f_i from 19 Hz to 44 Hz with a step of 0.5 Hz are used for case B. Using two layers on a halfspace is sufficient to find a theoretical fit to the experimental attenuation curve $A_R^E(\omega)$. The vector of design variables x includes the thickness of the layers and the material damping ratio in the layers and the halfspace. The other soil properties (P- and S-wave velocity as determined in the previous sections, and density $\rho =$ 1900 kg/m^3) are kept constant in the inversion procedure. The resulting material damping ratio profile is summarized in table 3.

SUMMARY AND VERIFICATION OF THE RESULTS

The profiles determined for the P- and S-wave velocity as well as the material damping ratio are combined in table 4 for measurement lines A and B. It is observed that both tests lead to almost the same soil profile. The S-wave velocity increases gradually from a value of around 120 m/s at the surface to around 430 m/s at larger depths. The P-wave velocity profile shows a sudden increase at a depth of about 5 m, revealing the groundwater table depth. The material damping ratio is 7% at the surface and gradually decreases to 2% at larger depths.

In order to assess the accuracy of the determined soil profiles, the results summarized in table 4 are used to calculate two theoretical transfer functions $\tilde{H}^T(k_r, \omega)$ corresponding to the both measurement lines A and B. These functions are shown in figures 6(a) and 6(b), for cases A and B, respectively. Both figures exhibit a very good agreement with the corresponding experimental transfer functions $\tilde{H}(k_r, \omega)$ presented in figures 3(a) and 3(b), demonstrating the accuracy of the determined soil profile.

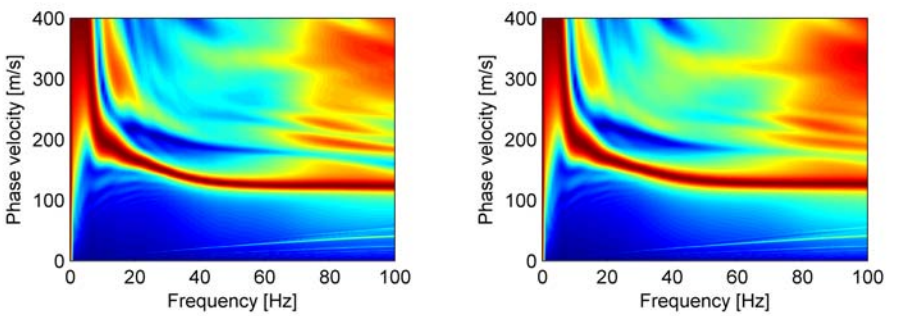

Figure 6. The theoretical $f-k$ spectrum $\tilde{H}^T(k_r, \omega)$ for the measurement lines (a) A and (b) B at the NGES.

CONCLUSION

This paper focuses on the determination of the soil properties at the site NGES, where an extensive measurement campaign has been carried out and the data has been made available to the community. The P- and S-wave velocity as well as the material damping ratio of the site NGES are determined in this paper. The SR technique along with the STA/LTA method are used to determine the experimental arrival time, from which the P-wave velocity profile is obtained. The classical SASW as well as the $f-k$ analysis are used to determine the experimental dispersion curve. The S-wave velocity profile is subsequently determined in an inversion procedure, where the a priori determined P-wave velocity profile is fixed. The half-power bandwidth is finally used to determine the attenuation of Rayleigh waves from the width of the peaks in the $f-k$ spectrum. The attenuation curve is inverted using the known values for the P and S-wave velocity profile.

The determined soil properties are finally used to simulate the experimental transfer function in the frequency-wavenumber domain. The correspondence between the experimental and the theoretical results is good, implying that dynamic soil properties are accurately determined.

ACKNOWLEDGEMENTS

The results presented in this paper have been obtained within the frame of the project G.0595.06 “In situ determination of material damping in the soil at small deformation ratios”, funded by the Re- search Foundation - Flanders and the project OT/05/41 “A generic methodology for inverse modeling of dynamic problems in civil and environmental engineering”, funded by the Research Council of K.U.Leuven. The second author is a postdoctoral fellow of the Research Foundation - Flanders. The financial support is gratefully acknowledged.

REFERENCES

Badsar, S., Schevenels, M., Haegeman, W. and Degrande, G. (2010). Determination of the damping ratio in the soil from SASW tests using the half-power bandwidth method, *Geophysical Journal International* **182**(3): 1493–1508. **URL:** *http://dx.doi.org/10.1111/j.1365-246X.2010.04690.*

Chopra, A. (2007). *Dynamics of structures*, third edn, Pearson Prentice Hall, Upper Saddle River, NJ.

Cuellar, V. and Valerio, J. (1997). Use of the SASW method to evaluate soil improvement techniques, *Proceedings of the 14th international conference soil mechanics and foundation engineering*, Hamburg, pp. 461–464.

Forbriger, T. (2003). Inversion of shallow-seismic wavefields: I. Wavefield transformation, *Geophysical Journal International* **153**(3): 719–734.

François, S., Schevenels, M., Thyssen, B., Borgions, J., Badsar, S. and Degrande, G. (2011). Design and efficiency of a vibration isolating screen in the soil, *Journal of Geotechnical and Geoenvironmental Engineering, Proceedings of the ASCE* . Submitted for publication.

Kausel, E. (2006). *Fundamental solutions in elastodynamics: a compendium*, Cambridge University Press, New York.

Kausel, E. and Roësset, J. (1981). Stiffness matrices for layered soils, *Bulletin of the Seismological Society of America* **71**(6): 1743–1761.

Kavazanjian, E., Snow, M., Poran, C. and Satoh, T. (1994). Non-intrusive Rayleigh wave investigations at solid waste landfills, *Proceedings of the first international congress on environmental geotechnics*, Edmonton, pp. 707–712.

Lai, C. (1998). *Simultaneous inversion of Rayleigh phase velocity and attenuation for near-surface site characterization*, PhD thesis, Georgia Institute of Technology.

Lai, C., Rix, G., Foti, S. and Roma, V. (2002). Simultaneous measurement and inversion of surface wave dispersion and attenuation curves, *Soil Dynamics and Earthquake Engineering* **22**(9-12): 923–930.

Madshus, C. and Kaynia, A. (2000). High-speed railway lines on soft ground: dynamic behavior at critical train speed, *Journal of Sound and Vibration* **231**(3): 689–701.

Nazarian, S. and Stokoe II, K. (1984). Nondestructive testing of pavements using surface waves, *Transportation Research Record* **993**: 67–79.

Nazarian, S., Stokoe II, K. and Hudson, W. (1983). Use of spectral analysis of surface waves method for determination of moduli and thicknesses of pavement systems, *Transportation Research Record* **930**: 38–45.

Park, C., Miller, R. and Xia, J. (1999). Multichannel analysis of surface waves, *Geophysics* **64**(3): 800–808.

Rix, G., Lai, C. and Spang Jr., A. (2000). In situ measurement of damping ratio using surface waves, *Journal of Geotechnical and Geoenvironmental Engineering, Proceedings of the ASCE* **126**(5): 472–480.

Roësset, J. (1998). Nondestructive dynamic testing of soils and pavements, *Tamkang Journal of Science and Engineering* **1**(2): 61–81.

Withers, M., Aster, R., Young, C., Beiriger, J., Harris, M., Moore, S. and Trujillo, J. (1998). A comparison of select trigger algorithms for automated global seismic phase and event detection, *Bulletin of the Seismological Society of America* **88**(1): 95–106.

Analysis of SASW, MASW and Passive Surface Wave Data Collected at the National Geotechnical Experimentation Site at Texas A&M University

A. J. Martin[1]

[1]GEOVision, Inc., 1124 Olympic Drive, Corona, CA 92881; PH (951) 549-1234; FAX (951) 549-1236; email: amartin@geovision.com

ABSTRACT

A surface wave data set consisting of spectral analysis of surface waves (SASW), multi-channel analysis of surface waves (MASW) and passive MASW data, acquired at the Texas A&M University NGES site, was provided to the academic and professional community for analysis using various techniques.

A comparison of the surface wave dispersion data acquired using the multiple methods was performed. Generally, the surface wave dispersion data acquired using the three techniques were similar. Analysis of the surface wave dispersion data was limited to forward and inverse modeling of the SASW data and combined active and passive MASW data using two commercial software packages. Several S-wave velocity models were generated to demonstrate the problem of non-uniqueness. Non-uniqueness, however, has a much smaller impact on depth averaged physical properties and the average S-wave velocity of the upper 30 m (V_S30) was found to vary by only a few percent between the various models.

INTRODUCTION

Shear-wave velocity (V_S) has long been known to be an essential parameter for evaluating the dynamic properties of soils. Common applications of V_S imaging include estimation of the average shear-wave velocity in the upper 30 m (V_S30), seismic risk studies, seismic hazard zonation, evaluation of liquefaction potential and characterization of strong motion seismic instrument sites.

Active surface wave techniques, such as the spectral analysis of surface waves (SASW) and multi-channel analysis of surface waves (MASW), and passive surface wave techniques, such as the array microtremor and refraction microtremor (passive MASW) techniques, are proven non-destructive seismic methods that can be used to determine the variation of V_S with depth (Stokoe et al., 1994; Brown, 1998; Park et al., 1999; Okada, 2003, Martin, et al., 2006 and Louie, 2001). The basis of surface wave methods is the dispersive characteristic of Rayleigh waves when propagating in a layered medium. The Rayleigh-wave phase velocity depends on the material

properties (primarily S-wave velocity with smaller contributions from P-wave velocity, Poisson's ratio and mass density) to a depth of about one wavelength. Surface wave testing consists of collecting surface wave data in the field, generating the dispersion curve and then using iterative forward or inverse modeling techniques to calculate the corresponding V_S profile. In urban environments, the combined use of active and passive surface wave techniques can limit the need to mobilize large energy sources such as weight drops, bulldozers and vibratory sources.

Active and passive surface wave techniques are used by numerous practitioners, both in industry and academia, to characterize subsurface S-wave velocity structure. Surface wave techniques are often applied to geotechnical site characterization as part of the design of critical structures and it is, therefore, very important to determine the relative strengths and limitations of the various surface wave techniques including the wide variety of data reduction and modeling methodology. Blind tests/benchmarking studies provide a mechanism by which to evaluate the various surface wave methods, data reduction and analysis techniques. To this end, surface wave data consisting of SASW, active MASW and passive MASW data were acquired at the National Geotechnical Experimentation Site (NGES) at Texas A&M University (TAMU) and provided to the academic and professional community for reduction and analysis using various techniques.

OVERVIEW OF SURFACE WAVE DATA

SASW, active MASW and passive MASW data were acquired along a profile at the TAMU NGES. SASW data were acquired at two locations centered at 18.6 m (Test Site 61) and 39 m (Test Site 128) along the profile (Figure 1). The SASW data were acquired in a common center point configuration with receiver spacings of 1.2 to 39 m. Both forward and reverse shot locations were occupied for each receiver spacing with the source offset from the near receiver typically between one and two times the receiver spacing. A sledge hammer was used for the 1.2 to 4.8 m receiver spacings and a vibratory energy source was generally used for the larger receiver spacings. The relative location of the center of each SASW array and the receiver array is presented in Figure 1.

MASW data were acquired along two arrays of 62 4.5 Hz vertical geophones spaced 0.61 m apart and centered at 18.6 m (Test Site 122_0) and 48.5 m (Test Site 98_220), respectively, as shown by the lines on Figure 1. The energy source for the MASW testing consisted of a sledgehammer (5 stacks) at five locations between 3 and 15.2 m from one end of the receiver array as denoted by the "x" symbols on Figure 1.

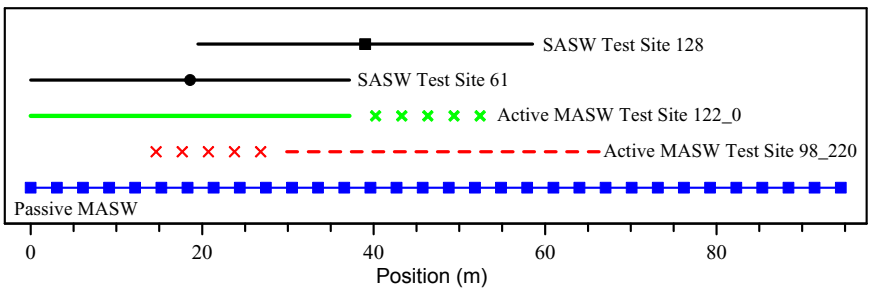

Figure 1. Relative position of SASW, active and passive MASW test locations along profile

Passive MASW data were acquired using 32 4.5 Hz geophones spaced 3 m apart and located between 0 and 94.5 m on the profile as shown in Figure 1. A total of twenty 32 second noise records were obtained using a sample rate of about 2 ms. An additional 6 noise records were obtained with a person jogging along the length of the array. Information on the noise conditions at the site by which to assess the applicability of the passive MASW technique was not available to the author. Array microtremor data were not acquired during this benchmarking exercise.

DATA REDUCTION

The SASW, active MASW and passive MASW data were reduced using several readily available commercial software packages. Some data reformatting was required to convert the provided data files into a format compatible with the software packages utilized. The primary interest of the author was comparison of the surface wave dispersion data acquired using the various surface wave methods.

SASW Data Reduction

The SASW data were reduced using WinSASW v1.23. SASW dispersion data were also extracted from selected MASW receiver pairs using a version of Geogiga Surface Plus (Geogiga, Inc.) containing modifications requested by the author. SASW dispersion data with a maximum wavelength of 30 m were extracted from hammer MASW records, a realistic limit for a sledge hammer energy source. The SASW dispersion data outlined above are presented in Figure 2 and were used as the basis for comparison with active and passive MASW data.

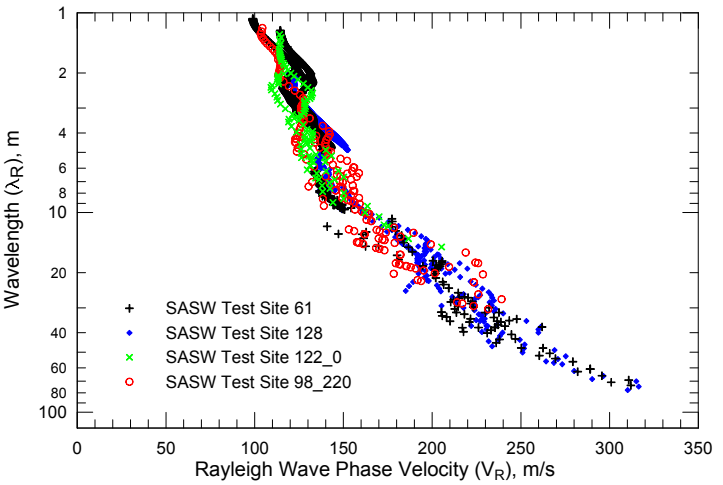

Figure 2. SASW dispersion data

Active MASW Data Reduction

The MASW data were reduced using SeisImager/SW (Oyo Corporation/Geometrics), Geogiga Surface Plus and/or SurfSeis 2 (Kansas Geological Survey). All of these software packages use the phase shift method (Park et. al., 1998) for the wavefield transformation and can be used interchangeably.

A comparison of the MASW dispersion data extracted using the entire receiver array to the SASW dispersion data is presented as Figure 3. The surface wave dispersion data were extracted from waveform data using an f-v transform and several strategies including: picking the dispersion curve for each shot record, combining the wavefield transforms from each shot record and then picking a single dispersion curve and muting to visible surface waves before applying the wavefield transform.

Although shown in Figure 3, MASW phase velocity data at wavelengths greater than 37 m (length of receiver array) were not used for data modeling. This is a realistic limit based on both the array length, significant scatter in the MASW phase velocities at wavelengths greater than 40 m and the fact that the sledge hammer source did not generate significant energy at frequencies below about 7.5 Hz. Both the SASW and long wavelength MASW data are subject to near field effects due to the non-planar wavefront.

Near field effects in MASW data have been the subject of significant research in recent years (e.g. O'Neill, 2003, Zywicki and Rix, 2005, Xu et. al., 2006, Bodet et. al., 2009, Yoon and Rix, 2009). This research demonstrates that near field effects, which also affect SASW data, often result in underestimated phase velocity at wavelengths greater than half the receiver spread length for linear arrays (Bodet et. al, 2009) or wavelengths greater than mean source to receiver distance (Yoon and Rix, 2009). Of course, field logistics dictate that near field effects have to be balanced with the loss of high frequency dispersion data, more significant contribution of lateral velocity variation and increased signal attenuation that result from longer receiver arrays.

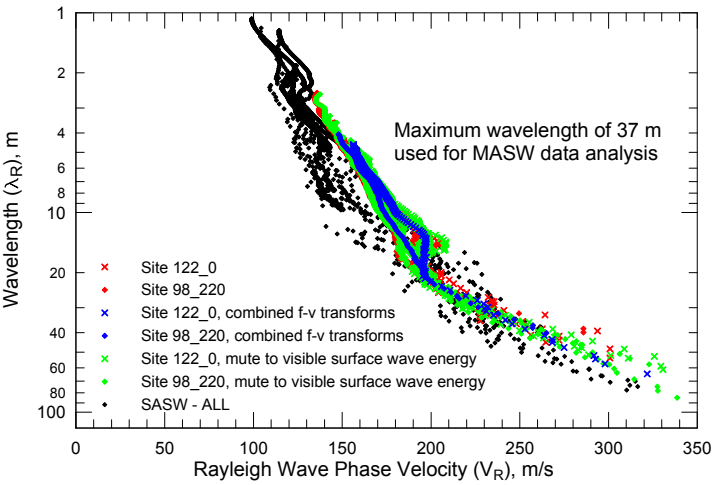

Figure 3. MASW testing at test sites 122_0 and 98_220

The MASW phase velocities are higher than those from SASW testing over the 5 to 12 m wavelength range. The smaller SASW receiver spacings effectively sample the central portion of the test area (Figure 1) and, therefore, lateral velocity variation is a plausible explanation for the difference in the dispersion curves. Reversed MASW shot locations and a center shot could have helped determine the degree to which near surface lateral velocity variation occurs at the site. Lower SASW phase velocities related to near field effects also warrants consideration. MASW phase velocities are also higher than SASW phase velocities at wavelengths greater than about 30 m indicating that V_S models developed from only MASW dispersion data may have higher velocities at depth than those developed from SASW data.

To further investigate the differences between the SASW and MASW dispersion curves, MASW dispersion analysis was conducted using a limited offset range from the near shots. Figure 4 presents a comparison of the SASW dispersion curves to MASW dispersion curves resulting from wavefield transformation of the near 16 to 31 geophones. A maximum wavelength limitation equal to the length of the utilized receiver array was utilized. As shown in Figure 4, there is a much better agreement between limited offset MASW dispersion data and SASW dispersion data. The geometry of the MASW test sites (Figure 1) is such that a similar region is sampled with the limited offset MASW data as with the small SASW receiver spacings; therefore, lateral velocity variation likely explains the improved agreement between

the two data sets. As a significant portion of the author's application of surface wave techniques is associated with estimating V_S30, a decision was made to generate a conservative velocity model by use of the lower phase velocity dispersion data. Therefore, a composite MASW dispersion data set was generated consisting of wavelengths greater than 12 to 17 m from the wavefield transforms of the entire seismic records and selected dispersion data from wavefield transform of offset limited seismic records.

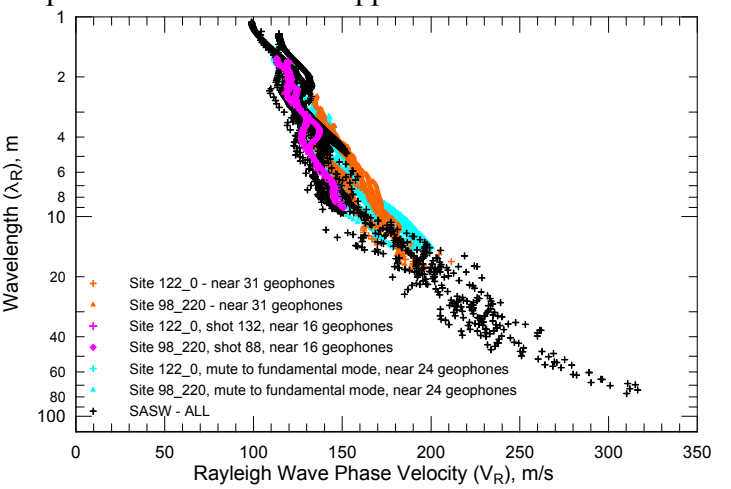

Figure 4. Comparison of MASW dispersion data over a limited receiver offset range and SASW dispersion data

Passive MASW Data Reduction

Under normal conditions the author would not consider using a passive linear array, also referred to as passive MASW or ReMi™, data without knowledge of the ambient vibration conditions at the site. Use of this array is typically limited to urban sites where the presence of numerous, omnidirectional vibration sources are a reasonable assumption. Under these conditions the technique can perform quite well, especially if tied to active surface wave data. Array based passive surface wave techniques are preferred, but not always possible (e.g. sidewalk is the only location to make measurements). Review of the passive MASW data indicated that the site was less than ideal for application of the technique, possibly due to a dominant cross line noise source, and passive dispersion data were extracted from only four (4) of the 20 noise records using both the ReMi™ and spatial autocorrelation (SPAC) techniques (Figure 5). A maximum wavelength limitation of 94.5 m, the receiver array length, was applied to the passive MASW dispersion data. No attempt was made to extract dispersion data from the passive surface wave records acquired with a person walking along the array.

There is very good agreement between the active and passive surface wave data even though the passive MASW dispersion analysis was conducted on only four of the 20 seismic records. There is significant

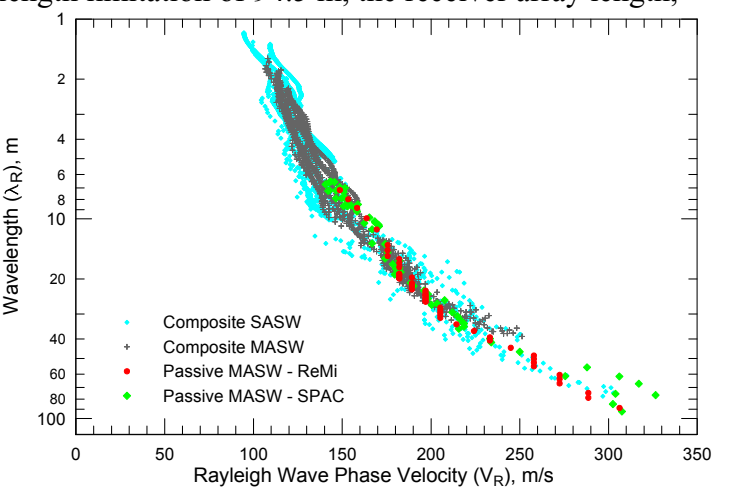

Figure 5. Comparison of Composite SASW, MASW and Passive MASW Dispersion Curves

scatter in the SPAC dispersion data at wavelengths greater than about 53 m with only the lower phase velocities used for modeling.

Representative Dispersion Curves

Prior to data modeling, especially if using inversion techniques, it is necessary to develop a regularly sampled representative dispersion curve. Numerous schemes exist for generating the representative dispersion curve including manual picking, direct averaging and more sophisticated averaging schemes. The moving average curve fitting routine outlined in Joh (1996) and as implemented in WinSASW V3.1.2 was used to generate representative dispersion curves for the SASW and combined active and passive MASW data sets. In retrospect, manual picking of a dispersion curve may have been more appropriate given the irregular sampling of the dispersion data from the various techniques. The representative dispersion curves were sampled at equal logarithmic wavelength increments.

DATA ANALYSIS

Analysis of the surface wave dispersion data was limited to forward and inverse modeling using two commercial software packages (WinSASW V1.23 and SeisImager SW) utilizing the plane wave, fundamental or effective mode Rayleigh wave assumption. Several V_S versus depth models were produced to demonstrate non-uniqueness. The water table depth was constrained by a simple 2-layer model of the first arrival seismic refraction data on the near offset MASW seismic records, which yielded a water table depth and P-wave velocity of saturated sediments of about 4.5 m and 1,825 m/s, respectively.

The S-wave velocity models were produced using the forward modeling routine in WinSASW V1 and 2D solution (fundamental mode, plane wave approximation) and the SeisImager SW package (10 layer model, 15 iterations of the inverse modeling routine, increase in velocity with depth constraint applied and not applied). WinSASW utilizes the dynamic stiffness matrix method (Kausel and Roesset, 1981) for the forward model, whereas SeismImager SW utilizes a form of the transfer matrix method (Thomson, 1950, Haskell, 1953).

The composite dispersion data, representative dispersion curve and theoretical dispersion curves and associated V_S models resulting from forward and inverse modeling of the SASW and combined active and passive MASW dispersion data are presented as Figures 6 and 7, respectively.

Although two different modeling techniques were used and multiple models were generated for each data set, V_S30 only ranges from 235 to 241 m/s (2.5 % variation) and 238 to 240 m/s (1 % variation) on the models derived from the SASW and combined active and passive MASW dispersion data, respectively. V_S30 appears relatively insensitive to model non-uniqueness and is likely more accurate than the actual V_S models; however, more testing is required, particularly from over parameterized inverse models.

CONCLUSIONS

The surface wave dispersion data acquired using all of the techniques are generally very similar. There is, however, a small difference in the MASW and

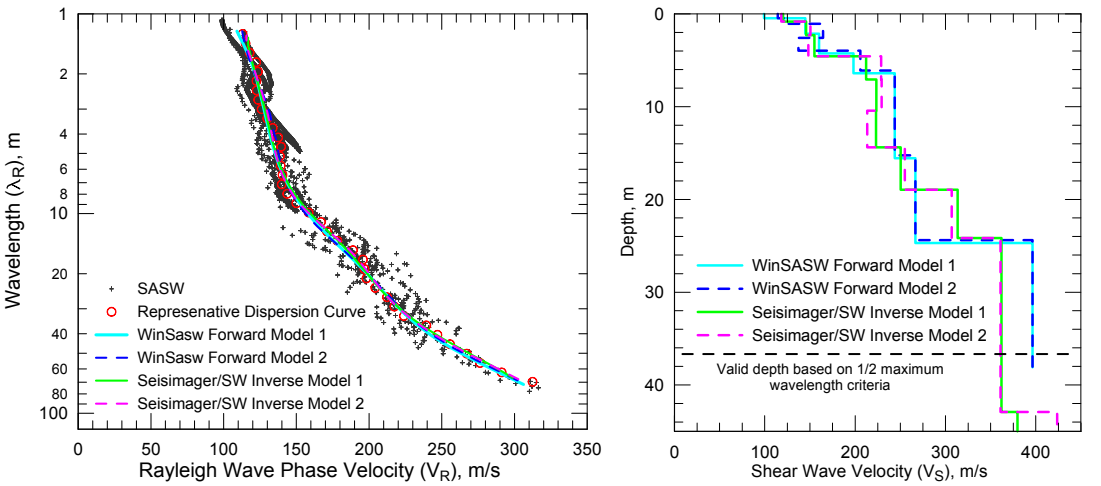

Figure 6. Composite and representative SASW dispersion curves and theoretical dispersion curves (left) and associated Vs models (right)

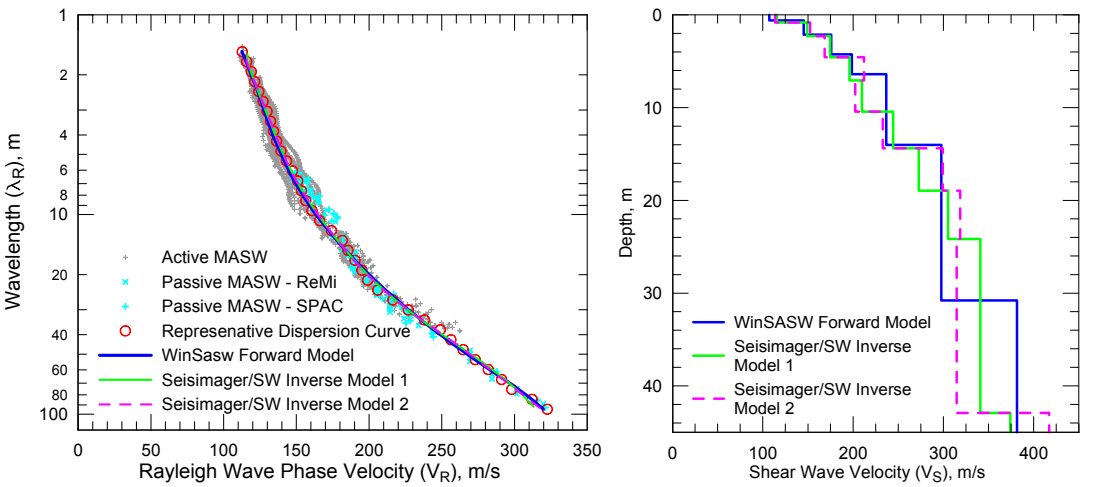

Figure 7. Composite and representative active/passive MASW dispersion curves and theoretical dispersion curves (left) and associated Vs Models (right)

SASW dispersion data over the 5 to 12 m wavelength range, likely the result of lateral velocity variation. MASW phase velocities are also higher than SASW phase velocities at wavelengths greater than 30 m although MASW phase velocities at wavelengths greater than 37 m were not used for analysis.

Several Vs models were generated for the SASW and combined active and passive MASW dispersion data to demonstrate non-uniqueness. Even though there are slight differences in the Vs models presented as Figures 6 and 7, the average velocity of the upper 30 m (V_S30) varies by less than 2.5% between models generated using the multiple techniques. Depending upon the degree to which near field effects impact the surface wave dispersion data, V_S30 could be slightly underestimated at this site.

Model improvements could be achieved using processing techniques such as 3D array based processing of the SASW data in an attempt to model multiple modes of wave propagation, the cylindrical wavefront and modal superposition. Multi-mode inversion of the MASW data could also result in more accurate Vs models.

REFERENCES

Bodet, L., Abraham, O., and Clorennec, D. (2009). "Near-offset effects on Rayleigh-wave dispersion measurements: physical modeling." *Journal of Applied Geophysics,* 68, 95-103.

Brown, L. T. (1998). "Comparison of V_S profiles from SASW and borehole measurements at strong-motion sites in Southern California." Master's Thesis, University of Texas, Austin.

Haskell, N. A. (1953). "The dispersion of surface waves on multilayered media." *Bulletin Seismological Society of America*, 17-34.

Joh, S. H. (1996). "Advances in interpretation and analysis techniques for spectral-analysis-of-surface-waves (SASW) measurements." Ph.D. Dissertation, University of Texas, Austin.

Kausel, E. and Roesset, J. M. (1981). "Stiffness matrices for layered soils." *Bulletin Seismological Society of America*, 71(6), 1743-1761.

Louie, J. N. (2001). "Faster, Better: Shear-Wave Velocity to 100 Meters Depth from Refraction Microtremor Arrays." *Bulletin of the Seismological Society of America*, 91 (2), 347-364.

Martin, A. J., Shawver, J. B. and Diehl, J. G. (2006). "Combined use of Active and Passive Surface Wave Techniques for Cost Effective UBC/IBC Site Classification", *Proceedings of the 8th National Conference on Earthquake Engineering*, San Francisco, California, paper no. 1013.

Okada, H. (2003). "The Microtremor Survey Method." *Geophysical Monograph Series Number 12*, Society of Exploration Geophysicists.

O'Neill, A. (2003). "Full-waveform reflectivity for modeling, inversion and appraisal of seismic surface wave dispersion in shallow site investigations." Ph.D. Dissertation, University of Western Australia, Perth.

Park., C.B., Miller, R.D. and J. Xia (1998), "Imaging dispersion curves of surface waves on multi-channel record." *68th Annual International Meeting of the Society of Exploration Geophysics*, Expanded Abstracts, 1377-1380.

Park., C. B., Miller, R. D. and Xia, J. (1999). "Multichannel analysis of surface waves." *Geophysics*, 64(3), 800-808.

Stokoe, K. H., II, Wright, S. G., Bay, J. A. and Roesset, J. A. (1994). "Characterization of geotechnical sites by SASW method.", *Geophysical Characterization of Sites*, Technical committee for XIII ICSMFE, A.A. Balkema Publisher, Rotterdam, Netherlands, 785-816.

Thomson, W. T. (1950). "Transmission of elastic waves through a stratified solid medium." *Journal of Applied Physics*, 21(2), 89-93.

Xu, Y., Xia, J. and Miller R. D. (2006). "Quantitative estimation of minimum offset for multichannel surface –wave survey with actively exciting source." *Journal of Applied Geophysics*, 59, 117-125.

Yoon, S. and Rix, G. J. (2009). "Near-field effects on Array-based surface wave methods with active sources." *Journal of Geotechnical and Geoenvironmental Engineering*, 135(3), 399-406.

Zywicki, D. J., and Rix, G. J. (2005). "Mitigation of near-field effects for seismic surface wave velocity estimation with cylindrical beamformers." *Journal of Geotechnical and Geoenvironmental Engineering*, 131(8), 970-977.

Active Risk Management in Geotechnical Engineering

W. Allen Marr[1], PE, PhD, NAE, F.ASCE

[1]President and CEO, Geocomp Corporation, 125 Nagog Park, Acton, MA 01720 wam@geocomp.com

ABSTRACT: *Active risk management, (ARM^{TM}),* is a systematic process of identifying, analyzing, planning, monitoring and responding to project risk ***over the life of the project***. It involves processes, tools, and techniques that help the project team minimize the probability and consequences of adverse events (threats) and maximize the probability and consequences of positive events (opportunities) throughout the life of the project. It is especially useful in projects with significant geotechnical risks. It provides the project team with more complete information on the risks they face in a format understandable to non-specialists – cost and schedule impacts. It identifies the uncertainties and potential events that create the most risk to the project and develops ways to minimize these uncertainties as they affect final project cost and schedule.

The concept of Active Risk Management applied to civil engineering projects has been developed by the author on a variety of projects over 35 years. This paper lays out the steps of Active Risk Management and discusses how they are applied in geotechnical engineering. It illustrates the use of the method with a practical example that shows the value of obtaining additional geotechnical information to reduce risk.

INTRODUCTION

Every construction project faces risks that threaten successful completion of the project as measured by cost, schedule and quality. The construction industry is seeking better ways to manage these risks. Since the 1970's, the author and his colleagues have worked with clients in the infrastructure market to identify and quantify risks for specific projects, then develop risk management strategies that provide the most benefit to the project in terms of cost, schedule and quality. This work has led to the concept of Active Risk Management which recognizes that risk management efforts must extend throughout the life of a project and must be based on information that is current and comprehensive. This document represents the synthesis of our experience with risk management into a logical and consistent approach that has saved clients large sums of money by actively managing risk throughout the project.

Project risk is an uncertain event or condition that potentially impacts the project objectives for cost, schedule, and quality. Impacts may be both positive and negative. A risk has a cause and, if it occurs, a consequence. Risk is the combination of the likelihood of the uncertain event times its consequence. A likely event with moderate consequences may expose the project to more risk than an unlikely event with high consequences. ***Risk management*** is a systematic process of identifying, analyzing, planning, monitoring and responding to risk. It involves processes, tools, and techniques that help the project team minimize the probability and consequences of adverse events and maximize the probability and consequences of positive events.

Many organizations practice some form of risk management on construction projects. Generally these activities focus on risk assessment and risk allocation by individual members of the project team. These activities are organized to manage that member's risk by transferring, avoiding, mitigating or accepting specific risk elements. This is not managing overall project risk. It may in fact increase total project costs because risks do not get allocated to the team member best positioned to manage that risk at an efficient cost.

ACTIVE RISK MANAGEMENT

The author has developed the concept of **Active Risk Management™** (ARM™) to describe an organized risk management strategy that transcends the entire project. ***Active risk management*** is a systematic process of identifying, analyzing, planning, monitoring and responding to project risk ***over the life of the project***. It involves processes, tools, and techniques that help the project team minimize the probability and consequences of adverse events (threats) and maximize the probability and consequences of positive events (opportunities) throughout the life of the project.

Active Risk Management provides the project team with more complete information on the risks they face in an understandable quantitative format – cost and schedule at risk – and does so in near real-time. This not only helps team members make informed decisions, but also monitor the progress of risk management efforts over the duration of the project.

Active Risk Management provides quantitative information on the impacts of each risk component to cost, schedule and quality so that the most significant risks can be managed with the most effective approach. It applies methods of uncertainty analysis with project management tools to consider all potential risks and find those with the highest potential impact on the project objectives.

The physical processes of construction inherently involve substantial uncertainty that creates risk to the owner, contractor and engineer. These risks are in addition to the conventional risks (those from injury, contract, regulatory, legal, financial, weather and others) associated with the project. No amount of planning and engineering can predict with 100-percent certainty how the various elements of the project will actually perform during construction. Among the unknowns are: the geologic profile; the engineering properties of each component of the geologic profile; the groundwater conditions; the in situ stresses; the effects of environmental conditions, construction activities, and time on the underground conditions; limitations of analysis and design methodologies; unknown obstructions; location,

condition and performance during construction of existing utilities and other structures; and interactions between the ground and structures. There may also be uncertainty in the forces from extreme events that the project will experience. On top of these are the uncertainties that derive from accidents, mistakes, poor judgment, and improper actions of the work force and other construction issues during the performance of the work. These types of risk are referred to as "operational risks". Operational risks are often ignored in the contractual, financial, and legal discussions of risk management; yet they may jeopardize the entire project.

One approach to managing risks is to develop a conservative design based on what the project team considers a worst-case scenario, and hope for the best. But unexpected factors, such as excessive ground movements or unexpected groundwater flow can damage completed work or adjacent facilities. These, in turn, can cause project delays, add substantial costs, degrade quality, or risk the health and safety of workers and the public. A more cost-effective way to manage risks is to design for the most likely scenario based on an investigation of the underground conditions and potential hazards. The design process includes a risk assessment to determine which sources of uncertainty dominate the operational risks, which risks can be reduced with design modifications, and which risks can be avoided with observation and remedial work during construction, i.e. monitoring how the site actually performs as construction begins, then making adjustments to the design and/or construction methodology as required by the observed performance. The risk assessment is continually reviewed and updated as new information becomes available. This approach is the essence of Active Risk Management™. The ARM™ method has similarities to Dr. Peck's Observational Method (Peck, 1969) from a geotechnical engineer's perspective, but looks more broadly at all potential risks to the project; makes quantitative estimates of the relative magnitudes of each risk element and its impact on cost, schedule and quality; and monitors Key Risk Indicators.

Active Risk Management uses historical data, expert judgment with tools from decision theory, and probability theory to make numerical assessments of each component of risk for construction. Measurements of actual conditions as they unfold and opinions from subject matter experts are integrated with formal analyses to produce a balanced quantitative assessment of each source of operational risk in terms of potential impact on cost and schedule. This approach has helped owners and contractors make informed decisions regarding design and construction of major facilities – decisions that have saved hundreds of millions of dollars by avoiding overly conservative approaches and focusing resources on the most beneficial actions.

Effective risk management consists of several steps that can be visualized as a continuous circle of improvement shown in Figure 1. Effective risk management requires the process of risk mitigation to be completed and repeated throughout the project duration as new information becomes available. Past risk management practice on many projects has typically been to prepare a risk assessment during the planning phase of a project, make some decisions on risk allocation, then do little formal work on risk management for the remainder of the project. This practice does not provide the substantial benefits of a complete risk management program. Effective risk management of project construction starts in the planning phase, and

Fig. 1: Circle of Risk Management

continues until after the facility is placed into service or risks are reduced to an acceptable level.

Numerous sources of risk exist on a complex project. It becomes easy to overlook or forget a significant source of risk that later threatens the project objectives. Using established methods and tools, qualitative risk analysis assesses the probability and the consequences of each identified risk to determine its overall importance. Risks to project cost and schedule involve two principal elements: uncertainties in quantities and unit costs for known elements and unknown conditions and events that are not covered in the baseline cost and schedule elements. During the planning phase of a project, quantities and unit prices may have considerable uncertainty. These uncertainties can be estimated by asking the sources of the information to expand their estimates to lowest possible value, highest conceivable value and the most likely value for each cost, quantity, and schedule item.

These types of variability have traditionally been handled by the estimators making individual conclusions about what amount to put into a price estimate and then adding a contingency to the project total cost. The problem with the contingency approach is that different estimators use different means to decide how much contingency to add to each cost item and then another contingency gets added to the total bid cost. No one knows what the final project price really represents relative to all the uncertainties that were or were not considered in the individual price elements.

APPLICATION ILLUSTRATION

Explicit consideration of the best estimates of the uncertainties in each element of the project costs can be used to obtain a range of probable cost for the project. This range can then be used to decide how much risk to accept in preparing the final bid price. This is illustrated with an example. A large earthworks project is estimated by conventional means to cost $495 million. The bid management team discusses uncertainties and risks and decides to add a 6% contingency to the base estimate for external risks making their total cost estimate $525 million.

A risk assessment breaks this global estimate of risks into an estimate of uncertainty in cost and schedule for each component of the project and for each potential risk event. Table 1 gives a summarized risk registry for the primary unknowns. A detailed review by item of the base cost and schedule with the project estimators results in a range for base cost and schedule. Table 1 summarizes the estimates for lowest possible value, the highest conceivable value and the most likely value (called mode) for costs, schedule and likelihoods. The values come from the subjective assessments by the project team members most familiar with the project. A review with the project team indicates 5 events with significant potential impact to the project cost and schedule that were not covered in the base cost and schedule estimate. Estimates

are made for the range of potential cost and schedule impacts to the project and for the likelihood that each of these events may occur. Note that uncertainty in the likelihood estimate is also included. These data are used as input to a numerical simulation run in a spreadsheet that develops a probability distribution for each uncertain element and numerically integrates the individual event distributions into one overall distribution on cost and another on schedule. These risk costs are added to the base cost uncertainties to obtain the overall uncertainty for project cost. Such estimates are shown by the six curves in Figure 2.

Table 1: Simplified Risk Registry

Risk Event	ID	Consequence (ranges are lowest, mode and highest estimates)	Likelihood and Sources of Data
Base	Base	475/500/550 millions 46/48/54 months	100% review of base estimates
Earthwork issues	A	5/6/7.5 millions 3/4/6 months	12-16-22% from project manager
Delays in shoring delivery	B	7/8/9 millions 4/5/6 months	10/20/25% from suppliers
Unexpected site conditions	C	30/54/90 millions 4/6/8 months	7-10-15% from geotechnical consultants
Bad weather	D	1/1.5/2.5 millions 1/1.3/2 months	9-12-15% from weather records
Approval Delays	E	0.2/0.25/0.3 millions 3/4/6 months	25-30-35% past experience
Additional Testing and Monitoring	F	1/1.2/1.5 millions No schedule impact	Likelihood for A reduced to 4/5.3/7.3%; Likelihood for C reduced to 0.7/1.0/1.5%

The seventh curve, ID F, is actually an opportunity. An additional testing program to reduce uncertainty in soil properties and a performance monitoring program to give early warnings to invoke contingency measures costs money but reduces uncertainty which lowers risk. The reduced uncertainty lowers risk costs by much more than the cost of the additional work.

Accounting for risk costs from event uncertainties in the example increases the best estimate of the base cost from \$495M to \$507 million. There is a 10% chance that the base cost could exceed \$530M. The range of probable cost for the project with all uncertainties and identified risks accounted for is \$492 to 554M (C_{10} and C_{90} exceedance values). Prudent decision makers would consider this range of probable cost in preparing budgets for the project and bids for the construction. It is useful to note that an estimate using mean values for unit prices and quantities and adding a 6% contingency to account for uncertainty in costs and quantities, but not including the unknown risks, would yield a cost of \$525M. Figure 2 shows that there is a 15% chance that this cost will be exceeded if risk events A-E are not considered and a 33% chance if risk events A-E are included. Most contractors would be very

uncomfortable bidding a project with a price that had a 33% chance of being exceeded.

Figure 3 shows the risk curves for schedule. The best estimate of likely time to complete the job is 48 months. Adding in the effects of potential external events shows that the chance of completing the project in 48 months is about 10%. There is a 10% chance that the project will take more than 56.6 months to complete. This additional time has a significant impact on the cost of the project.

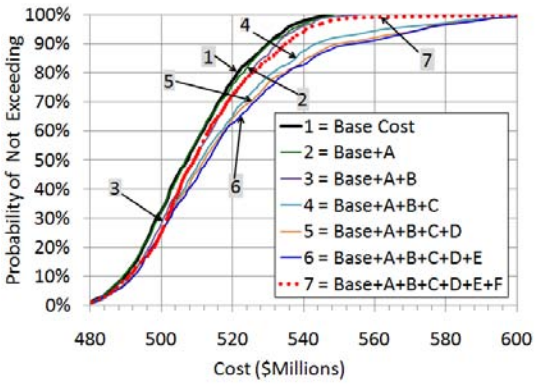

Fig. 2: Estimated Cost with Risk

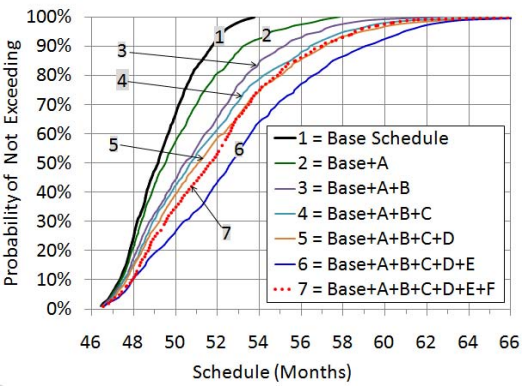

Fig. 3: Estimated Schedule with Risk

This example shows the effects of uncertainties on project costs and schedule estimates during the planning phase of a project. As the project progresses, new information alters the uncertainties. Pricing and quantities become more certain. As time passes, a risk event happens or doesn't happen which alters its probability to 0 or 1. Uncertainties in cost and schedule can also be reduced by collecting additional information that reduces uncertainty in risk events. Curve 7 shows the potential benefits of performing more testing on the earthen materials to reduce uncertainty in how they can be excavated and compacted, and of adding an instrumentation program to determine as early as possible how the work is performing and whether remedial actions may be required to prevent undesirable performance, such as a slope stability failure or a foundation failure, that increase cost or schedule.

Another useful outcome of the risk assessment is a ranking of the sources of risk by their relative impacts on estimated cost and schedule. Figures 4 and 5 show results for this example. The highest cost risk is caused by uncertainty in site conditions. Based on the cost and likelihood estimates of the team this uncertainty has an expected cost impact of $6.5M on the project and a schedule delay of 0.6 months.

ID F in Table 1 illustrates opportunity. By performing further site investigations to lower geotechnical uncertainty and adding a performance instrumentation-monitoring system, there is an expected cost increase of $1.2M but the value of the expected reduction in risk is $7M for a net potential gain of almost $6M and a schedule reduction of 1 month. The effect on the risk curves for cost and schedule are shown by the difference between curves 6 and 7 in Figures 2 and 3. For geotechnical engineers, results like these provide a great way to communicate the value of additional site investigations and performance monitoring programs to clients.

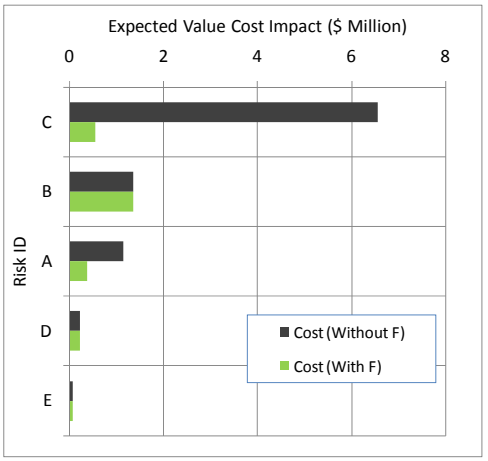

Fig. 4: Tornado Chart for Costs

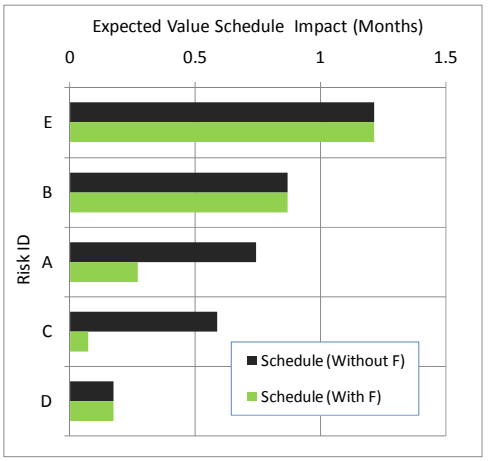

Fig. 5: Tornado Chart for Schedule

The Risk Management approach illustrated in this example occurs at the beginning of the project. It provides very useful information to help bid the project and develop strategies to manage the project to minimize risks during the execution. It provides a rational and consistent methodology to quantify all uncertainties in the project cost and schedule elements. To be most effective however, this risk assessment methodology should continue throughout the project with a monitoring and updating program to expose emerging risks and manage their consequences. This addition is what makes the Active Risk Management concept unique. The "F" event given in the example shows the potential benefit of continuing risk management through the project.

TEN STEP APPROACH TO ACTIVE RISK MANAGEMENT

The ARM^{TM} approach to risk management involves close teamwork among the Owner, the Engineer, the Contractor (if contract has been awarded) and a team of subject matter experts. The Owner provides information on the project scope and objectives and supplies other resources necessary to conduct the risk assessment. The Engineer provides information on possible risk

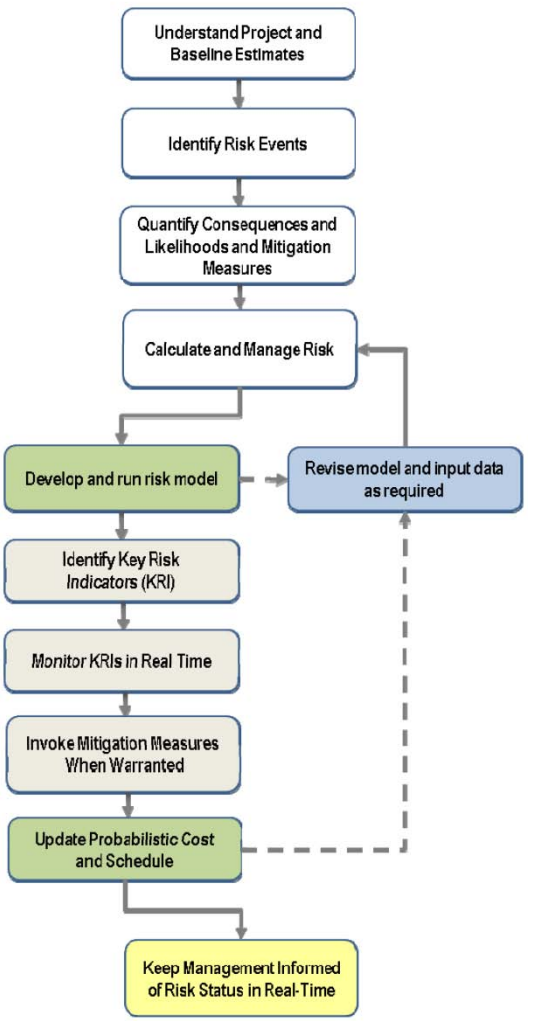

Fig. 6: Work Tasks for Active Risk Management Process

events, their likelihood of occurrence and their consequences. Perspective Contractors, or construction specialists, also provide information on possible risk events - especially those tied to construction means and methods, their likelihood of occurrence, and their consequences. The Risk Team facilitator provides the framework for a systematic examination of risk by the team; facilitates the definition of risk events, their likelihood of occurrence, and their consequences; tests the information for completeness and consistency with scientific requirements; develops and applies a mathematical model of risk; and interprets and reports the results to the project team. The Risk Assessment Team is comprised of professionals experienced in all aspects of planning, design, and construction of the facility. Independent consultants or subject matter experts whose expertise closely aligns with unique aspects of the project and who understand the essential elements of risk analysis may be added to the team.

Figure 6 illustrates the sequence of tasks we use to complete an active risk assessment program. The process runs in a linear sequence in which the specific work in each task depends on the results of previous tasks. Each task is self evident.

CONCLUSIONS

Active Risk Management provides the project team with complete information on the risks they face in an understandable format – cost and schedule at risk. It identifies the uncertainties and potential events that create the most risk to the project and develops ways to minimize these uncertainties on final project cost and schedule. This not only helps team members to make informed decisions, but also to monitor the progress of risk management efforts over the duration of the project. Active Risk Management provides clients with a continual assessment of their risk profile and how it is changing as the project progresses. Active Risk Management identifies specific actions that can be used to alter events and reduce consequences; thereby preventing unexpected and costly events. Active Risk Management seeks to contain and control the many costs that result from unexpected and uncontrolled events. The result can be savings that are many times the cost of the risk management effort.

The author's experience shows that the project's best interests are served when key participants take a proactive approach to minimizing the occurrence of significant unexpected events and controlling the significant consequences of undesirable performance. Using Active Risk Management concepts on significant projects around the world has shown that this methodology is best applied by whoever has the most at risk in a project's successful outcome. Depending on the project and its risk profile, this may be the Owner, the General Contractor, the Construction Manager, the Insurer or the Financer.

REFERENCES

Marr, W.A. (2006) "Geotechnical Engineering and Judgment in the Information Age," Keynote lecture. *ASCE GSP GeoCongress-2006*, Atlanta, GA.

Peck, R.B. (1969) "Advantages and Limitations of the Observational Method In Applied Soil Mechanics," *Geotechnique*, June, pp. 173-187.

Risk Assessment of Success Dam, California: Flood Related Potential Failure Modes

Loren Anderson[1], Michael Ruthford[2], Vlad Perlea[2], David Serafini[2], Jack Montgomery[2], and David Bowles[1]

[1]Utah State University, 8200 Old Main Hill, Logan, UT 84322; emails: Loren.Anderson@usu.edu and david_s_bowles@hotmail.com
[2]US Army Corps of Engineers, Sacramento District, 1325 J Street, Sacramento, CA 95814; emails:Michael.E.Ruthford@usace.army.mil, Vlad.G.Perlea@usace.army.mil, David.C.Serafini@usace.army.mil and Jack.Montgomery@usace.army.mil

ABSTRACT

Potential seismic deficiencies of Success Dam, California have been identified and a remediation plan for the dam is in the process of development. The dam is currently operated under reservoir pool elevation restriction to reduce risk until the long-term remediation is implemented. Justification of operation restrictions and establishing the priority of remediation activities required preparation of a baseline risk assessment. Seepage and piping failure modes made a significant contribution to the baseline risk, but were little affected by the operating restrictions that were used to reduce the earthquake-related failure modes. This paper describes the role of the flood-induced failure modes in the risk assessment and particularly the evaluation of the piping and seepage failure modes. The USACE Piping and Seepage Toolbox was used as an aid in estimating the probability of failure by the various piping and seepage failure modes.

INTRODUCTION

The existing Success Dam is located on the Tule River, about 6-miles east of the city of Porterville, Tulare County, California. The project includes both the Main Dam and Frazier Dike. The Main Dam is a 1,040 meter (3,404 feet) long compacted earthfill embankment dam with a maximum height of 44.2 meters (145 feet). Frazier Dike is a 2,365 meter (7,760 foot) long containment dike. It is a compacted, homogenous embankment with a maximum height of 12.8 meters (42 feet) as shown in Figure 1. The Sacramento District of the US Army Corps of Engineers is conducting a dam safety remediation of Success Dam to address issues associated with seismic and seepage stability of the embankment, control tower seismic stability, and the spillway PMF routing. The companion paper by Bowles et al (2011) describes the overall approach to the risk assessment and justification of the current operation restrictions. Another companion paper by Ruthford et al (2011) discusses the potential risk of failure due to seismic loading.

The portion of the risk at Success Dam due to flood loading can be classified into two general categories: (1) Flood Failure Modes: This category includes failure by wave erosion and overtopping of both the Main Dam and Frazier Dike; and (2) Flood-internal Failure Modes: This includes failure modes due to internal erosion of

the embankment and foundation and slope instability. These failure modes were only examined for the Main Dam, as Frazier Dike is only loaded during flood events.

The following sections describe the flood and flood-internal failure modes at Success Dam.

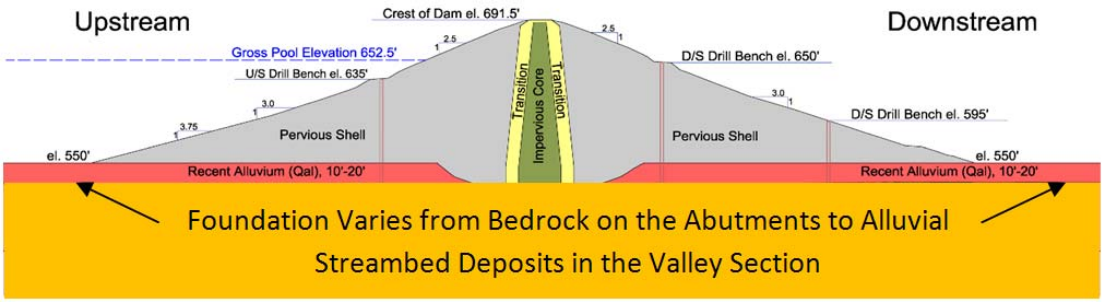

Figure 1. Typical Cross Section at the Maximum Section

FLOOD LOADING

Success Dam is currently operated with a restricted storage pool. This pool restriction limits the amount of irrigation water that can be stored during the summer months, but does not affect the flood conservation pool and therefore it has limited affect on the flood damage reduction capabilities of the dam outside the flood season. This is best illustrated by the flood control diagram for the project shown in Figure 2, which demonstrates that the potential operating restrictions only alter the operation of the reservoir outside of the flood season. This is an important factor when considering the risk-reduction benefits of any potential operating restriction, as any potential failure modes which are driven by flood events during the flood season will be unchanged by the operating restrictions.

The peak reservoir pool elevation versus annual exceedance probability (AEP) relationship for Success was estimated by first considering the historical operation of the dam up to the spillway crest which is at elevation 198.9 m (652.5 feet). Above this elevation pool levels were estimated based on flood modeling conducted by the Sacramento District. The current probable maximum flood (PMF) is projected to cause the pool to rise to an elevation of approximately 210.4 m (690.3 feet), which is below the crest of the dam at elevation 210.8 m (691.5 feet). In order to account for the risk of overtopping, the PMF was assigned an AEP of 1 in 10,000 in accordance with Corps' guidance and the peak inflow curve was extrapolated to simulate events with AEPs of up to 1 in 1,000,000.

To account for the effects of operating restrictions on the peak reservoir pool elevation versus AEP relationship, a daily reservoir simulation was run for the 41-year period of record that was available at the time of an earlier 2004 Study. Reservoir releases were limited to non-damaging discharge rates such that the storage pool is estimated to exceed the pool level specified by the operating restriction but only for relatively short periods of time. This simulation was conducted for potential operating restrictions (ORs) corresponding to pool elevations of 580, 600, 620, 630 and 640 (specified in feet).

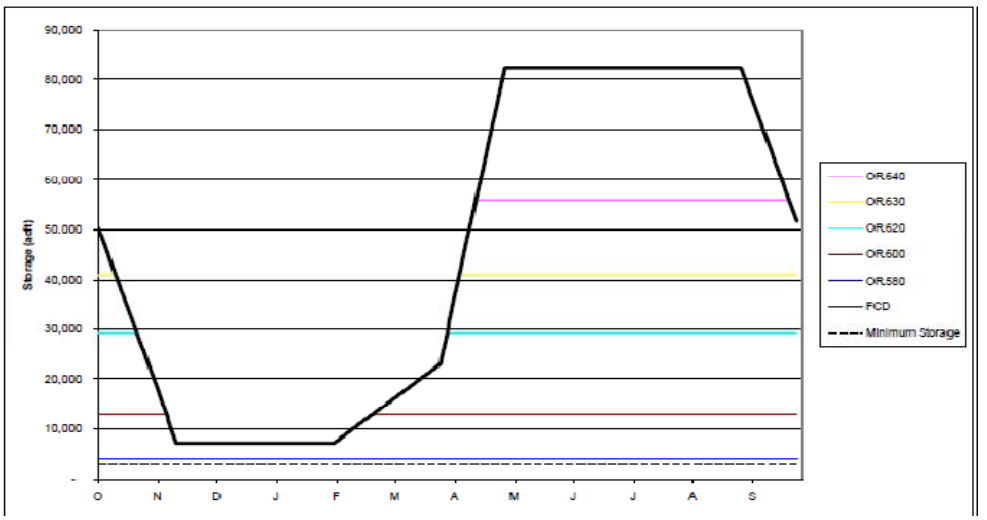

Figure 2. Flood control diagram for Success Dam showing normal operation (FCD) and potential operating restrictions.

The final curves are shown in Figure 3 for no restriction and the potential operating restrictions considered in the risk assessment. It is interesting to note that the curves all converge at an elevation of approximately 201.2 m (660 feet). Above this elevation, the effects of lower conservation pools for operating restrictions as illustrated in Figure 2 are estimated to be insignificant due to the large inflow volume relative to available reservoir storage.

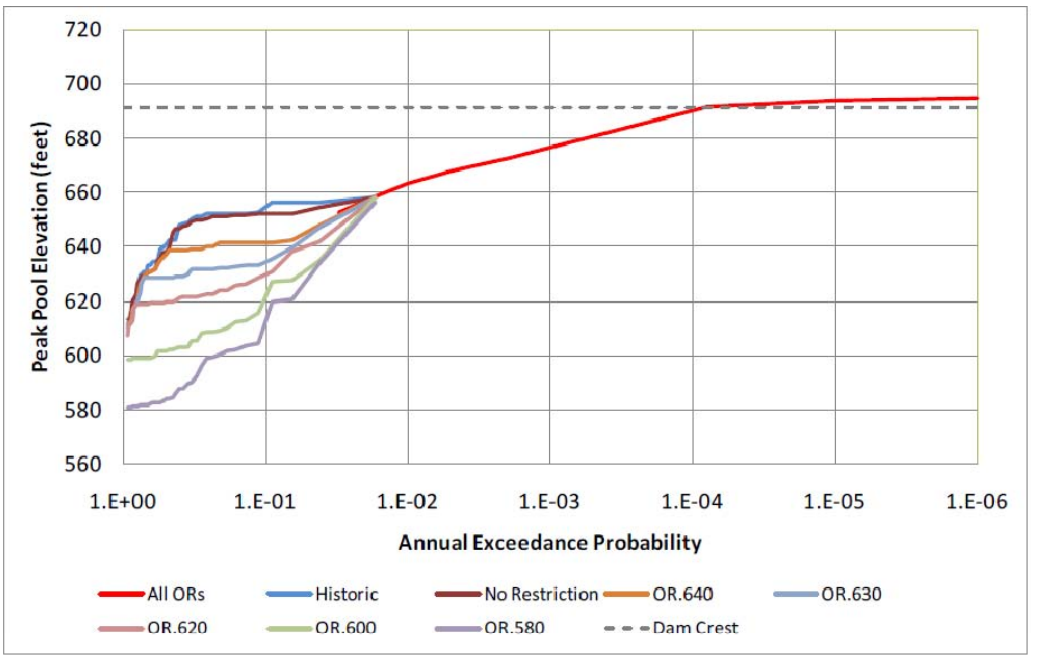

Figure 3. Peak reservoir pool elevation - AEP relationships for normal operation and potential operating restriction alternatives.

IDENTIFICATION OF POTENTIAL FAILURE MODES

After estimating the flood loading, the potential failure modes for Success dam were identified by the engineering team through a series of screening evaluations of the dam conducted for the 2004 risk assessment and the 2009 update. Three initiating mechanisms were identified which could lead to failure of the dam. These were an earthquake, a flood, and seepage either due to a flood or normal operation (called flood-internal for this study). Failure modes were only considered if they were judged to be credible (i.e., capable of causing dam failure, defined as an uncontrolled release of the reservoir) and significant for the risk assessment that was conducted.

The engineering team identified overtopping, wave erosion, slope instability and internal erosion as the primary flood induced failure mechanisms at Success Dam. A detailed assessment of piping risk at the Main Dam was aided by the Piping and Seepage Toolbox (Reclamation-USACE-URS-UNSW 2008). Each of the initiating mechanisms addressed in the toolbox was discussed as it related to Success Dam. Out of this screening six potential piping failure modes were identified for the Main Dam. As was mentioned earlier, only failure by overtopping was considered for Frazier Dike due to time constraints and the fact that the dike is only loaded during large flood events. Both the flood and flood-internal failure modes are discussed below. The seismic failure modes are described in a companion paper by Ruthford et al (2011).

EVALUATION OF POTENTIAL FLOOD FAILURE MODES

Three potential failure modes were considered under the general category of flood failure modes. These are wave erosion of the Main Dam, overtopping of the Main Dam and overtopping of Frazier Dike. The likelihood of each of these failure modes occurring was estimated by the engineering team for the risk assessment with consideration of the slope protection, material erodibility and the duration of the flood events. Table 1 was used to guide the judgment of the team. The team estimated the system response probability (SRP), or the conditional probability of failure, for each of the three failure modes in this category. Each of these three failure modes will be discussed briefly below.

Table 1. Probability mapping scheme (Reclamation-USACE-URS-UNSW 2008).

Verbal Descriptor	Probability
Virtually Certain	0.999
Very Likely	0.99
Likely	0.9
Neutral	0.5
Unlikely	0.1
Very Unlikely	0.01
Virtually Impossible	0.001

Wave Erosion. Failure by wave erosion was considered only for the Main Dam. The crest of the Main Dam is approximately 6.7 meters (22 feet) wide and the upstream slope is protected by rip rap, although there is concern that it does not meet current USACE criteria. The team judged that the risk due to wave erosion was negligible until the pool was within 1.5 meters (5 feet) of the crest. When the pool level reached the crest of the dam the team judged that the conditional probability of failure due to wave erosion was "very unlikely" which, using Table 1, corresponds to a probability of 0.01. As the dam begins to overtop the probability of failure due to wave erosion decreases to zero.

Overtopping. The probability of failure due to overtopping was estimated for both the Main Dam and Frazier Dike. In developing the judgment-based SRP relationship for overtopping, a number of factors were taken into consideration, including the following:

- The erodibility of the material on the downstream face of the dam
- The well maintained dam crest
- The potential duration of overtopping
- The protection of the groins where flow would be concentrated
- Comparisons with relationships developed for other dams.

Embankment overtopping would require a flood greater than the PMF at both the Main Dam and Frazier Dike. Figure 4 shows the estimated SRPs for Flood overtopping. In the case of the Main Dam, the relationship matches a standard one developed by RAC Engineers and Economists to represent embankment dams in good condition. In the case of Frazier Dike, the relationship corresponds to an embankment with relatively poor overtopping resistance.

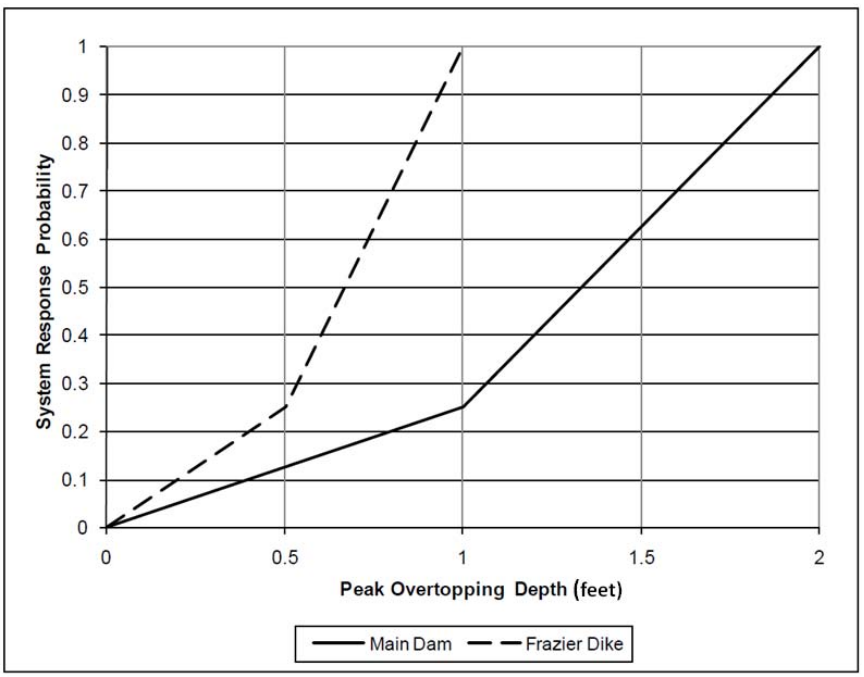

Figure 4. System response probabilities for overtopping at Success Dam.

EVALUATION OF POTENTIAL FLOOD-INTERNAL FAILURE MODES

The flood-internal risk at Success Dam is due to slope instability and piping at the Main Dam. These failure modes were not considered for Frazier Dike. The SRP relationships for the piping failure modes were estimated using guidance from the "Event Tree Method" proposed in the Piping and Seepage Toolbox (Reclamation-USACE-URS-UNSW 2008). The process of internal erosion and piping is broken down into five basic events of initiation, continuation, progression, intervention, and breach failure represented in the toolbox using an event tree model. Using the toolbox as a guide, engineering judgment was used to estimate the conditional probabilities of failure for each branch of these event trees for four reservoir pool elevations, thus providing a SRP relationship. Elevation 590 feet was considered to be a piping failure threshold for all piping failure modes. Estimates were also made for elevations 620, 656 (approximately the pool of record) and 689 feet [approximately the PMF peak pool level, which has since been revised to elevation 210.4 m (690.34 feet)]. Each of the seven potential flood-internal failure modes is discussed briefly below. The piping failure modes are listed in order of decreasing contributions to the total estimated probability of failure and the SRP relationships for each are shown in Figure 5.

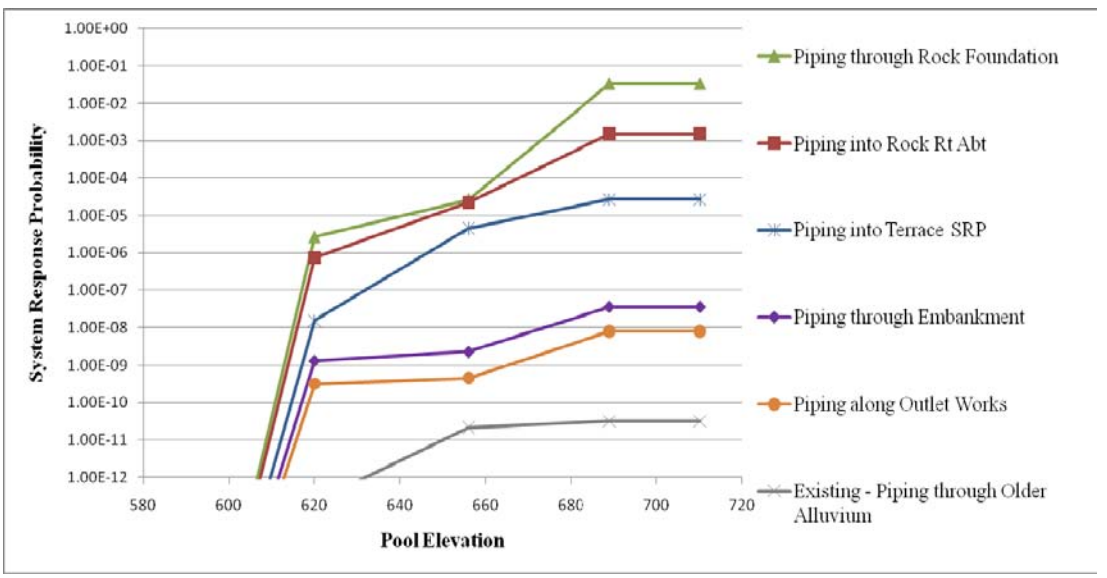

Figure 5. System response probabilities for the piping failure modes.

Slope Instability. The potential for static slope instability at the Main Dam was evaluated for the full range of pools under consideration. This was accomplished by performing a probabilistic slope stability analysis using the SLOPE/W and SEEP/W modules of Geostudio 2007(Geo-Slope 2007) and guidance from ETL 1110-2-561 (USACE 2006). The results of the analysis showed extremely small conditional probabilities of failure due to static slope instability [approximately 2 x 10^{-8} for pool elevation 210.6 m (691.1 feet)]. This is consistent with the relatively high static factors of safety (approximately 1.6 for this pool elevation) for the Main Dam. These results showed that static slope instability was not a significant risk driver for this

project. This result is in agreement with historical performance and past engineering analyses.

Piping through the rock foundation. Historical seepage and recent analyses of instrumentation data have shown that areas of the rock foundation in the right and left abutment develop artesian conditions under high pools. There is concern that joints in the foundation may not have been treated properly or may have infilled material which could erode, dramatically increasing the seepage through the upper portion of the bedrock, which could lead to sloughing and unraveling of the downstream shell.

Piping into the rock foundation. The core trench in the right abutment of the dam is founded on bedrock, which may or may not have been properly treated prior to material placement. This failure mode considers the possibility that the core material could be piped into open joints in the rock and exit unfiltered downstream. This could lead to breach of the dam through sinkhole development. This failure mode is different from the previous one in that material would be piped into the joints and exit downstream, as opposed to increased seepage being transmitted through the joints and into the downstream shell. This failure mode had a lower estimated probability of occurring than the previous one because it required that open joints are in contact with the core material.

Piping into the terrace deposits. In the left abutment of the Main Dam, the core trench is founded on a partially cemented older alluvial deposit, but the walls of the trench are exposed to a coarser-grained terrace deposit. This deposit does not meet filter criteria for the sandy clay core and there was concern that the transition material may have "pinched out" in this area. This concern was based on an interpretation of as-built drawings and construction photos, but upon a re-examination of the evidence the team judged that the likelihood of the transition material not being in place was "very unlikely". This reduced the overall SRP below the two failure modes above that are associated with the rock foundation.

Piping through a layer of high permeability in the core. The engineering team identified a possible issue of piping through a poorly compacted or high permeability zone through the core. This zone could have been caused by desiccation cracking of the core material due to seasonal shutdowns or due to the haul road, which ran across the core near the closure section of the embankment. Construction photos show evidence of both of these and there is little evidence of how the surfaces were prepared prior to placing the next lift of material. Although identified as a possible issue during the screenings, subsequent evaluations showed this failure mode poses a low likelihood of failure.

Piping through the embankment along the outlet works. Success Dam has an embedded circular conduit with seepage collars. The engineering team examined construction photos and as-built drawings and concluded that it appears that care was taken when placing core material around the conduit, but observations at other dams

have shown it is difficult to achieve good compaction around seepage collars. Further evaluations showed this failure mode had a low likelihood of failure.

Piping into the older alluvium foundation. Portions of the core trench of the Main Dam are founded in older alluvial materials. These materials are primarily cemented, but during construction some discontinuous layers of uncemented sand were discovered. This failure mode captures the possibility that one of these pervious layers is continuous and in contact with the core. Core material could be piped downstream and exit unfiltered into the shell or recent alluvium. If no crack filling takes place the pipe could progress to the reservoir leading to a dam breach through gross-enlargement or sinkhole development. This failure mode seemed to be virtually impossible to the engineering team, but was fully examined using the toolbox in order to definitively support the low likelihood of occurrence.

SUMMARY

Success Dam is currently under evaluation for possible remediation to address dam safety concerns stemming from both seismic and hydrologic loading. The loading for the flood and flood-internal failure modes is driven both by flood events and seasonal storage of irrigation water. Success Dam currently has an operating restriction, but this has only a limited effect on higher frequency floods. Several failure modes have been identified ranging from overtopping to foundation piping. System response probabilities for each failure mode were estimated by the engineering team and were used to estimate the overall project risk. The conditional system response probabilities show that the largest piping risk is due to the rock foundation, which is consistent with historical seepage observations and instrumentation data. Two companion papers describe the seismic failure modes (Ruthford et al 2011) and the overall approach to estimation of the dam failure risk at this project (Bowles et al 2011).

REFERENCES

Bowles, D. et al. (2011). “Risk assessment of Success Dam, California: Evaluation of operating restrictions as an interim measure to mitigate earthquake risk.” *GeoRisk 2011 ASCE Conference,* Atlanta, Georgia, USA.

Geo-Slope International (2007). “Geostudio 2007: Geotechnical Modeling Software”, Geo-Slope International, Calgary, Alberta, Canada.

Reclamation-USACE-URS-UNSW (2008). *Risk analysis for dam safety: A unified method for estimating probabilities of failure of embankment dams by internal erosion and piping*. August 2008. Version: Delta, Issue 2.

Ruthford, M., V. Perlea, D. Serafini, M. Beaty, L. Anderson, and D. Bowles. (2011). “Risk Assessment of Success Dam, California: Earthquake Induced Potential Failure Modes.” *GeoRisk 2011 ASCE Conference,* Atlanta, Georgia, USA.

USACE (2006). *Reliability analysis and risk assessment for seepage and slope stability failure modes for embankment dams*. Engineer Technical Letter (ETL) 1110-2-561. January 2006. Washington, D.C.

GEOTECHNICAL RISK IN THE PERUVIAN ANDES

A. Carrillo-Gil[1] and A.Carrillo-Acevedo[2]

[1] P.E., Fellow ASCE. Research Unit, Department of Civil Engineering, Ricardo Palma University, Jr. Emilio Fernandez 296, Of. 703, Santa Beatriz, Lima 01, Peru; Ph (511) 433-9591; FAX (511) 433-0299; e-mail: acsac01@speedy.com.pe
[2] P.E., Member, ASCE. 471 NW 82 Av. Suite 711, Miami, FL33126, USA; Ph 786 879 0415; FAX 305 261 1241; e-mail: arnaldo1124@gmail.com

ABSTRACT

Not many civil engineering technical documents confront an uncertainty comparable to the existing one in the calculations of the geotechnical risk in the Peruvian Andes. The reason of this uncertainty is the dispersion of values of calculation variables that engineers have to input into their models. After many research studies, it has been possible to obtain "reliability curves" about Andean slopes at the Peruvian North region. These curves represent the risk and reliability level for static and pseudo-static conditions (severe seismic conditions), having been determined that a reliability index greater than 2 is acceptable considering the uncertainty of soil and rock geotechnical parameters in the studied region. Analyses are made in order to establish a correlation between the estimated factor of safety, the reliability index, the terrain slope, and the corresponding vulnerability levels. It was found that in order to achieve an acceptable reliability level, the slopes should be less than 36 degrees with a static factor of safety of at least 1.25. Finally, for several history cases presented on professional practice and with the results of this research, it was possible to choose the best alternative of engineering solution, which will be directly associated to a certain cost of losses that would occur in the case that no solution will be adopted for the slopes on study.

INTRODUCTION

In many cases, slope researches and landslide studies involves rudimentary ways of calculation for risk estimation. These estimations rely on geotechnical engineer judgment and experience. Many important decisions come from the advice of a specialist and not from a detailed study and explicit quantification of risk. After a complete analysis of numerous professional works and research, it has been possible to gather a database related to the engineering, geomorphology and geology of the main sliding process in the Peruvian Andes. This analysis is done by making an estimation of the probable magnitude, frequency, and impact potential during a certain period. Together with engineer experience judgment, and justified with documentation, it allows to obtain generalizations including all the known threats in a determined zone, with the purpose of being monitored and managed in the future, making it easier to take earlier decisions and to determine where to address the limited economical resources of the studied regions.

SEISMIC AND GEOLOGY CONDITIONS

The Andes was formed at the limit of the Ocean Pacific, or Nazca Plate, and the South American plate. It extends as a narrow boundary along the South American continent until North America where is called the Rocky Mountains.

The Peruvian Andes consist of a mountain system naturally formed between Peru-Chile trench and the Amazonian plain. All stratigraphy**,** geomorphology, and seismicity from the Andes are a direct or indirect result of the subduction of the Nazca Plate below the South American Plate.

The Andes development began in the Late Paleozoic era. It continued in the Mesozoic era and acquires its definitive form in the Cenozoic era (Tertiary) until nowadays. In the modern Andes evolution, many recent failures are present such as folding on the old quaternary deposits, the quaternary volcanism, the uplift of the marine terrace, as well as seismic and volcanic activity. All these events have characterized the Andes as an active seismic belt.

The first profile of the Andes and the beginnings of the Andean subduction happened in the late Paleozoic, during the tectonic phase. This phase is responsible for the continental derive origins, readjustment and straighten up of the earth plates.

The seismicity of the Peruvian Andes happens because of interplate subduction events as a result of the contact zone rupture of the Nazca plate and the South American plate and intraplate events that happen within the two of them. During the subduction events, the region has experimented four great events in 1604, 1687, 1746, and 1868. Each event had a rupture length in a range of 150 to 500 Km. Earthquakes magnitudes estimations had a range of 8.0 to 8.8 based on the rupture length. The intraplate events that affect the Peruvian Andean region happen with more frequency with earthquakes magnitudes above 7.3 or even higher, mainly within the Nazca plate subduction.

PARAMETERS CHARACTERIZATION

Based on many engineering projects executed in the Peruvian Andes, a geotechnical characterization process of the present rocks and soils resistance parameters was done. This process had as objective to determine the variation of these parameters in order to be considered on a probabilistic way into the models to be used, especially, for the colluvium and rocks frequently found during the studies. The information was completed with field and laboratory tests. The material type colluvium statistic sample was obtained from researched material distribution graphs that represent the geotechnical parameters variations and describe the uniform behavior in a Gauss bell curve.

Slope Stability Analysis. Many slope stability analyses were executed using the typical profile from the Peruvian Andes (Figure 1), considering the superficial presence of a colluvium layer, formed by breccias packed with clays and limes; and underneath rock from different origins and quality, mainly lutites, sandstones, andesites, granites, and others.

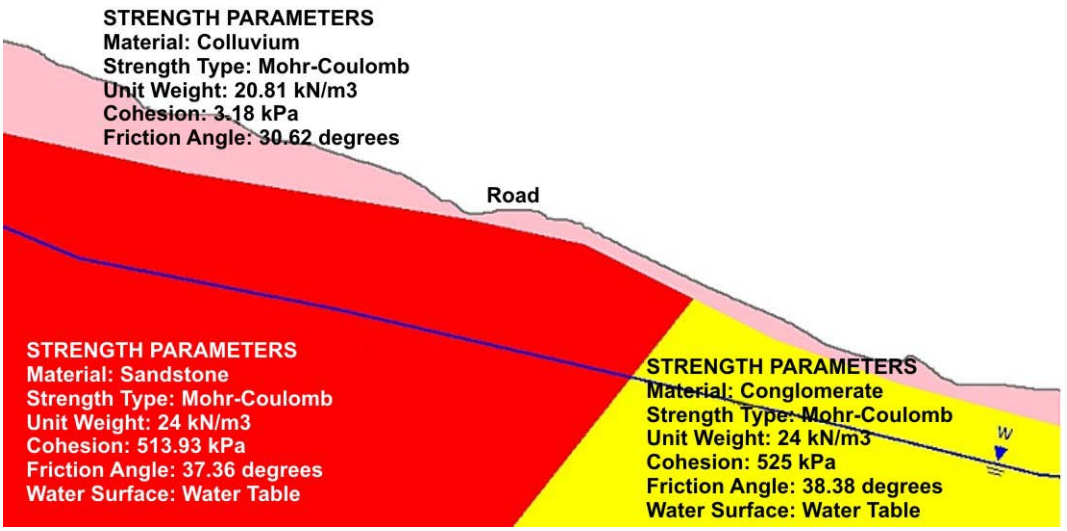

Figure 1. Typical geotechnical modeling

Due to the variability of input parameters, there is an uncertainty with respect to the geotechnical parameters of the soil. Therefore, each parameter was considered as a statistic probability distribution.

The probabilistic analysis gives a direct distribution of the factor of safety associated to a certain design and analysis situation. In these cases, a Monte Carlo simulation was adopted because of its simplicity in its methodology of analysis and because it is based from deterministic models for the procurement of results in a probabilistic form for each analyzed parameter.

RESULTS & DISCUSSION

With the realized probabilistic analysis, a sensitivity analysis to estimate the seismic risk was made on the analyzed surfaces of the geotechnical model, in order to determine the seismic acceleration value to activate a possible landslide on the study area. From the results, it was observed that landslides are probable to happen with acceleration values of 0.22g, considering all possible topographic conditions.

The probability of failure of the typical slope was managed through procedures of slope stability by engineering works. This works diminished the probability of failure, and therefore, lowered the potential risk value for a certain cost.

It was important to correlate the probability of failure of the slope with the vulnerability index of the region. Since those parameters are well known, the management for landslide risk can be more effective. The professional will be able to choose which factor to manage. To lower the failure probability of the slope represents a cost because of the required stabilization works. Vulnerability values are directly related to potential loss in the same region, and they are difficult to change. But, if the region has a very low degree of vulnerability, even with a very high value of probability of occurrence, the potential risk for landslide may not be relevant for that area.

Finally, diagrams in Figures 2 and 3 are obtained after a valorization process of risk. The results of the reliability analysis consider the slope inclination and the vulnerability of the zone where a reliable curve is achieved for static conditions (no seismic). Same procedure is applied for seismic conditions, considering accelerations between 0.20g and 0.30g.

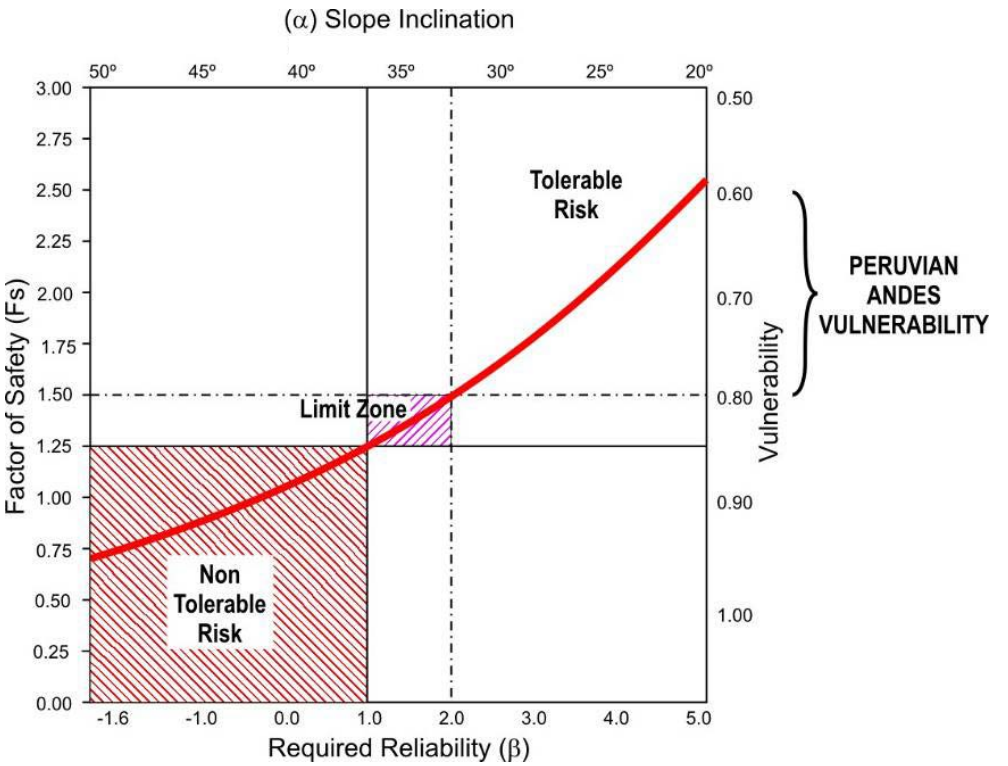

Figure 2. Mean curve of static reliability

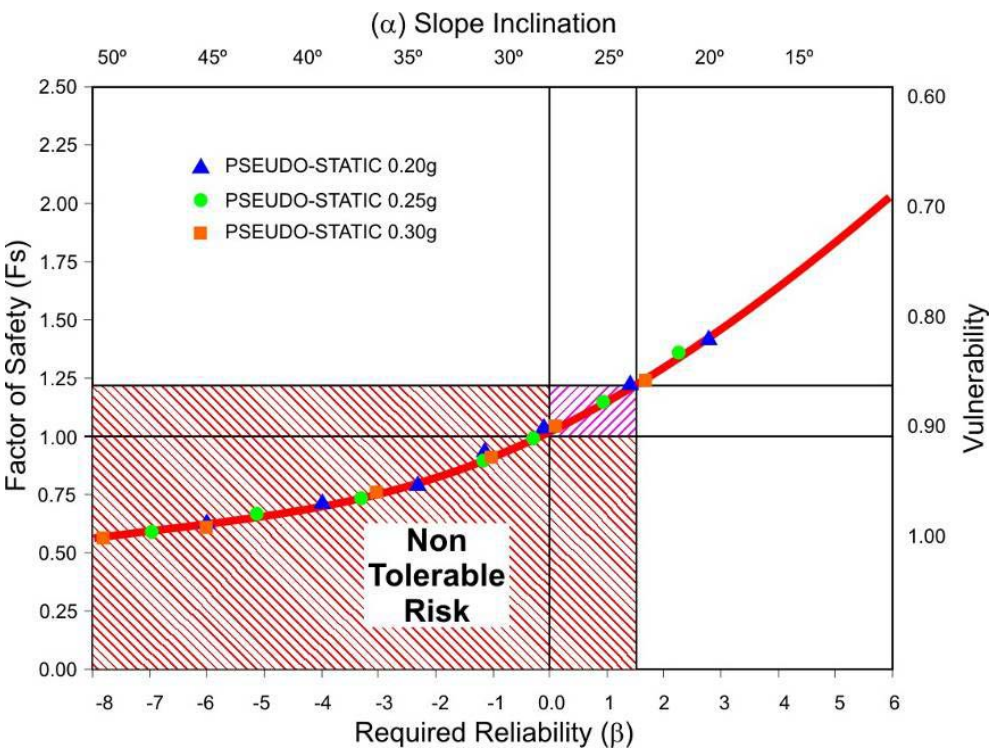

Figure 3. Mean curve of seismic reliability

CONCLUSIONS

It is important to obtain "reliability curves" for the slopes in the studied zone. These curves represent in a graphical and summarized way, the level of risk and reliability of the slopes. It was determined that a reliability value $\beta > 2$ allows ensuring acceptable reliability level considering all geotechnical parameters of the area. It shows that a correlation between calculated factors of safety, required reliability, and Peruvian Andes vulnerability exist. These graphs show that to get a good level of reliability, the slope inclination should be less than 36^{o} for a static safety value of 1.25. These values are related to a specific vulnerability level.

Finally, it is established that an analysis of landslides risk as part of a slope stability analysis, allows the professional engineer to choose the most effective solution. These solutions comply with acceptable reliability levels. The landslides destructibility can be quantified by a geotechnical control measures evaluated in the magnitude/frequency relation at the studied zone, especially when the rains are intense and frequent.

REFERENCES

AC Consultant Engineers SAC. (2003) "Historical Analysis of the Geotechnical Monitoring of the Conococha – Yanacancha Road", Technical Report, Lima, Peru.

AC Consultant Engineers SAC. (2004) "Final Report on the Supervision, Installation of the Geotechnical Instrumentation in Km. 24 of the Conococha – Yanacancha Road", Technical Report, Lima, Peru.

AC Consultant Engineers SAC. (2004) "Status Report Conococha – Yanacancha Access Road. Strategic Plan for Remediation of Km. 94. Stability Risk", Technical Report, Lima, Peru.

Carrillo A.G. (2003) "Slope Stabilization Systems: Some Peruvian Cases", Conference Soil and Rock, America 2003, 12th Pan-American Conference on Soil Mechanics and Geotechnical Engineering and 39th U.S. Rock Mechanics Symposium, Cambridge, Massachusetts.

Lee E.M. and Jones D.K.C. (2004) "Landslide Risk Assessment", Thomas Telford, London.

Torres, C. (2007) "Valuation of Landslide Risk", Thesis, Ricardo Palma University, Lima, Peru.

Quantified Risk Assessment of Shield Tunneling Effects on Urban Cement Concrete Pavement

Q. F. Hu[1] and H. W. Huang[2]

[1]Shanghai Institute of Disaster Preventation and Relief, Tongji University, 1239 Siping Rd, Shanghai 200092, P. R. China, PH (+86) 21-65983449; FAX (+86) 21-65987989; email: huqunf@tongji.edu.cn
[2]Department of Geotechnical engineering, Tongji University, 1239 Siping Rd, Shanghai 200092, P.R. China, .PH (+86) 21-65989273; FAX (+86) 21-65985017; email: huanghw@tongji.edu.cn

ABSTRACT

When a shield machine is tunneling under an urban cement concrete road, the pavement settlements or deformation can be progressed into four stages: upheaval, subsidence, consolidation and subside. Therefore, it is inevitable that urban roads are often damaged and broke because of these incompatible settlements during the shield tunnel construction. It finally leads to many typical failures such as spall, fracture, pavement depression and faulting of slab ends in cement concrete pavements. So it needs to analyze these differently typical destructions and discuss risk loss in the whole life of roads. A quantified model of risk assessment is established on three parameters: the maximum settlement (S_{max}), pavement condition index (*PCI*) and risk loss (*CR*). And a case study is shown here to elucidate that the proposed model is useful for the risk assessment of damage conditions of cement concrete roads due to shield tunnel construction.

INTRODUCTION

Generally, most of subway tunnels in soft soil areas are built under the urban highways in order to avoid the damage of adjacent buildings. When a shield machine is tunneling under an urban road, these pavement settlements or deformation can be progressed into four stages: upheaval, subsidence, consolidation and subsidence which can lead to change the soil conditions heavily under the road surface (Lee 1999, Leca 2000, Hu. 2005). Therefore, it is inevitable that the urban cement concrete roads are often damaged and broke because of these incompatible settlements during the shield tunnel construction. There are many typical failures such as spall, fracture, pavement depression and faulting of slab ends in cement concrete pavements. And it may result in some seriously social effects and big economic loss finally. This paper analyzed and quantified these differently typical destructions based on *The code of cement concrete pavement Maintenance in China*

(2001), and discussed all main cost including construction and maintenance in the whole life of roads. Then a risk assessment model for cement concrete pavements is established on three parameters: the maximum settlement, pavement condition index and potential risk los. And the quantified risk method is to elucidate in a case study. It states that the proposed method is useful for the risk assessment of road damage conditions due to shield tunnel construction and be referenced internationally in some similar projects.

DAMAGE TYPES AND ECONOMIC LOSS

The damage of cement concrete pavement is classified into four types: rupture, vertical settlement, joint damage and surface worsement referring from *the technical specification of cement concrete pavement maintenance for highways in China* (JTJ073.1-2001). As considering the detailed types during shield tunnel construction, it includes as follows: (1) rupture or crack of cement slabs, such as the longitude or transverse crack; inclined rupture and marine or corner crack etc. (2) vertical settlements, such as depression and blow ups etc. (3) joint damage, such as filling lost, pavement pumping, pot hole, blow-up and fault of slab ends etc. (4) surface worsement, such as mapping cracking, scaling and surface angularity. The surface worsement is often resulted from some material aging and tire abrasion, and it assumes that it is not involved in the period of the shield tunnel construction. The cement concrete pavement will become worse with the development of all different damage, and the road capacity is also decreased gradually for the bad pavement conditions. So the benefit and performance of cement concrete is lost heavily to maintenance when the pavement cannot provide its normal services finally. Rentz etc. (1998) analyzed the cost pattern for the whole life of pavement and established a life-time cost model which includes design and construction cost, management cost, operation cost and other fees.

According to the life-time cost pattern of a cement concrete pavement, the risk loss is due to its operation performance damaged by the shield tunnel construction. In the light of risk, the economic loss of risk assessment is included as follows: (1) the direction fees, such as the repair fees, the surface maintenance, rehabilitating and rebuilding etc. (2) the cost of operation and time loss resulted from the decreasing of transportation capacity and making a detour. (3) the cost of decreasing of operation conditions and pavement performance, such as gas consumption, tire abrasion and vehicle depreciation etc. (4) the accidents loss for the damaged pavement. As is known, the direct loss is the main part of four differently economic losses when the subway is advancing under the cement concrete pavement. So it is calculated in the quantified model of risk assessment based on the assessment model of cement concrete pavement condition (JTJ073.1-2001).

THE QUANTIFIED RISK ASSESSMENT MODEL

Some assumption is listed in order to establish a risk assessment model of shielding tunnel construction under a cement concrete pavement (Hu etc. 2005). (1) the condition of cement concrete pavement is good before the tunnel construction, and there are not some problems of slab crack. (2) the tunnel machine is advancing along the longitude center line of a cement concrete pavement, and it may leads to a soil loss under the pavement. The change of pavement thinness and other factors is not considered here. (3) the settlement of road under shield tunneling is calculated by the Peck's formula (Peck, 1969), and the volume of soil loss is equal to the tank of pavement settlement. (4) the potential damage of adjacent buildings is negligible, and it is not calculated in the established model.

The damage of cement concrete pavement is finished in a short time after the tunnel is advanced. The typical mode of pavement damage is crack, rupture, depression, stagger and pot holes etc. based on some projects' investigation of pavement damage. Therefore, the index of pavement damage ratio (*DBL*) is used to assess the damage condition of cement concrete pavement, which is calculated from the pavement condition index (*PCI*) according to *the technical specification of cement concrete pavement maintenance for highways in China* (JTJ073.1-2001). The formula of *DBL* from some survey of pavement condition is listed.

$$DBL = (\sum_{i=1}^{n}\sum_{j=1}^{m_i} DB_{ij} \cdot W'_{ij}) / BS \qquad (1)$$

Where: *DBL* is the damage ratio of cement concrete pavement. DB_{ij} is the slab number of the *i* damage with the *j* condition, and its value got from Table 1. W'_{ij} is a compensation factor of the *i* damage with the *j* condition, and is listed in Table 2. BS is the slab number in the investigating area of cement concrete pavement.

Table 1 the classification of damage for cement concrete pavement

type	Damage conditon	The condition and description of damage of damage
Intercross Crack	negligible	The slab is slightly damaged to crack in 2-3 blocks.
	middle	The slab is divided into medium-sized 3-4 blocks or slightly damaged to 5 blocks and more.
	serious	The slab is cut seriously into 4-5 blocks or divided into medium-sized 5 blocks and more.
Corner crack and one-direction rupture	negligible	The crack width of slab is less than 3 mm in the corner, or flush joint of different slabs is only slight crack.
	middle	The crack width of slab is between 3-10 mm in the corner, or the rupture of flush joint of different slabs is about 15 mm.
	serious	The crack width of slab is over 10 mm in the corner, or the rupture of flush joint of different slabs is more than 15 mm.

The risk assessment is carried out by in-suit investigation for the subway project. The damage of cement concrete pavement is resulted from the incompatible settlement or soil loss under shield tunnel construction. The deformation of the

pavement bottom is calculated by the Peck Formula (Peck, 1969), and the width of the displacement is

$$B_1 = 2 \cdot i(z_0) \tag{2}$$

$$i(z_0) = 0.575 z_0^{0.9} \cdot D^{0.1} \tag{3}$$

Where B_1 is the width of soil displacement from the effect of tunneling (m), $i(z_0)$ i is the horizontal distance from point of reflection on the curve of the soil displacement to the tunnel center (m), z_0 is the depth of tunnel center (m), and D is the diameter of tunnel (m).

Table 2 the coefficient for calculating *DBL* of cement concrete pavement

Damage type and condition		Intercross crack	Corner crack	Inclined crack or rupture
classification	negligible	0.60	0.20	0.20
	middle	1.00	0.70	0.60
	serious	1.50	1.00	1.00

The slab length and width of cement concrete pavement is 2 m34.5 m, and the buried depth of subway is about 12 m~ 15 m. The width of soil displacement under tunneling is at least 4.5 m by using the formula (2), so it easily causes the pavement damage if the soil displacement is controlled well under shield advancing. According to the model assumption, the different types of pavement damage are results in the tunneling and vehicles' load. Therefore, the crack mode is calculated by the method of geometry shown in Figure 1.

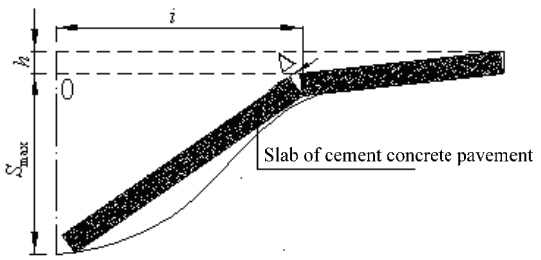

Figure 1 the sketch for calculating the crack of cement concrete pavement

The crack width of slab Δ is related to the depth of soil displacement from Figure 1, and the formula of Δ is

$$\Delta = h \cdot \arctan\left(\frac{S'_{\max}}{i(z_0)}\right) \tag{4}$$

Where Δ is the crack width of slab in cement concrete pavement (mm), h is the thickness of slab, and its value is 250 mm, $S'_{\max}$ is the maximum of soil displacement under tunneling (mm), and its value is got from the in-suit survey after the subway is advanced.

The pavement damage is classified through the assessment of the crack width Δ of slab. The center line of cement concrete pavement is calculated by the

below formula.

$$S_{\max}(z) = \frac{V_i}{2.5 \cdot i(z_0)} \tag{5}$$

$$V_i = \frac{1}{4}\pi \cdot [(D+g)^2 - D^2] \tag{6}$$

$$g = U_{3D}^* + \omega + 2t + \delta \tag{7}$$

Where $S_{\max}$ is the maximum of pavement displacement under tunneling (mm), V_i is soil loss during the shield tunneling, g is the thickness of soil loss, U_{3D}^* is the thickness of over excavation of shield machine advancing, ω is the factors of machine operation and construction condition. t is the shell thickness of shield machine tail, δ is the gap between the shell and the outer of tunnel linings.

Then put the formula (4) into formula (3), the initial crack width of cement concrete pavement under tunneling is got as follows.

$$\Delta_0 = h \cdot \arctan\left(\frac{S_{\max}}{i(z_0)}\right) \tag{8}$$

The damage classification of cement concrete pavement is established through calculating the crack width Δ and initial crack width Δ_0 of slab based on Table 1. The final damage of cement concrete pavement is listed in Table 3.

Table 3 the classification of damage for cement concrete pavement

Damage type	negligible	middle	serious
Δ / Δ_0	<3	$3\sim15$	>15

According to many investigations of subway construction, the average accident probability is about 10% (Hu, 2005). That is to say, there are four damaged slabs in the length of 100 m pavement. Therefore, the number of damaged slabs DB_{ij} and the total slab BS are respectively calculated on the pavement length L, pavement width B and the geometric dimension by risk investigation $a \times b$. The detailed formula is

$$DB_{ij} = \frac{L}{a} \cdot \frac{4}{100} = \frac{L}{25a} \tag{9}$$

$$BS = \frac{2L \cdot B}{a \cdot b} \tag{10}$$

Where L is the investigation length of cement concrete pavement (m), B is the pavement width (m), $a \times b$ is the geometric dimension of pavement (m^2).

Then put the formula (7) and (8) into formula (9), the pavement condition index PCI of cement concrete is given by the recommendation function (JTJ073.1-2001).

$$PCI = 100 - 15DBL^{0.439} \tag{11}$$

The quantified risk assessment of shield tunneling effects on cement concrete pavement is established the relationship of risk loss and the pavement condition index PCI based on the life-time cost of pavement (Rentz, 1998). The formula for the direction cost of risk loss is shown

$$MC = 0.34 + 3.44 \times 10^6 (100 - PCI) \cdot AADT \quad (12)$$

$$C_R = 8.5 \cdot L \cdot B \cdot MC \quad (13)$$

Where $AADT$ is the annual average daily traffic of the assessed pavement, MC is the maintenance cost of damaged pavement, C_R is the risk loss of cement concrete pavement under tunneling (Chinese Yuan).

A CASE STUDY AND DISCUSSION

In order to elucidate an example for the purposed risk assessment model, a case study is given as follows. The buried depth z_0 of a subway is 15 m and its inner diameter D is 5.2 m. The tunnel is located in the middle of a cement concrete pavement. The soil under the pavement is respectively 0~3 m rinse fill, 3~9 m grey soft silty clay, 9~16 m silty clay and 16~21 m grey clay.

The cement concrete pavement is a four-lane double way road, and the geometric dimension $a \times b$ is 5.0×4.5 m, the thickness of pavement slab is 25 cm. The width of pavement B is 9.0 m. The Average Daily Truck Traffic $ADTT$ is 2600. The total pavement length of running tunnel L is 1000 m.

The $i(z_0)$ is got from the formula (3) by choosing the $B = B_1 = 9.0$ m. Then the initial crack width is calculated by the formula (8) and its values is $\Delta_0 = 0.706$ mm. The annual average daily traffic of the assessed pavement is 10400 from $ADTT = 2600$. Therefore, the risk loss of cement concrete pavement is assessed by formula (12) and (13), and the final relationship of the maximum displacement and pavement condition index is shown in Figure 2. Then the risk loss of different maximum displacement is obtained in Figure 3.

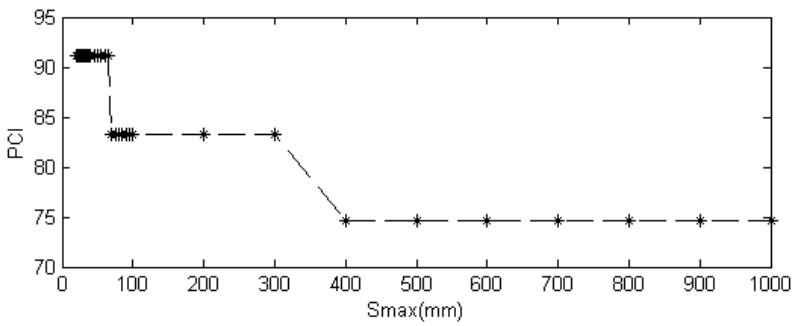

Figure 2 the relationship of pavement maximum settlement and its PCI

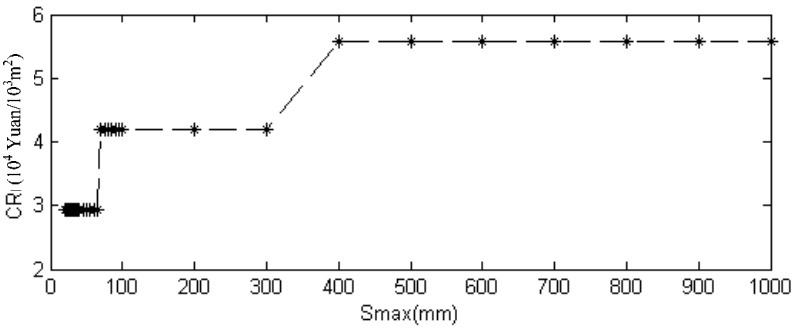

Figure 3 the relationship of pavement maximum settlement and its risk cost

When subway in soft soil areas is built under the urban highways, these pavement settlements or deformation can be progressed into four stages: upheaval, subsidence, consolidation and subside which can lead to change the soil conditions heavily under the road surface. The pavement damage is complicated to explain why the process happened during shield tunneling. But the damage types are similar for the cement pavement, which include crack, rupture, depression, stagger, pot hole and blow-up etc. The average settlement of cement concrete pavement is about 20 mm~ 40 mm during the shied tunneling if the construction is well controlled. Then it may lead to some negligible damage of pavement condition, and the pavement condition index decreases little gradually. The risk loss due to tunneling is the cost of routine maintenance, or may more than it. If there are some accidents to happen during the construction, and the maximum displacement is more than 40 mm, it would lead to some damage to the pavement and sharply decrease the pavement condition. Therefore the risk loss of cement concrete pavement also increased quickly. As it is shown if Figure 3 and Figure 4, the risk loss is about 30,000 Yuan/1000 m^2 if the maximum is 40 mm, and the risk loss is about 42,000 Yuan/1000 m^2 if the maximum is less than 300 mm. Finally, the risk loss is up to 58,000 Yuan/1000 m^2 if the settlement of pavement is more than 400 mm.

The risk loss of cement concrete pavement is pavement direct cost, and we did not consider some other fees like the cost of operation and time loss resulted from the decreasing of transportation capacity and making a detour, the cost of decreasing of operation conditions and pavement performance, and the accidents loss for the damaged pavement. If all those cost is considered in the quantified risk assessment model, the total risk loss would be increase three times of the calculated costs. Therefore, it is a must to pay much attention to control the machine operation and advancing velocity, and try to decrease the effects on the surrounding soil.

CONCLUSION

Some conclusions are drawn from the analysis and case study in the paper. They are listed as follows:

(1) The risk may be serious when a shield machine is advancing under a cement concrete pavement. It is resulted in much damage such crack, rupture, bumping, pot hole and blow-up etc., which affect the pavement operation performance and the traffic capacity. Therefore, it is a must to take some measure to decrease the effects on the pavement.

(2) The risk loss and pavement condition index are related the maximum settlement due to tunneling. If the maximum displacement of cement concrete pavement increased from 40 mm to 300 mm, the pavement condition index would decrease sharply with some pavement damage. The maximum of risk loss is up to 58,000 Yuan/1000 m^2 if the settlement of pavement is more than 400 mm. And cement concrete pavement would need an intermediate or heavy maintenance.

(3) There are about 10 accidents which will happen in the construction some subway in China. And the risk of tunneling is got a high attention in recent year. Some new codes and measures are taken gradually to decrease the damage effect of shield tunneling. The purposed model of of effect on cement concrete pavement will provide a method to do a quantified risk assessment for the subway projects.

ACKNOWLEDGEMENT

This work was carried out in the course of research sponsored by the China National Science Foundation under Grant No. 50879058. The authors also wish to thank Dr. L. Chen for his helpful suggestion and discussion.

REFERENCES

China National Engineering Code (2001). *The technical specification of cement concrete pavement maintenance for highways in China* (JTJ073.1-2001).

Hu Q. F, Huang H. W., Chen L. (2005). The Risk Evaluation on Effect of Shield Tunnel Construction on Urban Asphalt Pavement, *Chinese Journal of Underground Space and Engineering*, Vol. 4 (2) 263-267.

Lee, K. M. Ji H. W., Liu J.H. (1999) A case of ground mechanism of EPB shields tunneling in soft clay. *Geotechnical Aspects of Underground Construction in Soft Ground*. Tokyo, 251~256.

Leca E., Leblais Y., Kuhnhenn K. (2000). Underground works in soils and soft rock tunnelling. *Proceedings of International Conference on Geotechnical and Geological Engineering*, vol. 1, 220-268.

Rentz H. H (1998) Life-Cycle Cost Analysis in Pavement Design, *Report of U.S. Department of Transportation Federal Highway Administrator*. Publication No. FHWA-SA-98-079.

Risk Assessment of Success Dam, California: Earthquake Induced Potential Failure Modes

M. Ruthford[1], V. Perlea[1], D. Serafini[1], M. Beaty[2], L. Anderson[3], and D. Bowles[3]

[1]US Army Corps of Engineers, Sacramento District, 1325 J Street, Sacramento, CA 95814; emails: Michael.E.Ruthford@usace.army.mil, David.C.Serafini@usace.army.mil, and Vlad.G.Perlea@usace.army.mil
[2]Beaty Engineering, 16631 SW Timberland Drive Beaverton, OR 97007; email: mhb@beatyeng.com
Utah State University, 8200 Old Main Hill, Logan, UT 84322; emails: loren.anderson@usu.edu and david_s_bowles@hotmail.com

ABSTRACT

Seismic deficiency of Success Dam, California has been determined and the need of remediation for improving the performance of the dam under earthquake loading has been identified. Consequently, the dam is currently operated under reservoir pool elevation restriction, pending rehabilitation implementation. Justification of operation restrictions and establishing the priority of remediation activities required preparation of a baseline risk assessment. This paper describes the estimation of the inputs to the estimation of the probability of failure (breach of the dam) from earthquake loading using an event tree risk model. The inputs that are described include earthquake loading, liquefaction and deformation analysis and the development of the system response probability relationships for above core erosion, seepage erosion through cracks and tower induced failure modes. Two companion papers describe the potential failure modes related to flood events (Anderson et al 2011)and the overall risk assessment and justification of operation restrictions (Bowles et al 2011).

INTRODUCTION

The existing Success Dam is located on the Tule River, about 6-miles east of the city of Porterville, Tulare County, California. The District is conducting a dam safety remediation of Success Dam to address issues associated with seismic and seepage stability of the embankment, control tower seismic stability, and the spillway PMF routing. A companion paper by Bowles et al (2011) describes the overall risk assessment approach and justification of the current operation restrictions. It also describes how reservoir pool elevation was considered in the estimation of immediate and delayed earthquake-induced failure modes. Another companion paper by Anderson et al (2011) discusses the potential risk of failure due to causes other than the earthquakes.

The potential failure modes associated with the earthquake action as initiating event, were classified in three main categories:

- Above core erosion, possibly occurring when the pool is relatively high and the seismic settlement at the core location allows the water in reservoir to reach the unprotected downstream shell;
- Seepage erosion through cracks, following transverse cracking of the core and disruption of filters;
- Embankment and tower severe deformation that can lead to failure by piping into a rupture in the outlet works system.

Each of these potential failure modes and their contribution to the total risk are described in this paper. The system response probability relationships and their role in the event tree calculations of the probability of failure are described in the companion paper by Bowles et al (2011).

EARTHQUAKE LOADING

The site seismic activity can be induced by a series of faults as presented in Figure 1.

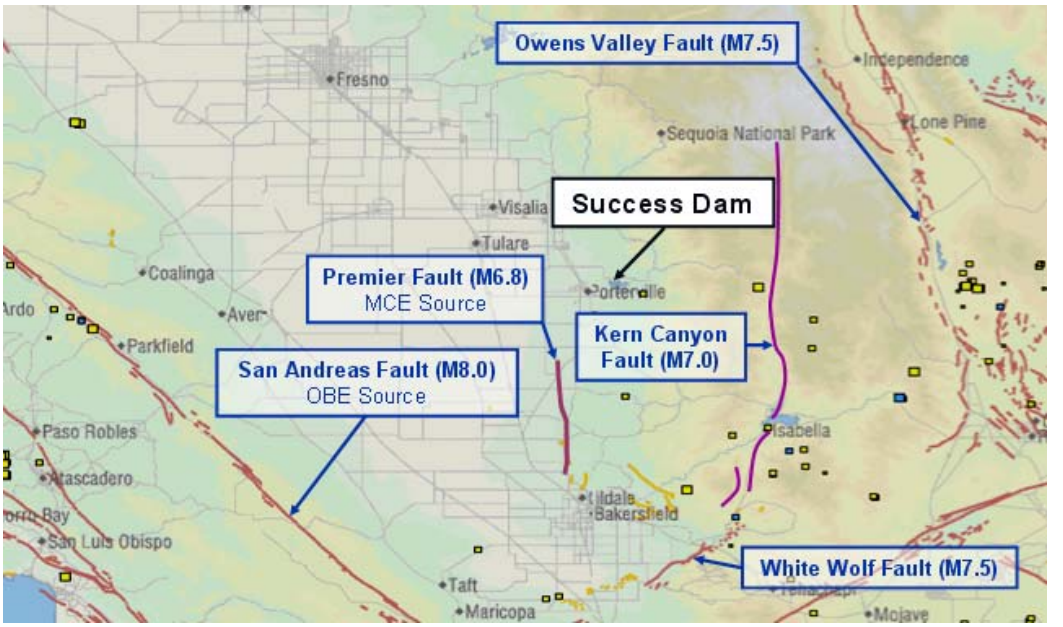

Figure 1. Primary seismic sources in vicinity of Success Dam.

The contributions of the various seismic sources to the mean peak horizontal acceleration hazard were determined by URS Corporation (2004). For risk assessment purposes the sources were grouped in three magnitude ranges, as follows:

- Large magnitude earthquakes, M > 7, where M is the moment magnitude; this group includes all faults shown on Figure 1 except the Premier Fault.
- Moderate magnitude, M = 6.5 … 7.0; seven faults assumed active were included in this category, of which only the closest to the dam site, Premier Fault, is shown on Figure 1.
- Background earthquakes, M < 6.5; numerous remaining faults and seismic source zones from the URS seismicity study were assigned to this category.

The contribution of each category to the total hazard was obtained by adding the probabilities of exceedance of various levels of induced earthquake intensity at the site (described through the Peak Ground Acceleration, PGA) generated by all seismic sources in a group. Figure 2 shows the result of this analysis. Each group of magnitude range was separately, but identically, evaluated in the risk analysis. These probability distributions and stage-duration relationships for reservoir pool elevations were used to represent the earthquake and pool level aspects of loading in the event tree calculations (see Levels 1 – 3 in the event tree in Figure 1 in the companion paper by Bowles et al (2011).

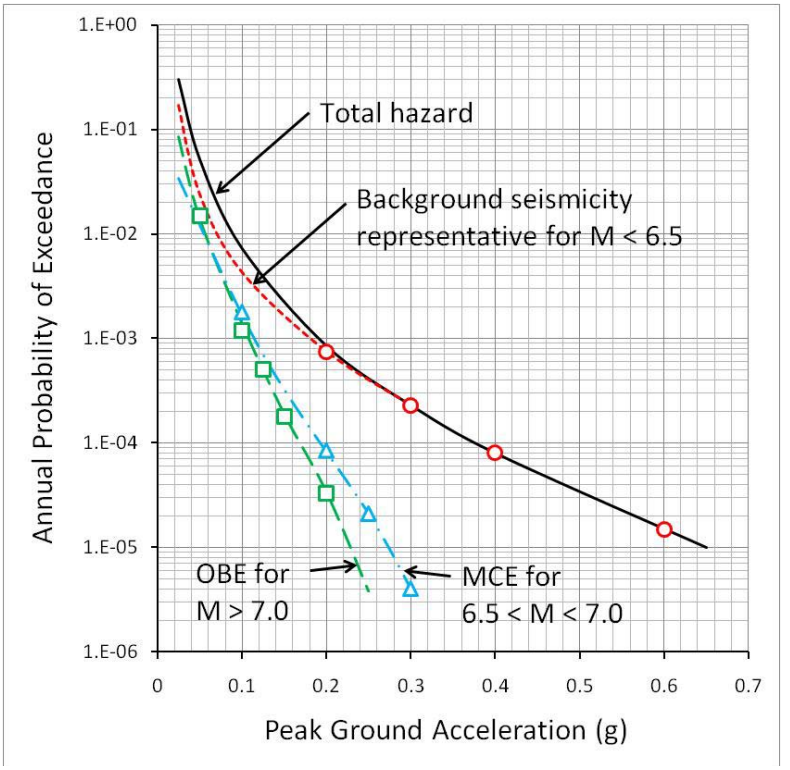

Figure 2. Contribution of seismic sources to mean peak horizontal acceleration hazard.

Previously, the behavior of the existing dam had been evaluated under two levels of seismic loading: OBE – operating basis earthquake and MCE – maximum credible earthquake. Because the OBE was determined to be generated by a strong, distant earthquake, its definition corresponds to the large magnitude group; the MCE, which deterministically was considered to be generated by the Premier Fault, was assumed to be representative for the moderate magnitude group. Each of these levels of seismic loading had been modeled in deformation analyses through 10 different time histories; for compliance with the basic requirement of the risk assessment of evaluating the "best estimate" of displacements, the time history inducing approximately the median deformation was selected for the risk analysis. The base time histories were subsequently scaled to various PGA values, as shown with dots (circles, triangles, or squares) in Figure 2.

RESULTS OF SEISMIC DEFORMATION ANALYSIS

The computer program FLAC (Fast Lagrangian Analysis of Continua), which is commercially available from Itasca Consulting Group, Inc. (2008), was used in the analyses. FLAC is a two-dimensional finite difference program that solves dynamic problems in the time-domain. The program provides many constitutive models that are useful for many situations. FLAC also allows the user to specify his/hers own constitutive models when additional refinements or features are needed. The user-defined model UBCSAND was used for the liquefiable zones in Success Dam and its foundation.

Figure 3 presents an example of the post-earthquake deformed shape and the maximum shear strain contours, as a representation of the developed shear surfaces.

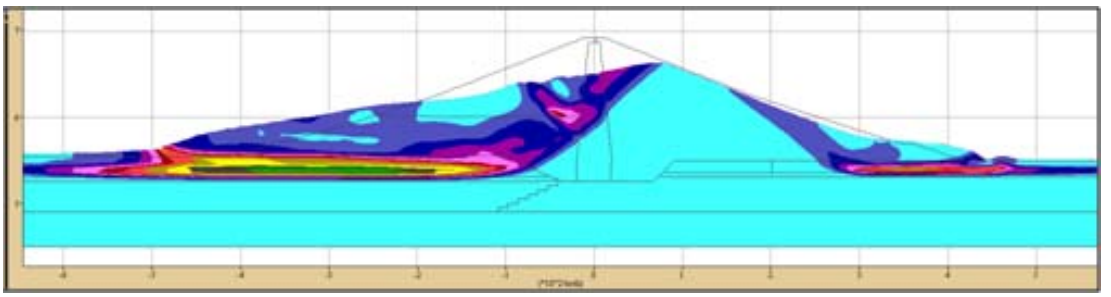

Figure 3. Deformed shape and contours of maximum shear strain increments.

The selected parameter to represent earthquake damage was the seismic settlement at crest, at the maximum dam section. Figure 4 shows the predicted settlement increase with the intensity of shaking. There are three groups of lines, corresponding to the three magnitude groups. The four lines of each group correspond to four different pool elevations. The settlement significantly decreases with lower pools making full pool the most critical.

Above Core Erosion (ACE) mode of failure. Due to the large available freeboard, overtopping of the crest would only be possible when a strong, long duration earthquake (M > 7, PGA = 0.2g) acts when the pool is full, as shown in Figure 5. However, settlement of the crest below the pool level at the time of the seismic event does not necessarily imply immediate overtopping. As shown in Figure 6, the computed deformed shape for this case shows the crest dropping below the pool level while a remnant of the downstream shell remains above the pool. If an ACE failure occurs, because the possibility of continuous and significant transverse cracks cannot be eliminated for this type of deformation, the probability that the breach would occur immediately after the earthquake was estimated to be 10% and 90% that it would occur within about 24 hours after the earthquake, depending on the pool level at the time of the earthquake [see Figure 1h in the compainion paper by Bowles et al (2011)].

Based on the deformed shape estimated using FLAC and shown in Figure 6, the remnant of downstream shell was estimated to have a width of 30 m (95 feet). Even if the actual deformations were 50% larger than computed, as shown with

arrows on Figure 6, there is still an estimated 18 m (63 feet) of shell material to resist an immediate failure. Although the downstream remnant will be heavily fractured, and the reservoir will be in direct contact with the relatively pervious shell material, this is still a significant consideration in a risk analysis since the shell could prevent or delay the failure of the dam. Unsaturated flow calculations show that the delay until initiation of failure may be on the order of 4-5 hours, enough to dramatically decrease the potential loss of life, due to the increase in warning time.

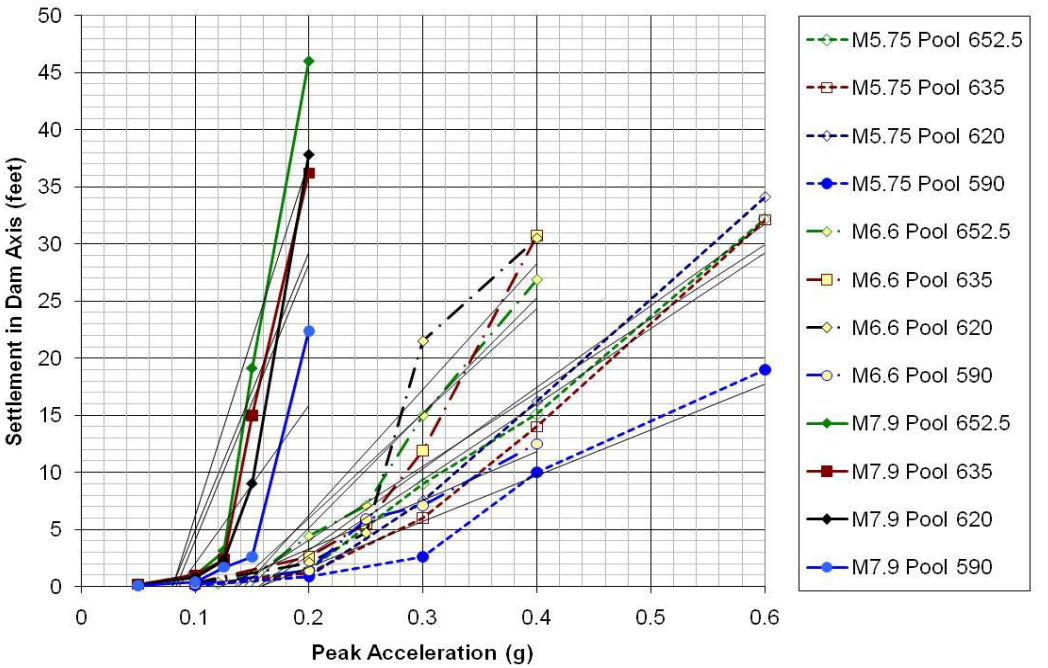

Figure 4. Seismic settlement as a function of PGA, M, and pool elevation.

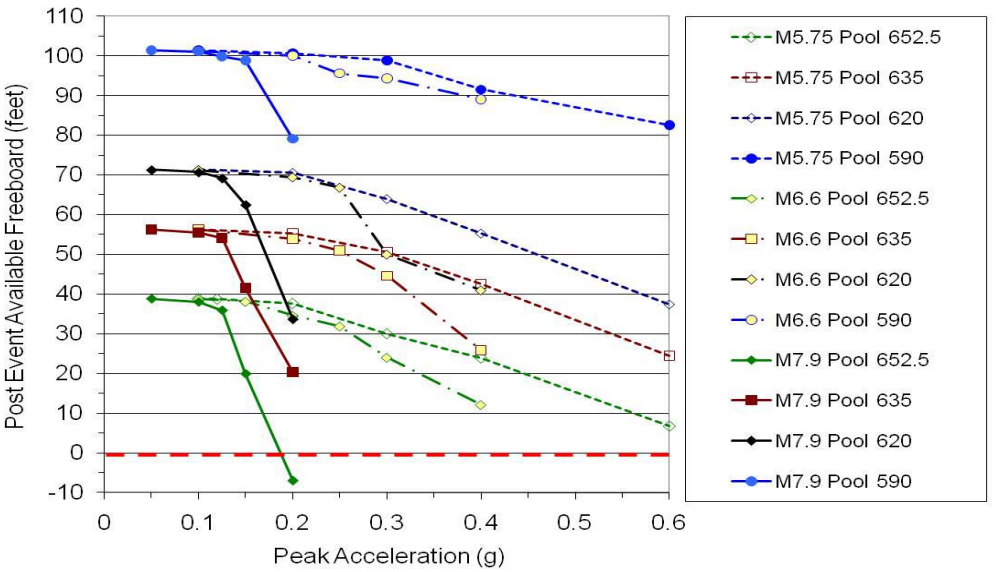

Figure 5. Available freeboard after seismic deformation.

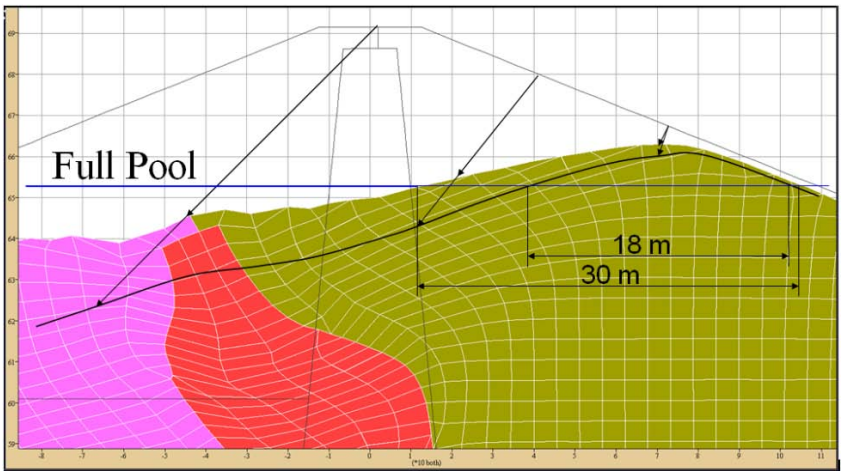

Figure 6. Settlement of crest below pool but without immediate overtopping.

Seepage Erosion through Cracks (SEC) failure. Transverse cracks through the core may have many causes including differential settlement at abutments or foundation discontinuities, abrupt changes in embankment deformations, amplified ground motions, and distress of the crest section through large deformations of the embankment. Historic observations have suggested that most transverse cracks within intact sections tend to be open to depths of less than about 6 m (20 feet). The maximum crack depth considered in this analysis was 9 m (30 feet). The depth of significant deformation as predicted in the FLAC analysis was also considered in evaluating crack depth. The relevant FLAC results are illustrated on Figure 7. It was assumed that core material subject to movements greater than 0.3 m (1 foot) will be more likely to experience distress and would be subject to continuous cracking. These cracks were considered likely when the 0.3 m (1 foot) displacement contour on the upstream edge of the core was below the pool elevation.

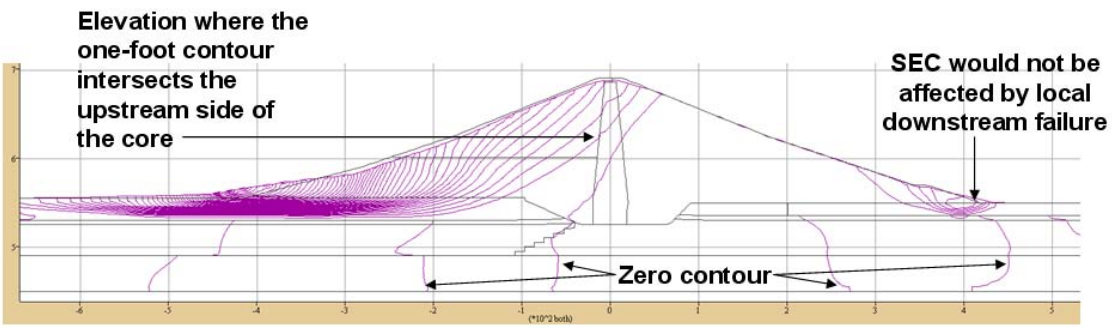

Figure 7. Evaluation of the depth of distress in the core.

Piping into a rupture in the outlet works system mode of failure. The control tower rises approximately 181 feet above the bedrock foundation. The configuration of the tower and conduit within the upstream shell are shown in Figure 8.

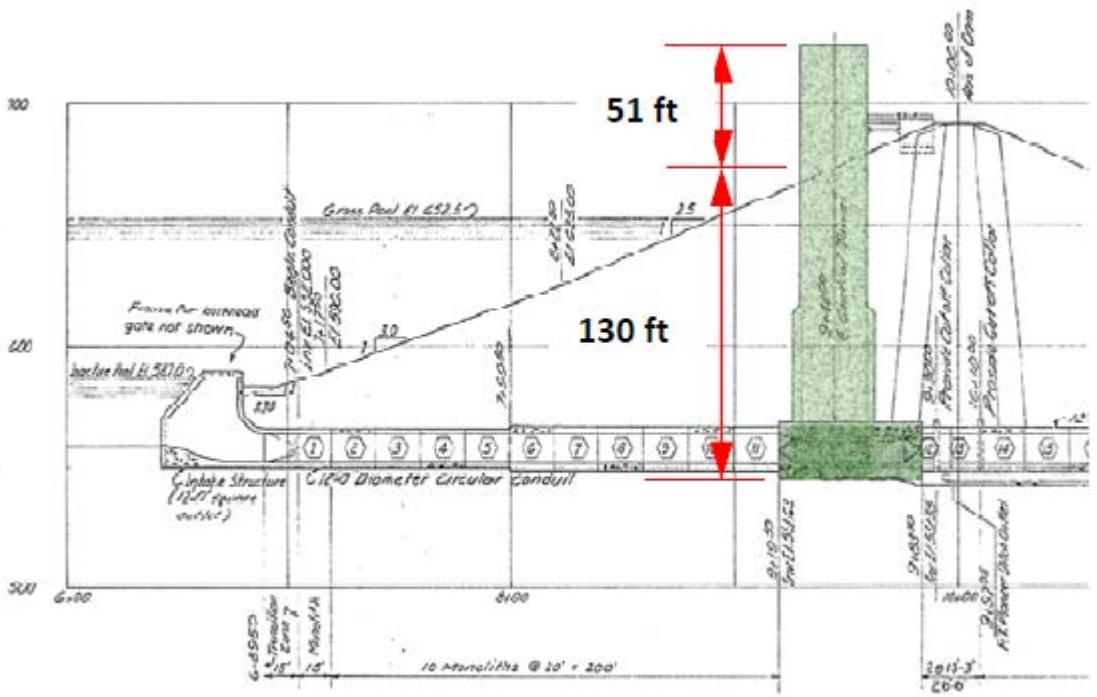

Figure 8. Cross section of control tower, intake structure and conduit.

A potential failure modes analysis identified three credible and significant seismic failure modes for the tower: 1) loss of outlet works function due to tower distress leading to eventual overtopping of the dam; 2) development of large open cracks in the tower creating a critical erosion path for upstream shell and core materials into the damaged tower and exiting through the conduit; and 3) opening of the joint between the tower and first downstream conduit section leading to erosion of core material into the conduit.

The loss of outlet works function was approximately linked to the predicted size of total crack opening in the tower. The tower was included in the FLAC analyses using beam elements with plastic hinges. The analyses showed that almost all of the predicted tower movement was due to rotation at the plastic hinge. The total crack width was estimated from the final hinge rotation assuming the tower rotated about its upstream edge. The FLAC model did not include the possibility of shear dislocation of the tower, although this response was subjectively addressed in the assessment.

The tower was assumed to remain functional for crack openings less than 0.06 m (0.2 feet), and to become permanently non-functional for crack openings greater than about 0.3 m (1 foot). This is an approximate assessment based on how the critical section may deform at failure and how these deformations could affect the operation of the mechanical equipment. Failure modes related to erosion of materials into the conduit were also related to a combination of crack size and reservoir elevation. These failure modes generally required crack openings significantly larger than 0.3 m (1 foot).

To incorporate tower response into the risk analysis, a relationship between total crack width and seismic loading was developed from the FLAC analyses. A key

factor in this assessment was the observation that tower response can be directly related to embankment deformation. The adopted relationship is shown by the trend line in Figure 9. This trend line was based on preliminary analysis results and lies somewhat below the final range of analysis predictions. An important conclusion from this figure is that crest settlements larger than 0.9 m (3 feet) are expected to lead to permanent loss of tower function.

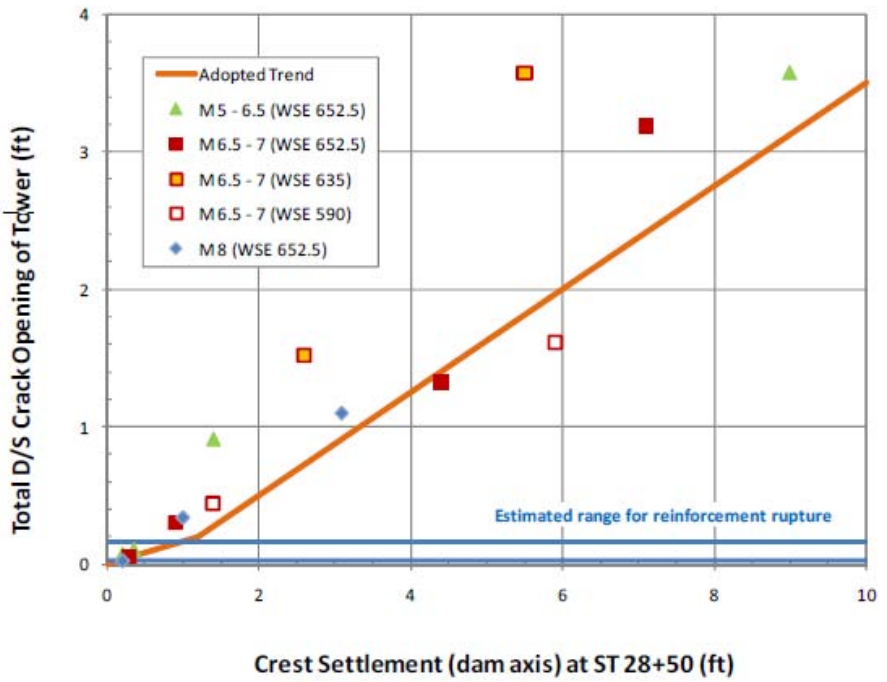

Figure 9. Approximate relationship for crack opening versus crest settlement.

Significance of results. The estimates of the performance of Success Dam presented in this paper were used to estimate the system response probability relationship (fragility curves) implemented in Levels 5-7, 9 and 10 of the event tree risk model as described in a companion paper (Bowles et al., 2011, see Figure 1).

REFERENCES

Anderson, L. M. Ruthford, V. Perlea, D. Serafini, J. Montgomery, and D. Bowles. (2011). Risk Assessment of Success Dam, California: Flood Related Potential Failure Modes. *GeoRisk 2011 ASCE Conference,* Atlanta, Georgia, USA.

Bowles, D. et al. (2011). "Risk assessment of Success Dam, California: Evaluation of operating restrictions as an interim measure to mitigate earthquake risk." *GeoRisk 2011 ASCE Conference,* Atlanta, Georgia, USA.

Itasca Consulting Group (2008). "FLAC, Fast Lagrangian Analysis of Continua, Version 6.0", Itasca Consulting Group, Minneapolis, Minnesota, USA.

URS Corporation (2004). "Deterministic and Probabilistic Seismic Hazard Analyses for Success Dam, California", prepared for the US Army Corps of Engineers, Sacramento District (unpublished).

A Parametric Study on Factors Affecting Ground Vibrations during Pile Driving through Finite Element Simulations

Mo Zhang[1] and Mingjiang Tao[2]

[1]Department of Civil and Environmental Engineering, Worcester Polytechnic Institute, 100 Institute Road, Worcester, MA 01609, email: mozhang@wpi.edu;
[2]Department of Civil and Environmental Engineering, Worcester Polytechnic Institute, 100 Institute Road, Worcester, MA 01609, Ph: 508-831-6487, Fax: 508-831-5808, email: taomj@wpi.edu.

ABSTRACT

Driven pile has often been used to provide loading support for civil infrastructure, but the induced ground vibration can cause damage to adjacent structures. The vibration risk associated with pile driving is often managed via monitoring ground vibrations that is quantified by peak particle velocity (PPV). Therefore, a rational approach to predict PPV is desired because the commonly used scaled-distance equations consider only the distance from driven piles and the input energy but ignore other important factors. To fulfill this knowledge gap, a finite element method based parametric study was performed to examine the influence of soil damping ratio, Young's Modulus of soil, and the number of loading pulses on ground vibrations due to pile driving. The results obtained from this study will aid geotechnical engineers in better managing the risk of pile driving to surrounding building by designing and executing a proper ground vibration monitoring plan.

INTRODUCTION

Driven pile has often been used to support major infrastructure, such as industrial and residential buildings, bridge, highway and other structures. However, pile driving inevitably causes varying degrees of ground vibrations, which may damage the surrounding structures. Prior to any pile driving operations, state departments of transportation (DOTs) usually perform risk analysis to address concerns associated with pile driving vibrations, by understanding the likelihood of damage from pile installation procedures. The extent of structure damage due to pile driving is well believed to relate with the amplitude of ground vibrations that is often quantified in terms of peak particle velocity (PPV). Currently, the PPV is approximated with the Scaled Distance (SD) approach, which can predict PPV value from the normalized distance by the energy transmitted from pile driving hammers to driven piles. One of such SD-based models was proposed by Wiss (Woods 1997) and reads:

$$PPV = k\left[\frac{D}{\sqrt{W}}\right]^{-n} \quad (1)$$

Where D is the horizontal distance from the driven pile, W is the hammer energy transferred to the pile, k is the ground vibration velocity at one unit of distance from driven piles, and n is the wave attenuation rate (Tao, Svinkin et al. 2009). The SD approach is easy to use and considers two important factors (i.e., hammer energy and distance) affecting ground vibration. However, other factors (e.g., soil properties,

soil-structure interactions) having significant influence on ground vibrations are not considered by the SD approach, and a better understanding of pile driving induced ground vibrations is needed. Therefore, this study aims to provide insights into the wave attenuation in the surrounding ground during pile driving and identify important soil parameters so that the pile driving associated risk can be better managed. In particular, the influence of soil damping ratio, Young's modulus of soils, and the number of pulse loading cycles on wave attenuation was examined through a finite element method (FEM)-based parametric study. This study will assist the geotechnical practitioners to further understand the ground vibration and manage the induced structure damages more efficiently.

2-D FEM MODEL FOR PILE DRIVING

Basic model

The basic 2-D FEM model for simulating pile driving was set up with PLAXIS 2D, as shown in Figure 1. The geometry was simulated as an axisymmetric model with the pile located along the axis of the symmetry. 15-noded elements were chosen to model the pile and the soil, with the interface being added between the pile and the soil. The left and right boundaries were horizontally fixed, and the bottom was fixed in both horizontal and vertical directions. To avoid spurious reflection, absorbent boundaries were used at the bottom and the right side of the model (Brinkgreve and Broere 2008). The soil was modeled as a single layer with the thickness of 50 m, and the ground water level was assumed at the bottom of the layer. The concrete circular pile, with its dimensions of 20 m by 0.4 m, is modeled as a linear elastic material. As sand and clay are typical soils encountered in the field, they will be used in this study, with typical values of their physical properties listed in Table 1.

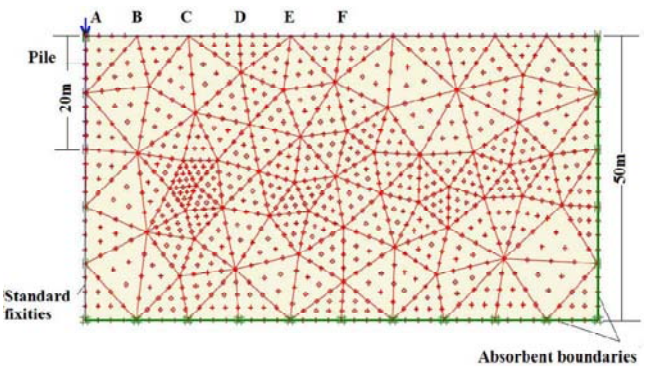

Figure 1. The geometry of the basic 2-D FEM model

Table 1. Typical values of soil physical parameters required in Plaxis

Soil	γ (kN/m^3)	E (kN/m^2)	μ	c (kN/m^2)	φ (°)	Model Type
Sand	17	50000	0.2	1	31	Hardening Soil
Clay	16	15000	0.3	2	24	Mohr-C. Undrained

Notes: γ is the unit weight, E is Young's Modulus, μ is Poisson's ratio, c is cohesion, and φ is frictional angle. The other properties were used as default values in PLAXIS 2D.

A dynamic distributed load of 5000kN/m^2 was uniformly applied on the top of the pile to simulate loading exerted by a pile hammer during pile driving, and the displacement of the pile under the dynamic distributed load can be readily obtained from the simulations. By plotting dynamic load vs. displacement of the pile, as shown in Figure 2a, the energy applied to the pile can be calculated as the area enveloped by the curve. Ground vibrations in terms of PPV at various distances from the driven pile can be obtained from the waveforms at various nodes (e.g., B to F shown in Figure 1). Then the relationship between the SD and PPV values can also be established from the FEM simulation results, as illustrated in Figure 2b. The values for k and n in the SD equation corresponding to the FEM simulation results can be determined from the best-fit line.

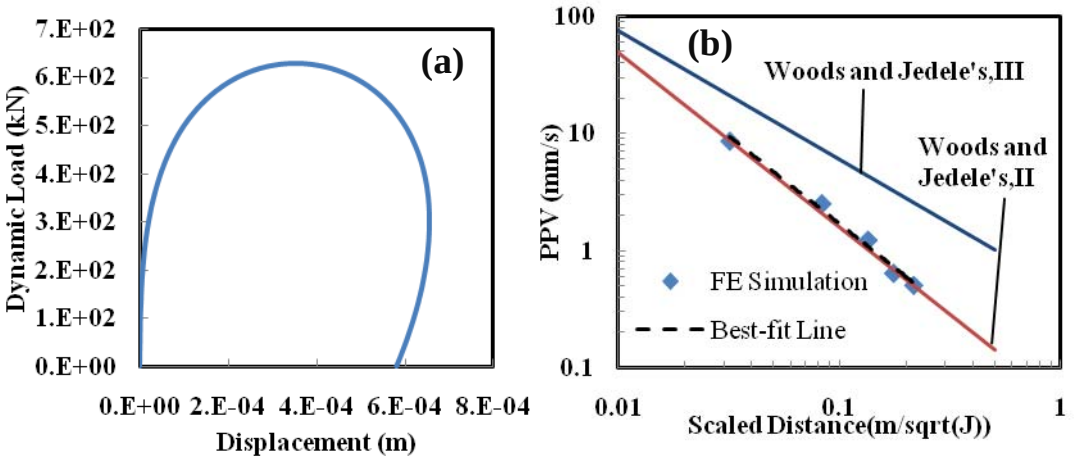

Figure 2. (a) A sample displacement vs. dynamic force curve; and (b) PPV vs. SD plots resulted from the FEM simulations and Woods and Jedele's equations

To verify the results from the FEM simulations, Woods and Jedele's equations for approximating PPV values were used in this paper because of their wide use in the pile driving practice and the lack of detailed information from pile driving case history data. Based on the SD concept and measured ground vibrations from field construction projects, Woods and Jedele developed a PPV vs. scaled distance chart for various soil types. The classification of soil types in Woods and Jedele's chart is largely of qualitative nature, in which only qualitative descriptions of the soils were given. In this chart n values (i.e., the slope in the log-log PPV vs. SD space to represent the wave attenuation rate in the soil) are 1.5 and 1.1 for soil classes II and III, respectively (Woods 1997). These two lines corresponding to soil classes II and III are also plotted in Figure 2b, and the FEM simulation results reveal similar trend of and are close to one of these two lines. This illustrates that the FEM model is capable of representing ground vibrations induced by pile driving. Note that the FEM simulation results are not necessary to fully agree with Woods and Jedele's lines, because the soil parameters in the model are not the same as those for soil class II and III.

Validation of using a single pulse of dynamic loading for modeling pile driving

To simplify FEM simulations, the dynamic loading applied to driven piles from the hammer was modeled by one single pulse of harmonic loading in this study.

In reality, however, a pile is usually driven by multiple hammer drops that can generate continuous wave propagations in the ground, and thus it is possible for adjacent grounds to experience vibrations of higher magnitudes due to the superimposition effect of successive waves. If the overlapping effect on ground vibrations cannot be neglected, the FEM simulation with one loading pulse will underestimate magnitudes of ground vibrations and thus a multi-pulse dynamic loading should be used. To investigate this superimposition effect, FEM simulations with different numbers (ranging from 1 to 5) of loading pulses were performed for both sand and clay. The time interval of 0.99 s was chosen for two consecutive pulses based on pile driving records from some construction projects in Louisiana. Waveform trends from the FEM simulations are similar in sand and clay, with the results showing that it takes a longer time for the wave to dissipate in clay and a larger extent of wave overlapping effect exists in clay. To be concise, only the dynamic response of the ground underlain by a clay layer was discussed herein. Figure 3a shows the dynamic response at ground surface point B located 9.18 meters away from the driven pile under five-pulse loading, expressed by the particle velocity time history. Except for a small increase from the first to the second peak, the other peaks are almost the same. Furthermore, the PPV vs. SD relationships for clay under various numbers of loading pulses were plotted in Figure 3b, which indicates that the FEM simulation results under different numbers of loading pulses are almost the same. Therefore, the PPV values (i.e., ground vibration magnitudes) at different distances from the pile are not affected significantly by the wave overlapping effect, and it is justified to simulate ground vibrations during pile driving by using a single pulse loading.

Determination of soil damping ratio

Soil damping ratio plays an important role in wave attenuation, so its influence on ground vibrations was investigated in this research. However, the damping ratio is difficult to determine because it is affected by many factors (shear strain, soil properties, etc). The estimation procedure of soil damping ratio is presented first before its influence on ground vibrations was examined by FEM simulations.

Soil's damping ratio is composed of viscous and hysteretic components. Viscous component is represented by the initial damping ratio, which is the constant item in Equation (2) and independent of the soil shear strain. Hysteretic component is affected by the reduction of soil shear modulus as shear strain increases and represented by the shear strain dependent item in Equation (2) (Tsang, Chandler et al. 2006).

$$\xi = \xi_i + \xi_{max}\left(\frac{\gamma}{\gamma+\gamma_r}\right) \quad (2)$$

where ξ_i is the initial damping ratio, ξ_{max} is the maximum hysteretic damping ratio corresponding to the hypothetical limiting condition of zero shear modulus, γ_r is the reference shear strain of soil, and γ is the cyclic shear strain (Tsang, Chandler et al. 2006). Initial and maximum hysteretic damping ratio can be estimated as (Tsang, Chandler et al. 2006):

$$\xi_i(\%) = 1.5 + 0.03\mathrm{PI}(\%) \leq 5.8 \quad (3)$$

$$\xi_{max}(\%) = 16 - 0.1\mathrm{PI}(\%) \geq 0.0 \quad (4)$$

where PI is the plasticity index.

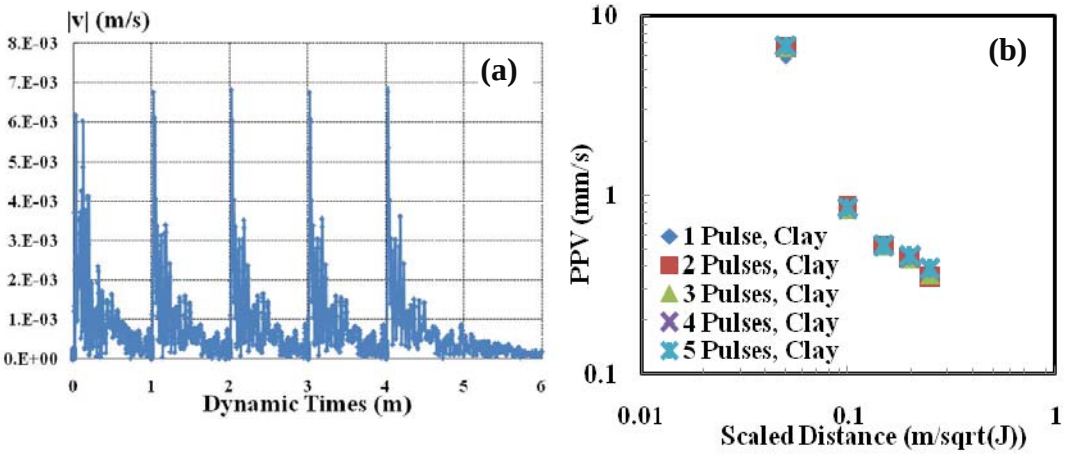

Figure 3. (a) Vibration time history at Point B under 5 loading pulses; and (b) PPV vs. SD under different number of loading pulses

With the above equations, the damping ratio range can reasonably be approximated if the PI is known. For the sand with a PI of 0, ξ_i is 1.5% and ξ_{max} is 16%; and for the clay with a PI of 30, ξ_i is 2.4% and ξ_{max} is 13%. When $(\gamma/(\gamma+\gamma_r))$ takes the value of 0 or 1 in Equation (2), the corresponding damping ratios are 1.5~17.5% for sand and 2.4~15.4% for clay. The soil damping ratios used for the subsequent parametric study were chosen from these ranges. In PLAXIS 2D, the material damping ratio is characterized by Rayleigh formulation and expressed by the Rayleigh damping coefficients α and β as:

$$[C] = \alpha[M] + \beta[K] \qquad (5)$$

where [C], [M] and [K] are damping, mass and stiffness matrices, respectively. α is a coefficient that determines the influence of mass on the damping and β is a coefficient that determines the influence of stiffness on the damping (Brinkgreve and Broere 2008). These two parameters are required inputs for the FEM dynamic simulations with Plaxis, which should be determined corresponding to a chosen damping ratio. A simple approximation method was proposed by Amorosi et al. with which α and β can be determined from the following relationship (Amorosi, Boldini et al. 2010):

$$\begin{Bmatrix}\alpha\\ \beta\end{Bmatrix} = \frac{\xi}{\pi f_m + \pi f_n}\begin{Bmatrix}4\pi^2 f_m f_n\\ 1\end{Bmatrix} \qquad (6)$$

where m and n are the vibration mode numbers, f_m and f_n are the natural frequencies at the corresponding vibration modes, which in turn can be estimated with the following equation :

$$f_n = \frac{V_S}{4H}(2n-1) \qquad (7)$$

where V_S is the shear wave velocity of the soil, and H is the thickness of the soil layer. It is common to choose one frequency at the first vibration mode and the other at the predominant frequency to approximate the damping coefficient (Park and Hashash 2004). Vibration modes 1 and 5 were selected herein to calculate f_n and f_m. Typical shear wave velocities were chosen as follows: 220 m/s for sand and 150 m/s for clay (Das 1993). Then the values for α and β were approximated for subsequent FEM simulations by using Eqs. (6) and (7) for chosen damping ratios.

RESULTS OF FEM PARAMETRIC STUDY

Influence of soil damping ratio on ground vibrations

Five different values of damping ratio were selected to investigate its influence on wave attenuation and ground vibrations during pile driving based on the FEM model described previously, with other model conditions and parameters remaining the same. The corresponding Rayleigh damping coefficients α and β, as listed in Table 2, were calculated with the natural frequencies of 1.83 HZ and 16.50 HZ using Equation (7). The log-log PPV vs. Scaled Distance charts obtained from the FEM simulations for these 5 cases are shown in Figure 4, and the corresponding k and n values for the SD equations are summarized in Table 2. Woods and Jedele's

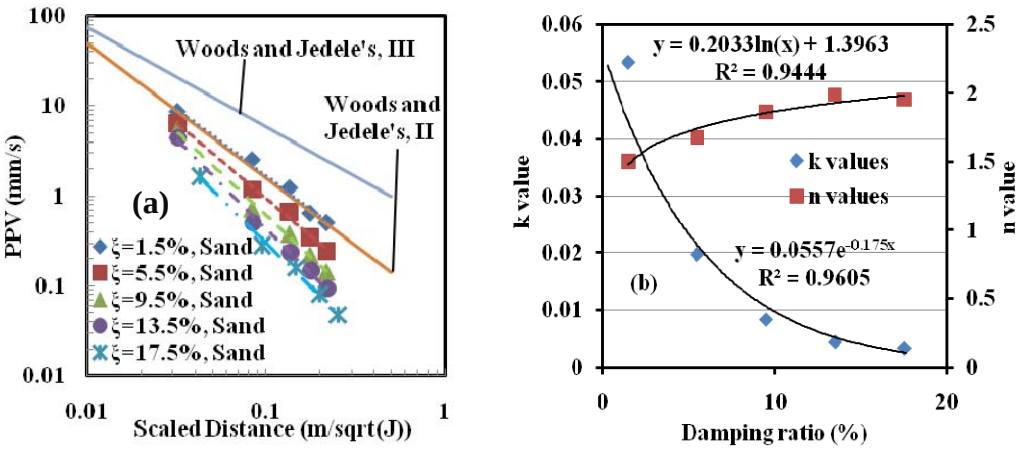

Figure 4. Influence of damping ratio values on ground vibrations: (a) PPV vs. SD with different damping ratio, and (b) the change of k and n with damping ratio

lines for soil class II and III are also presented in Figure 4a for comparison.

Table 2. Damping ratio parameters and derived SD equation's k and n values from FEM simulations on sand

Model #	Soil	Damping Ratio (%)	α	β	k	n
101	Sand	1.5	0.31102	0.00026	0.0533	1.501
102	Sand	5.5	1.1404	0.00095	0.0197	1.678
103	Sand	9.5	1.96978	0.00165	0.0084	1.861
104	Sand	13.5	2.79916	0.00234	0.0045	1.987
105	Sand	17.5	3.62854	0.00304	0.0034	1.952

It is apparent that the FEM simulation results follow the similar trend to those of Woods and Jedele's SD lines. As shown in Figure 4b and Table 2, when the damping ratio increases, k decreases and n increases. The maximum difference between the n values is about 0.45, which is relatively large given the fact that the n value falls within the range of 1 to 2. A more pronounced difference among k values is observed, with the maximum k value 16 times larger than the minimum one. It is

also apparent that strong relationships exist between damping ratio and k & n values, as indicated by Figure 4b, which shows that the influence of damping ratio on k & n values becomes smaller as it approaches the upper limit value (i.e., 17.5% for the sand in this study). It is well known that the material damping ratio represents the energy absorbent capacity of the soil. The larger is the damping ratio, the more energy is absorbed by soil, and the greater is the wave attenuation, which corresponds to a larger n value but a smaller k. Apparently, the influence of soil's damping ratio on wave attenuation and ground vibrations is well captured by the FEM simulations. In addition, the FEM simulation results in this study add some quantitative indicators to Woods and Jedele's SD equations, by relating soils' damping ratio to the k and n values.

Influence of Young's modulus of soil

In this section, the FEM simulations were performed for varying values of Young's Modulus that are given in Table 3. Figure 5 shows the corresponding FEM simulation results, with the derived k and n values summarized in Table 3. It is observed from these results that k decreases and n increases with the increasing Young's Modulus. The maximum difference among k values is 0.056 for sand and less than 0.01 for clay while the difference between the maximum and minimum n values is about 0.536 for sand, and 0.236 for clay. This indicates that the increasing of Young's Modulus hardly affects k values in the SD equations.

Table 3. Influence of Young's Modulus on ground vibrations

Model #	Soil	Young's Modulus (kPa)	Unit Weight(kN/m^3)	k	n
201	Sand	2.00E+04	15	0.0829	1.329
202	Sand	5.00E+04	17	0.0321	1.785
203	Sand	1.50E+05	22	0.0269	1.865
204	Clay	1.00E+04	16	0.0226	1.732
205	Clay	3.00E+04	18	0.0164	1.902
206	Clay	2.50E+05	20	0.0141	1.968

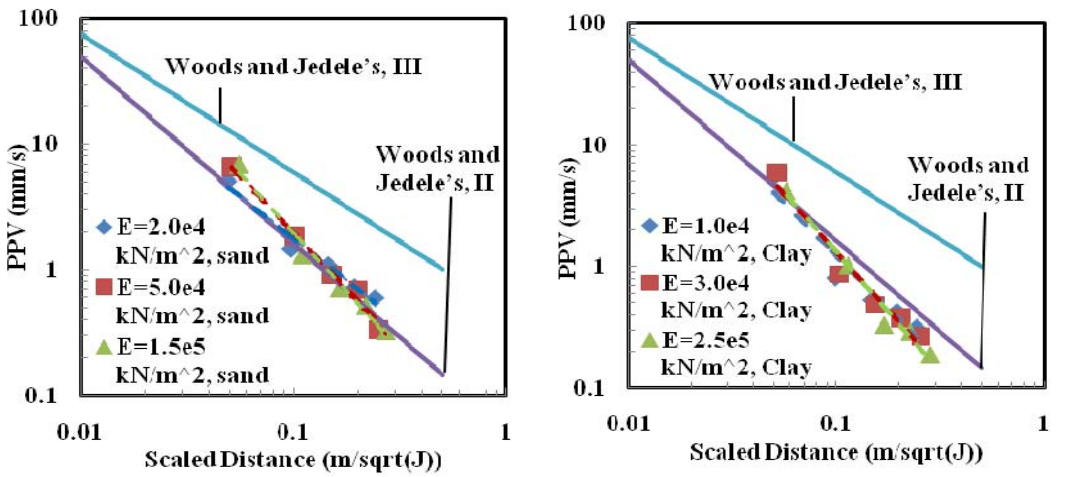

Figure 5. Influence of Young's modulus of soil on ground vibration: (a) sand; and (b) clay

CONCLUSIONS

Structure damage can be caused by ground vibrations during pile driving, which is mainly dependent on the amplitude of ground vibrations that in turn is affected by soil properties. A better understanding of soil properties' influence on ground vibrations is required for effectively managing the risk of pile driving. Based on the FEM simulation results, the following conclusions can be drawn:

The superimposition effect associated with multiple loading pulses on ground vibrations is not appreciable, when the time interval between two consecutive loading pulses was chosen to be 0.99 s. The 2-D FEM model used in this study can predict the magnitude attention of ground vibrations during pile driving and agrees with the results from the commonly used Woods and Jedele's equations.

The FEM simulation results indicate that a large damping ratio can greatly reduce the intensity of ground vibrations, as reflected by increased wave attenuation rate (i.e., n values in the SD equation) and decreased k values. The FEM results also show that the influence of Young's Modulus of the soil is similar to that of the damping ratio but to a less extent. Namely, a high Young's Modulus can also decrease the intensity of the ground vibrations in a way similar to soil damping ratio.

The parametric study in this paper can help geotechnical engineers manage the risk of pile driving more effectively by better understanding the influence of soil properties on pile driving induced ground vibrations, although the simplified 2-D FEM simulations cannot completely reflect the reality of pile driving processes.

ACKNONWLEDGEMENT

The authors thank Louisiana Department of Transportation and Development for providing financial support for this study under state project No. 736-9901589.

REFERENCES

Amorosi, A., D. Boldini, and Elia, G. (2010). "Parametric study on seismic ground response by finite element modelling." Computers and Geotechnics 37: 515-528.

Brinkgreve, R. B. J. and W. Broere (2008). PLAXIS 2D: Finite Element Code for Soil and Rock Analyses:[user's Guide]-Version 9.0, Balkema.

Das, B. M. (1993). Principles of Soil Dynamics, Brooks/Cole.

Park, D. and Y. M. A. Hashash (2004). "Soil damping formulation in nonlinear time domain site response analysis." Journal of Earthquake Engineering 8(2): 249-274.

Tao, M., M. Svinkin, and M. Zhang (2009). Update LADOTD Policy on Pile Driving Vibration Management-Interim Report to Louisiana Transporation Research Center, Department of Civil and Environmental Engineering, Worcester Polytechnic Institute, MA.

Tsang, H.-h., A. M. Chandler, and Lam, N. T.K. (2006). "Simple models for estimation period-shift and damping in soil." Earthquake Engineering and Stuctural Dynamics 35(15), 1925-1947.

Woods, R. D. (1997). NCHRP Synthesis of Highway Practice 253: Dynamic Effects of Pile Installations of Adjacent Structures.

Tunnel Face Support Pressure and Associated Risk

Mahmoud Ahmed, Ph.D., P.E.[1] and Magued Iskander, Ph.D., P.E., F.ASCE [2]

[1] Project Engineer, New York State Department of Transportation, Route 9A Project, 21 South End Ave, New York, NY 10280; PH (212) 267- 4113; FAX (212) 267-4114; email: mmahmoud@dot.state.ny.us
[2] Associate Professor, Polytechnic Institute of New York University, Six Metrotech Center, Brooklyn, NY 11201; PH (718) 260-3016; FAX: (718) 260-3433; email: iskander@poly.edu

ABSTRACT

Prediction of ground movements and risk assessment of damage to adjacent buildings and utilities have become an essential part of the success of tunneling projects in urban environments. First stage assessment of risk in tunneling zones involved evaluation of face stability conditions and ground movement induced by tunneling. This paper presents experimental work on the stability of a tunnel face using transparent soil models to estimate the magnitude of tunnel face minimum supporting pressure, failure pattern and extension of failed zone which can further be applied to tunnel risk analysis. The model tunnel was installed in a plexiglas box filled with transparent soil and was supported at the face by means of water pressure. Tests were performed by reducing supporting pressure until collapse occurred. Model tests were sliced optically with a laser sheet and images were captured for every decrement in tunnel supporting pressure. Later, these images were analyzed by Digital Image Correlation (DIC) and vector fields of incremental displacements were obtained. The value of minimum support pressure was obtained and geometry of the failure zones was found to be of chimney shape with a limited extension in front of the face. Contour plots of resultant ground movement at pre-collapse and post failure indicated that a minimum distance equal to the tunnel diameter should be considered above and a way form the tunnel for underground utilities risk assessment. A minimum support pressure was achieved with support pressures as low as 10 % of the effective vertical stress at the tunnel axis. The stability of the tunnel face was related to the coefficient of active earth pressure. In general, results of the study were in agreement with current knowledge of full-scale situations.

INTRODUCTION

Underground construction, in general, and tunneling in particular, imposes risks on owners, contractors and communities involved in the project. A primary concern for all entities involved in tunnel projects is the potential for large scale accidents during tunnel face collapse. For tunnels in metropolitan areas, there is a risk of damage to buildings, foundations and underground utilities which tend to be of greater risk because subsurface movement is usually larger than what appeared at the surface (Ahmed and Iskander, 2010). Additionally, lack of knowledge about subsurface ground reactions to tunneling can cause projects to overrun in budget and

schedule through what have been called "unforeseen conditions", an excuse frequently given to owners and the public. Finally, there is a risk that potential problems caused by tunneling and associated ground movement could lead to public protests and eventually may impact the course of the project. A good example for this scenario is the New Jersey Transit/ARC tunnel which was called off in October 2010 by the Governor of New Jersey State.

Risk on tunneling projects usually managed through engineering decisions made during the project development (Eskesen et al., 2004). These authors indicated that risk management processes can be significantly improved when all potential problems can be clearly identified and appropriate risk mitigation measures can be implemented in a timely manner. Accurate prediction of ground movements associated with differing face pressures in soft ground is essential for efficient construction and protection of nearby structures and utilities from damage. The higher the face pressure, the slower and more expensive the construction becomes (Mair and Taylor, 1997). On the other hand, reduced face pressures run the risk of excessive ground deformations (Peck, 1969); therefore it is necessary to know the minimum face pressures that result in acceptable ground movement. In addition to face collapse (active failure) the face support pressure must also prevent blow-out (passive failure) of the soil mass near the tunnel face.

Analytical methods and experimental data to estimate the tunnel face support pressure are in short supply, particularly for tunnels in saturated sand. The approach adopted in this research makes use of the recently developed transparent soil technology and associated image processing techniques (Iskander, 2010) to investigate the relationship between tunnel geometry, face support pressure, and ground deformation. A tunnel is pre-placed in a transparent soil model, which represents saturated sand. Tunnel face support is simulated using an internal pressure (σ_T) applied inside the tunnel (Fig. 1). Tests are conducted by reducing the tunnel pressure σ_T in stages until collapse of the soil occurs. Because the model is transparent, it can be sliced using a laser light sheet. In this research, the tunnel model was sliced parallel to and perpendicular to tunnel axis. Images of the soil, illuminated by a laser light sheet, were captured after each decrement of σ_T reduction and used to obtain corresponding 2D deformation fields. While this technique might not precisely model tunnel construction in the field, nevertheless it is capable of revealing patterns of face collapse and its relation to support pressure and tunnel geometry.

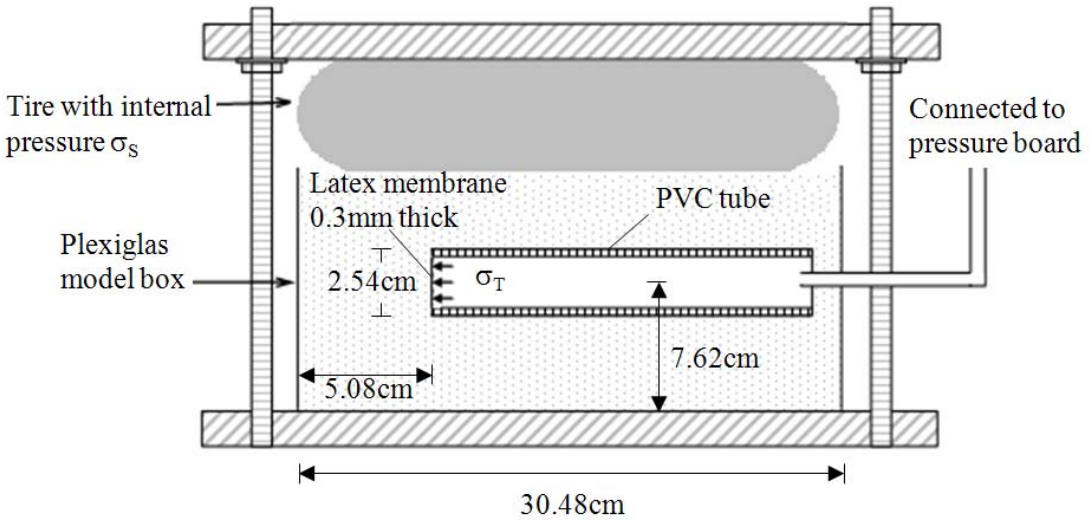

Figure 1. Tunnel model.

In addition to the tunnel container, the set up also included a Cohu 2622 black & white CCD camera, 35mW Melles Griot laser light source, a line generator lens, a loading frame, a test table, and a PC for image processing (Fig.2). The camera has a resolution of 640x480 pixels and is controlled by the PC through a Matrox Meteor 2/4 frame grabber. A macro-zoom lens with a variable focus length from 18-108 mm was mounted on the CCD camera.

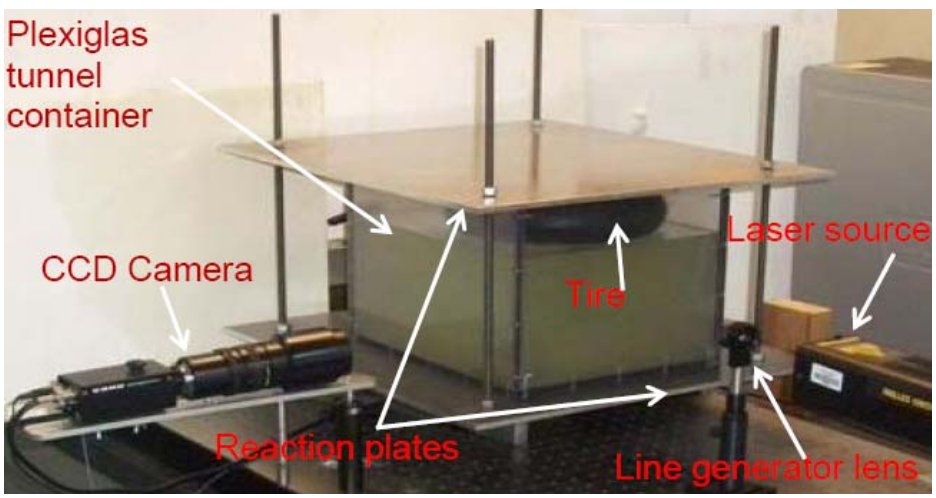

Figure 2. Experimental setup.

EXPERIMENTAL METHODOLOGY

To understand influence of important parameters, it is necessary to make certain assumptions and formulate a simplified model for tunnel construction (Fig. 3). The unsupported length, behind the face is taken equal to zero which is a reasonable assumption for shield driven tunnels. The self-weight of the soil above the tunnel (γC) is small and thus neglected. A surcharge σ_s is applied at the surface. Plane strain is assumed. A Plexiglas model 30.48 cm long, 25.4 cm wide and 20.32 cm high was used to contain the transparent soil. The dimensions of the model have been chosen in such a way, that the influence of the boundaries was minimized. The tunnel is modeled by a PVC tube of 2.54 cm diameter preinstalled inside the model at a depth of 12.7 cm (Fig. 1). A latex membrane (0.3 mm thick) of negligible strength was attached to the end of the tube to represent the tunnel face. The membrane was left slack to prevent mechanical influence on the displacement of the face. The tube (tunnel) was then filled with air under pressure to simulate the tunnel support pressure (σ_T) which can be read and controlled by the pressure board. In reality, such a support can be achieved by use of compressed air, bentonite slurry or earth pressure balance (E.P.B. shield). In this study, σ_T is assumed to be constant over the tunnel face, which best models the case of compressed air support, but also provides valuable information for slurry or E.P.B. shields. For application of surcharge or surface pressure σ_S, the Plexiglas model container was placed between two identical metal plates (Fig. 2) connected by four threaded rods. A rubber tire with internal pressure σ_S was placed on top of the transparent soil, and connected to the pressure board. The tunnel support pressure σ_T was increased such that $\sigma_T = \sigma_S = 69$ kPa at the beginning of the test. The tire was placed on to top of the transparent soil which was well leveled to assure uniform pressure distribution.

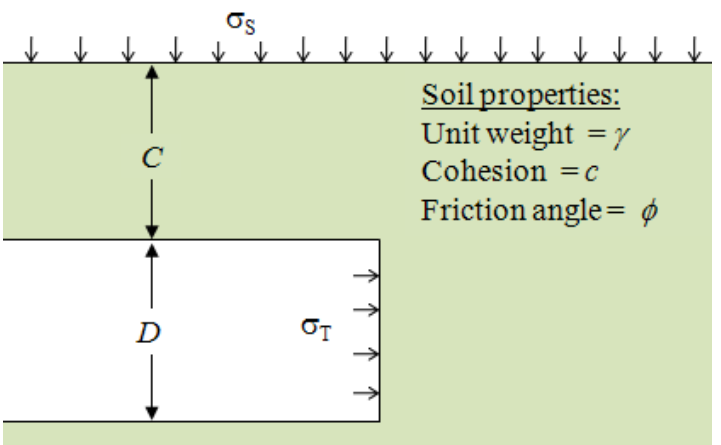

Figure 3: Important parameters in tunneling.

Active collapse of the tunnel is triggered by application of surcharge, σ_S, and self-weight, with the tunnel face pressure σ_T providing resistance against failure. Under passive conditions, these roles are reversed, and blow-out of the soil mass in

front of the tunnel face is caused by the tunnel pressure with resistance being provided by the surcharge and self-weight. In this study, only the active collapse of the tunnel face is considered in the analysis; because the blow-out of the soil in front of the tunnel face is less likely, thus of less practical interest.

Transparent sand used in this study (Sadek et al., 2002) has a unit weight of 8.53 kN/m^3, friction angle of 36°, particles size of 0.5 - 1.5 mm, specific gravity of 2.2, zero cohesion and 32 MPa modulus of elasticity. Time to set-up and run one of these transparent soil models depends on the depth of silica gel. Approximately 48 hours was required to fully saturate the silica gel and run one test. In order to achieve transparency in any transparent material, the refractive index of the solid and pore fluids must be matched. Application of layered soils in transparent soil models is possible when the refractive indices of all materials matched (Iskander, 2010). Such application is under consideration by the authors to study tunneling in layered soils (mixed-tunneling). Transparent material used in this study has been used previously to study pile penetration (Liu and Iskander, 2010) and shallow foundations (Iskander and Liu, 2010).

DISPLACEMENT MEASUREMENT

The interaction between laser light and transparent soils produces a distinctive speckle pattern. This speckle pattern manifests the interaction between the transparent soil matrix, impurities, entrapped air, and the laser. Small particle movements will result in changes in the speckle distribution in the plane of measurement. If the deformation is small, the contrast distribution resulting from the speckle effect will follow the particle movement. Images captured before and after deformation are analyzed using the cross-correlation function (DIC) which is a classic pattern recognition technique based on using correlation function to locate the best matching position of two images and thus predicting movements. Sadek et al. (2002) studied the accuracy of DIC application in transparent soil models. The results indicate that the calculated deformation using the developed system has an error on the order 0.1 pixel, which is equivalent to a 0.01 mm for optical settings used in this study.

For displacements measurement using DIC, the camera images are divided into rectangular regions called interrogation areas or interrogation windows. For each of these interrogation windows the image before and after each decrement of tunnel pressure are correlated to produce an average particle displacement vector. Doing this for all interrogation regions produce a vector map of average particle displacements. The position of the peak in the correlation plane corresponds directly to the average particle displacement within the interrogation area investigated. The vector from the center of the region to the peaks of cross-correlation function gives the magnitude and direction of the relative movement between two images.

ANALYSIS OF TEST RESULTS

Plots of face support pressure against face displacements for a tunnel with cover to diameter (C/D) ratio equal to 1.5 is presented in Fig. 4, where the tunnel support pressure, σ_T, normalized by the vertical effective stress, σ_V, at the tunnel axis

is plotted against tunnel face displacement, δ_h, measured at the center of the face, normalized by tunnel diameter, D. At the beginning (point O) $\sigma_T/\sigma_V = 1$, where σ_V ($\approx \sigma_S$ in this study) is the theoretical vertical pressure at the tunnel center line where the measurement was taken. As σ_T is reduced, no movement is observed at the face down to pressures that are very low compared to initial support pressure. For our tests, a distinctive pressures (at point A) represents the start of collapse and corresponding to σ_T/σ_V = 18 %. Chambon and Corté (1994) referred to pressure triggering collapse in centrifuge experiments on 5 tunnels in dry sand as the characteristic failure pressure, p_c. Based on their tests conditions (γ = 15.3–16.1 kN/m^3, p_c = 20.1–20.2 kPa, C/D = 1–2) σ_T/σ_v ranges between 11 % for C/D = 2 and 18% for C/D = 1. Our test and Chambon and Corté test are in agreement and have the same range for tunnel support pressure that triggers the collapse stage. Further reduction of support pressure beyond point A down to point B, results in small face displacement, which are approximately proportional to the reduction in σ_T. At Point B, the cumulative normalized displacements of the tunnel face is about 1% (Fig. 4). Again, this range compares favorably with the 0.7% reported by Chambon and Corté (1994) for dry sand.

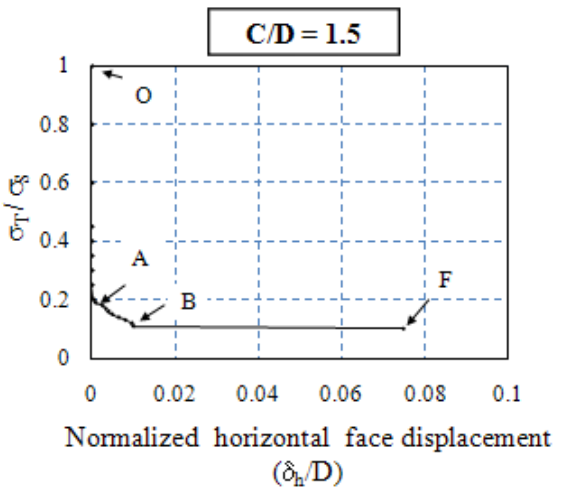

Figure 4. Plots of face support pressure against face displacements.

Displacement vectors and contour plots of resultant ground movement at Point B (pre-collapse) normalized by tunnel diameter are shown in Fig. 5 for C/D = 1.5. This figure presents the extension of ground movement ahead of the face and above the crown. It appears that ground movement extends approximately 1D in front of the tunnel face. Ground movements are largest near the face but propagate upward to form a narrow chimney.

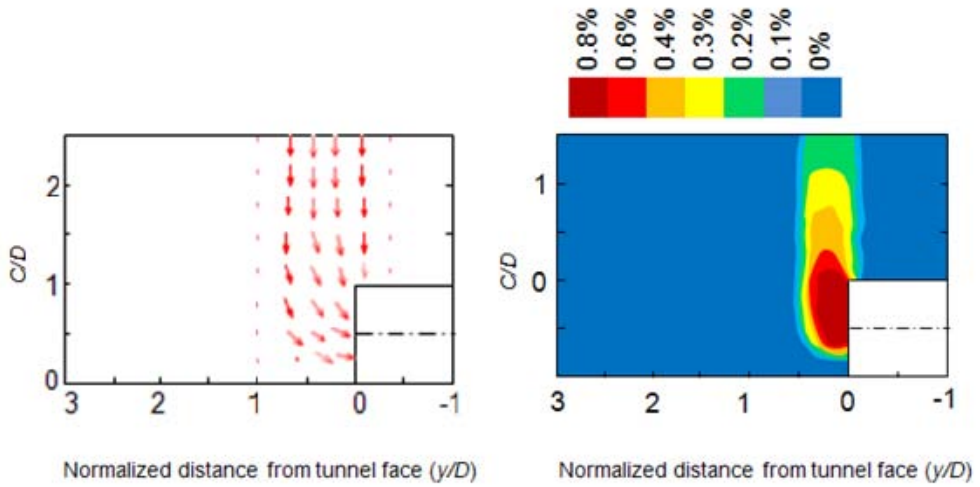

(a) **(b)**

Figure 5. (a) Displacement vectors (b) contour plots of ground movements at Point B (C/D = 1.5).

Knowledge of when Point B or local tunnel face failure occurs is not only important to ensure face stability but also to control and limit ground deformations associated with the tunneling. It appears that a small face support pressure approximately 10% of the vertical stress, applied to the tunnel face is sufficient to provide stable conditions against the action of earth pressure at the face which falls between the average of the data published by Oblozinsky and Kuwano (2006) and Chambon and Corté (1994). After Point B was reached (Fig. 4), further decrease of the supporting pressure led to sudden collapse (Point F) as transparent soil tended to slide into the tunnel and the failure envelope propagated progressively upward. Contour plots for resultant ground movements associated with Point F (failure) are shown in Fig. 6 for C/D = 1.5 and 4.5. The movements observed at failure (Fig. 6) are substantially larger than those observed at Point B (Fig. 5). The failed zone is relatively narrow and reaches approximately 1D above the tunnel crown, when arching of the soil prevented further deformation. The failed soil mass outcropped at the ground surface for the C/D =1.5 case. The observed failure zone is consistent with the prismatic wedge block failure mechanisms proposed by Horn (1961), Chambon and Corté (1994), Leca and Dormieux (1990) and Mollon et al. (2009).

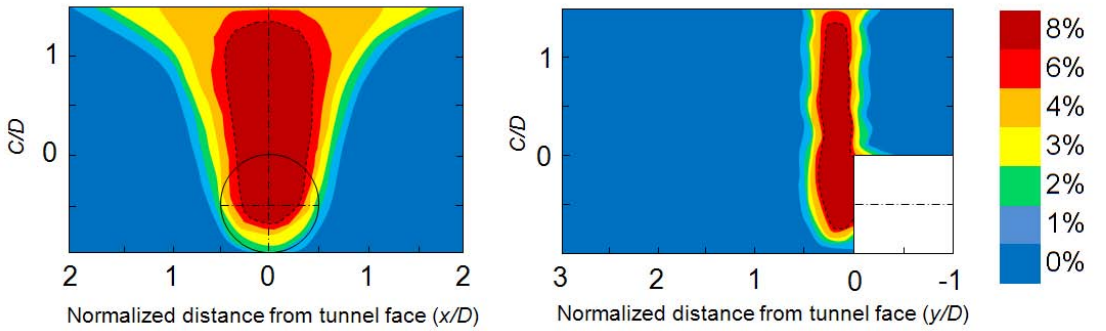

Figure 6. Contour plots of ground movements at Point F (C/D = 1.5).

CONCLUSIONS

An experimental method was developed to analyze the progression of ground movements with decreasing tunnel face pressure. The use of transparent soils permitted visualization of actual internal ground deformations under the test conditions. A minimum support pressure, $\sigma_{T,}$ was achieved with pressures as low as 10 % of the effective vertical stress, $\sigma_{V,}$ at the tunnel axis. The observed ground deformations can be divided into three stages in relation to lateral earth pressure coefficient, k_a, representing (1) Face Deformation ($1 > \sigma_T/\sigma_V > 0.8\ k_a$), involving little or no deformation; (2) Face Slip Stage ($0.8\ k_a > \sigma_T/\sigma_V > 0.5\ k_a$) involving increasing but stable deformation; and (3) Failure Stage ($\sigma_T/\sigma_V < 0.5\ k_a$) where excessive irrecoverable deformations occurred.

The observed failure mechanisms resembled a prismatic wedge in front of the tunnel face extending upward in the form of a vertical chimney confirming the mechanisms proposed by Horn (1961), and Chambon and Corté (1994). Contour plots of resultant ground movement at pre-collapse and post failure indicated that a minimum distance equal to tunnel diameter should be considered above and a way form the tunnel for underground utilities risk assessment.

REFERENCES

Ahmed, M. and Iskander, M. (2010) "Analysis of tunneling induced ground movements using transparent soil models" *ASCE Journal of Geotechnical and Geoenvironmental Engineering*, <http://dx.doi.org/10.1061/(ASCE)GT.1943-5606.0000456>.

Chambon, P. and Corté, J. F. (1994) "Shallow tunnels in cohesionless soil: Stability of tunnel face" *Journal of Geotech. Eng.*, 120, 1148–1165.

Eskesen, D., S., Tengborg, P., Kampmann, J and Veicherts, T. H. (2004)"Guidelines for tunnelling risk management: International Tunnelling Association, Working Group No. 2" *Tunnelling and Underground Space Technology*, 19, 217–237.

Horn, M. (1961) "Horizontal earth pressure on perpendicular tunnel face" *Proceedings of the Hungarian National Conference of the Foundation Engineer Industry*, Budapest, Hungary, 7–16.

Iskander, M. & Liu, J. (2010) "Spatial Deformation Measurement using Transparent Soil" *ASTM Geotechnical Testing Journal*, 33, 314-321, doi: 10.1520/GTJ102745.

Iskander, M. (2010). Modelling with Transparent Soils, Visualizing Soil Structure Interaction and Multi Phase Flow, Non-Intrusively. Springer ISBN: 978-3-642-02500-6.

Leca, E., and Dormieux, L. (1990) "Upper and lower bound solutions for the face stability of shallow circular tunnels in frictional material" *Geotechnique*, 40, 581–606.

Liu, J. and Iskander, M. (2010) "Laboratory Investigation of the Modeling Capacity of Synthetic Transparent Soils" *Canadian Geotechnical Journal*, 47, 451-460, DOI: 10.1139/T09-116.

Mair, R. J. and Taylor, R. N. (1997) "Bored tunnelling in the urban environment" (State-of-the-art report and theme lecture), *Proceedings of the 14th International Conference on Soil Mechanics and Foundation Engineering*, Hamburg, Germany, 4, 2353-2385.

Mollon, G., Dias, D., and Soubra, A. (2009). "Probabilistic analysis and design of circular tunnels against face stability" *Int. J. Geomech*., 9, 237–249.

Oblozinsky, P. and Kuwano, J. (2006) "Centrifuge experiment on stability of tunnel face in sandy ground" *Proceedings of the 5th International Conference on Geotechnical aspects of underground construction in soft ground*, TC28 of the ISSMGE, the Netherlands, 271-275.

Peck, R. B. (1969). "Deep Excavations and Tunneling in Soft Ground." *Proceedings, 7th International Conference on Soil Mechanics and Foundation Engineering*, Mexico City, State-of-the-art Volume, 225-290.

Sadek, S., Iskander, M., & Liu, J. (2002) "Geotechnical properties of transparent material to model soils" *Canadian Geotechnical Journal*, 39, 111-124.

Risk Analysis of Pile Pressing-in on an Adjacent Earth-Retaining Wall

Amy D.D. Lu[1] and Albert T. Yeung, Fellow, ASCE[2]

[1] Dept. of Civil Engrg., The University of Hong Kong, Pokfulam Road, Hong Kong; PH (852) 53779264; FAX (852) 25595337; email: ldd09@hku.hk
[2] Dept. of Civil Engrg., The University of Hong Kong, Pokfulam Road, Hong Kong; PH (852) 28598018; FAX (852) 25595337; email: yeungat@hku.hk

ABSTRACT

Pile pressing-in is a green pile installation technology that uses hydraulic jacks to press piles into the ground. It is environmentally friendly as it eliminates the noise and vibration nuisance as well as air pollution problems.

The current state of development of the pressing-in technique and equipment allows piles to be pressed-in very close to existing permanent or temporary earth-retaining walls. The piles being installed may induce additional lateral loads on the retaining wall and/or excessive movement of the wall, and may thus have detrimental effects on the stability of the wall. It is of great importance to understand these adverse effects that may be induced by pile pressing-in to ensure the stability of any nearby retaining walls. However, it is extremely expensive and time-consuming to conduct a full-scale evaluation. Therefore, laboratory evaluation using a scaled model was adopted in this research. The availability of a hi-tech tactile pressure sensor mat makes it possible to measure the normal stress on a laboratory-scale model retaining wall with high accuracy. Based on a series of laboratory tests, the variation of factor of safety against sliding k with distance between the pile and the retaining wall was quantified. Influences of the movement of the retaining wall on k were studied. Limitations of the current research are also discussed.

BACKGROUND

Pile pressing-in (also known as pile jacking) is an environmentally friendly pile installation method that uses hydraulic jacks to press piles into the ground. It is widely used worldwide, in particular in Asian countries including China, Singapore, and Malaysia (Lam and Li 2003). The versatility of the pressing-in technology makes it possible for pressed-in piles to be installed in very close proximity to existing earth-retaining walls. The situation often occurs in mountainous regions, where retaining walls are commonly used to improve slope stability or to make room for infrastructures. For better use of land resources, piles are sometimes constructed very close to the retaining wall. Moreover, pressing-in piles can be installed adjacent to temporary earth retaining walls supporting temporary excavations when different construction activities are progressing simultaneously.

The pressing-in piles may have detrimental effects on nearby retaining walls by increasing the lateral load on the retaining walls, inducing excessive movement of the

retaining walls, or both. It is vital to analyze the risk of such detrimental effects so as to ensure the stability of the existing earth-retaining walls and to avoid excessively conservative designs. However, relevant research has not been extensively conducted. As a result, there are many uncertainties in the design.

Several analytical methods were proposed to describe soil movement induced by pile installation, including the strain path method (Baligh 1995), shallow strain path method (Sagaseta and Whittle 2001), and cavity expansion method (Baligh 1985). However, these studies have not been extended to evaluate the effects of pile installation on nearby retaining walls. Henke (2009) used ABAQUS to simulate the effects of additional load on nearby retaining structure. However, there are no full-scale or laboratory-scale experiments conducted to evaluate the validity of Henke's simulations.

In this research, a series of laboratory-scale experiments has been performed to evaluate the additional load on the retaining wall, movement of the wall induced by pile pressing-in, and their interactions. Risk analysis on the factor of safety against sliding k has been conducted to express the potential risk explicitly.

EXPERIMENT DESIGN

In the past, it was very difficult to capture the stress distribution acting on a laboratory-scale retaining wall. The use of too few pressure cells cannot capture an accurate stress distribution. However, the use of too many pressure cells will advertently change the stiffness of the system (Talesnick 2005).

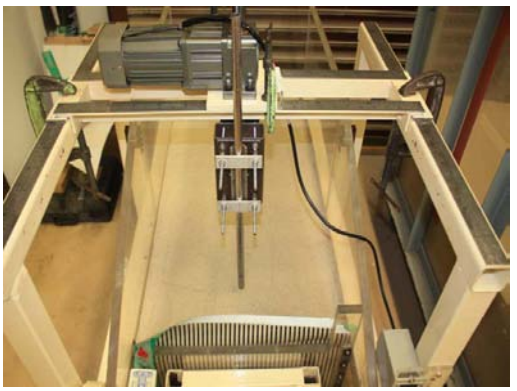

Figure 1. Laboratory apparatus.

The availability of grid-based Tekscan tactile pressure sensor mats makes it possible to measure the normal stress distribution accurately and continuously. In this research program, a 102 cm long and 50 cm wide apparatus made of plexglas as depicted in Fig. 1 was specifically designed, fabricated, and assembled. The front end wall of the apparatus is used to model an earth-retaining wall. The wall can undergo controlled translations, rotations, and any combination of translations and rotations as required. A Tekscan sensor Mat #5315 containing 2016 sensor cells had been installed on the inner surface of the retaining structure before the apparatus was filled with dry British standard sand compacted to relative density of 60%.

A speed-control motor with a maximum thrust of 140 kg is used to press a model pile into the sand. The motor is fixed onto a transverse beam by G-clamps. The transverse beam is supported by two longitudinal beams so that the motor can be located anywhere within the apparatus to press-in piles as shown in Fig. 1. Steel hollow circular model piles of diameter 1.5 cm with conical tip were used in the experiments.

EXPERIMENTAL RESULTS

Experiments were conducted to simulate the pile pressing-in operation and diff-

rent types of retaining wall movements including: (1) no movement; (2) translational movement; and (3) rotational movement. Piles were installed at different distances from the wall. The lateral stress distribution on the wall was measured as a function of pile penetration and wall movement.

Case 1: Rigid retaining wall. When the retaining wall is rigid, the only effect of pile pressing-in is the increase in lateral stress acting on the wall. The model pile is penetrated along the centerline of the apparatus at different distances from the wall. Consequently, the maximum increase in lateral stress induced by the pressed-in pile occurs at the central column of sensors on the sensor mat. The average lateral stress ratio measured along the central column of sensors $\gamma_{ave,c}$ induced by the pressed-in pile as a function of distance from the retaining wall is shown in Fig. 2. The average lateral stress ratio along the central column of sensors $\gamma_{ave,c}$ is defined as the average of the ratios of the lateral stresses induced by the pressed-in pile to the original lateral stresses measured by the central column of sensors. When the distance is 3 cm, $\gamma_{ave,c}$ is approximately 3.75. The average lateral stress ratio along the central column decreases rapidly with increase in distance between the pile and the retaining wall. After the pile distance reaches 20 cm, the rate of decrease is much slower. $\gamma_{ave,c}$ are approximately

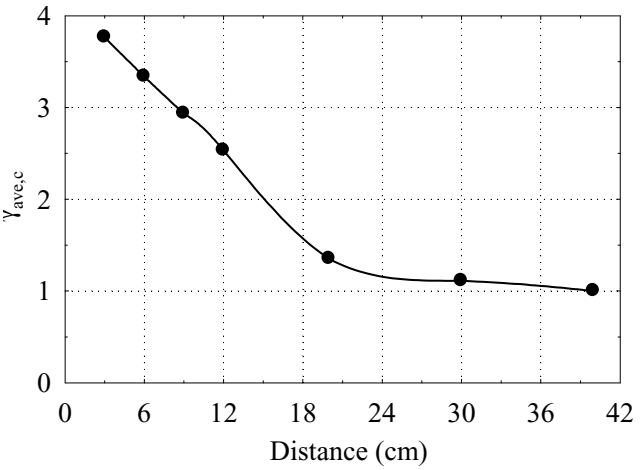

Figure 2. Average lateral stress ratio along the vertical centerline of the retaining wall versus pile distance.

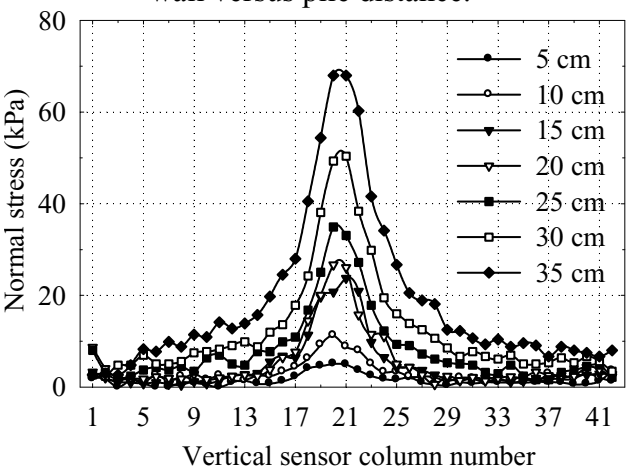

Figure 3. Lateral stress distribution in the transverse direction of the wall

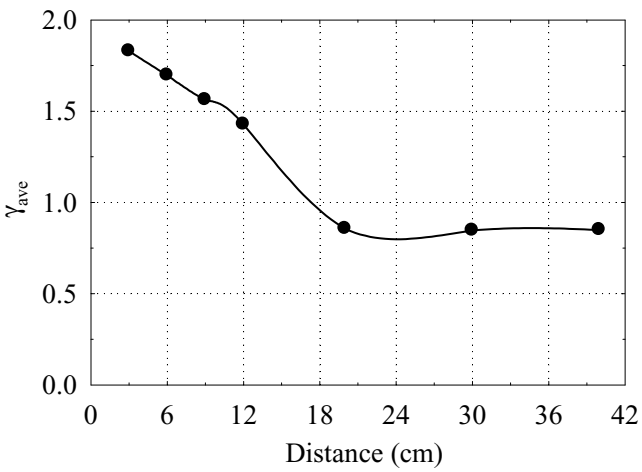

Figure 4. Average lateral stress ratio within the effective zone versus pile distance

1.5 and 1.1 for pile distances of 20 cm and 40 cm, respectively.

There is an effective zone within which there is a significant increase in normal lateral stress acting on the wall induced by pile pressing-in. The lateral stress distributions at the pile tip level along the transverse direction of the wall when the pile was pressed-in at 3 cm from the wall are shown in Fig. 3. It can be observed that the lateral stress increases with penetration depth. The average lateral stress ratio throughout the effective zone γ_{ave} as a function of pile distance as shown in Fig. 4 can thus be used to reflect the average effects of a single pressed-in pile.

Case 2: Translational retaining wall. When the retaining wall can translate, the lateral stress acting on the wall and amount of translation of the retaining wall are inter-dependent. The pile was first pressed-in at a distance of 6 cm from the retaining wall. The retaining wall was then translated outwards to 0.2 mm gradually. The resulting $\gamma_{ave,c}$ and γ_{ave} as a function of the amount of outward translation are shown in Figs. 5 and 6, respectively. It can be observed that both $\gamma_{ave,c}$ and γ_{ave} decrease with increase in outward translation. There appears to be a linear relationship between $\gamma_{ave,c}$ and outward translation as shown in Fig. 5. It can be observed in Fig. 6 that the total lateral load acting on the wall within the effective zone is reduced to the original value before pile pressing-in when the outward translation reaches 0.06 mm.

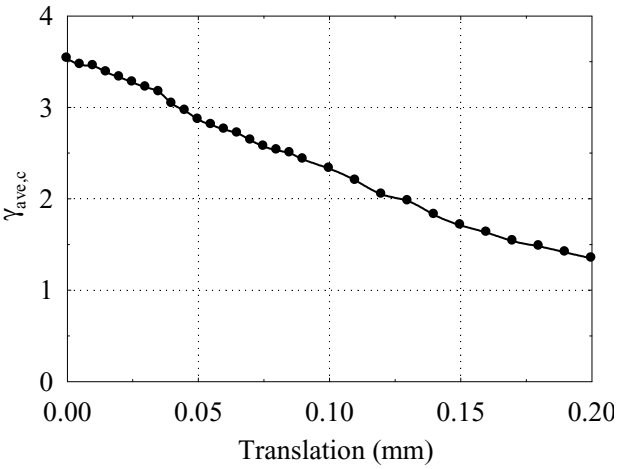

Figure 5. Average lateral stress ratio along the vertical centerline of the retaining wall versus translation

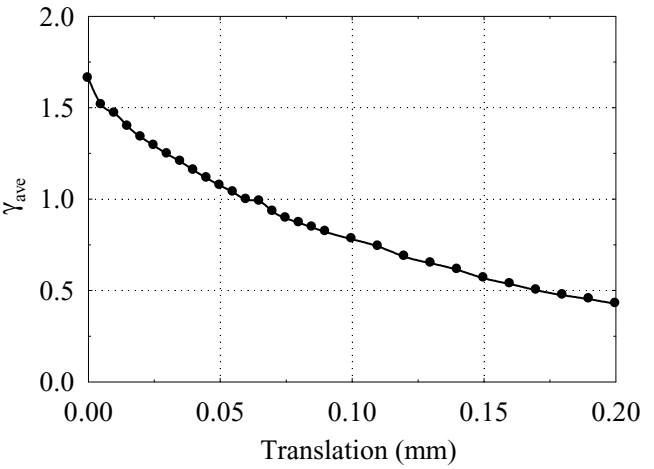

Figure 6. Average lateral stress ratio within the effective zone versus translation

Case 3: Rotational retaining wall. When the retaining wall can rotate, the lateral stress acting on the wall and the amount of rotation of the retaining wall are inter-dependent. Similar to Case 2, the pile was first pressed-in at a distance of 6 cm from the retaining wall. After the pile had been pressed-in, the retaining wall was rotated outwards about the base to 0.2°. The resulting $\gamma_{ave,c}$ and γ_{ave} as a function of the angle of rotation are shown in Figs. 7 and 8, respectively. It can be observed that both $\gamma_{ave,c}$ and γ_{ave} decrease with increase in outward rotation. It can be observed in Fig. 8 that total lateral load acting on the wall

within the effective zone decreases to the original value before pile pressing-in when the outward rotation is approximately 0.03°.

RISK ANALYSIS

As shown in the experimental results, pile pressing-in would induce considerable increase in lateral load on the retaining wall. However, translation and/or rotation of the retaining wall can reduce the increased lateral load to some extent.

A factor of safety against sliding k is utilized to express the associated risk explicitly. In practice, piles are pressed-in at a specific spacing. The effects of neighboring piles on the retaining wall may overlap. The overlapping may increase both the $\gamma_{ave,c}$ and γ_{ave} of a single pile. As a result, k will be reduced. On the other hand, if $\gamma_{ave,c}$ is considered as the increase in lateral stress ratio for the entire retaining wall, the estimation of k would be too conservative for a single pile, as the load increase on the retaining wall away from the centerline projection of the pile as shown in Fig. 3 is less. However, $\gamma_{ave,c}$ is adopted for the analysis to estimate k to account for the overlapping effects of multiple piles.

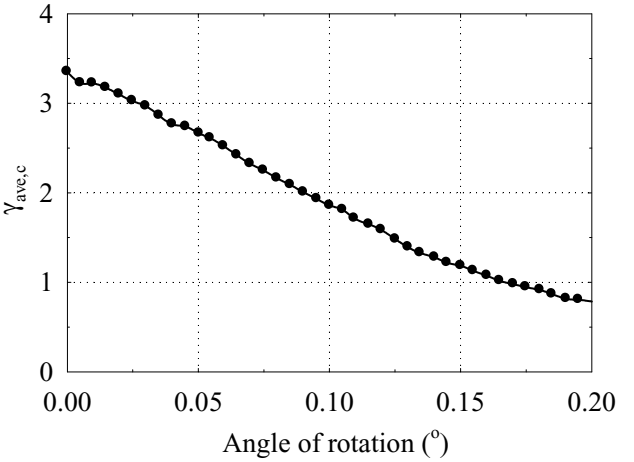

Figure 7. Average lateral stress ratio along the vertical centerline of the retaining wall versus rotation

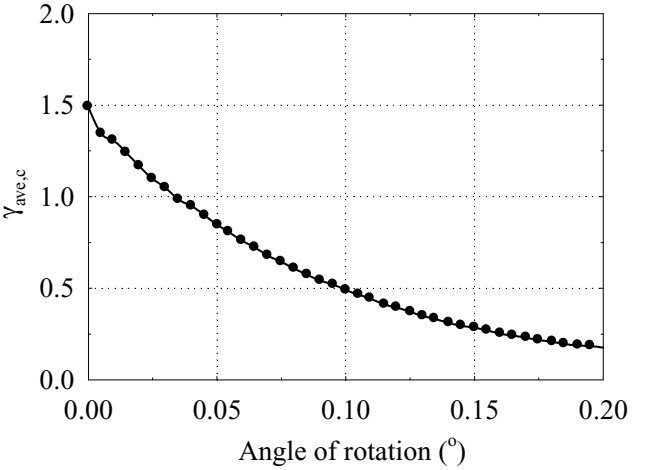

Figure 8. Average lateral stress ratio within the effective zone versus rotation

Assuming the original design factor of safety against sliding is k_0, i.e.,

$$k_0 = \frac{R_0}{F_0} \tag{1}$$

where F_0 = lateral load acting on the wall; and R_0 = resisting force. The lateral load acting on wall after pile pressing-in is denoted as F and is given by

$$F = F_0 \times \gamma_{ave,c} \tag{2}$$

Therefore, the factor of safety against sliding k becomes

$$k = \frac{R_0}{F} = \frac{k_0}{\gamma_{ave,c}} \Rightarrow \frac{k}{k_0} = \frac{1}{\gamma_{ave,c}} \tag{3}$$

When the pile distance is twice the pile diameter, k is decreased to approximately one third of the original design factor of safety k_0. As the pile distance increases, k increases but will not resume the value k_0 until the pile distance reaches approximately 40 cm as shown in Fig. 9.

The outward translation of the retaining wall would reduce the increased lateral load induced by pile pressing-in. The increase in k with outward translation of the retaining wall is shown in Fig. 10. When the outward translation reaches 0.2 mm, k/k_0 is approximately 0.75, which is twice the value for the rigid wall.

Similarly, the outward rotation would also reduce the increased lateral load induced by pile pressing-in. The increase in k with outward rotation of the retaining wall is shown in Fig. 11. When the angle of rotation is approximately 0.17°, the value of k resumes the original design factor of safety against sliding k_0. Further outward rotation will result in further increase in the factor of safety against sliding.

With regard to the factor of safety against overturning k', it can be defined as

$$k' = k \times \frac{L_0}{L} \qquad (4)$$

where L_0 = moment arm of the force about the base before pile pressing-in; and L = moment arm of the force about the base after pile pressing-in. As the

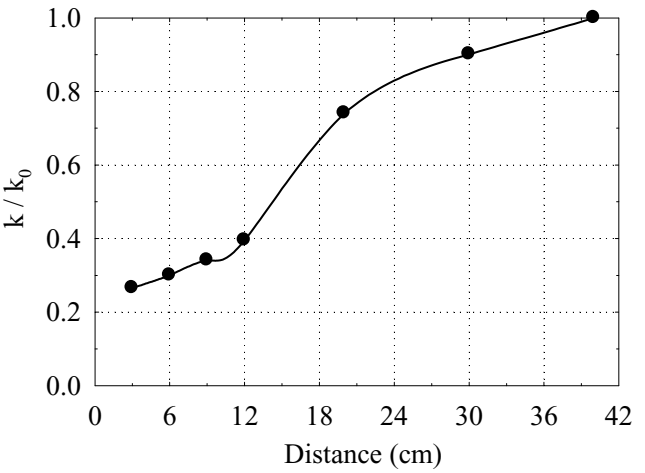

Figure 9. Factor of safety against sliding versus pile distance

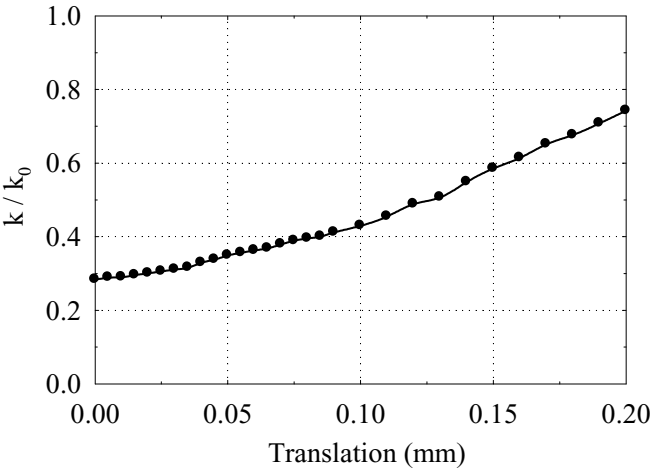

Figure 10. Factor of safety against sliding versus translation

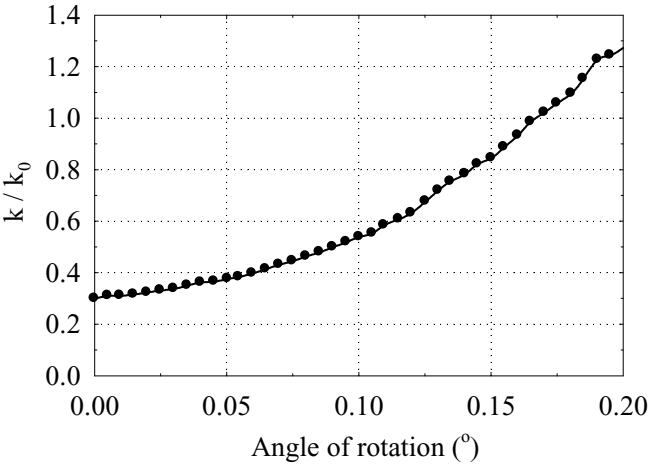

Figure 11. Factor of safety against sliding versus rotation

increased in lateral load on the retaining wall by pile pressing-in is more significant at the bottom than at the top as shown in Fig. 3, L should be smaller than L_0. As a result, k' is generally larger than k. Therefore, the factor of safety against sliding would be more critical than the factor of safety against overturning during pile pressing-in.

DISCUSSIONS AND CONCLUSIONS

When pressed-in piles are constructed in proximity of a retaining wall, the lateral stress acting on the retaining wall is increased, resulting in a decrease in the factors of safety against sliding and overturning of the retaining wall. There is a risk of failure of the retaining wall if the factor of safety is less than unity. However, the translation and rotation of the retaining wall can reduce the increased lateral stress. As the amount of movement increases, the lateral stress decreases and the risk of failure decreases. However, the amount of movement must be within serviceability limits. A methodology has been developed to evaluate the risk of failure on the basis of lateral stress increase induced by a single pressed-in pile, wall translation and rotation.

The current study is limited to laboratory-scale measurements of lateral stress increase induced by a single pile. Therefore, the results should be considered as preliminary. Scale effect should be considered for real life construction projects. Moreover, overlapping effects of multiple piles should be considered in further study.

ACKNOWLEDGEMENTS

The financial support provided to the first author for her graduate study by The University of Hong Kong is acknowledged. Moreover, the 2nd IPA Research Grant Award bestowed to the second author by the International Press-in Association to support the research is gratefully acknowledged.

REFERENCES

Baligh, M.M. (1985). "Strain path method." J. Geotech. Engrg., ASCE, 111(9), 1108-1138.

Gue, S.S. (1984). Ground heave around driven piles in clay. PhD thesis, University of Oxford, U.K.

Henke, S. (2009). "Influence of pile installation on adjacent structures." International Journal for Numerical and Analytical Methods in Geomechanics, 34(11), 1191-1210.

Lam, J., and Li, K.S. (2003). "Introduction." *Case histories of jacked piling in Hong Kong*, Centre for Research & Professional Development, Hong Kong, 1-35.

Randolph, M.F., Steenfelt, J.S., and Wroth, C.P. (1979). "The effect of pile type on design parameters for driven piles-design parameters in geotechnical engineering." *Proc., 7th. European Conf. Soil Mech.*, Brighton, Vol. 2, 107-114.

Sagaseta, C., and Whittle, A.J. (2001). "Prediction of ground movements due to pile driving in clay." *J. Geotech. Geoenvir. Engrg.*, ASCE, 127(1), 55-66.

Talesnick, M. (2005). "Measuring soil contact pressure on a solid boundary and quantifying soil arching." *Geotech. Test. J.*, ASTM, 28(2), 171-179.

Numerical Study on the Dynamic Behavior of Retaining Walls Backfilled with Shredded Tires

E. Huggins[1] and N. Ravichandran[2]

[1]Student, Department of Civil Engineering, Clemson University, Clemson, SC 29621; PH (864) 656-2818; FAX (864) 656 2670; email: ehuggin@clemson.edu
[2]Assistant Professor, 320 Lowry Hall, Department of Civil Engineering, Clemson University, Clemson, SC 29621; PH (864) 656-2818; FAX (864) 656 2670; email: nravic@clemson.edu

ABSTRACT

Previous research has shown that shredded tires are a beneficial replacement for conventional sand backfills in retaining walls as they reduce both material costs and structural wall size requirements. To further investigate the suitability of tire shreds as a backfill material, this study evaluates the performance of retaining walls backfilled with tire shreds under dynamic loading conditions. Projected lateral earth pressures and bending moments and shear forces on the structure are evaluated for both shredded tire backfill and conventional backfill sand using a geotechnical engineering finite element software, PLAXIS. Input information for material properties of soil, sand backfill, and shredded tires is determined from laboratory testing. Through this comprehensive dynamic simulation, the safety and performance of shredded tires is confirmed for structures under earthquake loading. This demonstrates the viability of shredded tires as an economical replacement for conventional sand in the construction of retaining walls in seismic zones.

INTRODUCTION

Approximately 78% of the more than 270 million discarded tires in the United States are disposed of as whole tires in landfills or illegal dump sites. Tire piles produce fire, environmental, and public health hazards. First, whole tires collect water and produce a warm, moist environment that is an ideal breeding ground for disease carrying mosquito populations. Whole tire piles also pose a fire hazard in that they are readily ignited by the slightest source and trap air making them nearly impossible to extinguish. In addition, as tires burn they produce liquid oil and toxic smoke that are damaging to the environment and harmful to individuals living in the area. The shredding of whole tires and use of shreds in civil engineering applications is one method for reducing tire stock piles and the risks associated with that disposal technique. One prominent use for tire shreds in civil engineering applications involves their use as a lightweight and low cost replacement for conventional backfill materials in retaining wall construction. In order for tire shreds to be implemented in this way, their safe performance in conjunction with retaining structures must be evaluated in both static and dynamic loading scenarios. In the construction of a retaining wall, the backfill material has a great impact on the behavior and proper functioning of the structure. In some areas, seismic loadings may complicate the normal behavioral expectations of such structures, and the structure and backfill must be designed to handle seismic loadings without compromising safety and performance. Typically, a coarse-grained sand or gravel is used because these

materials have a high permeability even when compacted which alleviates excess pore water pressure behind the wall. The properties that most affect backfill performance are permeability and shear strength parameters. Any material used for backfill must have a high enough permeability to allow water to drain freely and dissipate the excess pore water pressure behind the wall.

A potential design benefit of replacing sand backfill with rubber chips is their low unit weight. Unit weight of the backfill affects how much static load is applied to the structure. In addition, the underlying soil at the site must support the vertical load of the soil above it, and if the in situ soil is soft this may limit the weight of the backfill material that can be accommodated. Cecich et al (1996) found the unit weight of shredded tires to range from 35-38 pcf, which is less than a third of the weight of comparable sand backfill. These findings are supported by the findings of Lee et al (1999) which showed that shredded tires had a dry unit weight of 40 pcf. Even the rubber-sand with 40% tires by weight had a unit weight of 79.6 pcf which is significantly lower than that of pure sand (Lee et al, 1999). In a study by Warith et al (2004), the values for unit weight were very similar with compacted unit weights ranging from 40.7 pcf to 52.5 pcf. These significantly lower unit weight values can translate into significant design changes in retaining walls. In retaining walls designed for the study by Cecich et al (1996), the use of shredded tires reduced the volume of backfill required and reduced the dimensions of the retaining structures required to meet structural and geotechnical standards. Because the structures were carrying less load from the backfill, the risks of overturning, sliding, and strength failures were reduced and a less intense design was required for the same criteria and application. In addition, the reduced unit weight of tires is helpful in working with sensitive soil bases which are soft or demonstrate excessive settlement.

Shalaby and Khan (2005) investigated the use of tire shreds as a replacement for conventional road embankment fill in an area with boggy soil. The type of soil present in the area was expected to experience excessive settlement if conventional backfill were used. Measures typically required to improve the soil structure for road construction include applying a thick layer of base material capable of reducing stress on underlying soil, but the weight of this layer would be sufficient to produce undesirable settlement (Shalaby & Khan, 2005). This is an example of when tire shreds were used to cope with problematic soil conditions that may be present in the field instead of using ground improvement techniques or requiring the replacement of subgrade material with borrow (Shalaby & Khan, 2005).

MATERIALS AND MATERIAL PROPERTIES

For this study, it is necessary to model a retaining wall and soil system for both conventional backfill materials and shredded tire backfill. To describe the properties of the soil, the Mohr Coulomb model available in PLAXIS was used. Additionally, for the in-situ soil under the wall, the undrained material type is applied as the soil considered is saturated clay. Plate elements were used to represent the retaining wall and footing. The behavior of these plates is characterized using a Linear Elastic model. The values for each of the model parameters for the backfill materials and the in situ soil are shown in Table 1.

The permeability values for the various shredded tire sizes were obtained from results of a study by Khan et al. (2010). The friction angle and cohesion for each nominal size category were found in the comprehensive study on tire shred size and corresponding properties performed by Moo-Young et al. (2003). Similarly, the Proctor Test results of Moo-Young et al. (2003) were used in selecting the moist unit weight, or the unit weight for materials above the water table. Lee et al. (1999) performed computer simulations comparable to those in this study with comparable tire shreds and the value for the Young's Modulus at atmospheric pressure used by Lee et al. is used here and listed in Table 1. The unit weight and friction angle for the conventional backfill sand are based on design values suggested in a design recommendation report from the geotechnical engineering firm, S&ME (2010), and represent accepted properties of clean granular sand backfill for retaining structures. The Young's Modulus for the sand was taken from a study by Lee et al. (1999) in which similar computer simulations with sand were performed but for static analysis. The in-situ soil properties were based off of local area clays common to the authors' geographical region. A field test by S&ME (2010) in Anderson County, SC provided the subsurface exploration data used to calculate the soil strength parameters shown in Table 1. These values were calculated based on correlations between the adjusted blow count (N_{60}) and soil strength parameters. As such, the undrained shear stress was calculated using the correlation suggested by Hara et al. (1971) and the Young's Modulus was found using the this value and linear interpolation of factors devised by Duncan and Buchignani (1976).

Table 1: Properties of In Situ Soil and Backfill Materials Used in Simulations

Property	Nominal rubber size			Standard sand backfill	In situ clay
	2 in.	4 in.	6 in.		
Saturated unit weight (kN/m^3)	-	-	-	-	18.07
Moist unit weight (kN/m^3)	6.25	6.75	6.5	18.85	-
Young's modulus (kPa)	3395.2	3395.2	3395.2	47888.0	85992.5
Poisson's ratio	0.33	0.33	0.33	0.3	0.35
Permeability (cm/sec)	5.18	3.66	2.13	0.00116	1.16^{-6}
Friction angle (deg)	15	32	27	28	0
Cohesion (kPa)	394.5	373.5	373.5	0	110674.6

The material properties of the concrete retaining wall were based on typical properties for concrete commonly used in practice. This includes a unit weight of 150 pcf and a compressive strength of 5000 psi. The wall dimensions are directly taken from design specifications for a Nevada Department of Transportation Type 1 Retaining Wall, 16 ft in height (Nevada Department of Transportation, 2007). Based on these dimension specifications and typical concrete properties, the necessary input parameters required by PLAXIS were determined for the footing and the wall and are shown in Table 2.

Table 2: Properties of the Nevada DOT Retaining Wall and Footing Used in Simulations

Property	Wall	Footing
Young's modulus (GPa)	28	28
Cross-sectional area (cm^2)	854.7	1068.4
Moment of inertia (m^4)	0.0017	0.0033
Thickness (cm)	6.30	7.87
Weight (kN/m^2/m)	0.8874	1.1121

SIMULATION RESULTS AND DISCUSSION

The retaining wall-soil systems are modeled using a commercially available advanced finite element program, PLAXIS. This program allows for the modeling of two dimensional systems of structures and soil groups under both static and dynamic loading conditions. The finite element mesh used in this study is shown in Figure 1.

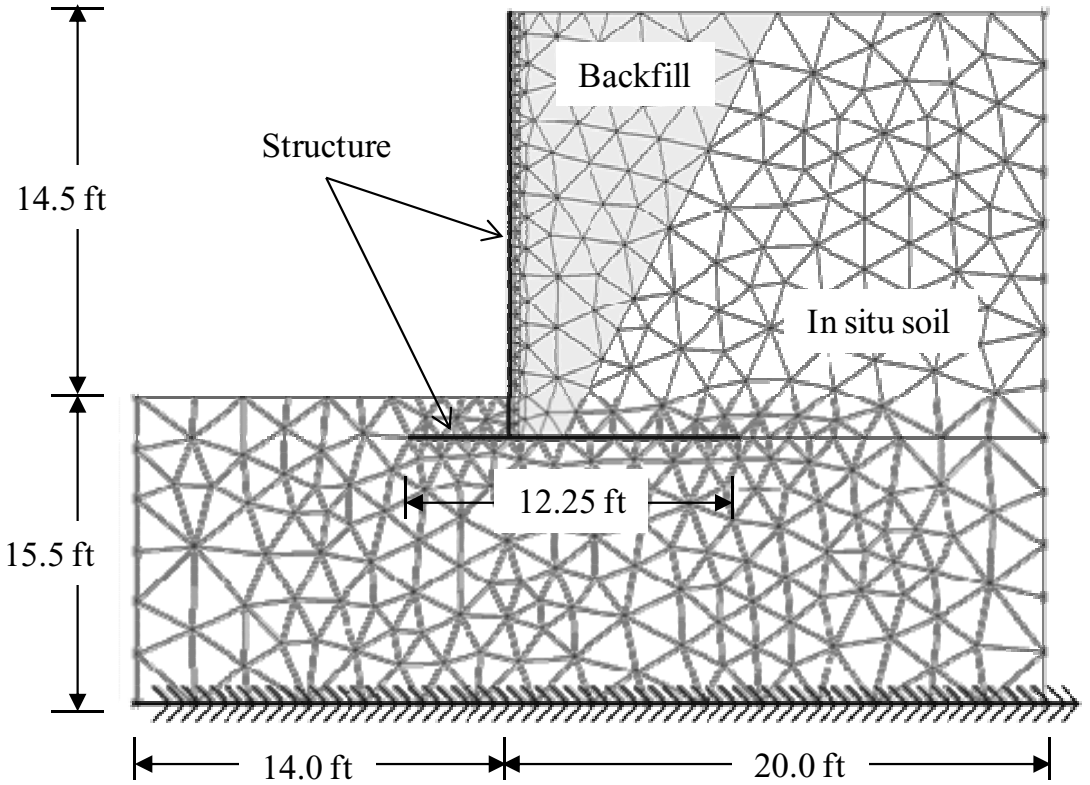

Figure 1: The PLAXIS mesh used in this study

This model consists of a cantilever retaining structure placed in saturated clay soil and backfilled with either clean sand or shredded tires depending on the case being observed. Four configurations were developed in which the backfill material is varied with all other parameters remaining constant. The boundaries are fixed against horizontal motion on the upright faces and are fully fixed along the base face. The absorbent boundaries allow for accurate simulation of earthquake scenarios by absorbing the waves travelling through the soil as they reach the boundaries rather than continually reflecting these waves back into the soil body. Finally, the model has a prescribed displacement applied to the base of the model as shown in Figure 1. The prescribed displacement is defined by entering acceleration time history data, which PLAXIS integrates to produce the applied displacement. The acceleration time history entered is shown graphically in Figure 2. Because the size of the tire shred and properties can vary considerably, three nominal sizes were considered in this study. The predicted maximum bending moment shear forces for these sizes are compared with the predictions from clean sand backfill.

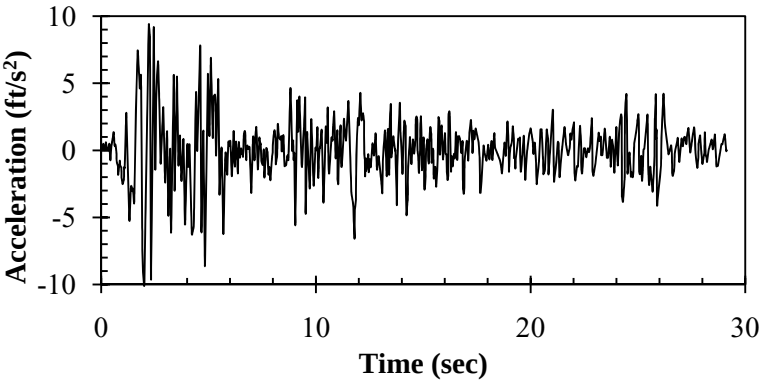

Figure 2: El Centro Earthquake Acceleration Time History

The Figure 3 shows the predicted maximum bending moment distribution for this retaining wall with various backfill conditions. As expected for the cantilever wall the maximum moment is achieved at the base of the vertical wall near the footing. The value of this moment is -49.42 kip-ft per foot of wall for the traditional sand backfill as shown in Figure 3(a). Figures 3 (b), (c), and (d) depict the moment distributions imparted on the wall by the 2-in., 4-in., and 6-in. shredded tire backfill respectively. All three diagrams for the shredded tire backfill, which are of equal scale, have almost identical force distributions on the wall. As a result, the distribution and magnitude of the moments imposed by each of the tire sizes are very similar. The maximum moments achieved are -28.70 kip-ft, -24.39 kip-ft, and -25.32 kip-ft for the 2-in, 4-in, and 6-in shredded tire backfill scenarios respectively. These similarities demonstrate that though the properties of the tire shreds vary with size, their behavior in this application and their interaction with the retaining structure is reasonably consistent between the sizes.

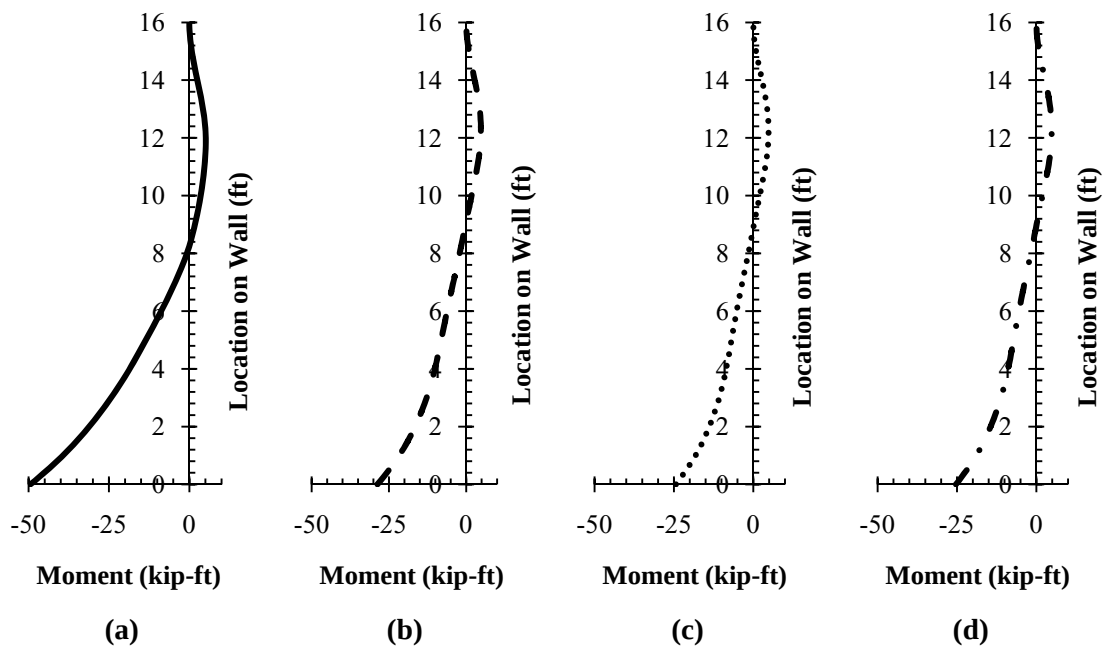

Figure 3: Maximum predicted bending moment distribution diagrams for the retaining wall with (a) Conventional Sand backfill, (b) 2-in Shredded Tires, (c) 4-in Shredded Tires, and (d) 6-in Shredded Tires

The Figures 4 shows the predicted maximum shear force distribution on the retaining wall with various backfill conditions. The maximum shear forces achieved are 10.99 kips, 7.88 kips, 6.95 kips, and 7.18 kips for the sand, 2-in, 4-in, and 6-in shredded tire backfill respectively.

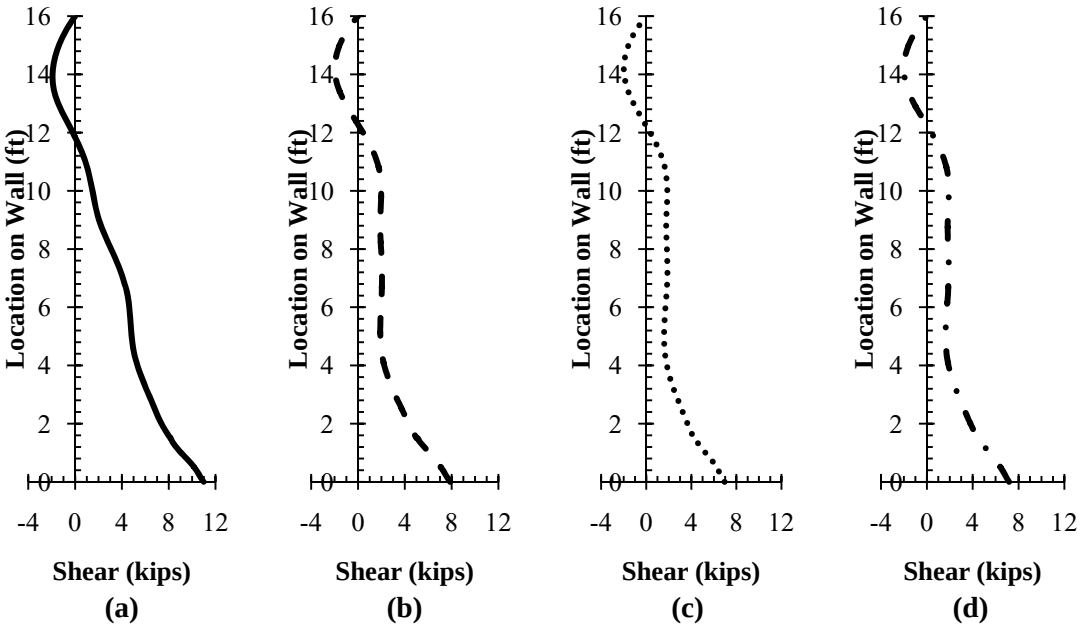

Figure 4: Maximum predicted shear distribution diagrams for the retaining wall with (a) Conventional Sand backfill, (b) 2-in Shredded Tires, (c) 4-in Shredded Tires, and (d) 6-in Shredded Tires

In addition to the shear force and moment exerted on the wall, it is important to study the displacement time history of the retaining wall with different backfill conditions. Predicted lateral displacement time history at the tip of the wall is shown with respect to time in Figure 5.

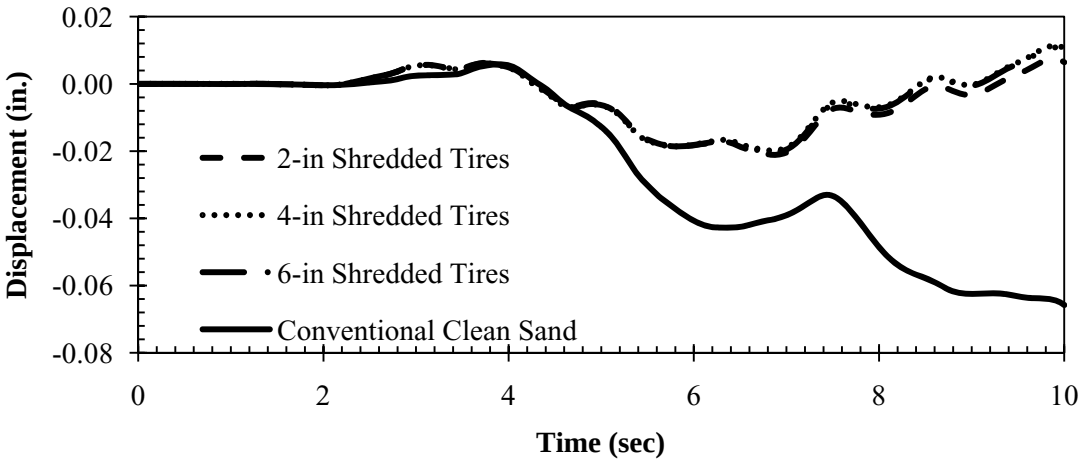

Figure 5: Displacement of the wall at the free end with different backfill

The displacement of the wall shows that after about 2 sec of dynamic loading, the wall starts to show apparent bending deformations that respond to the oscillating

loading. Note in the time history that at approximately 2 sec the maximum acceleration is experienced and this area of increased acceleration ends at approximately 5 sec. This would cause the lagged deflection response in the wall seen in Figure 5. The magnitudes of the displacements due to dynamic load application will presumably vary with the bending moment imposed on the wall by the backfill material. Both the magnitude and the pattern of deflection in response to dynamic loadings are worth noting in comparison to deflection in walls backfilled with shredded tires. The wall backfilled with the 2-in shredded tire experiences the greatest displacement. This displacement is also a departure from the displacement experienced by the walls backfilled with 4-in and 6-in shredded tires, which have more similar displacement values.

As seen in this graph, each of the walls backfilled with the shredded tire sizes has a very similar displacement pattern. All of the structures begin to oscillate after approximately 2 sec and continue to oscillate until the end of the test. Each of the walls experiences a maximum displacement at approximately 7 sec. It is also interesting to note that all of the walls reach a maximum deflection prior to the end of the test and actually rebound to almost their original shape by the end of the test. This is an important characteristic of the tire shred backfill to note and more importantly to compare to the behavior of sand backfills.

Table 3: Maximum Values for Wall Response Parameters by Backfill Type

Wall response parameter	Standard sand backfill	2in Nominal size rubber	4in Nominal size rubber	6in Nominal size rubber
Max. shear force (kips)	10.99	7.88	6.95	7.18
Max. bending moment (kip-ft)	-49.42	-28.70	-24.39	-25.32
Max. free end deflection (in)	0.274	0.110	0.079	0.080

RELIABILITY ANALYSIS

Dynamic response of retaining wall backfilled with shredded tire and subjected to dynamic load is one of the problems ideally suited for reliability analysis. Variations in situ soil parameters (friction angle and cohesion), shredded tire parameters (unit weight and friction angle) and geometry (height of the wall and slope of the backfill-in situ soil interface) can be taken into consideration. Mean value for the maximum bending moment, shear force, tip deflection can be found using FOSM considering the values listed in Tables 1 and 2 as the mean values and assuming appropriate coefficient of variations for these variable. Detail work is underway on this topic.

CONCLUSION

Simulation results show that the retaining walls backfilled with the sand showed both higher maximum deflection and a higher permanent deflection after the dynamic load was applied. The retaining wall with the sand backfill begins to deflect just after the maximum applied acceleration is experienced and the deflection both continues to increase and remains permanent at the end of the simulation. The deflection of the wall backfilled with sand is significantly greater during and after the dynamic loading sequence than the walls backfilled with the shredded tires. This can be explained largely by the significant decrease in unit weight and resulting lateral

load, both static and dynamic, experienced with the shredded tire backfill. A reduction in unit weight results in a reduction of dynamic force on the wall under the same applied accelerations. Additionally, once the dynamic load has ceased, the continued applied load to the wall is significantly less. This translates to reduced deflections in the wall during and after the dynamic load sequence is applied when shredded tires are used in place of heavier sand backfill.

As shown in Table 3, the most noticeable difference is between the bending moments imposed on the wall by the different backfills. The moment experienced by the wall with the conventional sand backfill is nearly twice that of the wall with the shredded tire backfill with little regard to tire shred size. The tire shred backfills also performed more favorably in all other categories with the wall experiencing less shear force and significantly less maximum deflection at the free end when the tire backfill was used. This demonstrates that not only do the shredded tire backfill materials consistently meet the standards for conventional sand backfill; they improve upon the behavior of conventional materials. Based on these favorable numerical results combined with observations of increased wall resilience, the conclusion is that shredded tires perform exceptionally well as retaining wall backfill materials in dynamic loading scenarios. In addition, the behavior similarities between tire shreds of different sizes show that size does not have a significant impact on retaining wall behavior under dynamic loadings.

REFERENCES

Cecich, V., Gonzales, L., Hoisaeter, A., Williams, J., & Reddy, K. (1996). Use of Shredded Tires as Lightweight Backfill Material for Retaining Structures. *Waste Management & Research, 14,* 433-451.

Duncan, J. M. & Buchignani, A.N. (1976). An Engineering Manual for Settlement Studies. Department of Civil Engineering, University of California, Berkeley.

Hara, A., Ohata, T., & Niwa, M. (1971). Shear modulus and shear strength of cohesive soils. *Soils and Foundations, 14(3),* 57-153.

Lee, J.H., Salgado, R., Bernal, A., & Lovell, C.W. (1999). Shredded Tires and Rubber Sand as Lightweight Backfill. *Journal of Geotechnical and Geoenvironmental Engineering, 125 (2),* 132-141.

Khan, A. A., Karanfil, T., & Grayson, J. M. (2010). Septic Tank Tire Chip Study: The Feasibility of Tire Chips as a Substitute for Stone Aggregate in Septic Tank Leach Fields.

Navada Department of Transportation (2007). Types 1A & 1B Cantilever Concrete Retaining Walls. *Standard Plans.*

Nevada Department of Transportation (2001). *Standard Specifications*

S&ME (2010). Subsurface Exploration: West Abutment Replacement Saluda Drive at Big Brushy Creek, Anderson County, SC. S&ME Project No. 1261-10-069. Report Prepared by Michael Revis, P.E. & David Swoap, P.E. (April 9).

Shalaby, A., & Khan, R.A. (2005). Design of unsurfaced roads constructed with large-size shredded rubber tires: a case study. *Resources, Conservation and Recycling, 44,* 318-332.

Warith, M.A., Evgin, E., & Benson, P.A.S. (2004). Suitability of shredded tires for use in landfill leachate collection systems. *Waste Management, 24,* 967-979.

Probabilistic Analysis of the Deflection of Retaining Wall in Deep Excavation

Y. G. Tang

Associate Professor, Department of Architecture, Hwa-Hsia Institute of Technology, No. 111, Gong Jhuan Rd., Chung Ho city, Taipei 23568, TAIWAN; PH (886-2)8941-5144; FAX (886-2)2941-5730; email: tang@cc.hwh.edu.tw

ABSTRACT

Deformation caused by excavations in urban areas is one of important problems geotechnical engineers have to cope with. The excavation-induced deformations deterministically estimated by conventional empirical/numerical methods can not consider the uncertainties of geotechnical engineering system. In this regard, the random finite element method (RFEM) is employed to investigate the influence of uncertainty on excavation-induced deformation. The RFEM combined random fields of soil properties with the finite element method through the Monte Carlo simulation. A well-documented excavation case history is employed in the RFEM analysis. Analysis results show that the RFEM is capable of providing reasonable estimations of the exceeding probability of wall deflection caused by excavation. The RFEM has a potential to be a convenient tool to account for the scatter in material and model parameters and thus can significantly upgrade the applicability and value of numerical analysis.

INSTRODUCTION

Prevention of damage to buildings adjacent to excavation is recognized as one of the most important tasks in the design of braced excavation in urban area. This task can be achieved through the prediction of excavation-induced wall and ground movements, with which the potential of damage to adjacent buildings can be estimated. In practice, the engineer often adopts the magnitude of retaining wall deflection as in indicator to evaluate the potential of damage to a building. Therefore, it is necessary to incorporate a suitable predictive method for estimating excavation-induced ground movements in the excavation design.

In the analysis of excavation, the finite element method (FEM) has been extensively applied to estimate the excavation-induced deformation. It should be noted that such deformation analysis using the FEM is deterministic, which means the model uncertainty and parameter uncertainty cannot be appropriately considered in the analysis. In other words, the computed wall and ground movements cannot reflect the degree of uncertainty of the random variables. This study combined the concept of random fields of soil properties and the Monte Carlo simulation into the FEM as random finite element method (RFEM). The RFEM can be used to conduct the probabilistic analysis to estimate the retaining wall deflection. In this study, a well-documented excavation case history is analyzed using the RFEM. The objective

of this paper is to apply the RFEM in the estimation of wall deflection considering the parameter uncertainty.

THE RANDOM FINITE ELEMENT METHOD AND SOIL MODEL

An obvious deficiency of conventional FEM for the excavation analysis is that the uncertainty of geotechnical problems cannot be considered. The "random finite element method" (RFEM) can be formed through the combination of the nonlinear finite-element methods and random field generation techniques. The principle of analysis procedure using the RFEM developed by Tang (2010) is shown in Figure 1. The procedure of analysis requires the implementation of the Monte Carlo simulation. This approach consists of two primary parts: 1) using random variables with specified joint probability distributions to represent these geotechnical uncertainties, and 2) performing a large number of deterministic FEM analyses to determine the relative frequency of maximum wall deflection.

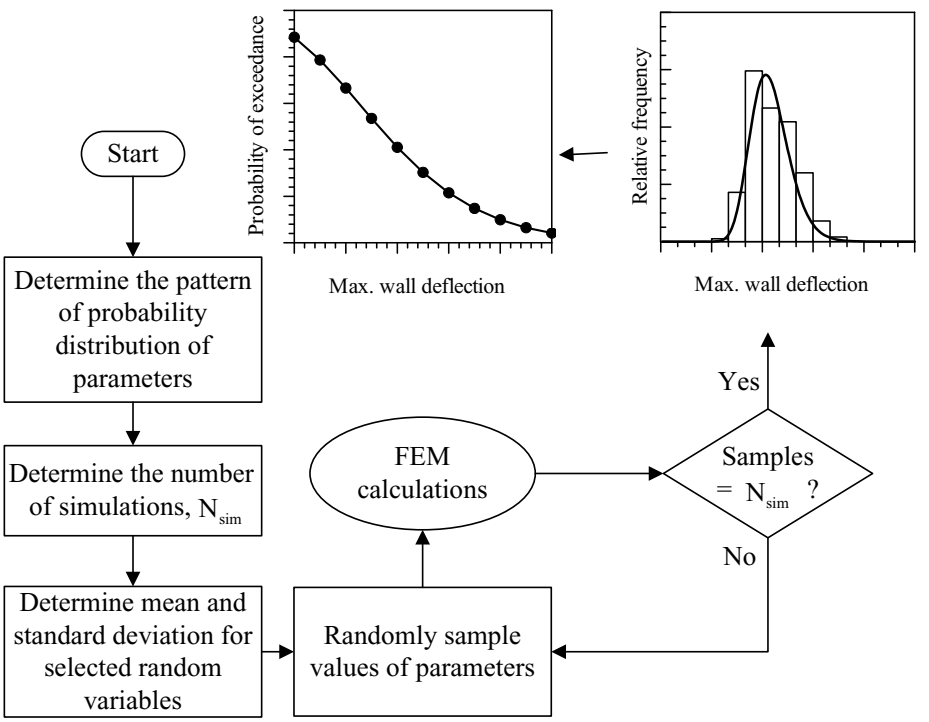

Figure 1. Principle of analysis procedure using the random finite element method (Tang 2010)

In this study, a two-dimensional FEM code AFENA (Carter and Balaam, 1990) is adopted to conduct the subsequent RFEM analysis. Specifically, the bar element was used to simulate the behavior of strut. Both the soil and support wall were simulated with the eight-node quadrilateral isoparameteric (Q8) elements. The support wall and strut were assumed to behave as a linear-elastic material, in which both the Young's modulus and the Poisson's ratio were assumed to be constants. In addition, the hyperbolic model (Duncan and Chang, 1970) was used to describe the

sandy layers. The MPP model, a simplified small-strain soil model validated by Kung et al. (2007), is used to represent the undrained behavior of clay. For simplicity, the MPP model is not introduced in detail here, and the reader can be referred to Kung et al. (2007) for details.

EXCAVATION CASE HISTORY

An excavation case history (called the Lurie Center) on the Chicago campus of the Northwestern University documented by Finno and Roboski (2005) is employed to conduct the probabilistic analysis of the deflection of retaining wall in the present study. A plan view of the area, approximately 80 m × 68 m in size, is shown in Figure 2. The four stage excavation is supported by a hot-rolled PZ-27 sheet pile wall on all sides, and the average maximum excavation depth is 12.8 m. The groundwater level was located at a depth of about 3 m. Figure 3 shows the stratigraphy and construction activities.

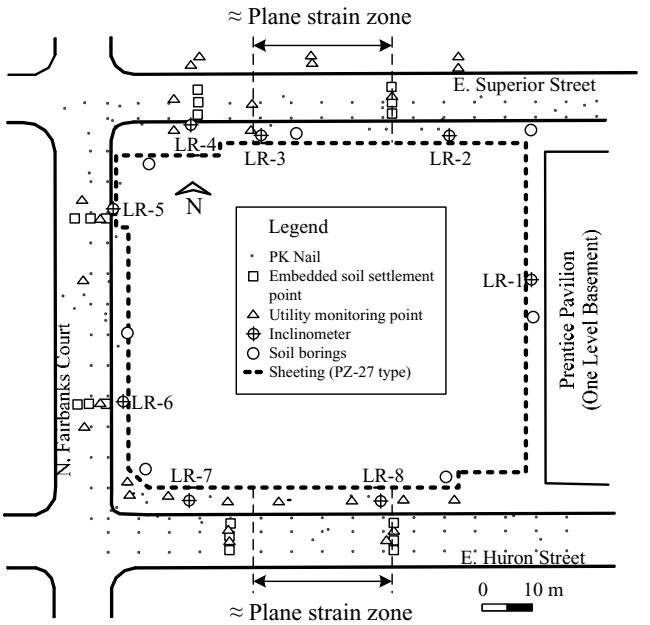

Figure 2. Plan view of the Lurie center case and the instrumentation plan (after Finno and Roboski, 2005)

Two levels of tied-back ground anchors are installed on the east wall owing to the presence of the basement of the Prentice Pavilion. These levels of tied-back anchors provided lateral support on the other three walls. Design ground anchor loads were 623, 534, and 623 kN for the first, second, and third levels, respectively. The anchors were installed at a horizontal spacing of 2.74 m on the first level and 1.83 m on the second and third levels. Both the first- and second-level anchors are founded in beach sand. All anchors were locked off to a prestress of 100% of the design load. The angles of tied-back installation are 20°, 10°, and 30° for the first, second, and third levels, respectively.

This study particularly focuses on the estimation of the maximum deflection of retaining wall. Figure 4 reveals the lateral soil deformations measured by inclinometer LR-3 and LR-8 (see Figure 2). The two inclinometers are installed in the north and south walls at the plane-strain zone and thus are comparable with the analysis results of RFEM using the two dimensional FEM code.

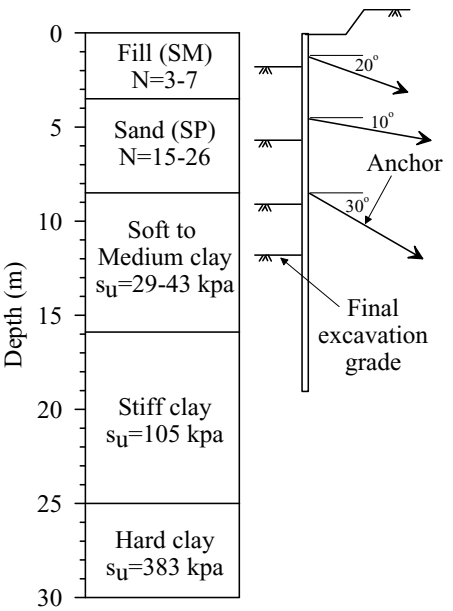

Figure 3. Stratigraphy and construction activities

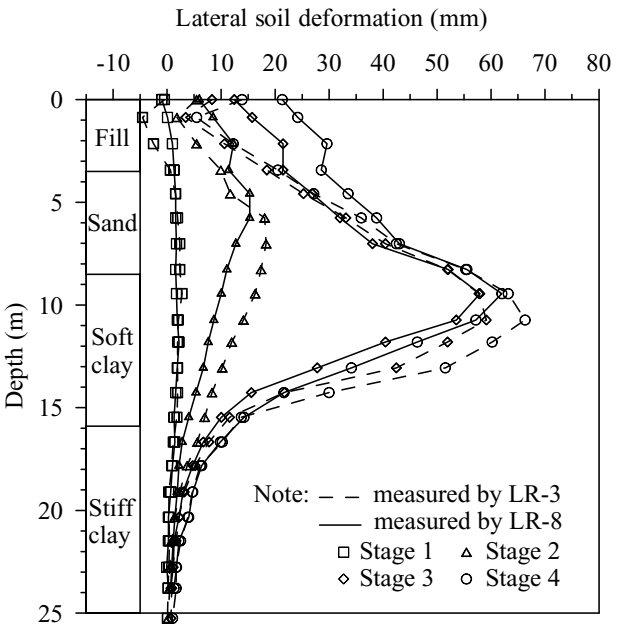

Figure 4. Lateral soil deformation observed in the Lurie Center case

PROBABILISTIC ANALYSIS ON WALL DEFLECTION

The soil and structure parameters used in the RFEM analysis are determined based on Kung et al. (2007), as shown in Table 1. Note that the sheet-pile wall was simulated by the solid element with the same bending and axial stiffness, and the equivalent thickness and modulus of the wall were determined based on the suggestion by Day and Potts (1993). The equivalent stiffness of anchors calculated by the horizontal spacing and the nominal stiffness is used in the analysis.

The stiffness modulus of soil is very sensitive to effects of sample disturbance and errors of testing equipment (Burland, 1989; Kung 2007). According to Tang and Kung (2010), the stiffness modulus and undrained shear strength of clay are two predominant factors in the FEM analysis of excavation. For simplicity, only the uncertainty of stiffness modulus of soil is considered in the analysis of this study. Specifically, the stiffness moduli, K for sandy layers and E_i/s_u for clayey layers, are selected to consider the uncertainty. The Lurie case history is analyzed in this study using the proposed RFEM. The soil parameters used in the RFEM are shown in Table 1 as proposed by Kung et al. (2007). The K and E_i/s_u shown in Table 1 represent the mean values. As to the determination of the uncertainty of K and E_i/s_u, this study adopted five scenarios of coefficient of variation (COV= 0.1, 0.2, 0.3, 0.4, and 0.5) to conduct the RFEM analysis, respectively.

Table 1. Soil parameters used in RFEM analyses

Depth (m)	γ_t (kN/m^3)	K_0	E_i/s_u	s_u/σ'_v	R_f	a	b	ν	K_s	c' (kpa)	ϕ' (°)	K=K_{ur}	n
Sandy layers (Duncan-Chang model)													
0-3.5	18.9	1.00	-	-	0.9	-	-	0.30	-	0	33	1000	0.5
3.5-8.5	19.6	0.46	-	-	0.9	-	-	0.30	-	0	33	1500	0.5
Clayey layers (MPP model)													
8.5-15.9	18.9	0.50	1300	0.25	0.9	0.00010	1.4	0.49	0.75	-	-	-	-
15.9-25.0	18.9	0.85	2500	0.60	0.9	0.00001	1.2	0.49	0.75	-	-	-	-

Note that the Gaussian assumption would lead to an estimation of uncertainty regarding data, it suffers from the limitation that the normal distribution is not representative of real data for the stiffness modulus (which is always positive) and, for this reason, lognormal probability density function for the input random variables will be considered in the following analysis.

For ensuring the accuracy of RFEM analysis and upgrade the efficiency of Monte Carlo simulations, various simulation numbers are selected to conduct the excavation deformation analysis to determine the adequate simulation number. Note that COV=0.3 is used in the analysis. Table 2 shows the mean and standard deviation of maximum deflection of retaining wall at various stages with different simulation number. Use of the simulation number of 1000 for RFEM analysis on the excavation case history is considered appropriate. Then, other four scenarios of COV (0.1, 0.2, 0.4, and 0.5) are performed using the proposed number of 1000.

Table 2. The mean and standard deviation of maximum deflection of retaining wall compared with different number of simulation

Num. of simulation	Maximum deflection of retaining wall (mm)			
	Stage 1	Stage 2	Stage 3	Stage 4
100	3.11(0.54)	11.16(2.08)	61.01(12.14)	71.14(13.54)
400	3.09(0.53)	11.20(1.80)	61.54(12.21)	71.64(13.65)
800	3.08(0.53)	11.15(1.73)	61.24(12.52)	71.49(14.11)
1000	3.08(0.53)	11.17(1.73)	61.33(12.35)	71.58(13.84)
2000	3.08(0.53)	11.15(1.75)	61.02(12.23)	71.26(13.74)
5000	3.09(0.54)	11.14(1.78)	60.86(12.50)	71.03(14.03)
10000	3.09(0.54)	11.12(1.76)	60.82(12.35)	71.01(13.84)

Note: number in () represents the standard deviation

Figure 5 shows the analysis results of maximum wall deflection on the Lurie case for excavation stage 4 using the RFEM with respect to various COV scenarios. Also shown in the same figure are the lognormal probability density functions with the same mean and standard deviation as estimated from the analysis dataset. It appears that the theoretical distribution is practically equal to the computed maximum deflection of retaining wall.

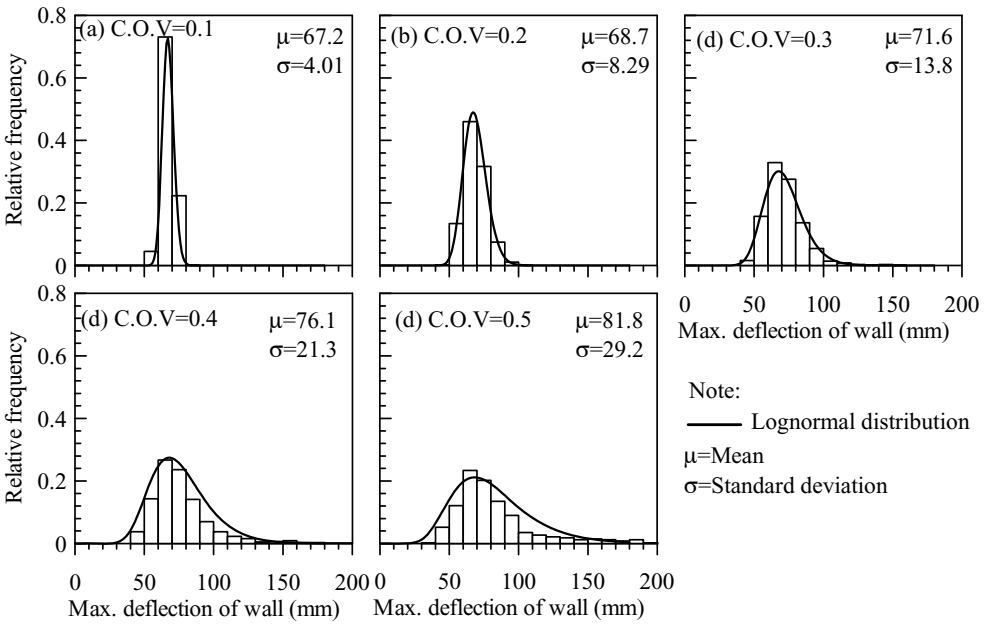

Figure 5. Histogram and lognormal distribution of the computed maximum deflection of retaining wall

According the analysis results, the two parameters of the lognormal distributions (i.e., λ and ξ) were obtained from the sample data. The probability of exceeding, P_e, can be easily obtained as follows:

$$P_e = 1 - \Phi\left(\frac{\ln x - \lambda}{\xi}\right) \quad (1)$$

where Φ denotes standard normal probabilities; x is random variable; λ and ξ, are the parameters of the lognormal distribution, which represent the mean and standard deviation of $\ln x$, respectively.

To facilitate probabilistic assessments of excavation-induced wall deflection, a simplified chart for estimating maximum deflection of retaining wall caused by excavation is established in Figure 6. In this figure, the probability of exceeding with respect to various maximum deflection of retaining wall in the Lurie case can be determined for stages 3 and 4. For example, when the maximum wall deflection is equal to 80mm at excavation stage 4, the probability of exceeding with respect to COV=0.1, 0.2, 0.3, 0.4 and 0.5 are 0.2%, 9.2%, 24.9%, 37.5%, and 45.7%, respectively. The results show that even though the same wall deflection is obtained in the analysis, various levels of risk may be encountered in light of various degree of uncertainty of soil parameters. This chart may provide additional valuable information to engineers for assessing the probability of exceeding of the maximum wall deflection caused by excavation.

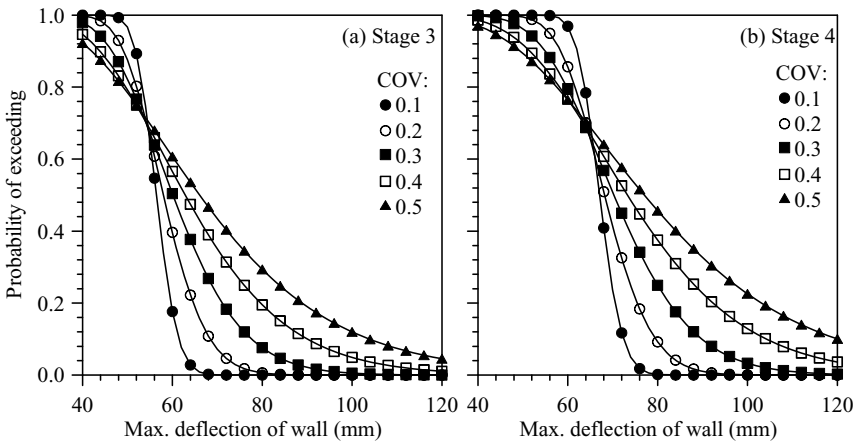

Figure 6. The probability of exceeding with respective to various maximum deflection of retaining wall

CONCLUSIONS

This study applied the RFEM in terms of a probabilistic approach to analyze the excavation-induced wall deflection. The RFEM approach involves the Monte Carlo simulation and random variables with specified joint probability distributions to consider the geotechnical uncertainty. The probability of computed maximum deflection of retaining wall caused by excavation can be determined through RFEM analysis. The wall deflection observed by a well-documented excavation case history is re-analyzed by the proposed RFEM. The results show that even though the same wall deflection is obtained by the deformation analysis, various levels of risk may be

encountered in light of various degree of uncertainty of the soil parameters. The determination of probability of exceeding can provide additional information for evaluating the probability of exceeding of the maximum wall deflection cased by excavation.

ACKNOWLEDGMENTS

The study on which this paper is based was supported by the National Science Council, Taiwan through Grant NSC 98-2221-E146-006. This financial support is greatly appreciated.

REFERENCES

Burland J. B. (1989). "Ninth Laurits Bjerrum Memorial Lecture: Small is beautiful-the stiffness of soils at small strain." *Canadian Geotechnical Journal*, 26, 499-516.

Carter, J. P., Balaam, N.P. (1990). *A general finite element algorithm.* Centre for Geotechnical Research, University of Sydney.

Day, R. A., and Potts, D. M. (1993). "Modeling sheet pile retaining walls." *computers and Geotechnics*, 15(3), 125-143.

Duncan, J. M., Chang, C. Y. (1970). "Nonlinear analysis of stress and strain in soils." *Journal of the Soil Mechanics and Foundations Division*, 96(5), 1629-1651.

Finno, R. J., and Roboski, J. F. (2005). "Three-dimensional reponse of a tied-back excavation through clay." *Journal of Geotechnical and Geoenvironmental Engineering*, ASCE, 131(3), 273-282.

Kung, G. T. C. (2007). "Equipment and testing procedures for small strain triaxial tests." *Journal of the Chinese Institute of Engineer*, 30(4), 579-591.

Kung, T. C., Hsiao, C. L., and Juang, C. H. (2007). "Evaluatioin of a simplified small-strain soil model for analysis of excavation-induced movements." *Canadian Geotechnical Journal*, 44, 726-736.

Tang, Y. G., and Kung, G. T. C. (2010). "Investigating the effect of soil models on deformations caused by braced excavations through an inverse-analysis technique." *Computers and Geotechnics*, 37, 769-780.

Tang, Y. G. (2010). "Probability-based method for predicting wall deflection caused by excavation using RFEM." *Journal of Zhejiang University-SCIENCE A*. (Under review)

Risk Management with Performance-based Geoengineering Monitoring: APM Tunnel Extension at Hartsfield-Jackson International Airport

By Thomas Allen Tye, PE[1] and W. Allen Marr, PE, PhD, NAE, F.ASCE[2]

[1]Geocomp Corporation, 2662 Holcomb Bridge Road, Suite 310, Alpharetta, GA 30022, ttye@geocomp.com
[2]Geocomp Corporation, 125 Nagog Park, Acton, MA, 01720, wam@geocomp.com

ABSTRACT

Atlanta's International Airport is adding a new $1.2 Billion International Terminal. The Automated People Mover (APM) trains are extended beneath an existing terminal to the new one via twin open-cut tunnels as wide as 67 feet. The excavation was braced by a soldier pile/lagging/tieback system and underpinning piers to depths of about 40 feet. Movement of the adjacent existing tunnel and building was a concern due to unbalanced earth loads and the potential for unexpected behavior.

To manage this risk, a real-time, performance monitoring program was used to provide early warnings of unacceptable or surprise performance to implement protective measures to stop/reduce the consequences. The risk management program included alarms generated from the system via email when measurements exceeded safe values and a plan of action to engage contingency measures. The plan was used to avert potential disaster as well as long delays in the construction schedule.

INTRODUCTION

The existing Automated People Mover (APM) underground train way is being extended to the new Maynard H. Jackson, Jr. International Terminal with a new east entrance to the airport. The project involves the open-cut excavation of 1200 linear-feet of twin tunnels as wide as 67 feet in fill soils of varying composition (see Figure 1). The tunnels were constructed in the area of Delta Air Lines' active baggage handling, Concourse E and Taxiway D. The tunnels also pass through existing structural walls at Concourse E, which required significant demolition of portions of these walls.

The existing conditions consist primarily of variable consistency fill soils described as medium dense to loose, silty fine to medium sands with N-values ranging from 6 to 30 bpf to depths of 30 to 40 feet underlain by some alluvial soils (clayey sands with organics), Piedmont residual soils (med dense silty sands), partially weathered rock (N>100), and rock (see Figure 2). The site is located in the Piedmont physiographic province and near the headwaters of the Flint River. The

eastern portion of the tunnel near the new concourse is constructed over the former Flint River.

Figure 1: Open Excavation Conc.E

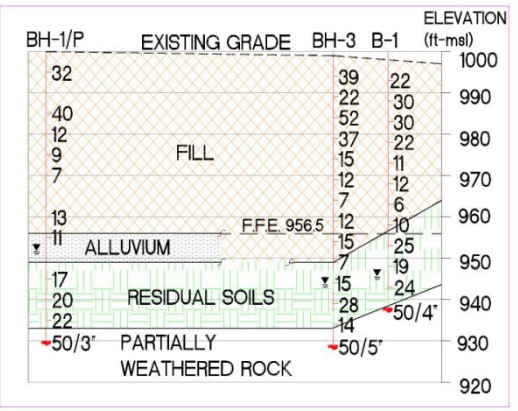

Figure 2: Cross Section of Area

The excavation bracing system designed by Berkel consisted of underpinning the existing pile caps with hand-excavated piers with a soldier pile and lagging system (exterior portions) and to depths of about 40 to 50 feet. The wall was laterally stabilized with three rows of prestressed tiebacks (Figure 3). During the initial meeting with the Holder Manhattan Moody Hunt/Berkel (design-build) team, the potential for significant movement of the existing adjacent tunnel due to the unbalanced earth load of the excavation was identified as a potential source of risk.

Excavating in variable consistency ground inherently involves uncertainties and can produce unexpected behavior. Deformations in loose pockets of soil can be erratic in pattern. This was further complicated by the fact that tunneling involves an unloading of the soil. Soil is stiffer in unloading; therefore, deformations may be quite small up to the point that the soil is near collapse. As a result, indications of impending movements can be small and impossible to detect without sensitive monitoring equipment placed in appropriate locations and monitored in real-time.

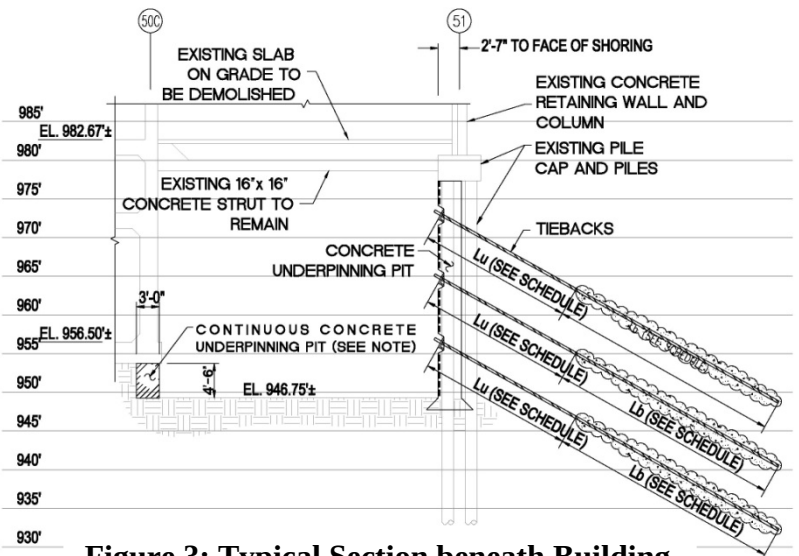

Figure 3: Typical Section beneath Building

A collapse or significant sudden large movements associated with excavation on this project could produce major consequences. Possible consequences identified included:

- Overstressing of beams in the concourse structure due to deformations of the columns adjacent to the tunnel excavation;
- Shifting of the existing and operating tunnel box due to removal of lateral support from one side;
- Sudden deflection that disrupts operation of the baggage handling equipment for Delta's entire operations;
- Collapse or sudden depression of an area in the Concourse E; and
- Excessive movement of a pile reducing or removing the support for its column that supports the overhead terminal structure.

Any of these potential failure modes could have caused a significant disruption in airport operations in the area of work, potential hazard to the safety of people and equipment, and create significant delays to tunnel construction while safety officials, airport authorities and others decided how to proceed. The resulting delays could be potentially damaging to the contractor and have major consequences to the overall development schedule for the airport. The design-build team noted that the consequences of failure were high and with even a small likelihood of failure, the risk would be high.

Risk is the combination of the likelihood of the uncertain event times its consequence. The consequences of sudden, unexpected deformation or ground collapse during excavation could be highly significant to the capital improvement program. Such significant consequences coupled with a somewhat probable chance of the occurrence of significant deformations and/or a collapse presented significant risk to the project.

RISK MANAGEMENT - PLANNING

Before the recommendations for performance monitoring were offered by Geocomp, a meeting was held with the design-build team to discuss the critical structural elements, concerns of the structural engineer and the operations issues of concern to the airport, Delta Air Lines (the primary user), and the FAA. The project plans and specifications but specified required measurements and threshold levels did not include details regarding the instrumentation or data collection system design. The excavation support and protection systems were to be monitored daily during excavation progress for as long as the excavation remained open. The structure, utilities, and other facilities were to be protected from damage caused by settlement, lateral movement, and other hazards that could develop during excavation support and protection system operations.

The meeting outlined the consequences of excessive movements and the design-build team recognized the risks involved with the 40-foot excavation beneath the existing terminal and adjacent to the existing active tunnel. The existing building

foundations consisted of augered cast-in-place piles with a single Diwidag bar in the center that offered little shear strength and lateral resistance. Movements of more than ½-inch (1.3 cm) could lead to shear of the piles and loss of support of the building. The tarmac and continuing airline operations were essential to continued operations and were sensitive to vertical settlements. The meeting led to the following points for consideration in the design of a monitoring program that would provide warnings of unacceptable deformations:

- sensitivity of the structural beams to small deflections,
- potential for the adjacent tunnel box to shift laterally due to the unbalanced earth pressure loads,
- critical fanhouse area and associated utilities,
- jacking of columns that had to be removed during load transfer to new foundation support elements,
- utility bridge and test track tunnel outside the Concourse E building that were sensitive to movements,
- dependency of the contingency planning involving the addition of additional horizontal braces if the existing tunnel box moved.

A proactive approach to managing these risks was to use a real-time monitoring program that would provide early warnings of unacceptable or surprise performance in time for protective measures to be implemented to stop the undesirable performance or reduce the consequences of that performance.

An effective monitoring program must have the following elements (Marr, 2007):

- Measure one or more Key Performance Indicators.
- Action Levels and responses must be established up front.
- Data must be reliable.
- Measurements must be taken with sufficient frequency to capture the unexpected performance at the earliest possible stage.
- Measurements must be evaluated in a timely manner.
- Preplanned action must be taken when Action Levels are reached.

Key performance indicators for this excavation and tunneling operation were identified to include the following:

- Lateral movement of soil on the sides of the tunnels away from the column piles in ways that would compromise the vertical capacity of the pile caps.
- Vertical deformations of the baggage handling facilities, Concourse walkway and columns.
- Horizontal deformation or rotation of any columns.
- Vertical deformation of structural walls that tunnels punch through
- Horizontal deformation of the Test Track tunnel before and during underpinning.

Instrumentation to monitor these performance indicators was installed prior to the start of excavation to establish baseline readings of the instrumentation and characterize the pre-construction background behavior of the monitoring system. These measurements were critical to minimizing the chance of a sudden collapse or unacceptable movement.

The design-build team established the Yellow Warning Level for deformations at 0.25-inch (0.6 cm) and the Red Alert-Stop Work Level at 0.5-inch (1.3 cm). An orange alert level was also established as an intermediate point between yellow and red (0.375-inch, 1.0 cm). At the Yellow Warning Level, Berkel and Geocomp were to confirm the data and check the area. At the Orange Alert Level, Berkel would take precautions to reduce the potential for further movement (see Table 1). Measurements above the Red Alert-Stop Work Level, Berkel would employ remedial measures to prevent further movement including the addition of bracing. Table 1 summarizes the actions to be taken after established observations or measurements. Establishing this table at the beginning of the project and having all team members use it proved to be a critical component of the risk management program.

Table 1: Risk Management Program -Action Levels and Responses

*** Any Orange or Red Alert needs an official report from Berkel/Geocomp/MME concerning causes of alert.**

Yellow Warning Level	
Action:	**Conference call with Berkel & Geocomp to determine any necessary action**
Triggers:	**Confirmed yellow measurement on any sensor within 50 ft (15.2 m) of excavation work**
	Lateral Movement of 0.25" (0.6 cm)
	Any Break or Loss of Load in Tieback
	New cracks in wall in excavated areas

Orange Alert Level	
Action:	**Conference call with Berkel, Geocomp, HMMH, SDL, ATC to determine any necessary action**
Triggers:	**Confirmed orange measurement on any sensor within 50 ft (15.2 m) of excavation work**
	Lateral movement of more than .375" (1 cm)
	Any break or loss of load in tieback
	New cracks in wall in excavated areas

Red Alert – Stop Work	
Action:	**Stop Work and replace excavated soil; conference call with Berkel, Geocomp, HMMH, SDL, ATC, AGD, HJDP to determine corrective action (cross bracing, rakers, additional backfill, etc.)**
Triggers:	**Confirmed red measurements on any sensor within 100ft (30.5 m) of excavation work**
	Lateral Movement of 0.5" (1.3 cm)
	Any Break or Loss of Load in Tieback
	New cracks in wall of excavated area more than 1/2" (1.3 cm)

AUTOMATED INSTRUMENTATION PROGRAM

As discussed above, the Key Performance Indicators for this work were deformations. Deformations can cause architectural and structural distress to the existing structures and potentially disrupt important airport operations, such as baggage handling, people traversing the concourse, and airplanes using the taxiway. The monitoring devices used for this project are described below.

Locations and numbers of instruments: The design-build team used collective knowledge and experience from monitoring tunnels, and results from discussions to make the plan for locations of instruments. Central to the recommendations was the

working premise that the deformation limits imposed by the design team were quite restrictive and left little room or time to alter the construction method at a given location before the maximum allowable value would be reached. This established the need for an automated, real-time monitoring system.

Automated Total Stations with prism targets: This system consisted of computer controlled total stations (AMTS) to measure the exact location of prism targets mounted at locations where deformations were to be monitored. At intervals of 1 to 3 hours, the AMTS machines measured the position of each target relative to reference targets located away from the zone of influence of tunneling. The only limitation with this approach was that there must be a clear line-of-sight between the AMTS and the target. Repeatability was approximately ±1 mm in x, y and z directions which made this an excellent device to detect early warning signs of deformations. Data from the AMTS were sent immediately by a cell modem connection to a central computer system at Geocomp headquarters for instant comparison of the measured value with allowable values.

Targets were placed on the columns and on the underpinning piers supporting the columns at about 1/3 depths of the excavation (about 10 feet, 3 m) within the excavation to monitor the movements. These locations provided information on column movement vertically and horizontally as well as rotation of the columns. Each of these deformation modes would directly affect the stresses in the structural beams supported by the columns.

In-place inclinometers in vertical casings: This system used electronic tilt sensors placed inside a 2.75" (70 mm) diameter plastic casing that was installed in underpinning piers supporting the pile caps. The device provided early indications of horizontal movement of soil away from the piles. Such movement potentially induces shear within the column for which the piles were not designed to resist. As the excavation advanced, readings could be taken as often as once every few minutes to give maximum protection to the piles from unexpected ground movement. The system was very precise, giving repeatable measurements at a single elevation to better than 0.01-inch (0.25 cm).

In-place inclinometers (IPI) were used over the traditional manual system with readings taken every few minutes. Frequent readings were important to help prevent movements than could occur within hours following local excavation. When the support system was in place and excavation completed, further movements would occur relatively slowly and the areas were monitored with the AMTS system and periodic manual monitoring of the inclinometers.

Inclinometer casings were installed between each pile foundation and the tunnel excavation because of the concern with a localized loss of ground that could occur due to loose, poor ground conditions. Such conditions could exist at any of the pile foundations and could be limited in horizontal extent to that single pile and/or pile cap. That ruled out the possibility of instrumentation at only a fraction of the pile caps because measurements on the instrumented fraction would not apply to potential

localized collapses at the non-instrumented locations. The approach taken was to install the inclinometer casing, read it with a manual readout system, then before the tunnel excavation reached that section, install the IPI string. Once excavation was completed in an area, the IPI string was removed and used at another location. Subsequent, less frequent readings were then obtained with the manual readout. This approach considerably reduced the cost for IPI sensors.

Data collection, management and reporting system: To provide real value to the project, instruments were read several times per hour within the active tunneling area and the data was evaluated within a few minutes to determine whether any threshold values were exceeded. Messages were sent to project staff within minutes to alert them of any measured values as soon as they exceeded threshold values. This massive data collection, management and reporting was done by computer and making it available over the web via Geocomp's iSiteCentral™ software. This system provided alarms with up to the minute information to the design-build team.

RISK MANAGEMENT PLAN UTILIZATION

On the morning of August 1, 2009, the monitoring system detected sudden deflection of 5/8-inch (1.6 cm) in several underpinning piers supporting the Concourse E building columns. The deflections shown graphically on the website (Figure 4) resulted in Red Alert–Stop Work level alarms to the project team. Other Yellow and Orange level alarms from the AMTS readings at the piers confirmed the IPI alarms/readings.

The alarm messages were delivered and Berkel personnel responded immediately. They observed that cracks had developed in underpinning piers supporting the building columns. It was observed that the area had been over-excavated before the next row of tiebacks was installed and that the water table was much higher than reported in the subsurface exploration report. This resulted in higher loads to the excavation bracing system than anticipated.

The design-build team decided that additional lateral bracing was required and placed beams against the piers to prevent further movement, as planned (Figure 5). It was concluded that an additional row of tiebacks would be added in this limited area to provide support in the lower levels of the wall in the area of the highest earth pressures.

CONCLUSIONS

The risk of the project was reduced based on the implementation of the Active Risk Management™ program and the following risk management objectives were achieved:

- Key Performance Indicators were measured and compared to action levels.
- Data provided was reliable, with redundancy, and transmitted quickly for immediate evaluation.

- Preplanned action was taken to prevent additional and potentially damaging movement.
- Construction was able to proceed without disruptions to the operation from unacceptable performance.

The risk management program indentified specific actions; thereby containing and controlling the many costs that resulted from the unexpected and uncontrolled events. Had these actions not occurred, the probability of large deflections that would have disrupted operations and delayed construction was high and the consequences would have far exceeded the cost of the risk management program.

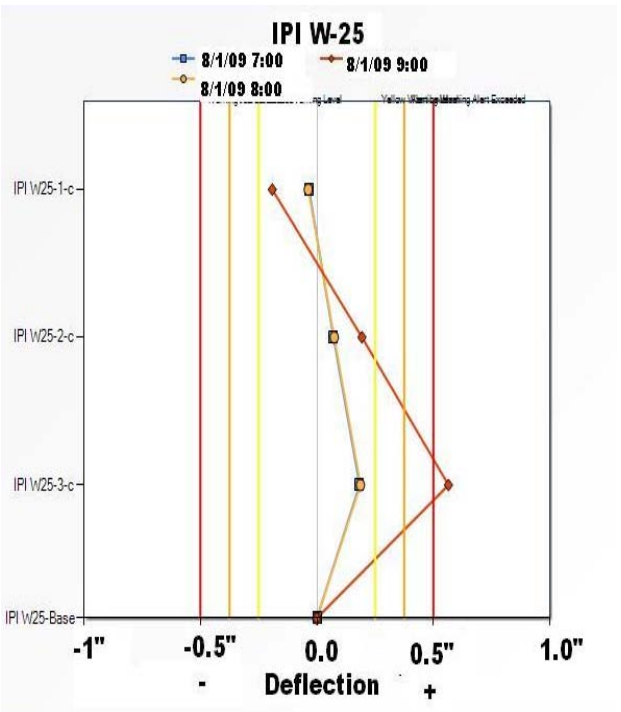

Figure 4: In-Place Inclinometer Chart

Figure 5: Lateral bracing

REFERENCES

Marr, W. A. (2007). "Why Monitor Performance?" *ASCE: GSP117.* Keynote paper presented to 7th International Symposium on Field Measurements in GeoMechanics, Boston.

Marr, W.A. (2005). "Automated Collection of Instrumentation Data." Boston Society of Civil Engineers Section, 2005.

Pennington, Steve, et al (2007). "Instrumentation During APM Construction at Dulles International Airport." *FMGM 2007: Seventh International Symposium on Field Measurements in Geomechanics*, Boston.

Probability-based Risk Assessment of Landslide/Slope Failure

Y. Y. Chi[1], Y. F. Lee[2], C. H. Juang[3], Y. L. Wu[4] and Y. P. Wu[5]

[1]Department of Land Management and Development, Chang Jung Christian University, Taiwan. email: yunyao@mail.cjcu.edu.tw
[2] Department of Leisure Recreation and Travel Management, Toko University, Taiwan. email: 2007LR03@mail.toko.eud.tw
[3] Department of Civil Engineering, Clemson University, Clemson, SC 29634, USA.; also affiliated with National Central University, Jhongli, Taoyuan, 320, Taiwan. email: hsein@clemson.edu
[4]Department of Land Management and Development, Chang Jung Christian University, Taiwan. email: ylw@mail.cjcu.edu.tw
[5]Department of Geotechnique and Engineering Geology, China University of Geosciences, China. email: wypyh@vip.sina.com

ABSTRACT

In this paper we present a framework for analyzing the rainfall-induced landslide risk and demonstrate it with a case study of Lushan hot-spring district in Nantou County in central Taiwan. This framework consists of three parts: (1) an approach for determining the probability of landslide/slope failure, (2) a procedure for estimating the landslide-induced losses, and (3) a procedure for computing the total landslide risk. The emphasis of the paper is on the determination of the probability of landslide/slope failure. The proposed framework is further demonstrated through a sensitivity analysis to investigate the influence of various degrees of parameter uncertainty.

INTRODUCTION

Landslides are a frequent natural disaster in Taiwan, the occurrence of which is often attributed to the ascending groundwater or the flood erosion during a torrential rainfall. The rainfall-induced landslide, especially located on the top slope in the development area, can cause severe property damage and/or casualties. The recent catastrophic event, the landslide at Xiao-lin village, which is located in Jiashian, Kaohsiung County, in southern Taiwan is a fresh reminder of the magnitude of the possible destruction and tragedy by large landslides. The Xiao-lin landslide, which was induced by Typhoon Morakot in August, 2009, buried more than 300 people at once. Naturally, landslide risk assessment is an important task facing both the engineer and the local authorities in mountainous Taiwan in which sustainable land use and

development policies must be enforced. In this paper, the focus is on landslide risk assessment, and a probabilistic approach is adopted for evaluating the landslide/slope failure potential. The landslide risk at a locality is defined by the products of the probability of landslide occurrence (P) and the loss as a result of the landslide (L).

In this paper, the framework for the landslide risk assessment is developed and demonstrated simultaneously by means of a case study of the Lushan, Taiwan area. Lushan, the literal meaning of which is Mountain Lu, is a popular hot-sprint mountain resort in central Taiwan (see Figure 1) with over 60 years of history of commercial operations. Because of the high commercial property values, it would be of special interest to conduct a landslide risk assessment so as to develop guidance for land use planning and regulation in the study area.

This framework consists of three parts: (1) an approach for determining the probability of landslide/slope failure, (2) a procedure for estimating the landslide-induced losses, and (3) a procedure for computing the total landslide risk. Here, the Hasofer-Lind (1974) reliability method is used to analyze the probability of slope failure. In the case study, the proposed framework is further demonstrated through a sensitivity analysis to investigate the influence of various degrees of parameter uncertainty. Different landslide risks induced by different conditional probabilities are then examined.

Figure 1. Location of the study area, Lushan, Nantou County, Taiwan

ELEMENTS OF LANDSLIDE RISK ASSESSMENT – A BRIEF REVIEW

1. Hasofer-Lind reliability analysis for the probability of landslide

The Hasofer-Lind (1974) reliability method is employed herein with an assumption that the input parameters follow the normal distribution (if they are not normal random variables, then the transformation must be performed to find their equivalent normal random variables). The reliability index (RI) is defined as:

$$RI = \min_{X \in F} \sqrt{\left[\frac{X_i - \mu_i}{\sigma_i}\right]^T R^{-1} \left[\frac{X_i - \mu_i}{\sigma_i}\right]} \quad (1)$$

where X_i is a random variable; μ_i and σ_i are the mean and standard deviation of X_i, respectively; R is correlation matrix of X_i; F is a failure region (corresponding to the domain in which FS $\leq$1). Once the reliability index RI is determined, the nominal probability of landslide can be obtained as:

$$P = \Phi(RI) \quad (2)$$

where Φ is the standard normal cumulative distribution function (note: this function is implemented in Excel® as NORMSDIST). A simple and effective approach using the Solver tool within the Excel spreadsheet, developed by Low et al.(1998), is used to solve for RI in this paper. Once the reliability index is determined, the reliability-based critical slip surface, the most probable slip surface, can be searched for and determined.

2. Slope stability analysis

In this paper, we adopt the modified Morgenstern-Price slice method (Chen and Morgenstern, 1983) as the performance function and then consider the input parameter uncertainties within the analysis framework of the Hasofer-Lind's reliability index. Chen and Morgenstern (1983) method of slices may be applied to circular and non-circular slip surfaces, in which the sliding mass is divided into several slices and the requirements for force and moment equilibrium should be fully satisfied for every thin slice. By examining overall force equilibrium and overall moment equilibrium, an expression for factor of safety (FS) is obtained.

3. Estimation of loss due to landslide

Estimation of the property loss is itself a complicated process. Here, the unit price appraisal method (Chen et al., 2007) is used to estimate the property loss. The following infrastructures are characteristic of our Lushan study area: structures (buildings and facilities), agricultural products (tea leaf, fruit, and vegetable) and roadways. Furthermore, Lushan is a popular scenic resort area, which generates revenue from tourism. Thus, for the landslide-induced loss estimation, both land use-related loss and tourist-related loss are included.

PROCEDURE FOR RISK ASSESSMENT OF LANDSLIDE

Step 1 - Determination of an initial slip surface and number of slices

Here, we use the lower part of an ellipse (Xie et al., 2003) to express the geometry of slip surface, as shown in Figure 2. Five variables, specifically the center of the ellipse (X_0, Y_0), the long axis of the ellipse (L_a), the short axis of the ellipse (L_b), and the inclination angle (θ) are assumed for defining the lower part of ellipse. The center (X_0, Y_0) is determined and the inclination angle (θ) is set based upon the slope angle. The long axis (L_a) determines the starting and end points of the slip surface, which should be determined based on the field investigation. The short axis (L_b) simulates the depth of the slip surface, which should be determined based upon the potential slip depth.

Regarding the method of slices, while the use of a greater number of slices can better simulate the slip surface, such a procedure is more computationally demanding. Here 12 slices is adopted.

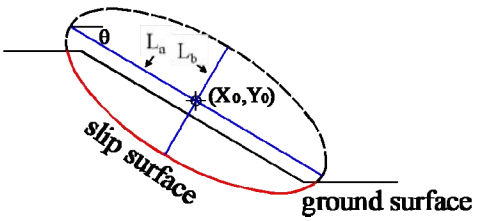

Figure 2. The geometry of slip surface as defined by the lower part of an ellipse (after Xi et al., 2003)

Step 2 - Determination of environmental variables

The shear strength parameters, including cohesion and friction angle, are treated as random variables, characterized with a mean value and a coefficient of variation. If the correlation between the random variables exists, the correlation matrix should be considered. The mean and the coefficient of variation of each of these random variables are determined based upon the test results.

Step 3 - Determination of the objective function and restrictions

In the Hasofer-Lind reliability analysis, the objective function expressed in Eq. (1) is to be minimized subjected to the constraint that $X \in F$. Thus, if the "design point" is on the safe side, the factor safety must be set to FS $\leq$ 1; otherwise, the factor safety must be set to FS > 1. Furthermore, the objective function must satisfy all restrictions of the Chen and Morgenstern (1983) method of slices.

Step 4 –Determination the reliability index and the corresponding slip surface

The previous steps can easily be set up in an Excel® worksheet, and the Solver in the Excel can be executed to minimize the objective function, which yields the reliability index RI. The probability of landside can then be determined using Eq. (2).

Step 5 – Estimation of landslide-induced property loss

Upon completion of steps 1 through 4, the loss estimation is then carried out using the unit price appraisal method. Using the Lushan area as an example, the loss is estimated category-by-category as follows:

Structures: The replacement cost of the structure is used to measure the value of the structural loss. The average number of floors in the study area is 2.8; specific data from Nantou County show the unit price (construction cost) for typical reinforced concrete structures to be 5,000 NT dollars/m^2. Thus, the loss value of all structures in the study area can be estimated by the average area per floor (m^2) multiplied by the average

number of floors multiplied by the unit construction cost (dollars/m2).

Agricultural products: The loss value of agricultural products is determined by the market price. According to the Taiwan agriculture statistics yearbook 2008, the production per unit area of tea, fruit, vegetable in Natou are 1,429 kg/ ha, 6,894 kg/ ha, and 17,904 kg/ ha, respectively. In 2008, the average unit market price of tea, fruit, vegetable are 166 NT dollars/kg, 80 NT dollars/kg, and 48 NT dollars/kg, respectively, according to the agricultural price query system in the Agriculture and Food Agency, Council of Agriculture, Taiwan. Thus, the market price of tea, fruit, vegetable are 237,214 NT dollars/ha, 551,520 NT dollars/ha, and 859,392 NT dollars/ha, respectively.

Roadways: The loss value of roadways is calculated by the construction cost. According to Chen et al. (2007), the unit construction cost of roadways is 30,000 NT dollars / m2. Based upon the field investigation, the average width of roadways is 8 meters. Therefore, the construction cost of roadways may be estimated by the total length multiplied by the average width multiplied by the unit construction cost.

Tourist revenue: Based upon the statistic of "Visitors to the Principal Scenic Spots in Taiwan by Month, 2008," the total number of tourists in Lushan is estimated at 349,125. The average expenditure in Taiwan is 1,915 NT dollars per person in 2008. Thus, the tourist revenue at Lushan is estimated at approximately 668,574,375 NT dollars.

LANDSLIDE RISK ASSESSMENT - CASE STUDY OF LUSHAN

1. Environmental conditions at Lushan, Taiwan

The Lushan hot spring area is located in the Nantou County in central Taiwan (Figure 1), with most of the hotels and restaurants built along or near the Ta-luo-wan River, as shown in Figure 3. The roads in the Lushan area include T14 (state system), N87 (county system), and the village roadways. Figure 3 also shows the topography and land use of the study area. The slopes that are prone to landslide lay in the north side of the hot spring district with slope aspect changing from southwest to southeast. The variation of gradient is small and the average gradient is approximately 27 degrees. One representative profile is selected for landslide risk assessment. Table 1 shows the shear strength parameters of the slate, sandy slate and fresh sandy slate. Possible variations, in terms of the coefficients of variation (COV), of these parameters are also estimated to account for the uncertainty in the estimated mean of the parameters. The knowledge of this variation allows us to treat the parameters as a random variable so as to perform a probabilistic analysis.

Table 1. Shear strength parameters and adopted values for reliability analysis

Rock stratum	c (t/m^2)	ϕ (degrees)
Slate (SL)	0.3 ~ 0.7	23 ~ 32
Sandy slate (SSL)	0.4 ~ 1.6	28 ~ 42
Fresh sandy slate (FSL)	12 ~ 38(2)	17 ~ 53(2)

(1) Direct shear tests were performed by Liming Engineering Consultants Co.

(2006) following ASTM and ISRM specifications.
(2) Estimated based upon the results of unconfined compressive strength tests.

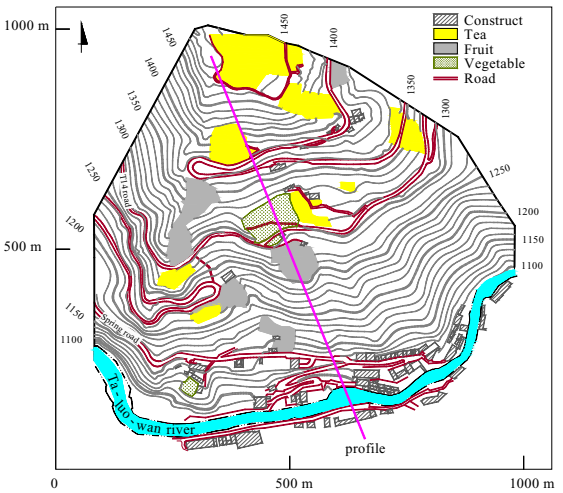

Figure 3. Topography and land use of the Lushan area

2. Analysis results of the landslide risk

A representative profile is selected for analysis of the landslide risk. Initially, a series of shear strength parameters based on Table 1 are adopted for reliability analysis that employs the Chen and Morgenstern (1983) method of slices. Table 2 shows the factor of safety (FS) and the probability of landslide occurrence (P) under different strength parameters. It is found that the factor of safety increases with increasing the strength parameter; otherwise, the probability of landslide occurrence decreases with increasing the strength parameter.

Table 2. Analysis results under different strength parameters

Scenario	SL		SSL		FS	RI	P	Landslide risk = P×L (million NT dollars)
	c	ϕ	c	ϕ				
1	0.5	20	1.0	30	0.760	1.7076	0.9561	2174.17
2	0.5	25	1.0	30	0.907	0.5644	0.7138	1623.18
3	0.5	28	1.0	30	0.923	0.4081	0.6584	1497.20
4	0.5	29	1.0	30	0.952	0.2726	0.6074	1381.23
5	0.5	30	1.0	35	1.008	0.0932	0.4629	1052.63
6	0.5	31	1.0	36	1.042	0.1679	0.4333	985.32
7	0.5	35	1.5	35	1.123	0.7132	0.2378	540.76
8	1.0	35	1.5	35	1.192	0.8462	0.1987	451.84

* The coefficient of variation of c and ϕ are 0.4 and 0.2 for SL and SSL
* The correlation between c and ϕ is 0.

It is assumed that loss of land-use and tourist revenue will be produced when a

landslide event happens in the Lushan area. As shown in Table 3, the losses of land-use and tourist revenue are 1,605 and 669 million NT dollars, respectively. The landslide risk attributed to loss of land use and loss of tourist revenue under scenario 1 is estimated as: 0.9561 × 2,274 = 2,174.17 million NT dollars (about 67.94 million US). Similarly, the landslide risk under other scenario can be computed as shown in Table 2.

Table 3. Estimation of loss (thousand NT dollars) at Lushan

Land use					Tourist revenue
Structure	Tea leaf	Fruit	Vegetable	Road	
265,812	1,003	1357	756	1,336,200	668,574

PARAMETRIC ANALYSES

The parametric analysis is performed herein to investigate the effect of the coefficient of correlation on the probability of landslide as shown in Figure 4. The negative correlation between c and ϕ reflects the fact that in strength testing, the cohesion decreases as the friction angle increases. The analysis results shows that the probability of landslide could be under-estimated if the correlation ρ is not incorporated in the reliability analysis as FS < 1. Otherwise, neglecting the correlation ρ may lead to overestimation of the probability of landslide occurrence as FS>1.

The effect of the uncertainty level of strength parameters (c and ϕ) on the probability of landslides is examined as well. As shown in Figure 5, the effect of assumed COV on the resulting P– FS curve for this slope stability is quite significant. At a given FS = 1.1, the probability of landslide is P = 0.30 and landslide risk = 682 million NT dollars when the strength uncertainty level is at COV(c) = 40% and COV(ϕ) = 20%. When the strength uncertainty level is reduced to COV(ϕ) = 20% and COV(c) = 10%, the same problem will yield P= 0.17 and landslide risk = 387 million NT dollars even the FS remains 1.1. Thus, the design based on FS can yield different probability of landslide. This confirms the well-known observation that the probability of landslide is a more consistent safety measure than the factor of safety.

SUMMARY AND CONCLUDING REMARKS

A probability-based framework for assessing the landslide risk is presented and demonstrated with a case study of the Lushan hot spring area in central Taiwan. The important features of the framework include (1) calculate the probability of landslide, and (2) quantify the landslide loss. The landslide risk assessment framework is shown to be effective in the case study of Lushan.

The probability of landslide is especially affected by the strength and their uncertainty levels. Thus, it is essential to make a concerted effort to reduce the uncertainty in the estimated strength in the field and laboratory investigation. Furthermore, it is also important to properly evaluate the possible correlations among the input parameters. The computed probability of landslide could be misleading if significant correlations exist but are not included in the reliability analysis.

ACKNOWLEDGMENTS

The second author wishes to acknowledge financial support of the National Science Council (NSC), Taipei, Taiwan through Grant No. NSC 99-2221-E-464 -002 –MY3.

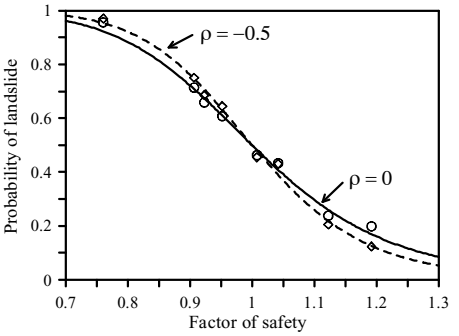

Figure 4. Probability of landslide under various degrees of parameter correlations

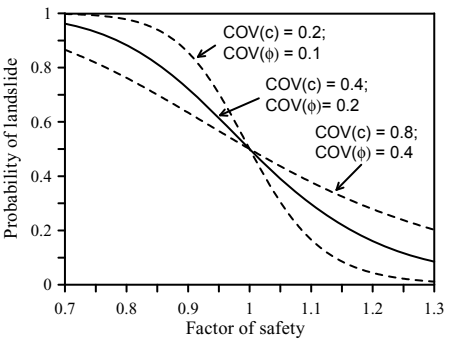

Figure 5. Probability of landslide under various degrees of parameter uncertainty

RENRERENCES

Chen, A. Y., and Morgenstern, N. R. (1983). "Extension to the generalized method of slices for stability analysis." *Canadian Geotechnical Journal,* 20(1), 104 - 119.

Chen, S. C., Wu, C. Y., and Huang, B. T. (2007). "Risk assessment of debris flow disaster in Songhe village." *Journal of Chinese Soil and Water Conservation*, 38(3), 287 - 298.

Hasofer, A. M., and Lind, N. C. (1974). "An exact and invariant first-order reliability format." *Journal of the Engineering Mechanics Division*, 100(EM1), 111 - 121.

Liming Engineering Consultants Co., Ltd, (2006). *Final report to investigations, managements, and planning projects of landslide area. Soil and Water Conservation Bureau*. (in Chinese).

Low, B. K., Gilbert, R. B., and Wright, S. G. (1998). "Slope reliability analysis using generalized method of slice." *Journal of the Geotechnical Engineering Division*, 124(4), 350 - 362.

Xie, M., Esaki, T., Zhou, G.., and Mitani, Y. (2003). "Three-dimensional stability evaluation of landslides and a sliding process simulation using a new

geographic information systems component." *Environmental Geology*, 43, 503 - 512.

Road Slopes Risk Assessment of the Northern Part of Gifu Prefecture Japan

Yusuke Honjo[1], Yu Otake[1], Shuzi Moriguchi[1] and Takashi Hara[1]

[1] Department of Civil Engineering, Gifu University, Gifu, Japan 501-1193
honjo@gifu-u.ac.jp

ABSTRACT: The road slope hazard, which is the occurrence rate of rock falls along the major roads, in the Northern part of Gifu prefecture, consists of Takayama, Furukawa and Gero areas (total 4,177 km^2), is evaluated in this paper. This rock fall rate is estimated in two flods. First, the relative rate of rock falls is estimated by the logistic regression analysis based on the inventory data of slopes along the major roads in the region which includes about 3000 slopes. The inventory data include past events records, as well as topological, geological and geotechnical characteristics of each slope evaluated by the experts in 1996. The slopes are also classified into three categories by the experts as "measures required', "continuous observation" and "no measure required". Based on this classification, the logistic regression analyses are carried out to rank the hazard of the slopes by their attributed characteristics as the explanatory variables. Once relative rate of rock falls are estimated for each slope, this rate is calibrated to the absolute rate by using the actual rock fall event records between 2004 and 2008. By these two folds estimation procedure, the absolute rate of rock fall for each slope along the roads are finally estimated. This study is a part of the development of a methodology for making road maintenance strategies based on risk. Thus, the information gained in this study is combined with other data for damage to propose the strategy for repair and maintenance plan of the road slopes in this region.

INTRODUCTION

In order to propose a methodology for making road maintenance strategies based on risk, we evaluated rock fall probability at each slope in Northern part of Gifu prefecture, which consists of Gero (851 km^2), Takayama (2534 km^2) and Furukwwa (792 km^2).

Risk of a road slope, R, is defined as the product of the loss at the rock fall, D, and probability of the occurrence of the event, P, R=DxP, for all slopes under consideration. The task in this paper is to evaluate P for each slope.

DESCRIPTION OF DATA

Two kinds of data sets are employed in this study: one is "Stability assessment tables (SAT)" and the other is "Rock fall accident record (RFAR)".

(1) **Stability assessment tables (SAT):** SAT are the result of very intensive country wide slope inspection done in 1996, by the experts on road slopes for many geological and geotechnical characteristics, as well as past accident records and measures taken for each slope.

Table 1 Items checked in SAT investigation and chosen in the logistic regression

Check items		Category no.	Rock falls					
			Gero		Takayama		Furukawa	
			T.S.	N.S.	T.S.	N.S.	T.S.	N.S.
Topography	Talus-cone topography	2			X	X		
	Past slope failure area	2	X					
	Clear slope curvature change	2				X		X
	Foot of table land	2	X	X				
	Erosion at slope bottom	2						
	Overhang in general slopes	2						
	Catchments topography	2	X					
	Past debris flow	2						X
	Convex topography at ridge end	2				X		X
	Overhang in ridge end slope	2	X					
Soil characteristics, geology, structure	Weak soil layers	3						
	Degree of rock weathering	3			X	X		
	Planes dipping to the slope	2						
	Soils on top of impermeable layer	3						
Surface conditions	Floating / rolling rocks	3		X			X	X
	Spring water	3						
	Slope covering conditions	3					X	
Configuration	Slope inclination (soil slope)	4						
	Slope inclination (rock slope)	4						
Abnormal phenomena	Spalling in rock slope	2					X	
	Gully erosion	2					X	X
	Scouring	2						
	Piping holes	2						
	Cave-in	2						
	heaving	2						
	Tree root bending	2					X	
	Tree falls	2			X	X		
	Joints	2						X
	Open joints	2	X					
	Abnormal behavior of countermeasures	2	X	X				X
	other abnormal phenomena	2	X					
	Abnormal phenomena in adjacent slopes	2		X	X	X	X	
Past record	Past rock fall record	3	X	X	X	X	X	X

(note) T.S.: treated slope, N.S.: natural slope, which are defined in FIG.1.

Table 1 lists items checked at that time. All the items are qualitative, and the investigators ranked each slope for each item according to the manual developed by the ministry of construction (RMTC, 1996). The number of categories for each item is listed in the table, most of which are 2 categories and some are 3 or 4.

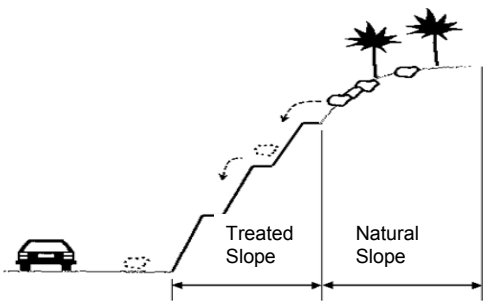

FIG.1. Definition of treated and natural slope

3023 slopes in the regions were investigated at that time (Table 2). Rock fall is an event where rocks in the slope fall to the road, and rock failure is an event where rock falls off from the original rock slopes. Each slope is evaluated by total scores that are accumulated from items the experts had given scores according to the given format. The slopes are also classified to three categories, namely measures required (MR), continuous observation (Ob) and no measures required (NM), by the experts themselves.

Among the three regions, Furukawa is the most mountainous region and less densely populated than the other two regions, whereas Takayama is most densely populated among the three.

Table 2 Number of slopes for SAT investigation and result of RFAR

region	Evaluation results	No. of slopes for SAT		Sub-total	Cumulative transformation rate		No. of failures in inventory slopes	No. of failures in non inventory slopes
		Rock fall	Rock failure		Rock fall	Rock failure		
Gero	M.R.	186	51	237	0.88	0.80	5	7
	Ob	399	68	467	0.51	0.34	12	
	N.M.	204	10	214	0.13	0.04	0	
	subtotal	789	129	918			17	
Takayama	M.R.	275	109	384	0.85	0.90	7	17
	Ob	517	380	897	0.42	0.43	7	
	N.M.	133	36	169	0.07	0.03	0	
	subtotal	925	525	1450			14	
Furukawa	M.R.	277	35	312	0.76	0.73	11	16
	Ob	126	20	146	0.42	0.32	5	
	N.M.	186	11	197	0.16	0.08	3	
	subtotal	589	66	655			19	
All region	M.R.	738	195	933	0.84	0.87	23	40
	Ob	1042	468	1510	0.45	0.40	24	
	N.M.	523	57	580	0.11	0.04	3	
Total		2303	720	3023			50	

(note) M.R.: Measure required, Ob: Continuous observation, N.M.: No measure required

(2) **Rock fall accident record (RFAR):** RFAR is a list of rock fall accidents taken place during 2004 to 2008 in the regions. The total accident number is relatively small, however they are records of the real events showing absolute frequency of the rock falls.

Unfortunately, not all accidents had taken place in the inventory slopes. About 40% of them occurred in slope not included in the inventory as shown in Table 2. Special consideration is required in treating such events.

It should also be noticed that Furukawa area had a higher number of accidents compared to the other two regions. Actually, Furukawa has only one third of the area compared to Takayama, yet the number of the events are almost the same.

METHOD OF ANALYSIS

The assessment of the road slopes are done in two steps: fist by the logistic regression analysis on SAT data to obtain relative failure probability of slopes, P_s; then RFAR data is used to calibrate P_s to the absolute failure probability, P_z.

The relative failure probability assessment: The logistic regression method is usually employed to analyze cases where dependent variables are measured on a binary scale, e.g. failure vs. non-failure (Cox, 1970; Dobson, 1983). In the present case, however, the outcomes are categorized into three cases, where measure required (M.R.), continuous observation (Ob) and no measure required (N.M.). Therefore, the dependent variables are given by the representative accumulation rate (Y) in the logistic regression analysis.

The calculation procedure of the representative accumulation rate (Y) is explained by taking case of the Gero area as an example. In the Gero rock fall case (see Table 2), there are 186 M.R., 399 Ob and 204 N.M. Y for each category is obtained as follows:

$$\text{M.R.: } Y_1 = \frac{204 + 399 + 186/2}{789} = 0.88,\ \text{Ob: } Y_2 = \frac{204 + 399/2}{789} = 0.51,\ \text{N.M.: } Y_3 = \frac{204/2}{789} = 0.13$$

The logistic regression model is given as follows:

$$Y = \frac{\exp\left[\mathbf{X}^{\mathrm{T}}\beta\right]}{1+\exp\left[\mathbf{X}^{\mathrm{T}}\beta\right]},\quad \ln\left[\frac{Y}{1-Y}\right] = \mathbf{X}^{\mathrm{T}}\beta \tag{1}$$

where $\mathbf{X}$ = explanatory variable vector, β = regression coefficient vector.

The logistic regression analysis is solved by R language (Venables and Ripley, 2001). The best combination of the independent variables is determined by stepwise regression procedure (the forward method) taking AIC and some engineering judgment as criteria.

The absolute failure probability assessment: In the second step, the relative failure probability, P_s, obtained in the first step is calibrated to the absolute failure probability, P_z, based on RFAR data. The calibration is made so as the mean absolute rock failure probability of each category of slope in each region coincides with the failure probability obtained from the RFAR data. A conversion factor from the relative to the absolute failure probability, i.e. P_s to P_z, is given in the formula below:

$$\frac{N_{iF}}{N_i} = \frac{\sum_{j=1}^{N_i} P_{Sij}}{N_i} \times K_i \quad \text{thus, } K_i = \frac{N_{iF}}{\sum_{j=1}^{N_i} P_{Sij}} \tag{2}$$

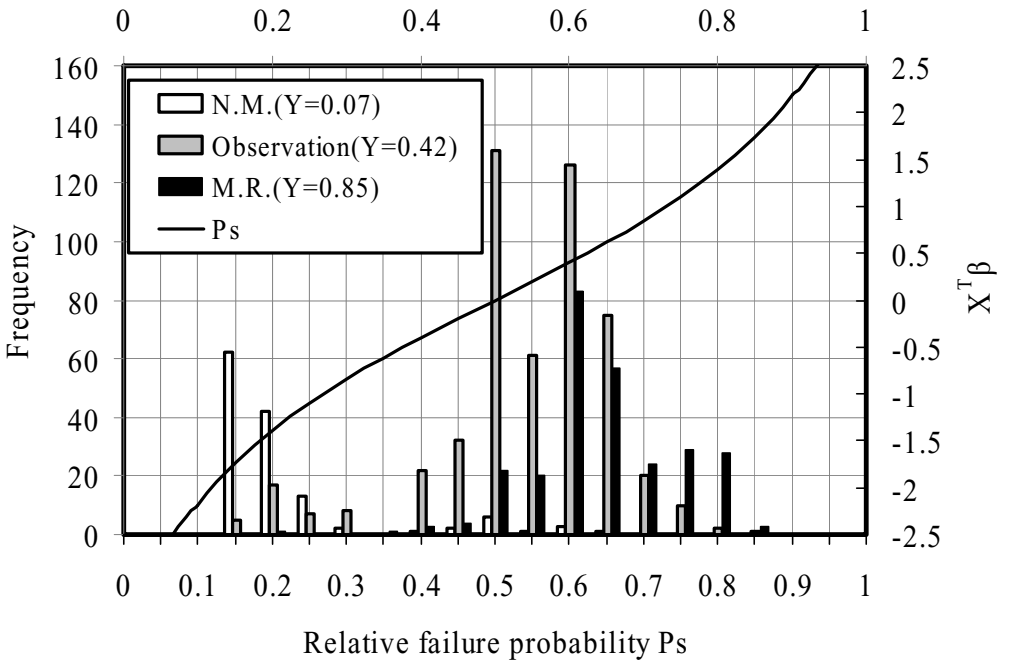

FIG. 2 Relative failure probability of natural slopes in Takayama area

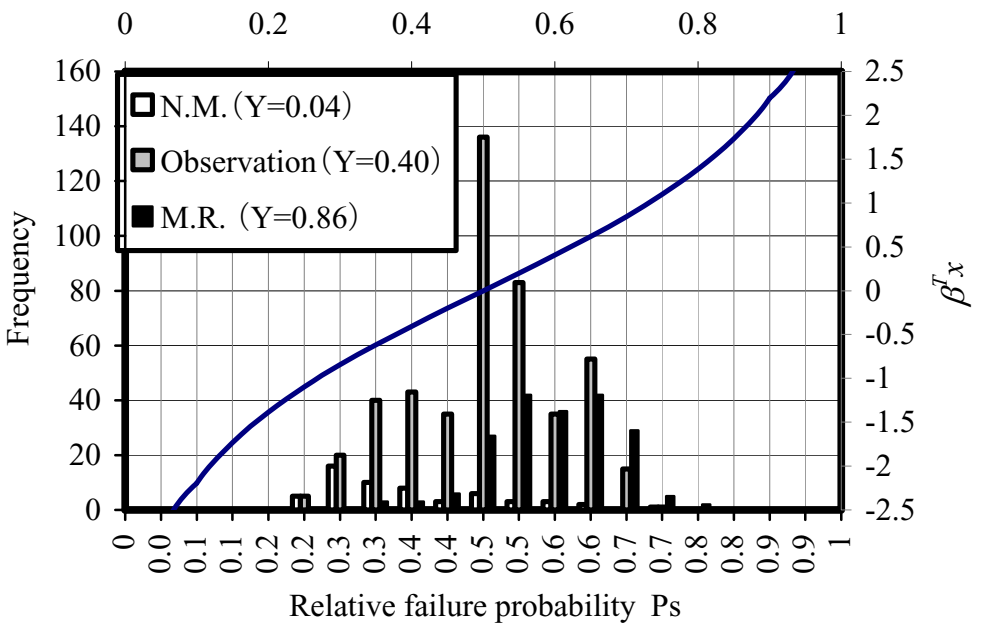

FIG. 3 Relative failure probability of rock failure in all areas

where N_i = total number of slopes in category i in a region, N_{iF} = number of failed slope in category i in a region, P_{sij} = the relative failure probability of j-th slope in category i in a region, K_i = the conversion factor for category i in a region.

The conversion factor was also adjusted for slope failures in non-inventory slopes by increasing the number of slope failures according to the ratio of the number of failures in each category. Thus, the conversion factor has been modified as

$$\frac{N_{iF}+N_{iF}^*}{N_i}=\frac{\sum_{j=1}^{N_i}P_{Sij}}{N_i}\times K_i^* \quad \text{therfore,} \quad K_i^*=\frac{N_{iF}+N_{iF}^*}{\sum_{j=1}^{N_i}P_{Sij}} \tag{3}$$

where N_{iF}^* = assigned number of failure in non-inventory slopes to the inventory slopes. Ki^* = conversion factor from the relative failure probability to the absolute.

RESULTS OF ANALYSIS

Relative failure probability assessment: The selected explanatory variables for rock falls in each area for the treated and natural slopes are presented in Table 1. In all models, 'past rock fall record' is selected. Other selected variables are different from a region to a region and from treated to natural slopes. Variables such as items related to 'topography', 'surface conditions' and 'abnormal phenomena' are selected.

It is chosen to build different models for the different regions so as to reflect the geological, geotechnical and other features of each region.

Logistic regression analysis for rock failure is also carried out. However those results are not presented in this paper due to the limitation of the space. A unified model is chosen in rack fall case because the explanatory variables selected are not very different from a region to another.

Figure 2 presents a result of logistic regression curve and the actual frequency distribution in Takayama region for the natural slopes. It is understood from the figure that the three categories of slopes, namely MR, Ob and NM, are fairly well separated. Especially the separation of NM to the other two is apparent, whereas MR and Ob are rather mixed. The general characteristics are the same for the other two regions.

Figure 3 shows obtained relative failure probability for rock failure in all regions. A unified model for all regions is adopted in this case. It is apparent that separations among the three categories are poor in this case, and many failure cases of different categories are overlapping. This reflects the fact that evaluation of rock failure probability is more difficult compared to rock fall.

Absolute failure probability assessment: The absolute failure probabilities for all slopes are presented in Figure 4. The followings are observed:

- The absolute failure probability generally is 2 to 3 times higher in Furukawa region compared to the other two regions. This is reflecting the number of rock fall accidents and total number of slopes that are shown in Table 2.
- Because the number of slopes susceptive to rock falls are much higher in Furukawa and Gero region, rock fall is much greater cause of accidents than rock failure in these two regions. It is different in Takayama region, where rock failure is also important compared to rock fall.

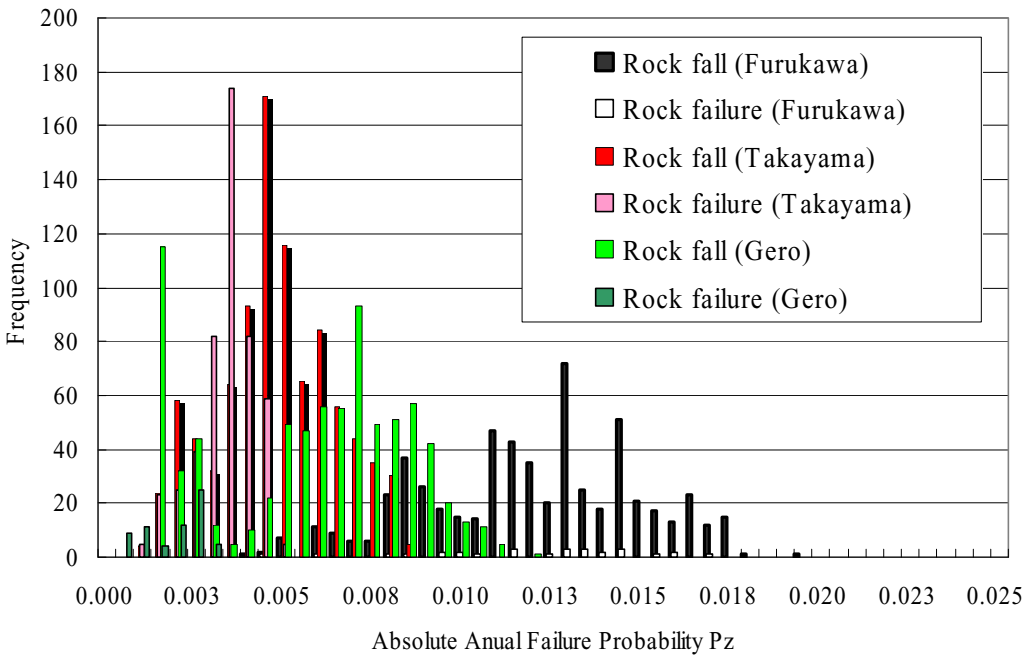

FIG. 4 Absolute annual failure probability by region and kind

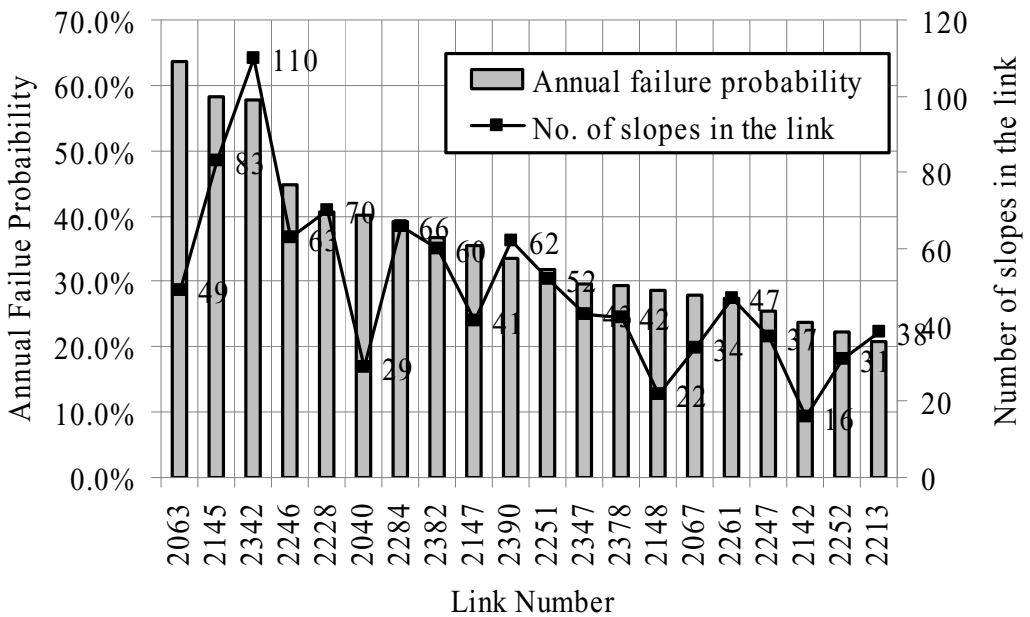

FIG. 5 Failure probability by Links (worst 20 links)

- It is observed in all regions that spreading of the absolute failure probability is wider in rock fall than in rock failure. It is also observed that the distributions of rock failure stay in the middle of those of rock fall. This is due to the narrower distribution of the relative failure probability of rock failure compared to those of rock fall we have observed in Figures 2 and 3.

This paper is a part of the study to propose a methodology for making road maintenance strategies based on risk. All the slopes evaluated above are slopes along the road in the Northern Gifu prefecture. The roads compose a network which consists of nodes and links. We can actually calculate the annual occurrence probability of rock fall on each link based on the results. Figure 5 actually presents the worst 20 links in the network with the higher failure probabilities. This information was linked to the economic loss caused by road closure induced by rock falls to evaluate the risk.

CONCLUSIONS

The conclusions that can be drawn from the analysis are as follows:

(1) The relative failure probability of each slope is successfully estimated based on SAT data by logistic regression analysis that takes into account the experts' evaluation, past accident records and measures taken at slopes.
(2) The absolute failure probability of each slope is estimated by calibrating the relative failure probability based on RFAR data. Since this failure probability has the same magnitude of failure rate to the real data, it can be used in the risk calculation.

ACKNOWLEDGMENTS

The authors appreciate the support of the special education and research found provided by MEXT. We thank Gifu prefecture for providing us the data. The authors are also grateful to H. Machida, H. Sawada, A. Yashma, Y. Takaghi, F. Kurauchi and Y. Kitaura, the member of the research team. The authors also thank one of the reviewers of this paper for his kind corrections and comments which have contributed a great deal to the improvement of English writings.

REFERENCES

Cox, D.R. (1970). *Analysis of Binary Data*, Chapman and Hall, London.

Dobson, A.J. (1983). *An Introduction to Statistical Modelling*, Chapman and Hall, London.

RMTC (1996): *Inspection manual for road hazard mitigation*, Road maintenance technology center foundation. (in Japanese)

Venables, W. N. and B. D. Ripley (1999) Modern Applied Statistics with S-plus, vol. 1 (third ed.), Springer-Verlag.

Managing Settlement Risk due to Tunneling Beneath Downtown Seattle

Michael A. Lach, P.E., M. ASCE[1]

[1] CDM, 14432 SE Eastgate Way, Suite 100, Bellevue, WA 98007

ABSTRACT

Seattle's Alaskan Way Viaduct is to be replaced by a 2.7-kilometer- (1.7-mile-) long, 17.5-meter- (57.5-foot-) diameter, deep-bored tunnel directly beneath the downtown urban core. Seattle Public Utilities (SPU) owns and maintains more than 1,300 water and sewer pipes in the vicinity of the proposed tunnel alignment. The Washington State Department of Transportation (WSDOT) prepared surface settlement estimates based on a uniform level of tunnel ground loss and identified utilities that could be damaged. SPU has a proactive asset management strategy and wanted to define the probable risks to its aging infrastructure from tunnel-induced deformations, taking into account uncertainty due to tunneling difficulty and problematic ground conditions. Probabilistic factors were used in developing a probabilistic distribution for ground deformations, allowing each utility to be evaluated for deformations that would exceed established limits. A risk matrix was developed to compare deformation limit exceedances with established levels, quantifying the utility system's overall risk and providing SPU with a solid strategy for mitigating the potential for system disruption.

PROJECT DESCRIPTION

The Alaskan Way Viaduct and Seawall Replacement Program (AWVSRP) is a project led by WSDOT in conjunction with federal and local agencies. The most significant portion of this project is a 2.7-kilometer- (1.7-mile-) long, 17.5-meter- (57.5-foot-) diameter bored tunnel, which will house State Route 99–a four-lane, limited access highway through downtown Seattle. The tunnel alignment will cross beneath high-rise buildings and busy city streets, as well as the infrastructure

supporting these elements, including more than 1,300 water and sewer pipes owned and maintained by SPU.

The tunnel will be excavated through glacially over-consolidated soils. Although these soils are very dense, continuous support of the ground will be required and the tunnel will be completed using a pressurized face tunnel boring machine (TBM).

SOURCES OF SURFACE SETTLEMENT

Tunnel-induced surface settlements can generally be divided into two categories: ground movement during optimal TBM operations and ground movement due to unforeseen events, or sub-optimal construction. The second category is rare and involves ground movements that are unpredictable as to their location or magnitude; therefore, this paper deals only with ground movement during optimal TBM operations.

These surface settlements are a result of pressure imbalances at the face, overcut and tail void, deflection of the tunnel liner and long-term consolidation of the surrounding soil resulting in ground loss (Cording and Hansmire, 1975). This ground movement typically manifests as a trough-like depression at the ground surface, taking a shape that can be modeled by the normal probability distribution curve (Schmidt, 1974). The depth and width of the settlement trough are dependent upon the tunneling methods, geologic setting and depth of the tunnel. In general, settlements decrease and the trough widens as the depth-to-diameter (Z/D) ratio increases.

The development of the settlement trough occurs over time with the passing of the TBM. Figure 1 shows the development of surface settlements at the base of this trough as measured on another similar local project. Zone 1 represents ground movement ahead of the TBM due to pressure imbalances at the face. Zone 2 includes settlement due to overcut and tail void, while Zone 3 represents deformation of the initial lining system and long-term consolidation.

PREDICTED SETTLEMENT

Geotechnical consultants for WSDOT developed predictions of tunnel-induced surface settlement on the AWVSRP project. These predictions were based on empirical relationships and linear-elastic numerical models, assuming that state-of-the-practice tunneling methods would be employed. The consultants also analyzed

the affect this settlement would have on utilities in the area. In this analysis, they compared the predicted settlement and shape of the settlement trough to published data estimating the allowable deflection limits of the utilities. This analysis resulted in a list of susceptible utilities.

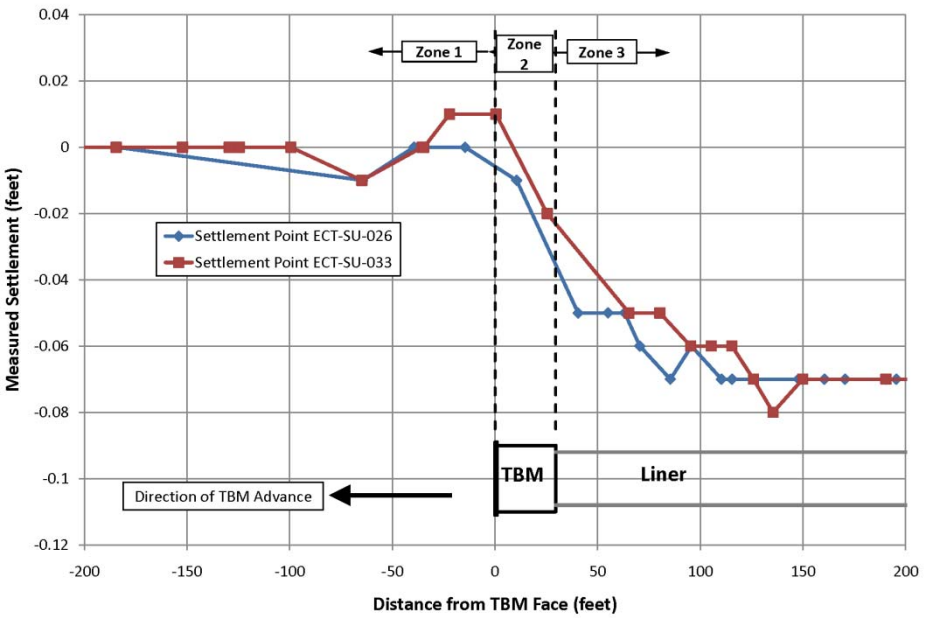

Figure 1. Development of Surface Settlement

There are two primary limitations of this analysis. First, settlement predictions do not consider variations in settlement magnitudes due to variations in workmanship in constructing the tunnel. Secondly, the results were expressed as a binary output: either the utility in question was susceptible or it was not. SPU wanted to understand the probable distribution of settlement (i.e., worst case, best case, most likely) with respect to spatial distribution of settlement along the tunnel alignment. SPU also needed to support risk management decisions that balance the risk of settlement exceeding amounts that can cause damage, the consequences of this damage and mitigation cost.

UNCERTAINTY AND PROBABILITY OF FAILURE

The first step in evaluating the risk to SPU's infrastructure was to identify and quantify uncertainties related to the surface settlement.

Sources of Uncertainty. The amount of settlement that occurs during tunneling operations typically varies from the amount predicted due to the following:

- The actual volume loss varies during tunneling . Typically, higher ground loss will be experienced when mining begins. During launching of the TBM, it is difficult to develop and maintain a consistent, proper soil pressure balance. For the first part of the tunnel drive the contractor gains experience with the TBM operation and ground conditions. Maintaining the proper soil pressure balance may also be difficult at the end of tunneling prior to TBM retrieval.

- Soil cohesive strength redistributes the stresses caused by ground loss at the tunnel. This leads to bridging or arching and results in lower surface settlement elevation than predicted by a fully elastic model. Therefore, typical evaluations will over-predict settlement for where there are overlying deep, stiff cohesive soils, which comprise much of the alignment.

- Sharp variations in ground conditions, equipment failures, or operator error can result in higher than planned ground volume loss.

In addition, historical development of Seattle's downtown urban core consisted of a significant amount of cut and fill operations. The presence of deep fills at the ground surface adds uncertainty in estimation of elastic properties used for the calculation of predicted settlement and could serve to exacerbate tunnel-induced settlements.

Quantifying Uncertainty. We felt that the uncertainty described in the previous section would be most heavily influenced by two factors: the stage of the mining operations and the depth of fill at the ground surface. To quantify this uncertainty, we divided the tunnel into six categories based on the mining conditions and four categories based on the fill conditions. For each of these categories, we developed probability factors which describe the probable deviation from the values predicted by WSDOT as described below.

For each category, we assigned expected and worst-case values for settlement based on experience with similar projects in the local area as reported in the technical literature (e.g., Cochran et al, 2003 and Lach and Sariosseiri, 2010). We developed probability factors where the mean was defined as the ratio of the expected value to the predicted value. Using the four-sigma rule, we then calculated a standard deviation assuming that the worst-case scenario would lay two standard deviations above the mean (USACE, 2006). These probability factors are summarized in Tables 1 and 2.

Table 1. Probability Factors for Mining Conditions

Condition	Description	Mean	Standard Deviation
1	Launch	1.5	1.0
2	Learning Curve	1.5	0.75
3	Normal mining w Z/D < 2	1.25	0.25
4	Normal mining w 2<Z/D<3	1.0	0.25
5	Normal mining w Z/D > 3	0.5	0.25
6	Retrieval	1.5	0.75

Table 2. Probability Factors for Fill Conditions

Condition	Description	Mean	Standard Deviation
1	Cut	0.75	0.25
2	Fill, < 10 feet	1	0.25
3	Fill, 10 - 20 feet	1.25	0.375
4	Fill, > 20 feet	1.5	0.5

We assumed that each probability function was the product of three independent variables: the WSDOT-predicted settlement (a constant) and the mining and fill condition factors (normal probability functions). We then combined these three variables using the "change of variables" method. This resulted in a single probability distribution function for each pipe location.

Probability of Unacceptable Performance. We defined performance in terms of acceptable deformations. SPU has set limits for joint pull-out, joint rotation, differential movement, and total movement for cast and ductile iron pipes. Typically, if work on a project causes one of their pipes to deform beyond these limits, SPU requires that the pipeline be replaced. We used these limits as our acceptable deformation criteria for these types of pipes.

For other pipes (e.g., reinforced concrete, vitrified clay, PVC pipes), SPU has not established acceptable deformation limits. We defined our acceptable deformation in these cases as the deformation that would be likely to cause some damage to the pipe. The selection of these values was based largely on criteria presented by Attewell et al (1986).

Using the probability distribution for the anticipated settlement, we calculated the probability that each utility in the project would exceed the established deformation limits.

RISK MATRIX

To establish a proactive risk management strategy, we developed four categories of importance and subdivided the probability of exceedance into four categories. These categories were used to develop a risk matrix that could be used in risk management and planning actions to mitigate damage during tunnel construction.

Criticality Levels. In order to establish recommended action levels for the utilities located along the tunnel alignment, we suggested that SPU use criticality levels (CL) for classifying the utilities. Assuming that larger pipes served more utility customers and would have larger economic consequences if damaged, our suggestion for the criticality levels was as follows:

- **CL1** – All pipes greater than 300 millimeters (12 inches) in diameter
- **CL2** – All pipes 250 or 300 millimeters (10 or 12 inches) in diameter
- **CL3** – All pipes 200 millimeters (8 inches) in diameter
- **CL4** – All pipes less than 200 millimeters (8 inches) in diameter

Action Level Matrix. The criticality levels were combined with four ranges of probability that the allowable deformations would be exceeded. From these categorizations, a two-dimensional risk action level matrix was built as shown in Figure 2. Each utility along the tunnel alignment was assigned one of the 16 action level categories.

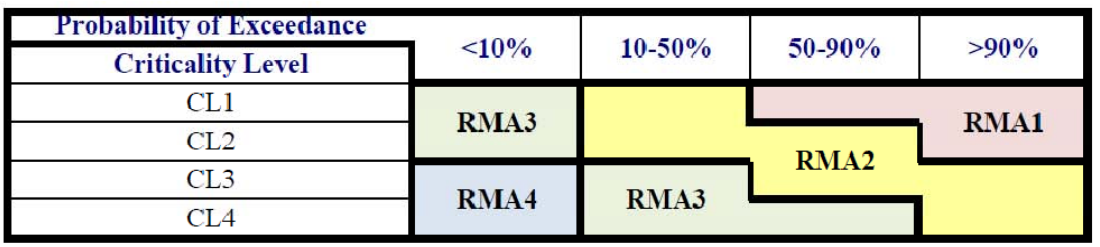

Figure 2. Risk Matrix

Risk Management Actions. As shown in Figure 2, the matrix can be divided into zones of risk management actions (RMA). For example, pipes that have a high criticality level (i.e., serve a large number of customers) and a high probability of exceeding the allowable deformation limits would require the most proactive approach. Suggested actions for the risk management actions were as follows:

- **RMA 1:** Temporarily re-route the utility while the TBM is mining in the vicinity. Replace the utility after the TBM has passed and settlement monitoring confirms movements have stopped.
- **RMA 2:** Replace the utility after the TBM has passed and settlement monitoring confirms movements have stopped. Have response plan in place to repair or re-route if utility damage is excessive during construction. Keep a repair team on 24-hour standby until after the TBM has passed.
- **RMA 3:** Monitor the specific utility for settlement (in addition to general surface settlement monitoring). Replace following construction if established deformation limits are exceeded.
- **RMA 4:** Rely on surface settlement monitoring in area. If settlement exceeds predicted values, evaluate and replace as appropriate.

One of the greatest strengths of this analysis is that the utility owner, in cooperation with the project owner and contractor, can redefine parameters based on the level of risk each party is willing to accept. Changes to the risk action matrix can be easily made through adjustments to the criticality levels, probability of exceedance categories, and zones of defined risk management actions. All of the risk evaluation calculations were compiled in a master spreadsheet where any category can be easily modified and the utilities regrouped into the various risk management action categories.

CONCLUSIONS

Utility owners, when faced with the prospect of major disruption to their networks due to large-scale construction projects, can utilize a probability-based risk assessment approach as a practical tool that can be used as part of a risk management decision process that balances the risk of settlement exceeding amounts that can cause damage, the consequences of this damage, and mitigation cost.

Evaluating the risk of damage due to excessive settlement in quantifiable probabilistic terms provides a level of flexibility that traditional analyses do not. Using this approach, and working closely with the project owner and contractor, will allow SPU to prioritize repair actions and minimize service disruptions, while minimizing unnecessary expenses.

ACKNOWLEDGEMENTS

The author would like to thank SPU for the opportunity to work on this project and the permission to share this knowledge with the geotechnical community. I would also like to thank WSDOT and their consultants, especially Shannon and Wilson and KPFF for laying the groundwork that was utilized for this analysis. Finally, credit must be given to our colleagues and partners on this project at Kennedy/Jenks Consultants.

REFERENCES

Attewell, P.B., Yeates, J., and Selby, A.R. (1986). *Soil Movements Induced by Tunneling and Their Effects on Pipelines and Structures*. Chapman & Hall.

Cochran, J., Pearia, T., Robinson, R., and Haynes, C. (2003). "Successful Application of EPB Tunneling for the Denny CSO Project, Seattle, Washington." *Proceedings of the 2003 Rapid Excavation and Tunneling Conference.* 1104-1116.

Cording, E.J. and Hansmire, W.H. (1975). "Displacements around Soft Ground Tunnels." *General Report of Session IV, 5th Panamerican Conference on Soil Mechanics and Foundation Engineering, Buenos Aires.* 571-632.

Lach, M.A. and Sarioseirri, F. (2010). "Tunnel-Induced Surface Settlement on the Brightwater Conveyance East Contract." *North American Tunneling, 2010 Proceedings.* 298-303.

Schmidt, B. (1974). "Prediction of Settlements due to Tunneling in Soil: Three Case Histories." *Proceedings of the 1974 Rapid Excavation and Tunneling Conference.* Vol. 2. 1179-1199.

USACE. (2006). *Reliability Analysis and Risk Assessment for Seepage and Slope Stability Failure Modes for Embankment Dams.* Engineer Technical Letter 1110-2-561.

Assessing the Probability of Occurrence of Earthquake-induced Landslides Offshore the U.S. East Coast: A First-order, Second Moment Approach

Eugene C. Morgan[1] and Laurie G. Baise[1]

[1]Dept. of Civil and Environmental Engineering, Tufts University, 200 College Ave., Medford, MA, 02155, USA; PH (617) 627-3098; eugene.morgan@tufts.edu

ABSTRACT

Submarine landslides pose a direct threat to offshore infrastructure, and an indirect threat to coastal communities via tsunami generation. Recent studies have investigated the potential role that submarine landslides play in causing tsunamis on the U.S. East Coast. This paper quantitatively assesses submarine landslide hazard offshore Long Island and New Jersey, as an example, but the method herein can be applied to the entire Atlantic margin. Using publicly available bathymetry, surficial sediment data, undrained shear strength values, and earthquake ground motion predictions, we map the conditional probability of slope failure over our entire study area. We calculate this probability using a first-order, second moment estimate of the variance of critical acceleration needed to overcome the resisting forces in the infinite slope stability analysis. We show that this first-order, second moment approximation serves as a convenient and computationally efficient way of assessing submarine landslide hazard over a broad region, while also accounting for the significant uncertainties in the slope stability parameters.

INTRODUCTION

Recent analyses of submarine landslide hazard offshore the U.S. East Coast have focused on the potential devastation caused by tsunamis generated from such events. Earthquakes are thought to serve as the primary trigger of tsunamigenic landslides in this region, much like the 1929 Grand Banks event (Fine et al., 2005). Ten Brink et al. (2009) estimates the distance to the continental slope that earthquakes of various magnitudes would have to be located to trigger significantly- sized landslides. Chaytor et al. (2009) evaluate the size distribution of observed landslides along the Atlantic margin, implying trends of future activity. Grilli et al. (2009) assess submarine landslide hazard at specific locations along the upper East Coast continental slope using a Monte Carlo-based approach. The goal of this paper is to supplement these previous studies with a purely quantitative approach that incorporates a large amount of data to give a full-coverage assessment of the probability of earthquake-induced submarine landslide occurrence.

A probabilistic assessment of slope stability not only accounts for uncertainty in parameter values, but can indicate factors most responsible for destabilization as well. First-order, second moment (FOSM) analyses provide a computationally

efficient way of estimating the probability of failure (Ang and Tang, 1984). This method requires a mathematical model of failure, and mean and standard deviation values for the parameters of that model. Taking the Taylor series expansion of the model about its mean parameter values, and ignoring higher order terms, gives analytical estimates of the mean and variance of the failure metric (e.g. factor of safety (FS)). Assuming a probability distribution for FS, the mean and variance parameterize the distribution for FS, which then yields estimates of the probability of failure. Neglecting correlation between parameters in the FOSM analysis results in a much simpler expression for the variance of FS, and Haneberg (2004) notes that doing so does not significantly affect the variance estimates.

Recent studies use the FOSM method to analyze subaerial landslide hazard (Suchomel and Masin, 2010; Chen et al., 2007; Haneberg, 2004; Giasi et al., 2003; Luzi et al., 2000), but the application of this method to submarine slope stability appears less frequently in the literature. Yang et al. (2007) compare FOSM to other probabilistic methods in evaluating the stability of a submerged, synthetic slope, and Cassidy et al. (2008) perform a retrospective FOSM analysis on a submarine slide that occurred in Finneidfjord, Norway in 1996. These studies evaluate 2-dimensional slope profiles, and we are not aware of any studies that apply the FOSM analysis over entire offshore regions.

This paper aims to provide a full-coverage, probabilistic slope stability analysis for an area covering the continental shelf and slope offshore Long Island and New Jersey. Such an analysis compliments previous studies in this area by quantitatively verifying their results while extending the assessment over the entire region and honoring publicly available data collected in the area. We show that FOSM provides an easily-implemented and reliable assessment that gives preliminary indications of potential failure "hotspots", which can then be used to direct more-detailed, future investigations.

STUDY AREA AND DATA

While the entire U.S. Atlantic margin generally has good data coverage, we focus on the slope offshore Long Island and New Jersey (Figure 1a) because this area has potentially high susceptibility to tsunami run-up, and submarine mass movements have been studied here previously (e.g., Grilli et al., 2009). We expect the analysis presented here to be repeatable along the U.S. East Coast, and other offshore locations around the world with similar types of data.

The relevant data that extends over our study area includes SRTM30 global topography (and bathymetry), surficial sediment classification, undrained shear strength (s_u) values, and probabilistic peak ground accelerations. The SRTM30 dataset (http://topex.ucsd.edu/WWW_html/srtm30_plus.html) has a grid resolution of 30 arc seconds (~1km), and incorporates higher-resolution bathymetry data where available (Figure 1a). The U.S. Geological Survey (USGS) East-Coast Sediment Analysis (http://woodshole.er.usgs.gov/openfile/of2005-1001/) classifies surficial sediments on the margin based on texture data and provides the interpretation as a polygon shapefile covering all of our study area (Figure 1b). Additionally, the USGS's usSEABED database (http://pubs.usgs.gov/ds/2005/118/index.html)

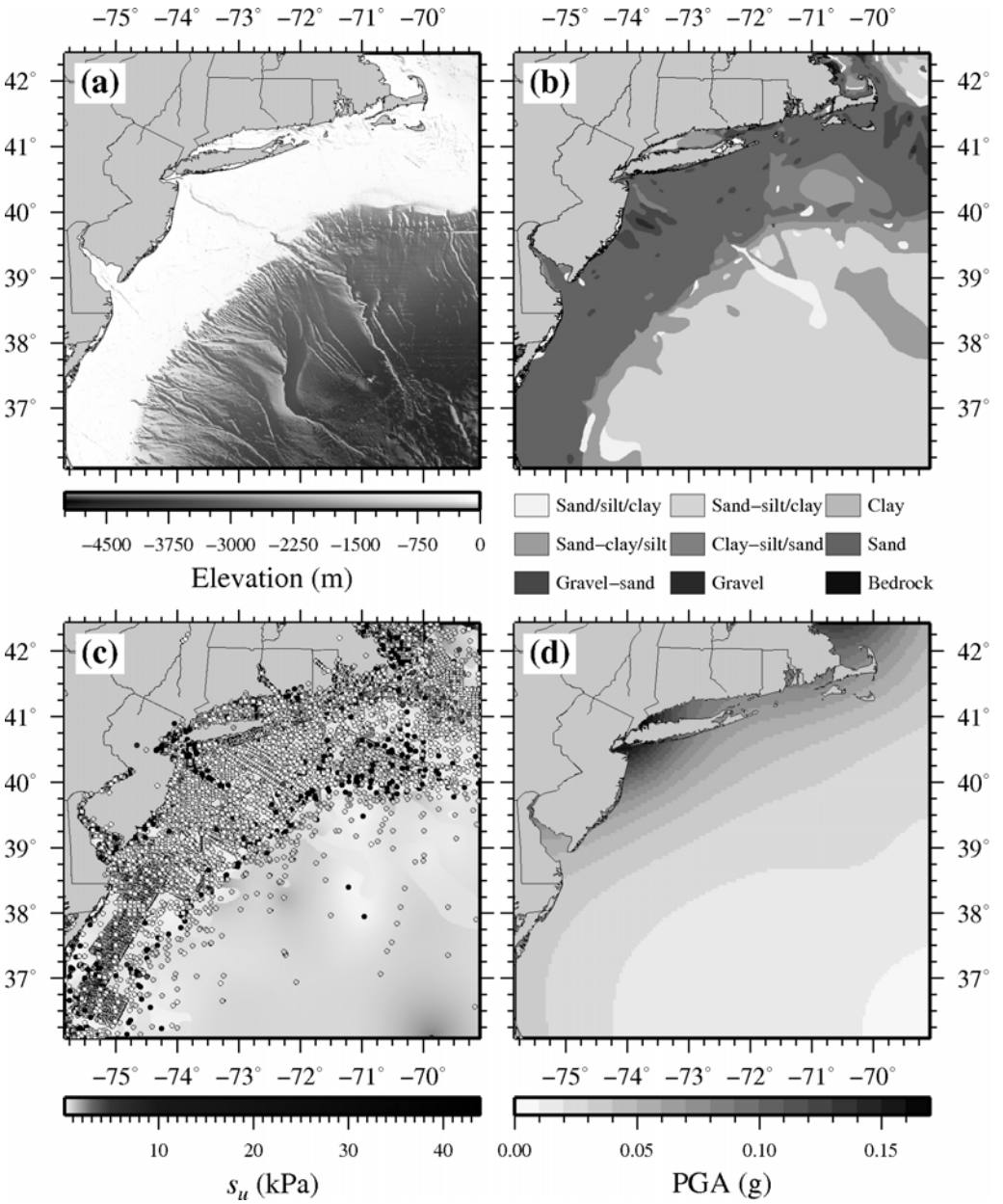

Figure 1. Location of study area, displaying a) SRTM30 bathymetry, b) East-Coast Sediment Analysis surficial sediment classifications, c) usSEABED s_u values within 1m below seafloor on top of the kriged s_u values, and d) peak ground acceleration (PGA) with 2% probability of exceedance in 50 years.

estimates s_u values (even for granular materials) from field and lab measurements including hand penetrometer strength, vane shear strength, cohesion values from triaxial and shear box tests, compressive shear strength at low confining pressures, and cone resistances, and also assess values based on soil and rock descriptions. In order to study shallow landslides, we filter out any s_u values from depths greater than 1m below seafloor (points in Figure 1c). To assess earthquakes as a potential

triggering mechanism for submarine landslides in this area, we use 2008 USGS National Seismic Hazard Maps for the East Coast which give earthquake peak ground accelerations (PGA) for various probability levels (we choose to look at the largest and rarest ground motions: 2% probability of exceedance in 50 years)(Figure 1d).

DATA PROCESSING

In order to make the subsequent calculation outlined in the next section, we convert all the necessary data layers to a raster format. Because the SRTM30 layer provides the highest resolution, we sample the other layers onto its grid. Slope angle (α) comes from computing the directional derivative of the SRTM30 elevation data, so does not need to be re-gridded. We use literature values for the total unit weights (γ) of the surficial sediments (values listed in Table 1), and so we rasterize the surficial sediment polygons to the SRTM30 grid. The effective unit weight (γ') used in the FOSM calculations comes from subtracting the unit weight of water (9.81 kN/m^3) from the total unit weight.

Table 1: Total unit weights (γ) and their standard deviations (σ_γ) used for each sediment type.

Sediment	γ (kN/m^3)	σ_γ (kN/m^3)	Sediment	γ (kN/m^3)	σ_γ (kN/m^3)
Sand/silt/clay	15.45	0.98	Sand	18.64	0.98
Sand-silt/clay	17.36	0.98	Gravel-sand	18.64	1.96
Clay	15.70	0.98	Gravel	20.60	1.96
Sand-clay/silt	17.36	0.98	Bedrock	29.43	0.98
Clay-silt/sand	14.52	0.98			

Gridding the usSEABED s_u values is more difficult because these data exist at discrete points. We interpolate these values to the SRTM30 grid by means of stratified kriging (base layer in Figure 1c). Stratified kriging differs from ordinary kriging in that it predicts s_u values only at grid cells that belong to the same surficial sediment unit as the data points. That is, this type of kriging stratifies the s_u data points by the sediment type they lie within, builds sample variograms from the stratified data, fits a variogram model to each variogram, and then predicts within each sediment unit based on the unit's respective model. Not only does the model honor (potential) differences in spatial correlation structure between sediment types, but will help mitigate the bias arising from denser s_u sampling near-shore. Also, kriging gives uncertainties (variances) with its predictions, making it compatible in providing parameters for the FOSM method.

FOSM FOR FS AND a_c

In our infinite slope stability analysis, we parameterize all the resisting forces with the undrained shear strength (s_u) given by the usSEABED dataset. Our static factor of safety is then FS = s_u /($\gamma' z \sin\alpha \cos\alpha$), where the driving force in the denominator results from the buoyant weight of the soil mass (γ' times thickness z) on the slope with angle α. For the FOSM method, we take the partial derivatives of FS

with respect to s_u and γ′, giving $\partial FS/\partial s_u = (\csc\alpha \sec\alpha)/(\gamma' z)$, and $\partial FS/\partial \gamma' = (-s_u \csc\alpha \sec\alpha)/(\gamma'^2 z)$. Here, we only take the derivatives with respect to s_u and γ′ because we assume that these two parameters contain all the uncertainty in FS; we measure α directly from the SRTM30 bathymetry and arbitrarily evaluate shallow-seated slides with z = 1m. Our mean FS estimate (mapped in Figure 2a) comes from evaluating the equation for FS at the mean parameter values ($\bar{x}_i = (\bar{s}_u, \bar{\gamma}')$), while the variance of FS (σ_{FS}^2) comes from FS evaluating $\sigma_{FS}^2 = \sum_i (\partial FS/\partial x_i)_{\bar{x}_i}^2 \sigma_{x_i}^2$, where $\sigma_{x_i}^2$ is the vector of variances for $x_1 = s_u$ and $x_2 = \gamma'$. Figure 2b shows the static factor of safety standard deviation σ_{FS}. We can repeat the FOSM method for the critical acceleration a_c, which includes the static factor of safety: $a_c = (FS-1)g \sin\alpha = s_u g/(\gamma' z \cos\alpha) - g \sin\alpha$, where g is gravity (Newmark, 1965). Taking the partial derivatives gives $\partial a_c/\partial s_u = (g \sec\alpha)/(\gamma' z)$, and $\partial a_c/\partial \gamma' = (-s_u g \sec\alpha)/(\gamma'^2 z)$. Again, our mean a_c estimate (Figure 2c) comes from evaluating the equation for a_c above at the mean parameter values, and variance from $\sigma_{a_c}^2 = \sum_i (\partial a_c/\partial x_i)_{\bar{x}_i}^2 \sigma_{x_i}^2$. Figure 2d shows the critical acceleration standard deviation σ_{a_c} in order to keep the units comparable to the a_c values. We can then calculate the probability of failure (P[fail], Figure 3) by parameterizing the normal cumulative distribution function with a mean equal to a_c and a standard deviation equal to σ_{a_c}, and plugging in the mapped PGA values (Figure 1d). In other words, P[fail] is the area of the normal density curve centered at a_c with standard deviation σ_{a_c} that lies below the given PGA value. Therefore, keep in mind that the probabilities of failure plotted in Figure 3 are conditional on the PGAs with 2% probability of exceedance in 50 years, which are the rarest (and thus largest) predictions of ground motion available from the USGS.

DISCUSSION

While areas of higher landslide hazard largely exist on steeper slopes, α is not the only variable controlling the distribution of failure probabilities in Figure 3. We see from Figure 2 that the lowest FS and a_c generally occur on the upper portion of the continental slope, which has the steepest slopes (2° < α < 53°), with the largest α occurring in incisions in the slope. From Figure 3, we see the largest P[fail] values (> 50%) share the same association, but a strict causative relationship between α and P[fail] cannot be made; numerous patches of P[fail] < 50% exist on the upper slope and some patches of P[fail] > 50% have shallow slope angles. While the upper slope largely contains sand-clay/silt with sand-silt/clay draping the lower slope and patches of sand/silt/clay, the lower probabilities are primarily associated with clay-silt/sand, which is lighter than the former three sediment types. Additionally, s_u has a strong influence on the spatial variation of P[fail] within the continental shelf.

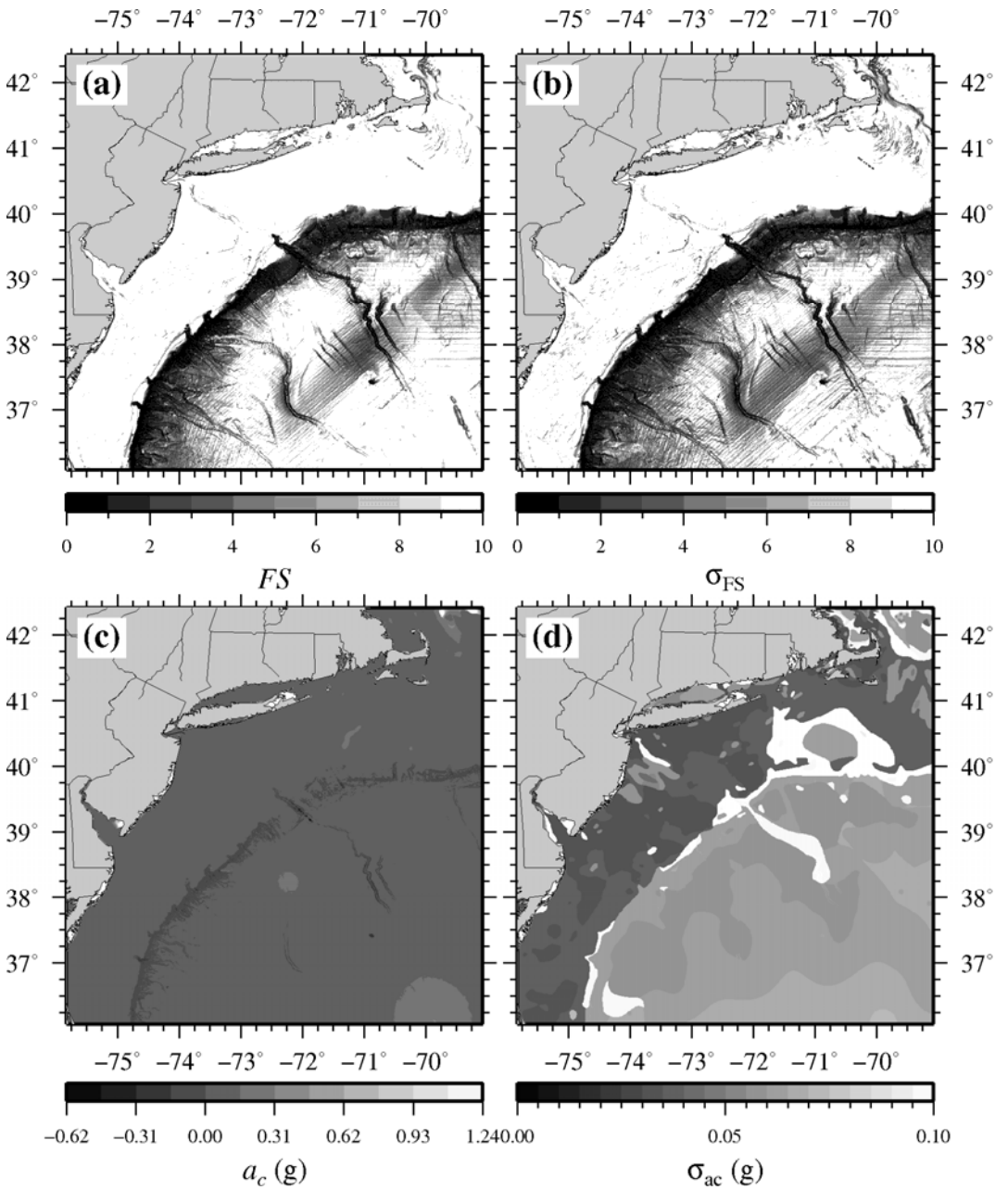

Figure 2: Results from the FOSM analysis with input data from Figure 1 and Table 1: a) static factor of safety FS clipped to values ≤ 10, b) standard deviation of static factor of safety σ_{FS}, also clipped to values ≤ 10, c) critical acceleration a_c, and d) σ_{a_c}. Note that negative a_c values are associated with Fs < 1. Values are shaded by the SRTM30 terrain to show their relationship to geomorphic features.

Figure 3 identifies specific areas of distinctly high landslide hazard. A small patch to the south on the upper slope (around -74.75°, 36.25°) has P[fail] > 80%, which is surrounded by significantly smaller probabilities. Large patches of higher probability exist off Delaware, owing to localized spots of low s_u and higher levels of

ground motion. Additionally, the canyon incised by the Hudson river (below Long Island) hosts higher probabilities than neighboring areas on the lower slope, but these hazardous areas do not extend beyond the canyon walls. In general, canyons in the slope host markedly higher probabilities of failure, and should be investigated in greater detail.

It is also important to note that the higher P[fail] values co-locate with negative a_c values on the continental slope, which in turn are associated with FS < 1. Even though the locations with FS < 1 have relatively low uncertainty ($\sigma_{FS} < 1$), they also lie in sparser s_u data coverage, so the shear strength of these slope sediments are not nearly as well-characterized as on the shelf. Similarly, using arbitrarily different γ values may reduce the distribution of FS < 1. Also, while the FS < 1 values generally have smaller uncertainty than larger FS values, negative a_c values have larger or just as large σ_{a_c} values as areas with larger a_c values. Namely, in Figure 2d, the upper slope generally has larger uncertainty (σ_{a_c}) than either the lower slope or shelf. Thus, we are not as confident in our estimates of the most hazardous areas as we are in the least hazardous areas.

CONCLUSION

While this study presents some significant findings, certain limitations in the analysis have yet to be overcome. For one, this analysis does not account for earthquake duration (i.e. Arias intensity) and Newmark displacements, which determine whether slope material will fail catastrophically or not. Exceeding a_c may cause the soil mass to slip, but will the soil mass slip far enough to completely fail? Here we have limited the calculations to z = 1m, when it should be fairly easy to iterate the calculations over a variety of landslide thicknesses. Deeper z values add the complexity of sub-seabed structure and parameter variation with depth into the analysis, but in order to address tsunami generation, this analysis must adequately consider landslide thickness. Furthermore, our estimates of γ are rudimentary at best, and having field measurements of γ would improve the results significantly. More accurate and widely-distributed s_u values would also improve the results.

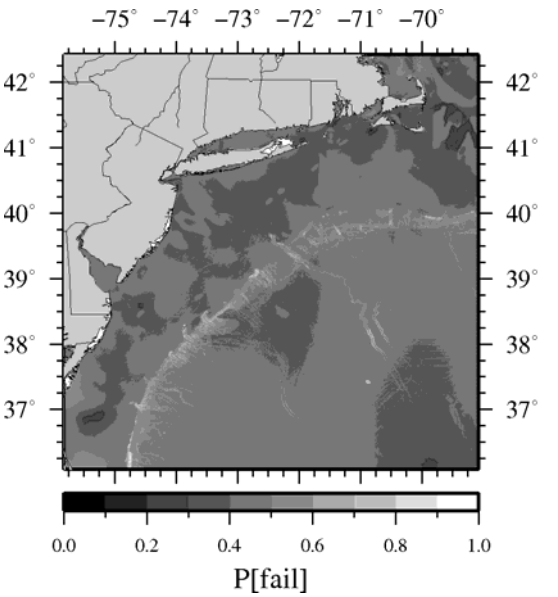

Figure 3: The probability of shallow slope failure given the peak ground accelerations with 2% probability of exceedance in 50 years (Figure 1d).

Despite the above limitations, this paper illustrates the viability of the FOSM method as a preliminary indicator of the most hazardous areas in an entire region. Via

FOSM analysis, one can easily construct an analytical expression for the uncertainty of a chosen failure metric, thus easing the computation of failure probabilities from a large amount of data.

REFERENCES

Ang, A. H.-S., Tang, W. H. (1984). *Probability Concepts in Engineering Planning and Design*. J. Wiley & Sons, New York.

Cassidy, M. J., Uzielli, M., Lacasse, S. (2008). Probability risk assessment of landslides: A case study at Finneidfjord. *Canadian Geotechnical Journal*, 45(9), 1250-1267.

Chaytor, J. D., ten Brink, U. S., Solow, A. R., Andrews, B. D., 2009. Size distribution of submarine landslides along the U.S. Atlantic margin. *Marine Geology* 264 (1-2), 16–27.

Chen, J. C., Jan, C. D., Lee, M. H., 2007. Probabilistic analysis of landslide potential of an inclined uniform soil layer of infinite length: theorem. *Environmental Geology*, 51(7), 1239–1248.

Fine, I.V., Rabinovich, A.B., Bornhold, B.D., Thomson, R.E., Kulikov, E.A., 2005. The Grand Banks landslide-generated tsunami of November 18, 1929: preliminary analysis and numerical modeling. *Marine Geology* 215 (1-2), 45-57.

Giasi, C. I., Masi, P., Cherubini, C., 2003. Probabilistic and fuzzy reliability analysis of a sample slope near Aliano. *Engineering Geology* 67 (3-4), 391 – 402.

Grilli, S. T., Taylor, O. D. S., Baxter, C. D. P., Maretzki, S. (2009). A probabilistic approach for determining submarine landslide tsunami hazard along the upper east coast of the United States. *Marine Geology*, 264(1-2), 74–97.

Haneberg, W. C., 2004. A rational probabilistic method for spatially distributed landslide hazard assessment. *Environmental & Engineering Geoscience* 10 (1), 27–43.

Luzi, L., Pergalani, F., Terlien, M. T. J., 2000. Slope vulnerability to earthquakes at subregional scale, using probabilistic techniques and geographic information systems. *Engineering Geology* 58 (3-4), 313–336.

Newmark, N. M., 1965. Effects of earthquakes on dams and embankments. *Geotechnique* 15 (2), 139–160.

Suchomel, R., Masin, D., 2010. Comparison of different probabilistic methods for predicting stability of a slope in spatially variable c-φ soil. *Computers and Geotechnics* 37 (1-2), 132 – 140.

ten Brink, U. S., Lee, H. J., Geist, E. L., Twichell, D., 2009. Assessment of tsunami hazard to the U.S. East Coast using relationships between submarine landslides and earthquakes. *Marine Geology* 264 (1-2), 65 – 73.

Yang, S., Nadim, F., Forsberg, C., 2007. Probability study on submarine slope stability. In: Lykousis, V., Sakellariou, D., Locat, J. (Eds.), *Submarine Mass Movements and Their Consequences*. Vol. 27 of Advances in Natural and Technological Hazards Research. Springer Netherlands, pp. 161–170, 10.1007/978-1-4020-6512-5 17.

An Innovative Landslide Risk Assessment System: Application to Highway Embankments

L. Pantelidis[1]

[1]Division of Engineering, Colorado School of Mines, Golden, CO 80401-1887, USA; email: lyssander_p@hotmail.com

ABSTRACT

In this paper a landslide risk assessment system referring to highway embankments is proposed. The system in question consists of three stages, a) the quantitative attribution of the failure hazard of embankments, b) the calculation of geometric characteristics of a possible failure and c) the quantitative attribution of consequences. As regards to the first stage, the failure hazard derives from the drained condition of embankments and the influence that climatic conditions have on their stability; the latter being the most common landslide-triggering factor. The second stage is based on existing methods and models; allowing for application in Highway Engineering the proposed system provides an assessment of the failure extent with regard to roadway elements. Finally, the third stage fully distinguishes the consequences to traveler's safety from those to traffic flow. Correspondingly, there are two risk values, where, the highest one is chosen every time. Based on the last, an alertness condition is assigned accompanied by recommended actions.

INTRODUCTION

Slope instabilities along highways are not only a major hazard for travelers but also create excessive maintenance costs and hinder traffic. Over the last decades a quite big number of qualitative and quantitative risk assessment systems referring to highway geotechnical assets has been proposed. The disadvantages and limitations of these systems have been discussed in detail by Pantelidis (2010c) and hence, no further reference is made here. The objective of the present paper is to propose a risk assessment system for highway embankments in order to ensure highway performance and safety. The system in question is a part of an overall risk assessment system that deals with both highway cuttings (rock and earth) and embankments (Pantelidis, 2009b). It is composed of three main stages, a) the quantitative attribution of the failure hazard of highway embankments, b) the calculation of the geometric elements of a possible failure and c) the quantitative attribution of the consequences.

QUANTITATIVE ATTRIBUTION OF FAILURE HAZARD

The determination of the failure hazard of embankments is done by quantifying their normal (drained) condition separately from the triggering mechanism for failure. A relevant flow chart, which however refers to rock cuttings, is given in Pantelidis (2009a, 2010a).

Normal (drained) condition of highway embankments. This stage is based on stability charts (e.g. Cousins, 1978) or closed form solutions (e.g. Pantelidis, 2008a,b). In a second phase and where it is possible, slope stability software could be used for the most hazardous embankments (embankments giving high *risk* value; see below). It is noted that, the question here is exclusively the *normal* condition of embankments (no pore water pressures or other loadings are taken into account).

Triggering mechanism for failure. The influence of water on the stability of highway embankments is taken into account in the proposed system by the Triggering Mechanism Factor (f_{TM}) which is given as the product of the critical precipitation ratio I_m/I_{cr} times the drainage factor f_D:

$$f_{TM} = \frac{I_m}{I_{cr}} \cdot f_D \qquad (1)$$

where, I_m is the mean annual precipitation height, I_{cr} the critical annual precipitation height (I_{cr}=700 mm, fixed conservative value; see Pantelidis, 2010a) and f_D the drainage factor of embankment. This step allows the system to be adapted to local climatic conditions (precipitation height) increasing its reliability.

The drainage factor (f_D) which was structured in a form of rating table (Table 1) is inferred through in situ observations relative to the potential of pluvial water to trigger instabilities (potential for infiltration and drainage of water, sub-factor f_{inf} and f_{dr} respectively). Table 1 has been calibrated in order to be compatible with the mean annual precipitation height. Such values are, generally, easier to be found comparing e.g. to the monthly or hourly precipitation height values.

Hazard Index. The Hazard Index (HI) reflecting the failure hazard of embankment is obtained from factors F (safety factor) and f_{TM} through the empirical chart of Figure 1. It was found that the ratio f_{TM}/F provide an excellent distinction between the prone and non-prone to fail embankments (Pantelidis, 2009b). The HI values range between 1 and 10 so as to be comparable with the respective ones referring to rock and earth cuttings (Pantelidis, 2009b, 2010a). This allows for the relative assessment of failure risk of different highway geotechnical assets in a highway maintenance management framework.

Table 1. Drainage factor f_D for typical embankments and on sloping ground.

Drainage sub-factor f_{dr} Drainage of infiltrated water through slope face of the embankment [2]	**Infiltration sub-factor f_{inf}** Infiltration of water in the body of the embankment[1]				
	Impossible or negligible[3]	Minor	Medium	Significant	Major[4]
Very good (naked face)	1	2.4	4.6	6.1	7.5
Good (e.g. some vegetation)	1	2.6	4.9	6.5	8.1
Medium	1	2.7	5.2	6.9	8.6
Poor (e.g. dense vegetation)	1	2.9	5.7	7.6	9.4
Very poor (e.g. very dense vegetation)	1	3	6	8	10

[1] It refers to flows from upslope (only in the case of embankments founded on sloping ground, e.g. water from ravines), infiltration from embankment slopes, unpaved shoulders etc.
[2] It refers mainly to the coverage with vegetation of the lower part (drainage zone) of slope face of embankments with grass and weeds. It could also refer to the coverage of slope with concrete etc.
[3] Well-maintained culvert/ditches, unpaved shoulders with adequate gradient, slopes with good coverage (e.g. dense vegetation) etc.
[4] No or bad-maintained culvert, wide and permeable shoulder, damaged ditches, high and bare slopes etc.

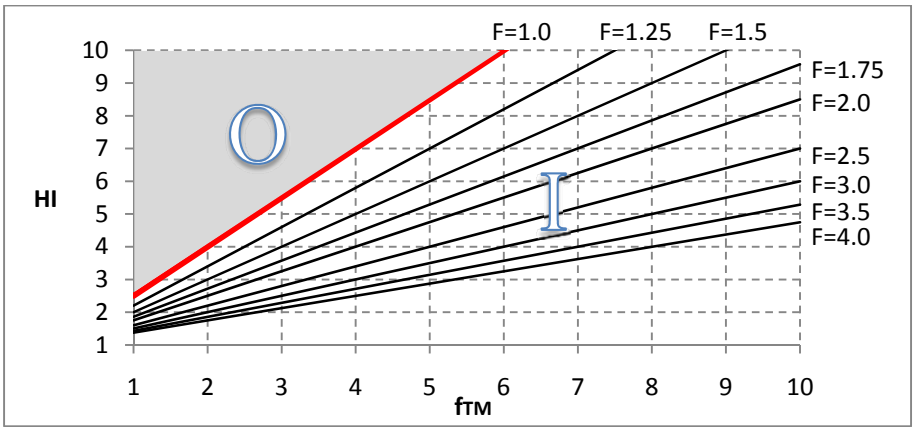

Figure 1. Triggering Mechanism Factor – Hazard Index chart. Area O: Impossible (F<1), Area I: Possible (F≥1). HI=1.5·(f_{TM}/F)+1.

CALCULATION OF THE GEOMETRIC CHARACTERISTICS OF A POSSIBLE FAILURE

This stage is based on models and methods such as those proposed by Pantelidis (2008a, 2008b, 2010b) and Khalili et al. (1996). It is assumed that road subsidence in the order of 0.15m is large enough to cause significant problems to traffic flow and threaten the safety of travelers.

QUANTITATIVE ATTRIBUTION OF FAILURE CONSEQUENCES

Consequences to traffic flow – Consequence Index CI_1

The consequences index CI_1 reflects the effects of a possible embankment failure to traffic flow, that is, the socioeconomic effects. Allowing for application in Highway Engineering the proposed system provides an assessment of the failure extent with regard to roadway elements (roadside area, ditch, lane width, total trafficked width). There are six predetermined scenarios both for National Roads and Motorways (Table 2 and 3 respectively), where, the failure extent is related with the remaining (free to traffic) width of the road. Each scenario corresponds to a consequence score or range of score (see Table 2 and 3). In the second case, the consequence score is given by Equation 2 taking into account the required Length of Detour (if any) and the Level of Service (LOS) of road through factor ΔCI (Figure 2). The Length of Detour refers to the additional travel length; the length that vehicles would cover anyway along the main road is subtracted from the total length of detour - if negative then equals zero. The Level of Service (AASHTO, 2004) characterizes the operating conditions on the facility in terms of traffic performance measures related to speed and travel time, freedom to maneuver, traffic interruptions, and comfort and convenience. The levels of service range from level-of-service A (least congested) to level-of-service F (most congested). Safety is not included in the measures that establish service levels. Perhaps, a more realistic approach is to choose the most unfavorable LOS referring to the time span or season of the year where an embankment failure is more possible. The decision is left on the user's judgment.

$$CI_1 = CI_{1,min} + \Delta CI \quad (2)$$

Table 2. Roadway Impedance for National Roads (2 lanes)

Case	Roadway Impedance
a	The failure affects only the unpaved shoulder or is extended up to the drainage ditch (if any). CI_1=1.
b	The amplitude of failure is extended up to the paved shoulder or the emergency lane (if any). CI_1=1.5.
c	One lane partially blocked. The remaining width of the trafficked surface is at least 5.5m (including the paved shoulder and emergency lane) permitting traffic flow in both directions. Additional Traffic Signs (e.g. traffic cones) facilitate traffic flow in both directions. CI_1=3.
d	Half the width of the road (up to the centerline) is blocked. Width of the remaining pavement is greater than 3.0m. Alternating traffic flow. Additional Traffic Signing is compulsory. The CI_1 value is taken from Equation 2 depending on the LOS (the length of detour equals zero). $CI_{1,min}$=4.5 (default value). Range of values CI_1=4.5–7.
e	The amplitude of failure is extended beyond the road centerline. Alternating traffic flow. Remaining road width about 2.50÷3.0m. Vehicles decelerate, but they still can go through. The CI_1 value is taken from Equation 2 depending on the LOS (the length of detour equals zero). $CI_{1,min}$=6 (default value). Range of values CI_1=6–8.5.
f	Road is totally blocked. Detour is compulsory. The CI_1 value is taken from Equation 2 depending on the length of detour and the LOS. $CI_{1,min}$=7.5 (default value). Range of values CI_1=7.5–10.

Table 3. Roadway Impedance for Motorways (4 lanes, separated pavements)

Case	Roadway Impedance
a	The failure affects only the unpaved shoulder or is extended up to the drainage ditch (if any). CI_1=1.
b	The amplitude of failure is extended up to the paved shoulder or the emergency lane (if any). CI_1=1.5.
c	One lane partially blocked. The remaining width of the trafficked surface in the direction affected by the failure is at least 6m, forming two traffic lanes. Additional Traffic Signing (e.g. traffic cones) is compulsory. Traffic flow is slow and uninterrupted. CI=3.
d	One lane totally blocked. The remaining width of the trafficked surface in the direction affected by the failure is greater than 3.0m (traffic in two lanes is merged to one lane). Vehicles decelerate, but they still can go through. Additional Traffic Signing is compulsory. The CI_1 value is taken from Equation 2 depending on the LOS (the length of detour equals zero). $CI_{1,min}$=4.5 (default value). Range of values CI_1=4.5–7.
e	One direction is blocked. Vehicles must make a detour to the slip road (if any) or to the contra flow through circulation diverters. The CI_1 value is taken from Equation 2 depending on the length of detour and the LOS. $CI_{1,min}$=6 (default value). Range of values CI_1=6–8.5.
f	Only one lane of the total road free to traffic. Vehicles in one direction must detour to the slip road (if any) or to the contra flow through circulation diverters (alternating traffic flow). The CI_1 value is taken from Equation 2 depending on the length of detour and the LOS. $CI_{1,min}$=7.5 (default value). Range of values CI_1=7.5–10.

Consequences to travelers' safety – Consequence Index CI_2

The consequences index CI_1 reflects the effects of a possible embankment failure to travelers' safety. As known, the required Stopping Sight Distance (SSD) of a vehicle, which at the moment when the driver perceives the danger on the road has a velocity v_o, is given by Equation 3 (AASHTO, 2004). Similarly, if the available sight distance, SD, is λ times smaller than SSD (λ=SD/SSD, where λ<1), Equation 3 can be transformed into Equation 4. Finally, Equation 4 is solved as for the impact velocity of vehicle v_{im} (the velocity by which the vehicle is inserted in the failed road

segment); see Equation 5. In the case of a road having zero lengthwise gradient, the impact velocity of vehicle can be directly obtained from Figure 3.

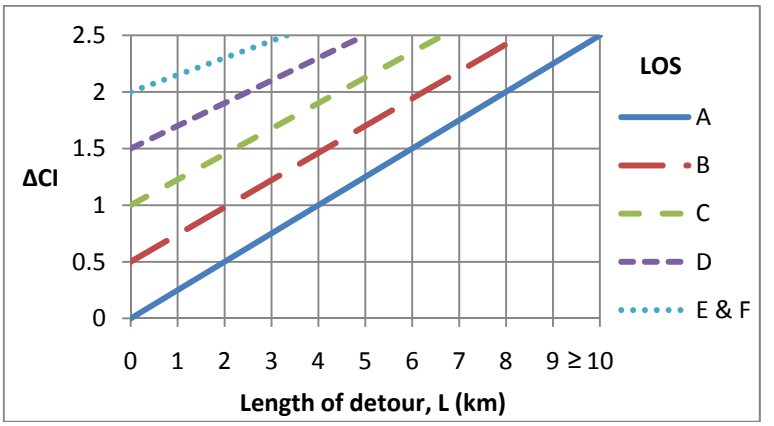

Figure 2. Factor ΔCI (Eq. 2). LOS [General operating condition]: A [Free flow], B [Reasonably free flow], C [Stable flow], D [Approaching unstable flow], E [Unstable flow] and F [Forced or breakdown flow] (AASHTO, 2004).

$$SSD = S_{reaction} + S_{breaking} = v_o \cdot t_r + \frac{v_o^2}{2\cdot\{\alpha+g\cdot\sin(i)\}} \quad (3)$$

$$SD = \lambda \cdot SSD = v_o \cdot t_r + \frac{v_o^2 - v_{im}^2}{2\cdot\{\alpha+g\cdot\sin(i)\}} \quad (4)$$

$$v_{im} = \{(1-\lambda)\cdot v_o \cdot [2\cdot t_r \cdot \{\alpha + g\cdot\sin(i)\} + v_o]\}^{0.5} \quad (5)$$

Where, v_{im} and v_o are the impact and the initial velocity of vehicle respectively (m/s), g=9.81 m/sec^2 and, according to AASHTO (2004): t_r=2.5sec (reaction time of 90% of drivers) and α=3.4 m/sec^2 (recommended deceleration rate). i is the lengthwise inclination angle of the road (positive for upgrades). λ=SD/SSD. $S_{reaction}$ and $S_{breaking}$ are the reaction and breaking distance as defined by AASHTO (2004). All distances are in meters.

The maximum consequence score (maxCI_2=10) was given to the case where a vehicle is inserted into the failure zone with speed greater or equal to v_s=50 km/h (suggested value), whilst the lowest (minCI_2=1) to the case where there is no impact. For intermediate impact velocities the consequences index CI_2 is distributed linearly following Equation 6.

$$CI_2 = 9\cdot v_{im}/v_s + 1 \quad (6)$$

RISK INDEX, LEVELS OF ALERTNESS CONDITION AND RECOMMENDED ACTIONS

As known, risk is expressed by the product of hazard and its consequences using the following general statement:

$$Risk = Hazard\ x\ Consequences \quad (7)$$

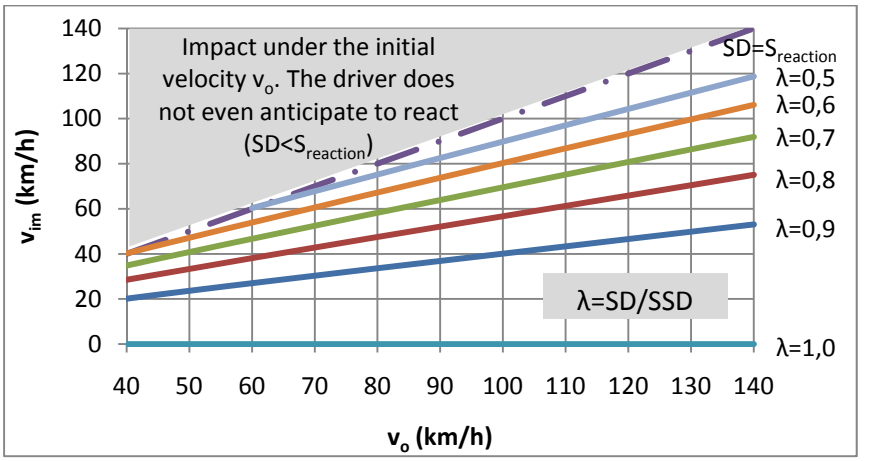

Figure 3. Nomograph for the calculation of impact velocity v_{im} of vehicle in case of highways having zero lengthwise gradient (Pantelidis, 2009b).

The above used definition Hazard x Consequences or otherwise expressed, "probability of an event times the consequences if the event occurs" is that of statistical decision theory. The main objective of the quantitative risk assessment is to illustrate the risk notion by a single mathematical value.

In the present study, the quantification of Risk, Hazard and Consequences is expressed by the Risk Index (RI_n), the Hazard Index (HI) and the Consequences Index (CI_n) respectively, thus:

$$RI_n = HI \times CI_n \quad (8)$$

where, n=1 refers to risk and consequences to travel flow and n=2 to risk and consequences to travelers' safety. The value of RI_n ranges between 1 and 100 as the values of HI and CI_n range between 1 and 10.

Correction of RI_1 value. As mentioned previously, the CI_1 refers to the socioeconomic consequences of a highway geotechnical asset failure, in this respect, a highway embankment failure. These consequences may be associated with disturbance and inconvenience to road users, their lost time (occupational or recreational), the additional travel costs following a detour, the blockade of community etc. Therefore, the greater the time for traffic flow restoration is, the greater the socioeconomic consequences are. The time needed for the complete restoration of traffic flow depends mainly on the readiness and the location of the Maintenance Centre as well as on the amplitude and depth of embankment failure. The time in question is taken into account by the proposed system using the semi-log diagram of Figure 4. This empirical diagram gives the corrected risk index value referring to travel flow ($RI_{1,c}$).

Total Risk Index. Examining the situation as a whole, the highest risk value between the one referring to travel flow (corrected value) and the one referring to travelers' safety is chosen. This value is called Total Risk Index:

$$TRI = \max\{RI_{1,c}, RI_2\} \quad (9)$$

Levels of Overall Alertness Condition and Recommended Actions. Each highway embankment investigated is classified to one of five distinct levels, the Severe, High, Medium, Low and Negligible following Table 4 (the TRI values are rounded to the nearest integer). The recommended actions to be undertaken for the five levels of the Overall Alertness Condition are also given in Table 4.

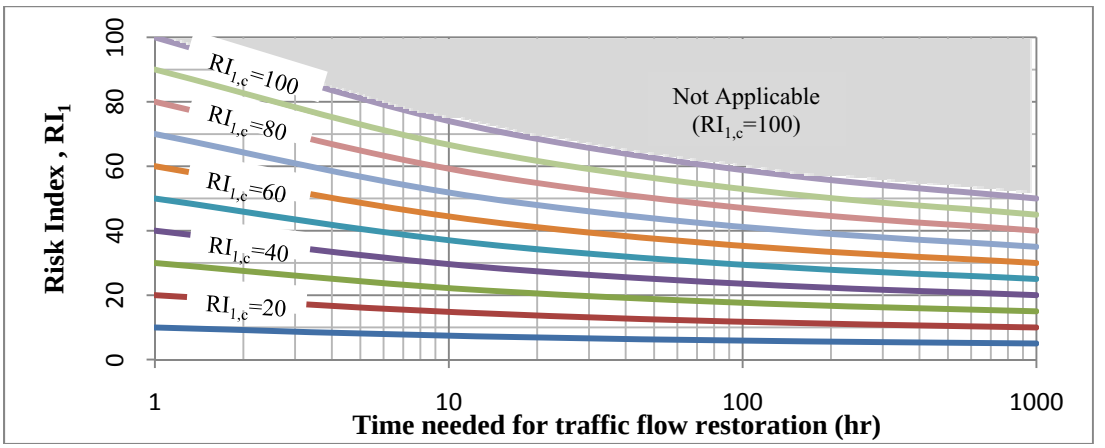

Figure 4. Corrected Risk Index $RI_{1,c}$. The corrected value derives from the RI_1 value and the time needed for traffic flow restoration (estimated value).

Table 4. Recommended Actions by Overall Alertness Condition (OAC).

OAC (TRI)	Recommended Actions
Severe (70-100)	State of immediate action. Stabilization and remedial measures have to be taken at highest priority. Thorough inspection every year after the remedial action.
High (45-69)	State of alert. Remedial action required within two years by order of precedence. Survey every year after the remedial action.
Medium (25-44)	State of vigilance. No immediate action is required. Additional preventive measures after further survey. Survey every two years.
Low (10-24)	State of awareness. No immediate action required. Site inspection and condition assessment every five years.
Negligible (1-9)	State of stability. No immediate or posterior action required.

SUMMARY AND CONCLUDING REMARKS

A landslide risk assessment system referring to highway embankments was the subject of the present paper. The system consists of three main stages, a) the quantification of the failure hazard of highway embankments, b) the calculation of the geometric characteristics of a possible failure and c) the quantification of consequences. The risk value for each embankment examined derives from the failure hazard and consequence value following the well-known definition of risk (Risk = Hazard x Consequences). In the first stage, the normal (drained) condition of embankment expressed by its safety factor, F, is combined with the triggering mechanism factor, f_{TM}. The last is a dimensionless site-specific factor related to the mean and critical precipitation height, such that the system to be adapted to local climatic conditions, as well as to in situ observations relative to the potential for infiltration and drainage of water in and from the embankment mass. In the second stage the amplitude and depth of a possible failure are determined through existing

methods and models; allowing for application in Highway Engineering the proposed system provides an assessment of the failure extent with regard to roadway elements (e.g. roadside area, ditch, lane width). Finally, in the third stage the consequences to traveler's safety are fully distinguished from those to traffic flow. Therefore, there are two risk values, where, the highest corresponds to the actual risk level. Based on the last, an alertness condition is assigned and recommended actions are given. The proposed system is the product of a thorough study of a large number of embankments from the wider area of North and West Greece, which either have failed or not.

ACKNOWLEDGEMENTS

The author wishes to thank Prof. D. Vaughan Griffiths and Prof. Gordon Fenton for their comments and suggestions.

REFERENCES

AASHTO (2004) *A Policy on Geometric Design of Highways and Streets (The Green Book)*, AASHTO, Washington.

Cousins, B. F. (1978). "Stability Charts for Simple Earth Slopes". *J. Geotech. Eng. Div.*, ASCE, 104(GT2), 267-279.

Khalili, N., Tai, K. S. and Fell, R. (1996). "A simplified method for estimating failure induced deformation." *Proc. 7th Intl. Symp. on Landslides*, Balkema, Rotterdam, Trondheim, Norway, 1263-1268.

Pantelidis, L. (2008a). "Stability against translational failure of non-cohesive embankments founded on natural slopes". *Proc. 12th International Association for Computer Methods and Advances in Geomechanics (IACMAG)*, IACMAG, Goa, India, 4645-4651.

Pantelidis, L. (2008b). "Stability of highway embankments constructed on sloping ground against translational failure." *Geomech. Geoeng*., Taylor & Francis, 3(3), 191-197.

Pantelidis, L. (2009a). "Rock slope stability assessment through rock mass classification systems." *Int. J. Rock Mech. Min. Sci*., 46(2), 315-325.

Pantelidis, L. (2009b). "System of quantitative and qualitative assessment of highway geotechnical assets failure hazard and relevant consequences (Title in Greek: Σύστημα ποιοτικής και ποσοτικής αξιολόγησης του κινδύνου αστοχίας γεωκατασκευών οδοποιίας και των συναφών επιπτώσεων)." PhD Thesis, Aristotle University of Thessaloniki, Greece.

Pantelidis, L. (2010a). "An alternative rock mass classification system for rock slopes." *Bull. Eng. Geol. Environ*., Springer, 69(1), 29-39.

Pantelidis, L. (2010b). "Semi-analytical model for the determination of vertical settlement of crest of road embankments founded on sloping ground." *Geomech. Geoeng*., Taylor & Francis, 5(3), 179-186.

Pantelidis, L. (2010c). "A critical review on highway slope instability risk assessment systems." *Bull. Eng. Geol. Environ*., Springer, Advance online publication.

Seismic Risk Assessment and Application in the Central United States

Zhenming Wang[1]

[1)]Kentucky Geological Survey, University of Kentucky, 504 Rose Street, Lexington, Kentucky 40506; PH (859) 323-0564; FAX (859)257-1147; email: zmwang@uky.edu

ABSTRACT

Seismic risk is a somewhat subjective, but important, concept in earthquake engineering and other related decision-making. Another important concept that is closely related to seismic risk is seismic hazard. Although seismic hazard and seismic risk have often been used interchangeably, they are fundamentally different: seismic hazard describes the *natural phenomenon* or *physical property* of an earthquake, whereas seismic risk describes the *probability* of loss or damage that could be caused by a seismic hazard. The distinction between seismic hazard and seismic risk is of practical significance because measures for seismic hazard mitigation may differ from those for seismic risk reduction. Seismic risk assessment is a complicated process and starts with seismic hazard assessment. Although probabilistic seismic hazard analysis (PSHA) is the most widely used method for seismic hazard assessment, recent studies have found that PSHA is not scientifically valid. Use of PSHA will lead to (1) artifact estimates of seismic risk, (2) misleading use of the annual probability of exccedance (i.e., the probability of exceedance in one year) as a frequency (per year), and (3) numerical creation of extremely high ground motion. An alternative approach, which is similar to those used for flood and wind hazard assessments, has been proposed.

INTRODUCTION

Dealing with uncertainty is a way of life, and there is always a certain degree of uncertainty when any decision is made. The world is full of uncertainties, ranging from climate change, to erratic financial markets, to natural disasters, to terror attacks, to personal health, to the most fundamental measurements of all: *time* and *space*. Risk is one of the most important considerations in everyday decision-making. Definitions and uses of risk are widely inconsistent and ambiguous throughout the world, however (Holton, 2004). For example, in financial terms, risk is often referred to as the unexpected variability or volatility of returns, including both worse-than-expected as well as better-than-expected returns. In occupational health, risk is defined as a combination of the likelihood of an occurrence of a hazardous event or exposure and the severity of injury or ill health that can be caused by the event or exposure. In statistics, risk is often defined as the probability of an undesirable event. Thus, risk is somewhat subjective and varies from profession to profession or user to user.

Risk assessment or quantification is a complicated process, ranging from pure subjective indexing, to empirical analysis, to semiempirical analysis, to pure statistical analysis. This can be seen in a global risk network report, “Global Risks 2007” by World Economic Forum (2007), which listed 23 core global risks that were

assessed by different organizations with different methods. The most common way to report results from a risk assessment is in terms of economic or human impacts.

The U.S. Army Corps of Engineers applied a portfolio risk analysis to identify risks posed by geohazards (floods, earthquakes, seepage, and others) on the dams along the Ohio River (Schaefer, 2006). According to this analysis, risk in terms of relative expected loss per year can be quantified as

$$R = HP_f P_b XL, \quad (1)$$

where H is the hazard (flood, earthquake, seepage, and others) in events per year, P_f is the conditional failure probability per hazard (event), P_b is the conditional breach probability per failure, X is the exposure (population or property), and L is loss (lives or dollasr) rate for the exposed population or property, respectively. The product of X and L is also called the consequence of the breach and exposure (people or property). The results showed that seepage poses the greatest risk to dams along the Ohio River (Schaefer, 2006).

Although risk assessment is complicated, it always starts with hazard assessment. The same is true for seismic risk. This paper will focus on the definitions and uses of seismic risk in earthquake science and engineering.

SEISMIC RISK ASSESSMENT

In order to better define and assess seismic risk, we first need to explore the basic concept of seismic risk as well as seismic hazard. Seismic risk is defined as "the probability that some humans will incur loss or that their built environment will be damaged" (McGuire, 2004, p. 8). Seismic hazard is defined as "a property of an earthquake that can cause damage and loss" (McGuire, 2004, p. 7). In other words, seismic risk describes the *probability* of loss or damage that could be caused by a seismic hazard, whereas seismic hazard describes the *natural phenomenon* or *property* of an earthquake (Scawthorn, 2008). Thus, seismic hazard and seismic risk are two fundamentally different concepts (Wang, 2009). This is illustrated in Figure 1, which shows massive landslides and rockfalls (seismic hazards) triggered by the Wenchuan earthquake and its aftershocks.

As shown in Figure 1, the driver and pedestrians (i.e., exposures), who were exposed to and vulnerable to the hazards, were taking a risk (probability) of an adverse consequence: being struck by a rockfall. Thus, seismic risk is a probable outcome (or consequence) from interaction (Φ) between a seismic hazard and exposure. Therefore, in qualitative terms, seismic risk can be expressed as

$$\textit{Seismic risk} = \textit{Seismic hazard } \Phi \textit{ Exposure}. \quad (2)$$

This conceptual (qualitative) relationship demonstrates that seismic hazard is a critical component of seismic risk: there is no seismic risk if there is no seismic hazard. But high seismic hazard does not necessary mean high seismic risk. This conceptual relationship also demonstrates that engineering design for seismic hazard mitigation may be different from design for seismic risk reduction. Seismic hazard may or may not be mitigated, but seismic risk can always be reduced by either mitigating seismic hazard, reducing exposure, or both. For example, earthquake fault rupture cannot be mitigated, but liquefaction can be mitigated by engineering measures. As shown in Figure 1, seismic hazard (rockfalls) may not be able to be

mitigated, but seismic risk can always be reduced by either mitigating seismic hazard (i.e., building barriers or other measures), reducing exposure (i.e., limiting traffic or pedestrians), or both. There will be no risk if the driver decides not to drive or pedestrians decide not to walk on the road (i.e., no exposure).

Figure 1. Seismic risk and hazard. Seismic hazard: rockfall triggered by an earthquake. Exposures: car, driver, and pedestrians. Consequence: struck by a rockfall. Seismic risk: the probability of being struck by a rockfall (adverse consequence) during the period that the car or pedestrians pass through the road section.

Quantitatively, seismic risk assessment is complicated and somewhat subjective because it not only depends on the desired measurement of consequence (i.e., outcome of physical interaction between seismic hazard and exposure), but also on how the hazard and exposure interact in *time* and *space*. The hazard and exposure might interact at a specific site (site-specific risk) or over an area (aggregate risk). In order to quantify seismic risk, a distribution or model must be assumed to describe how the hazard and exposure interact in time. For example, several models, such as the Poisson, empirical, Brownian passage time, and time-predictable, have been used to describe earthquake occurrence in time. Although the Poisson model may not be applicable, it is the most commonly used in seismic risk estimations (Cornell, 1968; Milne and Davenport, 1969; Wang, 2009, 2011). Assuming a Poisson distribution for earthquake occurrence in time, seismic risk, expressed in terms of a probability of ground motion exceeding a specified level (y) at least once during a period t (in years) for a given exposure at a site, can be estimated by

$$P_y[Y \geq y] = 1 - e^{-\frac{t}{\tau}}, \tag{3}$$

where τ is the average recurrence interval of the ground motion exceeding y. The relationship between ground motion y and average recurrence interval τ or frequency ($1/\tau$) is determined from a seismic hazard assessment, such as probabilistic seismic hazard analysis (PSHA), which will be discussed in detail in the next section.

Equation (3) can be used to estimate seismic risk for the car and pedestrians shown in Figure 1 if the rockfall occurrences follow a Poisson distribution. If the rockfall hazard is quantified as a mean diameter of 0.25 m or greater with an average occurrence frequency of once every hour along that section of the road, the risk for a car that take 3 minutes to pass through that section of the road is about a 5 percent probability of being struck by the rockfall; the risk is about a 28 percent probability for pedestrians who take 20 minutes to pass through the road section. Furthermore, pedestrians will almost certainly be killed if they are struck by a rockfall of 0.25 m or greater diameter, but the driver of a car might not be killed if the car is struck by a similar rockfall because the body of the car could protect the driver. If we assume that pedestrians will surely be killed (100 percent chance) when they are struck by the rockfall and there is about a 25 percent chance that a driver will be killed if a car is struck by the rockfall, the risk of being killed is about 28 percent for pedestrians and only about 1.25 percent for the driver of a car. Thus, seismic risk in terms of an exceedance probability of fatality can be expressed as

$$P_f = P_r[D_r \geq 0.25m] \cdot P_f[F|0.25m], \quad (4)$$

where $P_r[D_r \geq 0.25\text{m}]$ is the exceedance probability calculated from equation (3), and $P_f[F|0.25\text{m}]$ is the conditional fatality probability when $D_r \geq 0.25\text{m}$ occurs. The conditional fatality probability is obtained from fragility analysis, which is used to determine a relationship between the probability of a damage state and a hazard level: the so-called fragility curve (Scawthorn, 2008). Fragility curves for building damage or economic loss and ground motion are obtained from structural engineering analysis (Kircher and others, 1997). Thus, equation (4) can be used to estimate seismic risk in terms of a probability of building damage, economic loss, or other measures.

SEISMIC HAZARD ASSESSMENT

As previously discussed, seismic hazard is a key component in seismic risk assessment. The aim of a seismic hazard assessment is to quantify three parameters: level of ground motion or other measure, its spatial and temporal measurements, and associated uncertainties at a site of interest (Cornell, 1968; Wang, 2009, 2011). Many approaches have been used, but currently the most widely used approach is probabilistic seismic hazard analysis (PSHA).

Probabilistic Seismic Hazard Analysis (PSHA)

The basic concepts and formulations of PSHA were developed by Cornell (1968). Later, with the development of computers and software, PSHA gained wide acceptance as a computer model for seismic hazard assessment. Although PSHA has become a standard model for seismic hazard assessment in the United States, there have always been some serious concerns and problems associated with it. In 1988, the National Research Council organized a panel to review PSHA in response to concerns and problems raised from several studies, particularly those by the Lawrence Livermore National Lab and the Electric Power Research Institute in the early 1980's. The National Research Council panel identified many issues with PSHA, particularly in how to capture earth science information. The panel found that "because the 'aggregated' results of PSHA are not always easily related to the inputs, PSHA may

also obscure the unknown and uncertainties of earth sciences data and may lead to an unwarranted sense of accuracy in the value" (National Research Council, 1988, p. 5). The obscured unknowns and uncertainties of earthquake science in PSHA led to large differences in and disagreements on hazard estimates among practitioners and experts. This led to another review of PSHA by the Senior Seismic Hazard Analysis Committee (SSHAC), commissioned by the U.S. Nuclear Regulatory Commission, the U.S. Department of Energy, and the Electric Power Research Institute in 1997. The committee concluded that "many of the major potential pitfalls on executing a successful PSHA are procedural rather than technical in character" (SSHAC, 1997, p. xiv). This conclusion led to the establishment of procedural guidelines for executing a PSHA: the SSHAC-97 guidelines.

Thus, the serious concerns and problems with PSHA have never been addressed or resolved technically by either the National Research Council (1988) or SSHAC (1997). The concerns and problems were exemplified by the Yucca Mountain project (Stepp and others, 2001), which is the most comprehensive PSHA study ever executed in the United States according to the SSHAC-97 guidelines. This study resulted in an extremely high ground-motion estimate at the Yucca Mountain nuclear waste repository: about 10g PGA. This extreme estimate was not consistent with the precarious balanced rocks observed near the site (Brune and Whitney, 2000) and triggered widely debate and discussions among PSHA practitioners, seismologists, and engineers. It was concluded that the ground motion was overestimated for the Yucca Mountain project (Abrahamson and Hanks, 2008). Therefore, the most comprehensive PSHA study ever undertaken did not result in appropriate seismic hazard estimate. It is clear that there are some intrinsic problems with PSHA.

As stated by McGuire (2008), PSHA is a mathematical formulation derived from a rigorous probability analysis of distributions of earthquake magnitudes, locations, and ground-motion attenuation. Studies have shown that some of the assumptions and preconditions that PSHA is based on are not valid in seismology, however (Anderson and Brune, 1999; Wang, 2006, 2011; Wang and Zhou, 2007). Furthermore, as derived by Cornell (1968), PSHA calculates the annual probability of exceedance (i.e., exceedance probability in ONE year [t=1 year]) for a given ground-motion level from the "total probability theorem":

$$P[Y \geq y] \approx \sum v_i t\,(1\,year) \iint P[Y \geq y \,|\, M, R] f_{M,R}(m,r)\,dmdr\,, \qquad (5)$$

where Y and y are earthquake ground motions, M and m are magnitudes, R and r are distance, v_i is the rate (*per year*) of earthquakes for source i, $P[Y \geq y|M,R]$ is the conditional exceedance probability, and $f_{M,R}(m,r)$ is the probability density function (PDF), respectively. The summation is over all sources. But equation (5) has been commonly written in PSHA (McGuire, 2004, 2008) by omitting the precondition of t=1 *year* as

$$P[Y \geq y] \approx \sum v_i \iint P[Y \geq y \,|\, M, R] f_{M,R}(m,r)\,dmdr \qquad (6)$$

Thus, the annual probability of exceedance is the exceedance probability in ONE year (i.e., t=1 year) and a dimensionless quantity. Unfortunately, the annual probability of exceedance has erroneously been interpreted and used as the annual exceedence frequency or rate and a dimensional quantity with the unit of per year in PSHA

(Cornell, 1968; McGuire, 2004, 2008; Scawthorn, 2008; Petersen and others, 2008). This unfortunate error has made the risk (i.e., the probability of ground motion as defined by Cornell [1968]) becoming the hazard (i.e., the frequency [per year] of ground motion) (Scawthorn, 2008).

Therefore, PSHA is scientifically invalid. Use of PSHA becomes a pure computer model without sound physical and mathematical bases. Furthermore, seismic risks calculated from PSHA, such as the ground motions with 10, 5, and 2 percent probabilities of exccedance in 50 years (Petersen and others, 2008) and the building's collapse risks (Luco and others, 2007), are all artifacts.

Alternative Approaches

Similar to curves produced in flood and wind hazard analysis, a seismic hazard curve in terms of a ground motion and its exceedance frequency at a site can be constructed from the earthquake catalog, fault locations, and ground-motion attenuation relationships (Milne and Davenport, 1969; Wang, 2006, 2011). The relationship between the exceedance frequency f_y (per year) and ground motion y at a site takes the following form:

$$\ln(f_y) = a + b\ln(y), \tag{7}$$

where a and b are constants and determined from curve-fitting, such as the least-squares method. By applying equation (7) to input data from the 2008 national seismic hazard maps (Petersen and others, 2008), seismic hazard curves can be obtained (Fig. 2). Figure 2 shows the PGA hazard curves with different confidence (uncertainty) levels for Paducah, Ky.

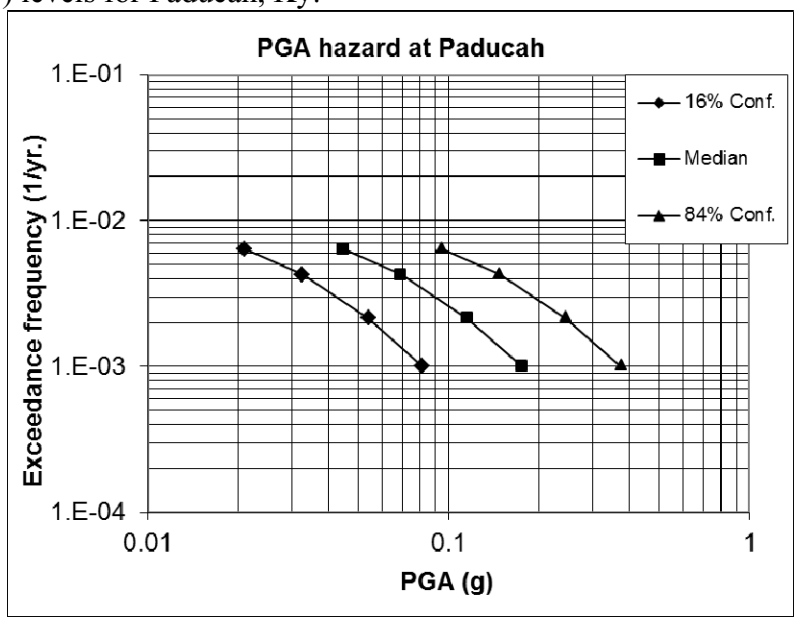

Figure 2. PGA hazard curves at Paducah, Ky.

The curves shown in Figure 2 are similar to the flood hazard curve derived from a flood hazard analysis and can be used to estimate seismic risk in a similar way (Wang and Ormsbee, 2005). As shown in Figure 2, a median PGA of 0.17g with an exceedance frequency of 0.001 (1/yr) could be expected in Paducah, Ky. According

to equation (3), the risk in terms of a probability of exceeding the median (50 % confidence) PGA of 0.17g in 50 years will be about 5 percent in Paducah. If a building's fragility is known, the risk in terms of exceedance probability that the building could be damaged can be estimated from equation (4). For example, if a building has a 50 percent probability of collapse when the building experiences a PGA of 0.17g, then the collapse risk for the building will be 2.5 percent (5% x 50 %) in 50 years.

CONCLUSIONS

Although seismic hazard and seismic risk have often been used interchangeably, they are fundamentally different. Seismic hazard is a natural phenomenon, such as ground shaking, fault rupture, or soil liquefaction, that is generated by an earthquake, whereas seismic risk is the probability that humans will incur loss or their built environment will be damaged if they are exposed to a seismic hazard. The differences between seismic hazard and seismic risk are of practical significance in earthquake engineering and other related decision-making because measures for seismic hazard mitigation may differ from those for seismic risk reduction. Seismic risk is quantified through a complicated process – seismic risk assessment which starts with seismic hazard assessment.

In a way similar to flood and wind hazard assessment, seismic hazard is assessed from instrumental, historical, and geological observations. In other words, seismic hazard is assessed from earth science. Although PSHA is the most widely used method for seismic hazard assessment, its results are not consistent with observations. For example, the extremely high ground motion (10g PGA or greater) derived from the PSHA study at the Yucca Mountain nuclear waste repository is not consistent with the precarious balanced rocks observed near the site. Studies have also shown that the mathematical formulation of PSHA is not valid and that annual probability of exceedance is a dimensionless quantity, but has been erroneously interpreted and used as an exceedance frequency (per year). Resulting seismic risk estimates from PSHA, such the ground motions with 2, 5, and 10 percent probabilities in 50 years, are all artifacts. An alternative approach, which is similar to flood and wind hazard analysis, provides consistent results that can be used directly in seismic risk assessment.

ACKNOWLEDGEMENTS

I thank Meg Smath of the Kentucky Geological Survey for editorial help. I appreciate the comments and suggestions from two unanimous reviewers, which help to improve the manuscript greatly.

REFERENCES

Abrahamson, N.A., and Hanks, T.C. (2008). "Points in hazard space: A new view of PSHA." *Seismological Research Letters*, **79**, 285.

Anderson, J.G., and Brune, J.N. (1999). "Probabilistic seismic hazard analysis without the ergodic assumption." *Seismological Research Letters*, **70**, 19–28.

Brune, J. N., and Whitney J.W. (2000). "Precarious rocks and seismic shaking at Yucca Mountain, Nevada." *USGS Digital Data Series*, **058**, Chapter M, 19p.

Cornell, C.A. (1968). "Engineering seismic risk analysis." *Bulletin of the Seismological Society of America*, **58**, 1583–1606.

Holton, G.A. (2004). "Defining risk." *Financial Analysts Journal*, **60**, 19–24.

Kircher, C.A., Nassar, A.A., Kustu, O., and Holmes, W.T. (1997). "Development of building damage functions for earthquake loss estimation." *Earthquake Spectra*, **13**, 663–682.

Luco, N., Ellingwood, B.R, Hamburger, R.O., Hooper, J.D., Kimball, J.K., and Kircher, C.A. (2007). "Risk-targeted versus current seismic design maps for the conterminous United States." *SEAOC 2007 Convention Proceedings*, 163–171.

McGuire, R.K. (2004). "Seismic hazard and risk analysis." Earthquake Engineering Research Institute, MNO-10, 240 p.

McGuire, R.K. (2008). "Probabilistic seismic hazard analysis: Early history." *Earthquake Engineering and Structural Dynamics.* **37,** 329–338.

Milne, W.G., and Davenport, A.G. (1969). "Distribution of earthquake risk in Canada." *Bulletin of the Seismological Society of America*, **59**, 729–754.

National Research Council. (1988). "Probabilistic seismic hazard analysis." Report of the Panel on Seismic Hazard Analysis: Washington, D.C., National Academy Press, 97 p.

Petersen, M.D., Frankel, A.D., Harmsen, S.C., Mueller, C.S., Haller, K.M., Wheeler, R.L., Wesson, R.L., Zeng, Y., Boyd, O.S., Perkins, D.M., Luco, N., Field, E.H., Wills, C.J., and Rukstales, K.S. (2008). "Documentation for the 2008 update of the United States national seismic hazard maps." *U.S. Geological Survey Open-File Report* 08-1128, 60 p.

Scawthorn, C. (2008). "A brief history of seismic risk assessment." *Risk Assessment, Modeling and Decision Support Risk, Governance and Society*, **14**, 5–81.

Schaefer, J. (2006). "Dam safety portfolio risk assessment." 6th Annual Technical Forum, Geohazards in Transportation in the Appalachian Region, August 2–3, 2006, Lexington, Ky.

Senior Seismic Hazard Analysis Committee (1997). "Recommendations for probabilistic seismic hazard analysis: Guidance on uncertainty and use of experts." Lawrence Livermore National Laboratory, NUREG/CR-6372, 81 p.

Stepp, J.C., Wong, I., Whitney, J., Quittmeyer, R., Abrahamson, N., Toro, G., Youngs, R., Coppersmith, K., Savy, J., Sullivan, T., and Yucca Mountain PSHA project members (2001). "Probabilistic seismic hazard analysis for ground motions and fault displacements at Yucca Mountain, Nevada." *Earthquake Spectra*, 17, 113–151.

Wang, Z. (2006). "Understanding seismic hazard and risk assessments: An example in the New Madrid Seismic Zone of the central United States." Proceedings of the 8th National Conference on Earthquake Engineering, April 18–22, 2006, San Francisco, Calif., Paper 416.

Wang, Z. (2009). "Seismic hazard vs. seismic risk." *Seismological Research Letters*, **80**, 673–674.

Wang, Z. (2011). "Seismic hazard assessment: Issues and alternatives." *Pure and Applied Geophysics*, **168**, 11–25.

Wang, Z. and Ormsbee, L. (2005). "Comparison between probabilistic seismic hazard analysis and flood frequency analysis." *EOS, Trans., AGU*, **86**, 45, 51–52.

Wang, Z., and Zhou, M. (2007). "Comment on 'Why do modern probabilistic seismic hazard analyses often lead to increased hazard estimates?' by Julian J. Bommer and Norman A. Abrahamson." *Bulletin of the Seismological Society of America*, 97**,** 2212–2214.

World Economic Forum (2007). "Global risks 2007." Cologne/Geneva, Switzerland, 34 p.

Implicit Expression Solution of Slope Reliability on Kinematical Element Method and Response Surface Method

Ping Cao[1] and Ke Zhang[2]

[1]School of Resources and Safety Engineering, Central South University, Changsha, Hunan, 410083, China; PH (+86) 0731-88879263; FAX (+86) 0731-88879612; email: pcao_csu@sina.com
[2]School of Resources and Safety Engineering, Central South University, Changsha, Hunan, 410083, China; PH (+86) 0731-88879263; FAX (+86) 0731-88879612; email: zhangke_csu@163.com

ABSTRACT

Kinematical element method is an advanced slope limit analysis technology with strict mechanical and mathematical basis, so calculation accuracy is higher than other methods. Considering slope reliability analysis of kinematical element method with implicit expression function, an improved method for calculating reliability which combines response surface method is presented. Kinematical element method is adopted to compute experimental points instead of traditional finite element method, which overcomes the disadvantage of time-consuming. Quadratic polynomial function is established to approximate response surface function. And first-order second-moment method is used to calculate the reliability index of response surface function. Engineering examples are analyzed with the method, the results are compared with limit equilibrium method and FEM. The effectiveness of the proposed method is proved. At last the effect of groundwater and blasting on reliability index and safety factor is discussed.

INTRODUCTION

Traditional method of slope stability analysis is based on determination model. However, a number of experiments and engineering examples show that the geotechnical conditions and parameters of slope are uncertain obviously. So it is more scientific and efficient to use analytical method combined with probability theory and determination method on slope stability study.

The establishment of the limit state equations in slope reliability analysis is expressed by calculating factor of safety. Fellenius method can construct explicit limit state equation directly. We can find the solution with analytical method and generally use the first-order second-moment method. As for other limit equilibrium method and numerical simulation method, limit state equation is expressed by implicit function and analytical method is required to calculate the derivative of function. So it is difficult to calculate it with analytical method. Response surface method (RSM) can solve the problem conveniently. Wong (Wong 1985) first applied this method to slope reliability analysis. And his research shows that the relative difference between the result of response surface method and the accurate result of direct monte carlo simulation technique ranges from 1% to 9%. Numerical

simulation technology, such as FEM and FLAC, is usually adopted to construct the response function (Wong 1985, Xu 2006, Sung 2009). But numerical simulation technology has a problem of wasting time. So some researchers (Xu 2006) combined response surface method with limit equilibrium method (Janbu, Spencer, Morgenstern, Sarma method) to calculate the reliability index. Limit equilibrium method makes some hypothesis for changing hyperstatic problem into static problem, so the calculation result is not strict.

To overcome the disadvantages of numerical simulation technology and limit equilibrium methods, Kinematical Element Method (KEM) is adopted to calculate the factor of safety. Kinematical element method is presented by Peter Gussman in 1982 (Gussmann 1982), and the method has a strict mechanical and mathematical basis. Assumptions errors about geometric shape of slip surface and forced form on soil slices could be eliminated. So calculation accuracy is higher than other methods.

PRINCIPLE OF KINEMATICAL ELEMENT METHOD

The theory system of KEM contains kinematics analysis, static analysis and optimization (Gussmann 1982, Gussmann 1992). Initial plastic sliding zone is approximately assumed, and divided into several sliding block elements called kinematical element. The relationship between normal stress and shear stress on slip velocity boundary condition should satisfy Mohr-Coulomb criterion.

According to the compatibility condition of movement for elements, we can obtain the following kinematics equations,

$$[K]\{V\}+\{\hat{V}\}=0 \tag{1}$$

where $[K]$ represents kinematics coefficient matrix, $\{V\}$ represents the vector of unknown displacements of elements, $\{\hat{V}\}$ represents the known displacements vector on flexible boundary.

After solving the above equations, determine directions of relative movement of elements, thus obtaining direction of tangential force applied on the element.

Then the static equilibrium equations of every element are established, and normal force applied on the element is taken as unknown quantity,

$$[K_S]\{N\}+\{F\}=0 \tag{2}$$

where $[K_S]$ represents static coefficient matrix, $\{N\}$ represents the vector of unknown norm stress on the element, $\{F\}$ represents the vector of known forces related to the body force, water pressure and cohesion.

Factor of safety is obtained by employing iteration process after solving the static equations. After that, the object function is selected as factor of safety, and the coordinates of nodes are selected as variables. And then, optimization Algorithm is used to search the true plastic zone and critical slip surface. Readers can consult literature (Gussmann 1982, Gussmann 1992, Cao and Gussmann 1999) for the detail of KEM.

RELIABILITY SOLUTION USING RESPONSE SURFACE METHOD

Response surface method. The basic principle of response surface method (RSM) is to fit performance function with approximate response surface function through designing a series of experimental points, especially around the checking point (Box and Wilson 1954, Wong 1985, Bucher 1990). Taking both accuracy and efficiency of calculation results into consideration, quadratic polynomial equation without cross terms which suggested by Bucher and Bourgund (Bucher and Bourgund 1990) is adopted.

$$g(X) \approx \hat{g}(X) = a + \sum_{i=1}^{n} b_i X_i + \sum_{i=1}^{n} c_i X_i^2 \tag{3}$$

where, a, b_i and c_i represent undetermined coefficients. n represents the number of variables.

According to the above formula, approximate explicit function with factor of safety can be expressed as follows,

$$F_S \approx a + \sum_{i=1}^{n} b_i X_i + \sum_{i=1}^{n} c_i X_i^2 \tag{4}$$

Performance function for slope stability is defined as,

$$g(X) = F_S - 1 = a + \sum_{i=1}^{n} b_i X_i + \sum_{i=1}^{n} c_i X_i^2 - 1 \tag{5}$$

Solution procedure. The reliability solution procedure is shown as follows,

Step 1. Select initial samples $X^{(1)} = (x_1^{(1)}, x_2^{(1)}, \cdots, x_n^{(1)})$, mean value point is generally chosen, i.e., $X^{(1)} = (\mu_{x1}, \mu_{x2}, \cdots, \mu_{xn})$.

Step 2. Evaluate (2n+1) values of performance function by KEM, i.e., $g(x_1^{(1)}, x_2^{(1)}, \cdots, x_n^{(1)})$ and $g(x_1^{(1)}, x_2^{(1)}, \cdots, x_i^{(1)} \pm f\sigma_i, \cdots, x_n^{(1)})$, where, coefficient f is taken as 3 for the first iteration and as 1 for the other iterations.

Step 3. According to (2n+1) values obtained in step 2, determine coefficients a, b_i, c_i by solving the equations (5). Thus, response surface function is established.

Step 4. Calculate the reliability index $\beta^{(k)}$ and corresponding checking point $X^{*(k)}$ of response surface function by first-order second-moment method, where k denotes the number of iteration.

Step 5. Check whether $\left|\beta^{(k)} - \beta^{(k-1)}\right| < \varepsilon$ meets accuracy requirement. If it does, then finish the iterations. Otherwise, new iteration point is obtained by interpolation,

$$X_M = \mu_{X_i} + \frac{g(\mu_{X_i})}{g(\mu_{X_i}) - g(X^*)}(X^* - \mu_{X_i}) \tag{6}$$

go back to step 2 until the reliability index is converged.

EXAMPLE ANALYSES

Example 1: Malkawi slope. The first example shown in Figure 1 is taken from literature (Malkawi 2000). The reliability index of the embankment was calculated by Malkawi using first-order second-moment method (FOSM) and Monte Carlo simulation method (MCSM). The calculating parameters subject to the normal

distribution and the mean soil parameters $c = 10\text{kPa}$, $\varphi = 10°$, $\gamma = 17.64\text{kN/m}^3$, and the coefficients of variation are 0.10, 0.05 and 0.01, for cohesion, friction angle, and the unit weight respectively. In literature (Malkawi 2000), four slope stability methods, which are Fellenius, Bishop, Janbu, and Spencer's methods, were employed to establish the limit state function. Tan (Tan 2005) also studied this slope by finite element method of small and large deformation. As is shown in Figure 1, the mean factor of safety calculated by KEM lies between ones calculated by FEM of small deformation and large deformation, and is appreciably higher than limit equilibrium methods, but the relative difference is less than 10%. The time of KEM for calculating safety factor is about 1.5s, which has fast computational speed.

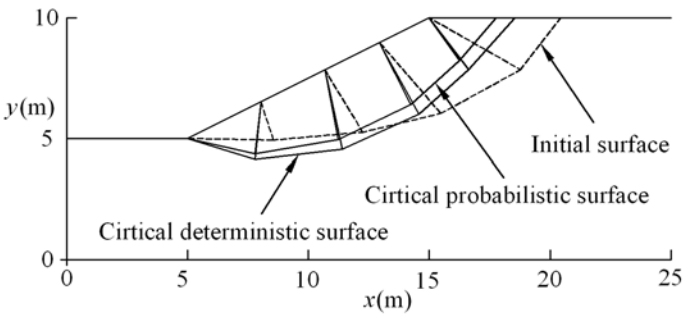

Figure 1. Cross-section and results for example 1.

According to the computing results of Malkawi, good agreement between FOSM and MCSM was achieved, except Spencer's method. Malkawi explained that the deviation was attributed to the errors on evaluating derivatives for the nonlinear formulation of safety factor. It is more difficult to calculate derivative for the complexity of KEM. For the reasons above, response surface method is used in this paper with no need of modifying original KEM program. The reliability index calculated by KEM of this paper is close to those by FEM in literature (Tan 2005). It is also found that there may be different from the critical deterministic surface and critical probabilistic surface in Figure 1.

Table 1. Comparison of results for reliability index of example 1.

Authors	Method	Factor of safety	Reliability index		
			FOSM	MCSM	RSM
Malkawi	Fellenius	1.28	3.5	3.5	/
	Bishop simplified	1.36	4.3	4.3	/
	Janbu simplified	1.31	3.6	3.0	/
	Spencer	1.29	3.5	5.5	/
Tan	FEM (small deformation)	1.46	4.55	/	/
	FEM (large deformation)	1.39	4.77	/	/
This paper	KEM	1.42	/	/	4.48

Example 2: Open pit slope of Jiagou aluminum mine. Section 8 of Jiagou aluminum mining slope is selected to study, which is shown in Figure 2. Upper part of the slope includes loess and clay, which easily leads to landslide. We sampled in

Mining Area, and tested physical and mechanical parameters. The mean soil parameters $\gamma = 18.25\text{kN/m}^3$, $c = 39\text{kPa}$, $\varphi = 22.4°$, and the standard deviations are 0.30, 3.83 and 1.33 for the unit weight, cohesion, and friction angle respectively. All random variables are characterized by normal distribution.

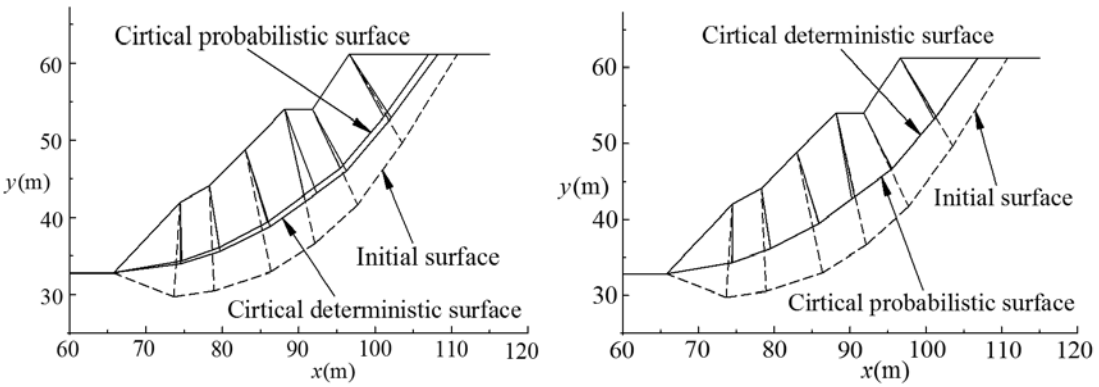

(a) General condition (b) Rich in water

Figure 2. Cross-section and calculation results for example 2.

General soil condition and soil condition which is rich in water are both considered. According to the relationship between water content and soil strength, the value of cohesion is reduced by 30%, and the value of friction angle is reduced by 10% under soil condition rich in water.

Table 2. Calculation results for example 2.

Condition	Reliability index	Probability of failure	Factor of safety
General condition	3.44	2.9×10^{-4}	1.244
Rich in water	-0.058	5.23×10^{-1}	0.996

Example 3: Open pit slope of Yongping copper mine. Take section 1-1 of Yongping copper mining slope as example. The slope height is 348m, and overall slope angle is $38.9°$. Eluvial-slope wash on the upper part has been stripped and the slope, which has no large surface active faults, is mainly made up of migmatite. We measured the shear strength by INSTRON 1346 electro-hydraulic servo tester. The mean rock parameter (from typical rock sample) $\gamma = 27\text{kN/m}^3$, $c = 590\text{kPa}$, $\varphi = 46.73°$, and the standard deviations are 1.80, 98.67 and 3.89 for the unit weight, cohesion, and friction angle respectively. All random variables are characterized by normal distribution. Through the result by KEM, the factor of safety is 1.899 and reliability index is 5.79 under natural self-weight condition. But taking the influence of underground water into account, the factor of safety is 1.586 and reliability index is 4.51.

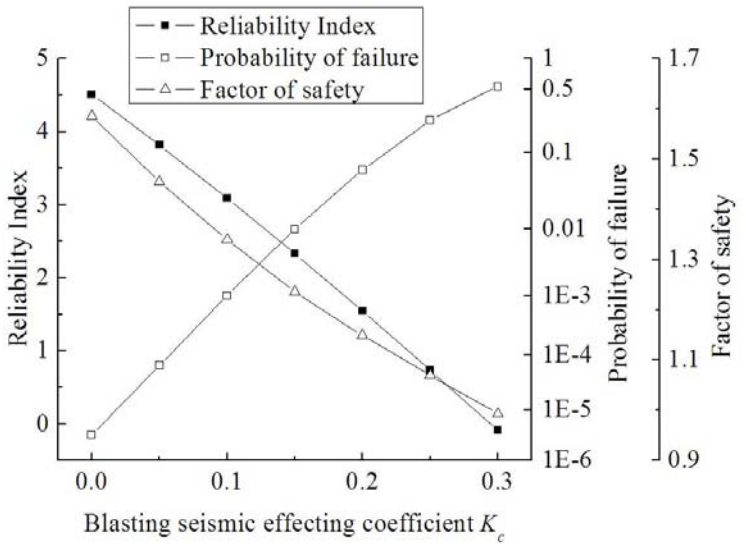

Figure 3. The influence of blasting to the stability of slope.

Excavation blasting is common in modern surface mining. Blasting load caused by blasting is one of main influence factors to slope stability in open pit mine. This paper mainly studies the effect of blasting on reliability index and minimum safety factor, with different blasting seismic effecting coefficient K_c considered. According to Figure 3, the factor of safety and reliability index decrease and the probability of failure increases as K_c increases. The relationship between K_c and reliability index is linear. Nonlinear relation is obtained between K_c and factor of safety, so as to probability of failure. When K_c exceeds 0.15, growth of probability of failure is remarkable. And when K_c=0.15, probability of failure is 9.9×10^{-3}, which is close to the acceptable failure probability (10×10^{-3} is taken as acceptable failure probability for this slope). Thus, slope in this state can be considered as a critical state. It's worth pointing out that when factor of safety is 1.236, the state of slope is considered as steady with traditional method. But for high discreteness of cohesion of this slope, it's more scientific to use reliability analysis approach.

For reference to on-site blast vibration monitoring data of Yongping copper mine, empirical formula about blasting seismic effecting coefficient K_c , explosive weight Q (the maximum explosive weight is used during segment blast) and distance R is expressed as follows,

$$K_c = \beta \cdot a/g \tag{7}$$

where, β, as the reduction coefficient of blasting dynamics, is taken as 0.175. a represents vibration acceleration, i.e., $a = 4587\left(\frac{\sqrt[3]{Q}}{R}\right)^{1.8}$.

According to the critical blasting seismic effecting coefficient, we can obtain the relationship between safety blasting distance R and explosive weight Q, i.e., and that is $R \geq 2.566 * \sqrt[3]{Q}$, which is shown in Figure 4. This formula provides practical guidance for the project production blasting.

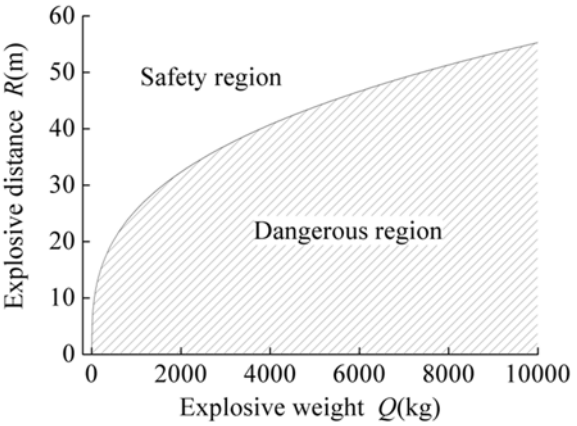

Figure 4. The relationship between explosive weight and distance.

CONCLUSIONS

In this paper, a new approach of slope reliability analysis, which combines with KEM and response surface method, is presented. Example application indicates that factor of safety and reliability index calculated by KEM is similar with those of limit equilibrium method, and are more close to those of FEM. There may be great difference between the cirtical deterministic surface and cirtical probabilistic surface. And the method of reliability analysis proposed by this paper can be widely used in the geotechnical engineering.

Groundwater and blasting has a large influence on the stability of slope. For Jiagou aluminum mining slope, soil weakening by water will cause landslide easily. For Yongping copper mining slope, The relationship between blasting seismic effecting coefficient and reliability index is linear. Nonlinear relation is obtained between blasting seismic effecting coefficient and factor of safety, so as to probability of failure. We could determine the critical blasting seismic effecting coefficient and critical factor of safety considering failure probability. After that, formula about safety blasting distance and explosive weight is presented. It is more scientific to evaluate the stability of slope when combining both probability theory and determination method.

REFERENCES

Box, G. E. P., and Wilson, K. B. (1954). "The exploration and exploitation of response surfaces: Some general considerations and examples." *Biometrics*, 10(1), 16-60.

Bucher, C. G., and Bourgund, U. (1990). "A fast and efficient response surface approach for structural reliability problems." *Structural Safe*, 7, 57-66.

Cao, P., and Gussmann, P. (1999). "Kinematical element method and slope stability analysis." *Chinese Journal of Rock Mechanics and Engineering*, 18(6), 663-666.

Gussmann, P. (1982). "Kinematical elements for soils and rocks." *Proc. 4th Int. Conf. on Num. Mech. in Geomech.*, Edmonton, 47-52.

Gussmann, P. (1992). "Die methode der kinem atischen element and adaptive optimierung." *Bauingenieur*, (67), 409-417.

Malkawi, A. I. H., Hassan, W. F., and Abdulla, F. A. (2000). "Uncertainty and reliability analysis applied to slope stability". *Structural Safety*, 22, 161-187.

Sung Eun Cho. (2009). "Probabilistic stability analyses of slopes using the ANN-based response surface." *Computers and Geotechnics*, 36, 787-797.

Tan, X. H., Wang, J. G., and Zhang, H. T. (2005). "Large deformation finite element reliability analysis of slope stability." *Chinese Journal of Rock Mechanics and Engineering*, 24(supp.2), 5308-5312.

Wong, F. S. (1985). "Slope reliability and response surface method." *J. Geotech. Geoenviron. Eng.*, ASCM, 111(1), 32-53.

Xu, B., and Low, B. K. (2006). "Probabilistic stability analyses of embankments based on finite element method." *J. Geotech. Geoenviron. Eng.*, ASCM, 32(11), 1444-1454.

Field Performance of a New Approach Slab System

Qiming Chen[1], P.E. and Murad Abu-Farsakh[2], P.E.

[1]Louisiana Transportation Research Center, Louisiana State University, Baton Rouge, LA 70808; PH (225) 767-9727; FAX (225) 767-9108; email: qchen1@lsu.edu
[2]Louisiana Transportation Research Center, Louisiana State University, Baton Rouge, LA 70808; PH (225) 767-9147; FAX (225) 767-9108; email: cefars@lsu.edu

ABSTRACT

The Louisiana Department of Transportation and Development has initiated a major effort to minimize the bridge end bump problem. As a result, a new design for the approach slab was proposed, which requires increasing the slab rigidity and the use of reinforced soil foundation (RSF) to support the slab and traffic loads. The Bayou Courtableau Bridge was selected as a demonstration project to evaluate and verify the new approach slab design system. The thickness of the approach slab is 16 inch. The end support of the approach slab is a 4.0-feet wide strip footing with soil underneath reinforced by geogrid. The first static load test was conducted right before the bridge opened to the traffic. The test results indicated that the west approach slab (with new design) remained its full contact supports from the soil while the east approach slab (with traditional design) started losing a portion of its supports from the soil.

INTRODUCTION

Background and problem. Bridge approaches are normally constructed with reinforced concrete slabs that connect the bridge deck to the adjacent paved roadway. The slab is usually supported on one side by the bridge abutment and on the other side by the embankment. Their function is to provide a smooth and safe transition of vehicles from roadway pavements to bridge structures and vice versa. However, complaints about the ride quality of bridge approach slabs still need to be resolved. The complaints usually involve a "bump" that motorists feel when they drive on or off bridges (Cai et al., 2007). This problem is commonly referred to as the bump at the end of the bridge mainly resulted from the differential settlement of the concrete approach slab relative to the bridge deck. It results in uncomfortable rides, dangerous driving conditions, and frequent repairs. Field observations indicated that either faulting at the roadway pavement/approach slab joint (R/S joint) or a sudden change in the slope grade at the approach slab/bridge joint (S/D joint) (as shown in Figure 1) causes this "bump" (Cai et al., 2007).

The settlement of the natural soil under the embankment, the compression of the embankment fill, and the stiffness of the concrete approach slabs contribute to the development of such a bump problem. Concrete approach slabs can lose their contacts and supports from soil due to the settlement of embankment soil on which the slabs are built (Figure 1). When settlement occurs, the slab will bend in a concave manner that causes a sudden change in slope grade of the slab. Traffic loads will be redistributed to the ends of the slab. Due to the redistribution of loading, vertical faulting at the R/S joint and a sudden change in the slope of grade

at the S/D joint may occur. Eventually, the rideability of the bridge approach slabs will deteriorate with time.

The bump at the end of a bridge problem affects 25 % of the bridges in the United States (approximately 150,000), and the amount of money spent every year on the repair of this problem nationwide is estimated to be at least $100 million (Briaud et al., 1997). There are several ways, such as pile supported embankment, lightweight embankment fill, etc., were tried to reduce the bump at the end of the bridge (Puppala et al., 2009). However, the cost of a particular solution may be prohibitive or exceed the life-cycle costs. The best current practices optimize the balance between proper design, proper construction, and acceptable maintenance while satisfying budget constraints and safety levels (Briaud et al., 1997).

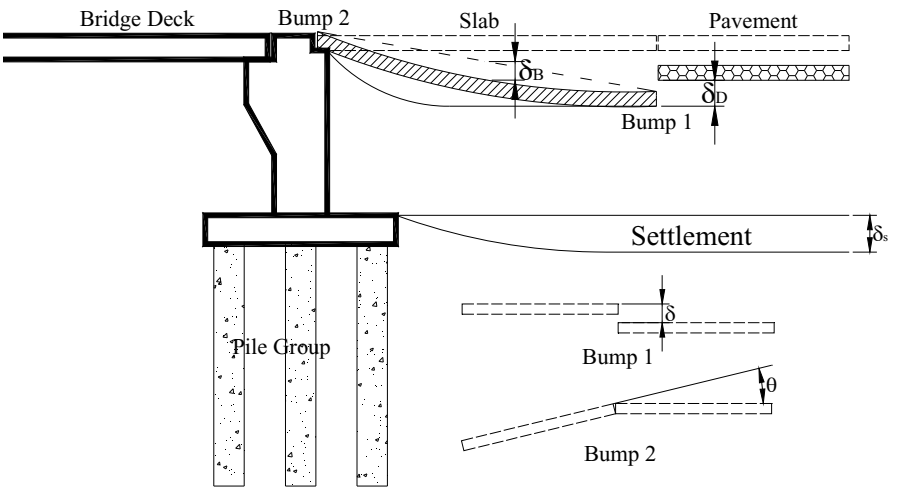

Figure 1. Illustration of approach slab and its interaction with soil

Potential solution. The Louisiana Department of Transportation and Development (LADOTD) has launched a major effort to solve the bridge bump problem by changing the design of approach slabs where differential settlement is expected. The objective is to find a feasible solution that makes approach slabs strong enough to allow them to lose a portion or all of their contact supports without detrimental deflection. In this solution, the flexural rigidity (EI) of the approach slabs will be increased by increasing the slab thickness and reinforcement, and therefore some embankment settlement will be allowed without a decrease in ride quality. As a result, the slab and traffic loads will be carried by the two ends of the slab rather than distributed over the length of the slab. Accordingly, a footing will be needed at the R/S joint. To increase the soil's bearing capacity and to reduce the footing settlement due to concentration load, the soil underneath the footing can be reinforced with geogrid reinforcement.

Several research projects were initiated by LADOTD in response to this need (Cai et al., 2005, Abu-Farsakh et al., 2007, Martinez, 2009). Cai et al. (2005) investigated the effect of embankment settlements on the performance of the approach slab using a 3-D finite element analysis. A correlation among the slab parameters, deflections of approach slabs, internal moments of the slab, and the differential settlement was established. A proper design of the approach slab was then provided to help mitigate the rideability problems of the slab in their study. Abu-Farsakh et al. (2007) identified the capability of geogrid reinforcement to

increase the soil's bearing capacity and to reduce the footing settlement. Typical design parameters for reinforcement layout were recommended and a step by step procedure for RSF design was provided in their study. To validate the findings and the design recommendations developed in these research studies and to update the design and construction guidelines of LADOTD for bridge approach slabs to mitigate bridge end bump problem, the Bayou Courtableau Bridge was selected to demonstrate the new approach slab design system. The field performance, including deformation and internal stresses of the concrete slabs, contact stresses between slab and embankment, stress distributions within reinforced soil foundation, and strain distributions along the geogrid, was monitored and will be presented in this paper.

DESIGN OF NEW APPROACH SLAB SYSTEM

Site description. The Bayou Courtableau Bridge as part of Louisiana Highway 103 in St. Landry Parish is located 2 miles east of I-49. Replacement of the old bridge, which was built in 1930, was required because of its low sufficiency rating (a rating of 10 or less), according to LADOTD. The sufficiency rating is a numerical value ranging from 0 to 100, with 55 percentage points applied to the structural adequacy, 30 percent points applied to the functional adequacy and serviceability, and 15 percent points applied to the essential for public use. A sufficiency rating of less than 50 qualify a bridge for replacement, while a sufficiency rating of less than 80 qualify a bridge for rehabilitation (LADOTD, 2004).

Design of approach slab system. The east approach slab of the bridge was designed according to standard (traditional) LADOTD's Bridge Design Specifications for comparison. The thickness of slab is 12 inch. The No. 6 steel bars were spaced 6 inch at the bottom of slab, while No.4 steel bars were installed at the top of slab at a spacing of 12 inch. The design of the west approach slab of the bridge was changed to feature the new proposed approach slab design system. The rigidity of the west approach slab was increased by increasing the thickness from standard 12 inch to 16 inch. The bottom slab steel bars was increased from No. 6 to No. 10 while other reinforcement configurations remained the same as the east approach slab. A 4 ft wide strip footing (B=4 ft) was placed at the roadway pavement/approach slab joint to support the slab and traffic loads. The soil underneath the footing was reinforced with six layers of geogrid placed at a spacing of 12 inch, as described in Figure 2. The width of geogrid was 20 ft. (5B). The embankment fill is a silty clay, having a liquid limit of 41 and a plastic index of 23. This soil contains 53% silt, 46% clay, and 1% sand. The maximum dry density of the soil is 99.4 lb/ft^3 with an optimum moisture content of 15.8% as determined by Standard Proctor test. This silty clay soil was classified as CL according to the Unified Soil Classification System (USCS), and A-7-6(24) according to the AASHTO classification system.

INSTRUMENTATION AND LOAD TESTING

Instrumentation plan. To monitor the performance of the new approach slab system, an instrumentation plan, which included foil strain gages, pressure cells, and "sister bar" strain gages (Figure 3), was developed and deployed. Five pressure cells were installed underneath the approach slabs of each side to

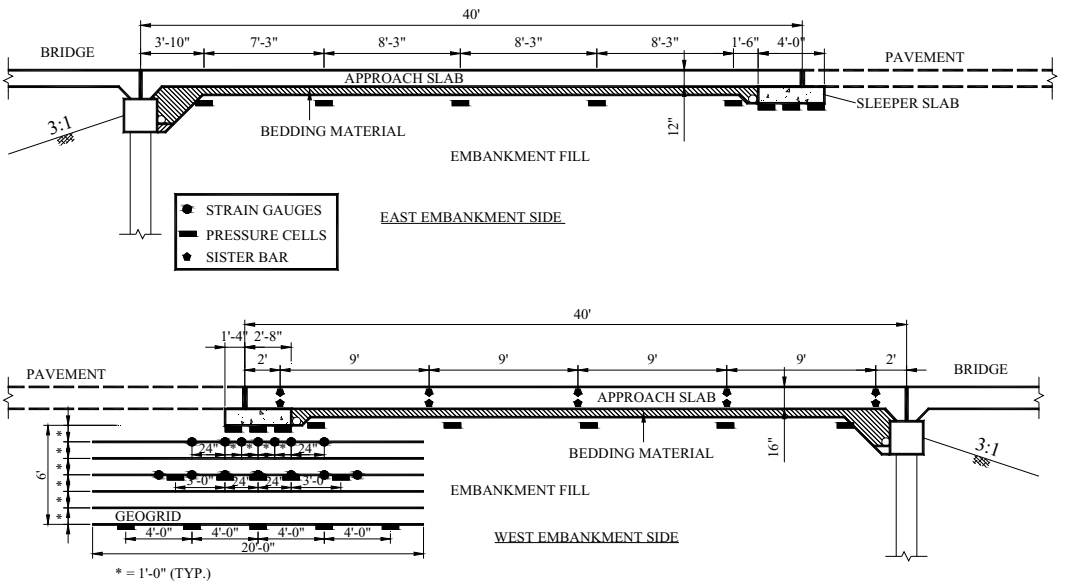

Figure 2. Standard and new approach slab design systems

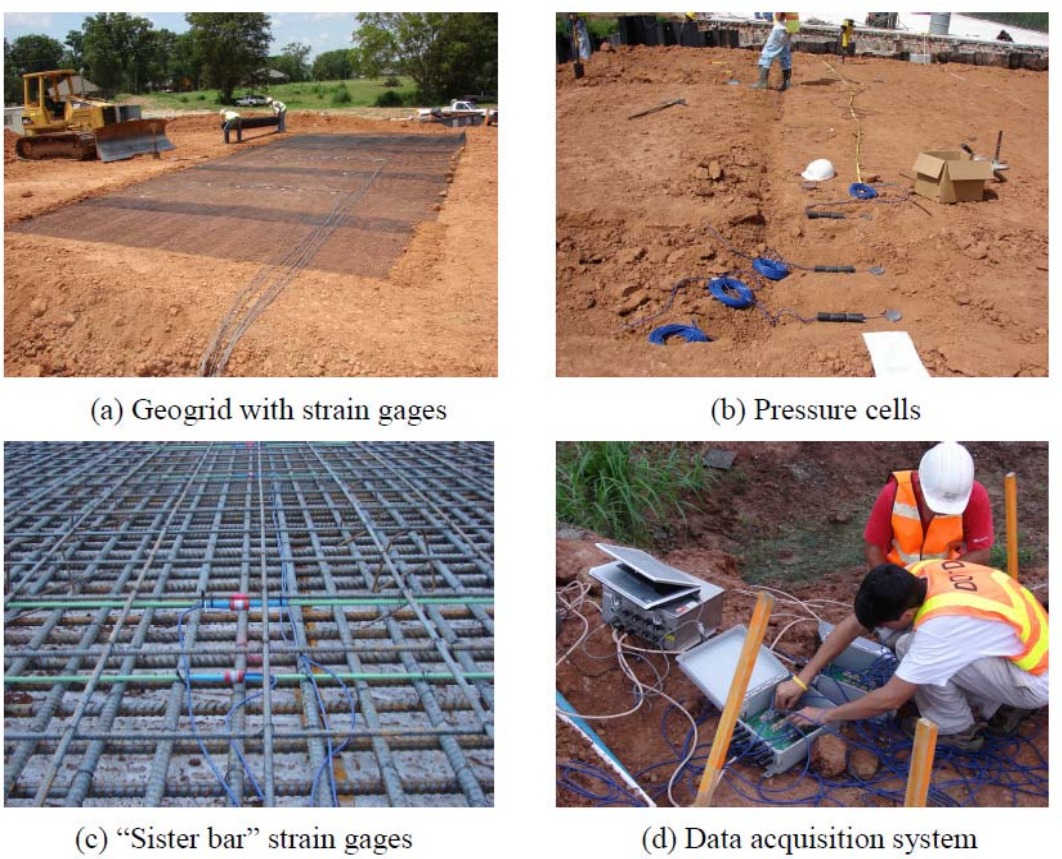

Figure 3. Photos of instrumentation and data acquisition system

investigate the contact stress between the slab and embankment, (Figure 2). To investigate the stress distribution within reinforced soil foundation, three pressure cells were installed below the strip footings of each side; and ten pressure cells were installed within the reinforced zone under the strip footing of the west approach slab (Figure 2). To investigate the strain distribution along the geogrid, two layers of geogrid were instrumented with the foil strain gages with locations

at 1 ft. below and 3 ft. below the strip footing as shown in Figure 2. To evaluate the internal stress of the approach slab, fifteen pairs of "sister bar" strain gages were installed within the west approach slab (Figure 3).

Static load testing. The first static load test was conducted right before the bridge opened to traffic (October, 2009). Dead loads were placed on the slab by positioning the 20-ton large cone truck at strategic locations. The axle distribution and loads per axle of the large cone truck are described in Figure 4.

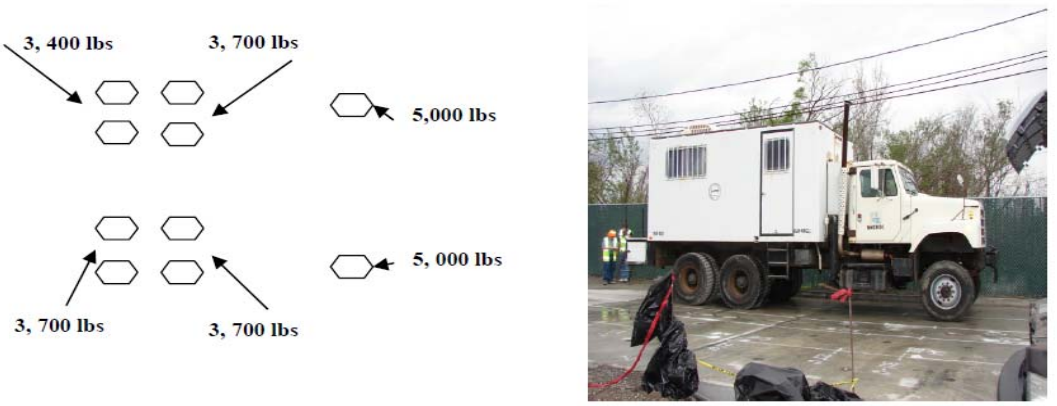

Figure 4. Large cone truck axle distribution and loads

RESUTLS AND ANALYSIS

Contact stress. Figure 5 presents the contact stress between the slab and embankment of each side when the 20-ton cone truck was positioned at the center of the slab in the traffic direction. As can be seen from Figure 5a, all pressure cells underneath the west concrete approach slab (except for the one close to the R/S joint) registered significant pressures. This observation suggests that the west approach slab maintained its contacts and supports from soil when it opened to the traffic. The negligible registered pressure of the pressure cell close to the R/S joint may be due to the edge lift induced (curling) by the center loading. On the other hand, Figure 5b shows that for the east approach slab, the pressure cell close to the B/S joint (i.e., the pressure cell underneath the front axle of the cone truck for truck position shown in the figure) registered negligible pressure. This observation may indicate that the east approach slab started partially losing its contacts and supports from embankment soil before it was opened to the traffic.

At this stage, the benefit of new approach slab system could not be identified because the west approach slab still remained its contacts and supports form the embankment soil. However, as the settlement of natural soil and compression of embankment fill continues, it is expected, with the time, that the west approach slab will gradually lose its contacts with the soil, and hence mobilizing the benefit of RSF. Once the west approach slab loses its supports from soil, the concept of new approach slab design will be realized. For this purpose, a second load test is being planned at Bayou Courtableau Bridge.

Internal strain of the west approach slab. Figure 6 shows the distribution of internal strains in the west approach slab that were measured when the large cone truck was positioned at the center of the slab in the traffic direction. The

compressive strains here are taken as positive. As indicated in the figure, tensile strains were developed at the bottom of the slab, while compressive strains were developed at the top of slab as a result of the cone truck load with the position shown in figure.

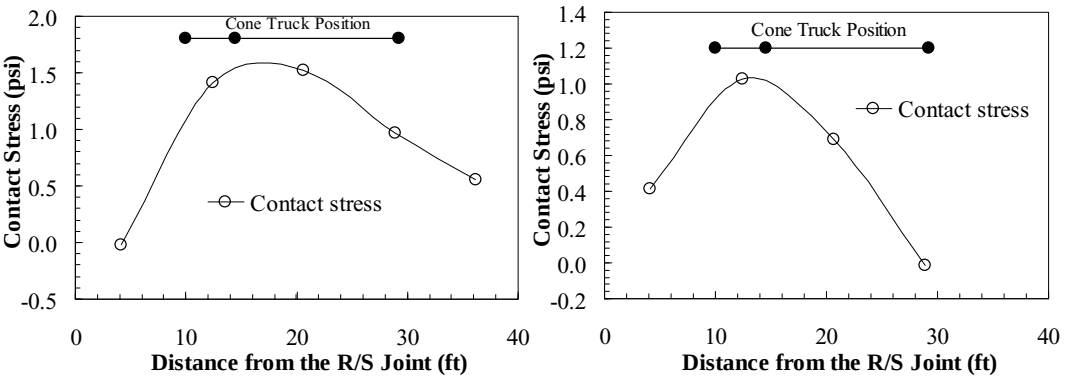

(a) West approach slab (b) East approach slab

Figure 5. Contact stress between approach slab and embankment

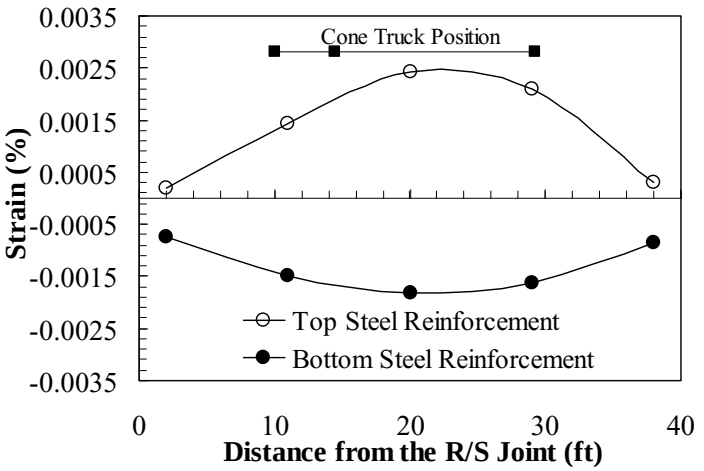

Figure 6. Internal strain distributions within the approach slab

Stress distribution within reinforced soil foundation. Figure 7 presents the variations of stress distributions within reinforced soil foundation measured when the rear wheels of the rear tandem axles of the large cone truck were located at the roadway pavement side of the R/S joint. As can be seen from the figure, the pressure registered by the pressure cells was greatest at the point between the rear tandem axles with a position closer to the front wheels of the rear tandem axles. This can be explained by the fact that the rear wheels of the rear tandem axles transferred the loads to the soil through two interfaces (pavement to footing, then to soil), while the front wheels of the rear tandem axles distributed the loads to the soil directly through the slab. As such, the dead loading from the rear wheels of the rear tandem axles would be distributed over a larger area of soil than that from the front wheels of the rear tandem axels.

Strain distribution along the geogrid. Figure 8 presents the variations of strains measured along the geogrids when the rear wheels of the rear tandem axles of the

large cone truck were located at the roadway pavement side of the R/S joint. The measured tensile strain was greatest at the point between the rear tandem axles, which is consistent with the location of the maximum measured pressure (Figure 7). The maximum measured strains were 0.5% for the georid located 1 foot below the footing and 0.15% for the geogrid located 3 foot below the footing. Both of them are way below the 2% strain, which is the value normally published by manufactures.

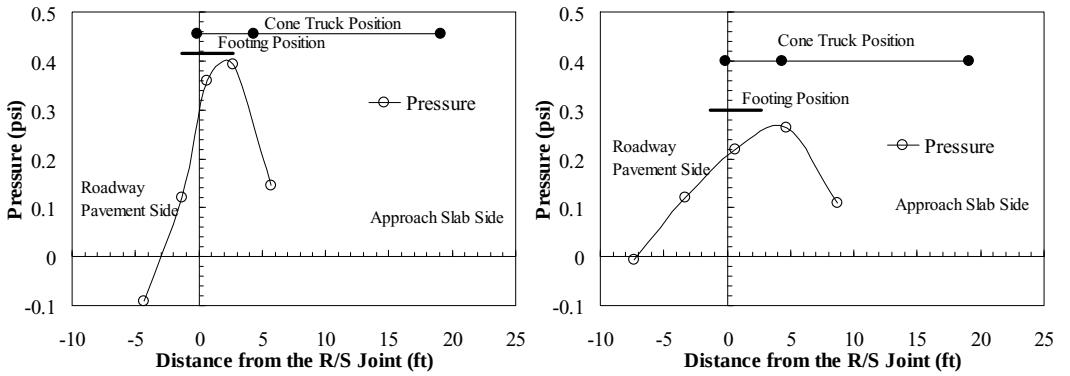

(a) 3 feet below the footing (b) 6 feet below the footing

Figure 7. Stress distributions within reinforced soil foundation

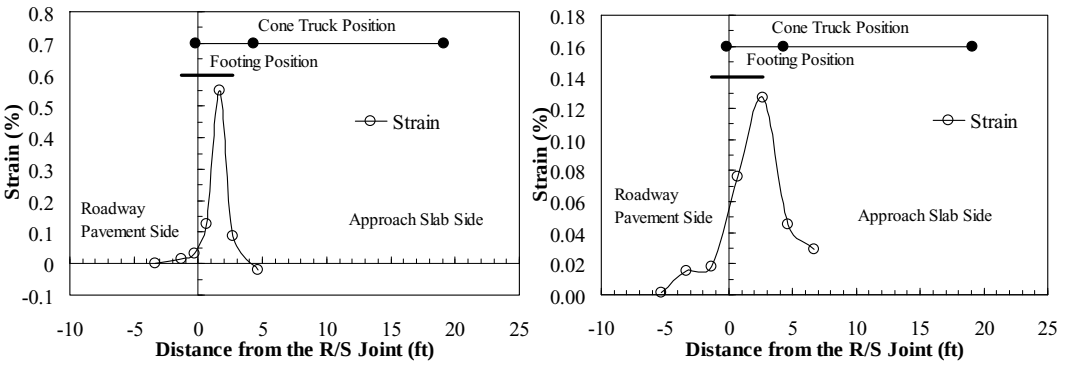

(a) 1 foot below the footing (b) 3 feet below the footing

Figure 8. Strain distributions along the geogrid

SUMMARY AND CONCLUSIONS

The bump at the end of the bridge is one of the major national bridge maintenance problems. LADOTD has launched a major effort to solve this problem by changing the design of approach slabs through increasing the rigidity of the approach slab with the introduction of reinforced soil foundation at the R/S joint to support the slab weight and traffic loads. The Bayou Courtableau Bridge, part of Louisiana Highway 103 in St. Landry Parish, was used as a demonstration project to verify the proposed new approach slab design system. The performance of the new approach slab design was preliminarily investigated by performing a static loading test through positioning a 20-ton large cone truck at strategic locations on the slab. The results of contact stresses between the slab and embankment indicate that the west approach slab, with new design, remained its contacts and supports from the soil, while the east approach slab, with standard

design, started partially losing its contacts and supports from the soil at the time when the bridge was ready for traffic. The internal strain distribution within the approach slab shows that the bottom of the slab is in tension while the top of the slab is in compression. The preliminary data on the measured stress distribution within the reinforced soil foundation and the strain distribution along the geogrid shed some lights on the performance and potential benefits of reinforced soil foundation in approach slab application. However, no definite conclusions can be reached on the superior performance of the new approach slab system from these limited data. A second test is therefore being planned at Bayou Courtableau Bridge to re-evaluate the performance of new approach slab design. In addition, other bridge site(s) will be used to demonstrate the new design methodology. With more data to come, the analysis will be extended, and more insight into the performance of the new approach slab system will be demonstrated.

REFERENCES

Abu-Farsakh, M. Y., Chen Q., and Yoon S. (2007). "Use of Reinforced Soil Foundation (RSF) to Support Shallow Foundation," Final Report, Louisiana Transportation Research Center, Baton Rouge, LA, Report No. FHWA/LA. 195 p.

Briaud, J.L., James, R.W., and Hoffman, S.B. (1997). "Settlement of bridge approaches (the bump at the end of the bridge)," NCHRP Synthesis 234, Transportation Research Board, National Research Council, Washington D.C., 75 p.

Cai, C.S., Voyiadjis, G. Z., and Shi, X. (2005). "Determination of interaction between bridge concrete approach slab and embankment settlement," Final Report, Louisiana Transportation Research Center (LTRC), Louisiana Department of Transportation and Development (LADOTD), Baton Rouge, LA, Report No. FHWA/LA.05/403, 150 p.

Louisiana Department of Development and Transportation (LADOTD). (2004). *Bridge Design Manual,* Louisiana Department of Development and Transportation, Baton Rouge, LA.

Martinez, M. (2009). "The rideability of a deflected bridge approach slab," Final Report, Louisiana Transportation Research Center (LTRC), Louisiana Department of Transportation and Development (LADOTD), Baton Rouge, LA, Report No. FHWA/LA.09/4457, 60 p.

Puppala, A.J., Saride, S., Archeewa, E., Hoyos, L.R., and Nazarian, S. (2009). "Recommendations for design, construction, and maintenance of bridge approach slabs: synthesis report," Final Report, Texas Department of Transportation, Austin, TX, Report No. FHWA/TX-09/0-6022-1, 186 p.

External Stability of Geotubes Subjected to Wave Loading

M. Khalilzad[1] and M. A. Gabr[2],

[1]Graduate Student, Dept. of Civil, Construction, and Environmental Engineering, North Carolina State University, Raleigh, NC 27695; email: mkhalil@ncsu.com
[2]Professor, Dept. of Civil, Construction, and Environmental Engineering, North Carolina State University, Raleigh, NC 27695; email: gabr@ncsu.com

ABSTRACT

Geotubes used as shoreline protective structures are formed using geotextile material that is hydraulically filled with soil to form desired dimensions. Historically, these structures are mainly used in the US for the dewatering of wet soils, and there is a focus in the literature on the internal stability aspects where filling pressure is specified such that rupture does not occur. After the 2008 Hurricane Ike hit on Galveston, failure of geotubes was observed in differential lateral displacement and rotation modes as well as due to the scour of the underlying foundation soil. External stability of geotubes is studied in this paper considering the effects of wave loading with the rising water level due to the storm surge. Results indicated that limit equilibrium analysis yielded factors of safety less than unity, yet, in some cases functionality is preserved as the lateral deformation can be tolerated and the height of the structure is maintained. Based on the parameters assumed in this paper performance aspects can be preserved during storm loading if the soil used to form the geotube is engineered to have soil elasticity modulus more than 1 MPa, and soil unit weight higher than 18 kN/m^3. At these values, the geotube exhibited the attributes of a rigid body response, with a minimal distortion of shape under the applied loading.

INTRODUCTION

The use of long geotextile-made containers that are hydraulically filled with soil, also referred as geotubes, can serve an alternative for the traditional coastal protection structures such as sea walls. In this case a tube is formed using geotextile materials and is hydraulically filled with a mixture of sand and water. Such an option is more attractive than hardened structures as they can be covered with sand and made to look analogous to natural dunes. However, while geotubes are used as costal protective structures, their design approach and construction materials are implemented in practice in the same fashion as when they are used for the dewatering of sludge materials. Issues related to internal stability and filling pressure are addressed in literature, but analysis of external stability is an issue needing more investigation.

Internal stability of geotubes including adequate seaming strength and the shapes to which they are formed under specified pumping pressure has been investigated in the past. For example, Liu (1981) presented a general solution for predicting the shape of a geotube as a function of the internal filling pressure. Kazimierowicz (1994) developed a formulation for a geotube filled with sand or mortar to provide the tensile force in the shell and the length of the contact between the geotube and its foundation. Leshchinsky et al. (1996) and Plaut and Suherman (1998) presented formulations for the geometry of geotubes and the circumferential stresses in the geotextile. The latter also extended the formulation to include the two cases of geotubes on deformable foundation and with water on one side. Plaut and Klusman (1999) analyzed stacked geotubes on deformable foundation in two configurations: one geotube on top of the other, and one geotube set on two geotubes underneath it. In all of these approaches, it has been assumed that the maximum tensile stress in geotextile occurs under hydraulic pumping pressure while geotubes are being filled. Contre (2002) presented a finite element model for the consolidation of geotubes and verified the former statement about maximum tensile stress occurring during the filling process. By conducting a series of hydraulic experiments, Yaliciner et al. (2006) studied the performance of perforated vertical walls constructed with geotextile tubes. The focus of the work was not on the external stability but on evaluating the reflection and transmission coefficient as a function of the wave characteristics. The authors suggested that this type of structures can be used as breakwaters where the design wave characteristics are in the acceptable lower limits.

Observations from geotube failures at Galveston, Texas, after hurricane Ike (2008) however showed that design aspects related to the external stability have been lacking. As shown in Figures 1 and 2, the geotube is exposed after the waves have washed away the cover sand "dune". It seems that failure under the wave impact occurred in different modes. Lateral translation of geotubes under a combined effect of sliding and rotating was observed in this case. Sinking the geotubes due to a low bearing capacity and scour of the foundation soil was also observed, as shown in Figure 1.

Figure 1. Geotubes at Galveston, TX after Hurricane Ike
[Photo by Dr. M. Overton, North Carolina State University]

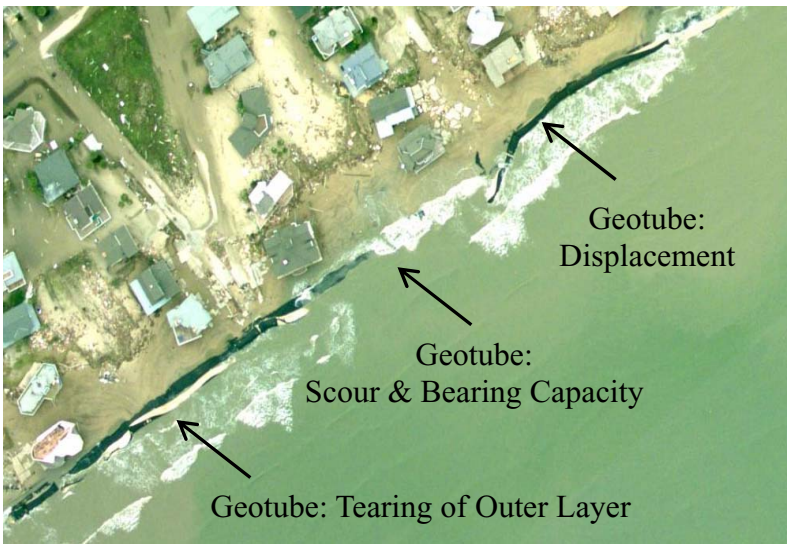

Figure 2. Different Modes of Failure after Hurricane Ike (Galveston, TX) [Google Earth View]

Work in this paper aims at investigating the deformation behavior of geotubes with an emphasis on the external stability under wave loading. First, a geotube with the same geometry as in Galveston case is studied using the limit equilibrium approach. The factors of safety against sliding and rotation are estimated under wave loading. Then, deformation analysis is performed using a finite element model to study the effect of material properties on the horizontal movement and tensile stresses in geotextile while the geotube is under a horizontal impulse loading representative of wave loading. A discussion on the appropriateness of limit equilibrium approach versus deformation analysis is presented.

LIMIT EQUILIBRIUM ANALYSIS

Limit equilibrium analysis is performed to assess the importance of external stability for a geotube system under wave loading. Previously, Shin and Oh (2007) studied the stability of a geotube under different wave heights assuming rigid body characteristics. They have used Hiroi's empirical equation (Hiroi, 1920) to estimate the hydrodynamic pulsating load due to wave action, and assumed an equivalent rectangular shape of loading with a zero initial water level.

In the analysis of the Galveston geotube case, a wave equivalent force is obtained from Liu (1981) and is expressed by:

$$F = \beta \gamma_w H_b^2$$

where F is the equivalent wave load, γ_w is the unit weight of water and β is an empirical coefficient depending on the ratio of d_s/H and d_s/H_b, where H, H_b and d_s are geotube height, wave height, and initial water height, respectively. The advantage of using Liu (1981) approach is the β factor is defined specifically for a structure with

an oval cross section shape, which is similar to that commonly formed for a geoteube. Referring to Liu (1981), the maximum impact force from the breaking waves happens when the initial water level is approximately at the vertical portion of the geotube (convex point). During a hurricane, water can be impounded behind the geotube because of the wave run-up exceeding the height of the geotube, or due to a plunging wave overtopping it. This trapped water, being a different height from water in front of the structure contributes to the uplift pressure on the geotube, which is also included for a robust analysis.

Analysis Parameters

In the limit equilibrium analysis, the geotube is assumed to behave as a rigid body for the purpose of external stability, and initially oval in shape. This approach was presented by Shin and Oh (2007). For the subject geotube, a value of 2 was assumed for the ratio of major and minor axes of the ellipse (WRP, 1998). The circumference of this ellipse in Galveston case was 9 m based on the Miratech documents (2003). For geotubes located at Bolivar Peninsula, the elevation of the base was at +1.55 m MSL (Mean Sea Level) and the minimum geotube height was 1.5 m (Heilman, 2003). The sea level varied between +0.3 to +3.5 m MSL based on the measurements obtained from gauges operated by National Ocean Service (NOS) of the National Oceanic and Atmospheric Administration (NOAA), as reported by Kraus and Lin (2009). Factors of safety are calculated for the geotube under two conditions; i) Case 1: the wave height is assumed 1.3 m (from the bottom of geotube) corresponding to a β of 3.5. This represents approximately 65% of the maximum measured surge, ii) Case 2: a smaller wave height of 1.0 m (approximately 50% of the maximum measured surge) is assumed with a β of 2.5. The wave force decreases from 62 kN/m to 25 kN/m when the wave height is decreased from 1.3 to 1.0 m, as both β and H_b decrease. In both cases, to get the maximum wave pressure for such surge level, the initial water level is assumed to be at the convex point of the geotube.

Results: Limit Equilibrium.

The results of the limit equilibrium analysis are shown in Figure 3 where the factors of safety against sliding and overturning are obtained for different soil unit weights. Since the soil unit weight may vary depending on the filling approach and placement, calculations are repeated for unit weights range of 17 to 21 kN/m^3 which are representative values for filling soil (Leshchinsky et al., 1996, Oh & Shin, 2006 and Shin & Oh, 2007). For Case 1 wave loading magnitude, the factors of safety against sliding and overturning are less than unity for all the unit weights indicating that the geotube is unstable in both failure modes (sliding and rotation). On the other hand, for Case 2, the factors of safety against overturning are higher than unity and the geotube is stable against rotating. However, in the sliding failure mode, it is stable only when the soil unit weight exceeds 18 kN/m^3.

There are of course several questions surrounding the assumption of a rigid body and the meaning or validity of such analysis. One main issue that is not however clear from the results of the limit equilibrium is the magnitude of deformation associated with the cases where the factor of safety is less than 1.0. It is possible that the geotube structure remains functional as it is able to tolerate a certain amount of

deformation without compromising its integrity. This issue is addressed next through the performance of deformation analysis.

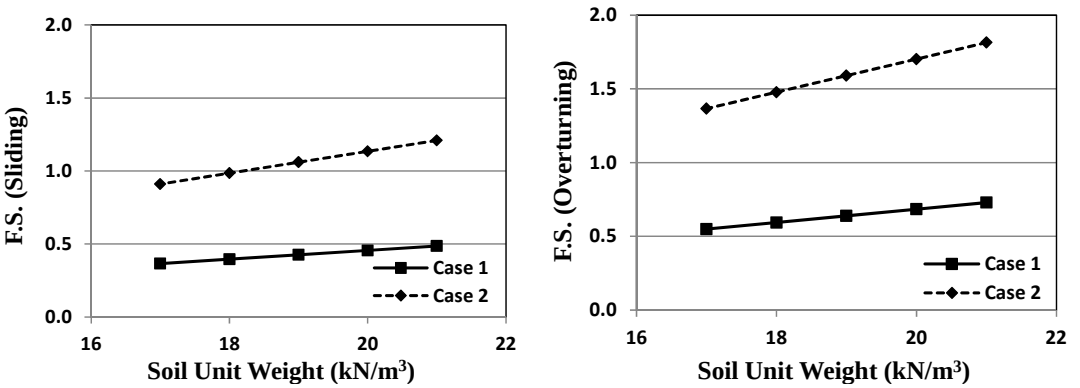

Figure 3. Factor of Safety against Sliding and Overturning

NUMERICAL MODELING

The numerical analysis of a geotube system involves certain complexities. These include unusual shape of the cross section for defining initial conditions, analysis of large deformations, contact between the geotextile and the soil at the interface, and moving boundary conditions as sliding occurs. Therefore, several simplifications are introduced in order to be able to study the effect of parameters impacting the behavior of a geotube under wave loading. These include the following: i) plane strain elements are used in the model implying that the geotube section is long enough; ii) geotextile elements are assumed to have elastic behavior while Mohr-Coloumb plasticity is assumed for the soil inside the geotube; iii) hydraulic properties of the soil and geotextile are not considered in this analysis; iv) friction between the geotextile and foundation is modeled at the interface while the geotextile and inner soil elements are assumed to be bound together; v) foundation layer is assumed to be non-yielding to reduce complication of the analysis with regard to bearing capacity; and vi) wave loading is applied as an equivalent horizontal pressure pulse.

Model Overview

The numerical model is developed using the computer program ABAQUS 6.9-EF. CPE3 elements (three-node linear plane strain triangle elements) are used for all three types of materials including geotextile, soil inside the geotube, and the foundation soil. The Mesh and model configuration are shown in Figure 4 and material properties are presented in Table 1 (the mesh is truncated at the bottom of the figure for clarity of presentation). The mesh is created using approximately 6200 elements and 5200 nodes. Boundary conditions include the constrained x and y displacements at the bottom of the foundation layer and constrained x displacements at the two sides of foundation layer. At the interface of geotextile and foundation layer, a contact was defined with a friction coefficient of 0.32 assigned to the

tangential interaction based on the recommendation of WRP Technical Note (1998). The interface of between the geotextile and inner soil is a constraint of type "*tied*". Loading conditions are the weight of the material in the form of *gravity* loads, a *hydrostatic pressure* applied over the outer surface of the geotextile where it is in contact with the initial water level. A horizontal impulse pressure equivalent to the wave impact is applied on the seaside surface of geotextile up to the elevation corresponding to the wave height. This loading is in the form of an impulse with 1 second duration to represent one cycle impact under storm surge.

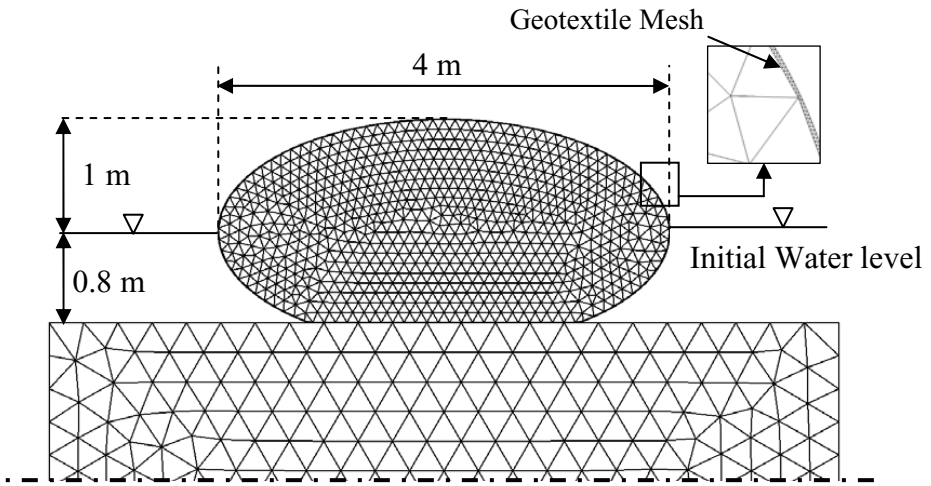

Figure 4. Finite Element Meshing and Model dimensions

Table 1. Reference Material Properties

Material	Density (Kg/m^3)	E (MPa)	υ	Φ(°)
Confined Soil	2000 (saturated)	0.5	0.3	26
Geotextile	400	5×10^3	0.4	N/A
Foundation	N/A	1×10^3	0.3	N/A

The analyses are performed in two steps. First, the geotube system with initial oval shape is placed under the gravity loading, thereby developing the initial stresses in the soil and geotextile. At this step, the geotube develops its shape due to the weight of contained soil. At the second step, a horizontal loading equivalent to the wave impact is applied to the model and the geotube deformation behavior is evaluated.

The deformed shapes after "step 2" are shown in Figure 5 assuming soil modulus varies from 0.1 to 2 MPa. The material properties including the density and elasticity modulus of the confined soil as well as the elasticity modulus of the geotextile influence the shape of the geotube at equilibrium. Results in Figure 5 show that below a specific limit for soil modulus (1 MPa in this analysis), translation occurs with distortion of the cross section shape. In addition, the geoteube-foundation contact interface length starts to increase which while may provide a higher resistance

to sliding, it lead to a reduction in the height. In addition, for the case of E greater than or equal to 1 MPa, deformation seems to occur mostly in a rigid body fashion with a minimal distortion of the cross section shape.

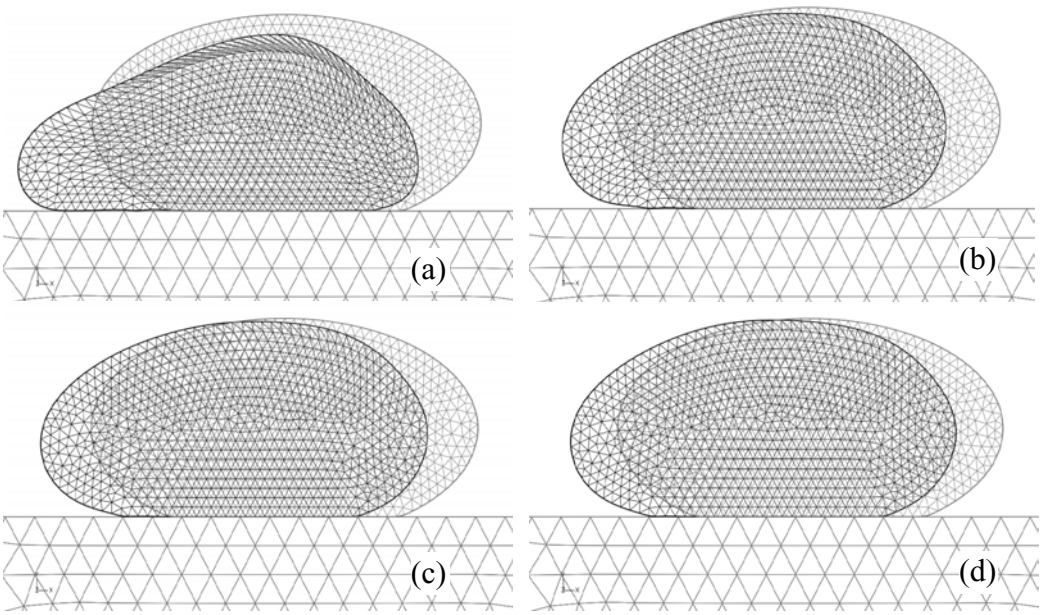

Figure 5. Geotube Deformed Shape under Horizontal Impact for Different Soil Elasticity Modulus [(a) E=0.1 MPa , (b) E=0.5 MPa, (c) E=1 MPa, (d) E=2 MPa]

PARAMETRIC STUDY

Effect of Soil Unit Weight

Correlating the results from the limit equilibrium to the deformation analyses reveal several interesting findings. When the geotube is stable under the wave impact (i.e. the limit equilibrium factor of safety is higher than unity), a relatively small displacement (less than 0.04m) is determined, as shown in Figure 6(a). This small displacement can be mainly attributed to the cross section distortion of the geotube under the external loading condition. When the geotube is unstable (i.e. the limit equilibrium factor of safety is less than unity), the soil unit weight has a large effect on the horizontal displacement under the wave impact. As shown in Figure 6(a), it is observed that the factor of safety against sliding is equal to or larger than unity for Case 2 when the unit weight is greater than 18 kN/m^3. Correspondingly, the horizontal deformation for this case is very small (0.06 m) for soil unit weights greater than 18 kN/m^3. On the other hand, as the soil unit weight decreases from 21 to 17 kN/m^3, the amount of geotube displacement increases from 0.39 to 0.75 m.

At the same time, the effect of soil unit weight on the mobilized tension in the geotextile is shown in Figure 6(b). A higher value of soil unit weight directly increases the in-plane tensile stresses in the geotextile, because the pressure applied to the surface of the geotextile increases. In this case, even though a lateral deformation of 0.39 m may be tolerated as the geotube retains its shape, the tension in

the geotxtile most likely exceeds allowable tensile strength (even with the avoidance of transversal seam orientation.)

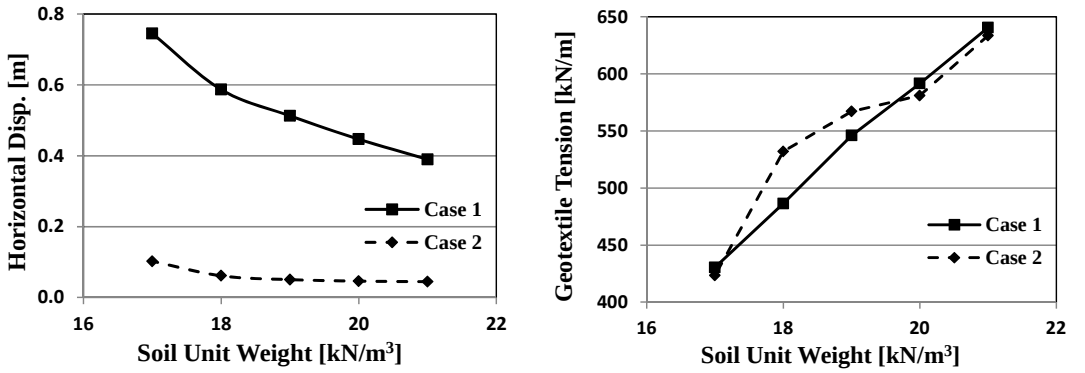

Figure 6. Effect of Soil Unit Weight on Geotube: (a) Interface Horizontal Displacement, and (b) Mobilized Tension in Geotextile

Effect of Elasticity Modulus

As seen in Figure 7(a), soil modulus of elasticity has a slight impact on the horizontal displacement of the geotube, but for elasticity modulus less than 0.5 MPa the geotube is more distorted because of the self-weight. In this case, the interface contact length between the geotube and foundation increases (Figure 5). This provides more resistance against lateral sliding of the geotube and therefore, horizontal deformation drops as a lower value of soil elasticity modulus (0.1 MPa) is assumed.

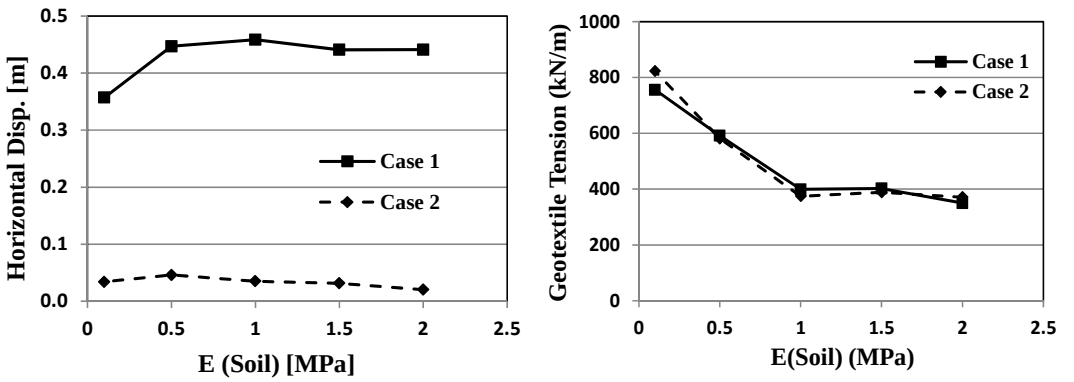

Figure 7. Effect of Soil Elasticity Modulus on Geotube: (a) Interface Horizontal Displacement, and (b) Mobilized Tension in Geotextile

Figure 7(b) shows the effect of soil elasticity modulus on the tension developed in the geotextile. It can be observed in that in both cases, as the soil becomes stiffer, less tension is mobilized in the geotextile as a less of distorted shape is developed. However, the soil elasticity modulus with a value greater than 1 MPa has negligible effect on the tension in geotextile. At this point, the soil is stiff to an extent that can carry the load without large deformations. This limit can be called the "*rigidity limit*" since it seems to define a value after which the geotube seems to exhibit attributes of a rigid body movement.

Effect of Soil Friction Angle

Assuming geotubes are filled with a granular soil, friction between the particles is the main source of strength for the filling soil. When the wave hits the geotube, a part of impact energy dissipates in the form of deformation of the filling material, and the remainder of the energy causes the geotube to move. As the friction angle of the filling soil increases, more of the energy of a wave impact is transformed into the movement of the geotube than being dissipated due to deformation. This can be observed in Figure 8(a). As soil friction angle changes from 18 to 22 degrees, the horizontal displacement increases from 0.40 to 0.48 m.

For Case 1 (the geotube is unstable according to the limit equilibrium analysis), as the soil friction angle increases, the maximum tension in the geotextile decreases (Figure 8b). Changing the friction angle from 18 to 22 degrees results in a reduction in geotextile tension from 750 to 680 kN/m. This seems to be because of the lower plastic shear strain of the soil at the higher shear strength. For example, in the previous case when the soil friction angle increases from 18 to 22 degrees, the maximum plastic shear strain decreases from 0.32 to 0.27. If the contained soil becomes plastic, it will undergo more strains. Hence, the strain and correspondingly the stress will be higher in the geotextile. In Case 2, the geotube is stable and deformations are small, (0.04 m) thus, the tension in the geotextile in approximately the same for different friction angles.

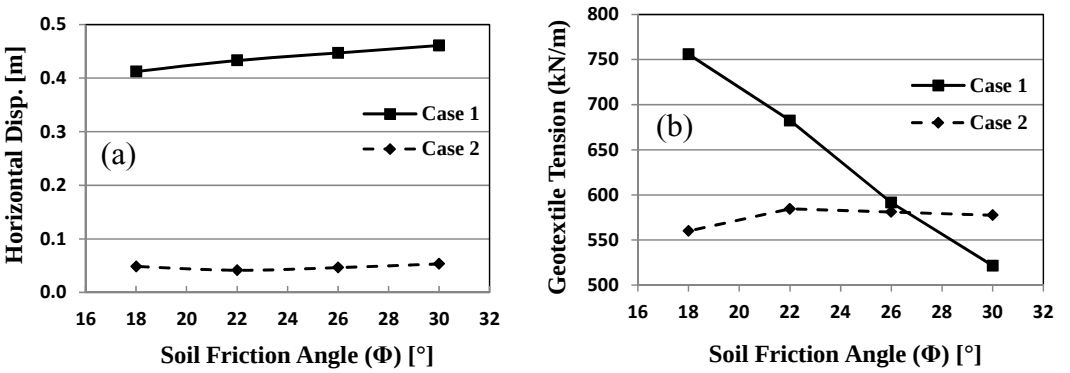

Figure 8. Effect of Soil Friction Angle on Geotube: (a) Interface Horizontal Displacement, and (b) Mobilized Tension in Geotextile

CONCLUSSION

The knowledge about the external stability of geotubes under the wave loading is limited in the literature. Uncertainties are involved in the design of this type of protective structure as several aspects are carried over from the practices related to the use of these structures for dewatering high water content materials. This study is focused on assessing the importance of external stability under the wave loading and aspects related to its determination. Based on the results obtained from the analytical and numerical models, the following conclusions are advanced:

i) Limit equilibrium analysis for the geotube representative of the those installed at Galveston shows that factors of safety against sliding and overturning are less than unity when the initial sea water level is at 0.8 m and wave height is 1.3 m. This is perhaps is not surprising since failure has been observed during Hurricane Ike in 2008.

ii) Parametric studies show that for the soil elasticity modulus less than 1 MPa (in this study), the contact length between the geotube and the foundation increases as the shape of the structure is distorted. This provides more resistance against geotube sliding and results in less displacement, but at the same time lead to reduction in its height.

iii) When the geotube is unstable, the soil unit weight plays an important role in the magnitude of the horizontal displacement of the geotube with increasing the soil unit weight considerably decreases the horizontal displacement. For Case 1 loading, half of the displacement was obtained when the soil unit weight was increased from 17 to 21 kN/m^3. Also, soil unit weight showed to have an increasing effect on the geotextile tension (e.g. in Case 2, if soil unit weight increases from 20 to 21 kN/m^3, the geotextile tension decreases from 640 to 590 kN/m)

iv) Soil elasticity modulus had a negligible effect on the horizontal displacement, however, and based on the parameters used in this study, there is a threshold above which the geotube exhibited the attributes of a rigid body. For the unstable geotube and when soil modulus is below 1 MPa, the horizontal displacement starts decreasing because of increasing the contact length (e.g. the displacement changes from 0.45 m to 0.36 m when the soil elasticity modulus varies from 0.5 to 0.1 MPa). With increasing the soil elasticity modulus, the geotextile tension decreases (e.g. increasing the soil elasticity modulus from 0.1 to 0.5 MPa results in 25 percent reduction in the geotextile tension)

v) Increasing the soil friction angle, more displacement is observed for an unstable geotube (e.g in Case 2, if soil friction angle changes from 18 to 22 degrees, the horizontal displacement also increases from 0.40 to 0.42 m). On the other hand, a higher friction angle leads to a lower tension in geotextile (e.g. a variation of the friction angle from 18 to 22 degrees results in a reduction in the geotextile tension from 750 to 680 kN/m.)

ACKNOWLEDGEMENT

Work in this paper was supported by the US Department of Homeland Security under Award Number: 2008-ST-061-ND 0001.

DISCLAIMER

The views and conclusions contained in this document are those of the authors and should not be interpreted as necessarily representing the official policies, either expressed or implied, of the US Department of Homeland Security.

REFERENCES

Cantre, S. (2002). "Geotextile tubes--analytical design aspects", *Journal of Geotextiles and Geomembranes*, Vol. 20, Issue 5, 305-319

Yalciner, A. C., Ergin, A. Pamukcu, S. and Derun B. A., (2006). "Performance of perforated breakwaters constructed with geotextile tubes". *Journal of Coastal Research, SI 39 (Proceedings of the 8th International Coastal Symposium)*, 750 -753.

Heilman, D. J., Perry, M. C., Thomas, R. C. and Kraus, N. C. (2008). "Interaction of Shore-Parallel Geotextile Tubes and Beaches Along the Upper Texas Coast." *US Army Corps of Engineers, ERDC/CHL CHETN-II-51*

Hiroi, I. (1920). "Evaluation of wave pressure." *Journal of JSCE* 6 (2), 435–449.

Kazimierowicz, K. (1994). "Simple analysis of deformation of sand-sausages." *5th International Conference on Geotextiles, Geomembranes, and Related Products*, Singapore, 775-778.

Kraus, N. C. and Lin L. (2009). "Hurricane Ike along the upper Texas coast: An introduction." *Shore & Beach*, Vol. 77, No. 2, 1-8

Leshchinsky, D., Leshchinsky, O., Ling, H. L., and Gilbert, P. A. (1996). "Geosynthetic tubes for confining pressurized slurry: some design aspects." *Journal of Geotechnical Engineering*, Vol. 122, No. 8, 682–690

Liu, G. S. (1981). "Design criteria of sand-sausages for beach defenses." *International Association for Hydraulic Research: Summaries of Papers Proceedings*, New Delhi, India, 123-131.

Miratech. (2003) "Sand Dune Construction, Bolivar Peninsula, Geotube Structures", http://www.texasgulfcoastonline.com/portals/0/PDFs/Sand_Dune_Construction_and_Geotubes_Bolivar_Peninsula.pdf

Oh, Y. I. and Shin, E. C. (2006). "Using submerged geotextile tubes in the protection of the E. Korean shore" *Coastal Engineering*, Vol. 53, No. 11, 879-895

Plaut, R. H., and Suherman, S. (1998). "Two-dimensional analysis of geosynthetic tubes." *Acta Mechanica*, 129(1-4), 207-218.

Plaut R.H. and Klusman, C.R. (1999). "Two-dimensional analysis of stacked geosynthetic tubes on deformable foundations." *Thin-Walled Structures*, 34 (1999), 179–194

Shin, E. C. and Oh, Y. I. (2007). "Coastal erosion prevention by geotextile tube technology." *Geotextiles and geomembranes*, 25 (4-5), 264-277.

WRP Technical Note (1998). "Geotextile Tube Structures for Wetlands Restoration and Protection." *WRP TN HS-RS-3.2*, January 1998.

Probabilistic Assessment of Commercial Design Guides for Steep Reinforced Slopes: Implications for Design

W.A. Kitch, M.ASCE, Ph.D., P.E.[1], R.B. Gilbert, M.ASCE, Ph.D., P.E.[2], and S.G. Wright, M.ASCE, Ph.D., P.E.[3]

[1] Associate Professor, Civil Engineering Department, California State Polytechnic University, 3801 W. Temple Avenue, Pomona, CA 91768-2557; PH (909)-869-3147; email: wakitch@csupomona.edu
[2] Professor, Department of Civil, Architectural and Environmental Engineering, University of Texas, Austin, 1 University Station C1700, Austin, Texas 78712-0273; PH (512) 232-3688; email: bob_gilbert@mail.utexas.edu
[3] Professor Emeritus, Department of Civil, Architectural and Environmental Engineering, University of Texas, Austin, 1 University Station C1700, Austin, Texas 78712-0273; PH (512) 471-4929; email: swright@mail.utexas.edu

ABSTRACT

Deterministic procedures are still the predominate methods used in reinforced slope design. These procedures generally use limit equilibrium methods based on accepted factors of safety. This paper presents a method of probabilistic analysis which is easily adapted to existing deterministic methods. The method is used to analyze the reliability of a two steep reinforced slopes designed using commercially published guidelines. The reliability of internal failure modes (passing within the reinforced zone) and composite failure modes (passing mostly outside of the reinforced zone) are computed and compared. The results indicate that internal and composite failure modes may be nearly equally likely leading to a total probability of failure of twice that of either mode. The paper present a design process to ensure that the probability of failure is controlled by composite failure modes and the reliability of internal modes is sufficiently high that they do not significantly reduce the total reliability of the slope.

SLOPE DESIGNS ANALYZED

This paper exams two reinforced slopes designed using typical deterministic methods and analyzes these designs using probabilistic methods. The slopes are 45° and 70° slopes reinforced with geogrids. Both designs consist of uniform cohesionless soil both within and below the slopes. The slopes were designed using guidelines published by Tensar (1988). These design guidelines were developed with a two wedge failure surface satisfying only force equilibrium, Schmertmann et al (1987). For a uniform soil with a given friction angle, ϕ, and slope angle, β, the key design parameters are: the length of the reinforcing elements, L, chosen so that composite failure modes have a satisfactory factor of safety, and the spacing, S, and allowable reinforcement force, R_a, selected so that internal failure modes have a

satisfactory factor of safety. The two slopes designed using the Tensar (1988) guidelines are shown in Figure 1.

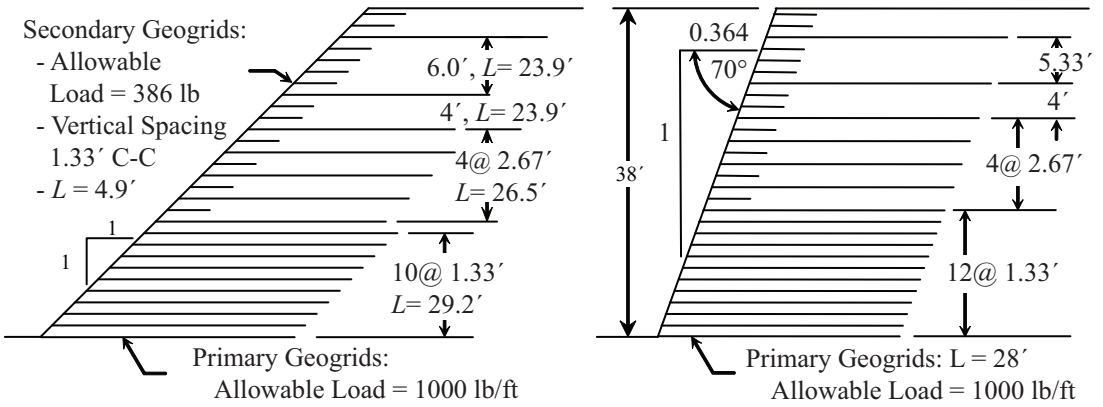

a) 45 Degree Slope b) 70 Degree Slope

Figure 1. Cross-sections of two reinforced slopes analyzed showing length and spacing of geogrid reinforcement

DETERMINISTIC ANALYSES

After the slopes were designed using the Tensar (1988) guidelines they were reanalyzed using UTEXAS3 (Wright 1991). This analysis used a full equilibrium method with circular failure surfaces. This allowed failures extending into base materials below the slopes to be investigated. It also allowed investigation of the relationship between allowable reinforcement force and reinforcement length and how these variables affect the location of the critical surface.

Nineteen distinct failure modes were investigated: 18 internal modes passing through the reinforced portion of each slope, and one composite mode passing predominately outside the reinforced portion of each slope but intersecting a few reinforcing elements. The failure modes were numbered 0 (zero) for the composite mode and 1 through 18 for the internal modes, the number indicated the lowest reinforcing elements through which the failure surface passed. Typical failure modes are shown in Figure 2.

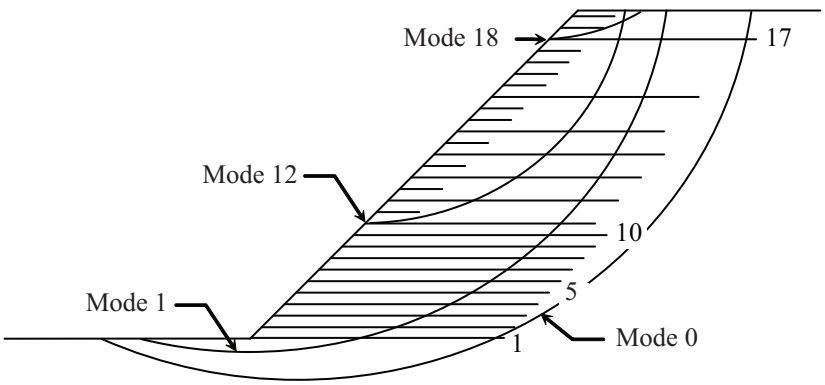

Figure 2. Failure modes of 45 degree showing numbering scheme

For each failure mode a search for the critical slip surface was performed to determine the local minimum factor of safety for that mode. The computed factors of safety for each mode are shown in Figure 3. Figure 3 shows that the Tensar (1988) design guidelines generate slope designs where the composite failure mode controls and the critical surface passes predominately below and behind the reinforced portion of the slope. Figure 3 also shows that the internal failure modes have a relatively uniform factor of safety. Both these observations are in keeping with the original intent of these design guidelines (Schmertmann et al, 1987).

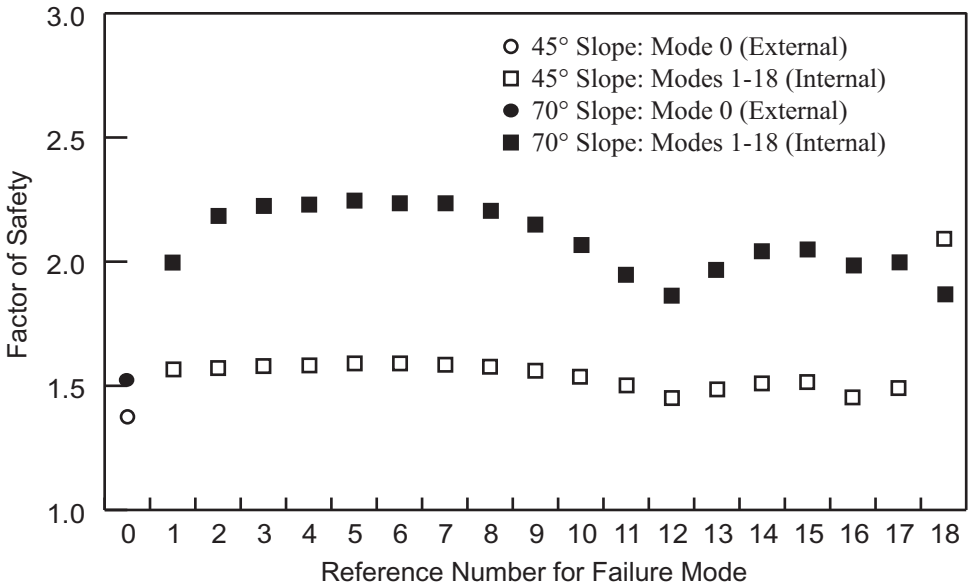

Figure 3. Comparison of the factors of safety computed for each failure mode

A second series of analyses was done to investigate the relationship between allowable reinforcement force and reinforcement length. In this series of analyses the vertical spacing of geogrids was kept the same, but the reinforcement length and allowable reinforcement force were varied. A large number of combinations of reinforcement length and force were analyzed; for each combination the minimum factor of safety was computed and the location of the critical circle identified. Figure 4, show the results of this analysis for the 45° slope. Figure 4 shows that for relatively long or weak reinforcement (the lower shaded portion of the figure) the failure mode is internal and the factor of safety is a function of only the reinforcement force. Figure 4 also shows that for relatively strong or short reinforcement, the failure mode is composite and the factor of safety is governed by the reinforcement length. Note that the transition from internal to composite failure mode is quite abrupt. It is also worth noting that the Tensar (1998) design guides have a composite failure mode close to the point where the failure surface transition from composite to internal.

PROBABILISTIC ANALYSES

Using the deterministic analyses as a starting point, the reliability index, β, was computed for each of the 19 failure modes. These analyses used two random variables: the shear strength or the soil, s, in the form of $s = \tan(\phi)$, and the

reinforcement force, R. The reinforcement length and spacing were assumed to have no significant variance. The limit state function was taken to be

$$g(s,R) = 1 - F(s,R) \tag{1}$$

Where, F is the factor of safety computed using standard limit equilibrium methods.

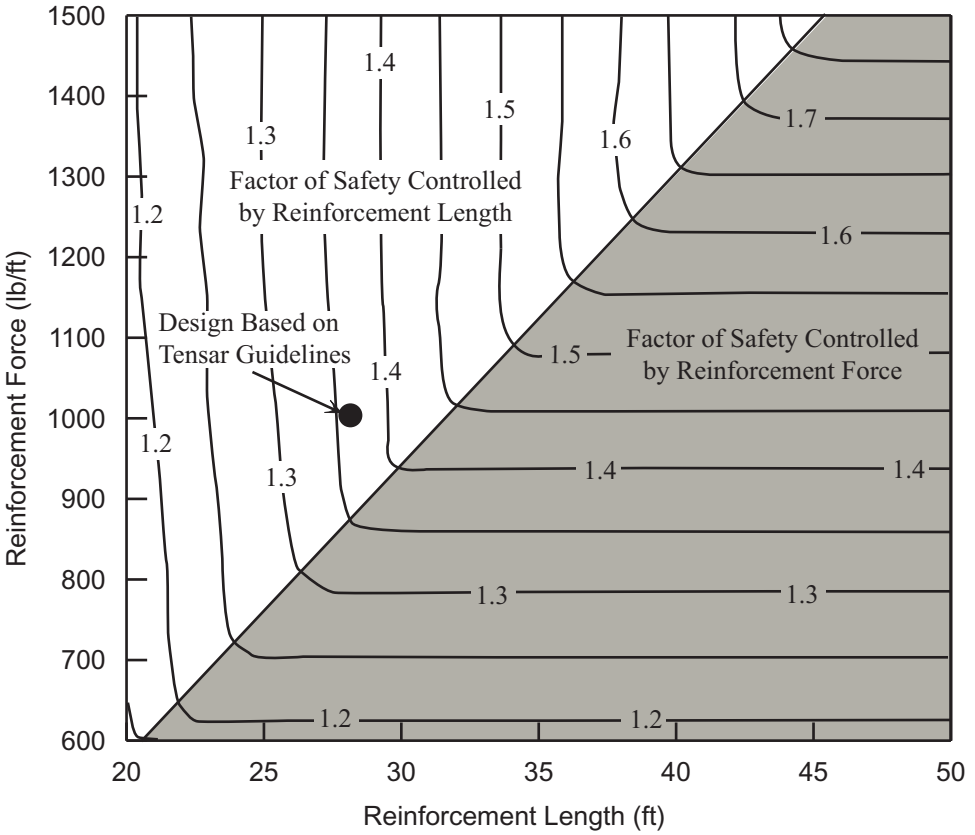

Figure 4. Factor of safety as a function of reinforcement length and force for the 45 degree slope

The mean-value first-order reliability index, β_{MV}, because of simple form

$$\beta_{MV} = \frac{1 - F(\mu_s, \mu_R)}{\sqrt{\frac{\partial F}{\partial s}\sigma_s^{\,2} + \frac{\partial F}{\partial R}\sigma_R^{\,2}}} \tag{2}$$

Where μ_s and μ_R are the mean values of the soil shear strength and reinforcement force and σ_s and σ_R are the standard deviations of the soil shear strength and reinforcement force (Ang and Tang, 1984, Madsen et al 1986). UTEXAS3 was used to find the minimum factor of safety for a given failure mode which was then $F(\mu_s, \mu_R)$. Four more computations with UTEXAS3 were then needed to numerically estimate the partial derivatives in Equation 2. The mean-value first-order reliability index was then computed knowing the standard deviations of the shear strength and reinforcement force (Kitch 1994).

Figure 5 shows the mean-value reliability index calculated for each of the 18 failure modes assuming a coefficient of variation of 0.1 for shear strength and 0.2 for reinforcement force for the 45° slope. From this figure it can be seen that mode 12

has the highest probability of failure (lowest β) for internal failure modes. Mode 0 represents the composite failure mode with the highest probability of failure.

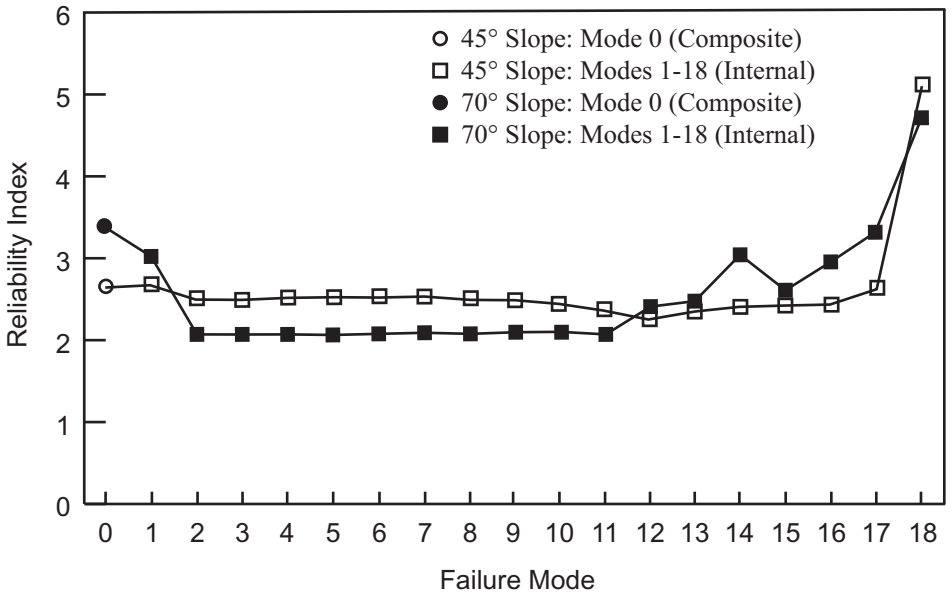

Figure 5. MFORM reliability indices for failure modes in each slope

UNCERTAINTY IN SOIL STRENGTH AND REINFORCEMENT FORCE

One advantage of the mean-value first-order reliability method is that it is easy to determine how variance of the random variables affects reliability. Once the mean value of the factor of safety, F, and the partial derivatives of F with respect to shear strength and reinforcement force are computed, the reliability index can be computed for any combinations of σ_s and σ_R without any further limit equilibrium computations, using Equation 2.

Published literature on the variability of shear strength of cohesionless soils and mobilized reinforcement force in reinforced slopes was reviewed (Kitch, 1994). Based on this review the values shown in Table 1 were determined. It should be noted that the estimates are for variability of a single known cohesionless soil. They do not include the uncertainty of the existence of an unidentified soil layer. These values are appropriate for a built up slope where the embankment soil is known and has been tested. They would not be appropriate for the remediation of an existing slope where there is a possibility of unidentified weak layers existing beneath or behind the reinforced slope. In Table 1, inherent variability considers only the variability of the material properties; model error considers uncertainties in how properties are determined and how they are modeled in the analysis process.

Table 1. Variability Estimates for Shear Strength and Reinforcement Force*

Variable	Coefficient of Variation	
	Inherent variability	Model error
Spatial average shear strength	0.10	0.15 – 0.18
Reinforcement Force	0.10	0.25

* From Kitch (1994)

From the data in Table 1, it is estimated that the coefficient of variation or shear strength could range from 0.10 to 0.20 ($=\sqrt{0.10^2+0.18^2}$) depending on whether or not model error is included. Similarly the coefficient of variation of reinforcement force could range from 0.10 to 0.27 ($=\sqrt{0.10^2+0.25^2}$). Using these ranges of variability, a sensitivity study was conducted to determine how the relative variability of soil strength and reinforcement force affected the probability of internal versus composite failure modes.

For the sensitivity study, the reliability of the critical internal failure mode was compared with that of the composite failure mode for coefficients of variation of the shear strength of 0.1, 0.2 and 0.3 and coefficients of variation of the reinforcement force ranged from zero to 0.5. The comparison of the reliabilities for internal and composite failure modes as a function of the coefficients of variation is shown in Figure 6 for both slopes.

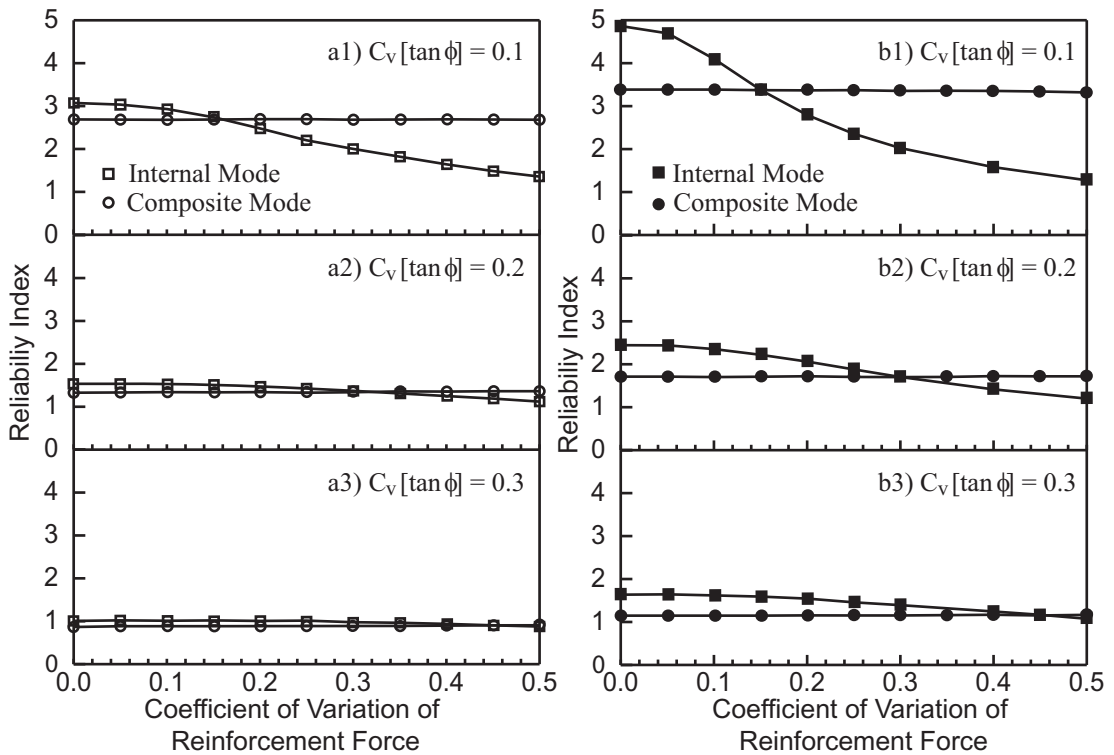

a) 45 Degree Slope b) 70 Degree Slope

Figure 6. Comparison of reliability index of internal and composite failure modes as a function of variability of reinforcement force and soil shear strength.

If we consider only inherent variability of the shear strength and the reinforcement force, then coefficients of each variable are approximately 0.10 (Table 1) and for both the 45° and 70° slope the most likely failure mode is internal. However, if we include model error then the coefficients of variation increase to 0.20 for shear strength and 0.27 for reinforcement force. In this case, not only do the reliabilities of the slopes decrease both the probability of an internal and composite failure modes are nearly equal as can be seen in Figures 6a and 6c.

IMPLICATIONS FOR ANALYSIS AND DESIGN

The analysis presented shows that reinforced slopes designed using the Tensar (1998) guidelines have their critical failure surface with the minimum factor of safety is a surface falling primarily outside of the reinforced portion of the slope. Newer procedures (Elias et al, 2000 and Tensar, 2003) generate similar designs. However, the probabilistic analysis indicates that for typical levels of uncertainty in the reinforcement force and soil shear strength, the internal and composite failures are nearly equally probable. Since the two modes are essentially independent the total probability of failure is the sum of the probabilities of failure of each. In the case where the probabilities of failure of each mode are equal the total probability is twice the maximum probability of failure of either mode. If the slope is designed such that the probability of failure of internal modes is significantly lower than the probability of composite modes then the probability of failure of the slope will be equal to the probability of failure of the composite mode.

The designer has little control over the variability of either soil shear strength or the reinforcement force. The mean soil shear strength is also limited by the availability of soils at or near the site. In this case the key remaining design variables are the reinforcement strength and spacing which control the mean reinforcement force, and the reinforcement length which will control the location of the composite failure mode and thereby the mean factor of safety of the composite failure mode.

If the coefficients of variation are fixed, the reliability of internal failure modes will be controlled by the mean reinforcement strength which can be increased by either decreasing the spacing of reinforcement or increasing the strength of individual reinforcing elements. In either case this is relatively inexpensive. The reliability of the composite failure mode will then be controlled by the mean factor of safety of the composite failure mode, which, in turn, will be controlled by the length of the reinforcement. Increasing the reinforcement length has a significant increase in the earthwork costs which will, in general, exceed the costs of any additional reinforcing material. Therefore the key design parameter for most slopes will be length of reinforcement used. Since the marginal costs of increasing reinforcement within the reinforced zone of the slope is low, it should always be possible to design a slope where the most probably failure surface is a composite surface. And the probability of failure will be controlled by the reinforcement length and the mean and coefficient of variation of soil strength.

Combining MFORM analyses with traditional limit equilibrium stability analyses is a useful in designing reinforced slopes. The process should start by estimating the mean value of the soil strength and the variability of the soil strength and reinforcement force. The coefficients of variation should be selected

conservatively. With this information, the analysis should proceed by determining the length of reinforcement required to provide an adequate reliability for the composite failure mode. Then the spacing and strength of reinforcement can be chosen so that the probability of failure of an internal failure is well below that of a composite failure.

It is relatively simple to expand a typical limit equilibrium analysis into an MFORM probabilistic analysis using any limit equilibrium slope stability analysis program that accommodates reinforcement. The process starts by locating the critical slip surface and computing the associated factor of safety using the mean value of the random variables, (in this case shear strength and reinforcement force). Once the critical surface is found, 2 more limit equilibrium computations must be performed for each random variable in order to compute the partial derivatives needed to compute mean-value reliability index (Equation 2). Once the partial derivatives have been computed, the reliability index can be computed for any combination of coefficients of variation of the random variables without further limit equilibrium computations. This makes MFORM a simple and powerful tool to investigate how changes in variability affect the reliability of various slope designs. No special probabilistic software is needed.

REFERENCES

Ang, A., and Tang, W. (1984). *Probability Concepts in Engineering Planning and Design, Vol II: Decision, Risk and Reliability*. John Wiley & Sons, New York, N.Y.

Elias, V., Christopher, B., and Berg, R. (2000). *Mechanically Stabilized Earth Walls and Reinforced Soil Slopes Design and Construction Guidelines*. FHWA-NHI-00-043.

Kitch, W. (1994). *Deterministic and Probabilistic Analyses of Reinforced Soil Slopes*, Ph.D. Dissertation, University of Texas, Austin TX.

Madsen, H., Krenk, S., and Lind, N. (1986). *Methods of Structural Safety*. Prentice-Hall, Englewood Cliffs, New Jersey.

Schmertmann, G., Chouery-Curtis, V., Johnson, R., and Bonaparte, R. (1987). "Design Charts for Geogrid-Reinforced Soil Slopes." *Geosynthetics '87 Conference Proceedings*, Industrial Fabrics Assoc. Intl., New Orleans, 108-120.

Tensar Earth Technologies, Inc. (1988). *Slope Reinforcement with Tensar Geogrids, TTN:SR1*. Tensar Corporation, Morow, GA.

Tensar Earth Technologies, Inc. (2003). *Sierra Slope Retension Design Guidelines*. TTN-Sierra-7.03, Tensar Corporation, Morow, GA.

Wright, S. (1991). *UTEXAS3: A Computer Program for Slope Stability Calculations, Users Manual*. University of Texas, Austin TX, Geotechnical Center.

Using Computer Simulations to Take a Closer Look at Load and Resistance Factors for Designing Geosynthetic-Reinforced Walls

Stanley M. Miller[1], M. ASCE, P.E.

[1]Professor Emeritus, Dept. of Civil Engineering, Univ. of Idaho, Moscow, ID 83844
Senior Engineer, STRATA Inc., Moscow, ID 83843
PH (208) 882-1006; FAX (208) 883-4750; email: smiller@stratageotech.com

ABSTRACT

As the LRFD (Load and Resistance Factor Design) Method is implemented in the geotechnical design of geosynthetic-reinforced earth structures for transportation projects according to AASHTO and FHWA guidelines, it would be useful to know how much conservatism is embedded in the prescribed load and resistance factors. Probabilistic analyses using traditional ASD methods (Allowable Stress Design) provide one way to assess the influence of current load and resistance factors on design recommendations. Such an analysis based on computer simulations has been applied to a published FHWA retaining-wall example, focusing on wall performance criteria such as sliding and eccentricity (overturning). The simulations rely on using beta probability distributions to model key input characteristics, including bivariate beta models for attributes that are correlated with each other. Initial results from this study indicate that the prescribed LRFD factors do not provide overly conservative design recommendations. The impacts of key LRFD factors on the computed probability of failure values for sliding also have been investigated for this retaining-wall example.

INTRODUCTION

The currently prescribed load and resistance factors for the LRFD (Load and Resistance Factor Design) Method used in the geotechnical design of geosynthetic-reinforced earth structures have been developed from engineering experience and empirical calibration with design results from traditional ASD methods (Allowable Stress Design). For load factors, maximum and minimum values are listed, and for design purposes the ones most critical to performance of the retaining wall are used for design calculations. Resistance factors for various design elements are reported as single values (e.g., 0.65, 0.75, or 1.0; U.S. DOT FHWA, 2009). As engineers gain experience with LRFD methods, it would be useful to know how much conservatism is embedded in the prescribed load and resistance factors and how sensitive are the design results to uncertainty in soil properties used in the stability calculations. For some projects focused on geosynthetic MSE (mechanically stabilized earth) walls,

reasonably conservative design assumptions can be implemented without adding significant costs to the project. However, such is not the case for many projects, and probabilistic analysis provides a framework to quantify the uncertainties, leading to better informed engineering decisions (Duncan, 2000; Griffiths and Fenton, 2007).

Computer simulations can be used to compare variability in ASD results with the design recommendations from LRFD based on limit states. The simulations rely on being able to describe/identify probability distributions for the input properties treated as variables. Each distribution is modeled as a probability density function (PDF), and a very useful PDF for geotechnical investigations is the general beta PDF. This is a flexible model defined over set limits (minimum and maximum) and takes on various shapes (symmetric, skewed right/left, uniform, exponential) given two specified shape parameters, defined herein as "r and s". Geotechnical experience and a few data from field sampling and laboratory testing can be used to describe a general beta PDF for any soil attribute of interest. For example, experience with an extensive data set from a soil-compaction study for an earth dam (Miller and Comstock, 2005) has shown that soil dry unit weights for five different compaction lifts had a minimum-to-maximum difference that ranged from 0.94 to 1.57 kN/m^3 (6 to 10 pcf), and two lifts showed a symmetric distribution of values, two lifts showed a skewed-right distribution of values, and one lift showed a slightly skewed-left distribution. Also, typical standard deviation values were about 0.31 kN/m^3 (2 pcf). Examples of general beta PDF's with various shape parameters are shown in Fig. 1.

One of the advantages of the general beta PDF model is that the user can specify four of the six descriptive parameters, and the remaining two can be calculated. This is particularly convenient for geotechnical soil attributes, because when adequate data are available to compute a sample mean and standard deviation and to identify the minimum and maximum values, then the shape parameters (r and s) of the beta PDF can be calculated for use in subsequent modeling. However, when very few data are available, the user can specify reasonable values for the minimum and maximum, as well as the shape parameters (r and s) that provide a reasonable symmetry or skew to the PDF, and then the mean and standard deviation can be calculated.

For many geotechnical ASD projects, Monte Carlo simulation provides a flexible, widely applicable tool (Chandler, 1996; Miller, 2009) to generate a realization of the discrete distribution of the output attribute (typically, the safety factor) using randomly selected values from PDF models of the input attributes. Interdependence between any two input variables can be accounted for using their linear correlation coefficient. For this particular study of geosynthetic-reinforced retaining walls, interdependent input attributes would be soil unit weight and soil friction angle, which tend to be directly related to one another (i.e., as soil unit weight increases, we expect the soil friction angle also to increase) with correlation coefficients likely ranging from 0.5 to 0.8. The computer simulations for this study relied on general beta and bivariate beta PDF models for the variable input attributes, and were conducted using Monte Carlo simulation programmed within the Mathcad® software package (PTC, 2010).

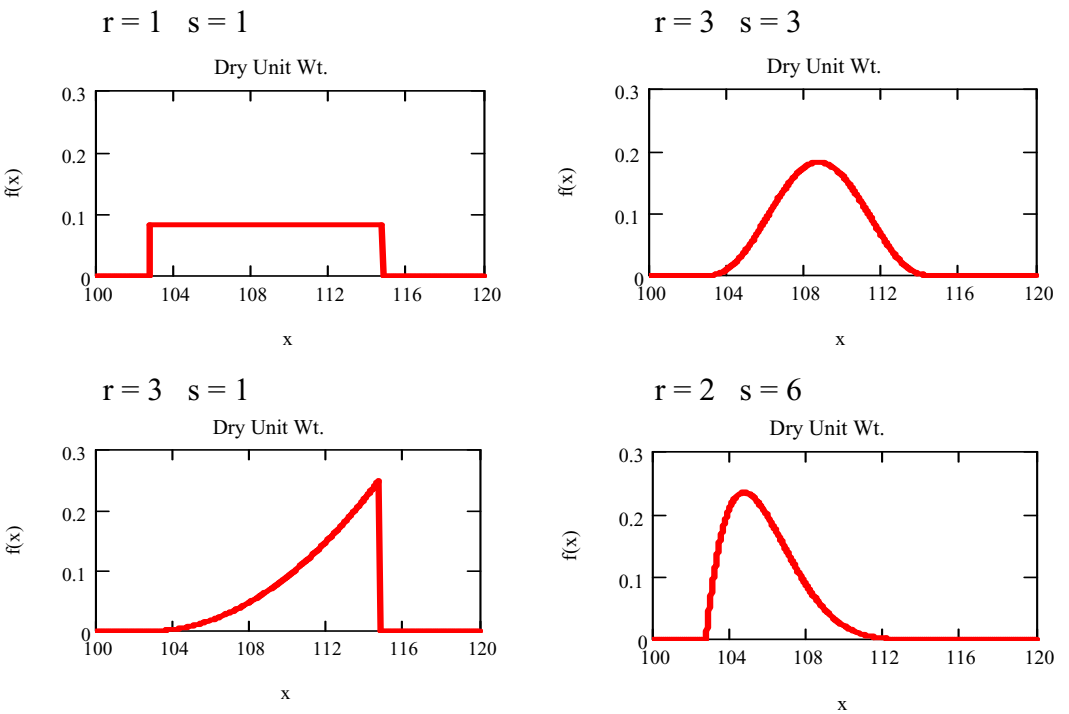

Figure 1. Examples of general beta PDF shapes for soil dry unit weight in pcf (adapted from Miller, 2009).

EXAMPLE OF LRFD CALCULATIONS FOR MSE WALL

A published LRFD example for a geosythetic-reinforced MSE wall in a FHWA Reference Manual (U.S. DOT FHWA, 2009) known as Example E1, has been used to compare LRFD results to probabilistic ASD results for sliding and overturning (eccentricity). Similar studies for analyzing bearing capacity and internal stability of the reinforcement also could be conducted, but were not included in the scope of this current paper. This example involves a 6.1-m (20-ft) high wall with a broken back-slope (2h:1v) and traffic surcharge (Fig. 2). LRFD is similar to ASD in that a coherent gravity mass is assumed for external stability, the shape of the internal failure paths is treated the same, and reinforcement layers are treated as discrete elements. The key differences are the way in which LRFD compares the loads and resistances, and how uncertainty is incorporated into the design process. It also relies on load-combination limit states, such as Strength I, Extreme Event I, and Service I, for design criteria. The Example E1 calculations for base sliding and overturning (eccentricity) were setup in Mathcad®, and those final results concur with those presented in the FHWA Manual in Appendix E (i.e., capacity-to-demand ratio, CDR, of 1.119; and an eccentricity ratio of 0.211, which is less than the prescribed value of 0.25). Note that the LRFD process does not really indicate how conservative the assumption is regarding the 5.49-m (18-ft) wide reinforced zone. However, if we reduce this width by small increments, the analysis shows that the smallest width that still meets the LRFD design criteria for sliding and eccentricity is 5.12 m (16.8 ft).

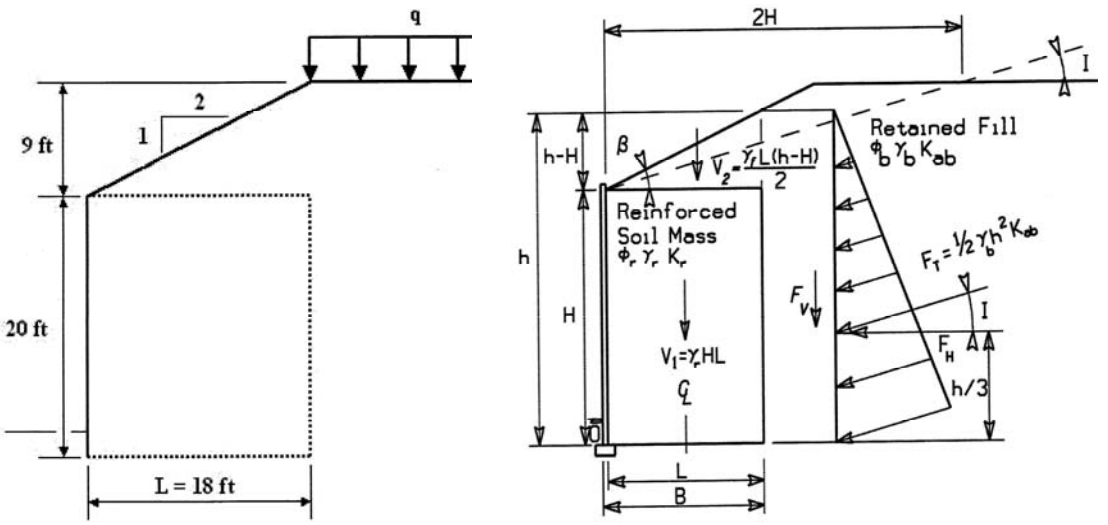

Figure 2. MSE wall geometry for Example E1, showing the assumed 5.49-m (18-ft) wide reinforcement zone (from U.S. DOT FHWA, 2009, Vol. II).

MONTE CARLO SIMULATION

For the previous analysis, the unit weights of the retained soil behind the geosynthetic zone (γ_b) and the reinforced-zone soil (γ_r) were considered to be constant, with a value of 19.64 kN/m^3 (125 pcf). Also, the shear strength values (friction angles) were considered constant for the retained soil (ϕ_r) and the foundation soil (ϕ_f). To consider how variability and uncertainty in these attributes may impact the design results, Monte Carlo simulations were conducted to compare the ASD and LRFD methods. The ASD analysis for sliding stability was similar to that used in LRFD, excluding the load and resistance factors; however, the stability analysis for overturning was based on calculating moments about the toe of the wall, instead of about the center of the base of the reinforced zone. The accepted design criteria for ASD is that the factor of safety (FOS) for sliding is $\geq$ 1.5 and the factor of safety for overturning is $\geq$ 2.0. By simulating hundreds of FOS values, we can compute the probability of an "inadequate design", P(ID), by computing the percentage of simulated FOS values that are less than the criteria values (1.5 for sliding and 2.0 for overturning). We also can compute the probability of failure as the percentage of simulated FOS values that are less than 1.0. In like manner, simulations based on the LRFD method will provide "factored" probabilities of failure, one for sliding (CDR $\leq$ 1), and one for eccentricity (probability that $e_{ratio} \leq 0.25$).

Mathcad® calculations for Example E1 (see attached Appendix) illustrate the simulation process with 2000 iterations and using bivariate beta PDF's to mimic the correlation between soil unit weight and friction angle. In the Appendix example, all input beta PDF's are assumed skewed right (r = 2; s = 6). Other simulations using uniform symmetric PDF's (r = s = 1) and center-modal symmetric ones (r = s = 6)

also were conducted using the same minimum-to-maximum variable ranges for unit weight and for friction angle. Simulation results are summarized in Tables 1 and 2.

The traditionally computed, deterministic results are shown in columns 2 and 3 of the tables. Selected combinations of beta PDF shape parameters for simulating soil unit weight and friction angle are given in column 4 of the tables; [1,1] provides a uniform distribution (equal probability across the interval); [6,6] provides a symmetrical, central-modal distribution similar to a truncated normal PDF; [2,6] provides a skewed-right distribution similar to a truncated lognormal PDF. A summary of the ASD simulation results is given in columns 5-8 of the tables. The term reported in column 8, F_{LRFDpf}, is the ASD factor of safety value that would yield the same probability of failure as that reported for the LRFD simulation; in other words, this is the ASD FOS value that most closely emulates the output of the LRFD analysis. Results from the LRFD simulations are reported in columns 9 and 10 of the tables.

Table 1. Simulation results for sliding analysis of MSE wall, Example E1; correlation coefficient assumed to be 0.7 for soil unit weight and friction angle.

Reinforced Length	ASD FOS	LRFD CDRsl	Beta PDF	ASD Simulation F_{mean}	P(ID)	P(F)	F_{LRFDpf}	LRFD Simulation CDR_{mean}	P(F)
5.49m (18ft)	1.628	1.119	r1,s1	1.630	0.106	0.000	1.451	1.120	0.029
			r6,s6	1.629	0.003	0.000	---	1.120	0.000
			r2,s6	1.507	0.465	0.000	1.451	1.038	0.097
5.12m (16.8ft)	1.527	1.053	r1,s1	1.530	0.392	0.000	1.449	1.055	0.202
			r6,s6	1.529	0.277	0.000	1.449	1.054	0.039
			r2,s6	1.414	0.967	0.000	1.448	0.977	0.792
4.57m (15ft)	1.375	0.954	r1,s1	1.379	0.783	0.000	1.443	0.956	0.761
			r6,s6	1.377	1.000	0.000	1.443	0.955	0.945
			r2,s6	1.274	1.000	0.000	1.422	0.886	1.000

Table 2. Simulation results for overturning analysis of MSE wall, Example E1; correlation coefficient assumed to be 0.7 for soil unit weight and friction angle.

Reinforced Length	ASD FOS	LRFD e Ratio	Beta PDF	ASD Simulation F_{mean}	P(ID)	P(F)	F_{LRFDpf}	LRFD Simulation $eRatio_{mean}$	P(F)
5.49m (18ft)	2.789	0.2112	r1,s1	2.792	0.000	0.000	---	0.2113	0.000
			r6,s6	2.789	0.000	0.000	---	0.2113	0.000
			r2,s6	2.694	0.000	0.000	---	0.2199	0.000
5.12m (16.8ft)	2.451	0.2489	r1,s1	2.454	0.000	0.000	2.441	0.2490	0.466
			r6,s6	2.451	0.000	0.000	2.441	0.2489	0.419
			r2,s6	2.369	0.000	0.000	2.441	0.2588	0.939
4.57m (15ft)	1.985	0.3225	r1,s1	1.987	0.557	0.000	2.190	0.3226	1.000
			r6,s6	1.985	0.675	0.000	2.086	0.3226	1.000
			r2,s6	1.919	0.983	0.000	2.050	0.3349	1.000

Several interesting observations of these simulation results are listed below:
1. The ASD probability of failure values for sliding and for overturning were always equal to zero, regardless of the reinforcement lengths considered here and regardless of whether the deterministic FOS was less than the commonly prescribed design value (1.50 for sliding and 2.00 for overturning). This suggests that the design FOS values for relatively simple MSE wall geometries (such as Example E1) likely are overly conservative, meaning that MSE walls designed using ASD analysis over the past 25 years have been designed with more conservatism than current MSE wall designs based on LRFD. This further assumes that soil unit weight and friction angle do not exceed reasonably expected variability, such as a range of 0.94 to 1.57 kN/m^3 (6 to 8 pcf) for unit weight and a range of 2 to 4 degrees for friction angle. Greater variability in these soil properties may decrease the level of conservatism.
2. Though deterministic design criteria may be met in the sliding and overturning analyses of MSE walls (whether by ASD or LRFD methods), there still may be a significant probability of failure that may be of concern to the design engineer. Note the LRFD simulation results for the 5.12-m reinforcement length in both tables, especially when the soil properties are assumed to have skewed-right distributions.
3. The probability of "inadequate design", P(ID), as used in the reported ASD analyses, may prove to be a better tool for comparison with LRFD results than the ASD P(F) values. This is due to the fact that the design FOS values for sliding and for overturning are "factored" to deal with uncertainties at the end of the ASD analysis, which is somewhat similar to the LRFD approach which instead relies on load and resistance factors up front in the analysis to account for those uncertainties. In other words, the ASD P(F) values based on the probability that the FOS takes on values less than 1.0 are actually "unfactored" and will be difficult to compare directly with LRFD P(F) values.

INFLUENCE OF LRFD FACTORS ON PROBABILITIES OF SLIDING

Like many typical MSE wall analyses with geogrid-reinforced zones, this Example E1 indicates that the sliding failure mode controls the design more than the overturning (eccentricity) mode. The following load and resistance factors are used to compute the CDR for sliding (U.S. DOT FHWA, 2009):

Horz. earth pressure:	γ_{EHmax} (1.5)	Vert. earth pressure (dead load):	γ_{EVmin} (1.0)
Live load surcharge:	γ_{LS} (1.75)	Resistance for base sliding:	Φ_S (1.0)

The FHWA-recommended factor values for a MSE "Strength-State" analysis are shown in parentheses above. By varying the value of one of these terms while holding the other three constant, we can investigate the influence of such changes by conducting Monte Carlo simulations and displaying the results on plots like those shown in Figures 3 – 6 (based on skewed-right input PDF's). It is important to note that the probability of failure for sliding equals approximately 0.10 in each case when a load or resistance factor is assigned its FHWA-recommended value. Thus, similar graphs can be generated for any specified wall geometry, so the designer can see the impact of modifying LRFD factors on the resulting P(F) values for that project.

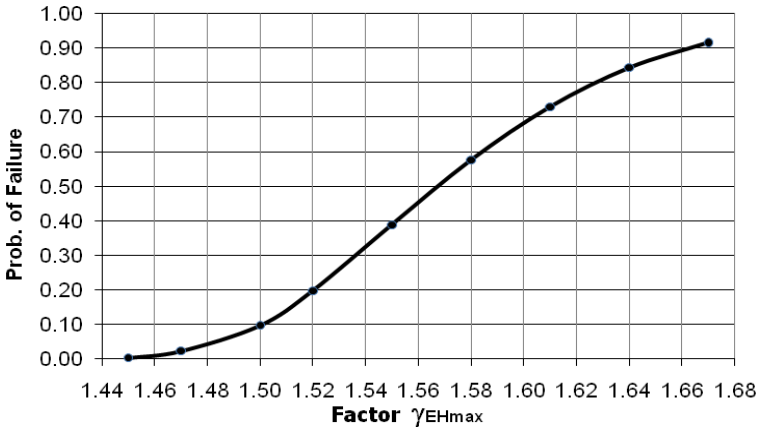

Figure 3. Relationship between $P(F)_{sliding}$ and γ_{EHmax} for FHWA Example E1.

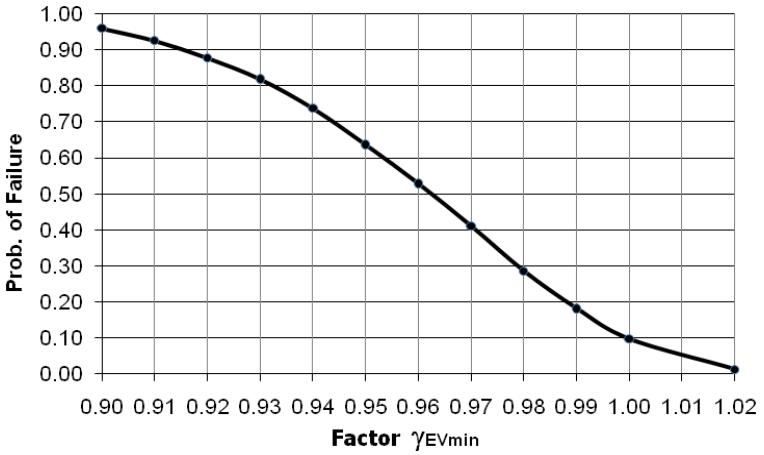

Figure 4. Relationship between $P(F)_{sliding}$ and γ_{EVmin} for FHWA Example E1.

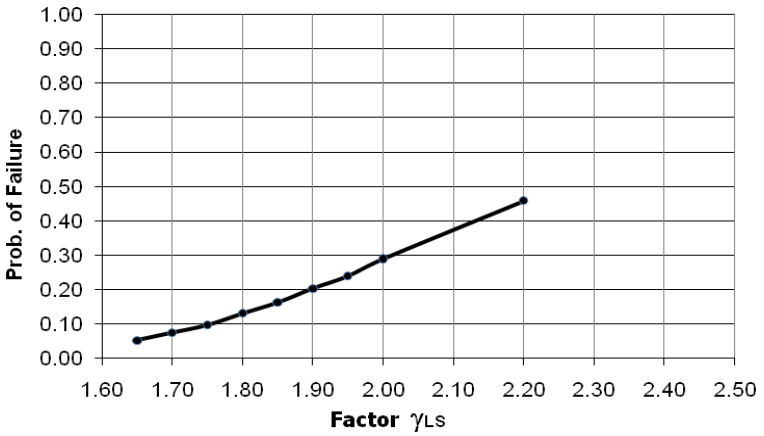

Figure 5. Relationship between $P(F)_{sliding}$ and γ_{LS} for FHWA Example E1.

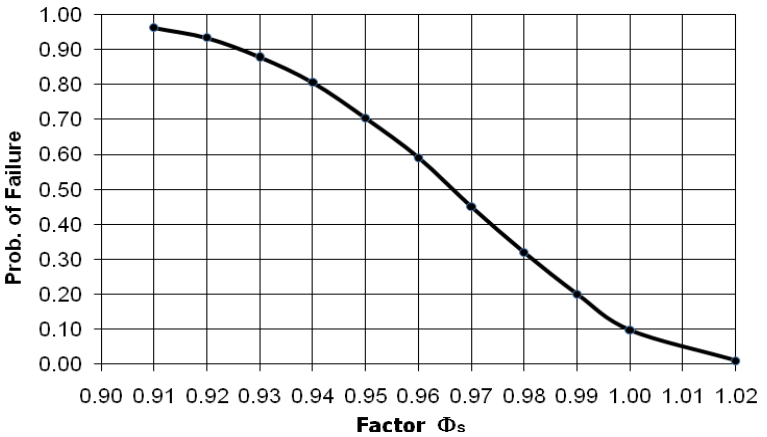

Figure 6. Relationship between $P(F)_{sliding}$ and Φ_S for FHWA Example E1.

CONCLUSIONS

Experience with these types of simulations for sliding and overturning analyses of MSE walls has shown that LRFD methods are not overly conservative in regard to the minimum recommended length of the geogrid reinforcements (e.g., L_{min} = 0.8H for sloping backfill surcharge). In fact, for simple wall geometries like that used in Example E1, LRFD design results appear to be slightly less conservative than those from traditional ASD analyses. Skewed-right PDF's for unit weight and friction angle always resulted in higher probability of failure values than those computed with symmetric PDF's.

Probabilistic simulations and sensitivity studies can provide valuable input to assist in the specification of load and resistance factors when desired probabilities of failure can be prescribed by site conditions, project objectives and usage, and/or risk assessments. Simulation examples based on skewed-right input PDF's for soil unit weight and friction angle have shown that the FHWA-recommended values for load and resistance factors tend to produce probability of sliding values equal to approximately 0.10 (for FHWA Example E1). Additional studies are recommended to also evaluate other potential failure modes, such as overturning, bearing failure, geogrid rupture or pullout, and global instabilities.

REFERENCES

Duncan, J.M. (2000). "Factors of safety and reliability in geotechnical engineering." *J. Geotech. & Geoenvir. Engrg.* 126(4), 307-316.

Chandler, D.S. (1996). "Monte Carlo simulation to evaluate slope stability." In *Uncertainty in the Geologic Environment: From Theory to Practice*, Geotech. Special Publ. No. 58, ASCE, 474-493.

Griffiths, D.V. and Fenton, G.A., eds. (2007). *Probabilistic Methods in Geotechnical Engineering*. Springer Wien Publ., New York, 346 p.

Miller, S.M. (2009). "Computational and visual tools for teaching probabilistic geotechnical design." In *Contemporary Topics in In-Situ Testing , Analysis, and Reliability of Foundations*, Geotech. Special Publ. No. 186, ASCE, 632-639.

Miller, S.M. and Comstock, C.M. (2005). "Geostatistical analysis of relative compaction during construction of an earthfill dam." In Proc. of 11th Intl. Conf. of IACMAG, Turin, Italy, 2, 523-530.

U.S. DOT FHWA (2009). "Design and construction of mechanically stabilized earth walls and reinforced slopes, Vol. I and II". Publ. No. FHWA-NHI-10-024, National Highway Institute, Washington, DC.

PTC (2010). website: www.ptc.com/products/mathcad, Parametric Technology Corp., 140 Kendrick Street, Needham, MA; October, 2010.

APPENDIX – Example of Mathcad® sheet for MSE wall simulations.

Modular Block Wall with Geogrid Reinf. & Broken Backslope: Example E1

Backslope is 2h:1v and assumed traffic load is equiv. to 2-ft thick soil layer

$^\circ := \text{deg}$

$H := 20 \quad H_b := 9 \quad I := 57.29578 \cdot \operatorname{atan}\left(\frac{H_b}{2H}\right) = 12.68 \quad \gamma_b := 125.0\ \text{pcf} \quad \gamma_r := 125.0\ \text{pcf}$

$\delta := I \cdot ^\circ \quad \beta := I \cdot ^\circ \quad \theta := 90 \cdot ^\circ \quad \phi_b := 30 \cdot ^\circ \quad \phi_f := 30 \cdot ^\circ \quad L := 16.8\ \text{ft} \quad h := H + H_b$

PROBABILISTIC METHOD

Beta pdf values for variable attributes

Retained soil unit wt. (pcf)	$\gamma_{bmin} := 121$	$\gamma_{bmax} := 129$	$\gamma_{br} := 2$	$\gamma_{bs} := 6$	
Reinforced soil unit wt. (pcf)	$\gamma_{rmin} := 122$	$\gamma_{rmax} := 128$	$\gamma_{rr} := 2$	$\gamma_{rs} := 6$	
Retained soil fric. angle (°)	$\phi_{bmin} := 28$	$\phi_{bmax} := 32$	$\phi_{br} := 2$	$\phi_{bs} := 6$	$\rho_b := 0.7$
Reinforced soil fric. angle (°)	$\phi_{rmin} := 29$	$\phi_{rmax} := 31$	$\phi_{rr} := 2$	$\phi_{rs} := 6$	$\rho_r := 0.7$
Foundation soil fric. angle (°)	$\phi_{fmin} := 28$	$\phi_{fmax} := 32$	$\phi_{fr} := 2$	$\phi_{fs} := 6$	

(note: ρ is the estimated correl. coef. between ϕ and γ for the soil material)

ASD Results

FOS sliding

Fsmin = 1.3138

Fsmax = 1.5989

Fsmean = 1.4154 Fssd = 0.0457

ProbID := CtP(FS$_s$, 1.5) = 0.95350

ProbFail := CtP(FS$_s$, 1.0) = 0.00000

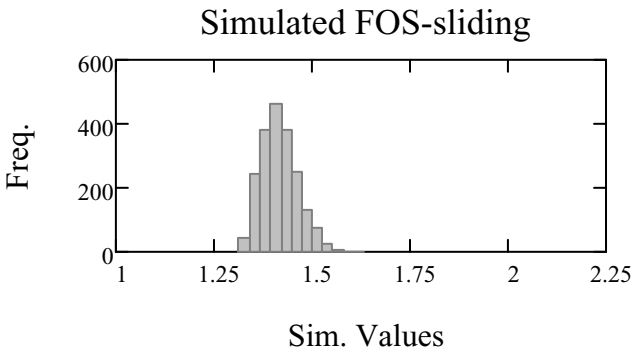

FOS overturning

Fomin = 2.2619

Fomax = 2.5312

Fomean = 2.3696 Fosd = 0.0444

ProbID := CtP(FS$_o$, 2.0) = 0.00000

ProbFail := CtP(FS$_o$, 1.0) = 0.00000

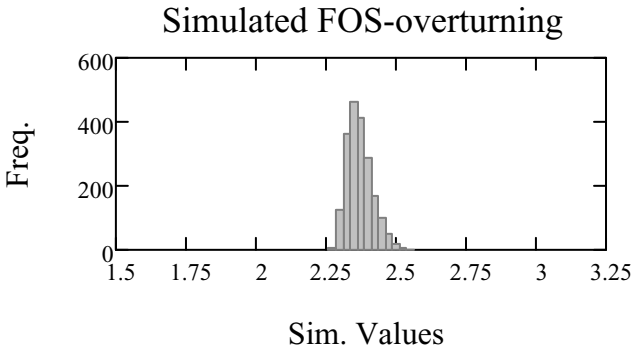

LRFD Results

CDR sliding

Csmin = 0.9095

Csmax = 1.1014

Csmean = 0.9780 Cssd = 0.0309

ProbFailc := CtP(CDR$_s$, 1.0) = 0.76550

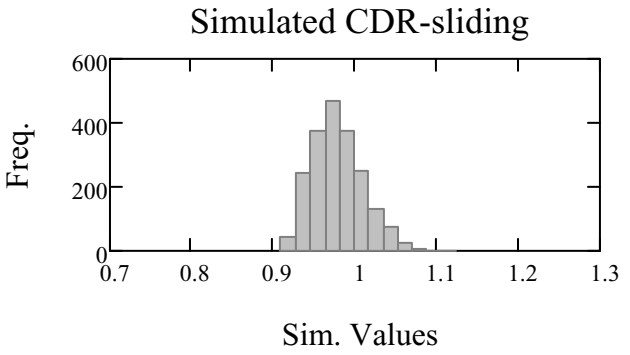

e/L eccentricity

emin = 0.2399

emax = 0.2725

emean = 0.2587 esd = 0.0054

ProbFaile := 1 − CtP(e$_r$, 0.25) = 0.92450

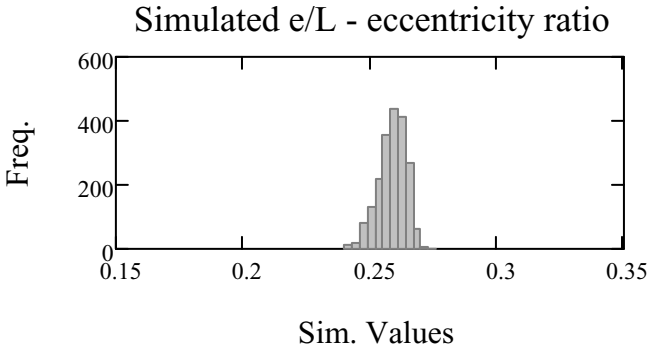

Impact of Non-Analytical Factors in Geotechnical Risk Assessment of Levees

Mary Perlea[1], Edward Ketchum[2],

[1]US Army Corps of Engineers, Sacramento District, 1325 J Street, Sacramento, CA 95814; Phone : 916-557-7185; email: Mary.p.perlea@usace.army.mil,
[2]US Army Corps of Engineers, Sacramento District, 1325 J Street, Sacramento, CA 95814; Phone : 916-557-5383; emails: Edward.A.Ketchum@usace.army.mil

ABSTRACT

This paper provides information on the impact of vegetation, rodents' activity, encroachments, utility penetration and riverbank and levee erosion on the performance of the levee system protecting the City of Sacramento, California. A geotechnical risk and reliability study was performed on the levees along the Sacramento River and tributaries to determine the risk of a poor performance of the existing levees. Seepage through the levee foundation and the slope stability were determined to be the major factors of poor performance for the levee system. Fragility curves estimating probability of poor performance of the levee system for different river stages were obtained by combining the analytically obtained fragility curves for seepage and slope stability with judgmental fragility for the other factors. This paper presents the example of a judgmental curve as concluded by an expert elicitation panel regarding the impact of non-analytical factors on the geotechnical performance of the levee system protecting the Sacramento area. The performance curves were used only for an economical evaluation of the levee, to determine the federal interest in the project, not for the design of the of the flood control system.

INTRODUCTION

Performance curves for a levee system are developed only for financial analyses on selected critical index points, as a composite based on the individual components of the levee performance curve, which include the seepage through the levee foundation and levee embankment and stability of the landside levee slope for steady state conditions, considering different river stages. The seepage portion and the stability portion of the levee performance curve are each based on standard engineering analyses that are repeatable and objective (meaning that different geotechnical engineers, using the same data set would come up with the same answers for the seepage and stability portion of the levee performance curves). Non-analytical factors such as vegetation on the levee slopes or within the levee vicinity, rodent activity, encroachments, utility penetrations, and erosion of the river bank and levee slopes, will have an impact on the performance of the levee embankment which cannot be determined analytically. All these external factors are part of a judgmental fragility curve. This portion of the levee performance curve is basically an educated opinion based upon the individual geotechnical engineer's professional experience. Because it is an educated opinion by a geotechnical engineer, two different geotechnical engineers could come up with drastically different judgment portions of

the levee performance curve. This problem is further compounded by the involvement of geotechnical engineers from different organizations and agencies, with different backgrounds and different professional experience. In science, engineering, and research, expert elicitation is the synthesis of opinions of experts of a subject where there is uncertainty due to insufficient data, when such data is unattainable because of physical constraints or lack of resources. Expert elicitation is essentially a scientific consensus methodology. Expert elicitation allows for parameterization, an "educated guess", for the topic under study, and its most common use is to quantify uncertainty. Expert elicitation is one of several methods acceptable in United States Corps of Engineers (USACE) guidance documents for use in reliability analyses and risk assessments and has been used for various Corps projects. The expert elicitation panel consisted of a wide array of experienced geotechnical engineers and levee maintaining agencies' personnel, with the objective being to develop the most likely impacts of vegetation, rodent activity, encroachments, utility penetration and erosion on levee performance, as well as uncertainty bands about these most likely impacts.

TYPES OF OPINIONS ELICITED

The experts provided opinions for the followings:

1. Define terms to reduce ambiguity in the descriptions, and state any necessary assumptions by examining and revising the description of issues presented to them.
2. Provide answers to issues as "Yes" or "No" with any explanations if necessary or requested.
3. Provide a probability value. Probability is defined as a measure of occurrence likelihood or chance, and is of two types: (a) objective probability is based on empirical information, and computed as the relative frequency, and (b) subjective probability is not based on empirical information, but inferred indirectly from relevant knowledge. Probabilities must meet the following conditions: (a) $0 \leq$ probability ≤ 1, and (b) sum of probabilities of all possible outcomes that are mutually exclusive is 1.
4. Provide values described by a triangular probability distribution. The triangular probability distribution is used to subjectively assess a variable or a parameter and its uncertainty, as shown in Figure 1. The best estimate is commonly placed in the middle. The experts will be asked a series of questions concerning specific topics. When possible all answers to questions will be given in the format of a triangular distribution. A response in the format will include, a minimum, maximum, and most likely value to the question from each respondent.
5. Provide a confidence interval on the value that a parameter or coefficient might take. Confidence intervals are ranges used to subjectively assess a variable or a parameter and its uncertainty. The relationship between a confidence level and the size of the interval is such that higher confidence produces wider intervals, and smaller confidence leads to narrower intervals.

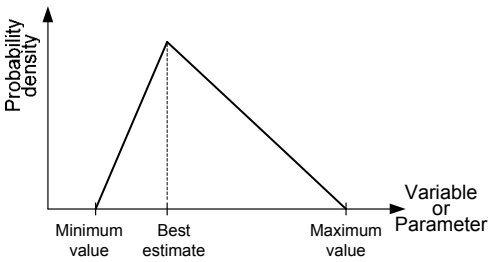

Figure 1. Probability Triangular Distributions.

PANEL COMPOSITION

The panel was composed of the nine (9) members as follows.

1. Facilitator – a well known expert in the subject. The facilitator will have no voting rights, he will assure the questions asked to the expert panel are related to the subject and the responses are unbiased and assure the panel addresses all questions.
2. The geotechnical engineer responsible for the development of the fragility curves, with no voting rights. He provides additional insight of the condition at the levee reaches examined.
3. Two members of the Engineering Department of the Corps of Engineers, with knowledge of the area analyzed and its past history.
4. One member of the Operation Department of the Corps of Engineers with past levee inspection and flood fight experience for the subject levee system.
5. Two highly recognized specialists in geotechnical and hydraulic aspects of the levee system, particularly regarding the seepage, slope stability, and erosion issues related to levee performance.
6. Two members of the California Department Resources, the official owners of the levees and directly responsible with the inspection, operation and maintenance of the system.

Several non-voting observers participated at the expert elicitation meetings were members of the Levee Maintaining agencies or other Corps of Engineers specialists. These observers provided witness testimony concerning past performance on the levee systems analyzed and on other levees in the California Central Valley.

LEVEES SYSTEMS ANALYZED

The Sacramento District of the Corps of engineers performed a feasibility study of the levee systems protecting the city of Sacramento and its neighborhood. The protected area was divided in three major basins:

1. Natomas Basin - is nearly a closed basin protected by a levee along the east bank of the Sacramento River between Natomas Cross Canal (NCC) and American River, continued by a levee along the north bank of the American River to the Natomas East Main Drainage Canal (NEMDC), a levee along the west bank of the NEMDC and along the west bank of the Pleasant Grove

Canal, and closed by the levee long the NCC to its confluence with the Sacramento River.

2. American River North Basin - protected by a levee along the American River north bank continued by a levee along the east bank of the NEMDC. Levees along the tributaries to the NEMDC such as Dry Creek and Arcade Creek north and south bank are also included in the system.
3. American River South Basin - protected by a levee along the south bank of the American River continued by a levee along the Sacramento River south of the American River. The levee systems and the basins are shown on Figure 2.

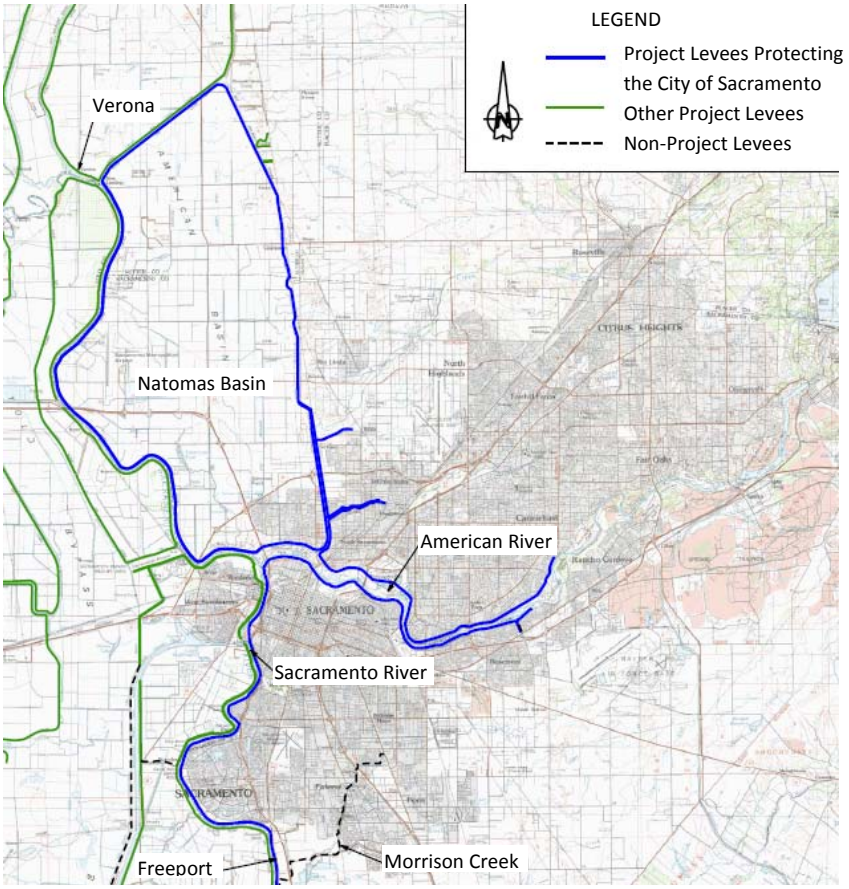

Figure 2. Sacramento Levee Systems.

Each basin was divided into multiple reaches with common geotechnical, geomorphologic and levee geometry aspects as well as economical and hydraulic aspects. A critical index point was selected for each reach. The selection of the index points was based on seepage and stability deterministic analyses considering the levee and foundation geotechnical conditions, and levee geometry. Geotechnical risk based analyses were performed to develop the stability and underseepage fragility curves. The judgmental fragility curve were determined by the expert elicitation based on known conditions of the vegetation on levee embankment or in the vicinity of the toes, encroachments, utility penetration, rodent activity, and erosion based on the location of the river and past history.

LEVEE EMBANKMENT FAILURE MODES

The team first question was to identifying what causes a levee to go into a poor performance mode, that is, what causes levees to fail or breach in case of no flood fighting or other action. The panel was asked to vote which ones are most likely to cause a levee to fail. The results (with the number of votes received) are provided below:

- Seepage – 10
- Erosion - 7
- Overtopping - 4
- Encroachments/Penetrations - 6
- Stability - 6
- Rodents - 6

Considering that the stability and seepage through the foundation of the levee and through the embankments are determined analytically, the following factors were considered having a significant contribution to the failure with no flood fighting involved. The results were as follows:

- Encroachments (in the levee embankment and/or foundation of the levee)
- Erosion (of the levee embankment and/or riverbank)
- Penetrations (through the levee embankment and/or levee foundation)
- Rodents activity (beavers and/or squirrels)
- Vegetation (brush and/or trees on the levee embankment and within a critical area of the toe of the levee)

It was noted that consideration of agreement in failure modes & influence, importance of the economic model versus level of protection & public safety can have a difference on the basis of risk and communication

NATOMAS BASIN, SACRAMENTO RIVER EAST BANK LEVEE - JUDGMENTAL CURVES

This is an example of determination of the judgmental curve for one index point on the levee along the east bank of the Sacramento River, protecting the Natomas Basin.

1. General Conditions**.** The levees are constructed of dredged sand over an impervious clay blanket underlain by s thick layer of sand. The levees are located in a high populated area, with heavy woody vegetation and encroachments extending on the levee waterside or landside slopes up to the levee crest. The Garden Highway runs on the levee crest along the east bank of the Sacramento River and north bank of the American River. The encroachments include residential and commercial buildings, apartment houses, gas station. Swimming pools were excavated close to the levee landside toes. Private fences between residential lots extend on the levee slope crossing the levee crest, making the access for inspection, maintenance and flood fighting difficult. Mature trees or brush, including hedges between the highways and private lots are grown on the levee slopes up to the levee crest. Utility penetrations such as water lines, sewer lines, and electrical conduits, culverts and pipes from interior drainage pump stations, and irrigation lines, are crossing the levees. On some areas of the reach the levee is oversized, with the crest at least 40

feet wide and extended as much as 60 feet wide along some reaches. A deep soil/cement/bentonite wall is authorized and planned to be constructed within this reach, there is also an existing shallow 30 to 40 feet deep seepage cut-off wall to mitigate the seepage through the levee embankment. Based on hydraulic analyses, there are expected low water velocities during high river stages due to Sacramento Bypass on the upper end which diverts the water in the Yolo Bypass. Figure 3 shows an apartment complex with gates, fences, trees constructed on the waterside levee slope up to the levee crown.

Figure 3. Apartment House and Woody Vegetation on the Waterside Levee Slope.

2. Impact of Vegetation on Levee Poor Performance. The existing vegetation consists of mature trees and brushes on both waterside and landside slopes of the levee, as well as along the levee toes. It was mentioned that the composition of the slurry wall may influence the behavior of the roots within the levee embankment. It was noted that one negative impact of the mature trees is possible uprooting due to windthrow which leaves behind big holes in the levee, exposing the sandy portion of the levee to more erosion, decreasing the levee slope stability, and increasing the seepage through the levee or its foundation. The water elevation in the river was considered also on the impact of the vegetation. The average impact of the vegetation on the poor performance of the levee after removing the high and low votes, was considered 3% for water at the levee crest.

3. Impact of Encroachments on levee poor performance. The existing conditions include power poles, residential homes as well as commercial buildings constructed on the fill on waterside berms or along the landside toe within the levee right of way. Fences and hedges along the private property line extending to the levee crown and along it prevent visibility of the levee slope for annual and periodic inspection. An urban developed area is located landside of the levee extended up to 10 feet from the levee toe. All these encroachments impede proper inspection of the levee and make difficult a flood fighting during high water stages. Swimming pools excavated close to the levee landside toe cutting into the impervious blanket increase seepage through the levee foundation. Excavated levee slopes and construction of unauthorized retaining walls into the levee slopes may lead to slope instability of the levee

embankment. The decision on the impact of the encroachment on the levee poor performance within this reach was 7% considering the water at the levee crest.

4. Impact of Penetrations on Levee Poor Performance. Along this reach there are two interior drainage pump stations which include discharge lines through the levee embankment. The conditions of the discharge lines are mostly unknown; there are no recent visual or video inspections available. The pump station discharge lines have flap gates and hand cranks that are 1914 vintage. Figure 4 shows the outlet structure of the pumping station. There is known seepage at joints into conduit.

Figure 4. Aged Pumping Station Outlet Structure

There are also other utility penetrations that may have a negative impact such as a big sewer force main and several irrigation lines. One sewer line constructed by directional drilling caved during installation. The levee settled a couple of inches and a big subsidence was observed under an abandoned house 50 feet from the levee landside toe. The area was repaired and it is monitored for further movements. There are also pressurized gas lines crossing the levee embankment. The impact of the penetration on the poor performance of the levee was rated 6% when the river reaches the crest of the levee.

5. Impact of Animal Burrows on the Levee Poor Performance. This reach of the levee system is heavily populated and animal burrowing is considered minimal. There is an active rodent abatement program. There is no history of animal burrow damages. The existing seepage cut-off wall may also prevent seepage through the levee even if animal burrow activity was observed in the past. Considering the high and low factors, the average voted impact on the levee performance was determined to be 3%.

6. Impact of Erosion on Levee Poor Performance. There is no Sacramento bank erosion history related to stream velocity or wind waves along this reach. Encroachments and vegetation on the levee slopes also reduce erosions of the riverbank and levee waterside slope. Considering the existing conditions the impact of erosion on the levee poor performance for this reach was considered 4% for the water at the levee crest.

7. Summary of Components on this Reach: Vegetation 3%; Encroachments 7%; Penetrations 6%; Animal Burrows 3%; Erosion 4%.

FRAGILITY CURVES FOR NATOMAS LEVEE ON SOUTH SACRAMENTO RIVER

The judgmental fragility curves considering the expert elicitation votes are provided in Figure 5.

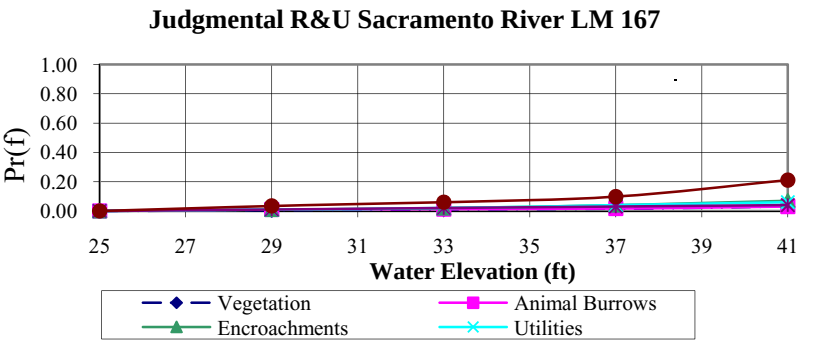

Figure 5. Judgmental Risk Based Fragility Curve.

Considering the seepage and stability analyses, the combined risk of poor performance is shown on Figure 6. As seen on Figure 6, the poor performance of the levee embankment at this location is determined by the seepage through the levee embankment. The judgmental impact on the performance is very limited.

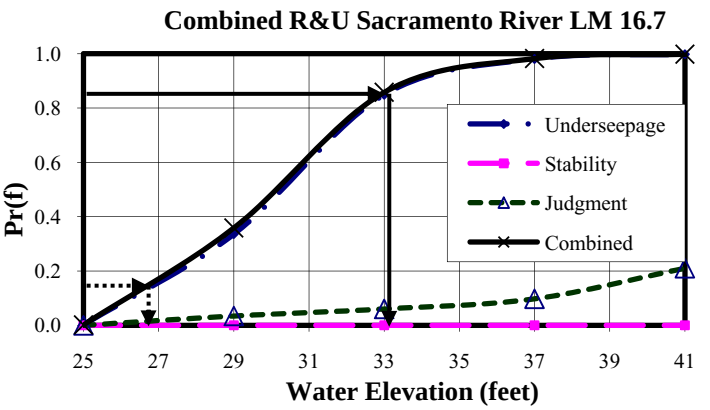

Figure 6. Combined Geotechnical Risk and Uncertainty Curve.

CONCLUSION

The expert elicitation panel determined that the non-analytical factors affecting the levee performance along this reach of the levee generally have a relatively low impact (up to 25%) on the levee performance. This impact should be considered in the evaluation of the levee conditions and particularly in the proposed mitigation measures. Some of the proposed remediation actions may reduce the negative impact of the non analytical factors. As an example, a soil/cement/bentonite

seepage cut-off wall proposed to mitigate the seepage through the levee embankment and through the foundation may reduce the impact of the rodents' activity or tree roots penetration. Some of the existing utilities penetrating the levee will be relocated up and above the seepage cut-off wall reducing the impact of the penetration. A seepage berm constructed landside of the levee toe will remove the vegetation growing on the landside, remove the encroachments, and fill up the excavation landside of the levee toe.

REFERENCES

US Army Corps of Engineers (2010). *Natomas Post Authorization Changer Report*, August 2010

US Army Corps of Engineers (2006). TL 1110-2-561 - *Reliability Analysis and Risk Assessment for Seepage and Slope Stability Failure Modes for Embankment Dams*

Rockfall and Mitigation Evaluation with 3-D Discrete Element Modeling

R. Zhang[1], A. Rock[2]
Metropolitan State College of Denver, Department of Engineering Technology, Denver, Colorado 80217; PH 303-556-8561; FAX: 303-556-2972; Email: rzhang@mscd.edu
[2]Lodex Engineering Corporation, 1745 Shea Center Drive, 4th Floor, Highlands Ranch, Colorado 80129; PH 720-344-5188; Email: arock@lodexeng.com

ABSTRACT

Rocks falling down a slope bounce, slide, roll, and launch. Cylindrically-shaped rocks pick up speed rolling like a log or barrel, then bounce end-over-end until nearly coming to a stop. The sharp corners of block-shaped rocks break off. Rocks pick up translational and rotational speed, bouncing and launching at greater trajectory heights until impacting the slope with sufficient force to break apart. Smaller fragments may stop relatively quickly, while larger fragments may undergo additional changes in size and shape while continuing to fall down the slope. Factors such as initial rock shape, size, initial fracture persistence, and anisotropic tensile strength can significantly affect rock trajectory heights, energies, and rollouts. This paper presents a numerical method to efficiently and accurately simulate rockfall to design barriers, attenuators, and catchments.

INTRODUCTION

Rockfall mitigation is important for safety and maintenance of railroads, highways, or other structures in mountainous regions. Although field testing is adventurous, it can be costly, hazardous, and time consuming, with limited results. Field testing often requires diversion of traffic, evacuation of personnel and equipment, or construction of barriers to protect existing structures. Hundreds of rocks of different sizes and shapes must be released from various locations on the slope in various seasons and weather conditions with high-speed video acquisition at numerous locations on the slope, unobscured by vegetation or terrain, to measure translational and rotational energies, trajectory heights, and break-up of the rocks. Native rocks must be used, as man-made rocks typically exhibit significantly different rockfall characteristics. The testing process must be repeated after constructing a rockfall mitigation strategy, or after any changes in slope conditions or vegetation occur. In many cases, rockfall mitigation strategies must be constructed prior to testing to protect existing structures, which in turn affect test results. These difficulties, limitations, and requirements often result in construction of mitigation strategies with limited or non-existent field testing data. However, without sophisticated numerical modeling tools, field testing may be the only available option for obtaining realistic and accurate results.

ENGINEERING APPROACH

The theoretical foundation for DEM is based on solving the equations of motion by numerical integration and the principle of dynamic relaxation. In general, DEM programs should at least include the following three aspects:

- Representation of contact and establishment of a correct contact constitutive model between discrete bodies.
- Representation of the properties of materials of discrete bodies which may be rigid, deformable, isotropic, anisotropic, homogeneous or heterogeneous.
- Representation of various discrete block shapes and establishment of certain data structures and algorithms to assess contacts and contact types.

The discrete element method specifically related to this simulation discretizes the particles as 3D spheres. Figure 1 shows two blocks ***I*** and ***II*** in contact. Their positions are defined by vectors $\boldsymbol{R_1}$ and $\boldsymbol{R_2}$. The blocks have masses m_1 and m_2, linear velocity vectors $\boldsymbol{v_1}$ and $\boldsymbol{v_2}$, and angular velocity vectors ω_1 and ω_2, respectively. The equation of motion for element *i* at discretized time step *n* is:

$$\mathbf{M}\mathbf{a}_\mathbf{n}^\mathbf{i} + \mathbf{C}\mathbf{v}_\mathbf{n}^\mathbf{i} + \mathbf{P}_\mathbf{n}^\mathbf{i}\left(\mathbf{x}_\mathbf{n}^\mathbf{i}\right) = \mathbf{f}_\mathbf{n}^\mathbf{i} \tag{1}$$

where

$\mathbf{x}_n^i$, $\mathbf{v}_n^i$ and $\mathbf{a}_n^i$ are the position, velocity and acceleration vectors of the *i*th element at the *n*th time step. The 3-D case results in:

$$\left(\mathbf{x}_n^i\right)^T = \left[\mathbf{x}_n^i, \mathbf{y}_n^i, \mathbf{z}_n^i, \theta_n^i\right]; \qquad ; \qquad \left(\mathbf{a}_n^i\right)^T = \left[\ddot{\mathbf{x}}_n^i, \ddot{\mathbf{y}}_n^i, \ddot{\mathbf{z}}_n^i, \ddot{\theta}_n^i\right]$$

where

M – mass matrix, (*kg, lbm*)
C – damping matrix, (*kg/s, lbm/s-*g_c), where g_c is the gravitational constant.
$\boldsymbol{P_i}$ –resultant contact force vector applied on the *i*th element at the *n*th step (*N*, *lbf*)
$\boldsymbol{f_n^i}$ – the boundary force or body force vector applied on the *i*th element at the *n*th step (*N*, *lbf*)

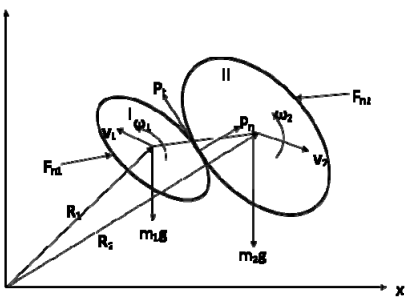

Figure 1. Element interaction

Figure 2 shows a rock with a cylindrical shape. The irregularity of the rock is represented as a collection of small spheres in a tight tetrahedral packing connected with appropriate constitutive models to describe rigidity, heterogeneity and fracture

of the rock block. A soft-contact model was chosen for this simulation since explicit integration can accurately replicate simultaneous bouncing, rolling, sliding, and launching.

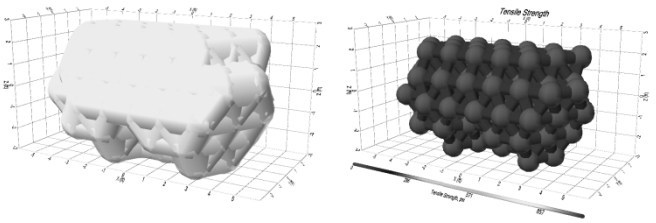

Figure 2. Rock shape and structure

MODEL CALIBRATION AND BACK-CALCULATION OF PARAMETERS

Numerical models have been successfully applied in structural engineering where the structure and mechanics of man-made materials are well understood. Care must be taken to correctly initialize and calibrate numerical models in geotechnical applications, where material properties are more difficult to measure and quantize. Typical parameters that need to be correctly initialized for the DEM model are the damping and stiffness coefficients of contact. The uncertainty and variety of geo-materials make correct input difficult. For rockfall problems, the irregular shapes and the different sizes of a rock, variations of slope properties, such as slope roughness, vegetation on the slope, and restitution and friction between the rock and the slope introduce complexity for correct initialization of the model.

Model calibration is required to correct for errors in representation. For example, the slope may be represented as a mesh of rigid triangles to form a rough approximation of the slope. Stochastic models that attempt to imitate equations of motion require extensive calibration to correct for errors in equation representation. Attempts to match stochastic models to comprehensive rockfall data collected globally for decades have proven difficult, resulting in overly conservative and occasionally unreliable rockfall estimates.

Models with correct equations of motion and accurate representation of the slope and rocks actually require little or no calibration. When initialized correctly, these models produce accurate results. This is the general engineering practice across all disciplines: 1) determine correct equations that accurately represent reality, and 2) determine accurate values for input parameters. No matter how accurate the equations, garbage in results in garbage out. Regardless of the accuracy of models and equations, engineers are indispensible.

In order to ensure accurate inputs, we have developed a technique that fine-tunes input parameters using known observations to produce accurate rockfall behavior and statistics. In order to determine correct model inputs for diverse geotechnical conditions, two steps are taken into account in the initialization: 1) using published,

measured, or observed data, such as impact energy, trajectory heights, and rollouts, and 2) integrating a back-calculation strategy in the models to guide correct parameter inputs for specific site investigations.

The rockfall simulation model is run dozens of times over a range of inputs varied simultaneously, to obtain optimum input parameters, as shown in Figure 3. When the user specifies a range for certain input parameters, with rollout data for a rock of a particular size and shape, or trajectory height or energy at a given location on the slope, the program will back-calculate the optimum input parameters within the specified range. The program performs a multi-dimensional search to determine input values that minimize errors in specified rollout, trajectory height, and/or energy data.

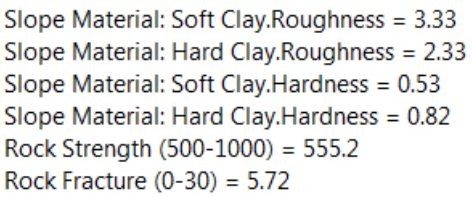

Figure 3. Optimum input paramter determination

The results of each simulation collected in the back-calibration phase are used to produce an interactive parameter analysis model. Figure 4 is a plot of the interactive parameter analysis model showing the relationship between rock fracture persistence and rock tensile strength on the kinetic energy of the rock at analysis partition 1. Changes in the input parameters at the top of the figure are immediately reflected in the outputs below. Interactive 2D and 3D plots of specified parameters aid the user in understanding the complex interactions of parameters. The plot in Figure 4 shows that the kinetic energy of rocks at analysis partition 1 increases with higher rock tensile strength and lower rock fracture persistence.

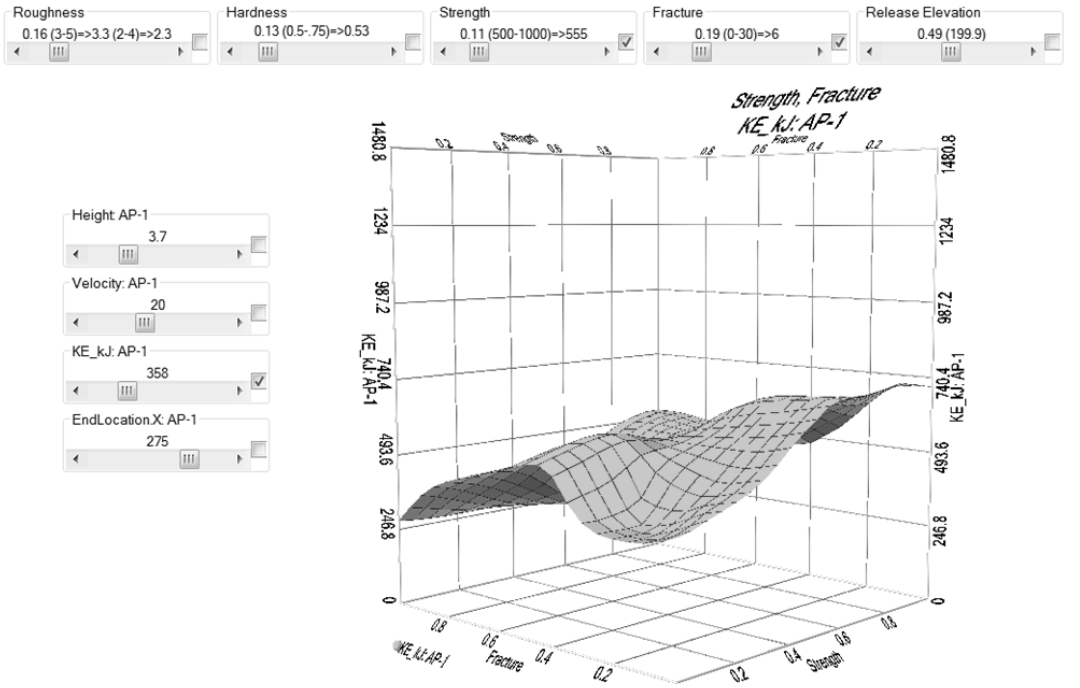

Figure 4. Interactive parameter analysis model

ROCKFALL HAZARD MITIGATION STRATEGIES AND RISK ANALYSIS

Once a sophisticated numerical modeling tool has been developed and properly initialized, it is ready for application. The model must first be initialized with the slope geometry. Although many survey options are available, we chose in this example to include a portion of a quarry surveyed using LIDAR data, shown in Figure 5. The rockfall release zone is shown near the top of the upper face in dark gray. Three analysis partitions are placed at the toe of each floor. The release zone is from strata with 1.5 m blocks near the top of the upper face. 100 rocks were released to obtain the unmitigated dispersion of trajectory heights, energies, and velocities, as shown in the right-most plot in Figure 5.

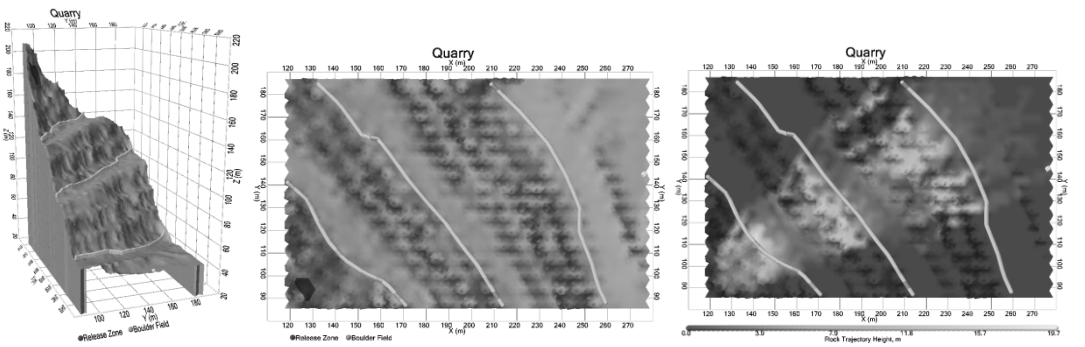

Figure 5. Orthogonal and top views from a LIDAR survey of a quarry with two upper working floors above the final floor.

Ideally, we would like to add more protection closer to the toe of the working floors. From Table 1, a wall 15 m high would be required at the toe of the top working floor to stop 90% of the rocks.

Table 1. Unmitigated Rockfall Results for Analysis Partition 1

Cumulative Probability	Trajectory Height (m)	Velocity (m/s)	Energy (kJ)
50%	6.1	24	6000
75%	10.5	32	10000
90%	14.4	36	13000
95%	16.0	38	14000
98%	16.9	40	15000

After examining the trajectory heights and energies in Figure 5 and the cumulative probabilities in Table 2, we decide to place a 7 m high attenuator below the release zone with an attenuating serviceable energy level of 1000 kJ.

Table 2. Rockfall Results for Attenuator 1

Cumulative Probability	Trajectory Height (m)	Velocity (m/s)	Energy (kJ)
50%	4.1	9	1000
75%	4.9	12	2000
90%	5.6	17	3000
95%	6.6	21	4000
98%	7.5	23	5000

The location of the attenuator and the resulting trajectory height dispersion plot are shown in Figure 6. Although the attenuator decreases the trajectory heights and velocities of rocks below the release zone, the attenuator is so close to the release zone that the dispersion appears unaffected.

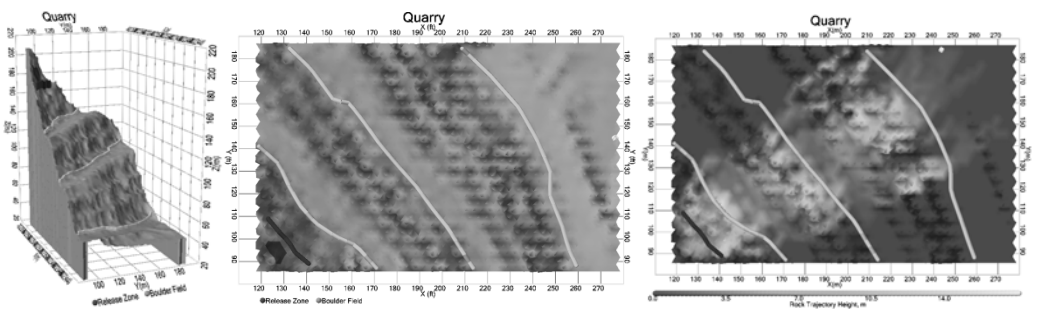

Figure 6. Placement of Attenuator 1, shown below release zone, with resulting rock trajectory dispersion.

The cumulative probabilities for Analysis Partition 1 after placement of Attenuator 1 are shown in Table 3. Comparing Table 3 with Table 1 for results at a cumulative probability of 75%, the velocities of rocks at the toe of the upper floor would decrease by 18%, energies would decrease by 25%, and the trajectory heights would decrease by 9%.

Table 3. Rockfall Results for Analysis Partition 1, Using Attenuator 1

Cumulative Probability	Trajectory Height (m)	Velocity (m/s)	Energy (kJ)
50%	6.9	22	6000
75%	9.6	27	8000
90%	12.9	30	9000
95%	13.9	32	10000
98%	15.7	33	10000

This process can be repeated to mitigate rockfall from the top of the slope to the bottom. Each time an attenuator or rockfall barrier is placed on the slope, this will have an effect on all rockfall statistics farther down the slope. Figure 7 shows frames of a large block clearing a rockfall barrier, fracturing upon impact on the other side, and coming to rest in fragments on a bench.

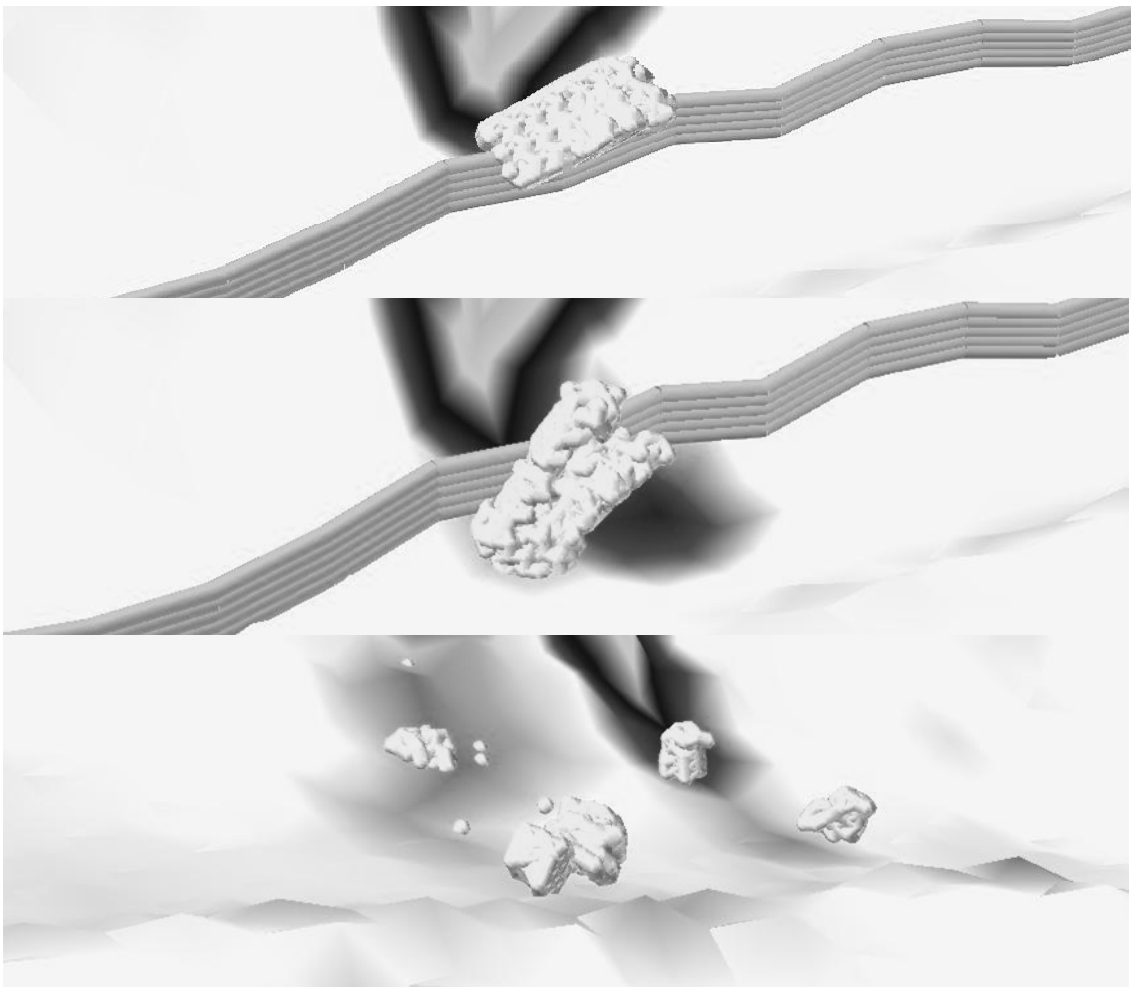

Figure 7. Large block bounces over barrier (a), fractures between sedimentary layers upon impact with the slope below the barrier (b), and results in deposition of fragments on a bench (c). Kinetic energy of fragments are plotted as contours on slope.

CONCLUSION

Rockfall mitigation is a complex process, requiring careful engineering. Numerical models, no matter how accurate, are not replacements for engineers. Engineers must take into account numerous factors, such as accessibility of certain regions on the slope, and the location, design, performance, number, and cost of barriers or attenuators. It is our hope that modeling tools such as this can assist engineers to design better rockfall mitigation systems in less time at a lower cost to provide protection for the maximum the number of roads and structures exposed to rockfall hazards.

ACKNOWLEDGEMENTS

CRSP-3D (Colorado Rockfall Simulation Program) was originally sponsored by the Colorado Department of Transportation (CDOT) as CRSP-5, with the Colorado School of Mines providing technical support as the original co-developers of CRSP. Yeh & Associates lead the task work for CRSP-3D under CDOT and FHWA-CFLHD technology deployment programs. We want to extend our thanks and gratitude to Rick Andrew, Howard Hume, and Ryan Bartingale (Yeh & Associates), Ty Ortiz (CDOT), Matt DeMarco, Khamis Haramy, and Roger Surdahl (FHWA) for their technical reviews, comments and coordination of the project. CRSP-3D has been rewritten and significantly expanded in scope, and is currently part of the Rockfall Mitigation System (RMS) module in the Mt Design package developed by Lodex Engineering.

REFERENCES

Donze, F., Richefeu V., and Magnier, S., "Advances in Discrete Element Method Applied to Soil, Rock and Concrete Mechanics," EJGE, 2008.

Lemos, J., "Discrete Element Modeling of Mansonry Structure," *International Journal of Architectural Heritage*, 2007, 1: 190 – 21

Jean, M., "Frictional Contact in Collections of Rigid or Deformable Bodies: Numerical Simulation of Geomaterial Motions," *Mechanics of Geomaterial Interfaces*, Elsevier Sciences Publishers, 1995, pp 463–486

Zhang, R., "Discrete Element Modeling of Granular Materials under Biaxial Conditions,", technical report, PhD thesis, University of Colorado, Boulder, CO., 1996

GeoRisk in the Design-Build Procurement Process

John Christos Daoulas, B.S., M.S., P.E.[1]

[1]Virginia Department of Transportation, Central Office Materials Division, 1401 East Broad Street, Richmond, Virginia 23219; PH (804) 221-7011; FAX (804) 328-3136; email John.Daoulas@VDOT.Virginia.gov

ABSTRACT

The use of the design-build procurement process by transportation agencies has become increasingly popular to accelerate advertisement of projects. The risks associated with this type of procurement process differ from the traditional design-bid-build process. This is particularly true for geo-engineering risks. These risks are of concern for both agencies and design-builders since they can result in escalation of contingency costs in the price proposal and unforeseen costs after award if not properly identified and mitigated. The purpose of this paper is to provide insight on how this particular issue is being addressed by the Virginia Department of Transportation (VDOT) in their DB program. The paper addresses key elements that should be considered in assessing geo-engineering risks and methods that can be used to mitigate these risks. The paper also addresses the importance in development of technical requirements to clearly define the project objectives to ensure greater uniformity and fairness in preparation of price proposals.

INTRODUCTION

The use of the design-build (DB) procurement process has become increasingly popular in recent years especially in the transportation industry. The allocation of responsibility to a single source (design-builder) gives an agency the ability to define total project costs and to decrease the time for project procurement and delivery. It also reduces the potential for disputes and claims that are commonly associated with the traditional design-bid-build (DBB) projects. The DB contractor has more flexibility in managing costs and schedule during both the design and construction phases. However, not all projects are appropriate for DB as outlined in the AASHTO Guide for Design-Build Procurement (2008) and Loulakis et al (2001). One factor listed in the AASHTO Guide is the agencies need to consider project risks related to subsurface conditions and how they can be adequately addressed during the DB procurement process.

There are a number of risks uniquely associated with the DB process that can result in additional project costs if these risks are not adequately identified, quantified and mitigated prior to submission of the price proposals. A leading risk category of concern for both the agency and DB contractor is geo-engineering risk. In particular, differing site conditions (DSC) which represent an adverse change in the subsurface conditions from those considered during the procurement/proposal phase of the project. Under the DBB process DSC risks are fully allocated to the agency. The logic is that the agency controls the design and therefore is in the best position to

manage this risk. In the DB process the agency is not in a position to control or manage this risk after award since the detailed design is the sole responsibility of the DB contractor. Conversely, during the procurement process the design-builder must rely upon the agency for the quality and quantity of geotechnical information provided in development of their preliminary plans and associated price proposal. Therefore, allocation of DSC risk can be problematic and typically becomes a point of contention between the agency and DB contractor. The method in which the DSC risk is allocated for DB projects varies among transportation agencies. The Virginia Department of Transportation (VDOT) currently allocates DSC as a shared risk in cost and/or time as defined by specific contract language.

Presented herein are the processes that VDOT uses to identify, quantify and mitigate geo-engineering risks during the development and procurement of DB projects. The methods presented have proven effective in mitigating geo-engineering risk and minimizing cost and schedule impacts on projects.

RISK IDENTIFICATION

The first step in the risk assessment process is to properly identify the risks. The process of identifying geo-engineering risk during the initial phases of procurement is essentially the same for both DB and DBB projects. There are three key elements needed to properly identify geo-engineering risk: project objectives, site and subsurface conditions, and past experience with similar projects in the region. The greater the knowledge of these three elements will likely result in a more accurate and meaningful risk identification process. Failure to consider any one of these three elements can result in improper assessment and mitigation of risk that can result in increased costs and delays during design and construction of a project.

Project Objectives. The design features included within the scope of work for a project are very important in assessing the type and magnitude of geo-engineering risk. Different types of project features such as bridges, tunnels, roads, dams, embankments, slopes, etc. will typically yield different types and magnitudes of geo-engineering risk under similar geologic conditions. There can also be differences in the short and long term performance risks for each of these features that need to be considered. For example, a cut slope in highly preconsolidated and fissured clays can exhibit a low risk for short term instability but can exhibit significant long term performance risk if not properly designed to consider residual shear strength and the long term effect of saturation from changes in surface or subsurface water. Design and performance requirements which can vary based upon project goals should also be examined. Examples include acceptable settlements for foundations and/or embankments, pavement smoothness, limits on vibrations to minimize impact on historical structures, long term durability requirements, and right-of-way restrictions. What may need to be done to achieve the desired design and performance requirements may also represent a risk from the standpoint of feasibility. Insufficient time and/or funds to perform an adequate site investigation before advertising the project poses another type of geo-engineering risk that should be considered.

Site and Subsurface Characteristics. Understanding the site and subsurface characteristics of the project site are another key aspect of geo-engineering risk identification. Typically, there are unique risks associated with particular geologic formations or structures such as, presence of sinkholes in karst terrain, and rock gouge and slickensides along fault zones. Regional and local ground water conditions are another key risk factor that must also be considered. Valuable knowledge of the geologic and ground water conditions for a particular site can generally be attained through literature research which usually includes previous geotechnical and ground water studies, geologic and agricultural maps, journals, and research studies. Mining maps, historical data, topographic surveys and aerial photos are other sources used to aid in the identification of potential geo-engineering risks especially those associated with previous man-made features.

Experience. It is widely recognized that risk identification is best achieved through knowledge and experience. In assessing geo-engineering risks, experience can extend beyond that of the agency's geotechnical engineers or engineering geologists. Local experience of individual contractors, field inspectors, geotechnical design consultants and even adjacent landowners have the potential for providing valuable insight in identifying geo-engineering risks associated with a particular project site. Documented experience in the form of "Lessons Learned" developed during the design and construction of past projects can be another valuable resource. The extent to which various sources of experience should be cultivated is dependent on the project type, complexity of the geologic conditions, and level of knowledge and experience of the geotechnical engineer or engineering geologist assigned to the project risk assessment team.

RISK RATING

The second step of the risk assessment process is to rate each risk event that has been identified. DB projects typically have expedited development and procurement phases which preclude the same level of iteration in identification and mitigation of risks typically afforded for a traditional DBB projects. Therefore, to aid in the development of an effective mitigation strategy, each risk event must be characterized according to its probability of occurrence during the duration of the contract and desired life of the project. The severity of the impact the occurrence of each risk event may have on the cost, time and/or long term performance of the project must also be assessed. Probability and statistical analysis, and analytical models can all be effective tools in risk rating provided there is sufficient time and data available to perform these analyses. However, such a quantitative analysis is not warranted on most VDOT projects and a more qualitative approach is taken to rate each risk event utilizing the same key elements used for risk identification as discussed above. There are various methods available for quantifying risk. A commonly accepted method used by VDOT is a two-dimensional matrix where the probability of occurrence and severity of impact are individually numerated on a scale of 1 to 3 (1- low, 2- moderate, 3- high). The overall risk rating for a particular event is determined my multiplying the probability rating by the corresponding

impact rating, resulting in a range of overall risk ratings of 1 to 9. For example, it may be determined that although the probability of a sinkhole forming in a particular karst terrain warranties a moderate rating of 2 the severity of impact if such an event occurred would result in a higher rating of 3. Therefore, the overall risk rating would be 6. The determination of the overall risk rating is further illustrated in Figure 1.

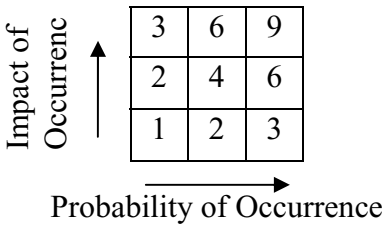

Figure 1.Risk Analysis Matrix

Overall risk ratings of 6 or higher are deemed high risk events that warrant particular actions to be taken to further assess and to mitigate the risk. Moderate risk events are those that have an overall risk rating of 4. An appropriate amount of assessment should also be provided for moderate risk events to include further research and field investigation to a magnitude that is typically less than high risk events. A risk event with an overall ranking of 3 or less are expected to have little impacts on the project cost, time and performance and typically does not warrant further assessment. However, low risk events should never be discarded since the initial rating of the risk event could change as a result of a change in the project objectives and/or as a result of new information that becomes available during the project development process.

RISK ALLOCATION

After the risks have been identified and rated the next step is to determine how each risk event will be allocated either as an agency risk, a design-builder risk, or a shared risk. The terms of the contract define how risks will be allocated for a particular project based on agency policies and project goals to include the party who is deemed to be in the best position to manage the risk. FHWA and AASHTO both provide guidelines on how to assess and allocate risk. For DB projects all geotechnical design risks are assumed to be allocated to the design-builder. However, this is generally true only up to the time of completion of the project to include a possible warranty period after which long term geotechnical related performance risk reverts back to the agency. The geo-engineering risk that generally represents the most concern on how this risk is allocated from the perspective of both the agency and the design-build contractor is *differing site conditions*. The method in which this risk is allocated can have significant impacts on contingency costs and potential claims for a project.

Differing Site Conditions. Differing site conditions (DSC) can either be Type 1 - Subsurface or latent physical conditions at the site differing materially from those

indicated in the contract documents; or Type 2 - Unknown physical conditions at the site of an unusual nature differing from those ordinarily encountered and generally recognized as to be inherent in work of the character provided for in the contract documents. For DBB projects the allocation of risk for DSC remains solely with the contracting agency for the duration of the project. However, this is not necessarily true for DB projects. The reason is the design-builder is generally in a better position to manage this risk through design and by the means and methods utilized to construct the project. In the case of VDOT the risk of DSC is allocated to the agency up to a specified amount of time after the date of commencement referred to as the Scope Validation Period. After this period the entire risk and associated cost and time impacts are allocated to the DB contractor with the exception of hazardous materials that is is retained by VDOT for the full duration of the project.

Long Term Performance. There are a number of geo-engineering related risks that need to be considered that can impact the long term performance and operation and maintenance (O&M) costs of a project. These risks for most VDOT DB projects are allocated to the agency after the construction of the project has been completed even though the design-builder is in the best position to manage this risk through the method of design and construction of the project. The exception is VDOT toll revenue generated public–private-partnership (P3) DB projects where the design-builder is required to operate and maintain the project for a specified period of time that can extend up to 60 to 90 years after project completion. The inability to control design for non-toll revenue projects where risks for performance and O&M costs are allocated back to the agency has been problematic for most transportation agencies. As a result agencies have been reluctant to use the DB method of procurement and have considered other alternate procurement methods such as Construction Management-at-Risk. However, long term performance risks can be mitigated through the terms of the contract provided the agency's project goals are well defined and the long term performance and O&M risks are clearly identified and rated. The mitigation strategies utilized by VDOT to address these types of long term risks are presented herein.

RISK MITIGATION

After the risk assessment has been completed and the geo-engineering risks identified, rated and allocated, a risk mitigation plan should be developed to address these risks in order of priority. The purpose of mitigation is to better characterize and seek reduction in the potential impact of a risk event through better management by the agency in preparation of the contract documents and by the design-builder in preparation of their proposal. The desired outcome is to reduce uncertainty thereby minimizing contingency costs included in the price proposal and to alleviate the potential for claims after award of the contract. The focus of the mitigation strategy should be on the risk events rated moderate to high. However, low risk events should not be discarded for the reasons previously stated. There are generally two ways that VDOT mitigates geo-engineering risk. The first is development of a geotechnical engineering data report (GEDR). The second is to establish a baseline of geotechnical

requirements within the contract documents the design-builder will need to comply with in development of their design and price proposal for the project. The design-builder can best mitigate their risk by selecting an experienced geotechnical engineer prior to proposal preparation to perform a detailed assessment of the geotechnical information provided by the agency and the technical and performance requirements included in the contract documents. The DB geotechnical engineer may also supplement this information with additional geotechnical data/insight they may have as well as seek clarification from the agency on design or performance requirements that may be in question prior to submission of the price proposal. VDOT offers each design-builder the opportunity to submit questions and attend a proprietary meeting to address any concerns or ideas they may have regarding the contract documents prior to submission of proposals.

In the case of a new road alignment in southwest Virginia, the highly variable geologic conditions were identified as a significant time and cost impact risk to the successful design, construction and long term performance of the proposed rock cut slopes. The GEDR was developed to mitigate this and other geo-engineering risks that resulted in bid prices below VDOT's construction estimate. Although attempted no significant claims for work orders due to DSC were granted after award. During design, the DB attempted to justify steepening the slopes as a cost savings measure based on the particular methodology used in their analysis. In absence of the design guidelines included in the contract documents the DB would likely have been successful in steepening the slopes resulting in an increase to the long term performance risks to VDOT and driving public.

Geotechnical Engineering Data Report. The purpose of the GEDR is to present factual geotechnical data and to identify geotechnical engineering issues that must be addressed to prospective design-builders in order for them to have a uniform basis for preparation of proposals for the project. The data provided is the result of a preliminary subsurface exploration and laboratory testing program performed to assess the surface and subsurface conditions that can reasonably be expected within the limits of the project as well as site specific geotechnical, geophysical, and surface conditions that the design-builder must consider in preparation of their price proposal. Historical data can also be included provided the data is of adequate quality and reliability for the purpose of proposal preparation. Another important element of the GEDR is the geotechnical engineer's or engineering geologist's assessment of how the geotechnical related conditions may affect the design and construction of project elements. This assessment along with the physical and site reconnaissance data can benefit the design-builder in better assessing their risks through preliminary design in preparation of the price proposal. For the agency the information attained can be useful in assessing the feasibility of the project goals and scope of work as well as development of appropriate geotechnical requirements for inclusion in the contract documents. For example, an agency objective could be to limit right-of-way (ROW) impacts which would require cut slopes to be constructed at 1.5H:1V but still maintain a minimum factor of safety (FS) of at least 1.5. However, based on the preliminary geotechnical assessment of the actual site and subsurface conditions it may be determined that the project goal as stated is not feasible and that the agency

would either have to relax the FS requirement and assume more risk in the long term performance of the slope or acquire additional ROW to flatten the slope so the desired FS can be achieved. Alternatively, a retaining wall could be added to the project scope. Since the design-builder must rely on this information and terms of the of the DSC clause within the contract documents, the GEDR also represents a legal document that is the basis for dispute resolution in event of a DSC claim.

Preliminary Subsurface Exploration/ Laboratory Testing Program. The level of geotechnical and geophysical investigation needed for preparation of a GEDR varies depending on project type, project site and geologic characteristics, and results of the risk assessment previously discussed. For example, construction of a turn lane addition in cuts in an area where there is no rock and the subsurface conditions are expected to be homogenous, may require only one or two borings with a couple of existing pavement cores. However, for the same turn lane in fills constructed over swampy soils, more, and deeper borings with shear and/or consolidation laboratory testing may be appropriate. The considerations used by VDOT in setting up an appropriate field investigation and laboratory testing program are similar for a DBB project outlined in VDOT's Materials Manual of Instructions (MOI). This includes literature review; site reconnaissance; selecting the appropriate type and spacing of borings/soundings; and selection of appropriate laboratory testing.

The main objective of the subsurface investigation program is to obtain sufficient information so the agency geotechnical engineer or engineering geologist can reasonably assess the feasibility of the project objectives and mitigate the level of uncertainty for the design-builder. VDOT uses the investigation requirements outlined in the MOI to establish an initial baseline that is modified to meet the project goals focusing on moderate to high risk events. This approach optimizes the investigation effort to address those geotechnical elements of the project site of most concern to both the agency and the design-builder. In most cases VDOT performs between 70 and 90 percent of what would be required for final design. The design-builder, under the terms of a VDOT contract, is required to perform a final geotechnical study to complete the minimum investigation requirements of the MOI and any additional investigations to support of their specific design.

Contract Terms. An effective ways to mitigate performance risk is through the technical requirements of the contract documents. Even though the design-builder is required to design the project according to acceptable federal, state, local and industrial standards, this does not always mean the project objectives and associated risks will be adequately addressed. For example, there is a number of combinations/layering of pavement materials that can be utilized to develop a pavement section that meets AASHTO standards based upon a particular structural number. However, experience has shown not all pavement sections with the same structural number will perform equally over the long term. For this reason VDOT DB contracts include minimum pavement sections the design-builder is required to include in their price proposal. This ensures the agency obtains the product they believe is best to help mitigate their long term O&M risks while also providing greater uniformity and fairness to the design-builders in development of their price

proposals. This same concept has also been applied to shallow bridge foundations on non-scourable rock where interpretation of AASHTO standards can be highly subjective. If the design-builder can adequately show during the scope validation period the minimum pavement or scour requirements included in the contract document are inadequate for the purpose of final design then the added costs incurred by the design-builder to modify the design are compensated accordingly. The main drawback with this mitigation strategy is the agency may be overly prescriptive within the technical requirements and restrict the design-builders' ability to provide meaningful innovation in their design. This can result in reduced cost savings for the project and/or undue allocation of design and construction risks for the agency.

CONCLUSIONS

Geo-engineering risks play a very important role in assessing the feasibility, cost, schedule, and successful long term performance of a DB project. These types of risks are of equal concern to both the agency and the DB contractor since they can have a significant impact on contingency costs included in price proposals and increase the potential for unforeseen costs and time delays after award of contract. It is to the agencies benefit to indentify and mitigate geo-engineering risks prior to submission of price proposals, regardless of how those risks are allocated, in order to minimize project costs and the potential for future claims. It is extremely important to allow sufficient time and provide adequate funding for quality site and subsurface investigation and laboratory testing programs. A thorough GEDR, based upon the results of these investigations must be prepared to address the moderate to high risks and contract terms developed for the specific performance risks identified in the risk assessment. The design-builder must assess how these risks are considered in their preliminary design during the procurement stage and communicate to the agency any concerns regarding these risks prior to development of their price proposal. The process outlined in this paper has been effective in addressing geo-engineering risk for projects procured through the VDOT DB program. Although the DB procurement process may differ between agencies, the identification, quantification and mitigation of geo-engineering risks is a key risk factor that needs to be appropriately addressed by both the agency and the design-builder to ensure success and long term performance of DB projects.

REFERENCES

American Association of State Highways and Transportation Officials (AASHTO). (2008). *AASHTO guide for design-build procurements,* Washington D.C.

Federal Highways Administration (FHWA). (October 2008). *Guide to risk assessment and allocation for highway construction management*, Washington D.C.

Loulakis, M.C. (2001). "Design build: does it guarantee project success?" *C-Risk Inc.*, http://www.c-risk.com/Article/mcl_design-build_0.1.htm.

Virginia Department of Transportation (VDOT). (2008). *Materials manual of instructions*, Richmond, Virginia.

Owner Involvement - Choosing Risk Factors for Shallow Foundations

By Roger A. Failmezger, P.E., F. ASCE[1] and Paul J. Bullock, Ph.D., P.E.[2]

Abstract: The engineer must always design to avoid injury and loss of life. However, other design decisions are purely economical. The owner should invest in the most economical foundation that will adequately support the building, considering both constructability and risk of failure. The owner chooses the site with its subsurface conditions, the structure and its foundation loads, and the available funding. The engineer must design a foundation that adequately supports the structure and balances the owner's cost with the performance of the foundation. Improved bearing capacity design methods have largely precluded stability failures, but excessive settlement remains problematic. The engineer measures the soil's deformation properties and predicts the amount of settlement that will occur. As some foundation movement will occur under any level of load, the engineer's design should allow a tolerable movement that also provides reasonable foundation cost. It may prove more cost effective to use smaller spread footings that settle a tolerable amount with a risk of minor repair rather than larger footings or deep foundations whose costs may overburden the construction budget. The authors present charts showing the probabilities of success of 90%, 95%, 99%, and 99.9% for limiting settlement plotted against its standard deviation. To increase the accuracy of the estimated settlement and the success probability, the settlement estimates are based on direct measurements of soil modulus using the Dilatometer. The charts are formatted for the owner to understand and to make the most appropriate choice for the building.

INTRODUCTION

Owners make many financial decisions on every project. They should choose the most economical foundation that will safely support their structure. Often, they choose a geotechnical engineer, who only performs a basic study for the project. This engineer typically does not measure the soil's deformation properties, but instead estimates those properties using crude correlations with as much as $\pm$200% error. This study can be adequate if the subsurface conditions are very favorable and column loads are relatively light. For marginal subsurface conditions or heavy column loads, the geotechnical engineer often recommends overly conservative foundation designs that sometimes include unnecessary deep foundations. Instead of making poor recommendations, the geotechnical engineer should perform a more thorough subsurface investigation that measures the soils' deformation properties. Then the engineer can confidently calculate the settlement for each column and size the footings so that the structure will settle uniformly. Otherwise, the owner, often unknowingly, pays an excessive price for the poor design.

[1] President, In-Situ Soil Testing, L.C., P. O. Box 83, Morattico, VA 22523, roger@insitusoil.com
[2] Tolunay-Wong engineers, Inc., 3636 NW 23rd Place, Gainesville, FL 32605, pbullock@tweinc.com

SITE INVESTIGATION TO QUANTIFY RISK

The engineer needs reasonably accurate deformation tests to accurately predict settlement of shallow foundations. The oedometer test, standard penetration test (SPT), cone penetrometer test (CPT), pressuremeter test (PMT), and dilatometer test (DMT) are commonly used for shallow foundation design. The applicability of these tests to quantify the risk of undesirable settlement is discussed below.

Oedometer Test: Sampling, followed by consolidation testing in an oedometer in the lab, provides an accurate test of deformation properties. However, testing is time-consuming and is typically performed at depth intervals exceeding 10 ft (3 m) or more. Sampling and handling disturbance may also significantly reduce the accuracy of the results. In general, the authors believe that in-situ testing provides more information, more quickly, with less cost.

Standard Penetration Test (SPT): Tests are commonly performed on 5-foot (1.5-meter) depth intervals at several borehole locations on a site. Because each boring could serve as a settlement prediction, there are usually enough data for numeric probability analyses. The test measures the number of hammer blows (N value) to drive a sampler 1 ft (0.30 m) into the soil. There are several acceptable hammer types, but these different hammer systems deliver different energies to the sampler. Unfortunately, the energy is rarely measured in the United States. (The new standard in Europe requires energy measurement.) The hammer energy transferred to the rods, when measured, varies from 30 to 95% of the theoretical potential energy of 4200 in-lb (475 N-m). The hammer type, while a critical factor for the energy, is often omitted from the boring log. If the geotechnical engineer does not know the energy used to drive the sampler, this significantly reduces the accuracy of any N-value interpretation.

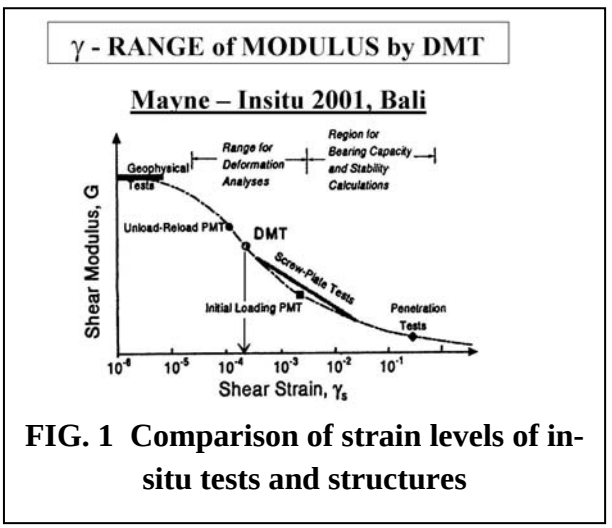

FIG. 1 Comparison of strain levels of in-situ tests and structures

The SPT is a dynamic penetration strength test and strains the soil to failure. As shown on Fig. 1, structural loads commonly strain the soil to intermediate levels. To determine the soil deformation modulus from the SPT N-value requires extrapolation from a strength parameter at failure strain to a deformation parameter at an intermediate strain, another possible source of error.

The dynamic penetration of the sampler in cohesive soil, especially sensitive soil, remolds the soil. In residual soils, the SPT destroys the latent rock structure. In both cases N-value correlations for the static deformation modulus are very poor or

invalid. In sands, modulus correlations are somewhat better. Duncan (2010) suggests a relatively high coefficient of variation for the accuracy of predicting settlement in sands using N_{60} values (N-value with energy corrected for 60% of the theoretical energy) of 0.67. In a perfectly homogeneous soil, the error in the method alone would require that the average value of settlement be 0.30 in (7.6 mm) to be 95% certain that a settlement of 1.00 in (25.4 mm) would not be exceeded. Therefore, even the best case scenario for the SPT, seems much too inaccurate to predict settlement.

Cone penetrometer tests (CPT): The CPT measures the tip resistance (q_T) using calibrated strain gauges, typically providing repeatable data at 0.03 to 0.16 ft (0.01 to 0.05 m) depth intervals. Therefore, there are sufficient data to quantify risk. Like the SPT, the test strains the soil to failure. While the quasi-static tip resistance, q_T, has reasonable accuracy and repeatability, the engineer must still extrapolate to a deformation modulus at an intermediate strain level. The commonly-used equation below relates the tangent modulus, M, to q_T, using a strength parameter to predict a deformation parameter.

$$M = (\alpha)\ (q_T),$$

Depending on stress history and soil type, the value of α ranges from 1 to 8 for cohesive soil, 3 to 11 for normally-consolidated sand, and 5 to 30 for over-consolidated sand. Most engineers use conservatively low values and tend to over predict settlement. The unknown range of α reduces the accuracy of settlement prediction from the CPT.

Pressuremeter tests (PMT): The pressuremeter test strains the soil to intermediate strains in static deformation. Thus, the PMT predicts settlement relatively well, though often relying on empirical methods. However, it is a relatively slow test to perform and typically only two to six tests can be performed in one day, often at depth intervals of 10 ft (3 m) or more. The quantity and the quality of the tests are highly dependent on the driller's skill and experience. Unfortunately, there are usually not enough tests performed for a risk assessment of settlement.

Dilatometer tests (DMT): Like the pressuremeter, the dilatometer uses static deformation to strain the soil to intermediate strains. The DMT provides the one-dimensional tangent modulus (M) with tests generally performed at depth intervals of 0.66 ft (0.20 m). In thin layers of compressible soils, tests are often performed at depth intervals of 0.33 ft (0.10 m) for better definition. Tests typically take about 1 minute to perform and a sounding provides sufficient data for risk assessment of settlement with DMT. The authors recommend the dilatometer test as the best choice of in-situ tests for the settlement prediction of shallow foundations. At numerous (20+) sites in a wide variety of soils, Schmertmann (1986) and Hayes (1986) separately predicted settlement using DMT and measured actual settlement of footings/embankments. With the exception of quick silts, they found a ratio of predicted to measured settlement of 1.07 with a coefficient of variation of 0.18 (Failmezger, Bullock, 2004).

OWNER'S EXPECTATIONS FOR DESIGN SERVICES

The engineer must perform design services to meet the standard of care, i.e. the level of service provided by an average engineer in the geographical area at the time of service. The engineer carries professional liability insurance that covers the risk only when his services do not satisfy the standard of care.

However, many owners want better than average design services. They want the engineer to design the foundation as economically as possible while safely supporting the structure. They want their structure to perform as intended, but they do not want to spend unnecessary money on the foundation. To perform a higher level of services, the engineer must perform a more sophisticated subsurface investigation that accurately quantifies the soils' deformation properties. A thorough investigation increases the engineer's knowledge and reduces the uncertainty of the design parameters of the soil, improving the accuracy of settlement estimates.

Smaller foundations generally settle more than larger ones. The owner must choose between the cost savings of a smaller foundation and the increased risks for unsatisfactory performance (e.g. cracks). Provided that the foundation is stable, the cost to repair any initial cracking is often far less expensive than the additional cost of an overly conservative foundation.

The owner's expectation of the engineer's service exceeds the level of service covered by professional liability insurance. The owner benefits financially from the better design services by having a smaller and less expensive foundation and logically should be the party to take this additional liability.

PREVALENT U.S.SHALLOW FOUNDATION DESIGN

The geotechnical engineer typically performs several standard penetration test (SPT) borings across the site, obtaining samples only for soil identification, gradation, Atterberg limits. Based on the engineer's experience, the SPT N-values, and limited lab data, the engineer then recommends an allowable bearing capacity, rounded to the nearest 500 psf (23.9 kPa), to the structural engineer for design. All footings are then sized based on this single design bearing capacity.

The column loads for the structure can vary considerably, requiring larger footings for heavier loads. A larger footing load strains a larger and deeper volume of soil with greater settlement. While the deformation properties of the underlying soil can vary significantly within the site, the engineer does not directly measure them and has relatively coarsely spaced data with which to work. The inherent variability in the field measurement of the N-value combined with a relatively crude design method leads to highly inaccurate settlement predictions using the SPT. Faced with so much uncertainty, the engineer typically recommends an overly conservative and expensive design.

IMPROVED SHALLOW FOUNDATION DESIGN

Dilatometer tests can help significantly reduce design uncertainty by providing depth profiles of repeatable and accurate deformation modulus values. Typically, the goal of foundation design is to minimize the settlement between any two points on the structure relative to the distance between them, or the angular distortions, to avoid unacceptable damage to the structure. Table 1 shows limits of angular distortion for different types of structures and their uses. The geotechnical engineer, the owner and structural engineer, working closely together, should choose the appropriate risk levels for angular distortion.

Table 1 Allowable Angular Distortion

Situation	Allowable Angular Distortion
Machinery sensitive to settlement	1/750
No cracking in buildings; tilt of bridge abutments; tall slender structures such a stacks, silos, and water tanks on a rigid mat; steel or reinforced concrete frame with brick block, plaster or stucco finish and length to height ratio greater than 5	1/500
Cracking in panel walls; problems with overhead cranes	1/300
Structural damage in buildings; flexible brick walls with length to height ratio greater than 4	1/150

The design procedure has the following steps:

1. Perform dilatometer soundings at the site,
2. Perform settlement calculations for each column,
3. Calculate the angular distortion between adjacent columns,
4. Determine the average and standard deviation values of angular distortion for the structure,
5. Quantify the standard deviation values from other sources of error,
6. Compute the overall standard deviation value for angular distortion,
7. Plot the average and overall standard values on the probability angular distortion design charts and determine if the design is satisfactory.

Perform dilatometer soundings: Perform DMT soundings to accurately characterize deformation properties at the site, focusing on weaker soils when encountered. Generally, perform soundings at the heavier column loads and at some of the perimeter columns. For columns, the sounding depths should extend at least two times the design footing width to define the modulus values within the footing's stress bulb. For wall footings, the depth should extend least four times the footing width. Both cases require additional depth where footing influence overlaps, and several deep soundings should be used to identify soft soils that may cause global settlement of the structure. Sites with heterogeneous deformation properties require more DMT soundings for proper site characterization.

Settlement Calculations: From each dilatometer sounding, the engineer predicts settlement using Schmertmann's method, multiplying the tangent modulus by the predicted elastic stress at depth increments equal to the DMT test interval. The load for the settlement calculation includes the column load, which lessens with increasing depth (stress bulb) and the weight of any additional fill, which is typically assumed infinitely large horizontally and imposes a uniform pressure to infinite depth. The engineer adjusts the footing dimensions so that settlement for the structure is as uniform as possible.

A settlement prediction must be made for each column. If there is no DMT sounding at the column location, then a weighted average settlement can be computed from the nearby DMT soundings. With this approach, the horizontal distance from each nearby DMT sounding to the column is calculated. The total distance of all nearby soundings is summed. The contributing settlement from a sounding equals the predicted settlement times its distance divided by the total distance. The predicted settlement for the column is the sum of the contributing settlements. The weighted average method only works if the soils' deformation properties do not significantly change between soundings. If there is significant variability, then a DMT sounding must be conducted at that column location.

Angular Distortion: The angular distortion is computed for all adjacent columns by dividing the predicted settlement difference or differential settlement by the horizontal distance between the columns. Any large values of angular distortion require a redesign for those footing dimensions to reduce the differential settlement.

Computing Average and Standard Deviation of Angular Distortion: Each value of computed angular distortion becomes part of the angular distortion data set. The average and standard deviation are calculated from this data set. The computed standard deviation represents the predicted settlement variability and accounts for the variability of the deformation modulus properties of the soil at the site.

Other Sources of Error: Other error sources include the accuracy of the Schmertmann DMT settlement method, the accuracy of the column loads, how well the contractor constructs the footings, and how well the inspector monitors the footing construction. From case study data, Failmezger and Bullock (2004) determined a coefficient of variation for Schmertmann's method of 0.18 for all soils except quick silts with an average predicted settlement 1.07 times the measured value. While the structural engineer can accurately predict the dead load of the column, he or she cannot accurately predict the live load. The structural engineer should provide the coefficient of variation for the column loads. The engineer must judge contractor and inspector error based on their qualifications, with a reduction for better expertise and a penalty for lower cost.

Overall Standard Deviation of Angular Distortion: If the sources of error are independent of each other, then the overall standard deviation is computed as the

square root of the sum each standard deviation squared. This is the maximum or conservative value of standard deviation. If these sources of error are partially dependent on each other, then a lower value of standard deviation could be used.

ANGULAR DISTORTION DESIGN CHARTS

The Beta probability distribution was chosen to determine the risk of angular distortion exceeding acceptable limits. The normal probability distribution was not used because its minimum/maximum end limits are negative infinity and positive infinity, both unrealistic. The log-normal probability distribution was not used because its end limits are zero and positive infinity, and positive infinity was unrealistic. The minimum and maximum end limits of the beta distribution are selected by the user and the authors chose the limits as $\pm$ three standard deviations from the mean. The minimum end limit was the larger of zero or the computed value. When the minimum end limit was greater than zero, the distribution was not skewed; when it was zero, the distribution was skewed right.

The area under a probability distribution curve is defined as 1.00. The area where the probability curve exceeds the angular distortion limit is the probability of failure. The probability of success is therefore 1.00 minus the probability of failure. The probabilities of success of 90%, 95%, 99%, and 99.9% were calculated for angular distortion limits of 1/750, 1/500, 1/300 and 1/150 for the average and overall standard deviation values of angular distortion. Plots of the average and standard deviation for those probabilities of successes are shown as Figs. 2 to 5 for limits of 1/750, 1/500, 1/300 and 1/150. If the probability distribution curve was bell-shaped and not skewed, then the relationship between the average value and standard deviation was linear. If the distribution curve became skewed right, then the relationship became non-linear.

Example Problem: The owner plans to construct a four story reinforced concrete office building with drywall interior walls. He desires probabilities of success of 99.99% against structural damage and 95% against drywall cracking. The geotechnical engineer performs dilatometer soundings at most of the column locations and determines the average value of angular distortion of 0.0022 and a standard deviation of 0.0002. The coefficient of variation for the dilatometer prediction method = 0.18 (case study database); for the loads = 0.20 (provided by the structural engineer); for the contractor/inspector = 0.10 (selected by qualifications). The standard deviation equals the coefficient of variation times the average value of angular distortion. Therefore, the standard deviation for the DMT method = 0.0040, for the loads = 0.0044, and for the contractor/inspector = 0.0022. The overall standard deviation was 0.0063. By plotting the average and overall standard deviation values on Fig. 4, we estimate a 96% probability of success. These values plot significantly to the left of the 99.99% line on Fig. 5. Therefore, the design satisfies the owners' needs.

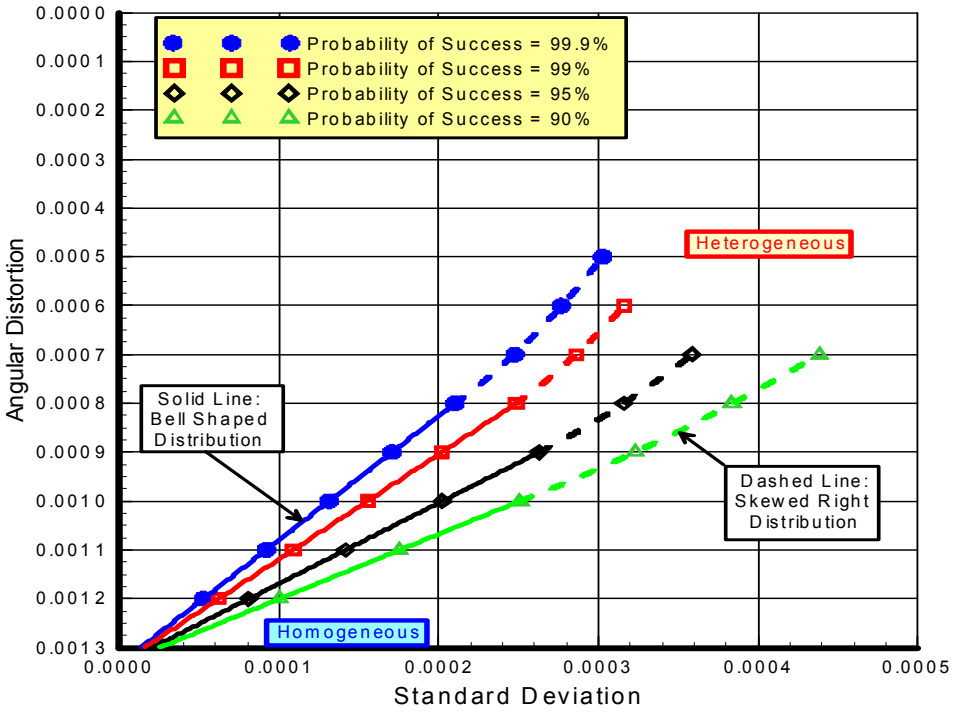

FIG. 2 Threshold Value of Angular Distortion = 1/750

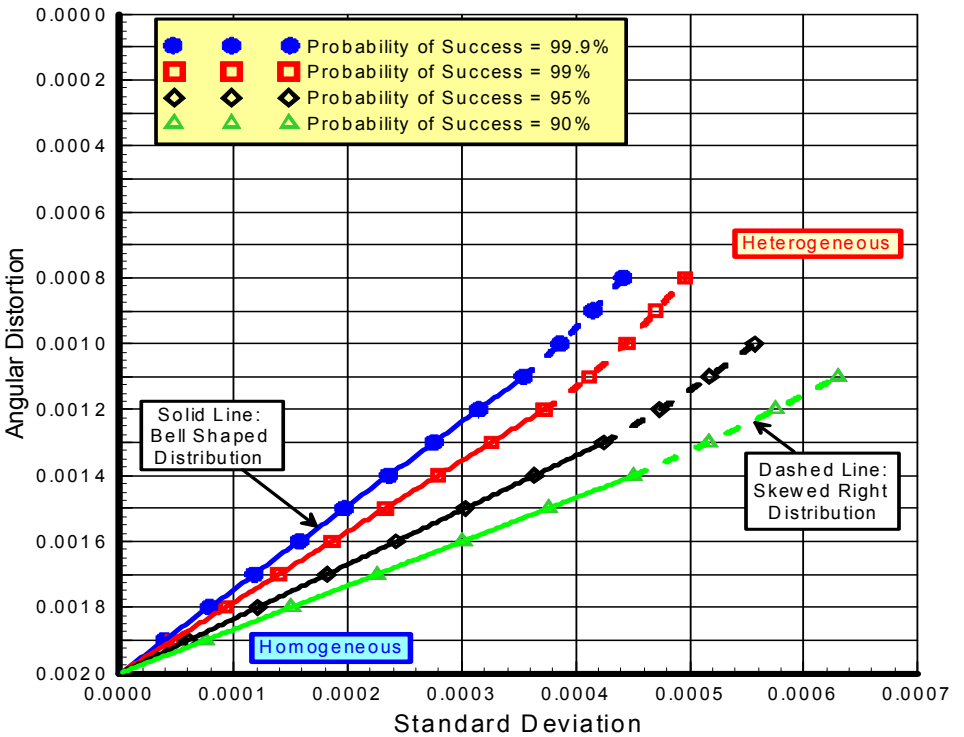

FIG. 3 Threshold Value of Angular Distortion = 1/500

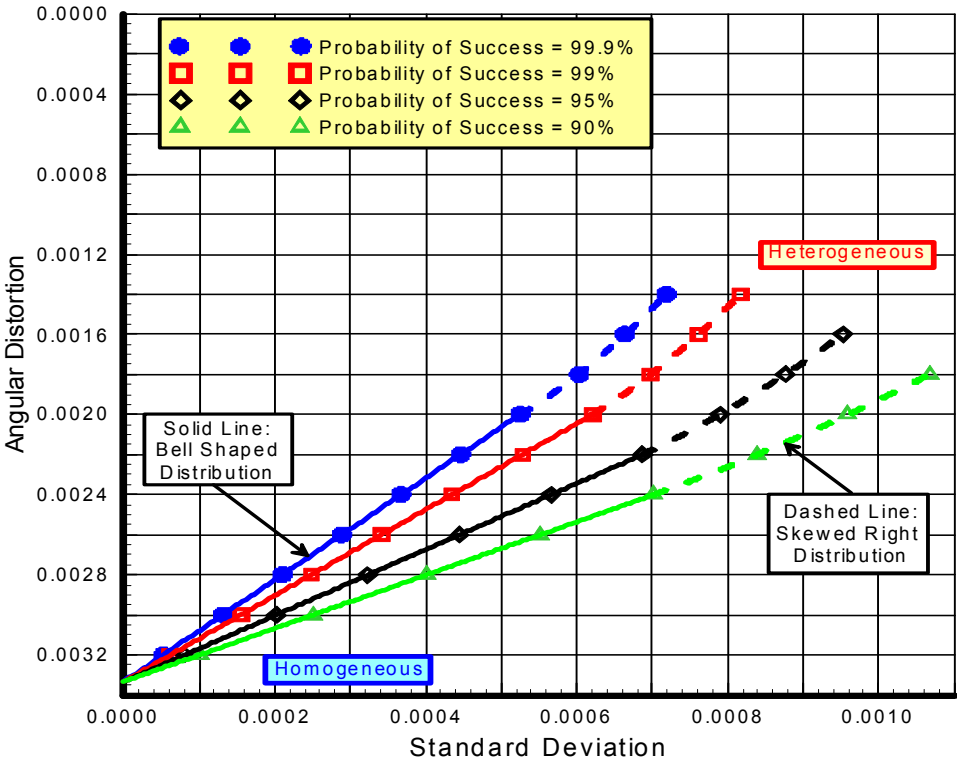

FIG. 4 Threshold Value of Angular Distortion = 1/300

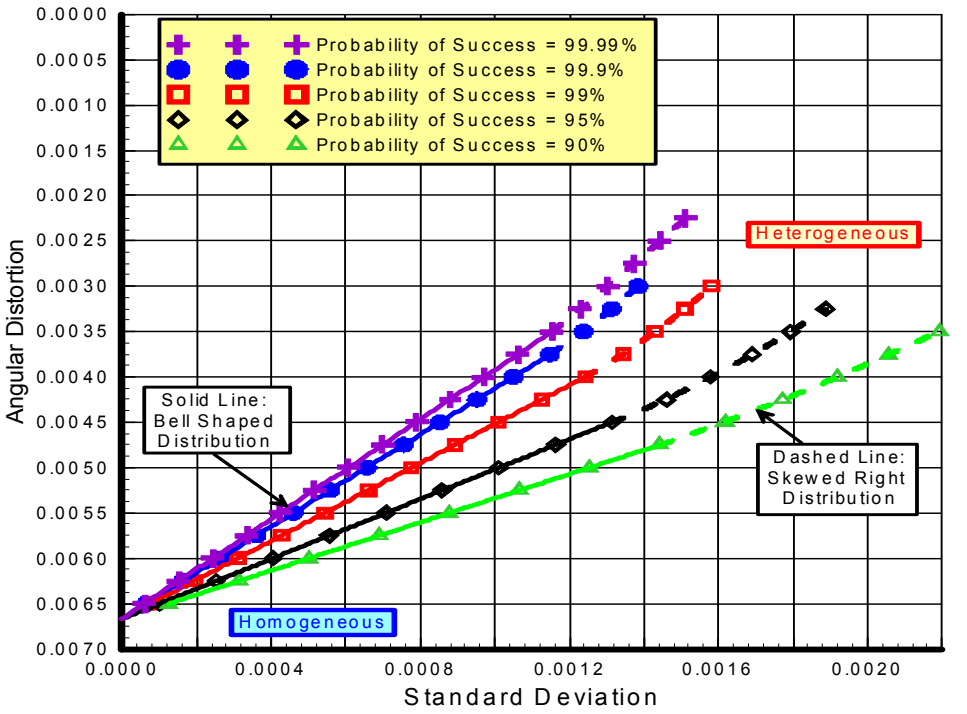

FIG. 5 Threshold Value of Angular Distortion = 1/150

CONCLUSIONS

1. For structures with intermediate to heavy loads or sites with heterogeneous subsurface conditions, the owner will financially benefit from a thorough subsurface investigation and a detailed settlement analysis for angular distortion of the shallow foundation system. With the proposed shallow foundation design method, the engineer can often design buildings to be safely supported on shallow foundations that otherwise may have been designed with deep foundations.
2. The relationship between the average and standard deviation of angular distortion for different probabilities of success is linear if the probability distribution curve is bell-shaped.
3. The owner can select the level of risk for angular distortion and balance the lower costs of an economical shallow foundation and the higher risk of angular distortion.
4. The authors do not recommend using SPT data for settlement predictions due to its inherent variability and the correlation required between N-value and deformation modulus.
5. The authors do recommend using DMT data to directly measure deformation modulus for risk assessment of shallow foundations.

REFERENCES

Briaud, J-L, 1992, *The Pressuremeter*, A.A. Balkema, Brookfield, VT.

Burland, J. B. and Burbridge, M. C., 1985, “Settlement of Foundations on Sand and Gravel”, Proc., Inst. of Civ. Engrs, Part 1, 78, 1325-1381.

Christian, John T., Oct. 23, 24, 1997, "Reliability Approaches in the Design of Slopes", Excellence in Geotechnical Engineering, Central Pennsylvania Section, ASCE and Pennsylvania Department of Transportation.

Duncan, J. Michael, April 2000, “Factors of Safety and Reliability in Geotechnical Engineering”, ASCE Journal of Geotechnical and Geoenvironmental Engineering, Vol 126, No. 4, pp. 307-316.

Failmezger, R. A., Rom, D., Ziegler, S. R., 1999, “SPT? A better approach of characterizing residual soils using other in-situ tests”, Behavioral Characterics of Residual Soils, B. Edelen, Ed., ASCE, Reston, VA, pp. 158-175.

Failmezger, Roger A., 2001, Discussion of “Factors of Safety and Reliability in Geotechnical Engineering.

Failmezger, Roger A., Bullock, Paul J., 2004, “Individual foundation design for column loads”, International Site Characterization ’02, Porto, Portugal

Failmezger, R. A. and Bullock, P. J., Handy, R. L., 2004, “Site variability, risk, and beta”, *Proc. Geotechnical and Geophysical Site Characterization*, Viana da Fonseca, A. and Mayne, P., editors, Rotterdam, pp. 913-920.

Harr, Milton E., 1977, Mechanics of Particulate Media: A Probabilistic Approach, McGraw-Hill, New York

Hayes, J.A., August 1986, "Comparison of flat dilatometer in-situ test results with observed settlement of structures and earthwork", Proceedings 39th Geotechnical Conference, Ottawa, Ontario, Canada.

Lambe, T. William, Whitman, Robert V., 1969, *Soil Mechanics*, John Wiley & Sons, New York

Lunne, T., Robertson, P. K. and Powell, J.J.M, 1997, *Cone Penetration Testing in Geotechnical Practice*, Blackie Academic and Professional, London, England.

Marchetti, Silvano, 1980, "In Situ Tests by Flat Dilatometer", *Journal of Geotechnical Engineering*, Vol. 106, No. GT3, pp. 299-321.

Mayne, P.W., 2001, Stress-strain-strength-flow parameters from enhanced in-Situ tests, *Proceedings, International Conference on In-Situ Measurement of Soil Properties and Case Histories*, Bali, Indonesia, pp. 27-47.

Mirza, C., 1998, "The high cost of low bid cost site characterization", *Proc. Geotechnical and Geophysical Site Characterization*, Robertson, P. K. and Mayne, P. W., editors, Rotterdam, pp. 227-232.

Monaco, P., Totani, G., Calabrese, M., 2006, "DMT-predicted vs observed settlements: a review of available experience", *Proceedings from the Second International Flat Dilatometer Conference*, Washington, D.C., pp. 244-252.

Pennsylvania Department of Transportation/Federal Highway Administration, 1988, *Report Number: FHWA-PA-87-024+84-24, Guidelines for Using the CPT, CPTU and Marchetti DMT for Geotechnical Design*, Volumes 1-4.

Schmertmann, J.H., 1978, "Use the SPT to Measure Dynamic Soil Properties? - Yes, But..!", *Dynamic Geotechnical Testing*, STP 654, ASTM, Philadelphia, PA.

Schmertmann, J.H., 1979, "Energy Dynamics of the SPT", *JGED*, GT8, ASCE, NY, NY.

Schmertmann, John H., 1986, "Dilatometer to compute foundation settlement", Proc., In-Situ '86: ASCE specialty conf. On use of in-situ tests and geotech engrg, ASCE, Reston, VA, pp. 303-321.

Skempton, A. W., 1986, "Standard penetration test procedures and the effects in sands of overburden pressure, relative density, particle size, ageing and overconsolidation," *Geotechnique 36*. No. 3, pp. 425-447.

Terzaghi, K., and Peck, R.B., 1948, *Soil Mechanics in Engineering Practice*, John Wiley & Sons, NY, NY.

U.S. Army Corps of Engineers, *EM 1110-2-1904 Settlement Analysis*, ASCE Press, NY, NY

Model Test Study of Soil Variation Impact on Shield Tunnel Segment Structure

Hongwei Huang[1], Dongming Zhang[1], Qunfang Hu[2] and Jie Zhang[1]

[1]Dept. of Geotechnical Engineering, Tongji University, 1239 Siping Road, Shanghai, 200092, PRC; PH +86 (0)21 6598 9273, +86 (0)21 6598 2386 and +86 (0)21 6598 5017; email: huanghw@tongji.edu.cn, 09zhang@tongji.edu.cn and cezhangjie@tongji.edu.cn
[2]Shanghai Institute of Disaster Prevention and Relief, 1239 Siping Road, Shanghai, 200092, PRC; PH +86 (0)21 6598 3449; email: huqunf@tongji.edu.cn

ABSTRACT

In recent 10 years, several accident cases and theories showed that soil distribution around the shield tunnel has direct or indirect impact on the failure models of tunnel segment structure. In this paper, a 1:38.75 ration physical model test is developed and carried out to clarify the impact of the soil variation on the mechanical behaviors of the tunnel segment structure. Some conclusions are put forward that soil variation does have an influence on the structure, but with different grades in different places of the segment structure. The value of displacement, bending moment of the segment structure located in the variation area increase dramatically, and the extremum points move to side of the varied soil in the structure. However, the structure located in the unvaried region remains almost the same status as that in the green field.

INTRODUCTION

In geo-engineering, the underground works, especially tunnels, are being paid more and more attentions to because of its fast, environmental friendly and efficient features. Metro lines and road tunnels in city have gained widely popularity to relieve the traffic pressure in China. Based on the investigation, nearly 33 metro lines in 10 cities are being operated today in mainland. In Shanghai, the operational mileage is 425km up to 2010, contributing nearly half of the total figure in China. Not only the length of the tunnel growing, but also the size of the tunnel is increasing. The diameter of tunnels can range from 6.2m for metro lines to 15m for road tunnels. Especially, the Shanghai Yangtze River shield tunnel is the biggest tunnel in the world with its 15m diameter. The metro lines and the road tunnels are built mostly by shield. As a result, the possibility that the shield crosses the different stratums both in longitudinal direction and in transverse section will become more likely (figure 1).

However, now the design of shield tunnel lining segment is mostly in condition of the homogeneous ground. It can hardly match the reality. The fact is that due to the soil variation, many failures of the segment have taken place, where the differential settlement, segment cracks, leakage and convergence deformation are the most significant (figure 2).

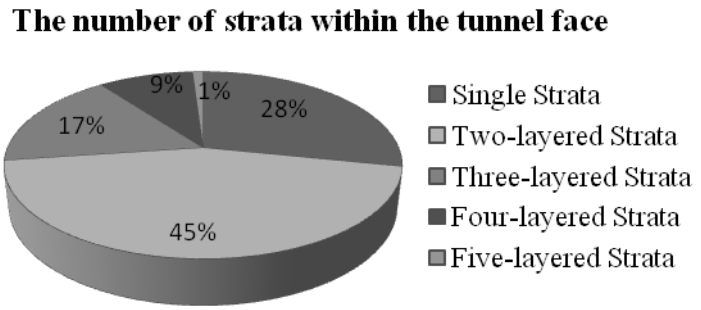

Figure 1. Number of strata within the Yangtze River shield tunnel face.

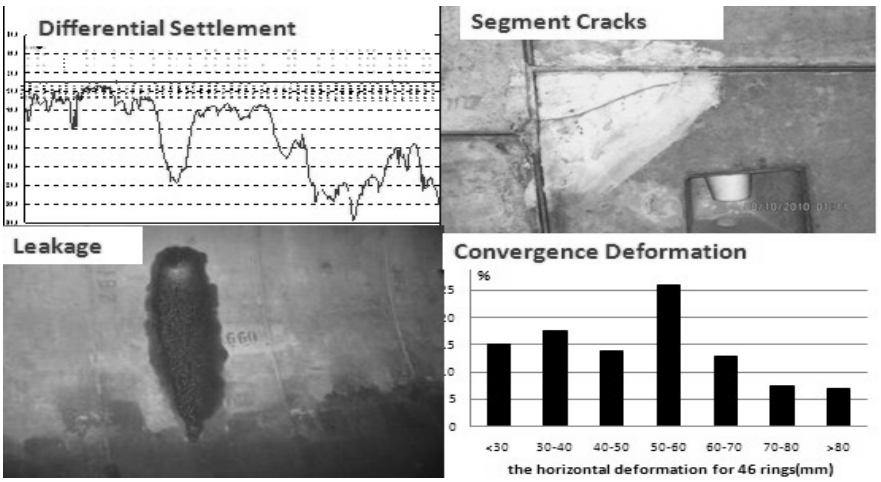

Figure 2. Main failure modes of metro lines in Shanghai.

In the past decades, many tunnel modeling techniques were developed all over the world (Meguid, et al. 2007), which include the classical trap door models (Chevalier, et al. 2009), rigid tube with flexible or movable face models (Fellin, et al. 2010), pressurized air bags, polystyrene foam and organic solvent, soil auguring, miniature TBM (Nunes, et al. 2009), etc. But they didn't consider the impact of the soil variation on the tunnel structure very much. In China, also a great many of researchers have designed many kinds of model test apparatus, such as a combined geo-mechanical model test system (Zhang, et al. 2007). All these kinds of model test apparatus have a common point, which is its big size. The conduction of every test is often exhausted and unsustainable. He, et al. (2008) has presented a model test to

figure out mechanical characteristics of segment lining structure under multi-layered strata, where the rock and the sand were simulated as the composite stratums. In a word, to conclude the current research level at home and abroad, the model test study of soil variation impacting on the segment lining structure is necessary and significant, especially for the small scale test to simulate the soil variation. On the basis of this knowledge, we have developed a small scale plane model test to clarify the impact of composite soil stratums on the segment lining structure.

TESTING PROGRAM

Simulation of Tunnel Segment Lining. The advantage of the model test is to reduce the engineering problems to a small scale condition which is easy to handle. It should obey the similarity principles. Otherwise, for the convenience of fetching the materials, A PE tube was used to model the Shanghai metro line with 38.75 for the geometry similarity ratio and 25.12 for the modulus similarity ratio. The thickness of the tube and the width of one ring were designed to match the similarity ratio. For a plane model test, 8 rings were simulated in total. The detailed similarity relation is showed by table 1.

Table 1. Parameters of the Test and the Prototype.

Content	Parameter	PE Tube	Metro Tunnel	Similarity Ratio
Tunnel	Diameter(m)	0.16	6.2	38.75
	Thickness(m)	0.0095	0.35	36.84
	Width of one ring(m)	0.025	1	40
	Elastic modulus(GPa)	1.373	34.5	25.13

For shield tunnel structure, the existence of the joints has weakened the stiffness of the ring, which is not only the key point for designing but also a complicated issue for modeling. Some joints modeling work has been done, where the joint can be simulated by small screw (Huang, et al. 2006), or modeled by making a slot (He, et al. 2008). Based on the stiffness-weakened mechanism of the joints and numerical analysis, a slot was incised with 4mm in depth and 2mm in width to model the segment joints showed by figure 3, in which transverse effective rigidity ratio η was given at 0.6 for the reality in Shanghai. The modeling of the lining segment structure is illustrated by figure 3. 12 pieces of strain gauges at the outside of the structure, together with 8 displacement sensors at the inside of the structure, were used to measure the moment and the deformation of the segment. In addition, we have placed 4 earth pressure sensors to find out the stress distribution around tunnel. The arrangement of the measurement is depicted by figure 4.

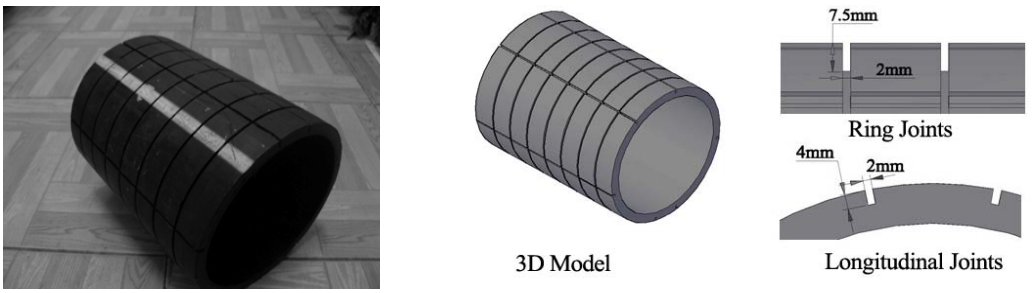

(a) The PE Tube **(b) The modeling of joints**

Figure 3. Modeling of lining segment.

Simulation of the soil variation. With the fact that the appearance of the multi-layered stratums located within the tunnel face was the normal condition as the data shows, two kinds of stratums with sharp different compressive modulus were introduced to simulate the multi-layered character. The purely fine sand (S1) and the muddy clay (S2) were modeled as the hard and soft soil, respectively. Because the emphasis of the research focused on the impact of modulus difference on the structure, where the elastic modulus of the PE tube was much larger than the soil, the values of the compressive modulus of the soil did not match the similarity ratio very well with 8.31MPa for S1 and 3.10MPa for S2. The dividing line between S1 and S2 was located at the spring of the tunnel section, which figure 5 has showed as test 3. Two homogeneous stratum tests, as test 1 and test 2, were conducted to compare with the composite stratums test. The size of the soil volume was 0.2m×0.56m×0.56m(thickness×length×width).

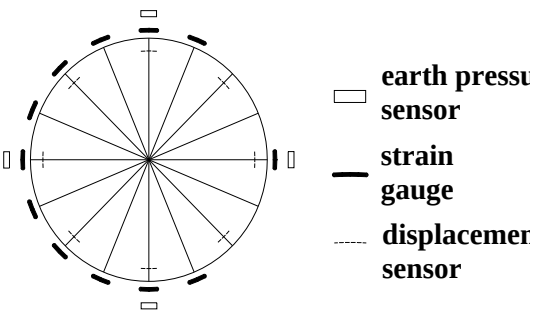

Figure 4. Measurement.

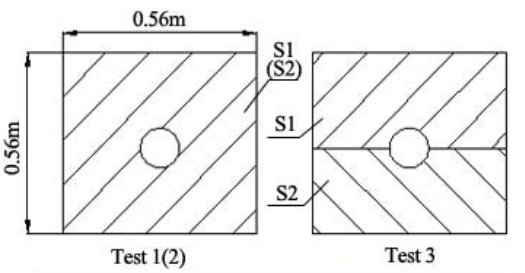

	S1	S2
E_s(Mpa)	8.32	3.1
Cohesion(kPa)	3	20
Friction angle	31.24	31.43
Gravity(kN/m3)	17	16

Figure 5. Simulation of soil variation.

Loading. The whole test apparatus had the size of 0.2m×1.0m×1.0m, consisted of the inner box containing soil and tunnel, outer boards supporting the loading reaction and the loading system that connected the forgoing two parts. The diagram and photograph are given by figure 6.

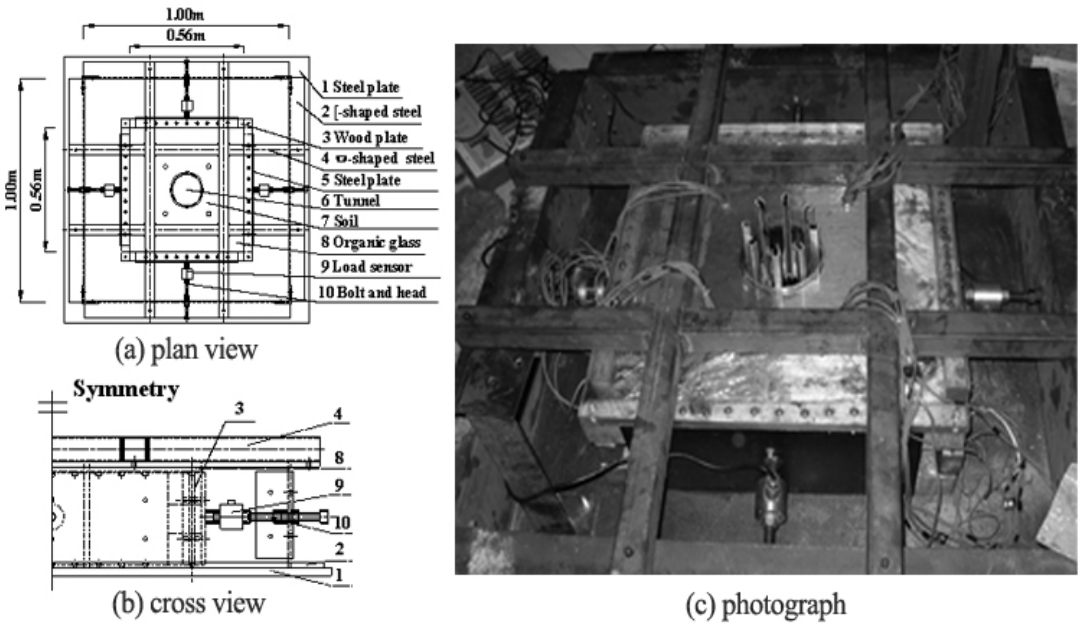

Figure 6. Test apparatus (a), (b) Diagram; (c) Photograph.

Limited by similarity ratio, the final load level of the test was 10.8kPa for vertical earth pressure and 5.4kPa for horizontal pressure. The load scale was so small that no common loading system, such as jack, could afford the real time and multilevel loads. A new but simple loading system was designed, which gave the loads by bolts showed by figure 6(b). We used spanners to apply the designed loads, and the sensor to read the loads in time. The final load level was derived for 5 steps with same intervals.

TEST RESULTS WITH INTERPRETATIONS

Deformation of the structure around the tunnel. Figure 7 shows the convergence deformation at the final load level. The results got from Test 1, Test 2 and Test 3 are plotted together to compare the difference due to soil variation. As showed in figure 7, we can see that in the homogeneous ground condition, the deformation is symmetrical with different values. The result in multi-layered ground condition is quite different from the ones above. Asymmetrical deformation has occurred, which top of the lining deforms 7.75mm and the bottom deforms 13.49mm with 5.43mm at the spring of the tunnel. It means that the displacement is impacted with different degrees in different places of the tunnel. If we consider that the green ground is S1 and the under layer is varied to S2, the deformation will be different in the varied side, which behaves more likely in S2 condition, with light difference in the unvaried side.

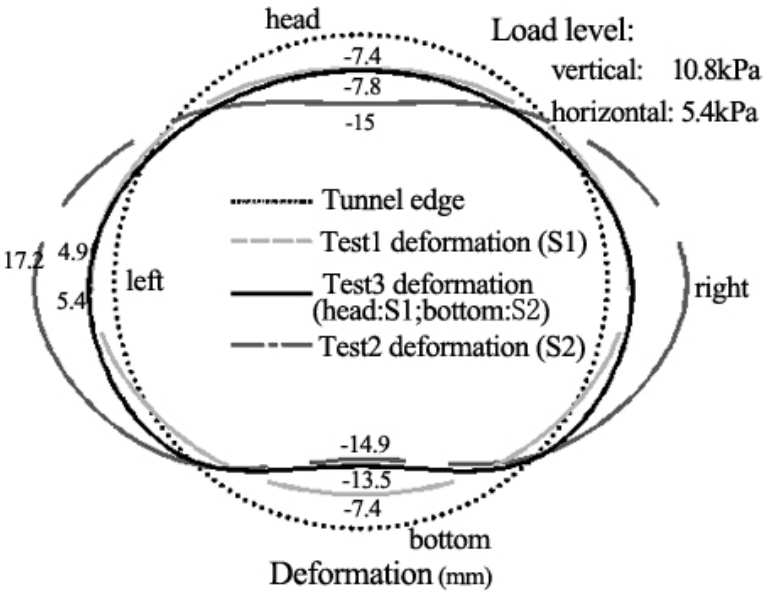

Figure 7. Convergence deformation.

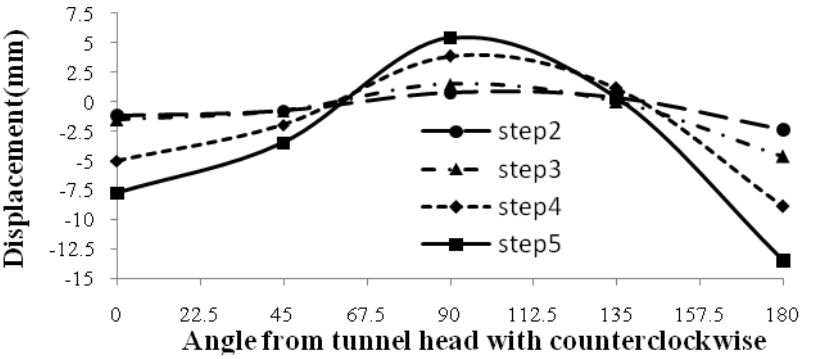

Figure 8. Differential deformation in Test 3.

The figure 8 has showed the displacement around the tunnel given at increasing load levels in Test 3. From figure 8, on condition that the compressive modulus ratio between S1 and S2 is 2.68 with dividing line locating at the spring, the deformation ratio (bottom deformation / the head deformation) is 1.75 averaged by different load levels and paralleled tests. He, et al. (2008) has given the deformation ratio at 1.57 on the condition that the modulus ratio of the two stratums was 15 and the dividing line located at 0.25D from the top of the tunnel. The truth has been proved that the different soil-structure interactions do have impact on the mechanical property of the lining structure with different degrees. The difference between the two deformation ratio results has proved that the modulus ratio and the multi-layered dividing line have fierce influences on the deformation behavior of the structure.

Moment of the structure around the tunnel. As figure 9 and figure 10 illustrate, the moment of the lining structure behaves almost the same rules as the deformation

of the structure does. The result of test 3 shows that moment of the tunnel head remains almost the same as in the homogeneous ground condition, while the bottom moment has changed dramatically with the moment ratio(bottom moment / head moment) at 2.15 averaged by different load levels and paralleled tests. The ratio derived by He, et al. (2008) is 2.51 where the condition is given above. From figure 10,we can also see the extremum point of the positive moment has moved to the side of varied soil (S2) for 22.5 degrees which is no longer at the spring of the tunnel depicted by the results of test1 and test2.

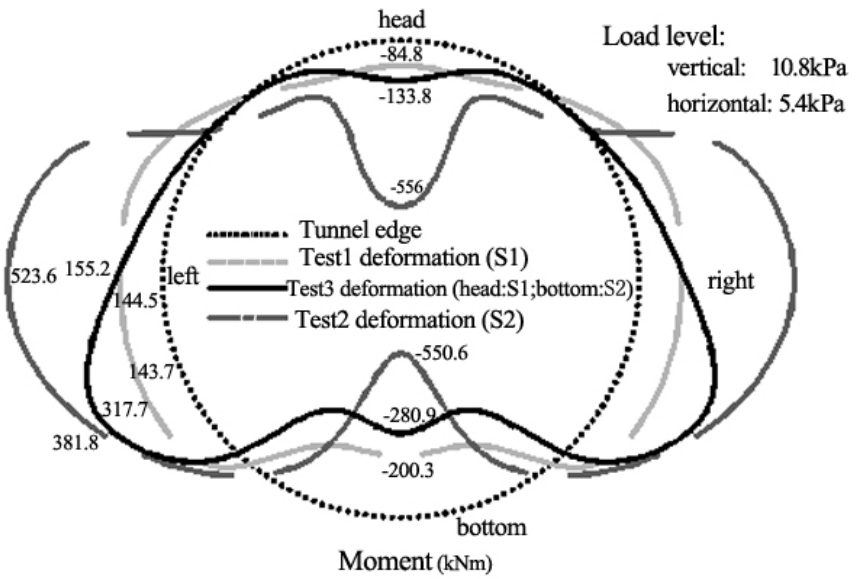

Figure 9. Moment around tunnel.

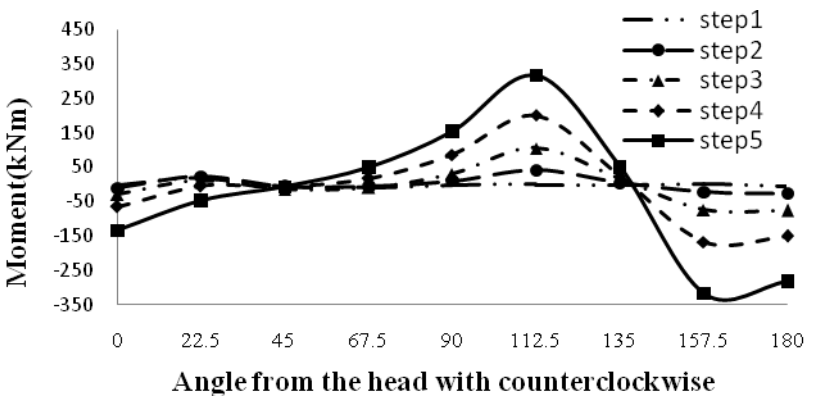

Figure 10. Differential moment in Test 3.

CONCLUSION

A small scale plane model test system was newly developed, and the shield tunnel lining structure and the soil variation expressed by the multi-layered stratums

were simulated successfully by applying the test system. Good repeatability of the test was confirmed. This suggests the test system is applicable to study the geo-technical problems including the impact of soil variation on tunnel structure.

The soil variation does impact on the tunnel lining structure, but with different grades in different places of the segment structure. On the condition that the modulus ratio between the two stratums is 2.68 where the multi-layer dividing line locates at the spring of the tunnel, average deformation ratio between the bottom and the top of the structure is 1.75, while the average moment ratio arrives at 2.15. The extremum point of the positive moment moves to the soft soil side for nearly 22.5 degree. However, the deformation and moment located in the unvaried area remain the same as that in the homogeneous ground.

Combined with the results derived by He, et al. (2008), the factors of the modulus ratio and the location of layer dividing line have fierce influences on the mechanical property of the shield tunnel lining structure. Since it's a small scale model test for preliminary study, more variation of soil conditions should be considered in the future work.

REFERENCES

Chevalier, B., Combe, G., Villard, P. (2009). "Experimental and Numerical Study of the Response of Granular Layer in the Trap-door Problem." In: Proceedings of 6th *Int. Conference on the Micromechanics of Granular Media, Golden, Colorado, 2009*. P.649-652.

Fellin, W., King, J. L., Kirsch, A., et al. (2010). "Uncertainty modeling and sensitivity analysis of tunnel face stability." *Structural Safety*, 32(6), 402-410.

He, C., Zhang, J. G., Yang, Z. (2008). "Model tests on mechanical characteristics of segment lining structure under multi-layered strata." *Chinese Journal of Geotechnical Engineering*, 30(10), 1537-1543.

Huang, H. W., Xu, L., Yan, J. L., et al. (2006). "Study on transverse effective rigidity ratio of shield tunnels." *Chinese Journal of Geotechnical Engineering*, 28(1), 11-18.

Meguid, M. A., Saada, O, Nunes, M A, et al. (2007). "Physical modeling of tunnels in soft ground: A review." *Tunnelling and underground space technology*, 23(2), 185-198.

Nunes, M.A., Meguid, M. A. (2009). "A study on the effects of overlying soil strata on the stresses developing in a tunnel lining." *Tunneling and Underground Space Technology*, article in press.

Zhang, Q. Y., Li, S. C., Guo, X. H. (2007). "A combined geomechanical model test system and its application in a bifurcation tunnel project." *Chinese Journal of Geotechnical Engineering*, 29(9), 1337-1343.

Mitigating Risk and Managing Foundation Cost & Schedule on "Mega" Transmission Line Projects: Beginning with the End in Mind

K. Yamatani, M.ASCE, P.E.[1] and A. Jahangir, P.E.[2]

[1]Kleinfelder, 180 Sheree Blvd., Suite 3800, Exton, PA 19341; PH (610) 594-1444; FAX (610) 594-2743; e-mail: kyamatani@kleinfelder.com
[2]Kleinfelder, 1340 Charwood Road, Suite I, Hanover, MD 21076; PH (410) 850-0404; FAX (410) 850-0049; e-mail: ajahangir@kleinfelder.com

ABSTRACT

"Mega" transmission line projects (MTLPs) span hundreds of miles through various geologic settings and changing subsurface conditions. Foundation Engineers, in conjunction with the project team, are tasked with developing strategies to overcome these and other challenges that are common to MTLPs. In a traditional project organizational structure for MTLPs, subsurface investigations are subcontracted to geotechnical consulting firms often after significant milestone decisions have been made that dramatically effect foundation design and construction costs and schedules and ultimately, the level of risk/reliability of the foundations.

This paper introduces a practical approach to providing Foundation Engineering services for MTLPs from project planning through foundation construction that will yield significant cost and schedule reductions (during subsurface investigation and construction) and mitigate project risk by increasing the reliability and efficiency of the foundation designs and foundation construction process. This is accomplished by implementing a phased subsurface investigation and a design approach that utilizes nomographs and through timely collaboration between the geotechnical consultant and the project team from project planning through foundation installation.

INTRODUCTION

"Mega" transmission lines are defined here as transmission lines that span distances of about 100 miles or more. Due to their length, mega transmission line projects (MTLPs) present unique technical and non-technical challenges to Foundation Engineers. Unlike commercial and/or industrial type projects which generally involve the design and construction of a handful of structures in a relatively small area, MTLPs consist of hundreds of structures spaced out over 100 or more miles, often traversing arduous terrain through various geologic settings and drastically different subsurface conditions. These MTLPs often intersect thousands of properties and roadway and stream crossings with unique access considerations. Aggressive project schedules, public sensitivity, changing structure locations, and unreliable cellular phone communication present additional project challenges.

To overcome these challenges, Foundation Engineers must collaborate with the project design team during project planning, throughout the investigation and design stage, and throughout foundation construction. For the purpose of this paper, Foundation Engineers are defined as engineers who collect and interpret subsurface conditions and

design the transmission tower foundations using the loads provided by others. The foundation engineering responsibilities are divided between Geotechnical Engineers and Foundation Structural Engineers. Geotechnical Engineers collect and interpret subsurface conditions and prepare subsurface design parameters while Foundation Structural Engineers use those design parameters to design foundations. The collaboration that is discussed in this paper starts between the Geotechnical Engineers and the Foundation Structural Engineers, and then it extends to rest of the project team including the contractors. A typical project team for a MTLP may include, but is not limited to:

- Owner;
- Construction/Program manager or Owner's engineer;
- Transmission line designers;
- Right-of-way agents;
- Foundation engineers;
- Construction coordinators; and
- Contractors (clearing, earthwork, foundation).

Foundation Engineers often engage in the project after significant work (line routing, survey, property acquisition/land owner negotiations, construction cost/schedule estimates, budget development, etc.) are complete and critical decisions that can affect project risks (structure types/locations, foundation types, boring quantities/locations, etc.) have been made. When inserted into this traditional project organizational structure, Geotechnical Engineers generally perform their work independently and develop recommendations for Foundation Structural Engineers to use in finalizing an engineering design which has already been budgeted and planned for. Hence, information collected during geotechnical/geological investigations is not fully utilized to the benefit of MTLPs.

A practical approach to providing Foundation Engineering services for MTLPs from project planning through foundation construction is introduced herein. This approach yields significant cost and schedule reductions during subsurface investigation and construction and mitigates project risk by increasing the reliability and efficiency of the foundation designs and foundation construction process. This is accomplished via timely collaboration between the Geotechnical Engineer, the Foundation Structural Engineer, and the rest of the project team during project planning, subsurface investigation, foundation design, and foundation construction.

Geological and geotechnical factors play an important role during project planning. Foundation type is a significant consideration in developing project schedules and budgets. Timely desktop evaluations provide valuable information for preliminary foundation type selection as well as future field investigation planning.

The subsurface investigation should provide sufficient information upon which foundation designs are based without being overly conservative in the design approach and without causing excessive delays during construction due to engineering re-design. To overcome these challenges, Foundation Engineers should conduct a targeted subsurface investigation and adopt a design approach that utilizes nomographs which facilitates real time foundation design change decisions during construction.

Foundation nomographs consisting of either graphs or tables that display required drilled pier sizes for various structure types and subsurface profiles, are based on the

collected information along the project alignment. Drilled pier foundations are considered in this paper because they are a common foundation for transmission line structures. Utilizing nomographs during foundation installation enables onsite geo-professional observers to evaluate the subsurface conditions at each foundation and evaluate the appropriate drilled pier length "on the spot." This process reduces over-drilling from conservative design assumptions and mitigates the risk of an undersized foundation at locations where subsurface investigations have not been performed at a structure.

PROJECT PLANNING

MTLP planning generally begins by identifying two geographical locations, where electricity is generated (or will be generated) and where electricity is needed. At this stage of the project, a team may be assembled to evaluate several corridors through which a MTLP will traverse to take electricity from point A to point B. There are many factors that project teams consider in their route selection during this preliminary planning phase. These factors may include, but are not limited to:

- Cost;
- Existing right-of-way;
- Environmental impact;
- Constructability;
- Current and/or future land use; and
- Community impact.

Generally, a project team, through community input, will evaluate these and other factors to refine their planning from corridors, which may be several miles wide, to a select handful of routes, which may only be hundreds of feet wide. After further evaluation, a final set of routes are then presented to a Public Utility Commission (PUC), which ultimately decides the final route along which the proposed transmission line will traverse. Geotechnical investigations, due in-part to cost, but also due to public relations considerations, are not initiated until the route selection is substantially complete.

Geotechnical investigations can become expensive in remote areas where clearing has not occurred, access roads are not yet built, there is no readily available water source for drilling, and the mobilization from one site to another may take hours, or sometimes, days. Public relations considerations are crucial to the success of a MTLP. During planning, it is important to gain the support of the communities through which the corridors and routes traverse. Private land owners generally do not look favorably upon drill rigs and other support vehicles tracking through their land for the sake of evaluating whether or not their back yard is a good place to put a transmission line. Hence, since transmission line structures will generally be located on a private land owner's property, geotechnical borings are generally not drilled until property acquisitions are substantially complete.

These considerations are valid. However, they should not discourage the project team from collecting geotechnical and geological information during the planning stages of a MTLP because they can have a dramatic effect on the very same factors, listed above, that are being considered as part of planning.

At this stage of the project, geotechnical consultants should conduct a desktop study. This is a relatively low cost way to collect publically available geotechnical and geological information, combine it with consultants' knowledge of a particular region, and present it in a way that will facilitate the evaluation of several different corridors/routes. A desktop study may identify the following features along each of the studied corridors/routes:

- Geologic regions or units;
- Ranges of engineering parameters associated with each geologic region;
- Geo-hazards (landslide prone areas, karst, expansive soils, collapsible soils, caliche, surface mine fills, deep mining activity, faults, etc.); and
- Ranges of anticipated soil overburden thickness.

At this stage of a MTLP, the goal of the desktop study is to divide the study area into a manageable number of regions that are geologically similar and develop subsurface profiles for each of these regions. A subsurface profile should consist of an estimate of the "average" or typical overburden thickness and engineering parameters for the overburden and bedrock, if the bedrock is considered to be within a reasonable depth below ground surface, typically about 50 feet. These subsurface profiles will generally not consider the "worst case" subsurface condition resulting from a potential geo-hazard. Rather, they are preliminary approximations of the average subsurface conditions from which estimates of the foundation costs may be developed.

Locations of geo-hazards are overlain on figures that display each of the studied corridors/routes and the boundaries of the regions for which individual subsurface profiles have been developed. Using these figures, the project team evaluates the relative risk, cost, and level of difficulty, from a geotechnical and geological perspective, of one corridor/route versus another. Importantly, this information is collected without disturbing land owners and without mobilizing expensive drilling rigs to evaluate corridors/routes that may not be selected for the transmission line.

SUBSURFACE INVESTIGATION / FOUNDATION DESIGN

Geotechnical consultants rarely drill a boring at every transmission line structure for MTLPs. This is costly and, likely, would not be feasible because the exact final location of each structure is often not known at this stage of the project. Therefore, geotechnical engineers are forced to develop recommendations for foundations in locations that may be thousands of feet from the nearest boring.

Hence, to reduce the risk of under-designing foundations, geotechnical consultants recommend conservative engineering parameters and conservative estimates of overburden depth for foundation design. Compounding this level of conservatism, foundation design engineers may select the "worst-case" set of parameters for their design and implement a "one size fits all" foundation for each type (tangent, angle, or dead-end) of transmission line structure. In this scenario, the effort to provide reliability of the foundation designs results in increased construction costs. To develop a more cost-effective subsurface investigation and foundation design, Geotechnical Engineers should collaborate with the Foundation Structural Engineer and the rest of the project team to discuss the implementation of a design/construction process which utilizes nomographs.

The nomograph process. The nomographs discussed in this paper are applicable to drilled pier foundations that are partially embedded in rock. They are graphs which present the required rock socket length for a drilled pier for various overburden depths. A separate nomograph is developed for each "design" subsurface profile with a specific loading condition. For example, if the Geotechnical Engineer recommends two subsurface profiles and the Foundation Structural Engineer recommends three structure load design cases, there would be a total of six nomographs. During construction, on-site geo-professional observers evaluate the soil/rock conditions in each foundation excavation, select the appropriate subsurface profile and load case, estimate the as-drilled overburden depth, and modify the design length of each drilled pier in real time. Figure 1 is a depiction of a generic nomograph.

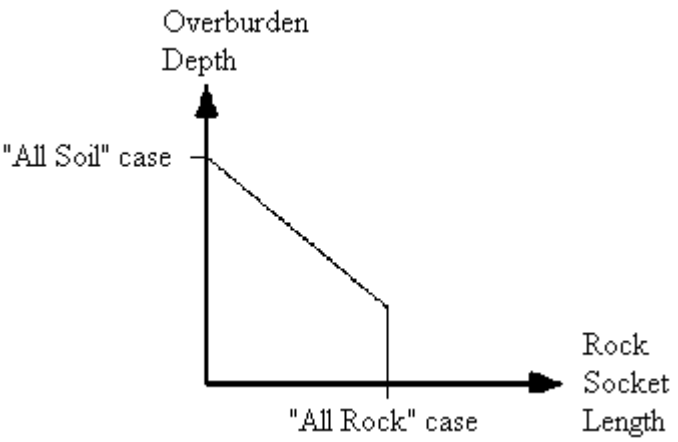

Figure 1. Sample Generic Nomograph.

Once the project team accepts the idea of using a nomograph approach, the Foundation Engineer can work with the project team to develop a targeted and efficient subsurface investigation. Having completed a desktop study, the Geotechnical Engineer has a better idea of the areas of high geotechnical risk and a rough idea of the ranges of expected overburden soils along the proposed alignments. The Foundation Structural Engineer will often know the probable location of heavily loaded structures such as long spans, angle structures, and dead-end structures. In addition, a probable foundation type and design methodology should be established by the Foundation Engineer.

The subsurface investigation should be designed in consideration of all of these factors. Now, instead of drilling borings to an arbitrary depth in arbitrary locations based on a goal of "x" borings per mile, the Geotechnical Engineer can develop a subsurface investigation that more effectively mitigates risk with a smaller quantity of borings drilled to appropriate depths. In addition, the field testing and laboratory testing program can be tailored to the probable foundation type and specific design methodology.

Once the initial phase of the subsurface investigation is complete, the Geotechnical Engineer, in conjunction with the Foundation Structural Engineer, selects an appropriate number of subsurface profiles to develop for foundation design. There are many factors to consider in this decision. The main factors are:

- Variability of subsurface conditions along the alignment;

- Cost (engineering effort) associated with developing each nomograph;
- The effect, real or perceived, of construction changes; and
- Construction schedule.

Ultimately, the subsurface profiles used for the development of nomographs should cover the range of subsurface conditions encountered during the investigation. To make this decision, the Geotechnical Engineer needs to understand which geotechnical parameters the foundation design is most sensitive to. This requires an understanding of the design methodology. The refinement and efficiency of the foundation designs increases with the quantity of subsurface profiles that are developed. For instance, the foundation designs for the entire alignment may be designed on a single "soft clay over rock" profile. However, if say 30% of the foundations are in a "dense sand over rock" setting, there those foundations will be over-designed unless they are based on an equivalent profile.

Recall, for a single subsurface condition, the number of required nomographs will equal the number of loading conditions. Multiple foundation design calculations for various overburden depths are required to develop each nomograph. Therefore, the cost to develop each nomograph should also be considered.

The more subsurface profiles that are used, the closer the as-drilled conditions will be to those which were used for design. As a result, the magnitudes of the field changes to the drilled pier lengths will decrease. These construction changes are necessary to either make the design more efficient (in the case where a drilled pier is shortened) or make the design more reliable (in the case where a drilled pier is lengthened to match the as-drilled subsurface conditions). Regardless, construction changes cause contractors to have less ability to predict schedule and cost. This should be considered, in addition to cost to develop nomographs, when evaluating the appropriate number of subsurface profiles to use.

Finally, the overall construction schedule needs to be considered. MTLPs are often fast-tracked and therefore, while there may be sound technical reasons to develop multiple nomographs, the construction schedule may only accommodate the development of nomographs for one or two subsurface profiles. The way in which the number of subsurface profiles affects the project logistics is shown in Figure 2.

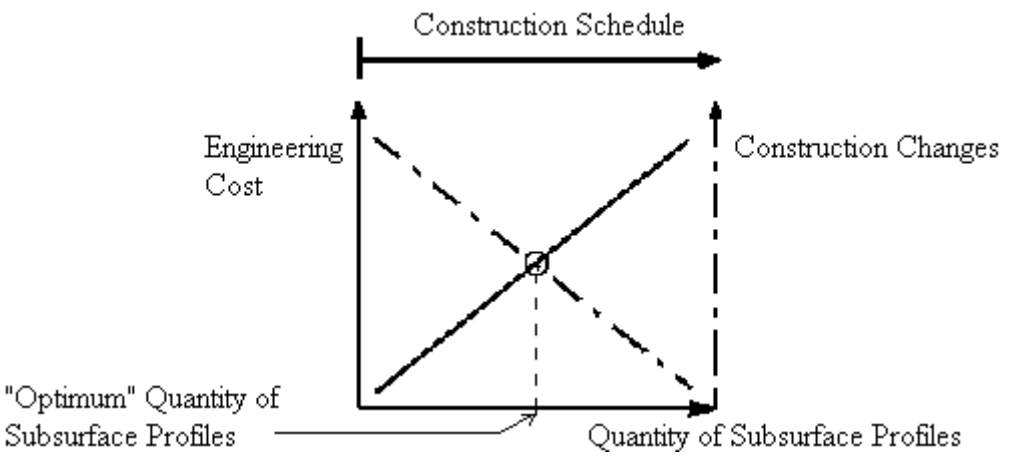

Figure 2. Relationship between subsurface profile quantity and project logistics.

CONSTRUCTION

The benefits of the approach described above will not be fully realized unless the collaboration between the Foundation Engineer and the rest of the project team continues through foundation construction. Now that nomographs are developed for the project, an onsite geo-professional observer that is familiar with the development of the subsurface profiles needs to accompany the drilled pier contractor during construction. The main responsibilities of the on-site geo-professional observer are:

- Identify the as-drilled subsurface conditions at each foundation;
- Select the subsurface profile that best represents the as-drilled conditions;
- Select the appropriate nomograph for the subsurface profile and the structure loading type;
- Estimate the depth of overburden;
- Select the appropriate rock socket length from the nomograph; and
- Communicate the foundation design change to the project team.

To properly identify the as-drilled subsurface conditions and select the appropriate subsurface profile, the on-site geo-professional observer must be familiar with the ranges of subsurface conditions that were considered in the development of the subsurface profiles. Hence, it is of paramount importance that these on-site personnel communicate with the Foundation Engineers prior to mobilizing to the project site and throughout construction. Ideally, the on-site geo-professional observer will be an employee of the geotechnical consultant to facilitate communication.

The on-site geo-professional observer must also communicate with the rest of the project team. Prior to construction, communication protocols should be developed so that the dissemination of information regarding construction changes is streamlined and efficient.

By using nomographs, a major logistical challenge, lack of cell phone service that often occurs, can be overcome. This is not an insignificant challenge. Consider the cost and schedule impact of identifying a “changed condition” that warrants a design change in a situation without nomographs. Assuming there is someone onsite who is qualified to identify a “changed condition”, that person would then need to make the Foundation Engineer aware of the changed condition, at which time, construction may stop. Provided they have cell phone service, they can call the Foundation Engineer who will then implement a re-design process which may take several hours or days. The re-design is communicated to the project team and back to the onsite personnel at which time, after significant delay, construction proceeds.

By using nomographs, design changes are made in real time by a qualified person that is capable of identifying a condition that warrants design change and is empowered to implement it. As a result, the project realizes significant cost and schedule savings while increasing the efficiency and reliability of every foundation design by tailoring the designs to the as-drilled subsurface conditions.

CONCLUSIONS

MTLPs include hundreds of structures and, in some cases, thousands of foundations. Therefore, even small changes to foundations designs can have a dramatic effect on the overall project cost and schedule when these changes are implemented thousands of times. During construction, schedule is paramount. Implementing a design approach that reduces the amount of contractor stand-by time while foundation re-design occur reduces foundation construction schedule and foundation installation cost. By tailoring each foundation design based on as-drilled conditions, they become efficient and more reliable. This is accomplished through timely collaboration between the Foundation Engineer and the project team from project planning through foundation installation. The benefits of implementing the practical approach to providing Foundation Engineering services described herein are:

- Geotechnical and geologic information is collected in a non-intrusive (desktop study) manner in a timely fashion (during project planning) to facilitate the evaluation of multiple corridors/routes being considered for the transmission line;
- Information presented in the desktop study may be used to develop more realistic foundation cost and schedule estimates;
- Using the desktop study, efficient subsurface investigations are developed that target high geologic risk areas and critical structure locations;
- The overall number of borings are reduced while achieving a higher level of reliability of the foundation design by implementing a nomograph approach that tailors each foundation design to the as-drilled conditions;
- By implementing nomographs, a “one size fits all” design is not used and significant construction cost and schedule savings are realized; and
- By implementing nomographs, design changes are implemented in real time thereby avoiding costly delays associated with re-design that would otherwise occur remotely.

To realize these benefits, the project team must incorporate the Foundation Engineer into the project team during early planning and maintain communication and collaboration throughout foundation construction.

REFERENCES

The Institute of Electrical and Electronics Engineers (IEEE). (2001). *IEEE Std 691-2001, IEEE Guide for Transmission Structure Foundation Design and Testing*, New York, NY.

United States Department of Agriculture, Rural Utilities Service (RUS). (2005). *RUS Bulletin 1724E-200, Design Manual for High Voltage Transmission Lines*, Washington, DC.

Comparison Study on Computer Simulations for Bridge Scour Estimation

Xinbao Yu[1], Junliang Tao[2] and Xiong (Bill) Yu[3*]

[1]Research Associate, Louisiana Transportation Research Center
[2]Graduate Research Assistant, Department of Civil Engineering, Case Western Reserve University, Cleveland, OH 44106
[3*]Assistant Professor, Department of Civil Engineering, Case Western Reserve University, Cleveland, OH 44106, xxy21@case.edu

ABSTRACT

This paper compares the use of 1D and 2D hydraulic models for bridge scour prediction. Two representative computational software developed by Federal Highway Administration (FHWA), HEC-RAS and Flo2dh, are used as the benchmark comparison bases. The procedures for model construction and scour estimation are illustrated by developing simulation examples. The comparison shows that 1D model using HEC-RAS, while is easy to construction, does not account for the effects of flow disturbance due to hydraulic obstructions. These include the spatial variation of the alignment angle, which significantly affects the depth of scour prediction. Higher dimensional mode such as Flo2dh captures the effects of flow field distribution. It is however difficult to use and requires deliberations to run proper simulations. Further development of computational simulation and visualization technologies is necessary and will help place computer aided bridge scour simulations into the hands of practitioners.

INTRODUCTION

The catastrophic collapse of the Schoharie Creek Bridge on the New York State Thruway in April 1987 during a near record flood, which caused 10 fatalities, focused the U.S. national attention on the bridge scour problem (NTSB 1987). Bridge scour or bridge sediments scour is the lowering of streambed around bridge piers or abutments. Over the last few decades, scour is the most common cause of the collapse of in-service bridges. It also contributes to high construction and maintenance cost for bridges over waterways. Federal Highway Administration (FHWA) design guide requires bridge foundations to withstand the effects of scour induced by floods of 100-year return period. Evaluation of bridge scour is mandatory for the design of new bridges or rehabilitation of the existing ones. Accurate scour prediction is essential for implementing an economic countermeasure design.

As computers become widely used in every aspects of engineering design, the way of performing hydraulic analysis has also changed dramatically. Hydraulic modelers become more relied on the “user friendly” modeling programs. However, sometimes, modelers are more well-trained with the computer program, but less well-trained with

the theory basis behind the program (Walton et al. 1997). For bridge scour analysis there are various existing modeling systems, for 1D simulation such as HEC-RAS and WSPRO, 2D simulation such as Flo2dh and SED2D, or 3D simulation such as Flow3D and CCHE3D (Walton et al. 1997). The modelers are facing with difficult task of choosing the appropriate tools for a given application.

One of the mostly widely used computer program for bridge scour analysis is HEC-RAS, a one dimensional hydraulic analyses program with scour estimation modules. It predicts scour at bridge crossing reasonably well for simple regular channel. It however was found either significantly overpredict or underpredict scour compared with actual field observation. For river channels with complex geometries or where lateral distribution of flow is of concern such as bridge openings, two or two dimensional model is preferred. Three-dimensional model provides the most realistic simulation of flow field under turbulence conditions adjacent to bridge piers and abutments. The modeling process, however, can be complex; besides, solving a 3D model requires significant amount of computational time. 1D and 2D hydraulic models remain most frequently used. With progresses in computational technology, this barrier will only be reduced with time.

This paper presents a comparison study of 1D and 2D models for bridge scour simulation. HEC-RAS and FESWMS Flo2dh are selected as representatives of 1D and 2D models. The procedures in model construction and typical results of simulation from these two programs are compared. A few important aspects were highlighted such as the effects of spatial topography on the flow field distribution and bridge scour prediction.

BACKGROUND

Introduction to HEC-RAS: HEC-RAS (River Analysis System) is bridge scour prediction software developed by the Army Corps of Engineers Hydrologic Engineering Center (HEC). It has been widely used by state DOTs and private design practitioners. The first version of HEC-RAS was released in July of 1995. The most current version at the moment of writing is version 4.0 Beta. The detailed hydraulic evaluations have been performed using techniques outlined in Hydraulic Engineering Circular No. 183 (Richardson and Davis 2001). It provides predictive scour-depth computations using parameters from a one-dimensional hydraulic analysis. Field observations show that bridge scour predicted by HEC-RAS generally overestimated the actual scour depth. One of the reasons is that scour prediction equations used in HEC-RAS was developed based on scaling up the laboratory results, which are difficult to satisfy both the hydraulic and hydrodynamic similitude. The assumption of one dimensional flow is another potential source of errors.

The basic computational procedure in HEC-RAS is based on solving the one dimensional energy equation. Energy losses are accounted for by friction (Manning's equation) and contraction/expansion (coefficient multiplied by the change in velocity head). The momentum equation is utilized in situations where the water surface profile is rapidly varied. These situations include mixed flow regime calculations (i.e., hydraulic jumps), hydraulics of bridges, and evaluating profiles at river confluences (stream junctions) (Brunner 2002).

Introduction to FESWMS Flo2dh: Flo2dh, part of the Federal Highway Administration's (FHWA) Finite Element Surface-water Modeling System (FESWMS), is a two-dimensional finite element model that was developed by the U.S. Geological Survey in cooperation with the FHWA (Parr et al. 2007). The software was developed for analyzing backwater and flow distribution at width constrictions and highway crossings of rivers and flood plains. It supports both supercritical and subcritical flow analysis. This code solves two dimensional flow equations based on the continuity of mass and momentum; it assumes a depth-averaged flow, as opposed to cross-section averaged flow in one dimensional models. This program can simulate movement of water and non-cohesive sediment in rivers, estuaries, and coastal waters. The software was special designed to model highway river crossings where complex hydraulic conditions exist, which is to address the shortcomings that conventional one-dimensional flow calculations cannot provide the needed level of solution details at these locations. This code, however, has not enjoyed widespread use due to difficulty in use and also the very limited number of actual applications that subjected to field verification.

Models for Scour Prediction

Computational software such as HEC-RAS and Flo2dh simulates the flow field under different levels of assumptions. They are combined with scour prediction formulas for scour depth estimation.

Scour occurring at bridge crossing generally include three components: 1) Long-term aggradation and degradation of the river bed, 2) general scour at bridge (including contraction scour and other general scour), and 3) local scour at the piers or abutments3). Based on the existence of sediment transportation, scour was classified as clear-water scour and live-bed scour. Two of the scour prediction formulas (i.e., Froehlich equation (Eq. (1)) and HEC-18 equation (or CSU equation, Eq. (2)) available in both programs are introduced below.

$$y_s = 0.35\phi(a')^{0.62} y_1^{0.47} Fr_1^{0.22} D_{50}^{-0.09} + a \qquad (1)$$

where ys is the depth of pier scour; ϕ is Correction factor for pier nose shape: ϕ = 1.3 for square nose piers; ϕ = 1.0 for rounded nose piers; and ϕ = 0.7 for sharp nose (triangular) piers; a′ is the projected pier width with respect to the direction of the flow, feet (m). y1 is the flow depth directly upstream of the pier in feet (m). Fr1 is Froude Number directly upstream of the pier; D50 is median diameter of the bed material, feet (m); a is the pier width4).

$$d_{sl} = 2.0K_1K_2K_3K_4 b^{0.65} y_a^{0.35} Fr_a^{0.43} \qquad (2)$$

where K1 = pier shape factor, K2 = flow alignment factor, K3 = bed condition factor, K4 = bed armoring factor, b = pier width, ya = approach flow depth, Fra= approach flow Froude number, and Va = depth-averaged velocity of the approach flow6).

Both HEC-RAS and Flo2dh predict scour depth utilizing the empirical scour prediction equation with the calculated quantities (for example, water depth and velocity of flow) or preset quantities (pier width, grain size of bed materials and other parameters). HEC-RAS can predict contraction scour, abutment scour and pier scour; while in Flo2dh, contraction scour and pier scour can be calculated. For comparison

purpose, only pier scour is studied in the paper.

HYDRAULIC MODELING

To perform scour analysis, a river model containing bridge crossing needs to be set up first. With this model, flow conditions (water depth and velocity of flow) at the bridge crossing can be determined.

Procedures of Modeling by HEC-RAS: To calculate scour at bridges, a hydraulic model that contains the bridge crossings must be developed at first. An example of HEC-RAS river model is shown in Figure 1a. To calculate energy losses due to construction of bridge crossing, four user-defined cross sections need to be specified on the river channel near the bridge.

The flow distribution option in the HEC-RAS software allows for additional output showing the distribution of flow for multiple subdivisions of the left and right riverbanks as well as the main channel. Information that can be output for each flow slice include the percentage of flow, flow area, wetted perimeter, conveyance, hydraulic depth and average velocity. Up to a maximum of 45 total slices can be output for each flow element (left riverbank, main channel, and right riverbank). After incorporating the flow distribution data and specifying the boundary conditions, steady flow analysis under subcritical regime can then be performed. This step determines the velocity and depth of flow around bridge crossing. An example output of flow distribution at a bridge crossing section is shown in Figure 1b.

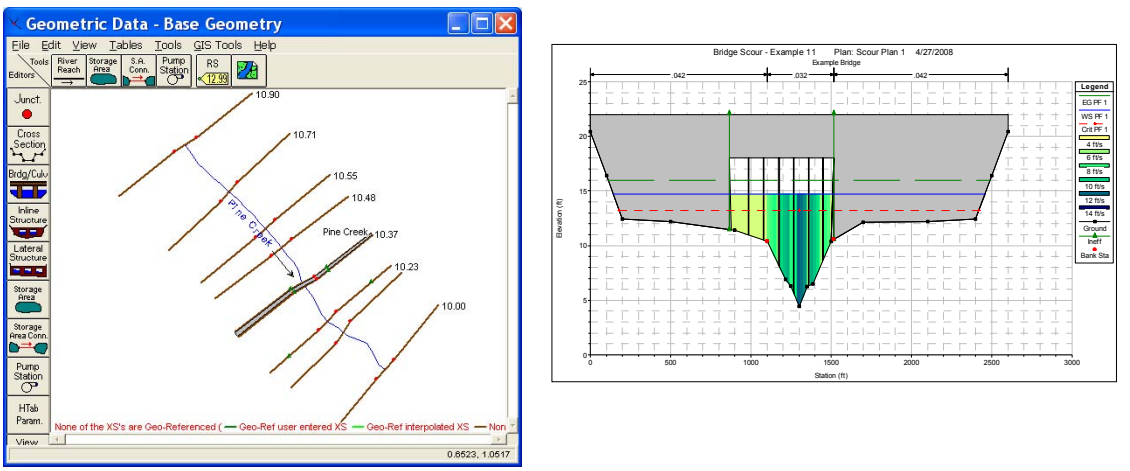

Figure 1. a) Screen shot of river model in HEC-RAS; b)Output of flow distribution at the bridge cross section

After the velocity and water level at the bridge cross section are obtained, scour analysis can be performed. For the pier scour analysis, the model has the option of using either the CSU equation (Eq. (2)) or the Froehlich equation (Eq. (1)). The predicted scour depth can then be visually presented. A screen shot of the program's scour analysis module with result display is shown in Figure 2.

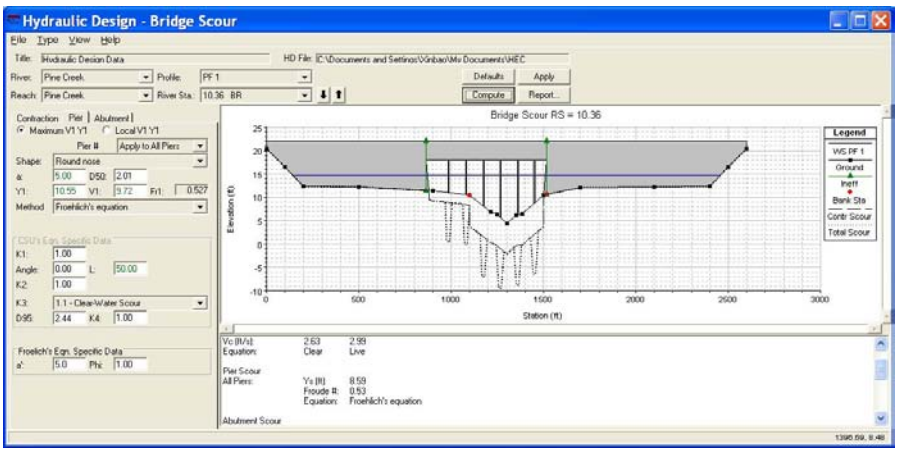

Figure 2. Screen shot of bridge scour analysis in HEC-RAS

Procedures of Modeling by FESWMS Flo2dh: The first step of using Flo2dh is to generate the topographic data for the river, including the location and elevation of riverbed. This can be created manually or using other river modeling software including HEC-RAS. An example of topographic data imported from HEC-RAS is shown in Figure 3.

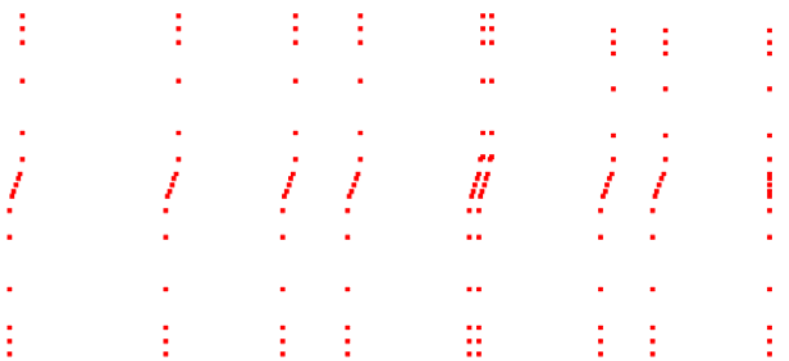

Figure 3. Scatter data points for mesh generating

The raw data of river topography can be refined. The refinement include, for example, extending the boundary of mesh in the downstream side to eliminate the effects of boundary truncation on flow field distribution. An example of refined mesh is shown in Figure 4.

After FEM mesh is constructed, material properties can then be assigned to each element. As shown in Figure 5, different colors indicate different types of materials. The elements corresponding to the bridge embankment can be disabled to block flow. The default simulation by Flo2dh is for wet river bank. A strip of elements on each side of bank can be disabled to simulate the effects of dry banks.

Piers can be added by changing the materials properties in the corresponding FEM mesh at the corresponding pier location. With the 2D flow field simulation capability, Flo2dh calculates the flow velocity, depth and angle of attack around bridge piers. These are then used to predict pier scour depth using Eqs. (1) and (2). A screen shot for the input parameters of pier scour calculation is shown in Figure 6. The parameters include the shape and geometry of piers and the characteristic particle sizes of sediment.

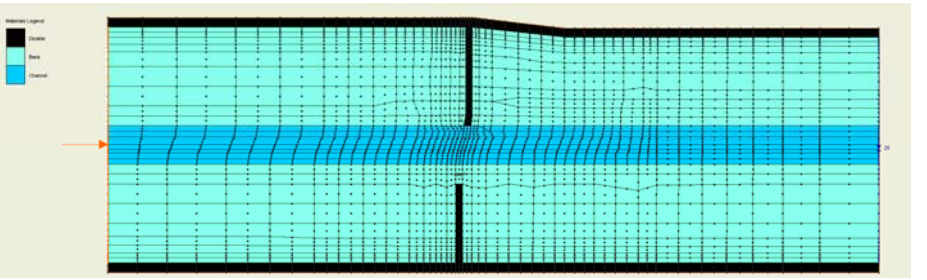

Figure 4. 2D mesh for bridge scour simulation

A COMPARISON STUDY ON 1D AND 2D SCOUR MODEL

Hydraulic Analyses Results: Both HEC-RAS and SMS programs were used to simulate scour at similar cross sections of bridges. The comparison is based on generating similar flow velocities. For this criteria, a flow rate of 80000ft^3/s is specified in Flo2dh at the upper stream boundary and water surface of 25 ft is specified at the downstream boundary. For HEC -RAS, an input flow rate of 30000 ft^3/s generates similar magnitude of flow velocity at the bridge cross section. A higher water surface boundary is also used in Flo2dh as lower boundary leads to an unstable solution. The calculated flow field by Flo2dh is shown in Figure 5.

In figure 5, the length of arrows is proportional to the magnitude of velocity. Darker blue color in the contour means larger velocity. This figure shows the bridge structures (piers) significantly changed the flow field. In addition to flow status, flow speeds greatly increase at the bridge crossing section. The disturbed flow attacks the bridge from different angles.

(a)

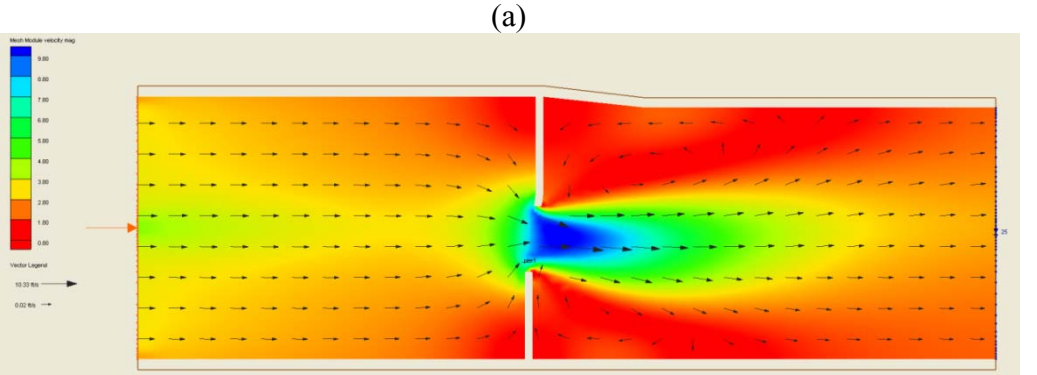

(b)

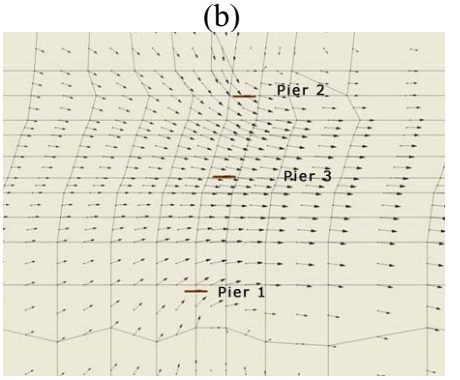

Figure 5. a) Example of flow field by Flo2dh, b) Distribution of velocity field around bridge model with 3 piers

The profiles of water level along the middle of the river bed are plotted in Figure 6a. Both shows disturbance at the location of bridge crossing. Due to the slight differences in the boundary conditions, the profile of water level obtained by Flo2dh, while has similar shape as that by HEC-RAS, has a flatter slope.

Figure 6b compares the flow velocity calculated by HEC-RAS and Flo2dh. For HEC-RAS, the distribution of flow velocity along two cross sections are plotted, i.e., the cross section along the bridge crossing and the cross section just upper stream of the bridge. The difference clearly shows the effects of bridge piers in obstruction of the flow. There are several obvious velocity drops on the velocity profile calculated by HEC-RAS. The location of these drops correspond to the location of piers, the discontinuity might also be attributed to the one-dimensional flow assumption by the HEC-RAS model.

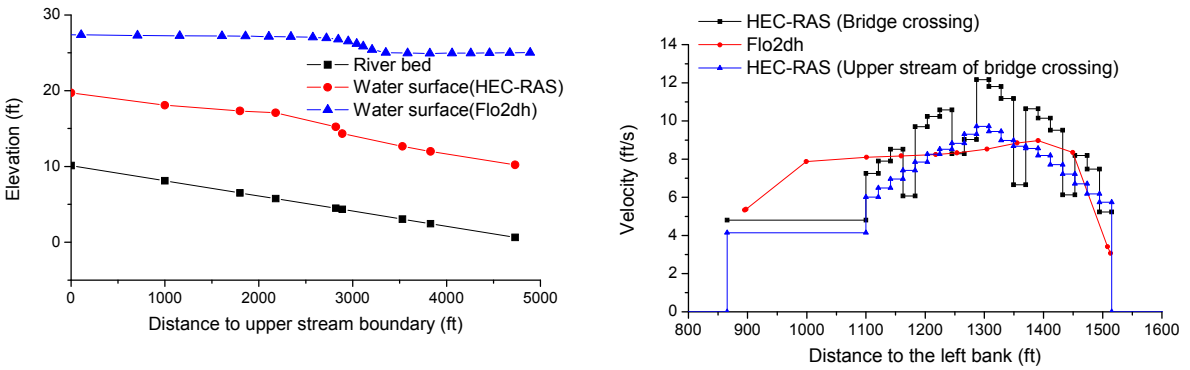

Figure 6. a) Water profile calculated by HEC-RAS and Flo2dh, b) Comparison of velocity magnitude at cross section with bridge piers

Bridge piers were introduced by equivalency principles in Flo2dh model by two different methods. The first method is to create an area with the same geometry as a bridge pier and set elevation of this area equal to the height of a pier. The second method is to increase the roughness of elements containing the pier to simulate the effect of a pier on the approaching flow). With the use of FEM analyses, the flow field obtained by Flo2dh is continuous.

Scour Analysis: HEC-RAS has option to calculate the scour for all the piers using the maximum velocity and water depth at the bridge cross section; or scour around each pier can be calculated separately using the local flow conditions at corresponding pier. The default option is the first approach, which is also used in this study. A maximum water depth of 10.55ft and velocity of 9.72ft/s was obtained from hydraulic analysis at the first upstream cross section of the bridge. With the flow condition determined, it requires to determine the alignment angle in order to estimate pier scour. Such information is generally obtained by survey the angle between flow direction of mainstream and direction of bridge deck.

Due to the lack of survey data, an alignment angle with bridge piers of 33.8° was used for scour prediction in HEC-RAS (the results of Flo2dh were used). The projection width of pier normal to the direction of flow, a′, was found to be 30.06 ft. Substituting these parameters to Eq. (1) and subjected to the constraints that scour depth needs to be smaller than 2.4a (HEC-RAS User Manual), a pier scour depth of 12 ft was determined. By use of using Eq. (2), with K1=1.0, K2=3.34 (alignment angle=33.8^{o}), K3=1.1 (clear water scour) and K4=1.0, the calculated scour depth is 38.23ft. There are significant differences in scour prediction depending on the scour models selected.

For analyses using Flo2dh, a velocity of 7.446ft/s and water depth of 14.848ft are determined at the pier location. The resultant pier scour depth is 11.51 ft using Froehlich equation (Eq. (1) but without the term that adds the pier width). A pier scour depth of 28.82ft with confident level 99% is obtained for design purpose. While using HEC-18 (CSU) equation (Eq. (2)), with K1=1.0, K2=3.21 (alignment angle=33.8o), K3=1.1 (clear water scour) and K4=1.0, the calculated scour depth is 32.52ft.

To examine the effects of alignment angle on pier scour, two more piers (shown in Figure 10) were added to into the bridge cross section in the Flo2dh model. The resultant scour adjacent to each pier was compared. Using Eq. (2), the pier in the middle has the minimum scour depth of 19.40ft. The scour depths at piers on the both sides are both about 31.21ft. The significant differences might be attributed to the effects of spatial distribution of flow speed and the consequence differences in the alignment angles around different piers. This clearly demonstrates the effects of flow field distribution on scour depth prediction. Rather than using a bulk value of alignment angles for all the piers, determination of flow field distribution helps to assess the scour potential along individual piers.

CONCLUSIONS

Computer assisted analyses will play increasing roles in bridge scour countermeasure design. This paper compares the bridge scour prediction by 1D and 2D models. HEC-RAS and Flo2dh are selected as benchmark comparison bases. The application procedures of both models are illustrated and compared by developing simulations examples. The results indicate scour prediction is significantly affected by the spatial distribution of flow field, especially the angle of alignment with bridge piers. For bridge with multiple piers, the spatial effects of flow field distribution have to be accounted for by realistically simulating the flow field distribution. 1D model such as HEC-RAS is incapable in this regard. Higher dimensional model such as Flo2dh has advantage in this regard. As most engineers experienced, high dimensional model was found to be much more complex and difficult to set up compared with 1D HEC-RAS model. There is a need to improve the simulation environment to place powerful scour simulation tools into the hand of practitioners. It needs to be pointed out, neither models discussed in this paper could account for the variations of river topography during the scour process. Further advancement in the areas of computational fluid dynamics and coupled fluid-particle interaction simulations are needed.

REFERENCES

National Transportation Safety Board (NTSB): Collapse of the New York Thruway (I-90) Bridge over the Schoharie Creek, near Amsterdam, New York, April 5, 1987. NTSB/HAR-88/02, *National Transportation Safety Board*, Washington, D.C., 1988.

Walton, Raymond, Bradley, J.B., and Grindeland, T.R.: 1-D or 2-D Models for River Hydraulic Studies, *Proceedings, IAHR/ASCE Conference*, San Francisco, California, August, 1997.

Richardson, E. V., and Davis, S. R.: Evaluating scour at bridges. FHWA NHI 01-001: Hydr. *Engrg. Circular No. 18*, 4th Ed., U.S. Department of Transportation, Washington, D.C, 2001.

Brunner, G.W.: HEC-RAS, River analysis system hydraulic reference manual: U.S. *Army Corps of Engineers Report* CPD-69, 2002.

Froehlich, D. C.: User's Manual for FESWMS FST2DH, Two-dimensional Depth-averaged Flow and Sediment Transport Model. U.S. Department of Transportation, Federal Highway Administration, McLean, Virginia, 2003.

Updating Uncertainties in Friction Angles of Clean Sands

Jianye Ching[1], M. ASCE, Jieru Chen[2], AM. ASCE, and Kok-Kwang Phoon[3], F. ASCE

[1] Associate Professor, Dept of Civil Engineering, National Taiwan University, Taipei, Taiwan. Tel: 886-2-33664328; Email: jyching@gmail.com
[2]National Chi Nan University, Dept of Civil Engineering, Nantou, Taiwan
[3]National University of Singapore, Dept of Civil & Environmental Engineering, Singapore

ABSTRACT

It is essential to characterize the uncertainties of soil shear strengths, including friction angles of sands. In particular, it is of practical interest to reduce the uncertainties in friction angles based on all available information by correlation, given the considerable cost of a typical site investigation. This study proposes a systematic way of constructing multivariate correlations on friction angles of clean sands. A set of simplified equations are obtained through Bayesian analysis for the purpose of reducing uncertainties. The inputs to the equations are the results of field and laboratory tests, and the outputs are the updated mean values and standard deviations of the friction angles. Test databases are used to demonstrate the consistency of the proposed simplified equations.

INTRODUCTION

Uncertainties in soil properties are commonly encountered in geotechnical engineering. More economical geotechnical designs can be achieved by updating uncertainties through site investigation. Reliability-based design (RBD) is known to provide a rational basis for propagating uncertainties in the design environment explicitly into the final design outcome (e.g. width of footing). However, one recurring criticism of RBD is that there is no particular motivation to use it because it seems to produce designs comparable to existing practice. One of the key objectives of this paper is to demonstrate that site investigation is not a *cost* item but an *investment* item, because updating of uncertainties through more and/or better tests can translate directly to design savings through RBD.

This paper focuses on the peak friction angle cohesionless soils. In practice, it is already well-known that field or laboratory test data, denoted as "test indices" from here on, can be used to estimate friction angles through correlations. In the literature, such pairwise correlations between various test indices and friction angles have been widely studied. A fairly comprehensive review of pairwise correlations between various test indices and friction angles is given in Kulhawy and Mayne (1990).

In reality, site investigation usually produces multivariate information. For instance, when borehole samples are drawn, SPT-N values are usually available, and the information regarding density and gradation can also be obtained through laboratory tests. Many of these test indices may be simultaneously correlated to friction angles if they are taken within distances where the spatial correlation is strong.

It is not obvious how to estimate the friction angle conditioning on multivariate test indices. In this paper, the practical issue of updating the mean and standard deviation (first two moments) of friction angles by incorporating multivariate test index information is addressed for reconstituted clean sands. The general approach proposed in Ching et al. (2010) for undrained shear strengths of clays is adopted in this study. A simplified graphical model is first proposed for reconstituted clean sands to describe the likely inter-dependency between friction angles and test indices. With this model and the pairwise correlations at hand, it is possible to update the first two moments of friction angles by incorporating multivariate information through Bayesian analysis.

The main contribution of this paper is a set of equations whose inputs are the observed multivariate test index values and outputs are the updated mean value and standard deviation of the friction angle for reconstituted clean sands. Due to the limited variety of sands in the pairwise correlations, these equations are strictly applicable to normally consolidated clean quartz sands.

SIMPLIFIED GRAPHICAL MODEL FOR FRICTION ANGLE

A simplified graphical model is proposed in Figure 1 to characterize the likely inter-dependency between friction angles and test indices for reconstituted clean sands. Note that assumptions on inter-dependency are of practical necessity: Bayesian analysis on multivariate correlations in general requires multivariate data points. Unfortunately, multivariate data points such as the triplets mentioned above are very rare in the literature. Pairwise data points (e.g. ϕ_p vs. D_r or ϕ_p vs. SPT-N) are much more prevalent. The strategy adopted in this study is to make plausible assumptions on inter-dependency between friction angles and test indices to mitigate this significant practical constraint. With these assumptions, it is possible to estimate the multivariate correlations with *only pairwise* data points.

The friction angle (ϕ_p) considered in this paper is the peak secant friction angle determined by drained triaxial compression tests. The peak friction angle can be further decomposed into two components: peak dilation angle ϕ_d and critical-state friction angle ϕ_{cv}. For the graphical model, the adopted test indices are limited to the following: (a) relative density (D_r) and mean confining pressure at failure p'; (b) SPT-N value $(N_1)_{60}$ corrected with respect to both energy ratio and overburden stress; (c) cone penetration test (CPT) tip resistance $q_{c1} = (q_c/P_a)/(\sigma_{v0}/P_a)^{0.5}$ corrected for overburden stress, where q_c is the cone resistance, σ_{v0} is the in-situ effective vertical stress, and P_a is the atmosphere pressure. The critical-state friction angle ϕ_{cv} and mean confining pressure at failure p' must be provided by the user.

PROBABILISTIC MODELS FOR PAIRWISE CORRELATIONS

Efforts were made in compiling a correlation database from the literature (see Table 1) to estimate the probabilistic models for the pairwise correlations. The data points in the database are mostly normally consolidated clean quartz sands. Therefore, the corresponding correlations may not be applied to highly overconsolidated sands, silty sands and gravels with high feldspar and mica content, sands with significant

aging effects, etc. For Bayesian analysis, the statistics (e.g. mean and standard deviation) of the following quantities are needed: (a) ϕ_d conditioning on {D_r, p'}; (b) ϕ_{cv}; (c) q_{c1} conditioning on ϕ_p; (d) $(N_1)_{60}$ conditioning on ϕ_p.

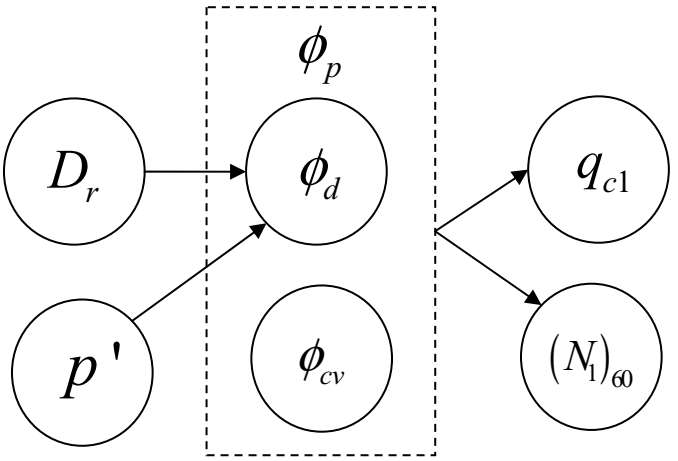

Figure 1 Graphical model for reconstituted clean sands

Table 1 Database for the pairwise correlations

Soil name	Reference	Correlation
Tonegawa sand	Kokusho and Yoshida (1997)	{D_r, p'} vs. ϕ_d
G25 gravelly sand	Kudo et al. (1990)	ϕ_p vs. $(N_1)_{60}$
Sacramento river sand	Lee and Seed (1967)	{D_r, p'} vs. ϕ_d
Brasted sand	Cornforth (1964, 1973)	
Glacial outwash sand	Hirschfield and Poulos (1964)	
Ham river sand	Bishop and Green (1965)	
Chattahoochee river sand	Vesic and Clough (1968)	
Various sands from literature	Kulhawy and Mayne (1990)	ϕ_p vs. q_{c1}

First two moments of ϕ_d conditioning on {D_r, p'}. The correlation between ϕ_d of sands and $\{D_r, p'\}$ is well known, e.g. Bolton (1986). The data points from Table 1 are mostly from triaxial tests on NC quartz sands. Their D_{50} ranges from 0.20 mm to 0.67 mm and their C_u ranges from 1.56 to 5.92. The predicted mean value of ϕ_d is

$$E\left(\phi_d \mid D_r, p'\right) = 3 \cdot I_R = 3\left(D_r \cdot \left[Q - \ln\left(p'\right)\right] - R\right) \quad (1.)$$

where I_R is the dilatancy index; Q and R are model parameters, chosen to be 11.5 and 0.8 in this study, respectively, to obtain a good fit; D_r is expressed as a fraction (not percentage) while the mean confining pressure at failure p' is in the unit of kN/m^2. The standard deviation of this transformation uncertainty is on average 1.96 degrees.

Estimation of ϕ_{cv}. According to Bolton (1986), for representative quartz sands, ϕ_{cv} is around 33°, while for representative feldspar sands, ϕ_{cv} is around 40°. Other researchers also provided estimates for possible values of ϕ_{cv} for many quartz sands, and the average value is about 32.5°. The mean function of ϕ_p conditioning on $\{D_r, p'\}$ is therefore

$$E\left(\phi_p \mid D_r, p'\right) = 3\left(D_r \cdot \left[Q - \ln\left(p'\right)\right] - R\right) + \phi_{cv} = 3I_R + \phi_{cv} \quad (2.)$$

and the standard deviation remains at 1.96 degrees.

First two moments of $(N_1)_{60}$ conditioning on ϕ_p. Data points from Table 1 were based on SPT conducted in calibration chambers containing clean quartz sands. Their D_{50} ranges from 0.34 mm to 1.13 mm, and C_u ranges from 1.95 to 5.65. Notice that these data points belong to only two types of sands. The mean function for $\ln[(N_1)_{60}]$ conditioning on ϕ_p is estimated to be

$$E\left(\ln\left[\left(N_1\right)_{60}\right] \mid \phi_p\right) = 0.161\phi_p - 3.724 \quad (3.)$$

The standard deviation for the above transformation is about 0.248, which is unrealistically low judging from the large measurement uncertainty of SPT-N tests. This may be due to the fact that only two types of sands are used to obtain this correlation and the high degree of control exercised in calibration chamber tests. Chen (2004) reported that the standard deviation is roughly doubled, i.e. 0.496.

First two moments of q_{c1} conditioning on ϕ_p. A correlation between friction angle and CPT reading was proposed in Kulhawy and Mayne (1990). This correlation is based on results from many calibration chamber tests on reconstituted clean NC and OC sands. Their D_{50} ranges from 0.16 mm to 1.00 mm, C_u ranges from 1.30 to 2.60 and OCR ranges from 1.0 to 14.7. The mean function for $\ln(q_{c1})$ conditioning on ϕ_p is estimated to be

$$E\left[\ln\left(q_{c1}\right) \mid \phi_p\right] = 0.127\phi_p - 0.307 \quad (4.)$$

The standard deviation for the above transformation is about 0.501.

BAYESIAN INFERENCE WITH MULTIVARIATE TEST DATA

Bayesian analysis is a natural way of handling multivariate information. If the variable of interest and the observed variable are *jointly* Gaussian, it is possible to derive all relevant conditional means and conditional standard deviations in closed-form. The updated mean and standard deviation (in degrees) of the friction angle conditioning on various combination of multivariate test data can be summarized as follows (note: $I_R = D_r[11.5-\ln(p')]-0.8$):

Conditioning on {D_r, p'} (based on Eq. (2.)):

$$E\left(\phi_p \mid D_r, p'\right) = 3I_R + \phi_{cv} \qquad \text{std}\left(\phi_d \mid D_r, p'\right) = 1.96 \tag{5.}$$

Conditioning on $(N_1)_{60}$ (based on Eq. (3.)):

$$E\left(\phi_p \mid (N_1)_{60}\right) = 6.22 \ln\left[(N_1)_{60}\right] + 23.167 \qquad \text{std}\left(\phi_p \mid (N_1)_{60}\right) = 3.086 \tag{6.}$$

Conditioning on q_{c1} (based on Eq. (4.)):

$$E\left(\phi_p \mid q_{c1}\right) = 7.819 \ln\left(q_{c1}\right) + 2.401 \qquad \text{std}\left(\phi_p \mid q_{c1}\right) = 3.919 \tag{7.}$$

Conditioning on {D_r, p'} and $(N_1)_{60}$ (based on Eqs. (2.) and (3.)):

$$\begin{aligned} &E\left(\phi_p \mid (N_1)_{60}, D_r, p'\right) = 1.996 I_R + 0.665\phi_{cv} + 2.081 \ln\left[(N_1)_{60}\right] + 7.751 \\ &\text{std}\left(\phi_p \mid (N_1)_{60}, D_r, p'\right) = 1.655 \end{aligned} \tag{8.}$$

Conditioning on {D_r, p'} and q_{c1} (based on Eqs. (2.) and (4.)):

$$\begin{aligned} &E\left(\phi_p \mid q_{c1}, D_r, p'\right) = 2.335 I_R + 0.778\phi_{cv} + 1.735 \ln\left(q_{c1}\right) + 0.5325 \\ &\text{std}\left(\phi_p \mid q_{c1}, D_r, p'\right) = 1.753 \end{aligned} \tag{9.}$$

Conditioning on $(N_1)_{60}$ and q_{c1} (based on Eqs. (3.) and (4.)):

$$\begin{aligned} &E\left(\phi_p \mid (N_1)_{60}, q_{c1}\right) = 3.84 \ln\left[(N_1)_{60}\right] + 2.993 \ln\left(q_{c1}\right) + 15.22 \\ &\text{std}\left(\phi_p \mid (N_1)_{60}, q_{c1}\right) = 2.423 \end{aligned} \tag{10.}$$

Conditioning on {D_r, p'}, $(N_1)_{60}$ and q_{c1} (based on Eqs. (2.), (3.), and (4.)):

$$\begin{aligned} &E\left(\phi_p \mid (N_1)_{60}, q_{c1}, D_r, p'\right) = 1.518 \ln\left[(N_1)_{60}\right] + 1.183 \ln\left(q_{c1}\right) + 1.814 I_R + 0.605\phi_{cv} + 6.015 \\ &\text{std}\left(\phi_p \mid (N_1)_{60}, q_{c1}, D_r, p'\right) = 1.524 \end{aligned} \tag{11.}$$

The most effective information is {D_r, p'} since the corresponding standard deviation is the smallest. It is also clear that the standard deviation decreases with increasing amount of information.

VALIDATION OF BAYESIAN EQUATIONS

Test database with data points of sands and gravels of known {D_r, p'}, $(N_1)_{60}$, q_{c1} and ϕ_p are compiled and studied to assess the performance for the Bayesian

equations given above (Eqs. (5.)-(11.)). Three test scenarios are considered: (a) scenario A: for this scenario, $\{D_r, p'\}$ and ϕ_p are known, and the $\{D_r, p'\}$ information is used to predict the mean values and 95% confidence intervals for ϕ_p by using Eq. (5.). These mean values are then compared with the actual values of ϕ_p, and the confidence intervals are also examined; and (b) scenario B: $\{D_r, p'\}$, q_{c1} and ϕ_p are known. Two types of predictions are made – predicting ϕ_p based on q_{c1} only by using Eq. (7.) (scenario B1) and predicting ϕ_p based on $\{D_r, p'\}$ and q_{c1} by using Eq. (9.) (scenario B2). Table 2 presents the test data points used in the various test scenarios. For all test scenarios, the performance of the Bayesian equations is presented in a plot where the horizontal axis is the updated (predicted) mean value of friction angle and the vertical axis is the measured value of friction angle. The two dashed lines parallel to the 1:1 solid line are the 95% confidence intervals.

Scenario A: The comparison is demonstrated in Figure 2. The prediction is in general satisfactory, judging from the fact that most markers are within the two dashed lines. A clear exception is the Erksak sand (ErS), for which the updated mean values of friction angles are obviously much larger than their actual values. The reason for causing this overestimation is not clear at this time.

Table 2 Test database for demonstrating the prediction results

Soil name	Symbol	Reference
Hokksund sand	HO	Parkin et al. (1980)
Lone Star #2	LS2	Villet and Mitchell (1981)
Ticino sand	TiS	Baldi et al. (1986)
Erksak sand	ErS	Been et al. (1987)
Leighton Buzzard	LB	Houlsby and Hitchman (1988)

Scenario B: Figure 3 shows the prediction results for reconstituted clean sands for scenarios B1 (prediciting ϕ_p based on q_{c1} only). The predictions are in general satisfactory. Note that the range between the two dashed lines is rather wide due to the large uncertainty in Eq. (7.). Figure 3 also shows the prediction results for reconstituted clean sands for scenarios B2 (prediciting ϕ_p based on $\{D_r, p'\}$ and q_{c1}). First, note that the range between the two dashed lines is significantly reduced after the inclusion of the $\{D_r, p'\}$ information. Despite the reduction of this range, most sands still lie within the narrow range, except the Erksak sand (ErS).

The performance of Eqs. (5.)-(11.) is in general satisfactory for reconstituted clean sands despite the presence of a few outliers (some Erksak and Ticino sands). Incorporating more information also helps to reduce uncertainties, i.e. make the two dashed lines closer. This is clear from the analysis results shown in Figure 3.

CONCLUSION

The main product of this paper is a set of equations whose inputs are the observed multivariate test index values and outputs are the updated mean values and

standard deviation of the friction angle. Due to the limited variety of sands in the pairwise correlations, these equations are strictly applicable to normally consolidated clean quartz sands. Several test databases are presented to verify the consistency of the proposed framework for estimating friction angles of reconstituted clean sands. The results show that the proposed framework can provide consistent prediction for the friction angle over reconstituted clean sands and can reduce the standard deviation of friction angle by incorporating more sources of information.

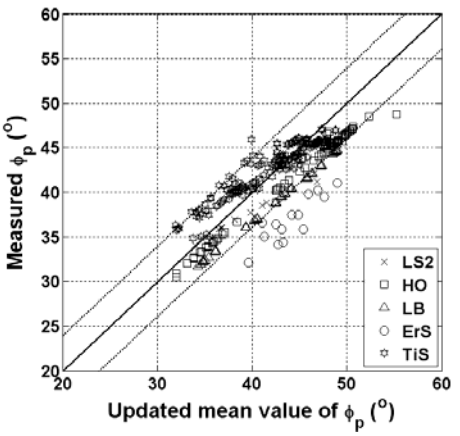

Figure 2 Prediction results for scenario A (predicting ϕ_p based on {D_r, p'}) on reconstituted clean sands in the test database.

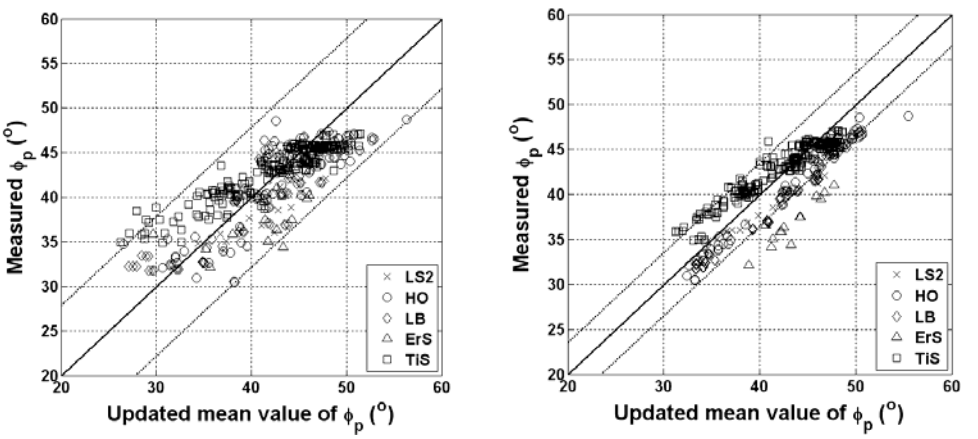

Figure 3 Prediction results for scenario B1 (left: predicting ϕ_p based on q_{c1} only) and B2 [predicting ϕ_p based on {D_r, p'} and q_{c1}].

REFERENCES

Baldi, G., Bellotti, R., Ghionna, V., Jamiolkowski, M. and Pasqualini, E. (1986). Interpretation of CPT's and CPTU's: drained penetration of sands. Proceeding, 4th International Geotechnical Seminar Field Instrumentation and In-Situ Measurement, Nanyang Technological Institute, Sigapore, pp. 143-156.

Been, K., Lingnau, B. E., Crooks, J. H. A., and Leach, B. (1987). Cone penetration

test calibration for Erksak sand. Canadian Geotechnical Journal, 24, pp. 601-610.

Bishop, A. W. and Green, G. E. (1965). The influence of end restraint on the compression strength of a cohesionless soil. Geotechnique, 15(3), pp. 243-266.

Bolton, M. D. (1986). The strength and dilatancy of sands. Geotechnique, 36(1), pp. 65-78.

Chen, J.R. (2004). Axial behavior of drilled shafts in gravelly soils. Ph.D. Dissertation, Cornell University, Ithaca, N.Y.

Ching, J., Phoon, K.-K. and Chen, Y.-C. (2010). Reducing shear strength uncertainties in clays by multivariate correlations, Canadian Geotechnical Journal, 47(1), 16-33.

Cornforth, D. H. (1964). Some experiments on the influence of strain conditions on the strength of sand. Geotechnique, 14(2), pp. 143-167.

Cornforth, D. H. (1973). Prediction of drained strength of sands from relative density measurements. Evaluation of Relative Density and Its Role in Geotechnical Projects Involuing Cohesionless Soils, ASTM, Philadelphia, STP 523, pp. 281-303.

Hirschlield, R.C. and Poulos, S. J. (1964). High-pressure triaxial tests on a compacted sand and an undisturbed silt. Laboratory Shear Testing of Soils (STP 361), ASTM, Philadelphia, pp. 329-339.

Houlsby, G. T. and Hitchamn, R. (1988). Calibration camber tests of cone penetrometer in sand. Geotechnique, 38(1), pp. 39-44.

Kokusho, T. and Yoshida, Y. (1997). SPT-N value and S-wave velocity for gravelly soils with different grain size distribution. Soils and Foundations, 37(4), pp. 105-113.

Kudo, K., Nishi, K., and Tanaka, Y. (1990). Static Mechanical Properties of Gravel Ground - Part 1: Influence of Gravel Content on Mechanical Properties. Report U090033, Central Research Institute of Electric Power Industry, Tokyo, 52 p. (in Japanese).

Kulhawy, F. H. and Mayne, P. W. (1990). Manual on estimating soil properties for foundation design. Report EL-6800, Electric Power Research Institute, Palo Alto.

Lee, K.L. and Seed, H. B. (1967). Drained strength characteristics of sands. Journal of Soil Mechanics and Foundation Division, ASCE, 93(6), pp. 117-141.

Parkin, A. K., Holden, J., Aamot, K., Last, N. and Lunne, T. (1980). Laboratory investigation of CPT's in sand. Report 52108-9, Norwegian Geotechnical Institute, Oslo, pp. 45.

Vesic, A. S. and Clough, G. W. (1968). Behavior of granular materials under high stresses. Journal of Soil Mechanics and Foundation Division. ASCE 94(3), pp. 661-688.

Villet, W. C. B. and Mitchell, J. K. (1981). Cone resistance, relative density, and friction angle. Cone Penetration Testing and Experience, Ed. G. M. Norris and R.D. Holtz, ASCE, New York, 1981, pp. 178-207.

Constructing Joint Distributions of Multivariate Geotechnical Data

Jianye Ching[1], M. ASCE, Kok-Kwang Phoon[2], F. ASCE, and Wen-Chao Huang[3]

[1] Associate Professor, Dept of Civil Engineering, National Taiwan University, Taipei, Taiwan. Tel: 886-2-33664328; Email: jyching@gmail.com
[2] Professor, Dept of Civil Engineering, National University of Singapore, Department of Civil Engineering, Singapore
[3] Assistant Professor, Dept of Civil Engineering, National Central University, Taiwan

ABSTRACT

This paper presents easy-to-use tools for constructing joint distributions given multivariate geotechnical data. Two scenarios are addressed (a) complete multivariate data: the Iman-Conover method will be adopted; (b) incomplete multivariate data: the Bayes' net will be adopted. Examples of multivariate geotechnical data will be presented to illustrate the procedures for constructing the joint distributions under both scenarios and to demonstrate the practical uses of these joint distributions for the purpose of site characterization.

INTRODUCTION

The benefits of constructing joint distributions for geotechnical data are rarely recognized in the literature. When multivariate geotechnical data exist in sufficient amount, it is of significant practical usefulness to construct a joint probability distribution function. The usefulness is reflected in the following: (a) it is possible to derive the mean and coefficient of variation (c.o.v.) of pairwise correlations systematically using the constructed joint distribution; (b) it may be possible to study theoretically using the joint distribution if new strong pairwise correlations can be found either among the original components or some derived components; (c) it may be possible to derive higher-order correlations, e.g. a pairwise correlation equation that depends on the value of a third variable; (d) based on the Bayes' rule, it may be possible to update the mean value and c.o.v. of a soil parameter given the information of other parameters.

When complete multivariate geotechnical data are available, joint distributions can be constructed in a practical way using the Iman-Conover method (Iman and Conover 1982). The Iman-Conover method is an easy-to-use approach for constructing joint distributions based on marginal distributions and rank correlations. In this paper, a database of 345 data points with known liquidity index (LI), undisturbed undrained shear strength (s_u), remolded undrained shear strength (s_u^{re}), preconsolidation stress (σ'_p), and vertical effective stress (σ'_v) will be analyzed as a demonstration. Note that complete multivariate data in this case means that LI, s_u, s_u^{re}, σ'_p and σ'_v are measured *at the same time* over a small uniform volume of soil.

When only partial information is available, constructing joint distributions is more challenging. In this paper, the Bayes' net will be adopted to analyze a database

with pairwise information for demonstration – only the pairs {OCR, s_u}, {N_{60}, s_u}, and {q_T-σ_{v0}, s_u} are known, where OCR is the overconsolidation ratio, N_{60} is the energy-ratio corrected SPT-N value, σ_{v0} is the total vertical stress, and q_T is the CPT reading corrected with respect to the pore pressure behind the cone. Note that partial multivariate data in this case means that OCR and s_u are measured over one volume of soil, SPT and s_u are measured over a second volume of soil, and CPT and s_u are measured over a third volume of soil. In other words, there may not be a volume of soil in which OCR, SPT, CPT and s_u are known at the same time. Clearly, partial multivariate data are more prevalent in the geotechnical engineering literature.

COMPLETE MULTIVARIATE GEOTECHNICAL DATA

A database consisting of 345 lightly overconsolidated and sensitive clay data points with simultaneously known {LI, s_u, s_u^{re}, σ'_p, σ'_v} information was compiled. This calibration database will be used to construct the joint distribution of {LI, s_u, s_u^{re}, σ'_p, σ'_v}. The data points are taken from 37 sites worldwide, covering a wide range of sensitivity, OCR, LI, and clay types, but fissured and organic clays are nearly absent in this database. Since s_u values depend on stress state, strain rate, sampling disturbance, etc., all s_u values are converted into mobilized s_u values by following the recommendations made by Mesri and Huvaj (1997).

For this case where complete geotechnical data are available, this study recommends a technique called the Iman-Conover (IC) method that was first proposed by Iman and Conover (1982). It is a straightforward yet powerful method that is able to construct the joint probability distribution of correlated random variables with known marginal distributions and rank correlations. Since marginal distributions and rank correlations can be estimated reasonably accurately even with limited number of data points, the IC method is quite practical. The marginal distributions can be easily estimated from the marginal data, e.g., estimate the probability distribution of LI based on the 345 LI data points. This can be easily achieved by comparing the histograms or by taking the quantile-quantile plot. Studies involving characterization of a ***single*** random variable are routinely carried out in the literature. The rank correlations among the five random variables are simply the Pearson or product-moment correlations among their *ranks*. Therefore, such rank correlations can be easily obtained by first converting {LI, s_u, s_u^{re}, σ'_p, σ'_v} to their ranks and then calculating the moment correlations. Studies involving characterization of correlation between ***two*** random variables are significantly more limited and characterization of correlation matrices for ***three or more*** random variables using actual data is virtually non-existent.

The IC method simulates samples of {LI, s_u, s_u^{re}, σ'_p, σ'_v} that follow marginal distributions and rank correlations estimated statistically from the above data. Hence, the IC method matches the joint probability distribution in the second-moment sense. The simulated samples, together with the calibration database, are shown in Figure 1. Not only the correlations among the original random variables {LI, s_u, s_u^{re}, σ'_p, σ'_v} are shown but the correlations among their derived quantities, including $S_t = s_u/s_u^{re}$, OCR = σ'_p/σ'_v, s_u/σ'_v, are also shown. The performance of the IC method in constructing the joint probability distribution is evident insofar as pairwise

correlations are concerned. The samples mimic the correlation behaviors of the database, even for those with nonlinear trends, e.g. LI-s_u^{re} and LI-S_t correlations.

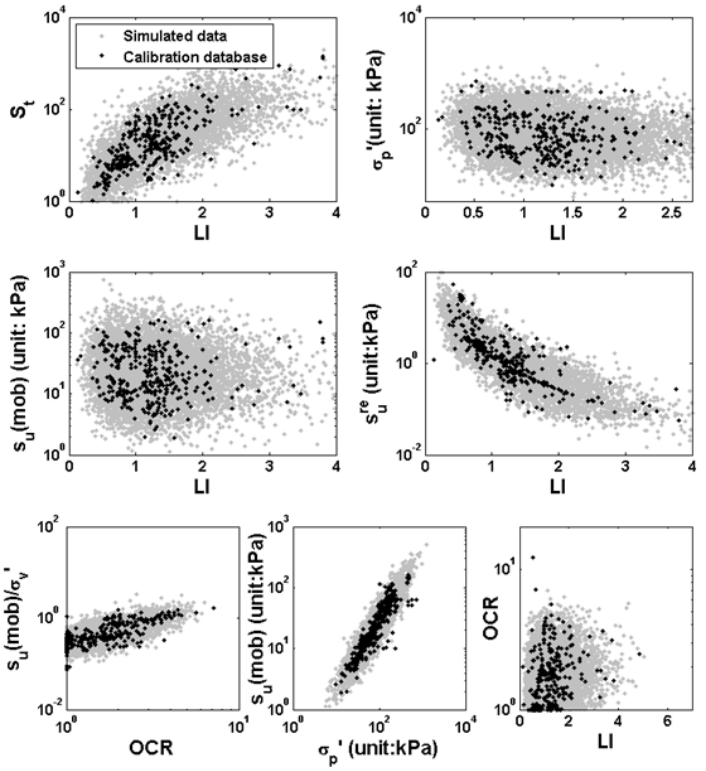

FIG. 1 Comparisons between the Calibration Database and the Simulated Data Points.

Given the simulated samples of {LI, s_u, s_u^{re}, σ'_p, σ'_v}, it is possible to find the means and coefficients of variation (c.o.v.) of some design parameters conditioning on LI. Among all LI-related correlations, LI seems to be strongly correlated to S_t and s_u^{re} (see Figure 1). When S_t range is specified, LI seems to be strongly correlated to s_u and σ'_p. The mean values and c.o.v.s conditioning on LI can be found by a simple maximum likelihood analysis over simulated data points. Table 1 summarizes all mean trends (m) and their standard deviations (s) for the natural logarithms of the design parameters of interest. The results provide estimates for the first two moments (m and s) of the logarithms of the parameters. By lognormality, the updated mean and c.o.v. of the parameter are simply $\exp(m+s^2/2)$ and $[\exp(s^2)-1]^{0.5}$, respectively.

It is interesting to explore if the IC method can capture higher-order dependency information in the database, namely, a pairwise correlation equation may occasionally depend on the value of a third variable. For illustration, the OCR-(s_u/σ'_v) correlation is studied. The goal is to study how this correlation equation is affected by S_t. Figure 2 compares the simulated data and the calibration data within OCR-(s_u/σ'_v) plots restricted to various S_t ranges. It is evident that the trend lines (solid lines) move slightly upwards for increasing S_t. This behavior seems to be consistent with an

independent validation database. This limited study appears to imply that third-order information is reasonably captured by the rank correlation based IC approach.

Table 1 Updated Mean and Standard Deviations of Logarithms of Parameters.

		Mean (m)	Standard deviation (s)
ln S_t		2.5 + 2.5 ln(LI)	1.074 – 0.039 LI
ln s_u^{re}		0.377 - 2.44 ln(LI)	0.738 – 0.007 LI
ln(σ_p')	S_t = 1~4	3.113 - 2.44 ln(LI)	0.867 – 0.032 LI
	S_t = 4~16	4.141 - 2.44 ln(LI)	0.815 – 0.001 LI
	S_t = 16~64	5.096 - 2.44 ln(LI)	0.751 + 0.029 LI
	S_t ≥64	6.144 - 2.44 ln(LI)	0.671 + 0.087 LI
ln(s_u)	S_t = 1~4	1.542 - 2.44 ln(LI)	0.887 - 0.070 LI
	S_t = 4~16	2.727 - 2.44 ln(LI)	0.827 – 0.012 LI
	S_t = 16~64	3.857 - 2.44 ln(LI)	0.797 – 0.000 LI
	S_t ≥64	5.071 - 2.44 ln(LI)	0.662 + 0.109 LI

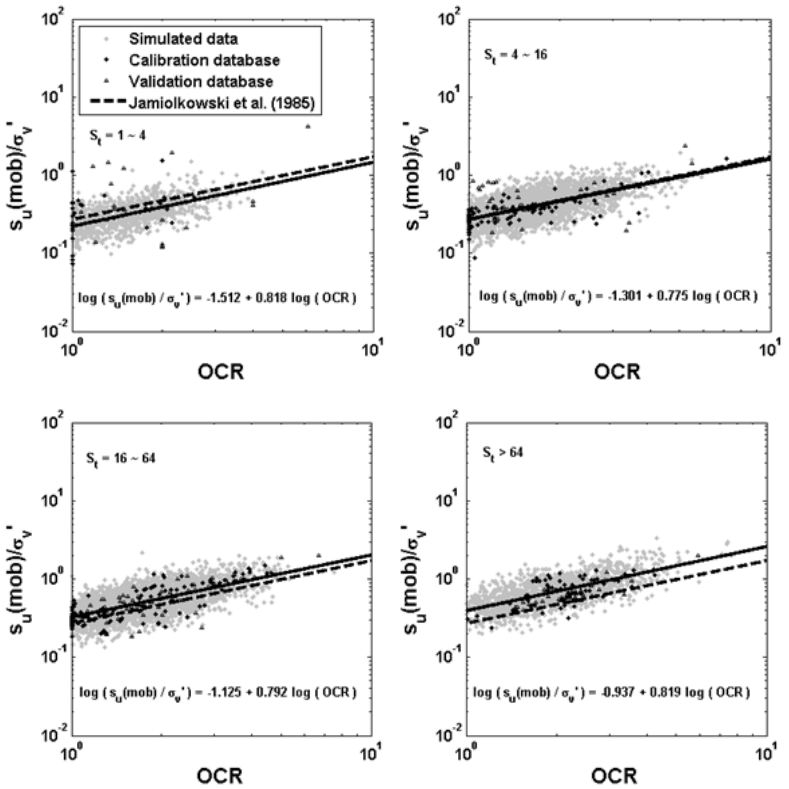

FIG. 2 Simulated Data versus Measured Data within OCR-(s_u/σ'_v) Plots Restricted to Various S_t Ranges. The Solid Lines are the Trends of the Simulated Data.

PARTIAL MULTIVARIATE GEOTECHNICAL DATA

A database where only pairs {OCR, s_u}, {N_{60}, s_u}, and {q_T-σ_{v0}, s_u} are known was compiled for this study. For brevity, q_T-σ_{v0} will be denoted by q"$_T$ from hereon.

All s_u values are converted into laboratory CIUC s_u values by following recommendations made by Kulhawy and Mayne (1990).

Since the rank correlation matrix cannot be fully populated based on available data, the IC method is not applicable, e.g., while the rank correlation between OCR and s_u is available, the rank correlation between OCR and N_{60} is not available. Given this incompleteness, it is necessary to postulate an underlying correlation structure for the multivariate data. A physically intuitive way of doing so is to adopt a simplified Bayes net model, as shown in Figure 3. The likely inter-dependencies between the four variables {s_u, OCR, N_{60}, q"$_T$} can be appreciated visually using such a Bayes net model. Note that assumptions on inter-dependencies are of practical necessity: analysis on multivariate correlations in general requires multivariate data points as demonstrated in the preceding section. Unfortunately, multivariate data points {s_u, OCR, N_{60}, q"$_T$} are very rare in the literature, while pairwise data points are much more abundant. With the assumptions embedded in the model, it is possible to find the four-dimensional joint distribution using *only pairwise* data points.

The underlying assumptions of this model are: (a) OCR is the main factor influencing the *normalized* undrained shear strength s_u/σ'_{v0}, and s_u in turn influences N_{60} and q"$_T$; (b) given s_u, its N_{60} and q"$_T$ are independent of OCR. In other words, once s_u is known, OCR does not contain further information of N_{60} and q"$_T$; (c) given s_u, its N_{60} and q"$_T$ are mutually independent. In other words, N_{60} and q"$_T$ are treated as two pieces of independent information for s_u. This model is deemed to be reasonable for unstructured unfissured inorganic clays. Needless to say, it is strictly a postulation at this stage and validation is necessary.

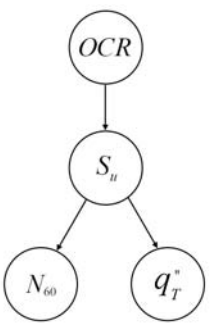

FIG. 3 Bayes Net Model for Clayey Soils

The model requires the first two moments of the following quantities: (a) s_u conditioning on OCR; (b) N_{60} conditioning on s_u; (c) q"$_T$ conditioning on s_u. These first moments are summarized from the pairwise database as follows:

$$E\left[\ln\left(s_u\right)|OCR\right]=0.640\cdot\ln\left(OCR\right)+\ln\left(\sigma'_{v0}\right)-0.874 \quad (1)$$

$$E\left[\ln\left(N_{60}\right)|s_u\right]=1.633\cdot\ln\left(s_u\right)-0.403\cdot\ln\left(\sigma'_{v0}\right)-3.845 \quad (2)$$

$$E\left[\ln\left(q''_T\right)|s_u\right]=\ln\left(s_u\right)+2.540 \quad (3)$$

and the standard deviations are respectively 0.237, 0.456, and 0.34.

If the transformation uncertainties of the above equations are assumed to be jointly Gaussian, based on the Bayes' rule, it is possible to obtain in closed form the mean value and c.o.v. of s_u given {OCR, N_{60}, q"$_T$}, as follows:

Conditioning on OCR:

$$E\left[\ln(s_u)\,|\,OCR\right] = 0.640\cdot\ln(OCR) + \ln(\sigma'_{v0}) - 0.874 \qquad Var\left[\ln(s_u)\,|\,OCR\right] = 0.237^2 \tag{4}$$

Conditioning on N_{60}:

$$E\left[\ln(s_u)\,|\,N_{60}\right] = 0.602\cdot\ln(N_{60}) + 0.243\cdot\ln(\sigma'_{v0}) + 2.363 \qquad Var\left[\ln(s_u)\,|\,N_{60}\right] = 0.277^2 \tag{5}$$

Conditioning on q"$_T$:

$$E\left[\ln(s_u)\,|\,q''_T\right] = 0.976\cdot\ln(q''_T) - 2.408 \qquad Var\left[\ln(s_u)\,|\,q''_T\right] = 0.336^2 \tag{6}$$

Conditioning on OCR and N_{60}:

$$\begin{aligned} &E\left(\ln(s_u)\,|\,N_{60}, OCR\right) = 0.373\cdot\ln(OCR) + 0.256\cdot\ln(N_{60}) + 0.685\cdot\ln(\sigma'_{v0}) + 0.476 \\ &Var\left(\ln(s_u)\,|\,N_{60}, OCR\right) = 0.180^2 \end{aligned} \tag{7}$$

Conditioning on OCR and q"$_T$:

$$\begin{aligned} &E\left(\ln(s_u)\,|\,q''_T, OCR\right) = 0.431\cdot\ln(OCR) + 0.326\cdot\ln(q''_T) + 0.674\cdot\ln(\sigma'_{v0}) - 1.418 \\ &Var\left(\ln(s_u)\,|\,q''_T, OCR\right) = 0.194^2 \end{aligned} \tag{8}$$

Conditioning on N_{60} and q"$_T$:

$$\begin{aligned} &E\left(\ln(s_u)\,|\,N_{60}, q''_T\right) = 0.362\cdot\ln(N_{60}) + 0.399\cdot\ln(q''_T) + 0.146\cdot\ln(\sigma'_{v0}) + 0.409 \\ &Var\left(\ln(s_u)\,|\,N_{60}, q''_T\right) = 0.215^2 \end{aligned} \tag{9}$$

Conditioning on OCR, N_{60}, and q"$_T$:

$$\begin{aligned} &E\left(\ln(s_u)\,|\,N_{60}, q''_T, OCR\right) = 0.291\cdot\ln(OCR) + 0.200\cdot\ln(N_{60}) + 0.220\cdot\ln(q''_T) + 0.534\cdot\ln(\sigma'_{v0}) - 0.187 \\ &Var\left(\ln(s_u)\,|\,N_{60}, q''_T, OCR\right) = 0.159^2 \end{aligned} \tag{10}$$

The above results provide the updated mean (m) and standard deviation (s) of $\ln(s_u)$. By lognormality, the updated mean and c.o.v. of s_u are simply $\exp(m+s^2/2)$ and $[\exp(s^2)-1]^{0.5}$, respectively.

Case study – A deep excavation site is extracted from Ou (2006). Standard penetration tests (SPT), vane shear test (VST), and cone penetration tests (CPT) were conducted. The readings are shown in Figure 4. The soil profile includes three thick clayey layers and three thin sandy layers. Figure 4 shows the results of the laboratory and field tests.

Based on the SPT, CPT, and OCR data and the formulas provided above (Eqs. 4-9), the updated means and 95% confidence intervals (±1.96 standard deviations) with respect to depth are plotted in Figure 5 for four combinations of information. For this case study, several undisturbed clay samples were extracted from the site, and

laboratory tests, including UU and CK_0U (K_0-consolidated undrained) tests, were conducted to determine the undrained shear strengths. These actual values of s_u are converted into their equivalent CIUC values and are plotted as asterisks. It is evident that the updated c.o.v. of s_u decreases as more information is taken into account. Moreover, although the confidence intervals become smaller, most of them still contain the measured s_u values. When all information is implemented, the updated c.o.v. of s_u is as low as 0.16. This demonstrates that the uncertainty in s_u can be effectively reduced by incorporating multivariate data.

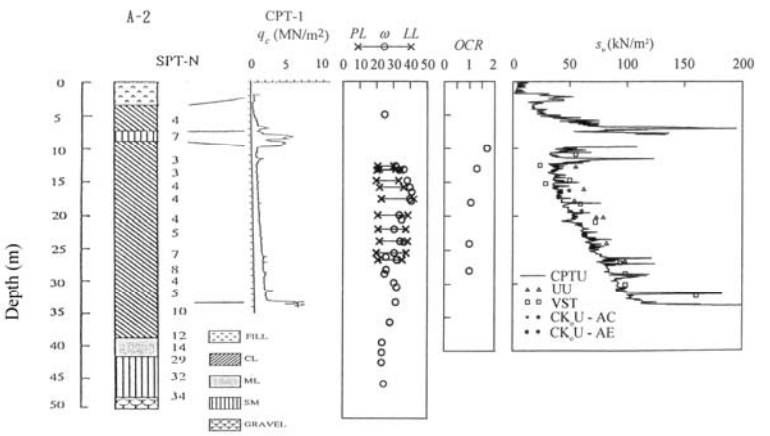

FIG. 4 The Soil Profile and Test Data Results (from Ou (2006))

CONCLUSION

Multivariate geotechnical data produced by different field/laboratory tests are typically available in a site investigation for sufficiently important structures. In this study, two scenarios are considered: (1) complete multivariate data and (2) incomplete multivariate data. For the first case, geotechnical parameters are measured *at the same time* over a reasonably small uniform volume of soil. For the second case, only a subset of the geotechnical parameters are measured over the same volume of soil. For example, the site investigation may involve measuring OCR and s_u over one volume of soil, SPT and s_u over a second volume of soil, and CPT and s_u over a third volume of soil. In other words, there may not be a volume of soil in which OCR, SPT, CPT and s_u are known at the same time. Clearly, the second scenario involving incomplete or partial multivariate data is more prevalent in practice.

A joint probability distribution is constructed using a database consisting of 345 sensitive clay data points with simultaneously known {LI, s_u, s_u^{re}, σ'_p, σ'_v} and the Iman-Conover (IC) method. The IC method only matches the actual joint probability distribution in the second-moment sense. Even if complete multivariate data are available, they are rarely available with sufficient quantity to estimate statistics beyond the second moments with confidence. Hence, the IC method is quite practical.

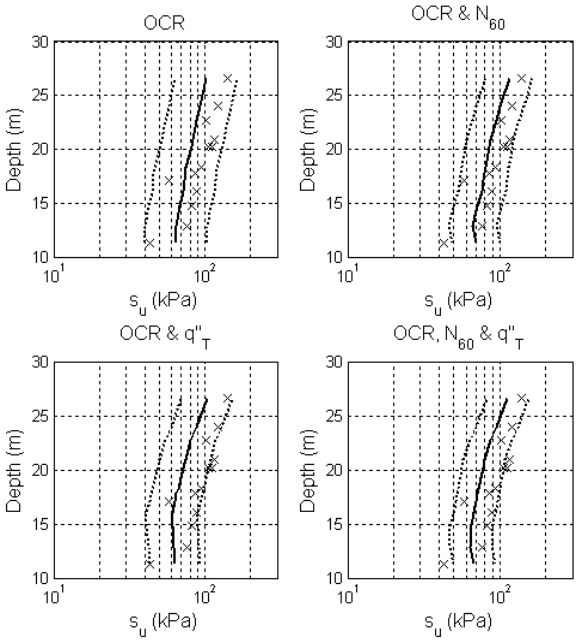

FIG. 5 Updated Mean and 95% Confidence Intervals of s_u with Respect to Depth

A second joint probability distribution is constructed for $\{s_u, OCR, N_{60}, q''_T\}$ using an incomplete database where only the pairs $\{OCR, s_u\}$, $\{N_{60}, s_u\}$, and $\{q_T-\sigma_{v0}, s_u\}$ are known. Given this incompleteness, the IC method is not applicable and it is necessary to postulate an underlying correlation structure for the multivariate data using a Bayes net model. The likely inter-dependencies between the four variables $\{s_u, OCR, N_{60}, q''_T\}$ can be appreciated visually using such a Bayes net model.

The practical usefulness of constructing a joint probability distribution is demonstrated. For the five-dimensional probability distribution pertaining to $\{LI, s_u, s_u^{re}, \sigma'_p$ and $\sigma'_v\}$, it is shown that the OCR-(s_u/σ'_v) correlation can be further refined by considering the effect of S_t. For the four-dimensional probability distribution pertaining to $\{s_u, OCR, N_{60}, q''_T\}$, it is shown that the uncertainty in the estimation of s_u can be effectively reduced by incorporating increasingly more information.

REFERENCES

Iman, R. and Conover, W. (1982). A distribution-free approach to inducing rank correlation among input variables. Communications in Statistics - Simulation and Computation, 11(3), 311–334.

Kulhawy, F.H., and Mayne, P.W. (1990). Manual on Estimating Soil Properties for Foundation Design. Electric Power Research Institute, Palo Alto, Calif. Report EL-6800.

Mesri, G. and Huvaj, N. (2007). Shear strength mobilized in undrained failure of soft clay and silt deposits. ASCE *Geotechnical Special Publication 173*, Geo-Denver.

Ou, C.Y. 2006. *Deep excavation engineering*, Scientific & Technical Publishing Co. Ltd.

Extension of CSRSM for the Parametric Study of the Face Stability of Pressurized Tunnels

Guilhem Mollon[1], Daniel Dias[2], and Abdul-Hamid Soubra[3], M.ASCE

[1]LGCIE, INSA Lyon, Université de Lyon, Domaine scientifique de la Doua, Bât JCA Coulomb, 20 Avenue Albert Einstein, 69621 Villeurbanne, France ; guilhem.mollon@insa-lyon.fr
[2]LGCIE, INSA Lyon, Université de Lyon, Domaine scientifique de la Doua, Bât JCA Coulomb, 20 Avenue Albert Einstein, 69621 Villeurbanne, France ; daniel.dias@insa-lyon.fr
[3]GeM, University of Nantes, Boulevard de l'université, BP 152, 44603 Saint-Nazaire cedex, France ; abed.soubra@univ-nantes.fr

ABSTRACT

The Collocation-based Stochastic Response Surface Methodology (CSRSM) is a powerful probabilistic method. It aims at replacing a complex deterministic model by a simple analytical expression (called meta-model) to reduce the time cost of the classical probabilistic methods. The meta-model is based on a Polynomial Chaos Expansion (PCE). The coefficients of the PCE are computed in this paper by regression from the response of the deterministic model at a limited number of collocation points. The conventional formalism of CSRSM requires performing a new set of deterministic computations each time the probabilistic parameters of the input random variables are slightly modified. An extension of CSRSM is therefore proposed in this paper. It allows the realization of a parametric study at a limited time cost without loss of accuracy. This is demonstrated by comparing the results obtained from the original CSRSM and its extension when performing a parametric study concerning the stability analysis of a pressurized tunnel face.

INTRODUCTION

As is well known, the most robust probabilistic approach is the Monte-Carlo simulation method. This method requires a large number of calls of the deterministic model especially for small values of the failure probability (e.g. about 1,000,000 samples for a failure probability of 10^{-5}).

Although the deterministic numerical methods (such as those based on the Finite Element Method FEM or the Finite Difference Method FDM) are appealing, these methods are difficult to use in a probabilistic framework particularly when employing MC simulation method. This is because these methods need a very long computation time. In order to overcome the above shortcoming, the Collocation-based Stochastic Response Surface Methodology (CSRSM) is applied herein. CSRSM makes possible the probabilistic study of a complex deterministic model by replacing it by an analytical expression (called meta-model) with a reduced time cost. This meta-model is expressed by a Polynomial Chaos Expansion (PCE). The coefficients of the PCE are determined in this paper by a regression approach using a limited number of calls of the deterministic model. The meta-model can then be used in the classical probabilistic methods such as the Monte Carlo simulation method. It should be mentioned that the conventional formalism of CSRSM requires performing a new set of deterministic computations each time the probabilistic parameters of the

input random variables are slightly modified. An extension of CSRSM is therefore proposed in this paper. It allows the realization of a parametric study at a limited time cost without loss of accuracy. As an illustrative application of CSRSM and its extension, one considers in this paper the probabilistic stability analysis of a pressurized tunnel face. The paper is organised as follows: A brief description of the deterministic model concerning the collapse pressure of a pressurized tunnel face is first presented. It is followed by the presentation of CSRSM and its extension. Finally, a verification of CSRSM (by comparison with the results of Monte Carlo simulation method) and a comparison between the results obtained from both CSRSM and its extension are presented and discussed.

DETERMINISTIC MODEL

The face stability analysis of a circular tunnel driven by a pressurized shield is of major interest. It requires the determination of a so-called "critical collapse pressure" of the tunnel face (denoted σ_c), i.e. the greatest one under which the tunnel face collapses. The deterministic model chosen in this study is analytical. It is based on the kinematical theorem of limit analysis. The collapse mechanism is translational. It is composed of five conical blocks (Fig. 1) with an opening angle equal to φ where φ is the soil friction angle.

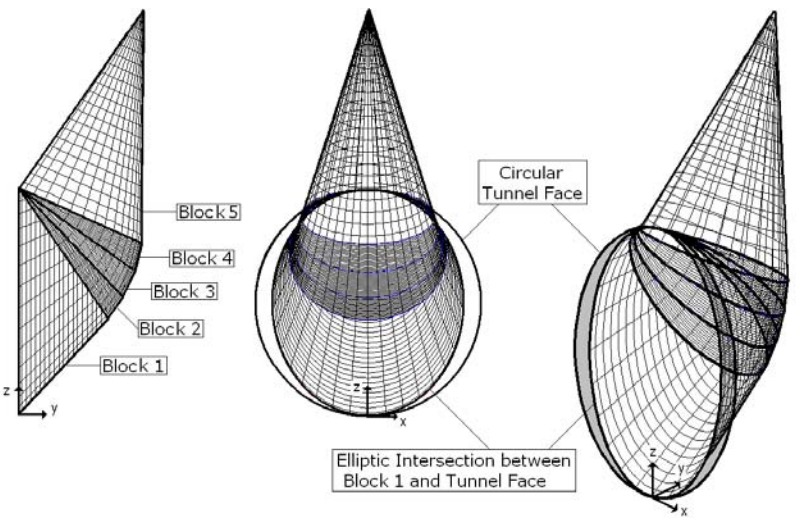

Figure 1. Five-block collapse mechanism

This mechanism was extensively presented in Mollon et al. [2009]: it is able to provide a quite correct estimation of σ_c despite the fact that it does not intersect the entire circular tunnel face as was observed experimentally by Takano et al. (2006). The analytical five-block model was chosen in this study because its extremely small time cost (smaller than 0.1s) makes it very convenient for the verification of CSRSM. This verification is performed by comparison with Monte Carlo simulation method which requires a great number of calls of the deterministic model. In this study, the output random variable is the critical collapse pressure, and the two input random variables are the friction angle (φ) and the cohesion (c) of the soil.

BRIEF DESCRIPTION OF CSRSM

In this section, the classical formalism of CSRSM (Isukapalli [1999], Sudret [2007], Phoon and Huang [2007] and Huang et al. [2009]) is presented in the case of two input random variables (φ and c). CSRSM aims at replacing the initial deterministic model by an approximate analytical expression (meta-model) when performing a probabilistic analysis. The meta-model is a Polynomial Chaos Expansion (PCE). For a PCE of order n, the meta-model is expressed in the basis of the multidimensional Hermite polynomials of order $\leq n$. For a given set of the probabilistic parameters of the input random variables (i.e. type of distribution and statistical moments of the random variables, and correlations between random variables); the unknown coefficients of the PCE are obtained in this paper by regression using the response of the deterministic model at a given number of collocation points. The different steps of CSRSM may be described as follows:

The two random variables (i.e. φ and c) have first to be represented in the PCE by two standard variables ξ_1 and ξ_2, which are normal uncorrelated variables with zero mean and unit variance. For a PCE of order n, the available collocation points are classically determined as follows: each standard variable is assumed to take the values of the roots of the one-dimensional Hermite polynomial of order n+1, and the available collocation points result from the combinations of all these roots for the different random variables. It should be noted that this method of choosing the collocation points is not mandatory as will be seen later in this paper. For the present case of two input random variables, the output random variable may be expressed by a PCE as follows:

$$U = \sum_{i=1}^{p} a_i \cdot \Gamma_i(\xi_1, \xi_2) \tag{1}$$

In this expression, the terms Γ_i are multidimensional Hermite polynomials (which constitute the basis of the PCE) and the terms a_i are unknown coefficients to be determined. The number p of terms in this summation and the number M of the available collocation points are given by:

$$p = \frac{(n+n_v)!}{n!\,n_v!} \tag{2}$$

$$M = (n+1)^{n_v} + \begin{cases} 0 & \text{if one of the roots of the } (n+1)^{\text{th}} \text{ univariate Hermite polynomial is 0} \\ 1 & \text{otherwise} \end{cases} \tag{3}$$

where n_v is the number of random variables. It should be mentioned that when the number n_v of the random variables is important, the number M of the available collocation points becomes much larger than the number p of the unknown coefficients. This leads to a linear system of equations where the number of equations is greater than the number of unknown. It is therefore necessary to make a judicious choice of the collocation points to be used in the regression process. Several methods exist (Isukapalli [1999], Sudret [2007]), but they are useless when using only two random variables as is the case in the present paper. Hence, all the available collocation points are considered in the analysis. To be introduced in the deterministic

model, the collocation points represented by vectors $(\xi_{1,m}, \xi_{2,m})$ (with $1 \le m \le M$) have to be expressed in the space of the physical variables corresponding to vectors (φ_m, c_m), using the following expressions:

$$\begin{bmatrix} \xi_{1C,m} \\ \xi_{2C,m} \end{bmatrix} = H \cdot \begin{bmatrix} \xi_{1,m} \\ \xi_{2,m} \end{bmatrix} \tag{4}$$

$$\begin{cases} \varphi_m = F_\varphi^{-1}\left[\Phi\left(\xi_{1C,m}\right)\right] \\ c_m = F_c^{-1}\left[\Phi\left(\xi_{2C,m}\right)\right] \end{cases} \tag{5}$$

In these equations, H is the Cholesky transform of the correlation matrix of φ and c, F_φ is the cumulative density function (CDF) of φ, F_c is the CDF of c, and Φ is the normal cumulative density function with zero mean and unit variance. When the response of the deterministic model (i.e. the value of σ_c) is obtained for each collocation point, the values of the PCE coefficients are determined by regression using the following equation:

$$\underline{\underline{N^t}} \cdot \underline{\underline{N}} \cdot \underline{a} = \underline{\underline{N^t}} \cdot \underline{f} \tag{6}$$

where *a*=column vector of the unknown coefficients, *f*=column vector of the deterministic responses, and N is a matrix given by:

$$\underline{\underline{N}} = \begin{bmatrix} \Gamma_{0,0} & \Gamma_{1,0}\left(\xi_{1,1}\right) & \Gamma_{0,1}\left(\xi_{2,1}\right) & \Gamma_{2,0}\left(\xi_{1,1}\right) & \Gamma_{1,1}\left(\xi_{1,1},\xi_{2,1}\right) & \Gamma_{0,2}\left(\xi_{2,1}\right) \\ \Gamma_{0,0} & \Gamma_{1,0}\left(\xi_{1,2}\right) & \Gamma_{0,1}\left(\xi_{2,2}\right) & \Gamma_{2,0}\left(\xi_{1,2}\right) & \Gamma_{1,1}\left(\xi_{1,2},\xi_{2,2}\right) & \Gamma_{0,2}\left(\xi_{2,2}\right) \\ \cdot & \cdot & \cdot & \cdot & \cdot & \cdot \\ \Gamma_{0,0} & \Gamma_{1,0}\left(\xi_{1,M}\right) & \Gamma_{0,1}\left(\xi_{2,M}\right) & \Gamma_{2,0}\left(\xi_{1,M}\right) & \Gamma_{1,1}\left(\xi_{1,M},\xi_{2,M}\right) & \Gamma_{0,2}\left(\xi_{2,M}\right) \end{bmatrix} \tag{7}$$

Once the unknown coefficients are determined, one obtains an analytical equation (i.e. a meta-model) that can be used in place of the deterministic model to perform a probabilistic analysis using (for example) Monte Carlo simulation method.

VERIFICATION OF CSRSM

A set of probabilistic parameters is chosen as a reference case for the two input random variables φ and c as follows: the two variables are considered as normal uncorrelated variables with μ_φ=17° and COV(φ)=10%, μ_c=7 kPa and COV(c)=20%. Characteristics of a soft clay are chosen because this kind of soil is likely to allow face instabilities. For this reference case, the coefficients of the PCEs of orders 2 to 5 are determined using the process described above. Fig. 2 shows the response surfaces (represented by lines of equal value of σ_c in a φ-c plane) as provided by the original deterministic model and by its approximations by the PCEs of orders 2 and 4. It clearly appears that both PCEs are able to provide a very good approximation of the original deterministic model in the central part (i.e. in the region of maximum probability of occurrence), but that the order 4 is much more accurate in the surrounding areas corresponding to zones with lower probabilities of occurrence.

A Monte-Carlo (MC) simulation with 10^6 samples is performed on the original deterministic model and on the PCEs of orders 2 to 5. This simulation is only made possible due to the very small time cost of the original deterministic model chosen in this paper, which allows a great number of samples. The results in terms of probability density function (PDF) and in terms of failure probability are shown in Figs. 3a and 3b respectively. It appears from Fig. 3a that the PDF obtained for the meta-models are in good agreement with the one of the original deterministic model, especially when the PCE order is larger than 2. Moreover, Fig. 3b shows that all the PCEs of order greater than 2 provide a good estimation of the failure probabilities at the distribution tail which is the zone of interest of the geotechnical engineer; the accuracy increases with the PCE order.

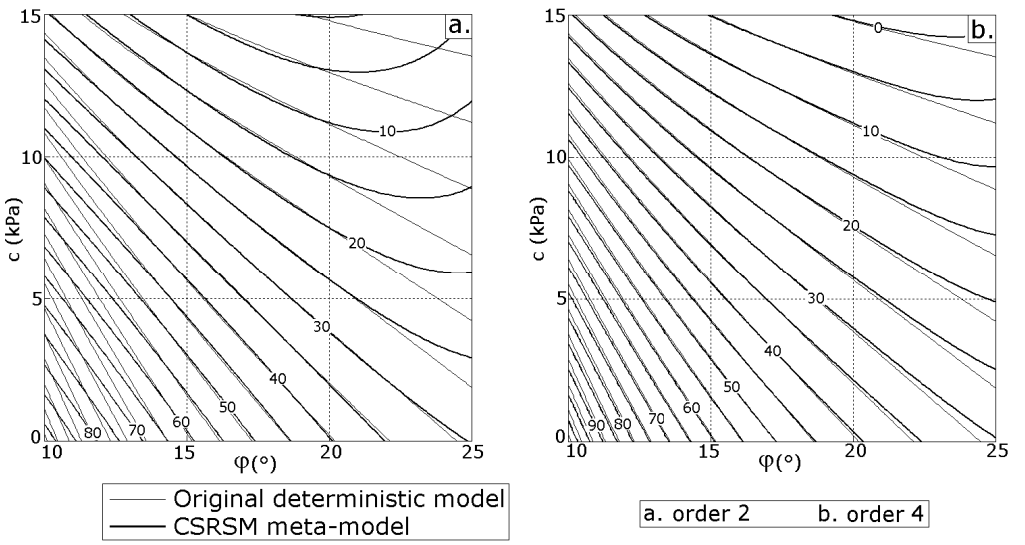

Figure 2. Response surfaces of the critical collapse pressure (in kPa) as provided by the original deterministic model and by the PCEs of orders 2 and 4

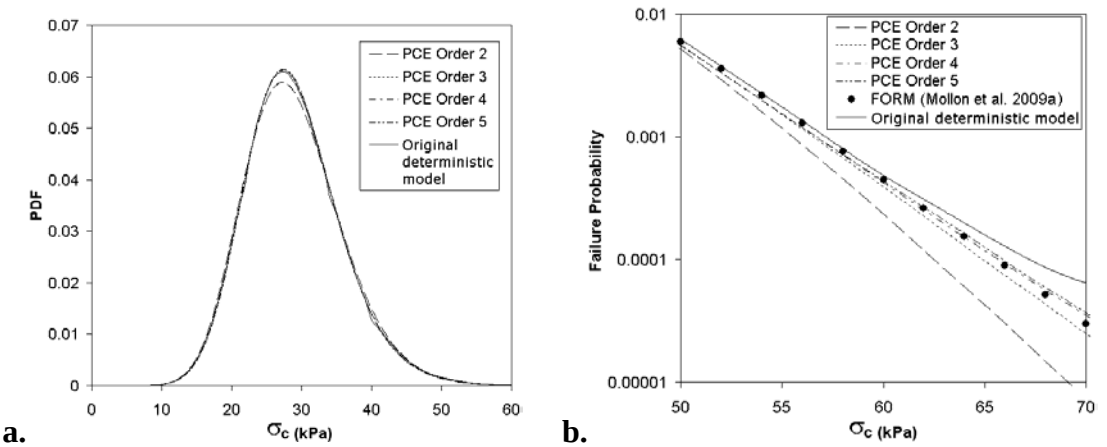

Figure 3. Results of the Monte-Carlo Simulation; a. PDF of σ_c; b. Failure probability

As a conclusion, the PCE of order 2 provides good results only in terms of trends, but the PCEs of orders 3, 4 and 5 provide very close probabilities to the ones of the original deterministic model. There is also a good agreement with FORM results obtained in a previous study (Mollon et al. [2009]). The PCE of order 4 seems

to be the best compromise between accuracy and computational cost, but the order 3 may reasonably be used for computationally-expensive models. Notice finally that the number of collocation points used for the fourth order PCE is equal to 25, which means that 25 calls of the deterministic model were needed to obtain this PCE.

EXTENSION OF CSRSM

CSRSM is an efficient and accurate tool for the probabilistic study of a mechanical model, but it suffers from the fact that its conventional formalism implies a new set of deterministic computations each time one of the probabilistic parameters of the input variables (such as the COV or the correlation coefficient) is changed. This is due to equations (4) and (5) which state that the position of the collocation points in the physical space is dependant on the correlation matrix and the CDF of the input variables. The time cost of a parametric study (when using a computationally-expensive model) is therefore very expensive, while such a study may be interesting because these parameters are usually not known with a great accuracy. This section presents an extension of CSRSM, which makes possible the use of existing deterministic results to carry on a parametric study with no additional time cost. This extension is based on the fact that the position of the collocation points described earlier is not mandatory and that it is possible to use other kinds of collocation schemes, without loss of accuracy of the meta-model. For example, Fig. 4a shows two response surfaces of σ_c in the physical φ-c plane. The first one corresponds to a PCE of order 4 used for the reference case described above, and the second one corresponds to a PCE of order 4 for a different probabilistic case (lognormal variables with μ_φ=17° and COV(φ)=8%, μ_c=7 kPa and COV(c)=25% and with a correlation coefficient $\rho_{\varphi c}$=-0.3). Since the type of the probability distributions, the COVs and the correlation coefficient have been changed, the collocation points are different with respect to the reference case. However, the two response surfaces appear very similar on the entire range of the parameters. This illustrates the claim that there is no need for new calls of the deterministic model for a parametric study. When a first set of deterministic computations has been performed and a new set of probabilistic parameters is chosen, one may compute the positions of the collocation points in the standard space which would have led to the physical collocation points that were already computed. These positions $\left(\xi'_{1,m},\xi'_{2,m}\right)$ are obtained by the following equations:

$$\begin{cases}\xi'_{1C,m} = \Phi^{-1}\left(F_\varphi\left(\varphi_m\right)\right)\\ \xi'_{2C,m} = \Phi^{-1}\left(F_c\left(c_m\right)\right)\end{cases} \tag{8}$$

$$\begin{bmatrix}\xi'_{1,m}\\ \xi'_{2,m}\end{bmatrix} = H^{-1}\begin{bmatrix}\xi'_{1C,m}\\ \xi'_{2C,m}\end{bmatrix} \tag{9}$$

This process provides a new set of collocation points $\left(\xi'_{1,m},\xi'_{2,m}\right)$ for which the corresponding deterministic results are already available. Equation (6) can therefore be applied to compute the coefficients of a new PCE, with no additional deterministic computation. A MC simulation with 10^6 samples is carried out for the new probabilistic properties described above, using the three following models: (i) the original deterministic model, (ii) the PCE of order 4 based on the conventional

CSRSM (which implies 25 new calls to the deterministic model), and (iii) the PCE of order 4 based on the proposed extension method (which uses only the existing 25 deterministic results and do not require any new call to the deterministic model).

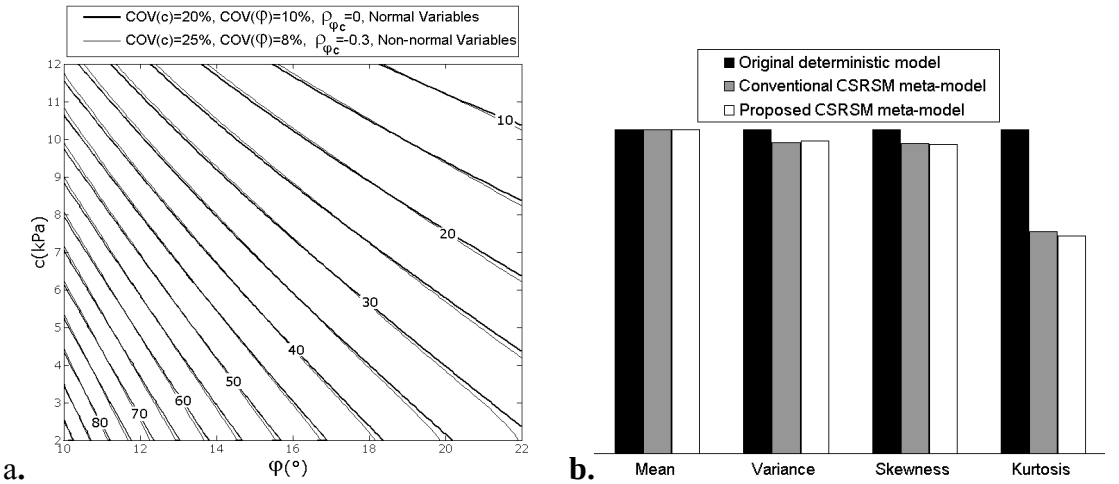

Figure 4. a. comparison between the response surfaces provided by two PCEs with different probabilistic parameters; b. Statistical moments of the conventional and proposed CSRSM (normalized to the ones of the original deterministic model)

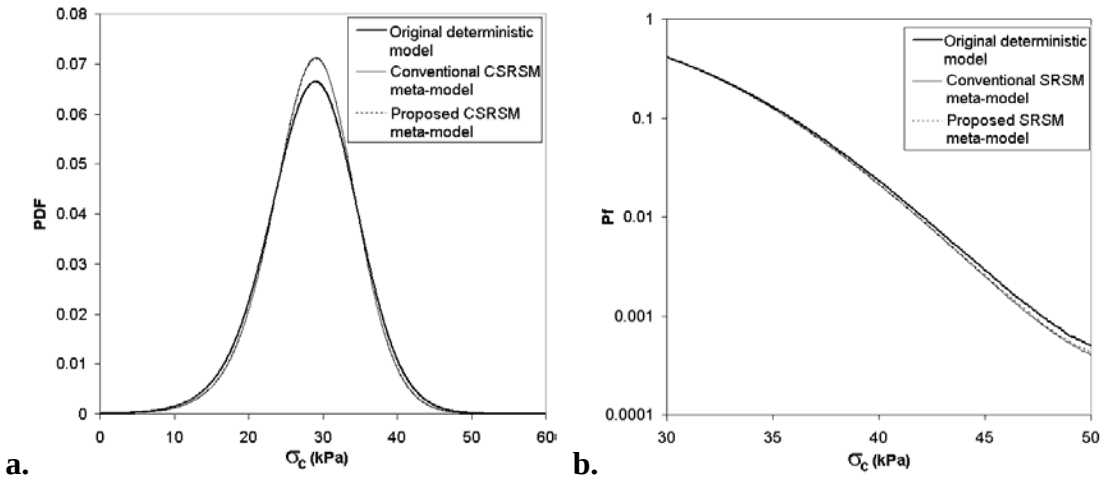

Figure 5. Comparison of the classical and the proposed CSRSM with respect to the original deterministic model; a. PDF of σ_c; b. Failure probability

Figs. 4b, 5a and 5b present a comparison between the three models, respectively in terms of the statistical moments of σ_c, in terms of the PDF of σ_c, and in terms of the probability of failure at the distribution tail. A very good agreement appears between the two meta-models. It clearly means that the proposed extension of CSRSM does not reduce the accuracy of the probabilistic results. Notice however that the proposed methodology is only relevant if the area covered by the new collocation points in the standard space is not too different from the one obtained using the original collocation scheme. From a practical point of view, it means that the changes made to the probabilistic parameters of the input variables should remain small during the parametric study.

CONCLUSION

The Collocation-based Stochastic Response Surface Methodology (CSRSM) is presented and applied to an analytical deterministic model (devoted to the determination of the critical collapse pressure of a pressurized tunnel face). CSRSM is first verified by a comparison with the results obtained from the Monte-Carlo (MC) simulation method. In a second time, an extension of the CSRSM is proposed, allowing a parametric study for no additional call to the deterministic model. The proposed extension method is verified by a MC simulation approach. It shows that the proposed collocation scheme does not reduce the accuracy of the meta-model. However, the proposed methodology is only relevant if the area covered by the new collocation points in the standard space is not too different from the one obtained using the original collocation scheme. From a practical point of view, it means that the changes made to the probabilistic parameters of the input variables should remain small during the parametric study.

REFERENCES

Huang, S.P., Liang, B., Phoon, K.K. (2009). "Geotechnical probabilistic analysis by collocation-based stochastic response surface method." *Georisk*, 3(2), 75-86.

Isukapalli, S.S. (1999). An uncertainty analysis of transport-transformation models, *Ph.D. thesis*, The State University of New Jersey, New Brunswick, New Jersey.

Mollon, G., Dias, D., and Soubra, A.-H. (2009). "Probabilistic analysis and design of circular tunnels against face stability." *Int. J. of Geomech., ASCE*, 9(6), 237-249.

Phoon, K.K., and Huang, S.P. (2007). "Geotechnical probabilistic analysis using collocation-based stochastic response surface method.", *Applications of Statistics and Probability in Civil Engineering*, Kanda, Takada and Furada (eds.), Taylor and Francis Group, London.

Sudret, B. (2007). "Global sensitivity analysis using polynomial chaos expansion.", *Reliability Engineering and System Safety*, 93, 964-979.

Takano, D., Otani, J., Nagatani, H., Mukunoki, T. (2006). "Application of X-ray CT on boundary value problems in geotechnical engineering – Research on tunnel face failure." Proceedings of Geocongress, ASCE, Atlanta.

Beam on Spatially Random Elastic Foundation

S. Haldar[1] and D. Basu[2]

[1]School of Infrastructure, Department of Civil Engineering, Indian Institute of Technology Bhubaneswar, Bhubaneswar 751013, India; PH (91) 674 230 6299; FAX (91) 674 230 1983; email: sumanta@iitbbs.ac.in
[2]Department of Civil and Environmental Engineering, University of Connecticut, 261 Glenbrook Road, Unit 2037, Storrs, CT 06269; PH (860) 486 5023; Fax: (860) 486 2298; email: dbasu@engr.uconn.edu

ABSTRACT

Beams on elastic foundations have been mostly analyzed using the Winkler model, in which a series of disjointed elastic springs are used to represent the foundation soil. However the two-parameter Vlasov's foundation model gives better representation of beam-soil interaction since it incorporates normal and shear resistance of soil. Previous studies examined response of beams on elastic foundation model considering model parameters as deterministic quantity. In contrast to previous studies, this paper examines the response of beams resting on elastic soil media with spatial random variations of soil Young's modulus. The randomness in the soil properties is incorporated in the two-parameter Vlasov's foundation model and, subsequently, the beam responses are obtained. Statistics of beam response are obtained by Monte Carlo simulation approach. It is observed that the soil inherent variability alters the beam response significantly.

INTRODUCTION

Beams on elastic foundations (BEF) are mostly analyzed using the classical Winkler model. In the case of Winkler model, the compressive resistance of soil against beam deflection is quantified in terms of a spring constant k [force/length^2/length], which is often related to the modulus of subgrade reaction (Hetenyi 1946). The value of the Winkler parameter k depends on the soil type, depth of soil layer and on the relative stiffness of the structure and the soil (Vallabhan and Das 1988). The major drawback of the Winkler model is that it cannot capture the soil resistance arising out of the shear strains in soil. Moreover, the equations available for estimating k are mostly developed empirically without a solid basis of mechanics. In fact, Vallabhan and Das (1988) observed that the Winkler model may lead to unconservative designs in the case of uniform beam loading.

The two-parameter Vlasov foundation model is superior to the Winkler model because soil resistance due to both compression and shear can be accounted for in this model. In this model, the parameter k accounts for the compressive resistance while the parameter t accounts for the shear resistance that develop between soil layers displaced differentially in the vertical direction (Vallabhan and Das 1988). A major advantage of the Vlasov model is that the two model parameters can be rationally related to the fundamental elastic soil properties, e.g., soil Young's

modulus (E_s) and Poisson's ratio (v), using the variational principles of mechanics. Several research studies have been carried out on the response of beams on two-parameter elastic foundations subjected to static load (Harr *et al.* 1969, Jones and Xenophontos 1977, Nogami and Lam 1987, Vallabhan and Das 1991). In all these studies the soil was assumed to be spatially uniform. However, due to the inherent variability of soil properties, there are uncertainties associated with the estimation of the two model parameters. Consequently, a probabilistic analysis of BEF is necessary to estimate the uncertainties associated with the predictions of beam responses.

The significance of the variability of natural soils and its influence on foundation response have been widely recognized in several pioneering research works (e.g., Lumb 1966, Vanmarcke 1983, Phoon and Kulhawy 1999, Lacasse 2001). *In situ* soil properties generally exhibit a spatial variation that follows a trend with distance with a scatter. Such a variation is described by the mean, the coefficient of variation and the correlation distance of the soil properties. In a spatially varied soil, properties at adjacent locations are correlated and the distance up to which significant correlation exists is termed as the correlation distance. That spatial variability of soil properties significantly affects the response of foundations is well established (Griffiths and Fenton 2001). A comprehensive study on the response characteristics of beams on elastic foundation considering the spatial variability of soil properties is rather limited. Guo and Weitsman (2002) presented a solution technique for BEF problem on non-uniform elastic foundations due to static load using *Green's function*. Griffiths *et al.* (2008) analyzed laterally loaded pile considering the random heterogeneity of soil by using the Winkler model in conjunction with the random finite element model.

In this paper, the response of beams resting on spatially varying foundations is investigated using the two parameter Vlasov model. The governing differential equations for beam and soil displacements are developed using variational principles. The randomness in the soil properties is incorporated by assuming two-dimensional non-Gaussian homogeneous random fields for Young's modulus E_s of soil. The Poisson's ratio is assumed to be a constant. The statistics of beam response, as influenced by the variance and spatial correlation lengths of E_s are examined using the Monte Carlo simulation approach.

ANALYSIS

Governing differential equation

An Euler-Bernoulli beam, of length L and width b and with free ends, is assumed to rest on a linear elastic continuum of uniform thickness that overlies a rigid layer. The beam is assumed to be loaded uniformly (Fig. 1). A plane strain condition is assumed with the thickness of the analysis domain equal to the beam thickness b. The origin of the coordinate axes is fixed at the left corner of the beam. It is assumed that the deformation in the elastic layer, due to the loaded beam, is restricted up to a certain distance on either side of the beam. Based on a convergence study the distance is fixed to equal to the beam length L. Thus, the length of analysis

domain is $3L$ spanning from $-L$ to $2L$. The potential energy of the beam-soil system is given by,

$$\Pi = \int_{-L}^{0}\int_{0}^{H}\frac{b}{2}\left(\sigma_x\varepsilon_x+\sigma_z\varepsilon_z+\gamma_{xz}\tau_{xz}\right)dxdz+\int_{0}^{L}\int_{0}^{H}\frac{b}{2}\left(\sigma_x\varepsilon_x+\sigma_z\varepsilon_z+\gamma_{xz}\tau_{xz}\right)dxdz$$
$$+\frac{b}{2}\int_{0}^{L}E_bI_b\left(\frac{d^2\bar{w}}{dx^2}\right)^2dx+\int_{L}^{2L}\int_{0}^{H}\frac{b}{2}\left(\sigma_x\varepsilon_x+\sigma_z\varepsilon_z+\gamma_{xz}\tau_{xz}\right)dxdz-\int_{0}^{L}q\bar{w}(x)dx \quad (1)$$

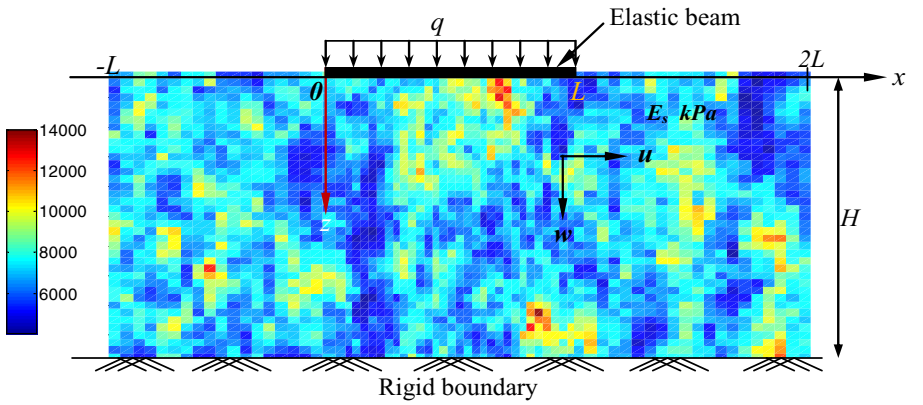

Figure 1. A beam on a spatially varying elastic foundation.

where E_bI_b is the flexural stiffness of the beam, H is the depth of the elastic soil layer, σ and ε represent the stress and strain tensors in the soil with the subscripts representing x and z the corresponding components, q is the uniformly distributed load on the beam and $\bar{w}(x)$ is the beam deflection. The soil Young's modulus $E_s(x, z)$ is assumed to be a spatial function of x and z. The Poisson's ratio $\nu(x,z)$ of the soil layer is assumed to be a constant.

The vertical displacement $w(x,z)$ in the elastic soil layer is expressed as $w(x,z)=\bar{w}(x)\cdot\phi(z)$ where $\bar{w}(x)$ is the surface deflection of soil which is the same as the beam deflection at the beam-soil interface. The function $\phi(z)$describes how the deflections within soil mass decreases with increasing depth z from the beam, and it is assumed that $\phi(0)=1$ which ensures the compatibility between the beam and the underlying layer and that $\phi(H)=0$ which ensures that the displacements are zero at the boundary with the rigid layer. The displacement $u(x,z)$ in the horizontal direction is assumed to be zero for the entire domain.

Relating soil displacements with strains and strains with stresses using plane elasticity, the potential energy Π can be expressed in terms of the displacement functions $\bar{w}$ and ϕ. Minimizing the potential energy of the beam-soil system (i.e., by setting $\delta\Pi = 0$) and separately considering the variations of $\bar{w}$ and ϕ, the governing differential equations for the beam-soil system can be developed. Collecting the terms associated with $\delta\bar{w}$ in the equation $\delta\Pi = 0$ and setting them equal to zero gives

$$-2t_1\frac{d^2\overline{w}_1(x)}{dx^2}+k_1(x)\cdot\overline{w}_1(x)=0 \qquad (\text{for } -L\le x\le 0) \tag{2}$$

$$E_bI_b\frac{d^4\overline{w}_2(x)}{dx^4}-2t_2(x)\cdot\frac{d^2\overline{w}_2(x)}{dx^2}+k_2(x)\cdot\overline{w}_2(x)=q \quad (\text{for } 0\le x\le L) \tag{3}$$

$$-2t_3(x)\frac{d^2\overline{w}_3(x)}{dx^2}+k_3(x)\cdot\overline{w}_3(x)=0 \quad (\text{for } L\le x\le 2L) \tag{4}$$

with the displacement boundary conditions $\overline{w}_1(x=-L)=0$, $\overline{w}_1(x=0)=\overline{w}_2(x=0)$; $\overline{w}_3(x=2L)=0$ and $\overline{w}_3(x=L)=\overline{w}_2(x=L)$ and force boundary conditions

$$-2t_1(x)\cdot\frac{d\overline{w}_2}{dx}=E_bI_b\frac{d^3\overline{w}_2}{dx^3}-2t_2(x)\cdot\frac{d\overline{w}_2}{dx} \qquad (\text{at } x=0) \tag{5}$$

$$E_bI_b\frac{d^3\overline{w}_2}{dx^3}-2t_2(x)\cdot\frac{d\overline{w}_2}{dx}=-2t_3(x)\cdot\frac{d\overline{w}_3}{dx} \qquad (\text{at } x=L) \tag{6}$$

$$E_bI_b\frac{d^2\overline{w}_2}{dx^2}=0 \qquad (\text{at } x=0 \text{ and } L) \tag{7}$$

In the above equations, $\overline{w}_1$, $\overline{w}_2$ and $\overline{w}_3$ represent the function $\overline{w}(x)$ in the domains $-L\le x<0$, $0\le x\le L$ and $L\le x\le 2L$, respectively. Finite element (FE) approach is used to solve the above equations. The soil parameters k_j and t_j in the above equations are defined for each domain (j = 1, 2 and 3), and can be expressed for the elastic soil discretized into thin layers as

$$2t_j(x)=b\sum_{i=1}^{N}\frac{E_s(x,i\Delta z)}{2(1+\nu)}\phi(i\Delta z)^2\Delta z \tag{8}$$

$$k_j(x)=b\sum_{i=1}^{N}\frac{E_s(x,i\Delta z)(1-\nu)}{(1+\nu)(1-2\nu)}\left(\frac{\Delta\phi(i\Delta z)}{\Delta z}\right)^2\Delta z \tag{9}$$

where Δz = depth interval, N is the total number of discretised layer with $H = N\Delta z$, the subscript i represents the soil layers, and the subscript j = 1, 2 and 3 represent the domains $-L\le x\le 0$, $0\le x\le L$ and $L\le x\le 2L$, respectively.

Collecting the terms associated with $\delta\phi$ in the equation $\delta\Pi = 0$, the following differential equation is obtained,

$$-m\frac{d^2\phi}{dz^2}-\frac{d\phi}{dz}\frac{dm}{dz}+n\phi=0 \tag{10}$$

with boundary conditions $\phi(0) = 1$ and $\phi(H) = 0$ where

$$m(z)=b\sum_{j=1}^{N_1}\frac{E_s(j,z)(1-\nu)}{(1+\nu)(1-2\nu)}\overline{w}(j)^2\Delta x+b\sum_{j=N_1}^{N_2}\frac{E_s(j,z)(1-\nu)}{(1+\nu)(1-2\nu)}\overline{w}(j)^2\Delta x$$
$$+b\sum_{j=N_2}^{N_3}\frac{E_s(j,z)(1-\nu)}{(1+\nu)(1-2\nu)}\overline{w}(j)^2\Delta x \tag{11}$$

$$n(z) = b\sum_{j=1}^{N_1}\frac{E_s(j,z)}{2(1+\nu)}\left(\frac{\Delta\overline{w}(j)}{\Delta x}\right)^2\Delta x + b\sum_{j=N_1}^{N_2}\frac{E_s(j,z)}{2(1+\nu)}\left(\frac{\Delta\overline{w}(j)}{\Delta x}\right)^2\Delta x +$$

$$b\sum_{j=N_2}^{N_3}\frac{E_s(j,z)}{2(1+\nu)}\left(\frac{\Delta\overline{w}(j)}{\Delta x}\right)^2\Delta x \; ; \; x(j=1)=-L,\; x(j=N_1)=0,\; x(j=N_2)=L\;, x(j=N_3)=2L \qquad (12)$$

The values $\overline{w}(x)$ are obtained from the FE solution and used to compute the values of *m(z)* and *n(z)* as defined in Eq. (11) and Eq. (12) respectively. A finite difference (FD) approach is utilized to solve the values $\phi(z)$ considering two boundary conditions, namely, $\phi(0)$ = 1 and $\phi(H)$ = 0. The above equations comprise spatial variation of soil's Young's modulus [i.e. $E_s(x,z)$]. Therefore, two dimensional homogeneous spatially correlated random field is generated.

Modeling of random field

The spatial variability of the soil properties can be expressed concisely using the random field theory. In the most general terms, a random field is essentially a random (or stochastic) process consisting of an indexed (i.e. ordered according to one or more reference dimensions) set of random variables (Vanmarcke 1983). A parametric study of the beam response is performed assuming a range of values of scale of fluctuation (2m-45m) and coefficient of variation (20-80%) of E_s for the log-normally distributed random field.

The variations of the soil properties *in situ* soil represented by the mean, coefficient of variation and correlation distance affect the design values. In a random field modeling, the assumption of log-normal distribution for soil properties is appropriate as the soil properties are always non-negative. Hence, if the soil property E_s is considered as random variable and assumed to be a log-normally distributed value, represented by parameters like mean $\mu_{\ln E_s}$, standard deviation $\sigma_{\ln E_s}$ and correlation distance $\delta_{\ln E_s}$. A detailed procedure for the generation of isotropic correlation log-normal random field using *Cholesky decomposition* is given in Haldar and G.L.S. Babu (2008).

Solution scheme

The analysis presented in this paper considers a 15 m long beam with a depth and width of 0.5 m subjected to a uniformly distributed load (UDL) of 50 kN/m. Vallabhan and Das (1988) shows that beam responses depend on soil depth (*H*). Hence, present study considers value *H* equals to 10 m for analysis purpose. Based on the characteristic length of beams on elastic foundations (Vesic 1961), the beam is moderately long. A uniform value of $E_s = 7\times10^3$ kPa is first assumed in order to obtain the deterministic response of the beam. The same value of E_s is adopted as the mean μ_{Es} and the random field is generated for a range of coefficient of variation COV_{Es} and correlation distance δ_z. The values of the different parameters used in the analysis are given in Table 1.

In order to solve the differential equations the beam was discretised into 25 elements and the foundation at the left and right side of the beam were divided into 20 elements each along the x direction. In order to solve the differential equation of $\phi(z)$ and to obtain the parameters k_j and t_j, the elastic soil was discretised vertically into 40 elements. Solution of $\phi(z)$ was obtained using the finite difference method. Since the solution for the beam response requires the value of $\phi(z)$ a priori, an iterative procedure is employed. Initially a linear profile of $\phi(z)$ is assumed retaining appropriate boundary conditions and beam deflection $\overline{w}(x)$ was obtained. Beam deflection values were then used in solving differential equation of $\phi(z)$ and a new profile of $\phi(z)$ was obtained. Iterations were continued until the difference in the beam deflection values at any node, between two consecutive iterations, was less than 1×10^{-5}. Spatially correlated random field of E_s was mapped onto the 2D field. Each grid was assigned an E_s value which varied from one element to the next. Monte Carlo simulation approach was used in the generation of the sample functions of 2D log-normal random field. In the present analysis, 100 Monte Carlo simulations were performed since the fluctuation in the mean and standard deviation of beam response falls within a tolerable range. Each realization produced different beam responses. Hence, the statistics of beam responses were obtained by ensemble averaging. The beam response was investigated in terms of the normalized correlation distance δ_z/L.

Table 1. Beam and soil data.

Beam data	Value	Soil data	Value
Length L (m)	15	Mean μ_{Es} (kPa)	7×10^3
Width b (m)	0.5	Soil depth H (m)	10
Depth (m)	0.5	Poisson's ratio υ	0.2
Young's modulus (kPa)	2.1×10^7	COV_{Es} (%)	20, 50, 80
UDL q (kN/m)	50	Correlation distance, δ_z (m)	2.25, 22.5, 45

RESULTS AND DISCUSSION

The physical significance of COV_{Es} and δ_z is evident in Figs. 2(a)-(d), which show gray scale representation of possible realization of E_s. The darker shades represent weaker zones. The results of Figs. 2(a) and (c) indicate that the increase in COV increases the variability of the soil. Figs. 2(c) and (d) show the effects of the correlation distance. At low values of δ_z, the field is more varied while, with an increase in δ_z, the field becomes more homogeneous.

In order to estimate the statistical parameters of the beam responses from Monte Carlo simulations, it is assumed that the beam responses follow log-normal distribution similar to the soil Young's modulus. The results obtained from Monte Carlo simulations are presented in Fig. 3. The mean values of maximum beam deflection and maximum bending moment are obtained for selected ranges of COV and correlation distance of E_s. Figs. 3(a) and (c) show the influence of the correlation distance and variability on the estimated mean maximum deflection (μ_{Wmax}) and maximum bending moment of beam (μ_{Mmax}).

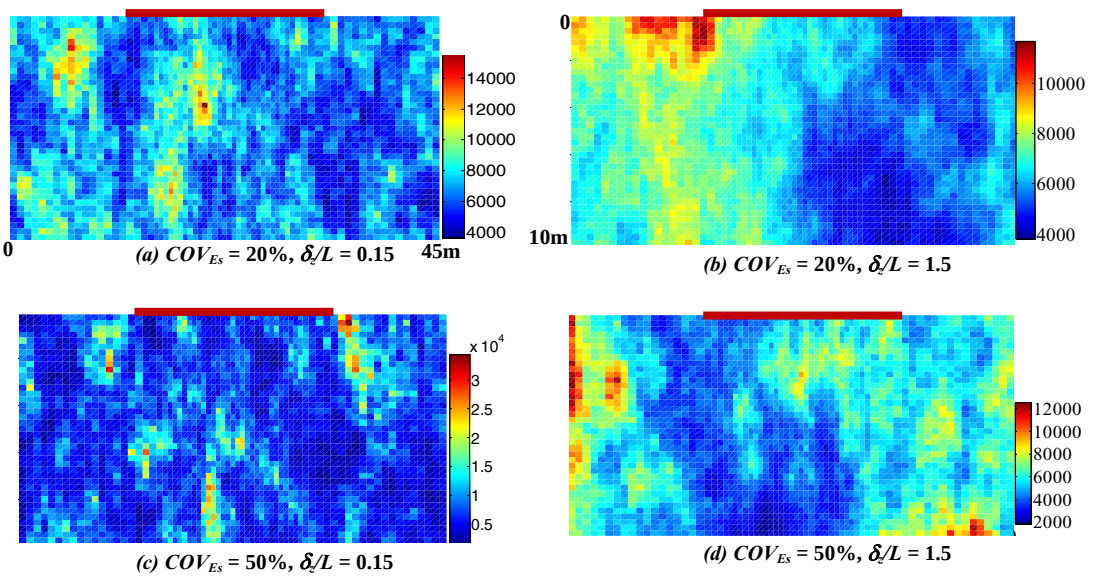

Figure 2. Realization of random field.

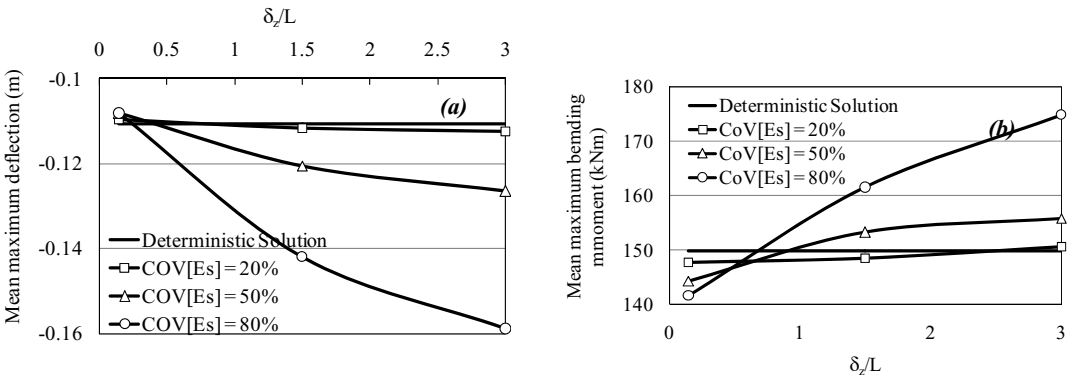

Figure 3. Influence of *COV* and δ_z of E_s on (a) μ_{Wmax} (b) μ_{Mmax}.

The maximum beam deflection for homogenous soil is estimated as 0.11 m, while Fig. 3(a) shows a significant increase in the mean maximum deflection for spatially varying soil. For example, if *COV* and δ_z/L of E_s are 80% and 3, respectively, the value of the μ_{Wmax} may be 43% more than maximum deflection for the corresponding homogeneous soil. In general, the mean maximum deflection increases with an increase in the values of COV_{Es} and δ_z/L. Similar observations were made for the mean maximum bending moment. Fig. 3(b) shows that the maximum bending increases with increase in the values of *COV* and δ_z/L of E_s.

CONCLUSION

The present study highlights the influence of the spatial variation of soil Young's modulus on the beam response considering the two-parameter Vlasov foundation model. Based on a parametric study it was found that, with increase in the coefficient of variation in the soil elastic modulus, there occurs an increase in the

mean values of the maximum beam deflection and bending moment. It was also found that greater values of the correlation distance and coefficient of variation give greater values of beam deflection and bending moment compared with the beam response for homogeneous soil. This effect is, however, subdued at low soil variability and correlation distance.

REFERENCES

Griffiths, D.V., and Fenton, G.A. (2001). "Bearing capacity of spatially random soil: the undrained clay Prandtl problem revisited." *Geotechnique*, 51(4), 351-359.

Griffiths, D.V., Paiboon, J., Huang, J., and Fenton, G.A. (2008). Numerical analysis of beams on random elastic foundations. *Proceedings of the 9th International Congress on Numerical Methods in Engineering and Scientific Applications, CIMENICS'08*, 19-25.

Guo, Y.-J., and Weitsman,Y.J. (2002). "Solution method for beams on nonuniform elastic foundations." *Journal of Engineering Mechanics, ASCE*, 128 (5), 592-594.

Haldar, S., and G.L.S. Babu (2008). "Effect of soil spatial variability on the response of laterally loaded pile in undrained clay." *Computers and Geotechnics*, 35, 537-547.

Harr, M.E., Davidson, J.L., Pombo, L.E., Ho, D.-M., Ramaswamy, S.V., and Rosner, J.C. (1969). "Euler beams on a two parameter foundation model." *Journal of Soil Mechanics and Foundation Engineering, ASCE*, 95(SM4), pp. 933-948.

Hetenyi, M. (1946). *Beams on elastic foundations*. Ann Arbor. University of Michigan Press.

Jones, R., and Xenophonotos, J. (1977). "The Vlasov foundation model." *International Journal of Mechanical Sciences*, 19, 317-323.

Lacasse, S. (2001). "37th Terzaghi Lecture: Geotechnical Solutions for the Offshore Synergy of Research and Practice." *ASCE National Convention 2001*, Houston.

Lumb, P. (1966). "The variability of natural soils." *Canadian Geotechnical Journal*, 3(2), 74-97.

Nogami, T., and Lam, Y.C. (1987). "Two-parameter layer model for analysis of slab on elastic foundation." *Journal of Engineering Mechanics, ASCE*, 113(9), 1279-1291.

Phoon, K.-K., and Kulhawy, F.H. (1999). "Evaluation of geotechnical property variability." *Canadian Geotechnical Journal*, 36, 625-639.

Vallabhanm C.V.G., and Das, Y.C. (1988). "Parametric study of beams on elastic foundations." *Journal of Engineering Mechanics, ASCE*, 114(12), 2072-2082.

Vallabhanm C.V.G., and Das, Y.C. (1991). "Modified Vlasov model for beams on elastic foundations." *Journal of Geotechnical Engineering, ASCE*, 117(6), 956-966.

Vanmarcke, E.H. (1983). *Random fields: analysis and synthesis*. MIT Press, Cambridge.

Vesic, A.B. (1961). "Bending of beams on isotropic elastic solid." *Journal of Engineering Mechanics, ASCE*, 87(EM2), 35-53.

Teaching Reliability at the Undergraduate Level

[1]Robb Eric S. Moss, Ph.D., P.E., M.ASCE

[1]California Polytechnic State University, San Luis Obispo, CA 93401 Email: rmoss@calpoly.edu PH: 805-756-6427

ABSTRACT: For Cal Poly's Civil and Environmental Engineering curriculum a stand-alone introductory course called Engineering Risk Analysis introduces concepts of reliability analysis. This course encompasses all the sub-disciplines in civil and environmental engineering. After five years of teaching this course there are a number of lessons that may be useful to other instructors including; solving a simple example problem using multiple methods, focusing on the normal and lognormal distributions for a quick preliminary solution, using reliability spreadsheet solutions, and allowing the students to develop their own applications of probabilistic tools. A discussion of the course format, references and resources, pedagogy devices, and in-class examples are covered. The higher goal of this course is to educate students in probabilistic methods, familiarize them with risk analysis procedures, and to elevate the basic level of understanding of uncertainty in engineering and how to properly deal with it.

INTRODUCTION

The different fields that fall under the umbrella of Civil and Environmental Engineering are reaching maturation in terms of design and analysis techniques. Almost all problems in these fields can be cast as a relationship between load and resistance or demand and capacity. The amount of data available for assessing performance of a particular design technique increases and statistical analysis can be performed. The more data that is available the more it is apparent that treating design and analysis probabilistically is the proper way to capture respective uncertainties in the load and resistance. The movement towards LRFD (Load and Resistance Factor Design) codes is because properly accounting for the uncertainty provides not just a better answer (i.e., closer to the true answer) but can also result in cost savings.

To provide graduating engineers with an understanding and appreciation of probabilistic methods I have created an upper division technical elective course called Engineering Risk Analysis that encompasses all the fields in Civil and Environmental Engineering. This course targets undergraduate students nearing the end of their degree as well as graduate students just beginning their degree. The course material is heavy on applied probabilistic methods drawing examples from Structural,

Geotechnical, Water, Transportation, and Environmental Engineering problems to demonstrate tangible applications.

The motto for the class is "uncertainty exists, deal with it". This class allows student to become familiar with the probabilistic tools available for applied risk analysis and runs them through many examples so that they have practice tackling whatever type of problem may crop up in their own practice. This class strives for the next generation of engineers to be conversant and comfortable in probabilistic analysis.

COURSE OUTLINE AND OBJECTIVES

Engineering Risk Analysis is a ten week course (one quarter) with two 110 minute lectures a week and has the following course outline;

- Data Reduction and Sample Statistics
- Set Theory and Probability
- Random Variables and Probability Distributions
- Functions of Random Variables
- Reliability Analysis and Error Propagation
- Introduction to Decision Theory
- LRFD

Students are required to have completed all of their introductory courses in Structural, Geotechnical, Water, Transportation, and Environmental Engineering as well as a course in Statistics for Engineers. This has them well prepared to take a basic example from any field and examine it from a probabilistic perspective. The prerequisite statistics course covers statistical methods well and only a brief review is required, however probability is not addressed in detail in the statistics course and a substantial amount of time is spent covering this during the quarter. A thorough understanding of the fundamentals of probability is a must to progress to reliability methods.

As with most probabilists in engineering I teach this course from a Bayesian perspective. The primary reason is because failure data is often sparse, full scale failures cannot generally be duplicated in a controlled manner, and sample sets are highly heterogeneous and non-ergodic. Subjective probability is often needed to augment the meager objective probability measures available. The subjective probability can be from *a prior* information, expert consensus, and engineering judgment. Philosophically this follows the degree-of-belief definition of probability which is consistent with the design process in Civil and Environmental Engineering problems and is also consistent with hazard forecasting and hazard mitigation.

In this course we work primarily the normal and lognormal probability distributions. This simplifies the mathematics greatly in a number of areas and provides a reasonable first-order approximation for most engineering problems. References for other theoretical distributions are many and if students understand the basis for using a theoretical distribution they can often easy increase the complexity of the analysis by using other distributions once they have run through it with the normal or lognormal.

The guiding principle and objective of this course; all undergraduate engineering

students should be able to perform simple reliability analysis. By presenting reliability in a simplified format not only do the students gain the ability to evaluate load versus resistance in a probabilistic manner but more importantly they leave the class with a new perspective on engineering. This perspective is that uncertainty exists in every aspect of engineering and that they must deal with it either implicitly or explicitly. For most students this is a subtle but profound paradigm shift that alters the way they view all subsequent engineering problems.

The class culminates in a self-directed project where the students are asked to take some of their newly acquired tools and apply them to an engineering problem of their choosing. The project is purposely left open ended to allow for exploration of topics and tools. The projects do not necessarily have to use reliability methods but the better students often gravitate towards this because they find it a powerful extension of their engineering abilities. Examples of successful student projects are presented later in this manuscript.

RESOURCES

There are a number of excellent resources that I have drawn heavily from in developing this course, although no single text or reference suffices. The discussion of statistics draws from the venerable Benjamin and Cornell (1970) which is dated but I find does the best job presenting the simple applied statistics needed for the course. Discussion of probability, set theory, probability distributions, functions of random variables, and Monte Carlo simulations closely follows the excellent revised text by Ang and Tang (2007). The first edition of this text is what most current engineers "cut their teeth on". While that was a good text, it was often hard to navigate and opaque on some topics. The second edition of this text is far superior, taking the strong points of the first edition (Ang and Tang 1975) and adding to it better explanations, more and better examples, and computation solutions; the way most problems are solved in this era of inexpensive computation effort.

Once through the topic of functions of random variables by mid-quarter, enough ground has been covered to move into reliability. Here the class starts with Baecher and Christian (2003) which I find provides the most clear and concise review of reliability methods. Other references have been drawn from including Ang and Tang (1990), Der Kiureghian (2001), and Stewart and Melchers (1997).

After spending a fair amount of lecture time on component reliability the class ventures into systems analysis, decision trees, and broader risk topics. Here along with material drawn from the references mentioned above a number of examples are drawn from my own research and consulting experience. I find it useful to bring in an external speaker who does environmental risk analysis to present a couple complex projects utilizing the tools we have covered in a basic manner in class.

With reliability behind us we can now discuss the basis of LRFD codes and how the factors are developed. I find the presentation by Baecher and Christian (2003) is accessible to the students and the given examples show the utility of LRFD over WSD/ASD (working stress design/allowable stress design.

EXAMPLE PROBLEMS

The most useful example is one that I borrow from Baecher and Christian (2003). Here my bias for geotechnical engineering is obvious, but the "cut slope" problem is so simple and accessible to students that it is hard to justify using another. The problem deals with a vertical cut in cohesive soil. Figure 1 shows the geometry and details of the problem.

As mentioned previously students in the class are required to complete all their introductory engineering courses so they have had an introduction to geotechnical engineering and are familiar with soil mechanics. This problem is used to explore a suite of reliability solution techniques; exact solution(s), first order second moment (FOSM), first order reliability method (FORM), second order reliability method (SORM), and Monte Carlo Simulations. With FORM and SORM, whereas solutions following the improved Hasofer-Lind algorithm (Zhang and Der Kiureghian 1995) are presented for completeness, the focus is on simplified spreadsheets solutions (Low and Tang 1997; Phoon 2008; Phoon and Nadim 2004) because of their accessibility to students with a limited advanced mathematics background. The "cut slope" problem reinforces the concepts covered when discussing functions of random variables. It is also useful for exploring how correlation between independent variables can influence the component reliability.

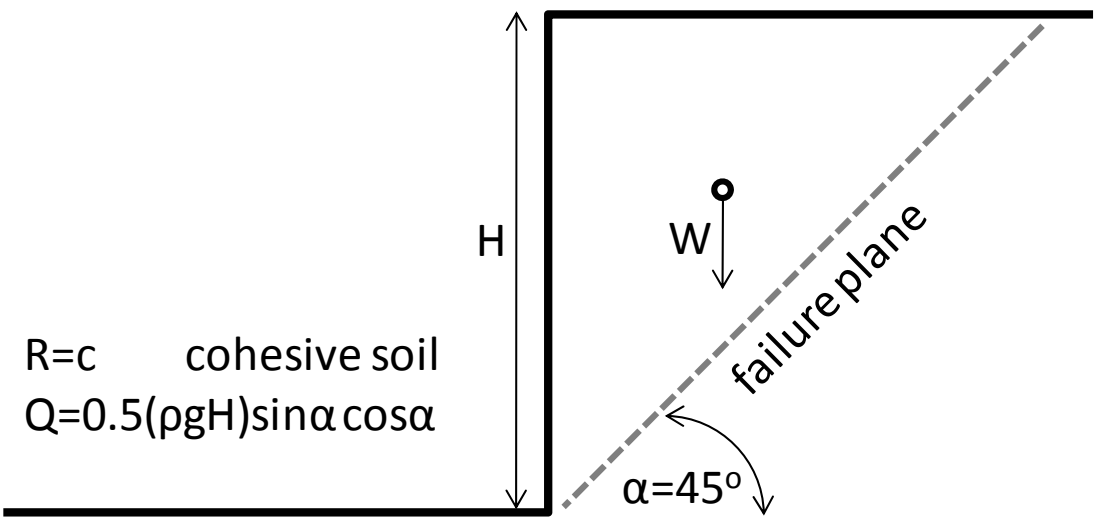

FIG. 1. Cut slope problem used to demonstrate exact, FOSM, FORM, SORM, and MC reliability solution methods. In this figure H is the vertical cut height, W the weight at the centroid of the soil mass above the failure plane, alpha (α) the failure plane angle, R the resistance which is equal to the soil cohesion (c), and Q the load which is the product function shown that includes density (ρ) and gravity (g).

PEDAGOGICAL TECHNIQUES

After teaching this course for five years I have found some pedagogical techniques that are useful. Often the hurdle in this class is getting the students through the section on elementary probability. After covering Venn diagrams, set theory, and the rules of probability we spend the bulk of two lectures going through example problems. The trick with problems of elementary probability is that there are often different means of solving them, whether using *a prior* probability, Venn diagrams, and/or invoking the rules of probability. But the most difficult aspect of elementary probability problems is taking a word statement and writing it correctly in set theory with the appropriate probability terms and set theory symbology. To help the students a simple rubric is repeated over and over in problem solving;

a) Declare all knowns (an obvious but often overlooked step),
b) Write the problem statement in set terminology (this takes much practice), and
c) Reduce the stated to a calculatable form by invoking the rules of probability (often the easiest step).

In this section of the class I assign a set of homework and ask the students to work in pairs. I encourage group discussions among pairs and forewarn them that these problems, although they appear simple, often require a good deal of time to work through. The day the homework is handed in I often take lecture time to go through the problems one by one, show them my solution to the problem, and have an in class discussion. The written solutions to these problems are provided with clear step by step declarations following the above rubric and explicitly stating how the steps were arrived at. I have found that this careful and thorough coverage is necessary to assist the students through the crux of probability and lays the foundation for the reliability section to come.

A second pedagogical technique that is used is restricting our use of probability distributions to the normal and lognormal. This provides mathematical simplicity in almost all cases and allows for the concepts of probability and reliability to be focused on rather than dwelling on the menagerie of probability distributions and their nuances. This allows the class to progress through reliability in one quarter and gives the students a means of performing a first-order estimate of reliability for the bulk of engineering problems. There are many texts and other references that exist on other theoretical probability distributions and I provide some discussion where it may be necessary to diverge from the normal and lognormal. But for most applications the normal and lognormal are sufficient to give a close enough approximation for first-order engineering assessment.

STUDENT PROJECTS

The quarter culminates in students picking a particular topic of interest from their discipline and applying some of the tools they acquired during the course. The student project deliverables are a short written report and a short oral presentation. This is often the most rewarding portion of the course from an instructor's perspective. Some of the more interesting student projects over the years include;

- A student was interested in power distribution systems and used a recent journal publication to develop uni-, bi-, and tri-modal estimates of systems

failure for a particular grid arrangement with a specific correlation structure.

- A structural student was interested in reliability of timber beams for home construction. There was some statistical information in the literature on the strength properties of timber beams but the student decided to augment the sample statistics by collecting over a hundred popsicle sticks and individually testing them to failure to better characterize the variance. The mean results when scaled were in good agreement with the published mean results, and the variance (and frequency distribution) was much better characterized thanks to the experiments.
- A traffic student was interested in the probability of cars stopping for "right on red" situation and, finding no data available, spent several hours at a local corner collecting data to inform the analysis. The presentation was rather lively as the discussion included scores of samples where cars were not stopping at the light at all regardless of pedestrians (including babies in strollers) in the crosswalk.

Typical projects include error propagation through common engineering design equations (e.g., open channel flow, reinforced concrete deign, waste water discharge concentration), or statistical analysis with an elementary probability statement at the end (e.g., traffic flow, construction cost analysis). But there are a number of these projects that are developed enough to end up as chapters in master's theses or incorporated into research reports. In this sense the class is a resource for the department in providing a probabilistic perspective for any student in Civil and Environmental Engineering looking to develop that aspect of their research. The key to the student projects is that they are open ended with the topic driven by the student's interest, resulting in a more intimate mastery of some of the tool introduced in the class.

SUMMARY

Presented is a discussion of a course positioned in Cal Poly's Civil and Environmental Engineering curriculum that introduces reliability to upper division undergraduates, as well as first year graduate students. My goal in creating this course was to emphasize applied statistics and probability to enable the students to perform simple first-order estimates of the probability of failure for any problem they may encounter.

To achieve this the fundamentals are covered in a purposeful, detailed, and applied manner so that the students master sample statistics, elementary probability, simple probability distributions (normal and lognormal), functions of random variables, component reliability, and systems reliability. This requires a large number of in class examples that follow a problem solving rubric and show clear step by step solutions. The class culminates in a student directed project on a topic of their choosing where the tools developed in the class are applied.

Success in developing this class is demonstrated by the large number of student who go on to incorporate probabilistic methods into their engineering thought process and carry that over into their practice or research. This class strives to imbue the next generation of engineers with an appreciation of uncertainty in Civil and

Environmental Engineering problems and to arm them with tools for dealing with this uncertainty in an explicit manner.

REFERENCES

Ang, A. H.-S., and Tang, W. H. (1975). *Probability Concepts in Engineering Planning and Design: Volume I. Basic Principles*. John Wiley and Sons, Inc.

Ang, A. H.-S., and Tang, W. H. (1990). *Probability Concepts in Engineering Planning and Design: Volume II-Decision, Risk, and Reliability*, Published by the Authors.

Ang, A. H.-S., and Tang, W. H. (2007). *Probability Concepts in Engineering: Emphasis on Applications to Civil and Environmental Engineering. 2nd Edition*. John Wiley and Sons, Inc., New York.

Baecher, G. B., and Christian, J. T. (2003). *Reliability and Statistics in Geotechnical Engineering*, John Wiley and Sons, Inc.

Benjamin, J., and Cornell, C. A. (1970). *Probability, Statistics, and Decision for Civil Engineers*, McGraw-Hill, New York.

Der Kiureghian, A. (2001). "Course Notes from CE229: Structural Reliability." UC Berkeley.

Low, B. K., and Tang, W. H. (1997). "Efficient Reliability Evaluation Using Spreadsheet." *Journal of Engineering Mechanics*, 123(7), 749-752.

Phoon, K.-K. (2008). "Reliability-Based Design in Geotechnical Engineering." Taylor and Francis, New York.

Phoon, K.-K., and Nadim, F. (2004). "Modeling Non-Gaussian Ramom Vectors for FORM: State-of-the-Art Review (keynote)." *International Workshop on Risk Assessment in Site Characterization and Geotechnical Design*, Indian Institute of Science, Bangalore, India, 55-85, November 26-27.

Stewart, M. G., and Melchers, R. E. (1997). *Probability risk assessment of engineering systems*, Chapman&Hall.

Zhang, Y., and Der Kiureghian, A. (1995). "Two improved algorithms for reliability analysis." *Proceedings 6th IFIP WG 7.5 working conference on reliability and optimization of structural systems*, 297-304,